

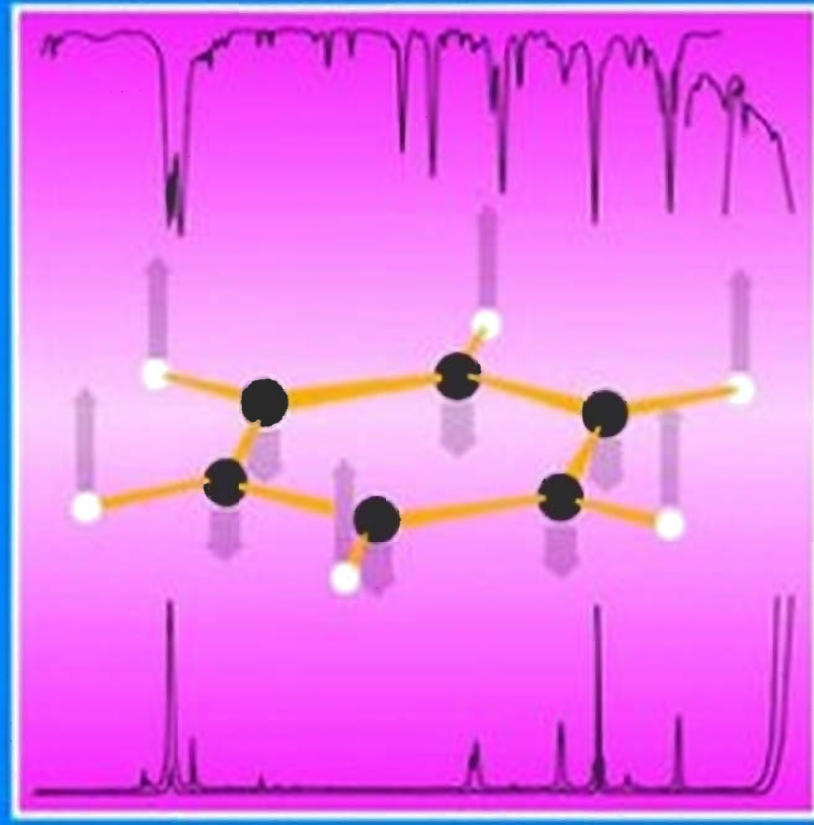
Infrared and Raman Spectroscopy

**Methods and
Applications**

Edited by Bernhard Schrader

Contributors:

D. Bougeard
M. Buback
A. Cao
K. Gerwert
H. M. Heise
G. G. Hoffmann
B. Jordanov
W. Kiefer
E.-H. Korte
H. Kuzmany
A. Leipertz
E. Lenz
J. Liquier
A. Roseler
H. Schnockel
B. Schrader
H. W. Schrotter
M. Spiekermann
E. Taillandier
H. Willner



Infrared and Raman Spectroscopy

Edited by Bernhard Schrader



© VCH Verlagsgesellschaft mbH, D-69451 Weinheim (Federal Republic of Germany), 1995

Distribution:

VCH, P.O. Box 101161, D-69451 Weinheim (Federal Republic of Germany)

Switzerland: VCH, P.O. Box, CH-4020 Basel (Switzerland)

United Kingdom and Ireland: VCH (UK) Ltd., 8 Wellington Court, Cambridge CB1 1HZ (England)

USA and Canada: VCH, 220 East 23rd Street, New York, NY 10010-4606 (USA)

Japan: VCH, Eikow Building, 10-9 Hongo 1-chome, Bunkyo-ku, Tokyo 113 (Japan)

ISBN 3-527-26446-9

Infrared and Raman Spectroscopy

Methods and Applications

Edited by Bernhard Schrader

Contributors:

D. Bougeard, M. Buback, A. Cao,
K. Gerwert, H. M. Heise, G. G. Hoffmann, B. Jordanov,
W. Kiefer, E.-H. Korte, H. Kuzmany, A. Leipertz, E. Lentz, J. Liquier,
A. Röseler, H. Schnöckel, B. Schrader, H. W. Schrötter,
M. Spiekermann, E. Taillandier, H. Willner



Weinheim · New York · Basel · Cambridge · Tokyo

Prof. Dr.-Ing. Bernhard Schrader
Soniusweg 20
D-45259 Essen (Heisingen)

This book was carefully produced. Nevertheless, authors, editor and publisher do not warrant the information contained therein to be free of errors. Readers are advised to keep in mind that statements, data, illustrations, procedural details or other items may inadvertently be inaccurate.

Published jointly by
VCH Verlagsgesellschaft mbH, Weinheim (Federal Republic of Germany)
VCH Publishers, Inc., New York, NY (USA)

Editorial Director: Dr. Steffen Pauly

Library of Congress Card No.: applied for

British Library Cataloguing-in-Publication Data:
A catalogue record for this book is available from the British Library

Die Deutsche Bibliothek- CIP-Einheitsaufnahme
Infrared and raman spectroscopy : methods and applications /
ed. by Bernhard Schrader. Contributors: D. Bougeard ... –
Weinheim ; Basel ; Cambridge ; New York, NY ; Tokyo :
VCH, 1995

ISBN 3-527-26446-9
NE: Schrader, Bernhard [Hrsg.]; Bougeard, Daniel
© VCH Verlagsgesellschaft mbH, D-69451 Weinheim (Federal Republic of Germany), 1995
Printed on acid-free and low-chlorine paper

All rights reserved (including those of translation into other languages). No part of this book may be reproduced in any form – by photoprinting, microfilm, or any other means – nor transmitted or translated into a machine language without written permission from the publishers. Registered names, trademarks, etc. used in this book, even when not specifically marked as such, are not to be considered unprotected by law.

Composition: U. Hellingen, D-69253 Heiligenkreuzsteinach
Printing: Strauss Offsetdruck GmbH, D-69509 Mörlenbach
Bookbinding: Fikentscher Großbuchbinderei, D-64295 Darmstadt
Printed in the Federal Republic of Germany

Preface

Infrared spectroscopy is now nearly 100 years old, Raman spectroscopy more than 60. These methods provide us with complementary images of molecular vibrations: Vibrations which modulate the molecular dipole moment are visible in the infrared spectrum, while those which modulate the polarizability appear in the Raman spectrum. Other vibrations may be forbidden, 'silent', in both spectra. It is therefore appropriate to evaluate infrared and Raman spectra jointly. Ideally, both techniques should be available in a well-equipped analytical laboratory. However, infrared and Raman spectroscopy have developed separately. Infrared spectroscopy became the 'work-horse' of vibrational spectroscopy in industrial analytical laboratories as well as in research institutes, whereas Raman spectroscopy up until recently was essentially restricted to academic purposes.

This is due to the fact that fluorescence of impurities may completely mask a Raman spectrum if it is excited, as usual before 1986, in the visible range of the spectrum. Since the quantum yield of fluorescence exceeds that of the Raman effect by a factor of about one million, traces of fluorescent compounds – ubiquitous impurities like stop cock grease, the 'whitening dyes' (blancophores) of many detergents, or the products of photochemical or oxidation processes or of the pyrolysis of pure samples – may preclude the observation of Raman spectra which are excited by radiation in the visible (VIS) or ultraviolet (UV) region. However, most of these fluorescent compounds do not show electronic absorption bands in the near infrared (NIR) region. Therefore, in a Raman spectrum which is excited by radiation in the NIR, fluorescence should not appear. During the late 1980s it was demonstrated (Hirschfeld and Chase, 1986) that most samples afford undisturbed Raman spectra excited with the radiation of a neodymium doped yttrium aluminum garnet (Nd:YAG) laser at a wavelength of 1064 nm.

Thus, Raman spectroscopy as well as infrared spectroscopy can now be applied – either individually or in combination – to most problems where they appear useful.

This book intends to supply the basic information necessary to apply the methods of vibrational spectroscopy, to design experimental procedures, to perform and evaluate experiments. It does not intend to provide a market survey of the instruments which are available at present, because such information would very soon be outdated. However, the general principles of the instruments and their accessories, which remain valid, are discussed. Details concerning sample preparation and the recording of the spectra, which is the subject of introductory courses, are assumed to be known. Special procedures which are described in monographs, such as Fourier transformation or chemometric methods, are also not exhaustively described. This book has been written for graduate students as well as for experienced scientists who intend to update their knowledge.

After a short outline of the early history of infrared and Raman spectroscopy (Section 1), a general survey is given of different aspects of vibrational spectroscopy (Section 2). This survey is sufficient for readers who intend to get an impression of the fundamentals of vibrational spectroscopy. It serves as a common basis for subsequent chapters, which describe special experimental features, the theory, and applicational details: Section 3, Tools for infrared and Raman Spectroscopy; Section 4, Vibrational spectroscopy of different classes and states of compounds; Section 5, Evaluation procedures, and Section 6, Special techniques and applications.

In order to provide comprehensive and up-to-date information, several specialists of vibrational spectroscopy have contributed chapters dealing with their particular fields. The editor did not make considerable effort to force the authors to use exactly the same nomenclature. The nomenclature used by different authors reflects the common usage in the pertinent literature of the individual fields. There are typical but established differences in the nomenclature used by chemists and physicists – chemists prefer to think in terms of molecules and their properties, whereas physicists like to concentrate on phenomena and formalisms. However, the IUPAC and IUPAP rules as well as the SI units are obeyed wherever suitable and possible. The literature citations of all chapters are collected in a common section at the end of this book, arranged according to the name-date system (Ebel and Bliefert, 1990).

This book has emerged from manuscripts prepared for advanced courses on vibrational spectroscopy, for lectures, and for encyclopedic articles. I would like to thank all authors for dedicating their spare time to this work and to express my gratitude to all who helped me organize the manuscript, especially Frau Anne Tamburano, who typed large parts of the manuscript and produced the bibliography and the index. My wife Christa helped me prepare draft manuscripts and to organize the whole book. Mrs. Barbara Hoeksema did a great job to remove Germanisms and to improve the English. Heinz Sprünken has drawn many figures, Elke Manzel has recorded several spectra. Many colleagues, especially Prof. Dr. Wolfgang Kiefer, Prof. Dr. Heinz W. Schrötter, Dr. Goran Baranović, Dr. Gabor Kereszty, Dr. David Moore, and his wife, Viera gave important advice for improving the text. Dr. Steffen Pauly, VCH Publishers, helped considerably to produce a consistent book.

I would like to invite the readers of this book to give comments and recommendations which could improve it.

Support of the basic research, the results of which are reported throughout this book, by the Fonds der chemischen Industrie, the Deutsche Forschungsgemeinschaft, the Bundesministerium für Forschung und Technologie, the Minister für Wissenschaft und Forschung, Nordrhein-Westfalen, and the Volkswagen-Stiftung is gratefully acknowledged.

Essen, Spring 1994

Bernhard Schrader

Table of Contents

1	Early history of vibrational spectroscopy	
	(<i>B. Schrader</i>)	1
2	General survey of vibrational spectroscopy	
	(<i>B. Schrader</i>)	7
2.1	Molecular vibrations	8
2.2	Methods of observing molecular vibrations	13
2.3	The infrared spectrum	16
2.4	The Raman spectrum	18
2.5	Frequencies of the vibrations of typical model molecules	26
2.5.1	Stretching vibrations of linear triatomic molecules	27
2.5.2	Stretching vibrations of cyclic molecules and molecular chains	30
2.5.3	General rules concerning vibrations	32
2.5.4	Estimating force constants	34
2.6	Vibrational spectra of molecules in different states	35
2.7	The symmetry of molecules and molecular vibrations	38
2.7.1	Symmetry operators, symmetry elements	39
2.7.2	Point groups, space groups	41
2.7.3	Selection rules of the vibrations of molecules and crystals	44
2.7.3.1	Definition of a group, multiplication tables	44
2.7.3.2	Representations of a group	45
2.7.3.3	Irreducible representations	47
2.7.3.4	The character table	48
2.7.4	The number of vibrational states belonging to the different symmetry species	50

2.7.5	The number of vibrational states of a molecular crystal	51
2.7.6	Vibrational spectra of thiourea molecules and crystal modifications	54
2.7.6.1	Vibrational states of the free thiourea molecule	54
2.7.6.2	Vibrational states of the thiourea molecule under the constraints of its site symmetry	56
2.7.6.3	Vibrational states of the unit cell of crystalline thiourea	56
2.7.6.4	Correlation of the motional degrees of freedom of thiourea	57
2.7.7	Infrared and Raman activity of lattice vibrations	61

3 Tools for infrared and Raman spectroscopy (*B. Schrader*) 63

3.1 The optical conductance 65

3.1.1	The optical conductance of spectrometers	67
3.1.2	Properties of grating spectrometers	69
3.1.3	Properties of prism spectrometers	72
3.1.4	Optical conductance of prism and grating spectrometers	72
3.1.5	Optical conductance of interferometers	73
3.1.6	Application of dispersive spectrometers and interferometers to vibrational spectroscopy; the Jacquinot advantage	75
3.1.7	Interference filters	76
3.1.8	Lasers	77

3.2 Polarized radiation (*B. Jordanov*) 78

3.2.1	The Stokes - Mueller formalism	79
3.2.1.1	The Stokes vector	79
3.2.1.2	The Mueller matrices	83
3.2.2	Polarization optics	89
3.2.2.1	Linear polarizers	89
3.2.3	Retarders	94

3.3 Properties of the components of optical spectrometers (*B. Schrader*) 97

3.3.1	Radiation sources	97
3.3.2	Imaging and conducting optical elements	100
3.3.3	Radiation detectors, signal-to-noise ratio	106
3.3.4	Optimizing vibrational spectroscopy as an analytical method	108
3.3.4.1	Basic information theory	108
3.3.4.2	Information theory applied to analytical chemistry	111
3.3.5	The precision of spectrometric analysis and the limit of detection	115
3.3.6	Multichannel and multiplex techniques, the Fellgett advantage	120

3.4	Spectrometers for the near, middle, and far infrared range	123
3.4.1	Radiation sources	124
3.4.2	Spectral apparatus	124
3.4.3	Detectors	126
3.4.4	Sample arrangements	126
3.4.5	Radiation balance of an IR spectrometer	131
3.5	Raman spectrometers	135
3.5.1	Radiation sources	136
3.5.2	Spectral apparatus	136
3.5.3	Sample techniques	138
3.5.3.1	Theory	138
3.5.3.2	Sample arrangements for Raman spectroscopy	143
3.5.3.3	Micro and 2D scanning arrangements	148
3.5.4	The radiant power of Raman lines	151
3.5.4.1	Radiation balance of a Raman scattering sample, considering absorption by the sample or the solvent	153
3.5.5	Special features of Raman spectroscopy in the NIR range	155
3.5.5.1	Influence of the characteristics of sample and spectrometer	155
3.5.5.2	Conclusions concerning optimization of NIR Raman spectroscopy	161
3.6	Nonlinear Raman spectroscopy (<i>W. Kiefer</i>)	162
3.6.1	Nonlinear Raman processes	163
3.6.1.1	Spontaneous scattering: hyper Raman effect	163
3.6.1.2	Stimulated Raman effect	164
3.6.1.3	Nonlinear Raman spectroscopies based on third-order susceptibilities	166
3.6.2	Instrumentation for nonlinear Raman spectroscopy	172
3.6.2.1	Hyper Raman spectroscopy	172
3.6.2.2	Coherent anti-Stokes Raman spectroscopy (CARS)	172
3.6.2.2.1	Scanning pulsed CARS	173
3.6.2.2.2	Multiplex CARS	176
3.6.2.2.3	Femtosecond time-resolved CARS	176
3.6.2.2.4	High resolution cw-CARS	178
3.6.2.2.5	Special laser beam arrangements for CARS	180
3.6.2.3	Stimulated Raman gain and inverse Raman spectroscopy (SRGS, IRS)	182
3.6.2.4	Photoacoustic Raman spectroscopy (PARS)	185
3.6.2.5	Ionization detected stimulated Raman spectroscopy (IDSRS)	186

4 Vibrational spectroscopy of different classes and states of compounds 189

4.1 Organic substances (*B. Schrader*) 189

- 4.1.1 Chain molecules, polymers 192
- 4.1.1.1 General features 192
- 4.1.1.2 Special properties of the spectra of polymers 195
- 4.1.2 C=C vibrations 195
- 4.1.3 Conjugated and cumulated C=C systems 197
- 4.1.4 X=Y=Z derivatives 199
- 4.1.5 Acetylene derivatives 202
- 4.1.6 Nitriles 202
- 4.1.7 Saturated isocycles 202
- 4.1.8 Dependence of the C-halogen vibrations on the constitution, the configuration, and the conformation 205
- 4.1.9 The substitution pattern of benzene derivatives 208
- 4.1.10 The ether moiety 209
- 4.1.11 CH₃-X groups 209
- 4.1.12 The carbonyl group in different environments 212
- 4.1.13 Azo compounds, peroxides, disulfides 215
- 4.1.14 R-SO_n-R and R-SH groups 215
- 4.1.15 Nitro groups 215
- 4.1.16 Substances of biological interest 220
- 4.1.17 Solvents 222

4.2 Inorganic substances (*H. Schnöckel and H. Willner*) 223

- 4.2.1 Introduction 223
- 4.2.2 Application of vibrational spectroscopy in inorganic chemistry 224
- 4.2.2.1 Qualitative and quantitative analysis of known compounds 224
- 4.2.2.2 Qualitative analysis of unknown compounds. Interpretation of vibrational spectra with the help of empirical rules 225
 - 4.2.2.2.1 Characteristic frequencies 225
 - 4.2.2.2.2 Vibrational coupling 226
 - 4.2.2.2.3 Influence of bonding on vibrational frequencies 229
 - 4.2.2.2.4 Discussion of structure and bonding with the help of vibrational spectroscopy 234
 - 4.2.2.2.5 Geometry, composition, and symmetry 234
 - 4.2.2.2.6 Assignment of vibrational absorptions. Normal coordinates 236
 - 4.2.2.2.7 Intensity of vibrational bands 239
 - 4.2.2.2.8 Isotopic substitution 240
 - 4.2.2.2.9 Force constants 242
 - 4.2.2.2.10 Significance of force constants for chemical bonding. Comparison with other properties of bonds 244

4.2.2.3.7	Prediction of the vibrational spectra of unknown species	246
4.2.2.4	Vibrational spectra of crystals from a chemical point of view	247
4.2.3	Selected examples of structural examination by vibrational spectroscopy, classified by compounds	249
4.2.3.1	Gaseous compounds	249
4.2.3.2	Solutions	250
4.2.3.3	Solids	251
4.2.3.3.1	Molecular solids	251
4.2.3.3.2	Isolated groups of ionic compounds	251
4.2.3.3.3	Solid ionic compounds	252
4.2.4	Conclusion	252
4.3	Rotation-vibration spectra of gases (<i>H.M. Heise and H.W. Schrötter</i>)	253
4.3.1	Infrared spectra of gases (<i>H.M. Heise</i>)	256
4.3.1.1	Introduction	256
4.3.1.2	Linear molecules	258
4.3.1.3	Symmetric top molecules	267
4.3.1.4	Spherical top molecules	270
4.3.1.5	Asymmetric top molecules	272
4.3.2	Raman spectra of gases (<i>H.W. Schrötter</i>)	277
4.3.2.1	Introduction	277
4.3.2.2	Selection rules and examples of spectra	278
4.3.2.2.1	Diatomlic molecules	279
4.3.2.2.2	Linear molecules	286
4.3.2.2.3	Symmetric top molecules	290
4.3.2.2.4	Spherical top molecules	292
4.3.2.2.5	Asymmetric top molecules	294
4.3.2.3	Raman scattering cross sections	295
4.3.2.4	Conclusion	297
4.4	Matrix-isolated molecules (<i>H. Schnöckel and H. Willner</i>)	297
4.4.1	Introduction	297
4.4.2	Vibrational spectra of matrix-isolated molecules	298
4.4.3	Basic experimental details	299
4.4.4	Methods of matrix preparation and formation of guest species	302
4.4.5	Molecules in the vapor phase	303
4.4.5.1	Molecules in the vapor phase formed by chemical reaction	306
4.4.6	Spontaneous chemical reactions in a matrix (Cryochemistry)	309
4.4.7	Photochemical reactions in a matrix	312

4.5	Crystals (<i>D. Bougeard</i>) 314
4.5.1	Vibration of an unidimensional diatomic chain 314
4.5.2	Qualitative extension to a three-dimensional lattice 316
4.5.3	Single crystal spectroscopy 317
4.5.3.1	Infrared spectra 318
4.5.3.2	Raman spectra 318
4.5.4	An investigated example: calcium carbonate 319
4.5.4.1	Calcite 319
4.5.4.2	Aragonite 320
4.5.5	Applications 322
4.6	Liquid crystals: orientational order and optical anisotropy (<i>E.-H. Korte</i>) 323
4.6.1	Introduction to liquid crystals 323
4.6.2	Degree of order and optical anisotropy of nematics 325
4.6.3	Evaluation of order and orientation 333
4.6.4	The cholesteric helical structure: analysis and application 334
4.6.5	From nematic anisotropy to cholesteric optical activity 343
4.7	Infrared and Raman spectroscopy of biomolecules (<i>A. Cao, J. Liquier, and E. Taillandier</i>) 344
4.7.1	Nucleic acids 345
4.7.1.1	Experimental methods: IR and classical Raman spectroscopy 345
4.7.1.1.1	Solutions 345
4.7.1.1.2	Films and fibers 345
4.7.1.1.3	Crystals 346
4.7.1.2	What does the vibrational spectrum of a nucleic acid look like? 346
4.7.1.3	The three main families of nucleic acid double helix conformations 347
4.7.1.3.1	The B → A conformational transition 348
4.7.1.3.2	The B → Z conformational transition 350
4.7.1.3.3	Hydrogen-deuterium exchange 351
4.7.1.3.4	Infrared linear dichroism 352
4.7.1.3.5	Crystal studies 353
4.7.1.4	Triple helices 354
4.7.1.5	DNA-drug interactions 354
4.7.2	Proteins-pigments 355
4.7.2.1	IR and classical Raman spectroscopy 356
4.7.2.1.1	Band assignment and protein conformation 356
4.7.2.1.2	Treatment of data 356
4.7.2.1.3	Membrane proteins 357
4.7.2.2	Recent techniques 358
4.7.2.2.1	Resonance Raman spectroscopy 358
4.7.2.2.2	Surface enhanced Raman spectroscopy 361

4.7.2.2.3	Near IR FT Raman spectroscopy	361
4.7.2.3	The cytochrome c system	362
4.7.2.4	Nucleoproteins	362
4.7.2.4.1	Chromatin	362
4.7.2.4.2	Viruses	363
4.7.3	Biomembranes	364
4.7.3.1	Characteristic wavenumbers and spectral regions usually used for membrane studies	364
4.7.3.1.1	Infrared absorption bands	364
4.7.3.1.2	Characteristic Raman bands	365
4.7.3.2	Phospholipid model membranes	365
4.7.3.2.1	Phase transitions investigated by vibrational spectroscopy	366
4.7.3.2.2	The interdigitated phase	366
4.7.3.2.3	Effect of drugs on phospholipid model membranes	367
4.7.3.2.4	Interactions with ionophores	368
4.7.3.2.5	Effect of polycations on charged lipids	369
4.7.3.3	Phospholipid bilayers in the presence of cholesterol, membrane proteins, and peptides	369
4.7.3.3.1	Effect of cholesterol	369
4.7.3.3.2	Interactions with membrane proteins	370
4.7.3.3.3	Interaction with hormones	370
4.7.3.3.4	Effect of toxins	371
4.7.3.4	Glycolipids	371
4.8	Conducting polymers, semiconductors, metals, and superconductors (<i>H. Kuzmany</i>)	372
4.8.1	Infrared and Raman spectroscopy of systems with free carriers and resonance transitions	373
4.8.2	Infrared and Raman spectroscopy of conjugated polymers	377
4.8.3	Infrared and Raman spectroscopy of organic charge-transfer crystals	396
4.8.4	Infrared and Raman spectroscopy of semiconductors	399
4.8.5	Infrared and Raman spectroscopy of metals and superconductors	401
4.8.6	Infrared and Raman spectroscopy of fullerenes	407
4.8.7	Summary and conclusion	410
5	Evaluation procedures	411
5.1	Quantitative analysis, automatic quality control (<i>M. Spiekermann</i>)	411
5.1.1	General	411
5.1.2	Relation between measured quantities and concentration	413
5.1.3	Quantitative analysis by IR spectroscopy	415
5.1.3.1	Calibration methods based on band maxima	416

5.1.3.2	Calibration methods based on integrated intensities	419
5.1.3.3	Quantitative analysis based on derivative spectroscopy	423
5.1.3.4	Single component analysis	424
5.1.3.5	Multicomponent analysis	427
5.1.3.6	Analysis of binary mixtures without external calibration	429
5.1.3.7	Quantitative reflection spectroscopy	430
5.1.4	Quantitative analysis by Raman spectroscopy	430
5.1.5	Examples	431
5.1.5.1	Quantitative analysis of liquid solutions	431
5.1.5.2	Gases	433
5.1.5.3	Solids	434
5.1.6	Quality control	436
5.1.7	Chemometrics	444
5.2	Calculation of frequencies and intensities of vibrations of molecules and crystals (<i>D. Bougeard</i>)	445
5.2.1	General formulation	445
5.2.2	Internal coordinates	448
5.2.3	Symmetry coordinates	450
5.2.4	Summary of the coordinate systems	450
5.2.5	Program packages for normal coordinate treatment	451
5.2.6	Potential energy functions	451
5.2.7	Physical significance of force constants	453
5.2.7.1	Valence stretching	453
5.2.7.2	Interaction force constants	454
5.2.8	Vibrational frequencies of crystals	456
5.2.8.1	General treatment	456
5.2.8.2	Potential function	457
5.2.8.2.1	Van der Waals interactions	457
5.2.8.2.2	Hydrogen bond	458
5.2.8.2.3	Electrostatic interaction	458
5.2.8.3	Concluding remarks on solid state calculations	459
5.2.9	Vibrational intensities	459
5.2.9.1	Classical methods	460
5.2.9.1.1	Electro-optical theory	460
5.2.9.1.2	Polar tensors	462
5.2.9.2	Quantum chemical methods	462

6	Special techniques and applications	465
6.1	Applications of non-classical Raman spectroscopy: resonance Raman, surface enhanced Raman, and nonlinear coherent Raman spectroscopy (W. Kiefer)	465
6.1.1	Introduction (with M. Spiekermann)	465
6.1.2	Resonance Raman spectroscopy (RRS)	466
6.1.2.1	Resonance Raman theories	468
6.1.2.1.1	The sum-over-states picture (with M. Spiekermann)	468
6.1.2.1.2	The time-dependent picture	473
6.1.2.2	Applications of resonance Raman spectroscopy (with M. Spiekermann)	482
6.1.2.2.1	Anharmonicity constants from overtone progressions	482
6.1.2.2.2	Accurate determination of excited state repulsive potential functions of diatomic molecules in the gaseous phase	482
6.1.2.2.3	Determination of excited state structure of polyatomic molecules	485
6.1.2.2.4	Resonance Raman spectroscopy of biochemical and biological systems	486
6.1.2.2.5	Various applications of resonance Raman spectroscopy	488
6.1.3	Surface enhanced Raman scattering (SERS)	489
6.1.3.1	SERS theories	490
6.1.3.2	Techniques for SERS	493
6.1.3.3	Some applications of SERS	495
6.1.4	Applications of nonlinear Raman spectroscopy	498
6.1.4.1	Hyper Raman spectroscopy	498
6.1.4.2	Coherent anti-Stokes Raman spectroscopy (CARS)	501
6.1.4.2.1	Spectroscopy of gas-phase molecules (with A. Leipertz)	502
6.1.4.2.2	Femtosecond time-resolved studies in liquids and solutions	505
6.1.4.2.3	Resonance CARS of the solid state	507
6.1.4.3	Stimulated Raman gain and inverse Raman spectroscopy (SRGS, IRS)	511
6.1.4.4	Photoacoustic Raman spectroscopy (PARS)	513
6.1.4.5	Ionization detected stimulated Raman spectroscopy (IDSRS)	515
6.2	Principles and application of near-infrared spectroscopy (M. Buback)	518
6.2.1	Introduction	518
6.2.2	Near-infrared spectra of small molecules	520
6.2.3	Near-infrared spectra of selected organic compounds	531
6.2.4	Quantitative analysis via near-infrared spectroscopy	537
6.2.5	Concluding remarks	541
6.3	Vibrational optical activity (VOA) (G. G. Hoffmann)	543
6.3.1	Vibrational circular dichroism (VCD)	543
6.3.1.1	Introduction	543
6.3.1.2	Instrumental techniques	544

6.3.1.3	Theoretical models	551
6.3.1.3.1	The degenerate coupled oscillator (DCO) model	551
6.3.1.3.2	The fixed partial charge (FPC) model	552
6.3.1.3.3	The charge flow (CF) model	552
6.3.1.3.4	The localized molecular orbital (LMO) model	552
6.3.1.3.5	The dynamic polarization (DP) model	553
6.3.1.3.6	The inertial motion (IM) model	553
6.3.1.3.7	The bond moment (BM) model	553
6.3.1.3.8	The atomic polar tensor (APT) model	554
6.3.1.3.9	The ring current mechanism	555
6.3.1.3.10	The magnetic field perturbation method (MFP)	555
6.3.1.3.11	The sum-over-states vibronic coupling (VC) method	557
6.3.1.4	Experimental results	557
6.3.2	Raman optical activity (ROA)	561
6.3.2.1	Introduction	561
6.3.2.2	Instrumental techniques	561
6.3.2.3	Theoretical models	565
6.3.2.3.1	The molecular polarizability and optical activity tensors	565
6.3.2.3.2	The bond polarizability model	567
6.3.2.4	Experimental results	569
6.3.3	Conclusions	572
6.4	Foundations and features of infrared reflection techniques (<i>E.-H. Korte and A. Röseler</i>)	572
6.4.1	Introduction	572
6.4.2	Physical background	573
6.4.3	Modelling and evaluation	582
6.4.4	Experimental techniques	586
6.4.4.1	Specular reflection spectra	586
6.4.4.2	Spectroscopic ellipsometry	589
6.4.4.3	Attenuated total reflection	593
6.4.4.4	Reflection absorption	596
6.4.4.5	Diffuse reflection	598
6.4.4.6	Competing techniques	602
6.5	Continuous extraction technique (<i>E. Lentz</i>)	603
6.5.1	Introduction	603
6.5.2	The ATR membrane technique	603
6.5.2.1	ATR membrane cell	603
6.5.2.2	Basic aspects of ATR theory	604
6.5.2.3	Selection of the internal reflection element	605
6.5.2.4	Selection and preparation of membranes	605
6.5.3	Membrane processes	609

6.5.3.1	Enrichment factor	609
6.5.3.2	Time constant of the extraction process	611
6.5.3.3	The Nernst diffusion layer	611
6.5.3.4	Improvement of the detection limit	612
6.5.4	Alternative membrane procedures	613
6.5.4.1	Non-reversible enrichment	613
6.5.4.2	Optical fibers covered with membranes	613
6.5.4.3	Combination of continuous distillation and head space analysis	615
6.5.4.4	Measurement of the transmission of the membrane	616
6.6	Investigation of fast reactions and intermediates (<i>K. Gerwert</i>)	617
6.6.1	Introduction	617
6.6.2	Methods	619
6.6.2.1	Principles of FTIR	619
6.6.2.2	Time-resolved FTIR techniques	621
6.6.2.2.1	Static FTIR	621
6.6.2.2.2	Rapid scan	621
6.6.2.2.3	Stroboscope technique	624
6.6.2.2.4	Step scan	625
6.6.2.3	Time-resolved conventional IR techniques	625
6.6.3	Application to bacteriorhodopsin	626
6.6.3.1	Introduction	626
6.6.3.2	Sample preparation	626
6.6.3.3	An example of a static (low temperature) FTIR measurement, the <i>BR</i> to <i>K</i> transition	628
6.6.3.4	An example for band assignment, the <i>BR</i> to <i>L</i> transition	629
6.6.3.5	An example of the stroboscope technique: the <i>L</i> to <i>M</i> transition	631
6.6.3.6	An example of the rapid scan method: the <i>M</i> to <i>BR</i> conversion	634
6.6.4	Application to bacterial photosynthetic reaction centers	636
6.6.5	FT-Raman spectroscopy	637
6.7	Application of high-pressure techniques (<i>M. Buback</i>)	640
6.7.1	Introduction	640
6.7.2	Optical cells for vibrational spectroscopy of fluids at high pressures and temperatures	642
6.7.3	Vibrational spectra of polar fluids	648
6.7.4	Chemical transformations in the dense fluid phase studied by high-pressure spectroscopy	652
6.8	Low- and high-temperature techniques, spectrometric determination of sample temperature (<i>A. Leipertz and M. Spiekermann</i>)	658
6.8.1	General	658
6.8.2	Temperature determination by IR spectroscopy	664

6.8.2.1	Determining the rotational temperature from the rotational structure of vibration-rotation bands	664
6.8.2.1.1	Determination of the rotational temperature of C=O	664
6.8.2.1.2	Making use of the distance between the maxima of <i>P</i> and <i>R</i> branch	665
6.8.2.2	Deriving the vibrational temperature from the intensities of overtones and combination bands	666
6.8.2.3	Temperature determination by simulating band contours	667
6.8.2.4	The procedure of line reversal	668
6.8.3	IR emission spectra	668
6.8.4	Temperature determination by linear Raman spectroscopy	671
6.8.4.1	Rotational temperature from the intensity distribution in purely rotational Raman spectra	671
6.8.4.1.1	Intensity ratio of two lines in the Stokes wing	672
6.8.4.1.2	Taking into account all rotational lines of the Stokes and the anti-Stokes wing	672
6.8.4.2	Determining the vibrational temperature from the intensity distribution of vibrational-rotational Raman bands	674
6.8.4.2.1	Temperature determination by simulating band profiles	675
6.8.4.2.2	Intensity ratios of vicinal maxima of vibrational transition bands ('hot bands')	676
6.8.4.2.3	Ratios of integrated intensities of Stokes and anti-Stokes vibrational Raman bands	676
6.8.5	Applications	679
6.8.5.1	Reaction kinetics	679
6.8.5.2	Phase transitions	683
6.8.5.3	Rotational isomerism	684
6.8.5.4	Unstable substances	687
6.8.5.4.1	Carbocations	688
6.8.5.4.2	Protonated organic compounds	689
6.8.5.5	Intermolecular and intramolecular interactions	691
6.8.5.6	Macromolecules	692
6.8.5.7	Coupling of thermogravimetric analysis with IR spectroscopy	693

7 Character tables 695

8 Literature 711

9 Index 765

Contributors

Prof. Dr. Bougeard

Centre National de la Recherche
Scientifique
Laboratoire de Spectrochimie Infrarouge
et Raman
Université des Sciences et Techniques de
Lille Flandres Artois
LASIR: Bât. C5
59655 Villeneuve d'Ascq
France

Prof. Dr. J. M. Buback

Institut für Physikalische Chemie
Universität Göttingen
Tammannstraße 6
37077 Göttingen
Germany

Prof. Dr. A. Cao

U.F.R. Santé-Medecine-Biologie
Humaine
Laboratoire C.S.S.B.
Unité de Recherche Associée au C.N.R.S.,
1430
Université Paris Nord
74 rue Marcel Cachin
93012 Bobigny Cedex
France

Prof. Dr. K. Gerwert

Institut für Biophysik
Ruhr-Universität Bochum
Postfach 102148
44780 Bochum
Germany

Dr. H. M. Heise

Institut für Spektrochemie und
angewandte Spektroskopie
Bunsen-Kirchhoff-Straße 11
44139 Dortmund
Germany

Dr. G. G. Hoffmann

Institut für Physikalische und
Theoretische Chemie
Universität Essen
Fachbereich 8
45117 Essen
Germany

Dr. B. Jordanov

Institut für Organische Chemie
Bulgarische Akademie der
Wissenschaften
1113 Sofia
Bulgaria

Prof. Dr. W. Kiefer

Institut für Physikalische Chemie
Universität Würzburg
Marcusstraße 9-11
97070 Würzburg
Germany

Dr. E.-H. Korte

Laboratorium für spektroskopische
Methoden der Umweltanalytik
Institut für Spektrochemie und
angewandte Spektroskopie
Rudower Chaussee 5, Geb. 11.1
12489 Berlin
Germany

Prof. Dr. H. Kuzmany

Institut für Festkörperphysik
Universität Wien
Strudlhofgasse 4
1090 Wien
Austria

Prof. Dr.-Ing. A. Leipertz

Lehrstuhl für Technische Thermodynamik
Friedrich-Alexander-Universität
Erlangen-Nürnberg
Am Wechselgarten 9
91058 Erlangen
Germany

Dipl. Chem. E. Lentz

Institut für Physikalische und
Theoretische Chemie
Universität Essen
Fachbereich 8
45117 Essen
Germany

Prof. Dr. J. Liquier

U.F.R. Santé-Medecine-Biologie
Humaine
Laboratoire C.S.S.B.
Unité de Recherche Associée au C.N.R.S.,
1430
Université Paris Nord
74 rue Marcel Cachin
93012 Bobigny Cedex
France

Dr. A. Röseler

Laboratorium für spektroskopische
Methoden der Umweltanalytik
Institut für Spektrochemie und
angewandte Spektroskopie
Rudower Chaussee 5, Geb. 11.1
12489 Berlin
Germany

Prof. Dr. H. Schnöckel

Institut für Anorganische Chemie
Lehrstuhl Analytische Chemie
Universität Karlsruhe
Engesserstraße, Geb. 30.45
76128 Karlsruhe
Germany

Prof. Dr.-Ing. B. Schrader

Institut für Physikalische und
Theoretische Chemie
Universität Essen
Fachbereich 8
45117 Essen
Germany

Prof. Dr. H. W. Schrötter

Sektion Physik
Ludwig-Maximilians-Universität München
Schellingstraße 4/III
80799 München
Germany

Prof. Dr. M. Spiekermann

Fachbereich Angewandte
Naturwissenschaften
Fachhochschule Lübeck
Stephensonstraße 3
23562 Lübeck
Germany

Prof. Dr. E. Taillandier

U.F.R. Santé-Medecine-Biologie
Humaine
Laboratoire C.S.S.B.
Unité de Recherche Associée au C.N.R.S.,
1430

Université Paris Nord
74 rue Marcel Cachin
93012 Bobigny Cedex
France

Prof. Dr. H. Willner

Institut für Anorganische Chemie
Universität Hannover
Callinstraße 9
30167 Hannover
Germany

1 Early history of vibrational spectroscopy*

Around 60 B. C., T. Lucretius Carus wrote:

Forsitan et rosea sol alte lampade lucens possideat multum caecis fervoribus ignem circum se, nullo qui sit fulgore notatus, aestiferum ut tantum radiorum exaugeat ictum.

(Perhaps the sun, shining with a high rosy torch, is surrounded by more fire with invisible heat, which is not recognized by its glare, thus amplifying the heat-transferring power of the rays (citation from Nonnenmacher, 1961)).

Mariotte in 1686 noticed that heat emerging from a fireplace can be focused by a mirror but does not pass through a glass plate. This observation was confirmed by Scheele in 1781. Herschel decomposed the radiation of the Sun with a prism. Using mercury thermometers with blackened bulbs, Herschel in 1800 showed that there is invisible but heat-transporting radiation beyond the red end of the solar spectrum. Most of the components of present infrared spectrometers were already described during the nineteenth century (Jones, 1981): thermopiles made of antimony/bismuth junctions which employ the thermoelectric effect, discovered by Seebeck (1823), were produced by Nobili (1830). Melloni (1833) discovered the transparency of sodium chloride for infrared radiation. He used it to construct the first mid-infrared spectrometer (Melloni, 1835). Ångström (1868) determined the exact wavelengths of the Fraunhofer lines in the solar spectrum by using diffraction gratings – which had already been made and used by Fraunhofer himself in 1821 – with up to 10000 lines per inch (about 4000 lines per cm)! Bell (1881) constructed the photophone, the photoacoustic detector. Langley (1881) invented the bolometer and, using his own IR spectrometer, already detected sulfur dioxide in the atmosphere of Pittsburgh (personal communication of E.K. Plyler, cited by Jones, 1981). Langley also described (1883) the 'window' in the spectrum of atmospheric water vapor between 8 and 12 μm . Using a combined grating and prism spectrometer, Langley (1884) was able to determine the refractive index of sodium chloride to about 5 μm . He thus made it possible to calibrate the wavelength scale of infrared prism spectrometers. Michelson introduced the two-beam interferometer in 1890.

The first spectra of molecular vibrations were observed in 1881 by Abney and Festing. They prepared photographic emulsions, which were sensitive in the near infrared region

* Chapter 1 is contributed by B. Schrader, Essen

up to 1200 nm, and photographed the absorption spectra of 48 organic liquids with path lengths up to 60 cm by using 3 1/2 prisms, mostly in a double pass arrangement. "When we find a body having a band at 0.74 μm and another beginning at 0.907 μm and ending at 0.942 μm , we may be pretty sure that we have an ethyl radical present. In the aromatic group the critical line is at wavelength $\lambda = 0.867 \mu\text{m}$. If that line be connected with a band we feel certain that some derivative of benzene is present...". "It seems highly probable by this delicate mode of analysis that the hypothetical position of any hydrogen which is replaced can be identified ..., a point of prime importance to organic chemistry". – Abney and Festing knew that these bands are associated with the hydrogen in the molecule, but they did not know that they were observing the overtones and combinations of normal vibrations of C–H, N–H, and O–H bonds.

Ångström (1889, 1890) recorded the absorptions of carbon monoxide, carbon dioxide, carbon disulphide, methane, benzene, and others in the wavelength range up to 8 μm , using a rock-salt prism spectrometer with lenses and a bolometer. Around the same time, Julius (1892) obtained the infrared spectra of some 20 organic compounds up to a wavelength of 10 μm in a cell with rock salt windows and at a sample thickness of about 0.2 mm. "He found that all compounds containing the methyl, CH_3 group had an absorption band at 3.45 μm ." He arrived at the conclusion "that the absorption of heat waves is due to intramolecular movements; in other words, the internal structure, i.e., the grouping of the atoms in the chemical molecule, determines the character of the absorption. He found that the chemical atom lost its identity in a compound; i.e., the effect is not 'additive', so that one can not foretell the absorption spectrum of the compound from a knowledge of the spectra of the constituent elements" (Coblentz, 1905). Using a KCl prism, Rubens and Aschkinass (1898) observed the emission and absorption spectra of CO_2 and water vapor up to 20 μm .

In 1905, Coblentz published an atlas containing absorption spectra of 120 organic compounds, as well as emission and reflection spectra (e.g., of the Moon) in the range up to 15 μm . He recorded these spectra during a two-year post-doctoral project, using instruments he built in the course of his graduate research program. He clearly described the differences between the absorption spectra of o-, m- and p-xylene, by having absorption bands at 13.6, 12.9, and 12.66 μm respectively. "In some compounds there is evidence that certain bands, e.g., the 3.43 μm band, are due to a definite group of atoms, e.g. the CH_3 -groups in the chain compounds and terpenes; in other compounds the evidence is just as strongly in favor of the manner of bonding of the atoms, e.g., the methylene hydrocarbons of the petroleum distillates; still other compounds, e.g., benzene and its derivatives, especially *phenyl mustard oil*, in which we have the characteristic vibration of the mustard oils superposed upon the vibration of the benzene nucleus, show that both the groups of atoms and their manner of bonding with other atoms, as well as the kind of atom have a great influence upon the absorption curve" (Coblentz, 1905). He observed that different isomers give rise to different spectra, and that there are also characteristic vibrations of the CH_2 or CH_3 , NH_2 , C_6H_6 , NO_2 , OH , and NCS groups.

Unfortunately, the importance of this work, published by a physicist, and its consequences was not acknowledged by chemists. It was not until the Second World War that this new method began to find broad acceptance.

In the laboratories of BASF (Badische Anilin- and Soda-Fabrik) at Ludwigshafen, the importance of infrared spectroscopy for industrial purposes was realized as early as the 1930's. The first IR instrument with a modulated beam was built by Lehrer in 1937 and modified to a double beam instrument with optical compensation in 1942. Luft described the first non-dispersive infrared analyzer in 1943. He used the gas to be analyzed as absorber in a photo-acoustic detector cell. Thus, the instrument was sensitive only to this gas. He also provided a survey of early industrial applications of infrared spectroscopy (Luft, 1947).

Based on the servo techniques developed during the Second World War automatically recording infrared spectrometers were introduced to the market in the United States. Especially the Perkin-Elmer Model 21 stimulated the application of infrared spectrometry worldwide. In 1957, some 100 Model 21 spectrometers were sold along with about 300 of the low-cost Model 137, Infracord.

During the 1960s further improvements made infrared spectroscopy a very useful tool used worldwide in the analytical routine laboratory as well as in many fields of science. Grating spectrometers replaced the prism instruments due to their larger optical conductance (which is explained in Sec. 3 of this book). The even larger optical conductance of interferometers could be employed after computers became available in the laboratory and algorithms which made Fourier transformation of interferograms into spectra a routine. The computers which became a necessary component of the spectrometers made new powerful methods of evaluation possible, such as spectral subtraction and library search.

The Raman effect also allows the observation of vibrational spectra; it provides information which complements that obtained by IR spectroscopy. This effect had been repeatedly predicted. Lommel (1878) described certain anomalies of fluorescence, the color of which is dependent on the nature of the sample and the frequency of the exciting radiation, with the necessity of bands with the frequency $\nu \pm \omega$, if a damped anharmonic oscillator of the frequency ω is irradiated with light of the frequency ν . Smekal (1923), Kramers and Heisenberg (1925), Schrödinger (1926), and Dirac (1927) predicted the Raman effect by applying quantum mechanics to molecules. Raman was looking for the optical analogue of the Compton effect, when, on February 7, 1928, his co-workers Krishnan and Venkateswaran observed 'modified scattering' of sunlight, which Raman identified as Kramers-Heisenberg effect. A short paper describing 'A New Type of Secondary Radiation' by Raman and Krishnan was cabled to Nature on February 16th, 1928. Other papers followed (Raman et al., 1928).

In France, Rocard (1928) immediately attributed this novel effect to optical modulation by the oscillating molecule. Cabannes (1928) described the new effect as 'optical beating' and predicted the existence of pure rotational Raman scattering in anisotropic molecules. In the Soviet Union, Landsberg and Mandelstam (1928) published their results on the light scattering of quartz, describing lines which differed from those expected by Debye's theory. They explained this phenomenon as inelastic scattering of light quanta.

In the United States, Wood (1928) realized that he had already recorded Raman lines on his photographic plates when he investigated resonance fluorescence. He introduced the term 'anti Stokes' for scattered light, whose quanta have a higher energy than those of the exciting light (see Sec. 2.4).

Since Raman was the first to publish a spectrum of scattered light containing frequency-shifted lines, he received the Nobel prize for physics on December 11, 1930, "for his work on the 'diffusion' of light and for the discovery of the effect which bears his name."

As mentioned above, the basic theory of the Raman effect was developed before its discovery. However, at this time numerical calculations of the intensity of Raman lines were impossible, because these require information on all eigenstates of a scattering system. Placzek (1934) introduced a 'semi-classical' approach in the form of his polarizability theory. This provided a basis for many other theoretical and experimental studies. Physicists and chemists worldwide realized the importance of the Raman effect as a tool for qualitative and quantitative analysis and for the determination of structure.

It soon became apparent that the Raman effect was "not a substitute for infrared spectroscopy", which in the thirties was a much more difficult technique than Raman spectroscopy, but a "complement to be evaluated in connection with infrared spectroscopy" (Schaefer and Matossi, 1930). Kohlrausch (1931, 1938, 1943) in particular explored the relation between Raman spectra and molecular structures. However, until about 1950, Raman spectroscopy was applied more often than IR spectroscopy and it was only rarely that the two types of spectra were jointly evaluated. The reverse became true after 1950, when automatically recording infrared spectrometers were introduced to the market. Infrared spectroscopy found its place in routine analysis.

The most important stimulus to the development of Raman spectroscopy has been the laser, invented by Maiman in 1960. During a short period the mercury arcs were replaced by these really monochromatic and most powerful light sources. At the same time the photographic plates were replaced by photomultipliers, and scanning grating spectrometers replaced the prism spectrographs. Also, the introduction of double and triple monochromators, an elaborate sample technique (Kiefer, 1977), and later of diode arrays and charge-coupled devices (CCDs) contributed considerably to the development of Raman spectroscopy. This is also true of 'non-classical' Raman effects, utilizing resonance and non-linear phenomena. Nevertheless, the main obstacle to an application as routine method of analytical chemistry could not be removed until the late 1980's: the fluorescence of the impurities which are found in most 'real life' samples. Excited by radiation in the visible (or UV) region of the spectrum it is by orders of magnitude stronger than the Raman effect. In addition, the technical developments which have improved the quality of the spectra and the convenience of recording them, however, are somewhat compromised by the higher price of the instruments. As a result, the scope of these instruments has remained much the same, and the number of Raman spectrometers in use has been still only a small fraction of the number of infrared spectrometers.

There is a real chance of a breakthrough of Raman spectroscopy in routine analytics. Excitation of Raman spectra by near-infrared radiation and recording with interferometers, followed by the Fourier transformation of the interferogram into a spectrum – the so-called NIR-FT-Raman technique – has made it possible to obtain Raman spectra of most samples uninhibited by fluorescence. In addition, the introduction of dispersive spectrometers with multi-channel detectors and the development of several varieties of Raman spectroscopy has made it possible to combine infrared and Raman spectroscopy whenever this appears to be advantageous.

The following chapters describe the most important work in the different fields. Comprehensive reviews of the history of vibrational spectroscopy have been published by Jones (1981, 1985). Möller and Rothschild (1971) have compiled a complete bibliography of far-infrared spectroscopy covering the period between 1892 and 1969. Reviews of the history of the Raman effect have been published by Brandmüller and Kiefer (1978) and by Long (1988).

2 General survey of vibrational spectroscopy*

Molecules consist of atoms which have a certain mass and which are connected by elastic bonds. As a result, they can perform periodic motions, they have *vibrational degrees of freedom*: All motions of the atoms in a molecule relative to each other are a superposition of so-called *normal vibrations*, in which all atoms are vibrating with the same phase and *normal frequency*. Their amplitudes are described by a *normal coordinate*. Polyatomic molecules with n atoms possess $3n - 6$ normal vibrations (linear ones have $3n - 5$ normal vibrations), which define their *vibrational spectra*. These spectra depend on the masses of the atoms, their geometrical arrangement, and the strength of their chemical bonds. Molecular aggregates such as crystals or complexes behave like 'super molecules' in which the vibrations of the individual components are coupled. In a first approximation the normal vibrations are not coupled, they do not interact. However, the elasticity of bonds does not strictly follow Hooke's law. Therefore overtones and combinations of normal vibrations appear.

Infrared and Raman spectrometers are the most important tools for observing vibrational spectra. Depending on the nature of the vibration, which is determined by the symmetry of the molecule, vibrations may be *active* or *forbidden* in the infrared or Raman spectrum. The following characteristics are most relevant to the application of vibrational spectra throughout chemistry and physics. They are to be explained and illustrated in detail in the subsequent chapters:

1. Vibrational spectroscopy involves different methods, the most important of which are infrared (IR) and Raman spectroscopy.
2. The IR and Raman spectra of two molecules are different, if these molecules have different constitutions, isotopic distributions, configurations, conformations or if their environments are different for whatever reason. This also includes the infrared or Raman optical activity of enantiomers.
3. Definite substances can be identified by their IR and Raman spectra, interpreted like fingerprints.
4. The spectra show certain bands, i.e., *characteristic vibrations*, which are typical of particular groups of atoms and which are defined by definite ranges of frequencies **and** intensities in the IR *and* the Raman spectra. These may be employed for the elucidation of the molecular structure.
5. Molecular structures may also be derived from the spectra by employing model calculations.

* Chapter 2 is contributed by B. Schrader, Essen

6. The intensities of the bands in the spectrum of a mixture are usually proportional to the concentrations of the individual components. It is thus possible to determine the concentration of one substance or to carry out a multi-component analysis.
7. Vibrational spectra of substances in any state can be recorded; the spectra of one substance in different phases are similar, but they differ with respect to the activity and intensity of vibrations, their frequency, the half width, and the fine structure of the bands.
8. IR and Raman spectra can usually be recorded non-destructively. After the spectra have been recorded, the sample can be recovered and used for other purposes. Raman spectra can be recorded from samples in a closed ampoule.
9. The recording and evaluation of IR and Raman spectra may be automatized. The spectra may be obtained *on-line* and in *real time*.
10. The time needed to record a vibrational spectrum is of the order of seconds to minutes or, with special equipment, may even be less.

2.1 Molecular vibrations

Each atom has three *degrees of freedom*: it can move independently along each of the axes of a Cartesian coordinate system. If n atoms constitute a molecule, there are $3n$ degrees of motional freedom. Three of these degrees – the translational ones – involve moving of all atoms simultaneously in the same direction parallel to the axes of a Cartesian coordinate system. Another three degrees of freedom also do not change the distance between atoms, they describe rotations, e.g., about the principal axes of the inertial ellipsoid of the molecule. The remaining $3n - 6$ degrees are motions which change the distances between atoms: the lengths of the chemical bonds and the angles between them. Since these bonds are elastic, periodic motions occur. All vibrations of an idealized molecule result from superposition of $3n - 6$ non interacting normal vibrations.

The simplest model of a vibrating molecule describes an atom bound to a very large mass by a weightless spring (Fig. 2.1-1 a). The force F which is necessary to move the

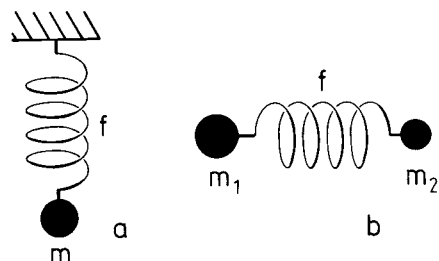


Figure 2.1-1 Models of a harmonic oscillator, **a** mass m on a spring with the force constant f , **b** two masses, m_1 and m_2 , connected by a spring with the same force constant.

atom by a certain distance x from an equilibrium position is proportional to the force constant f , a measure of the strength of the bond. This is Hooke's law:

$$F = -f \cdot x \quad (2.1-1)$$

The negative sign shows that the force is directed opposite to the elongation. According to Newton's law, the force is also proportional to the mass m and its acceleration, the second derivative of the elongation with respect to the time t :

$$F = m \cdot \frac{d^2x}{dt^2} \quad (2.1-2)$$

Both equations can be combined:

$$m \cdot \frac{d^2x}{dt^2} = -f \cdot x \quad (2.1-3)$$

This second order differential equation possesses the solution

$$x = x_0 \cdot \cos(2\pi \nu t + \varphi) \quad (2.1-4)$$

describing the motion of the atom as a harmonic oscillation. Here ν is the vibrational frequency and φ the phase angle. The second derivative of x by the time is found to be:

$$\frac{d^2x}{dt^2} = -4 \pi^2 \nu^2 x_0 \cos(2\pi \nu t + \varphi) = -4 \pi^2 \nu^2 x \quad (2.1-5)$$

Insertion into Eq. 2.1-3 yields

$$4 \pi^2 \nu^2 m = f \quad \text{or} \quad \nu = \frac{1}{2\pi} \sqrt{f/m} \quad (2.1-6)$$

This is the frequency of the vibration of a mass connected to a very large mass by an elastic spring. If we now consider a diatomic molecule the mass m is called *reduced mass* of a diatomic molecule with the masses m_1 and m_2 (Fig. 2.1-1 b):

$$\frac{1}{m} = \frac{1}{m_1} + \frac{1}{m_2} \quad (2.1-7)$$

Thus, we obtain an equation describing the frequency of the vibrations of a diatomic molecule:

$$\nu = \frac{1}{2\pi} \sqrt{f(\frac{1}{m_1} + \frac{1}{m_2})} \quad (2.1-8)$$

Eq. 2.1-8 gives the frequency ν (in Hz, s^{-1}) of the vibration. In vibrational spectroscopy, it is common to measure 'frequencies' in wavenumber units $\tilde{\nu}$ (waves per unit length), which is the reciprocal wavelength λ :

$$\tilde{\nu} = \frac{\nu}{c} = \frac{1}{\lambda} \quad (2.1-9)$$

If atomic mass units are employed and the force constants are measured in N/cm (= mdyne/Å), the frequency of the vibration of a diatomic molecule is given by:

$$\tilde{\nu}/\text{cm}^{-1} = 1303 \sqrt{f(\frac{1}{m_1} + \frac{1}{m_2})} \quad (2.1-10)$$

A C-H group with atomic masses of 12 and 1 units, respectively, in which the atoms are connected by a bond with a force constant f of 5 N/cm thus has a frequency of $\tilde{\nu} = 3033 \text{ cm}^{-1}$.

Since the center of gravity is immobile when a molecule vibrates, the amplitudes are inversely proportional to the masses of the atoms:

$$\frac{x_1}{x_2} = \frac{m_2}{m_1} \quad (2.1-11)$$

The absolute amplitudes of normal vibrations are of the order of 1 ... 10 pm.

Force constants of chemical bonds are approximately proportional to the bond order. Force constants of carbon-carbon single, double, and triple bonds have approximate values of 4.5, 9.4 and 15.7 N/cm, respectively. The significance of force constants for chemical bonding is discussed in detail in Sections 2.5.4 and 4.2.2.3.6.

The potential energy of a molecule which obeys Hooke's law is obtained by integrating Eq. 2.1-1:

$$V = \frac{1}{2} f r^2 \quad (2.1-12)$$

in which $r = x - x_e$, x_e is the Cartesian coordinate of the potential minimum. The graph of this function is a parabola; it is referred to as a 'harmonic' potential, because the model performs a 'harmonic' vibration. The atoms move with a definite frequency, according to the cosine function in Eq. 2.1-4. The bonds in actual molecules, however, are not obeying Hooke's law exactly. The force needed to compress a bond by a definite distance is larger than the force required to stretch this bond. Graphs describing harmonic as well as real, anharmonic potentials are shown in Fig. 2.1-2. Anharmonic molecular potentials may be represented by approximate functions, e.g., the Morse function (1929):

$$V = D[1 - \exp(-\sqrt{f_e/2D} \cdot r)]^2, \quad (2.1-13)$$

f_e is the force constant near the potential minimum and D stands for the dissociation energy.

There are other empirical potential functions which are especially useful to describe intermolecular potentials, i.e., the potentials between atoms, which are not connected by chemical bonds. Two of these (the Buckingham and the Lennard-Jones potential) are discussed in Secs. 2.5.4 and 5.2.

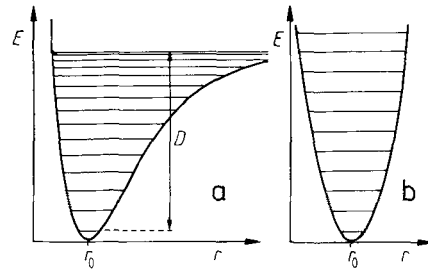


Figure 2.1-2 **a** Anharmonic, **b** harmonic potential with energy states according to quantum mechanics, E energy, r distance between the masses, r_0 equilibrium distance, D dissociation energy. The lowest energy level has the quantum number $v = 0$, followed by $v = 1, 2, \dots$.

According to classical mechanics, a harmonic oscillator may vibrate with any amplitude, which means that it can possess any amount of energy, large or small. Quantum mechanics, however, shows that molecules can only exist in definite energy states. In the case of harmonic potentials, these states are equidistant,

$$E_i = h \cdot \nu (v_i + 1/2), \quad v_i = 0, 1, 2, \dots \quad (2.1-14)$$

while for anharmonic potentials the distances between energy levels decrease with increasing energy (Fig. 2.1-2).

These energy levels are numbered v_i , the vibrational quantum number. At $v_i = 0$, the potential energy has its lowest value, which is not the energy of the potential minimum. The former exceeds the latter by $1/2 h \cdot \nu_i$. This is the so-called *zero point energy*. This energy cannot be removed from the molecule, even at temperatures approaching absolute zero.

For polyatomic molecules the frequency of normal vibrations may be calculated by applying the Lagrange equation to expressions of the kinetic and potential energy of the molecule (Wilson et al., 1955; Sec. 5.2).

The kinetic energy of a molecule is definitely given by the masses of the atoms and their velocities:

$$T = 1/2 \sum_i m_i \cdot \dot{x}_i^2 \quad (2.1-15)$$

Generally, the potential function of a polyatomic molecule can be described by a Taylor series:

$$V(r) = V_0 + \sum_i f_i r_i + \frac{1}{2} \sum_{i,j} f_{ij} r_i r_j + \frac{1}{6} \sum_{i,j,k} f_{ijk} r_i r_j r_k + \dots \quad (2.1-16)$$

where the r_i are suitable displacement coordinates from the equilibrium geometry at a potential minimum and the constants

$$f_i = \left(\frac{\partial V}{\partial r_i} \right)_0; \quad f_{ij} = \left(\frac{\partial^2 V}{\partial r_i \partial r_j} \right)_0; \quad f_{ijk} = \left(\frac{\partial^3 V}{\partial r_i \partial r_j \partial r_k} \right)_0 \quad (2.1-17)$$

are called linear, quadratic, cubic etc. force constants. The potential can be defined such that $V_0 = 0$. By definition, the second term in Eq. 2.1-16 is equal to zero, because the molecule is regarded as to be in its equilibrium (Califano, 1976):

$$\sum_i f_i r_i = 0.$$

The cubic and higher terms are difficult to determine; they have many components with a comparatively small value. Therefore, with a good approximation, an acceptable potential function has the form

$$V = \frac{1}{2} \sum_{i,j} \left(\frac{\partial^2 V}{\partial r_i \partial r_j} \right)_0 r_i r_j = \frac{1}{2} \sum_{i,j} f_{ij} r_i r_j \quad (2.1-18)$$

The diagonal force constants f_{ii} with $i = j$ describe the elasticity of a bond according to Hooke's law. The constants with $i \neq j$, the *interaction force constants* however, describe the change of the elastic properties of one bond when another bond is deformed (Sec. 5.2).

Thus, the force constants of the bonds, the masses of the atoms, and the molecular geometry determine the frequencies and the relative motions of the atoms. Fig. 2.1-3 shows the three normal vibrations of the water molecule, the symmetric and the antisymmetric stretching vibration of the OH bonds, ν_s and ν_a , and the deformation vibration δ . The normal frequencies and normal coordinates, even of crystals and macromolecules, may be calculated as described in Sec. 5.2. In a symmetric molecule, the motion of symmetrically equivalent atoms is either symmetric or antisymmetric with respect to the symmetry operations (see Section 2.7). Since in the case of normal vibrations the center of gravity and the orientation of the molecular axes remain stationary, equivalent atoms move with the same amplitude.

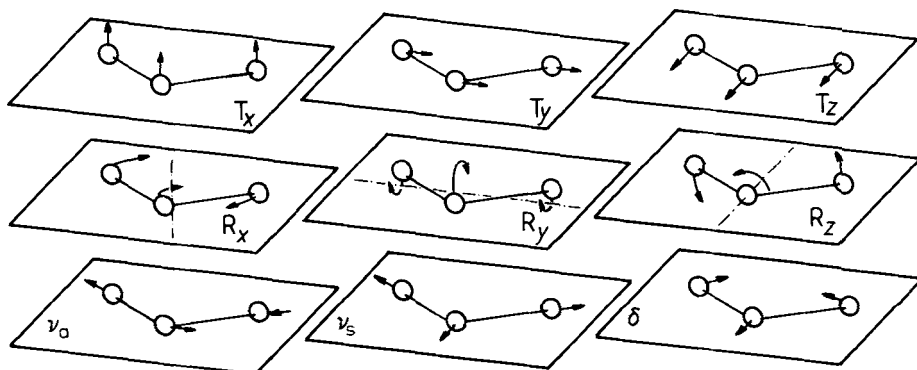


Figure 2.1-3 Motional degrees of freedom of the water molecule, T_i are translations and R_i rotations of the whole molecule, $i = x, y, z$; ν_s is the symmetric, ν_a the antisymmetric stretching vibration, δ the deformation vibration.

The vibrations may be described by different sets of basis coordinates. To start with, there are the changes of the $3n$ *Cartesian coordinates* X of the molecule. Chemists favor descriptions of the motions and the force constants in terms of bond lengths and bond angles. These are known as *internal coordinates* R . The equivalent internal coordinates of a molecule which possesses a certain symmetry, may change either *in-phase* or *out-of-phase*. The simultaneously occurring relative changes of the bond parameters of equivalent bonds are described by *symmetry coordinates* S . *Normal coordinates* Q describe motions as linear combinations of any set of basis coordinates. Different coordinate systems can be transformed into each other by matrix multiplication. For further details, see Sec. 5.2.

In reading the following sections, it might be useful to keep in mind that molecular potentials are not exactly harmonic, but that the harmonic approximation is generally sufficient. We have seen, that classical mechanics describes molecular vibrational frequencies. Yet only quantum mechanics can specify the change of energy of the vibrational states and the interaction with the light quanta which are absorbed, emitted, or scattered by a molecule.

Vibrational frequencies of typical model molecules are discussed in Sec. 2.5, applications in organic chemistry are found in Sec. 4.1, and their use in inorganic chemistry is described in Sec. 4.2. The calculation of molecular vibrations is treated in Sec. 5.2.

2.2 Methods of observing molecular vibrations

According to quantum mechanics the molecule can take up an amount of energy $h\nu_s$ to reach the first vibrationally excited state. Light quanta in the infrared region with a wavelength λ of $2.5 \dots 1000 \mu\text{m}$ possess energies of $h\nu = hc\tilde{\nu}$ with $\tilde{\nu} = 4000 \dots 10 \text{ cm}^{-1}$. A molecule which is irradiated with a continuous spectrum of infrared radiation may absorb light quanta which have this energy. The spectrum of the remaining radiation shows an absorption band at a frequency ν_s . Fig. 2.2-1a demonstrates this process. In this diagram the vibration of a diatomic molecule or one vibrational degree of freedom of a polyatomic molecule is excited by a transition from the energy level $v = 0$ to $v = 1$ (Eq. 2.1-14) of the anharmonic potential of the electronic ground state S_0 .

The same vibration may be excited by a completely different mechanism, i.e., by inelastic scattering of light quanta of higher energy, the so-called Raman effect, illustrated in Fig. 2.2-1b. The molecules are irradiated with monochromatic radiation in the ultraviolet, visible, or near-infrared region of the spectrum, whose quanta have the energy $h\nu_0$. During an inelastic impact of a light quantum with a molecule, vibrational energy $h\nu_s$ can be exchanged. Thus, light quanta are scattered which have a lower or higher energy, according to

$$h\nu_R = h\nu_0 \mp h\nu_s \quad (2.2-1)$$

in which $h\nu_s$ is the vibrational energy. The energy quanta $h\nu_R$ give rise to a Raman spectrum. At the same time, the exciting light quanta are also elastically scattered, a

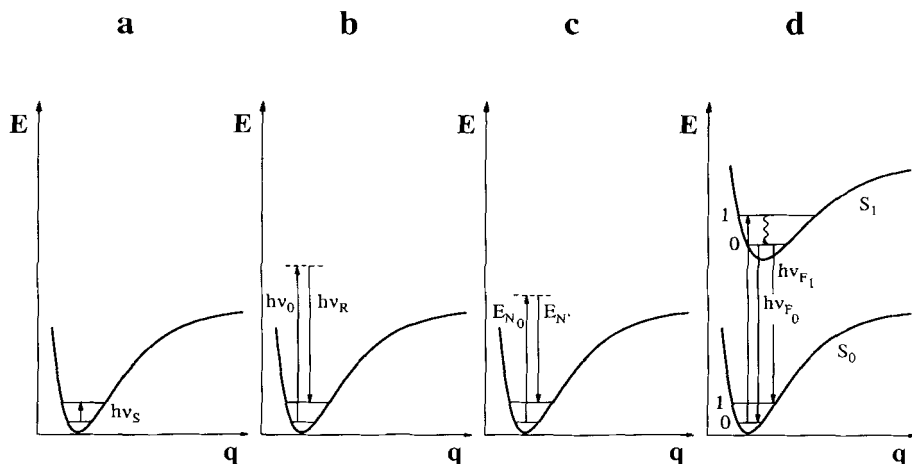


Figure 2.2-1 Observation of the excitation of a vibrational state in the electronic ground state S_0 , by a, infrared absorption; b, Raman scattering; c, inelastic neutron scattering; d, fluorescence.

phenomenon referred to as Rayleigh scattering. In this case, the scattered quanta have the same energy $h\nu_0$ as the exciting radiation.

Fig. 2.2-1c illustrates a similar process, the inelastic scattering of neutrons. Irradiating molecules with mono-energetic neutrons produce scattered neutrons according to an energy balance equivalent to Eq. 2.2-1. While Raman scattering as well as infrared absorption of symmetric molecules obeys strict selection rules, which allow or forbid the activity of certain vibrations in these spectra, inelastic scattering of neutrons is not subject to such rules. It is not usually applied in analytical chemistry, but it is used to study lattice vibrations of crystals in solid-state physics and dynamics of liquids.

Finally, fluorescence spectra (especially, of gases) may also disclose vibrational states of a molecule in its electronic ground state (Fig. 2.2-1d). Molecules which are irradiated with light quanta whose energy is sufficiently high to allow transition of valence electrons to excited states, may return to the ground state by emitting light quanta of lower energy. Such *fluorescence spectra* may show subbands arising from a transition from the electronic excited state to different vibrational states of the electronic ground state. Fluorescence spectroscopy is a valuable tool for trace analysis, because its quantum yield, i.e., the ratio of emitted to absorbed energy quanta, is high. However, it is not usually applied in analytical chemistry to investigate vibrational states.

For molecules which are in the same state under the same condition, all of the methods illustrated in Fig. 2.2-1 may supply identical values for the vibrational frequencies of molecules in the electronic ground state. The methods, however, which are generally applied to most molecules are infrared and Raman spectroscopy – they are the topic of this book.

Insert 10 cents into a Coke machine and receive a Coke: INFRARED; insert 1 Dollar and receive a Coke and 90 cents change: RAMAN (Assigned to A. Einstein, personal communication by Prof. F. A. Miller).

Infrared and Raman spectroscopy provide complementary images of molecular vibrations, because in these spectroscopic techniques the mechanisms of the interaction of light quanta with molecules are quite different.

Interaction of infrared radiation with a vibrating molecule is only possible if the electric vector of the radiation field oscillates with the same frequency as does the molecular dipole moment. A vibration is infrared active only if the molecular dipole moment is modulated by the normal vibration,

$$\left(\frac{\partial \mu}{\partial q} \right)_0 \neq 0, \quad (2.2-2)$$

where μ is the molecular dipole moment and q stands for the normal coordinate describing the motion of the atoms during a normal vibration.

A similar condition must be fulfilled for a vibration to be observed in the Raman spectrum. When a molecule is exposed to an electric field, electrons and nuclei are forced to move in opposite directions. A dipole moment is induced which is proportional to the electric field strength and to the molecular polarizability α . A molecular vibration can only be observed in the Raman spectrum if there is a modulation of the molecular polarizability by the vibration,

$$\left(\frac{\partial \alpha}{\partial q} \right)_0 \neq 0. \quad (2.2-3)$$

If the conditions, Eqs. 2.2-2 and 2.2-3, are fulfilled by symmetry, then the vibrations

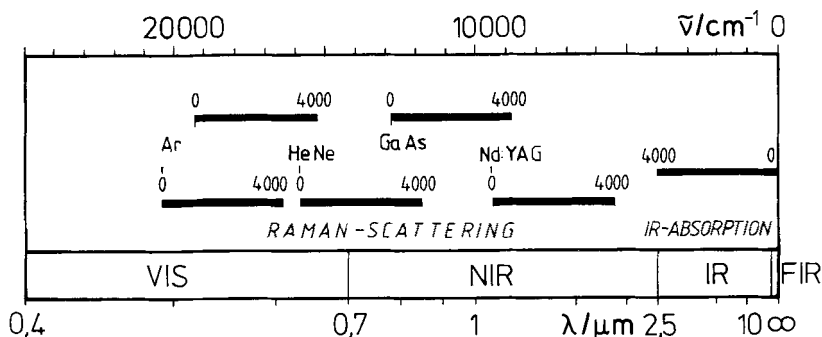


Figure 2.2-2 The visible, near, middle and far infrared region of the spectrum drawn in a scale linear in wavenumbers. The infrared (IR) and far-infrared (FIR) spectrum is recorded by absorption of light from a continuous spectrum in the range of $\lambda = 2.5 \dots 100 \mu\text{m} \cong \tilde{\nu} = 4000 \dots 100 \text{ cm}^{-1}$ and $\lambda = 100 \dots 1000 \mu\text{m} \cong 100 \dots 10 \text{ cm}^{-1}$. Raman spectra can be excited by monochromatic radiation, emitted by different lasers in the visible (VIS) or near-infrared range (NIR). Molecules emit Raman lines with a frequency difference $\Delta\tilde{\nu}$ to that of the exciting frequency $\tilde{\nu}_0$ between 0 and ± 4000 or $\pm 10000 \text{ cm}^{-1}$. Usually only the Raman spectrum which is shifted to smaller wavenumbers, the 'Stokes' Raman spectrum, is recorded. Its range is indicated by bars for different exciting lines: Ar⁺ laser at 488 and 515 nm, HeNe laser at 623 nm, GaAs laser at 780 nm, and Nd:YAG laser at 1064 nm.

are said to be *allowed* or *active* in the infrared or Raman spectrum, respectively; if they are not fulfilled by symmetry, they are said to be *forbidden* or *inactive* (Sec. 2.7.3.4).

Fig. 2.2-2 shows a range of Raman spectra excited by different spectral lines, and of the infrared spectrum. If a linear wavenumber scale is used, all spectra have the same length. The absorption spectrum between 4000 and 10 cm^{-1} covers the infrared (IR) region with a wavelength of $2.5 \dots 100\text{ }\mu\text{m}$ and the far infrared (FIR) region, $100 \dots 1000\text{ }\mu\text{m}$. The range of the emitted Raman spectra extends from the frequency of the monochromatic exciting radiation $\tilde{\nu}_0$ to $\tilde{\nu}_0 - \Delta\tilde{\nu}$ with $\Delta\tilde{\nu} = 0 \dots 4000\text{ cm}^{-1}$. The ranges of Raman spectra, excited by common types of lasers are shown: Ar-ion laser 488 and 515 nm, HeNe laser 633 nm, GaAs 780 nm, Nd:YAG 1064 nm.

2.3 The infrared spectrum

Infrared spectra are usually recorded by measuring the transmittance of light quanta with a continuous distribution of the sample. The frequencies of the absorption bands ν_s are proportional to the energy difference between the vibrational ground and excited states (Fig. 2.3-1). The absorption bands due to the vibrational transitions are found in the

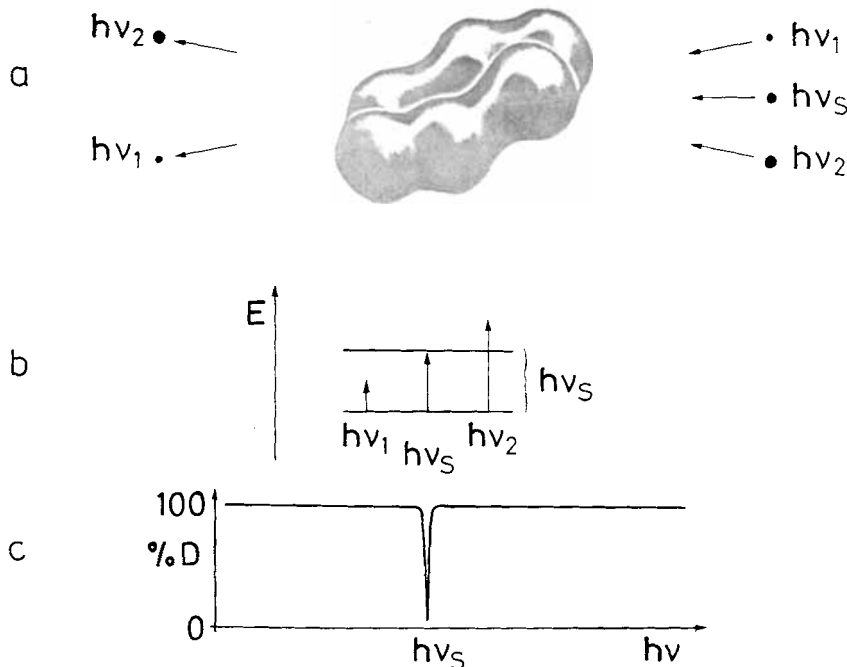


Figure 2.3-1 Principle of infrared absorption: **a** Quanta of the energy $h\nu_1$, $h\nu_S$ and $h\nu_2$ hit the molecule, only $h\nu_S$ is absorbed; **b** term diagram; **c** infrared absorption spectrum.

wavelength region of $\lambda = 2.5 \dots 1000 \text{ } \mu\text{m}$, which is equivalent to a wavenumber range of $\tilde{\nu} = 4000 \dots 10 \text{ cm}^{-1}$.

There are $k = 3n - 6$ normal vibrations of a non-linear molecule with n atoms. These vibrations may only absorb infrared radiation if they modulate the molecular dipole moment $\boldsymbol{\mu}_K$, (which is a vector with the components μ_x , μ_y , and μ_z):

$$\boldsymbol{\mu}_k = \boldsymbol{\mu}_0 + \left(\frac{\partial \boldsymbol{\mu}}{\partial q_k} \right)_0 q_k + \frac{1}{2} \left(\frac{\partial^2 \boldsymbol{\mu}}{\partial q_k^2} \right)_0 q_k^2 + \dots \quad (2.3-1)$$

with

$$q_k = q_k^0 \cdot \cos(2 \pi \nu_k t + \varphi_k) \quad (2.3-2)$$

the k th normal coordinate. The Cartesian components of the displacement of each atom during a normal vibration q_k are described by the components of the eigenvector matrix $\mathbf{L} = [l_{ki}]$ calculated by diagonalization of the secular determinant, as discussed in Sec. 5.2.

$$q_k = \sum_{i=1}^{3n} l_{ki} x_i, \quad x_i = \sum_{k=1}^{3n-6} (L^{-1})_{ik} q_k \quad (2.3-3)$$

If the potential is anharmonic, the higher terms of the potential energy according to Eq. 2.1-16 are not negligible, the *mechanical anharmonicity* gives rise to overtones, vibrations with the double, triple, or multiple frequency of the fundamentals. Overtones are also produced by the higher terms of the dipole moment according to Eq. 2.3-1, the *electrical anharmonicity*. Since both equations may contain mixed terms, combinations of two or more normal vibrations, i.e., sums or differences, are produced. These appear in the spectra, but usually only with small intensity. Also Raman spectra show overtones and combinations due to mechanical and electrical anharmonicities (see below).

Most analytical applications of infrared spectroscopy are based on the Bouguer-Lambert-Beer law, describing the absorption of a light flux Φ_0 by a sample:

$$\Phi_{tr} = \Phi_0 \cdot 10^{-A} = \Phi_0 \cdot 10^{-\epsilon cl} \quad (2.3-4)$$

Here, A is the (decadic) absorbance; ϵ represents the molar (decadic) absorption coefficient, customarily expressed in $\text{dm}^3/\text{mol} \cdot \text{cm}$, equivalent to $1000 \text{ cm}^2/\text{mol}$; c stands for the concentration in mol/dm^3 ; and l for the thickness of the sample in cm . These definitions are not strictly in accordance with SI standards. Nevertheless, they are used in this book, because millions of data in these units are published. The transmittance or transmittance factor is given by $\tau = \Phi_{tr}/\Phi_0$, the absorptance or absorption factor is equal to $\alpha = 1 - \tau$. For pure samples, the linear decadic absorption coefficient $a = \epsilon \cdot c$ is employed. Theoretical problems are sometimes approached by using the 'Napierian' coefficients, which are defined by

$$\Phi = \Phi_0 \cdot e^{-B} = \Phi_0 \cdot e^{-\kappa cl} \quad (2.3-5)$$

where B is the Napierian absorbance and κ stands for the molar Napierian absorption coefficient. κ may be called the molar absorbance cross-section and $\sigma = \kappa/N_A$ is the cross-section per molecule, N_A being the Avogadro constant.

The macroscopic and molecular properties are related by the integral Napierian absorption coefficient

$$A = \int_{band} \kappa d\tilde{\nu} \quad (2.3-6)$$

The integral Napierian absorption coefficient of the k th normal vibration is given by

$$A_k = \frac{N_1 \pi}{3 c} \left[\left(\frac{\partial \mu_x}{\partial q_k} \right)_0^2 + \left(\frac{\partial \mu_y}{\partial q_k} \right)_0^2 + \left(\frac{\partial \mu_z}{\partial q_k} \right)_0^2 \right] \quad (2.3-7)$$

in which N_1 is the number of molecules per cm^3 .

2.4 The Raman spectrum

If a light quantum $h\nu_0$ hits a molecule, an *elastic scattering* process, i.e., *Rayleigh scattering* of quanta with energy $h\nu_0$, has the highest probability. The *inelastic* process, during which vibrational energy is exchanged, has a much lower probability; it is called *Raman scattering* (Fig. 2.4-1). It emits quanta of energy $h\nu_0 \mp h\nu_s$. At ambient temperature most molecules are in their vibrational ground state. According to Boltzmann's law, a much smaller number is in the vibrationally excited state. Therefore, the Raman process, which transfers vibrational energy to the molecule and leaves a quantum of lower energy ($h\nu_0 - h\nu_s$) has a higher probability than the reverse process. – While studying fluorescence spectra, Stokes in 1852 (Stokes, 1880) postulated that the wavelength of light produced by fluorescence or phosphorescence is always longer than that of the exciting light. In analogy, Raman lines are referred to as *Stokes* lines and *anti-Stokes* lines, respectively (Wood, 1928), Fig. 2.4-1. Stokes lines are caused by quanta of lower energy. Since their intensities are higher than those of anti-Stokes lines, only they are usually recorded as Raman spectrum.

Fig. 2.4-2 shows the Boltzmann distribution of excited vibrational states with energies of $h\nu = hc\tilde{\nu}$ (with $\tilde{\nu} = 0 \dots 4000 \text{ cm}^{-1}$) of an ensemble of molecules at temperatures of 10, 30, 100, 300, 1000, 3000 and 10 000 K, respectively. Thus, the ratios of the intensities of the Stokes and anti-Stokes Raman lines of the same frequency shift make it possible to determine the temperature of a sample (see discussion of Eq. 2.4-10).

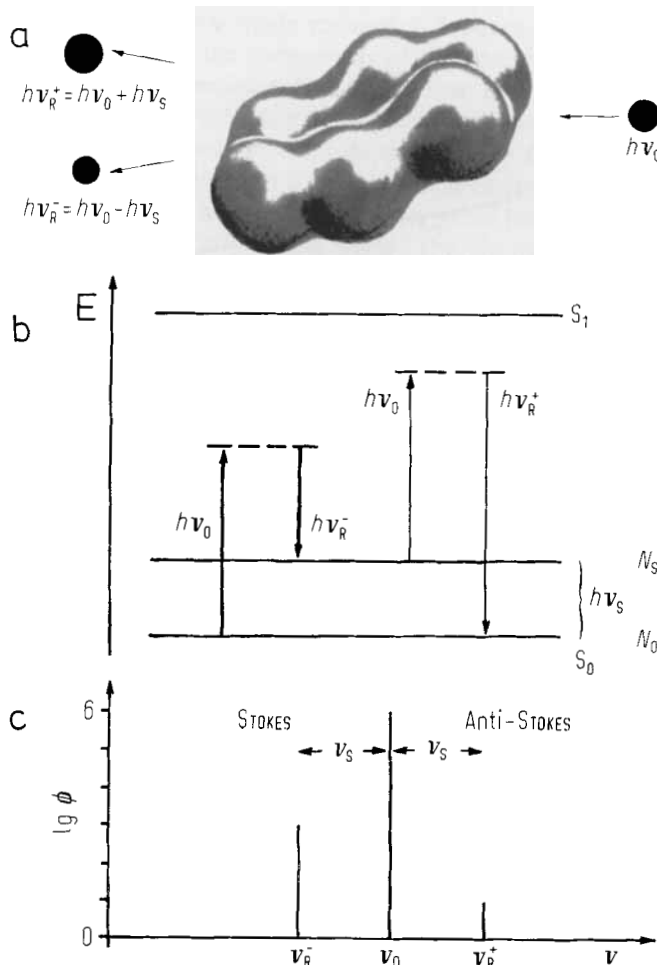


Figure 2.4-1 Principle of Raman scattering: **a** Quanta of the energy $h\nu_0$ hit the molecule, an elastic impact scatters the quantum $h\nu_0$, inelastic impacts scatter quanta which have energies smaller or larger by the amount of the vibrational energy, $h\nu_s$. **b** Term diagram: the irradiation with light quanta $h\nu_0$ of molecules in the vibrational ground state may lead to molecules in the vibrational excited state, quanta with energy $h\nu_R^- = h\nu_0 - h\nu_s$ are scattered. Since some molecules are, according to Boltzmann's law already in the excited state, also the process is possible which produces quanta of larger energy, $h\nu_R^+ = h\nu_0 + h\nu_s$. **c** Raman spectrum: two lines are seen, which differ from the frequency of the exciting radiation (the Rayleigh peak ν_0) by the vibrational frequency; the Raman line with the lower frequency (the *Stokes* line) is stronger, than with the larger frequency (the *anti-Stokes* line) weaker. Their intensity ratio is given by the ratio of the occupancies of both levels.

The absolute intensity of a line provides information about the molecular structure. It shows the modulation of the molecular polarizability by a vibration.

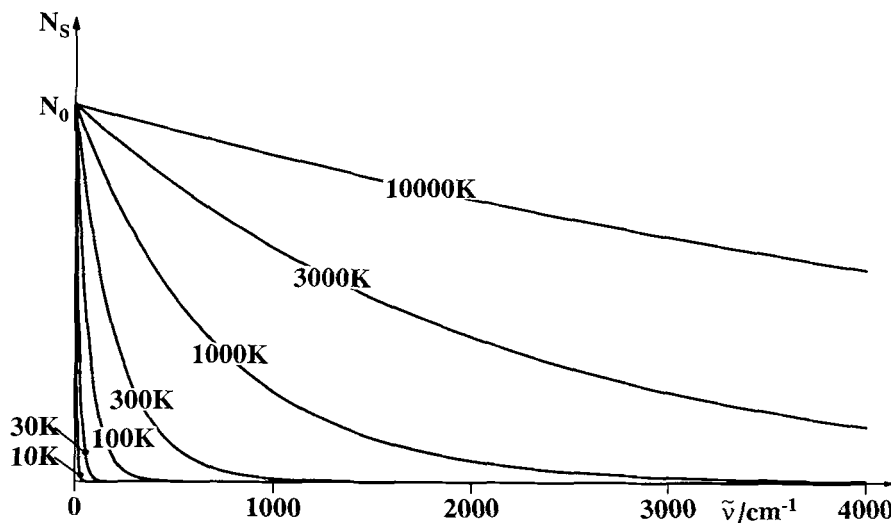


Figure 2.4-2 Boltzmann distribution $N_s = N_0 \cdot e^{-hc\tilde{v}/kT}$ over the vibrational states of the energy $hc\tilde{v}$ in a harmonic potential, with $\tilde{v} = 0 \dots 4000 \text{ cm}^{-1}$ and a temperature of $T = 10, 30, 100, 300, 1000, 3000$ and $10\,000 \text{ K}$.

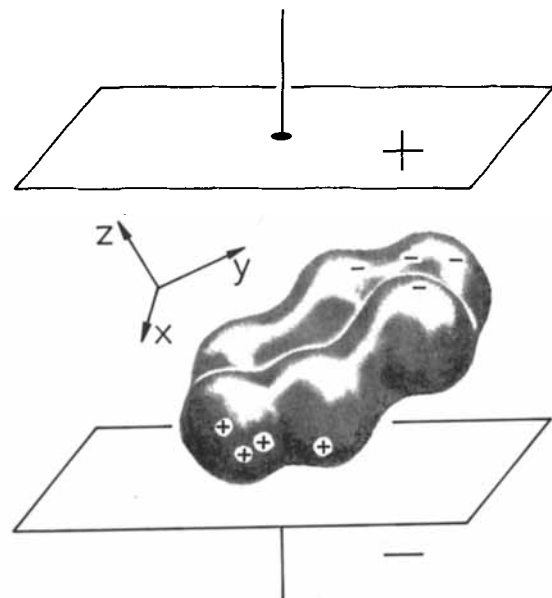


Figure 2.4-3 Molecular dipole moment induced by an electric field.

Fig. 2.4-3 shows a nonpolar molecule, such as benzene, which is thought to be placed in an electric field, represented by the space between the plates of a charged capacitor. The negatively charged plate attracts the nuclei, while the positive plate attracts the

electrons. Thus, a dipole moment is induced. In order to quantitatively describe this dipole moment, the components of the vector of the electric field are denoted by E_x , E_y , and E_z in a molecular fixed Cartesian coordinate system. This coordinate system is usually defined according to the symmetry properties of the molecule (see Sec. 2.7.1). The induced dipole moment depends on the flexibility of the electrons and nuclei of the molecule, described by the polarizability α . Obviously, the polarizability of the π -electrons can be regarded to be higher in the plane of the atoms of the benzene molecule than perpendicularly to this plane. The electric field gives rise to an induced dipole moment μ' , described by its components:

$$\begin{aligned}\mu'_x &= \alpha_{xx} E_x + \alpha_{xy} E_y + \alpha_{xz} E_z \\ \mu'_y &= \alpha_{yx} E_x + \alpha_{yy} E_y + \alpha_{yz} E_z \\ \mu'_z &= \alpha_{zx} E_x + \alpha_{zy} E_y + \alpha_{zz} E_z\end{aligned}\quad (2.4-1)$$

All α_{ij} are components of a tensor α , which projects one vector, the electric field vector E , to produce another vector μ' , the induced dipole moment. This can be written in matrix notation as

$$\begin{bmatrix} \mu'_x \\ \mu'_y \\ \mu'_z \end{bmatrix} = \begin{bmatrix} \alpha_{xx} \alpha_{xy} \alpha_{xz} \\ \alpha_{yx} \alpha_{yy} \alpha_{yz} \\ \alpha_{zx} \alpha_{zy} \alpha_{zz} \end{bmatrix} \cdot \begin{bmatrix} E_x \\ E_y \\ E_z \end{bmatrix} \quad \text{or as}$$

$$\mu' = \alpha E \quad (2.4-2)$$

When the charge of the capacitor is reversed, the induced dipole moment is also reversed. When a molecule is exposed to an alternating electric field of high frequency ν_0 , the induced dipole moment will also alternate with the same frequency. Thus, the molecule emits electromagnetic radiation of the frequency ν_0 . Rayleigh scattering is due to this process.

The flexibility of electrons and nuclei in a molecule depends on their mutual distance. If the distance is small, an external field has a smaller influence on the particles than if the distance is large. Therefore, the polarizability of a molecule can be modulated by a vibration. Consequently, the induced dipole moment and therefore also the amplitude of the emitted field are modulated by the frequency of the vibration. The molecule behaves like the radio antenna of an AM station, which emits signals produced by amplitude modulation of a certain carrier frequency with a signal frequency ν_s (Fig. 2.4-4). Analysis of the emitted field with a spectrometer shows a central frequency as well as side bands at a distance of $\pm\nu_s$ cm⁻¹. According to the Boltzmann distribution, a side band with a lower frequency emitted by a molecule has a higher intensity than the side band with the higher frequency.

As a consequence, polyatomic molecules produce Raman spectra like the one shown in Fig. 2.4-5. The molecules are excited by the radiation of an argon ion laser at 515 nm.

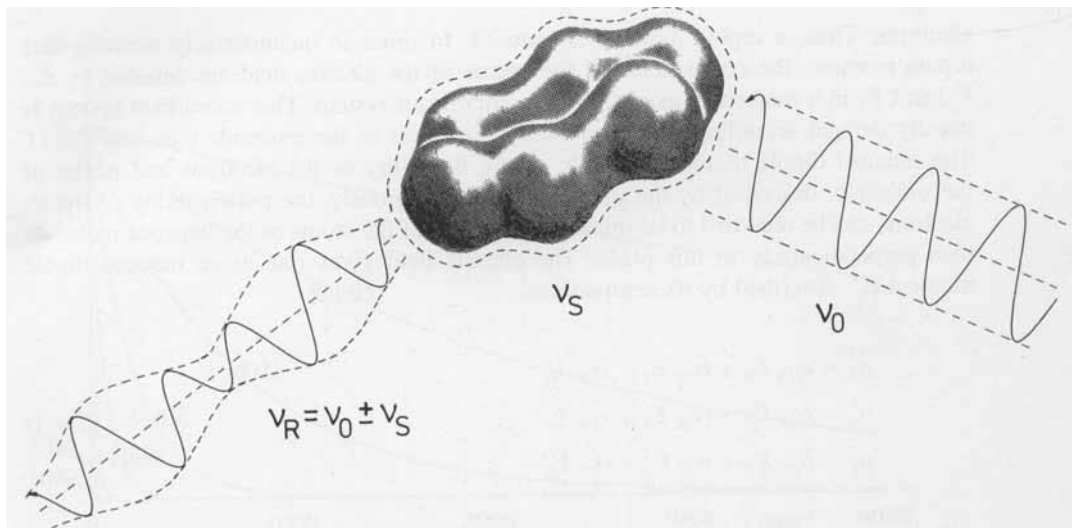


Figure 2.4-4 Modulation of the scattered light by a molecular vibration.

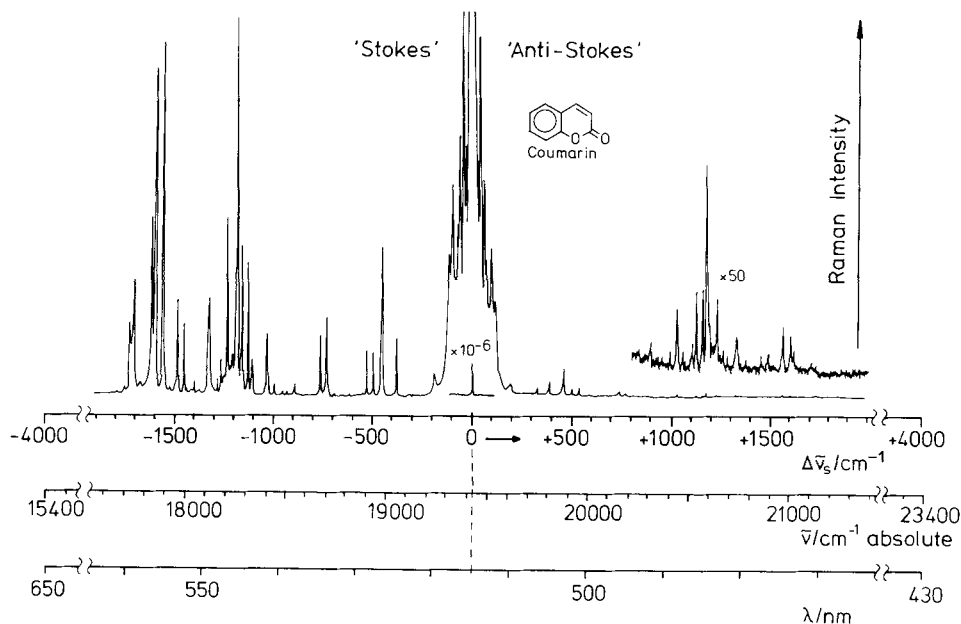


Figure 2.4-5 Raman spectrum of Coumarin, excited with the radiation of the Ar⁺-laser at $\lambda = 514.53 \text{ nm}$ equivalent to $\bar{v} = 19430 \text{ cm}^{-1}$.

The Raman lines at larger wavelengths are much stronger; they reflect those quanta which transfer radiation energy to the molecule by exciting its vibrations. The absolute wavelength scale and the absolute wavenumber scale are not well suited to represent the

Raman spectrum. In order to make Raman spectra easier to evaluate, frequency *shifts* are usually recorded; the exciting radiation defining the zero frequency shift.

Eq. 2.4-3 describes the modulation of the polarizability of a molecule by a vibration with the frequency ν_k :

$$\alpha_k = \alpha_0 + \left(\frac{\partial \alpha}{\partial q_k} \right)_0 q_k^0 \cdot \cos 2\pi \nu_k t + \dots \quad (2.4-3)$$

Here q_k^0 represents the normal coordinate (compare Equation 2.3-2, 3). As a consequence of irradiation, the magnitude of the electric field vector is modulated with the frequency ν_0 , and the molecule shows an induced dipole moment:

$$\mu'_k = \alpha_0 E_0 \cos 2\pi \nu_0 t + \left(\frac{\partial \alpha}{\partial q_k} \right)_0 q_k^0 E_0 \cos 2\pi \nu_0 t \cdot \cos 2\pi \nu_k t \quad (2.4-4)$$

This is equivalent to

$$\begin{aligned} \mu'_k = & \alpha_0 E_0 \cos 2\pi \nu_0 t + \frac{1}{2} \left(\frac{\partial \alpha}{\partial q_k} \right)_0 q_k^0 E_0 [\cos 2\pi(\nu_0 - \nu_k)t + \\ & + \cos 2\pi(\nu_0 + \nu_k)t] \end{aligned} \quad (2.4-5)$$

A Hertzian dipole emits electromagnetic radiation. Its intensity S is proportional to the square of the absolute value of the second time derivative of the induced dipole moment: $S \propto \langle |\ddot{\mu}'_k|^2 \rangle$. Thus, the first of the terms in Equation 2.4-5 describes Rayleigh scattering, the second term concerns Stokes, and the third anti-Stokes Raman scattering. This equation, however, does not show the individual intensities of Stokes and anti-Stokes lines.

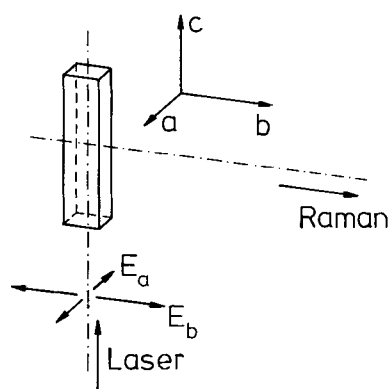


Figure 2.4-6 Orientation of the electric field vector of the exciting vibration with respect to the 'plane of observation', the bc plane.

Placzek's theory (1934) which treats molecules as quantum objects and electromagnetic fields classically, satisfactorily describes the Raman effect on the condition that the exciting frequency differs considerably from the frequencies of electronic as well as of vibrational transitions.

The Raman spectrum of a liquid which is obtained with the experimental arrangement outlined in Fig. 2.4-6 is described by the following equation. The sample is irradiated along the c axis, the Raman radiation is observed in the direction of the b axis of a laboratory fixed Cartesian coordinate system (90° geometry). The sample is irradiated with linearly polarized radiation whose electric vector is oriented in the a direction. This is perpendicular to the plane of observation defined by the directions of irradiation and observation. The calculation of the absolute radiant power of a Raman line is discussed in Sec. 3.5.4. The observed radiant power is proportional to the integral Raman scattering coefficient (the absolute differential Raman scattering cross-section) $d\sigma/d\Omega$ in $\text{cm}^2 \cdot \text{sr}^{-1}$ with σ the cross-section and Ω the solid angle. It is, for the 'Stokes line' of a Raman-active vibration $\tilde{\nu}_k$ given by (Schrötter and Klöckner, 1979):

$$\left(\frac{d\sigma}{d\Omega} \right)_{k\perp} = \frac{\pi^2}{45 \epsilon_0^2} \cdot \frac{b_k^2 \cdot (\tilde{\nu}_0 - \tilde{\nu}_k)^4}{1 - \exp(-hc\tilde{\nu}_k/kT)} \cdot g_k \cdot (45 \bar{\alpha}'_k^2 + 7 \gamma'_k^2) \cdot L \quad (2.4-6)$$

Here, $\tilde{\nu}_0$ and $\tilde{\nu}_k$ represent the frequency of the exciting radiation and the excited vibration, respectively, and g_k is the degree of degeneracy of this vibration (see Sec. 2.7.2). The expression $g_k \cdot (45 \bar{\alpha}'_k^2 + 7 \gamma'_k^2)$ is known as the *scattering activity*, $b_k^2 = h/8\pi^2 c \tilde{\nu}_k$ is the square of the 'zero point amplitude' of the vibration. Eq. 2.4-6 may be simplified:

$$\left(\frac{d\sigma}{d\Omega} \right)_{k\perp} = \frac{h}{2^3 c \epsilon_0^2} \cdot \frac{(\tilde{\nu}_0 - \tilde{\nu}_k)^4}{\tilde{\nu}_k [1 - \exp(-hc\tilde{\nu}_k/kT)]} \cdot g_k \cdot \left(\bar{\alpha}'_k^2 + \frac{7}{45} \gamma'_k^2 \right) \cdot L \quad (2.4-6')$$

The internal field factor

$$L = (n_R/n_0)(n_R^2 + 2)^2(n_0^2 + 2)^2 / 3^4 \quad (2.4-7)$$

(with n_0 and n_R the refractive indices at the wavelength of the exciting and the Raman radiation, respectively) takes into account the increase of the incident and scattered electric field due to the dielectric nature of the scattering medium (Eckhardt and Wagner, 1966; Nestor and Lippincott, 1973).

If the electric vector of the exciting radiation is oriented in b direction, parallel to the plane of the direction of irradiation and observation, then the scattering coefficient is given by:

$$\left(\frac{d\sigma}{d\Omega} \right)_{k\parallel} = \frac{h}{2^3 c \epsilon_0^2} \cdot \frac{(\tilde{\nu}_0 - \tilde{\nu}_k)^4}{\tilde{\nu}_k [1 - \exp(-hc\tilde{\nu}_k/kT)]} \cdot g_k \cdot \left(\frac{6}{45} \gamma'_k^2 \right) \cdot L \quad (2.4-8)$$

In the case of anti-Stokes Raman scattering with the electric vector of the exciting radiation oriented perpendicularly to the plane of observation, the scattering coefficient is:

$$\left(\frac{d\sigma}{d\Omega} \right)_{k\perp}^+ = \frac{h}{2^3 c \epsilon_0^2} \cdot \frac{(\tilde{\nu}_0 + \tilde{\nu}_k)^4}{\tilde{\nu}_k [\exp(hc\tilde{\nu}_k/kT) - 1]} \cdot g_k \cdot \left(\bar{\alpha}'_k^2 + \frac{7}{45} \gamma'_k{}^2 \right) \quad (2.4-9)$$

The ratio of the coefficients of the Stokes and anti-Stokes Raman lines is given by:

$$\left(\frac{d\sigma}{d\Omega} \right)_{k\perp}^- / \left(\frac{d\sigma}{d\Omega} \right)_{k\perp}^+ = \left(\frac{\tilde{\nu}_0 - \tilde{\nu}_k}{\tilde{\nu}_0 + \tilde{\nu}_k} \right)^4 \cdot \exp(hc\tilde{\nu}_k/kT) \quad (2.4-10)$$

This equation allows contact-free determination of the sample temperature. In order to evaluate it, the measured intensities have to be transformed into absolute values, and they must be corrected with respect to the spectral sensitivity of the spectrometer (see Secs. 3.5.4 and 6.8.4.2.3). As shown in Fig. 2.4-2 the optimum range of the Raman bands employed for this purpose is depending on the expected temperature range. The intensity ratio has to be of a value which can be measured with a large signal-to-noise ratio. For the measurement of sample temperatures near room temperature Raman lines in the range $0 \dots 500 \text{ cm}^{-1}$ are useful, for temperatures of about 100 K Raman lines with a wavenumber of less than 200 cm^{-1} should be employed.

In these equations discussed above, $\bar{\alpha}'_k$ and γ'_k stand for the isotropic and the anisotropic part of the change of the polarizability, respectively, given by the equations below (in order to simplify these equations, the subscript k has generally been omitted in all terms):

$$\bar{\alpha}' = \frac{1}{3} [\alpha'_{xx} + \alpha'_{yy} + \alpha'_{zz}] \quad (2.4-11)$$

$$\begin{aligned} \gamma'^2 &= \frac{1}{2} [(\alpha'_{xx} - \alpha'_{yy})^2 + (\alpha'_{yy} - \alpha'_{zz})^2 + (\alpha'_{zz} - \alpha'_{xx})^2 + \\ &\quad + 6(\alpha'_{xy}^2 + \alpha'_{xz}^2 + \alpha'_{yz}^2)] \end{aligned} \quad (2.4-12)$$

The terms $\alpha'_{ij} = \left(\frac{\partial \alpha_{ij}}{\partial q} \right)_0$ are the components of the tensor of the polarizability change resulting from a normal vibration q . This tensor is usually symmetric. The polarizability has the dimension $\text{J}^{-1} \text{C}^2 \text{m}^2$. In the old literature the polarizability has been described as a volume, since there is an analogy to the molecular volume, in $\text{\AA}^3 = 10^{-24} \text{cm}^3$. If the polarizability, given in SI units is divided by $4\pi\epsilon_0$ (in $\text{J}^{-1} \text{C}^2 \text{m}^{-1}$), then a volume results, the *polarizability volume*. The normal coordinates are 'mass weighted' and have the dimension $\text{cm} \cdot \text{g}^{1/2}$.

Very useful information may be derived from the intensities in spectra which are obtained with the electric vector of the exciting radiation oriented parallelly and perpendicularly to the plane of observation (Eqs. 2.4-7 and 2.4-8). The ratio of the two scattering coefficients is known as the *depolarization ratio* ρ :

$$\rho_k = \frac{S_{k\parallel}}{S_{k\perp}} = \frac{6\gamma'_k{}^2}{45\alpha'_k{}^2 + 7\gamma'_k{}^2} \quad (2.4-13)$$

If the Raman radiation is observed through a polarizer with its electric vector perpendicular to the plane of scattering ($\parallel c$ in Fig. 2.4-6) then the equation 2.4-13 changes:

$$\rho_k = \frac{S_{k\parallel}}{S_{k\perp}} = \frac{3\gamma_k'^2}{45\alpha_k'^2 + 4\gamma_k'^2} \quad (2.4-13')$$

In Sec. 2.7.3.4 it is demonstrated that the depolarization ratio may be used to determine the symmetry of the vibrations of molecules in the liquid state, see also Long (1977).

As already pointed out, this description of the Raman effect is based on the 'polarizability theory' (Placzek, 1934) which is valid in a good approximation if the exciting frequency ν_0 is much higher than the frequency of the vibrational transition ν_v , but lower than the frequency of the transition to the electronic excited state ν_e . If, on the other hand, ν_0 is approaching ν_e , then resonances occur which considerably enhance the intensities of the Raman lines, i.e., the *resonance Raman effect*. This effect and its applications are described in Sec. 6.1 and also in Secs. 4.2 and 4.8.

Raman spectra, as infrared spectra show overtones and combination bands. These are due to mechanical anharmonicities (Eq. 2.1-16) as well as to electrical anharmonicities (higher terms in Eq. 2.4-3).

If the exciting radiation has a very high intensity, as in 'giant laser pulses', the induced dipole moment (Eq. 2.4-1) is larger than in the linear approximation:

$$\mu' = \alpha E + \frac{1}{2}\beta E^2 + \frac{1}{6}\gamma E^3 + \dots \quad (2.4-14)$$

This produces 'non-linear effects', such as hyper Raman scattering, CARS, and other effects. They are described in Secs. 3.6 and 6.1.

2.5 Frequencies of the vibrations of typical model molecules

Vibrational spectra contain information about every aspect of the molecular structure. This information can be evaluated by comparing observed infrared and Raman spectra with those calculated from systematically modified model molecules until the best adjustment is achieved (see Sec. 5.2). However, very simple calculations may help to assign the observed bands to structural features or to predict the effect of a change of the molecular or crystal structure as a result of a chemical reaction or a phase transition.

Such estimations have been known since the early days of vibrational spectroscopy (Kohlrausch 1931, 1938, 1943) and are discussed also by Herzberg (1945), Siebert (1966), Nakamoto (1978), Colthup, Daly and Wiberley (1990), Schrader (1968, 1980) and Weidlein, Müller and Dehnicke (1982). Examples are given in this book in Secs. 4.1

and 4.2.2.2. Such models usually ignore anharmonicity and interaction force constants, they treat molecules just as systems of balls, connected by springs, based essentially on Eq. 2.1-10:

$$\tilde{\nu} = C \sqrt{f \left(\frac{1}{m_1} + \frac{1}{m_2} \right)} \quad (2.5-1)$$

Here, $C = 1303$, if $\tilde{\nu}$ is given in cm^{-1} , the force constant f in N/cm , and the masses m_1 and m_2 in atomic mass units.

2.5.1 Stretching vibrations of linear triatomic molecules

Symmetrical molecules

Eq. 2.5-1 can be applied directly to the calculation of the stretching frequencies of a symmetrical linear triatomic molecule. The molecule contains two bonds, therefore, we expect two stretching vibrations. During the *in-phase* or *symmetric stretching* vibration, the middle atom does not move. Therefore, the frequency is equal to that of a ball with the mass m_1 connected by a spring with the force constant f to an infinite mass m_2 (Fig. 2.5-1 a). Therefore, the frequency of the symmetric stretching vibration is given by:

$$\tilde{\nu}_s = C \sqrt{f \left(\frac{1}{m_1} + \frac{1}{\infty} \right)} = C \sqrt{\frac{f}{m_1}}. \quad (2.5-2)$$

For the *out-of-phase* or *anti-symmetric stretching* vibration, the ball with the mass m_2 can be regarded as being split into two halves which are moving at the same frequency and phase (Fig. 2.5-1 b). Therefore, its frequency is given by:

$$\tilde{\nu}_{as} = C \sqrt{f \left(\frac{1}{m_1} + \frac{2}{m_2} \right)}. \quad (2.5-3)$$

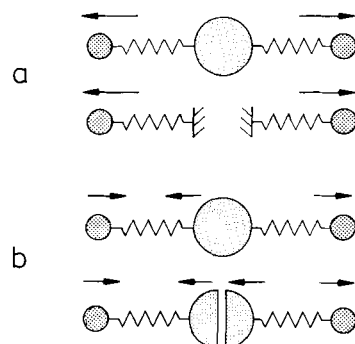


Figure 2.5-1 Stretching vibrations of a symmetric linear triatomic molecule, **a** symmetric (in-phase) stretching vibration, **b**, antisymmetric (out-of-phase) stretching vibration.

As a consequence we see that the symmetric vibration is independent of the mass of the atom in the center. However, the frequency of the anti-symmetric vibration is strongly dependent on the mass of the middle atom, especially when it is not very large. If all three atoms have the same mass m_1 , then the frequency of the anti-symmetric vibration is given by:

$$\tilde{\nu}_{as} = C \sqrt{f\left(\frac{1}{m_1} + \frac{2}{m_1}\right)} = C \sqrt{\frac{3f}{m_1}}. \quad (2.5-4)$$

For a bent triatomic symmetrical molecule with a bending angle α , the frequencies of the symmetric and anti-symmetric vibrations are given by:

$$\tilde{\nu}_{s,as} = C \sqrt{f\left(\frac{1}{m_1} + \frac{1 \pm \cos \alpha}{m_2}\right)}. \quad (2.5-5)$$

The frequency difference between the in-phase and the out-of-phase vibration and their relative magnitude depends on the bond angle α , as demonstrated in Fig. 2.5-2. If $\alpha > 90^\circ$, then the in-phase vibration has a lower frequency than the out-of-phase vibration; if, on the other hand, $\alpha < 90^\circ$, then the in-phase vibration is found at a higher frequency than the out-of-phase vibration. At 90° , the frequencies of the two vibrations are equal.

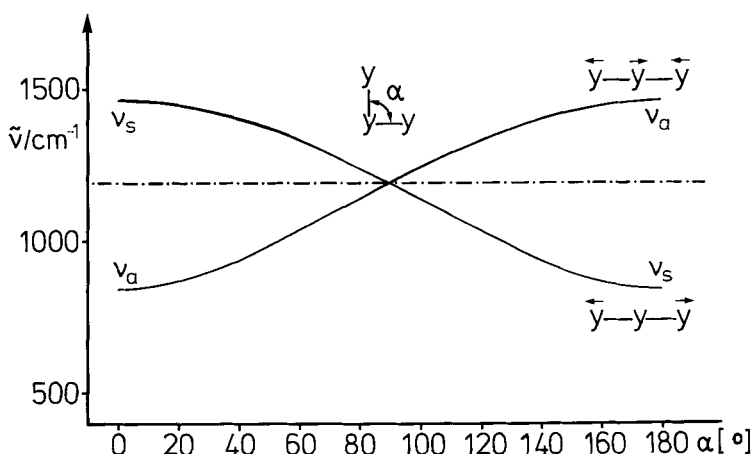


Figure 2.5-2 Stretching vibrations of a symmetric angular triatomic molecule Y-Y-Y, depending on the bond angle α , Y \cong C; $f_1 = f_2 = 5 \text{ N} \cdot \text{cm}^{-1}$; ν_s : symmetric (in-phase), ν_a : antisymmetric (out-of-phase vibration), the trace $\cdots \cdots$ shows the frequency of the uncoupled oscillators.

Unsymmetrical linear triatomic molecules

Two special cases are discussed here: A linear X-Y≡Y molecule with a variable mass of the atom X and a linear Y···Y···Y molecule with variable force constants. Both demonstrate characteristic localized vibrations as well as coupled vibrations of both bonds.

The frequencies of the stretching vibrations of the X-Y≡Y molecule model (corresponding to X-C≡C or X-C≡N) are shown in Fig. 2.5-3. The atomic mass of X is variable. If X has the mass 1 (corresponding to H), then there are two characteristic vibrations, i.e., the X-Y and the Y≡Y vibration. Even if X has a large mass (corresponding to C, F, Cl, Br, I), there is a characteristic X-Y and a Y≡Y vibration.

If the X atom, on the other hand, has a mass of 2 or 3 (corresponding to D and T), then according to Eq. (2.5-1) the two uncoupled oscillators (X-Y and Y≡Y) have almost the same frequency. As a result, there are no characteristic frequencies of individual bonds,

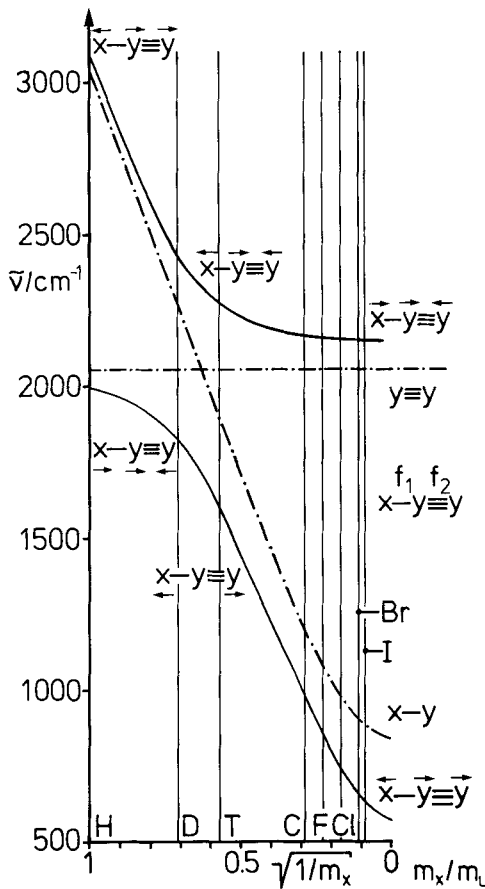


Figure 2.5-3 Stretching vibrations of a linear triatomic molecule, X-Y≡Y, X ≡ H, D, T, C, F, Cl, Br, I; Y ≡ C; $f_1 = 5 \text{ N} \cdot \text{cm}^{-1}$, $f_2 = 15 \text{ N} \cdot \text{cm}^{-1}$; the trace ····· shows the frequencies of the uncoupled oscillators.

but only an in-phase and an out-of-phase vibration of the two bonds at lower resp. higher frequency.

Fig. 2.5-4 demonstrates the case of equal masses and variable force constants. The $\text{Y}-\text{Y}\equiv\text{Y}$ model shows characteristic vibrations of the $\text{Y}-\text{Y}$ bonds at low frequencies while those of the $\text{Y}\equiv\text{Y}$ bonds are found at high frequencies. If the force constants are changed to become equal both isolated oscillators have the same frequency. They are, however, coupled and show an in-phase vibration at a low and an out-of-phase-vibration at a high frequency.

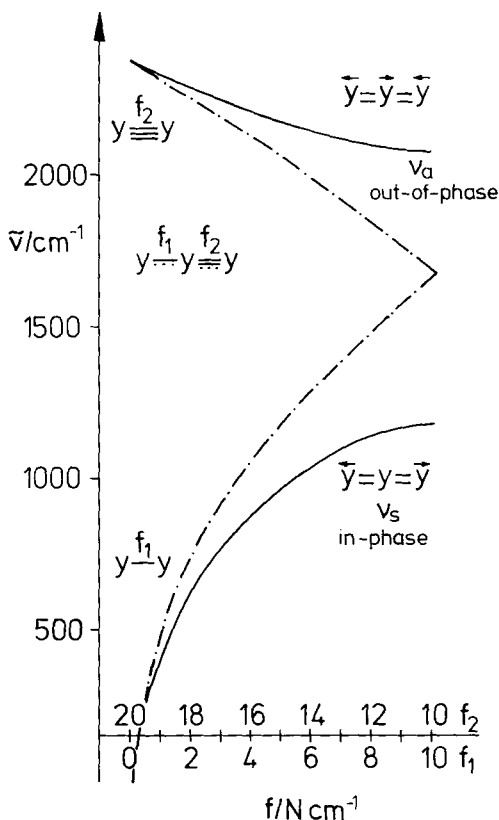


Figure 2.5-4 Stretching vibrations of a linear triatomic molecule with variable force constants, from $\text{Y}-\text{Y}\equiv\text{Y}$ to $\text{Y}=\text{Y}=\text{Y}$, $\text{Y} \equiv \text{C}$; $f_1 = 0 \dots 10 \text{ N} \cdot \text{cm}^{-1}$, $f_2 = 20 \dots 10 \text{ N} \cdot \text{cm}^{-1}$; the trace $\cdots \cdots$ shows the frequencies of the uncoupled oscillators.

2.5.2 Stretching vibrations of cyclic molecules and molecular chains

The *in-phase* (ip) and *out-of-phase* (oop) vibrations of the bonds in planar rings with an even number of atoms, as well as those in a zig-zag chain of infinite length (Fig. 2.5-5) follow the same equation:

$$\tilde{\nu}_{ip,oop} = C \sqrt{\frac{2f}{m}} (1 \pm \cos \alpha) \quad (2.5-6)$$

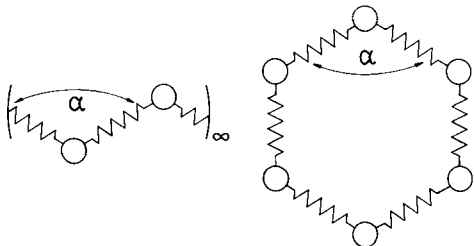


Figure 2.5-5 Models of an infinite chain and a ring with an even number of atoms having a bond angle α .

In the special case of a linear chain with $\alpha = 180^\circ$, the in-phase vibration has the frequency 0, it is a translation of the whole molecule. The out-of-phase-vibration of the linear chain has a frequency of

$$\tilde{\nu}_{oop} = C \sqrt{\frac{4f}{m}} \quad (2.5-7)$$

In addition to this special vibration, in which neighboring atoms move antiparallel with the same absolute amplitude, an infinite number of other vibrations exists where neighboring atoms have different amplitudes.



Figure 2.5-6 Zig-zag chains of different length, bond angle $\alpha = 109.5^\circ$, $m \equiv C$, $f = 5 \text{ N} \cdot \text{cm}^{-1}$; the trace \dots shows the frequency of the uncoupled oscillators.

The following equation gives the spectrum of the $n-1$ frequencies of a finite zig-zag chain of n atoms with a valence angle α :

$$\tilde{\nu}_i = C \sqrt{\frac{2f}{m}} \left(1 + \cos \alpha \cdot \cos \frac{i\pi}{n} \right), \quad i = 1 \dots (n-1) \quad (2.5-8)$$

These frequencies (calculated with $\alpha = 109.5^\circ$, $m = 12$ atomic mass units and $f = 5 \text{ N/cm}$) are shown in Fig. 2.5-6. It demonstrates that a connection of several similar oscillators to form chains results in exactly as many chain frequencies as there are equal coupled bonds. Although infinitely long chains exhibit infinitely many chain vibrations, only the highest and the lowest of these frequencies are visible in the optical spectra. For long chains, the upper and lower frequency limits (for $i = 1$ and $n - 1$, respectively) approach the values given by Eq. (2.5-6). Indeed, only the lowest and highest of these frequencies are observed in the infrared and Raman spectra of macromolecules.

Such calculations are very approximate, especially because coupling with the bending vibrations of the chain and those of other groups (C-H bonds), the interaction force constants, and the anharmonicity are ignored. This is discussed elsewhere in this book (see the following section as well as Secs. 4.2 and 5.2). However, these calculations allow insight into typical properties of vibrating molecules.

2.5.3 General rules concerning vibrations

- If two oscillators with different frequencies are coupled, then the low frequency is shifted to a lower value, the high frequency to a higher value. This effect is more pronounced the smaller the difference between the original frequencies is.
- If in a molecule n oscillators of the same frequency are coupled, then there are n different stretching normal vibrations in which all oscillators participate, but with different phases. These vibrations are observed at a higher respectively lower frequency than those of the isolated oscillator. The difference between frequencies increases with the strength of the coupling. The frequency of an isolated oscillator can be derived from the observed frequencies of the coupled vibrations by

$$\bar{\nu} = \sqrt{\frac{1}{n} \sum_{i=1}^n \tilde{\nu}_i^2}. \quad (2.5-9)$$

- All normal vibrations are symmetric or anti-symmetric with respect to the symmetry operations of the molecule, i.e., they may be characterized by a symmetry species (irreducible representation), see Sec. 2.7.
- If in a vibrating system any mass is increased or any force constant is reduced, then all vibrational frequencies are either reduced or they remain constant, but no frequency is increased (Rayleigh's rule).
- If a molecule contains a bond or a group whose vibrational frequency (viewed as an isolated unit) differs considerably from those of adjacent groups, then there are always vibrations which are primarily localized on this specific bond or group. Such vibrations therefore exhibit frequencies as well as infrared and Raman intensities which are *characteristic* of this particular bond or group. Examples are groups with isolated multiple bonds or groups with heavy atoms in an environment of single bonds between light atoms (e.g., saturated hydrocarbons).

- There are two main types of vibrations. Those which change bond lengths are called *stretching* vibrations and those which change bond angles are *bending* and *torsional* vibrations. Bending vibrations deform mainly bond angles at one atom, while torsional vibrations change the dihedral angle between planes defined by the ligands at both atoms of a bond.
- The number of vibrational degrees of freedom of a non-linear molecule with n atoms is

$$f = 3n - 6, \quad (2.5-10)$$

while for a linear molecule this number is $f = 3n - 5$. For a non-linear and noncyclic molecule with b chemical bonds, the number of stretching degrees of freedom is (Decius, 1949):

$$n_b = b \quad (2.5-11)$$

The number of bending degrees of freedom is:

$$n_\Phi = 4b - 3n + n_1 \quad (2.5-12)$$

Here, n_1 is the number of singly bonded (terminal) atoms.

The number of torsions is equivalent to the number of non-terminal bonds:

$$n_\tau = b - n_1 \quad (2.5-13)$$

- The observed normal vibrations are a linear combination of these degrees of freedom. In addition, combinations of normal vibrations may be visible, i.e., *harmonics*, *sum* and *difference 'tones'*. Combination tones usually show weak bands.
- An overtone (of a deformation) vibration which has about the same frequency as a fundamental (stretching) vibration of the same bonds may '*mix*' with the fundamental to produce two bands of nearly equal intensity. This effect, which may produce supernumerary bands is called *Fermi resonance* (Fermi, 1931). A necessary condition for Fermi resonance is that the overtone and the fundamental must belong to the same symmetry species (see Sec. 2.7).
- If a molecule is already in a vibrational excited state when it undergoes a further excitation, a *hot band* may be observed which – due to anharmonicity – has a lower frequency compared to the transition from the ground state.
- Some characteristic vibrations have been given special descriptive names (Mecke 1932). Stretching vibrations of an XY group are called $\nu(XY)$, symmetric deformation (or scissoring) vibrations of XY_2 or XY_3 groups are referred to as $\delta(XY_2)$ or $\delta(XY_3)$, other deformation vibrations are called wagging $\omega(XY_2)$, rocking $\rho(XY_2)$, or twisting $\tau(XY_2)$. Vibrations of CH_2 and CH_3 groups are shown in Fig. 4.1-1 (Section 4.1). Deformation vibrations of an atom out of a plane defined by three neighboring atoms are called out-of-plane vibrations γ . An example is the $\gamma(C-H)$ vibration of the hydrogen atoms on a benzene ring. If in-plane and out-of-plane deformations of heavy atoms are described (instead of H atoms) Δ and Γ may stand for δ and γ .

2.5.4 Estimating force constants

Force constants may be calculated on the basis of observed spectra or by quantum-chemical methods. They are heavily dependent on the definition of the force field used for the calculation (see Sec. 5.2). However, for estimations of the general behavior of the observed frequencies, the simple valence force field SVFF, (compare Sec. 5.2) is sufficient. It takes into account the force constants of bond stretchings and different kinds of angle deformations. It neglects interaction force constants which describe the changes of the elastic properties of one bond when others are deformed. The stretching force constants have values between 1 and 25 N/cm. They are tabulated in the books cited in the second paragraph of Sec. 2.5. Siebert (1966) found an equation which allows approximate calculation of force constants of any single bond:

$$f_{XY} = 7.20 \cdot \frac{Z_X \cdot Z_Y}{n_X^3 \cdot n_Y^3} \quad (2.5-14)$$

Here, Z_i are the atomic numbers and n_i are the principal quantum numbers of its valence electrons. The force constant for a C-C single bond is calculated to be 4.05 N/cm, the experimental value is 4.45 N/cm. Siebert also describes the relation between the force constant f_N of a multiple bond of the order N to that of a single bond f_1 and the lengths r_N and r_1 of these bonds:

$$f_N = \frac{N \cdot f_1 \cdot r_1}{r_N} \quad (2.5-15)$$

As a rough estimate, the force constant of a multiple bond is proportional to the bond order. Force constants of angle bending motions are one order of magnitude smaller than stretching force constants.

For the description of the elastic forces within molecular crystals and between atoms of the same molecule which are not directly connected by a chemical bond but which are approaching each other (as in biomolecules), intermolecular force constants are necessary (see Secs. 5.2). These may be calculated using atom-atom potential functions. Kitaigorodsky (1973) introduced a 'universal potential' of the Buckingham type (in kcal /mol):

$$V(r) = 3.5[8600 \exp(-13 r/r_0) - 0.04(r_0/r)^6] \quad (2.5-16)$$

The parameter r_0 is equal to or by about 10 % larger than the van-der-Waals radii of the approaching atoms. The second derivative of this equation gives the force constant (in N/cm) as a function of the interatomic distance (Schneider et al., 1975) :

$$f_{X \dots Y} = -0.041(r_0/r)^8 + 35320(r/r_0)^2 \exp(-13 r/r_0) \quad (2.5-17)$$

If the atoms carry charges, then there is a contribution to the force constants, according to Coulomb's law:

$$f_{X \dots Y, \text{Coul}} = 4.613 \frac{q_X \cdot q_Y}{r^3} \quad (2.5-18)$$

Here, q_X and q_Y are the charges of the atoms X and Y in atomic charge units and r its distance in Å. If the charges have opposite signs, then the contribution to the force constant is negative.

Since the intermolecular force constants are mainly due to the repulsive part of the potential, simple exponential functions are often sufficient to describe the intermolecular force constants (Fig. 2.5-7; Harada and Shimanouchi, 1967; Schrader, 1978).

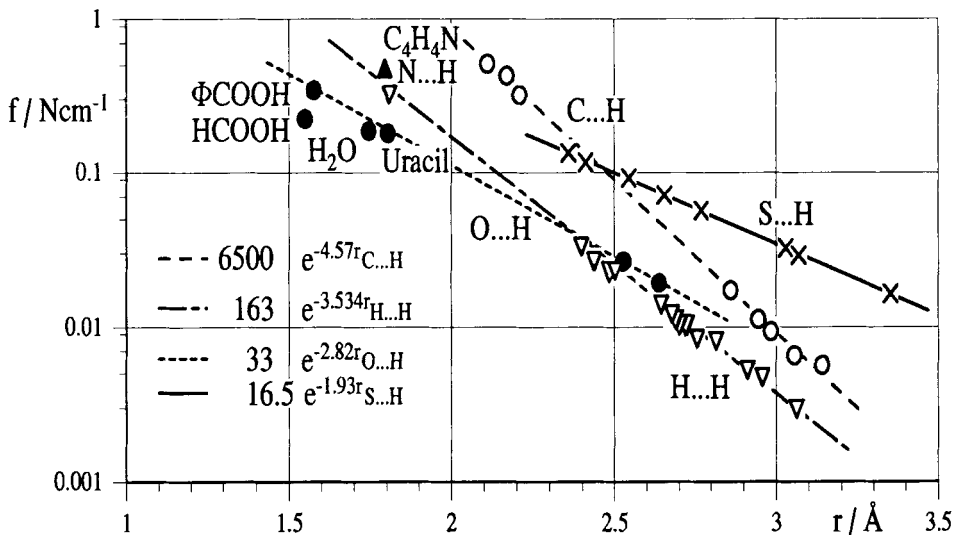


Figure 2.5-7 Interatomic force constants for different non-bonded pairs of atoms, $\Phi = C_6H_5$.

2.6 Vibrational spectra of molecules in different states

The spectra of infrared and Raman active normal vibrations (see Sec. 2.7) depend on whether the sample is in the liquid, gaseous or crystalline state. However, the main features which are needed to identify a molecule or to elucidate its structure are clearly visible in spectra of any state.

In the gaseous state coupling of the vibrational transitions with the rotational degrees of freedom give rise to rotational-vibrational bands (Fig. 2.6-1A). The structures of these bands characterize the shape of a molecule and its symmetry (see Sec. 2.7). Spectral lines in the far-infrared range and in low-frequency Raman spectra are due to pure, quantized rotations of the molecules. Infrared and Raman spectra of gases are discussed in detail in Secs. 4.3.1 and 4.3.2.

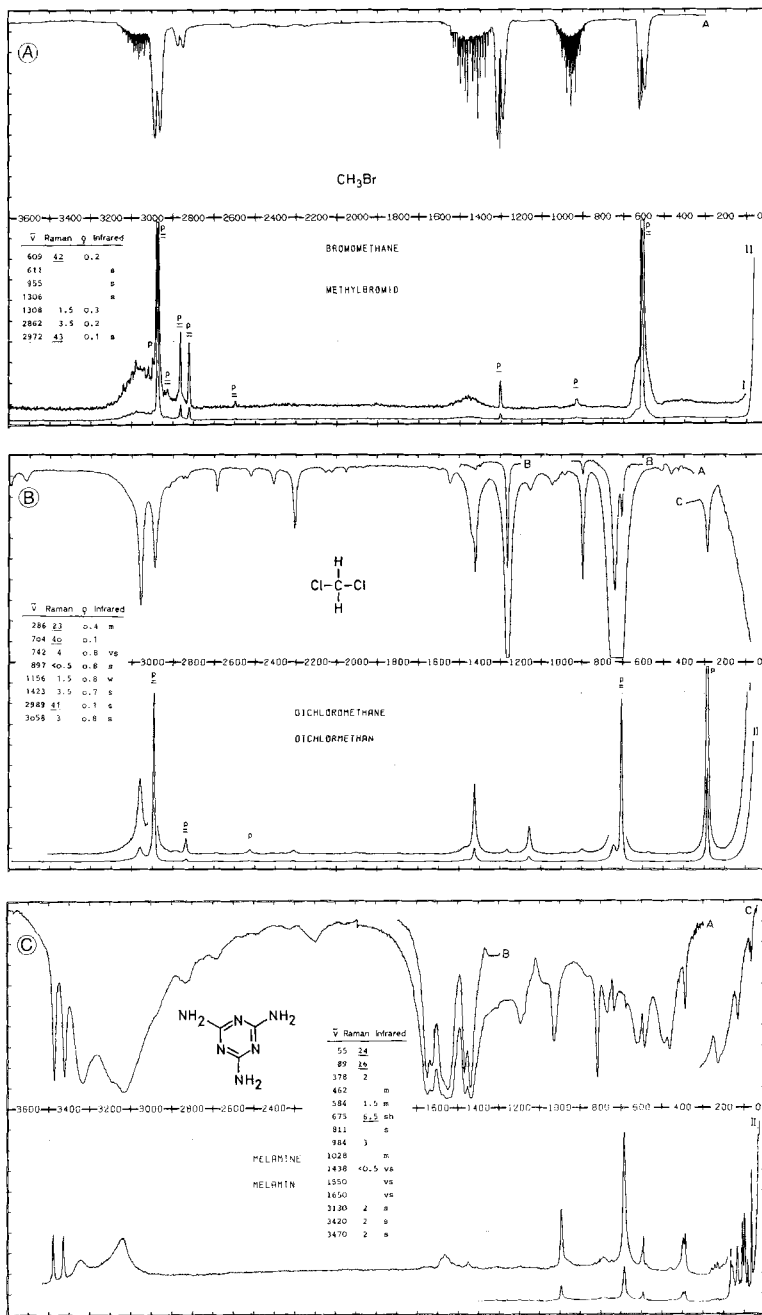


Figure 2.6-1 Infrared (above) and Raman (below) spectrum of A a gas: bromomethane, B a liquid: dichloromethane, and C a crystal powder: melamine, from Schrader (1989) A2-43, A2-40, and I13-01.

Spectra of samples in the liquid state (Fig. 2.6-1B) are given by molecules which may have any orientation with respect to the beam of the spectrometer. Like in gases, flexible molecules in a liquid may assume any of the possible conformations. Some bands are broad, since they are the sum of spectra due to different complexes of interacting molecules. In the low frequency region spectra often show 'wings' due to hindered translational and rotational motions of randomly oriented molecules in associates. These are analogous to the lattice vibrations in molecular crystals, which, however, give rise to sharp and well-defined bands. The depolarization ratio ρ of a Raman spectrum of molecules in the liquid state (Eqs. 2.4-11...13) characterizes the symmetry of the vibrations, i.e., it allows to differ between totally symmetric and all other vibrations (see Sec. 2.7.3.4).

Spectra of molecules in the crystalline state, i.e., of molecular crystals, are obtained from molecules which are at fixed positions (sites) in the lattice (Fig. 2.6-1C). Normal (first-order) infrared and Raman spectra can be seen as spectra of 'hyper molecules', the unit cells (Schneider 1974, Schneider et al., 1975). As a consequence, any molecular vibration is split into as many components as there are molecules present in the unit cell. Their infrared and Raman activity is determined by the symmetry of the unit cell. In addition, the translational and rotational degrees of freedom of molecules at their sites are 'frozen' to give rise to lattice vibrations: translational vibrations of the molecules at their sites and rotational vibrations about their main inertial axes, so-called librations.

In Fig. 2.6-2 outlines the change of the vibrational spectrum of a free molecule, as it is introduced into a molecular crystal. First, its center-of-mass and its axes are fixed with regard to the crystal axes. The *oriented gas model* allows an estimation of the relative infrared and Raman intensities of all components of a molecular vibration by taking into account the relative phases of the same vibration in the different molecules constituting the unit cell and the angle between the Cartesian axes of the molecules and the crystal. However, molecules are deformed by intermolecular static forces within the lattice. Thus, they usually have a lower symmetry than free molecules. This *site symmetry model* also is not sufficient, since it neglects dynamical interactions, i.e., coupling of the vibrations of neighboring molecules. These effects can be treated by the *factor group model*, which regards the unit cell as a vibrating hyper molecule. All vibrations of the free molecules are split into as many components as there are molecules in the unit cells, this is called *factor group splitting*. Moreover, all unit cells in a crystal also couple, i.e., they produce *optical and acoustical branches*. Since the wavelengths of the radiation employed for infrared and Raman spectroscopy are several orders of magnitude longer than the dimensions of the unit cells, first-order infrared and Raman spectra show only those vibrational states of the crystal where the wave vector approaches 0. This means that neighboring unit cells vibrate in phase. The factor group model is therefore a good model for the interpretation of infrared and Raman spectra of molecular crystals.

These facts are discussed in detail in Secs. 2.7 and 4.5. Many other crystals, e.g., ionic crystals, semiconductors, or metals, are three-dimensional macromolecules consisting of molecules or atoms which have essentially lost their individuality. These are discussed in Sec. 4.8.

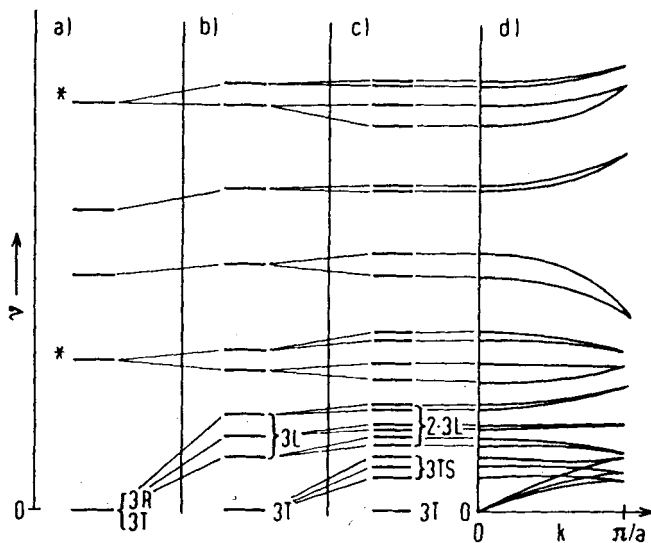


Figure 2.6-2 Variation of the frequencies by the incorporation of a tetraatomic molecule with two degenerate vibrational states (*) in a crystal lattice. **a** spectrum of the free molecule, R = rotations, T = translations; **b** static influence of the crystal lattice. The degenerate states split, the free rotations change into librations L ; **c** dynamic coupling of the vibrations of molecules within a primitive unit cell with $z = 2$ molecules. Each vibrational level of a molecule splits into z components and $3z - 3$ translational vibrations TS and $3z$ librations L appear; **d** dependence of the vibrational frequencies on the wave vector k of the coupled vibrations of all unit cells in the lattice. The three 'acoustic branches' arise from the three free translations with $\tilde{\nu} = 0$ (for $k \rightarrow 0$) of the unit cell; all vibrations of the unit cells with $\tilde{\nu} \neq 0$ (for $k \rightarrow 0$) give 'optical branches'.

2.7 The symmetry of molecules and molecular vibrations

"The word *symmetry* comes from the greek word *symmetria* and may be defined as harmony or balance in the proportions of parts to the whole. Symmetry is associated with beauty – with pleasing proportions or regularity in form, harmonious arrangement or regular repetition of certain characteristics. Nature shows many examples of symmetry: plants, animals, crystals and man's culture always employed symmetry – in architecture, painting, sculpture and music. Four types of symmetry can be found:

1. the radially symmetry type (wheel type),
2. the bilateral symmetry type,
3. the serial symmetry type and
4. the asymmetric type" (Ferraro and Ziomek, 1975).

Brandmüller (1980) and Claus (1980) discuss symmetry in science and art as well as in music.

Symmetry is a common quality in science; most properties of elementary particles, atoms, and molecules are symmetric, Brandmüller (1986), Brandmüller and Winter (1985), Brandmüller and Claus (1988). Since symmetry strictly defines relations between molecular spectra and molecular structures, the present section focuses on the mathematical tools which are necessary to apply symmetry concepts to vibrational spectroscopy.

The most important information gained by using these tools is the number of vibrations which have definite properties regarding infrared or Raman activity and which are characterized by the names of symmetry species or, in the language of mathematics, irreducible representations. A good introduction to chemical applications of group theory has been published by Cotton (1990). Standard publications on the application of group theory to infrared and Raman spectroscopy are the books of Herzberg (1945), Bhagavantam and Venkatarayudu (1969), and Wilson, Decius, and Cross (1955). General applications to spectroscopy are discussed by Bunker (1979). The theory of symmetry in chemistry is described by Wald (1985) and Steinborn (1993). Applications of group theory to the spectra of crystals have been described by Turrell (1972), Behringer (1973), Schrader (1978), and Rousseau et al. (1981), while Papoušek and Aliev (1982) applied group theory to spectra of gaseous samples.

2.7.1 Symmetry operators, symmetry elements

The symmetry of many molecules and especially of crystals is immediately obvious. Benzene has a six-fold symmetry axis and is planar, buckminsterfullerene (or just fullerene or footballene) contains 60 carbon atoms, regularly arranged in six- and five-membered rings with the same symmetry (point group I_h) as that of the Platonic bodies pentagon dodecahedron and icosahedron (Fig. 2.7-1). Most crystals exhibit macroscopically visible symmetry axes and planes. In order to utilize the symmetry of molecules and crystals for vibrational spectroscopy, the symmetry properties have to be defined conveniently.

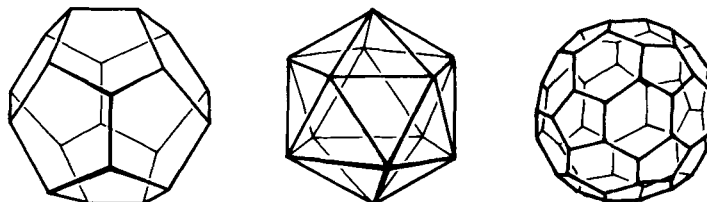


Figure 2.7-1 Three objects belonging to the same point group I_h : the pentagondodecahedron, the icosahedron, and the buckminsterfullerene.

For treating symmetry properties of molecules, *symmetry operators* are defined, which, when applied to a molecule, bring it into coincidence with itself. For molecules there are five types of symmetry operators:

- E Identity operator, a trivial but necessary operator (see Sec. 2.7.3.1)
- i Inversion operator, representing reflection at a center of symmetry
- σ Reflection operator, representing reflection on a plane
- C_n^k n -fold rotation operator, describing k successive rotations by an angle of $2\pi/n$ about an n -fold rotation axis (proper axis), n is the order of the axis, with $n = 2, 3, 4, \dots$; $k = 1, 2, \dots, (n-1)$ or $n \rightarrow \infty$; $k = 1, 2, \dots, \infty$.
- S_n^k n -fold rotation-reflection operator, defining k successive rotation-reflections about an n -fold rotation-reflection axis (improper axis): rotation by an angle of $2\pi/n$, followed by reflection on a plane perpendicular to the axis, with $n = 3, 4, \dots$; $k = 1, 2, \dots, (n-1)$ or $n \rightarrow \infty$; $k = 1, 2, \dots, \infty$.

An object is definitely *chiral* if it does not allow any S_n symmetry operation, where n may be any number; in this connection it is important to realize that S_1 would be identical to σ , S_2 to i (Fig. 2.7-2).

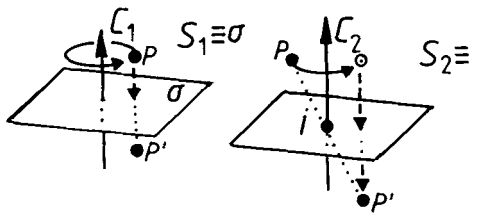


Figure 2.7-2 A symmetry operation S_1 , rotation by 360° with following reflection is identical with σ , a reflection by the horizontal plane; an operation S_2 , rotation by 180° with following reflection is identical with i , the inversion.

Further, *symmetry elements* are defined, these are the geometrical loci of all points which remain invariant when a symmetry operation is carried out. The names of the symmetry elements introduced by Schoenflies (1891) are given below, followed by the 'international' notation, introduced by Hermann (1928) and Mauguin (1931):

Notation by:	Schoenflies	Hermann/Mauguin
Identity	E	1
Center of symmetry	i	$\bar{1}$
Symmetry plane	σ	m
Proper axis	C_n	$2, 3, 4 \dots$
Improper axis	S_n	$\bar{2}, \bar{3}, \bar{4} \dots$

In order to standardize the application to molecules, the orientation of planes and axes is conventionally specified as follows:

- The axis with the highest order n is called the *main axis* and is by definition oriented in a *vertical* direction.
- A plane which is *perpendicular* to this axis is referred to as a *horizontal* plane σ_h .

- A plane which *includes* the main axis is a *vertical* plane σ_v . A vertical plane which bisects two C_2 axes which are oriented perpendicularly to the main axis is defined as a *dihedral* plane σ_d .
- A molecule-fixed Cartesian coordinate system is oriented such that its origin coincides with the center of mass and the axes coincide with the main inertial axes of the molecule. A rotation axis can thus be identified by a Cartesian axis, for example $C_n^k(z)$. The main axis is usually defined as the z axis. Planes are identified by the axes they contain: $\sigma(xy)$ or σ_{xy} .
- In the case of planar molecules with a symmetry according to the point group C_{2v} (see following section), it is recommended (Mulliken, 1955) to make the C_2 axis the z axis and to orient the x axis perpendicularly to the plane of the molecule (see Fig. 2.7-6). In planar molecules belonging to the point group D_{2h} , the x axis is oriented perpendicularly to the plane of the molecule, while the z axis should pass through the largest number of atoms; or, if this rule is not decisive, the z axis should intersect with the maximum number of bonds.

2.7.2 Point groups, space groups

Several symmetry operators may be applied to the same molecule, these constitute a *point group*. A group is a well defined concept in mathematics (see Sec. 2.7.3.1). The name *point group* indicates that at least one point (the center of mass) remains unmoved, when the symmetry operations are carried out. There is a limited number of point groups of molecules. Crystallographs count 32 point groups, since only operators related to 1-, 2-, 3-, 4- and 6-fold symmetry axes may be applied to parallelepipeds filling the space of crystals. In molecular spectroscopy, 5-, 7-, and 8-fold symmetry axes also exist, which increases the number of point groups in this field.

Point groups are usually characterized by symbols, introduced by Schoenflies in 1891 (Schoenflies, 1891, 1923). Group theory was first applied to molecular vibrations by Brester (1923) and Wigner (1931), see also Rosenthal and Murphy (1936). IUPAC recommendations have been published by Mulliken (1955), a revised recommendation is in preparation (Sullivan, 1994). IUPAC as well as IUPAP recommend the use of the Schoenflies notation, whereas the International Union of Crystallography uses the 'international' notation, introduced by Hermann (1928) and Mauguin (1931), see Hahn (1987). The Schoenflies symbols representing the point groups of molecules are defined as follows. All groups contain the identity operator. They contain further the symmetry operators connected to the following symmetry elements:

- C_1 no other symmetry elements,
- C_n an n -fold proper axis,
- D_n an n -fold proper main axis C_n and n 2-fold axes C_2 perpendicular to the main axis,

- D_{nh} an n -fold proper main axis C_n , n 2-fold axes C_2 perpendicular to the main axis and a 'horizontal' mirror plane perpendicular to the main axis,
 C_{nh} a C_n main axis and a 'horizontal' mirror plane perpendicular to the main axis,
 C_{nv} a C_n main axis and n 'vertical' symmetry planes σ_v ; if n is an even number, there are $n/2$ planes σ_v and $n/2$ planes σ_d bisecting the angles between σ_v ,
 D_{nd} an n -fold proper main axis C_n , n 2-fold axes C_2 perpendicular to the main axis, and n 'vertical' planes σ_d bisecting the angles between all neighboring C_2 axes,
 S_n an n -fold improper main axis S_n ,
 T all axes of a regular tetrahedron,
 T_d all axes and planes of a regular tetrahedron,
 O all axes of a cube,
 O_h all symmetry elements of a cube,
 I_h all symmetry elements of an icosahedron,
 $C_{\infty v}$ a C_∞ axis and an infinite number of 'vertical' planes σ_v ,
 $D_{\infty h}$ a C_∞ axis, an infinite number of 'vertical' planes σ_v and a 'horizontal' plane σ_h .

Molecules may be assigned to point groups according to the algorithm shown in Fig. 2.7-3.

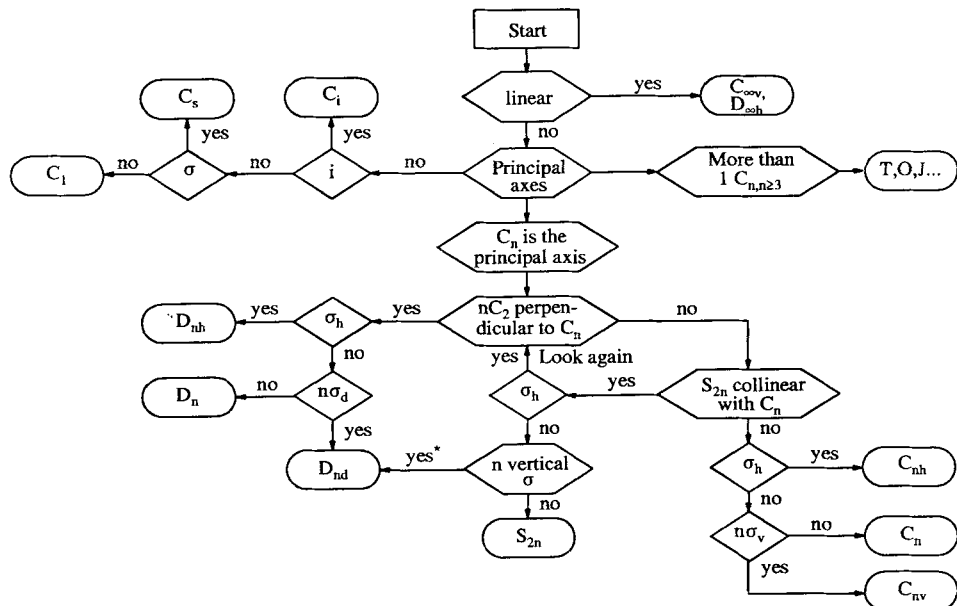


Figure 2.7-3 Algorithm for the determination of the point group belonging to a given object (Noggle, 1976).

Fig. 2.7-4 for instance, exhibits four-atomic molecules belonging to 11 different point groups. The molecules can be distinguished by the number of their vibrations in the

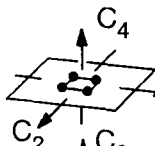
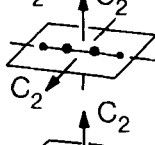
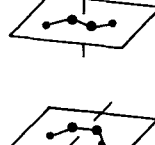
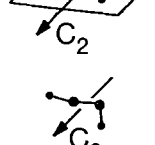
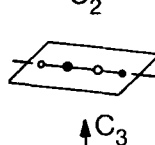
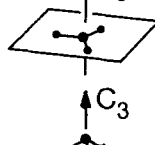
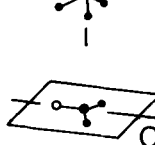
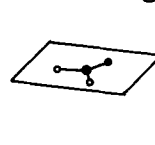
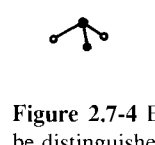
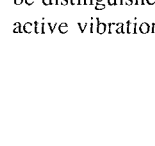
Point-group	Raman-active	Infrared	Different Species
 C_4	$1A_{1g}$ $1B_{1g}$ $1B_{2g}$	$1E_u$	3^*
 D_{4h}	$2\Sigma_g^+$ $1\Pi_g$	$1\Sigma_u^+$ $1\Pi_u$	3
 $D_{\infty h}$	$3A_g$	$1A_u$ $2B_u$	2
 C_{2h}			
 C_{2v}	$1A_2$ $2B_2$	$3A_1$	3
 C_2		$4A$ $2B$	2
 $C_{\infty} C_{\infty v}$		$3A$ $2E$	2
 D_{3h}	$1A'_1$ $2E$	$1A''_1$	3
 C_{3v}		$2A_1$ $2E$	2
 C_{2v}		$3A_1$ $1B_1$ $2B_2$	2
 C_s		$5A'$ $1A''$	2
C		$6A$	1

Figure 2.7-4 Examples of tetra-atomic molecules belonging to different point groups. They can be distinguished by the number of polarized and depolarized Raman active vibrations, the infrared active vibrations and the coincidences of frequencies of infrared and Raman active bands.

infrared and Raman spectra, its depolarization ratio, and coincidences between infrared and Raman active bands.

For crystals the symmetry operators of the 32 crystallographic point groups are combined with the combination of unit translations, thus creating 230 *three-dimensional space groups*. Their properties are tabulated in the International Tables for X-Ray Crystallography (Hahn, 1987). Point groups and space groups are groups in the mathematical sense. Their basic properties are discussed in the following section.

During all normal vibrations the moving atoms deform a molecule or a crystal such that the deformed object is either symmetric or antisymmetric with respect to the different symmetry operations belonging to its point group. 'Symmetric' means that the symmetry operation transforms one atom to an equivalent atom which is moving in the same direction. 'Antisymmetric' means that the equivalent atom is moving in the opposite direction.

Objects which have C_n or S_n axes with $n > 2$ have 'degenerate' vibrations, i.e., two (or more, for cubic or icosahedral point groups or linear molecules) vibrations have the same frequency. Carrying out a symmetry operation leads to a linear combination of degenerate vibrations.

Regarding the property 'symmetric', 'antisymmetric', or 'degenerate' with respect to all symmetry operations, vibrations can be classified according to symmetry species. Each symmetry species possesses certain spectroscopic characteristics, like 'forbidden in IR and Raman spectra', or 'IR-active with dipole moment change in x -direction', or 'modulates the xy component of the polarizability tensor'. They are given in 'character tables' (Figure 2.7-6), Sec. 7.

The next section describes the application of group theory to molecular vibrations and its consequences, e.g. the determination of the number of vibrations of all symmetry species.

2.7.3 Selection rules of the vibrations of molecules and crystals

2.7.3.1 Definition of a group, multiplication tables

A set of elements a, b, c, \dots constitutes a *group* $G[a, b, c, \dots]$ if the following four rules are obeyed:

1. For every pair of elements a and b , there exists a binary operation \circ which yields the *product* $a \circ b = c$, in which c is an element of the set (closure law).
2. The *associative law* holds: $a \circ (b \circ c) = (a \circ b) \circ c$.
3. Every group contains an *identity element (neutral element)* e , such that for every element a in the set, $a \circ e = e \circ a = a$.
4. There is an *inverse* a^{-1} for every element a in the set, such that $a \circ a^{-1} = a^{-1} \circ a = e$.

The number of elements in a group is called its *order* g . A group may have a finite or infinite order (finite or infinite group). All symmetry operators of a point or a space group fulfill the conditions 1 – 4.

It should be noted, that the *elements of a point group* are the *symmetry operators*; these are not to be confused with *symmetry elements*, i.e., the geometric loci of all points which are invariant under a symmetry operation.

A group can be described by its multiplication table which defines all possible combinations of the elements of a finite group. If the number of elements in the group (group order) is g , the group multiplication table consists of g rows and g columns.

The point group C_{2v} , for example, is characterized by the following group multiplication table (explanation of symbols in Figure 2.7-6):

C_{2v}	E	$C_2(z)$	$\sigma_v(xz)$	$\sigma'_v(yz)$
E	E	$C_2(z)$	$\sigma_v(xz)$	$\sigma'_v(yz)$
$C_2(z)$	$C_2(z)$	E	$\sigma'_v(yz)$	$\sigma_v(xz)$
$\sigma_v(xz)$	$\sigma_v(xz)$	$\sigma'_v(yz)$	E	$C_2(z)$
$\sigma'_v(yz)$	$\sigma'_v(yz)$	$\sigma_v(xz)$	$C_2(z)$	E

2.7.3.2 Representations of a group

A symmetry operator causes a *symmetry operation*. It moves a molecule into a new orientation, equivalent to its original one.

Symmetry operations may be represented by algebraic equations. The position of a point (an atom of a molecule) in a Cartesian coordinate system is described by the vector r with the components x , y , z . A symmetry operation produces a new vector r' with the components x' , y' , z' . The algebraic expression representing a symmetry operation is a matrix. A symmetry operation is represented by matrix multiplication.

A general rotation of a Cartesian coordinate system is described by:

$$\begin{bmatrix} x' \\ y' \\ z' \end{bmatrix} = \begin{bmatrix} c_{xx} & c_{xy} & c_{xz} \\ c_{yx} & c_{yy} & c_{yz} \\ c_{zx} & c_{zy} & c_{zz} \end{bmatrix} \cdot \begin{bmatrix} x \\ y \\ z \end{bmatrix} \quad (2.7-1)$$

Here, the c_{ij} are directional cosines of angles between the positive directions of the respective 'old' and 'new' axes (Fig. 2.7-5).

The transformation matrix $D(R)$ is known as a *representative of an operator R* (i.e., of an element of a point group). The matrices corresponding to all operators of a group are referred to as a *representation of the group*.

The identity operation is represented by:

$$\begin{bmatrix} x' \\ y' \\ z' \end{bmatrix} = \begin{bmatrix} 1 & 0 & 0 \\ 0 & 1 & 0 \\ 0 & 0 & 1 \end{bmatrix} \cdot \begin{bmatrix} x \\ y \\ z \end{bmatrix} \quad (2.7-2)$$

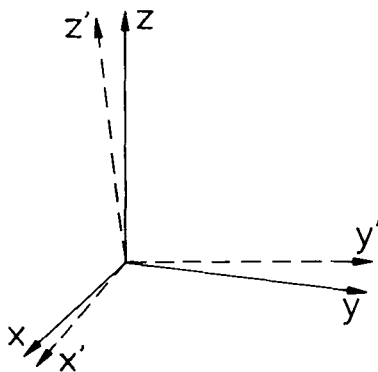


Figure 2.7-5 Definition of the rotation of a Cartesian coordinate system by an arbitrary angle.

An inversion is represented by the following matrix:

$$\begin{bmatrix} x' \\ y' \\ z' \end{bmatrix} = \begin{bmatrix} -1 & 0 & 0 \\ 0 & -1 & 0 \\ 0 & 0 & -1 \end{bmatrix} \cdot \begin{bmatrix} x \\ y \\ z \end{bmatrix} \quad (2.7-3)$$

A reflection at a plane containing the x and y axis is represented by:

$$\begin{bmatrix} x' \\ y' \\ z' \end{bmatrix} = \begin{bmatrix} 1 & 0 & 0 \\ 0 & 1 & 0 \\ 0 & 0 & -1 \end{bmatrix} \cdot \begin{bmatrix} x \\ y \\ z \end{bmatrix} \quad (2.7-4)$$

A (proper) clockwise rotation of a vector about the z -axis is directly derived from the matrix of the directional cosines (active transformation):

$$\begin{bmatrix} x' \\ y' \\ z' \end{bmatrix} = \begin{bmatrix} \cos\phi & -\sin\phi & 0 \\ \sin\phi & \cos\phi & 0 \\ 0 & 0 & 1 \end{bmatrix} \cdot \begin{bmatrix} x \\ y \\ z \end{bmatrix} \quad (2.7-5)$$

In case the coordinate system is rotated clockwise or the vector is rotated counter-clockwise (passive transformation) some elements of the matrix change its sign:

$$\begin{bmatrix} x' \\ y' \\ z' \end{bmatrix} = \begin{bmatrix} \cos\phi & \sin\phi & 0 \\ -\sin\phi & \cos\phi & 0 \\ 0 & 0 & 1 \end{bmatrix} \cdot \begin{bmatrix} x \\ y \\ z \end{bmatrix} \quad (2.7-5')$$

A rotation-reflection (improper rotation) about the z -axis is represented by a similar matrix, the zz -element changes its sign:

$$\begin{bmatrix} x' \\ y' \\ z' \end{bmatrix} = \begin{bmatrix} \cos\phi & -\sin\phi & 0 \\ \sin\phi & \cos\phi & 0 \\ 0 & 0 & -1 \end{bmatrix} \cdot \begin{bmatrix} x \\ y \\ z \end{bmatrix} \quad (2.7-6)$$

Transformations of this type are called orthogonal, they do not change lengths or angles of objects.

All matrices are mathematical expressions of symmetry operators. These matrices fulfill, with the matrix multiplication as the binary operation, the requirements for a group in a mathematical sense which is isomorphic to the corresponding point group. For instance, two symmetry operators $C_2(z)$ and $\sigma(yz)$ of a symmetry group C_{2v} combine to give a product $\sigma(xz)$. The matrices $\mathbf{D}(C_2(z))$ and $\mathbf{D}(\sigma(yz))$ corresponding to the symmetry operators $C_2(z)$ and $\sigma(yz)$ must be multiplied with each other to afford the matrix $\mathbf{D}(\sigma(xz))$ corresponding to $\sigma(xz)$. Therefore, an analogous multiplication table may be applied to the matrix representatives. The group Γ of the matrices $\mathbf{D}(E)$, $\mathbf{D}(C_2(z))$, $\mathbf{D}(\sigma(yz))$, and $\mathbf{D}(\sigma(xz))$ is called the matrix representation of the point group C_{2v} .

2.7.3.3 Irreducible representations

Every atom of a molecule has three degrees of freedom, i.e., it can move independently along each of the axes of a Cartesian coordinate system. A molecule containing n atoms therefore has $3n$ motional degrees of freedom. In order to classify these, g symmetry operators of the point group of the molecule have to be applied to them.

This results in a representation by a group of g square matrices, each having the dimension $3n \times 3n$.

A so-called similarity transformation reduces these matrices to matrices of the same dimension, but which are composed of submatrices of a lower order arranged along the diagonal. It is now called a block-factored matrix.

$$\left[\begin{array}{c} \mathbf{D}(i) \\ \vdots \\ \mathbf{D}(i) \end{array} \right] \xrightarrow{\mathbf{S}^{-1} \mathbf{D}(i) \mathbf{S}} \left[\begin{array}{cccc} \mathbf{R}_1 & 0 & \dots & 0 \\ 0 & \mathbf{R}_2 & \dots & 0 \\ \vdots & & \ddots & \vdots \\ 0 & 0 & \dots & \mathbf{R}_n \end{array} \right]$$

The trace, i.e., the sum of the diagonal elements of the matrix representing a symmetry operator is called the 'character' of this operator and is symbolized by χ . Equivalent symmetry operators (conjugate operators) form a class. Symmetry operators of the same class have the same character, since the equivalent representation matrices have the same trace.

For many applications of group theory it is sufficient to use the characters of the 'irreducible representations' (see following section) instead of the original representations.

If a transformation matrix \mathbf{S} can be found which transforms the matrices $\mathbf{D}(i)$ of a given representation to a block-factored matrix form, this representation is considered to be *reducible*.

If it is impossible to find a transformation which can further reduce all submatrices $\mathbf{R}_1 \dots \mathbf{R}_n$, then all matrices $\mathbf{D}(i)$ of a given representation are said to be completely reduced.

When the equations representing the symmetry operations of a molecule are related to normal coordinates instead of Cartesian coordinates, the representation will be completely

reduced. Normal coordinates are the result of 'normal coordinate calculations' described in Sec. 5.2.

The submatrices are also representations, i.e., so-called *irreducible representations*. The completely reduced representation can be regarded as the direct sum (represented by the symbol \oplus) of n_i multiples of irreducible representations Γ_i , where n_i is a positive number or zero:

$$\Gamma_{\text{red}} = n_1 \Gamma_1 \oplus n_2 \Gamma_2 \oplus \dots \quad (2.7-7)$$

For an n -atomic molecule, the sum of the numbers of normal coordinates n_i equals the number of motional degrees of freedom $3n$:

$$\sum_i n_i = 3n \quad (2.7-8)$$

The following statement is an important consequence of the representation theory:

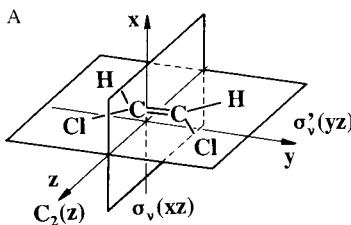
The number of inequivalent irreducible representations is equal to the number of classes in the group of symmetry operators.

2.7.3.4 The character table

A character table lists all possible different irreducible representations (species) of a point group (Fig. 2.7-6). Along the top row, the symmetry operators are listed, collected in classes (in the case of the point group C_{2v} , each symmetry operator is a class by itself). In the left column, the names of the vibrational species are given, corresponding to the irreducible representations. The rows of a character table define its symmetry properties by the characters of the irreducible representations. In the point group C_{2v} there are four classes, i.e., four species exist.

Generally their names indicate the result of the application of a symmetry operator:

- A symmetric with respect to the main axis of symmetry
- B antisymmetric with respect to the main axis of symmetry
- ' symmetric with respect to a plane of symmetry
- " antisymmetric with respect to a plane of symmetry
- g* symmetric with respect to the center of symmetry (from German *gerade*)
- u* antisymmetric with respect of the center of symmetry (from German *ungerade*)
- E* doubly degenerate with respect to the main axis
- T* triply degenerate with respect to the main axis
- G* fourfold degenerate with respect to the main axis
- H* fivefold degenerate with respect to the main axis
- 1, 2, 3 (as subscripts) symmetric or antisymmetric with respect to a rotation axis (C_n) or a rotation-reflection axis (S_n) or, if the other symbols are not sufficient to specify different species



B

①	C _{2v}	④	E	C ₂	$\sigma_v(xz)$	$\sigma'_v(yz)$	⑥	⑦
②	(2mm)	③						
③	A ₁		1	1	1	1	z	x ² , y ² , z ²
	A ₂	⑤	1	1	-1	-1	R _z	xy
	B ₁		1	-1	1	-1	x, R _y	xz
	B ₂		1	-1	-1	1	y, R _x	yz

Figure 2.7-6 A: Assignment of the Cartesian coordinate axes and the symmetry operations of a planar molecule of point group C_{2v} . **B:** Character table, 1 symbol of the point group after Schoenflies; 2 international notation of the point group; 3 symmetry species (irreducible representations); 4 symmetry operations; 5 characters of the symmetry operations in the symmetry species: +1 means *symmetric*, -1 *antisymmetric*; 6 *x*, *y*, *z* assignment of the normal coordinates of the translations, direction of the change of the dipole moment by the infrared active vibrations, R_x , R_y , and R_z stand for rotations about the axes specified in the subscript; 7 x^2 , xy , ... assign the Raman active species by the change of the components of the tensor of polarizability, α_{xx} , α_{xy} ,

The species of the point group C_{2v} are named A_1 , A_2 , B_1 , and B_2 . The characters of the different irreducible representations are shown in Fig. 2.7.-6. In the sixth column symbols of Cartesian coordinates are given: z in the row of the species A_1 means that the z coordinate does not change its sign when all different symmetry operations are applied. The coordinate x changes its sign, if a rotation about C_2 or a reflection at $\sigma'_v(yz)$ is applied: x transforms as the species B_1 . The translation T_x as well as the component of the dipole moment μ_x transform in the same way. Therefore, vibrations of the species B_1 modulate the dipole component μ_x : They are thus infrared active. Therefore, all vibrations which are infrared active belong to a species characterized with a Cartesian coordinate. For a molecule belonging to the point group C_{2v} vibrations of species A_1 , B_1 and B_2 are infrared active, since they are modulating the component μ_z , μ_x and μ_y , respectively, of the dipole moment.

Analogous arguments are true for the different rotations: R_z , a rotation about the z axis changes its sign when it is reflected at any symmetry plane. Therefore, it transforms as A_2 . R_y transforms as B_1 and R_x as B_2 .

The last column of a character table lists the products of Cartesian coordinates which transform as the respective symmetry species. It can be shown (Wilson, Decius and Cross (1955)) that the components of the polarizability tensor α_{xx} , α_{xy} ,... transform

in the same way. This means that all vibrations are Raman active or 'allowed' in the Raman spectrum, which belong to a species characterized by any product of Cartesian coordinates in the last column. The activity and special features of vibrations in the resonance and hyper Raman effect are explained by Schrötter (1982) and are tabulated by Weidlein et al. (1982).

Vibrations which are not allowed, are 'forbidden' in the infrared (or Raman) spectrum.

An important consequence of molecular symmetry concerns molecules which have a center of symmetry. It is *the rule of mutual exclusion*:

A vibration which is symmetric with regard to the center of symmetry is forbidden in the infrared spectrum, whereas a vibration which is antisymmetric to the center of symmetry is forbidden in the Raman spectrum.

The depolarization ratio of the Raman lines in the spectrum of a liquid compound, which is easy to measure, provides a means of distinguishing totally symmetrical vibrations from the rest.

Vibrations of totally symmetric species (defined by the first row of the character tables) emit Raman lines which are *polarized*: the depolarization ratio ρ_k can assume, according to Eqs. 2.4-11 ... 13 values of $0 \leq \rho < 6/7$. All other Raman-active vibrations are emitting lines which are depolarized, they have a depolarization ratio of $6/7$. The value $6/7$ is appropriate for an arrangement, where the Raman radiation s investigated without an analyzer. If an analyzer is used $3/4$ has to be taken instead. Cubic and icosahedral point groups are a special case: the depolarization ratio for totally symmetric vibrations is 0.

Changes of each component of the scattering tensor of the unit cell can be directly observed. The arrangement of the crystal with regard to the spectrometer is described by a nomenclature recommended by Porto et al. (1966). In this system, $a(bc)d$ stands for irradiation in a direction by radiation polarized in b direction, Raman radiation polarized in c direction is observed in d direction. Here, a, b, c, d indicate any crystal axes.

2.7.4 The number of vibrational states belonging to the different symmetry species

An important consequence of group theory, i.e., the so-called **great orthogonality theorem**, is the basis of the equation for calculating the numbers n_i of the vibrations belonging to a symmetry species i :

$$n_i = \frac{1}{g} \sum_R k(R) \chi_i(R) \chi(R) \quad (2.7-9)$$

The group order g equals the number of symmetry operators of this group.

The summation is extended over all classes of symmetry operators R .

$k(R)$ is the number of elements in each class (number of conjugate symmetry operators R in a class).

$\chi_i(R)$ is the character of the species (irreducible representation) i for the symmetry operator R found in the character table.

$\chi(R)$ is the character of the reducible representation of the symmetry operator R. It is proportional to the number of units (atoms, molecules, unit cells) whose center of mass is not moved by a symmetry operation. Let the number of such units be $u(R)$. The sign and magnitude of the contribution of each unit to $\chi(R)$ is determined by the transformation properties of a vector. For linear motions, this is a polar vector (Fig. 2.7-7a). The character of the reducible representation $\chi(R)$ equals the product of the number of particles whose position is not moved by the symmetry operation and the character of the transformation of a polar vector $\chi_t(R)$:

$$\chi(R) = u(R)\chi_t(R) \quad (2.7-10)$$

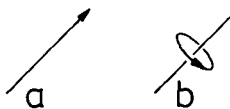


Figure 2.7-7 Symbolic representation of **a**, a polar and **b**, an axial vector.

The characters of the transformation of a polar vector by different symmetry operators are shown in Table 2.7-1 (Schrader, 1978).

In order to find the character of the representation of rotational motions and librations, the transformation properties of an axial vector (Fig. 2.7-7b) have to be taken into account. This vector is defined not only by its length and orientation, but also by a definite sense of rotation inherent to it. For linear molecules with only two degrees of rotational freedom, the $\chi_r(R)$ values for C_2 and σ depend on the orientation of the molecular axis to the symmetry elements. All values of $\chi_r(R)$ are also included in Table 2.7-1.

By analogy to Eq. 2.7-10, $\chi(R)$ is defined by:

$$\chi(R) = u_r(R)\chi_r(R) \quad (2.7-11)$$

Examples for this procedure are given in section 2.7.6.

2.7.5 The number of vibrational states of a molecular crystal

The theoretical background which is relevant for this section can be found in a number of publications: Bhagavantam and Venkatarayudu (1969), Turrell (1972), Behringer (1973), Schrader (1978), and Rousseau et al. (1981).

There are two types of crystals (Kleber 1961): in *homodesmic* lattices, mainly one type of force is acting between the atoms. Examples are the metals, diamond, and NaCl. Regarding vibrational spectroscopy these crystals act as units, whose vibrational states are properties of the whole crystal. There is no similarity to the spectra of the constituents.

Table 2.7-1 Number of vibrational states of molecules and unit cells

$n_i = \frac{1}{g} \sum_R k(R) \chi_i(R) \chi_t(R) u(R)$	(I)	
$n_i = \frac{1}{g} \sum_R k(R) \chi_i(R) \chi_r(R) u_r(R)$	(II)	
g	Order of point group)	
R	Symmetry operator) from character table	
$k(R)$	Number of conjugate symmetry operators R in a class)	
$\chi_i(R)$	Character of operator R in symmetry species i)	
$\chi_t(R)$	Character of the transformation of a polar vector,	
$\chi_r(R)$	Character of the transformation of an axial vector by a symmetry operator R :	
R	E C_2 C_3 C_4 C_6 i σ S_3 S_4 S_6	
	\perp	
$\chi_t(R)$	3 -1 0 1 2 -3 1 -2 -1 0	
a	3 -1 0 1 2 3 -1 2 1 0 non-linear	
$\chi_r(R)$	b 2 -2 0 -1 0 1 2 0 -2 1 0 -1 linear molecule	
$u(R), u_r(R)$	Number of units, the centres of mass of which remain invariant under symmetry operation R :	n_i Degrees of freedom belonging to species i :
(Equation I)		
$u(R) = u_p'(R)$	Atoms in vibrating system	p'_i Total degrees of freedom
$= u_T(R) = 1$	Vibrating system (molecule or unit cell)	T_i Translations
$= u_t(R)$	Molecules per unit cell minus 1	t_i Translational vibrations
(Equation II)		
$u_r(R) = z (= 1)$	Polyatomic molecules in unit cell (molecule)	r_i Librations (Rotations)
Inner vibrations: $p_i = p'_i - T_i - t_i - r_i$		

In (I) and (II) the sum is to be taken over symmetry operators R of different classes of conjugate elements only. — For $\chi_r(R)$ different values have to be taken for non-linear (set a) and linear (set b) molecules. For linear molecules the characters for the operators C_2 and σ depend on whether the molecular axis is parallel, \parallel , or perpendicular, \perp , to the symmetry elements.

In *heterodesmic* lattices however, there are different kinds of bonds acting. A molecular crystal is an example. The atoms within a molecule are bound by strong covalent bonds, whereas the atoms of different molecules are bound by weak van-der-Waals bonds. The molecules keep their individuality. Their vibrational spectra in the crystalline state are quite similar to the spectra of the same molecules in the gaseous, liquid or matrix-isolated state. However, the orientation of the molecules and the intermolecular forces and interactions are exactly defined. The intensities of the different bands in spectra given by different orientations of a single crystal reflect this orientation. This is a great advantage in contrast to the other collections of molecules, where molecules are statistically ordered, having a range of different orientations and interactions.

The wavelengths of radiation employed in infrared and Raman spectroscopy (200 to 20 000 nm) are several orders of magnitude longer than the dimensions of a unit cell in a crystal (0.2 to 2 nm). Therefore, only the vibrational states are visible in the spectra, where neighboring unit cells vibrate with a phase difference close to 0. This means that the geometry as well as the statical and dynamical properties of **one** unit cell are representative of the typical properties of uniquely packed molecules.

These properties are analyzed by a procedure consisting of three steps:

- Rigid molecules are oriented definitely: *the oriented gas approach*
- Molecules as objects of static forces are deformed and reduce their symmetry: *the site symmetry approach*
- All molecules within a unit cell couple dynamically: *the factor group approach*

Only for the interpretation of spectra of higher order or those of ionic crystals, semiconductors, or metals, the vibrational states of the whole crystal have to be regarded.

The factor group of a space group (Bhagavantam and Venkatarayudu, 1969) is simply the group of symmetry operators of a space group when the elementary translation operators are ignored; these do not contribute to the selection rules. The factor group is found by taking the Schoenflies symbol of the space group and deleting the superscript, e.g., D_{2h}^{16} becomes D_{2h} .

One has to take into account, however, that the unit cell which is relevant for spectroscopy is the **primitive** (or Wigner-Seitz) unit cell. It is a parallelepiped from which the entire lattice may be generated by applying multiples of elementary translations. Face- and body-centered cells are multiple unit cells. The content of such a cell has to be divided by a factor m to obtain the content of a primitive unit cell. This factor m is implicitly given by the international symbol for a space group: P and R denote primitive cells ($m = 1$), face-centered cells are denoted A , B , C ($m = 2$), and F ($m = 4$), and body-centered cells are represented by I ($m = 2$). Examples are described by Turrell (1972).

The factor group of any space group is isomorphic to one of the 32 point groups. The procedure for the classification of vibrations of free molecules can also be applied accordingly for the classification of the vibrations of molecular crystals, as explained by Table 2.7-1.

2.7.6 Vibrational spectra of thiourea molecules and crystal modifications

The examples discussed in this section are derived in studies concerning urea and thiourea and its inclusion compounds: Kutzelnigg et al. (1961) and Schrader et al. (1959, 1960, 1971), Takahashi et al. (1967), D'Orazio and Schrader (1976), and Bleckmann et al. (1971).

In the following section the symmetry species of the thiourea *molecule* are denoted by *lower-case* letters, while that of the *unit cell* of the crystal is indicated by *capital* letters. The Cartesian coordinate axes of the free molecules are labeled u , v , and w , those of the crystal a , b , and c (see Figs. 2.7-8 and 2.7-9; Schrader et al., 1971).

2.7.6.1 Vibrational states of the free thiourea molecule

'Free' thiourea molecules at room temperature may be regarded as planar with a symmetry according to the point group C_{2v} . The two-fold axis is the u axis, the molecular plane is defined by the u and v axes. Table 2.7-2 shows the characters of the species a_1 , a_2 , b_1 , and b_2 belonging to symmetry operators labeled according to the u , v and w axes. Below in this table are the $\chi_t(R)$ and $\chi_r(R)$ characters representing the transformation of a polar and an axial vector by a symmetry operator R , they are taken from Table 2.7-1. The number of atoms which do not change their position, when the symmetry operator R is applied, is given in the following row by $u(R) = u_{p'}$. Equation I of Table 2.7-1 then allows to calculate the number of vibrational degrees of freedom p' belonging to the different species. All $u_{p'} = 8$ atoms are invariant under the identity operation E . Under the operation $C_2(u)$ $u_{p'} = 2$ atoms, C and S, remain invariant. The same is true of reflection at $\sigma(uw)$. Under the operation $\sigma(uv)$, all 8 atoms remain invariant, because they are situated on the uv plane.

Table 2.7-2 Vibrational states of the 'free' thiourea molecule

C_{2v}	E	$C_2(u)$	$\sigma(uw)$	$\sigma(uv)$	p'	T	t	r	p
a_1	1	1	1	1	8	1			7
a_2	1	1	-1	-1	3			1	2
b_1	1	-1	1	-1	5	1		1	3
b_2	1	-1	-1	1	8	1		1	6
χ_t	3	-1	1	1					
χ_r	3	-1	-1	-1					
u'_p	8	2	2	8					
u_T	1	1	1	1					
u_t	0	0	0	0					
u_r	1	1	1	1					

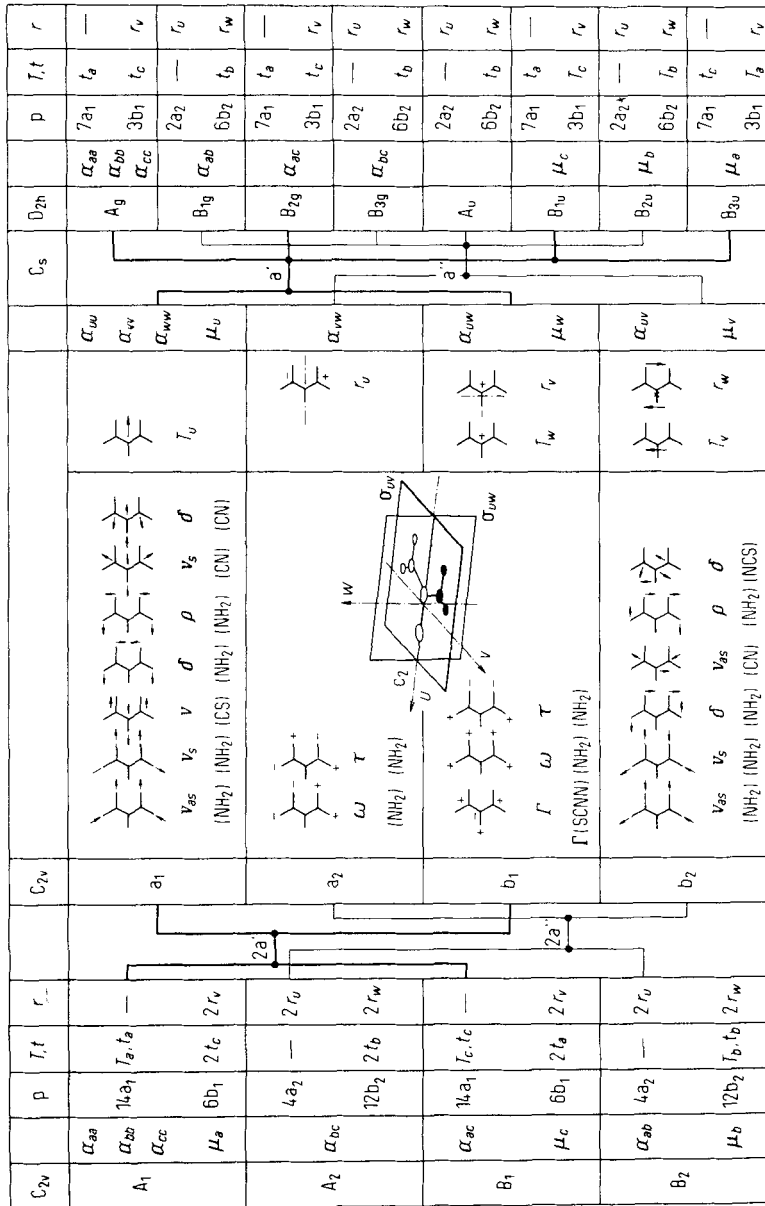


Figure 2.7.8 Vibrational species of thiourea as free molecule, point group C_{2v} , and under the constraints of the site symmetry, C_3 , of the unit cell at room temperature, D_{2h}^{16} , as well as of the ferroelectric modification, C_{2h}^2 ; Cartesian coordinate axes of the molecule: u , v , w ; crystal axes: a , b , c ; T translational vibrations, t librations, p internal vibrations (Schrader et al., 1971).

The number of translational degrees of freedom T_i and the number of rotations r_i are calculated by inserting $u(R) = u_T = 1$ into Eq. I of Table 2.7-1 or by inserting $u_r(R) = 1$ into equation II. The corresponding values are found in the character tables.

The number of vibrations of individual species are calculated according to $p_i = p'_i - T_i - r_i$. These results are reproduced schematically in the middle part of Fig. 2.7-8, where the respective infrared and Raman activities are labeled ' μ_x ' and ' α_{xy} ', with $x, y = u, v, w$. As a final test, the sum of all vibrational degrees of freedom can be calculated; it should be $3n - 6$ for nonlinear and $3n - 5$ for linear molecules.

2.7.6.2 Vibrational states of the thiourea molecule under the constraints of its site symmetry

The site symmetry of a molecule is the symmetry of the lattice point of its center of mass. If a complete $X\text{-ray}$ structure analysis is carried out then the site symmetry of the molecules is known. If only the space group is known, inspection of the space group diagrams in the International Tables (Hahn, 1987) may show the possible positions. These tables list the number and the symmetries of all equivalent positions and their coordinates for unit cells of all space groups, together with their diagrams. The probable site symmetry may be found by comparison of the number of molecules per unit cell and the number of equivalent lattice points. It may be of some help to realize that the site symmetry point group must be a subgroup of both the molecular symmetry point group and the point group isomorphic to the factor group.

Four thiourea molecules per unit cell are arranged in a crystal lattice with the space group D_{2h}^{16} , as shown in Fig. 2.7-9.

When free molecules are incorporated in a lattice, their axes are first oriented, i.e., $v \parallel b$; the angle between the u and the a axis is $\theta = 63.6^\circ$. This is one aspect of the 'oriented gas model'. However, as Fig. 2.7-9a shows, the molecules are not exactly planar; the hydrogen atoms are directed toward the neighboring S atoms. The symmetry plane $\sigma(uv)$ of the free molecule is thus lost, the new point group of the molecule is determined by the symmetry of the lattice site, C_s . According to the site symmetry model, the a_1 and b_1 species are therefore combined to afford a species a' , while the a_2 and b_2 species afford a'' , see Table 2.7-3 and Fig. 2.7-8.

2.7.6.3 Vibrational states of the unit cell of crystalline thiourea

Four thiourea molecules at C_s sites are the building blocks of the unit cell of the crystal of the space group D_{2h}^{16} . The point group which is relevant for the selection rules is found by deleting the superscript, which yields D_{2h} . Table 2.7-4 lists the details and results of the application of Eqs. I and II from Table 2.7-1. As shown in Fig. 2.7-8, the results are assigned to the components of the polarizability tensor α_{xy} and the dipole moment vector μ_x of the crystal, with x and $y = a, b, c$, which explains the Raman and infrared activity. We see that in addition to the translations of the whole crystal T_x , most

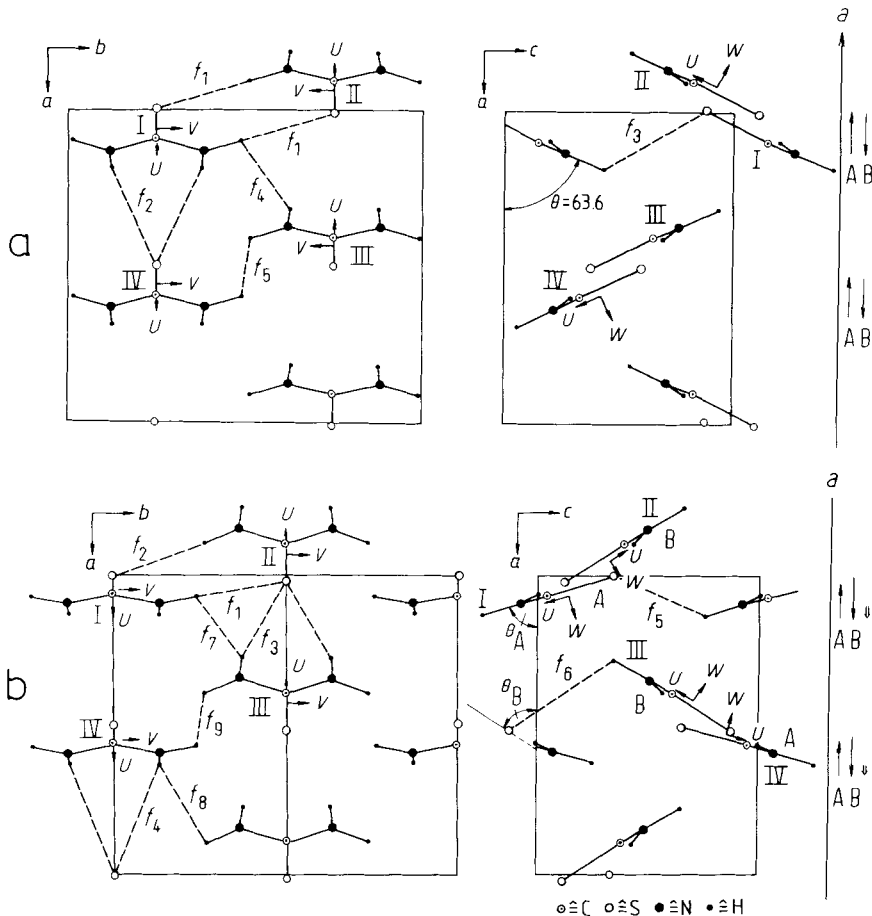


Figure 2.7-9 Unit cell of thiourea, **a** at 300 K, D_{2h}^{16} , $z = 4$, $\Theta = 63.6^\circ$, $a = 7.655$, $b = 8.537$, $c = 5.520 \text{ \AA}$; **b** at 110 K, C_2^2 , $z = 2 \cdot 2$, $\Theta_A = 60.5^\circ$, $\Theta_B = 70.6^\circ$, $a = 7.516$, $b = 8.519$, $c = 5.494 \text{ \AA}$ (Schrader et al., 1971).

species contain one or two translational vibrations t_x where the centers of gravity of the molecules vibrate with a different phase relation along the crystal axes $x = a$, b , and c . In addition, r are the frozen rotations, referred to as rotational vibrations or librations (from latin *libra* = balance).

2.7.6.4 Correlation of the motional degrees of freedom of thiourea

In order to analyze the motions within a molecular crystal, it is of great value to have both the Raman and the IR spectra of single crystals. If the crystal is oriented properly, it is thus possible to assign the observed spectra to vibrational species of the unit cell. If, as

Table 2.7-3 Vibrational states of the thiourea molecule at its lattice site

C_s	E	$\sigma(uw)$	p'	T	t	r	p
a'	1	1	13	2		1	10
a''	1	-1	11	1		2	8
χ_t	3	1					
χ_r	3	-1					
u'_p	8	2					
u_T	1	1					
u_t	0	0					
u_r	1	1					

Table 2.7-4 Vibrational states of the unit cell of the thiourea crystal at room temperature

D_{2h}	E	$C_2(c)$	$C_2(b)$	$C_2(a)$	i	$\sigma(ab)$	$\sigma(ac)$	$\sigma(bc)$	p'	T	t	r	p
A_g	1	1	1	1	1	1	1	1	13	2	1	10	
B_{1g}	1	1	-1	-1	1	1	-1	-1	11	1	2	8	
B_{2g}	1	-1	1	-1	1	-1	1	-1	13	2	1	10	
B_{3g}	1	-1	-1	1	1	1	-1	1	11	1	2	8	
A_u	1	1	1	1	-1	-1	-1	-1	11	1	2	8	
B_{1u}	1	1	-1	-1	-1	-1	1	1	13	1	1	1	10
B_{2u}	1	-1	1	-1	-1	1	-1	1	11	1	0	2	8
B_{3u}	1	-1	-1	1	-1	1	1	-1	13	1	1	1	10
χ_t	3	-1	-1	-1	-3	1	1	1					
χ_r	3	-1	-1	-1	3	-1	-1	-1					
u'_p	32	0	0	0	0	0	8	0					
u_T	1	1	1	1	1	1	1	1					
u_t	3	-1	-1	-1	-1	-1	3	-1					
u_r	4	0	0	0	0	0	4	0					

in the case of thiourea, the selection rules of the unit cell are of the point group D_{2h} , then three different infrared and six different Raman spectra can be recorded and assigned uniquely to the changes of the components of the dipole moment and the polarizability.

Fig. 2.7-8 shows the correlation diagram of the motional degrees of freedom of a free molecule, a molecule at its lattice site, and a unit cell. The vibrations of the species a_1 and b_1 as well as of a_2 and b_2 combine to give the symmetry species a' and a'' of the molecule at its crystal site. Since there are four molecules in the unit cell, all vibrational degrees of freedom split into four components. This is called *factor group*

splitting. Vibrations of species a' give rise to the Raman active vibrations A_g and B_{2g} and the infrared active vibrations B_{1u} and B_{3u} . On the other hand, a'' vibrations create two Raman active vibrations B_{1g} and B_{3g} and one infrared active vibration B_{2u} . The vibration A_u is forbidden.

The spectra of well oriented single crystals are reproduced in Figs. 2.7-10 and 11 (Schrader et al., 1971). The observed bands can nicely be assigned with the help of the oriented gas model. The v axis of the molecule is parallel to the b axis of the crystal. The vibrations of b_2 species which modulate μ_v of the molecules therefore show strong infrared bands in the B_{2u} spectrum, where the dipole moment changes in the b direction of the crystal. In the Raman spectra, these bands appear as B_{1g} and B_{3g} species. Bands of the molecular species a_1 which modulate the component μ_u of the dipole moment produce more intense bands in the species B_{1u} than in B_{3u} . This is due to the fact that the angle between the u axis of the molecule and the c axis of the crystal is small (26.4°), whereas the angle with the a axis is 63.6° . Vibrations which modulate the molecular dipole moment in u direction are therefore according to the oriented gas model in the infrared spectrum B_{1u} by a factor of $(\cos 26.4) / (\cos 63.6) \approx 4$ stronger than in the spectrum B_{3u} . This is indeed reflected by the spectra shown in Fig. 2.7-10. Similar arguments apply to the different intensities of the vibrations in the Raman spectra. These are discussed in detail by Schrader et al. (1971) and Schrader (1978). Deviations of these relative intensities, calculated by the oriented gas model, and the observed spectra reveal the interactions of the molecules in the crystal. The extent of this 'factor group splitting' of the components of the same molecular vibration in the different crystalline species also reveal intermolecular interactions. These may be due to interactions of the transition dipole moments of neighboring molecules or the influence of the intermolecular force constants (Bleckmann et al., 1971).

Of special interest is the observation of spectral changes caused by phase transitions. Thiourea undergoes a phase transition to form a ferroelectric modification which is stable

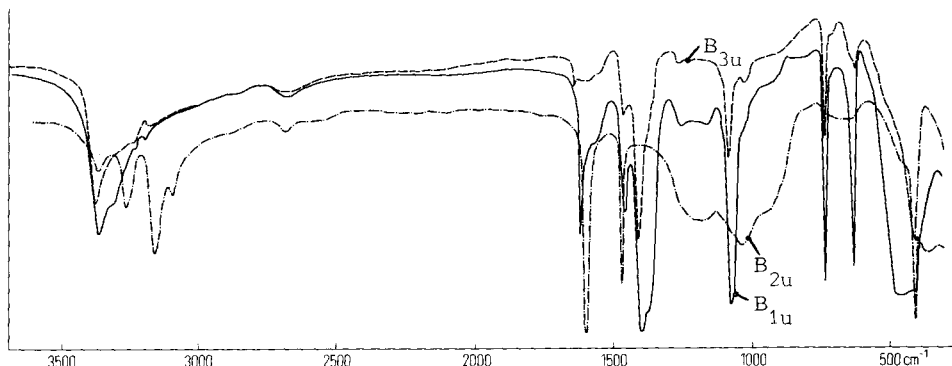


Figure 2.7-10 Infrared spectra of a thiourea single crystal, recorded by using the ATR technique with polarized radiation, 300 K, —— $B_{1u}(\mu_c)$, - · - · - $B_{2u}(\mu_b)$, - - - $B_{3u}(\mu_a)$ (Schrader et al., 1971).

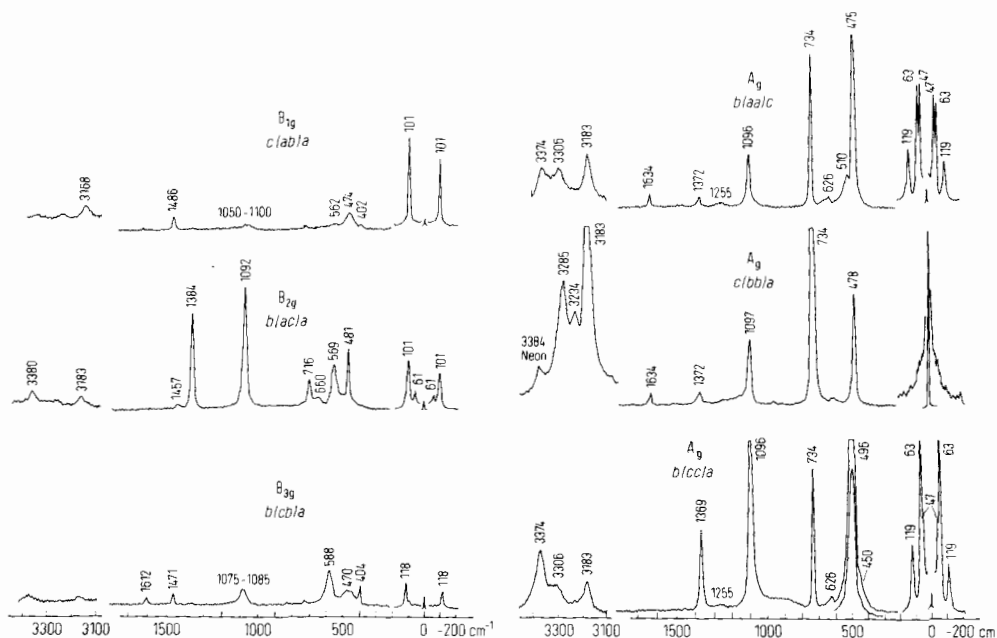


Figure 2.7-11 Raman spectra of the thiourea single crystal at 300 K, excited by using the radiation of a HeNe laser, 50 mW at 633 nm, $c(ab)a$ indicates irradiation in c direction, with radiation polarized parallel to the a axis, Raman radiation is observed in a direction with an analyzer oriented parallel to the b axis.

below 169 K. It has the space group C_{2v}^2 , with 4 molecules at two different sites. In this modification, the u axes of the molecule are not arranged antiparallel, as they are at room temperature. The molecules are arranged at different angles (29.5 and 19.4 °) between the u axis of the molecule and the c axis of the crystal. The dipole moments of neighboring molecules are not compensated, the whole crystal has a dipole moment, which can be switched by an external electrical field. Further splittings appear in the observed spectra and discontinuities are observed in the temperature dependence of the spectra of the lattice vibrations (Schrader et al., 1971). The correlation between the degrees of freedom of the molecules and the ferroelectric modification of the crystal is shown in the left part of Fig. 2.7-8.

The conclusion is that the infrared and Raman spectra of molecular single crystals can reveal an enormous amount of information regarding the structure of and interactions within molecular crystals. These spectra are therefore an interesting complement to the studies of X-ray or neutron diffraction.

2.7.7 Infrared and Raman activity of lattice vibrations

Independent of a thorough analysis, some general rules concerning the IR and Raman activity of librations and translational vibrations of molecules in a crystal lattice might be valuable:

1. A crystal with only one molecule per unit cell does not possess translational vibrations.
2. Molecules with a site symmetry C_i or point groups containing the inversion operator do not possess translational vibrations in Raman-active species, and they do not have librations in IR-active species.
3. Molecules with a site symmetry T_d and O_h cannot show any librations in their Raman or IR spectra.

According to rules (1) and (2) hexamethylenetetramine $C_6H_{12}N_4$ with the space group T_d^3 and one molecule per primitive cell cannot show any optically allowed lattice vibrations. Indeed, the Raman and IR spectra do not show any bands in the low-frequency region. Oxamide with one molecule per primitive cell C_i^1 at sites C_i shows three Raman bands, i.e., the three librations. Naphthalene with two molecules per primitive cell C_{2h}^5 at sites C_i shows six librations in the Raman spectrum. Three translational vibrations are allowed in the IR spectrum.

‘Activity’ of vibrations in optical spectra means only that these are allowed by the symmetry. They may, however, modulate the polarizability or the dipole moment to such a small extent that these vibrations do not give rise to observable bands. However, ‘inactivity’ of vibrations based on symmetry considerations means that the intensity is absolutely 0.

According to Raman and Nedungadi (1939) and Kastler and Rousset (1941), librations should show strong Raman bands if the difference between the polarizability values of the molecules perpendicular to the axis of libration is large. This can be observed in most examples. However, the statement that translational vibrations can only show weak Raman bands is definitely not true in some cases. In thiourea and melamine, for example, the strongest band of the Raman spectrum is due to a translational vibration. Its high intensity is explained by the change of the molecular orbitals due to intermolecular dynamical interactions (Schrader et al., 1971; Schneider et al., 1975; D’Orazio and Schrader, 1976).

Many other examples of the properties of internal and lattice vibrations in molecular crystals, especially their changes during phase transitions and intermolecular interactions, have been reported by Schrader (1978).

3 Tools for infrared and Raman spectroscopy*

Infrared and Raman spectra are electromagnetic spectra in the optical range. The underlying elementary processes are discussed in Sec. 2.2. Infrared spectra cover the middle infrared (MIR, $2.5 \dots 25 \text{ } \mu\text{m} \hat{=} 4000 \dots 400 \text{ cm}^{-1}$) and far infrared (FIR, $25 \dots 1000 \text{ } \mu\text{m} \hat{=} 400 \dots 10 \text{ cm}^{-1}$) range. In this region, most molecules show absorption or emission bands arising from symmetry-allowed interaction with the radiation field. The energy of the absorbed and emitted light quanta is equivalent to the energy difference between the lower vibrational states of the electronic ground state of a molecule.

Raman spectra are emission spectra excited by monochromatic radiation in the ultraviolet (UV, $0.2 \dots 0.4 \text{ } \mu\text{m} \hat{=} 50000 \dots 25000 \text{ cm}^{-1}$), visible (VIS, $0.4 \dots 0.7 \text{ } \mu\text{m} \hat{=} 25000 \dots 14300 \text{ cm}^{-1}$), or near infrared (NIR, $0.7 \dots 2.5 \text{ } \mu\text{m} \hat{=} 14300 \dots 4000 \text{ cm}^{-1}$) region. They are due to modulation of incident light by molecular vibrations. This is an inelastic scattering process of low probability. Faint spectral lines are emitted – the Raman spectrum – whose energy difference relative to the energy of the exciting line is equal to the energy difference between the lower vibrational states.

Infrared and Raman spectrometers usually combine a radiation source, a sample arrangement, a device for spectral dispersion or selection of radiation, and a radiation detector, connected to appropriate recording and evaluation facilities. An ideal spectrometer records completely resolved spectra with a maximum signal-to-noise ratio. It requires a minimum amount of sample which is measured nondestructively in a minimum time, and it provides facilities for storing and evaluating the spectra. It also supplies information concerning composition, constitution, and other physical properties. In practice, spectrometers do not entirely meet all of these conditions. Depending on the application, a compromise has to be found.

The following paragraphs describe the relevant properties of spectrometers. Terms, symbols and units are used according to IUPAP and IUPAC recommendations (Fassel, 1972; Mills, 1988). The most relevant ones are summarized in Table 3.1-1. For practical purposes, it is advantageous to use cm instead of the SI unit m for length, since the dimensions of most radiation sources, samples, and detectors are of the order of cm. Besides, this ensures coherence with the accepted wavenumber unit cm^{-1} . Items 1 and 2 in the table apply generally; while items 3, 4, 5, and 6 relate to the source of radiation, and 7 and 8 concern the irradiated object (the sample or the detector). It may be necessary to define some quantities for a small spectral region, a bandwidth of wavelengths or wavenumbers. The differential quotient may be indicated by a subscript, such as L_λ or $L_{\tilde{\nu}}$, and the respective property is known as a *spectral* property, e.g., *spectral radiance*.

* Chapter 3 is contributed by B. Schrader, Essen except section 3.2 and 3.6

Table 3.1-1 Nomenclature and symbols used to describe sources of radiant energy and their activity [IUPAC, Fassel 1972]

I Name	II Symbol	III Definition	IV Dimensions	V SI unit	VI Practical unit
1. radiant flux or radiant power Φ		power in the form of radiation	power	W	W
2. (radiant) energy Q		$Q = \int_0^t \Phi \, dt$	energy	J	W s = J
3. radiant intensity I		$I = \Phi/\omega$	$\frac{\text{power}}{\text{solid angle}}$	W sr ⁻¹	W sr ⁻¹
4. radiance $B \dots L$		$L = \frac{\Phi}{S\omega \cos \varepsilon}$	$\frac{\text{power}}{\text{solid angle} \times \text{area}}$	W sr ⁻¹ m ⁻²	W sr ⁻¹ cm ⁻²
5. (radiant) emissivity J		$J = \frac{\Phi}{V\omega}$	$\frac{\text{power}}{\text{solid angle} \times \text{volume}}$	W sr ⁻¹ m ⁻³	W sr ⁻¹ cm ⁻³
6. (radiant) energy density u		$u = Q/V$	energy/volume	J m ⁻³	J cm ⁻³
7. irradiance E		$E = \Phi/S$	power/area	W m ⁻²	W cm ⁻²
8. (radiant) exposure H		$H = \int_0^t E \, dr$	$\frac{\text{power} \times \text{time}}{\text{area}}$	J m ⁻²	W s cm ⁻² = J cm ⁻²

Reference to 3 to 8:

It must be kept in mind that the basic quantity in this system, the radiant flux Φ , may vary in space and direction. Therefore the area S , the solid angle ω and the volume V in the defining equations 3 to 8 must be small enough to give meaningful loc values for the derived quantities.

Reference to 4, 7 and 8:

S refers to the area of the radiating element for the term radiance, and to the area of the irradiated element for the term irradiance and (radian) exposure; ε is the angle between the normal to the surface and the direction of the radiating beam, which is assumed to be confined to a narrow solid angle.

3.1 The optical conductance

Any optical system transports electromagnetic radiation. This radiant power may comprise information in terms of wavelength distributions, intensity, polarization, and phase, either in space or in time. An optical system is essentially constituted either by imaging elements, such as lenses or mirrors, or conducting elements, such as optical fibers (Sec. 3.3.2). An optical system usually comprises a series of imaging elements. These are combined with elements which produce or detect radiation or interact in different ways with it.

The radiant flux Φ (power, W) transported by any optical system from the source to the detector may be described by the following equation:

$$\Phi = L G \tau \quad (3.1-1)$$

Here, L is the *radiance* (power/solid angle · area, W/cm² · sr) of the light source, G stands for the *optical conductance* (solid angle · area, sr · cm²), and τ represents the *transmission factor of the system*.

The concept of *optical conductance* was introduced by Hansen (1949), based on relations discussed by Abbe (1871) and Helmholtz (1874). It is defined by a IUPAC recommendation (Fassel 1972) and is similar to quantities known as 'throughput' or 'etendue'.

Let us assume that dF_1 is a surface element of a component of an optical system with a surface area F_1 , and dF_2 is a surface element of the next component with an area F_2 . The intervening distance between the two surface elements is a_{12} . α_1 and α_2 are the angles between the intervening line and the normals of the surface elements (Fig. 3.1-1). If the medium between F_1 and F_2 has the refractive index n , then the *optical conductance* G is **defined** by the integral:

$$G = n^2 \int_{F_1} \int_{F_2} (\cos\alpha_1 \cos\alpha_2 / a_{12}^2) dF_1 dF_2 \quad (3.1-2)$$

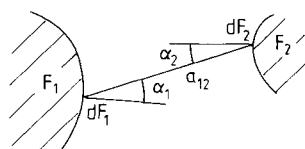


Figure 3.1-1 Parameters for the definition of the optical conductance (Schrader, 1990).

The direction in which the radiation travels is of no relevance. A typical component of an optical system is an area F radiating at (or being irradiated from) a solid angle Ω . It has an optical conductance of:

$$G = n^2 F \Omega \quad (3.1-3)$$

The solid angle of a cone with the half angle Θ is:

$$\Omega = 2\pi (1 - \cos\Theta) = 4\pi \sin^2(\Theta/2) \approx \pi \sin^2\Theta \quad (3.1-4)$$

The approximation

$$G \approx F \pi NA^2, \quad (3.1-5)$$

in which NA is the numerical aperture ($NA = n \sin \Theta$), is only valid for small angles Θ .

The optical conductance of a system with the areas F_1 and F_2 at a distance a_{12} may be approximated if $F_1, F_2 \ll a_{12}^2$:

$$G \approx n^2 F_1 F_2 / a_{12}^2 \quad (3.1-6)$$

In a correctly designed optical instrument each imaging element produces an image of the preceding imaging element upon the following one. On all successive elements, the images of the first two elements (e.g., the source and the next element which collects its radiation) alternate. For such an instrument, the optical conductance between any two apertures in a sequence is invariant (Fig. 3.1-2). As a result, the radiance observed at any cross-section of the beam of an optical instrument is invariant, except for loss by reflection, absorption, or scattering (which is accounted for by the transmission factor τ of the whole instrument). The optical conductance of the part of the arrangement which for theoretical or technical reasons cannot be enlarged determines the effective optical conductance of the entire instrument. This is usually the monochromator or interferometer, sometimes the source, the detector or an optical fiber. In the case of microscopes, it is often determined by the objective and the sample.

In this context, the refractive index in Eqs. 3.1-2, 3.1-3, and 3.1-6 is assumed to be $n = 1$, valid for air or vacuum between the optical elements. The *optical* conductance $G = G_0 \cdot n^2$ in this case is equal to the *geometrical* conductance G_0 .

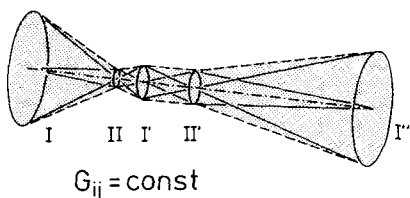


Figure 3.1-2 For a correctly designed optical instrument the optical conductance of any pair of subsequent elements is constant. Images of the preceding element are produced by the following element ($I \rightarrow I' \rightarrow I'' \rightarrow \dots; II \rightarrow II' \rightarrow \dots$), from Schrader (1980).

The optics of optical instruments can be calculated in good approximation by the 'lens equation', assuming 'thin' lenses (Sec. 3.3.2):

$$1/f_2 = 1/a_{12} + 1/a_{23} \quad (3.1-7)$$

and the relation:

$$r_1/r_3 = a_{12}/a_{23} \quad (3.1-8)$$

where f_2 is the focal length of the lens (or the mirror) [2], a_{12} is its distance from the preceding element [1], a_{23} is its distance to the following element [3], and r_1 and r_3 are the beam radii at the elements [1] and [3], respectively (Fig. 3.1-3). The optics of usual spectrometers is adequately described by these approximations, although they ignore the existence of principal points and surfaces and the difference between front and back focal lengths. Only at small f -numbers ($f/2r$) of 1.0 or less, more laborious calculations are necessary (see handbooks of optics).

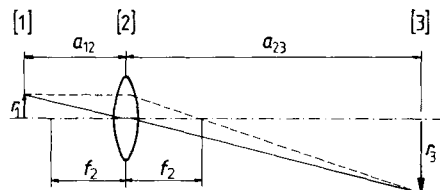


Figure 3.1-3 Imaging properties of a lens.

3.1.1 The optical conductance of spectrometers

The flux through a spectrometer within a small spectral region is appropriately described by Eq. 3.1-1. In this book, the optical properties are usually related to wavenumbers (Eq. 3.1-9) by the *spectral radiance* $L_{\tilde{\nu}}$ (radiance per wavenumber), by the *spectral optical conductance* $G_{\tilde{\nu}}$ (optical conductance per wavenumber), and by $\Delta\tilde{\nu}$, the *bandwidth* of the instrument (in wavenumber units):

$$\Phi = L_{\tilde{\nu}} G_{\tilde{\nu}} (\Delta\tilde{\nu})^2 \tau \quad (3.1-9)$$

$L_{\tilde{\nu}}$ is a property of the radiation source, it is discussed in Sec. 3.3.1. $G_{\tilde{\nu}}$ depends on the type of spectrometer, which may be dispersive or interferometric, and τ is the overall transmission factor of the entire instrument.

The resolving power

The practical resolving power is the ratio of the wavelength (or wavenumber) and the resolution, which may be chosen by changing the dimensions of slits or apertures, $R = \lambda/\Delta\lambda = \tilde{\nu}/\Delta\tilde{\nu}$. Its upper limit is R_0 , the theoretical resolving power, determined by the properties of the dispersive elements or by the path length of interfering rays. $\delta_0\lambda$ or $\delta_0\tilde{\nu}$ is referred to as theoretical resolution.

$$R_0 = \frac{\lambda}{\delta_0\lambda} = \frac{\tilde{\nu}}{\delta_0\tilde{\nu}} \quad (3.1-10)$$

For grating spectrometers, R_0 is determined by the number of the rules of the grating and the order of diffraction (Eq. 3.1-12); while for interferometers it is determined by the shift of the moving mirror (Eq. 3.1-34).

The diffraction pattern of a circular aperture

Images are produced by constructive interference of wavelets. When an ideal lens with the diameter $D = 2R$ is irradiated by a plane wave with the wavelength λ , it produces an interference pattern at the focal region, known as the Airy disc. Its radius is determined by the fact that the length of the rays from the edge of the lens may only differ by less than $\lambda/2$ in order to produce constructive interference (Fig. 3.1-4). The first dark ring about the central maximum is produced by interference of rays from the edge of the lens with a difference in length of $\lambda/2$. Its radius is proportional to the wavelength and inversely proportional to the diameter D of the lens:

$$r = 1.22 \cdot \lambda \cdot f/D \quad (3.1-11)$$

The central disk contains 83.8 % of the radiation energy; the remaining energy is distributed over the surrounding rings (7.2, 2.8, 1.5, 1.0, ... %).

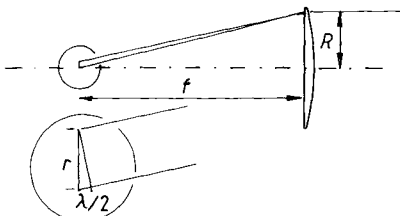


Figure 3.1-4 Diffraction pattern of a circular aperture of the diameter $D = 2R$, the first dark ring about the central maximum has the radius r .

Principle of dispersive instruments

Two monochromatic rays with the wavelengths λ_1 and λ_2 passing a lens at slightly different angles are assumed to be *resolved* if the maximum of the diffraction pattern of

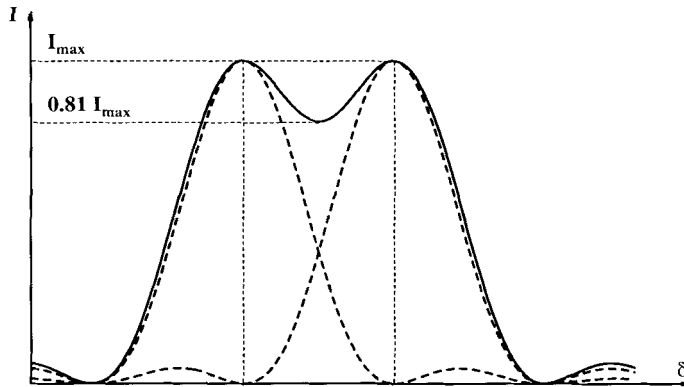


Figure 3.1-5 Two monochromatic rays are regarded as resolved, when the first minimum of the diffraction pattern of one ray is coincident with the maximum of the other ray: Rayleigh criterion.

λ_1 is at the position of the first minimum of the pattern of λ_2 . In this case, the *Rayleigh criterion* is satisfied (Fig. 3.1-5). The different angles are a consequence of the angular dispersion $d\varphi/d\lambda$ of the dispersive elements: the gratings or prisms.

3.1.2 Properties of grating spectrometers

A diffraction grating contains many parallel lines, 'grooves', on a planar or concave support. These grooves may be engraved mechanically, in which case they are known as rules. If they are produced by photographic recording of an interference pattern, these grooves are referred to as lines. The word 'holographic grating' is incorrect and is not recommended (Butler and Laqua, 1993). At some 'blaze angle' or at a 'blaze wavelength', the gratings may have their maximum efficiency, determined mainly by the form of the grooves. Gratings may be used either as transmitting or as reflecting elements. Reflecting gratings are usually coated with a highly reflective layer.

The significant data of a grating are: the total number of grooves N ; the distance between neighboring grooves, the grating constant a ; the length of the grooves or – in the case of a circular grating – its diameter. For a concave grating, either the focal length or the radius of the curvature has to be known.

For a grating which is to be used to disperse radiation with the wavelength λ , the grating constant can have any value between $\lambda/2$ and a high multiple of λ . The total number of rules N defines the number of interfering rays, differing in length by $m \cdot \lambda$, which produce a beam of radiation with the wavelength λ at the m th order of diffraction (Fig. 3.1-6). Therefore, the theoretical resolving power R_0 (Eq. 3.1-10) of a grating is given by:

$$R_0 = m \cdot N \quad (3.1-12)$$

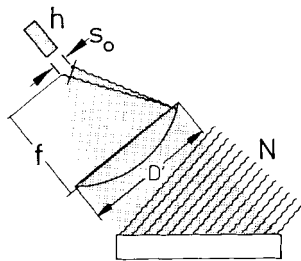


Figure 3.1-6 The main components of a grating spectrometer: N is the number of interfering rays, given by the number of rules; s_0 is the half width of the diffraction pattern of the collimator lens with the diameter D' and the focal length f , it determines the 'optimal' slit width (Laqua, 1980), h is the slit length.

The dispersion of the spectrum produced by a grating is described by the grating equation (which is analogous to Bragg's equation):

$$\sin \varphi_1 \pm \sin \varphi_2 = \pm m \lambda / a \quad (3.1-13)$$

φ_1 is the angle of incidence and φ_2 is the angle of diffraction, both measured relative to the grating normal O (Fig. 3.1-7). The positive sign is taken if both rays are on the same side of the normal. If they are on different sides, the sign of $\sin \varphi_2$ is taken negative; if $|\varphi_2|$ is larger than $|\varphi_1|$, the negative sign for m is taken. Differentiation yields the change of φ_2 with the wavelength, i.e., the *angular dispersion*:

$$\frac{d\varphi_2}{d\lambda} = m / (a \cdot \cos \varphi_2) \quad (3.1-14)$$

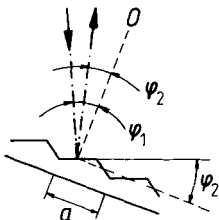


Figure 3.1-7 The parameters of the grating equation: a is the grating constant and φ_1 and φ_2 are the angles of incidence and diffraction, measured relative to the grating normal O .

As described above (Eq. 3.1-11), the collimator or 'camera' lens or mirror of a grating spectrometer produces a diffraction pattern. A monochromatic beam produces a pattern of the width $\delta_0 \varphi_2$, which according to Fig. 3.1-8 is described by the equation:

$$\delta_0 \varphi_2 = \lambda / D' \quad (3.1-15)$$

Eq. 3.1-14 quantifies the relation between $\delta_0 \varphi_2$ and the spectral bandwidth $d\lambda$, which is distributed over this minimum resolved angle. It determines the theoretical resolution and is therefore referred to as $\delta_0 \lambda$ (Eq. 3.1-10):

$$\delta_0 \varphi_2 = m \cdot \delta_0 \lambda / (a \cdot \cos \varphi_2) \quad (3.1-16)$$

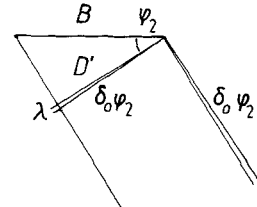


Figure 3.1-8 The resolution of a grating spectrometer. D' is the width of the diffracted beam and B the width of the grating.

Division of Eq. 3.1-15 by Eq. 3.1-16 gives an expression describing the theoretical resolving power R_0 :

$$R_0 = \lambda / \delta_0 \lambda = D' \cdot m / (a \cdot \cos \varphi_2) \quad (3.1-17)$$

With

$$\cos \varphi_2 = D' / B = D' / N \cdot a \quad (3.1-18)$$

(B the width of the grating is equal to $N \cdot a$) it follows that:

$$R_0 = m \cdot N \quad (3.1-19)$$

Eq. 3.1-16, on the other hand, gives:

$$\frac{\delta_0 \varphi_2}{\delta_0 \lambda} = m / (a \cdot \cos \varphi_2) = m \cdot B / a \cdot D' = R_0 / D' \quad (3.1-20)$$

Obviously, the theoretical resolving power is also given by:

$$R_0 = D' \cdot \frac{\delta_0 \varphi_2}{\delta_0 \lambda} \quad (3.1-21)$$

The *linear dispersion* is:

$$\frac{dx}{d\lambda} = \frac{d\varphi_2}{d\lambda} \cdot f \quad (3.1-22)$$

Here, f is the focal length of the 'camera' lens. The *geometrical slit width* s , which allows selection of the bandwidth $\Delta\lambda$, is:

$$s = \frac{dx}{d\lambda} \cdot \Delta\lambda = f \cdot \frac{\delta\varphi_2}{\delta_0\lambda} \cdot \Delta\lambda = f \cdot \frac{R_0}{D'} \cdot \Delta\lambda \quad (3.1-23)$$

Its minimum value, with $s_0 = 2r$ was already given by Eq. 3.1-11.

3.1.3 Properties of prism spectrometers

For a prism spectrometer with a symmetrically arranged prism with the refractive index n at an angle γ (Fig. 3.1-9), the angular dispersion is given by

$$\frac{d\varphi}{d\lambda} = 2 \frac{dn}{d\lambda} \left(\frac{1}{\sin^2 \gamma/2} - n^2 \right)^{-1/2} \quad (3.1-24)$$

where $dn/d\lambda$ is the *material dispersion* or *dispersive power*. The theoretical resolving power of a prism is determined by the different lengths of the extreme rays, measured in terms of numbers of waves:

$$R_0 = b \cdot \frac{dn}{d\lambda} \quad (3.1-25)$$

where b is the length of the base of the prism. By analogy with the derivation for the grating, the geometrical slit width s for a bandwidth $\Delta\lambda$ is again

$$s = f \cdot \frac{R_0}{D'} \cdot \Delta\lambda \quad (3.1-26)$$

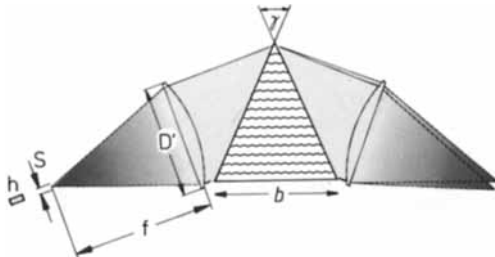


Figure 3.1-9 The significant features of a prism spectrometer: b length of the basis, γ angle of the prism, D' diameter of the collimator lens with the focal length f , s width and h length of the entrance slit.

3.1.4 Optical conductance of prism and grating spectrometers

According to Eq. 3.1-6, the optical conductance of an optical instrument equals the product of the areas of succeeding active elements, divided by the square of their distance:

$$G = \frac{s \cdot h \cdot D' \cdot H}{f^2} \quad (3.1-27)$$

Here, s is the width and h is the length of the entrance slit, D' stands for the width, and H represents the height of the beam at the grating or prism. Eqs. 3.1-23 and 3.1-26 yield the slit width s for a desired band width $\Delta\lambda$. Substitution in Eq. 3.1-27 gives

$$G = \frac{h \cdot H}{f} \cdot R_0 \cdot \Delta\lambda \quad (3.1-28)$$

Eqs. 3.1-19 and 3.1-25, which describe the relation between the characteristics of gratings and prisms and the theoretical resolving power R_0 , give the optical conductance of grating and prism spectrometers. We may write

$$G = G_\lambda \cdot \Delta\lambda \quad (3.1-29)$$

where G_λ is the optical conductance per wavelength unit. From $R_0 = \lambda/\Delta\lambda = \tilde{\nu}/\Delta\tilde{\nu}$, it follows that

$$\Delta\lambda = \Delta\tilde{\nu}/\tilde{\nu}^2 \quad (3.1-30)$$

Eq. 3.1-28 can thus be modified to give

$$G = \frac{h \cdot H}{f \cdot \tilde{\nu}^2} \cdot R_0 \cdot \Delta\tilde{\nu} \quad (3.1-31)$$

or

$$G = G_{\tilde{\nu}} \cdot \Delta\tilde{\nu}. \quad (3.1-32)$$

$G_{\tilde{\nu}}$, the optical conductance per wavenumber of grating and prism spectrometers, is therefore described by:

$$G_{\tilde{\nu}} = \frac{h \cdot H}{f \cdot \tilde{\nu}^2} \cdot R_0 \quad (3.1-33)$$

3.1.5 Optical conductance of interferometers

The famous Michelson interferometer records interferograms caused by interference of two beams of different lengths. The length of one of the beams is varied by a moving mirror (Fig. 3.1-10). The theoretical resolving power of a Michelson interferometer simply equals the number of wavelengths over a certain distance, given by twice the displacement of the moving mirror (Fig. 3.1-10):

$$R_0 = 2\Delta l/\lambda = 2\Delta l \cdot \tilde{\nu} \quad (3.1-34)$$

However, the rays are not strictly parallel:

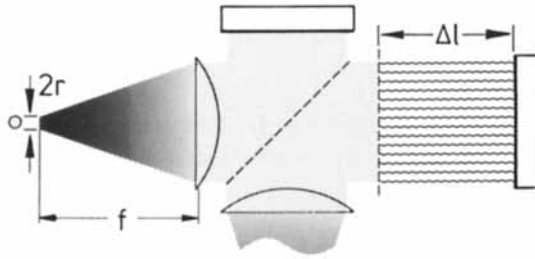


Figure 3.1-10 The significant features of an interferometer: Δl displacement of the moving mirror, $2r$ diameter of the Jacquinot stop.

True point sources cannot emit radiation, true parallel beams cannot transport radiation: the optical conductance of instruments with such elements would be 0!

Equivalent to the entrance slit of a grating or prism spectrometer, interferometers have also to use an aperture, known as Jacquinot stop. This is necessary in order to make use of the resolving power through displacement of the moving mirror. The rays emerging from the edge of this stop are somewhat longer than the rays which emerge from its center. The difference in length between these rays increases with the shift of the moving mirror. An exact calculation (Griffiths and de Haset, 1986) yields the relation between the allowed radius of the Jacquinot stop r , the focal length of the entrance optics, and the theoretical resolving power, determined by the displacement of the moving mirror:

$$r = f \cdot \sqrt{2/R_0} \quad (3.1-35)$$

According to Eq. 3.1-6, the optical conductance of an interferometer is therefore given by

$$G = G_{\tilde{\nu}} \cdot \Delta \tilde{\nu} = G_{\lambda} \cdot \Delta \lambda = \frac{r^2 \cdot \pi \cdot F_1}{f^2} = \frac{2 \cdot \pi \cdot F_1}{R_0} \quad (3.1-36)$$

Here, r is the radius of the Jacquinot stop, F_1 stands for the area of the beam at the beam splitter, and R_0 represents the resolving power, determined by the displacement of the moving mirror. For the optical conductance per unit bandwidth G_{λ} or $G_{\tilde{\nu}}$, we obtain:

$$G_{\lambda} = \frac{2 \cdot \pi \cdot F_1}{\lambda} \quad (3.1-37)$$

and

$$G_{\tilde{\nu}} = \frac{2 \cdot \pi \cdot F_1}{\tilde{\nu}} \quad (3.1-38)$$

The optical conductance of an interferometer is therefore given by:

$$G = \frac{2 \cdot \pi \cdot F_1}{\tilde{\nu}} \Delta \tilde{\nu} \quad (3.1-39)$$

3.1.6 Application of dispersive spectrometers and interferometers to vibrational spectroscopy; the Jacquinot advantage

The first present-day infrared spectrometers used prism monochromators. During the 1960's, these were replaced by grating instruments, which have a larger optical conductance throughout the entire spectral range. In the seventies, interferometers were introduced, since they further increased the optical conductance considerably (Jacquinot, 1954), combined with the multiplex or Fellgett advantage (Fellgett, 1958) (see Sec. 3.3.4).

Raman spectroscopy underwent almost the same change in instrumentation from prism to grating spectrometers. However, interferometers were only seldom used (Jennings, Weber and Brault, 1986).

The Raman spectrum to be analyzed contains mainly the exciting radiation with the frequency $\tilde{\nu}_0$, which is a result of Rayleigh and Tyndall scattering as well as reflection and refraction at particles and cuvettes. This radiation is accompanied by very strong lines and 'wings', which are due to rotational and translational vibrations of molecules in the condensed phase, with wavenumber shifts of up to about 80 cm^{-1} from the exciting line. The 'real' Raman lines have an intensity which is lower by several orders of magnitude, $10^{-6} \dots 10^{-12}$. The statistical noise of the quantum flux of the exciting radiation and the 'Rayleigh wings', i.e., the shot noise, is according to Poisson statistics proportional to the square root of the intensity. When the interferogram is transformed into a spectrum, this noise is distributed and appears as a background noise throughout the entire spectrum. It is even stronger than the strongest Raman lines. This *multiplex disadvantage* (Hirschfeld, 1976 b) has prevented the use of interferometers for Raman spectroscopy. However, if the Rayleigh line and its wings are completely eliminated from the radiation to be analyzed, then Raman spectra can be recorded. In this case, the Jacquinot advantage is complemented by a multiplex advantage (Secs. 3.5.2, 3.5.5).

As early as 1954, Jacquinot pointed out that interferometers have a considerably higher optical conductance than prism or grating spectrometers. In order to quantify this relation we use Eqs. 3.1-33 and 3.1-39 and add G or I as a superscript to designate the spectral optical conductance of grating instruments and interferometers, respectively:

$$G_{\tilde{\nu}}^G = \frac{h \cdot H}{f \cdot \tilde{\nu}^2} \cdot R_0 \quad (3.1-33 \text{ a})$$

According to this equation, the ratio between the length of the slit h and the focal length of the collimator f is relevant for the spectral optical conductance of a grating spectrometer. It is usually on the order of 0.01; values of up to 0.2 are only reached in very special cases (the old model 81 Cary Raman spectrometer with an 'image slicer', made in 1960).

R_0 is defined by the width of the grating D' (which for square gratings is approximated by the length of the grooves H), divided by the grating constant a . As pointed out above, the grating constant has a value between $\lambda/2$ and a high multiple of λ ; a good approximation is $a \approx \lambda = 1/\tilde{\nu}$. Therefore, R_0 may be approximated by $H \cdot \tilde{\nu}$. Eq. 3.1-33a

may thus be changed to

$$G_{\tilde{\nu}}^G \approx \frac{hH^2}{f\tilde{\nu}} \quad (3.1-40)$$

To compare this relation with the properties of an interferometer described by Eq. 3.1-39, we choose the beam area of the interferometer F_1 equal to the beam area at the grating H^2 . The spectral optical conductance of an interferometer thus equals:

$$G_{\tilde{\nu}}^I = \frac{2\pi H^2}{\tilde{\nu}} \quad (3.1-41)$$

Therefore, the ratio of the optical conductance of an interferometer and that of a grating spectrometer, the *Jacquinot Advantage*, is given by

$$\frac{G_{\tilde{\nu}}^I}{G_{\tilde{\nu}}^G} \approx \frac{2\pi f}{h} \quad (3.1-42)$$

We can see that this is a geometrical factor, independent of the wavelength range. For spectrometers with the same beam area at the grating and at the beam splitter, it is usually on the order of 500. However, common interferometers generally have a smaller beam area than grating instruments, which is why the Jacquinot advantage determined by comparing actual instruments is of the order of 100.

A comparison of the properties of grating spectrometers and interferometers should also include the total transmittance τ of the entire instrument. For infrared grating spectrometers and interferometers, τ is of about the same magnitude, i.e., about 40 %. Raman spectrometers are confronted with 'unshifted radiation' of very high intensity, which exceeds that of a typical Raman line by a factor of $10^6 \dots 10^{12}$. Therefore, triple monochromators on the one hand and interferometers with potent Rayleigh filters on the other hand have to be employed. Single monochromators have transmission factors of about 40 %; for a triple monochromator, τ would be 6.4 %. A combination of a Michelson interferometer with a powerful Rayleigh filter may have a somewhat higher transmittance.

In conclusion it can be stated that the spectral optical conductance for a prism spectrometer, a grating spectrometer, and a Michelson interferometer are approximately as 1 : 10 : 1000.

A comparison of grating instruments and interferometers is not complete without discussing the so-called multiplex advantage and some other consequences of the geometry of the instruments. This is discussed in Sec. 3.5.2.

3.1.7 Interference filters

Interference filters are used in photometers and spectrometers as fixed wavelength or tunable wavelength filters. An interference filter, equivalent to a Fabry-Perot etalon,

is a multiple beam interferometer. Between two semitransparent mirrors there is multiple constructive interference for all wavelengths, the multiples of which equal exactly the double optical length of the cavity. The standing waves are known as modes (Fig. 3.1-11), and the transmission maxima are given by

$$m \cdot \lambda = 2 \cdot d \cdot n; \quad \tilde{\nu} = m/2dn. \quad (3.1-43)$$

In Fabry-Perot etalons, the cavity encloses air, a gas, or vacuum, while for interference filters transparent dielectric layers are used. The real length of the interfering beam is N times the length of the cavity, due to multiple reflection. N , the so-called *finesse*, is determined by the reflectivity ρ of the mirrors: $N = \pi \cdot \sqrt{\rho}/(1 - \rho)$. Therefore, the resolving power, as above, equals the length of the interfering beam in units of the wavelength:

$$R_0 = 2dnN/\lambda \quad (3.1-44)$$

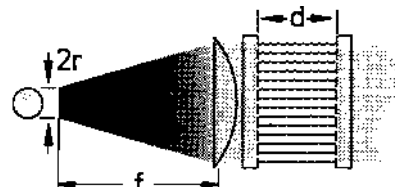


Figure 3.1-11 The significant features of Fabry-Perot-Etalons or interference line filters.

The radius of the Jacquinot stop is given by Eq. 3.1-35, while the spectral optical conductance of interference filters is quantified by Eq. 3.1-39. Interference filters have multiple transmission peaks for different orders m (Eq. 3.1-43). Unwanted peaks are 'blocked' by additional interference or absorption filters. The resolving power of an interference filter is usually somewhat less than that of grating spectrometers or interferometers. As a consequence the Jacquinot stop is large. This results in a high optical conductance. Filters with wedge-shaped cavities are used as tunable interference filters. Interference filters are usually constructed to transmit a small wavelength range. When used as a reflector, an interference filter has reflection minima at the maxima of the transmission at different orders m .

3.1.8 Lasers

A laser is a radiation source which produces a very high spectral radiance in a small spectral range at a fixed wavelength. A laser combines a radiation source with spectral isolation of its radiation – two important components of a spectrometer. The word laser is an acronym which stands for light amplification by stimulated emission of radiation. The essential elements of a laser are: an active medium; a pumping process to produce a population inversion; and a suitable geometry or optical feedback elements (Moore et al., 1993). Most lasers are essentially Fabry-Perot interferometers whose cavities contain

atoms or molecules in a state which allows stimulated emission of radiation, amplifying the standing waves, the *modes*, according to Eq. 3.1-43. Lasers produce coherent radiation with a definite phase relationship between the waves, both spatially as well as temporally.

Tunable lasers allow selection of the emission wavelength within a definite wavelength range. They function both as radiation sources and as monochromators.

Lasers are ideal radiation sources for Raman spectroscopy. They usually have a large resonator with highly reflecting windows, therefore, the resolving power may be very high. The optical conductance however, is very low, since the diameter of the laser beam and its solid angle are small. By concentrating the stimulated emission in the standing waves, the allowed modes of the resonator, a very high spectral radiance is produced. It is several orders of magnitude higher than 'classical' radiation sources, such as hot filaments, plasmas, semiconductors, or the sun. Thus, high radiant fluxes are available and may be transported even through optical systems with a low optical conductance, such as optical fibers.

3.2 Polarized radiation*

Light consists of electromagnetic waves whose vibrations are transverse to the propagation direction. Such a wave package contains beams vibrating randomly in different manners. If the vibrations, however, exhibit some spatial preference then the light beam is said to be *polarized*.

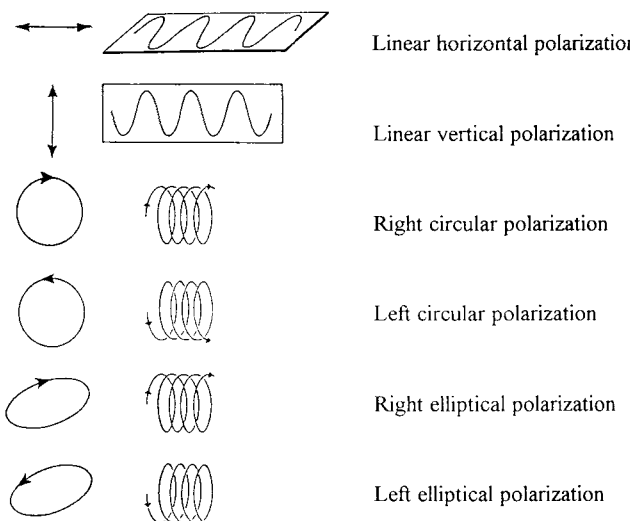


Figure 3.2-1 Schematic representation of various types of polarization.

* Section 3.2 is contributed by B. Jordanov, Sofia

When the vibration of the electric vector of the radiation wave proceeds in one plane, the light is *linearly polarized*. The vibration plane itself is called the *polarization plane*. The propagation of the electromagnetic wave may also proceed in a helix with circular or elliptical shape. The radiation is then understood to be *circularly* or *elliptically* polarized, having in mind that the sense of rotation of the electric vector determines an additional quality of the polarization – its “handedness”. The latter term originates from the specific geometry of human hands that has led to the meanings of “left” and “right”. Depending on that how the propagating electric vector rotates, clockwise or anti-clockwise, the resulting polarization is said to be *right* or *left*. Fig. 3.2-1 portrays the possible types of polarization.

3.2.1 The Stokes – Mueller formalism

To obtain knowledge about the polarization state and intensity of a light bundle having passed through a train of optical elements is a task of great practical value. A few general approaches exist which phenomenologically combine the relationships between the properties of the light bundle and the optical devices. According to the way of displaying the intensity and polarization state of the beam emerging from the optical train the following representations exist: the Poincaré sphere, the Stokes vector, the Jones vector and the so-called quantum mechanical analogy representations. Since they all reflect the same laws of optics they are equally true and only the nature of a definite optical problem to be solved determines which of them can more efficiently be used. For some reasons, which will be discussed later in a more detailed manner, the concept of the Stokes vector representation has gained more popularity. First, it could be reduced to some simple rules for performing calculations of intensity in various cases of polarization, and second, the corresponding mathematical procedure can undergo a convenient algorithmic representation also for use with computers. Therefore, in this section only the Stokes-Mueller formalism will be considered which reflects the Stokes vector approach. We shall kindly ask the reader to refer to the old but excellent monograph “Polarized Light” by Shurcliff (1962) for information about the other representations describing the polarization of light. Certainly there also exist much newer treatments of the problem (Gerard and Burch, 1975; Azam and Bashara, 1977; Röseler, 1990; Jensen et al., 1978; Schellman and Jensen 1987).

3.2.1.1 The Stokes vector

The appearance of Stokes’ publication, in which the concept of a vector representation of the beam description parameters was introduced, renders back to 1852. It, however, has remained for many years unnoticed (Shurcliff, 1962). The need for a general systematic and effective procedure for solving the exponentially growing quantity of optical problems has led to the rediscovery of Stokes’ approach to polarized radiation. Mueller’s contribution consists of developing a matrix calculus for evaluation of the four elements of the Stokes vector which are a set of quantities describing the intensity and polarization of a light beam.

The four parameters that are elements of the Stokes vector have the dimensions of intensity ($\text{W} \cdot \text{sr}^{-1}$). Each of them corresponds actually to a time-averaged intensity, and not to an instantaneous intensity value. Each of them shows how the intensity of a beam changes under the effect of a polarization device with standardised properties.

Various notations have been introduced by different authors for the elements of the Stokes vector. We shall use in this chapter the symbols most frequently applied nowadays since they have gradually turned to a general convention. Thus

$$\mathbf{S} = \begin{bmatrix} S_0 \\ S_1 \\ S_2 \\ S_3 \end{bmatrix} \quad (3.2-1)$$

stands for the Stokes vector in most of the numerous publications of the last ten years dealing with Stokes-Mueller's treatments of optical problems. S_0 is the overall beam intensity, S_1 is the horizontal linear dichroism, S_2 is the linear dichroism at $+45^\circ$ with respect to the horizontal line and S_3 is the right circular dichroism (see Sec. 3.2.1.2 C). Each element should otherwise be interpreted as the intensity transmitted by either a horizontally oriented linear polarizer (S_1), or by a polarizer oriented at $+45^\circ$ (S_2), or finally, by a right circular polarizer (S_3). Fig. 3.2-2 visualises schematically the elements of the Stokes vector.

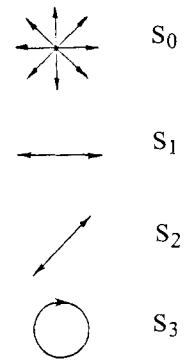


Figure 3.2-2 Polarization forms corresponding to the four Stokes parameters of a light beam. S_0 – unpolarized, S_1 – horizontally polarized, S_2 – polarized at $+45^\circ$, S_3 – right circularly polarized.

If the x - and y -amplitude components of the electric vector of the radiation are denoted by a_x and a_y , and the phase shift between them by δ , then the quantitative expressions of the Stokes vector elements are defined as follows:

$$S_0 = \langle a_x^2 + a_y^2 \rangle$$

$$S_1 = \langle a_x^2 - a_y^2 \rangle$$

$$S_2 = \langle 2a_x a_y \cos \delta \rangle$$

$$S_3 = \langle 2a_x a_y \sin \delta \rangle$$

The angular brackets mean time averaging of the amplitude expressions. It is often convenient to work with the so called normalised Stokes vector obtained after dividing all Stokes' elements S_0, S_1, S_2 , and S_3 by the first one, S_0 . The normalised Stokes vector displays the relative state of the beam having passed one or more optical elements. Let us consider a few typical cases and their description by means of the Stokes vector.

1. Unpolarized light: $a_x = a_y$

$$S_0 = 2a_x^2$$

$$S_1 = 0$$

$$S_2 = \langle 2a_x^2 \cdot \cos \delta \rangle = 2a_x^2 \langle \cos \delta \rangle = 0$$

$$S_3 = \langle 2a_x^2 \sin \delta \rangle = 2a_x^2 \langle \sin \delta \rangle = 0$$

Since the amplitudes are independent of the phase shifts the latter remain in the brackets and give exactly the zero average value of $\cos \delta$ and $\sin \delta$ in the interval $0 < \delta < 360$. In other words the unpolarized light could be considered as consisting of beams containing all possible phase shifts. Therefore, the Stokes vector of an unpolarized beam is written down as:

$$\mathbf{S} = \{2a_x^2, 0, 0, 0\}$$

or in a normalised form \mathbf{S}_n

$$\mathbf{S}_n = \{1, 0, 0, 0\}$$

2. Horizontally polarized beam: $a_y = 0$

$$S_0 = a_x^2$$

$$S_1 = a_x^2$$

$$S_2 = 0$$

$$S_3 = 0$$

$$\mathbf{S} = \{a_x^2, a_x^2, 0, 0\}$$

and normalised

$$\mathbf{S}_n = \{1, 1, 0, 0\}$$

3. Beam polarized at 45° : $a_x = a_y, \delta = 0$

$$\begin{aligned} S_0 &= 2a_x^2 \\ S_1 &= 0 \\ S_2 &= 2a_x^2 \\ S_3 &= 0 \\ S &= \{2a_x^2, 0, 2a_x^2, 0\} \\ S_{\mathbf{n}} &= \{1, 0, 1, 0\} \end{aligned}$$

4. Right circularly polarized beam: $a_x = a_y, \delta = \pi/2$

$$\begin{aligned} S_0 &= 2a_x^2 \\ S_1 &= 0 \\ S_2 &= 0 \\ S_3 &= 2a_x^2 \\ S &= \{2a_x^2, 0, 0, 2a_x^2\} \\ S_{\mathbf{n}} &= \{1, 0, 0, 1\} \end{aligned}$$

It is obvious from the above consideration that a vertically polarized beam ($a_x = 0$), a beam polarized at -45° ($a_x = a_y, \delta = \pi$), and a left circular polarized beam ($a_x = a_y, \delta = \pi/2$) will have the following Stokes vectors:

$$\begin{aligned} S &= \{a_y^2, -a_y^2, 0, 0\}; & S_{\mathbf{n}} &= \{1, -1, 0, 0\} \\ S &= \{2a_y^2, 0, -2a_y^2, 0\}; & S_{\mathbf{n}} &= \{1, 0, -1, 0\} \\ S &= \{2a_y^2, 0, 0, -2a_y^2\}; & S_{\mathbf{n}} &= \{1, 0, 0, -1\} \end{aligned}$$

All these results are summarised in Table 3.2-1.

Table 3.2-1 Stokes vectors describing the possible polarization states of light

Polarization state	Normalized Stokes vectors
Unpolarized	{1, 0, 0, 0}
Horizontally polarized	{1, 1, 0, 0}
Vertically polarized	{1, -1, 0, 0}
Polarized at 45°	{1, 0, 1, 0}
Polarized at -45°	{1, 0, -1, 0}
Right circularly polarized	{1, 0, 0, 1}
Left circularly polarized	{1, 0, 0, -1}

3.2.1.2 The Mueller matrices

The basic concept of the Stokes-Mueller calculus is that the transformation of the state of a beam under the action of an optical element could unequivocally be described by multiplying its Stokes vector S_0 by a matrix M (Mueller matrix) from the left. The resulting new Stokes vector S_r represents the altered state of the beam.

$$S_r = MS_0 \quad (3.2-2)$$

The effect of several elements through which a beam may pass is described by the matrix product of the Mueller matrices M_i corresponding to each of the optical elements E_i . The matrix product is build up from right to left in the sequence in which the beam enters each of these elements, $E_n, \dots, E_3, E_2, E_1$.

$$S_r = M_n \dots M_3 M_2 M_1 S_0 \quad (3.2-3a)$$

$$M = M_n \dots M_3 M_2 M_1 \quad (3.2-3b)$$

$$S_r = MS_0 \quad (3.2-3c)$$

$$(M_1 \Leftrightarrow E_1, M_2 \Leftrightarrow E_2, \dots, M_n \Leftrightarrow E_n)$$

M could be considered as an equivalent Mueller matrix corresponding to a hypothetical equivalent optical element \mathcal{E} which substitutes for the overall effect of E_1, E_2, \dots, E_n . In many cases the equivalent element \mathcal{E} can really exist so that the analysis on the basis of the Stokes-Mueller method would often be able to predict the simplest solution to a given optical problem. Let us consider a few typical examples for the application of the method.

A. Ideal horizontal linear polarizer

Such a device has the property to convert unpolarized light into horizontally polarized light, eliminating all vertical components of the unpolarized radiation. Therefore, the overall beam intensity of the polarized beam would be half of that of the unpolarized one, i.e.

$$S_0 = \{1, 0, 0, 0\} - \text{unpolarized beam}$$

$$S_r = \{1/2, 1/2, 0, 0\} = 1/2\{1, 1, 0, 0\} - \text{polarized beam}$$

The transformation itself has the form:

$$\begin{bmatrix} 1/2 \\ 1/2 \\ 0 \\ 0 \end{bmatrix} = \begin{bmatrix} 1/2 & 1/2 & 0 & 0 \\ 1/2 & 1/2 & 0 & 0 \\ 0 & 0 & 0 & 0 \\ 0 & 0 & 0 & 0 \end{bmatrix} \cdot \begin{bmatrix} 1 \\ 0 \\ 0 \\ 0 \end{bmatrix}$$

$$S_r \qquad \qquad \qquad M \qquad \qquad \qquad S_0$$

B. Linear retarder with $\delta = \pi$ (polarization rotator)

The purpose of such a device consists in changing the orientation of the polarization plane of a beam by 90° . That means the initial Stokes vector $\{1, 1, 0, 0\}$ of a horizontally polarized beam becomes $\{1, -1, 0, 0\}$ after passing through the retarder. Retarders are most often birefringent crystals of definite thickness. If the fast and slow axes of such a crystal orthogonal to each other are crossed at 45° with respect to the polarization plane, the retarder rotates the latter by 90° . The Stokes-Mueller transformation corresponding to this experiment should be:

$$\begin{bmatrix} 1 \\ -1 \\ 0 \\ 0 \end{bmatrix} = \begin{bmatrix} 1 & 0 & 0 & 0 \\ 0 & -1 & 0 & 0 \\ 0 & 0 & 1 & 0 \\ 0 & 0 & 0 & -1 \end{bmatrix} \cdot \begin{bmatrix} 1 \\ 1 \\ 0 \\ 0 \end{bmatrix}$$

$S_r \qquad \qquad M \qquad \qquad S_\theta$

Note that an ideal retarder does not change the intensity of the incoming beam.

Similar approaches can be applied to each type of polarization devices. A generalised representation of the Mueller matrices can be created separately for polarizers and retarders which acquires then a very compact form from which Mueller matrices for all possible types of polarizers and retarders can be derived. Since the matter exceeds the scope of the present consideration only a few Mueller matrices will be listed while for more details the reader could again refer to Shurcliff (1962).

C. The polarization sensitive sample

When spectroscopy with polarized light or other optical polarization measurements are performed the studied sample becomes one element of the optical train which transmits the beam from the radiation source to the detector. Four optical phenomena might take place in a sample sensitive to polarized radiation. We list them below together with their physical definition:

- | | | |
|------|------------------------------------|--|
| i. | Linear dichroism | $LD = (A_{ } - A_{\perp})/2$ |
| | Linear dichroism at 45° | $LD' = (A_{+45^\circ} - A_{-45^\circ})/2$ |
| ii. | Linear birefringence | $LB = 2\pi (n_{ } - n_{\perp})/\lambda_{vac}$ |
| | Linear birefringence at 45° | $LB' = 2\pi (n_{+45^\circ} - n_{-45^\circ})/\lambda_{vac}$ |
| iii. | Circular dichroism | $CD = (A_L - A_R)/2$ |
| iv. | Circular birefringence | $CB = 2\pi (n_L - n_R)/\lambda_{vac}$ |

where $A_{||}$ and A_{\perp} mean the absorbance of the anisotropic sample, parallel and perpendicular to a prior orientation direction respectively. A_R and A_L signify the absorbance of

the optically active sample with respect to right and left circularly polarized radiation. The remaining symbols n_{\parallel} and n_{\perp} are the so called ordinary and extraordinary refractive indices of the anisotropic sample while n_R and n_L are the refractive indices with respect to right and left polarized radiation. Finally λ_{vac} is the radiation wavelength in vacuum. It has been derived (Jensen et al., 1978) that the Mueller matrix of an anisotropic sample expressed in terms of LD , LB , CD , and CB has in general the form:

$$\mathbf{M} = e^{\mathbf{H}}, \text{ where} \quad (3.2-4)$$

$$\mathbf{H} = \begin{pmatrix} A & LD & LD' & -CD \\ LD & A & -CB & -LB' \\ LD' & CB & A & LB \\ -CD' & LB' & -LB & A \end{pmatrix} \quad (3.2-5)$$

Performing the exponentiation according to equation (3.2-4) leads to long expressions for each element of \mathbf{M} which are given by Jensen et al. (1978). This most general representation certainly assumes that a sample exhibits all possible effects. Such cases, if not excluded, are relatively rare. Much more often simpler cases appear when either the pair of LD and LB or that of CD and CB can be simultaneously present in one sample. Depending on the conditions of the experiment one term of pairs might also be eliminated so that the sample gives rise to only a pure polarization optical phenomenon. A table is listed below containing the Mueller matrices for samples with a single polarization phenomenon.

In the listed matrices the \sin , \cos , \sinh , and \cosh functions arise from the exponentiation according to equation (3.2-4). Here, A stands for the Napierian absorbance.

Let us consider some examples for the application of the Stokes-Mueller calculus.

A. Absorption of linearly polarized radiation by a linear dichroic sample

Let the transformation of the Stokes vector \mathbf{S}_0 for an unpolarized light beam be written down as

$$\mathbf{S}_r = \mathbf{M}_S \mathbf{M}_P \mathbf{S}_0 \quad (3.2-6)$$

for radiation which has passed through a polarizer and a linear dichroic sample. \mathbf{M}_P and \mathbf{M}_S are the Mueller matrices of the polarizer and the sample. Setting up the matrix product $\mathbf{M}_S \mathbf{M}_P$ with the matrices \mathbf{M}_P from Table 3.2-2 and \mathbf{M}_S from Table 3.2-3 gives

$$\begin{aligned}
 \mathbf{M}_S \mathbf{M}_P &= \frac{1}{2} e^A \begin{bmatrix} \cosh LD & \sinh LD & 0 & 0 \\ \sinh LD & \cosh LD & 0 & 0 \\ 0 & 0 & 1 & 0 \\ 0 & 0 & 0 & 1 \end{bmatrix} \cdot \begin{bmatrix} 1 & 1 & 0 & 0 \\ 1 & 1 & 0 & 0 \\ 0 & 0 & 0 & 0 \\ 0 & 0 & 0 & 0 \end{bmatrix} = \\
 &= \frac{1}{2} e^A \begin{bmatrix} \cosh LD - \sinh LD & \cosh LD + \sinh LD & 0 & 0 \\ \cosh LD - \sinh LD & \cosh LD + \sinh LD & 0 & 0 \\ 0 & 0 & 0 & 0 \\ 0 & 0 & 0 & 0 \end{bmatrix}
 \end{aligned}$$



Figure 3.2-3 Possible arrangements of sample and polarizer in an *LD* experiment.

Table 3.2-2 Classification of ideal optical devices and their corresponding Mueller matrices

Linear polarizers			
Polarization	Mueller matrix	Polarization	Mueller matrix
$\leftrightarrow \theta = 0^\circ$	$\frac{1}{2} \begin{bmatrix} 1 & 1 & 0 & 0 \\ 1 & 1 & 0 & 0 \\ 0 & 0 & 0 & 0 \\ 0 & 0 & 0 & 0 \end{bmatrix}$	$\uparrow \theta = 90^\circ$	$\frac{1}{2} \begin{bmatrix} 1 & -1 & 0 & 0 \\ -1 & 1 & 0 & 0 \\ 0 & 0 & 0 & 0 \\ 0 & 0 & 0 & 0 \end{bmatrix}$
$\nearrow \theta = 45^\circ$	$\frac{1}{2} \begin{bmatrix} 1 & 0 & 1 & 0 \\ 0 & 0 & 0 & 0 \\ 1 & 0 & 1 & 0 \\ 0 & 0 & 0 & 0 \end{bmatrix}$	$\nwarrow \theta = -45^\circ$	$\frac{1}{2} \begin{bmatrix} 1 & 0 & -1 & 0 \\ 0 & 0 & 0 & 0 \\ -1 & 0 & 1 & 0 \\ 0 & 0 & 0 & 0 \end{bmatrix}$
Retarders			
Retardation	Mueller matrix	Retardation	Mueller matrix
right circular	$\begin{bmatrix} 1 & 0 & 0 & 0 \\ 0 & 1 & 0 & 0 \\ 0 & 0 & 0 & -1 \\ 0 & 0 & 1 & 0 \end{bmatrix}$	left circular	$\begin{bmatrix} 1 & 0 & 0 & 0 \\ 0 & 1 & 0 & 0 \\ 0 & 0 & 0 & 1 \\ 0 & 0 & -1 & 0 \end{bmatrix}$
Circular polarizers			
Polarization	Mueller matrix	Polarization	Mueller matrix
right circular	$\frac{1}{2} \begin{bmatrix} 1 & 0 & 1 & 0 \\ 0 & 0 & 0 & 0 \\ 0 & 0 & 0 & 0 \\ 1 & 0 & 1 & 0 \end{bmatrix}$	left circular	$\frac{1}{2} \begin{bmatrix} 1 & 0 & -1 & 0 \\ 0 & 0 & 0 & 0 \\ 0 & 0 & 0 & 0 \\ -1 & 0 & 1 & 0 \end{bmatrix}$

The same matrix product is obtained if the multiplication $\mathbf{M}_P\mathbf{M}_S$ is performed instead of $\mathbf{M}_S\mathbf{M}_P$. That means the matrices \mathbf{M}_P and \mathbf{M}_S commute, and since one-to-one correspondence exists between the Mueller matrices and the optical elements which they represent, the mathematical commutation signifies that the places of the polarizer and the sample could be interchanged in the optical train. In other words the optical schemes in Fig. 3.2-3 turn out to be equivalent.

Only reasoning of technical nature could lead to a decision whether scheme a or b should be preferred in an experiment. Exactly the same result is obtained if one takes from Table 3.2-2 the Mueller matrix for the perpendicular polarizer.

B. Absorption of circularly polarized radiation by an optically active sample

In a real experiment circular polarization is obtained as a result of converting linearly polarized light by a retarder crossed at 45° to the polarization plane. Therefore, an optical train composed of polarizer (45°), retarder (0°) and optically active sample can be represented in terms of the Stokes-Mueller formalism (Fig. 3.2-4) as follows:

$$\mathbf{S}_r = \mathbf{M}_S \mathbf{M}_R \mathbf{M}_P \mathbf{S}_0. \quad (3.2-7)$$

The matrices of the 45° polarizer \mathbf{M}_P , of the retarder \mathbf{M}_R and of the optically active sample \mathbf{M}_S multiply consequently from the left the Stokes vector \mathbf{S}_0 of the unpolarized beam.

The matrices \mathbf{M}_P and \mathbf{M}_R are taken from Table 3.2-2, and the sample matrix from Table 3.2-3 respectively. The matrix product $\mathbf{M}_S \mathbf{M}_R \mathbf{M}_P$ can be set up as:

$$\mathbf{M}_S \mathbf{M}_R \mathbf{M}_P = \frac{1}{2} e^{-A} \begin{bmatrix} \cosh CD & 0 & 0 & \sinh CD \\ 0 & 1 & 0 & 0 \\ 0 & 0 & 1 & 0 \\ \sinh CD & 0 & 0 & \cosh CD \end{bmatrix} \cdot \begin{bmatrix} 1 & 0 & 0 & 0 \\ 0 & 1 & 0 & 0 \\ 0 & 0 & 0 & -1 \\ 0 & 0 & 1 & 0 \end{bmatrix} \cdot \begin{bmatrix} 1 & 0 & 1 & 0 \\ 0 & 0 & 0 & 0 \\ 1 & 0 & 1 & 0 \\ 0 & 0 & 0 & 0 \end{bmatrix}$$

The inspection of the matrix products $\mathbf{M}_S \mathbf{M}_R$, $\mathbf{M}_R \mathbf{M}_P$, $\mathbf{M}_R \mathbf{M}_S$ and $\mathbf{M}_P \mathbf{M}_R$ shows that the matrices \mathbf{M}_S and \mathbf{M}_R , as well as \mathbf{M}_P and \mathbf{M}_R , do not commute at all ($\mathbf{M}_S \mathbf{M}_R \neq \mathbf{M}_R \mathbf{M}_S$, $\mathbf{M}_R \mathbf{M}_P \neq \mathbf{M}_P \mathbf{M}_R$). Hence, no interchange of sample and retarder or of retarder and polarizer is allowed. The system consisting of a linear polarizer at 45° and a retarder acts as a circular polarizer with a Mueller matrix \mathbf{M}_C (see Table 3.2-3).

$$\mathbf{M}_R \mathbf{M}_P = \begin{bmatrix} 1 & 0 & 0 & 0 \\ 0 & 1 & 0 & 0 \\ 0 & 0 & 0 & -1 \\ 0 & 0 & 1 & 0 \end{bmatrix} \cdot \begin{bmatrix} 1 & 0 & 1 & 0 \\ 0 & 0 & 0 & 0 \\ 1 & 0 & 1 & 0 \\ 0 & 0 & 0 & 0 \end{bmatrix} = \begin{bmatrix} 1 & 0 & 1 & 0 \\ 0 & 0 & 0 & 0 \\ 0 & 0 & 0 & 0 \\ 1 & 0 & 1 & 0 \end{bmatrix}$$

\mathbf{M}_R	\mathbf{M}_P	\mathbf{M}_C
----------------	----------------	----------------

It is also easily seen that as a whole the matrix product $\mathbf{M}_R \mathbf{M}_P$ does not commute with $\mathbf{M}_S [\mathbf{M}_S (\mathbf{M}_P \mathbf{M}_R) \neq (\mathbf{M}_R \mathbf{M}_P) \mathbf{M}_S]$. Therefore, if circular dichroism is to be measured the scheme presented in Fig. 3.2-4. opens the only opportunity for that.

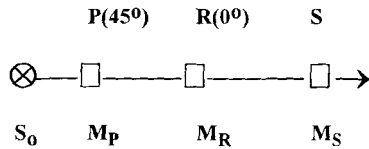


Figure 3.2-4 Arrangement of the optical devices in a CD experiment.

Table 3.2-3 The Mueller matrices for samples possessing only a single polarization property

Sample	Phenomenon	Mueller matrix
isotropic	pure absorption	$e^{-A} \begin{bmatrix} 1 & 0 & 0 & 0 \\ 0 & 1 & 0 & 0 \\ 0 & 0 & 1 & 0 \\ 0 & 0 & 0 & 1 \end{bmatrix}$
anisotropic	pure linear dichroism LD	$e^{-A} \begin{bmatrix} \cosh LD & -\sinh LD & 0 & 0 \\ -\sinh LD & \cosh LD & 0 & 0 \\ 0 & 0 & 1 & 0 \\ 0 & 0 & 0 & 1 \end{bmatrix}$
anisotropic	pure linear birefringence LB	$e^{-A} \begin{bmatrix} 1 & 0 & 0 & 0 \\ 0 & \cos LB & -\sin LB & 0 \\ 0 & \sin LB & \cos LB & 0 \\ 0 & 0 & 0 & 1 \end{bmatrix}$
anisotropic	pure linear dichroism at 45°	$e^{-A} \begin{bmatrix} \cosh LD' & 0 & -\sinh LD' & 0 \\ 0 & 1 & 0 & 0 \\ -\sinh LB' & 0 & \cosh LB' & 0 \\ 0 & 0 & 0 & 1 \end{bmatrix}$
anisotropic	pure linear birefringence at 45°	$e^{-A} \begin{bmatrix} 1 & 0 & 0 & 0 \\ 0 & \cos LB' & 0 & \sin LB' & 0 \\ 0 & 0 & 1 & 0 \\ 0 & -\sin LB' & 0 & \cos LB' \end{bmatrix}$
optical active	pure circular dichroism	$e^{-A} \begin{bmatrix} \cosh CD & 0 & 0 & \sinh CD \\ 0 & 1 & 0 & 0 \\ 0 & 0 & 1 & 0 \\ \sinh CD & 0 & 0 & \cosh CD \end{bmatrix}$
optical active	pure circular birefringence (optical rotation)	$e^{-A} \begin{bmatrix} 1 & 0 & 0 & 0 \\ 0 & \cos CB & \sin CB & 0 \\ 0 & -\sin CB & \cos CB & 0 \\ 0 & 0 & 0 & 1 \end{bmatrix}$

These two examples give some idea about the use of the Stokes-Mueller method and show its effectiveness. All Mueller matrices for optical polarization components used in the present chapter have been taken at “exact positions” such as 0° , 90° , 45° , etc. in order to avoid complicated expressions which might obscure the principle of the method. Of course, any arbitrary position of the optical elements could be considered by the Stokes-Mueller method. In such cases the “rotated Mueller matrix” $\mathbf{M}(\theta)$ is obtained as a result of the transformation.

$$\mathbf{M}(\theta) = \tilde{\mathbf{R}}(\theta)\mathbf{M}(0)\mathbf{R}(\theta) \quad (3.2-8)$$

$\mathbf{R}(\theta)$ is an orthogonal rotation matrix. The symbol tilde (\sim) means here “transposed” and $\mathbf{M}(0)$ is the Mueller matrix of the given optical element corresponding to 0° . If e.g. a linear polarizer is rotated at an angle θ the above transformation should look like as follows:

$$\mathbf{M}(\theta) = \begin{bmatrix} \cos 2\theta & -\sin 2\theta & 0 & 0 \\ \sin 2\theta & \cos 2\theta & 0 & 0 \\ 0 & 0 & 1 & 0 \\ 0 & 0 & 0 & 1 \end{bmatrix} \cdot \begin{bmatrix} 1 & 1 & 0 & 0 \\ 1 & 1 & 0 & 0 \\ 0 & 0 & 0 & 0 \\ 0 & 0 & 0 & 0 \end{bmatrix} \cdot \begin{bmatrix} \cos 2\theta & \sin 2\theta & 0 & 0 \\ -\sin 2\theta & \cos 2\theta & 0 & 0 \\ 0 & 0 & 1 & 0 \\ 0 & 0 & 0 & 1 \end{bmatrix}$$

3.2.2 Polarization optics

Devices which cause a spatial preference of the vibrations of the electromagnetic waves are called in general *polarizers*. Depending on the polarization type, polarizers are *linear*, *circular* or *elliptical*. Close to polarizers stand retarders. They are devices whose effect is manifested only upon polarized radiation. Otherwise retarders remain neutral with respect to unpolarized light. They possess the property to split the electric vector (the magnetic one too, respectively) of the electromagnetic wave into two usually orthogonal components and to create a phase difference between them. Exactly the latter feature, expressed alternatively that one of the split components retards with respect to the other, gives the name *retarders* to the considered devices. Often circular or elliptical polarizers are combinations of a linear polarizer with a retarder. The polarization devices will be considered separately below.

3.2.2.1 Linear polarizers

Five different optical phenomena are used for producing linear polarization: dichroism, birefringence, reflection, reflection-transmission by metal gratings (grids), and scattering.

Polarizers could have two functions: first to produce linear polarizations and second to detect and analyse existing polarization. In this second function polarizers are named *analyzers*.

A linear polarizer is characterized by its degree of polarization P which shows the completeness of the polarization achieved (Born, 1933). Two ways exist for the quantitative description of P . The first one uses the alternative meanings of “polarized” and “unpolarized”. One could state this way that the radiation emerging from a polarizer consists of a completely polarized fraction I_p and of a completely unpolarized one I_u . Then the degree of polarization is defined as:

$$P = I_p / (I_p + I_u) \quad (3.2-9)$$

Another definition of P employs the notion for the dominance of one of the orthogonally polarized light components over the other. In terms of it the meanings “dominant component” and “inferior component” are introduced denoting their intensities as I_d and I_i respectively. Thus P expressed in terms of them becomes

$$P = (I_d - I_i) / (I_d + I_i) \quad (3.2-10)$$

It is obvious that both definitions give the same numerical value for P , since the presence of an inferior opposite polarizations of intensity fraction I_i neutralises a fraction of the same intensity in the dominant polarization. Thus the remainder $I_d - I_i$ is exactly I_p and both denominators in the above two expressions are obviously equal. One can immediately notice that both definitions do not take into consideration the state of the incident light, and therefore, they are dependent on the latter. When, however, the beam falling onto a polarizer is completely unpolarized then the degree of polarization is called *polarizance*. It actually is the true characteristic of the polarizer.

Polarizers could be characterized by means of their transmittance with respect to polarized light. Thus the ratio of the so called major principal transmittance t_1 and the minor principal transmittance t_2

$$R_t = \frac{t_1}{t_2} \quad (3.2-11)$$

is called *principal transmittance* of the polarizer. Obviously it becomes infinity for an ideal polarizer.

Other characteristics could be derived from Eq. (3.2-11), but for their definition the reader could refer to Shurcliff's monograph (1962).

When a polarizer is rotated with respect to the polarization plane of already polarized incident radiation the transmitted intensity obeys the law of Malus

$$\frac{I}{I_0} = \frac{1}{2} \cos^2 \theta \quad (3.2-12)$$

where evidently I_0 and I are incident and emerging intensities and is θ the angle between the polarization plane of the incident light and that of the polarizer. Let us consider several types of polarizers:

A. Dichroic polarizers

These devices are based on the anisotropic absorption of light. Usually molecular crystals exhibit this property and tourmaline is the classical example for this. For practical purposes, however, micro crystals are oriented in polymer sheets. Polymers containing chromophors become after stretching dichroic polarizers. The devices produced in this manner are called *polaroids*. They have found a broad application in many technologies. Their application in spectroscopy is limited to the near ultraviolet and to the visible and near infrared range of the spectrum. In vibrational spectroscopy polaroids are employed as analyzers only for Raman spectroscopy.

B. Birefringence polarizers

Birefringence is an optical phenomenon manifested by the splitting of an unpolarized ray into two components of opposite polarization when entering an anisotropic medium. Both beams propagate in the birefringent medium with different velocities and this determines their different refractive indices usually denoted as n_o and n_e . If the incoming beam enters this birefringent medium at an angle different from the normal incidence then both beams trace different optical paths. One of the beams follows strictly Snell's law of refraction ($\sin\alpha / \sin\beta = n_o$, α – angle of incidence, β – angle of refraction) and is called *ordinary*. The other one deviates from this law of optics and therefore carries the name *extraordinary*. Uniaxial single crystals are most frequently used for making birefringent polarizers. Birefringence is observed only when the light beam propagates along a crystal axis perpendicular to the so called *optical axis* of the crystal. The latter determines the "non-birefringent" direction in the crystal along which light propagates with "ordinary velocity" and hence experiences "ordinary refraction". If $n_o > n_e$ the birefringent medium is conventionally assumed to be called *positively anisotropic*. In the opposite case, $n_o < n_e$ it is called *negatively anisotropic* (Born, 1933).

The principle of the birefringent polarizers is easily understood. It consists in removing one of the linearly polarized beams so that the other one remains for use in other devices.

Polarizers named after their inventors are known as such of Nicol, Ahrens, Glan-Foucault, Glan-Thompson, Wollaston and others. All they have primarily been based on anisotropic natural crystals. Nowadays these types of polarizers are produced from synthetic birefringent crystals with controlled purity.

The Glan-Foucault prism will be considered here as a simple representative of birefringent polarizers. A birefringent crystal, e.g. calcite, known to be of positive anisotropy ($n_o = 1.658$ and $n_e = 1.486$), is cut firstly in the form of a parallelepiped (Fig. 3.2-5a) and then split into two triangle prisms in a way that the splitting plane is not parallel to the optical axis (Fig. 3.2-5b). The splitting angle Θ is calculated to be above the critical angle Θ_C ($\sin\Theta_C = 1/n_o$) of total internal reflection for the ordinary ray and under this value for the extraordinary one. Both triangle prisms are mounted together in a holder so that their oblique faces stay strictly parallel to each other with an air gap between them.

A light beam falling normally on the entrance face of the polarizer is split into ordinary and extraordinary beams that propagate together until they reach the oblique face where the ordinary beam experiences total reflection. The extraordinary beam polarized perpendicularly to the optical axis of the crystal enters the second triangle prism and emerges from it with unchanged polarization. The symmetric construction of the polarizers ensures that both sides can be used as a beam entrance.

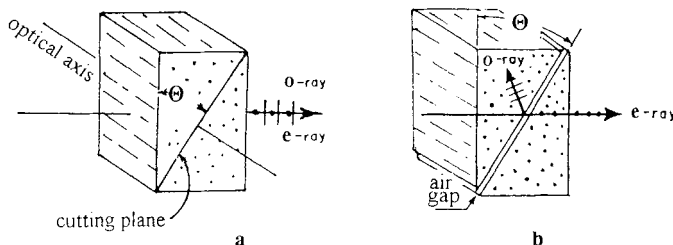


Figure 3.2-5 The Glan-Foucault polarizer; **a** – bulk calcite crystal with denoted cutting plane, **b** – polarizer construction.

All other types of birefringent polarizers listed above exploit the same physical principle and differ only in their construction. Immersion media are more often used instead of the air gap in order to achieve a rigid device. Birefringent polarizers are mainly used in Raman spectroscopy for polarization of the radiation of a laser light source.

C. Brewster polarizers

The physical principle of these polarizers rests on the so called Brewster reflection that is theoretically explained by the Fresnel theory of reflection and refraction. Each dielectric medium reflects at a definite angle Φ_B , called Brewster angle, only radiation which is polarized perpendicularly to the plane of incidence. The Brewster angle is determined by the refractive index of the medium according to the relationship $\tan \Phi_B = n$. The transmitted radiation contains both parallel and perpendicular polarizations in proportions depending again on the refractive index according to the Fresnel formulae (Born, 1933) (Fig. 3.2-6).

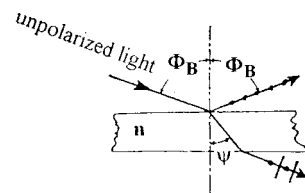


Figure 3.2-6 Principle of the Brewster polarizer. A beam reflected at the Brewster angle Φ_B is completely polarized vertically to the plane of incidence (the drawing plane); the refracted beam at angle ψ is of mixed polarization.

Brewster polarizers were widely used in infrared spectroscopy in two varieties. The first of them directly utilizes the reflected beams that contain the pure perpendicular component while the second type functions in transmission. Frequently used materials for Brewster polarizers are selenium (in old designs), silver bromide, KRS-5, germanium and silicon. The general requirement for the material used in these types of polarizers is to have a large refractive index. The higher the latter is the better parallel and perpendicular components of radiation separate.

The reflection polarizers have the disadvantage of declination of the beam direction from the optical axis of the instrument, and therefore, additional reflection elements must be introduced in order to restore the initial beam direction. Fig. 3.2-7a, b shows two possible designs of reflection Brewster polarizers. Their obvious advantage is the higher polarization purity achieved by one or two active reflection elements.

Brewster polarizers functioning in transmission consist of several plates or foils of high refractive index ordered in a holder at the Brewster angle. The plates (foils) consequently eliminate the perpendicular component of radiation thus filtering the parallel component. Old constructions with fragile selenium foils are known. Other constructions use silver bromide or KRS-5. The side displacement of the beam by the plates is compensated for, making use of the symmetric constructions displayed in Fig. 3.2-7c.

Brewster polarizers are almost not used anymore in IR spectroscopy since their relatively big sizes represent a definite disadvantage. Nowadays they are practically replaced by the convenient grid polarizers.

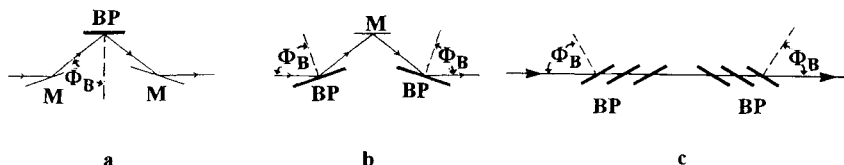


Figure 3.2-7 Brewster polarizers with one reflection (a), with two reflections (b) and in transmission (c); M – plane mirrors, BP – Brewster plates, Φ_B – Brewster angle.

D. Grid polarizers

These types of polarizers are constructed from either a free standing grating or a grating laid on a substrate of an IR-transparent material. Their compact form and space-saving size have made them widely applicable in IR polarization spectroscopy.

The geometrical condition for a grating to serve as a neat polarizer imposes the following requirement: the grating line spacing must lie under the diffraction limit for the shortest wavelength λ_{sh} of the used spectral range. This could easily be seen from the diffraction equation (Schröder, 1987), compare Eq. 3.1-13,

$$\sin \beta = \pm(m\lambda/a + \sin \alpha) \quad (3.2-13)$$

which gives the angle of diffraction β for diffraction of order m (see Fig. 3.2-8) as a function of the angle of incidence α , of the wavelength λ and of the grating constant a . The (+) and (-) signs in Eq. (3.2-13) refer to beams diffracted at angles above and below the value of the so called angle of mirror reflection (blaze angle). If $\lambda_{sh}/a + \sin \alpha > 1$ then diffraction occurs no more and the grating serves only as a neat polarizer, the beam being transmitted and reflected as by a semi-transparent mirror.

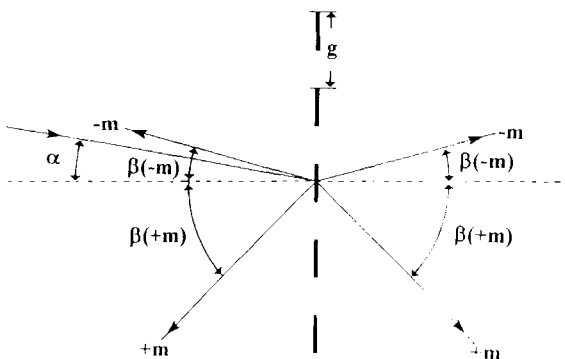


Figure 3.2-8 Beam diffraction on a grating with constant g in transmission and reflection; α – angle of incidence, β – angle of diffraction, $\pm m$ – order of diffraction.

The transmitted radiation is polarized perpendicularly to the grating lines while radiation parallel to them is reflected by the grid. Grid polarizers on substrates such as KRS-5, ZnSe, BaF₂, polyethylene and others are widely used today in IR spectroscopy. Free standing gratings are also in use especially for polarizing far infrared radiation despite of their sensitivity towards shocks and vibrations. They are free of secondary effects of absorption, reflection and refraction the substrate might cause.

3.2.3 Retarders

Retarders are usually devices which rotate the polarization plane of radiation or convert linearly polarized radiation into a elliptically or circularly polarized one. Their basic physical function consists in decomposing the electric vector of the linearly polarized radiation into two mutually orthogonally polarized components between which a phase difference (*retardation*) is created. Depending on the physical phenomenon that causes the retardation effect practical retarders based on birefringence and total internal reflection are known and used.

A. Birefringence retarders

When linearly polarized radiation enters a birefringent medium normally at an azimuth α of the electric vector with respect to the optical axis of the medium this electric vector splits into two orthogonally polarized components phase shifted at an angle (Born, 1933)

$$\delta = 2\pi\tilde{\nu}d\Delta n \quad (3.2-14)$$

where $\tilde{\nu}$ is the radiation wavenumber, d the thickness of the birefringent medium in cm, and Δn the linear birefringence ($\Delta n = n_o - n_e$). The azimuth α determines the ratio of the ordinary and extraordinary components (E_o and E_e) of the electric vector split into directions parallel and perpendicular to the optical axis of the birefringent medium.

$$E_o/E_e = \tan \alpha \quad (3.2-15)$$

Eq. (3.2-14) shows that the phase shift strongly depends on the radiation frequency at a constant d . The dependence upon n is usually slight and smooth.

Let two important cases be considered here. The first one concerns the situation when a phase difference of $k\pi$ may be created by varying some parameters of Eq. (3.2-14). This could require $\tilde{\nu}d\Delta n = k/2$, k being an integer. In this case the radiation emerging from the birefringent medium remains in the same polarization state but the value of its azimuth doubles. In other words, the polarization plane turns out to be additionally rotated by an angle α . Such a device is called a *half-wave plate* or *polarization rotator*. The meaning “half-wave plate” originates from the fact that the ordinary and extraordinary waves are shifted by an angle π if one does not take into account the multiple k . The polarization rotator is broadly used for rotating the polarization plane of laser radiation and particularly therefore very often applied in Raman spectroscopy.

The second case refers to generating circularly polarized light by means of birefringent retarders. If the azimuth α of the electric vector is set at $\pm 45^\circ$ and δ at $k\pi/2$ ($\tilde{\nu}d\Delta n = k/4$) respectively, the emerging radiation turns out to be circularly polarized. Such an optical element is often called *quarter wave plate* since $\delta = k\pi/2$ means a quarter wave displacement between the ordinary and extraordinary wave. The necessity of setting the azimuth at $+45^\circ$ arises from the requirement for circular polarization of an electromagnetic wave, its electric vector needs two equal components E_o and E_e on exit of the retarder.

Birefringent retarders are made of anisotropic uniaxial crystals such as calcite, α -quartz, sapphire, zinc sulphide, cadmium selenide and others. As Eq. (3.2-14) shows, the produced retardation is exact for a definite wavenumber or for its multiples. Between them all remaining possible polarization states are passed through.

Birefringence can be produced by mechanical stress exerted on optically isotropic media like glass and cubic crystals. Devices based on this phenomenon are used for polarization modulators. The so called *photoelastic modulators* (PEM) are widely used for measuring circular dichroism. The mechanical stress in the PEMs is produced by

means of piezoelements stuck on two opposite side walls of the isotropic material usually formed as an octagonal prism. The piezoelements are driven by rectangular voltage in the kilo-Hertz region, typically between 30 and 70 kHz. The voltage amplitude determines the maximum phase difference induced in the PEM material, for a given wavelength. Hence, for a period of voltage alternation all possible intermediate polarizations are obtained. A PEM is usually constructed to produce optionally maximum phase shifts of $\pm\pi$ and $\pm\pi/2$. As it was pointed out above, the produced phase shift is strongly and periodically depending on the radiation frequency. Therefore, artificial electronic or digital processing is performed in order to correct the frequency dependence of δ .

B. Totally reflecting retarders

If linearly polarized light is totally reflected the outgoing radiation is in general elliptically polarized depending on the angle of incidence, on the refractive index of the totally reflecting material and on the azimuth of the electric vector of the incoming radiation. The total internal reflection decomposes the electric vector into two components, one parallel to the plane of incidence and the other perpendicular to it, between which a phase difference δ is created given by the equation (Born, 1933)

$$\tan(\delta/2) = \left[\cos\varphi \sqrt{(\sin^2\varphi - n^{-2})} \right] / \sin^2\varphi \quad (3.2-16)$$

in which φ is the angle of incidence. The ratio of the amplitudes of the parallel E_p and the perpendicular E_s component of the totally reflected wave are determined by the azimuth α of the linearly polarized incident radiation analogously to Eq. (3.2-15)

$$\tan\alpha = E_p/E_s \quad (3.2-17)$$

Totally reflecting retarders are used for producing circular polarization. This can be done if $\alpha = \pm 45^\circ$, and if for a given n , φ is chosen in a way to create $\delta = \pi/2$ according to Eq. (3.2-16). Evidently this can be achieved for one reflection if the refractive index n is high enough. Optical materials with $n > 2.4$ fulfill this requirement and retarders in the

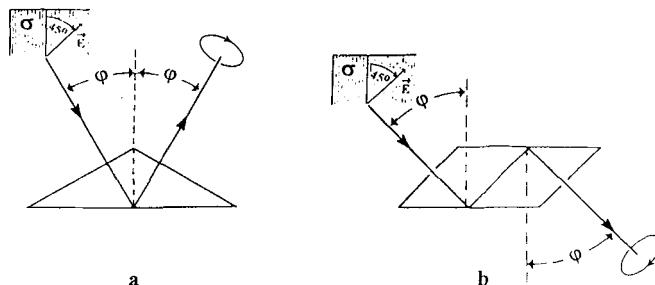


Figure 3.2-9 Totally reflecting circular retarders: **a** with a single reflection, **b** with two reflections; φ – angle of incidence calculated from Eq. 3.2-16 to produce $\delta = \pi/2$; the incoming electric vector \vec{E} forms an angle of 45° with the plane of incidence σ (the drawing plane).

form of triangle prisms can be manufactured from them (Fig. 3.2-9a). Such materials are ZnSe, KRS-5, Si, Ge, GaAs and others. A single reflection is, however, insufficient to produce circular polarization for materials whose refractive index lies below 2.4 (Korte et al., 1988). Therefore, retarders are made from them in the form of an oblique rectangular prism (Fig. 3.2-9b). Such a prism is called a *Fresnel rhombus*.

Eq. (3.2-16) shows that the frequency dependence of δ is manifested through the dependence of the refractive index n on the radiation frequency. Since the spectral range in which optical materials are used is far enough from their absorption bands the dependence of n and hence of δ on the frequency is a slightly and smoothly changing function in this spectral interval. Therefore, totally reflecting retarders are almost achromatic optical devices.

3.3 Properties of the components of optical spectrometers

This section provides a general description of the components of a spectrometer. The special features of spectrometers constructed for different methods of vibrational spectroscopy, especially the specific sample arrangements, are described in Secs. 3.4 and 3.5.

The cardinal element of a spectrometer, the spectral apparatus which is necessary for the selection or discrimination of radiation of different wavelengths, has been discussed above. It is used in connection with elements which generate, transport, and detect radiation. These components of an optical system are:

- Radiation sources
- Elements which produce images of preceding elements upon subsequent elements
- Elements which conduct radiation: light guides, optical fibers
- Sample arrangements
- Elements which transform radiation into electrical signals: radiation detectors.

The general properties of these components are discussed in short in the following sections. It is also shown how they determine the quality of solutions of analytical problems.

3.3.1 Radiation sources

An allowed transition between two energy states $E_2 > E_1$ of an atom, molecule, or crystal produces a light quantum with the energy $h\nu_{12}$. The reverse transition, from E_1 to E_2 , occurs if a light quantum $h\nu_{12}$ is absorbed:

$$E_2 - E_1 = h\nu_{12}. \quad (3.3-1)$$

If these are the energy states of an ensemble of species which are in a thermal equilibrium, then the absorption or emission can be described by Planck's and Kirchhoff's laws. The emitted or absorbed radiant power is released by or incorporated in the thermal reservoir. In this case, the ensemble is known as a *thermal radiator* or *absorber* and the corresponding process is referred to as *thermal emission* or *absorption* of radiant energy.

If, however, the population of the energy state E_2 is a consequence of a non-thermal process, then the emission of radiation as a result of a transition from E_2 to E_1 is referred to as *luminescence*. There are different types of luminescence:

- Electrical discharges in a plasma produce continuous and line spectra
- Chemical reactions may produce chemoluminescence
- Mechanical processes produce tribo and sono luminescence
- Recombinations of charge carriers in semiconductors produce electroluminescence
- Processes involving photons are called photoluminescence: fluorescence, phosphorescence, Brillouin and Raman scattering.

Luminescence processes usually produce incoherent radiation. The population of the energy states E_2 and E_1 , according to Boltzmann's law, may be described by a temperature. These states are not usually in thermal equilibrium with the other energy states of the ensemble, which normally correspond to a low temperature.

If the energy state E_2 is occupied through a *pumping process*, then a population inversion $N_{E_2} > N_{E_1}$ may be achieved. According to *Boltzmann's law*, negative temperatures would describe the occupation of these energy states. Such a luminescence process makes stimulated emission of coherent radiation possible – this is a laser.

In vibrational spectroscopy, usually classical (thermal) radiation sources are employed to measure absorption in the NIR, MIR, and FIR range, however, lasers will be used increasingly depending on the progress of development. Lasers are used nearly exclusively for Raman spectroscopy.

The laws of Planck and Kirchhoff

Any object at a temperature above absolute zero emits thermal radiation, it is a *thermal radiator*. Ideally, its atoms or molecules are in a thermal equilibrium, the entire ensemble has a definite temperature. In contrast to lasers, thermal radiation sources produce non-coherent radiation. Its quanta have a random phase distribution, both spatially and temporally. *Planck's law* defines the *spectral radiance of a black body: the radiant power per solid angle, per area, and per wavelength* $L_{\lambda,T}$ (Eq. 3.3-2) or *per wavenumber* $L_{\tilde{\nu},T}$ (Eq. 3.3-3):

$$L_{\lambda,T} = \frac{2hc_0^2\lambda^{-5}}{\exp(hc_0/k\lambda T) - 1} \quad (3.3-2)$$

$$L_{\tilde{\nu},T} = \frac{2hc_0^2\tilde{\nu}^3}{\exp(hc_0\tilde{\nu}/kT) - 1} \quad (3.3-3)$$

The radiant flux Φ transmitted by a thermal radiation source through a spectrometer is calculated by multiplying the spectral radiance by the spectral optical conductance, the square of the bandwidth of the spectrometer, and the transmission factor of the entire system (Eq. 3.1-9). Fig. 3.3-1 shows the Planck function according to Eq. 3.3-3. The absorption properties of non-black body radiators can be described by the Bouguer-Lambert-Beer law:

$$\tau = \Phi/\Phi_0 = 10^{-\epsilon \cdot c \cdot d} \quad (3.3-4)$$

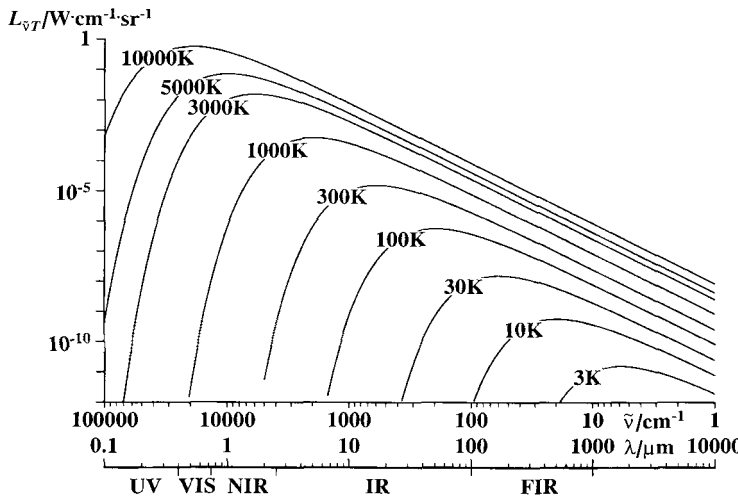


Figure 3.3-1 The spectral radiance of a black body of $T = 10000, 5000, 3000, 1000, 300, 100, 30, 10$ and 3 K in the range of $\tilde{\nu} = 1 \dots 10^5 \text{ cm}^{-1} \hat{=} \lambda = 10^4 \dots 0.1 \mu \text{m}$.

Kirchhoff's law states that for a sample at a given temperature T , the absorption factor α equals the emission factor ϵ_K , the *emittance* of the same sample:

$$\alpha \equiv 1 - \tau = 1 - \Phi/\Phi_0 = \epsilon_K \quad (3.3-5)$$

$$\epsilon_K = (1 - 10^{-\epsilon \cdot c \cdot d}) \quad (3.3-6)$$

In these equations, d is the sample thickness, ϵ is the molar decadic absorption coefficient and c stands for the concentration. For pure samples, $\epsilon \cdot c$ should be replaced by a , which is the linear decadic absorption coefficient of the sample. For a *black body radiator*, the emission factor is $\epsilon_K = 1$.

The Planck-Kirchhoff law allows a good approximation of the spectral radiance of any thermal radiator, the sources as well as the samples and detectors. Thermal radiators are characterized by a definite temperature as well as by their absorption coefficients $\epsilon(\tilde{\nu})$ or $a(\tilde{\nu})$, which describe the characteristic spectrum of the radiator:

$$L_{\tilde{\nu},T} = \frac{2hc_0^2\tilde{\nu}^3}{\exp(hc_0\tilde{\nu}/kT) - 1} \cdot \left(1 - 10^{-\epsilon(\tilde{\nu}) \cdot c \cdot d}\right) \quad (3.3-7)$$

$$L_{\tilde{\nu},T} = \frac{2hc_0^2\tilde{\nu}^3}{\exp(hc_0\tilde{\nu}/kT) - 1} \cdot \left(1 - 10^{-a(\tilde{\nu}) \cdot d}\right) \quad (3.3-8)$$

The spectral radiance determines the exchange of thermal radiation energy. The radiant flux exchanged by a spectrometer or any other optical system with a spectral optical conductance $G_{\tilde{\nu}}$ between two thermal radiators, A and B , is given by

$$\Phi = (L_{\tilde{\nu},T_A}^A - L_{\tilde{\nu},T_B}^B) \cdot G_{\tilde{\nu}} (\Delta\tilde{\nu})^2 \cdot \tau \quad (3.3-9)$$

The direction of the net radiant flux at a given frequency depends on the sign of the expression $(L_{\tilde{\nu},T_A}^A - L_{\tilde{\nu},T_B}^B)$. All elements of a spectrometer receive radiation from several radiators, including the spectrometer itself, while simultaneously acting as radiators. Thus, the balance of thermal radiation of any element in a spectrometer can be calculated, for example that of the sources, samples and detectors of near-, middle, and far-infrared spectrometers.

3.3.2 Imaging and conducting optical elements

Imaging elements

Lenses are the most important imaging elements. According to the laws of refraction, they provide images of radiating objects. The most common lenses have spherical or planar surfaces. Lenses which converge incident light beams are called positive; they may be either biconvex, plano-convex, or of the convergent meniscus type. They are characterized by a positive focal length. Lenses which diverge an incident beam are called negative; they may be biconcave, plano-concave, or of the divergent meniscus type. These lenses are characterized by a negative focal length (Fig. 3.3-2).

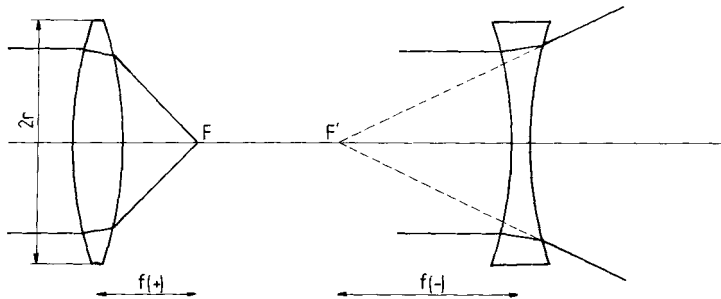


Figure 3.3-2 Definition of the focal length of a positive and a negative lens.

For any refracting material the speed of light is inversely proportional to the refractive index:

$$c_i \cdot n_i = c_0 \quad \text{or} \quad c_1/c_2 = n_2/n_1 \quad (3.3-10)$$

Here, c_0 is the speed of light in vacuum. According to Huygens' principle, the rays are refracted as described by Snellius' law of refraction:

$$\sin \alpha_1 / \sin \alpha_2 = n_2/n_1 \quad (3.3-11)$$

The imaging properties of a lens are most simply described by the lens equation (see Fig. 3.3-3):

$$1/f = 1/a_1 + 1/a_2 \quad (3.3-12)$$

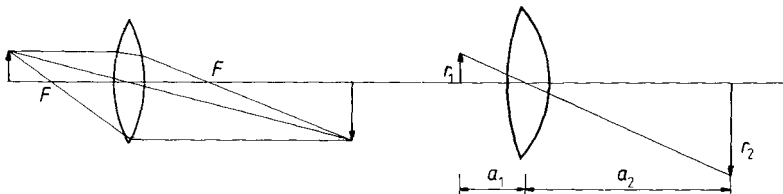


Figure 3.3-3 Imaging properties of lenses.

The magnification or conjugate ratio m is given by:

$$m = r_1/r_2 = a_1/a_2 \quad (3.3-13)$$

If two lenses are combined at a distance which is short compared to the focal length, then the focal length of the resulting combination is given by:

$$1/f_{res} = 1/f_1 + 1/f_2 \quad (3.3-14)$$

If the distances of the images on both sides of the lens are quite different, asymmetric lenses should be used (Fig. 3.3-4). Ideally, the angle of refraction on both surfaces of the lens should be equal. A lens which has a small f -number $= f/2r$ of the order of 1, and a very large or very small conjugate ratio (compared to 1), has to be plano-convex, aspheric, or a positive meniscus. This is often true of sample optics in Raman spectroscopy (Sec. 3.5.3.2). For such lenses, the equations given above are only approximations; the focal lengths are to be measured relative to the principal points (see textbooks of optics). There are special systems which operate with cylindrical lenses to transform a point object into a line image or to change the height of an image without changing its width.



Figure 3.3-4 Arrangement of asymmetric lenses with small f -numbers.

Lenses are not ideal. They produce various types of aberrations. Chromatic aberration due to material dispersion, i.e., the dependence of the refractive index on the wavelength is particularly important for spectroscopy. Therefore, the focal length of a single lens depends on the wavelength of the radiation. The refractive index usually increases, while the focal length decreases with decreasing wavelength. 'Achromatic' combinations of lenses of different materials have to be used for imaging over a wider spectral range.

By analogy with lens optics, mirror systems may be used. Mirror systems have the advantage that they do not show chromatic aberrations: the focal lengths and all imaging-properties are independent of the wavelength of the radiation. It is thus possible to adjust reflecting optical systems with visible light and to use them with UV or IR radiation. For rays near the optical axis, the focal length of a spherical concave mirror equals half the radius of the curvature. In addition to spherical convex or concave mirrors, aspherical mirrors are also frequently used:

- In the case of paraboloid mirrors, all rays passing through the focus are reflected parallel to the optical axis (or vice versa).
- With ellipsoid mirrors, all rays passing through the first focus are reflected to pass the second focus.

This is true even of very large solid angles. Such mirrors are therefore often used as a basis of irradiating, light collecting, and light concentrating systems. Toroid mirrors are also sometimes used. They have a shape like the surface of bicycle inner tubes. Toroids, like cylindrical lenses, transport radiation from a point object to a line image.

The optical conductance of an imaging system should be adapted to that of the other components of the spectrometer. In most cases, Eq. 3.1-6 is sufficient for its calculation.

Conducting optical elements

Optical fibers were originally developed mainly for communication links. Now their importance is steadily increasing in many other technical applications. In optical spectroscopy, optical fibers are used especially for the 'on-line' investigation of remote samples without its transport. Silica fibers have a transmission factor sufficient for connection over short distances in the UV/VIS range. Their maximum transmission, however, is in the NIR range, where connections over several kilometers are possible. Fig. 3.3-5 shows the transmission curve of a typical silica fiber in the optical range. Fibers developed for the MIR range are produced from oxides, chalcogenides, and halides of different elements (Klocek and Sigel, 1989; Katsuyama and Matsumura, 1989). Optical fibers, as ATR crystals (Sec. 6.7), are based on the total reflection of radiation inside a material which has a higher refractive index than its surroundings.

According to Snellius' law

$$\sin \alpha_1 / \sin \alpha_2 = n_2 / n_1 \quad (3.3-15)$$

if $n_2 > n_1$, and if the angle α_1 reaches 90° , radiation is totally reflected (Fig. 3.3-6 a).

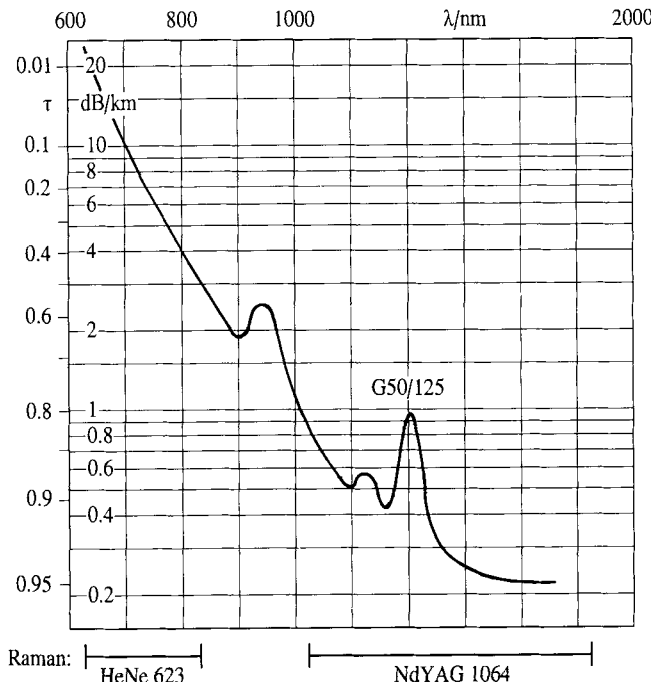


Figure 3.3-5 Transmission of a quartz fiber in the near-infrared region, τ is the transmittance of a fiber with a length of 1 km, below are the ranges of the Raman spectrum excited by the HeNe laser at 623 and the Nd:YAG laser at 1064 nm.

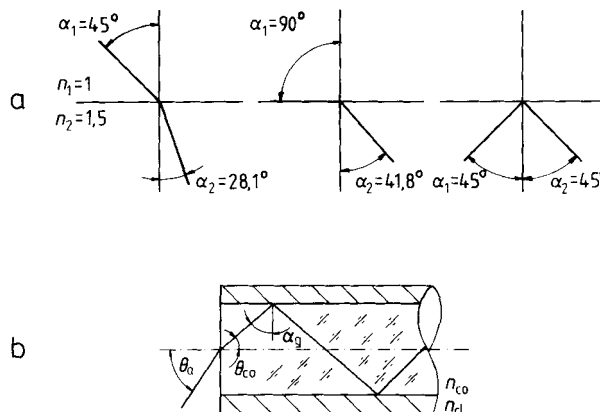


Figure 3.3-6 Law of refraction: **a** at the interface between two media with $n_1 = 1$ and $n_2 = 1.5$ all rays with $\alpha_2 > 41.8^\circ$ are totally reflected; **b** if α_g is the angle of total reflection at the interface between core and clad of an optical fiber, then Θ_{co} is the largest angle of rays relatively to the optical axis inside the fiber and Θ_a the largest angle outside.

In this case the angle of total reflection α_g is given by:

$$\sin \alpha_g = n_1/n_2 = n_{cl}/n_{co} \quad (3.3-16)$$

Optical fibers are cylinders made of a transparent material, the 'core', with a refractive index of $n_2 = n_{co}$, surrounded by a 'cladding', i.e., a material with a lower refractive index $n_1 = n_{cl}$ (Fig. 3.3-6 b). If radiation from inside the core hits the wall under an angle exceeding α_g , it is totally reflected. The maximum angle inside the core, at which the radiation is totally reflected is, with respect to the optical axis of the fiber:

$$\Theta_{co} = 90^\circ - \alpha_g \quad (3.3-17)$$

The properties of optical fibers are often characterized by the 'numerical aperture' $NA = n \sin \Theta$. It is given by:

$$\begin{aligned} NA &= n_{co} \sin \Theta_{co} = n_{co} \cos \alpha_g = n_{co} \sqrt{1 - \sin^2 \alpha_g} = \\ &= n_{co} \sqrt{1 - (n_{cl}/n_{co})^2} = \sqrt{n_{co}^2 - n_{cl}^2} \end{aligned} \quad (3.3-18)$$

Since

$$NA = n_{co} \sin \Theta_{co} = n_a \sin \Theta_a = \sqrt{n_{co}^2 - n_{cl}^2} \quad (3.3-19)$$

the angle Θ_a of the cone of the radiation in air which may be transported by the fiber with $n_a = 1$, equals:

$$\Theta_a = \sin^{-1} \sqrt{n_{co}^2 - n_{cl}^2} \quad (3.3-20)$$

Even a small difference between the refractive indices (e.g., 0.02) allows aperture angles, which are sufficient for many applications (e.g., 10°).

Since they are used in communication systems the transmission properties of optical fibers are usually listed in dB values. These are related to the transmission factor τ by the following equations:

$$\text{dB} = 10 \cdot \log(1/\tau); \quad \tau = 10^{(\text{dB}/10)} \quad (3.3-21)$$

For all applications in spectroscopy it is necessary to adapt the optical conductance of the fiber to the other elements of the instrument. Laser radiation can be transported easily by one fiber, but its connection to a spectrometer principally needs a bundle of fibers, because spectrometers have an optical conductance which usually exceeds that of one fiber. Besides, irradiation of the entrance slit of a grating spectrometer requires the fibers to be arranged in a row, while an interferometer requires a circular arrangement at an image of the Jacquinot stop. The optical conductance of one fiber may be approximated by

$$G_F \cong r^2 \pi^2 N A^2 \quad (3.3-22)$$

where r is the radius of the core. Unfortunately, it is not possible to completely match the areas of the optical beams. Even with dense packing and very thin cladding, the *filling factor* is usually less than 75 %. Including the reflection losses at the fiber tips, the overall transmittance of fiber bundles does not exceed 66 %, while single fibers reach as much as 85 %. In reflection spectroscopy, the fibers of two bundles of a Y-type system are statistically mixed at the tip near the sample. If, as in Raman spectroscopy, laser radiation as well as Raman radiation is to be transported, arrangements of 7, 19, or 37 fibers are useful, in which the respective central fiber is responsible for the transport of the laser radiation (Fig. 3.3-7a). It is even more advisable to use a relatively thin one to transport the laser radiation to the sample. This fiber is in the center of an arrangement of 3, 4, 8, 12, or 14 fibers with a large diameter which transport the Raman radiation (Fig. 3.3-7b).

The connection to the other elements of the instrument should be designed such as to fully exploit the available fiber aperture and to find the best possible match to the optical properties of radiation sources, of emitting, absorbing or scattering samples as well as with the images of slits, Jacquinot stops, and gratings or beam splitters.

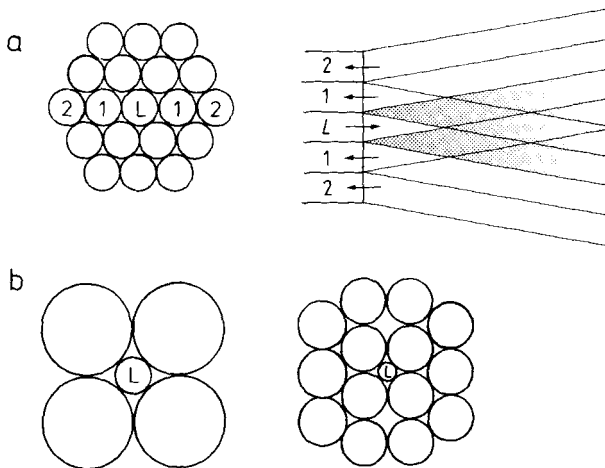


Figure 3.3-7 Fiber bundles for Raman spectroscopy. The diameter of the fiber for the exciting radiation is **a** the same, **b** smaller than that of the fibers transporting Raman radiation.

3.3.3 Radiation detectors, signal-to-noise ratio

The radiation detector is the essential part of every spectrometer. It employs different elementary processes to transform an *input*, e.g., radiant power (W), irradiance ($\text{W} \cdot \text{cm}^{-2}$), or radiant energy ($\text{W} \cdot \text{s}$) into an *output*, e.g., an electric charge, a current, or a potential. This is either recorded directly as a spectrum or processed after being digitized in order to solve analytical problems. The ratio between detector output and detector input is defined as the **responsivity** of the detector (IUPAC, 1992). Related to the responsivity is the **quantum efficiency**, which describes the number of elementary events produced by one incident photon.

Some radiation detectors, i.e., photoemissive detectors (vacuum phototubes or photomultipliers) or semiconductor detectors (photodiodes or phototransistors) directly produce an electrical signal by quantum effects. Their output is strongly dependent on the wavelength of the detected radiation. Thermal detectors, i.e., thermocouples and thermopiles, bolometers, pyroelectric detectors, or pneumatic and photoacoustic detectors record a temperature increase through radiation and convert this into an electrical signal. This is proportional to the flux of the absorbed radiant power, independent of the wavelength.

Array detectors are arrangements of many detector elements, they allow the imaging of objects or multichannel recording of spectra.

The output of a detector exhibits undesirable fluctuations which are called *noise*. This noise may be classified as:

- *thermal* or *Johnson noise* due to the thermal agitation of current carriers in a resistive element,
- *temperature noise* due to the statistical processes of heat exchange between a detector and its surroundings, which produces a fluctuation of the electric signal,

- *generation-recombination noise* due to the statistics of charge carriers,
- *contact noise* due to current fluctuations across electrical contacts,
- *radiation noise* due to statistical fluctuations of photon fluxes according to Poisson statistics,
- *dark current noise* due to the sum of noise currents in the absence of a signal,
- *shot noise*, which is the sum of the radiation noise and the statistical component of the dark current noise.

The smallest signal that can be determined is limited by the noise. The *noise equivalent power (NEP)* Φ_N is the incident radiant power (W) resulting in a signal-to-noise ratio of 1 within a given bandwidth of 1 Hz and at a given wavelength (see Fig. 3.3-14a). The reciprocal of the *NEP* is defined as the *detectivity D*. It is useful to normalize the detectivity by referring it to the sensitive area A of the detector and to the frequency bandwidth Δf of the measurement, resulting in the normalized detectivity D^* :

$$D^* = D(A\Delta f)^{1/2} = \frac{1}{\Phi_N} \cdot (A\Delta f)^{1/2} [\text{W}^{-1}\text{cm}^{-2}\text{s}^{-1/2}] \quad (3.3-23)$$

Fig. 3.3-8 shows the D^* values of different types of detectors as a function of the wavelength and the wavenumber, together with the number of light quanta which are

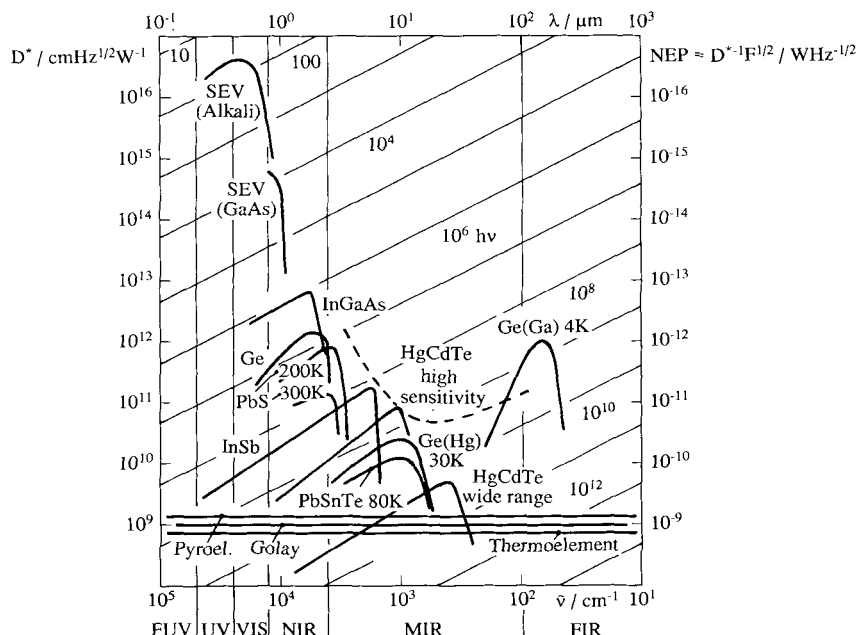


Figure 3.3-8 Normalized detectivity D^* and equivalent number of light quanta for different detectors for optical radiation. FUV, UV, VIS, NIR, MIR, FIR: far ultraviolet, ultraviolet, visible, near, middle, and far infrared region.

equivalent to the radiant power. Thermal detectors, such as thermocouples, pyro-electric detectors, and the Golay cell possess a uniform detectivity throughout the entire spectral range (idealized they behave as black body absorbers). Detectors which transform light quanta directly into electrical signals have a larger detectivity, but only within a limited spectral range. The diagram clearly indicates that the number of light quanta which are necessary to produce the *NEP* in the infrared range is several orders of magnitude larger than in the visible and the UV region.

The frequency distribution of noise is characterized by a power spectrum. There are two types. First, *white noise*, whose noise power is independent of the frequency. This noise arises from the statistics of electrons or photons and of the thermal energy of conductors. White noise can be reduced by extending the measuring time. Second, *excess low frequency noise, flicker, or 1/f noise* is due to fluctuations, drift and schlieren. It can be reduced by modulation. All types of noise are reduced by multiplex procedures, multichannel techniques, and multiple recording (Schrader, 1980).

The limit of detection and the precision of quantitative analyses depend on the signal-to-noise ratio of the recorded spectra. The purpose of the optimization of a spectrochemical procedure is to increase the signal-to-noise ratio. This is discussed in the following section.

3.3.4 Optimizing vibrational spectroscopy as an analytical method

Analytical chemistry aims at transforming physical and chemical properties of a sample into information about its composition.

Information concerning **all** aspects of the molecular structure and intermolecular interactions is encoded in the vibrational spectra. The art of vibrational spectroscopy can be defined as finding the optimum approach to extracting information from the spectra of molecules and to transform it into relevant answers to analytical questions, the most simple of which are: *what?* and *how much?* There are three steps which should be optimized:

1. Recording spectra in which the necessary information is encoded
2. Extracting this information
3. Decoding this information to afford solutions to analytical problems.

The theory of some of the procedures discussed in the following sections are described in several books, for example by Doerffel and Eckschlager (1981), Danzer et al. (1987 a, b) and Massart et al. (1988).

3.3.4.1 Basic information theory

An information channel transmits information from an information source to an information sink. On its way, the information is contaminated with noise (Fig. 3.3-9). Shannon (1948) studied the transmission of information by short-wave telegraphy. His results may

be applied to any process involving information transfer. The information in a telegram may be encoded in terms of *zeros* and *ones*. The information specifying which of the values, 0 or 1, a particular digit has assumed is referred to as the information unit. We call it a *bit*, an abbreviation of 'binary digit'.

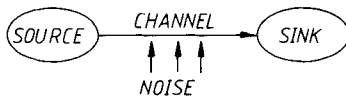


Figure 3.3-9 Information channel.

Consider a set of N different objects, which may be human individuals, chemical compounds, or values of an analytical measure. The problem here is to select one of these objects possessing a certain property by answers to definite questions.

A 'wise' question has the property that the probability p of each of the alternative answers, i.e., 'yes' or 'no', is $p = 0.5$. A 'stupid' question yields an answer with a probability near 1 or 0. With n 'wise' questions regarding two alternative properties, it should be possible to divide the set sequentially n times into two sets, each of which contains $N/2^n$ objects. After n divisions by wise questions, *one* object is finally left, and this is the wanted object:

$$N \cdot (1/2)^n = 1; \quad 2^n = N; \quad n = \text{ld} N. \quad (3.3-24)$$

In order to select one object out of N objects, $n = \text{ld} N$ bit of information is needed. $\text{ld} N$ is the *logarithmus dualis* of N , i.e., the logarithm of N to the base 2. For example: In order to select one out of 1024 objects, $\text{ld} 1024 = \text{ld} 2^{10} = 10$ bit of information is required.

Any information process, e.g., receiving a telegram may be regarded as answering a series of questions which allow alternative or multiple choice answers. It defines an information deficit, referred to as the entropy H , which is a positive quantity:

$$H = - \sum_i p_i \cdot \text{ld} p_i \quad (3.3-25)$$

Here p_i may be the probability of each of the letters to occur in the telegram. Information reduces this entropy:

$$I = H_{\text{begin}} - H_{\text{end}} \quad (3.3-26)$$

When all questions have been answered uniquely, the entropy is zero. The maximum information which can be obtained by a question allowing multiple choice between m answers is thus given by

$$I = H = - \sum_{i=1}^m p_i \cdot \text{ld} p_i$$

with

$$\sum_{i=1}^m p_i = 1 \quad (3.3-27)$$

The information which is gained by answering an alternative (dual choice question) is given by

$$I_2 = -p_2 \cdot \text{ld} p_2 - (1-p_2) \cdot \text{ld}(1-p_2) \quad (3.3-28)$$

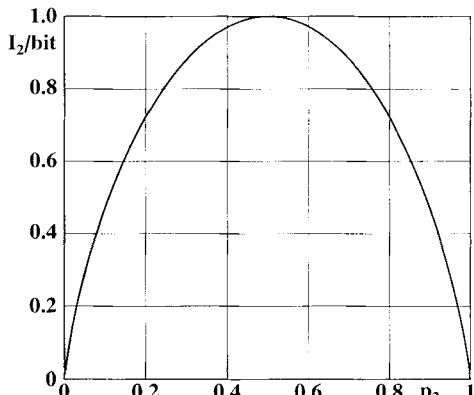


Figure 3.3-10 The information supplied by answering a question with two alternative answers having a probability p_1 and p_2 ; $p_1 = (1 - p_2)$.

For a 'wise' alternative, p_2 is 0.5, therefore $I_2 = 1$. If the answer is *a priori* certain, then it follows that $p_2 = 0$ or 1 and $I_2 = 0$ (Fig. 3.3-10). If there is an m -fold multiple choice with an equal probability of $1/m$ for each case, decision yields the following information:

$$I_N = - \sum_{i=1}^m \frac{1}{m} \cdot \text{ld} \frac{1}{m} = \text{ld} m \quad (3.3-29)$$

The same information is obtained if consecutive decisions are reached between choices with different values of m , either as alternatives or as multiple choice questions (Fig. 3.3-11). This allows to calculate how much information a certain analytical procedure may supply or how much information is needed to solve a particular analytical problem. An analytical measure, such as a melting point or a refractive index with 3 significant digits, may supply $\text{ld } 999 = 9.96 \cong 10$ bit. In order to identify one compound in a spectral collection of N different samples, $\text{ld } N$ bit are required; to identify one out of 100 000 spectra, at least 16.61 bit are needed.

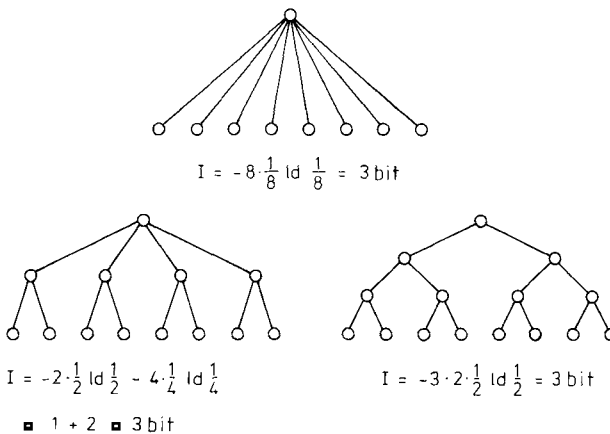


Figure 3.3-11 Three different ways to select one object from 8 objects by answering 'wise' questions. All supply 3 bit of information.

Processing and transporting information needs time. An information channel may be characterized by its channel capacity R_0 , measured in bit/s. An ideal channel transfers information which can be recognized with a probability of almost 1. Noise introduced into the channel reduces the probability of recognizing the information to p' .

$$R' = R_0(1 - (p' \cdot \text{ld} p' - (1 - p') \cdot \text{ld}(1 - p'))) \quad (3.3-30)$$

If the probability p' is reduced by 1 %, i.e., from 1.0 to 0.99, then the channel capacity R' is reduced by 8 %. If p' is reduced by 10 % to 0.90, the channel capacity decreases to 53 %. If p' is 0.5, then the channel can be switched off. Throwing a coin produces the same information: 0 bit.

3.3.4.2 Information theory applied to analytical chemistry

A spectrometric analytical procedure is regarded as a sequence of processes which transform information, coded differently and transmitted by different media (Fig. 3.3-12). The analytical problem is defined by words and numbers concerning the sample, the desired information, and the scenario of the complete procedure. It begins with the collection of a sample and its preparation. The information is originally encoded by the energy states of the sample. The spectrometer transforms this information by absorption or emission processes into numbers of light quanta at different energies. A detector produces electric currents which are transformed into binary numbers. These are finally processed by a computer to supply the answer to the problem: the concentration or amount of sample, its identity or structure. Each step in which information is transformed may introduce systematic or random errors, thus reducing the accuracy and precision of the result. Therefore, each step of an analytical procedure has to be carefully optimized, unequivocally defined, and documented. Following strictly such *complete analytical procedure*

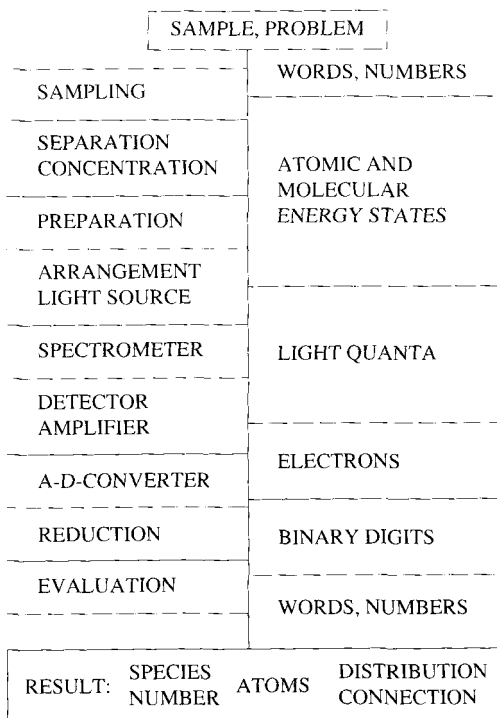


Figure 3.3-12 Definition of a 'complete analytical procedure'.

is necessary in order to obtain optimum, reliable, and reproducible results, independent of the time, the laboratory, or the analyzing individual.

The analytical information may be a flux of light quanta. It is transformed into a signal $\Phi(t)$, a voltage or current, by a radiation detector. Together with this signal, a stochastic variation, noise, is inevitably measured. The noise arising from most processes can be described by a Gaussian distribution of signals. The noise can be determined by recording the signal amplitudes of a 'blank sample' for a 'sufficient long' period of time (Doerffel and Eckschlager, 1981). A blank sample is a sample that does not intentionally contain the analyte (IUPAC, 1976). During this time, when the signal is given by a blank, the mean of $\overline{\Phi_{bl}(t)}$ defines the 'zero' point on the intensity scale (Fig. 3.3-14 a).

$$\Phi_{bl} = \overline{\Phi_{bl}(t)} \quad (3.3-31)$$

A sample containing analyte produces a signal Φ_S :

$$\Phi_S = \overline{\Phi_s(t)} - \overline{\Phi_{bl}(t)} \quad (3.3-32)$$

with $\overline{\Phi_s(t)}$ the mean value of the signal given by the analyte. The signal-to-noise ratio SNR is defined as

$$SNR = \frac{\Phi_S}{\Phi_N} \quad (3.3-33)$$

where

$$\Phi_N = \Phi_{bl,max}(t) - \Phi_{bl,min}(t) \quad (3.3-34)$$

The standard deviation of the intensity of the blank signal (Dörffel and Eckschlager, 1981) is approximately given by:

$$\sigma_{bl} \approx \Phi_N / 5 \quad (3.3-35)$$

Referring to the Sect. 3.3.3 the *NEP* of a detector would correspond to an *SNR* of 1, thus to a signal which is proportional to $5 \sigma_{bl}$ (Fig. 3.3-14a).

Spectroscopy as a two-dimensional analytical procedure provides ideally a number of independent channels of information, each at a definite wavenumber $\tilde{\nu}$ with a width of $\Delta\tilde{\nu}$. Let Φ_u and Φ_l define the upper and the lower limit of the usable intensity range, respectively, and σ the standard deviation of the measured intensity values. On the assumption that these values obey a Gaussian distribution the potential amount of information I_{pot} which a spectrometer may transfer during a time τ is given by (Eckschlager, 1969; Doerffel and Hildebrandt, 1969; Kaiser, 1970; Doerffel and Eckschlager, 1981):

$$I_{pot} = \frac{\tau}{\tau_A} \cdot \frac{\tilde{\nu}_u - \tilde{\nu}_l}{\Delta\tilde{\nu}} \cdot \text{ld} \frac{(\Phi_u - \Phi_l)\sqrt{n_A}}{\sigma \cdot \sqrt{2\pi e}} \quad (3.3-36)$$

Here, τ is the measuring time, τ_A represents the time needed for one measurement, σ is the standard deviation, $\tilde{\nu}_u$ and $\tilde{\nu}_l$ are the upper and lower values of the spectrometric parameters: wavenumbers, wavelengths, or masses; $\Delta\tilde{\nu}$ is the resolvable band width, $(\tilde{\nu}_u - \tilde{\nu}_l)/\Delta\tilde{\nu}$ defines the number of resolvable channels, n . Finally, n_A is the number of parallel determinations performed during the time τ_A .

In general, the potential amount of information which may be obtained by spectroscopy as a two-dimensional analytical procedure is given by

$$I_{pot} = n \cdot \text{ld } S, \quad (3.3-37)$$

where n is the number of resolvable channels and S stands for the number of resolvable intensity steps.

This potential amount of information can only be supplied if each channel produces information which is independent of that supplied by other channels (Fig. 3.3-13a; Schrader et al., 1981). However, spectra consist of bands in which neighboring data points are strongly correlated. Spectral lines may be described by Gaussian or Lorentzian functions, in which parameters define the position, intensity and halfwidth. The information content of a spectrum therefore consists of these significant parameters of all lines or unresolved bands (Fig. 3.3-13b). This makes it possible to store spectra in a reduced form.

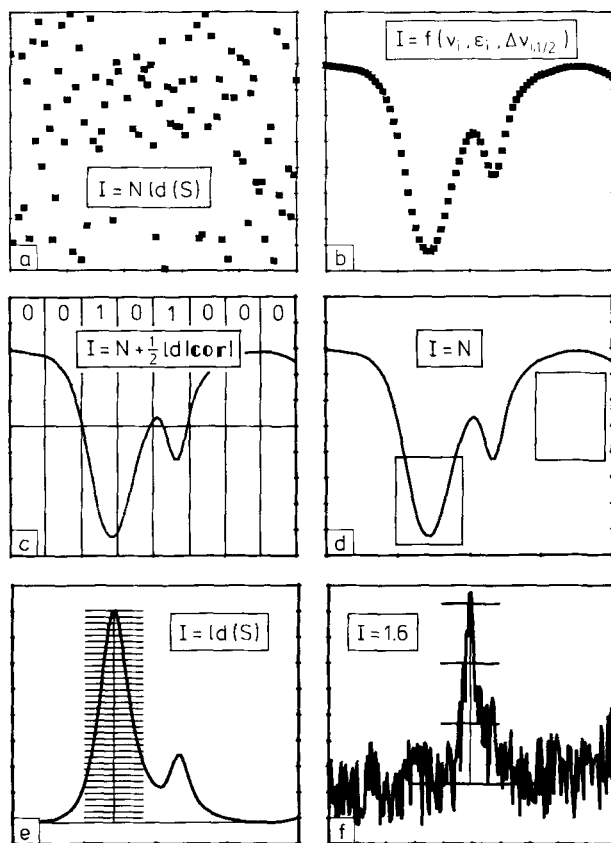


Figure 3.3-13 The information contained in a vibrational spectrum (see text).

For some applications it is sufficient to reduce the information provided by a spectrum by defining relatively broad channels. A 'one' appears only at a position of a band maximum with an intensity larger than a definite threshold value. All other channels produce a 'zero' (Fig. 3.3-13c). A certain correlation between different bands, e.g., the CH stretching and bending vibrations at 2900 and 1450 cm^{-1} , which reduces the available information, is taken into account by the determinant of the correlation matrix (Dupuis et al., 1978b).

There are programs which evaluate spectra by answering questions such as 'are there bands of an intensity between Φ_u and Φ_l at a frequency range between $\tilde{\nu}_u$ and $\tilde{\nu}_l$?' Each channel produces 1 bit of information (Fig. 3.3-13d), which may be used by 'expert systems' to evaluate characteristic vibrations (Schrader and Meier, 1975). Quite promising seem to be the new approaches to interpretation by learning programmes using neural networks and 'fuzzy logic' (Zupan and Gasteiger, 1991).

This discussion demonstrates that the number of resolvable channels in terms of information theory does not necessarily increase with the resolving power of the instrument.

This number, however, is a property which depends on the distribution of information in the spectrum. The optimum is obviously reached, if the resolution of the evaluation procedure is equivalent to the width of the bands in the spectrum (see Sec. 3.3.5).

The precision of quantitative analyses depends on the number of resolvable intensity steps (Fig. 3.3-13e and f). For trace analyses near the limit of detection, the number of steps may be quite small. As shown by Eq. 3.3-36, the number of steps is inversely proportional to the standard deviation of the measurement. It is therefore necessary to discuss the influence of the measuring conditions upon the standard deviation, since it is directly related to the signal-to-noise ratio in the spectrum.

3.3.5 The precision of spectrometric analysis and the limit of detection

A large signal-to-noise ratio is an essential factor to enhance the precision of an analytical procedure. We have seen that the intensity of a signal in a spectrum is proportional to the spectral optical conductance of the instrument. This section describes how the parameters of the measurement affect the signal-to-noise ratio.

A *calibration curve* defines the relation between an analytical signal Φ , produced by a definite component of a sample, the *analyte*, and the amount of this component or its concentration. Calibration curves usually have a linear range – sometimes after the analytical signal has been linearized (Fig. 3.3-14b). If there is a linear relation between the concentration c (or amount) of the sample and the observed signal Φ , its slope is called *sensitivity* γ :

$$\Phi = \gamma \cdot c, \quad \gamma = \left(\frac{\partial \Phi}{\partial c} \right) \quad (3.3-38)$$

The limit of detection, expressed as the concentration (or the amount) of the component of interest, is derived from the smallest measure, that can be detected with reasonable certainty for a given analytical procedure (IUPAC, 1976).

Kaiser (1970) defined the limit of detection as the concentration c derived from the smallest measure Φ_l , given by

$$\Phi_l = \overline{\Phi_{bl}(t)} \pm k \cdot \sigma_{bl}, \quad (3.3-39)$$

where $\overline{\Phi_{bl}(t)}$ is the mean of the blank measures, σ_{bl} is its standard deviation, and k is a numerical factor chosen according to the confidence level desired. The positive sign has to be chosen for emission, the negative sign for absorption processes. Blank measures Φ_{bl} , refer to the measures observed on a sample that does not intentionally contain the analyte and otherwise has essentially the same composition as the material under study (IUPAC, 1976).

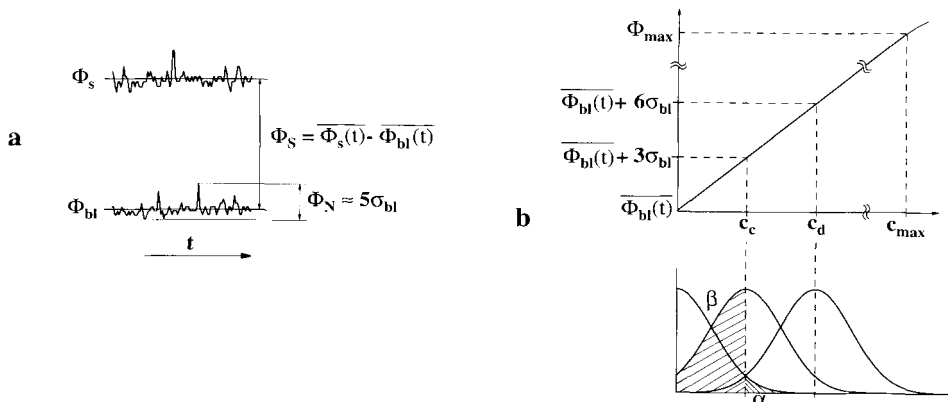


Figure 3.3-14 a Definition of the signal power Φ_s and the noise power Φ_N ; the *signal/noise* ratio SNR is defined by Φ_s/Φ_N ; the standard deviation of the blank is approximately given by $\sigma_{bl} \approx \Phi_N/5$; b definition of the detection limit c_c (Kaiser, 1970) and the decision limit c_d , the α - and the β -error (see text).

The minimum detectable concentration (or quantity) corresponds to

$$\underline{c} = (\Phi_l - \overline{\Phi_{bl(t)}})/\gamma \quad (3.3-40)$$

If, in the case of an emission process, we can assume a normal distribution of the measured values, then c_c , with $k = 3$, is the lowest concentration this procedure can detect (Kaiser, 1970):

$$\underline{c}_c = 3\sigma_{bl}/\gamma \quad (3.3-41)$$

Signals for which $\Phi \geq (\overline{\Phi_{bl(t)}} + 3\sigma_{bl})$ can be interpreted as 'component present' with a probability of 99.87 %. Only a small fraction will be misinterpreted: a signal from a true blank may be interpreted as 'component present' with a risk of $\alpha = 0.13 \%$. This is called the α error. However, the probability of *not* detecting the component when it is present, is $\beta = 50\%$ if $\Phi \leq (\overline{\Phi_{bl(t)}} + 3\sigma_{bl})$! Since this large β error is unacceptable, another value for the detection limit has been introduced, by which the detected component can definitely be distinguished from a blank (Fig. 3.3-14; Massart et al., 1988):

$$\underline{c}_d = 6\sigma_{bl}/\gamma \quad (3.3-42)$$

They define the $3\sigma_{bl}$ limit as the *detection limit* and the $6\sigma_{bl}$ limit as the *determination limit*. They define further a *determination limit*, at which quantitative determinations of the component with a defined standard deviation can be made. This determination limit is defined as

$$\underline{c}_q = k_q \sigma_{bl} / \gamma \quad (3.3-43)$$

in which the relative standard deviation of the determination σ_{rq} equals $1/k_q$. Thus, a relative standard deviation of $\sigma_{rq} = 5\%$ requires a value of $k_q = 20$. This means that the relative standard deviation of \underline{c}_c is 33.33 % and that of \underline{c}_d is 16.67 %.

There are several means of lowering the detection limit in vibrational spectroscopy. The intensity of a *Raman* band is for a given spectrometer and sample arrangement proportional to the flux of the exciting radiation Φ_0 , the concentration c (in molecules per cm^3), the effective molecular Raman scattering cross section Σ'_{RA} , and the effective thickness of the scattering sample d :

$$\Phi_{RA} \propto \Phi_0 \cdot c \cdot \Sigma'_{RA} \cdot d \quad (3.3-44)$$

The sensitivity, $\gamma_{RA} = \left(\frac{\partial \Phi_{RA}}{\partial c} \right)$, for Raman spectroscopy is therefore:

$$\gamma_{RA} \propto \Phi_0 \cdot \Sigma'_{RA} \cdot d \quad (3.3-45)$$

The radiation flux in *infrared* spectroscopy is given by the Lambert-Beer law:

$$\Phi_{IR} = \Phi_0 \cdot \exp(-\Sigma'_{IR} \cdot c \cdot d) \quad (3.3-46)$$

Again, Σ'_{IR} stands for the effective molecular cross section in IR spectroscopy, while c is the number of molecules per cm^3 , and d the sample thickness. In analyses near the detection limit the exponent is small, which makes it possible to approximate the exponential function: $\exp(-x) \approx 1 - x$:

$$\Phi_{IR} \approx \Phi_0 (1 - \Sigma'_{IR} \cdot c \cdot d) \quad (3.3-47)$$

The sensitivity of trace analysis by IR spectroscopy is therefore:

$$\gamma_{IR} \approx -\Phi_0 \cdot \Sigma'_{IR} \cdot d \quad (3.3-48)$$

In infrared absorption spectroscopy, we have to take the negative sign in Eq. 3.3-39. Thus, with Eq. 3.3-43, we obtain in Raman *and* infrared spectroscopy the same equation:

$$\underline{c} \approx \frac{k \sigma_{bl}}{\Phi_0 \cdot \Sigma' \cdot d} \propto \frac{k' \cdot NEP}{\Phi_0 \cdot \Sigma' \cdot d} \quad (3.3-49)$$

As discussed in connection with Fig. 3.3-14, σ_{bl} is proportional to the *NEP* of a detector, which can be described by the number of light quanta N_N of the energy $h\nu$ which produces a *SNR* of 1 (Fig. 3.3-8).

$$\underline{c} \propto \frac{k' \cdot N_N \cdot h\bar{\nu}}{\Phi_0 \cdot \Sigma' \cdot d} \quad (3.3-50)$$

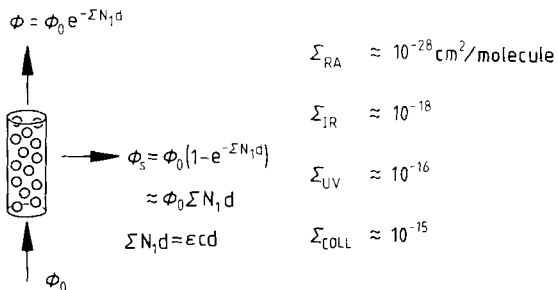


Figure 3.3-15 Typical molecular cross-sections: Σ_{COLL} collision cross-section, Σ_{UV} , Σ_{IR} , Σ_{RA} cross-section for UV, IR, and Raman spectroscopy.

Fig. 3.3-15 shows the typical molecular cross sections. For the elementary process of Raman spectroscopy, Σ_{RA} is of the order $10^{-28} \text{ cm}^2/\text{molecule}$. The cross section in infrared absorption is about 10 orders of magnitude *larger*. The diagram, Fig. 3.3-8, indicates that the number of photons which are equivalent to the *NEP* ($\simeq D^{*-1}$) is for measurements in the infrared range *smaller* by about 10 orders of magnitude compared to those for a typical *NEP* for measurements with photomultipliers. Thus, the smaller cross section of the Raman process (Sec. 3.5.4) is compensated for by a smaller number of photons necessary to produce a Raman signal which can be recognized in the noise.

Thus, the detection limits of infrared and Raman spectroscopy are of the same order of magnitude. In the case of dispersive spectrometers, this limit has been estimated to be about 1 pg of analyte in the sample (Schrader, 1980). It is several orders of magnitude higher than that of UV or fluorescence spectroscopy (less than 1 ag), because in this case both the number of photons equivalent to the *NEP* is small and the cross section is large, being nearly of the order of the gas kinetic cross section.

Therefore, due to their relatively high detection limit the methods of vibrational spectroscopy have to be carefully optimized in order to be able to compete with methods such as mass or fluorescence spectrometry which have much lower detection limits.

Eq. 3.3-50 gives us a clue on how to reduce the detection limit (and how to enhance the precision) by optimizing the measuring technique.

- Φ_0 should be maximized by enhancing both the spectral radiance of the radiation source and the optical conductance of the spectrometer.
 - The effective thickness of the sample should be increased by using appropriate sample techniques (Secs. 3.4.4 and 3.5.4).
 - The effective molecular cross section should be maximized (see below).
 - The noise should be reduced by cooling the detector and minimizing its effective area. Its influence can be reduced by employing multichannel and multiplex techniques, by accumulating spectra, and by increasing the measuring time.

The effective molecular cross section in vibrational spectroscopy

The sensitivity γ is the derivative of the signal by the concentration (Eqs. 3.3-38, 45, 48). It should be as high as possible in order to reduce the detection limit and to enhance the precision. Ideally, a sample should give rise to a narrow line with a high peak intensity, and the spectrometer should only 'see' the spectral band at which γ is at its maximum. This is possible with spectrometers which use tunable lasers as radiation sources for absorption spectroscopy or by using spectrometers with high resolution, e.g., for trace analyses of atmospheric gases.

The line widths in vibrational spectroscopy are a function of the measuring conditions and of the state of the sample. The natural line width of about 10^{-8} cm^{-1} is not usually resolved. The Doppler effect at room temperature contributes 10^{-3} cm^{-1} . The contribution due to impacts and intermolecular interactions for a gas at 1 mbar is 10^{-5} cm^{-1} and for 1 bar it is 10^{-2} cm^{-1} . The resulting line width in the spectra of crystals is of the order $1 - 5 \text{ cm}^{-1}$, and for a liquid it may reach 20 cm^{-1} .

Fig. 3.3-16 shows that the line width increases as the pressure of a gas increases (even by adding an inert gas at constant partial pressure of the analyte). As a result of condensation of the gas to a liquid, the entire band is reduced to one line. Solidification further reduces the band width. Since the integral intensity remains constant, the intensity of the band maximum increases, and so does the sensitivity (Schrader et al., 1981). In short: *Reducing the sample temperature increases the sensitivity.*

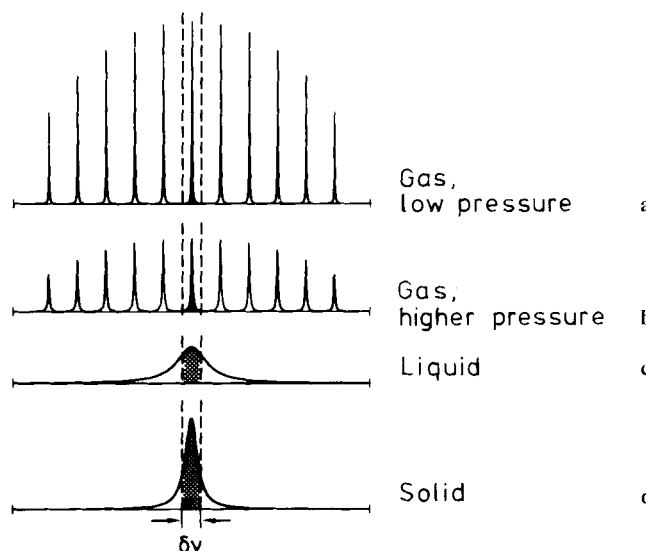


Figure 3.3-16 Vibrational-rotational band of a gas at **a** low, **b** higher pressure, **c** after condensation to a liquid, **d** solidified.

The molecular cross section of the ordinary Raman effect can be considerably enhanced. If the exciting radiation has a higher frequency, the intensity increases basically by the fourth power of the frequency. Moreover, there is a further increase as electronic absorption bands are approached: the pre-resonance and resonance Raman effect (Sections 3.6 and 6.1). Further, the so-called surface-enhanced Raman effect (SERS) increases the molecular cross section. Both effects produce an enhancement of several orders of magnitude (Gerrard, 1991) (see Sec. 6.1). However, these two effects have to be carefully adapted to the specific properties of the investigated molecules. Photochemical decomposition and excitation of fluorescence may make it impossible to record a Raman spectrum. The described techniques may thus be of considerable importance for the solution of special problems, but they are by no means routine techniques to be generally used.

An important parameter of a spectrometer is the relative bandwidth RB . It is defined by the spectral bandwidth of the spectrometer relative to the linewidth to be recorded.

If the detector is the main source of noise, $RB = 2$ would be appropriate. If, however, the background is the main source of noise, then it is advisable to use a narrow bandwidth, $RB \leq 1$ (Schrader et al., 1981). The best approach to optimizing the conditions consists in measuring the SNR at different spectral bandwidths. Fig. 3.3-17 (Schrader, 1980) illustrates this problem.

Ramsay (1952) studied the changes of the maximum absorbance and the half width of a band in the recorded spectrum with the relative bandwidth (RB) for continuous scanning spectrometers. He found that if $RB = 1$, the recorded half width increases by about 60 % and that the observed maximum absorbance is about 70 % of the true value. If $RB < 0.2$, the deviation is of the order of 1 %.

An important means of enhancing the signal-to-noise ratio is the time constant of the recording equipment. Schubert (1958), using scanning spectrometers, showed how the time constant τ_c of the recording system changes the shape of a band. The optimum (the Schubert factor) is reached at $\tau_c = 0.25 \tau_s$, where τ_s is the time needed to scan the half width of the band (the *duration of the signal*).

3.3.6 Multichannel and multiplex techniques, the Fellgett advantage

The detector noise of a spectrometer operating in the visible range can be very low (as for a grating Raman spectrometer with a cooled photomultiplier). In this case, the main source of noise is the statistical noise of the analyzed radiation Φ_S , according to Poisson statistics: $\Phi_N \simeq \sqrt{\Phi_S}$. The signal-to-noise ratio, SNR , is therefore given by:

$$SNR = \Phi_S / \sqrt{\Phi_S} = \sqrt{\Phi_S} \quad (3.3-51)$$

This relation is valid for every wavelength channel. The measuring time which is available for each channel is the total time τ , divided by the time τ_A needed to measure one channel. The time which is necessary to record the entire spectrum with M channels is

$M \cdot \tau_A$, and the signal-to-noise ratio of each channel remains the quantity given by Eq. 3.3-51.

Increasing the available total time τ increases the SNR by $\sqrt{\tau/\tau_A}$. If several detectors are measuring all M channels of a spectrum simultaneously, then it is possible to either record the entire spectrum within the time, necessary for measuring only one channel, or to increase the signal-to-noise ratio, SNR , for each channel by \sqrt{M} , this is the *multichannel advantage*:

$$SNR = \sqrt{\Phi_S \cdot M} \quad (3.3-52)$$

Such multichannel arrangements can be realized by using several single detectors operating simultaneously, and by employing array detectors with many detector elements. Charge-coupled devices, CCDs, are composed of many independent 'pixels', usually arranged in a 2-dimensional array, which store the charge, generated by light quanta. The charge pattern corresponds to the irradiation pattern. CCDs have the same advantages as a photo plate, which may be understood as a simultaneous multichannel detection system. Moreover CCDs may be used repeatedly. In combination with a suitable spectral apparatus, array detectors are very useful for spectral imaging, the mapping of the distribution of molecules with specific spectral bands at a surface (Treado et al., 1992).

In infrared spectroscopy, the detector noise is usually much higher than the noise from other sources. In this case, multiplex recording provides an additional advantage. An interferogram contains the detector noise only once, independently of the number of spectral channels. Fourier transformation produces a spectrum where the SNR_I of each spectral element is related to that of one line, SNR_S by:

$$\frac{SNR_I}{SNR_S} = \sqrt{M} \quad (3.3-53)$$

This is known as the *multiplex advantage*, or Fellgett advantage (Fellgett, 1958; Griffiths and de Haseth, 1986). However, if the radiation is the primary source of noise, especially if there are weak emission lines to be detected accompanied by strong emission lines, then there is a *multiplex disadvantage*. This is especially true in the visible or near infrared region. Fourier transformation distributes the statistical noise of the strong bands over the entire spectrum. It is thus necessary to eliminate the strong emission lines in order to be able to observe the weak lines.

Noise may be also produced by inappropriate recording conditions: If the spectral bandwidth of the spectrometer (Fig. 3.3-17c) is large compared to the spectral line the noise of the unresolved background contributes to the signal-to-noise ratio. In order to reproduce the shape of a spectral band the width of the steps has to be small enough compared to that of the band to be recorded (Fig. 3.3-17b). 'Smoothing', e.g., by the Savitzky-Golay polynome fit procedure (Savitzky and Golay, 1964; 1972) may also enhance the signal-to-noise ratio. This procedure separates spectral bands with a half width, which is expected for the analyte, from the noise. This is adjusted by the parameters of the polynome. Porchet and Günthard (1970) concluded that a spectrum stored in digital form is best treated by a quadratic polynome for $2\xi + 1$ points if there are ξ digital channels per half width of the band (Fig. 3.3-17b).

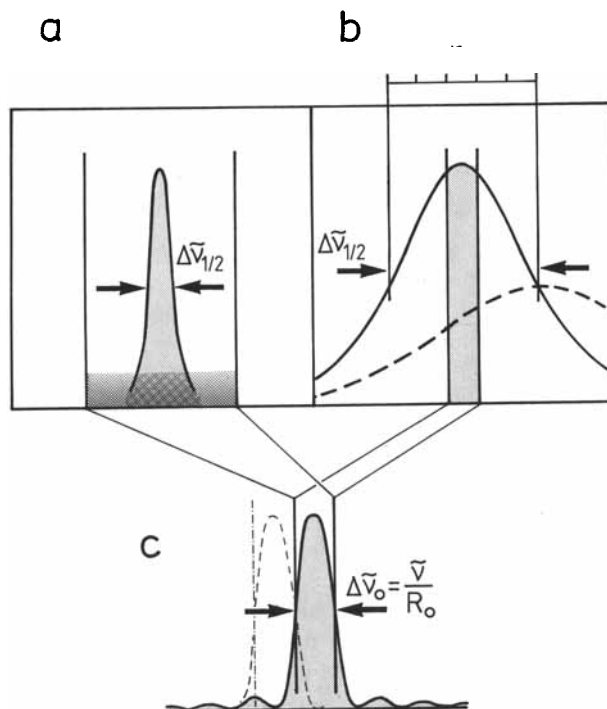


Figure 3.3-17 Relation between the optimal spectral band width $\Delta\tilde{\nu}_0 = \tilde{\nu}/R_0$ and the line width $\Delta\tilde{\nu}_{1/2}$, R_0 is the resolving power of the spectrometer. For a the sensitivity is low since the spectral band width is larger than the line width, also the background contributes to the noise, for b the resolution of the spectrometer is sufficient to yield a high sensitivity. c Relation between bandwidth and resolving power.

Finally, the analogue-to-digital converter should have a resolving power which is large enough (see Griffiths and de Haset, 1986) with respect to the intensity steps (Fig. 3.3-13e and f).

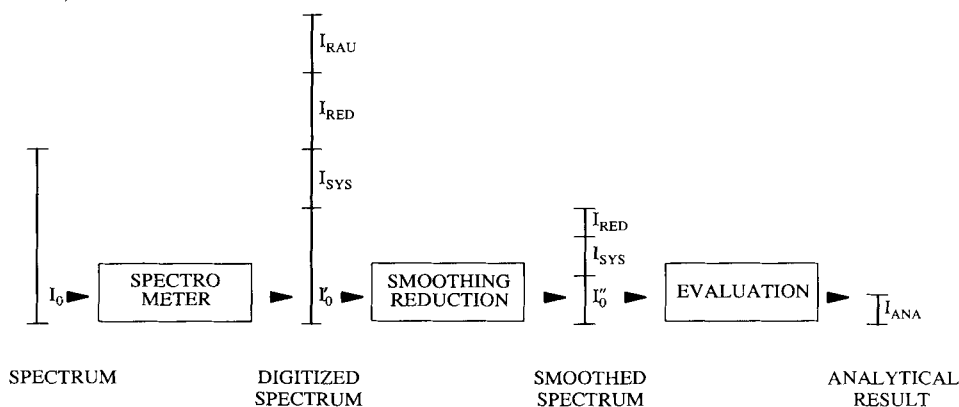


Figure 3.3-18 Handling of information by a spectrometer.

Fig. 3.3-18 outlines information handling in a spectrometer. A spectrum contains some useful information: the parameters of its bands, called I_0 . The spectrometer usually produces many more bits: for each of the n channels, S intensity steps are resolved supplying $n \cdot \lg S$ bit. This includes a certain portion of I_0 , however, most bits are due to noise (I_{RAU}), systematic errors (I_{SYS}) and redundant information (I_{RED}), measured in regions where no bands occur. The first step of an evaluation procedure may consist in eliminating regions which contribute no information. In addition the signal-to-noise ratio may be enhanced by a polynome fitting procedure (Savitzky and Golay, 1964). Finally, a spectrum may be described by the parameters of all bands: position, intensity, and width. Thus, a *smoothed* and *reduced* spectrum is produced. An evaluation program transforms this spectrum into answers to analytically relevant questions. This may be just 1 bit: 'Yes' or 'No' as an answer to the question 'Is compound X present (at a concentration exceeding some definite level)?'; it may also be a quantitative single or multi-component analysis (with about 10 bit per component), or it may concern identification by comparison with a spectral collection (with $\lg N$ bit for one selected spectrum out of a collection of N spectra).

3.4 Spectrometers for the near, middle, and far infrared range

In all ranges of the infrared, the near, middle, and far infrared (NIR, MIR, and FIR) mainly the *absorption* of radiation by a sample is evaluated. *Emission* spectra are only rarely recorded, even though they are a powerful tool for solving problems which cannot be investigated by other methods: investigations of remote samples (in astronomy and for environmental analysis), of reactions of substances on catalysts, and of layers on surfaces (Mink and Kereszty, 1988) (Sec. 3.3.1). Other techniques of investigating surface layers, e.g., ATR technique and ellipsometry in the infrared range, are described in Sec. 6.4.

Optical activity in the infrared range, as well as Raman optical activity, is a very important tool for the investigation of chiral compounds. Each band in a spectrum shows a certain optical activity, depending on how chiral features are modulated by the vibration. In principle, this affords much more information about the structure of chiral molecules and aggregates than do optical rotatory dispersion, ORD, and circular dichroism, CD, measured in the UV/VIS range, which only show properties of the chromophoric system. However, infrared circular dichroism (IRCD) – and Raman circular intensity difference (RCID) effects are inversely proportional to the masses of the particles interacting with the radiation. Consequently, vibrational optical activity is about 10^4 times weaker than the optical activity of the valence electrons. Today, only few scientists are working in this field. There is some hope that these methods may develop into powerful tools in structural chemistry, especially of bio-molecules (Sects. 6.3 and 4.6.4)

Microscopy in the infrared range is a rapidly developing technique which has many applications. In combination with Raman microscopy, it is used in micro technology, biology and medicine, and in product and environmental control (Sec. 3.5.3.3).

3.4.1 Radiation sources

The most common radiation sources are thermal ones. In the NIR region quartz-halogen lamps are mainly used. These emit the radiation of a tungsten wire, which is a 'grey' body at about 3000 K, the emissivity of which has been studied by De Vos, 1954, Rutgers and De Vos, 1954, 1973.

The absorption bands of most thermally resistant window materials in the MIR range make it necessary to use emitters which are stable towards the constituents of the atmosphere, especially to oxygen. The Nernst glower, a mixture of yttrium and zirconium oxides, used to be most popular. At room temperature the Nernst glower is an insulator; it has to be preheated in order to become a conductor. At working conditions, its emission spectrum is similar to that of a black body at 1800 K. The Nernst glower has a number of disadvantages; it is mechanically unstable and has a short lifetime. The so-called globar (glow bar) is more stable. This is a rod or tube with a diameter of 6 – 8 mm, made of SiC, which is a conductor at room temperature. It is heated by a high current at low voltage. Its emission is about 75 % of that of a black body at about 1400 K (Brügel, 1950).

In the FIR region, the mercury arc lamp is most frequently used. Its spectrum is emitted from the plasma as well as from the red glowing silica wall (Bohdansky, 1957).

Since there are only few – and expensive – tunable lasers available for the infrared range, they are not popular for routine applications. However, there are instances where CO₂ lasers (with a high efficiency) are used to excite emission spectra (Belz et al., 1987). Semiconductor lasers have been developed for monitoring atmospheric trace gases (Grisar et al., 1987).

3.4.2 Spectral apparatus

The first infrared spectrometers were prism instruments (Sec. 1). Around 1950, they were replaced by grating spectrometers, because the latter afford a higher spectral optical conductance (about one order of magnitude) and can be optimized for any optical range. Their popularity in analytical spectroscopy reached its maximum between 1970 and 1980. Now, grating spectrometers are being increasingly replaced by Michelson interferometers, which afford a much higher spectral optical conductance (about two orders of magnitude). In addition to the Jacquinot advantage, Michelson interferometers also profit from the multiplex advantage, which scanning grating spectrometers lack (Sec. 3.3.6).

Michelson interferometers also have the advantage of being much more tolerant to misadjustment of the sample arrangement, since they have circular Jacquinot stops, compared to the straight small entrance slits of grating spectrometers (Hirschfeld, 1977 b).

Interferometers can easily be adapted to the required resolution. One interferometer may either provide the very high resolution needed for a analysis of gas spectra, or a high optical conductance at a lower resolution, which is ideal for quick and reliable routine analysis. Their simple, rugged construction make interferometers suitable even for the industrial environment, where they serve in production and quality control. Due to the development of modern micro electronics, the necessary Fourier transformation can now be performed in real time by micro processors, together with the other procedures needed to evaluate the spectra for analytical purposes.

As an example of a modern commercial interferometer, the optical diagram of a Bruker IFS 66, is shown in Fig. 3.4-1. It allows working in the optical range from 40000 to 20 cm⁻¹ (250 nm to 500 μm), to exchange different internal and external radiation sources and detectors, and to connect various accessories, such as a Raman module or an infrared or Raman microscope.

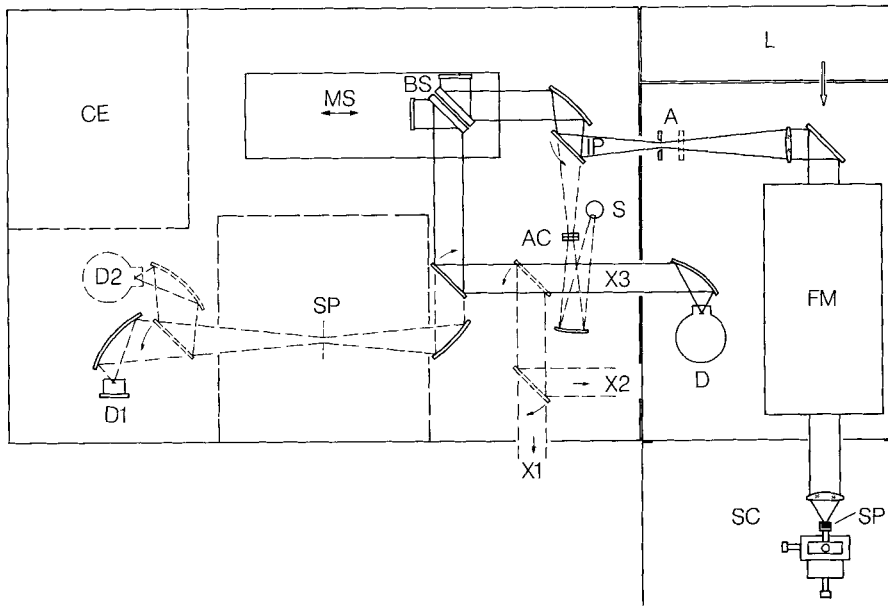


Figure 3.4-1 Optical diagram of a commercial Michelson interferometer for infrared and Raman spectroscopy (Bruker IFS 66 with Raman module FRA 106). CE control electronics, D1/D2 IR detectors, BS beamsplitter, MS mirror scanner, IP input port, S IR source, AC aperture changer, X1 — X3 external beams, A aperture for Raman spectroscopy, D detector for Raman spectroscopy, FM Rayleigh filter module, SC sample compartment with illumination optics, L Nd:YAG laser, SP sample position.

In the NIR, and, more rarely, in the MIR, interference filters are sometimes employed for spectral dispersion. Sets of individual filters and variable circular filters are used especially in simple spectrometers for production control and environmental monitoring.

A modification of the Debye-Sears effect, i.e., the modulation of the refractive index by acoustical waves functioning as tunable grating, is now applied to fast scanning NIR spectroscopy: The Acousto-Optic Tunable Filter (AOTF), (Harris and Wallace, 1969; Chang, 1981). In combination with array detectors, chemical imaging is possible (Treado et al., 1992).

3.4.3 Detectors

The properties of detectors are discussed in Sec. 3.3.3. The noise produced in detectors of infrared radiation is usually of thermal origin. Today, the number of detectors operating at room temperature (Golay cell, thermocouple, pyroelectric detectors) is therefore decreasing. Thermoelectric coolers based on the Peltier effect are used for temperatures down to -30°C . Liquid nitrogen (-196°C), and sometimes even liquid helium (4 K) are also employed. 'Closed cycle refrigerators' are usually not employed for cooling the detectors in analytical laboratories, since they may produce noise due to their mechanical vibrations. Cooled semiconductor quantum detectors (MCT, mercury-cadmium-telluride) have their advantageous low *NEP* only in a restricted wavelength range (Fig. 3.3-8). Therefore, several of these detectors are often combined in a spectrometer for alternative use. Semiconductor array detectors are gaining importance, especially in the NIR range. They can be used in special infrared spectrometers for process control.

Some detectors employ the optothermal effect: the absorbed modulated infrared radiation heats the sample and its environment, thus producing sound waves which are recorded with a microphone. They can be combined with scanning spectrometers and interferometers. A Golay cell (Golay, 1949) measures the optothermal pressure change by a light beam which is deflected by a reflecting membrane. The first infrared process spectrometer, the URAS, already employed the absorption bands of a detector gas to specifically analyze the concentration of this particular gas in a sample. This is a *non-dispersive spectrometer* already mentioned in Sec. 1.

3.4.4 Sample arrangements

Sample arrangements have to fulfill the following conditions:

- a limited amount of sample should be arranged such as to maximize the sensitivity of the spectrometer
- the sample should fit the optical conductance of the spectrometer
- the sample technique should be easy and it should be possible to completely recover the investigated sample.

The sample arrangement of an interferometer is usually placed between the interferometer and the detector. Cuvettes with windows made of IR-transmitting material (Table 3.4-1) contain either a pure liquid sample or a solution usually in a thickness of 5 ... 200 μm – defined by means of a 'spacer' – sometimes, without a spacer ('capillary') it may be even less. If the available amount of sample is very small or the concentration of the substance to be analyzed is very low, then the sample arrangement has to be optimized for this purpose as 'micro' or 'trace' arrangement respectively.

Table 3.4-1 Properties of some commonly used infrared optical materials^a

Optical material	Chemical composition	Transmission range (in 10^4 cm^{-1}) ^b	Refractive index ^c	Range of refr. index measurements ^d	Remarks
Crystal quartz	SiO_2	8.33 - 0.22	1.66 - 1.17 o 1.69 - 1.53 e	5.40 - 0.14 5.40 - 0.49	sens. to HF
Fused silica	SiO_2	8.33 - 0.22	1.53 - 1.40	4.68 - 0.27	
Calcite	CaCO_3	5.00 - 0.18	1.90 - 1.62 o 1.58 - 1.47 e	5.00 - 0.46 5.05 - 0.30	
Sapphire	Al_2O_3	7.14 - 0.15	1.83 - 1.59	3.77 - 0.18	good strength, no cleavage
Magnesium fluoride	MgF_2	9.09 - 0.13	1.43 - 1.38 o 1.41 - 1.37 e	4.67 - 0.92	
Magnesium oxide	MgO	4.00 - 0.12	1.77 - 1.62	2.77 - 0.19	
Irtran 1 ^e	MgF_2	1.00 - 0.12	1.38 - 1.23	1.00 - 0.11	polycryst.
Irtran 5 ^e	MgO	2.50 - 0.11	1.72 - 1.41	1.00 - 0.11	
Lithium fluoride	LiF	8.33 - 0.11	1.44 - 1.11	5.17 - 0.10	sens. to acids
Irtran 3 ^e	CaF_2	2.50 - 0.08	1.43 - 1.27	1.00 - 0.09	polycryst., no cleavage
Calcium fluoride, Fluorite	CaF_2	7.69 - 0.08	1.47 - 1.31	4.37 - 0.10	sens. to NH_4^+ salts, insol. in water
Arsenic trisulfide glass	As_2S_3	1.67 - 0.08	2.69 - 2.36	1.78 - 0.08	

Table 3.4-1 Continued

Optical material	Chemical composition	Transmission range (in 10^4 cm^{-1}) ^b	Refractive index ^c	Range of refr. index measurements ^d	Remarks
Irtran 2 ^e	ZnS	1.00 - 0.07	2.29 - 2.15	1.00 - 0.08	insol. in most solvents
Gallium arsenide	GaAs	1.00 - 0.07	3.34 - 2.12	1.28 - 0.04	
Silicon	Si	0.83 - 0.07	3.50 - 3.42	0.74 - 0.09	long wavelength limit on purity
Barium fluoride	BaF ₂	4.00 - 0.07	1.51 - 1.40	3.77 - 0.10	insol. in water
Cadmium sulfide, hexagonal	CdS	2.00 - 0.06	2.56 - 2.31 ^o 2.60 - 2.31 ^e	1.82 - 0.71	
Arsenic modified selenium glass	SeAs	1.25 - 0.05	2.58 - 2.47	0.99 - 0.07	
Irtran 4 ^e	ZnSe	2.22 - 0.05	2.48 - 2.32	1.00 - 0.05	polycryst.
Gallium antimonide	GaSb	0.55 - 0.05	3.82 - 2.12	0.55 - 0.05	
Amorph. selenium	Se	0.60 - 0.04	2.2	0.2	soft
Germanium	Ge	0.55 - 0.04	4.10 - 4.00	0.48 - 0.08	
Sodium chloride	NaCl	4.76 - 0.04	1.52 ^f		
Silver chloride	AgCl	2.50 - 0.03	2.00 ^f		sens. to light, very soft
Potassium chloride	KCl	4.76 - 0.03	1.82 - 1.23	5.40 - 0.03	

Table 3.4-1 Continued

Optical material	Chemical composition	Transmission range (in 10^4 cm^{-1}) ^b	Refractive index ^c	Range of refr. index measurements ^d	Remarks
Silver bromide	AgBr	0.22 - 0.03	2.31	0.2	light sensitiv
KRS5	TlBr-TlI	2.00 - 0.02	2.37	0.1	toxic
Potassium bromide	KBr	4.00 - 0.02	1.59 - 1.46	2.47 - 0.04	sens. to water, alcohol, hygroscopic
Potassium iodide	KI	4.00 - 0.02	2.05 - 1.56	4.00 - 0.03	
Cesium bromide	CsBr	3.33 - 0.02	1.73 - 1.56	2.50 - 0.02	hygroscopic, soft
Cesium iodide	CsI	4.00 - 0.01	2.04 - 1.64	3.57 - 0.02	hygroscopic, soft
Diamond	C	4.00 - 0.01	2.44 - 2.41	2.08 - 1.51	
Polyethylene (1 mm)	$(\text{CH}_2)_\infty$	0.05 - 0.005		very soft	

^aThe Table is compiled from The Infrared Handbook (W.L. Wolfe and G.J. Zissis, Eds.), Environmental Research Institute of Michigan, 1989., Chap.7.

^bThe cutoff is defined as 10% external transmittance for 2 mm thickness.

^cAt constant temperature (25 - 27 °C) and for the end values of the measurement range.
o - ordinary ray, e - extraordinary ray.

^dIn 10^4 cm^{-1}

^eIrran® is the trade mark of the Eastman Kodak Co.

^fAn average value.

Fitting the sample cell to the optical conductance – trace analyses

Eq. 3.3-49 can be rearranged to give the minimum absorbance A_{min} defining the detection limit:

$$A_{min} = \underline{c}\epsilon d \simeq \frac{k\sigma_{bl}}{\Phi_0} \quad (3.4-1)$$

At a given A_{min} the limit of detection is inversely proportional to the absorption coefficient ϵ and the thickness of the sample d :

$$\underline{c} = \frac{A_{min}}{\epsilon d} \quad (3.4-2)$$

With the known optical conductance of the spectrometer, we can calculate the minimum volume needed to fill a cuvette fitting the optical conductance of the spectrometer and

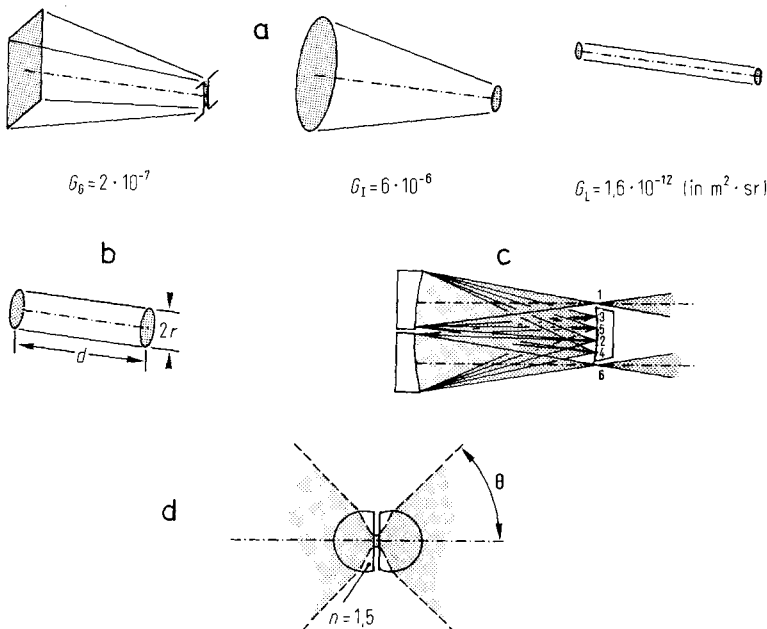


Figure 3.4-2 **a** Approximate optical conductance of a grating spectrometer, an interferometer ($R = 1000$ at 1000 cm^{-1}) or a laser; **b** cuvette of minimal volume for trace analyses of gases; **c** multiple reflexion cell (White cell); **d** cell for liquids with minimal volume.

providing a certain sample thickness. This minimum volume is obtained if the images of both determining apertures – the cross section of the beam at the beamsplitter and the Jacquinot aperture (or the cross section at the grating and the entrance slit) – have the same radius (Fig. 3.4-2b). For a certain sample thickness d it is given by

$$r = \sqrt[4]{Gd^2/\pi^2} \quad (3.4-3)$$

The volume needed to fill this cuvette is:

$$V = \sqrt{G} \cdot d^2 \quad (3.4-4)$$

Since the optical conductance of an interferometer, of a grating spectrometer, and of a laser has a ratio of approximately 100 : 1 : 10⁶, the necessary relative volumes are 10 : 1 : 10³ (Fig. 3.4-2a).

If a gas with very large sample thickness but with a restricted volume has to be fitted to a spectrometer, then so-called White cuvettes (White, 1942) can be used (Fig. 3.4-2c). They allow multiple passes of a beam through the same volume.

If a light pipe is used as cuvette for GC-IR coupling with Θ , the acceptable half angle of the beam, its inner diameter which fits the optical conductance, is given by

$$r = \sqrt{G/(2\pi^2(1 - \cos\Theta_{max}))} \quad (3.4-5)$$

Fitting the sample cell to the optical conductance – micro analysis

Beam condensors, by using a pair of ellipsoid mirrors, produce very small images of the Jacquinot stop or the entrance slit at the sample position. The size of these images may be even further reduced by making use of a Weierstrass sphere. Weierstrass (1856) showed that a spherical lens has two 'aplanatic points'. If a sphere of a glass with a refractive index n is introduced into an optical system which has a focus at a distance of $r \cdot n$ from its center, then the beam is focused inside the sphere at a distance of r/n from the center (Fig. 3.5-9). In this case the angle Θ in Eq. 3.4-5 may approach 90°. Thus, a sample with a very small area can fully fit the optical conductance of the spectrometer (Fig. 3.4-2d). Microscopes usually have an optical conductance which is considerably lower than that of spectrometers. In this case, the sample and the objective are the elements limiting the optical conductance (Schrader, 1990; Sec. 3.5.3.3).

3.4.5 Radiation balance of an IR spectrometer

Most IR spectrometers used in analytical laboratories measure absorption spectra using thermal radiation sources with detectors at room temperature or at a lower temperature.

Sometimes a heated sample is employed as the radiation source (e.g. Belz et al., 1987). The radiation balance, i.e., the flux from the emitter to the detector, can easily be determined by calculating the optical conductance of the spectrometer and by making use of the laws of Planck and Kirchhoff.

According to Eq. 3.3-9, the flux through a spectrometer is given by:

$$\Phi = (L_{\tilde{\nu}, T_A}^A - L_{\tilde{\nu}, T_B}^B) \cdot G_{\tilde{\nu}} \cdot (\Delta\tilde{\nu})^2 \cdot \tau.$$

The optical conductance of an interferometer equals $G_{\tilde{\nu}} \cdot \Delta\tilde{\nu} = 2\pi F_1 / R_0$ (Eq. 3.1-36). The beam area of the IFS 66 Bruker interferometer is $F_1 = 1.75^2 \cdot \pi = 9.62 \text{ cm}^2$. If the spectral bandwidth is $\Delta\tilde{\nu} = 4 \text{ cm}^{-1}$ at a frequency of 1000 cm^{-1} , then R_0 is 250. This determines $G = G_{\tilde{\nu}} \cdot \Delta\tilde{\nu} = 0.24 \text{ cm}^2 \cdot \text{sr}^{-1}$. An ideal beam splitter would have a transmittance factor of 0.5; in practice, however, it is lower, all losses by reflection, refraction, and scattering throughout the entire instrument further reduce the overall transmittance to a quantity of the order of $\tau = 0.1$. Thus, $G \cdot \Delta\tilde{\nu}^2 \cdot \tau = 0.097 \text{ cm} \cdot \text{sr}$. The radiance $L_T(\tilde{\nu}) = L_{\tilde{\nu}, T}(\tilde{\nu}) \cdot \Delta\tilde{\nu}$ (power per area and solid angle) of a Planck black body for a bandwidth of $\Delta\tilde{\nu} = 4 \text{ cm}^{-1}$ at different temperatures is listed in Table 3.4-2.

Table 3.4-2 Radiance of a Planck black body at $\tilde{\nu} = 1000 \text{ cm}^{-1}$ for a spectral bandwidth of $\Delta\tilde{\nu} = 4 \text{ cm}^{-1}$

T/K	$L_T / \text{W} \cdot \text{cm}^{-2} \cdot \text{sr}^{-1}$
3000	$77.41 \cdot 10^{-4}$
1000	$18.82 \cdot 10^{-4}$
350	$0.79 \cdot 10^{-4}$
300	$0.40 \cdot 10^{-4}$
77	$3.65 \cdot 10^{-11}$
4	$2.9 \cdot 10^{-159}$

Table 3.4-3 Radiant flux (W) flowing from a hot (A) to a cold (B) Planck black body through a spectrometer with the properties of the Michelson interferometer Bruker IFS 66 (Fig. 3.4-1)

T_A	T_B	Φ / W
3000	300	$7.47 \cdot 10^{-4}$
1000	300	$1.40 \cdot 10^{-4}$
1000	77	$1.44 \cdot 10^{-4}$
1000	4	$1.44 \cdot 10^{-4}$
350	300	$3.85 \cdot 10^{-6}$
350	77	$7.70 \cdot 10^{-6}$
350	4	$7.70 \cdot 10^{-6}$
300	77	$3.85 \cdot 10^{-6}$
300	4	$3.85 \cdot 10^{-6}$

The radiant flux through a spectrometer at a given bandwidth equals $\Phi = (L_T^A - L_T^B) \cdot G$; A and B define a black body at higher and lower temperature, respectively. A radiant flux flows from the hot to the cold Planck black body, i.e., a radiation source, the sample, or the detector. Combinations of practical significance are listed in Table 3.4-3.

Actually existing emitters are not black bodies. More realistic values may be calculated according to the Planck-Kirchhoff law, Eqs. 3.3-4 to 3.3-8. Table 3.4-4 shows typical molar decadic absorption coefficients for infrared absorption bands of character-

Table 3.4-4 Infrared molar decadic absorption coefficients ϵ for vibrations of typical organic molecules (Jones and Sandorfy, 1956)

Frequency $\tilde{\nu}$ / cm ⁻¹	Nature of Vibration	Compound	Absorption coefficient ϵ / L · mol ⁻¹ · cm ⁻¹
3530	Free $\nu_a(\text{NH}_2)$	Prim. amide	130
3415	Free $\nu_s(\text{NH}_2)$	Prim. amide	120
3305-3270	$\nu(\equiv\text{C}-\text{H})$	Monosub. acetylene	100
3100-3000	$\nu(\text{:C}-\text{H})$	Aromatic compounds	20-60
3090-3080	$\nu(=\text{C}-\text{H})$	$\text{RHC}=\text{CH}_2$	25-35
3085-3075	$\nu(=\text{C}-\text{H})$	$\text{R}_1\text{R}_2\text{C}=\text{CH}_2$	25-30
3030-3010	$\nu(=\text{C}-\text{H})$	cis $\text{R}_1\text{HC}=\text{CHR}_2$	30-40
3027-3020	$\nu(=\text{C}-\text{H})$	trans $\text{R}_1\text{HC}=\text{CHR}_2$	30-40
2962	$\nu_e(\text{CH}_3)$	Sat. hydrocarbon	150
2926	$\nu_a(\text{CH}_2)$	Sat. hydrocarbon	75
2872	$\nu_s(\text{CH}_3)$	Sat. hydrocarbon	90
2853	$\nu_s(\text{CH}_2)$	Sat. hydrocarbon	45
2270	$\nu_a(\text{N}=\text{C}=\text{O})$	Alkyl isocyanate	1300-2000
2260-2190	$\nu(\text{C}\equiv\text{C})$	Disub. acetylene	1
2140-2100	$\nu(\text{C}\equiv\text{C})$	Monoalkylacetylene	5
2000-1650	Overtones and combin.	bands of benzene derivatives	1-10
1820-1650	$\nu(\text{C}=\text{O})$	Carbonyl compound	250-1250
1678-1668	$\nu(\text{C}=\text{C})$	trans $\text{R}_1\text{HC}=\text{CHR}_2$	2
1662-1652	$\nu(\text{C}=\text{C})$	cis $\text{R}_1\text{HC}=\text{CHR}_2$	5-10
1658-1648	$\nu(\text{C}=\text{C})$	$\text{R}_1\text{R}_2\text{C}=\text{CH}_2$	30
1648-1638	$\nu(\text{C}=\text{C})$	$\text{RHC}=\text{CH}_2$	25-45
1610-1590	$\nu(\text{RING})$	Arom. hydrocarbon	20-100
1590-1588	$\delta(\text{NH}_2)$	$\text{R}-\text{NH}_2$ (dil. sol.)	180-210
1500-1480	$\nu(\text{RING})$	Arom. hydrocarbon	50-100
1467	$\delta(\text{CH}_2)$	Lin. aliph. chain	8
1380-1378	$\delta_s(\text{CH}_3)$	Lin. aliph. chain	5
1280-1150	$\nu_a(\text{C}-\text{O}-\text{C})$	Ester, lactone, etc.	500-1200
980-965	$\gamma(\text{HC}=\text{CH})$	trans $\text{R}_1\text{HC}=\text{CHR}_2$	100
720	$\rho(\text{CH}_2)$	$-(\text{CH}_2)_n-$ ($n > 4$)	3
671	$\gamma(\text{CH})$	Benzene	500

istic vibrations of organic molecules. If in Eq. 3.3-4: $\tau = \Phi/\Phi_0 = 10^{-\epsilon \cdot c \cdot d}$ the concentration c is given in mol · L⁻¹ and the thickness d in cm, then the molecular decadic absorption coefficient ϵ has the dimension L/mol · cm – the same dimension as used in UV spectroscopy. The strongest bands in the UV spectrum have ϵ values of about 10⁵ (Perkampus, 1992), whereas in infrared spectroscopy very strong bands have ϵ values of about 10³ (Jones and Sandorfy, 1956; Schrader 1989), see Table 3.4-4. Since all solvents show a continuous background absorption in the infrared range, only relatively concentrated solutions or the pure samples are investigated. Therefore, very thin samples are investigated, with a thickness of about 5 to 200 μm. Thus the exact determination of infrared absorption coefficients is quite difficult. Jones and coworkers (Bertie et al., 1991) have developed a procedure for the exact determination of the optical constants. Staat, Heise and Korte (1983) have described the systematical and statistical errors in the determination of the IR absorption coefficients and a procedure to avoid and compensate for them.

The frequencies and intensities of characteristic IR bands given in Table 3.4-4 are described and discussed in detail in Section 4.1.

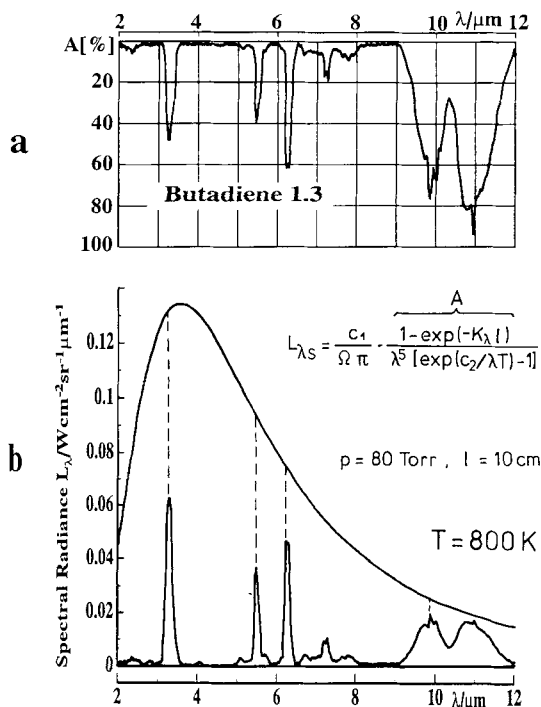


Figure 3.4-3 a Infrared absorption spectrum of butadiene at a pressure of 107 mbar at room temperature, thickness 10 cm; b infrared emission spectrum of the same sample at $T = 800\text{ K}$ compared to the emission spectrum of a black body of 800 K, recorded with Leitz prism spectrometer (Gutberlet, 1978).

Fig. 3.4-3 shows the infrared emission spectrum (the spectral radiance) of a sample of butadiene gas at $p = 107$ mbar in a cuvette with a thickness of 10 cm at 800 K, compared to the emission spectrum of a black body at the same temperature. It is interesting to note that – as theory predicts – the percentage emission of butadiene compared to that of a black body almost equals the percentage absorption of the same gas at room temperature as recorded with an ordinary spectrometer.

A very interesting alternative to using hot sources or samples and cold detectors is to record IR spectra with a cooled sample and a detector at room temperature. The same equations are valid, but the features of the sample can be measured with a higher resolution (Mink and Kereszty, 1988). If the thickness of a sample for emission spectroscopy is too large, then its spectrum approaches that of a black body. In this case, a steep thermal gradient is imposed upon the sample: heating the front and cooling the back, or *vice versa* can help resolve the spectral features of thin layers (Jones and McClelland, 1989).

3.5 Raman spectrometers

A Raman spectrum is excited by irradiating a sample with coherent or non-coherent monochromatic radiation in the ultraviolet, the visible, or the near-infrared range. By an elementary process described in Sec. 2.4, the sample produces usually non-coherent radiation: the strong Rayleigh line at the frequency of the exciting radiation and weak lines at frequencies shifted from the frequency of the exciting radiation by definite quantities, the Raman spectrum.

If coherent radiation with a very high intensity is applied continuously or as pulse, non-linear effects can be observed which produce coherent Raman radiation. This is due to the quadratic and cubic terms of Eq. 2.4-14, which describe the dipole moment of a molecule induced by an electric field. *Non-linear Raman spectroscopy* and its application are described in separate chapters (Secs. 3.6 and 6.1), since this technique is quite different from that of the '*classical*' Raman effect and it differs considerably in its scope.

The classical Raman effect produces only very weak signals. There are two techniques which very successfully enhance this effect. The *resonance Raman spectroscopy RRS* is making use of the excitation of molecules in a spectral range of electronic absorption. The *surface-enhanced Raman spectroscopy SERS* employs the influence of small metal particles on the elementary process of Raman scattering. These two techniques may even be combined: *surface-enhanced resonance Raman effect SERRS*. Such spectra are recorded with the same spectrometers as classical Raman spectra, although different conditions of the excitation and special sample techniques are used (Sec. 6.1).

Raman spectroscopy of gases is discussed in Sec. 4.3.2, the Raman optical activity in Sec. 6.3.

Up to the present most Raman spectra were recorded with scanning instruments, sequential spectrometers, with excitation in the visible range. New developments are now changing this situation:

- Array detectors make it possible to employ the multichannel advantage and to construct compact instruments without moving parts, useful for process control.
- Excitation of Raman spectra in the near-infrared range excludes fluorescence of samples and impurities, which used to mask the Raman spectra of 'real life' products. The very low intensity of Raman spectra in this range, which is proportional to the fourth power of the frequency, can be overcome by interferometers which employ the Jacquinot and multiplex advantage. Special features of NIR FT Raman spectroscopy are described in Sec. 3.5.5.

3.5.1 Radiation sources

Before the invention of lasers in 1960 (Maiman), radiation emitted by the mercury arc, especially at 435.8 and 404.7 nm, has been used for exciting Raman spectra (Brandmüller and Moser, 1962). Today, most types of lasers ('continuous wave' (cw) and pulsed, gas, solid state, semiconductor, etc.), with emission lines from the UV to the NIR region, are used as radiation sources for the excitation of Raman spectra. Especially argon ion lasers with lines at 488 and 515 nm are presently employed. NIR Raman spectra are excited mainly with a neodymium doped yttrium-aluminum garnet laser (Nd:YAG), emitting at 1064 nm.

For certain special purposes, e.g., the excitation of resonance Raman spectra, tunable dye lasers and solid state lasers are used, e.g., the chromium doped Alexandrite laser and the titanium doped sapphire laser (Demtröder, 1991).

3.5.2 Spectral apparatus

A Raman spectrometer has to analyze weak Raman radiation at different wavelengths and the very strong 'Rayleigh radiation', i.e., 'unshifted' radiation at the wavelength of the exciting radiation. This is produced at or in the sample by Rayleigh scattering, reflection, or refraction at powder particles or the sample container. The Rayleigh line has a radiant power which may exceed that of the Raman lines by about 10^6 up to 10^{15} .

The necessary resolving power of a Raman spectrometer is higher than that of an infrared spectrometer. A line at $\Delta\tilde{\nu} = 1000 \text{ cm}^{-1}$ in the Raman spectrum with a half width of 1 cm^{-1} , observed in the visible spectrum near 500 nm (20000 cm^{-1}), needs a resolving power of $R = 20000$. For a line at $\tilde{\nu} = 1000 \text{ cm}^{-1}$ in the infrared with a half width of 1 cm^{-1} , $R = 1000$ is sufficient. The necessary resolving power can usually be made available by common prism and grating spectrometers or by interferometers. Raman spectra of gases require instruments with a resolving power R up to $10^5 \dots 10^6$. They are recorded with specially designed grating spectrometers (Brodersen, 1979; Weber, 1979) or interferometers (Jennings, Weber and Brault, 1986).

In dispersive spectrometers, the Rayleigh radiation may produce stray radiation in the entire spectrum, the intensity of which may be higher than that of the Raman lines. Interferometers transform the Poisson distribution of the light quanta of the Rayleigh radiation into white noise, which overlays the entire Raman spectrum. Therefore, *all types of spectrometers must have means to reduce the radiant power of the exciting radiation accompanying the Raman radiation.*

Dispersive spectrometers usually achieve this end by employing double or triple monochromators. Each monochromator distributes stray radiation of about 10^{-5} of the power of the exciting radiation over the entire spectrum. Consequently, sequential spectrometers for the scanning of Raman spectra employ multiple monochromators, i.e., double or even triple monochromators with additive dispersion (Fig. 3.5-1 a).

As early as 1940, Reitz used a 'double spectrograph' with combined positive and negative dispersion for the reduction of stray light as he recorded Raman spectra of crystal powders on photographic plates.

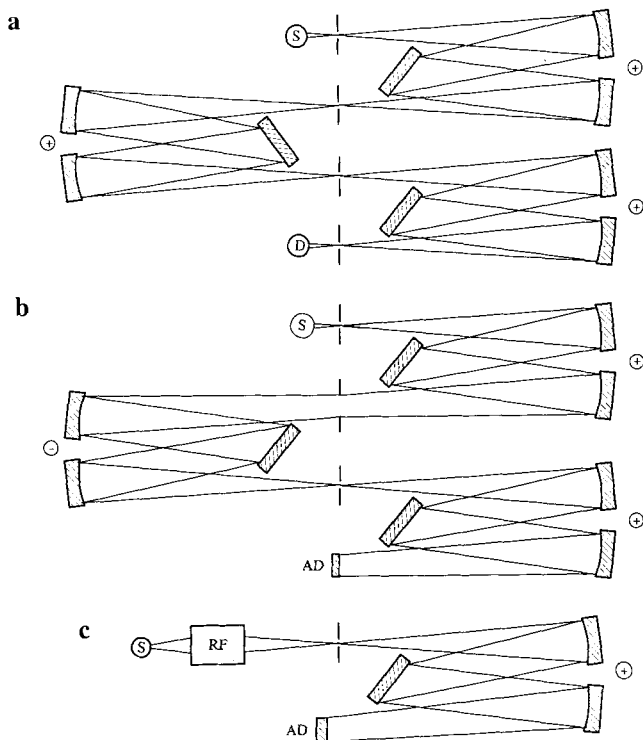


Figure 3.5-1 Types of Raman spectrometers: **a** scanning spectrometer with triple additive monochromators, S source, D detector; **b** instrument with subtractive double monochromator combined with polychromator and array detector AD; **c** Rayleigh filter RF with polychromator and array detector.

In modern 'simultaneous spectrometers', arrays of detector elements (AD in Fig. 3.5-1): photodiode arrays, or CCDs (charge-coupled devices), are arranged in a polychromator (a spectrograph). Here, each element records a different spectral band at the same time, thus making use of the multichannel advantage. A subtractive double monochromator preceding the polychromator can be used to virtually remove the exciting line from the spectrum (Fig. 3.5-1b). An alternative to a subtractive double monochromator is a 'Rayleigh filter', which specifically removes the exciting line (Fig. 3.5-1c). This combination constitutes the basic instrument for 'real time-online' instruments for many applications in industry and environmental control.

There are different types of spectrometers with detector arrays. Due to the limited number (256, 512 or 1024) of available detector elements compared to the number of resolvable spectral elements, the spectrometers permit either low resolution over the entire spectral range, or high resolution within a limited range. Alternatively, the technique described by Knoll et al. (1990) may be used: They employed scanning a multichannel instrument, which combines the merits of the scanning technique with those of the multichannel technique.

Michelson interferometers can be combined with Rayleigh line filters (or subtractive double monochromators) in order to prevent the consequences of the *multiplex disadvantage* (Secs. 3.1.6, 3.3.6; Fig. 3.4-1).

Rayleigh line filters may be produced as interference edge, band, or line filters, as so-called notch filters (Hirschfeld and Chase, 1986), or as 'holographic' filters (Peltier and Reeder, 1991), which specifically reflect the Rayleigh line. Semiconductor band gap filters (Schulte et al., 1991) have also been used. Christiansen filters (Gobrecht et al., 1965) exploit the different dispersion (the dependence of the refractive index on the wavelength, $n(\lambda)$) of particles and an immersion medium. Christiansen filters have their transmission maximum at the wavelength where both media have exactly the same refractive index. An 'ideal' Rayleigh filter has been described by Rasetti already in 1930. He used the mercury resonance radiation at 253.6 nm to excite Raman spectra of gases and placed one drop of mercury in the spectrograph to achieve selective absorption of this line. With this arrangement, he was able to observe pure rotational Raman lines with a simple spectrograph. This technique can also be used with other elements, such as rubidium or cesium (Indralingam et al., 1992). A Bruker notch filter reduces the exciting radiation as well as the Rayleigh wings in the range of $\pm 50 \text{ cm}^{-1}$ to about 10^{-13} , while the Raman spectrum, however, is for shifts greater than $\pm 100 \text{ cm}^{-1}$, only reduced to about 50 % (Schrader and Simon, 1988).

3.5.3 Sample techniques

3.5.3.1 Theory

A sample arrangement should make it possible to record Raman spectra within a short time period with a high SNR by using a small amount of sample. In order to optimize the

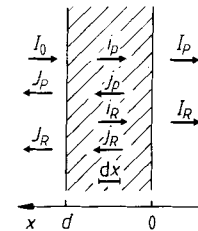
sample arrangement, it is of utmost importance to take into account and make proper use of the optical properties of the sample: the absorption, the elastic and inelastic scattering. These are represented by:

- the linear Napierian absorption coefficient α ,
- the linear Napierian scattering coefficient r ,
- the linear Napierian Raman scattering coefficient s .

These coefficients have the dimension of reciprocal length (Mills, 1988), in this context, cm^{-1} . Kubelka and Munk (1931) described the optical properties of pigments by employing the parameters α and r . The Kubelka-Munk theory is the basis of diffuse reflection spectroscopy (Sec. 6.4). We have extended the Kubelka-Munk approach in order to describe the Raman scattering of crystal powders (Schrader and Bergmann, 1967). The results can also be applied to liquids and transparent solids. The procedure is as follows:

The radiation balance of a layer with the thickness d having an 'infinitely large' surface, irradiated homogeneously from one side with exciting radiation, is given by the solution of four coupled linear first-order differential equations (Eqs. 3.5-1...4). This is a boundary value problem, with the definitions given in Fig. 3.5-2. We are discussing

Figure 3.5-2 Definition of the light fluxes inside and outside a sample of thickness d for the application of the theory of Kubelka and Munk (1931) and Schrader and Bergmann (1967): Exciting radiation I_0 , unshifted radiation leaving the back I_P , and the front surface J_P , Raman radiation leaving the back I_R , and the front surface J_R ; i_P , j_P , i_R , and j_R are the respective light fluxes inside the sample.



the properties of a layer with the thickness d , one surface of which is irradiated homogeneously with the intensity I_0 (radiant power per area). Here, i and j are the intrinsic intensities directed parallel and antiparallel to the exciting radiation, respectively. I and J are the radiation intensities emerging from the surfaces with the subscripts P and R representing, respectively, unshifted ('primary') and Raman radiation.

$$-di_P = -(r + \alpha)i_Pdx + rj_Pdx \quad (3.5-1)$$

$$dj_P = -(r + \alpha)j_Pdx + ri_Pdx \quad (3.5-2)$$

$$-di_R = -(r + \alpha)i_Rdx + rj_Rdx + s(i_P + j_P)dx \quad (3.5-3)$$

$$dj_R = -(r + \alpha)j_Rdx + ri_Rdx + s(i_P + j_P)dx \quad (3.5-4)$$

In order to simplify the solutions, a parameter k is introduced which is related to r and α :

$$k^2 = 2r\alpha + \alpha^2 \quad (3.5-5)$$

The solutions are given by the following equations:

$$I_P = I_0 \frac{k}{(\alpha + r) \sinh kd + k \cosh kd} \quad (3.5-6)$$

$$I_R = I_0 \frac{s \cdot k \cdot (k^2 d - r) \sinh kd + (r + \alpha)kd \cosh kd}{[\alpha + r) \sinh kd + k \cosh kd]^2} \quad (3.5-7)$$

$$J_P = I_0 \frac{r \sinh kd}{(\alpha + r) \sinh kd + k \cosh kd} \quad (3.5-8)$$

$$J_R = I_0 \frac{sk}{\alpha} \cdot \frac{k \sinh^2 kd + (\alpha + r) \sinh kd \cosh kd - krd}{[(\alpha + r) \sinh kd + k \cosh kd]^2} \quad (3.5-9)$$

It is particularly important to know the intensity of the Raman radiation relative to the unshifted radiation scattered in the same direction for forward scattering (0° arrangement):

$$\frac{I_R}{I_P} = \frac{s}{\alpha} \cdot \frac{k^2 d - r + (\alpha + r)kd \coth kd}{\alpha + r + k \coth kd}, \quad (3.5-10)$$

and for backward scattering (180° arrangement):

$$\frac{J_R}{J_P} = \frac{s \cdot k}{r \cdot \alpha} \cdot \frac{k \sinh kd + (\alpha + r) \cosh kd - \frac{krd}{\sinh kd}}{(\alpha + r) \sinh kd + k \cosh kd}. \quad (3.5-11)$$

These equations have been employed for the determination of absolute Raman scattering coefficients of crystal powders (D'Orazio and Schrader, 1974, 1976). Experiments have confirmed the consequences of this theory (Kłosowski and Steger, 1979).

In conventional Raman spectroscopy Raman spectra are recorded from colorless samples with exciting radiation in the visible range of the spectrum. In this case, the absorption of the exciting and Raman radiation by the sample is at its minimum, and the linear decadic absorption coefficient ($a = \epsilon \cdot c$) is of the order of $10^{-3} \dots 10^{-5} \text{ cm}^{-1}$.

However, if Raman spectra are recorded in the NIR range, the coefficient a may be of the order $10^{-1} \dots 10^2 \text{ cm}^{-1}$. This is due to the overtones and combinations of the X-H stretching vibrations (X may be any element) in the infrared range (Fig. 3.5-3; Luck, 1963; Visapää, 1965; Buback, 1977). The Napierian absorption coefficient α is related to a by $\alpha = a \cdot \ln 10$.

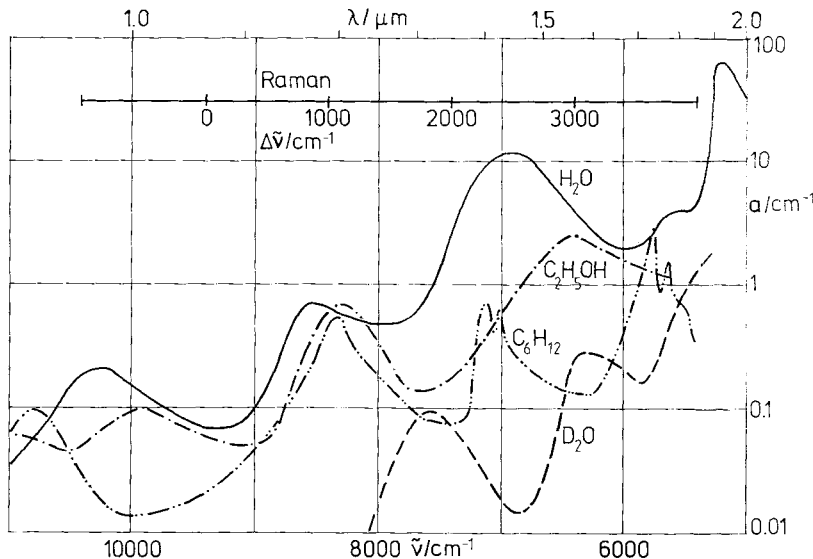


Figure 3.5-3 Linear decadic absorption coefficient of H_2O , D_2O , Ethanol, and Cyclohexane in the near infrared region. Insertion: range of the Raman spectrum, excited by the Nd:YAG laser with radiation of $\lambda = 1064 \text{ nm}$.

For the purposes of this discussion, α is assumed to equal 0.1 cm^{-1} , a suitable value for 'real life' samples.

The scattering coefficient r for crystal powders, is approximately inversely proportional to the diameter of the particles (Kortüm, 1969). For coarse, medium and fine powders, r is approximately 10 , 100 , and 1000 cm^{-1} , respectively. In the case of pure liquids, solutions, fibers, and single crystals, r is approximately 0 .

In this context, the Raman scattering coefficient s is assumed to be equal for all samples. Only relative intensities of the Raman spectrum are discussed.

Figs. 3.5-4 a and b show the relative intensities J_R and I_R of the Raman radiation of samples with different thicknesses in the back-scattering and the forward-scattering arrangement, according to Eqs. 3.5-9 and 3.5-7. Figs. 3.5-4 c and d show the reflectance ρ and the transmittance τ of the exciting radiation according to Eqs. 3.5-8 and 3.5-6, with $J_P/I_0 = \rho$ and $I_P/I_0 = \tau$.

Liquids can be assumed as samples with an elastic scattering coefficient r approaching 0 . The diagrams for $r = 0$ show that in the back-scattering arrangement (Fig. 3.5-4 a), the intensities of the Raman lines increase with the sample thickness. Fig. 3.5-4 c demonstrates that under the same conditions the intensity of unshifted radiation is very low. In the forward scattering arrangement, however, the intensity of the Raman lines also increases with the thickness of the sample (Fig. 3.5-4 b), but the Raman radiation is mixed with a very large amount of unshifted radiation (Fig. 3.5-4 d).

Thus, *liquids are best investigated with a back-scattering arrangement with a large effective thickness*.

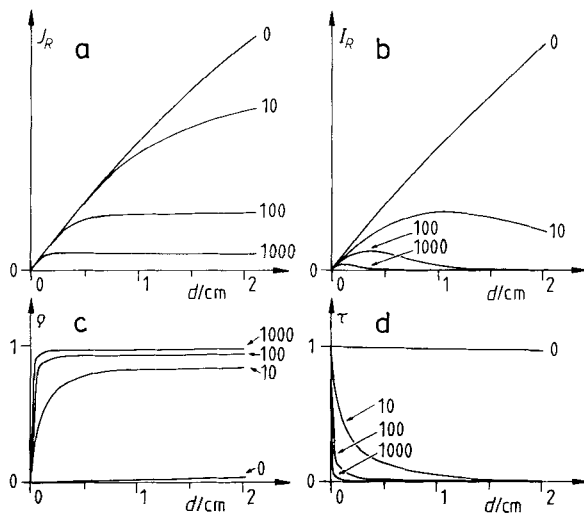


Figure 3.5-4 Raman radiation at **a** the front J_R , and **b** the back I_R , **c** reflectance ρ , and **d** transmittance τ , of samples with a thickness between 0 and 2 cm and coefficients of unshifted scattering $r = 0, 10, 100, 1000 \text{ cm}^{-1}$ representing liquids, coarse, medium, and fine powders, respectively.

Coarse, medium, and fine crystal powders have an elastic scattering coefficient of about 10, 100, or 1000 cm^{-1} , respectively. With the back-scattering arrangement (Fig. 3.5-4 a), the intensity of the Raman lines increases with the thickness of the sample. In the case of fine powders ($r = 1000$), this intensity reaches a small limiting value at a small thickness. For larger grains ($r = 10$ or 100), a higher limiting value is reached at a larger thickness. The same samples show a reflectivity ρ (Fig. 3.5-4 c), which approaches for larger scattering coefficients r higher limiting values at smaller thicknesses. The limiting value for $r = 1000$ is $\rho = 98.6\%$, for $r = 100$ is $\rho = 95.6\%$, and for $r = 10$ is $\rho = 86.8\%$.

This is a useful prerequisite for the optimization of sample arrangements: the low intensity of the Raman radiation can be considerably enhanced by utilizing multiple reflections of the exciting and the emerging Raman radiation at the sample and an external spherical mirror.

Thus, *multiple reflection arrangements* may have a high efficiency, which is nearly independent of the size of the grains!

Fig. 3.5-4 b shows the intensity of the Raman radiation of a forward-scattering arrangement. At an 'optimum thickness', the Raman radiation has a maximum, which increases as the elastic scattering coefficient decreases. The exciting radiation which emerges from the sample (Fig. 3.5-4 d) has a lower intensity if the elastic scattering coefficient r is higher.

Compared to back-scattering arrangements, forward-scattering arrangements produce lower absolute intensities of the Raman lines. However, the ratio of the Raman line intensity relative to the intensity of the exciting radiation emerging from the sample exceeds that of a back-scattering arrangement by one or two orders of magnitude.

Thus, the optimum sample arrangement for Raman spectroscopy of crystal powders with a low absorption coefficient is a forward-scattering (0°) arrangement of coarse crystallites with an optimum thickness in a multiple scattering arrangement. These are the conditions for the investigation of colorless samples in the visible range of the spectrum.

In the case of relatively high absorption coefficients, as in NIR-excited Raman spectroscopy, coarse powders should be investigated with a back-scattering (180°) multiple reflection arrangement.

3.5.3.2 Sample arrangements for Raman spectroscopy

Conventional Raman spectroscopy employs nonabsorbing samples and grating spectrometers. The liquid sample is irradiated with the exciting radiation, usually a laser beam. In a direction perpendicular to the laser radiation, an image of this part of the sample is produced by the entrance optics, irradiating the grating with the Raman radiation through the entrance slit (Fig. 3.5-5 a).

For nonabsorbing crystal powders, the 0° multiple reflection arrangement shown in Fig. 3.5-8 g has proven to be superior to other arrangements, because it combines a high intensity of the Raman radiation with the maximum ratio of Raman/exciting radiation, I_R/I_P . All of the Raman spectra of crystal powders reproduced in the Raman/Infrared Atlas (Schrader, 1989) have been recorded with an arrangement according to this principle.

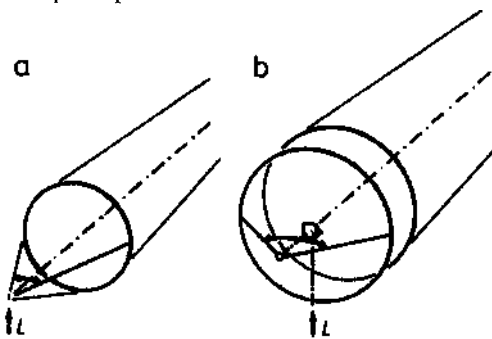


Figure 3.5-5 Sample arrangement for Raman spectroscopy. Optimal illumination of **a** a grating spectrometer in the 90° arrangement; **b** of an interferometer in the 180° arrangement.

As explained in the preceding paragraph absorbing samples (as for NIR-excited Raman spectroscopy) should be arranged in a 180° back-scattering arrangement. Interferometers which are employed for this purpose have a circular entrance aperture, i.e., the Jacquinot stop (instead of the entrance slit of a grating spectrometer). For NIR FT Raman spectroscopy the 180° back-scattering arrangement (Fig. 3.5-5 b) is therefore recommended for three reasons:

- The intensities observed under these conditions are the highest.
- The exciting radiation irradiates a conical volume of the sample. The Raman radiation emerging from this volume irradiates optimally the beam splitter of the interferometer through the circular Jacquinot aperture.
- A circular spot is more aberration-tolerant than a line of the same area and thus can be demagnified further (Hirschfeld, 1977). In other words, the Raman radiation of a smaller spot on the sample can be collected within a larger solid angle. This means a further optimization of the arrangement.

Conventional Raman spectroscopy utilizes rectangular or cylindrical cuvettes. A given spectrometer collects maximum intensity of Raman radiation of a sample, if the sample is placed in the focal region of a laser beam and if a maximum amount of the Raman radiation emerging from this sample is collected by a sample optics of the spectrometer within a maximum solid angle (Schrader, 1980). As mentioned in Sec. 3.1, the optical conductance of the entrance optics should have the same value as that of the interferometer or monochromator. Inspection of conventional sample arrangements shows that these conditions were often **not** fulfilled optimally:

- The focus of the observing optics in a rectangular cell is blurred, and so is the focus of the exciting radiation (rays with a larger angle relative to the optical axis in a rectangular or cylindrical cell have a different focal point than rays with a small angle to the axis (Fig. 3.5-6 a). The deviation of the focal point Δf (in %) as a function of the angle Θ of the ray relative to the normal of the refracting surface is shown in Fig. 3.5-7.
- The effective solid angle of the collected Raman radiation of a sample in a rectangular cell is only about 40 % of the solid angle of a suitable high-aperture optical system (Fig. 3.5-6 a, b).

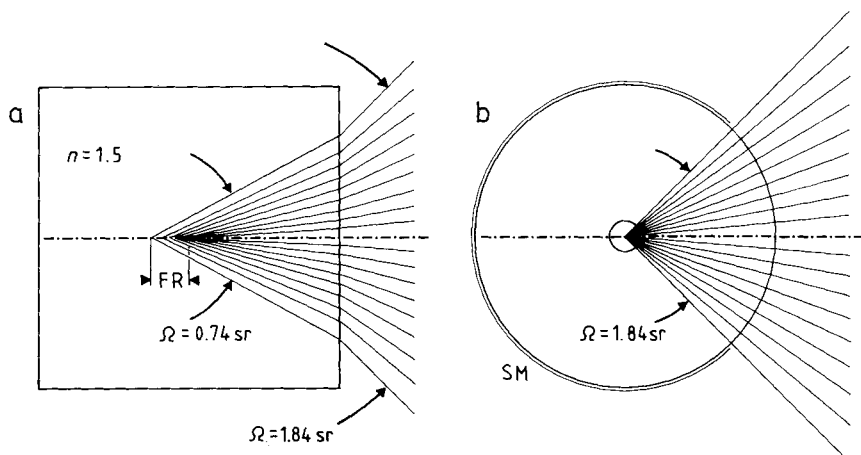


Figure 3.5-6 Arrangement of **a**, a rectangular cell and **b**, a spherical cell at the focus of the entrance lens of a Raman spectrometer. The effective solid angle is by a factor of 2.5 larger for a spherical cell compared to the rectangular cell. FR focal range, SM surface mirror.

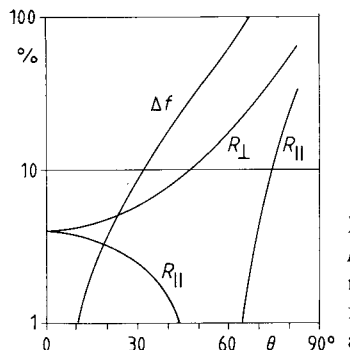


Figure 3.5-7 Shift of the focus Δf and reflectance R_{\parallel} and R_{\perp} in % for different angles Θ of a ray relative to the normal of the entrance window of a rectangular cell, calculated for $n_{cell} = 1.5$. For a spherical cell $\Delta f = 0$ and all R are about 4 %.

- Reflection losses at the surface of the cuvettes may be high and are strongly dependent on the angle of refraction and the direction of the electric vector relatively to the plane of incidence (Fig. 3.5-7).

There is a newly developed spherical cuvette which does not have these disadvantages (Schrader, 1987). The foci are not blurred, the effective solid angle of the collected Raman radiation is equal to that of the sample optics (Fig. 3.5-6 b), and the reflection losses are small and equal, because for every ray $\Theta = 0^\circ$. The losses can be reduced further by suitable anti-reflection coating of the surface range of irradiation and observation. The other part of the surface of the spherical cuvette should be covered with a reflecting material. Any sample placed at the center of the sphere constitutes with this surface mirror as second element a multiple reflection arrangement. Samples at the center of the cell have a spectral radiance which exceeds that of an ordinary sample arrangement by about one order of magnitude. The necessary amount of sample is of the size of the focal region of the exciting laser beam. It may well be less than 1 mm^3 . The sample at the focus of the laser beam may be effectively cooled if the sphere is made from a material which has a high thermal conductance, such as sapphire.

Furic and Durig (1988) have independently described some advantages of the spherical cuvette.

Fig. 3.5-8 shows different sample arrangements which are suitable for Raman spectroscopy. Fig. 3.5-8 a exhibits the conventional rectangular cuvette, which is not regarded as optimal. Fig. 3.5-8 b shows the spherical cell for liquids and powders. For a sample in a melting point capillary a small amount of glycerol may be used as immersion liquid between the capillary and the material of the sphere. Alternatively, the substances may be brought directly into the center of the sphere, and the boring may be closed by stoppers made of polytetrafluoroethylene. The sample may also be introduced with stainless steel cannulas fixed with epoxy cement. This flow-through arrangement can also be used as detector for chromatography, even with samples under high pressure for supercritical fluid chromatography. The center volume of the sphere itself may be spherical, a shape which is obtained by combining two half spheres. The diameter of the sphere can be very small and its wall may be thin. Large diameters are not recommended, because they would only increase the amount of sample and the losses by absorption. We successfully use spheres of 10 mm diameter, made from sapphire, with a sample volume of about 1 mm^3 in the center. Sapphire gives rise to a Raman spectrum of a few sharp and

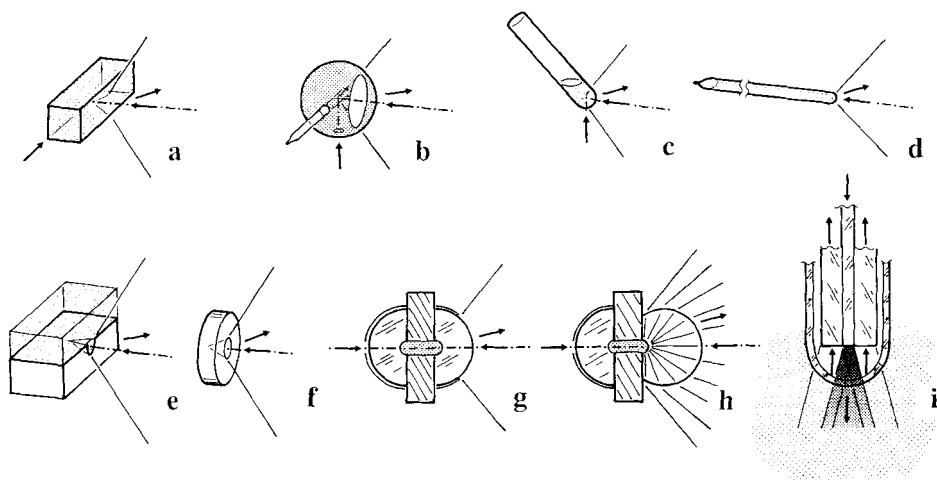


Figure 3.5-8 Sample arrangements for Raman spectroscopy: **a** rectangular cell, **b** spherical cell for liquids and powders which are in a melting point capillary at the center of the sphere with a reflecting surface; **c** liquid in an NMR tube, the axis of which has an angle of 45° relative to the axis of the entrance optics. The cuvettes **a - c** may be used in a 90° or a 180° arrangement; **d** light pipe cuvette; **e** arrangement for solids or surface layers: The sample is placed upon a block of aluminium or stainless steel with a polished conical indentation, providing a multiple reflection arrangement; **f** tablet with a cone-shaped bore; **g** arrangement for Raman spectroscopy of powders in 0° and 180° arrangement, the half spheres have a reflecting surface which reflects the exciting and Raman radiation back to the sample, which is not collected by the entrance optics; **h** same as **g** but one half sphere is exchanged against a Weierstrass lens (Weierstrass, 1856), which collects the radiation emitted into a solid angle of $\sim 2\pi$; **i** sample head for a two-way bundle of optical fibers for spectroscopy of liquids or powders. The head can be introduced directly into the sample, it is protected by a cover in order to prevent sticking and pyrolysis of the sample at the central fiber which transports the exciting radiation from the laser to the sample.

weak lines (Porto and Krishnan, 1967). They can easily be subtracted from the recorded spectrum and may be employed as intensity standards (Mattioli et al., 1991). Sapphire has a high thermal conductance, it is hard and very stable. Fused synthetic quartz is also suitable, glass has a stronger Raman spectrum, consisting of broad bands (Fig. 3.5-17).

Fig. 3.5-8 c shows a sample in an NMR tube. The angle of the tube axis relative to the axis of observation is 45°. When the Raman radiation is observed through the spherical bottom of the tube, some of the advantages of the spherical cell are exploited. All arrangements of Figures 3.5-8a...c can be utilized in a 180° (back-scattering) or a 90° arrangement.

Fig. 3.5-8 d shows a cuvette which is axially irradiated. Depending on the refractive index of the sample and the cuvette material and its length, the Raman spectrum may be very strong, as a consequence of utilizing the advantages of a light pipe. This cuvette is especially suitable for observing Raman spectra of dilute solutions. In the NIR range, it is advantageous to use solvents without X-H bonds, such as carbon tetrachloride,

carbon disulphide, or deuterated solvents, e.g., D₂O, since these have a smaller absorption coefficient in this region.

Figs. 3.5-8 e – h show sample facilities for solids and powders which employ different multiple reflection arrangements. Conical arrangements of powders were used for Raman spectroscopy long ago (Brandmüller and Moser, 1962). These devices make use of the advantages of multiple reflection and refraction at the surfaces of the grains in a powder. A multiple reflection system may be equipped with a metal mirror, like the cone-shaped indentation of the metal block shown in Fig. 3.5-8 e. Any flat sample whose surface is to be investigated may be placed on top of the mirror. Fig. 3.5-8 f shows a tablet with a conical or cylindrical bore in which multiple reflection at the internal surface of the sample occurs.

Figs. 3.5-8 g and h show a sample cell which may be used either as a 0° or as a 180° arrangement (forward or backward scattering). The reflecting half sphere, together with the sample surface, allows multiple reflection at the irradiated surface of the sample. The portion of radiation emerging from the other side of the sample, which is not collected by the spectrometer, is also reflected back to the sample. Most Raman spectra of the Raman /Infrared Atlas of Organic Compounds (Schrader, 1989) were recorded with a cell which is analogous to that shown in Fig. 3.5-8 g, often from tablets. Pressing a powder into a tablet usually reduces the scattering coefficient and thus enhances the intensity of the Raman spectrum. Fig. 3.5-8 h shows a so-called Weierstrass sphere (Weierstrass, 1856; Born, 1933; Wittke et al., 1989) placed on top of the sample. The Weierstrass sphere is an aplanatic system which makes it possible for the entrance optics of the spectrometer to collect all radiation which is emitted by the sample in a solid angle of nearly 2π . Fig. 3.5-9 demonstrates the principle of the Weierstrass sphere. If a sphere with a refractive index n and a radius r is placed in a focused beam such that the focus has a distance of the center of the sphere of $n \cdot r$, then inside the sphere the beam is focused with a distance from the center of r/n .

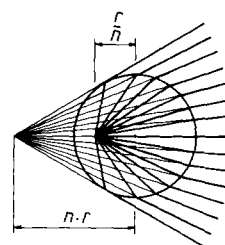


Figure 3.5-9 Principle of the Weierstrass lens: The refractive index of a sphere with a radius r is n . A beam which would have — without the sphere — a focus at a distance of $n \cdot r$ from the center of the sphere is focused inside the sphere at a distance of r/n from the center.

Fig. 3.5-8 i finally exhibits another universal sample head. It utilizes an optical fiber (Christie and McCreery, 1990; Schrader et al. 1988) to transport the exciting radiation to the sample. A bundle of fibers, usually with a larger diameter (Fig. 3.3-7), is arranged around the central fiber in order to transport Raman radiation from the sample to the spectrometer. The connection to the spectrometer is at its optimum if the optical conductance of the fiber bundle is as high as that of the spectrometer. The end of the fiber bundle is covered with a shield (NMR tube) to prevent sticking and pyrolysis of particles at the end of the laser fiber. It can be used to cool the head if the laser power

is high. This sample head may be inserted into any liquid or solid sample or even in a chemical reactor. A lens, a pair of spheres or a conducting cone at the end of the fiber bundle may be used to collect Raman radiation from a large solid angle and to send it through the fibers. It works as a transformer of the cross-section; according to the equation $F_1 \cdot \Omega_1 = F_2 \cdot \Omega_2$ it is inversely proportional to the solid angle - for a constant optical conductance.

As a variant of the end-on arrangement shown in Fig. 3.5-8d, the sample cuvette may be made very long, e.g., as a quartz tube of some tenths of a millimeter in diameter and several meters long. It can be used for trace analyses and for producing a very strong Raman spectrum with an unexpected high intensity of over- and combination tones (Schrader, 1960; Walrafen and Stone, 1972; Walrafen, 1974; Kiefer, 1977; Schmid and Schröter, 1981).

3.5.3.3 Micro and 2D scanning arrangements

For a given light flux of a laser source, the flux of the Raman radiation is inversely proportional to the diameter of the focus of the laser beam at the sample. This means that **an optimized Raman sample is a micro sample** (Schrader and Meier, 1966; Schrader, 1980). The minimum focal diameter of the laser beam is of the order of the wavelength of the laser radiation.

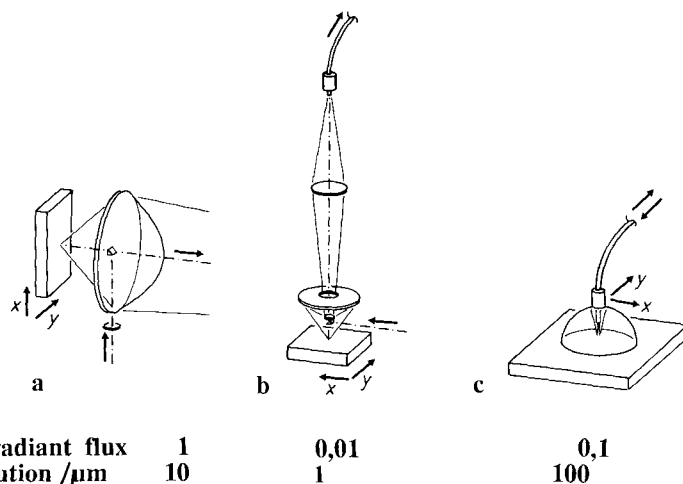


Figure 3.5-10 Scanning micro arrangements for Raman spectroscopy: **a** normal sample arrangement; **b** arrangement using a microscope and fiber optics; **c** scanning of surfaces with fiber optics and half-spheric mirror, which reflects the part of the exciting and Raman radiation back to the sample which is not directly collected by the fiber bundle (Schrader, 1990).

There are several possibilities of adapting a micro sample to a spectrometer. The most straightforward approach uses the ordinary 180° sample arrangement (Fig. 3.5-10 a). The spatial resolution is given by the irradiated volume of the sample and the resolution of

the observing system. In practice, laser beams can be concentrated to foci with a diameter of about 8 times the wavelength, e.g., 4 microns for excitation by laser radiation at 488 or 515 nm and 8 microns at 1064 nm. Even if the focus of the laser beam is of this magnitude, the effective volume is determined by the nature of the sample. Fig. 3.5-11 illustrates typical cases (Schrader, 1990). A sample which may internally reflect the laser beam (Fig. 3.5-11 a) will show a halo around the focal region. This can be prevented by applying an absorbing layer at the back of the sample. A transparent sample transmits Raman radiation from the entire irradiated lobe to the spectrometer (Fig. 3.5-11b). A sample such as a crystal powder which scatters radiation by reflection and refraction at the surface of its grains, gives rise to a blurred halo whose diameter increases with the size of the grains (Fig. 3.5-11c). The size of this diffusion halo may be calculated by a procedure resembling the Kubelka-Munk approach (Kubelka and Munk, 1931; Kubelka, 1948; Schrader and Bergmann, 1967), Sec. 3.5.3.1.

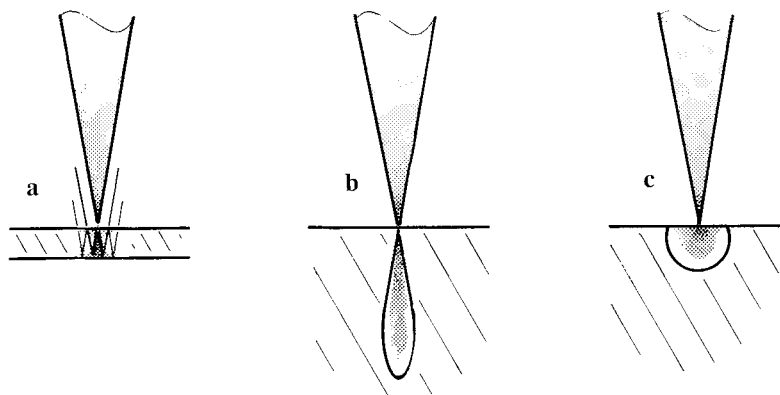


Figure 3.5-11 Volume of a sample the Raman scattering of which is observed, when irradiated by a focused laser beam in a 180° arrangement: **a** layer with internal reflection; **b** transparent absorbing material; **c** diffusely scattering material (Schrader, 1990).

If the spatial resolving power has to be high, then the Raman radiation must be observed through microscope objectives (Fig. 3.5-10 b). Unfortunately, these objectives have a somewhat lower optical conductance than the regular sample arrangement (Schrader, 1990). As a result, the observed Raman spectrum is also considerably weaker. A microscope may be connected to the spectrometer by a mirror system or by optical fibers, as shown in Fig. 3.5-10 b. Optical fibers are especially useful for NIR FT Raman spectroscopy, because the transmission of the fibers may be at its maximum exactly in the range of a Raman spectrum excited by a Nd:YAG laser (Fig. 3.3-5).

The spatial resolving power is especially large, if the *confocal technique* is applied (Schrader et al., 1993, 1994). A focus of a laser beam is produced by a microscope objective of large numerical aperture at the spot of the sample to be investigated (Fig. 3.5-12). The radiation emerging from this spot is projected by the objective onto a diaphragm with a hole of the size of the projected laser focus. Only the radiation passing

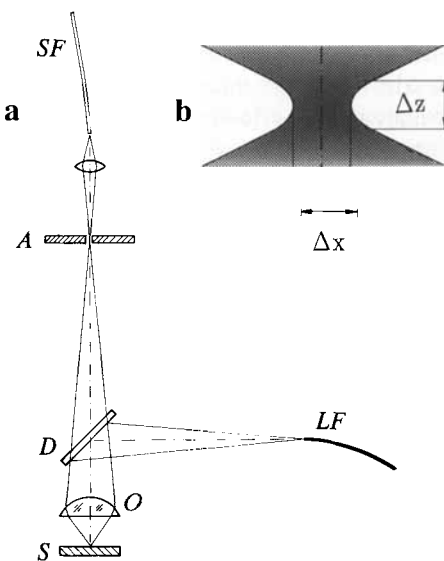


Figure 3.5-12 Principle of a confocal microscope: **a** *LF* fiber transporting the laser radiation, *D* dichroitic mirror, *O* objective, *S* sample, the Raman radiation produced in the illuminated spot of the sample is focused upon the diaphragm *A*, only the radiation from the spot is focused at the fiber *SF*, which transports the Raman radiation to the spectrometer; **b** focal range in the illuminated sample, Δx spatial, Δz depth resolution.

this diaphragm is analyzed by the spectrometer. Thus only the Raman spectrum from the spot is analyzed, the stray radiation from the surrounding is suppressed. The spatial resolution is after Abbe's equation given by $\Delta x \geq \lambda/2 NA$, the depth resolution is according to Berek's equation $\Delta z \geq \lambda/2 NA^2$.

Fig. 3.5-10 c shows another sample arrangement which makes use of a fiber-optical connection from the laser to the sample and back to the spectrometer. It is specially designed for the scanning of surface layers, e.g., of precious prints or paintings. The half spheric concave mirror reflects the portion of exciting radiation and Raman radiation back to the sample which has been scattered by the sample and is not collected by the optical fiber. Thus the mirror as a component of a multiple reflection system enhances the observed intensity of the Raman lines by a factor of 2 to 8, depending on the properties of the sample.

2 *D* mapping of a sample may be achieved with an $x - y$ drive which transports the sample at the focal region of the spectrometer or the microscope (Fig. 3.5-10 a, b; Schrader, 1990). If fiber optics is employed, the fiber head may be moved while the sample remains stationary. For each resolved sample point, a spectrum may be recorded and stored. A map showing the intensity distribution of different Raman lines illustrates the distribution of specific compounds over the surface.

The temperature of the observed spot on the sample can be monitored (by evaluation of the 'Stokes/anti-Stokes' intensity ratio, Eq. 2.4-10) without the expense of extra recording time (Schrader et al., 1990). This procedure is highly recommended if temperature sensitive samples are investigated. The sample temperature may be reduced by reducing the laser power, by placing a half sphere of sapphire upon the sample (with a drop of immersion fluid providing thermal and optical contact), or by blowing cold nitrogen gas upon the sample.

Delhaye and Dhamelincourt (1975) were the first to combine a Raman spectrometer with a microscope. Kiefer (1988) described the Raman spectroscopy of single particles of aerosols by the optical levitation technique, an approach which is even possible with a compact spectrometer (Hoffmann et al., 1992). Raman spectra recorded with NIR FT Raman microscopes have proven the value of this technique (Messerschmidt and Chase, 1989; Bergin and Shurwell, 1989; Simon and Sawatzki, 1991). Examples of micro Raman spectra obtained from different spots on certain biological samples have been published (Schrader, 1990; Puppels et al., 1991).

3.5.4 The radiant power of Raman lines

This section demonstrates how to calculate the flux (radiant power) of Raman radiation which is produced by irradiating a sample with laser radiation, analyzed by a spectrometer and recorded by a radiation detector (see Eq. 3.1-1).

Sec. 2.4, Eq. 2.4-6' shows that the differential Raman scattering cross section of a vibration of degeneracy g_k with the frequency $\tilde{\nu}_k$ of molecules in a liquid, excited by radiation with the frequency $\tilde{\nu}_0$ equals:

$$\left(\frac{d\sigma}{d\Omega} \right)_{k\perp} = \frac{h}{2^3 c \epsilon_0^2} \cdot \frac{(\tilde{\nu}_0 - \tilde{\nu}_k)^4}{\tilde{\nu}_k [1 - \exp(-hc\tilde{\nu}_k/kT)]} \cdot g_k \cdot \left(\bar{\alpha}'_k^2 + \frac{7}{45} \gamma'_k \right) \quad (3.5-12)$$

Redefining $\tilde{\nu}_0$ as the reference frequency, $\tilde{\nu}_{ref}$, and – dividing this equation by $(\tilde{\nu}_{ref} - \tilde{\nu}_k)^4$, affords the '*absolute normalized Raman scattering cross section*' (Eq. 3.5-13). It has been tabulated for several compounds by Schrötter and Klöckner, 1979. Typical values for liquids excited by radiation from an argon ion laser at 488 nm are listed in Table 3.5-1. Raman scattering cross sections of gases are discussed by Schrötter in Sec. 4.3.2.3.

Table 3.5-1 Integrated absolute normalized Raman scattering cross sections of liquids, excited with radiation of $\lambda_{ref} = 487.99$ nm $\hat{=} \tilde{\nu}_{ref} = 20487$ cm⁻¹ (Schrötter and Klöckner, 1979)

Compound	Band $\tilde{\nu}_k/\text{cm}^{-1}$	$\left(\frac{d\sigma}{d\Omega} \right)_{k\perp} \cdot (\tilde{\nu}_{ref} - \tilde{\nu}_k)^{-4} / 10^{-48} \text{cm}^6 \text{sr}^{-1}$
C ₆ H ₆	992	245
C ₆ H ₅ CH ₃	1002	127
C ₆ H ₅ NO ₂	1345	766
CS ₂	656	310
CCl ₄	459	134
CHCl ₃	666	54
CHCl ₃	762	32
C ₆ H ₁₂	802	68

$$\left(\frac{d\sigma}{d\Omega} \right)_{k\perp} \cdot (\tilde{\nu}_{ref} - \tilde{\nu}_k)^{-4} = \frac{h}{2^3 c \epsilon_0^2} \cdot \frac{g_k}{\tilde{\nu}_k [1 - \exp(-hc\tilde{\nu}_k/kT)]} \cdot \left(\bar{\alpha}'_k^2 + \frac{7}{45} \gamma'_k \right) \quad (3.5-13)$$

The term on the right-hand side of this equation represents the microscopic parameters of the sample. According to Placzek's theory (1934), this expression should be independent of the frequency of the exciting radiation. In the absence of a resonance or pre-resonance Raman effect, it would be equal for all exciting lines. The term on the left-hand side normalizes the observed Raman intensity by including the $\tilde{\nu}^4$ factor. These values have the dimension $\text{cm}^6 \cdot \text{sr}^{-1}$.

Eysel and Bertie (1988) considered the 'absolute normalized Raman scattering cross section' of the ring breathing vibration of liquid benzene at 992 cm^{-1} a standard for the measurement of relative Raman scattering cross sections of a number of compounds. When applying it as standard they made use of a 'divided spinning cell', developed by Kiefer and Topp (1974).

We will now proceed to calculate the radiant power of the totally symmetric ring stretching vibration of benzene at 992 cm^{-1} , which is excited by the radiation of a Nd:YAG-Laser at 1064 nm and analyzed by the detector of an interferometer with a Raman module.

The absolute Raman scattering cross section of this vibration is given by (Schrötter and Klöckner, 1979; Eysel and Bertie, 1988):

$$\left(\frac{d\sigma}{d\Omega} \right)_{k\perp} \cdot (\tilde{\nu}_{ref} - \tilde{\nu}_k)^{-4} = 200 \cdot 10^{-48} \text{ cm}^6 \text{ sr}^{-1} \quad (3.5-14)$$

The intensity of the observed radiation is proportional to this quantity, i.e., to the $\tilde{\nu}^4$ factor of the exciting frequency ($\tilde{\nu}_0$ and $\Delta\tilde{\nu}_k$ represent the wavenumber of the Nd:YAG laser radiation at 9398 cm^{-1} and the Raman shift of 992 cm^{-1} , respectively), and to the number of molecules per unit volume, $N_1 = 6.773 \cdot 10^{21} \text{ cm}^{-3}$. The 'Raman scattering coefficient' s of this line is thus given by:

$$s = \left(\frac{d\sigma}{d\Omega} \right)_{k\perp} \cdot (\tilde{\nu}_{ref} - \tilde{\nu}_k)^{-4} \cdot (\tilde{\nu}_0 - \tilde{\nu}_k)^4 \cdot N_1 \cdot L_n = 2.7 \cdot 10^{-8} \text{ cm}^{-1} \text{ sr} \quad (3.5-15)$$

Here, $L_n = (n_R/n_0)(n_R^2 + 2)^2(n_0^2 + 2)^2/3^4$ is the 'internal field factor', with n_0 and n_R the refractive indices of the sample at the frequencies of the exciting and the scattered radiation respectively (Nestor and Lippincott, 1973, see Eq. 2.4-7). Approximated with $n_0 \approx n_R = 1.5011$ its value is $L_n = ((n_0^2 + 2)/3)^4 = 4.04$. The radiance L_R ($\text{W cm}^{-2} \text{ sr}^{-1}$) of a Raman scattering sample is proportional to the power of the exciting radiation, divided by the cross section of the beam and multiplied with the Raman scattering coefficient and the thickness of the observed sample. Assuming that $\Phi_0 = 1 \text{ Watt}$ is the radiant power of the exciting radiation, $r = 0.05 \text{ cm}$ is the beam radius of

the exciting radiation at the sample, and $d = 0.1$ cm is the thickness of the irradiated sample whose Raman radiation is collected, then the resulting radiance is:

$$L_r = \frac{\Phi_0}{r^2 \cdot \pi} \cdot d \cdot s = 3.47 \cdot 10^{-7} \text{ Wcm}^{-2}\text{sr}^{-1} \quad (3.5-16)$$

We analyze Raman radiation with an IFS 66 Bruker interferometer with the FRA 106 Raman module. The optical conductance of an interferometer is given by Eq. 3.1-36: $G = 2\pi F_1 / R_0$. The area at the beam splitter is $F_1 = r^2\pi$, with $r = 1.75$ cm. The resolving power for the Raman line at $\tilde{\nu} = (9398 - 992) = 8406 \text{ cm}^{-1}$ and at a bandwidth of $\Delta\tilde{\nu} = 4 \text{ cm}^{-1}$ equals $R_0 = \tilde{\nu} / \Delta\tilde{\nu} = 2101$. Thus:

$$G = 2\pi^2 \cdot 1.75^2 / 2101 = 0.029 \text{ cm}^2\text{sr} \quad (3.5-17)$$

The transmission factor of the entire instrument (including interferometer and Rayleigh filter) is estimated to be $\tau = 0.1$. Finally, the radiant power of the Raman line equals:

$$\Phi_R = L_R \cdot G \cdot \tau = 1 \cdot 10^{-9} \text{ Watt} \quad (3.5-18)$$

This value is calculated for a '90° arrangement', according to a sample with a spherical surface of the sample cuvette, such as in Figs. 3.5-8 b or 3.5-8 c. If, however, a rectangular cuvette is used, as shown in Fig. 3.5-8 a, this quantity has to be divided by the square of the refractive index of benzene, $n^2 = 1.5011^2 = 2.2533$ (compare the discussion following Eq. 3.1-6). If, finally, an arrangement as in Fig. 3.5-8 d, i.e., an end-on cuvette in an '180° arrangement' is used, a much higher radiant power as that of Eq. (3.5-18) is recorded.

The calculated quantity is considerably higher as the *NEP* of a modern Ge semiconductor detector which is cooled with liquid nitrogen. Its *NEP* is about 10^{-15} W, thus even weak Raman lines may be recorded with a large signal-to-noise ratio.

This calculation, however, does not yet take into account the absorption of exciting and Raman radiation by the sample. For colorless samples, it is very low in the visible range of the spectrum, but in the NIR region it cannot be ignored.

3.5.4.1 Radiation balance of a Raman scattering sample, considering absorption by the sample or the solvent

In the region of NIR FT Raman spectroscopy, at $\tilde{\nu} = 5000 \dots 10000 \text{ cm}^{-1}$, substances with X-H bonds (X = any element) show overtones and combinations of the normal frequencies. They may have considerable intensity as demonstrated by Fig. 3.5-3 with the NIR absorption spectra of liquid H₂O, D₂O, ethanol, and cyclohexane. The linear decadic absorption coefficient a of water at a Raman shift of about 2500 cm^{-1} is of the order of 10. The transmission of a layer of $d = 1$ cm is given by:

$$\tau = \Phi / \Phi_0 = 10^{-a \cdot d} = 10^{-10} \quad (3.5-19)$$

Consequently, in order to perform quantitative analyses by NIR excited Raman spectroscopy, it is necessary to consider the absorption of the sample or the solvent.

The exciting **and** the Raman radiation may be absorbed by the sample or the solvent. The different geometrical arrangements are influenced differently.

90° arrangement:

The flux of the exciting **and** the Raman radiation is reduced, the radiance of the Raman radiation, Eq. 3.5-16, changes according to Lambert-Beer's Law:

$$L'_R = \frac{\Phi_0}{r^2 \cdot \pi} \cdot d \cdot s \cdot 10^{(-a_0 \cdot d_0)} \cdot 10^{(-a_R \cdot d_R)} \quad (3.5-20)$$

L'_R is the Raman radiance after the correction, a_0 , d_0 , a_R , and d_R stand for the linear decadic absorption coefficient and the thickness of the sample for the exciting and the Raman radiation, respectively. In case of a spherical cuvette (Schrader, 1987; Figs. 3.5-6b; 3.5-8b), d_0 and d_R are equal to the radius of the sphere and we obtain:

$$L'_R = \frac{\Phi_0}{r^2 \cdot \pi} \cdot d \cdot s \cdot 10^{(-a_0 + a_R) \cdot d} \quad (3.5-21)$$

180° arrangement:

The same equation is valid for the 180° arrangement if the cell is spherical (Fig. 3.5-8 b). A capillary cell in the 180° arrangement acts as a light pipe, due to the total reflection of the exciting and Raman radiation within the critical angle at the surfaces between the liquid and the wall or at the outer surface of the wall, depending on the respective refractive indices (Fig. 3.5-8 d). The intensity of the Raman radiation is inversely proportional to the effective cross section $r^2\pi$ of the light pipe. For small diameters, small absorption coefficients, and long cells, the intensity may thus be quite high (see last paragraph of Sec. 3.5.3.2; Schrader, et al., 1991):

$$L'_R = \frac{\Phi_0}{r^2 \cdot \pi} \cdot \frac{s}{a_0 + a_R} \cdot (1 - 10^{-(a_0 + a_R) \cdot d}) \quad (3.5-22)$$

Two different situations are possible: for a small thickness, L'_R is approximately proportional to the length of the capillary (compare the discussion concerning Fig. 3.5-4 a). If the thickness d is much larger than $1/(a_0 + a_R)$, the following value is approached:

$$L'_{R\infty} = \frac{\Phi_0}{r^2 \cdot \pi} \cdot \frac{s}{a_0 + a_R} \quad (3.5-23)$$

3.5.5 Special features of Raman spectroscopy in the NIR range

'Classical' Raman spectroscopy is based on exciting radiation in the visible region. It had been first mainly radiation of the line at 435.8 nm of the mercury plasma, after 1960 of the Ruby laser line at 694 nm, later it was the emission of the He-Ne laser at 632.8 nm, and at present that of the Ar⁺ laser at 488 or 515 nm (Fig. 2.2-2). Most samples do not normally show absorption bands in the visible region and the radiation detectors, usually photomultipliers, have a quite uniform responsivity (Sec. 3.3.3) in this range. As already pointed out, the disadvantage of classical Raman spectroscopy is its sensitivity against the fluorescence of impurities which could mask Raman spectra completely.

The situation changes dramatically, when exciting radiation from the near-infrared range is employed. The energy of the quanta at 1064 nm of the Nd:YAG laser is only 46 % of those of the 488 nm Ar⁺ laser line. This is not enough to excite fluorescence of most samples. Raman spectroscopy in the NIR region is therefore virtually immune against fluorescence due to impurities. In order to use its advantages it is necessary to be aware of possible drawbacks. In the NIR region all compounds containing X-H – bonds (X may be any element) show absorption bands due to overtones and combinations of the normal vibrations, Fig. 3.5-3. They may considerably reduce the intensity of the Raman lines and thus complicate quantitative analyses. Moreover, according to the laws of Planck and Kirchhoff, such overtones and combinations may give rise to thermal emission of the same order of magnitude as the Raman lines or which is even stronger. In addition, radiation detectors for the NIR region considerably change their spectral responsivity in the range of the Raman spectrum. Finally, there may be other sources of background which may potentially superimpose the Raman spectrum.

3.5.5.1 Influence of the characteristics of sample and spectrometer

Fig. 3.5-13 demonstrates the influence of sample and instrumental parameters on the intensities of the observed Raman lines, excited with the Nd:YAG laser at 1064 nm. The lower abscissa shows the absolute wavenumber scale, the upper abscissa represents the Raman shift. The relative intensity of Raman radiation is calculated by Eq. 3.5-9, taking into account the absorption coefficient ($a \text{ cm}^{-1}$) of water (Fig. 3.5-3) and a constant Raman scattering coefficient s (assumed to be equal to 1 cm^{-1}). The elastic scattering coefficients as parameters, $r = 0, 10, 100, 500 \text{ cm}^{-1}$, describe the properties of a liquid, a coarse, a medium, and a fine powder, respectively. The traces show the relative output voltage of a Germanium detector.

The wavenumber dependence of the intensity mainly arises from the changing absorption coefficient of water, as shown by Fig. 3.5-3. In the region of the strong absorption band associated with the first overtone of the OH stretching vibration ($2 \cdot 3400 = 6800 \text{ cm}^{-1}$ absolute, Raman shift $\approx 2500 \text{ cm}^{-1}$), the intensity is strongly reduced for all samples. If $r = 0$ (both upper curves), i.e., in the case of a liquid sample, the diagram shows that increasing the length of a capillary cell from $d = 1$ to 2 cm only increases the

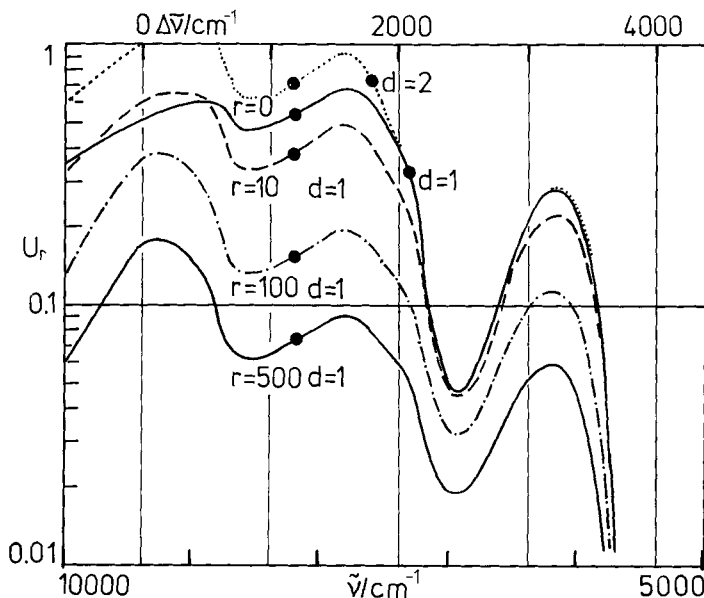


Figure 3.5-13 Influence of sample and instrument parameters on the observed intensity of a Raman line under the conditions of NIR FT Raman spectrometers. The relative output voltage of the Ge detector (cooled with liquid nitrogen) is given for a sample with the absorption spectrum of water. The upper curves, $r = 0$, represent a liquid sample with a thickness of 1 and 2 cm, respectively. The lower traces, $r = 10, 100$, and 500 , represent a coarse, medium and fine powder, respectively. Abscissa: below absolute wavenumbers, above Raman shift.

intensity in the regions of weak absorption (Raman shifts $< 1800 \text{ cm}^{-1}$). In the case of powdered samples, the coarse powder ($r = 10$) produces a higher intensity than the fine powder ($r = 500$), even in the region of the strong absorption band.

This example illustrates that measurements of absolute scattering coefficients and quantitative analyses are somewhat more difficult in NIR FT Raman spectroscopy than in the visible region, where absorption can usually be neglected. In any case, it is necessary to carefully calibrate (D'Orazio and Schrader, 1974, 1976) the spectral sensitivity of the instrument.

Thermal emission and other processes interfering with the Raman spectrum

Since hydrogen-containing samples have strong absorption bands in the NIR range, they may behave as 'gray' or even 'black' emitters, according to the combination of Planck's with Kirchhoff's law (Eq. 3.3-8). Samples which contain 'black' particles like soot or fine metal particles behave like black bodies. The particles are heated in the laser beam and emit Planck radiation, which at somewhat elevated temperatures is as strong as that of weak Raman lines.

Sec. 3.5.4 demonstrates that, by analyzing a sample of benzene in a 90° arrangement with an NIR FT Raman spectrometer, a laser power of 1 Watt produces a radiant power

of $\Phi = 1 \cdot 10^{-9}$ Watt at a Raman shift of 992 cm^{-1} . However, laser powers of 0.1 W are quite common in NIR FT Raman spectroscopy, and Raman lines with an intensity of 1/1000 of that of the benzene line (corresponding to $1 \cdot 10^{-13}$ W) should be visible in the Raman spectrum.

A black body of 480 K (207°C) sends $1 \cdot 10^{-13}$ W through the same spectrometer to the detector; at 760 K (487°C) it would be $1 \cdot 10^{-9}$ Watt.

The diagram of the Planck function, Fig. 3.3-1, demonstrates further that for smaller absolute wavenumbers there is a strong increase of the thermal emission.

Fig. 3.5-14 shows several emission curves reflecting the spectral radiance of a sample at temperatures of 0, 25, and 50°C , respectively, calculated by Eq. 3.3.8 and multiplied by the characteristics of the Germanium detector. The full lines show the Planck emission of a black body whereas the broken lines show that of water at a thickness of 1 cm. These diagrams illustrate that an increase of the sample temperature by 25°C raises the thermal emission by more than one order of magnitude! In addition, they demonstrate that in the region of the Raman spectrum between 0 and 3000 cm^{-1} , the intensity of the emission increases by 5 to 6 orders of magnitude. Only in the range of small Raman shifts, $< 2000\text{ cm}^{-1}$, the emission is not 'black'. This demonstrates the characteristic features of typical emission spectra (discussed in the next paragraph) with maximum intensity at a Raman shift of $3000 - 3300\text{ cm}^{-1}$.

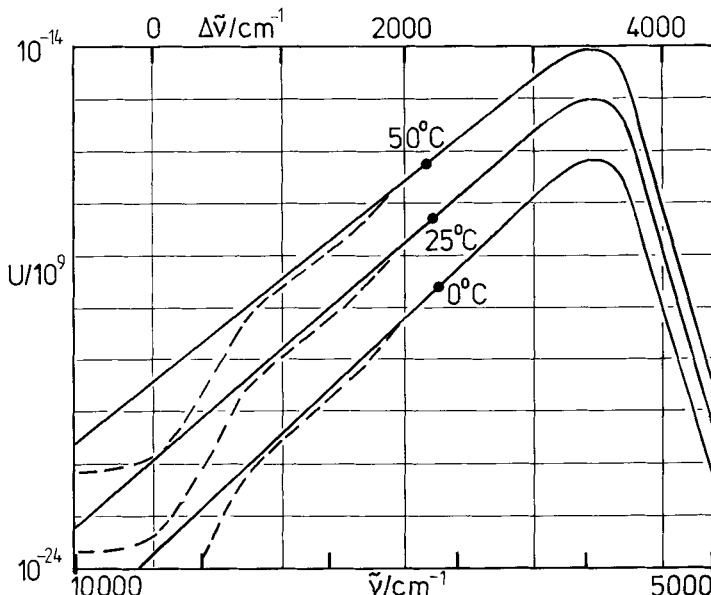


Figure 3.5-14 Thermal emission: Relative signal, recorded by a Germanium detector of a sample, thickness 1 cm, with the absorption properties of water (broken lines) and of a black body (full lines) in the range of the Raman spectrum excited with the Nd:YAG laser at 1064 nm .

A sample of black paraffinic crude oil (Fig. 3.5-15 a) gives a spectrum which is quite similar to that of a black naphthenic crude oil and to those of other similar samples. Its

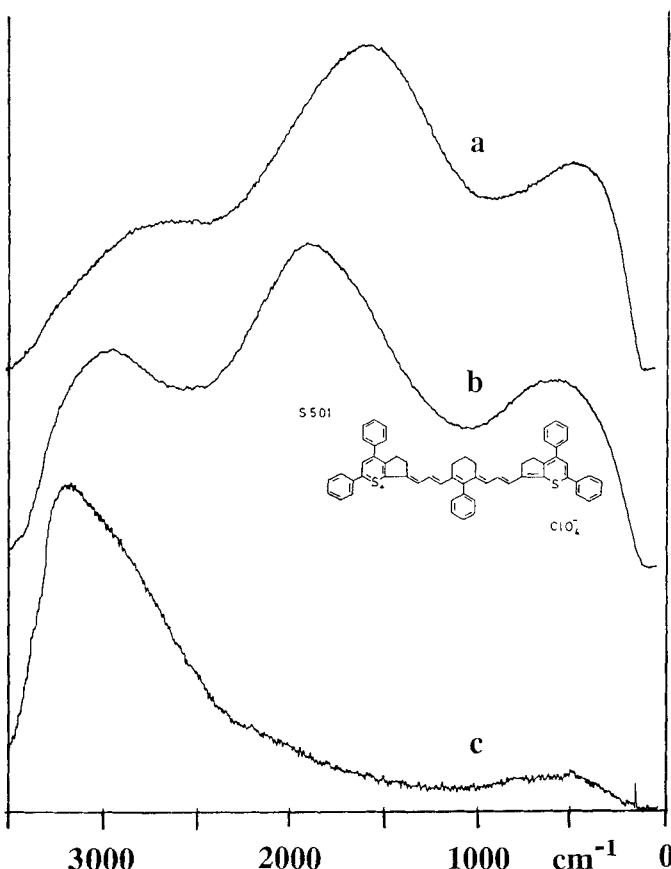


Figure 3.5-15 **a** Spectrum of a paraffinic crude oil, 20 mW, 100 scans; **b** fluorescence spectrum of a cyanine dye (Pollard et al., 1983) with absorption maximum at 1420 nm, 10 mW, 250 scans; **c** Spectrum of 0.93H-erionite at room temperature (Salzer et al., 1991).

three pronounced maxima prove that it is not the spectrum of a black body radiator as simulated in Fig. 3.5-14, which should have only one maximum at about 3100 cm^{-1} .

Large π -electron systems can absorb light quanta of low energy and, as a result, undergo transitions to excited states. During allowed transitions back to the ground state fluorescence may be emitted. π -Electron systems in species such as polycyclic aromatics with many rings and cyanine dyes may be large enough for light quanta of the Nd:YAG laser at 1064 nm to excite fluorescence. We investigated the fluorescence of a laser dye, a cyanine with an allowed absorption band at 1400 nm (Pollard et al., 1983). The spectrum is shown in Fig. 3.5-15 b. Again it shows three maxima, but at different positions and differing intensities than in Fig. 3.5-15a. Thus both spectra seem to be typical of samples that exhibit allowed fluorescence; since the quantum yield of fluorescence is larger than that of the Raman scattering, it is to be expected that the fluorescence will conceal

the Raman spectra of such samples. Since further shift of the exciting line to the infrared region seems not to be helpful or possible there is no remedy against such fluorescence.

Some other samples show a strong background even when the probability of the presence of a large π -electron system is very low. An example is given by ion exchangers in the H form and by certain types of zeolite, such as erionite (Salzer et al., 1991). Its spectrum is shown in Fig. 3.5-15 c. This is another example of compounds which are known to show continuous background in the Raman spectrum, but which however cannot be explained in terms of fluorescence. Pilz and Kriegsmann (1987) investigated this behavior. They found that this continuum has an intensity distribution of typical Stokes and anti-Stokes branches and also shows the $\tilde{\nu}^4$ dependence which is well known for Raman scattering. They assigned the continuum to stretching vibrations of strongly hydrogen-bonded OH groups exhibiting 'superpolarizability'. They found this for spectra of chalcedony and zeolite type silicates. The background appears after the ion exchange from the alkali type to the H type. This phenomenon was already observed in infrared spectra by Zundel et al. (1962, 1989). This effect is not an artifact, which may be overcome by changing experimental conditions; it is an expected property of the sample.

Fig. 3.5-16 demonstrates another typical case. Here experimental conditions change the spectrum. Fig. 3.5-16 a, excited with an unfocused laser beam of 100 mW, shows a weak Raman spectrum superimposed on a background. When the laser power is increased, Fig. 3.5-16 b, the intensity of the Raman lines increase, the background is much stronger and a very strong maximum at about 3100 cm^{-1} appears. Finally, as illustrated in Fig. 3.5-16 c, with a focused laser beam, that even with lower power produces a

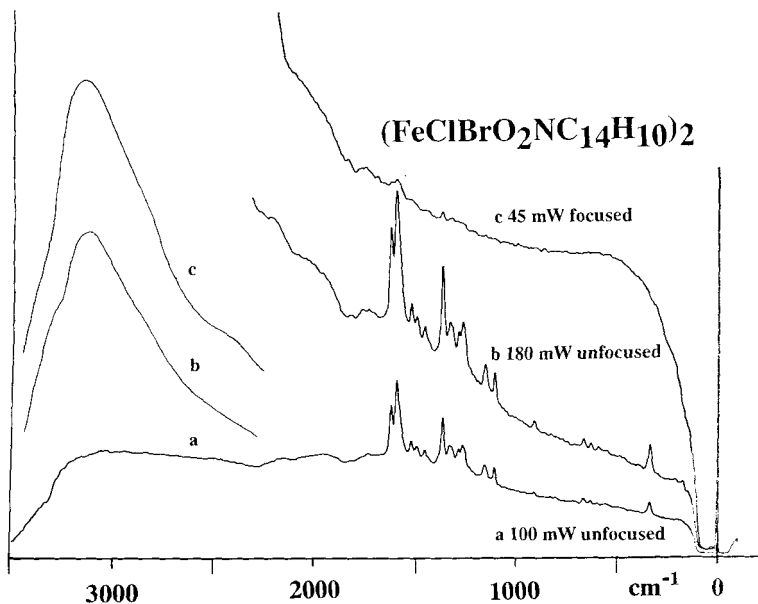


Figure 3.5-16 Spectrum of an organic iron complex, 100 scans, 8 cm^{-1} , **a** exciting radiation 100 mW, unfocused; **b** 180 mW, unfocused; **c** 45 mW, focused, for **b** and **c** the intensity of the range above 2200 cm^{-1} is reduced to 1/3 (Sawatzki, unpublished).

much larger sample irradiance, the Raman lines are nearly completely covered by a strong background. Apparently, this is an example of a competition between the emission of Raman scattering and thermal Planck-Kirchhoff emission. The behavior of this organic iron complex seems to be a typical process for certain compounds containing transition metals.

Mortensen et al. (1991) have described that traces of iron produce a heavy continuous background in the NIR region, whereas in the visible region the same samples give Raman spectra with low background. Many samples containing traces of transition metals exhibit broad background. Iron is an ubiquitous impurity in most laboratory glassware. This means that the background observed on a Raman spectrum *may* be a property of the cuvette material rather than one of the sample.

As a result, cuvettes for Raman spectroscopy should be carefully selected. They may, due to their impurities, add a background to the spectrum of the sample. In addition, all cuvette materials produce their own Raman spectra, which have to be considered, when the Raman spectra of the sample are evaluated. Fig. 3.5-17 a shows a Raman spectrum of a typical optical glass BK7, Fig. 3.5-17 b that of quartz glass suprasil, and Fig. 3.5-17 c of sapphire. Suprasil is a synthetic quartz which does not normally contain impurities. Therefore, Suprasil 'of ESR quality' is highly recommended as Raman cuvette material. Also, sapphire is a good cuvette material, as it is very hard, inert, has a good thermal conductance, and shows only weak but sharp Raman lines (Porto and Krishnan, 1967). It is used for the production of the 'universal Raman cell' (Schrader, 1987). The sharp Raman lines of sapphire observed in the spectra of the sample may be subtracted from the spectrum or used as internal standard for quantitative analyses (Mattioli et al., 1991).

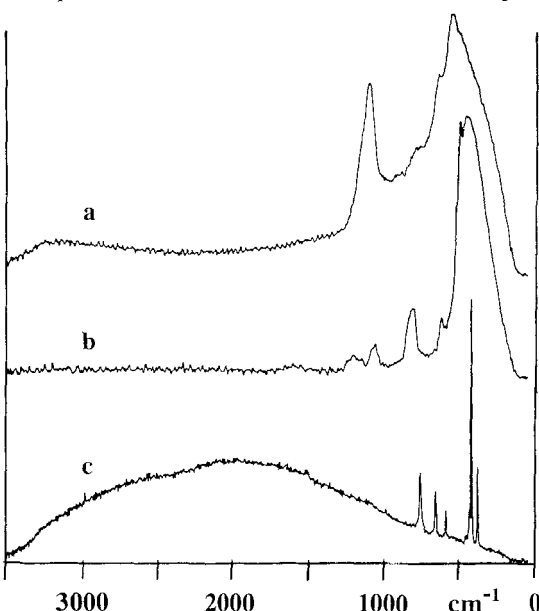


Figure 3.5-17 Raman spectra of: **a** optical glass BK7; **b** quartz glass suprasil; **c** sapphire (with traces of chromium).

However, sapphire may contain chromium as an impurity (from earlier production of ruby laser material at the same place). The sapphire spectrum in Fig. 3.5-17c shows such a continuum; it is not displayed by extremely pure sapphire. Sapphire which is contaminated with chromium shows – when irradiated by the radiation of an argon ion laser at 488 or 515 nm – the typical ruby lines at 694 nm.

3.5.5.2 Conclusions concerning optimization of NIR Raman spectroscopy

The following rules may be regarded as a guideline to optimize Raman spectroscopy in the NIR using interferometers (Schrader et al., 1991).

- With any sample, recording should begin with low laser power. While observing the interferogram and the resulting spectra, fine adjustment of the sample is possible. The laser power may then be increased until the maximum intensity of the Raman spectrum is reached, while no thermal emission (as in Fig. 3.5-16 c) is visible.
- A solid compact sample or a tablet produced from powder may be placed directly in the sample holder. The spectrum is often improved by irradiating a fine hole within the sample with the laser beam and by analyzing the Raman radiation emerging from the hole. The multiple reflection of exciting and Raman radiation inside the hole enhances the efficiency of the transformation of laser radiation into Raman scattered radiation.
- If only a small amount of solid sample is available, it should be placed in the center of a sapphire or suprasil sphere coated with a reflecting layer at those parts of the surface which is not used for illumination of the sample or for observing the Raman radiation (Schrader, 1987) but which have an antireflection coating at these parts.
- If a liquid is to be investigated and enough sample is available, the best arrangement is a capillary cell in a 180° geometry. For a limited amount of liquid, it is recommended to use a sapphire sphere, prepared according to the preceding paragraph and to place the sample in the center.
- Single crystals may be mounted on a goniometer head. Depending on the problem, 90° or 180° arrangements may be used.
- Polarizers may be employed to measure the scattering tensor of crystals or the depolarization factor of liquids (Hoffmann et al., 1991).

When a strong background is observed, there are several ways of reducing it:

- Absorbing particles may be removed by filtration through a Millipore Filter.
- Cooling the sample (by blowing cold nitrogen gas over it) reduces thermal emission.
- The Raman/Planck emission ratio may be enhanced by irradiating the sample with pulsed laser radiation, but only during the active recording phase of the interferometer (Cutler and Petty, 1991).
- Real fluorescence of impurities may be reduced by filtration of the liquid sample or a solution over charcoal or aluminum oxide.
- Background emission caused by transition metals in the cuvette material is eliminated by employing cuvettes made of suprasil.
- If these procedures do not help, the background emission may be a typical property of the sample which cannot be altered.

The quality of the spectra can be improved further by the following procedures:

- It is advisable to periodically calibrate the sensitivity of the spectrometer by measuring the spectrum of a Planck source. For this purpose, an iodine-quartz lamp may be used to irradiate a white email as a secondary standard (D'Orazio and Schrader, 1976). Further, the laser power should be monitored periodically.
- The sample temperature may be controlled by measuring the *Stokes/anti-Stokes* intensity ratio of Raman scattered radiation (Schrader et al., 1990), Eq. 2.4-10. This is of importance when temperature-sensitive samples or phase transitions are investigated.
- The water content of the atmosphere may give rise to sharp absorption lines, overtones of the IR absorption bands, in the region of a Raman shift of $2000 - 2700 \text{ cm}^{-1}$ (for excitation by a Nd:YAG laser). Such absorptions can be removed by purging the instrument with dry air.
- Since NIR laser radiation is invisible, it is advisable – while wearing safety glasses – to employ an infrared night vision instrument with a macro lens for the fine-adjustment of the sample.

3.6 Nonlinear Raman spectroscopy*

The introduction of lasers into Raman spectroscopy has stimulated this traditional field of molecular spectroscopy in various aspects. In conventional Raman spectroscopy a renaissance began by simply replacing the light source. Many new techniques, specially adapted to the coherent emission of the new Raman excitation source, were developed which permit the molecular spectroscopist to record Raman spectra of a great variety of compounds, from deeply coloured or even black materials, to highly fluorescent molecules. Parallel to these achievements there has been a rapid development of fundamentally new methods. These are based on the contributions of the nonlinear part of the induced dipole moment (spontaneous effects) or the induced polarization (coherent effects) to the intensity of the frequency shifted light. In the first case, the Raman signal is generated in a spontaneous, incoherent but nonlinear optical process, whereas in the second case the Raman information is contained in a coherent laser beam whereby the nonlinear polarization acts as a coherent light source.

In this section we first give a survey on the most common nonlinear Raman processes, i. e. the (incoherent) hyper Raman scattering and several forms of coherent nonlinear Raman scattering. We then describe the instrumentation needed to perform several practical kinds of these nonlinear laser spectroscopies. Applications of nonlinear Raman spectroscopy will be found in Sec. 6.1.

* Section 3.6 is contributed by W. Kiefer, Würzburg

3.6.1 Nonlinear Raman processes

3.6.1.1 Spontaneous scattering: hyper Raman effect

Let us first briefly discuss spontaneous nonlinear Raman spectroscopy on an isolated single molecule. Generally the induced dipole moment \vec{p} in a molecular system is written in the form

$$\vec{p} = \alpha \vec{E} + \frac{1}{2} \beta \vec{E} \vec{E} + \frac{1}{6} \gamma \vec{E} \vec{E} \vec{E} + \dots \quad (3.6-1)$$

where α is the polarizability, β the hyperpolarizability and γ the second hyperpolarizability. The α , β , γ , etc. are tensors of rank 2, 3, 4, etc., respectively. \vec{E} is the electric field, $\vec{E} \vec{E}$ is the dyadic product of two electric fields, etc. The nonlinear terms in Eq. (3.6-1) are usually small compared to the linear term which gives rise to normal, linear Raman scattering. However, when the electric field is sufficiently large, as is the case when for instance a Q-switched laser is focused on the sample, contributions from the second term in Eq. (3.6-1) are sufficiently intense to be detected. This scattering is at an angular frequency $2\omega_L \pm \omega_R$, where ω_L is the angular frequency of the exciting laser beam and $-\omega_R$ and $+\omega_R$ are the Stokes and anti-Stokes hyper Raman displacements, respectively. Also scattering at angular frequency $2\omega_L$ may occur, depending on the symmetry of the molecule. Scattering at angular frequencies $2\omega_L$ and $2\omega_L \pm \omega_R$ is called hyper Rayleigh and hyper Raman scattering, respectively.

The hyper Raman effect is a three-photon process involving two virtual states of the scattering system. The level scheme for hyper Rayleigh and hyper Raman scattering is presented in Fig. 3.6-1. Two laser photons of angular frequency ω_L are simultaneously scattered to give a photon at angular frequency $2\omega_L$ (hyper Rayleigh), at angular frequency $2\omega_L - \omega_R$ (Stokes hyper Raman) or $2\omega_L + \omega_R$ (anti-Stokes hyper Raman) when a molecular vibration (or rotation) is excited or destroyed, respectively. Thus, hyper Raman lines are found in the spectral neighbourhood of the second harmonic ($2\omega_L$) of the incident laser radiation. It should be mentioned, that Rayleigh scattering always occurs, but hyper Rayleigh scattering occurs only if the scattering material does not have a center of symmetry. Frequency doubled radiation consists of hyper Rayleigh scattering from a pure crystal and consequently a crystal used for frequency doubling must not have a centro symmetric unit cell.

The importance of the hyper Raman effect as a spectroscopic tool results from its symmetry selection rules. These are determined by products of three dipole moment matrix elements relating the four levels indicated in Fig. 3.6-1. It turns out that all infrared active modes of the scattering system are also hyper-Raman active. In addition, the hyper Raman effect allows the observation of “silent” modes, which are accessible neither by infrared nor by linear Raman spectroscopy. Hyper Raman spectra have been observed for the gaseous, liquid and solid state. A full description of theory and practice of hyper-Raman spectroscopy is given by Long (1977, 1982).

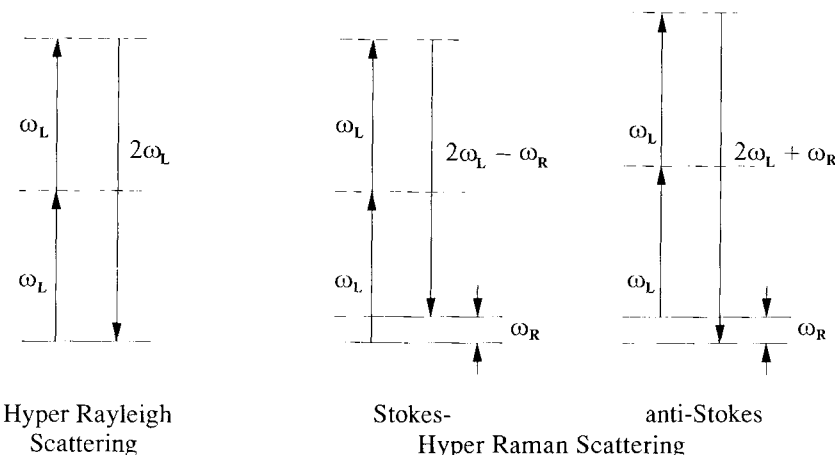


Figure 3.6-1 Schematic level diagram for hyper Rayleigh and hyper Raman scattering.

3.6.1.2 Stimulated Raman effect

The stimulated Raman process is schematically represented in Fig. 3.6-2. A light wave at frequency ω_S is incident on the material system simultaneously with a light wave at angular frequency ω_L . While the incident light beam loses a quantum ($\hbar\omega_L$) and the material system is excited by a quantum $\hbar\omega_R = \hbar(\omega_L - \omega_S)$, a quantum $\hbar\omega_S$ is added to the wave at frequency ω_S , which consequently becomes amplified.

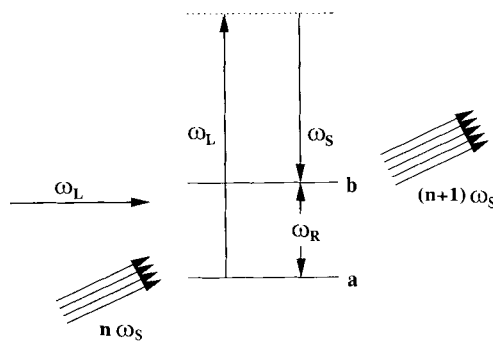


Figure 3.6-2 Schematic diagram for stimulated Raman scattering as a quantum process.

A theoretical description of the stimulated Raman effect in terms of a nonlinear Raman susceptibility was presented by Bloembergen (1963) soon after the experimental discovery of this effect. He showed that a polarization at Stokes angular frequency ω_S is generated via the third-order nonlinear susceptibility $\chi^{(3)}$. Including a degeneracy factor, (see Sec. 3.6.1.3) the polarization oscillating at angular frequency ω_S is given by (Berger et al., 1992):

$$\vec{P}^{(3)}(\omega_S) = \frac{6}{4} \varepsilon_0 \chi^{(3)}(-\omega_S; \omega_L, -\omega_L, \omega_S) |\vec{E}(\omega_L)|^2 \vec{E}(\omega_S) \quad (3.6-2)$$

For the case that the pump angular frequency ω_L and the Stokes angular frequency ω_S differ by a molecular angular eigenfrequency ω_R , i. e. $\omega_L - \omega_S = \omega_R$, the third-order nonlinear susceptibility has a negative imaginary part. This leads to a negative absorption coefficient or an exponential gain at the Stokes frequency ω_S proportional to the laser intensity at pump frequency ω_L (Bloembergen, 1978). The gain factor g , which describes this exponential growth, has been shown to depend on the differential Raman cross section $d\sigma/d\Omega$ as well as on the linewidth Γ of the molecular transition (ω_R) in the following way (Bloembergen, 1967)

$$g(\omega_S) \propto \left(\frac{d\sigma}{d\Omega} \right) \frac{\Gamma}{(\omega_L - \omega_S - \omega_R)^2 + \Gamma^2} \quad (3.6-3)$$

Optimum gain is found at the centre of the Raman line where $\omega_R = \omega_L - \omega_S$. There, the gain constant for stimulated Raman scattering at Stokes frequency is given by

$$g_s \propto \left(\frac{d\sigma}{d\Omega} \right) \cdot \frac{1}{\Gamma} \quad (3.6-4)$$

From Eq. (3.6-4) we immediately recognize that in stimulated Raman scattering processes where only *one* input laser field with frequency ω_L is employed, a coherent Stokes wave is generated for those Raman modes which have the highest ratio between differential Raman cross section and linewidth Γ . The latter corresponds to the dephasing time T_2 of the physical system, $\Gamma = 1/T_2$, and reflects the damping of the system.

In this classical description of stimulated Raman scattering a coherent light beam at Stokes angular frequency ω_S is produced by a pump field at $\omega_L = \omega_S + \omega_R$. The distinctive feature of stimulated Raman scattering is that an assemblage of coherently driven molecular vibrations provides the means of coupling the two light waves at angular frequency ω_L and ω_S by modulating the nonlinear susceptibility.

From the fact that the Stokes beam interacting with the pump laser beam automatically establishes correct phasing of the molecular oscillators so as to ensure propagation of the Stokes beam, it follows that Raman gain is possible for any direction of propagation of the Stokes beam with respect to the pump beam. However, the greatest Stokes intensity should be observed from a Raman cell along the direction of its greatest illuminated length, unless some other considerations are introduced.

In the ordinary Raman effect, few molecules are found in their excited vibrational state. The strong pumping action of a laser beam changes this situation drastically, so that an appreciable fraction of all molecules in the laser beam are soon made available for anti-Stokes emission. Classically, the anti-Stokes radiation is generated by the interaction of the laser beam with molecular vibrations, but the phase of the latter is established by the still more intense Stokes radiation. As a consequence, an index-matching requirement

exists for this three-wave process. The direction of emission of the anti-Stokes intensity is given by the momentum matching condition (Bloembergen, 1967)

$$\vec{k}_{AS} = 2\vec{k}_L - \vec{k}_S \quad (3.6-5)$$

Since in condensed phases there is dispersion of the linear index of refraction, $n = n(\omega)$ and because

$$|\vec{k}| = \frac{n(\omega) \cdot \omega}{c} \quad (3.6-6)$$

one immediately recognizes that a collinear arrangement between pump, Stokes and anti-Stokes beams is not possible. However, a direction can be found which satisfies the vector equation 3.6-5, but it confines the S and AS photon pairs to conical beams coaxial with the laser beam. Fig. 3.6-3 shows the required construction, the cones being generated by rotating the plane of the figure around \vec{k}_L .

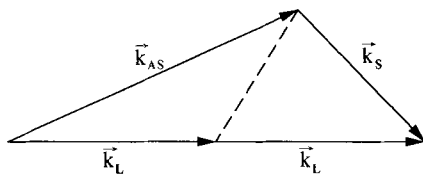


Figure 3.6-3 Momentum conservation for stimulated anti-Stokes Raman scattering (Representation of Eq. 3.6-5).

Similarly to the generation of coherent fundamental Stokes and anti-Stokes radiation, higher-order stimulated Stokes and anti-Stokes emission can be produced when high pump intensities are employed.

3.6.1.3 Nonlinear Raman spectroscopies based on third-order susceptibilities

From the foregoing short discussion on stimulated Raman scattering it became clear that during this nonlinear process coherently driven molecular vibrations are generated and that there is strong coupling between the mechanical waves and the light waves when the frequency difference between pump and Stokes beam matches the molecular vibrational frequency. In what usually is named as stimulated Raman effect only one input laser field (ω_L) is used for this type of excitation. We have seen in Sec. 3.6.1.2 that only particular Raman modes, i. e. those with highest gain factors, give rise to stimulated Stokes emission. Thus, for molecular spectroscopy in which the interest dominates to determine *all* Raman active modes, excitation with one strong laser field would not serve the purpose, although it would provide very high signals in the form of a coherent beam, but unfortunately, only at one particular vibrational frequency. However, the advantages of stimulated Raman scattering, being high signal strength and coherent

radiation, can be fully exploited by a very simple modification of the type of excitation. The trick is simply to provide the molecular system with an intense external Stokes field by using a second laser beam at Stokes frequency ω_S instead of having initially the Stokes field produced in the molecular system by conversion of energy from the pump field. Thus, by keeping one of the two lasers, e. g. the laser with angular frequency ω_L , fixed in frequency and the other one, e. g. the laser beam at Stokes angular frequency ω_S tunable, one is now able to excite selectively coherent molecular vibrations at any desired angular frequency ω_R . A variety of Raman techniques based on this idea has been developed, which combine the wide spectroscopic potentials of spontaneous Raman spectroscopy and the high efficiency of scattering, strong excitation and phasing of molecular vibrations in a macroscopic volume of substance, that is, as already emphasized, the features inherent in stimulated Raman scattering. Certainly, progress in these techniques was connected mainly with the achievements in the development of tunable lasers. The following acronyms of some of these nonlinear (coherent) Raman techniques have been widely used (Harvey, 1981; Kiefer and Long, 1982): CARS (Coherent anti-Stokes Raman Spectroscopy), CSRS (Coherent Stokes Raman Spectroscopy), PARS (Photoacoustic Raman Spectroscopy), RIKE (Raman Induced Kerr Effect), SRGS (Stimulated Raman Gain Spectroscopy), IRS (Inverse Raman Scattering), ASTERISK (a four colour technique, so named because of the arrangement of the planes of polarization in the experiment), HORSES (Higher-Order Raman Spectral Excitation Studies) and IDSRS (Ionization Detected Stimulated Raman Spectroscopy). The basic principles of some of these techniques will be discussed next under a common point of view.

A schematic diagram for some of the methods mentioned above is illustrated in Fig. 3.6-4. The common physical aspect is the excitation of Raman-active molecular vibrations (or rotations) in the field of two laser beams with angular frequencies ω_L and ω_S in such a way that their difference corresponds to the angular frequency of the molecular vibration ω_R ($\omega_L - \omega_S = \omega_R$). The strong coupling between the generated coherent molecular vibrations with the input laser fields via the third-order nonlinear susceptibility opens the possibility for the various techniques. As mentioned in Sec. 3.6.1.2 an anti-Stokes signal at angular frequency $\omega_{AS} = \omega_L + \omega_R = 2\omega_L - \omega_S$ is generated when the momentum matching condition (Eq. 3.6-5, Fig. 3.6-3) is fulfilled. However, in contrast to stimulated Raman scattering where the coherent signal is generated with only one input laser beam (ω_L), the anti-Stokes intensity is not scattered into a cone as described above. Instead, it is scattered in one direction, which lies in the plane given by the two laser beam directions \vec{k}_L and \vec{k}_S and which is determined by the momentum vector diagram shown in Fig. 3.6-3. Therefore, this so-called CARS spectroscopy is simply performed by measuring the signal $S(2\omega_L - \omega_S) = S(\omega_L + \omega_R)$, which is a coherent beam emitted into a certain direction. These coherent signals with anti-Stokes frequencies are generated each time the frequency difference of the input laser fields matches the molecular frequency of a Raman active transition.

The mixing of the two laser fields can also produce radiation on the Stokes side of the ω_S -laser. The direction of this Coherent Stokes Raman Scattering (CSRS) signal is again determined by a corresponding momentum conservation diagram, which leads to a different direction (see Fig. 3.6-4), labelled by $S(2\omega_S - \omega_L)$. From the symmetry of these two generated coherent beams, there seems to be no reason to favour the CSRS or

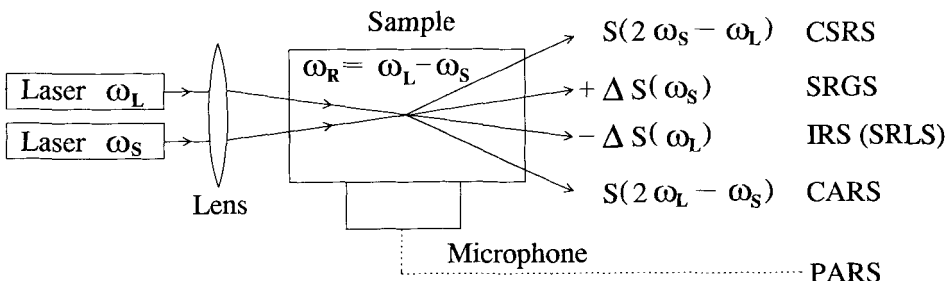


Figure 3.6-4 Schematic diagram for a few techniques in nonlinear (coherent) Raman spectroscopy (CSRS: Coherent Stokes Raman Spectroscopy; SRGS: Stimulated Raman Gain Spectroscopy; IRS: Inverse Raman Spectroscopy (= SRLS: Stimulated Raman Loss Spectroscopy); CARS: Coherent anti-Stokes Raman Spectroscopy; PARS: Photoacoustic Raman Spectroscopy).

CARS technique but, since $2\omega_S - \omega_L = \omega_S - \omega_R$ is too low wavenumber of both ω_L and ω_S there is strong tendency for CSRS to be overlapped by fluorescence. Furthermore, the CSRS signal is in principle weaker than the CARS signal. For these reasons the CARS technique is more frequently used.

The interaction of the electric fields of the two input laser beams with angular frequencies ω_L and ω_S with the electric field associated with the coherent molecular vibrations can yield also a gain or a loss in the power of the laser beams. The method where the gain at the Stokes frequency (labelled in Fig. 3.6-4 by $+ \Delta S(\omega_S)$) is measured is generally referred to as “Stimulated Raman Gain Spectroscopy” whereas the “Inverse Raman Scattering” is the terminology commonly used to designate the induced loss at the pump laser frequency (Fig. 3.6-4, $- \Delta S(\omega_L)$). IRS is also often called Stimulated Raman Loss Spectroscopy (SRLS).

From an experimental point of view, it is quite evident that for the four nonlinear coherent Raman techniques discussed until now, one either measures the radiation generated at anti-Stokes frequency (CARS, $\omega_{AS} = 2\omega_L - \omega_S$) or at Stokes frequency (CSRS, $2\omega_S - \omega_L$) or one determines the change ΔS in the laser beam power (ω_L : IRS; ω_S : SRGS). In order to get full Raman information of the medium, it is necessary to tune the frequency difference $\omega_L - \omega_S$; then, successively all Raman-active vibrations (or rotations, or rotation-vibrations) will be excited and a complete nonlinear Raman spectrum is then obtained.

In Photoacoustic Raman Spectroscopy (PARS) the sample is illuminated again by the two laser beams ω_L and ω_R the same way as shown in Fig. 3.6-4, i.e. with spatial and temporal overlapping. Due to the stimulated Raman effect, a population of a particular energy level (ω_R) of the sample is achieved. As the vibrationally excited molecules relax by means of collisions, a pressure wave is generated in the sample and this acoustic signal is detected by a sensitive microphone. In the PARS technique one usually modulates either one or both of the laser beams. When frequency matching is achieved ($\omega_R = \omega_L - \omega_S$) pressure variations are generated in the sample and an acoustic signal at the laser modulation frequency is detected. Again, by tuning one of the two laser frequencies one can obtain complete Raman information from the sample.

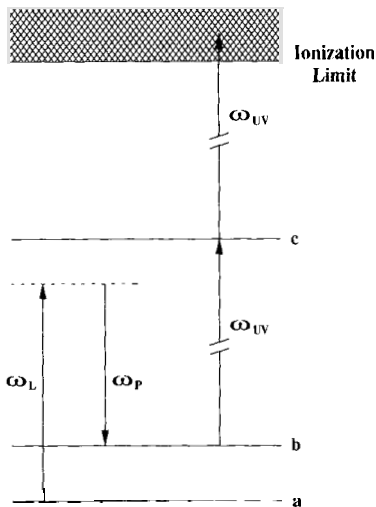


Figure 3.6-5 Energy-level diagram illustrating the two excitation steps of Ionization Detected Stimulated Raman Spectroscopy (IDSRS).

Esherick and Owyong (1983) have developed a double resonance method called Ionization Detected Stimulated Raman Spectroscopy (IDSRS). This technique combines the high sensitivity of resonant laser ionization methods with the advantages of stimulated Raman spectroscopy, e. g. the high spectral resolution. IDSRS is closely related to IR-UV double resonance ionization methods (Esherick and Anderson, 1980; Anderson and Esherick, 1980). The excitation process, illustrated in Fig. 3.6-5, can be briefly described as a two-step photoexcitation process followed by ion/electron detection. In the first step two intense narrow-band lasers (ω_L, ω_P) are used to pump a molecule from its ground state (a) to a vibrationally excited level (b) via the stimulated Raman process. The vibrationally excited molecules are then selectively ionized in a second step via a two-photon process by a UV laser tuned to be resonant with an electronic state (c) in the molecule. The technique allows an increase in sensitivity of over three orders of magnitude because ions can be detected with higher sensitivity than photons (see Sec. 3.6.2.5).

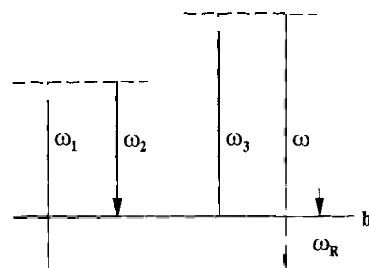


Figure 3.6-6 Schematic diagram representing the four-wave mixing process: a polarization is generated at

The nonlinear Raman techniques discussed above are special cases of a general four-wave mixing process, which is schematically illustrated in Fig. 3.6-6. Here, three independent fields with angular frequencies ω_1 , ω_2 , and ω_3 may be incident upon the matter. A fourth field, which is phase coherent relative to the input fields, is then generated at angular frequency $\omega = \omega_1 - \omega_2 + \omega_3$. When the angular frequency difference $\omega_1 - \omega_2$ equals the Raman excitation angular frequency ω_R , the signal wave at ω is enhanced, indicating a Raman resonance. Since this is a driven excitation, the coherent nature of the process results in a generated field which propagates in a specific direction with a wave vector \vec{k} defined by the vector relation

$$\vec{k} = \vec{k}_1 - \vec{k}_2 + \vec{k}_3 \quad (3.6-7)$$

As an example, the special phase matching condition for the stimulated Raman effect or the one for CARS (Eq. 3.6-5) is contained in Eq. 3.6-7 ($\vec{k}_1 = \vec{k}_3 = \vec{k}_L$ and $\vec{k}_2 = \vec{k}_S$). The phase matching condition is a consequence of the coherent generation of the signal field and dispersion in the linear refractive index of the matter. When the latter is significant (as in condensed media), it is required that the input fields overlap at the specific angle which satisfies Eq. 3.6-7. This overlap condition is illustrated in Fig. 3.6-7 for the general case of coherent Raman processes.

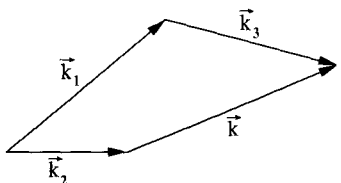


Figure 3.6-7 Phase matching condition for the general case of coherent Raman processes.

Although this phase matching condition can be bothersome and leads to loss of signal if not fulfilled, it has the advantage that all of the generated signal can be easily collected. Discrimination against fluorescence is thus much better achieved than in spontaneous (conventional) Raman spectroscopy. Another major advantage of the nonlinear coherent Raman techniques over conventional Raman spectroscopy is the ability to obtain Raman spectra with very high resolution which is solely determined by the line width of the input sources. The experimental requirements for high resolution measurements utilizing these techniques preclude the necessity of using monochromators, interferometers, or other apparatus usually used in conventional Raman spectroscopy. Since precisely controlled, tunable, narrow-line-width laser sources with appreciable power are available commercially, high resolution molecular spectroscopy, which for quite a long time was only possible by infrared absorption, has become feasible also in the visible region through these nonlinear techniques.

Similarly to the phase matching condition, also the induced third-order polarization can be written in a general form for all the nonlinear coherent Raman processes discussed above. The induced polarization which radiates a signal field of angular frequency $\omega = \omega_1 - \omega_2 + \omega_3$ is given by (Berger et al., 1992):

$$\vec{P}^{(3)}(\omega) = \frac{D}{4} \varepsilon_0 \chi^{(3)}(-\omega; \omega_1, -\omega_2, \omega_3) \vec{E}(\omega_1) \vec{E}^*(\omega_2) \vec{E}(\omega_3), \quad (3.6-8)$$

where D is a frequency degeneracy factor and hence depends on the specific process.

As examples, the nonlinear polarization which is the source term for the observed signal generated in the overlap of the incident laser beams (with e.g. parallel polarizations) becomes for CARS ($\omega = \omega_{AS}$; $\omega_1 = \omega_L$; $\omega_2 = \omega_S$; $\omega_3 = \omega_L$):

$$\vec{P}_{CARS}^{(3)}(\omega_{AS}) = \frac{3}{4} \varepsilon_0 \chi^{(3)}(-\omega_{AS}; \omega_L, -\omega_S, \omega_L) \vec{E}(\omega_L) \vec{E}^*(\omega_S) \vec{E}(\omega_L), \quad (3.6-9)$$

or for stimulated Raman gain spectroscopy:

$$\vec{P}_{SRGS}^{(3)}(\omega_S) = \frac{6}{4} \varepsilon_0 \chi^{(3)}(-\omega_S; \omega_L, -\omega_L, \omega_S) \vec{E}(\omega_L) \vec{E}^*(\omega_L) \vec{E}(\omega_S), \quad (3.6-10)$$

which is the same as Eq. 3.6-2. For the other processes and for details we refer to Berger et al., 1992.

Explicit expressions for the nonlinear susceptibilities have been derived from a quantum mechanical treatment (Flytzanis, 1975; Yuratich and Hanna, 1977; Yuratich et al., 1979; Eesley, 1981; Prior, 1984). It is certainly beyond the scope of this section to discuss this here. We solely refer here to the detailed treatment.

Finally, we mention that also the equations describing the intensities of the observed signal of the various methods have been derived in detail (Maker and Terhune, 1965; Yuratich and Hanna, 1977; Yuratich et al., 1979; Nibler and Pubanz, 1988). Since CARS is the mostly applied nonlinear Raman technique we give in the following the equation for the intensity I_{AS} (W m^{-2}) of the generated anti-Stokes radiation. Following the treatment of Nibler and Pubanz (1988) and likewise the notation of Maker and Terhune (1965) one arrives at the expression for the intensity of the CARS signal:

$$I_{AS} = \frac{\omega_{AS}^2}{n_L^2 n_S n_{AS} \varepsilon_0^2 c^4} |\chi_{CARS}^{(3)}|^2 I_L^2 I_S L^2 \operatorname{sinc}^2\left(\frac{\Delta k L}{2}\right) \quad (3.6-11)$$

where n_i is the refractive index at angular frequency ω_i , I_L and I_S are the intensities of the incident pump and Stokes laser beams, respectively, L is the length over which the beams are mixed through the sample (interaction length) and the Δk is the wave vector mismatch, i.e. $\Delta k = |2k_L - k_S - k_{AS}|$. Δk is a direct result of the fact that the propagating waves move in and out of phase because of dispersion in the sample. The dependence of I_{AS} on the square of the CARS susceptibility is characteristic of parametric processes. $\chi_{CARS}^{(3)}$ can be directly related to the differential Raman cross section $d\sigma/d\Omega$ as well as to the number density N (Yuratich and Hanna, 1977). We finally note that the phase matching factor in the CARS intensity, i.e. the $\operatorname{sinc}(x) = \sin(x)/x$ function, is essentially unity under most experimental conditions, which are usually chosen such that $\Delta k = 0$ for maximum signal.

3.6.2 Instrumentation for nonlinear Raman spectroscopy

3.6.2.1 Hyper Raman spectroscopy

Hyper Raman scattering signals are typically five to seven orders of magnitude weaker than those of linear Raman scattering. Larger hyper Raman signals are observed under resonant conditions (Washington et al., 1977; Ziegler and Roebber, 1987) and in surface-enhanced hyper Raman scattering (Murphy et al., 1982; Golab et al., 1988; Nie et al., 1990).

Since hyper Raman scattering is an incoherent process which does not require phase matching, it is preferentially observed at an angle of 90° from the incident laser direction. As for any spontaneous phenomenon, a double monochromator is used in most cases. Initial hyper Raman spectra were generated with a Q-switched ruby laser operating at approx. 1 Hz (Terhune et al., 1965) and detected with a synchronously gated photomultiplier tube and subsequently with optical multichannel detection (Verdieck et al., 1970; Savage and Maker, 1971; French and Long, 1975). The use of cw pumped acousto-optically Q-switched Nd:YAG lasers (repetition rates of 5 kHz), synchronously gated photomultiplier tubes (Vogt, 1976; Schmid and Schröter, 1977), and synchronously gated two-dimensional single-photon counting detectors (Vogt, 1987; Acker et al., 1989) has improved the signal-to-noise ratio of hyper Raman spectra. Considerable further improvements have been obtained with mode-locked pulses (at 82 MHz) from a Nd:YAG laser to observe the surface-enhanced hyper Raman signal from pyridine adsorbed on silver (Golab et al., 1988). In these studies hyper Raman signals were observed with intensities close to spontaneous Raman scattering. They showed that surface enhanced hyper Raman scattering (SEHRS) has become a useful spectroscopic technique. In view of the recent advances in laser and detector technology, significant improvement in SEHRS sensitivity will come rapidly from the use of an intensified CCD camera for hyper Raman signal detection and the use of a continuously tunable mode-locked Ti:Sapphire laser as the excitation source (Yu and Nie, 1992).

3.6.2.2 Coherent anti-Stokes Raman spectroscopy (CARS)

CARS is the most widely practiced nonlinear Raman spectroscopy technique (Nibler and Knighten, 1978). The major experimental advantage of CARS (and of most nonlinear coherent Raman techniques) is the large signal produced. In a typical CARS experiment in a liquid or a solid, the applied laser power of the pump and Stokes laser (10^4 – 10^5 W) generate an output power of up to 1 W (Levenson, 1982), while conventional Raman scattering would give collected signal power of $\sim 10^{-4}$ W with the same lasers. Since the CARS output is directional, the collection angle can be five orders of magnitude smaller than that needed in spontaneous scattering. Taken together, these two factors imply that CARS is nine orders of magnitude less sensitive to sample fluorescence than spontaneous scattering. The advantage is actually even greater since the CARS signal is at a higher frequency than any of the input laser frequencies.

However, there are some disadvantages of CARS: (i) an unavoidable electronic background nonlinearity that alters the line shape and can limit the detection sensitivity; (ii) a signal that scales as the square of the spontaneous scattering signal (and as the cube of the laser power; see Eq. 3.6-11), making the signals from weakly scattering samples difficult to detect; and (iii) the need to fulfill the phase matching requirements of Sec. 3.6.1.3. While other techniques avoid these difficulties, CARS remains still the most popular coherent nonlinear technique.

There are several experimental possibilities to realize coherent anti-Stokes Raman spectroscopy. Some of the most practical ones will be discussed next.

3.6.2.2.1 Scanning pulsed CARS

A typical CARS device for condensed phase spectroscopy which has been developed at the University of Würzburg (Materny et al., 1992b) is shown in Fig. 3.6-8. Because it contains two tunable (ω_L, ω_S) laser sources it is also suitable to perform resonance CARS

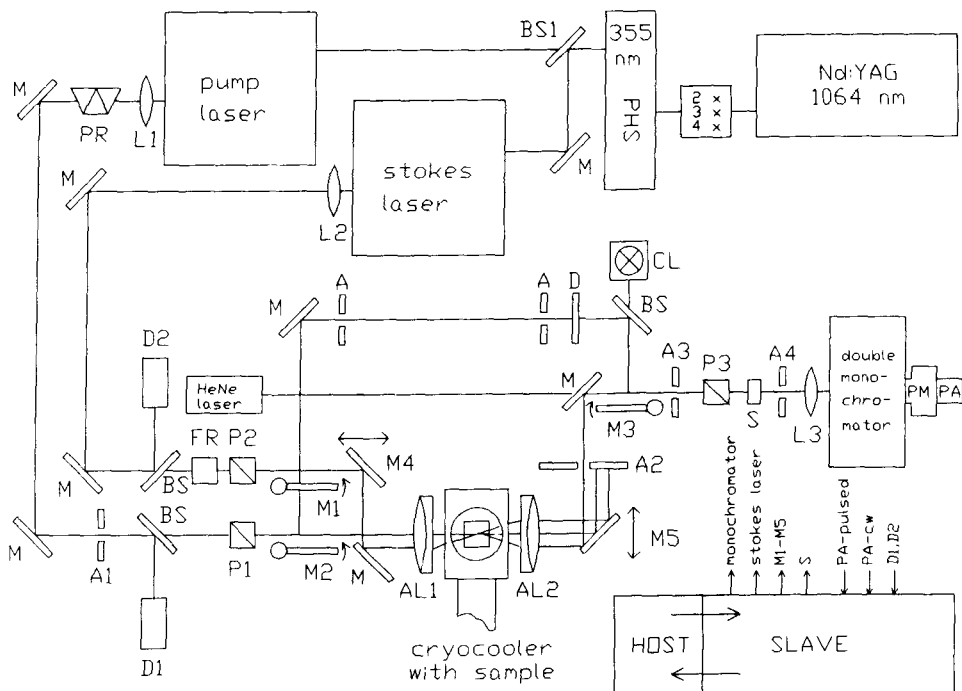


Figure 3.6-8 Experimental set-up for CARS spectroscopy in the condensed phase. A = aperture; AL = achromatic lens; BS = beam splitter; CL = calibration lamp; D = diffuser; D1, D2 = diodes; FR = double Fresnel rhombus; L = lens; M = mirror; P = Glan-Thompson polarizer; PA = preamplifier; PHS = Prism Harmonic Separator; PM = photomultiplier; PR = linear dispersing prism arrangement; S = shutter (Materny et al., 1992a).

spectroscopy in liquids or in solids (Materny and Kiefer, 1992a and 1992b; Materny et al., 1992b; Leuchs and Kiefer, 1993). For the simultaneous pumping of the two dye lasers a pulsed (10 Hz) Nd:YAG-laser with a harmonic generator and a prism harmonic beam separator (Spectra Physics Quanta Ray models GCR-4, HG-4 and PHS-1, respectively) are used. The third harmonic of the Nd:YAG laser with wavelength at 355 nm is split into two beams by a 2:1 beam splitter (BS1 in Fig. 3.6-8). These beams are then used to pump the two dye lasers. They supply the pump (ω_L) and Stokes (ω_S) beam, respectively. The outputs of the dye lasers are corrected for divergence by lenses L1 and L2 with long focal length. Dye luminescence of the pump laser is removed by a linear dispersing prism arrangement (PR) followed by an aperture (A1). The output of the dye lasers can be chosen to be horizontally or vertically polarized. To achieve exact polarization conditions Glan-Thompson polarizers (P1, P2) are added. The polarization of the Stokes beam can be turned separately by means of a double Fresnel rhombus (FR). The two laser beams are crossed and focused on the sample by an achromatic lens (AL1). The crossing angle can be tuned by changing the distance of the two parallel laser beams. The latter is achieved by moving the phase conditioning mirror M4 in the way indicated in Fig. 3.6-8.

The CARS signal (ω_{AS}) which is generated in the sample under a certain angle is made parallel to the pump and Stokes beam after passing an achromatic lens (AL2). Moving mirror M5 the way as indicated in Fig. 3.6-8 while tuning the Stokes laser wavelength leads to a compensation of the change of the observation angle. This is important to have the CARS beam in a final fixed position for further rigorous separation from the two dye laser beams. Part of the latter is performed by the apertures A2 and A3. After passing an analyzer (P3), a shutter (S) and a further aperture (A4), the CARS beam is finally focused by L3 on the entrance slit of a double monochromator (Spex 1680) which suppresses remaining laser or stray light.

For the purpose of alignment a He-Ne-Laser is installed which fixes the optical axis of the double monochromator. The signal path is aligned according to this axis. When the Stokes laser frequency is tuned, mirrors M4 and M5 are simultaneously moved under computer control to compensate for dispersion (phase-matching). The monochromator can be calibrated by means of several calibration lamps (discharge lamps, CL) when mirror M3 is switched into the right position. Putting mirrors M1 or M2 at 45° with respect to the laser beams, the pump or Stokes beam, respectively, can be directed to the monochromator for exact determination of the laser wavelengths.

The CARS signal is detected by a Model RCA C31024A fast photomultiplier (PM). The intensities of pump and Stokes laser are measured by photodiodes D1 and D2, respectively. The output signals of PM, D1 and D2 serve as input signals for the computer system. By means of the D1 output the pump laser triggers the complete electronic system for each laser shot. The computer controls the stepping motor of the double monochromator, the wavelength of the Stokes laser, positions of mirrors 1-5 and the shutter.

Instead of a solid sample mounted in a cryocooler as shown in Fig. 3.6-8 also a cell for liquids can be used at the same place which then allows to take CARS spectra of liquids.

The apparatus can also be easily modified for CARS difference spectroscopy, which allows the simultaneous measurement of CARS spectra of two different samples under identical conditions (Weippert and Kiefer, 1992a-c). CARS difference spectroscopy can be used similarly as Raman difference spectroscopy (Kiefer 1973, 1977; Asthana and Kiefer, 1993) for accurate determination of small frequency shifts and bandwidth changes in liquid mixtures, particularly when the sample is fluorescent.

Experimental problems may arise for CARS spectroscopy on samples with strong and broad absorption in the spectral region of interest. In such cases, the usual measurement procedure in which the CARS spectra are taken in transmission may be limited or even impossible. To overcome these difficulties a backscattering CARS technique has been developed by Weippert et al. (1993). The backward CARS signal is normally negligibly small compared with the forward signal because of a large phase mismatch (Pfeiffer et al., 1990). However, in the case of strongly absorbing samples the short interaction length L (see Eq. 3.6-11), which is then in the sub-micrometer range, causes the phase-matching condition to become less significant. Then, the backscattering CARS signal of strongly absorbing samples can have intensities even higher than those obtained in the conventional way, i. e. in a forward directed beam arrangement.

In order to observe backward scattered CARS signals from the surface of an opaque sample a special CARS set-up has been made, which is essentially the standard configuration as displayed in Fig. 3.6-8 with specific modifications. The latter is shown in detail in Fig. 3.6-9. Here, the sample area from Fig. 3.6-8 is reproduced together with the modification. In this case, the Stokes beam runs parallel above the pump beam. Both

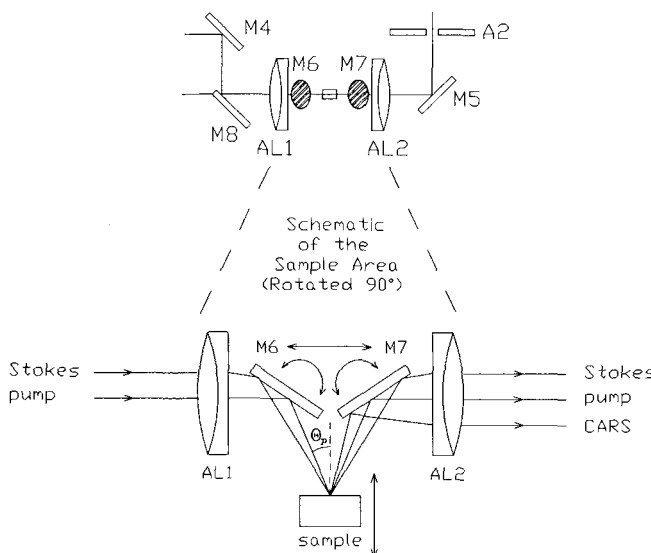


Figure 3.6-9 Modification of the pulsed CARS set-up shown in Fig. 3.6-8 for backscattering measurements. Shown is only the modified sample area (Weippert et al., 1993).

are focused by the achromatic lens AL1 and then deflected downwards by the mirror M6. The common focus is on the surface of the sample. The reflected upcoming beams including the generated CARS beam are reflected by mirror M7 so that after lens AL2 they again travel horizontally. This arrangement permits the CARS study of the surface of a highly absorbing sample which could be either a solid or a liquid.

Most of the CARS studies performed up to now were on gaseous samples. The main reason for this is the exceptionally high resolution combined with reasonable signal strengths. Although the nonlinear susceptibility $\chi_{CARS}^{(3)}$ of a gas is about two orders of magnitude smaller than that of a typical liquid, the interaction length can be much larger. There is nearly no dispersion of the medium if excitation is away from absorption and, hence, the phase-matching condition (Eq. 3.6-5) requires a collinear beam arrangement. Since the optical breakdown threshold for gases is orders of magnitude higher than for liquids or solids, the high output power produced by the second harmonic of a Nd:YAG laser ($\omega_L = 532$ nm) and a dye laser (angular frequency ω_S) pumped simultaneously by ω_L can be profitably employed. Thus, the CARS signal produced in gases with such a relatively simple CARS apparatus can be nearly as large as in liquids (Nibler and Knighten, 1978). The high intensity beams with angular frequencies ω_L and ω_S can be combined using a dichroic beam splitter. The CARS beam (ω_{AS}) can be best separated from the incident beams using a prism, dichroic mirrors or interference filters rather than a monochromator as shown in Fig. 3.6-8.

3.6.2.2 Multiplex CARS

Scanning CARS measurements require quite long recording times which may be too long with respect to the evolution of physical phenomena to be studied (e. g. chemical reactions). For such cases multiplex CARS is an attractive alternative to the single-frequency pulsed techniques. In multiplex CARS, the Stokes beam at ω_S is produced by a broad band laser (typically $150\text{-}200\text{ cm}^{-1}$) and the full spectrum ($150\text{-}200\text{ cm}^{-1}$) at anti-Stokes angular frequency ω_{AS} is recorded in a single laser shot (Nibler et al., 1977). A spectrograph with an optical multichannel analyzer (preferentially a cooled CCD camera) is needed for this purpose. In this case, however, the resolution is limited by the spectrograph and/or the optical multichannel analyzer employed.

It should be noted that the multiplex CARS signal obtained from a single laser shot is comparatively small. However, averaging over many shots gives CARS spectra of similar quality as scanning CARS spectra if the lasers have comparable output powers.

3.6.2.3 Femtosecond time-resolved CARS

Time-resolved coherent anti-Stokes Raman scattering has produced much important information on the dynamics of molecular vibrations and rotations (Laubereau and Kaiser, 1978; Duppen et al., 1983; Akhmanov et al., 1985; Angeloni et al., 1988). Particularly vibrational dephasing time constants in liquids and solids could be determined with this technique (Laubereau et al., 1978; Kohles and Laubereau, 1987; Weber and Rice, 1988; Bron et al., 1989). In these experiments pump and tunable Stokes beams serve to produce

a coherent polarization oscillation in a medium at a resonant vibrational frequency. A separate time-delayed probe beam then generates an anti-Stokes signal whose intensity decreases with time due to dephasing and population-changing collisions. For solids and liquids, dephasing times are only a few picoseconds but in low density gases the signals persist for much longer periods (Laubereau and Kaiser, 1978).

Recent technical developments in ultrashort-pulse lasers enable the CARS spectroscopist to obtain coherent light pulses shorter than 100 fs. This time scale corresponds to the period of molecular vibrational motions ($100 \text{ fs} \approx 100\text{-}150 \text{ cm}^{-1}$ depending on the shape of the pulse, for example). One is therefore able to coherently excite many vibrational modes at a time and monitor relaxation processes in real time.

Femtosecond time-resolved CARS experiments were first reported by Leonhardt et al. (1987). Following studies (Zinth et al., 1988; Zinth and Kaiser, 1988) showed beating patterns and fast decays of the coherent signal for several molecular liquids. Okamoto and Yoshihara (1990) reported the observation of femtosecond time-resolved CARS under various polarization conditions. They also observed time-resolved CARS under preresonance and rigorous resonance conditions, which gave useful information on the vibrational relaxation in electronically excited states. With their femtosecond time-resolved CARS apparatus, the schematic diagram of which is displayed in Fig. 3.6-10, they were able to study the femtosecond vibrational dephasing of a variety of molecular vibrations (Inaba et al., 1991, 1992, 1993; Okamoto et al., 1993a, 1993b), among them the $\text{C}\equiv\text{N}$

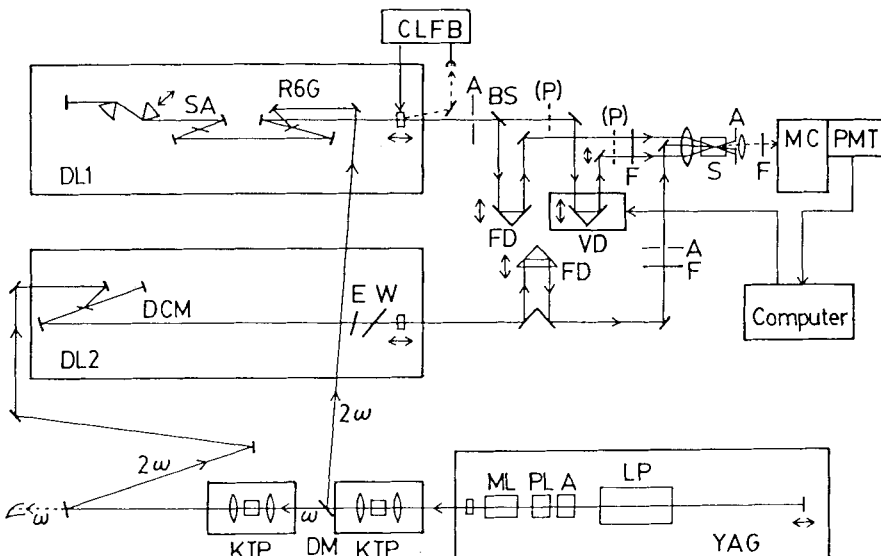


Figure 3.6-10 Schematic diagram of a femtosecond time-resolved CARS apparatus. YAG, cw mode-locked Nd:YAG laser; ML, mode locker; PL, polarizer; LP, laser pot; DM, dichroic mirror; DL1, femtosecond dye laser; SA, saturable absorber; CLFB, cavity-length feedback system; DL2, picosecond dye laser; W, tuning wedge; E, étalon; FD, fixed delay; VD, variable delay; BS, beam splitter; P's, half-wave plates (when necessary); F's, filters; S, sample; MC, monochromator; PMT, cooled photomultiplier. (Okamoto and Yoshihara, 1990).

and C≡C stretching vibration in liquid nitriles and liquid alkynes, respectively (see Sec. 6.1.4.2.2).

The basis of the experimental femtosecond CARS apparatus developed by Okamoto and Yoshihara (1990) which is reproduced in Fig. 3.6-10 is essentially the same as that of Leonhardt et al. (1987) and Zinth et al. (1988) with the addition of the possibility to change the polarization of the laser radiation. The main parts of the system are two dye lasers with short pulses and high repetition rates, pumped by a cw mode-locked Nd:YAG laser (1064 nm, repetition rate 81 MHz). The beam of the first dye-laser which produces light pulses with 75-100 fsec duration is divided into two parts of equal intensities and used as the pump and the probe beam. After fixed (for the pump beam) and variable (for the probe beam) optical delay lines, the radiation is focused onto the sample together with the Stokes radiation produced by the second laser (DL2), which is a standard synchronously pumped dye laser. The anti-Stokes signal generated in the sample is separated from the three input laser beams by an aperture, an interference filter, and a monochromator, and detected by a photomultiplier. For further details we refer to Okamoto and Yoshihara (1990).

Although time-resolved CARS is a powerful spectroscopic tool to study the vibrational relaxation of molecular systems, the information on dephasing dynamics via scattering from the isotropic part of the Raman tensor is often obscured by additional contributions due to the anisotropic component of the scattering tensor introducing also orientational relaxation effects and the nonresonant part of the third order nonlinear susceptibility (Fickenscher and Laubereau, 1990). An elegant femtosecond three colour polarization CARS technique has been developed which by proper choice of the polarization geometry allows to suppress the unwanted contributions by several orders of magnitude (Laubereau and Purucker, 1992; Li et al., 1992; Fickenscher et al., 1992; Purucker et al., 1993). For polarization CARS see Sec. 3.6.2.2.5.

3.6.2.2.4 High resolution cw-CARS

One of the main advantages of CARS and also of other nonlinear Raman spectroscopies is the high resolution that can be achieved in spectra of gases at low pressures. The reason for this is that the instrumental resolving power in these techniques depends only on the convoluted linewidths of the lasers used for excitation, whereas in linear Raman spectroscopy the resolution is determined by the monochromators used to disperse the observed scattered Raman light.

High resolution (ca. 10^{-3} cm $^{-1}$) CARS spectra can be achieved with single-mode cw lasers. The obvious disadvantage, however, is the drastically reduced CARS signal level due to the low power levels of cw lasers. The first cw CARS experiment was reported by Barrett and Begley (1975) followed by experiments performed by Henesian et al. (1976) and Fabelinsky et al. (1977). More recently Schrötter et al. (1988, 1989, see also Frunder et al., 1986) have developed a very efficient cw CARS spectrometer with a resolution of 0.001 cm $^{-1}$ (30 MHz). The high efficiency was achieved by intracavity excitation in an argon ion ring laser modified from a commercial laser head (Frunder et al., 1986). In this way an intracavity power of 100 to 200 W in a single longitudinal mode at 514.5 nm, selected by an intracavity etalon, was obtained. Fig. 3.6-11 shows the

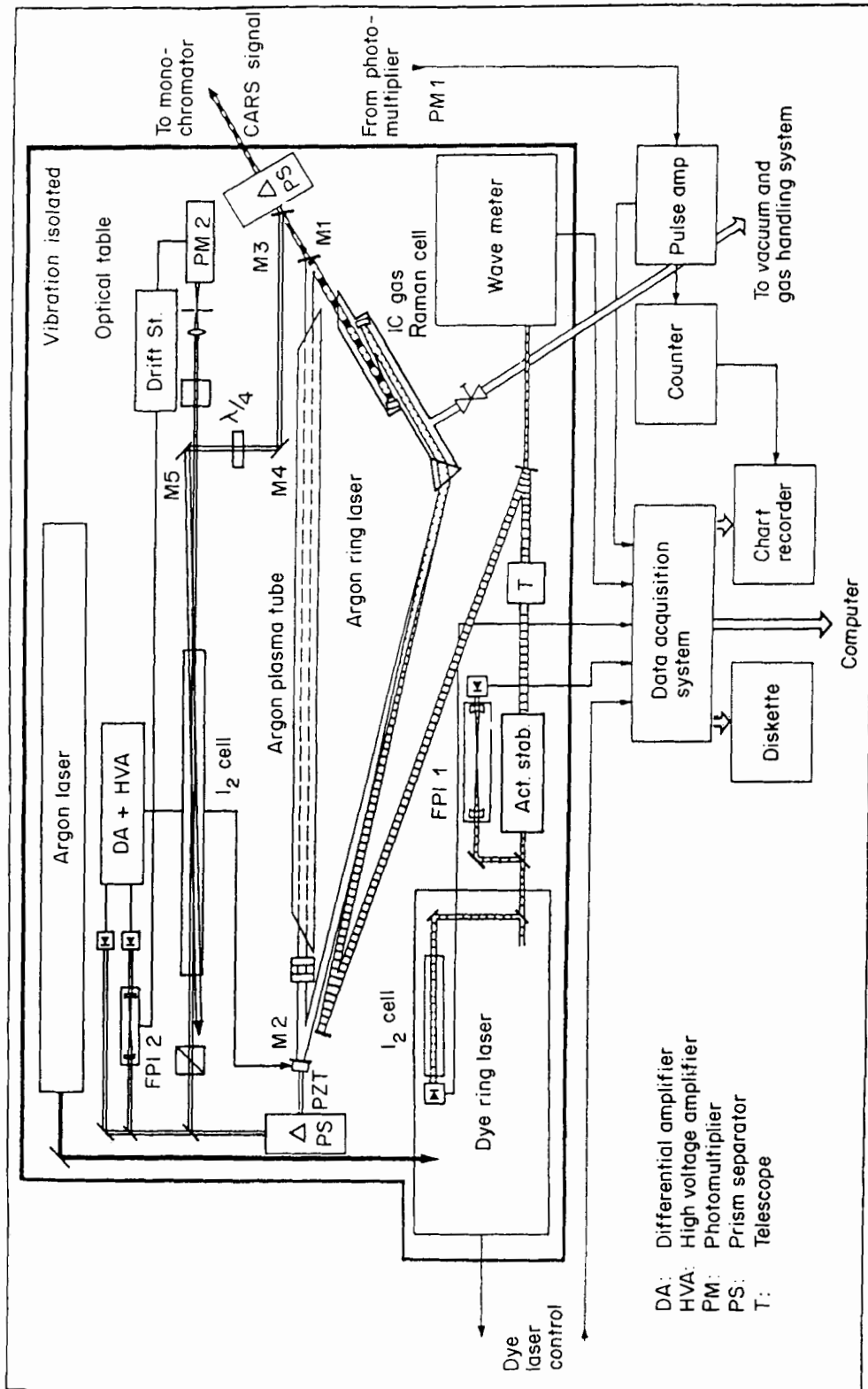


Figure 3.6-11 Schematic arrangement of a cw CARS spectrometer with actively stabilized argon ion and dye ring lasers (Schrötter et al., 1988).

schematic arrangement of the argon ion ring laser in the CARS spectrometer including the provisions for an active stabilization to a hyperfine component in the absorption spectrum of iodine. The second, tunable laser frequency is provided by a commercial dye ring laser pumped by a second argon ion laser. The beam of the dye ring laser is coupled into the cavity of the argon ion laser at the prism and is focused collinearly with the argon laser beam inside a specially constructed gas cell for intracavity CARS excitation. The generated CARS beam is transmitted by the dichroic end mirror of the argon ion laser and spectrally purified by a prism and a grating monochromator. With this sophisticated set-up high resolution CARS spectra can be generated in the spectral region from about 2000 to 3500 cm⁻¹ (see Fig. 4.3.2-14 for an example). Another example of high resolution CARS spectra is given in Fig. 6.1-20.

3.6.2.2.5 Special laser beam arrangements for CARS

As mentioned previously, the incident pump and Stokes laser beams must be aligned in a precise manner so that the CARS generation process is properly phased. Since gases are virtually dispersionless, i. e. the refractive index is nearly a constant over a wide frequency range, the photon energy conservation condition $\omega_{AS} = 2\omega_L - \omega_S$ indicates that phase matching occurs when the input laser beams are aligned parallel to each other. However, collinearity poses a problem in regard to spatial resolution. Therefore, Eckbreth (1978) has introduced a method that permits large angular separation of the input laser beams and hence high spatial resolution, while still satisfying the phase-matching requirement. In this approach (see Fig. 3.6-12) the ω_L pump beam is

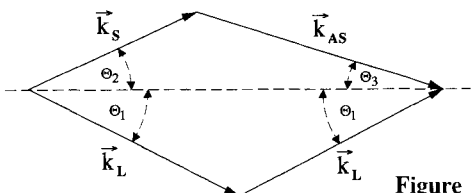


Figure 3.6-12 Phase matching for BOXCARS.

split into two components, which are crossed at an angle of $2\Theta_1$. The ω_S Stokes beam is introduced at angle Θ_2 , producing phase-matched CARS at angle Θ_3 . Based upon the shape of the phase-matching diagram, this technique has been termed BOXCARS (Eckbreth, 1978). The appropriate phase-matching angles are readily related from simple geometric considerations as follows (Eckbreth, 1978)

$$n_S \omega_S \sin \Theta_2 = n_{AS} \omega_{AS} \sin \Theta_3 \quad (3.6-12)$$

$$n_S \omega_S \cos \Theta_2 + n_{AS} \omega_{AS} \cos \Theta_3 = 2n_L \omega_L \cos \Theta_1 \quad (3.6-13)$$

It should be pointed out that the wave vectors need not reside in the same plane. The BOXCARS phase-matching diagram could be folded along the dotted line in Fig. 3.6-12. With this folded BOXCARS arrangement (Shirley et al., 1980) a great advantage

arises because the CARS beam is completely spatially separated from the incident wave mixing components, even at zero Raman shifts, allowing to perform CARS experiments for pure rotational transitions. The actual geometry of the laser and CARS beams for such a folded BOXCARS arrangement is shown in Fig. 3.6-13. Folded BOXCARS has been employed to examine for example the rotational CARS spectrum of air and N₂ (Shirley et al., 1980). The spectra could be scanned to within 7 cm⁻¹ of the pump frequency by using a single monochromator.

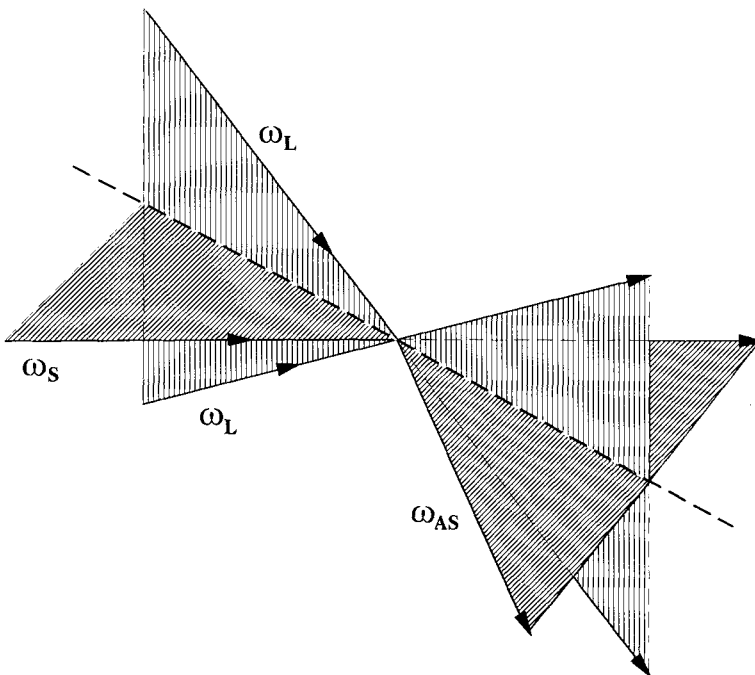


Figure 3.6-13 Geometry of laser beams for Folded-BOXCARS.

Another practical CARS technique places the Stokes beam inside the pump beam when using a Nd:YAG laser with Donut profile as pump laser source (Marko and Rimai, 1979). This method which has been termed USED (unstable resonator spatially enhanced detection) CARS (Eckbreth et al., 1984; Eckbreth and Anderson, 1985) also increases the spatial resolution.

As already mentioned shortly in Sec. 3.6.2.2.3 background contributions which may limit the CARS sensitivity in observing weak Raman resonances can be eliminated by applying special polarization arrangements for the laser and CARS beams. This has been already demonstrated by Song et al. in 1976. They have shown in a four-colour CARS experiment that, by proper orientation of the laser polarizations, background contributions can be eliminated, resulting in undistorted line shapes. A review of this technique and

numerous applications have been reported by Brakel and Schneider (1988). The basic idea of this so-called polarization CARS lies in the fact that the Raman signals which arise from Raman resonant and nonresonant response of the medium have normally different polarizations. As a consequence, the non-resonant contribution can be eliminated by means of a polarization analyzer. Polarization CARS can be performed in the scanning as well as in the multiplex mode.

3.6.2.3 Stimulated Raman gain and inverse Raman spectroscopy (SRGS, IRS)

As outlined in Sec. 3.6.1.3, both stimulated Raman gain spectroscopy (SRGS) and inverse Raman spectroscopy (IRS) or stimulated Raman loss spectroscopy (SRLS) fall into the class of coherent nonlinear Raman techniques. SRGS and IRS differ only in that spectra are obtained in the former case by using a Stokes shifted probe laser to scan the gain profile produced by a pump laser source, whereas in the latter case of IRS, an anti-Stokes shifted probe laser is used to scan the absorption profile (loss) on the opposite side of the spectrum relative to the pump frequency (Jones and Stoicheff, 1964; Owyong et al., 1978; Owyong, 1981). Thus, scanning of the frequency of one of the laser sources relative to the other results in a direct display of the Raman spectrum. The only difference in respect to the spontaneous Raman spectrum will be that, since this is a stimulated process, the signal will scale as the difference in population between the upper and lower level rather than being directly proportional to the lower-level population.

The advantages of SRGS and IRS are that the signal (in contrast to CARS) is linearly proportional to the spontaneous Raman scattering cross section (and to the product of the two laser intensities), and that the phase-matching condition is automatically fulfilled and there is no nonresonant background. As already mentioned in Sec. 3.6.1.3 the resolution of the nonlinear Raman techniques is limited only by the laser linewidths. These qualities give the stimulated Raman techniques particular appeal under conditions where interference from background luminescence is problematic or in situations where very high resolution is required. The main disadvantage of these techniques, however, is that they are quite sensitive to laser noise. The latter requires high stability in laser power.

Pioneering work on stimulated Raman spectroscopies was performed using pulsed high-power laser sources in order to induce appreciable Raman gain or loss that could be easily observed (Jones and Stoicheff, 1964). Later techniques employed stable cw lasers and detect the small ($\sim 10^{-5}$) changes in intensity due to Raman gain or loss (Owyong et al., 1978; Owyong, 1979 and 1981).

Due to complexity only a few stimulated Raman gain and loss spectrometers with main application in high resolution molecular spectroscopy have been built since the fundamental developments by Owyong et al. in 1978. An important improvement has been the realization of the quasi-cw stimulated spectrometer (Owyong, 1979), wherein a single-mode stable cw laser provides a low-noise probe source and a high-power repetitively pulsed laser system provides the pump source. Such a scheme is diagrammatically shown in Fig. 3.6-14 for inverse Raman (Raman loss) spectroscopy (Owyong, 1979).

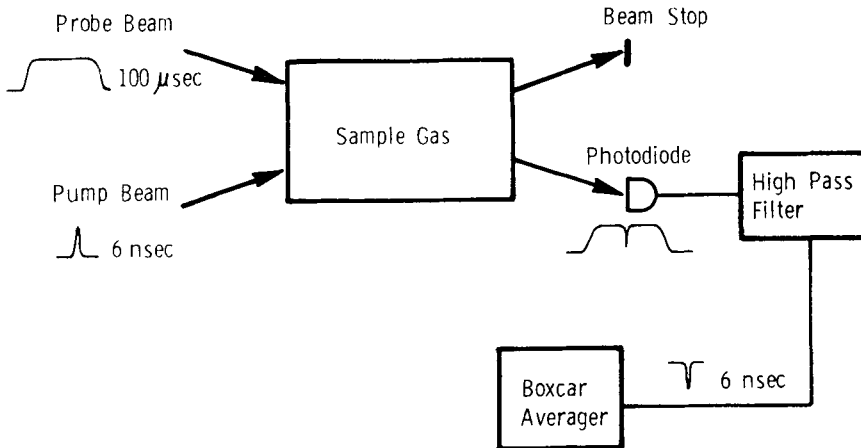


Figure 3.6-14 Schematic for quasi-cw inverse Raman spectroscopy (Owyoung, 1978).

Here, the anti-Stokes shifted probe laser (angular frequency in this case is ω_L) is temporally gated on for a time ($100 \mu\text{s}$) that is long compared to the high power pump pulse (angular frequency ω_S , 6 ns), yet short enough to result in a low duty cycle, and thus preclude premature saturation of the detector. As the two beams cross in the sample at their common focus, the Stokes gain or anti-Stokes absorption produced by the pump beam is reflected in an amplitude modulation of the probe beam. Elimination of the background probe level is achieved by high-pass filtering. Such an approach thus incorporates both the large gains in sensitivity using a high-power pump source and the stable noise free advantage of a cw probe laser. Also, since the pump source is repetitively pulsed, a boxcar averager may be used to provide signal averaging which increases the signal-to-noise ratio even further. Similar to pure cw systems, the spectrum is obtained by scanning either the pump or the probe laser, which allows the gain or absorption profile to be displayed directly.

The construction of a spectrometer for high resolution stimulated Raman spectroscopy based on the quasi-cw approach described above, has been reported recently by Bermejo et al. (1990). Their experimental set-up is shown in Fig. 3.6-15. It is also suitable to perform high resolution IR absorption spectroscopy. A frequency stabilized single mode argon ion laser delivers the probe beam. The tunable pump beam is produced by means of an argon ion pumped stabilized dye ring laser, whose output is amplified by a three stage dye amplifier which is pumped by a pulsed, frequency doubled Nd:YAG laser. A Fabry-Perot interferometer and a wavemeter serve for the accurate wavelength determination of the dye laser output. Part of the power of the pump and probe laser beams is used for generating a tunable, narrowband difference frequency by means of non-linear mixing in a LiNbO₃ crystal. Hence, simultaneous recording at high resolution IRS and infrared difference frequency spectra is possible with this instrumentation. Both resolution and absolute accuracy of the observed Raman transitions are of the order of 10^{-3} cm^{-1} . For examples of spectra see Sec. 6.1.4.3.

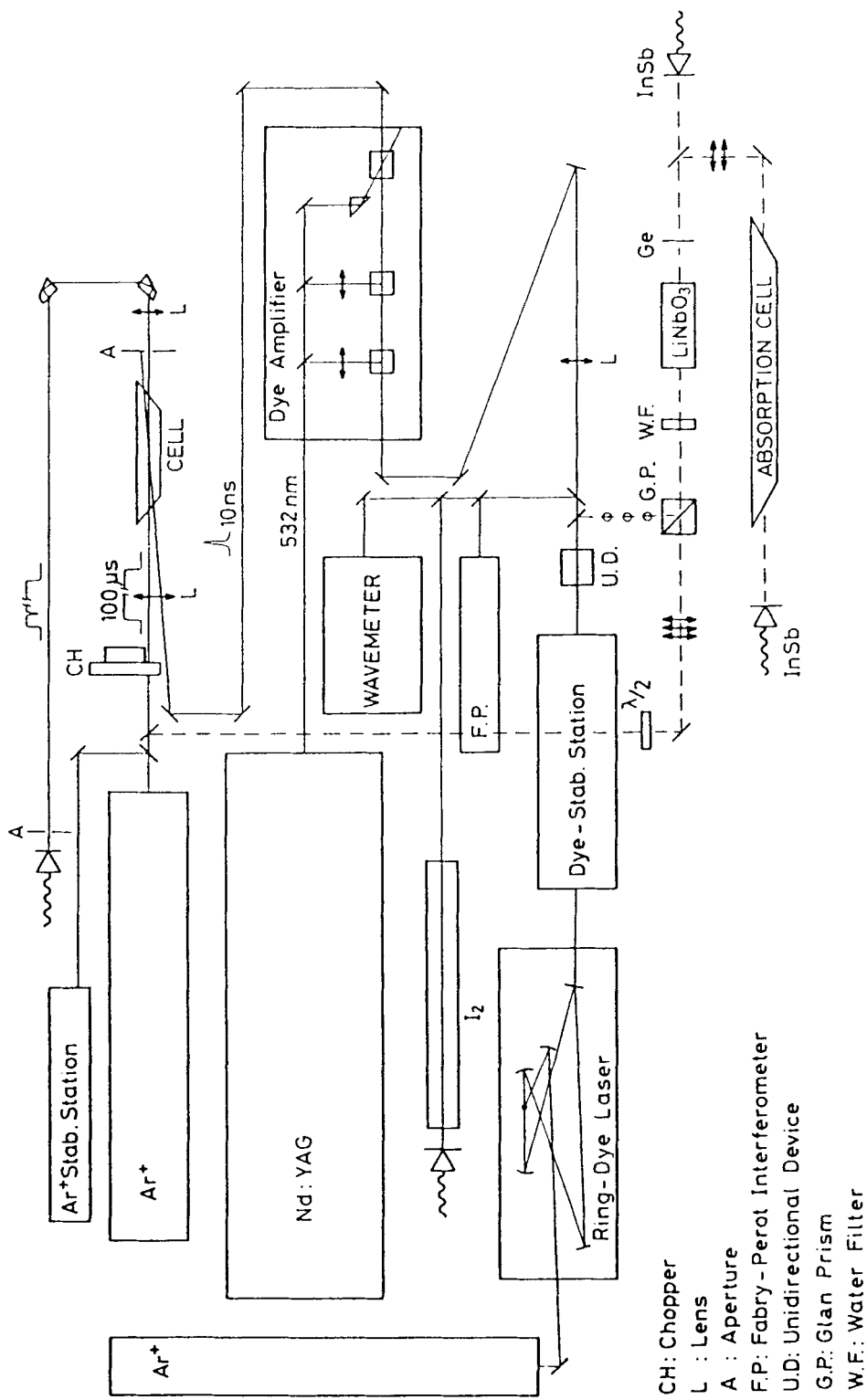


Figure 3.6-15 Schematic arrangement of a high resolution quasi-cw inverse Raman and frequency difference IR spectrometers (Bermejo et al., 1990).

3.6.2.4 Photoacoustic Raman spectroscopy (PARS)

Acoustic detection of the Raman process using cw laser sources was first performed by Barrett and Berry (1979). As discussed in Sec. 3.6.1.3 in PARS the energy is deposited in the sample by the stimulated Raman process and the PARS signal is detected by sensitive acoustic methods. The use of high-power pulsed laser sources again gave great improvements in the sensitivity of this technique. This method is limited by the requirement of a static ("quiet") sample and by the pressure necessary to transfer the acoustic signal to the microphone. The advantage of the method which originates from the nonoptical nature of the detection is the absence of a Rayleigh line, because no energy can be deposited into the sample at zero Raman frequency (ω_R), which enables to record pure rotational Raman spectra without any interference caused by Rayleigh scattering (Barrett, 1981; Barrett and Heller, 1982; Barrett et al., 1982).

Since the pioneering work by Barrett and coworkers only a few PARS experiments have been applied to some molecular gases (Brodnikowskii et al., 1985; Duval et al.,

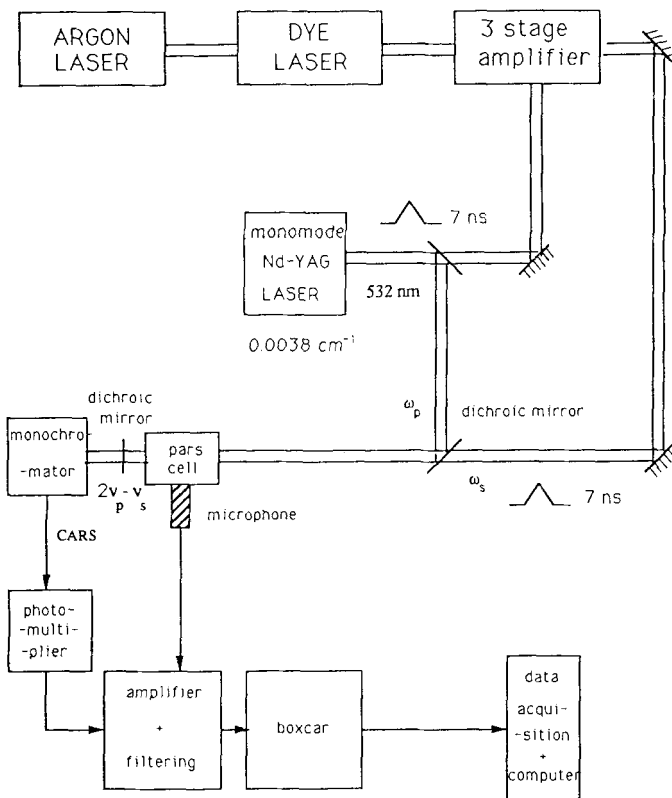


Figure 3.6-16 Schematic representation of a PARS-CARS experimental set-up (Rotger et al., 1992).

1986). The high potentiality of this technique when combined with the advantage of high-resolution spectroscopy using narrow line-width lasers has been demonstrated recently by Rotger et al. (1992). By a simple modification of their CARS apparatus (Millot et al., 1988) they were able to perform high resolution (0.005 cm^{-1}) PARS spectroscopy of gases at about 10 Torr $\approx 1.3 \text{ kPa}$. Their system, which is essentially a CARS set-up where in the sample cell a condenser microphone is inserted just in front of the beam focal point, is shown in Fig. 3.6-16. Pump (ω_L) and Stokes (ω_S) lasers are a frequency doubled single mode Nd:YAG laser and a pulsed amplified tunable dye laser, respectively. For examples of spectra see Sec. 6.1.4.4.

3.6.2.5 Ionization detected stimulated Raman spectroscopy (IDSRS)

As shortly discussed in Sec. 3.6.1.3 IDSRS combines high resolution stimulated Raman spectroscopy with highly sensitive resonant laser ionization to achieve an increase in sensitivity of over three orders of magnitude. The experimental apparatus to perform IDSRS is partially diagrammed in Fig. 3.6-17 (Esherick et al., 1985). The sensitivity of the technique is primarily limited by the level of background ionization present even when the Raman pump sources are off resonance. By using a segmented electrode design in conjunction with a differential amplifier (see Fig. 3.6-17), it is possible to differentially detect the IDSRS signal relative to the background signal arising from regions where

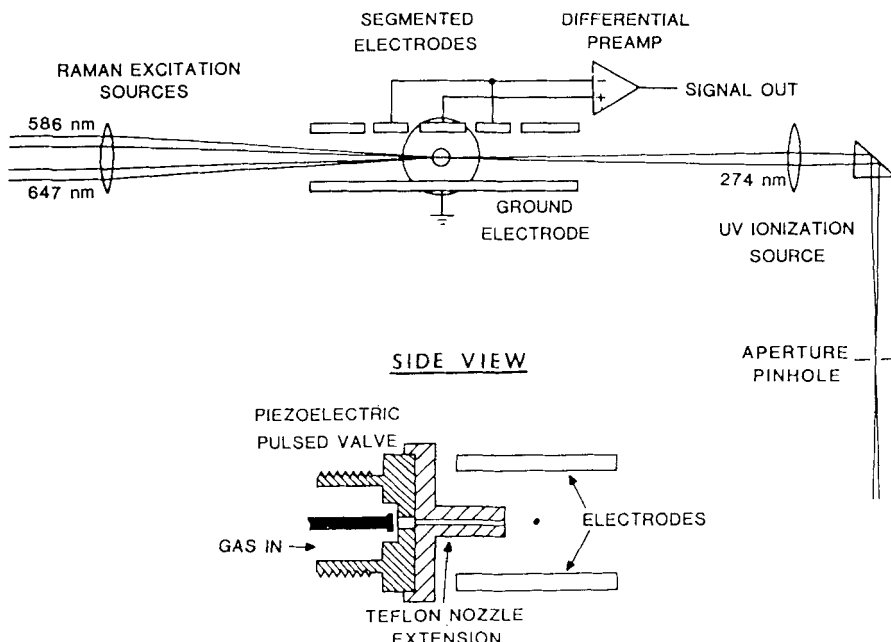


Figure 3.6-17 Diagram of part of the experimental apparatus for Ionization Detected Stimulated Raman Spectroscopy (IDSRS) (Esherick et al., 1985).

the three input laser beams do not cross. The background signal can thus be suppressed, significantly increasing the overall signal-to-noise. High spectral resolution in the first step of the process is achieved by using two near-Fourier-transform limited bandwidth (0.002 cm^{-1}) pulsed sources to drive the stimulated Raman transition. The latter two light sources originate from a single-mode cw krypton ion laser (647 nm) and a tunable single-mode cw dye laser (in Fig. 3.6-17: 586 nm), respectively. Both of these sources are pulse amplified up to $\sim 1\text{MW}$ in Nd:YAG-pumped dye-amplifier chains. Since the resolution of the Raman spectrum is dependent only on the visible Raman excitation sources, the linewidth requirements on the UV ionization laser are much less stringent. The frequency doubled output of a commercial Nd:YAG pumped dye laser is therefore sufficient for this source.

High resolution Raman spectra are obtained by scanning the frequency of one of the Raman excitation sources and monitoring the ionization signal as a function of the frequency difference between this laser and the second, fixed frequency, pump laser.

Since IDSRS involves the detection of ions, it can be readily implemented with mass-selective detection of those ions (Henson et al., 1989; Hartland et al., 1990; Henson et al., 1991). In fact, ion-mass analysis (by time-of-flight techniques, for example) greatly enhances the capabilities of the IDSRS technique.

Besides the frequency domain versions of mass-selective IDSRS, in which the frequency is scanned while photo-ions are detected, the same group has also developed Fourier transform versions of this scheme (FT-IDSRS) (Hartland et al., 1990). In this method the two stimulating Raman excitation beams are directed through a Michelson interferometer before being combined with the ionization UV laser field (see Fig. 3.6-18).

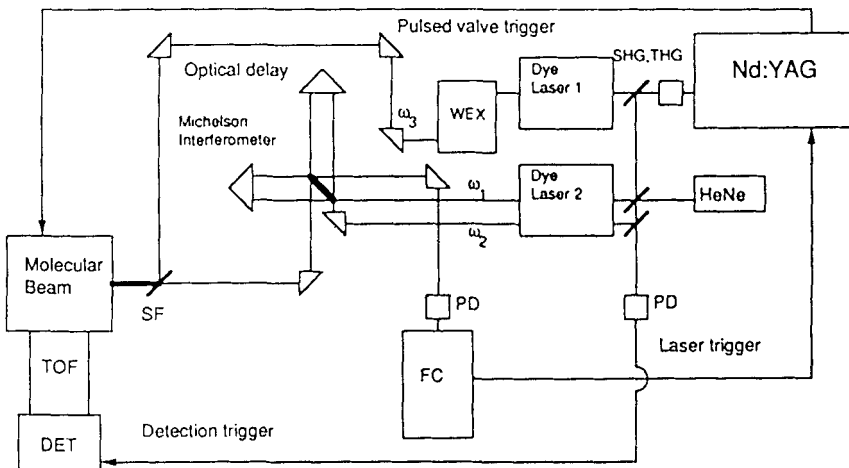


Figure 3.6-18 Apparatus configuration for mass-selective interferometric IDSRS experiments. HeNe, single-mode, frequency-stabilized He-Ne laser; SHG, THG, second- and third-harmonic-generating crystals; WEX, wavelength extender for frequency doubling with automatic crystal tracking; PD's, photodiodes; FC, fringe-counting electronics for generating trigger pulses from the He-Ne laser output; SF, Suprasil flat or dichroic beam splitter for combining ω_1 , ω_2 , and ω_3 ; TOF, DET, time-of-flight tube and ion-detection electronics (Hartland et al., 1990).

Photo-ions are then detected as a function of interferometer delay. The result is an interferogram that upon Fourier transformation yields a Raman spectrum whose resolution does not depend on the bandwidths of the Raman excitation sources but, instead, on the delay range of the interferometer scanned in the experiment. Mass-selective IDSRS and FT-IDSRS have been employed in a number of studies, including one of the benzene dimer (Henson et al., 1991). For examples of IDSRS spectra see Sec. 6.1.4.5.

4 Vibrational spectroscopy of different classes and states of compounds

4.1 Organic substances*

Inorganic substances are composed of any atoms of the periodic table in any of the various valence states. As demonstrated in Sec. 4.2 their vibrational spectra reflect this variety, however, ordered by well defined rules.

In contrast, organic substances are composed of only certain different kinds of atoms connected by a few different types of bonds. The great variety of organic compounds is mainly due to the many possibilities of combining these basic arrangements to molecules of different constitution, configuration, size, and substitution pattern.

The world of organic substances is therefore constituted by a multitude of different combinations of a certain number of definite groups of atoms. They may each be characterized by vibrations of definite frequency modified by definite interaction patterns.

Thus the concept of characteristic vibrations is especially useful in the field of organic chemistry. Already discussed by COBLENTZ in 1905, characteristic vibrations may be defined as follows:

If a bond or a group whose vibrational frequency (viewed as an isolated unit) differs considerably from those of adjacent groups, it shows vibrations which are primarily localized at this specific bond or group. Such vibrations therefore exhibit frequencies as well as intensities in the infrared and Raman spectrum which are characteristic of this particular bond or group.

Characteristic vibrations of many organic compounds, mainly based on Raman spectra, are discussed by Kohlrausch (1943). In two famous books Bellamy (1975, 1980) compiled and discussed the characteristic vibrations of all groups of relevance in organic chemistry, mostly derived from infrared spectra. Colthulp, Daly and Wiberley in 1990 published a very useful book discussing vibrational spectroscopy with special consideration of group frequencies and their dependence on the molecular environment. Freeman (1974) and Dollish et al. (1974) discussed the characteristic vibrations shown by the Raman spectra of organic compounds. Lin-Vien et al. (1991) published the first comprehensive compilation of the infrared and Raman characteristic frequencies of organic

* Section 4.1 is contributed by B. Schrader, Essen

molecules. They also show infrared and Raman spectra of typical molecules reproduced from published collections of spectra.

In this section of the present book a general survey of characteristic vibrations in organic molecules is given. By a specific discussion of typical features of the characteristic vibrations of distinct groups and of typical classes of compounds, their inherent dependence on bond properties, symmetry, structural characteristics and their environment is demonstrated. Since infrared and Raman spectra supply complementary images of a vibration, both spectra are discussed simultaneously and combined infrared and Raman spectra are reproduced as examples. They are taken from the atlas published by Schrader (1989).

Table 4.1-1 lists the range of the frequencies and the infrared and Raman intensities of typical characteristic vibrations of organic compounds. The Eq. 2.5-1 can be used as a guide through this table with reference to the rules discussed in Sec. 2.5. In the following discussion X, Y, and Z are, if applicable, denoting atoms of typical organic molecules: C, O, N, S, and the halogens.

Approximatively, the vibrational spectrum of organic compounds may be divided in typical regions: The X-H stretching vibrations are located in the highest frequency region, between 3700 and 2500 cm⁻¹. The next region, between 2500 and 2000 cm⁻¹, exhibits stretching vibrations of groups with triple bonds as well as the antisymmetric stretching vibrations of groups with cumulated double bonds, X=Y=Z. The following region, between 2000 and 1500 cm⁻¹, exhibits stretching vibrations of double bonded X=Y groups. X-H deformation vibrations are observed between 1500 and 1000 cm⁻¹. The region between 1300 and 600 cm⁻¹ shows stretching vibrations of single bonds of atoms of the second period. The next region shows bending vibrations of these groups and stretching vibrations of groups with heavier atoms. Finally, between 200 and 20 cm⁻¹ the lattice vibrations of crystalline molecules are found. These are vibrations of the molecules which may be regarded as 'frozen' translational and rotational degrees of freedom: translational vibrations and librations. They are discussed in Secs. 2.6, 2.7.6.3, and 2.7.7.

Table 4.1-1 Characteristic frequencies and Raman and infrared intensities of groups in organic compounds

Vibration [a]	Region [cm ⁻¹]	Raman	Intensity[b]	IR
$\nu(\text{O}-\text{H})$	3650–3000	w		s
$\nu(\text{N}-\text{H})$	3500–3300	m		m
$\nu(\equiv\text{C}-\text{H})$	3300	w		s
$\nu(=\text{C}-\text{H})$	3100–3000	s		m
$\nu(-\text{C}-\text{H})$	3000–2800	s		s
$\nu(-\text{S}-\text{H})$	2600–2550	s		w
$\nu(\text{C}\equiv\text{N})$	2255–2220	m–s		s~0
$\nu(\text{C}\equiv\text{C})$	2250–2100	vs		w~0
$\nu(\text{C}=\text{O})$	1820–1680	s~w		vs

Table 4.1-1 continued

Vibration [a]	Region [cm ⁻¹]	Raman	Intensity[b]	IR
$\nu(C=C)$	1900–1500	vs–m		0–w
$\nu(C=N)$	1680–1610	s	m	
$\nu(N=N)$, aliph. subst.	1580–1550	m	0	
$\nu(N=N)$, arom. subst.	1440–1410	m	0	
$\nu_a((C-)NO_2)$	1590–1530	m	s	
$\nu_s((C-)NO_2)$	1380–1340	vs	m	
$\nu_a((C-)SO_2(-C))$	1350–1310	w–0	s	
$\nu_s((C-)SO_2(-C))$	1160–1120	s	s	
$\nu((C-)SO(-C))$	1070–1020	m	s	
$\nu(C=S)$	1250–1000	s	w	
$\delta(CH_2), \delta_a(CH_3)$	1470–1400	m	m	
$\delta_s(CH_3)$	1380	m–w, s, if at C=C	s–m	
$\nu(CC)$, aromatics	1600, 1580	s–m	m–s	
	1500, 1450	m–w	m–s	
	1000	s (in mono-, m-, and 1,3,5- derivatives)	0–w	
$\nu(CC)$, alicyclics, aliph. chains	1300–600	s–m	m–w	
$\nu_a(C-O-C)$	1150–1060	w	s	
$\nu_s(C-O-C)$	970–800	s–m	w–0	
$\nu_a(Si-O-Si)$	1110–1000	w–0	vs	
$\nu_s(Si-O-Si)$	550–450	vs	w–0	
$\nu(O-O)$	900–845	s	0–w	
$\nu(S-S)$	550–430	s	0–w	
$\nu(Se-Se)$	330–290	s	0–w	
$\nu(C(arom.)-S)$	1100–1080	s	s–m	
$\nu(C(aliph.)-S)$	790–630	s	s–m	
$\nu(C-Cl)$	800–550	s	s	
$\nu(C-Br)$	700–500	s	s	
$\nu(C-I)$	660–480	s	s	
$\delta_s(CC)$, aliph. chains				
$C_n n = 3\dots 12$	400–250	s–m	w–0	
$n > 12$	2495/n			
Lattice vibrations in molecular crystals (librations and translational vibrations)	200–20	vs–0	s–0	

[a] ν stretching vibration, δ bending vibration, ν_s symmetric vibration, ν_a antisymmetric vibration.

[b] vs very strong, s strong, m medium, w weak, 0 very weak or inactive.

Stretching vibrations of atoms with different electronegativity modulate the molecular dipole moment, thus, they show strong infrared bands. Vibrations of bonds between equal atoms show infrared bands of very low intensity, however, they modulate the molecular polarizability and therefore show strong Raman bands. The intensity of the bands in the infrared spectrum is zero – the bands are forbidden in the infrared spectrum – if the environment of both atoms is equivalent by symmetry.

4.1.1 Chain molecules, polymers

4.1.1.1 General features

The aliphatic hydrocarbons are composed of skeletons of C atoms with CH₃–, CH₂–, and CH groups or just H atoms as substituents. The typical vibrational modes and the names of the vibrations of CH₂ and CH₃ moieties are summarized in Fig. 4.1-1.

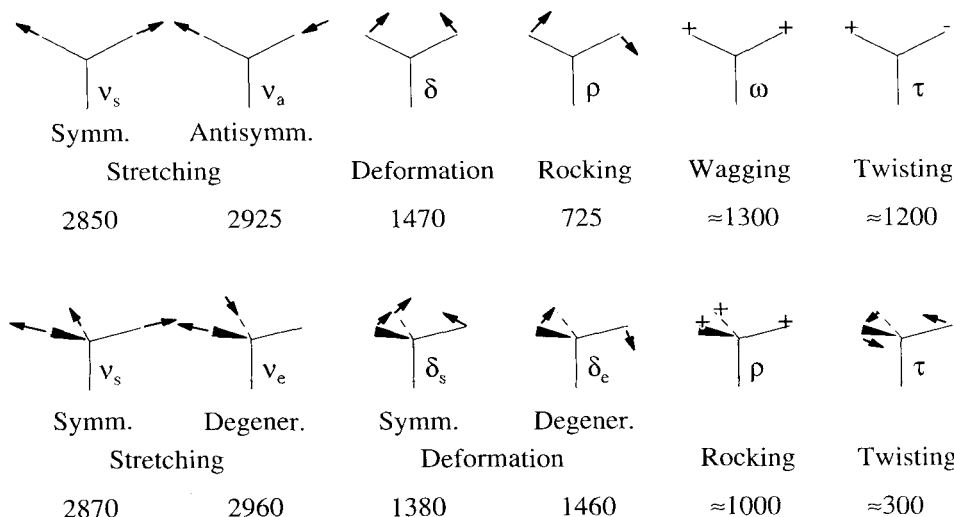


Figure 4.1-1 Characteristic vibrations of CH₂ and CH₃ groups and the approximate position of their frequencies in the spectra of hydrocarbons.

The typical vibrations of long zig-zag chains of –CH₂– groups are exemplified by the polyethylene spectra (Fig. 4.1-2 A). The IR spectrum exhibits no C–C backbone vibrations, however, it shows the antisymmetric and symmetric CH stretching vibration of the CH₂ group at 2920 and 2848 cm⁻¹, respectively, the CH₂ deformation vibration at 1463 and 1473 cm⁻¹, and the rocking vibration at about 725 cm⁻¹. This band is typical of –(CH₂)_n– chains with n > 4, which is, for instance, also shown in the spectrum of nylon 6 (Fig. 4.1-2B).

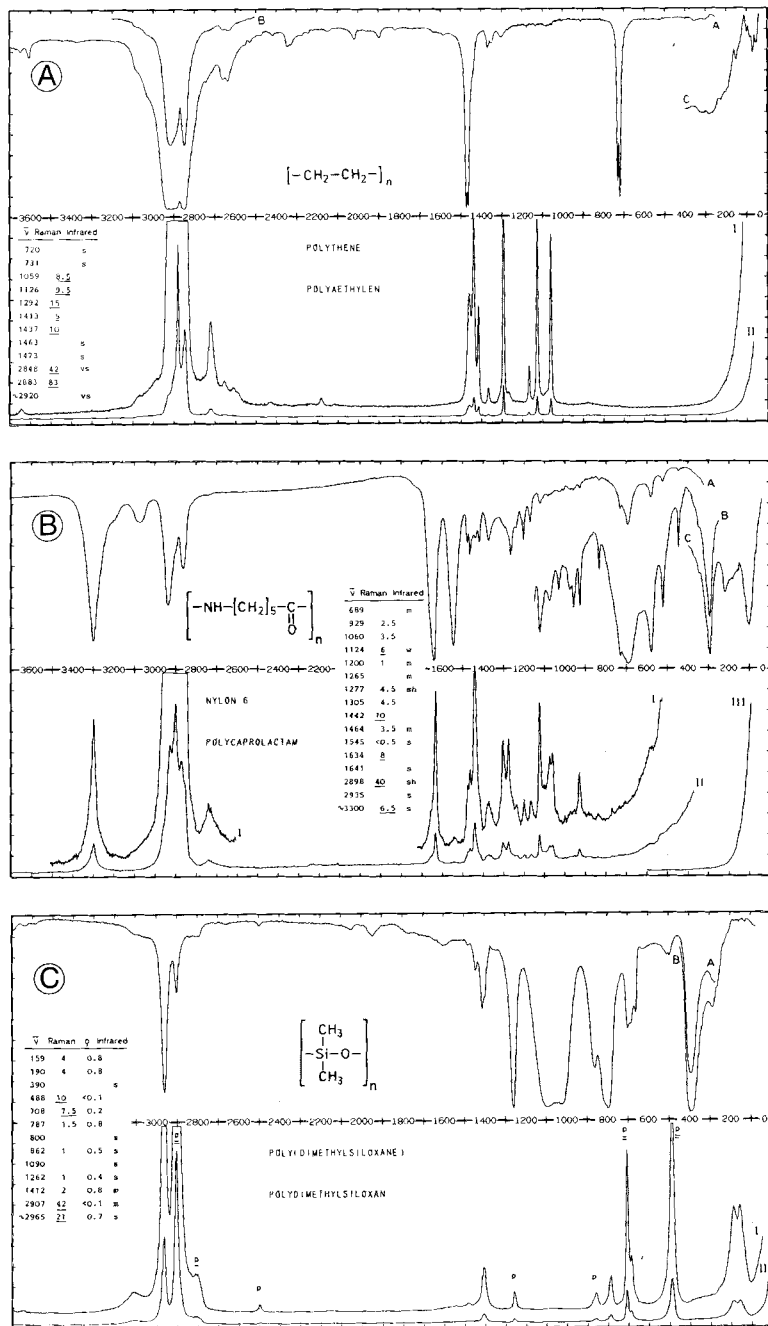


Figure 4.1-2 Vibrational spectra of A polyethylene, B nylon 6, and C polydimethylsiloxane, from Schrader (1989): N-01, N-10, and N-09.

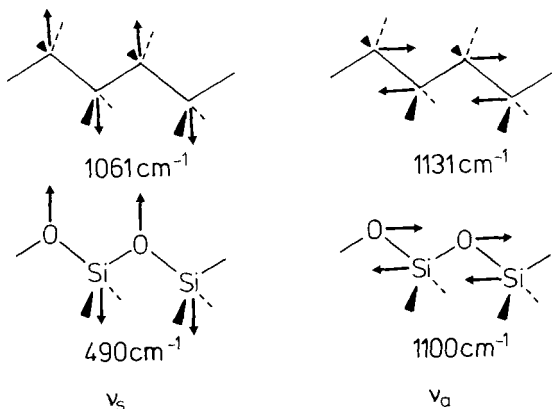


Figure 4.1-3 Symmetric and antisymmetric stretching vibrations of zig-zag chains. In the C–C chain, both vibrations are IR inactive and Raman active (rule of mutual exclusion: at the center of each bond there is a local center of symmetry). As the Si–O–Si chain vibrates, on the other hand, all Si atoms move against all O atoms: both vibrations are IR active. Both vibrations are Raman allowed; ν_s causes the greater polarizability change. The frequencies of these vibrations are affected by the substituents; the listed values correspond to polyethylene and polydimethylsiloxane, respectively (Fig. 4.1-2C).

In the infrared spectrum of polyethylene (Fig. 4.1-2A) this band is split into a doublet at 720 and 731 cm^{-1} . This 'factor group splitting' (Fig. 2.6-1 and Sec. 2.7.6.4) is a result of the interaction between the molecules in crystalline lattice areas. It may be used to investigate the crystallinity of polymers (Drushel and Iddings, 1963; Luongo, 1964). Polyethylene has a unit cell of the factor group D_{2h} (compare Secs. 2.7.5 and 2.7.6.3) which contains a $-\text{CH}_2\text{--CH}_2-$ section of two neighboring chains. Each of these sections has a center of inversion in the middle of the C–C bond (Fig. 4.1-3). Therefore the rule of mutual exclusion (Sec. 2.7.3.4) becomes effective: The vibrations of the C–C bonds cannot be infrared active and further there are no coincidences of vibrational frequencies in the infrared and Raman spectrum of linear polyethylene.

In the Raman spectrum of polyethylene the main peak of the bending vibrations is observed at 1437 cm^{-1} , while a wagging vibration shows a weak band at 1370 cm^{-1} and a twisting vibration gives a strong band at 1295 cm^{-1} . The stretching vibrations of the C–C chain are observed at 1126 and 1059 cm^{-1} , respectively, in the Raman spectrum (Figs. 4.1-2A and 4.1-3). A normal coordinate calculation of polyethylene is published by Tasumi et al. (1962).

Already Kohlrausch (1943) has pointed out that linear paraffines show a Raman band in the range 250 ... 400 cm^{-1} , the frequency of which decreases with increasing length of the chain. Schaufele and Shimanouchi (1967) have demonstrated that this 'longitudinal acoustical vibration' can be observed in the Raman spectra of crystalline linear hydrocarbons as well as in polymers with folded chains.

The infrared spectrum of polyamide (nylon 6), shown in Fig. 4.1-2B, additionally exhibits the typical bands of a secondary amide: an N–H stretching vibration at 3300 cm^{-1}

and three typical bands representing the amide group: the so-called Amide I band at 1640 cm^{-1} , the Amide II band at 1550 cm^{-1} , and the Amide III band at 1250 cm^{-1} . These bands are primarily due to coupling between the C=O and the C–N stretching with the N–H bending coordinate. This nomenclature was introduced because such vibrations usually involve several adjacent bonds (Miyazawa et al., 1956). Of minor importance are the Amide IV and VI bands at 620 and 600 cm^{-1} , respectively, as well as the Amide V band at 700 cm^{-1} , they are assigned to deformations of the C=O and the N–H in the amide group. As demonstrated by the spectrum of nylon 6, the Raman spectrum clearly shows the NH stretching vibration as well as the Amide I and the Amide III band. The amide bands play a leading role in investigations of the conformation of protein molecules (Secs. 4.7 and 6.6).

Fig. 4.1-2C exhibits an –Si–O–Si– chain in the silicone polymer, whose antisymmetric Si–O–Si stretching vibration is represented by a strong band at 1100 cm^{-1} in the IR spectrum, while the symmetric vibration gives rise to a strong Raman band at 490 cm^{-1} (Fig. 4.1-3).

4.1.1.2 Special properties of the spectra of polymers

The examples discussed in the preceding section demonstrate that infrared and Raman spectra of polymers are at first sight quite similar to those of molecules of low molecular weight. Spectra of non-crystalline polymers like poly(methylmethacrylate) resemble those of liquids, while those of polymers of high crystallinity are similar to those of molecular crystals. The characteristic vibrations of the constituents of the chains are visible as well as those of the substituents.

Typical features of the spectra of polymers are the changes introduced when the polymer chains are oriented by strain. When observed with polarized radiation the changing orientation of the molecular chains is visible by pleochromism of the infrared bands or the changes of the polarizability in the Raman spectra. Stress relaxation and the effects of fatigue and fracture may be observed, especially when the spectral subtraction technique is applied. These methods are well described by Siesler and Holland-Moritz (1980). In the 'Atlas of polymer and plastics analysis' by Hummel and Scholl (1991) the methods of polymer analysis are described exhaustively and the spectra of plastic material and its constituents are collected.

4.1.2 C=C vibrations

The vibration of the C=C double bond is observed in the region between 1900 and 1500 cm^{-1} (Table 4.1-2); the bands of isolated double bonds in unstrained chains are found between 1680 and 1640 cm^{-1} .

In "strained" ring systems, such as three-membered rings, however, the unusual position of the $\nu(\text{C}=\text{C})$ is apparently not due to an abnormal bonding condition or "tension". However, there is a strong mechanical vibrational coupling in an X–C=C–X system with

Table 4.1-2 Characteristic frequencies of the C=C bond in cm⁻¹

R = CH ₃ 1648	1669	1681	1672	1658
R = Alkyl 1641	1654	1667	1666	1648
1515	1621	1571	1672	1672
1525	1632	1768	1877	1780
1566	1641	1685	1686	1678
1614	1656	1685	1687	1657
1649	1678	1685	1668	1651
1650	1681	1614	1570	1672

a highly obtuse X-C=C angle. This is confirmed by model calculations which reproduce the observed frequency shifts as a result of mechanical coupling, not of a change of force constants (Takahashi and Schrader, unpublished). If the characteristic frequency of the isolated X-C bonds is higher than that of $\nu(C=C)$, then coupling shifts the $\nu(C=C)$

band to a lower frequency; this effect is particularly apparent in deuterated cyclopropene, where this band shifts to 1525 cm^{-1} . If the isolated $\nu(\text{C}-\text{X})$, however, would have a lower frequency, then $\nu(\text{C}=\text{C})$ shifts to a higher frequency (dimethylcyclopropene: $\nu = 1875\text{ cm}^{-1}$). This resonance repulsion is enhanced as the $\nu(\text{C}-\text{X})$ frequency approaches that of $\nu(\text{C}=\text{C})$.

All $\nu(\text{C}=\text{C})$ vibrations give rise to sharp and narrow Raman bands of high intensity. IR spectra, on the other hand, frequently exhibit comparatively weak $\text{C}=\text{C}$ vibrations. A symmetrical substitution in *trans* position introduces a center of inversion at the center of the $\text{C}=\text{C}$ bond; due to the rule of mutual exclusion (Sec. 2.7.3.4) the $\text{C}=\text{C}$ vibration must then be forbidden in the infrared spectrum.

4.1.3 Conjugated and cumulated $\text{C}=\text{C}$ systems

Conjugation with other unsaturated groups shifts the $\nu(\text{C}=\text{C})$ frequency to lower values, as, for instance, in the spectrum of acrylonitrile (Fig. 4.1-4A). Conjugation of several $\text{C}=\text{C}$ groups results in just as many coupled $\text{C}=\text{C}$ vibrations, which – depending on the symmetry and on the spatial arrangement – may be IR and/or Raman active.

Model calculations have demonstrated that the position of the *in-phase* and the *out-of-phase* $\text{C}=\text{C}$ vibration in a diene exhibit a characteristic dependence on the dihedral angle (Fig. 4.1-5) (Schrader and Ansmann, 1975). The *in-phase* $\text{C}=\text{C}$ vibration in an *s-trans* diene, showing a strong Raman band, is observed at a higher frequency (isoprene, 2-chloro-1,3-butadiene, Figs. 4.1-4B and C) than the *out-of-phase* vibration, which shows a strong infrared band. In the case of *s-cis* dienes (1,3-cyclohexadiene, Fig. 4.1-6A), the strong band in the Raman spectrum, the *in-phase* vibration is found at a lower frequency than the *out-of-phase* vibration, which is represented by a somewhat stronger IR band. These facts are useful for the elucidation of the structure of sterically hindered $\text{C}=\text{C}-\text{C}=\text{C}$ systems in chains or rings.

A similar coupling may be observed for α, β -unsaturated aldehydes and ketones. Table 4.1-3 shows that the *s-cis* or *s-trans* conformation of the $\text{C}=\text{C}-\text{C}=\text{O}$ systems is indicated by the difference of the frequencies of the $\text{C}=\text{O}$ and the $\text{C}=\text{C}$ stretching vibration as well as by its relative intensity in the infrared and the Raman spectrum and the depolarization factor in the Raman spectrum (Oelichmann et al., 1982).

Table 4.1-3 General infrared and Raman characteristics for estimation of the conformation of α, β -unsaturated ketones and aldehydes (Oelichmann et al., 1982)

	s-cis	s-trans
$\Delta\nu = \nu(\text{C}=\text{O}) - \nu(\text{C}=\text{C})$	$> 60 (\approx 68)$	$< 60 (\approx 40)$
Infrared intensity $A_{\text{C}=\text{O}}/A_{\text{C}=\text{C}}$	$< 2.6 (\approx 1.4)$	$> 2.6 (\approx 5.2)$
Raman intensity $I_{\text{C}=\text{O}}/I_{\text{C}=\text{C}}$	$< 0.5 (\approx 0.25)$	$> 0.5 (\approx 0.7)$
Depolarization ratio $\rho(\text{C}=\text{O})$ (Raman)	$> 0.3 (\approx 0.4)$	$< 0.3 (\approx 0.2)$

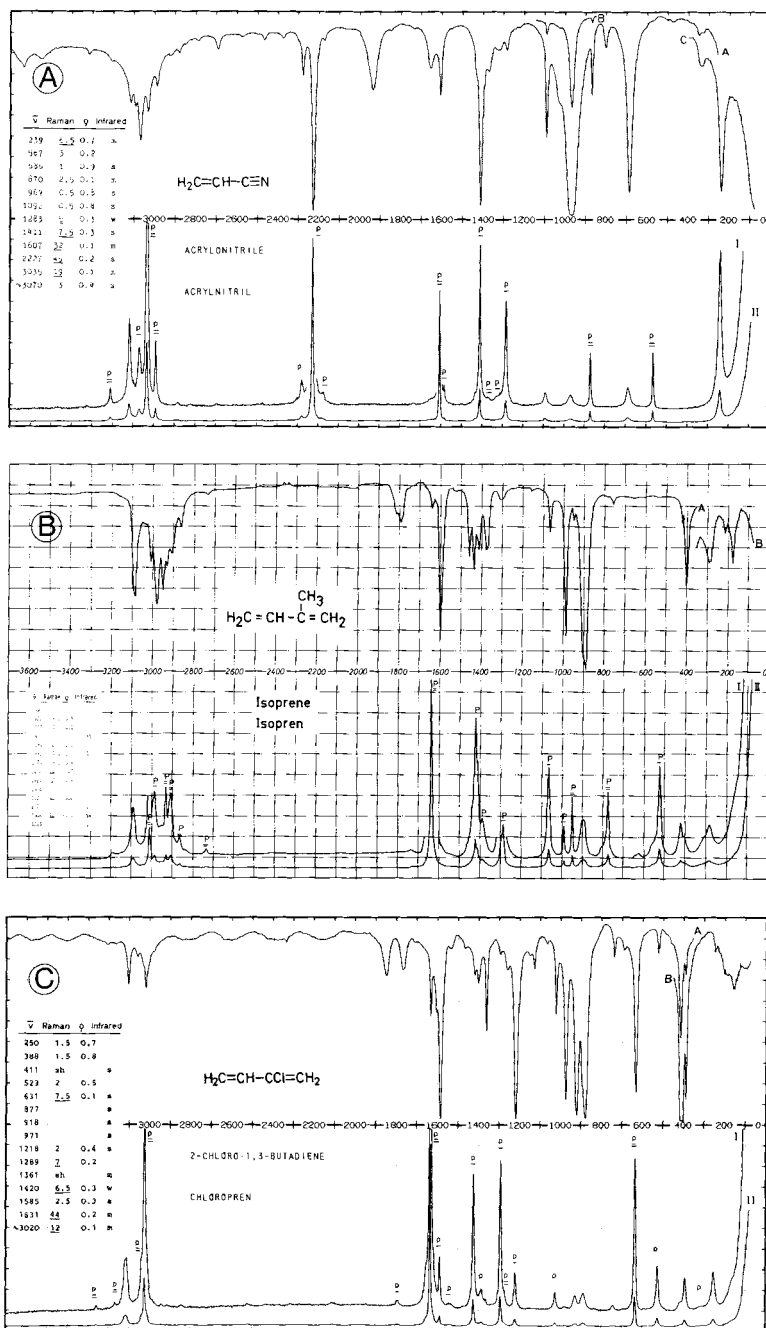


Figure 4.1-4 Vibrational spectra of A acrylonitrile, B isoprene, and C 2-chloro-1,3-butadiene, from Schrader (1989): C3-05, C2-01, and C2-14.

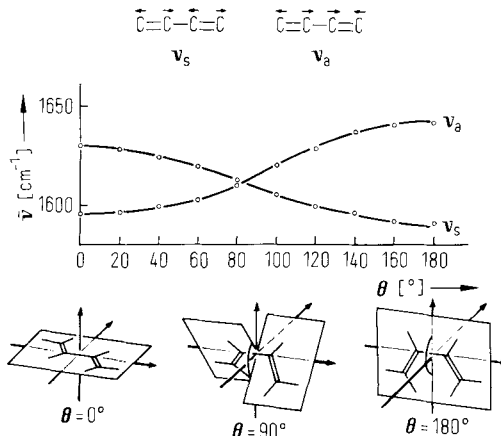


Figure 4.1-5 Pattern of the *in-phase* and the *out-of-phase* vibration, ν_s and ν_a of a conjugated diene during transition from *s-trans* ($\Theta = 0^\circ$) to *s-cis* ($\Theta = 180^\circ$).

Polyenes exhibit two strong Raman bands between 1600 and 1500 cm^{-1} and between 1200 and 1100 cm^{-1} , respectively. These are attributed to *in-phase* vibrations of the $\text{C}=\text{C}$ and $\text{C}-\text{C}$ bonds, respectively, throughout the entire chain. Examples include *all-trans*-retinol (Fig. 4.1-6B), β -carotene, and carotene-containing proteins, obtained, for instance, from lobster shells (Rimai et al., 1973; Oseroff and Callender, 1974). Polyene sequences with approximately twenty conjugated double bonds, formed by HCl elimination from polyvinyl chloride as a result of aging, also show these Raman bands at 1495 and 1115 cm^{-1} (Peitscher and Holtrup, 1975). These bands are enhanced as a consequence of the resonance Raman effect, which makes it possible to detect such groups in polymers and natural materials, even at low concentration.

By analogy with CO_2 , the cumulated $\text{C}=\text{C}=\text{C}$ system of substituted allenes exhibits an *out-of-phase* stretching vibration at about 1950 cm^{-1} and an *in-phase* vibration between 1100 and 1000 cm^{-1} (Fig. 2.5-4). The former gives rise to a strong IR band, while the latter possesses a strong Raman band (Fig. 4.1-6C).

4.1.4 X=Y=Z derivatives

The region around 2200 cm^{-1} exhibits a number of other *out-of-phase* vibrations of $\text{X}=\text{Y}=\text{Z}$ systems, such as allyl isothiocyanates and isocyanates. Depending on the nature of these molecules, the resulting vibrations exhibit strong infrared and/or strong Raman bands (Figs. 4.1-7B and C). This region also shows the stretching vibrations of the $-\text{C}\equiv\text{C}$ and the $-\text{C}\equiv\text{N}$ groups.

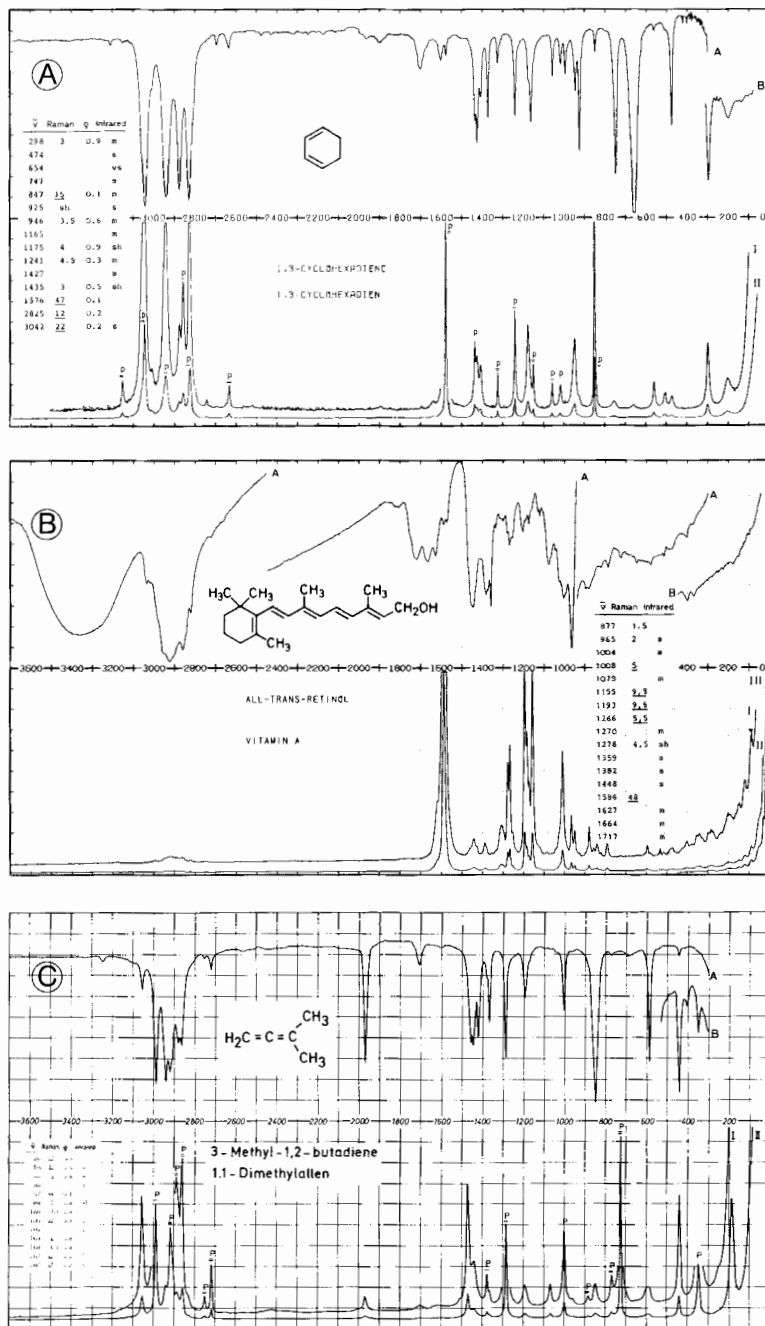


Figure 4.1-6 Vibrational spectra of A 1,3-cyclohexadiene, B all-trans-retinol, and C 3-methyl-1,2-butadiene, from Schrader (1989): E6-04, C4-01, and C5-01.

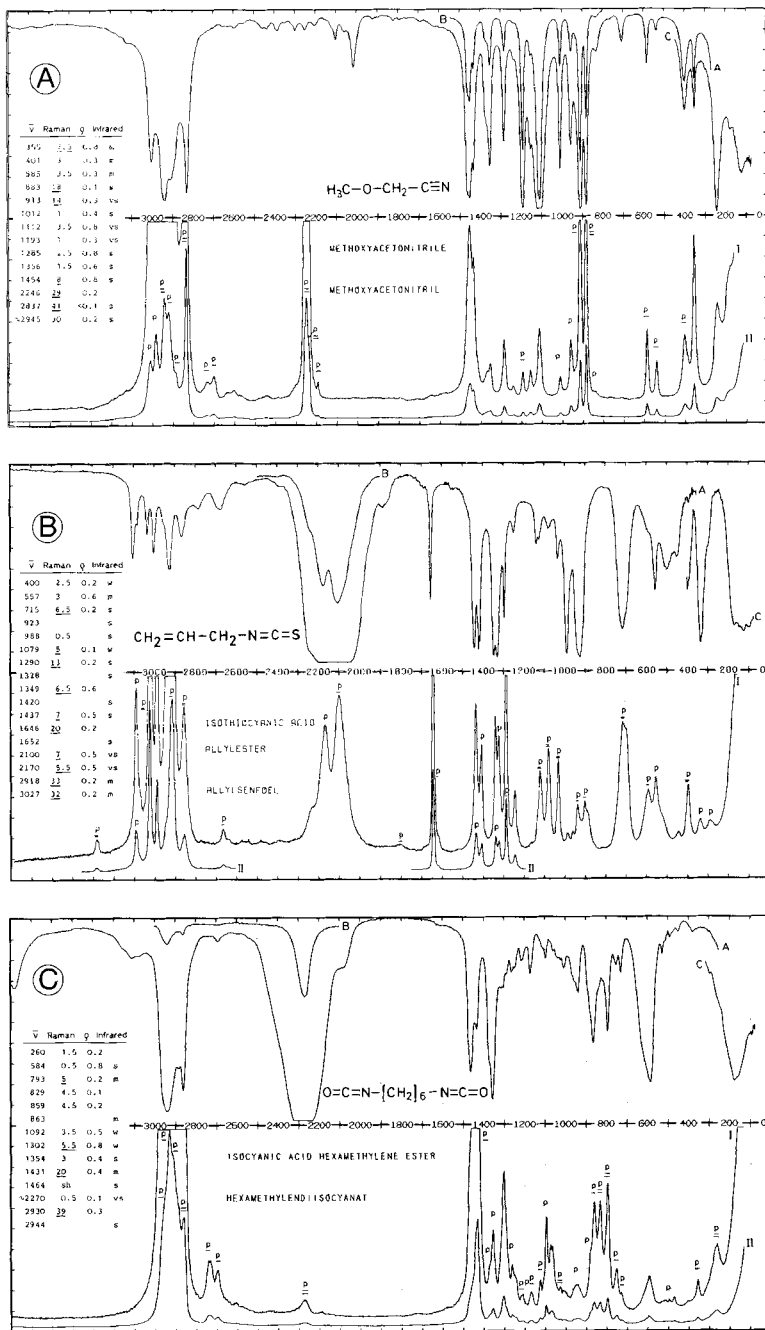


Figure 4.1-7 Vibrational spectra of A methoxyacetonitrile, B allyl isothiocyanate, and C hexamethylene diisocyanate, from Schrader (1989): B9-06, C1-12, and B12-02.

4.1.5 Acetylene derivatives

A terminal $\text{C}\equiv\text{C}-\text{H}$ group is characterized by a $\nu(\text{C}-\text{H})$ vibration at 3300 cm^{-1} (which is quite narrow compared to a $\nu(\text{N}-\text{H})$ band, which occurs in the same range) and by the broad $\delta(\text{C}-\text{H})$ band at 620 cm^{-1} , both of which are strong in the infrared but weaker in the Raman spectrum. A terminal $\text{C}\equiv\text{C}$ group shows a strong $\nu(\text{C}\equiv\text{C})$ Raman band and a weak infrared band at 2100 cm^{-1} (Fig. 4.1-8A). As a result of the inversion center, symmetrically disubstituted $\text{C}\equiv\text{C}$ groups do not exhibit an IR band at 2100 cm^{-1} (Fig. 4.1-8B). If, on the other hand, the $\text{C}-\text{C}\equiv\text{C}-\text{C}$ system is bent, as in cyclooctyne, it does give rise to a weak IR band, as demonstrated in Fig. 4.1-8C. All of these $\text{C}\equiv\text{C}$ stretching vibrations exhibit very strong Raman bands. They are often doubled as a result of resonance with the overtone of the $\text{C}-\text{C}\equiv$ stretching vibration (Fermi resonance, Sec. 2.5.3) and by ‘hot bands’ (Klaeboe et al., 1970). The Raman spectra of alkyl substituted acetylenes show a strong $\delta(\text{C}-\text{C}\equiv)$ band at 340 cm^{-1} (Fig. 4.1-8A, B, C).

The linear iminoboranes, $\text{R}-\text{B}\equiv\text{N}-\text{R}$ behave quite similar as the isoelectronic $\text{R}-\text{C}\equiv\text{C}-\text{R}$ system, the di-tert-butyl derivatives have a stretching frequency of the central bond at 2009 and 2226 cm^{-1} , respectively, with a force constant of the iminoborane being 82% of that of the ethyne (Klaeboe et al., 1985).

4.1.6 Nitriles

The $-\text{C}\equiv\text{N}$ group is represented by a sharp, strong $\nu(\text{C}\equiv\text{N})$ band in the Raman as well as in the IR spectrum, as shown in Fig. 4.1-4A. Electronegative substitution makes the $\nu(\text{C}\equiv\text{N})$ IR band so weak that it may be no longer recognizable in the IR spectrum itself (Fig. 4.1-7A). The corresponding Raman band, on the other hand, is always strong.

4.1.7 Saturated isocycles

Open-chain molecules may have different conformations; rotation around single bonds shifts several bands. As a consequence, the observed spectra exhibit relatively broad bands resulting from overlapping of the spectra of the conformational isomers. In ring systems, on the other hand, free rotation is largely inhibited or at least limited. The resulting IR and Raman spectra thus show very narrow bands. The number of bands increases as the size of the molecules increases and the symmetry is reduced (Figs. 4.1-9, 4.1-13, 4.1-19).

Raman spectra of saturated unsubstituted carbocycles exhibit not only bands which are typical of CH_2 groups, but also bands representing characteristic *in-phase* vibrations of $\text{C}-\text{C}$ bonds: cyclopropane at 1188 cm^{-1} (Fig. 4.1-10), cyclobutane at 1001 cm^{-1} , cyclopentane at 886 cm^{-1} , and cyclohexane at 802 cm^{-1} . These vibrations are also found in many substituted ring systems: C_3 between 1220 and 1200 cm^{-1} , C_4 between 930 and 850 cm^{-1} , C_5 between 810 and 800 cm^{-1} , and C_6 between 800 and 700 cm^{-1} .

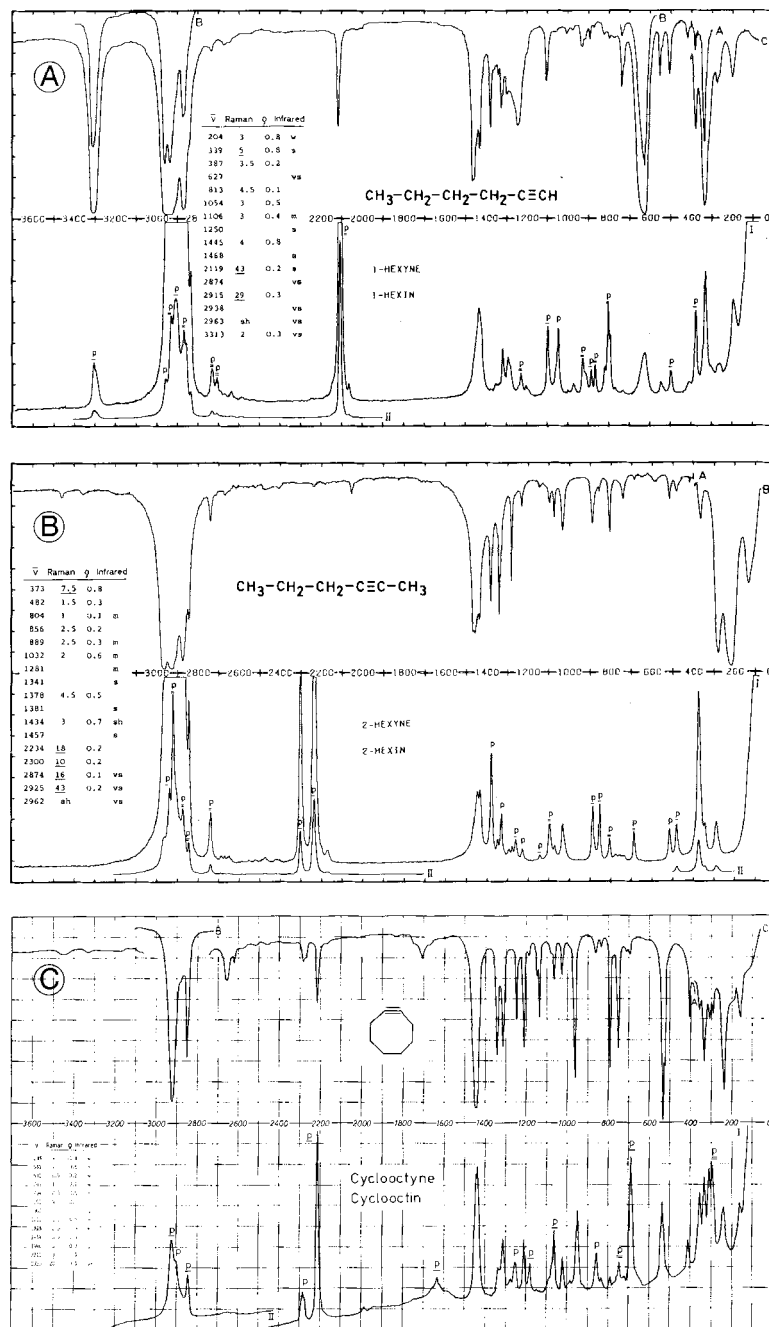


Figure 4.1-8 Vibrational spectra of A 1-hexyne, B 2-hexyne, and C cyclooctyne, from Schrader (1989): D1-03, D1-04, and E10-10.

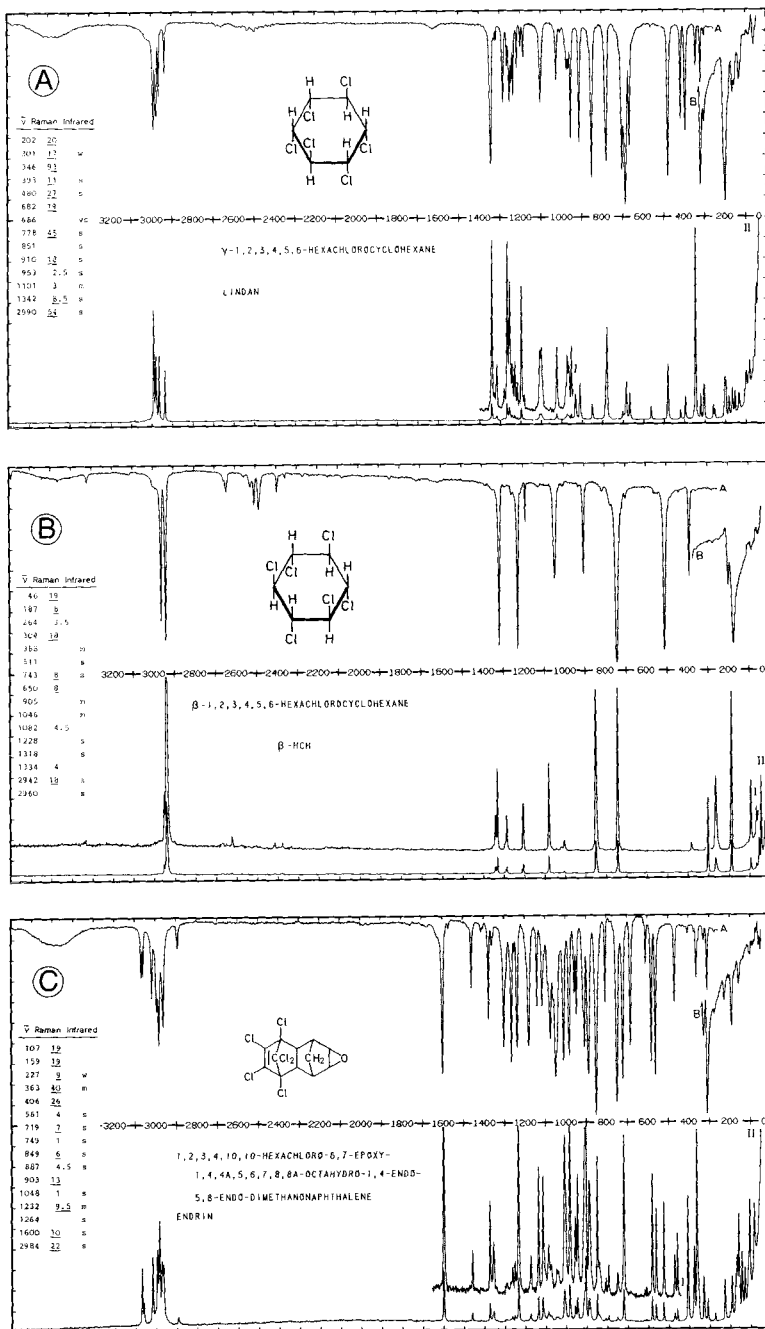


Figure 4.1-9 Vibrational spectra of A γ-, B β-1,2,3,4,5,6-hexachlorocyclohexane, and C endrin, from Schrader (1989): E1-18, E1-19, and J1-23.

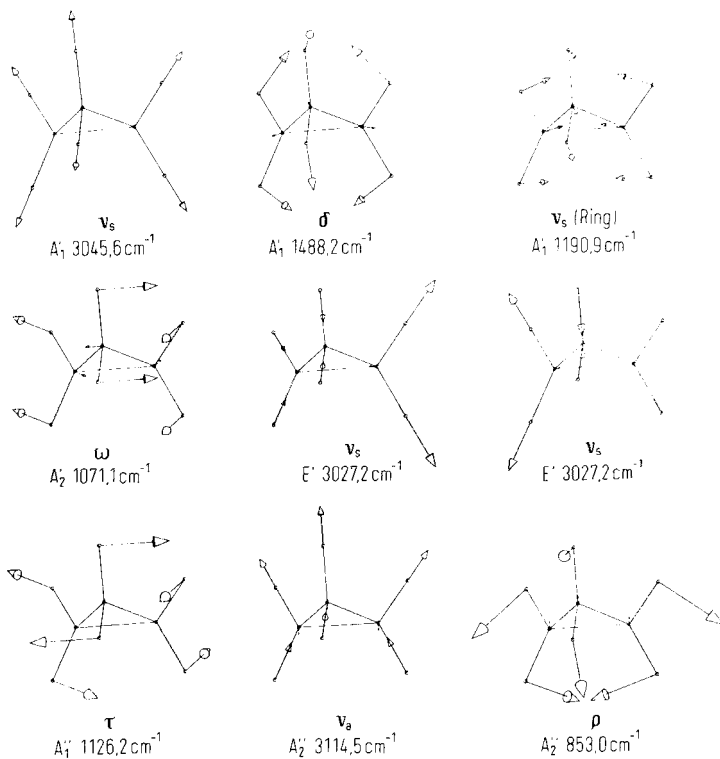


Figure 4.1-10 Typical normal vibrations of cyclopropane. The length of the vector arrow and the diameter of its head are proportional to the amplitude. The name of the characteristic vibrations, the vibrational species of the point group D_{3h} and the calculated frequencies are given (Spiekermann et al., 1980).

The γ isomer of 1,2,3,4,5,6-hexachlorocyclohexane (Fig. 4.1-9A), an insecticide, gives rise to a large number of sharp bands which have the same IR and Raman frequencies. The β isomer (Fig. 4.1-9B), on the other hand, exhibits fewer bands and shows no bands which coincide in the IR and the Raman spectrum. This confirms its structure, which possesses a center of symmetry (rule of mutual exclusion). The insecticide endrine, too, shows a complicated pattern of bands, but due to the low symmetry the IR and Raman spectrum coincide to a large extent (Fig. 4.1-9 C).

4.1.8 Dependence of the C-halogen vibrations on the constitution, the configuration, and the conformation

In the region between 900 and 500 cm^{-1} , the spectra shown in Figs. 4.1-9 and 4.1-11 exhibit a number of bands whose frequencies as well as IR and Raman intensities are determined by the number and the relative orientation of C–Cl bonds. There are several

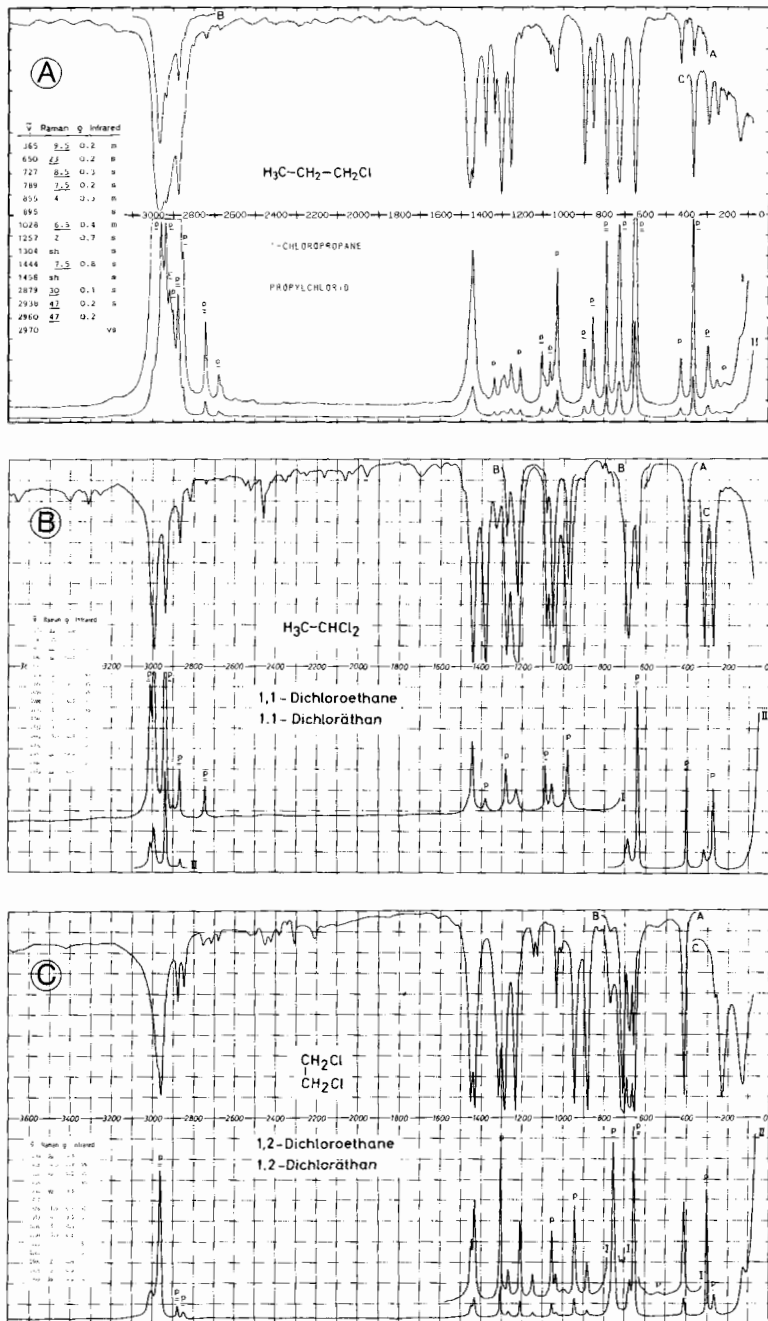


Figure 4.1-11 Vibrational spectra of A chloropropane, B 1,1- dichloroethane, and C 1,2- dichloroethane, from Schrader (1989): A2-60, A2-13, and A2-18.

mechanisms which contribute to this phenomenon, they are discussed by Kohlrausch, 1943; Mizushima et al., 1956; Dollish et al., 1974; Bellamy, 1975; Schrader and Meier, 1975; Colthup et al., 1990; and Lin-Vien et al., 1991.

One halogen atom located in a molecule which does not possess conformational isomers gives rise to one C–X vibration, with high intensity both in the IR and in the Raman spectrum (Fig. 2.6-1A, methyl bromide).

Fig. 4.1-12 shows the position of the characteristic vibration of a C–X bond with X=Cl, Br, or I, dependent on the nature of the carbon atom and the atom in *antiperiplanar* (*ap*) position relative to the C–X moiety. The nature of the C atom is given by P, S, and T for primary, secondary, and tertiary, respectively, as subscripts the atoms in *ap* position are denoted (Mizushima et al., 1956). In the conformer of 1-chloropropane (Fig. 4.1-11A) which has a C atom in the *ap* position (P_C in Fig. 4.1-12), the C–Cl vibration is found at 727 cm⁻¹, while the conformer with a hydrogen atom in the *ap* position (P_H) shows a band at 650 cm⁻¹. Cyclohexane derivatives show corresponding bands: an axial C–Cl (S_{H'H'}) is observed at 688 cm⁻¹, equatorial C–Cl (S_{CC}) at 733 cm⁻¹. The position of the conformational equilibrium determines the relative intensities of these two bands, which are strong both in the Raman and in the IR spectrum.

If two halogen atoms are located on the same C atom, then the two C–X bonds of the CX₂ group show an *in-phase* vibration as well as an *out-of-phase* vibration. The former gives rise to a low frequency band which is stronger in the Raman spectrum, while the latter, which is observed at higher frequency, is represented more strongly in the IR spectrum. Fig. 2.6-1B shows the corresponding methylene chloride bands at 704 and 742 cm⁻¹, while Fig. 4.1-11B exhibits those of 1,1-dichloroethane at 642 and 691 cm⁻¹, respectively.

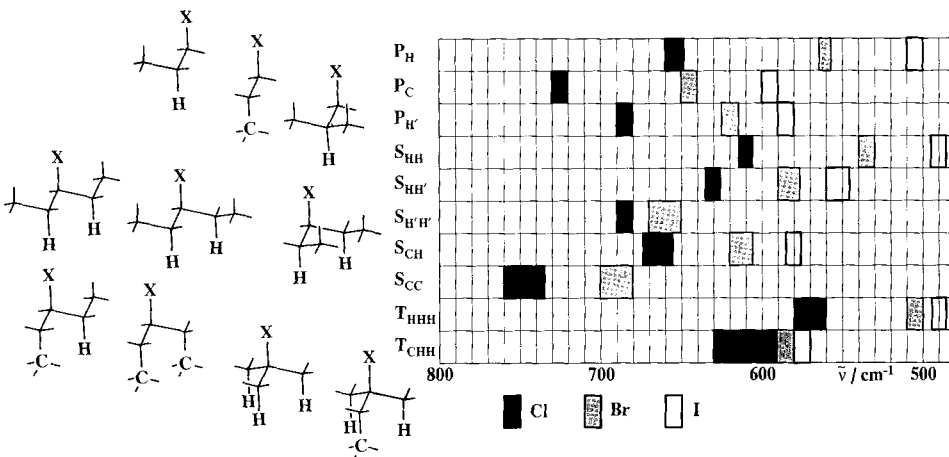


Figure 4.1-12 Characteristic frequencies of C–X bonds (X = Cl, Br, I) in hydrocarbons; P primary, S secondary, T tertiary C atom, the subscripts denote the atoms in *trans* (*antiperiplanar*) position to the C–X bond. For cyclohexane derivatives S_{H'H'} stands for an axial, S_{CC} for an equatorial C–X bond (Schrader and Meier, 1975).

As demonstrated by the spectra of 1,2-dichloroethane shown in Fig. 4.1-11C, two halogen atoms in 1,2-position also show *in-phase* as well as *out-of-phase* vibrations. The *antiperiplanar* conformation is subject to the exclusion rule: ν_s : Raman 750 cm⁻¹; ν_a : IR 708 cm⁻¹. In the case of the *synclinal* conformation, on the other hand, the *in-phase* vibration at 645 cm⁻¹ is stronger both in the IR and in the Raman spectrum than the *out-of-phase* vibration at 677 cm⁻¹. Freely rotating 1,2-dihalogen compounds therefore show four different C-Cl stretching vibrations (Fig. 4.1-11C).

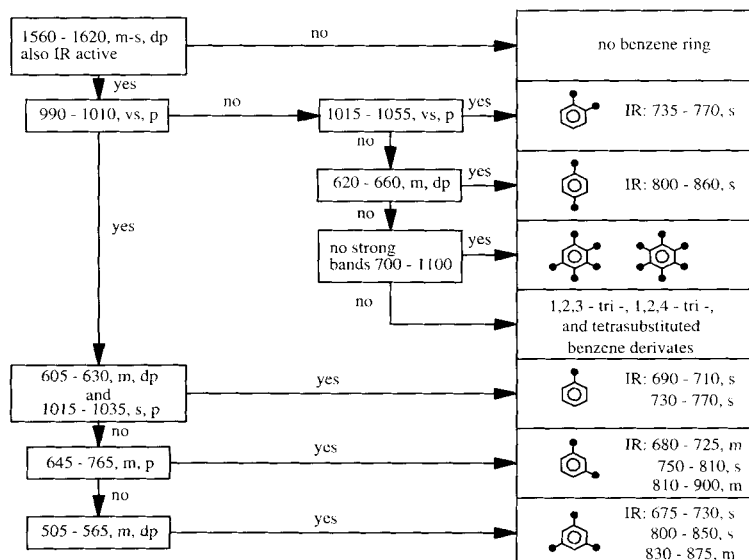
All conformational equilibria are dependent on the temperature and the medium: Klaeboe et al., 1957; Klaeboe and Nielsen, 1960.

4.1.9 The substitution pattern of benzene derivatives

The benzene ring shows a number of stretching and bending vibrations whose frequencies and intensities depend on the types and positions of the substituents.

Schrader and Meier (1972) have demonstrated that in this case, too, joint interpretation of Raman and IR spectra leads to more reliable conclusions concerning the substitution pattern than does evaluation of only one type of spectrum. Table 4.1-4 shows an algorithm which is meant to facilitate the determination of the substitution pattern.

Table 4.1-4 Diagram for the determination of the substitution pattern of benzene derivatives by characteristic Raman bands; intensity: m medium, s strong, vs very strong; degree of polarization: p highly polarized, dp depolarized, IR stands for characteristic IR band



In the region around 1600 cm^{-1} , all benzene derivatives exhibit IR as well as Raman bands of medium intensity due to *out-of-phase* stretching vibrations of the ring (compare Fig. 4.1-13). Occasionally, these bands may overlap with $-\text{NH}_2$ deformation vibrations. The absence of bands in the region around 1620 to 1560 cm^{-1} both in the IR and the Raman spectrum very likely points to the absence of benzene rings. Further interpretation is based on the Raman bands around 1000 cm^{-1} representing combined stretching and deformation vibrations of the ring atoms, together with those of bending vibrations observed at lower frequencies. *Mono* substitution is characterized by a pair of bands at 1000 and 1030 cm^{-1} (Fig. 4.1-13A). In the case of *meta di* substitution, the band at 1030 is not observed (Fig. 4.1-13B), while *ortho di* substitution results in a very strong band between 1055 and 1015 cm^{-1} ; *para di* substitution finally is characterized by the absence of a strong band in the region around 1000 cm^{-1} (Fig. 4.1-13C). In Table 4.1-4 other significant Raman bands as well as IR bands are included which may be used to confirm the interpretation of the spectra.

The characteristic pattern of overtone bands and combination vibrations between 2000 and 1660 cm^{-1} in the IR spectra of alkyl substituted benzene derivatives as well as the *out-of-plane* deformation vibrations of the hydrogen atoms in the IR spectra are frequently less reliable as indicators of the substitution pattern, especially in the presence of polar substituents, in which case their position tends to shift, and they often overlap with bands of substituents.

4.1.10 The ether moiety

The C–O–C group exhibits an *in-phase* and an *out-of-phase* stretching vibration. The *out-of-phase* vibration gives rise to a very strong IR band at 1060 to 1150 cm^{-1} , while the *in-phase* vibration, which is observed between 970 and 800 cm^{-1} , shows only weak bands. The relatively high frequency of the CH_2 bending vibrations at 1470 to 1480 cm^{-1} , which appears especially in the IR spectrum, is characteristic of ethers (Fig. 4.1-14A).

4.1.11 $\text{CH}_3\text{-X}$ groups

Methoxy groups and other X– CH_3 groups are easily characterized by the considerable dependence of the symmetric deformation vibration of the CH_3 group on the X atom.

Table 4.1-5 Frequencies of the symmetric CH_3 bending vibration of $\text{CH}_3\text{-X}$ groups with different X atoms, in cm^{-1}

	B	1310	C	1380	N	1410	O	1445	F	1475
			Si	1256	P	1295	S	1310	Cl	1355
Zn 1185			Ge	1235	As	1250	Se	1282	Br	1305
Cd 1129			Sn	1190	Sb	1200			I	1252
Hg 1205			Pb	1165	Bi	1160				

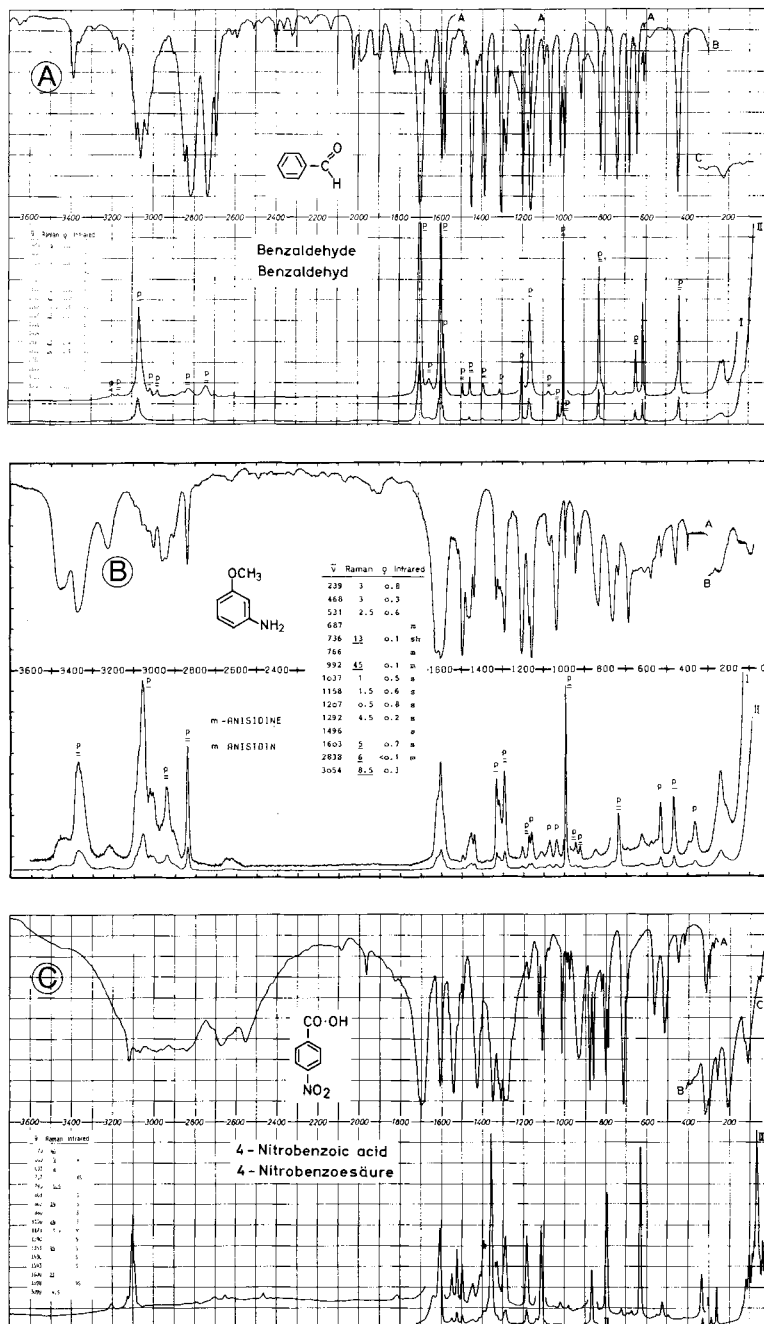


Figure 4.1-13 Vibrational spectra of A benzaldehyde, B *m*-anisidine, and C *p*-nitrobenzoic acid, from Schrader (1989): F1-14, F4-19, and F5-07.

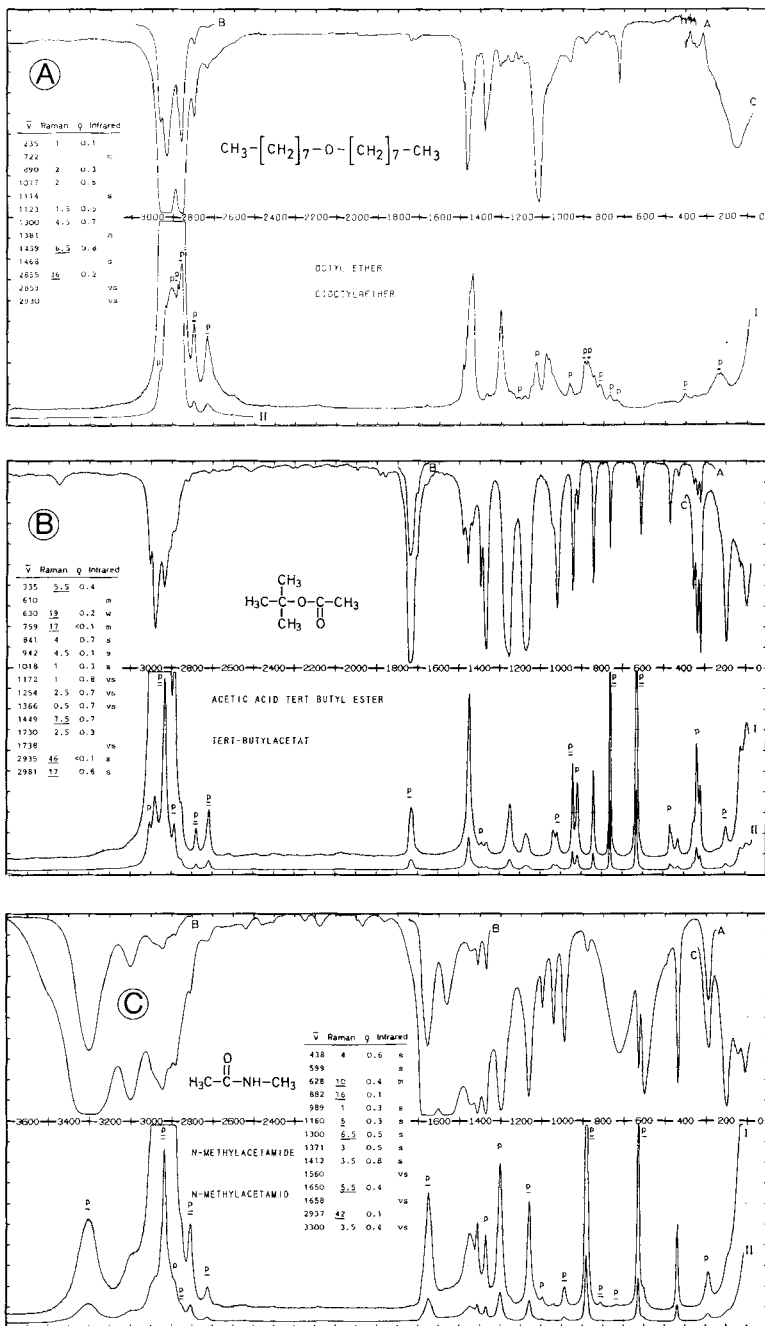


Figure 4.1-14 Vibrational spectra of A octyl ether, B acetic acid tert butyl ester, and C N-methylacetamide, from Schrader (1989): A4-05, B4-25, and B6-08.

This is a consequence of variation of the mass of X, the C–X stretching force constant, and the X–C–H deformation force constant. Table 4.1-5 shows the variation of this vibration with the position of the X atom within the periodic system. Colthup (1980) describes model calculations by the CNDO/2 method which explain this behavior.

The symmetric deformation vibration is represented by a medium to strong IR as well as Raman band. Examples of this vibration are shown in the following figures of this section:

N–CH₃: Fig. 4.1-14C; O–CH₃: Figs. 4.1-7A, 4.1-13B, 4.1-19B;

Si–CH₃: Fig. 4.1-2C; S–CH₃: Figs. 4.1-16C, 4.1-18A, B, C;

Br–CH₃: Fig. 2.6-1A (Sec. 2.6).

An additional feature especially for the recognition of O–CH₃ and N–CH₃ groups consists in relatively strong and sharp bands at 2830 cm⁻¹ and around 2800 cm⁻¹ in the IR and Raman spectra.

The symmetric CH₃ deformation vibration of C–CH₃ groups is normally observed at 1380 cm⁻¹. This vibration usually gives rise to an IR band of medium intensity, while the corresponding Raman band tends to be weak. If, however, the CH₃ group is a substituent of an unsaturated carbon atom, then the Raman spectrum also exhibits a band of medium intensity (Figs. 4.1-4B, 4.1-6B, 4.1-8B, 4.1-19A). If there are several CH₃ groups located on one carbon atom, then this deformation vibration is split by coupling (Figs. 4.1-6B, 4.1-14B, 4.1-16B). Isopropyl and tert-butyl groups are recognized in this way (Colthup, 1980).

4.1.12 The carbonyl group in different environments

The carbonyl group exhibits a very strong IR band and a medium to strong Raman band in the region between 1850 and 1650 cm⁻¹. Table 4.1-6 shows the position of the carbonyl frequency under the constraints of mesomeric, inductive, and geometric effects as well as dynamical interactions. A number of simultaneously present bands helps to characterize the nature of the C=O group:

<i>Aldehyde</i>	(Fig. 4.1-13A): 2820, 2720 cm ⁻¹ , both in the IR and the Raman spectrum.
<i>Carboxylic acid</i>	(Figs. 4.1-13C, 4.1-15A): 3500 – 2500 cm ⁻¹ , broad band only in the IR; 1420, 1320 – 1200 cm ⁻¹ , dimers of carboxylic acids: broad IR band at 920 cm ⁻¹ .
<i>Carboxylic acid esters</i>	(Fig. 4.1-14B): two very strong IR bands in the region between 1300 and 1050 cm ⁻¹ .
<i>Carboxylic acid anhydride</i>	(Fig. 4.1-15C): two bands at 1820 and 1760 cm ⁻¹ , respectively, one or two strong IR bands at 1300 – 1000 cm ⁻¹ .
<i>Carboxylic acid chloride</i>	(Fig. 4.1-15B): strong C–Cl vibration at 600 cm ⁻¹ (IR and Raman).
<i>Carboxylic acid amide</i>	see Figs. 4.1-2B and 4.1-14C and Sec. 4.1.1.

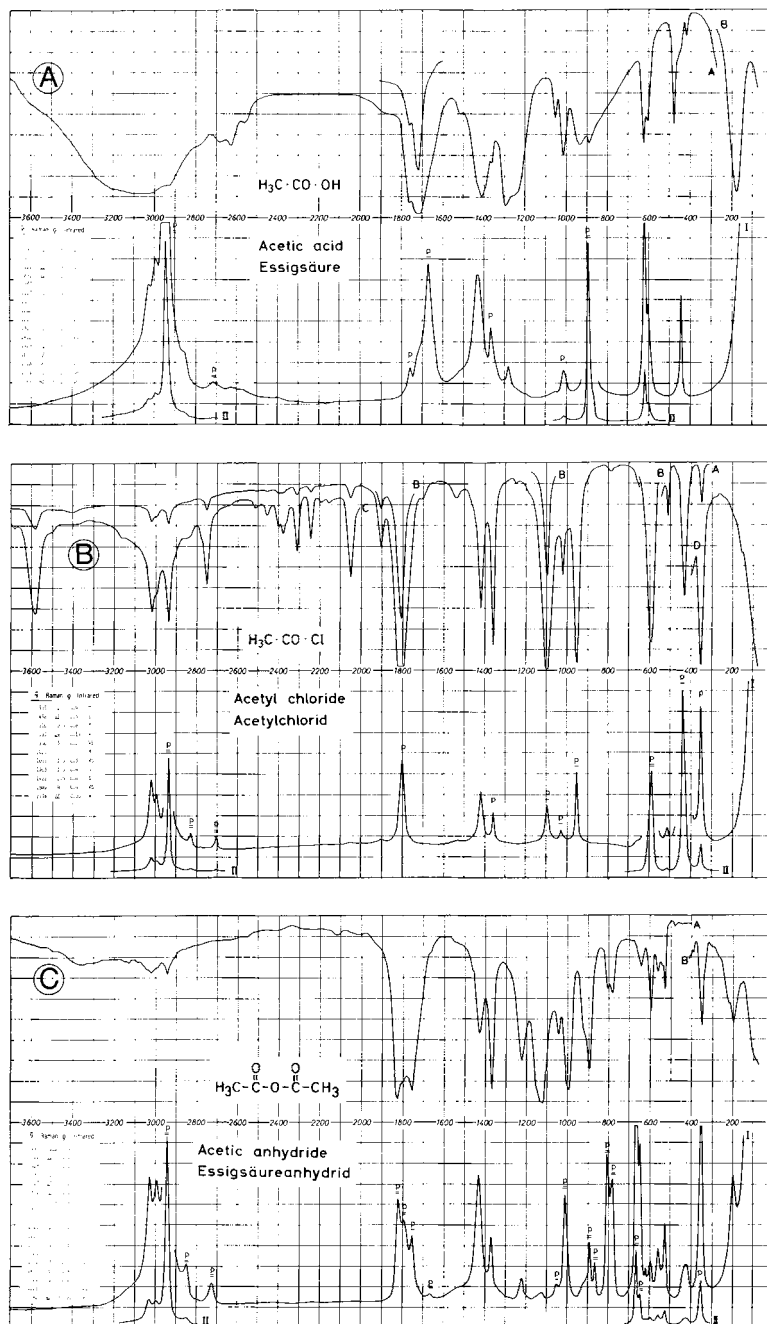


Figure 4.1-15 Vibrational spectra of A acetic acid, B acetyl chloride, and C acetic anhydride, from Schrader (1989): B3-05, B6-02, and B5-01.

Table 4.1-6 Characteristic frequencies of carbonyl derivatives X-CO-Y in a condensed undiluted phase, in cm^{-1}

$\begin{array}{c} \text{Y} = \\ \diagdown \end{array}$ $\begin{array}{c} \text{X} = \\ \diagup \end{array}$	$-\text{O}^- \ominus$	$-\text{NR}_2$	$-\text{NHR}$	$-\text{NH}_2$	$-\text{C}=\text{C}-$	$-\text{C}_6\text{H}_5$	$-\text{SR}$	$-\text{R}$	$-\text{H}$	$-\text{OH}$	$-\text{OR}$	$-\text{O}-\text{C}=\text{C}-$	$-\text{Cl}$	$\begin{array}{c} \text{O} \\ \parallel \\ -\text{O}-\text{C}-\text{R} \end{array}$
$-\text{C}\equiv\text{C}-$	—	—	—	—	—	(1643)	—	1675	1692	(1690)	1718	—	—	—
$-\text{C}=\text{C}-$	1545	—	1653	1663	1660	1699	—	trans: 1670 cis: 1700	1700	1705	1720	—	1748	1778 1721
C_6H_5-	1552 1434	1639 (1529)	(1651) 1671	1663	1699	1667	1653	1693	1710	1695 1632*	1717	1730	1774 1731	1778 1720
	—	—	1628	1658	—	1665	—	1684	—	1689 1645*	1723	1748	—	1767 1710
$\text{H}_3\text{C}-$	1583 1421	1640	1655 1555	1679 1625	trans: 1674 cis: 1693	1687	1692	1722	1715	1715 1675*	1740	1763	1806	1825* 1756
R-	1565 1429	1638	1640 1540	1670 1637	trans: 1670 cis: 1700	1693	1690	1716	1725	1722 1652*	1735	1742	1790	1805* 1745
H-	1603 1365	1670 1502	1666 1525	1690 1610	1700	1710	—	1738	(1746)	1754 1654*	1720	1727	—	—
$\text{Cl}_3\text{C}-$	1655	—	—	1699	—	1718	—	1767	1768	1742 1687*	1769	—	1803	—
$\text{F}_3\text{C}-$	1689 1448	—	1727 1711	1703 1626	—	1721	—	1761	1770	1785 1770	1789	1800	1810	1880 1812
	—	1658	—	—	—	—	1699	—	—	1713	—	—	—	—
	—	1639	1653	—	1684	—	—	1709	—	—	1730	—	—	1818 1772
	—	1689	1690	—	1716	—	—	1744	—	—	1770	—	—	1854 1782
	—	—	—	—	—	—	—	1782	—	—	1830	—	—	—

* Raman band

Amino acid

(Figs. 4.1-17A, B, C): both the amino group and the carboxyl group of crystalline amino acids are zwitter ions. The carboxylate ion give rise to two strong bands, one between 1610 and 1550, and another one at 1400 cm^{-1} , respectively. The ammonium group is represented by a broad band in the region between 3200 and 2200 cm^{-1} and also by a band around 1590 to 1500 cm^{-1} .

4.1.13 Azo compounds, peroxides, disulfides

The IR spectra of molecules containing C–X–X–C and C–Y=Y–C moieties only exhibit a weak band representing the vibration of the central bond if this center is asymmetrically substituted or if the substituents of the central bond are not arranged in *trans* position.

The Raman spectra of all aliphatic azo compounds, on the other hand, show a medium to weak N=N stretching vibration at 1570 cm^{-1} (Fig. 4.1-16A). In the spectra of azo compounds with mixed aliphatic and aromatic substitution this vibration is observed at 1520 cm^{-1} , and aromatic azo compounds give rise to a band at about 1425 cm^{-1} .

Peroxides, too, are Raman active; they exhibit a band at 860 cm^{-1} (Fig. 4.1-16B). Disulfides are characterized by the very strong Raman band of the S–S stretching vibration at 500 cm^{-1} (Figs. 4.1-16C, 4.1-17C). This band, together with the $\nu(\text{C–S})$ vibration at 500 – 750 cm^{-1} , strong in the Raman spectrum, is employed to elucidate the conformation of disulfide bridges in proteins (Lord, 1977).

4.1.14 R–SO_n–R and R–SH groups

The S–H stretching vibration gives rise to a sharp, strong Raman band at 2500 cm^{-1} (Fig. 4.1-17B). All compounds containing C–S bonds exhibit corresponding stretching vibrations represented by a weak IR band but by a strong Raman band between 500 and 750 cm^{-1} (Figs. 4.1-17B, C; Figs. 4.1-18A, B, C).

The SO stretching vibration in sulfoxides is observed between 1070 and 1020 cm^{-1} (Fig. 4.1-18B). Sulfones show an antisymmetric vibration at 1350 to 1300 cm^{-1} and a symmetric one at 1160 to 1120 cm^{-1} (Fig. 4.1-18C). Both bands are strong in the IR, but only the symmetric one gives rise to a strong Raman band.

4.1.15 Nitro groups

Nitro groups show a spectral pattern which is similar to that of sulfo groups. The antisymmetric (*out-of-phase*) stretching vibration of the N–O bonds gives rise to a strong IR band between 1590 and 1530 cm^{-1} . The symmetric (*in-phase*) stretching vibration of the NO₂ group exhibits a strong IR band and a very strong Raman band at 1380 to 1340 cm^{-1} . Aromatic nitro compounds show this band at lower (Fig. 4.1-13C) aliphatic nitro compounds at higher frequencies.

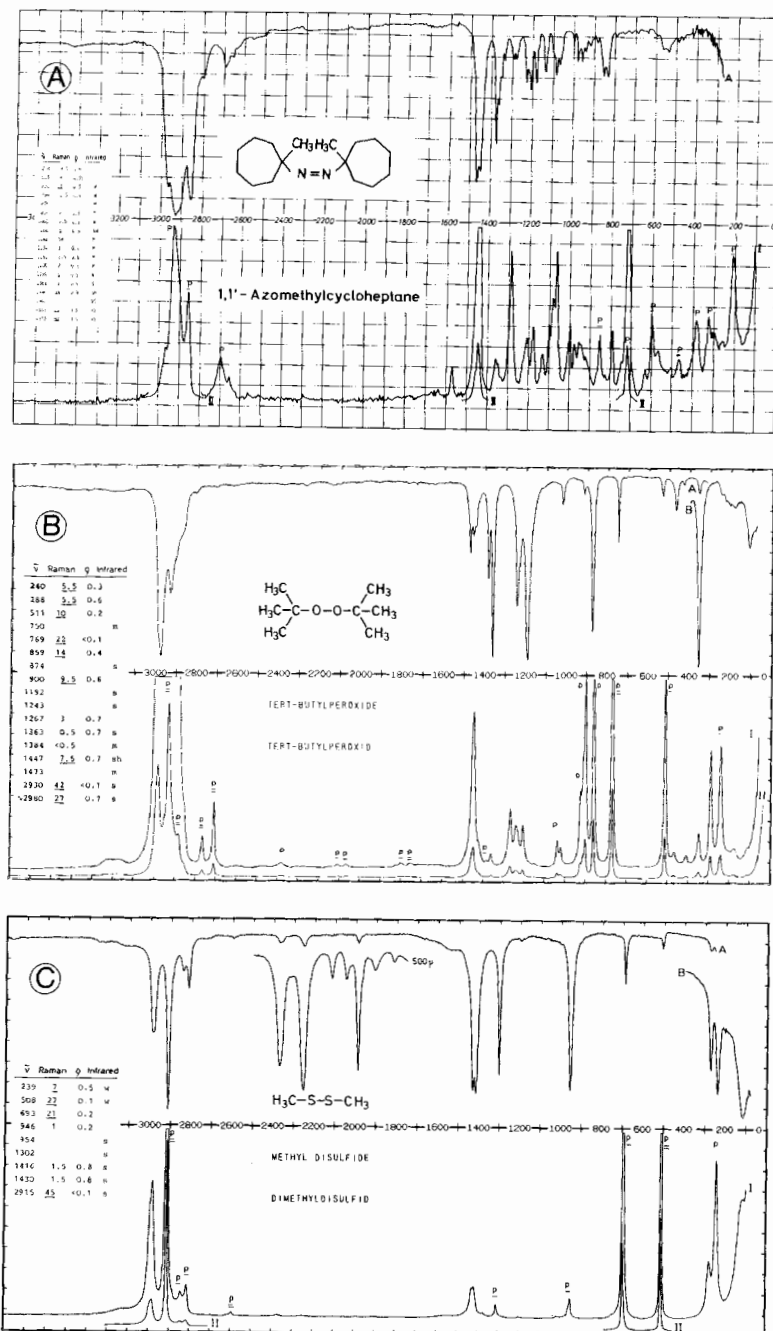


Figure 4.1-16 Vibrational spectra of A 1,1'-azomethylcycloheptane, B tert-butylperoxide, and C methyl disulfide, from Schrader (1989): E5-02, A6-01, and A11-03.

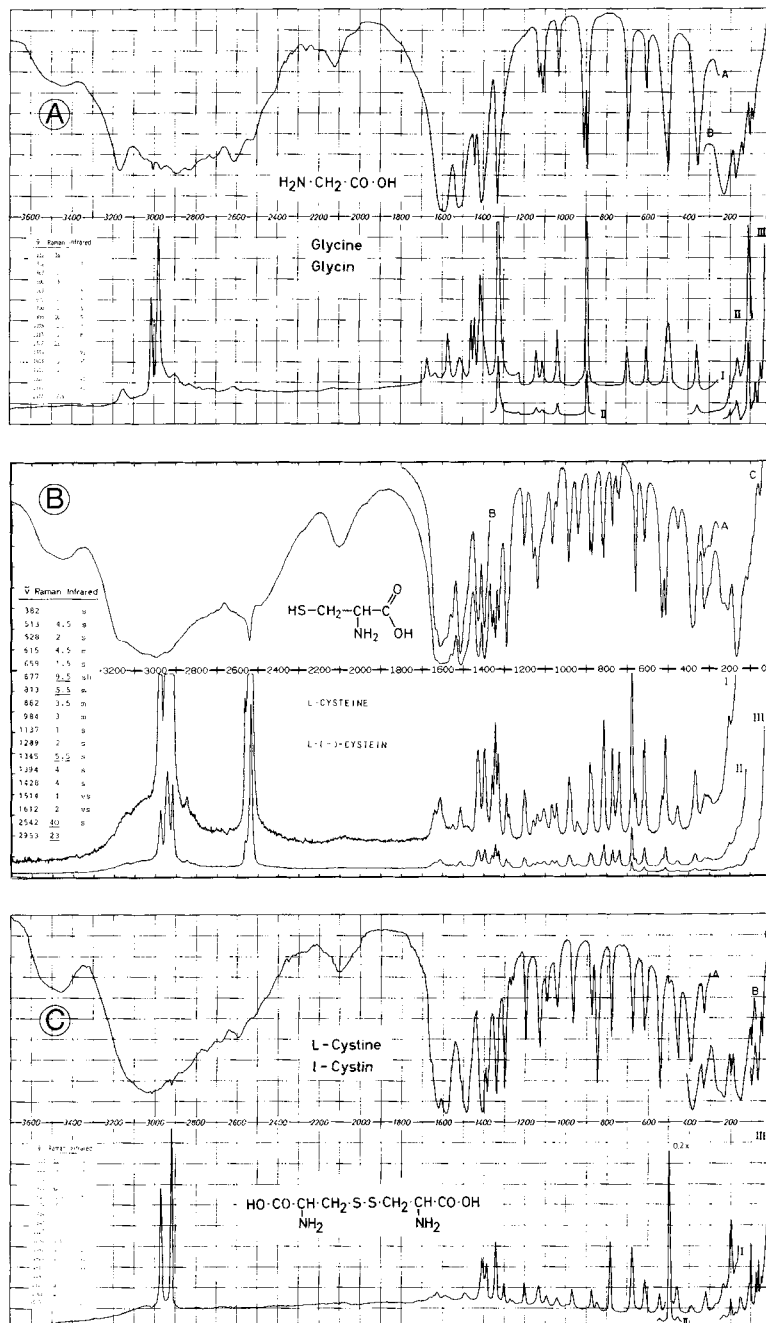


Figure 4.1-17 Vibrational spectra of A glycine, B L-cysteine, and C L-cystine, from Schrader (1989): B7-02, B7-05, and B7-01.

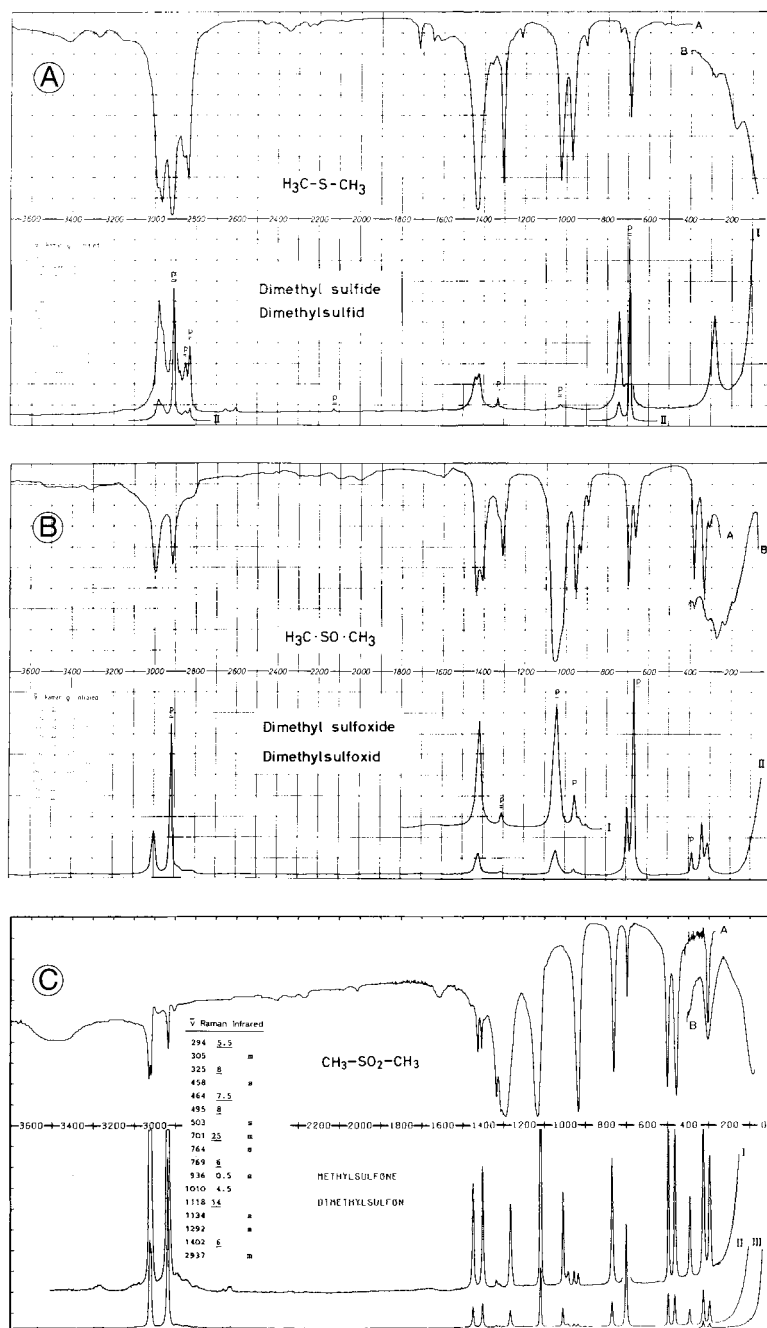


Figure 4.1-18 Vibrational spectra of A dimethyl sulfide, B dimethyl sulfoxide, and C methylsulfone, from Schrader (1989): A10-01, B13-01, and B13-03.

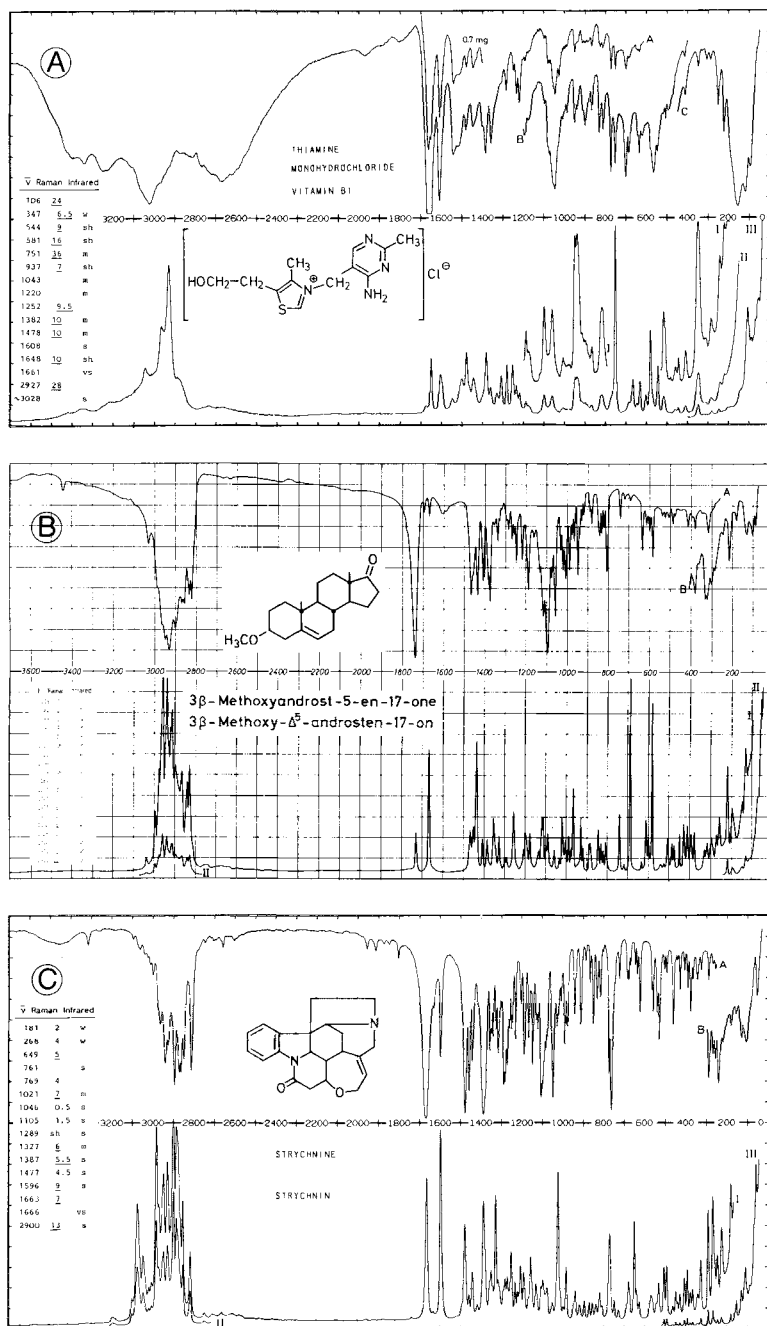


Figure 4.1-19 Vibrational spectra of A thiamine, B 3 β -methoxyandrost-5-en-17-one, and C strychnine, from Schrader (1989): J8-11, L-04, and J8-08.

4.1.16 Substances of biological interest

Joint interpretation of the IR and Raman spectra of biomolecules, which frequently lack symmetry properties, may afford more extensive information concerning the primary, secondary and tertiary structure, than does the interpretation of one type of spectrum only. Many systems can only be investigated in aqueous solution, a good solvent for Raman spectroscopy. The technique of resonance Raman spectroscopy facilitates investigations of pigments and the NIR FT Raman spectroscopy allows the investigation of nearly all samples which has not been possible before due to absorption and fluorescence. Spectra of biomolecules are exhaustively discussed in Sec. 4.7. Here only some general features are discussed.

Fig. 4.1-19 shows spectra of crystalline natural substances. The spectrum of thiamine, shown in Fig. 4.1-19A, exhibits a number of the already mentioned bands: OH, NH₂, aromatic and aliphatic C-H groups, vibrations of aromatic rings and of the CH₃ group on aromatic rings.

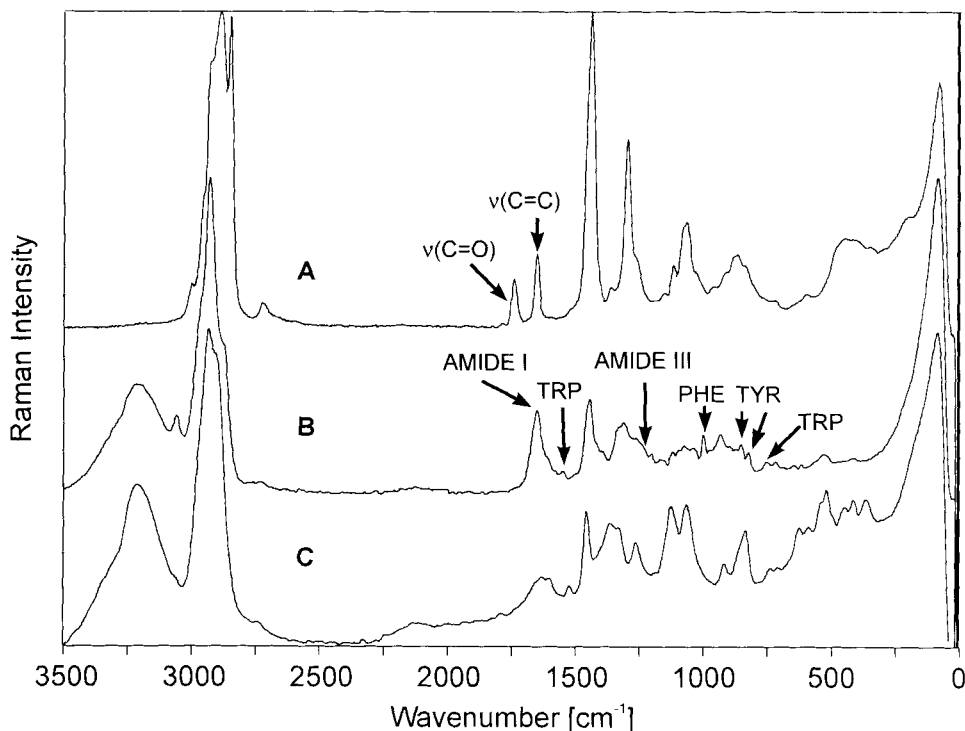


Figure 4.1-20 NIR FT Raman spectra of food ($\lambda_O = 1064$ nm, $\Delta\tilde{\nu} = 4 \text{ cm}^{-1}$): A butter, showing a typical spectrum of a fat (15 min, 270 mW); B turkey breast, a typical protein spectrum (60 min, 270 mW); C banana, a typical carbohydrate spectrum (60 min, 550 mW), from Keller et al., 1993.

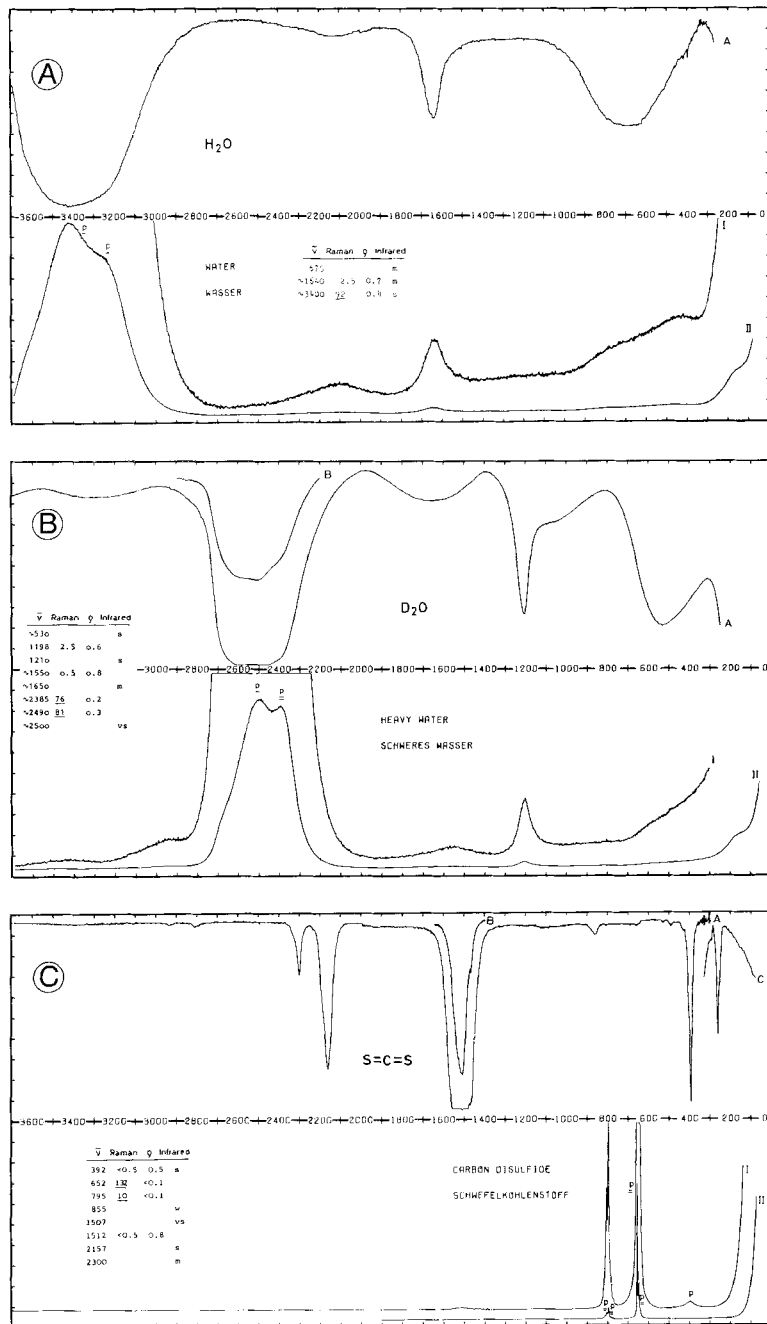


Figure 4.1-21 Vibrational spectra of A H_2O , B D_2O , and C CS_2 , from Schrader (1989): O-02, O-03, and O-01.

The spectrum of the steroid (Fig. 4.1-19B) clearly shows the non-conjugated C=O group in the D ring by a strong IR band at 1737cm^{-1} , as well as the isolated C=C bond by a strong Raman band at 1666 cm^{-1} . A dualistic interpretation scheme allows the estimation of the steroid structure by bands in the Raman and infrared spectrum (Schrader and Steigner, 1970, 1971, 1973).

The spectrum of strychnine shown in Fig. 4.1-19C exhibits bands representing CH bonds at saturated and unsaturated C atoms, an amide I vibration, and an *ortho di* substituted benzene ring. The large number of sharp bands and the extensive coincidences between all IR and Raman spectra shown in Fig. 4.1-19 point to multiaxial, only moderately symmetric rigid molecules.

The new NIR FT Raman spectroscopy now allows the investigation of food (Keller et al., 1993). Fig. 4.1.20 shows typical Raman spectra of food components: carbohydrates, proteins, and lipids. Fig. 4.1-20C shows the Raman spectrum of a banana with the *out-of-phase* and *in-phase* vibrations of the C–O–C groups of the carbohydrates at about 1100 and 850 cm^{-1} . Fig. 4.1-20B, a Raman spectrum of turkey breast shows the amide I and III bands and some bands which can be directly assigned to amino acids. The Raman spectra of lipids allow the determination of the amount of *cis* and *trans* disubstituted C=C bonds: Fig. 4.1-20A, butter (Keller et al., 1993). NIR Raman spectroscopy has good chances as tool for the investigation of living tissues, especially in medical diagnostics (Keller et al., 1994; Schrader et al., 1995).

4.1.17 Solvents

Water is only moderately suitable as a solvent for IR spectroscopy, since even thin layers of water give rise to a broad IR spectrum with a strong background (Fig. 4.1-21A). Although the Raman spectrum of water exhibits the same bands, these are usually much weaker than those of the solute. In D_2O (Fig. 4.1-21B), all vibrational frequencies are shifted, so that overlapping of the solvent bands with those of the solute can be avoided.

CS_2 is a nonpolar solvent which is particularly well suited for Raman spectrometry. CS_2 gives rise to very few bands only, and the bands of dissolved compounds are prominent even at low concentration. The CS_2 spectra are shown in Fig. 4.1-21C.

4.2 Inorganic substances*

4.2.1 Introduction

X-ray diffraction analysis has developed into a standard method of elucidating the composition and structure of solids in inorganic chemistry. It is therefore often debatable whether or not it is also necessary to employ vibrational spectroscopy. Unquestionably, X-ray analysis is the method of choice for the detailed structure determination of complex compounds, as new ones, e.g., cluster compounds containing many metal atoms, are synthesized ever more frequently. In these cases, only certain structural elements can be identified with the aid of vibrational spectroscopy. Besides these scopes of inorganic chemistry, there is an increasing interest in small reactive molecules for the discussion of structure and bonding and of reaction mechanisms. These species exist only under extreme conditions, e.g., at low pressure (interstellar space), or isolated in solid noble gases. Spectroscopy offers the tool to solve these problems. Vibrational spectroscopy in particular provides information about the dynamics of molecules, since it is often possible to calculate accurate force constants in small molecules. Together with bond distances and bond energies, these provide a good measure of bond strengths. Fundamental principles of vibrational spectroscopy are discussed in detail in other chapters of this book. Understandably, these principles are valid for all classes of chemical substances. Therefore, there is in principle no reason why a distinction should be made between inorganic and organic vibrational spectroscopy. In organic chemistry, carbon and a few other elements play a leading role, while in inorganic chemistry all elements of the periodic table are involved. Vibrational spectroscopy of inorganic substances is therefore broad in scope: it covers a wide range of energies of observed absorptions and involves a variety of technical methods. Interesting problems in this field which can be solved with the aid of vibrational spectroscopy constitute the central theme of this contribution. In accordance with the authors' interests, these issues are often approached from a chemical angle. Initially, methods and rules which are pertinent to the discussion of inorganic chemistry are explained by means of examples. The chapter then proceeds from purely analytical use as the main application of vibrational spectroscopy in inorganic chemistry to structural examinations. These involve comparing the measured spectra with those resulting from quantum chemical calculations in order to obtain information about the geometrical and electronic structure of a molecule. In the second short part, the potential and the limits of structural determination by vibrational spectroscopy are demonstrated by means of selected examples from modern inorganic chemistry. Frequencies and other structural data relating to common species mentioned in this text were extracted from textbooks without being specifically labeled as quotations (Siebert, 1966; Nakamoto, 1978; Weidlein et al., 1981, 1982 and 1986). Vibrational spectra of inorganic substances in particular are also discussed in detail by Ebsworth et al. (1987). A good introduction

* Section 4.2 is contributed by H. Schnöckel, Karlsruhe and H. Willner, Hannover

to the theory of vibrational spectroscopy, including examples from inorganic chemistry, was written by Gans (1975).

4.2.2 Application of vibrational spectroscopy in inorganic chemistry

4.2.2.1 Qualitative and quantitative analysis of known compounds

There is no question that the main application of vibrational spectroscopy in inorganic chemistry is the analysis of known substances, since species which differ from each other with respect to the masses of the involved atoms and to their (geometrical and electronic) connectivity exhibit a different vibrational spectrum. Vibrational spectroscopy is therefore basically employed to detect smallest amounts of a certain compound in a large excess of other components. For the preparative chemist, vibrational spectroscopy is thus a standard method of identifying products and of determining their degree of contamination by other compounds. Interpreting a spectrum is easier today than it used to be, since the fingerprint method involves comparing the measured spectra by aid of computers with reference spectra which are stored in electronic data files. Furthermore, sophisticated techniques connected with the optical operation of spectrometers (e.g., IR laser) as well as in the computational field (e.g., fast FT techniques, subtraction of spectra), which are described in more detail in other sections of this book, have considerably lowered the limits at which contaminations can be detected through IR and Raman spectroscopy. Today, even small contaminations in the ppm range can be detected. This is important, for example, in the analysis of pure silicon by the electronic industry. The content of substitutional carbon and interstitial oxygen in silicon is determined by measuring the infrared absorption caused by the local vibrational mode at 607 cm^{-1} and 1106 cm^{-1} , respectively, with a detection limit in the low ppm range (Stallhofer and Huber, 1983).

Typical features of vibrational spectroscopy in analytical chemistry are:

- rapid scanning by FT methods,
- preservation of the sample during measurement,
- simultaneous detection of different components of a mixture during one scan.

If, as usual, the spectra are not scanned in % transmission but in absorption, it is easy to quantitatively analyze the compound in question (absorbance \sim concentration). If the resolution of the instrument is higher than the half-width of a recorded band, then the height of the band is proportional to the concentration of the species.

Several analytical applications are presented below. For example, monitoring the composition of exhaust fumes by infrared spectroscopy plays an important role in the adjustment and development of car engines.

A new analytical technique, fluorine combustion analysis, is based on the fact that fluorides of elements in high oxidation states are thermodynamically stable, often volatile, and very strong infrared absorbers (Jacob, 1989). This method is especially suited to the

analysis of ceramics, glass and hard metals. In a typical run, about 1 mg of a sample is combusted in a large excess of fluorine in a nickel bomb at 20 bar and 600 °C. The resulting gas mixture is subsequently expanded in an infrared cell and sampled by an FTIR instrument.

In environmental analytical chemistry, high-resolution FTIR spectroscopy ($\Delta\tilde{\nu} < 0.005 \text{ cm}^{-1}$, below pressure line broadening) is used to determine the concentration of trace compounds in the atmosphere, e.g. CH₄, N₂O, O₃, CCl₂F₂, CCl₃F, H₂CO, NO₂, HNO₃, HF, HCl, etc. Infrared absorption spectra of the atmosphere are recorded at different elevation angles by using the sun as an IR source. For HF, which is formed by industrial activities alone, a vertical column abundance of 10^{15} molecules per cm² was observed at the Jungfraujoch observatory in the year 1989 (Bruker Report, 1990).

One more example from the field of matrix isolation may be mentioned. Samples of air were collected at the Schauinsland in the Black Forest (SW Germany). The trace impurities were enriched in frozen CO₂ matrices (Griffith and Schuster, 1987). These samples were analyzed both qualitatively and quantitatively by IR spectroscopy. Besides the absorptions of many well known species such as N₂O, CCl₃F, CCl₂F₂, OCS, CS₂, HONO, CH₃C(O)OONO₂ (PAN), new absorptions were observed which could not be assigned. The most remarkable result obtained from these investigations was the dramatic increase in the concentration of HONO between 8 a.m. and 5 p.m.

4.2.2.2 Qualitative analysis of unknown compounds. Interpretation of vibrational spectra with the help of empirical rules

4.2.2.1 Characteristic frequencies

IR spectroscopy is often used for the first approximate characterization of a new compound, since it is a fast and simple method. Over the past few years, Raman spectroscopy has also gained significance as new techniques (e.g., FT methods) were developed. It is especially in inorganic chemistry that Raman spectroscopy has a considerable advantage over IR methods, since sensitive samples can be measured in closed glass tubes. In order to interpret vibrational spectra, one often starts with the simple concept that typical frequencies can be related to certain pairs of atoms. Absorptions in certain frequency ranges should provide information about particular groups of atoms in the unknown species. Typical ranges of frequencies of stretching vibrations of organic compounds as well as of bending vibrations, e.g., $\rho(\text{CH}_2)$; $\tau(\text{CH}_2)$, $\omega(\text{CH}_2)$ are listed in Section 4.1 (Table 4.1-1, Figure 4.1-1) of this book. On the other hand, it is more difficult to discuss vibrational spectra of inorganic compounds, since, due to the size of the periodic table, a wide variety of heterogeneous bonding occurs. Therefore, two books containing only tables of stretching vibrations have been published (Weidlein et al., 1981 and 1986).

The frequencies of diatomic species provide a starting point for the assignment of vibrations in larger molecules. However, the situation in diatomic molecules is fundamentally different from that in larger molecules, as in the latter case coupling has to be taken into account (see also Sec. 2.5). Without critical consideration of such influences,

bands might be assigned incorrectly, and an erroneous conclusion might be drawn with respect to the molecular structure (Sec. 4.2.2.2).

Most of the element-hydrogen vibrations are hardly perturbed by coupling. This is due to the low atomic mass of the H atom, which moves mainly in this normal mode. These frequencies therefore provide an excellent measure of the force constants of a bond. These constants are a measure of the resistance of a bond to stretching from the equilibrium position. The M-H vibrations of the hydrides of elements of the second period correspond mostly to intense absorptions in the IR spectrum. Their frequencies increase in the following sequence:

(M-H)	B-H	C-H	N-H	O-H	F-H
$\tilde{\nu}/\text{cm}^{-1}$	2550	3000	3400	3700	4000

This trend is to be expected because the difference in electronegativities which are derived from bond strengths increases in the same manner. The vibrations of transition metal hydrides lie in the range between 1800 cm^{-1} (Cr-H) and 2150 cm^{-1} (Pt-H). Although M-H bonds are most easily identified by IR spectroscopy, other methods are also successfully applied. NMR techniques have certain advantages, especially in detecting hydrogen in diamagnetic transition metal complexes (Crabtree, 1990).

Apart from the influence of coupling, which usually must be taken into account, there is another more basic reason why the frequencies of diatomic molecules are not directly comparable. One has to distinguish between singly and multiply bonded systems. While the vibrational frequency in the N_2 molecule lies at 2330 cm^{-1} , molecules containing N-N single bonds exhibit vibrations as low as 930 cm^{-1} .

For the discussion of stretching vibrations of all types of bonds the aforementioned tables are recommended (Weidlein et al., 1981 and 1986). Only one topic in inorganic chemistry should be mentioned here: metal-metal bonds are often identified by their characteristic vibrations. They are usually observed in the Raman spectrum or in the Resonance Raman (RR) spectrum. In this way a variety of polynuclear metal species were detected in solid noble gases (Moskovits, 1986). In addition to the frequency range of these vibrations, which allow the characterization of certain species, overtones observed in the RR spectrum are important for the calculation of dissociation energies. Raman spectroscopy was used successfully to characterize metal-metal bonds in new compounds which are stable at room temperature: the first compound with an Al-Al bond was detected in this way (Uhl, 1988).

4.2.2.2 Vibrational coupling

In principle, it is not possible to equate the frequency of a diatomic A-B molecule with the frequency of an A-B group in a larger molecule. This is demonstrated by some triatomic molecules. A well-known example which illustrates this point is the difference between the CO frequency in the IR spectrum of the CO molecule (2136 cm^{-1}) and

that of the CO₂ molecule (2349 cm⁻¹). The IR-active stretching vibration of CO₂ has a higher energy than that of CO, although bonding is much stronger in CO than in CO₂. This is caused by the vibrational coupling of both CO groups in CO₂, which results in a repulsion of the two CO frequencies. The higher one is IR-active at 2349 cm⁻¹, the lower one is observed in the Raman spectrum at 1343 cm⁻¹. The latter vibration is additionally disturbed by special coupling, known as Fermi resonance.

Fermi resonance is observed if an overtone or a combination band has nearly the same energy as a fundamental. Coupling leads to a blue shift of the higher frequency and to a red shift of the lower one. Simultaneously, the intensity of the overtone increases while that of the fundamental decreases. In the CO₂ molecule there is a resonance between the symmetrical stretching vibration (1343 cm⁻¹, calculated without Fermi resonance) and the overtone of the deformation vibration (1334 cm⁻¹). Two other examples of Fermi resonance are:

CCl₄: $\nu_s (A_1) + \delta(T_2)$, (459 + 315 = 774 cm⁻¹) $\leftrightarrow (\nu_{as}(T_2) 780 \text{ cm}^{-1})$; observed (with Fermi resonance): 791 and 762 cm⁻¹ (Becher et al., 1974).

S=Si=O: (The spectrum of this molecule ($C_{\infty v}$), which is unstable with respect to polymerization, can only be obtained in solid noble gases):

$2\nu_{(SiS)} (A_1)$ (2·643 = 1286 cm⁻¹) $\leftrightarrow \nu_{(SiO)} (A_1)$ (ca. 1269 cm⁻¹); observed (with Fermi resonance): 1265 and 1290 cm⁻¹ (Schnoeckel, 1980).

Although perturbations of harmonics caused by Fermi resonance are not rare, the observed frequency changes are normally smaller than in the cases which have just been described. These interactions are mostly recognized if more than the expected number of absorptions are observed in the region of fundamental vibrations, or if the measured frequency shifts caused by isotopic substitution do not tally with the calculated ones (4.2.2.3.4).

As in the CO₂ molecule, there is strong vibrational coupling between the two NO groups in the isoelectronic NO₂⁺ species. The observed difference between both stretching vibrations is therefore large: ν_{as} : 2360 cm⁻¹, ν_s : 1396 cm⁻¹ (Hisatsune et al., 1962).

The theoretical treatment of linear AB₂ molecules to calculate force constants is simple, since in this case the symmetry coordinates are identical with the normal coordinates (2.3.2): the three expected vibrations belong to different irreducible representations (Σ_g^+ (ν_1), Σ_u^+ (ν_3), Π_u (ν_2)). Thus, a simple mathematical relation exists between the frequencies on the one hand and the force constants and the geometry (masses and distances) on the other hand (e.g., Siebert, 1966): the difference between the two stretching vibrations caused by coupling is large if the mass m_A of the central atom is small and if the force constant $f(AB)$ is large (Gans, 1975):

$$\nu_3^2 - \nu_1^2 \sim \mu_A \cdot f(AB) \quad \text{with } \mu_A = 1/m_A$$

The influence of this mechanically caused coupling is demonstrated by the following examples: Extremely light and extremely heavy central atoms exist in the species F–H–F[−] and F–Xe–F. The difference between ν_1 and ν_3 is therefore expected to be large in F–H–F[−] and small in F–Xe–F. This is in accordance with the experimental results:

	F–H–F	F–Xe–F
ν_1/cm^{-1}	600	515
ν_3/cm^{-1}	1455	557

The influence of the force constant $f(AB)$ on the extent of coupling becomes obvious if two species containing the same central atom are compared, e.g., CO_2 and CS_2 . Their force constants differ considerably: $f(\text{CO}) = 15.6 \text{ N/cm}$, $f(\text{CS}) = 7.6 \text{ N/cm}$. Thus, the difference between ν_3^2 and ν_1^2 in CO_2 is about twice as large as the difference between the two vibrations in CS_2 :

	CO_2	CS_2
ν_1/cm^{-1}	1343	658
ν_3/cm^{-1}	2349	1533

A detailed comparison between the frequency equations of ν_1 and ν_3 indicates that in addition to the mechanical contribution to coupling, an electronic factor also has to be taken into account. This is due to the fact that the bond strength does not really remain constant during the distortion of a bond. The restoring force of an $A - B$ bond, which is proportional to $f(AB)$, depends on whether the neighboring bond is extended or compressed. For this reason the interaction constant $f(AB)'$ was introduced. The coupling in a linear AB_2 molecule is influenced by $f(AB)'$ in the following manner: the difference between ν_3^2 and ν_1^2 caused by mechanical coupling is reduced by a term which is proportional to

$$(\mu_A + \mu_B) \cdot f(AB)'$$

This is true because $f(AB)'$ is normally positive. However, since it is much smaller than $f(AB)$ (its value is generally less than 10% of that of $f(AB)$), the electronic influence on the coupling is much smaller than the mechanical one.

The coupling situation changes if the bond angle in an AB_2 molecule becomes smaller than 180° . In this case, only the antisymmetric stretching vibration corresponds to a normal vibration, while the deformation and the symmetric stretching vibration have the 'same symmetry' and therefore mix. If the bond angle is 90° , the two stretching coordinates are orthogonal to each other. ν_s should be equal to ν_{as} if no other interactions had to be taken into account. However, the interaction between ν_s and δ causes ν_s to appear at a higher energy level than ν_{as} . In any case, coupling is reduced as the bond angle decreases from 180° to 90° . This manifests itself in a reduction of the difference between the AB stretching vibrations:

180°	134°
NO_2^+	NO_2
$2360 \text{ cm}^{-1}/1396 \text{ cm}^{-1}$	$1618 \text{ cm}^{-1}/1320 \text{ cm}^{-1}$

In bent AB_2 molecules, as in linear ones, coupling is also influenced by the mass of the central atom. This influence has been demonstrated elegantly by frequency calculations for some hypothetical molecules with additional variation of the bond angle: e.g., C–Hg–C, C–C–C, Hg–C–Hg (Weidlein et al., 1982).

Strong coupling is often observed in linear $A-B-C$ molecules. A correct assignment is sometimes critical, since their symmetry allows the two stretching vibrations to mix. Despite the presence of identical CN bonds in the molecules HCN, DCN, and TCN, the frequency of the CN stretching is therefore observed at the following wavenumbers (cm^{-1}): 2097 (HCN), 1924 (DCN), 2460 (TCN). In HCN and DCN, $\nu_{(\text{CN})}$ is reduced through interaction with the higher frequencies of the CH or the CD group, respectively. The high CN frequency in TCN, on the other hand, is caused by interaction of the low-lying CT vibration. This problem has been discussed in detail, along with the amplitudes and the potential-energy distribution of these motions (Weidlein et al., 1982).

The closer the two stretching frequencies in an $A-B-C$ molecule are, the stronger the coupling is. This means that frequencies which differ very much have nearly the same energy as the respective isolated AB or BC groups. The CN frequency of the OCN^- ion therefore differs from that of the SCN^- species: 2165 cm^{-1} (OCN^-) versus 2066 cm^{-1} (SCN^-). The interaction between $\nu_{(\text{CN})}$ and $\nu_{(\text{CS})}$ at 743 cm^{-1} in SCN^- is small, $\nu_{(\text{CN})}$ in the SCN^- species is therefore nearly equal to that of the uncoupled CN group, with $f(\text{CN}) = 16 \text{ N/cm}$ (Siebert, 1966). OCN^- , in contrast, shows strong coupling between $\nu_{(\text{CN})}$ and $\nu_{(\text{CO})}$, which according to normal coordinate analysis should be found at 1245 cm^{-1} , because of Fermi resonance between $\nu_{(\text{CO})}$ and $2 \cdot \delta$ (exp: $1302 \text{ cm}^{-1}/1207 \text{ cm}^{-1}$; $\delta: 632 \text{ cm}^{-1}$). As a consequence of this strong coupling, both frequencies differ considerably from those of the isolated groups. The stretching vibrations in the OCN^- ion are therefore better described as symmetric and antisymmetric motions.

While coupling in the triatomic species discussed here is relatively easy to estimate, since it is limited to the interaction of two vibrations, coupling in larger molecules can only be understood with the help of normal coordinate analysis (c.f. Sec. 4.2.2.3.2).

4.2.2.2.3 Influence of bonding on vibrational frequencies

The bonding situation determines the values of the force constants, and these constants are jointly responsible for the observed frequencies. Force constants are influenced much more by changes in the bonding than, for instance, by bond distances. However, frequencies also depend on the coupling situation, which is why it is advisable to be careful in drawing conclusions about the bonding from the frequencies.

The force constants of a given bond order depend mainly on the position of the constituent atoms within the periodic table. Within one period, the force constant increases with increasing group number. Since the atomic mass increases in the same sequence, this trend is not so pronounced in the frequencies:

	Al-Al	Si-Si	P-P	S-S	Cl-Cl
f/Ncm^{-1}	1.1	1.6	2.0	2.6	3.2
$\tilde{\nu}/\text{cm}^{-1}$	373	440	460	520	557

Within one group, the frequencies decrease with increasing period, since the bond strength decreases and the atomic mass increases:

	F-F	Cl-Cl	Br-Br	I-I
f/Ncm^{-1}	4.45	3.2	2.4	1.6
$\tilde{\nu}/\text{cm}^{-1}$	892	557	317	213

Since force constants are approximately proportional to the bond order, the following comparison of molecules containing multiply bonded phosphorus is informative:

	P-P	-P=P-	P≡P
	[1]		[2]
f/Ncm^{-1}	1.9	3.4	5.5
$\tilde{\nu}/\text{cm}^{-1}$	460	610	775

[1] (Hamaguchi et al., 1984)

[2] (Huber and Herzberg, 1979)

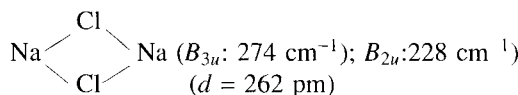
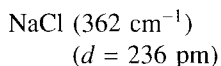
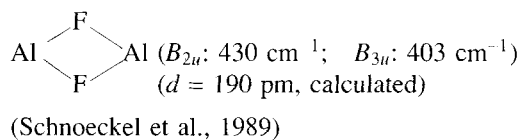
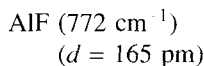
To demonstrate the influence of the bonding on the force constants and on the frequencies, molecules containing bonds between two identical atoms have been discussed intentionally, since force constants are mainly influenced by covalent contributions.

With increasing polarity of the bond the force constant decreases (N/cm):

MgCl ₂	2.05	(Lesieki and Nibler, 1976)
SiCl ₂	2.4	(Bürger and Eujen, 1974)

In the following section additional influences of the bonding situation on the vibrational frequencies are discussed: increasing the coordination number decreases the frequency.

Unless otherwise stated, these frequencies are related to the following (matrix isolated) molecular species:



(Huber and Herzberg, 1979)

(Ismail et al., 1975)

NaCl (solid): The coordination number of each atom in the NaCl lattice is six. Therefore, further weakening of the $\text{Na}-\text{Cl}$ bond is observed (c.f. Sec. 4.2.2.4). An instructive example illustrating the difference between terminal and bridging bonds is found among the boranes:

$\nu(\text{B}-\text{H})$	terminal	2600 cm^{-1}
$\nu(\text{B}-\text{H})$	bridging	1700 cm^{-1}

If the coordination number is increased through protonation, an increase in the positive charge alone would lead to a higher frequency. The former influence often dominates (symmetry species in brackets):



Sometimes, however, both influences cancel each other:



Increasing the formal oxidation number in the following isoelectronic molecules, which have the same coordination number, leads to higher frequencies and higher force constants:

SiF_2	:	5.5 N/cm
OPF	:	10.3 N/cm (PO), 4.7 N/cm (PF)
SO_2	:	10.3 N/cm

(Binnewies and Schnoeckel, 1990)

This trend is enhanced if the positive charge increases simultaneously:

	AlCl_4^-	SiCl_4	PCl_4^+
$\nu_1(A_1)/\text{cm}^{-1}$	350	423	450
$f(A_1) = f_r + 3f_{rr}/(\text{Ncm}^{-1})$	2.5	3.7	4.2

In this sequence, the totally symmetric stretching vibrations are compared, since they are the only ones in this irreducible representation in which the symmetry coordinate is identical with the normal coordinate. However, the same trend is often observed for the degenerate stretching modes $\nu_3(F_2)$, although in this case interaction with the deformation mode of the same symmetry $\nu_4(F_2)$ can in principle lead to frequency changes:

	ReO_4	OsO_4
$\nu_3(F_2)/\text{cm}^{-1}$	916	954

In octahedral molecules, the expected trend is evident in all Raman active vibrations, since each of these corresponds to a normal mode:

	$\nu_1(A_{1g})$	$\nu_2(E_g)$	$\nu_5(F_{2g})$	(cm^{-1})
PF_6^-	735	563	462	
SF_6	769	640	522	

If oxidation number and coordination number increase simultaneously, the expected frequency shifts cannot be predicted with confidence, since both properties lead to opposing frequency changes. The influence of the increased oxidation number generally dominates:

	XeF_2	XeF_4	XeOF_4	
$\nu_s (\text{XeF})/\text{cm}^{-1}$	515 (Σ_g^+)	543 (A_{1g})	576 (A_1)	
$\nu(\text{PF})$ (cm^{-1}) and $f(\text{PF})$ (N/cm)				
PF	P(O)F	PF_3	P(O)F_3	PF_5
838	811	860 (E)	990 (E)	640 $\nu_s(\text{PF}_2)_{ax}$ 945 $\nu_{as}(\text{PF}_2)_{ax}$
		892 (A_1)	873 (A_1)	817 $\nu_s(\text{PF}_2)_{eq}$ 1026 $\nu_{as}(\text{PF}_2)_{eq}$
4.9	4.7	5.4	6.3	

Inductive and mesomeric properties within the bonds are also reflected in the frequencies. This is firstly demonstrated for some compounds containing PO double bonds, and secondly for SiO double bonds (cm^{-1}):

OPF_3	OPCl_3	OPBr_3	OPF	OPCl	OPBr
1415	1290	1260	1295	1258	1253

(Binnewies and Schnoeckel, 1990)

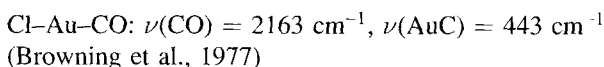
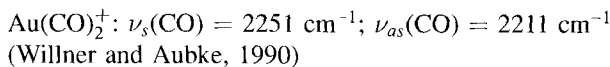
$\text{O}=\text{SiF}_2$	$\text{O}=\text{SiCl}_2$
1309	1240

(Schnoeckel, 1980 a, b)

The triatomic and tetraatomic species were investigated in solid noble gases. In organic chemistry, mesomeric influences are often discussed in connection with the bonding of carbonyl groups (c.f. Sec. 4.1.12). Similar arguments are used in inorganic chemistry to rationalize frequency shifts in metal carbonyls. The CO ligand in these compounds is able to accept electron density from the metal atom via π orbitals. This back-donation of electrons from occupied d orbitals of the metal to antibonding π^* orbitals of CO strengthens the metal-carbon bond and weakens the CO bond. Decreasing the positive charge on the metal atom therefore favors changes in the bonding in the same sequence. Particularly weak CO bonds are consequently found in negative species:

	$\text{Ni}(\text{CO})_4$	$\text{Co}(\text{CO})_4$	$\text{Fe}(\text{CO})_4^{2-}$
$\nu(\text{CO})/\text{cm}^{-1}$	2132 (A_1)	1918 (A_1)	1788 (A_1)
$\nu(\text{MC})/\text{cm}^{-1}$	380 (A_1)	439 (A_1)	464 (A_1)

On the other hand, the CO frequencies of metal carbonyls in which the metal atom has a positive oxidation number are often higher than that of the CO molecule. In this case, however, the metal-carbon bond is weak:



In the neutral $\text{Au}(\text{CO})$ species, isolated in solid noble gases, $\nu_{(\text{CO})}$ is lower: 2039 cm^{-1} (McIntosh and Ozin, 1977).

4.2.2.3 Discussion of structure and bonding with the help of vibrational spectroscopy

4.2.2.3.1 Geometry, composition, and symmetry

Linkages between different atoms can be discussed under the general aspect of geometry. This is mentioned in the section about characteristic frequencies. As a transition between the more qualitative analysis of the preceding chapter to the more structural approach of the present section, some comments on different possibilities of bonding in ambidentate ligands are presented. By using vibrational spectroscopy it is often possible to distinguish between the following linkages: –CN and –NC; –OCN and –NCO; –CNO (fulminate) and –ONC (isofulminate); –SCN and –NCS. All types of complexes containing these species have been discussed (Nakamoto, 1978):

- With the help of isotopic substitution and frequency calculations the isomers Me_3SiCN and Me_3SiNC were unambiguously identified (Linton and Nixon, 1958).
- It is almost impossible to distinguish between the –OCN and the –NCO linkage by X-ray diffraction. A recent study (Seppelt and Oberhammer, 1985) showed that, according to spectroscopic data including electron diffraction, the isomer pentafluoroselenium cyanate SeF_5OCN is favored; this compound had previously been described as pentafluoroselenium isocyanate.
- Systems containing thiocyanate ligands have been studied extensively. The stretching vibrations of the linear SCN group are affected differently by linkages via nitrogen or sulfur. The frequencies in the spectrum of the ion are: $\nu_1: 2053 \text{ cm}^{-1} (\nu_{(\text{CN})})$; $\nu_3: 750 \text{ cm}^{-1} (\nu_{(\text{CS})})$; $\nu_5: 480 \text{ cm}^{-1} (\delta_{(\text{SCN})})$.

In S-bonded complexes, the intensive CN vibration is shifted to slightly higher frequencies (2110 cm^{-1}) than in N-bonded systems (2100 cm^{-1}). However, a more definitive measure is provided by the CS frequency, which is generally of weak intensity: its frequency increases in the case of N-coordination (800 cm^{-1}), while a decrease is observed in compounds with metal-sulfur bonds (720 cm^{-1}). These frequency shifts can be explained by changes in the bonding, illustrated by the following structures: $-\text{S}-\text{C}=\text{N}$ and $\text{S}=\text{C}=\text{N}-$. In this, as in many other cases, the results obtained by vibrational spectroscopy were shown to be reliable by determining the crystal structures of particular examples by X-ray methods.

To obtain information about the geometry of molecules, e.g., about the number of AB bonds in an AB_n system, the spectra have to be analyzed more carefully. In a non-linear molecular compound, the total number of vibrations is $3n - 6$ ($n = \text{number of atoms}$). In order to discuss the geometry, one must first look at the number of stretching vibrations. This number corresponds to the number of AB bonds. As a result of the symmetry, the number of observed stretching vibrations is sometimes smaller, e.g., only two vibrations are usually observed for AB_3 -systems, since one of them is doubly degenerate. This is true for species with D_{3h} - and with C_{3v} -symmetry.

The observability of vibrations in the Raman and/or IR spectrum, the polarization of the vibrations, and the distribution in different representations can be deduced from the

symmetry of the species, i.e., from the point group to which the species belongs. The selection rules, which are based on the point group, are described in Sec. 2.7.3. Only a few simple examples are therefore presented here in order to illustrate the discussion of structure and symmetry:

AB_2 molecules: For bent species (C_{2v}), three vibrations should be detected in the IR spectrum as well as in the Raman spectrum. Sulfur dihalides provide a good example to demonstrate this fact: SF_2 (Ne matrix) shows the following absorptions in the IR spectrum: $\nu_s(SF_2) = 834 \text{ cm}^{-1}$; $\delta(FSF) = 358 \text{ cm}^{-1}$; $\nu_{as}(SF_2) = 808 \text{ cm}^{-1}$ (Haas and Willner, 1978). Since SF_2 is unstable with respect to disproportionation, no Raman spectrum has yet been obtained. However, the IR and the Raman spectrum of SCl_2 can easily be measured: $\nu_s(S^{35}Cl_2) = 527 \text{ cm}^{-1}$; $\nu_{as}(S^{35}Cl_2) = 525 \text{ cm}^{-1}$ (IR, Ne matrix), (Bielefeld and Willner, 1980); $\delta(CISCl) = 208 \text{ cm}^{-1}$ (Frankiss and Harrison, 1975). In both cases, the expected bent structure is derived from the IR spectrum as well as from the Raman spectrum by simply counting the number of bands.

In the case of a linear AB_2 molecule, two absorptions (ν_{as} , δ) should be observed in the IR and one (ν_s) in the Raman spectrum. Corresponding spectra were obtained for noble gas dihalides:

$$\begin{aligned} XeF_2: \nu_s &= 515 \text{ cm}^{-1} \text{ (Raman)}, \\ \delta &= 213 \text{ cm}^{-1} \text{ (IR)}; \\ \nu_{as} &= 557 \text{ cm}^{-1} \text{ (IR)}. \end{aligned}$$

Many of these conclusions from vibrational spectroscopy have been confirmed by other techniques, such as diffraction methods. This is also true for some alkaline-earth dihalides, which were investigated as matrix-isolated species by IR and Raman spectroscopy and studied in the gas phase with the help of electron diffraction: e.g., $MgCl_2$: electron diffraction in the gas phase: $d_{(MgCl)} = 219 \text{ pm}$, $\alpha = 180^\circ$ (Gershikov and Spiridonov, 1981); matrix-isolated $MgCl_2$: $\nu_1 = 327 \text{ cm}^{-1}$, $\nu_2 = 93 \text{ cm}^{-1}$, $\nu_3 = 601 \text{ cm}^{-1}$ (Lesieki and Nibler, 1976). The bonding and the structures of all alkaline-earth metal dihalides have been discussed in detail (Spoliti et al., 1980).

In discussing binary compounds, XeF_6 should be mentioned because of its fascinating vibrational spectrum. Due to the presence of a lone electron pair in the valence shell of the Xe atom, a distortion from O_h symmetry can be expected. The situation is, in fact, complex, which is illustrated by the vibrational spectra: spectra taken in the gas phase at different temperatures point to an equilibrium of isomers (Claassen et al., 1972).

Vibrational spectroscopy is a common method of obtaining information about the structure and symmetry of carbonyl complexes (Braterman, 1976; Kettle, 1977). This is because these compounds mostly exhibit intense, sharp absorptions in the range from 2100 cm^{-1} to 1800 cm^{-1} , where the sensitivity of the IR instrument is high. Since CO vibrations are almost free of coupling with the lower-energy modes of the molecule, even the relatively narrow frequency range of the CO vibration affords reliable information about the bonding between the CO group and the metal. Furthermore, the number of CO groups corresponds to the number of CO absorptions; of course degenerate modes must be accounted for with respect to the degree of degeneracy (in ()):

$\text{Mo}(\text{CO})_6$: A_1 : 2121 cm^{-1} ;
 E_g : 2025 cm^{-1} (2);
 F_{1u} : 2000 cm^{-1} (3)

In an analogous manner the structures of many mononuclear carbonyls were elucidated through their IR and Raman spectra only.

Many metal carbonyls prepared in solid noble gases can only be investigated by spectroscopic methods. Vibrational spectroscopy has been a successful tool for probing the structures and bonding of these reactive species. A famous representative of this large group of compounds is $\text{Pd}(\text{CO})_4$, which is only stable below 80 K (Moskovits and Ozin, 1976).

Today, however, polynuclear carbonyls are of primary interest. Their structure is frequently so complicated that it cannot be derived from the vibrational spectra by applying selection rules. Only certain structural elements, such as terminal and bridging CO groups, can be identified. Reliable information about the structure of these species can only be obtained by X-ray diffraction methods.

Vibrational spectra of solid carbonyls often differ from those in solution. The latter often exhibit very complicated spectra, since many isomers exist in an equilibrium. Even the interpretation of vibrational spectra of the species $\text{Fe}_3(\text{CO})_{12}$, whose size is small compared to many of the large carbonyl clusters which have been investigated during the past few years, is controversial (Cotton and Hunter, 1974).

4.2.2.3.2 Assignment of vibrational absorptions. Normal coordinates

An assignment is the correlation between a measured vibrational spectrum and the normal vibrations of a molecule. The shapes and numbers of normal vibrations can be derived theoretically. In general, complete assignment is not possible for large, unsymmetrical molecules. On the other hand, the vibrations of small, highly symmetrical molecules can often be assigned easily by using selection rules, e.g., by their absence in the IR and/or the Raman spectrum. In this way the symmetries of small species can be identified, as described in the previous chapter.

The depolarization ratio of a band is very helpful in assigning vibrations in the Raman spectra of gases and liquids (Sec. 2.7.3.4). Vibrations of a totally symmetric representation can thus be distinguished from those associated with lower symmetry: The breathing mode of the tetrahedral SiCl_4 molecule at 424 cm^{-1} , for instance, is the strongest band in one Raman spectrum but unobserved in another, depending upon the directions of the polarized radiation for excitation and observation.

Both the rotational fine structure and the contours of bands are helpful in assigning vibrations of gaseous compounds with a known structure. It is well known that vibrational transitions of diatomic AB molecules without changes in the rotational state (Q -branch, $\Delta J = 0$) are not allowed in the IR spectrum. Likewise, selection rules exist for linear molecules, spherical tops, symmetric and asymmetric tops. With different irreducible representations, these lead to characteristic band contours, which are discussed in detail in another part of this book (Sec. 4.3).

The unambiguous assignment of the vibrations of small molecules helps to assign the bands of larger species. It is important to remember that the assignment of the frequency range and the intensities must match that of analogous compounds. Finally, a correct assignment can be verified by calculating the force constants. Only those frequencies which have been assigned correctly can be reproduced in a calculation involving force constants which are reasonable with respect to the type of bonding. Besides, calculated isotopic shifts will only tally with the measured ones if the assumed assignment is correct.

After a vibration has been identified as a fundamental, a second problem arises in correlating the vibration with a definitive movement of the atom within its molecule. According to the theory, every fundamental as a normal vibration has to be described by a normal coordinate. A normal coordinate is a linear combination of coordinates which represent the movements of the atoms within a molecule relative to the equilibrium position. Internal coordinates are usually preferred. They represent distortions of bond lengths between chemically bonded atoms or movements involving changes in the bond angles. Every characterization of a fundamental as a stretching or a deformation vibration means that, strictly speaking, the normal coordinate is identical with the internal coordinate. No other coordinates are involved in this vibration. This situation, however, is rare. In most cases, therefore, assignment means that a specific coordinate makes a predominant contribution to a fundamental. For small molecules, for which reliable force constants can be calculated, the assignment can be confirmed by an analysis of the normal coordinates. As a result, one obtains the contributions of the internal coordinates to the normal coordinate. For some vibrations the assignment to localized movements is possible. The simplest example of a pure stretching vibration is the fundamental of a diatomic AB species:

$$\tilde{\nu} = 1303 \sqrt{f(\mu_A + \mu_B)}$$

with $\tilde{\nu}$ / cm⁻¹; f / Ncm⁻¹; $\mu_A = 1/m_A$

For the matrix-isolated $^{28}\text{Si}^{16}\text{O}$ molecule, for instance, the following values have to be substituted:

$$1226 \text{ cm}^{-1} = 1303 \sqrt{9.01 \left(\frac{1}{27.98} + \frac{1}{15.99} \right)}.$$

The vibrational frequencies of most diatomic species, some of which only exist at high temperature or during electrical discharge, have been tabulated (Huber and Herzberg, 1979). They may be obtained from the fine structures of the electronic emission spectra. Alternatively, many of them were identified directly as matrix-isolated species by IR or Raman spectroscopy.

Molecules of the type $\text{H}_x\text{A} - \text{BH}_y$ are sometimes discussed in a simplified manner as pseudo-diatomc species. Sensible results are obtained by this approximation if the

A-B vibration is distinct from the stretching and bending vibrations of the AH_x and BH_y groups. This is not the case with the molecule $H_2C=CH_2$. The CC stretching vibration at 1623 cm^{-1} lies close to the CH_2 deformation mode with the same symmetry (1342 cm^{-1}). Therefore, erroneous results are obtained for the force constant $f(\text{CC})$ if the mass of the CH_2 group is used in the formula for the diatomic oscillator (Becher and Adrian, 1970). In contrast, the situation is simpler if the *A* and *B* atoms are heavier. In bonds in which elements of the third period are involved, the element-element vibrations are hardly influenced by AH vibrations of the same symmetry:

$$\begin{aligned} H_2P-PH_2: \quad \nu(P-P) &= 437\text{ cm}^{-1} \\ H_3Si-SiH_3: \quad \nu(Si-Si) &= 435\text{ cm}^{-1} \end{aligned}$$

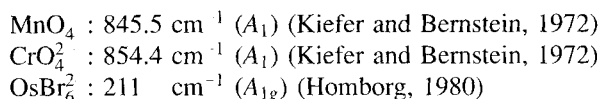
In some highly symmetrical molecules, a symmetry-adapted coordinate as a linear combination of internal coordinates can be identical with a normal coordinate. This is true for the following totally symmetric vibrations:

	$D_{\infty h}(A_g)$	$D_{3h}(A'_1)$	$T_d(A_1)$	$O_h(A_{1g})$
	CO_2	BF_3	$SiCl_4$	SF_6
$\tilde{\nu}_s / \text{cm}^{-1}$	1336	888	424	769

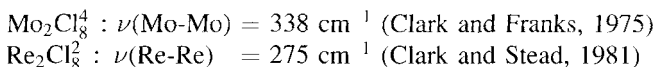
From these frequencies and with the help of the corresponding *G*-Matrix elements (Wilson et al., 1955), the symmetry-adapted force constants (*F*) can be calculated directly. In the vibrations discussed here, *F* is a linear combination of stretching and interaction force constants f_r and f_{rr} :

$$\begin{aligned} SF_6: F(A_{1g}) &= f_r + 4f_{rr} + f_{rr'} = 6.62\text{ N/cm} \\ CO_2: F(A_g) &= f_r + f_{rr} = 16.82\text{ N/cm} \\ BF_3: F(A'_1) &= f_r + 2f_{rr} = 8.83\text{ N/cm} \\ SiCl_4: F(A_1) &= f_r + 3f_{rr} = 3.76\text{ N/cm} \\ SF_6: F(A_{1g}) &= f_r + 4f_{rr} + f_{rr'} = 6.62\text{ N/cm} \end{aligned}$$

A further aid in assigning a band is its observation in the Resonance Raman (*RR*) spectrum. In *RR* spectroscopy, the exiting frequency coincides with a symmetry-allowed electronic transition. In general, only the totally symmetric vibrations are therefore enhanced in the *RR* spectrum (c.f. Sec. 6.1). The entire *RR* spectrum consists only of a few bands and their overtones. In the following highly symmetric species the totally symmetric breathing modes are easily identified:



With species containing metal-metal bonds, many overtones of the corresponding vibration may be observed in the *RR* spectrum:



Furthermore, some pure metal clusters such as Cr₂ and Cr₃ (DiLella et al., 1982), V₂ (Cossé et al., 1980), Fe₂ (Moskovits and DiLella, 1980) and similar species, such as Te₃ (Schnoeckel, 1984) were identified and characterized as matrix-isolated species by *RR* spectroscopy.

For more details, a review of the applications of *RR* spectroscopy in inorganic chemistry is recommended (Clark and Dines, 1986).

4.2.2.3.3 Intensity of vibrational bands

Thus far, this contribution has been concerned mainly with the energies of vibrational transitions. Intensities were considered only in connection with Fermi resonance and *RR* spectroscopy. In this section a few short comments about the intensity of vibrational bands in ‘normal’ IR and Raman spectra are presented. The intensity depends on the electronic structure of the species, since changes in the dipole moment ($\partial\mu$) and in the polarizability ($\partial\alpha$) during a vibration are caused by changes in the electron density.

$$I(\text{IR}) \sim \left(\frac{\partial\mu}{\partial Q} \right)^2 \quad I(\text{Raman}) \sim \left(\frac{\partial\alpha}{\partial Q} \right)^2$$

in which Q is the normal coordinate. The intensity of a vibrational band depends on two quantities, μ or α , and Q . While values of Q can be derived from normal coordinate analysis based on classical physics, μ and α can be obtained only by quantum-chemical calculations. Many semi-empirical and *ab initio* programs offer options to also calculate intensities. Today it is therefore possible to calculate the vibrational frequencies and their intensities in the IR and Raman spectra of small unknown species (Sec. 4.2.2.3.6). On the other hand, electronic structural data can be discussed with reference to the measured Raman intensities (Chantry and Plane, 1960 and 1961).

In certain circumstances, the relative intensities of the IR absorptions of a compound help to estimate bond angles. This procedure is useful for molecules containing two or more symmetrically equivalent diatomic oscillators. The angle between the oscillators can be obtained from the ratio of the relative intensities of the in-phase and the out-of-phase motions. This method has been applied successfully to calculate bond angles between the CO groups in metal carbonyls, since as a first approximation the CO vibrations do not mix with the other lower-energy motions, and since the changes in the dipole moment are collinear with the CO bond (Darling and Ogden, 1972 and 1973). The bond angles of some unstable, coordinatively unsaturated metal carbonyls generated in solid noble gases were calculated by this method (e.g., Fe(CO)₃, Fe(CO)₄, (Burdett et al., 1978)).

4.2.2.3.4 Isotopic substitution

According to the Born-Oppenheimer approximation, the potential function of a molecule is not influenced by isotopic substitution. Frequency shifts caused by isotopic substitution therefore provide experimental data in addition to the fundamentals which can yield information about the structure of a species. However, the half-widths of absorptions are too large to be resolved by the experimental techniques which are normally used, which is why these methods cannot reveal small isotopic shifts (some cm^{-1}). The half-widths of the bands are reduced drastically by applying the matrix-isolation technique (c.f. Sec. 4.4). The absorptions of many matrix-isolated species can therefore be characterized with the help of isotopic substitution, i.e., the molecular fragment which is involved in the vibration can be identified. The large $^{28}\text{Si}/^{29}\text{Si}$ shift of the most intense IR absorption of matrix-isolated $\text{S}=\text{Si}=\text{S}$ from 918 cm^{-1} to 907 cm^{-1} , for instance, demonstrates that silicon participates considerably in this vibration (Schnoeckel and Koeppe, 1989). The same vibration is shifted by 4 cm^{-1} if only one ^{32}S atom is substituted by a ^{34}S atom. The band at 918 cm^{-1} must be assigned to the antisymmetric stretching vibration, since the central A atom in an AB_2 molecule with $D_{\infty h}$ -symmetry counts twice as much as the B atoms in the G -matrix (c.f. Wilson et al., 1955).

It is often possible to derive the number of identically bonded atoms just from the splitting pattern of a band which is caused by isotopic substitution. This is demonstrated by some Cl-containing species. Since the natural $^{35}\text{Cl}/^{37}\text{Cl}$ distribution is approximately 3:1, the $X\text{-Cl}$ vibrations in a species which contains only one $X\text{-Cl}$ group afford two absorptions whose relative intensities are three and one: e.g., Al-Cl (Ar matrix): 455 cm^{-1} (3), 449.6 cm^{-1} (1) (Schnoeckel, 1976).

If two equivalent $X\text{-Cl}$ bonds are involved in a vibration, three bands with an intensity ratio of 9:6:1 ($^{35}\text{Cl}/^{35}\text{Cl}$; $^{35}\text{Cl}/^{37}\text{Cl}$; $^{37}\text{Cl}/^{37}\text{Cl}$) are observed: e.g., O=SiCl_2 (Ar matrix): $\nu_{as}(\text{SiCl}_2) = 637.5 \text{ cm}^{-1}$ (9); 634.6 cm^{-1} (6), 631.7 cm^{-1} (1) (Schnoeckel, 1980 b). If three equivalent $X\text{-Cl}$ bonds participate in a vibration, the splitting pattern is more difficult to interpret, since, due to the antisymmetrical vibration, the double degeneracy which is characteristic of symmetrically substituted species ($X^{35}\text{Cl}_3$ and $X^{37}\text{Cl}_3$) is not observed in unsymmetrically substituted species. In an $X\text{Cl}_4$ molecule with T_d symmetry, a nine-fold splitting of the antisymmetrical stretching vibration (F_2) will result:

natural abundance	point group	molecule	symmetry of the IR active modes
32.5%	T_d	$X^{35}\text{Cl}_4$	F_2
42.2%	C_{3v}	$X^{35}\text{Cl}_3^{37}\text{Cl}$	A_1, E
20.5%	C_{2v}	$X^{35}\text{Cl}_2^{37}\text{Cl}_2$	A_1, B_1, B_2
4.4%	C_{3v}	$X^{35}\text{Cl}^{37}\text{Cl}_3$	A_1, E
0.4%	T_d	$X^{37}\text{Cl}_4$	F_2

Some of these species, such as SnCl_4 (Koeniger and Mueller, 1975) and GeCl_4 (Koeniger et al., 1975), were investigated extensively in solid noble gases in order to measure

the isotopic shifts. These are needed to limit the number of solutions in a force constant calculation (Sec. 4.2.2.3.5). To the same end, a number of isotopomers of oxo-anions were investigated by IR. In order to obtain sharp bands, the following species are sometimes incorporated in high dilution in solid matrices, such as alkali halides: ClO_4^- , SO_4^{2-} , SeO_4^{2-} , CrO_4^{2-} and WO_4^2 (Becher et al., 1973 and 1976). Isotopic shifts between ^{92}Mo and ^{100}Mo were measured in order to obtain a force field of the MoO_4^2 anion (Müller et al., 1974). For more information about the metal isotope effect on molecular vibrations, the review of Mohan et al. (1975) is recommended.

Since the vibrations of molecules are anharmonic, it is important to remember that the frequencies of the different isotopomers only afford the same force constant if the amplitudes are assumed to be infinitesimally small. The distortion which is caused by the different anharmonicity of the vibrations in isotopomeric molecules is often small compared to the accuracy of the measurement. This is especially true for small isotopic shifts (about $1\text{-}5 \text{ cm}^{-1}$). As a result of the development of new, improved techniques (e.g., FT-spectrometers, matrix isolation), frequencies can sometimes be determined with an accuracy of more than 0.1 cm^{-1} . If isotopic shifts can be measured so accurately, they have to be corrected for anharmonicity, even if the isotopic shift is in the range of a few cm^{-1} . Since the required exact anharmonicity constants are generally unknown, an approximation has been suggested (Becher, 1968) which proved to be practicable, except for H/D substitution. This method involves using the anharmonicity constant x_e of a simpler compound which contains the same bond as the investigated compound. If no other data are available, x_e values of the diatomic species (Huber and Herzberg, 1979) have to be used. The corrected isotopic shift $\Delta\nu_{corr}$ is calculated using the following expression:

$$\Delta\nu_{corr} = \Delta\nu_{exp} + 2 \cdot x_e \Delta\nu_{exp}$$

The geometry and the force constants of a molecule determine the isotopic shifts of the vibrational frequencies. However, the products of the vibrational frequencies of two different isotopomers within the same irreducible representation are related by the Teller-Redlich product rule. For two symmetry-equivalent vibrations the following expression is obtained:

$$\frac{\nu_1 \cdot \nu_2}{\nu'_1 \cdot \nu'_2} = \sqrt{\frac{|G|}{|G'|}}$$

$|G|$ and $|G'|$ are the determinants of the G matrices of two isotopomeric molecules which can be calculated from the geometry of the molecule and from the atomic masses of the atoms involved (Wilson et al., 1955). If the geometry of a species is given, assignments are easily checked with the help of the frequencies of an isotopomeric molecule.

According to the Teller-Redlich rule, only three of the four experimentally obtained quantities (ν_1 , ν_2 , ν'_1 , ν'_2) are independent. In this case, therefore, a maximum of three force constants can be determined by isotopic substitution. If, on the other hand, more isotopic data are available, geometric parameters can be determined. This method is used extensively to calculate the bond angles 2α of AB_2 molecules from the antisymmetric harmonic stretching vibration ω_3 :

$$\sin \alpha = \frac{m_A m_A^i [m_B (\omega_3)^2 - m_B (\omega_3^i)^2]}{2 m_B m_B^i [m_A (\omega_3^i)^2 - m_A (\omega_3)^2]}$$

4.2.2.3.5 Force constants

In describing motions of atoms in molecular vibrations, internal coordinates are usually preferred to Cartesian coordinates. If the changes of bond lengths and bond angles which result from the displacement of atoms are used, the force field of a vibrating molecule is in accordance with the connectivity, since outside its equilibrium position the atom feels forces which are directed along chemical bonds. The increase in potential energy caused by the movements of atoms along internal coordinates is normally described by the approximation of harmonic vibrations:

$$V = \frac{1}{2} \sum_i \sum_j \left(\frac{\partial^2 V}{\partial r_i \partial r_j} \right)_0 r_i r_j = \frac{1}{2} \sum_i \sum_j f_{ij} r_i r_j$$

(in which r refers to the internal coordinates and f refers to the force constants). If one coordinate appears twice in one term, then f_{ii} is a stretching or a bending force constant. In the former case, the abbreviations f , f_r , k_r or K_r are used, while d , f_α , or H_α are used in the latter case. The potential curve of the discussed approximation is a parabola. The restoring forces which affect the atoms after minor distortions from the equilibrium position therefore obey a linear relation:

$$\text{Force} = f \cdot \Delta r$$

Stretching constants have the dimension N/m or N/cm. In the latter case, the same numerical value is obtained as with the dimension mdyn/Å, which continues to be used. A dimension of deformation constants is N·cm/rad². However, deformation constants are often given in the same dimension as stretching constants. In this case the dimension is adjusted by dividing it by 1 cm²/rad².

If two different coordinates (r_i and r_j) occur in one potential energy term, interaction force constants are obtained. Their value differs from zero if distortions in one coordinate r_i change the equilibrium position in r_j .

The mathematical procedures for the calculation of force constants are described in Section 5.2 of this book. For calculations involving small (triatomic) species, the book by Fadini and Schnepel (1985) is recommended. A review covering force constant calculations has been presented by Becher (1968). In this chapter only relevant aspects are discussed. Force constant calculations mainly rely on correct assignments of the observed frequencies. These are compared with calculated frequencies, which can be obtained, for example, by the Wilson method (Wilson et al., 1955). First, the G -matrix based on the known or an assumed geometry is calculated. The eigenvalues (frequencies) of the vibrations for different sets of force constants are then calculated. Their values are derived mostly from the force constants of similar species. Since the measured frequencies can be reproduced with an infinite number of sets of force constants, additional experimentally

obtained quantities, such as isotopic shifts, must be considered in order to reduce the number of solutions.

The observed frequencies (ν) have a lower energy than the harmonic vibrations (ω_e). As a first approximation, the following relation involving one anharmonicity constant x_e can be derived: $\nu = \omega_e (1 - 2x_e)$. Thus, force constants derived from experimentally determined frequencies are too small for harmonic approximation; differences up to 8% are sometimes found with X-H vibrations. However, this problem will not be discussed in more detail, since in practice force constants are usually calculated from measured frequencies.

Force constant calculations are facilitated by applying symmetry concepts. Group theory is used to find the appropriate linear combination of internal coordinates to symmetry-adapted coordinates (symmetry coordinates). Based on these coordinates, the G matrix and the F matrix are factorized, which makes it possible to carry out separate calculations for each irreducible representation (c.f. Secs. 2.7.3.3 and 5.2). The main problem in calculating force constants is the choice of the potential function. Up until now, it has not been possible to apply a potential function in which the number of force constants corresponds to the number of frequencies. The number of remaining constants is only identical with the number of internal coordinates (simple valence force field SVFF) if the interaction force constants are neglected. If this force field is applied to symmetric molecules, there are often more frequencies than force constants. However, the values are not the same in different irreducible representations, a fact which demonstrates the deficiencies of this force field (Becher, 1968).

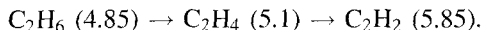
In the general valence force field (GVFF), all f_{ij} constants are taken into account. To n normal vibrations of the same symmetry correspond n stretching or deformation constants and $n(n-1)/2$ interaction constants. The GVFF is the most appropriate potential function from a chemical point of view. However, for a few small molecules all force constants of the GVFF have been calculated reliably, since with decreasing symmetry and with increasing molecular size the number of force constants by far exceeds the number of frequencies. Restrictions to the potential function have therefore been recommended for many problems.

The different approaches to performing a normal coordinate analysis are demonstrated for the molecule $Mn(CO)_5Br$. On the one hand, 30 normal vibrations were analyzed on the basis of the GVFF in a careful investigation involving 54 force constants (Ottensen et al., 1973). On the other hand, an approximation was introduced (Cotton and Kraihanzel, 1962, 1963, 1964), which makes it possible to calculate the CO-vibrations of the same molecule by using only 5 force constants: 2 different $f(CO)$ and 3 different interaction constants $f(CO/CO)$ (Cotton et al., 1967). This method is based on the idea that the CO vibrations with their high frequencies can be separated from the lower energy vibrations. The calculations are simple, since the G matrix contains only the diagonal elements ($\mu_C + \mu_O$). These simplified calculations were performed for many XY-stretching vibrations in carbonyl, nitrosyl, and cyanide complexes in order to confirm assignments, to interpret the intensities of CO vibrations, and to discuss the bonding.

Understandably, the force constants obtained by the GVFF method differ from those calculated with the help of the Cotton and Kraihanzel approximation (1962, 1963, 1964). However, the latter form a reasonable basis on which to compare similar molecules.

4.2.2.3.6 Significance of force constants for chemical bonding. Comparison with other properties of bonds

Changes in chemical bonds can be deduced from force constants. These changes correlate with the valence electron configurations of the involved atoms and with substituents which change the electron densities of the bonded atoms. This principle has been applied to a large number of organic compounds (Becher, 1968). A change in the chemical bonds is demonstrated by two examples: the CH-stretching force constant increases in the following sequence (N/cm):



This increase is plausible, since the *s* contribution increases in the same sequence (sp^3 - sp^2 - sp - hybridization). The C-C bonds in the following hydrocarbons provide an elegant example of the correlation between force constants and bond order:

	C-C C ₂ H ₆	C=C C ₆ H ₆	C=C C ₂ H ₄	C≡C C ₂ H ₂
$f(\text{CC})/\text{Ncm}^{-1}$	4.4	6.7	9.1	15.6
$d(\text{CC})/\text{pm}$	154	139	134	120

This chart demonstrates that changes in the bonding are reflected better by force constants than by bond distances. Many empirically derived relations were reported between these quantities (Badger, 1934; Gordy, 1946; Jensovsky, 1962). The same is true for the relation between stretching force constants and bond energies. But here is a difference: while the force constant represents the bond strength, which resists small distortions from the equilibrium distance, the bond energy represents the total bond strength during considerable distortion up to dissociation. A large bond energy is generally associated with a large force constant, but a variety of examples demonstrate that a chemical bond cannot be described by a single bonding parameter alone. Although the deep trough of a potential energy curve (representing the bond energy) normally has a steep slope near the minimum (a measure of the force constant), many ionic molecules exhibit a potential energy - bond distance function which goes through a deep minimum but increases with a flat slope. These opposite trends of bond energy and force constant are evident even in the single bonds of diatomic halogens:

	F ₂	Cl ₂	Br ₂
d/pm	142	199	228
f/Ncm^{-1}	4.5	3.2	2.4
bond energy/kJmol ⁻¹	159	243	205

In this respect it is also interesting to compare the bonding parameters in the BF/BF_3 pair and the AlF/AlF_3 pair of molecules (Schnoeckel et al., 1989):

	bond energy/kJmol ⁻¹	f_r/Ncm^{-1}	d/pm
BF	755	7.9	126
BF_3	645	7.3	131
AlF	675	3.9	165
AlF_3	592	4.8	163

In the pair BF/BF_3 , the higher bond energy of BF corresponds to a higher force constant and a smaller distance, as expected. In AlF, probably because of a greater ionic contribution, the force constant is smaller and the bond distance longer; but the bond energy is higher than in AlF_3 . The most remarkable molecule in this series is BF with its particularly strong bond. This is also confirmed by quantum chemical calculations, which are best visualized by the structure ${}^-\text{B}=\text{F}^+$ (Schnoeckel et al., 1989). All bonding parameters therefore show a weakening of the B-F bond in the sequence $\text{BF} \rightarrow \text{BF}_3$.

Chemical intuition is often better reflected in force constants and distances than in values of bond energies. This is demonstrated by the isoelectronic molecules SiF_2 , OPF, and SO_2 . In accordance with the force constants and the distances, single bonds have to be written in the Lewis structure of SiF_2 and double bonds in that of SO_2 (Binnewies and Schnoeckel, 1990):

	SiF_2	O=P=F	SO_2
atomization enthalpy/kJmol ⁻¹	1115	1065	1033
stretching force constant/Ncm ⁻¹	5.5	10.3	4.7
bond distance/pm	159	145	157
			143

However, there is an opposite trend in the bond energy. This is plausible, since the polarity of the bonds increases in the sequence $\text{SO}_2 \rightarrow \text{OPF} \rightarrow \text{SiF}_2$.

In the last few years there has been growing interest in molecules containing multiple bonds between atoms of higher periods. From this point of view, analogous carbon and silicon compounds were studied extensively. Important structural information was obtained from the vibrational spectra of reactive, matrix-isolated molecules such as SiO , SiS , SiO_2 , OSiS , and SiS_2 . The following table compares the respective force constants, bond distances, and bond energies (the latter two are obtained from quantum chemical calculations) with similar data of analogous carbon compounds (Schnoeckel and Koeppe, 1989):

X=Y X=Y=Z	$f(XY)$ Ncm ⁻¹	$f(YZ)$ Ncm ⁻¹	bond energy kJmol ⁻¹	$d(XY)^*$ pm	$d(YZ)^*$ pm
O=C	18.6		1072	110.6	
S=C	8.5		709	151.9	
O=C=O	15.6		799	113.6	
O=C=S	15.7	7.2		112.5	157.2
S=C=S		7.7	572	154.7	
O=Si	9.1		794	148.9	
S=Si	5.0		616	191.5	
O=Si=O	9.2		622	148.3	
O=Si=S	9.0	4.9		148.5	190.3
S=Si=S		4.9	533	190.7	

* For better comparison only calculated values (ab initio) are listed.

It is remarkable that, in contrast to the carbon-containing compounds, there is no difference between the force constants of SiO and SiO₂ or between those of SiS and SiS₂. On the other hand, the recorded trend among the bond energies of these molecules matches the expectation. The conclusion is that double and triple bonds in silicon compounds are similar if the bonds are distorted only slightly compared to the equilibrium position (force constant); while these bonds differ if the change of distance is large (bond energy). Quantum chemical calculations indicate that the predominant portion of the bond energy in SiO₂ has to be attributed to ionic interactions. This explains the preferred formation of solid SiO₂ crystals with stable Si–O–Si single bonds, while the less polar CO₂ still contains CO double bonds and forms a molecular lattice at low temperature.

4.2.2.3.7 Prediction of the vibrational spectra of unknown species

The discussions presented in this section (4.2.2.3) demonstrate that force constants are sensitive indicators of small changes in bonding. This means that the gradient of the potential curve near the equilibrium distance is easily affected by changes in the electronic structure. Thus, only sophisticated quantum chemical calculations make it possible to describe the potential curve with sufficient accuracy to obtain reliable force constants. At present, these calculations are performed for small molecules in order to obtain the entire vibrational spectrum: apart from the frequencies, which, however, must be scaled, reliable values are obtained for the intensities of the bands. This method is gaining significance for the identification of reactive species. It was employed, for instance, to prove the photochemical isomerization of matrix-isolated dihalomethanes (Maier et al., 1990). However, the frequencies of unknown species can also be calculated by classical methods (Sec.4.2.2.3.5). These calculations are based on the force constants of known molecules containing similar bonds. Furthermore, the intensities can be predicted empirically, since spectra of species representing almost all conceivable bonding possibilities are known. In the past, the structures of a large number of molecules were elucidated by these methods. Later, these results were largely confirmed by quantum chemical calculations. Because of the rapid development in computer technology and the increasing availabil-

ity of fast computers, quantum chemical calculations for the simulation of spectra of unknown species will gain importance in the near future.

4.2.2.4 Vibrational spectra of crystals from a chemical point of view

Important technical improvements in Raman and IR spectroscopy have also opened up new approaches to solving solid-state problems (c.f. Secs. 2.6, 2.7.5, 4.5, 4.8). In contrast to the wide range of applications of vibrational spectroscopy to molecular inorganic compounds, this method is less commonly used in solid state chemistry, although just such investigations of the lattice dynamics are crucial to the solution of current problems, e.g., high temperature superconductivity. Physically orientated groups are mainly working in this field. According to the more chemically oriented field in which the authors are active, these problems are discussed from an angle which is common in the interpretation of molecular compounds: e.g., is it possible to discuss the bonding in solid-state compounds on the basis of force constants derived from lattice modes?

A lattice, in contrast to a molecule, has an infinite number of vibrational degrees of freedom. According to the theory of lattice vibrations, the vibrations of the unit cell are regarded as being representative of all these motions. After subtracting three degrees of freedom for translation, $3n - 3$ optical modes remain for a unit cell containing n atoms. The infinite number of vibrations result from the different phases of the motions in the neighboring cells. The description of the Raman and IR spectra is, however, largely restricted to those vibrations which are in the same phase in all unit cells. The symmetry of all vibrations and the selection rules for their observation is determined by the factor group (Sec. 2.7.5). Its relation to the point group of a molecular compound is demonstrated by the IR and the Raman spectrum of the anion WO_4^{2-} in scheelite (CaWO_4), shown by the following table:

Point group	Site group	Factor group	Assignment
T_d	S_4	C_{4h}	
A_1	A	A_g B_u	$\nu_s(\text{WO}_4)$
E	A B	A_g B_u B_g A_u	$\delta_s(\text{WO}_4)$
F_2	B E	B_g A_u E_g E_u	$(\nu, \delta)_{as}(\text{WO}_4)$

In the first step, the vibrations of the hypothetical isolated species are analyzed with respect to its point group. Secondly, the symmetry of the species in the static lattice (the site symmetry) is determined. The site is normally of lower symmetry than the isolated species. If the species are highly symmetrical, splitting of the degenerate vibrations is observed. In the last step, the correlations between the different groups in the unit cell are analyzed (factor group analysis, Sec. 2.7.6). Since the unit cell of the scheelite crystal contains two WO_4^2- species, twice as many vibrations are observed as expected from site group analysis.

A further problem in the interpretation of vibrational spectra of solid state compounds arises from the different phases of the vibrations in neighboring cells, leading to a wave described by the wave vector k . In the absence of a phase difference, k equals zero. This is the basis for the factor group analysis. If the vibrational motions are oriented parallel to the direction of the wave caused by the phase differences, a longitudinal branch results; while transverse branches result from orthogonal vibrational motions. Furthermore, it is necessary to differentiate between optical and acoustic modes. In the optical mode of the NaCl lattice, Na^+ and Cl^- ions have opposite displacements, while the acoustic modes are caused by in-phase motions of Na^+ and Cl^- .

From the frequency of the transverse optical mode in a simple AB lattice with $k = 0$ a force constant can be derived which is a measure of the restoring forces experienced by the atoms as they are distorted from the equilibrium position. This force constant, $F(\text{lattice})$, is a linear combination of internal force constants, since in a lattice a linear combination of equilibrium distances and angles yields a coordinate of this vibration. Based on this assumption, the GF method (Wilson et al, 1955) can be applied. For diamond (or zinc blende), the following relation is obtained:

$$\lambda = 4/3 \cdot 2\mu_c \cdot F(\text{lattice})$$

$$\lambda = \tilde{\nu}^2 \cdot 10^{-6} \cdot 0.5891 \quad (\tilde{\nu} \text{ in cm}^{-1}; \quad F \text{ in N/cm})$$

The observed Raman frequencies of diamond (1332 cm^{-1}) and of silicon (507 cm^{-1}) afford the following force constants:

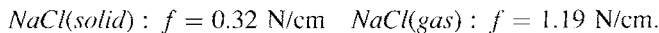
$$F(\text{diamond}) = 4.7 \text{ N/cm}, \quad F(\text{silicon}) = 1.6 \text{ N/cm}$$

These values are in the same range as the force constants of CC and SiSi bonds in molecular compounds:

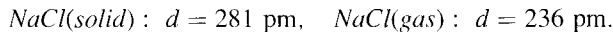
$$f(\text{CC}) = 4.4 \text{ N/cm}, \quad f(\text{SiSi}) = 2.4 \text{ N/cm}$$

Obviously, the addition of the values of all interaction force constants which are involved in $F(\text{lattice})$ simplify the result: $F(\text{lattice}) \approx f_r$. Analogous relations between $F(\text{lattice})$ and the observed frequencies have been discussed for solid NaCl and CaF₂ (Becher,

1972). As expected, the calculated force constants are much smaller than those of the isolated molecule:



This change in the bonding is also reflected in the bond distances:



4.2.3 Selected examples of structural examination by vibrational spectroscopy, classified by compounds

4.2.3.1 Gaseous compounds

While vibrational spectroscopy is a well-known method of determining the structures of stable compounds, new techniques open up new possibilities of also analyzing unstable species. In analogy to O=C=O, which is discussed in Section 4.2.2.2, the isoelectronic unstable species HN=C=NH was studied by FTIR methods. The two CN stretching vibrations are similar to those of CO₂: $\nu_{as}(\text{CN}) = 2104.70 \text{ cm}^{-1}$; $\nu_s(\text{CN}) = 1285 \text{ cm}^{-1}$ (Birk and Winnewisser, 1986). An unstable carbon oxide, the linear species O=C=C=C=C=O, was also investigated in the gas-phase (Holland et al., 1988) and as a matrix isolated species (Maier et al., 1988).

Comparable to CO₂ is the molecule CSe₂. It was investigated by high-resolution FTIR spectroscopy because precise structural determination of free molecules by microwave spectroscopy are limited to molecules which have a permanent dipole moment. Hence, other molecules have to be investigated by electron diffraction or high-resolution infrared techniques. Two recently studied examples are the $D_{\infty h}$ species CSe₂ and HF₂⁻. The following molecular constants with the standard error in parentheses of C⁸⁰Se₂ were measured: $\nu_1 = 369.1331(12) \text{ cm}^{-1}$ (obtained from a combination band), $\nu_2 = 313.0539(10) \text{ cm}^{-1}$, $\nu_3 = 1301.8774(5) \text{ cm}^{-1}$. From the rotational fine structure the equilibrium bond length $r_e(\text{C}^{80}\text{Se}) = 169.35536(19) \text{ pm}$ was determined (Bürger and Willner 1988).

Spectra of the linear anion FHF⁻ in the gas phase were obtained by diode laser spectroscopy: $\nu_1 = 583.6539(13) \text{ cm}^{-1}$, $\nu_2 = 1286.0284(22) \text{ cm}^{-1}$, and $\nu_3 = 1331.1502(7) \text{ cm}^{-1}$. From the resulting rotational constants an equilibrium F–F internuclear distance of 227.771(7) pm was calculated (Kawaguchi and Hirota, 1987). In the class of binary hydrides, boron compounds are especially interesting. A recent FTIR investigation revealed the out-of-plane vibration of unstable BH₃: 1140.8757(39) cm^{-1} (Kawaguchi et al., 1987). These data confirm the results of a recent matrix study which showed an absorption at 1132 cm^{-1} for the same vibration (Kaldor and Porter, 1971). A detailed

spectroscopic investigation of the stable B_2H_6 molecule has been published. With the help of 114 data obtained from the vibrational spectra of six isotopomers, 30 of the 33 independent force constants were calculated (Duncan et al., 1983). Although B_2H_6 is a well-known species, the existence of similar hydrides of heavier third-group elements is controversial. Recently, Downs et al. (1989) successfully investigated the sensitive compound Ga_2H_6 . From the average $P - R$ branch separation they concluded a Ga–Ga distance of 260 pm, which is in excellent agreement with recent electron diffraction data (Pulham et al., 1991) and with the corresponding distance in related molecules.

Boron nitrogen compounds and boron hydrides have stimulated particular theoretical interest throughout the last three decades. Some of the very simple species were investigated by FTIR methods:

$\text{H}-\text{B}=\text{N}-\text{H}$ was generated from $\text{B}_2\text{H}_6/\text{NH}_3$ in an electrical discharge (Kawashima et al., 1987). The BN-stretching vibration was measured at $1786.19308(72)$ cm^{-1} (^{11}B); $1823.40107(86)$ cm^{-1} (^{10}B). For the substituted species $\text{Me}-\text{B}=\text{N}-\text{Me}$, isolated in solid noble gases, the same vibration was observed at 2107 cm^{-1} (^{10}B) and 2054 cm^{-1} (^{11}B) (Paetzold et al., 1988). The simplest aminoborane $\text{H}_2\text{B}=\text{NH}_2$ was also investigated for the first time by FTIR spectroscopy. The BN vibration is measured at 1337.474 cm^{-1} (Gerry et al., 1985).

During the past few years, multiple bonds involving elements of higher periods have gained interest. In particular, many species containing PX multiple bonds were investigated. The $\text{CH}_3\text{C}\equiv\text{P}$ molecule is a good example. The CP stretching vibration is observed at $1437.4748(29)$ cm^{-1} (Ohno et al., 1987).

A new technique of investigating short-lived species is fast time-resolved IR spectroscopy. With the help of this method the first gas phase spectrum of naked $\text{Cr}(\text{CO})_5$, generated by photolysis of $\text{Cr}(\text{CO})_6$, was obtained (Seder et al., 1985). The structure is similar to that shown by matrix experiments: C_{4v} .

4.2.3.2 Solutions

Species which are isolated in solid noble gases may also be regarded as dissolved species (Sec. 4.4). One important advantage of matrix isolation over gas phase work is the ease of studying chemical reactions. An impressive example is the formation of dimeric SiO_2 in solid argon (Mehner et al., 1990). Many species were investigated at a slightly higher temperature in liquid Xe or Kr. This method was applied to the photochemical reaction between $\text{Fe}(\text{CO})_2(\text{NO})_2$ and 1,3-butadiene (Gadd et al., 1987). A similarly interesting technique of investigating organometallic compounds is their incorporation in polymers: photo-induced decarbonylation of $\text{Fe}(\eta^5-\text{C}_5\text{H}_5)(\text{CO})_2(\text{COMe})$ was observed in PVC film matrices (Hooker et al., 1984). A variety of investigations were performed in liquid NH_3 : Raman spectroscopy was used to follow the complexation of $\text{Hg}(\text{CN})_2$ by CN. The species $\text{Hg}(\text{CN})_2(\text{NH}_3)_2$, $\text{Hg}(\text{CN})_3(\text{NH}_3)^-$, and $\text{Hg}(\text{CN})_4^{2-}$ were identified (Earl et al., 1985).

A particularly interesting reaction in liquid Cl_2 (-100°) was performed by Seppelt (1976). The first formation of AsCl_5 from AsCl_3 and Cl_2 was monitored by Raman spectroscopy.

Finally, many aqueous solutions which are important to inorganic and analytical chemistry were studied by Raman spectroscopy at room temperature. The species HgCl_2 , HgCl_3 , and HgCl_4^{2-} , for instance, were identified in an aqueous HCl solution containing HgCl_2 (Bentham et al., 1985). The equilibrium between H^+ , CrO_4^{2-} and $\text{Cr}_2\text{O}_7^{2-}$ was also monitored by Raman spectroscopy (Michel and Cahay, 1986).

Solid solutions of BH_4^- in alkali halide single crystals were also investigated at room temperature in order to obtain information about changes in the symmetry caused by the matrix material (Memon et al., 1982).

Raman spectroscopy has also developed into a powerful tool for investigating high-temperature solutions: with the aid of this technique, many salt melts were studied. The species $\text{Al}_2\text{Cl}_6\text{F}$, AlCl_3F , AlCl_2F_2 , and AlClF_3 , for instance, were identified in fluoride-containing chloroaluminate melts (Gilbert et al., 1988).

4.2.3.3 Solids

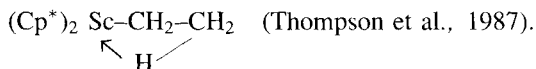
4.2.3.3.1 Molecular solids

The species Cl_2O_6 is difficult to handle. Its structure in the solid state was first concluded from vibrational spectra (Piva et al., 1971). These results are in accordance with the crystal structure (ClO_2^+ , ClO_4^-) (Tobias and Jansen, 1987). Two non-equivalent Cl atoms also exist in the gas phase, as shown by the matrix spectra of Cl_2O_6 (Jansen et al., 1988).

With the help of Raman spectroscopy many structural results have been obtained in the fascinating field of new cyclic sulfur molecules (Steudel, 1982). Out of the nearly immeasurable number of results in transition element chemistry, only two detailed studies shall be mentioned:

- Single crystal IR and Raman spectra yield a complete assignment of all CO modes in $\text{Ru}_3(\text{CO})_{12}$. The D_{3h} symmetry found in solution remains in the solid phase (Gilson and Evans, 1984).
- Low-temperature FTIR and Raman spectra of $\text{Re}_2(\text{CO})_{10}$ have been reported, together with ^{13}C data. These were used to make a full assignment, including Raman-active overtones. The results are generally in good agreement with D_{4h} symmetry, but there is some evidence of a slight distortion in solution (Harvey and Butler, 1985).

An important mechanism in organometallic chemistry is the activation of C-H bonds. This 'agostic' hydrogen can be detected by IR spectroscopy. Characteristic low-lying CH bands, for instance, are observed in the compound



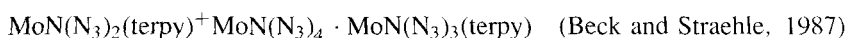
4.2.3.3.2 Isolated groups of ionic compounds

A prominent example of the application of vibrational spectroscopy in this field is the NO_4^- ion. The structure deduced from Raman spectra (Jansen, 1977) was later confirmed

by X-ray diffraction methods (Jansen, 1979). There are also many other cases in which the original structure obtained by vibrational spectroscopy was later or simultaneously confirmed by X-ray studies:

- $O_3Mo-O-MoO_3^{2-}$ (Becher et al., 1978; Becher and Fenske, 1978).
- Further examples of the large field of transition metal oxides are the compounds $VO_2F_2^3$ (Leimkuehler et al., 1986) and $(Mo_4O_{12}F_3)^{3-}$ (Buchholz and Mattes, 1986).

Besides metal oxides, many nitrides were initially identified by their characteristic IR frequencies. Out of the large variety of investigated compounds, only one with a single $M\equiv N$ group: $V(\equiv N)Cl_2(Py)_2$ (Willing et al., 1987) and one species containing three distinct $Mo\equiv N$ units (terpy = 2,2':6',2''-terpyridin):



shall be mentioned. The latter exhibits only a single sharp $Mo\equiv N$ vibration.

A very symmetrical ion of special interest to solid state chemistry is tetrahedral Si_4^4 . The Raman and the IR absorptions of this species were identified in the spectra of K_3LiSi_4 and K_7LiSi_8 (Kliche et al., 1987).

At least two detailed normal coordinate analyses are mentioned:

- $Mo_2Cl_8^4$ and other species containing metal-metal bonds were studied by Larson et al. (1986).
- The vibrational spectra of the highly symmetric (I_h) $B_{12}X_{12}^{2-}$ species ($X=H, F, Cl, Br$) were analyzed for the first time (Cyvin et al., 1986).

4.2.3.3 Solid ionic compounds

Most of these investigations were performed by physicists. Investigations on high-temperature superconducting materials, such as $YBa_2Cu_3O_7$, are also interesting for inorganic chemists. Since the number of publications in this field is immense, a review of the spectroscopy of inorganic substances listing about 100 references is recommended (Davidson, 1989), see also Sec. 4.8.

4.2.4 Conclusion

In the future, as in the past, vibrational spectroscopy will play a significant role in inorganic chemistry. Besides fast analysis with the help of fingerprint methods, one of its most important areas of application will be in the characterization of transient species. Knowledge of the bonding in such species provides the experimental background for an important topic in chemistry: the understanding of reaction mechanisms. In these investigations, quantum chemical *ab initio* calculations of vibrational spectra will gain importance.

We would like to thank Dr. G.S. McGrady for proof reading chapters 4.2 and 4.4. The support of our own matrix work over the course of several years by the Deutsche Forschungsgemeinschaft (DFG) is gratefully acknowledged.

4.3 Rotation-vibration spectra of gases*

In the gaseous or vapour phase molecules can rotate freely, which leads to a modification of their vibrational spectra by some significant rotational fine structure. The study of rotation-vibration transitions for the analysis of molecular structure and rotation-vibration interaction can be carried out using infrared and Raman spectroscopy (Hollas, 1982). The pure rotational spectra in the vibrational ground state and, to a lesser extent due to reduced intensities, in excited vibrational states can be observed in the microwave and in the far infrared region for molecules with a permanent dipole moment. For symmetric molecules without a dipole moment, but with a polarizability allowing for anisotropic scattering, the pure rotational Raman spectra (see, e.g., Weber, 1979) are an equivalent source of information on the interatomic structure, since the rotational energies depend on the molecular moments of inertia. The structure of the rotation-vibration spectra of gaseous compounds, of which some are presented as examples, will be discussed. The various applications of gas phase IR and Raman spectroscopy to problems of gas analysis will not be covered.

Infrared experimental techniques nowadays are dominated by Fourier-transform (FT) and laser techniques, whereas, besides the established 'dispersive laser Raman spectroscopy' using mono- and polychromators, also the FT-Raman technique with near-infrared excitation has been recently applied (Dyer and Hendra, 1992), although this is considered not to be ideally suited to Raman studies of gases due to the inherently low intensity of the scattered radiation. The concept of high resolution is different when comparing IR and Raman spectroscopy, where for the latter often a limitation by the half width of the exciting laser line is met. For a free running laser the natural line width, e.g., of the Ar^+ ion laser is about 0.15 cm^{-1} , which limits high resolution studies, unless single-moded lasers are used.

Such single-mode lasers, often pulse amplified by dye laser amplifiers pumped by injection-locked Nd:YAG lasers, are used in nonlinear Raman techniques by which an instrumental resolution better than 0.001 cm^{-1} is achieved (Esherick and Owyong (1982), Schrötter et al. (1988a)).

In many cases, the infrared and Raman rotation-vibration spectra contribute complementary structure data, particularly for highly symmetric molecules. Due to the significantly different selection rules a greater line density is observed for Raman due to a larger selection of allowed changes in the rotational energy compared to infrared gas spectra. Raman spectroscopy is, on these grounds, also a valuable supplement to infrared studies.

* Section 4.3 is contributed by H. M. Heise, Dortmund and H. W. Schrötter, München

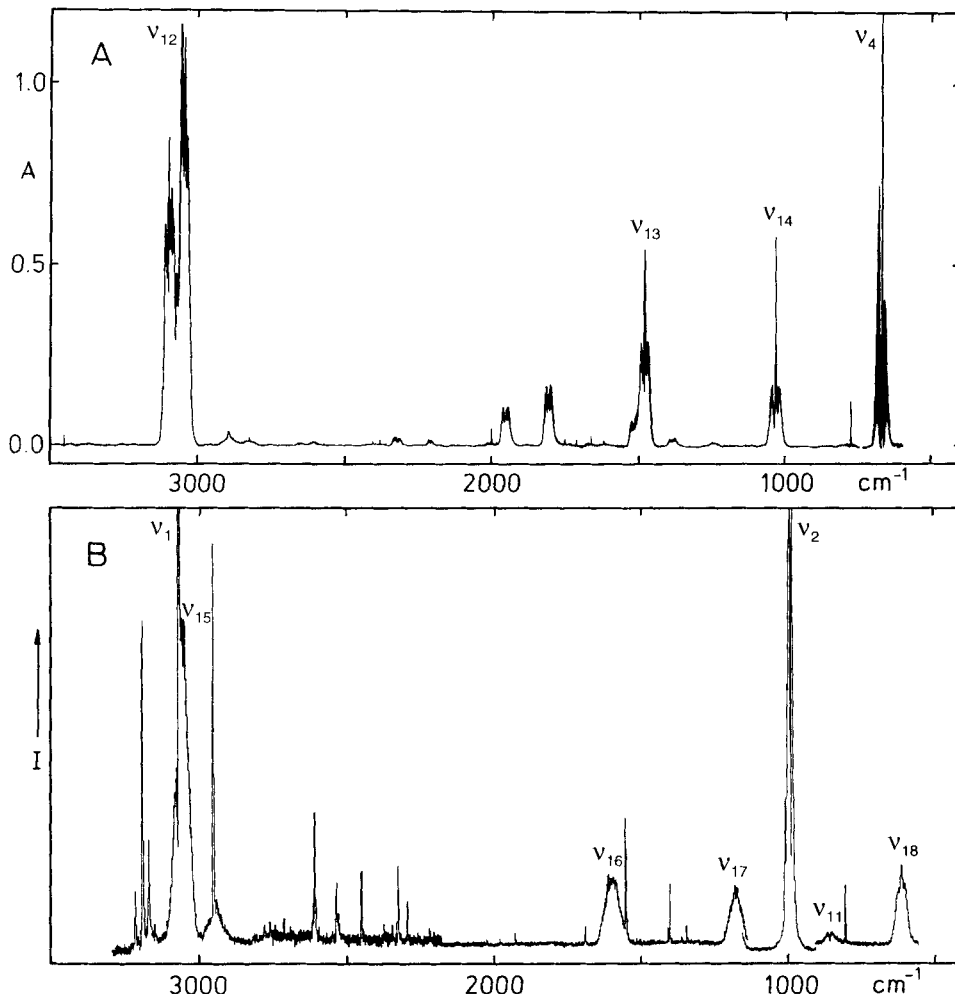


Figure 4.3-1 Rotation-vibration spectrum of C_6H_6 : **A** infrared spectrum in absorbance units; for the experimental conditions, see also Fig. 4.3.1-9. **B** Raman spectrum, compiled from several spectra recorded under different conditions, but plotted on an approximately equivalent intensity scale. The peaks of ν_1 and ν_2 are off scale (pressure 13 kPa, laser power 6 to 10 W at 514.5 nm, spectral slitwidth about 2 cm^{-1}).

The vibrational selection rules treated in Sec. 2.7 are strictly valid in the gas phase, because intermolecular interactions are mostly absent. As an example we present the rotation-vibration infrared and Raman spectra of benzene C_6H_6 in Fig. 4.3-1 on a common scale. According to the rule of mutual exclusion (see Sec. 2.7.3.4), none of the fundamentals should coincide in the two spectra. Of the 20 normal vibrations of C_6H_6 four are infrared active ($1A_{2u}$, $3E_{1u}$), seven Raman active ($2A_{1g}$, $1E_{1g}$, $4E_{2g}$), and nine

Table 4.3-1 Compilation of the wavenumbers $\tilde{\nu}_n$ of the fundamental vibrations of benzene C_6H_6 and C_6D_6 with notation according to Herzberg (1945). The values in parentheses give the uncertainty in units of the last decimal quoted

n	Symmetry	Activity	$\tilde{\nu}/\text{cm}^{-1}$	C_6H_6 Reference	$\tilde{\nu}/\text{cm}^{-1}$	C_6D_6 Reference
1	A_{1g}	Raman	3073.94(5)	Hollinger (1978a)	2303.44(3)	Hollinger (1979)
2	A_{1g}	Raman	993.063(15)	Hollinger (1978a)	945.583(15)	Hollinger (1979)
3	A_{2g}		1350	Brodersen (1956)	1061.4	Thakur (1986)
4	A_{2u}	IR	673.973 ₂ (2)	Lindemayer (1988)	496.2136(7)	Cabana (1974)
5	B_{1u}		3057	Brodersen (1956)	2284.5	Pulay (1981)
6	B_{1u}		1010	Brodersen (1956)	970	Pulay (1981)
7	B_{2g}		990	Brodersen (1956)	829	Pulay (1981)
8	B_{2g}		707	Brodersen (1956)	599	Pulay (1981)
9	B_{2u}		1309.8(3)	Berman (1987)	1282(3)	Thakur (1986)
10	B_{2u}		1148.5(3)	Berman (1987)	823.677	Plíva (1989)
11	E_{1g}	Raman	847.1	Hollinger (1978b)	660	Pulay (1981)
12	E_{1u}	IR	3047.9008 ₀ (3)	Plíva (1982)	2289.3(1)	Thakur (1986)
13	E_{1u}	IR	1483.985 ₄ (1)	Plíva (1983)	1335.2212(1)	Plíva (1990)
14	E_{1u}	IR	1038.267 ₀ (2)	Plíva (1984)	814.2969(2)	Plíva (1989)
15	E_{2g}	Raman	3056.7(1)	Hollinger (1978b)	2272.5	Hollinger (1979)
16	E_{2g}	Raman	1600.9764(8)	Plíva (1987)	1558.3	Hollinger (1979)
17	E_{2g}	Raman	1177.776(10)	Hollinger (1978b)	867.0	Hollinger (1979)
18	E_{2g}	Raman	608.13(1)	Hollinger (1978b)	580.2(1)	Callomon (1966)
19	E_{2u}		967	Brodersen (1956)	787	Pulay (1981)
20	E_{2u}		398	Brodersen (1956)	347	Pulay (1981)

forbidden in both effects ($1A_{2g}$, $2B_{1u}$, $2B_{2g}$, $2B_{2u}$, $2E_{2u}$). In addition to the fundamentals, many overtone and combination bands are evident in both spectra, but no coincidence is observed. In Table 4.3-1, the wavenumbers of the fundamental vibrations of C_6H_6 and C_6D_6 are compiled from the literature. For many cases, the accuracy of the Raman values is comparable to that of the infrared values, whereas the indirectly determined values of the inactive vibrations are not so well established yet, because they mostly rely on force field calculations. The basis for these are, in addition to the highly symmetric benzene species mentioned, also isotopically labelled molecules with D and ^{13}C ; see for example, Thakur et al. (1986). The problem is further complicated by the fact, that the vibrational potential of the molecule is anharmonic. For the determination of anharmonicities, vibrational bands other than the fundamentals have to be assigned and evaluated. In order to provide additional experimental data for an anharmonic force field of the benzene molecule, the second order Raman bands of C_6H_6 and C_6D_6 were recorded to determine anharmonicity constants of the free benzene molecule (Eppinger et al., 1992). This work was continued with an investigation of the Raman spectrum of 1,3,5- $C_6H_3D_3$ by Zeindl et al. (1993).

4.3.1 Infrared spectra of gases*

4.3.1.1 Introduction

The study of the rotation-vibration spectra of polyatomic molecules in the gas phase can provide extensive information about the molecular structure, the force field and vibration-rotation interaction parameters. Such IR-spectra are sources of rotational information, in particular for molecules with no permanent dipole moment, since for these cases a pure rotational spectrum does not exist. Vibrational frequencies from gas phase spectra are desirable, because the molecular force field is not affected by intermolecular interactions. Besides, valuable support for the assignment of vibrational transitions can be obtained from the rotational fine structure of the vibrational bands. Even spectra recorded with medium resolution can contain a wealth of information; 'hot bands', for instance, provide insight into the anharmonicity of vibrational potentials. Spectral contributions of isotopic molecules, certainly dependent on their abundance, may also be resolved.

Most fundamental rotation-vibration bands are located in the mid-infrared region from $4000 - 400\text{ cm}^{-1}$. A few vibrational bands appear in the far infrared where purely rotational spectra of light molecules with two or three atoms are also observed. This is in contrast to heavier polyatomic molecules: the study of their rotational spectra is the domain of the microwave spectroscopist who employs different equipment, particularly, monochromatic tunable radiation sources. Rotational constants determined from IR-work are therefore usually less accurate than those obtained by microwave spectroscopy.

* Section 4.3.1 is contributed by H. M. Heise, Dortmund

When investigating rotational-vibrational transitions one is mostly interested in the wavenumber position of the individual rotational lines to derive molecular parameters. The majority of commercial IR-spectrometers including grating and FT-instruments offer a maximum spectral resolution between 0.1 cm^{-1} and 2 cm^{-1} . Up to 1980, special grating spectrometers for high resolution studies were constructed capable of a spectral resolution of 0.025 cm^{-1} (see, e.g., Braund et al., 1980). Nowadays, there are commercial research FT-instruments approaching even a resolution of 0.002 cm^{-1} , so that studies can be carried out with resolutions bordering on those of laser spectroscopy where resolving powers of $\tilde{\nu}/\Delta\tilde{\nu} \sim 10^7$ and better are available. FT-spectrometers afford a high spectral wavenumber reproducibility; however, the precision of the wavenumber measurement depends definitely on the spectral linewidth, and the signal-to-noise ratio available.

High resolution studies by conventional spectroscopy are genuinely hampered by Doppler-broadening of the rotation-vibration lines in the low pressure regime. Individual Doppler-shifted frequencies contribute to the (normalized) Doppler-broadened line shape, due to the distribution of molecular velocities along the direction of observation

$$f_D(\tilde{\nu} - \tilde{\nu}_0) = \{(\ln 2/\pi)^{1/2}/\gamma_D\} e^{-\ln 2(\tilde{\nu} - \tilde{\nu}_0)^2/\gamma_D^2}$$

The corresponding halfwidth of such a Gaussian line profile, with its center at wavenumber $\tilde{\nu}_0$, can be calculated according to

$$\begin{aligned} 2\gamma_D &= \{8N_L kT(\ln 2)/M\}^{1/2} \tilde{\nu}_0/c \\ &= 7.15 \cdot 10^{-7} \tilde{\nu}_0 (T/M)^{1/2} \end{aligned}$$

where N_L is the Avogadro constant, k the Boltzmann constant, T temperature in (K) and M the molecular weight in atomic mass units. Special laser techniques have been developed to render Doppler-free spectroscopy possible; the high resolution of laser spectrometers is an asset in this context, see Demtröder (1991).

Another phenomenon to be considered is the collision or pressure broadening of lines. The resulting line shape can be described by a (normalized) Lorentzian function

$$f_c(\tilde{\nu} - \tilde{\nu}_0) = (\gamma_c/\pi)/\{(\tilde{\nu} - \tilde{\nu}_0)^2 + \gamma_c^2\}$$

The pressure and temperature dependence of the halfwidth parameter γ_c is given by

$$\gamma_c(T, p) = \gamma_c(T_0, p_0)(p/p_0)(T_0/T)^n$$

A compilation of values for γ_c and n of different small molecules was provided by Rothman et al. (1987).

In general, there are two approaches to recording gas phase spectra. A spectrum may be recorded of a sample at atmospheric pressure, with the investigated compound embedded in a matrix of air or another transparent gas, so that foreign gas broadening dominates. The second approach involves measuring a sample, preferably a pure compound, at reduced pressure, so that self-broadening prevails. At low pressure, usually several hPa, Voigt-profiles (see, e.g., Bakshi and Kearney, 1989) with contributions from Doppler and pressure broadening can be observed.

If adequate spectral resolution is available, infrared spectra of molecules in the gas phase can be highly structured. The varying molecular complexity and symmetry makes it necessary to employ different models for spectrum interpretation. These models may be characterized by considering the molecular moments of inertia. Generally, the moment of inertia I_α of a rigid body with n point masses rotating about the axis α is defined as

$$I_\alpha = \sum_{i=1}^n m_i r_i^2$$

with r_i the perpendicular distance between the particle of mass m_i and the axis passing through the center of mass. It is customary to designate the three perpendicular principal axes of the inertial tensor as a , b , and c with the convention of $I_a \leq I_b \leq I_c$ for the individual principal moments of inertia. There are four categories (see Tab. 4.3-2).

Table 4.3-2 Different categories of rotator models

Rotator model	Moments of inertia	Examples
linear rotor	$I_a = I_b$ and $I_c = 0$	CO, C ₂ H ₂
spherical rotor	$I_a = I_b = I_c$	SiCl ₄ , SF ₆
symmetric top	$I_a = I_b < I_c$	C ₆ H ₆ , cyclo-C ₃ H ₆
oblate	$I_a < I_b = I_c$	CH ₃ F, C ₂ H ₆
prolate		
asymmetric top	$I_a < I_b < I_c$	CH ₂ O, H ₂ O

Principal axes can easily be identified in a molecule which possesses symmetry elements: e.g., symmetry axes that coincide with principal ones, and a symmetry plane that is oriented perpendicularly to one of the principal axes. The simplest models discussed here are rigid rotor – harmonic oscillator models, which can be extended on demand to better fit the spectral data. For a more complete coverage, the reader is referred to other text books. As a first introduction to infrared rotation-vibration spectra the author prefers Barrow (1962). The topic is discussed in greater details by publications such as by Allen and Cross (1963), Herzberg (1945, 1950), and Hollas (1982).

4.3.1.2 Linear molecules

The rotational energy levels of a linear molecule treated as a rigid rotor can simply be calculated by quantum mechanics

$$E_J = \hbar/(8\pi^2 c I_b) J(J+1) = BJ(J+1)$$

Each level, with its unit usually given in cm^{-1} , is designated by the quantum number J , which is likewise related to the total angular momentum, while B is the rotational constant. For a diatomic molecule the moment of inertia I_b can be calculated from the nuclear masses m_1, m_2 and the equilibrium distance r :

$$I_b = \frac{m_1 m_2}{m_1 + m_2} r^2 = \mu r^2$$

with μ representing the reduced mass of the molecule.

Minor effects of the non-rigidity of the molecule, which are especially noticeable at higher rotational states, may be accounted for by extension with the term $-DJ^2(J+1)^2$ resulting from rotation-vibration interaction; D is referred to as molecular centrifugal distortion constant. Due to vibrational motion, the equilibrium distance is influenced and the observed rotational constant is a quantum mechanical average over this motion. For a polyatomic molecule, the dependence of the rotational constant on the vibrational states, is approximated closely by

$$B_{[v]} = B_e - \sum_i \alpha_i (v_i + d_i/2)$$

in which B_e is the equilibrium rotational constant, α_i represents small vibration-rotation interaction constants, and d_i stands for the degeneracy of the i -th vibrational state. The expression $[v]$ represents the vibrational quantum numbers (v_1, v_2, \dots) . For a diatomic molecule with only one fundamental vibration this expression may be simplified.

The transitions of an infrared rotation-vibration band are governed by corresponding rotational selection rules. It is customary to refer to the low wavenumber set of lines with $\Delta J = -1$ as the P -branch, while the high wavenumber part with $\Delta J = +1$ is known as the R -branch (for further labeling, see Fig. 4.3-2). Neglecting the centrifugal distortion, the wavenumbers of the rotational lines of a vibrational transition $(v' \leftarrow v'')$ with wavenumber $\tilde{\nu}_0$ can be described by a single equation

$$\tilde{\nu} = \tilde{\nu}_0 + (B'_{[v]} + B''_{[v]})m + (B'_{[v]} - B''_{[v]})m^2$$

Generally, constants and quantum numbers with single and double prime refer to the upper and the lower state, respectively. It is $m = J'' + 1$ for the R -branch and $m = -J''$ for the P -branch. Wavenumber combinations of pairs of lines with common upper or lower rotation-vibration state can give the corresponding rotational constants of the ground or excited vibrational state:

$$\Delta_2 F'' = R(J'' - 1) - P(J'' + 1) = 4B''_{[v]}(J'' + 1/2)$$

and

$$\Delta_2 F' = R(J'') - P(J'') = 4B'_{[v]}(J'' + 1/2)$$

Combination differences are often used to confirm the assignment of rotational quantum numbers.

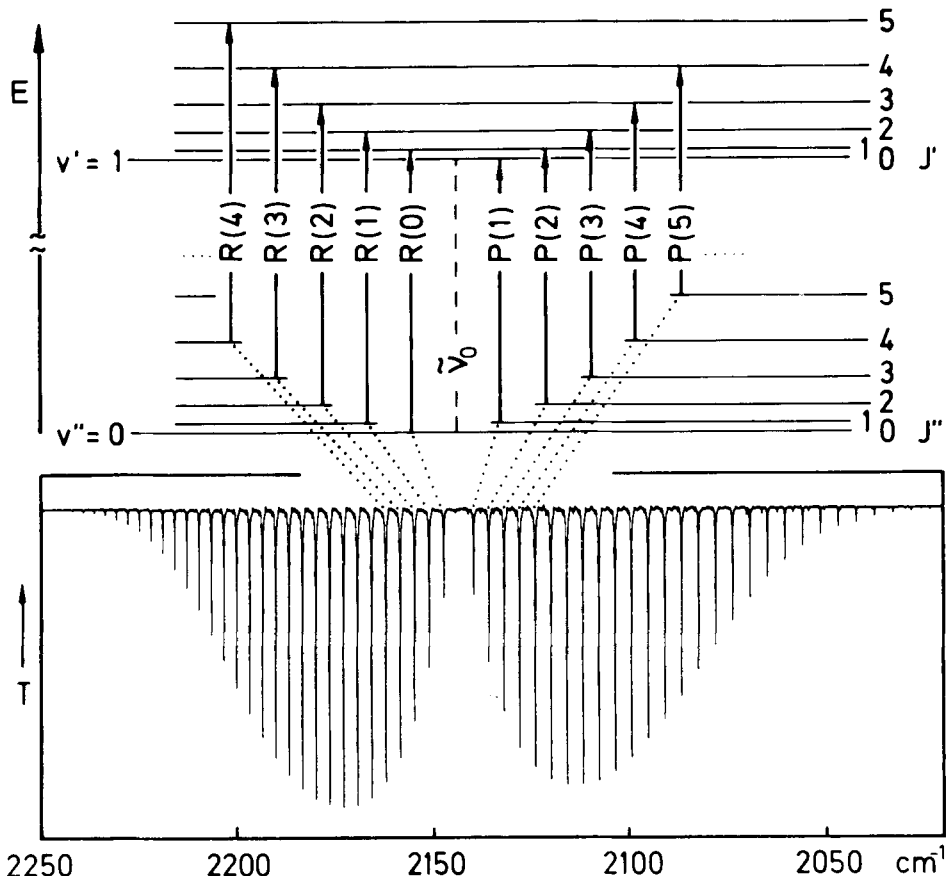


Figure 4.3-2 Assignment for the rotation-vibration lines of the CO fundamental vibration band.

As an example of the rotation-vibration band of a diatomic molecule, the nitrogen-broadened spectrum of $^{12}\text{C}^{16}\text{O}$ is shown in Fig. 4.3-2. An additional band appears, less intense, but shifted, which is attributed to the $^{13}\text{C}^{16}\text{O}$ isotope. Fig. 4.3-3 displays an overview spectrum including the overtone region for the $(2 \leftarrow 0)$ transition, with an inset magnifying the spectral features around the fundamental band at low pressure, which are not resolved at low resolution. In Tab. 4.3-3 the corresponding band centers, including band intensities of different isotopes – the latter also reflect their natural abundance – are presented. As a reference, the hot band $(2 \leftarrow 1)$ of the main isotope is also listed. The intensities of the main band lines of the $^{12}\text{C}^{16}\text{O}$ isotope are drastically reduced compared to the lines of the less intense bands. This is due to convolution effects, since the true line halfwidth is still much smaller than the spectral resolution used. This can have a dramatic impact on quantitative work: in order to record true line intensities, the spectral resolution should be chosen appropriate, i.e., it should be smaller than the true

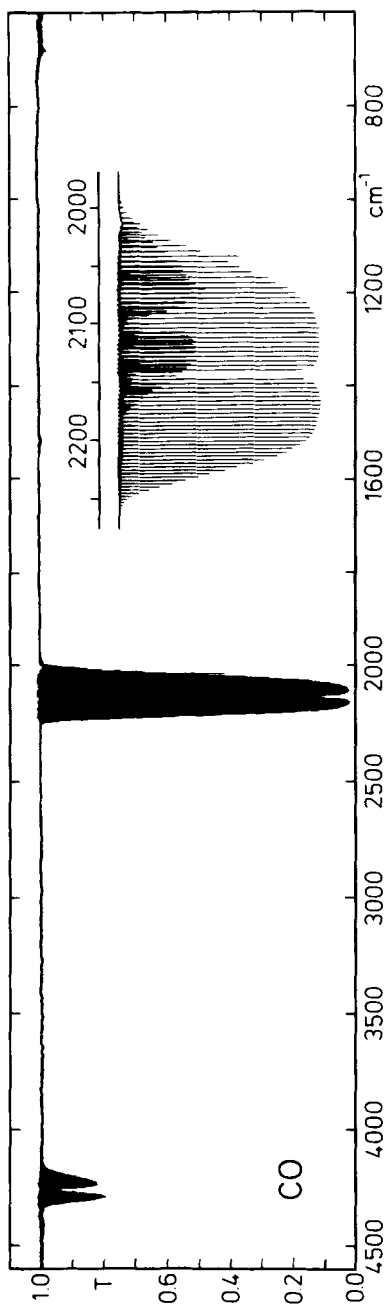


Figure 4.3-3 Spectrum of CO with pressure of 54 hPa, temperature of 25 °C and optical pathlength of 10 cm at a spectral resolution of 0.05 cm^{-1} ; the fundamental region is enlarged in the inset showing also the rotation-vibration features of the $^{13}\text{C}^{16}\text{O}$ isotope (see also text).

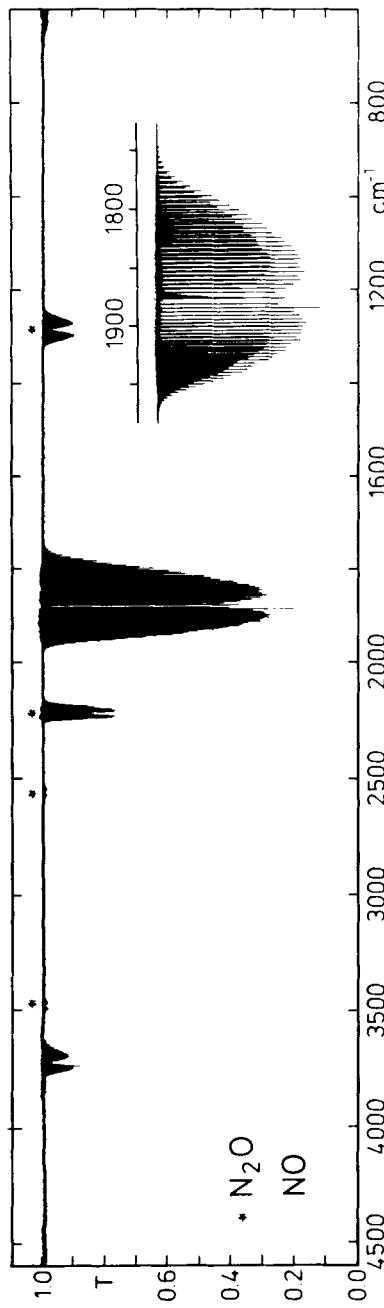


Figure 4.3-4 Spectrum of NO and its impurity of N_2O (total pressure 20 hPa, 25 °C, 10 cm) at a spectral resolution of 0.05 cm^{-1} ; in the inset high resolution details of the NO fundamental are shown.

Table 4.3-3 Infrared fundamental vibration wavenumbers of different isotopic species of CO (Rothman et al., 1987)

Band Center cm^{-1}	Isotope	Sum of Intensity @ 296 K $10^{21} \text{ cm}^{-1}/(\text{molec. cm}^{-2})$
2143.272	$^{12}\text{C}^{16}\text{O}$	9813
2116.791 (2 ← 1)	$^{12}\text{C}^{16}\text{O}$	0.5
2116.296	$^{12}\text{C}^{17}\text{O}$	3.5
2096.067	$^{13}\text{C}^{16}\text{O}$	105
2092.123	$^{12}\text{C}^{18}\text{O}$	19

line halfwidth. The effect of different instrument line shape functions has been described by Ramsay (1952) and Anderson and Griffiths (1975).

The selection rules $\Delta J = \pm 1$ afford a so-called parallel band with a change in dipole moment along the molecular axis, which is particularly obvious in diatomic molecules. NO, for instance, is an exception to this rule, because its ground state possesses an electronic orbital angular momentum about the molecular axis characterized by quantum number $\Lambda = 1$ (π -state). Stable molecules, normally with $\Lambda = 0$, are referred to as having Σ -states. The electronic spin gives rise to a multiplet term structure. In the case of NO, for instance, spins with $S = -1/2$ and $1/2$ are found. The quantum number of the resulting electronic angular momentum is either $\Omega = 3/2$ or $1/2$, which is designated as a right subscript to the state notation, while the left superscript represents the multiplicity $2S + 1$, e.g., $^2\pi_{3/2}$ and $^2\pi_{1/2}$. In these cases, models equivalent to the symmetric top apply (for details, see Herzberg, 1950). The selection rule $\Delta J = 0$ is thus allowed, giving rise to the so-called Q -branch of a rotation-vibration band (see Fig. 4.3-4). By using high resolution spectroscopy the multiplet structure is evident. The assignment of lines to the different states can be carried out considering that the quantum number J , which is always halfintegral here and designates the total angular momentum including the electronic component, cannot be smaller than Ω . As a consequence, there is a gap around the Q -branch resulting from the missing level with $J = 1/2$ of the $^2\pi_{3/2}$ -state. The energy difference between the two π -states can be estimated from the corresponding line intensities, which reflect the Boltzmann population density of the levels (see below).

In Fig. 4.3-4 a few bands are marked by an asterisk. We recorded the NO-spectrum of a sample which had been produced a year earlier. Decomposition afforded a certain percentage of N_2O , giving rise to additional parallel bands. This leads us to the spectra of polyatomic linear molecules, for which degenerate vibrational states exist. Rotation-vibration interaction is creating a vibrational angular momentum with allocated quantum number l_i (allowed values are $v_i, v_i - 2, \dots, -v_i$) for these states, so that similar arguments as mentioned above for molecules with electronic angular momentum apply. The induced Coriolis force will split the degenerate levels causing so-called l -type doubling. The oscillating dipole moment is oriented perpendicularly to the molecular axis, and all three branches with $\Delta J = 0, \pm 1$, of a so-called perpendicular band appear.

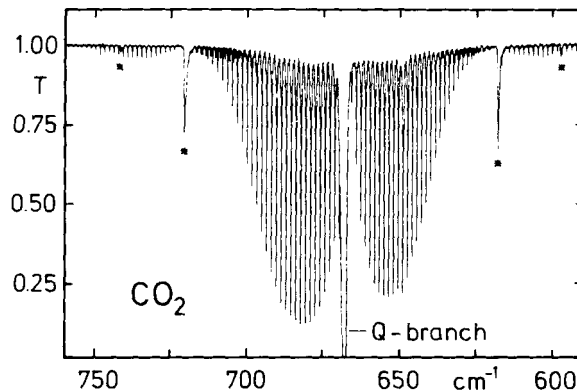


Figure 4.3-5 Rotation-vibration band (ν_2) of atmospheric CO_2 (atmospheric pressure 1000 hPa, 25°C, 400 cm) at a spectral resolution of 0.05 cm^{-1} (for a discussion of the Q -branches marked by an asterisk see text).

This is exemplified in Fig. 4.3-5, which shows the bending ν_2 -fundamental of CO_2 . There are other prominent Q -branches in this section of the spectrum. At this point, it is necessary to discuss different notations in use, since the vibrational energy state is usually characterized by the quantum numbers of the three fundamental modes and the angular moment, i.e., $(v_1 v_2^{\dagger} v_3)$. However, Fermi resonance between the vibrational states of $(1\ 0^0\ 0)$ and $(0\ 2^0\ 0)$, mixes levels, which makes the assignment ambiguous. Similar resonances occur at higher levels. This is the case, for example, with the two infrared-active combination bands above 3500 cm^{-1} which involve these two levels (see Fig. 4.3-6). This uncertainty is avoided by using a notation with an additional fifth parameter. The convention concerning the assignment of the upper and lower levels mentioned is $(1\ 0^0\ 0\ 1)$ and $(1\ 0^0\ 0\ 2)$, respectively. For further reading see Rothman and Young (1981) and the references cited therein. In Tab. 4.3-4 the assignment of the

Table 4.3-4 Infrared vibration bands of CO_2 around the ν_2 fundamental (Rothman et al., 1987)

Band Center cm^{-1}	Upper level	Lower level	Intensity @ 296 K $10^{22} \text{ cm}^{-1}/(\text{molec. cm}^{-2})$
741.724	11 ¹ 01	02 ² 01	76
720.805	10 ⁰ 01	01 ¹ 01	1396
668.115*	03 ³ 01	02 ² 01	369
667.752*	02 ² 01	01 ¹ 01	6257
667.380	01 ¹ 01	00 ⁰ 01	79452
618.029	10 ⁰ 02	01 ¹ 01	1364
597.338	11 ¹ 02	02 ² 01	49

* these hot bands have not been resolved (see Fig. 4.3-5)

observed infrared CO₂ bands under the experimental conditions chosen with dominating pressure broadening is given. In the spectrum of a CO₂ sample, obtained at low pressure, high resolution shows many more spectral details which can be demonstrated by the ν_3 -fundamental (see inset of Fig. 4.3-6). The corresponding assignment, including bands of isotopic species, is found in Tab. 4.3-5.

Table 4.3-5 Observable infrared vibration bands around ν_3 of CO₂ (unless stated, the normal isotope is implied); data from Rothman et al. (1987)

Band Center cm ⁻¹	Upper level	Lower level	Isotopic species	Intensity @ 296 K 10 ²² cm ⁻¹ / (molec. cm ⁻²)
2349.143	00 ⁰ 11	00 ⁰ 01		955357
2336.632	01 ¹ 11	01 ¹ 01		73666
2332.113	00 ⁰ 11	00 ⁰ 01	¹⁶ O ¹² C ¹⁸ O	3518
2327.433	10 ⁰ 12	10 ⁰ 02		1789
2326.598	10 ⁰ 11	10 ⁰ 01		1079
2324.141	02 ² 11	02 ² 01		2838
2283.488	00 ⁰ 11	00 ⁰ 01	¹⁶ O ¹³ C ¹⁶ O	9598
2271.760	01 ¹ 11	01 ¹ 01	¹⁶ O ¹³ C ¹⁶ O	817

An important aspect in band contour analysis are the relative line intensities within a vibrational band. These can easily be calculated on the basis of the population in the rotational states of the vibrational ground state, if the population density of the excited vibrational states can be neglected. An exception are, e.g., low energy torsional vibrations, where the excited states can be considerably populated even at room temperature. The Boltzmann distribution defines the temperature dependence of the population density for various energy levels at the thermodynamical equilibrium. For further discussion, it should be noted that the rotational levels for a linear molecule have a degeneracy of $(2J + 1)$. This degeneracy can be removed by applying a magnetic or electric field, as in Zeeman or Stark-spectroscopy. In this case, there is another rotational integral quantum number M_J with $|M_J| \leq J$, because the components of the angular momentum in the direction of the field are also quantized. Thus, the existing degeneracy has to be considered in the Boltzmann distribution of the J -th rotational level

$$N_J = (2J + 1)N_0 e^{-BJ(J+1)hc/(kT)}$$

where N_0 is the number of molecules in the ground state $J = 0$. By differentiation, it can be shown that the rotational state with the greatest population density is at

$$J_{max} = (kT/2hcB)^{0.5} - 0.5 = 0.5896(T/B)^{1/2} - 0.5$$

In the case of CO, for instance, J_{max} at room temperature can be found at $J = 7$ (see also Fig. 4.3-2). Knowledge of the rotational constant B makes it possible to estimate the temperature of a gas on the basis of the P - and R -branch intensity maxima (Sec. 6.8.2.1). If the rotational fine structure cannot be resolved, it is possible to use the distance between the P - and R -branch maxima for this purpose:

$$\Delta\tilde{\nu}_{PR}^{max} = (8BkT/\hbar c)^{1/2} = 2.3583(BT)^{1/2}$$

Line intensities are also governed by symmetry properties of the rotation-vibration states, which may show degeneracies arising from different orientations of existing nuclear spins. For each nucleus with spin quantum number I , there are $2I+1$ possible orientations of the spin with $M_I = -I, \dots, +I$, as discussed before in connection with the rotational quantum number M_J . Two examples will demonstrate the effects that have to be taken into account.

In the first category, let us consider nuclei with an integral spin quantum number (e.g., D with $I = 1$, ^{16}O and ^{12}C with $I = 0$; for the last two nuclei actually no spin function is involved). The CO_2 molecule is said to obey Bose-Einstein statistics, according to which the total wave function approximated by a product of electronic, vibrational, rotational and nuclear spin contributions must be symmetric with respect to the symmetry operation of exchanging nuclei. In practically all stable molecules, the electronic and vibrational ground state are totally symmetric. It can be shown that the rotational wave functions with even J quantum numbers are also totally symmetric, whereas states with an odd J are antisymmetric. In the case of CO_2 , it can be concluded that only rotational states with even values of J exist in the vibrational ground state. This is in contrast to the first excited antisymmetric stretching vibrational state of CO_2 , where only rotational levels with odd J values exist. The line spacings for the P - and R -branches are thus twice as large as those where all rotational states are allowed. Besides, in this example the central gap is only half as large as in the more general case, represented by the isotopic $^{18}\text{O}^{12}\text{C}^{16}\text{O}$ molecule which lacks a center of symmetry. The reader may verify the resulting line pattern of the normal isotope by comparing the rotational level structure and spectrum of CO shown in Fig. 4.3-2. However, with high resolution spectra provided the line density of hot band transitions is twice as high as that of the fundamentals (see Fig. 4.3-6 and Tab. 4.3-5). For the more complicated term scheme and selection rules in these cases, see Allen and Cross (1963).

The situation is different for molecules that possess nuclei with half integral spin quantum numbers. The list of examples includes ^1H with $I = 1/2$ or Cl with $I = 3/2$, both of which obey Fermi-Dirac statistics, which requires that the total molecular eigenfunction be antisymmetric. This may be exemplified by the spin statistical weights of the rotational energy levels of C_2H_2 . For the protons in this molecule three symmetric spin functions and one antisymmetric can be formulated, which must be paired with rotational states of appropriate symmetry. As a consequence, antisymmetric states with odd J -quantum numbers are found to be triply degenerate on the premise of a totally symmetric electronic and vibrational state. This results in an alternating line intensity in a rotation-vibration band, which may be of valuable assistance for the assignment of rotational quantum numbers, and may provide information about the molecular symmetry.

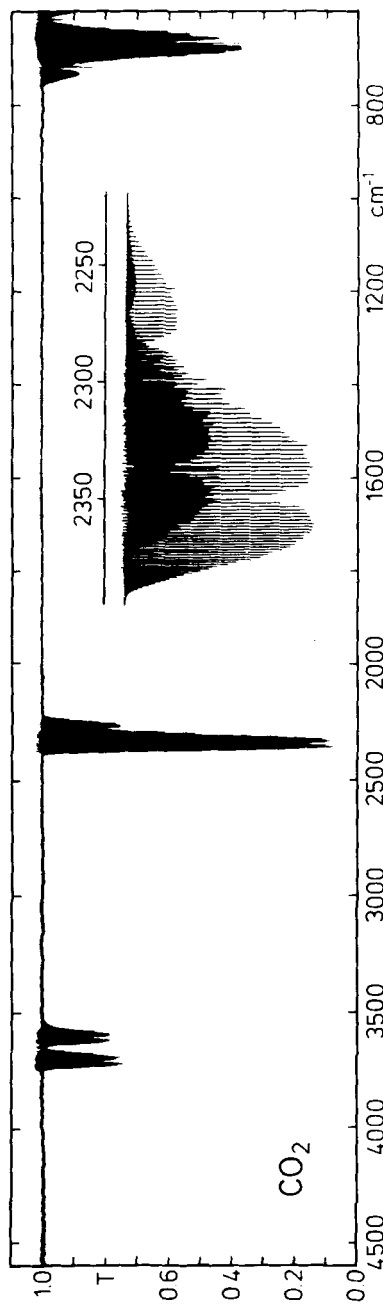


Figure 4.3-6 Rotation-vibration spectrum of CO_2 (8 hPa, 25 °C, 10 cm) with high resolution inset for the ν_3 -fundamental at a spectral resolution of 0.05 cm^{-1} .

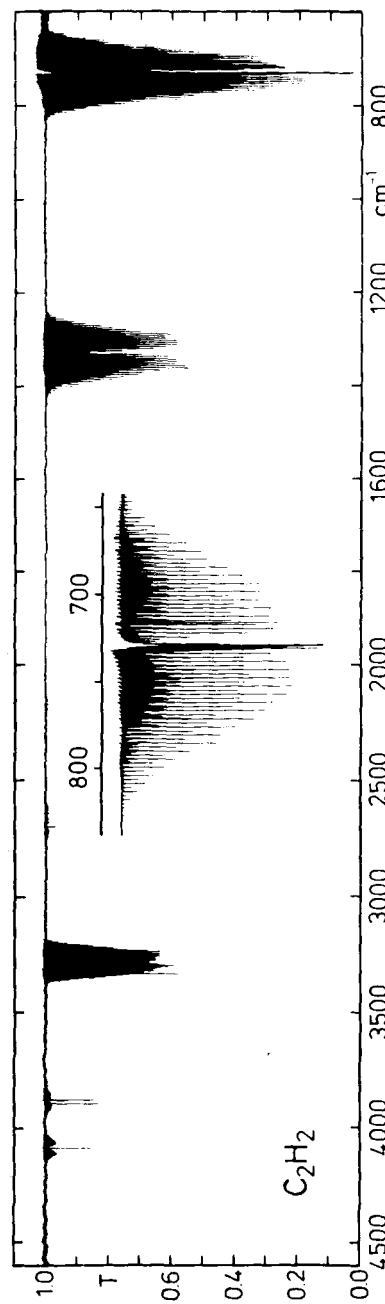


Figure 4.3-7 Rotation-vibration spectrum of C_2H_2 (5 hPa, 25 °C, 10 cm) at a spectral resolution of 0.05 cm^{-1} ; with the inset the intensity alternation due to spin statistics in the ν_5 -fundamental is illustrated (the underlying fine structure is from a hot band transition with its Q-branch shifted to lower wavenumbers compared to the fundamental).

This fine structure is presented clearly in the inset of Fig. 4.3-7, showing the perpendicular fundamental ν_5 of C_2H_2 . The absence of such effects in the spectrum of N_2O indicates that this linear molecule has no symmetrical structure with equivalent nitrogen atoms.

4.3.1.3 Symmetric top molecules

Before discussing the spherical rotor, it is appropriate to focus on the rotational energy levels for symmetric rotors (see also Tab. 4.3-2). For the rigid prolate top, the rotational energy is given by

$$E_{JK} = B_{[v]}J(J+1) + (A_{[v]} - B_{[v]})K^2$$

A succession of levels like those of a linear molecule can be calculated for each quantum number K , which in this case describes the quantized component of the angular momentum about the unique a -axis. K cannot exceed J , the quantum number for the total angular momentum, i.e., $K = 0, \pm 1, \dots \pm J$. For an oblate symmetric top the rotational constant $A_{[v]}$ has to be replaced by $C_{[v]}$. In relation to the case of $K = 0$, other K quantum numbers allowed will thus result in lower energies E_{JK} , which is in contrast to the prolate top with a positive term of $(A_{[v]} - B_{[v]})$. Evidently, all rotational levels with $K \neq 0$ are doubly degenerate. It should be noted that each level still possesses an M -degeneracy of $(2J+1)$ as discussed in connection with the linear molecule. This is due to space quantization.

A molecule which is a symmetric top on account of its symmetry (accidentally symmetric tops are not considered), exhibits two types of normal vibrations, because the oscillating dipole moment may either be oriented parallel to the top axis or perpendicularly to it. The infrared selection rules for a so-called parallel band are

$$\left. \begin{array}{l} \Delta J = \pm 1, K = 0 \\ \Delta J = 0, \pm 1, K \neq 0 \end{array} \right\} \Delta K = 0$$

For such a band, only stacked levels of the same K -value can be involved in a transition, resulting in subbands with three ${}^Q P_K$, ${}^Q Q_K$ and ${}^Q R_K$ -branches (the exception is $K = 0$ with a missing Q -branch, as in the case of the linear molecule). The superscript Q in the branch symbol stands for the corresponding ΔK selection rule. Due to the restriction $J \geq K$, some of the low J -lines in the K -subbands are missing. For the subband origins we find

$$\tilde{\nu}_o^{Sub}(K) = \tilde{\nu}_o + \{(A'_{[v]} - B'_{[v]}) - (A''_{[v]} - B''_{[v]})\}K^2$$

Finally, the complete parallel band is a superposition of all subbands. The composite of such a band resembles the perpendicular band of a linear molecule, apart from additional

K -splitting of the lines in the branches. This is only minor as long as the difference between the rotational constants of the lower and the upper vibrational state is small. The infrared spectrum of CH_3I (prolate top) shows examples of parallel band features with a PQR structure like that for a linear molecule (see Fig. 4.3-8).

The second type of fundamental vibrations involves an oscillating dipole moment, oriented perpendicularly to the unique molecular axis. The corresponding infrared selection rules for the rotational transitions are given by

$$\Delta J = 0, \pm 1 \quad \text{and} \quad \Delta K = \pm 1$$

Each K quantum number in the lower vibrational state with the exception of $K = 0$, gives rise to two subbands. The subband origins can be calculated according to

$$\begin{aligned}\tilde{\nu}_o^{Sub}(K) = & \tilde{\nu}_o + (A'_{[v]} - B'_{[v]}) \pm 2(A'_{[v]} - B'_{[v]})K + \\ & + \{(A'_{[v]} - B'_{[v]}) - (A''_{[v]} - B''_{[v]})\}K^2\end{aligned}$$

The equations for the individual P , Q and R subband branches are the same as those for linear molecules. In order to distinguish between different subband branches, one uses the superscript P and R for the corresponding ΔK selection rule, e.g., ${}^P Q_{K''}(J'')$ for a Q -branch transition with $\Delta K = -1$. The Q -branches may stand out against the other wide spread branch lines. This is true of our example of the CH_3I spectrum, which exhibits several perpendicular bands (see Fig. 4.3-8). This spectrum also shows the line intensity alteration in the Q branches as a result of spin statistics.

So far we have neglected rotation-vibration interaction. The rotational energy levels in a degenerate vibrational state of a symmetric top with a threefold or higher symmetry axis receive a contribution from Coriolis coupling. This is expressed by the additional term of $\pm 2\zeta_{[v]} A'_{[v]} K$, with ζ , the Coriolis coupling constant, terminating the degeneracy of the levels. The transitions in a perpendicular band involving ground state and degenerate vibrational state are thus affected by the shift of the individual subband origins, so that a new effective upper state rotational constant $A'_{[v]}(1 - 2\zeta_{[v]})$ can be obtained from the subband centers, leaving the rotational subband structure unaffected. The notably different Q branch spacings in the three most intensive perpendicular bands of CH_3I can be explained by this extended model.

In Fig. 4.3-9 a high resolution spectrum of NH_3 (oblate symmetric top) is displayed. The most intense infrared vibration, which is the ν_2 fundamental, shows the features of a parallel band, although with the notable structure of a Q branch doublet at 931.7 cm^{-1} and 968.3 cm^{-1} . This doublet arises from inversion doubling, which is due to the two possible opposite pyramidal configurations of the molecule. The corresponding double minimum vibrational potential leads to a splitting of the vibrational levels with two components for ν_2 , e.g., 0^s , 0^a and 1^s , 1^a etc.; the energy differences between the first two term pairs are 0.8 cm^{-1} and 35.8 cm^{-1} , respectively. The superscript reflects the symmetry of the state. In the infrared spectrum, the two bands discussed can be assigned to transitions between components of opposite parity, e.g., $1^a \leftarrow 0^s$ and $1^s \leftarrow 0^a$. Analysis of the spin functions indicates that, if $K = 0$, for symmetry reasons of the total wave function only either the

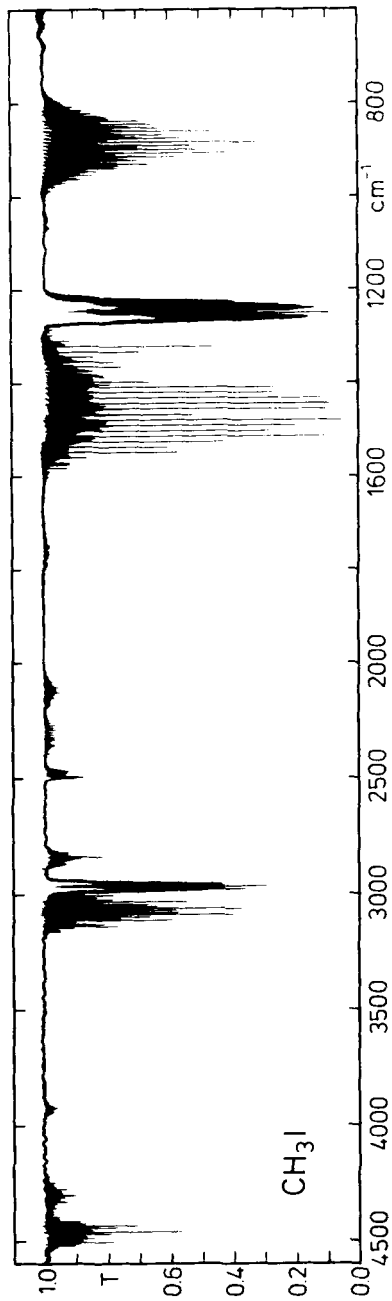


Figure 4.3-8 Rotation-vibration spectrum of CH_3I (prolate symmetric top; 41 hPa, 25°C , 10 cm) at a spectral resolution of 0.05 cm^{-1} .

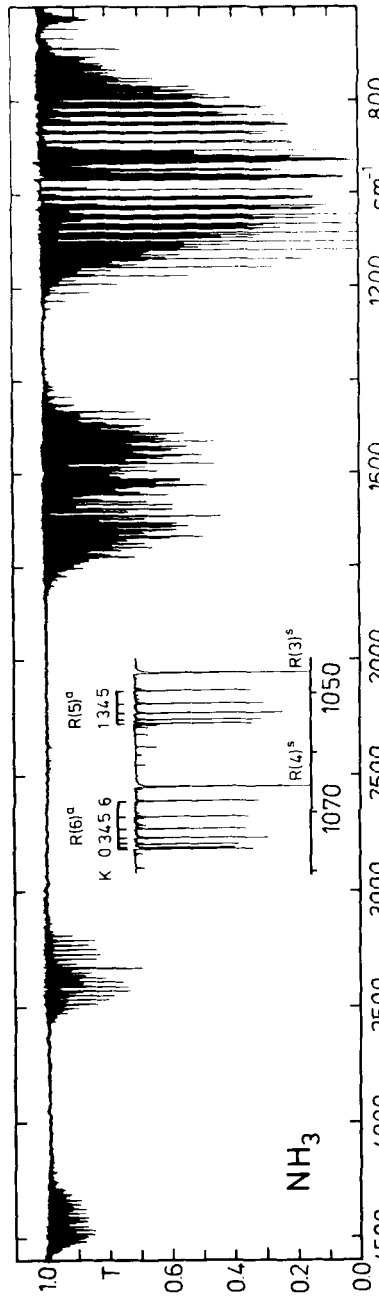


Figure 4.3-9 Rotation-vibration spectrum of NH_3 (7.5 hPa, 25°C , 10 cm) at a spectral resolution of 0.05 cm^{-1} ; the K -structure of the R' -branch lines of the ν_2 -fundamental can easily be resolved (see inset).

upper or, depending alternately on the J quantum number, the lower doublet level can exist (see also the fine structure of some R^a -branch lines for the $1^s \leftarrow 0^o$ transitions in Fig. 4.3-9; the K -splitting in the other band is not resolved). The second parallel band (ν_1 at 3336.2 cm^{-1}) is split much less, due to inversion doubling with $\Delta\tilde{\nu} = 1.8\text{ cm}^{-1}$. The ν_4 fundamental at 1627 cm^{-1} is a perpendicular band with the Q branch lines compressed in a smaller spectral interval compared to that of the CH_3J -spectrum. Another example of a spectrum which resembles those recorded with lower resolution, is the gas phase spectrum of benzene shown in Fig. 4.3-10. The fingerprint region below 2000 cm^{-1} exhibits the most intense fundamental (ν_4), which is a parallel band, at 671 cm^{-1} . The two perpendicular bands at 1485 cm^{-1} (ν_{13}) and 1037 cm^{-1} (ν_{14}) demonstrate similar features.

Finally, it should be noted that certain overtone and combination bands, or the spectrum of an accidentally symmetric rotor may give rise to hybrid bands with both parallel and perpendicular band features.

4.3.1.4 Spherical top molecules

Tetrahedral molecules, such as CH_4 and CF_4 , or octahedral ones, such as SF_6 , are described by the spherical top model, for which the same rotational term values can be calculated as for a linear molecule. This is due to the fact that this is the limiting case of a symmetric top, with all rotational constants being equal, eliminating the K dependence of the rotational energy terms with quantum number J . In addition to the spatial degeneracy, this yields a total of $(2J + 1)^2$ terms for each J value, neglecting nuclear spin effects. Thus, the infrared selection rule of $\Delta J = 0, \pm 1$ brings about a PQR branch structure in which the PR separation determined by contour analysis is by a factor of $\sqrt{2}$ larger than that found for a linear molecule with the same rotational B constant. This result is only due to the different degeneracies of the rotational levels for the two molecular models. The simple rotational energy expression only applies to nondegenerate vibrational levels. If the rigid rotor model for the degenerate states is relaxed, Coriolis interaction will give rotational fine structure clusters caused by term splitting.

The CH_4 spectrum, presented in Fig. 4.3-11, may serve as an example. A closer look at the PQR structure of the ν_3 fundamental at 3020 cm^{-1} reveals the line clusters. Magnification of some of the P branch lines, such as $P(7)$, discloses five components of similar intensity. The primary splittings, as mentioned above, occur in the upper J' -levels, each of which contains $J' - 1$ components. High resolution laser spectroscopy can even resolve 10 transitions, the additional of which arise from splittings in the ground state due to centrifugal effects. In practice, experiments often show, that the simple model applied to analyze the rotational fine structure is frequently inadequate. The higher the resolution, the more complicated the molecular models will be needed. Complex Hamiltonians are employed to simulate spectra and to verify the assignment. The subject is discussed in greater theoretical detail in monographs by Papousek and Aliev (1982) and Amat et al. (1971).

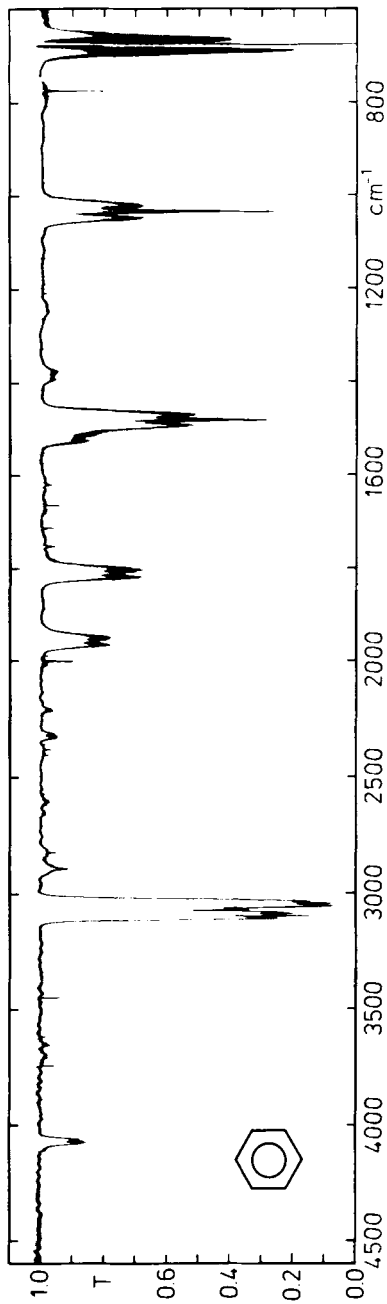


Figure 4.3-10 Rotation-vibration spectrum of C_6H_6 (oblate symmetric top; 55 hPa and 10 hPa for lowest wavenumber interval, 25°C , 10 cm) at a spectral resolution of 0.05 cm^{-1} .

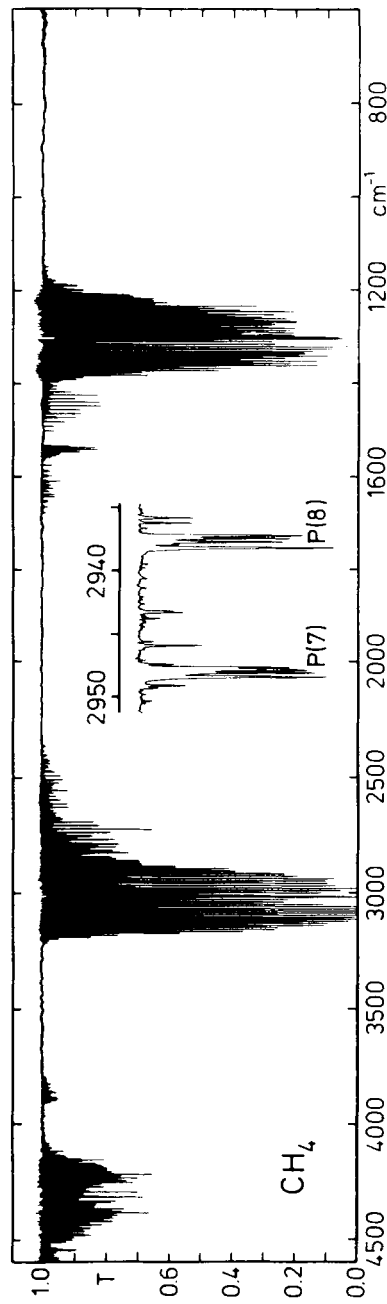


Figure 4.3-11 Rotation-vibration spectrum of CH_4 (spherical top; 56 hPa, 25°C , 10 cm); some rotational fine structure is also shown at a spectral resolution of 0.05 cm^{-1} .

4.3.1.5 Asymmetric top molecules

There is a large class of molecules for which all three rotational constants are different, although such molecules do not necessarily lack all symmetry. The rotational energy levels and the spectra of such molecules are rather complex. As a consequence of the asymmetry, the K degeneracy of the symmetric top levels is lifted, so that $(2J + 1)$ levels of different energy for each J value exist. The degree of asymmetry can be expressed by different parameters, a common one is defined by

$$\kappa = (2B - A - C)/(A - C)$$

For the prolate symmetric top with $B = C$ we find $\kappa = -1$ and for the oblate one with $A = B$: $\kappa = +1$. The rotational energy can thus be expressed as

$$E(J, \tau) = J(J + 1)(A + C)/2 + E_{J,\tau}(\kappa) \cdot (A - C)/2$$

where the index τ is a labeling integer ranging from $-J$ to J as E increases. A schematic diagram is shown in Fig. 4.3-12 from which the energy level correlation with the symmetric top models is evident. This correlation provides the basis for the double subscript notation of $K_1 K_2$ for the levels, which is alternatively used for the quantity τ . The index τ is related to the prolate quantum number K_1 and to the oblate K_1 by $\tau = K_1 - K_1$.

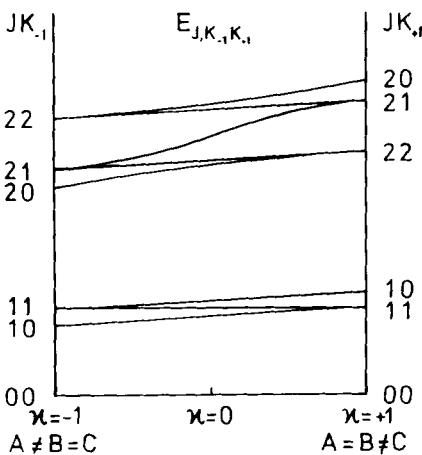


Figure 4.3-12 Schematic diagram of the lowest rotational energy levels of an asymmetric top molecule.

Unfortunately, explicit solutions for rotational levels exist only at low J values. This problem used to be solved by employing tabulations for the so-called reduced energy $E(\kappa)$, which is now conveniently calculated by computer programs.

The infrared spectra of the asymmetric top molecule obey the general selection rules $\Delta J = 0, \pm 1$. Due to symmetry reasons, we have to distinguish between three different types of vibrational bands, depending on the direction of the transition moment relative to the three principle axes. Orientation parallel to the a axis, for instance, constitutes a type A band, etc.. Considering the limiting symmetric top cases will assist our systematic band shape analysis. The A type and the C type band of a near prolate top, for example, resemble a parallel and a perpendicular band, respectively. In the near oblate case this has to be reversed. It helps to use the double K notation for the rotational levels, considering the corresponding infrared selection rules of a symmetric top. Group theoretical arguments show that these are just specializations of the more general cases described below. For A type bands we find

$$ee \leftrightarrow eo \text{ and } oe \leftrightarrow oo$$

by which even/odd changes of the corresponding K numbers are described. Note that a parity change occurs only for K_1 . For C type bands, the oscillating dipole moment is oriented along the principle axis of the largest moment of inertia. For the oblate symmetric top molecules with figure axis c , a parallel band will result. Exchanging the above K_1 and K_1 subscripts affords the selection rules

$$ee \leftrightarrow oe \text{ and } eo \leftrightarrow oo$$

Generally, changes in the subscripts by more than zero or one, as by demand of the symmetric top limits, result in less intensive transitions.

For B type bands, the oscillating dipole moment is oriented along the axis defining the intermediate principle moment of inertia, so that both symmetric top limits correspond to perpendicular bands, giving rise to the general selection rule

$$ee \leftrightarrow oo \text{ and } oe \leftrightarrow eo$$

Wherever this is applicable in rotational fine structure analysis, the customary approach involves analyzing the spectra in terms of a near prolate or oblate top. Deviations from this approximation decrease with increasing quantum number K . For a more extensive discussion, for example of the subband structure in symmetric top spectra, the reader is referred to Allen and Cross (1963).

The spectra of different asymmetric top molecules may serve to outline the theoretical aspects. One of the most important spectra, especially for atmospheric studies, is that of H_2O ($\kappa = -0.44$). The mid-infrared range (see Fig. 4.3-13) is dominated by two wide wing rotation-vibration bands; the high wavenumber band at 3756 cm^{-1} has been assigned to the antisymmetric stretching vibration ν_3 , which has the feature of an A type band. The other band, with its center at 1595 cm^{-1} , is the bending ν_2 fundamental, with the B type characteristic of showing a minimum instead of a prominent Q branch. Finally, the symmetric vibration ν_1 is of the same symmetry as ν_2 ; however, this B type band with its center at 3657 cm^{-1} overlaps considerably with ν_3 .

The second example, C_2H_4 , which is a planar molecule with an asymmetry parameter of $\kappa = -0.92$, exhibits all three types of bands, which indicates that the molecule

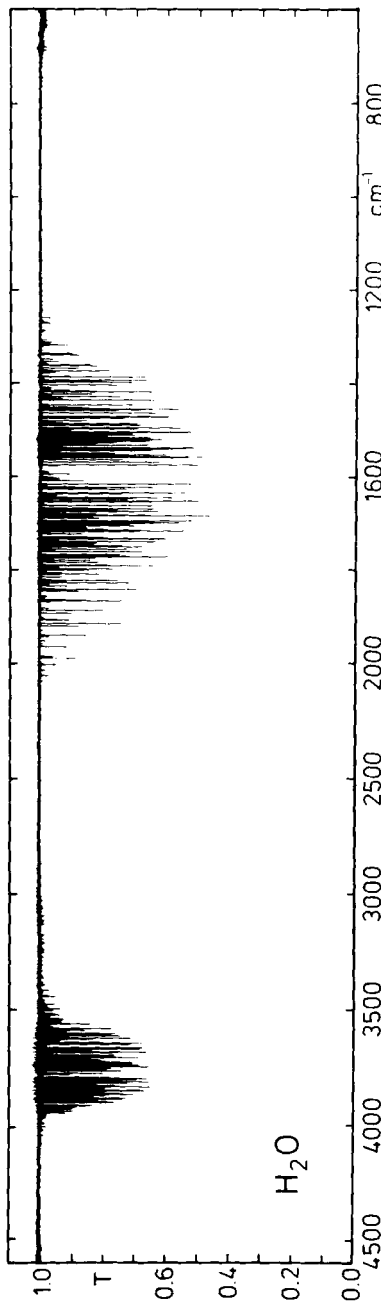


Figure 4.3-13 Rotation-vibration spectrum of H_2O (asymmetric top; 4 hPa, 25 °C, 10 cm) at a spectral resolution of 0.05 cm^{-1} ; above 600 cm^{-1} some lines from pure rotational transitions can be seen.

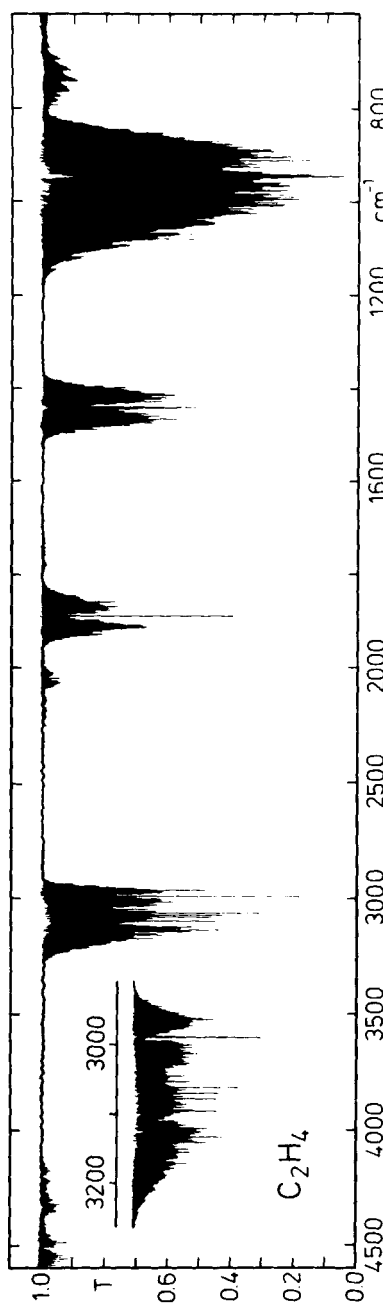


Figure 4.3-14 Rotation-vibration spectrum of C_2H_4 (asymmetric top; 18 hPa, 25 °C, 10 cm) at a spectral resolution of 0.05 cm^{-1} ; for clarity the CH-stretching region is enlarged.

possesses transition moments along all three different principal axes (see Fig. 4.3-14). The most intensive rotation-vibration band at about 950 cm^{-1} is assigned to ν_7 . It is a *C* type band with a pronounced resemblance to a perpendicular band of a prolate symmetric top. At low resolution, the high line density in the band center gives rise to a dominating *Q* branch. There are other single *Q* branches, especially at high wavenumbers of the band.

For clarity, the wavenumber scale of the CH-stretching region is magnified: besides the *A* type band at 2989.5 cm^{-1} (ν_{11}), there is a *B* type band at higher wavenumbers whose rotation-vibration lines go through a marked intensity minimum (3105.5 cm^{-1} : ν_9). Further two *A* type bands of medium intensity (1443.5 cm^{-1} : ν_{12} and a combination band at 1889.6 cm^{-1} , assigned to $\nu_7 + \nu_8$) can be observed.

There are asymmetric tops, for example of C_s symmetry, like the CH_3CHO molecule, where the transition moment is not always uniquely parallel to one of the principle axes but may be defined within the symmetry plane, giving rise to hybrid bands. In the latter case, mixtures of type *A* and *B* are possible (for illustration, see the spectral region below 1200 cm^{-1} in Fig. 4.3-15, containing four different band shapes which do not significantly change at lower spectral resolution (from high to low wavenumbers, the sequence is *B* type, *A/B* hybrid, *A* and *C* type).

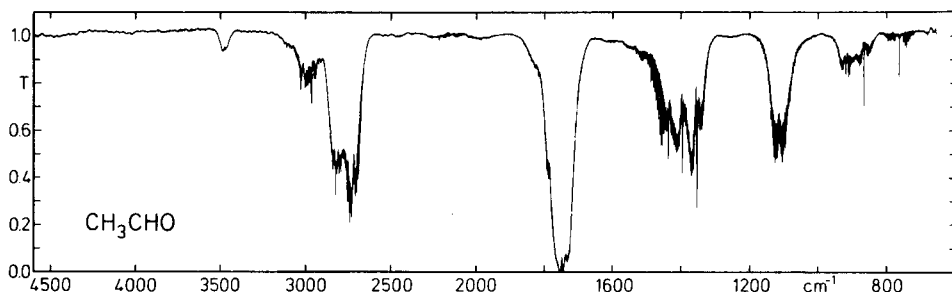


Figure 4.3-15 Rotation-vibration spectrum of CH_3CHO (asymmetric top; 38 hPa, 25°C , 10 cm) at a spectral resolution of 0.05 cm^{-1} .

Bandshape analysis is a source of valuable additional information for the symmetry assignment of a vibration on the grounds of the transition moment. At medium resolution, the resulting envelopes are still characteristic of the different types of bands. A by now classical publication by Ueda and Shimanouchi (1968) graphically presents a systematic investigation of envelopes of different asymmetric top molecules obtained by model calculations, including the effect of different slit functions commonly used with grating spectrometers. This approach is limited by the fact that the upper and lower state rotational constants are assumed to be the same. The influence of the relative values on the envelope may be almost as dramatic as the degree of asymmetry. Besides, resonances with other levels may perturb the overall features and intensities of a band. In the context of this book, this subject can only be touched on; it has been discussed in greater detail, for example, by Overend (1975) and Mills (1965). Concerning band

contour analysis, we should like to refer to the *PR* separations for the bands of linear and spherical molecules mentioned earlier. Several attempts have been made to quantify these features of symmetric and asymmetric tops. A classical review paper is that of Seth-Paul (1969) which provides useful approximations for vibrational assignment.

The large number of investigations of gaseous compounds in the infrared, make it impossible to present a compressed, complete overview on this subject. The state of the science up to 1945 has been described comprehensively in the classic books by Herzberg (1945, 1950) who compiled an excellent source of information on individual molecules. Today, there is an abundance of publications on high resolution studies by means of FT-IR spectrometers and diode lasers. Special techniques of simplifying infrared spectra by using free jet expansions for rotational and vibrational cooling of the investigated molecule have been developed (see, e.g., Davies and Morton-Jones, 1987). The overall complexity of rotation-vibration spectra has been demonstrated in an impressive manner by Graner (1981), who illuminates the essentials of high resolution work. This publication describes the investigations of methyl bromide spectra with all its isotopic varieties, critically considers perturbations, and aims at an almost complete set of harmonic and anharmonic constants. Using the rotation-vibration interaction parameters, the equilibrium rotational constants A_e and B_e of each of the isotopic molecules were evaluated, enabling the corresponding equilibrium structure for the CH_3Br molecule to be calculated.

A comprehensive publication by Heise et al. (1981) demonstrates the value of medium resolution work for the assignment of fundamentals of a larger, nine-atom molecule like $\text{CH}_3\text{CH}_2\text{CN}$ and its isotopic species. In this case, complete consideration of combination bands is of great assistance. In order to calculate a valence force field, the wavenumbers of the fundamentals have, as in most cases, not been corrected for anharmonicities and evident Fermi resonance effects. This gains an added degree of complexity as the molecular size increases.

An extensive and regularly updated database listing line frequencies, broadening parameters and intensities of a variety of molecules with a small number of atoms has been compiled. This database is particularly valuable for atmospheric studies and fundamental laboratory spectroscopy research. The most recent contribution by Rothman et al. (1987) also provides an extensive list of references, adding further details to the original studies. In this context, we would like to recommend a publication by Pugh and Rao (1976), which reviews intensity data, i.e., infrared band strengths of molecular vibrations, and provides an extensive list and description of the pertinent measurement techniques.

4.3.2 Raman spectra of gases*

4.3.2.1 Introduction

Soon after the discovery of the Raman Effect in liquids (Raman and Krishnan, 1928; Raman, 1928a; Raman, 1928b) also the first Raman spectrum of a gas, namely the vapor of ethyl ether, was observed by Ramdas (1928). Then Wood (1929) constructed a sample cell of 1.5 m length and a corresponding mercury arc lamp in a closely coupled configuration and photographed the Raman spectra of HCl and NH₃. In a series of papers Rasetti (1929a; 1929b; 1929c; 1930a; 1930b) investigated the rotational and rovibrational Raman spectra of H₂, N₂, O₂, and NO. Particularly important was the clear evidence for the 2 : 1 intensity ratio of even and odd rotational levels in N₂ (Rasetti, 1929a; 1929b; 1930a) which confirmed the validity of Bose statistics for the nitrogen nucleus (Heitler and Herzberg, 1929) two years before the discovery of the neutron. Although Placzek and Teller (1933) worked out the complete theory of rotational structure in Raman scattering, only very little experimental activity followed until about 1950.

As soon as water-cooled low pressure mercury arcs had been developed in Toronto (Welsh et al., 1952), the resulting low linewidths of the exciting lines facilitated the resolution of rotational structure in the spectra. In a long series of investigations Stoicheff (1959) and Weber (1973) and their collaborators recorded photographically the pure rotational Raman spectra of a great number of molecules under high resolution, while Welsh and coworkers in Toronto (Stansbury et al., 1953; Welsh et al., 1955; Feldman et al., 1955 and 1956; Romanko et al., 1955; Mathai et al., 1956; Welsh, 1956; Allin et al., 1967; Fast et al., 1969) studied rotation-vibrational Raman bands.

In the laboratories of Bernstein in Ottawa (Yoshino and Bernstein, 1958a; 1958b; 1959; Schrötter and Bernstein, 1961; 1964; Kecki and Bernstein, 1965; Bernstein, 1967) and Moser in Munich (Holzer and Moser, 1964; 1966; Holzer 1968a; 1968b; Perzl and Moser, 1968; Hornischer and Moser, 1972) Raman intensities were measured in gases and vapors using mercury excitation and photoelectric recording. The results of these investigations were collected in a review article (Murphy et al., 1969).

For all these experiments scattering volumes of about 10 L at atmospheric pressure were required. Through the introduction of lasers as light source in Raman spectroscopy a drastic reduction of the scattering volume became possible. In principle only an effective scattering volume of about 10⁻⁸ cm³ in the focus of a laser beam is required. The first Raman spectrum of a gas excited by a laser was published by Weber and Porto (1965). The decisive advantage of the technique was demonstrated by Barrett and Adams (1968) through excitation of the rotation-vibrational spectra of O₂, N₂, and CO₂ in the resonator of an argon ion laser. The results of many investigations have been reviewed by Weber (1976, 1979) and Brodersen (1979). Experimental aspects and chemical applications of gas-phase Raman spectroscopy were the subject of a more recent review (Murphy, 1991).

* Section 4.3.2 is contributed by H. W. Schrötter, München

4.3.2.2 Selection rules and examples of spectra

The formulae for the rovibrational energy levels of the different rotor type molecules have been given in Sec. 4.3.1. For Raman transitions different rotational selection rules have to be applied in addition to the vibrational Raman selection rules treated in Sec. 2.7.3. Generally transitions with $\Delta J = -2, -1, 0, +1$, and $+2$ are possible and the corresponding branches are designated as *O*-, *P*-, *Q*-, *R*-, and *S*-branches. For totally symmetric vibrations the 'isotropic' scattering is concentrated in the *Q*-branch and therefore these polarized branches are the most prominent features in Raman spectra of gases. Figure 4.3-16 shows as an example the Raman spectrum of hydrogen chloride HCl at a pressure of 100 kPa (Schrötter, 1982). At right, next to the exciting line, we see the nearly equidistant lines of the pure rotational Raman spectrum, originating from $\Delta v = 0, \Delta J = +2$ transitions, at left the strong *Q*-branch of the vibrational band ($\Delta v = +1, \Delta J = 0$), and next to it the lines of the *S*-branch ($\Delta v = +1, \Delta J = +2$) and the *O*-branch ($\Delta v = +1, \Delta J = -2$). We see that the vibration-rotation Raman band differs in its appearance from an infrared absorption band of a diatomic molecule (see Fig. 4.3-2). Under higher resolution the *Q*-branch is resolved into distinct rotational lines as shown in Fig. 4.3-17. Further we see two overlapping *Q*-branches of the isotopomers H^{35}Cl and H^{37}Cl . In order to understand the structure of a *Q*-branch and the information that can be extracted from it we take a closer look of the theory.

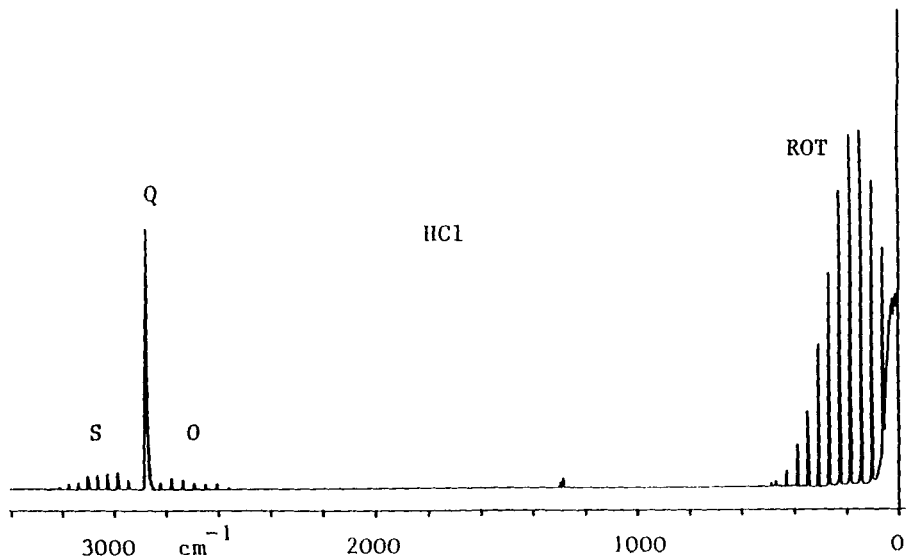


Figure 4.3-16 Raman spectrum of hydrogen chloride HCl at a pressure of 100 kPa. Slitwidth 2 cm^{-1} , time constant 1 s, scanning speed $50 \text{ cm}^{-1}/\text{min}$, laser power 800 mW at 514.5 nm (recorded by Hochenbleicher, see Schrötter, 1982).

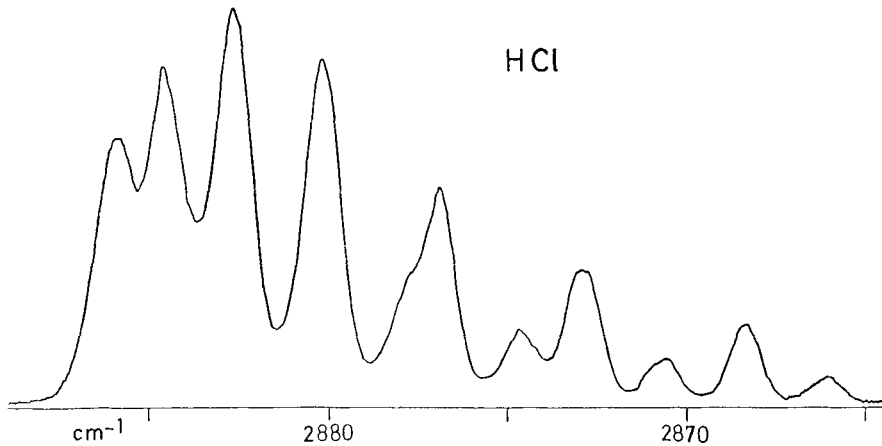


Figure 4.3-17 Raman spectrum of the *Q*-branch of HCl. Slitwidth 1 cm^{-1} , scanning speed 5 $\text{cm}^{-1}/\text{min}$, other conditions as in Fig. 4.3-16.

4.3.2.2.1 Diatomic molecules

The vibration-rotation energy levels of a diatomic molecule are given in traditional notation (Herzberg, 1950) by the expression

$$\begin{aligned} \frac{E(v, J)}{hc} = & \omega_e \left(v + \frac{1}{2} \right) - \omega_e x_e \left(v + \frac{1}{2} \right)^2 + \omega_e y_e \left(v + \frac{1}{2} \right)^3 + \dots \\ & + B_e J(J+1) - \alpha_e \left(v + \frac{1}{2} \right) J(J+1) + \gamma_e \left(v + \frac{1}{2} \right)^2 J(J+1) + \dots \\ & - D_e J^2(J+1)^2 - \beta_e \left(v + \frac{1}{2} \right) J^2(J+1)^2 + \delta_e \left(v + \frac{1}{2} \right)^2 J^2(J+1)^2 + \dots \\ & + H_e J^3(J+1)^3 + \dots \end{aligned}$$

where ω_e is the wavenumber of the harmonic vibration, $\omega_e x_e$ and $\omega_e y_e$ anharmonicity constants, B_e the equilibrium rotational constant, D_e and H_e the equilibrium centrifugal distortion constants of first and second order, α_e , β_e , γ_e and δ_e the equilibrium vibration-rotation interaction constants. The constants of higher order are included for completeness, they are required to describe the spectra obtained in modern high resolution Raman (and infrared) investigations.

The selection rules $\Delta v = +1$ and $\Delta J = 0$ lead to the expression for the wavenumbers in the *Q*-branch

$$\begin{aligned} \tilde{\nu}_Q(J) = & \omega_e - 2\omega_e x_e + \frac{13}{4}\omega_e y_e + \dots \\ & - (\alpha_e - 2\gamma_e)J(J+1) - (\beta_e - 2\delta_e)J^2(J+1)^2 + \dots \end{aligned}$$

and correspondingly $\Delta v = +1$ and $\Delta J = \pm 2$ to those for the *S*-branch (with $m = 2J + 3$) and the *O*-branch (with $m = -2J + 1$)

$$\begin{aligned}\tilde{\nu}_{S,O}(m) &= \omega_e - 2\omega_e x_e + \frac{13}{4}\omega_e y_e - \frac{3}{4}\alpha_e + \frac{3}{2}\gamma_e - \frac{9}{16}\beta_e + \frac{9}{8}\delta_e + \dots \\ &+ \left(2B_e - 2\alpha_e + \frac{5}{2}\gamma_e - 3D_e - 3\beta_e - \frac{15}{4}\delta_e + \frac{27}{8}H_e + \dots \right) \cdot m \\ &\cdot \left(\frac{1}{4}\alpha_e - \frac{1}{2}\gamma_e + \frac{11}{8}\beta_e + \frac{11}{4}\delta_e \right) \cdot m^2 \\ &\left(D_e + \beta_e + \frac{5}{4}\delta_e - \frac{34}{8}H_e \right) \cdot m^3 \\ &- \left(\frac{1}{16}\beta_e + \frac{1}{8}\delta_e \right) \cdot m^4 + \frac{3}{8}H_e \cdot m^5 + \dots\end{aligned}$$

Omitting the higher order constants we get the simpler formulae

$$\tilde{\nu}_Q(J) = \tilde{\nu}_0 - \alpha J(J+1) + \dots$$

for the *Q*-branch,

$$\tilde{\nu}_S(J) = \tilde{\nu}_0 + (2B - 3D) \cdot (2J + 3) - D(2J + 3)^3 + \dots$$

for the *S*-branch, and

$$\tilde{\nu}_O(J) = \tilde{\nu}_0 + (2B - 3D) \cdot (2J - 1) + D(2J - 1)^3 + \dots$$

for the *O*-branch, which are usually sufficient to describe medium resolution Raman spectra of diatomic molecules. We see that the structure of the *Q*-branch is essentially determined by the vibration-rotation interaction constant $\alpha = B_0 - B_1$, the difference of the rotational constants in the ground vibrational and the first excited state, B_0 and B_1 .

The pure rotational Raman spectra of homonuclear diatomic molecules are of particular importance for the determination of internuclear distances, because these molecules have no permanent dipole moment and therefore can not be investigated by microwave or far infrared spectroscopy in the usual way. The formula for the *S*-branch describes the pure rotational Raman spectrum with $\tilde{\nu}_0 = 0$. A good test for sensitivity and resolution of a Raman spectrometer is the recording of the pure rotational spectrum of air in the laboratory. Fig. 4.3-18 shows such a spectrum obtained recently with a commercial scanning Raman spectrometer by Castellucci et al. (1993). The nitrogen lines show the characteristic intensity alternation ratio 2:1 of lines with even and odd J values due to nuclear spin statistics, whereas the oxygen lines with even J are missing, see the discussion in Sec. 4.3.1.2 which shall not be repeated here. The two lines of oxygen and nitrogen near 60 cm^{-1} are 0.67 cm^{-1} apart and are clearly resolved in Fig. 4.3-18 using a spectral slit width of 0.3 cm^{-1} .

The Raman spectrum of gases can now also be recorded with Fourier-Transform Raman spectrometers with near infrared excitation (Dyer and Hendra, 1992). Fig. 4.3-19 shows a survey spectrum of air obtained in 4 hours of sampling time (Bruker, 1993). The region of the rotational spectrum is presented on an expanded scale in Fig. 4.3-20, it can be compared with Fig. 4.3-18. The intensities of the lines below about 80 cm^{-1} are weakened by the Rayleigh line suppression filter and the resolution is limited to 1 cm^{-1} , mainly by the laser used for excitation.

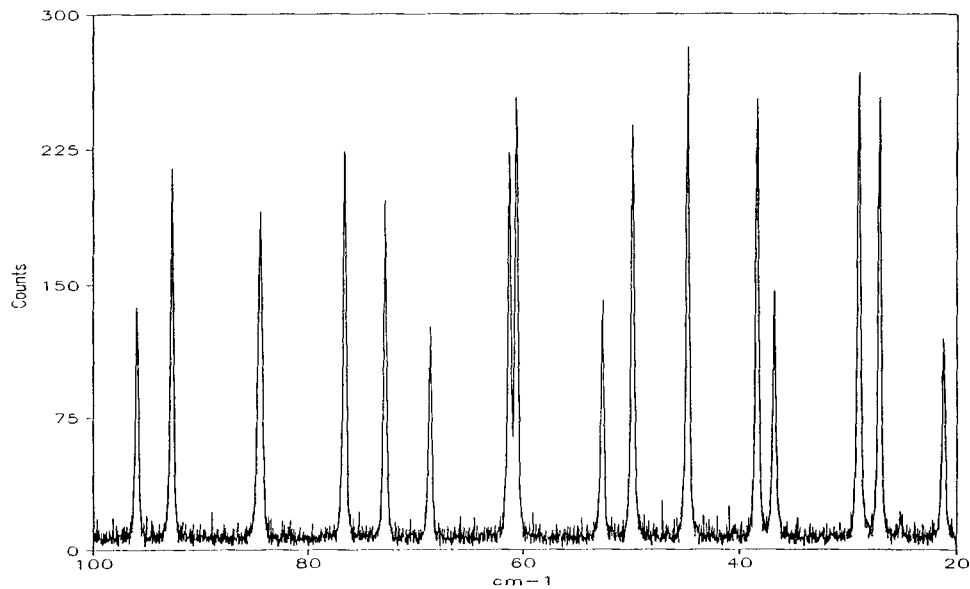


Figure 4.3-18 Part of rotational Raman spectrum of air at ambient pressure. Slitwidth 0.3 cm^{-1} , laser power 4 W at 514.5 nm (Castellucci et al., 1993).

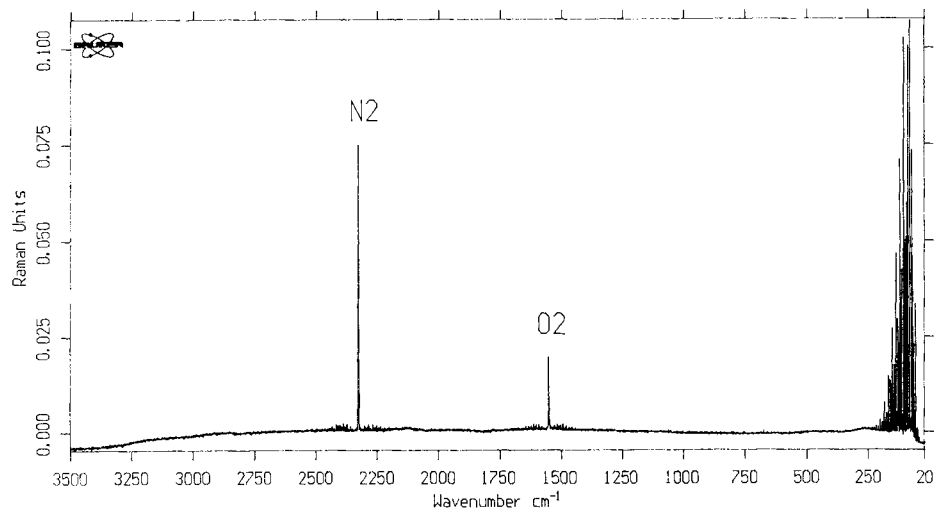


Figure 4.3-19 FT-Raman spectrum of air at ambient pressure in a multireflection cell. Recording time 240 min., resolution 1 cm^{-1} , laser power 380 mW at 1064 nm (Bruker, 1993).

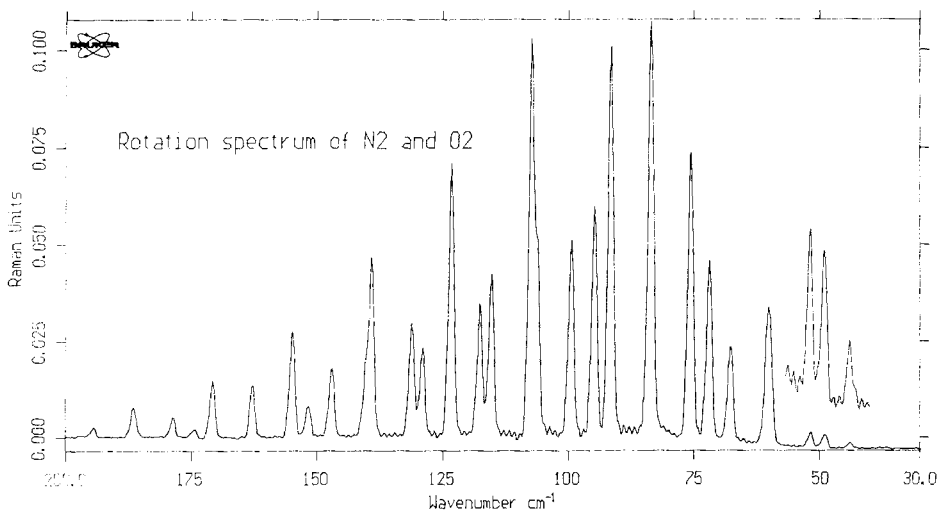


Figure 4.3-20 Expanded section of FT-Raman spectrum of air from Fig. 4.3-19 (Bruker, 1993).

The Raman spectrum of nitrogen was investigated by Bendtsen (1974) with photographic recording, by Frunder et al. (1986) with coherent anti-Stokes Raman scattering (CARS), and by Lavorel et al., (1987) and Tabyaoui et al., (1990) with high-resolution inverse Raman scattering (IRS). In the latter work the *Q*-branches of the fundamental and the first hot band of N₂ at about 1300 K were measured with high accuracy to obtain refined values of the spectroscopic constants. From these results the equilibrium internuclear distance $r_e = 109.7697(15)$ pm can be deduced (Lavorel et al., 1992).

The oxygen molecule has two unpaired electrons and therefore a triplet ground state $^3\Sigma_g^-$. The resulting triplet structure in the rotational Raman spectrum of $^{16}\text{O}_2$ which had been detected by mercury lamp excitation (Jammu et al., 1966) was further investigated experimentally (Renschler et al., 1969) and theoretically (Lepard, 1970). Through computer-simulation of the spectra (Altmann et al., 1972) it could be shown that an intermediate approximation between Hund's coupling cases (b) and (a) yields the best agreement between theory and experiment, in the rotational as well as in the rotation-vibrational spectrum observed by Rich and Lepard (1971). The best resolution in spontaneous Raman spectroscopy has been achieved by Loëte and Berger (1977) in the *Q*-branch of $^{16}\text{O}_2$ which is shown in Fig. 4.3-21. Line splittings in the *Q*-branch were observed by CARS with flashlamp pumped dye lasers (Ouazzany et al. 1987) and by inverse Raman spectroscopy in a molecular beam (Hill et al. 1983). Part of the latter spectrum is shown in Fig. 4.3-22. Different isotopomers of oxygen were studied by Edwards et al. (1981). Using the stimulated Raman gain technique Rouillé et al. (1992) recorded *Q*-branch spectra of the fundamental and the first two hot bands of $^{16}\text{O}_2$ at temperatures of 295 K and 1350 K, respectively (see Fig. 4.3-23) and refined the molecular constants; in this work it was also possible to resolve the triplet structure in the *O*- and *S*-branches of the fundamental band.

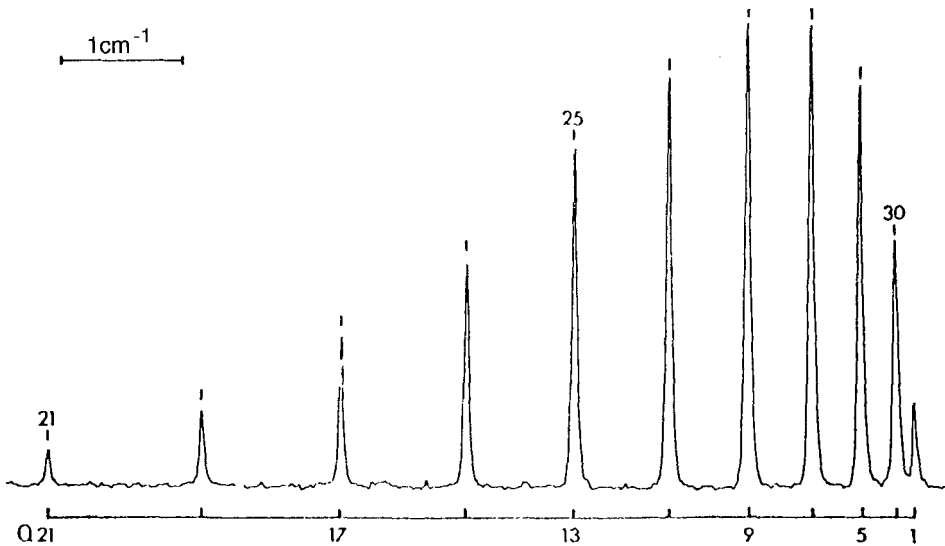


Figure 4.3-21 Raman spectrum of the Q -branch of $^{16}\text{O}_2$ with a resolution of 0.05 cm^{-1} at a pressure of 1.06 kPa . Photographic recording, exposure time 30 h (Loëte and Berger, 1977).

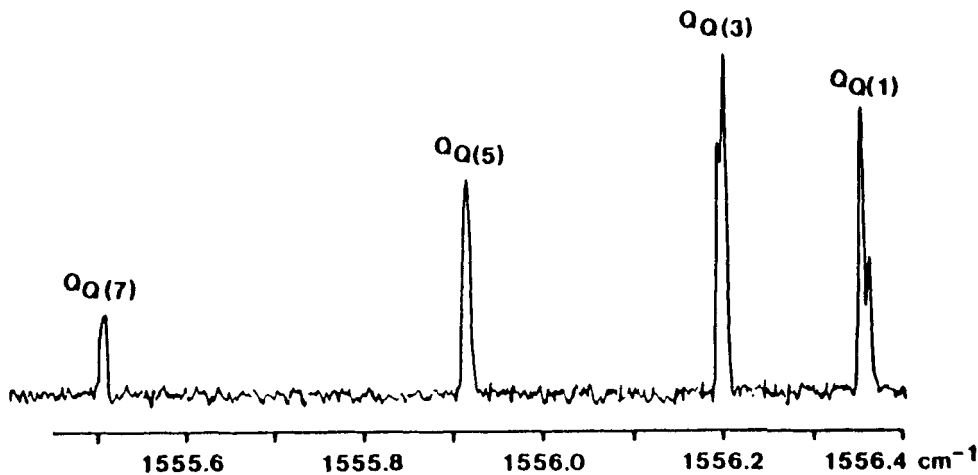


Figure 4.3-22 Inverse Raman spectrum of the Q -branch of $^{16}\text{O}_2$ at a temperature of 40 K in a molecular beam (Hill et al., 1983).

The Raman spectra of all isotopomers of hydrogen were investigated by Edwards et al. (1979, 1986) and Veirs and Rosenblatt (1987). Using the technique of Fourier-Transform Raman spectroscopy in the visible Jennings et al. (1986, 1987) determined the molecular constants of H_2 and D_2 with high accuracy. Density shifts of the Q -branch lines of H_2 were measured by Rahn and Rosasco (1990) at temperatures from 295 K to 1000 K .

Stricker and Hochenbleicher (1973) and Edwards et al. (1976) investigated the spectrum of fluorine by spontaneous Raman and Gilson and Purnell (1982) by CARS

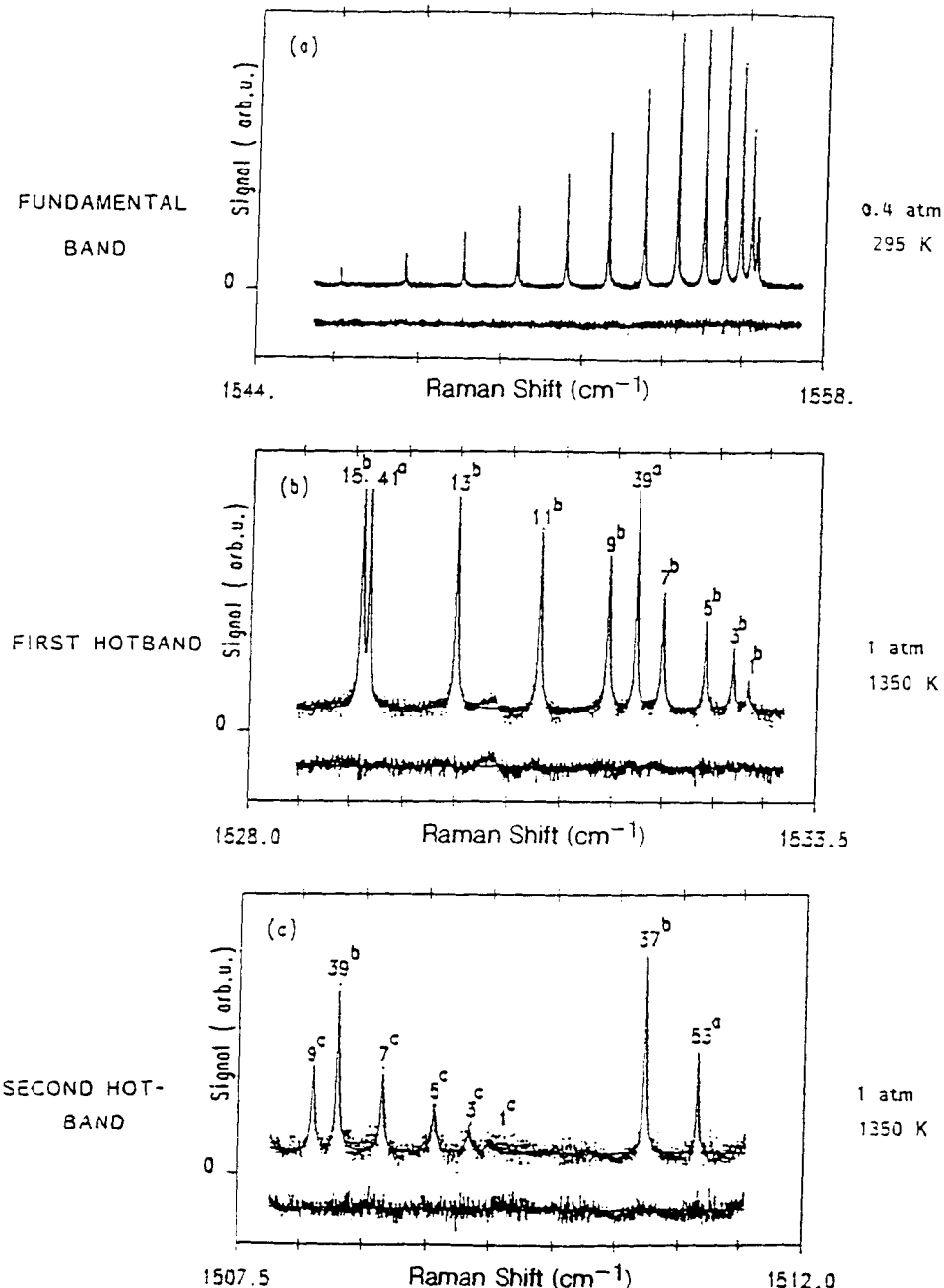


Figure 4.3-23 Inverse Raman spectra of Q -branches of $^{16}\text{O}_2$ in the fundamental (a) (40 kPa at 295 K) and the first (b) (100 kPa at 1350 K) and second (c) (100 kPa at 1350 K) hot bands. Lines marked (a), (b), and (c) correspond to the fundamental and the first and second hot bands, respectively. The curves under the spectra represent the residuals between experimental and calculated spectra (Rouillé et al., 1992).

spectroscopy. Recently Martinez et al. (1993) recorded the high-resolution stimulated Raman spectrum of F_2 and determined the equilibrium molecular constants given in Table 4.3-6. The resulting equilibrium distance for F_2 is $r_e = 141.2617(11)$ pm.

Raman spectra of chlorine, bromine, and iodine gas were first recorded by Holzer et al. (1970) with argon laser excitation, the latter two halogens showed a strong resonance Raman effect. The numerous results of later investigations are presented in Sec. 6.1. on the resonance Raman effect.

As already mentioned in Sec. 4.3.1.2, the unpaired electron in the molecule NO gives rise to two states $^2\Pi_{3/2}$ and $^2\Pi_{1/2}$. A Raman transition between these states is allowed and was detected by Rasetti (1930b) at about 120 cm^{-1} . This electronic Raman effect was rotationally resolved by Fast et al. (1969) and Rich and Welsh (1971). The rotational

Table 4.3-6 Molecular constants for the electronic ground state of F_2 (in cm^{-1})

	Martinez 1993	Gilson 1982	Edwards 1976	Stricker 1973
B_e	0.889325 ± 0.000012	0.88980 ± 0.00004		0.892 0.002
B_0	0.882953 ± 0.000009		0.88331 ± 0.00004	0.8847 ± 0.0010
α_e	(1.25952 $\pm 0.00018) \cdot 10^{-2}$			(1.3 $\pm 0.3) \cdot 10^{-2}$
α_0		(1.2972 $\pm 0.0007) \cdot 10^{-2}$		
γ_e	-(1.707 $\pm 0.008) \cdot 10^{-4}$			
D_e	(3.0 $\pm 0.4) \cdot 10^{-6}$	(3.40 $\pm 0.07) \cdot 10^{-6}$		
D_0	(3.1 $\pm 0.4) \cdot 10^{-6}$		(3.48 $\pm 0.06) \cdot 10^{-6}$	(4.9 $\pm 1.0) \cdot 10^{-6}$
β_e	(6.4 $\pm 0.2) \cdot 10^{-8}$			
β_0		(8 $\pm 1) \cdot 10^{-8}$		
δ_e	-(8.1 $\pm 1.0) \cdot 10^{-9}$			
$H_e \approx H_0$	-(3.0 $\pm 0.4) \cdot 10^{-10}$			
ω_e	916.929 ± 0.010			917.1 ± 3.5
$\omega_e x_e$	11.322 ± 0.006			11.8 ± 1
$\omega_e y_e$	-0.1057 ± 0.0007			
r_e	(141.2617 $\pm 0.0010)$ pm	(141.426 $\pm 0.004)$ pm	(141.31 $\pm 0.08)$ pm	

structure of the vibrational *Q*-branch was resolved by pulsed CARS (Beckmann et al., 1981) and by IDSRS (ionization-detected stimulated Raman scattering, Esherick and Owyong, 1983).

4.3.2.2.2 Linear molecules

The intensity distribution in the rotational Raman spectra of the linear molecules CO₂ and N₂O which are partly excited to the 01¹0 vibrational level at room temperature

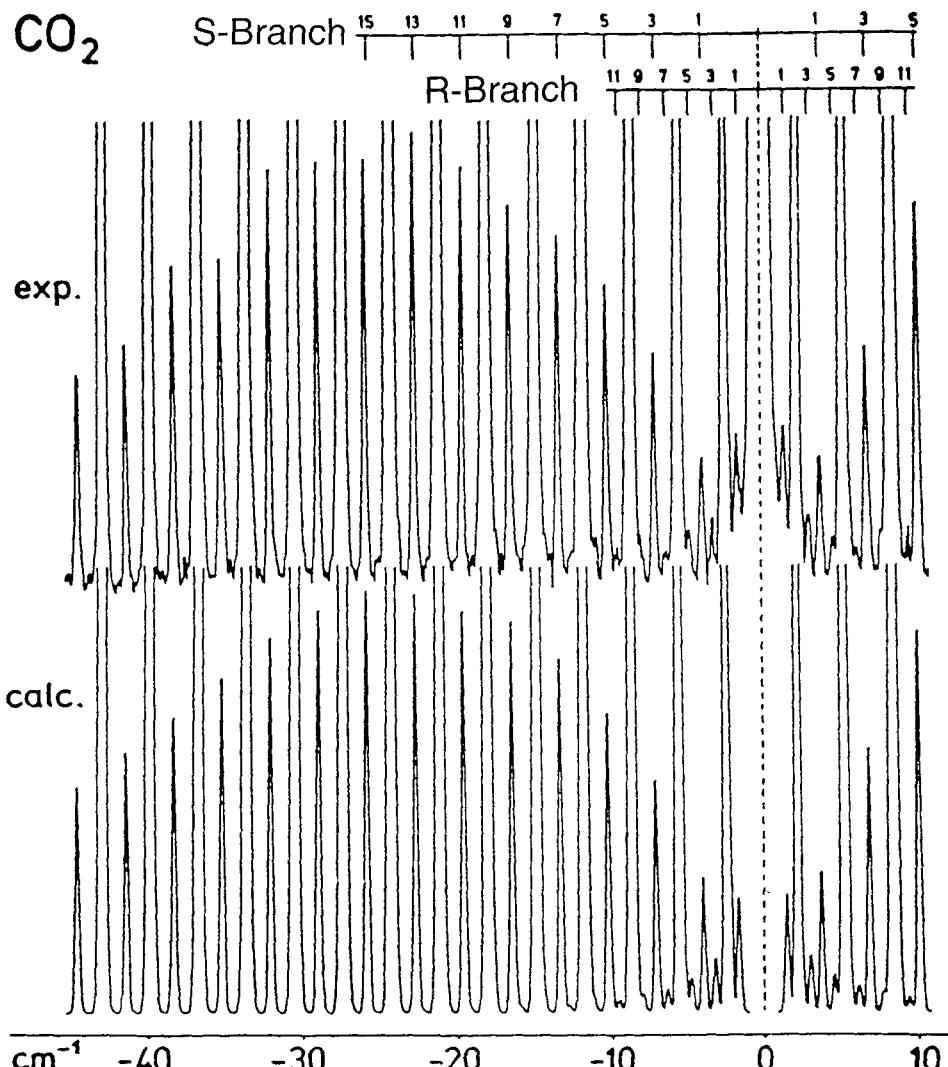


Figure 4.3-24 Part of the pure rotational Raman spectrum of CO₂ at a pressure of 10 kPa. Slitwidth 0.21 cm⁻¹, scanning speed 0.2 cm⁻¹/min, laser power 8 W at 514.5 nm. The S-branch lines of the molecules in the vibrational ground state are off scale (Altmann et al., 1976).

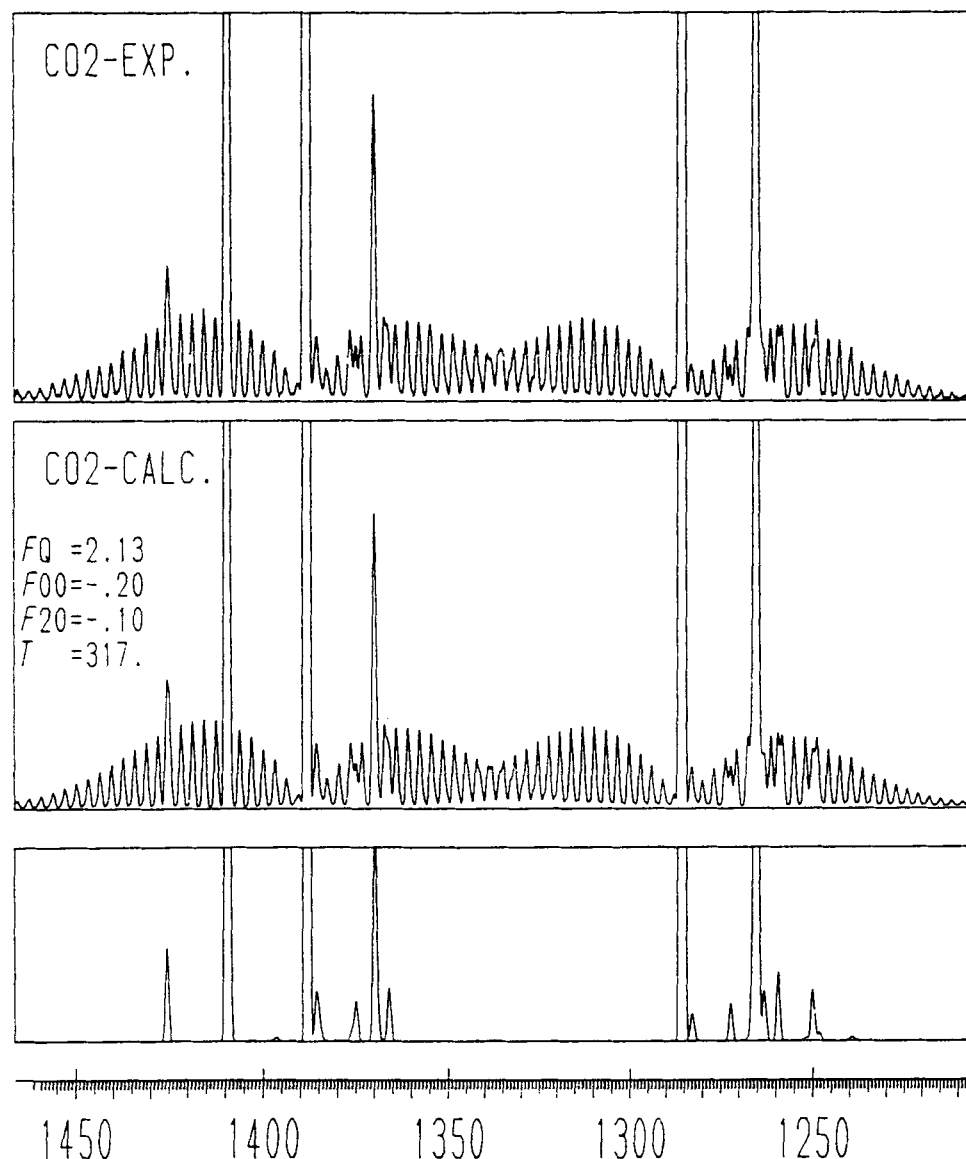


Figure 4.3-25 Raman spectrum of natural CO₂ in the Fermi resonance region at a pressure of 40 kPa. Slitwidth 0.8 cm⁻¹, laser power 9 W at 514.5 nm, multiple pass cell. Upper spectrum experimental, middle spectrum calculated, lower spectrum isotropic contribution to calculated spectrum (Finsterhözl, 1982).

has been investigated (Altmann et al., 1976) and *R*-branch lines were resolved down to 1.5 cm^{-1} . The *S*- and *R*-branches of the vibrationally excited molecules are shown in Fig. 4.3-24 for CO_2 .

The Σ -diads in the vibrational Raman spectrum of CO_2 and its isotopic variants were measured and their intensity distribution simulated (Srinivasan et al., 1977; Finsterhölzl et al., 1978; Klöckner et al., 1978; Finsterhölzl, 1982; Wienecke et al., 1986). In Fig. 4.3-25 the experimental and the calculated Raman spectra of natural CO_2 in the Fermi resonance region are presented, the lowest (calculated) spectrum showing only the *Q*-branches of the Fermi doublet of $^{12}\text{C}^{16}\text{O}_2$ and its hot bands and those of the isotopomers $^{13}\text{C}^{16}\text{O}_2$, $^{12}\text{C}^{16}\text{O}^{18}\text{O}$, and $^{12}\text{C}^{16}\text{O}^{17}\text{O}$, occurring in natural abundances of 1.1 %, 0.4 %, and 0.08 %, respectively, which explain some fine details in the experimental spectrum. The structure of the *Q*-branch of the (10⁰02) component at 1285 cm^{-1} has been resolved by CARS (Ouazzany et al., 1988), stimulated Raman (Saint-Loup et al. 1990) and photoacoustic Raman spectroscopy (Rotger et al., 1992).

The differential Raman scattering cross sections and depolarization ratios in the Fermi resonance region of carbon disulphide CS_2 were measured and interpreted in terms of three bond polarizability parameters and the cubic force constant k_{122} (Montero et al., 1984).

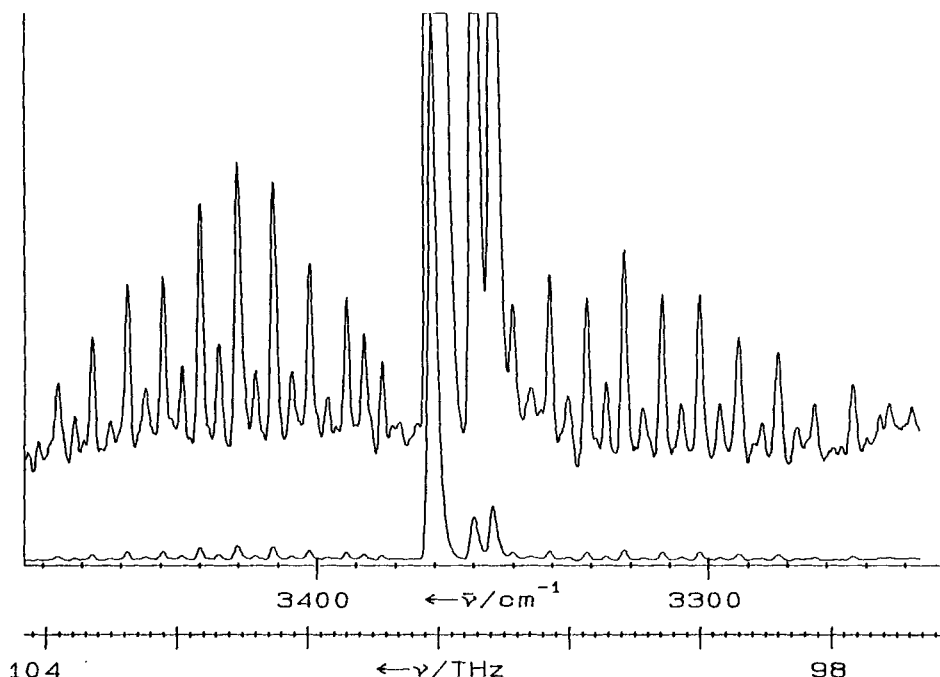


Figure 4.3-26 Raman spectrum of ν_1 band of acetylene C_2H_2 . Slitwidth 2 cm^{-1} , laser power 2.5 W at 514.5 nm , $10\text{ s}/\text{channel}$, upper spectrum 20fold sensitivity (Meßler and Schröter, 1992).

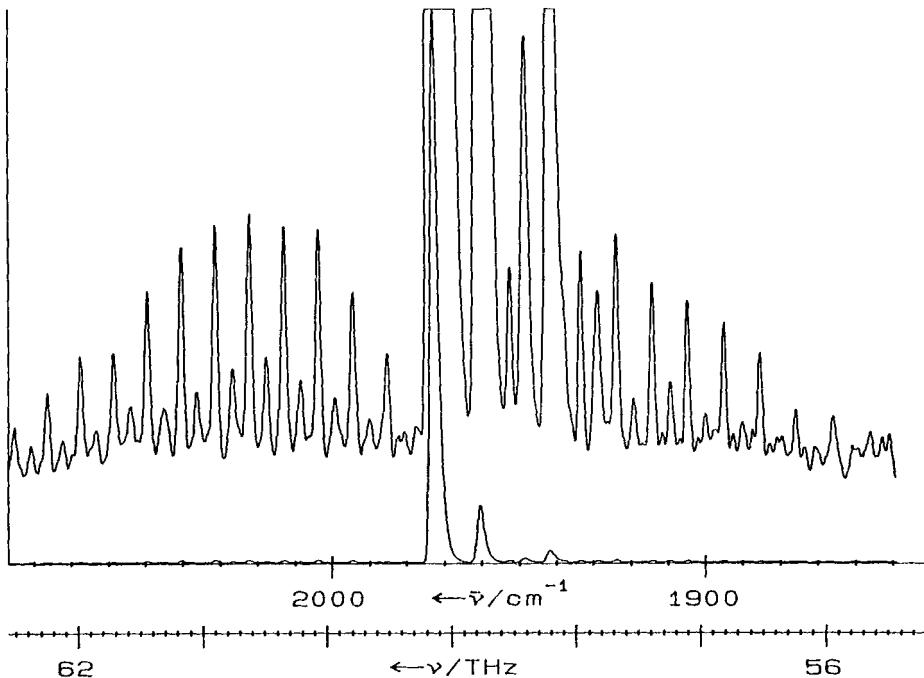


Figure 4.3-27 Raman spectrum of ν_2 band of acetylene C_2H_2 . Slitwidth 1.5 cm^{-1} , laser power 2.5 W at 514.5 nm , $10\text{ s}/\text{channel}$, upper spectrum 100fold sensitivity (Meßler and Schrötter, 1992).

The Raman spectrum of acetylene was the subject of many investigations (Finsterhözl et al., 1977 and 1981; Wang and Weber, 1978; Kostyk and Welsh, 1980; Weber et al., 1984). In Figs. 4.3-26 to 4.3-28 we show photoelectrically recorded survey spectra of the ν_1 , ν_2 , and ν_4 bands of C_2H_2 at 14.6 kPa at medium resolution (Meßler and Schrötter, 1992). In addition to the customary wavenumber scale in cm^{-1} a frequency scale in THz is given. In the ν_1 and ν_2 bands the Q -branches of hot bands originating from the ν_4 , ν_5 , and $2\nu_4$ levels are evident as well as the ν_2 Q -branch of $^{12}\text{C}^{13}\text{CH}_2$. Hot bands are not so evident in the ν_4 band of the degenerate bending vibration, but they contribute significantly to the band contour consisting of O -, P -, R -, and S -branches, with a weak Q -branch in the center. Through recording of the second order rovibrational Raman spectrum of C_2H_2 the anharmonicity constant x_{22} , which had been predicted by Strey and Mills (1976), could be determined by analyzing the combination band $\nu_1 + \nu_4$ which overlaps with $2\nu_2$ (Finsterhözl et al., 1981). The harmonic force field of acetylene was determined from Raman intensities of the fundamentals of C_2H_2 , C_2D_2 and C_2HD (Murphy and Montero, 1981) and the Raman intensities of overtones and combination bands of these species were measured and compared with values calculated from an anharmonic force field (Domingo et al., 1982). The intensity distribution in the $2\nu_4$ band was studied in detail (Liebrecht et al., 1988). The structure of the Q -branches was

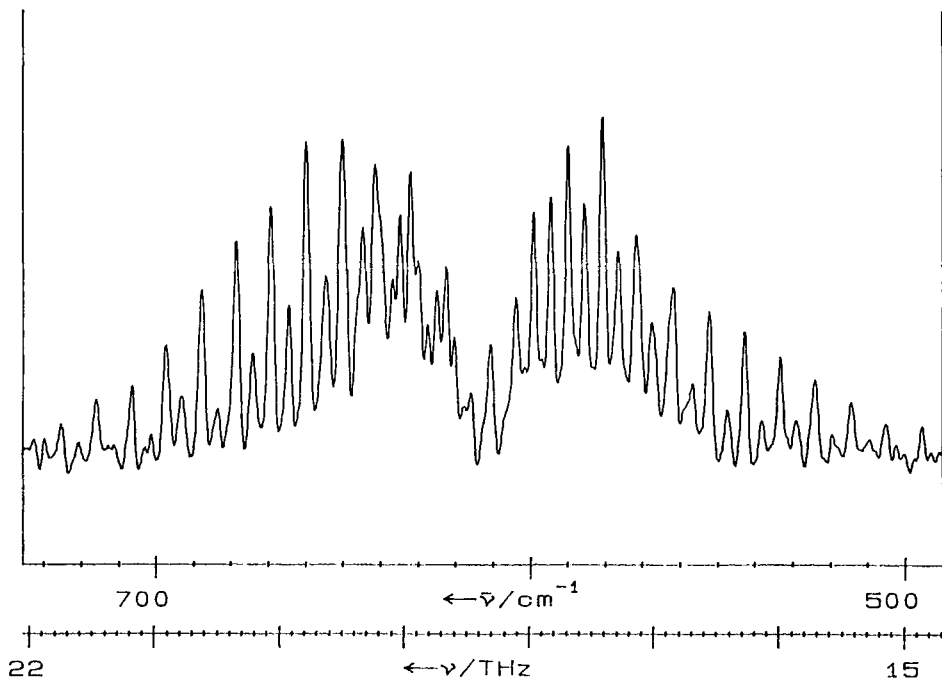


Figure 4.3-28 Raman spectrum of ν_4 band of acetylene C_2H_2 . Slitwidth 2 cm^{-1} , laser power 2.5 W at 514.5 nm , 8 s/channel (Meßler and Schrötter, 1992).

resolved using CARS spectroscopy by Fabelinsky et al. (1977) for ν_2 and by Nitsch and Kiefer (1977) for ν_1 and is reinvestigated using inverse Raman spectroscopy by Santos et al. (1993).

4.3.2.2.3 Symmetric top molecules

For a nonrigid symmetric top molecule there are three different centrifugal distortion constants D^J , D^{JK} , and D^K . The rotational energy levels of the vibrational level v of an oblate symmetric top can be represented by

$$\frac{E_v(J, K)}{hc} = \tilde{\nu}_v + B_v J(J+1) + (C_v - B_v)K^2 - D_v^J J^2(J+1)^2 - D_v^{JK} J(J+1)K^2 - D_v^K K^4$$

where $\tilde{\nu}_v$ is the vibrational term value, B_v and C_v are the rotational constants and K is the quantum number of the component of the angular momentum along the molecular symmetry axis. For purely rotational Raman transitions the selection rules are

$$\Delta v = 0, \Delta J = \pm 1, \pm 2 \text{ and } \Delta K = 0$$

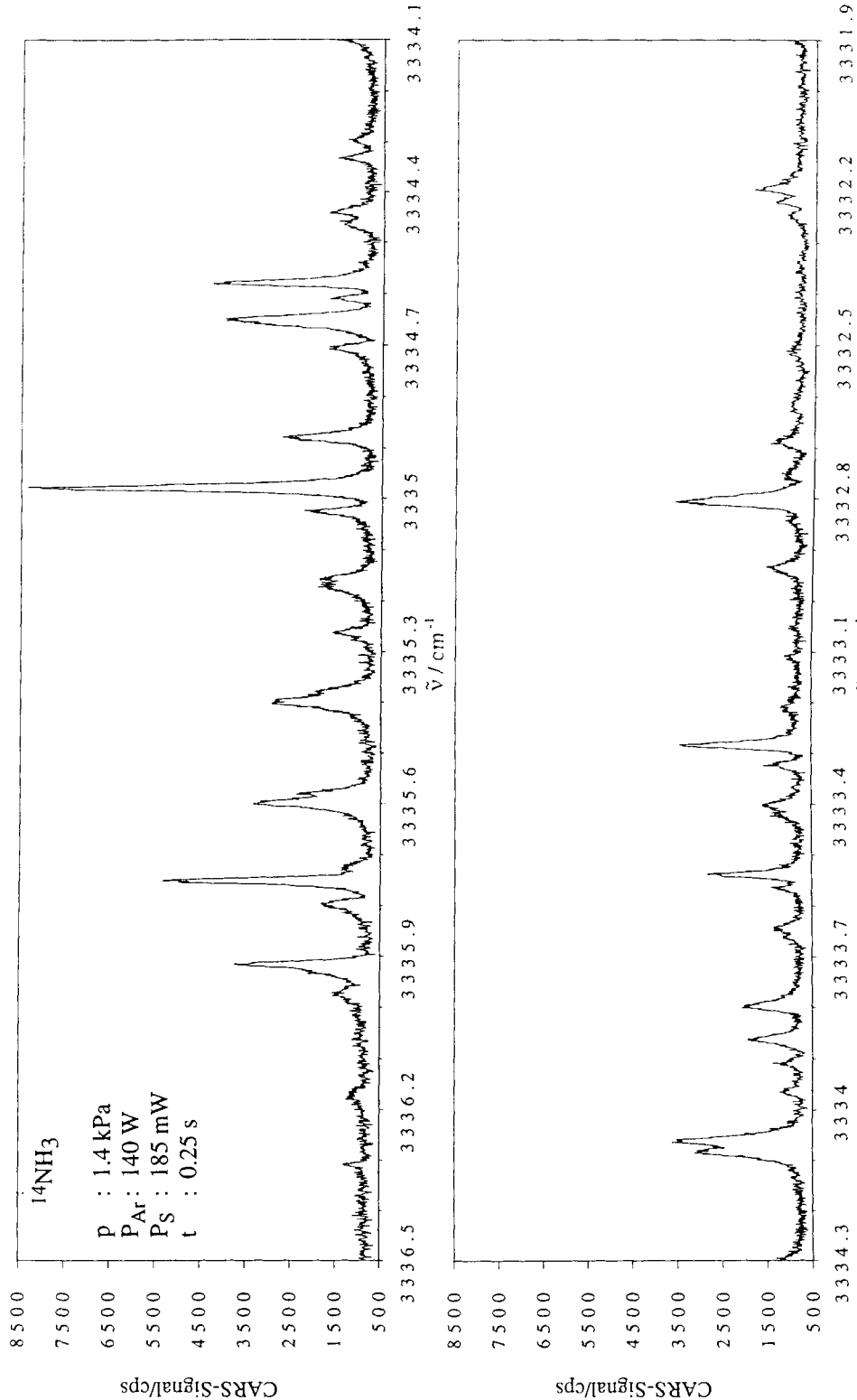


Figure 4.3-29 CARS spectrum of ν_1 band of ammonia $^{14}\text{NH}_3$. Pressure 1.4 kPa, argon laser intracavity power 140 W, dye laser power 185 mW, integration time 0.25 s/channel (Jonuscheit et al., 1994).

and lead to the expressions for the *S*-branch of the ground state $v = 0$

$$\tilde{\nu}_S(J, K) = (2B_0 - 3D_0^J \cdot 2D_0^{JK} K^2)(2J + 3) - D_0^J(2J + 3)^3$$

and the *R*-branch transitions

$$\tilde{\nu}_R(J, K) = (2B_0 - 2D_0^{JK} K^2)(J + 1) - 4D_0^J(J + 1)^3.$$

Evidently the rotational lines are split depending on the value of the constant D_0^{JK} .

In the rotational Raman spectrum of ammonia NH₃ this *K*-splitting could be resolved (Cloppenburg et al., 1979).

Actually all energy levels of the ammonia molecule are split into symmetric and antisymmetric levels with respect to inversion and for Raman transitions the additional selection rules $s \leftrightarrow s$ and $a \leftrightarrow a$ hold. The inversion splitting in the *Q*-branch of the ν_1 vibration was resolved using CARS spectroscopy by Angstl et al., (1985). Fig. 4.3-29 shows a recent recording of this *Q*-branch at a pressure of 1.4 kPa (Jonuscheit et al. 1994).

The vibrational spectrum of the benzene molecule as a good example for the rule of mutual exclusion was already treated in the introduction to Sec. 4.3. The pure rotational Raman spectrum of benzene (see Weber 1979) and the rotational structure of several vibrational Raman bands of C₆H₆ (Hollinger and Welsh, 1978; Jensen and Brodersen, 1979) and C₆D₆ (Hollinger et al., 1979) were also investigated. Using the technique of IDSRS (ionization-detected stimulated Raman scattering) in a molecular beam experiment Esherick et al. (1985) resolved the rotational structure of the ν_{16} band which is in Fermi resonance with $\nu_2 + \nu_{18}$. The two Fermi sub-bands could be recorded separately by selectively tuning the ionizing UV laser into resonance with electronic transitions from one of the two states. An extensive analysis of the deconvoluted spectra by Plíva et al. (1987) yielded deperturbed spectroscopic constants for the interacting states.

After the initial work of Romanko et al. (1955) the rovibrational Raman spectrum of ethane C₂H₆ was thoroughly investigated regarding intensities (Martin and Montero, 1984; Domingo and Montero, 1987), the energy levels of the torsional ν_4 mode (Fantoni et al., 1986; Fernández-Sánchez et al., 1989), and fundamentals, overtones and combinations from 600 to 6500 cm⁻¹ (van Helvoort et al., 1987). More recently also the torsional Raman spectra of partially deuterated ethane molecules were studied (Fernández-Sánchez and Montero, 1991). The *Q*-branch of the ν_3 band of ¹²C₂H₆ was resolved using inverse Raman spectroscopy (Bermejo et al., 1992) and its structure analysed in terms of a vibrational-torsional coupling Hamiltonian.

4.3.2.2.4 Spherical top molecules

Methane as the prototype of spherical tops was the subject of a great number of investigations, of which only some can be mentioned here. At high resolution the structure of rovibrational bands becomes very complicated due to tensorial splittings. Moreover Fermi and Coriolis resonances lead to interactions between fundamentals and overtone and combination bands of CH₄; therefore theoretical models for the "dyade" ν_2 and ν_4 (Champion, 1977) and the "pentade" ν_1 , ν_3 , $2\nu_2$, $\nu_2 + \nu_4$ and $2\nu_4$ (Lolck et al., 1982 and Poussigue et al., 1982) have been developed and sets of molecular constants were determined by adjustment to all available experimental high resolution IR and Raman

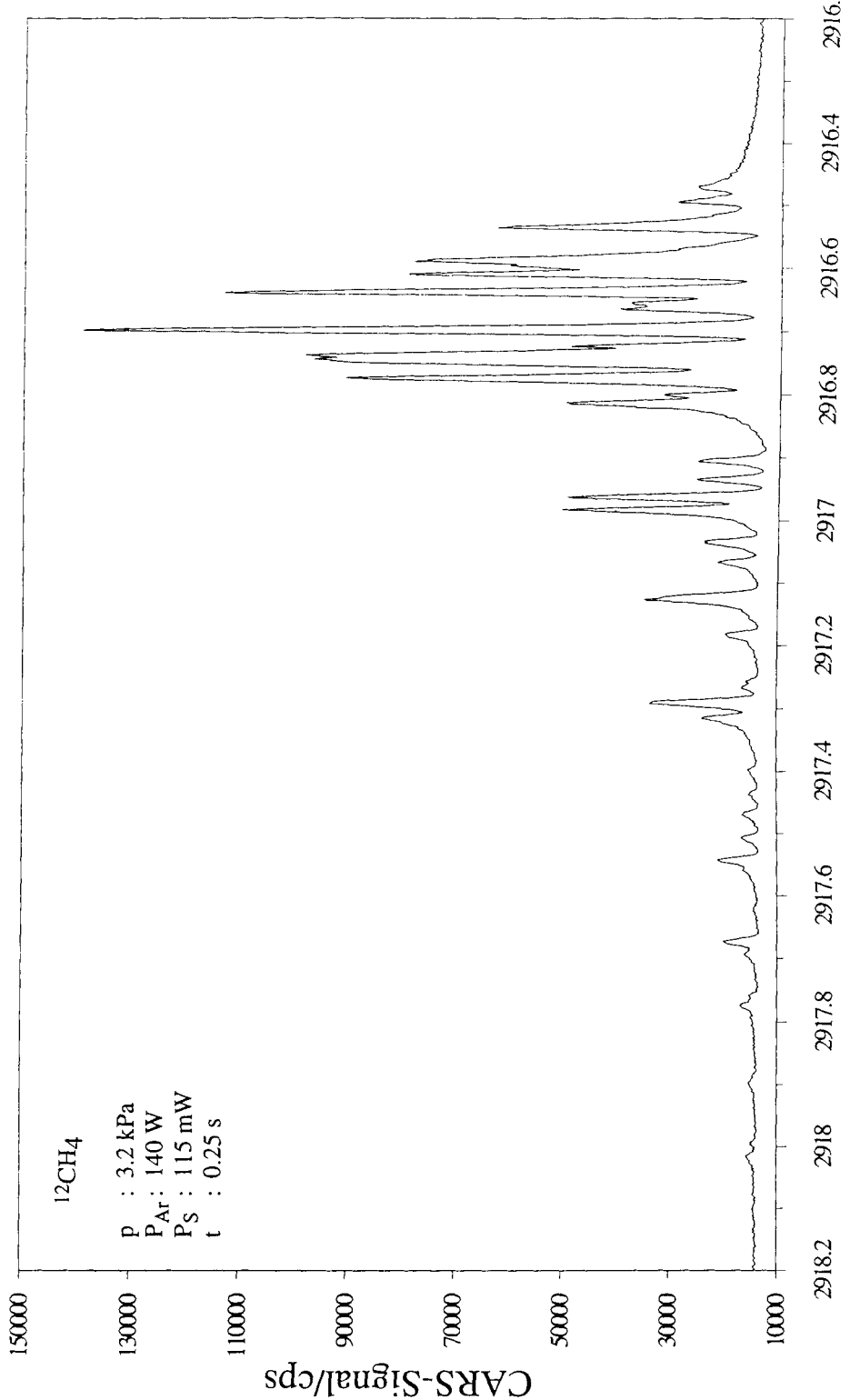


Figure 4.3-30 CARS spectrum of ν_1 band of methane $^{12}\text{CH}_4$. Pressure 3.2 kPa, argon laser intracavity power 140 W, dye laser power 115 mW, integration time 0.25 s/channel (Jonuscheit et al., 1994).

data. The ν_1 band had just been resolved by Owyong et al., (1978) and Kozlov et al., (1979) using stimulated Raman gain and CARS techniques, respectively.

Further experimental investigations of the ν_1 band of CH_4 by CARS (Fründner et al., 1983) and inverse Raman techniques (Valentini et al., 1980; Esherick and Owyong, 1982; Santos et al., 1992; Bermejo et al., 1992) have led to a steady improvement in wavenumber accuracy which is now claimed to be $\pm 0.001 \text{ cm}^{-1}$. Fig. 4.3-30 shows a recent recording of the cw CARS spectrum at a pressure of 3.2 kPa (Jonuscheit et al., 1994). Other detailed studies concerned the $2\nu_2$ band of $^{12}\text{CH}_4$ (Millot et al., 1991), the ν_1 and $\nu_2 + \nu_4$ Q -branches of $^{12}\text{CD}_4$ (Esherick et al., 1983; Lolck et al., 1985a; 1985b; Millot et al., 1992), the ν_1 band of $^{13}\text{CH}_4$ (McDowell et al., 1980; Jouvard et al., 1991) and ν_1 , $2\nu_2$ and $2\nu_4$ of $^{13}\text{CD}_4$ (Millot et al., 1988).

The interacting ν_1 and ν_3 bands of natural silane (Lavorel et al., 1990; Millot et al., 1990; Lavorel et al., 1993) and of stannane $^{116}\text{SnH}_4$ (Tabyaoui et al., 1991) have been measured by high resolution infrared and stimulated Raman spectroscopy. All these results were compiled in the T.D.S. data bank (Tomsk-Dijon Spectroscopy project) and were incorporated into a comprehensive model for the rovibrational spectra of methane and other spherical top molecules (Babikov et al., 1993; Champion et al., 1992).

4.3.2.2.5 Asymmetric top molecules

The main feature of the vibrational Raman spectrum of water vapour H_2O is the ν_1 band whose Q -branch extends from about 3630 to 3657 cm^{-1} (Bribes et al., 1976). The rotational Raman spectrum was investigated in the region 20 to 800 cm^{-1} (Murphy, 1977a) as well as the complete rovibrational Raman spectrum consisting of the ν_1 and ν_3 stretching vibration bands extending from 3400 to 4200 cm^{-1} (Murphy, 1978) and the bending mode ν_2 at 1595 cm^{-1} and its overtone $2\nu_2$ at 3152 cm^{-1} (Murphy, 1977b). As basis for the evaluation of CARS spectra of water vapour the temperature and pressure dependence of the ν_1 band was measured by high resolution inverse Raman spectroscopy (Rahn and Greenhalgh, 1986; Greenhalgh and Rahn, 1990).

The Raman spectrum of hydrogen sulfide H_2S has been investigated at medium resolution in connection with the measurement of Raman scattering cross sections (Schrotter and Klöckner, 1979). Later the Q -branch of the ν_1 band was resolved using the cw CARS technique (Fründner et al., 1985) and analysed by comparison with data from Fourier transform IR spectra (Lechuga-Fossat et al., 1984).

Ethylene has no dipole moment and a center of symmetry and therefore the Raman spectrum is an important source of structural information. After the early work on the rotational (Dowling and Stoicheff, 1959) and rovibrational Raman spectrum (Feldman et al., 1956) these spectra were thoroughly studied in a series of publications (Hills and Jones, 1975; Hills et al., 1977; Foster et al., 1977). Overtones and combination bands were measured in an *intracavity* Raman experiment by Knippers et al. (1985). The Q -branch of the ν_2 band was resolved by pulsed CARS spectroscopy in a molecular beam experiment (Byer et al., 1981).

4.3.2.3 Raman scattering cross sections

Relative and absolute Raman scattering cross sections have been measured by a number of groups and were summarized by Schrötter and Klöckner (1979). The formula for the total differential Raman scattering cross section of a vibrational-rotational band has been given in Eq. 2.4-6; the 'internal field factor' L is equal to 1 for gases, see also Sec. 3.5.4.

The mean value of the absolute differential Raman scattering cross section of the Q -branch of nitrogen was established to be (Schrötter and Klöckner 1979)

$$\left(\frac{d\sigma}{d\Omega} \right)_{Q,N_2} = (5.05 \pm 0.1) \cdot 10^{-48} (\tilde{\nu}_0 - \tilde{\nu}_{N_2})^4 \frac{\text{cm}^6}{\text{sr}},$$

where $\tilde{\nu}_{N_2}$ is 2331 cm^{-1} . The validity of the ν^4 -law was confirmed from 350 nm to 630 nm within experimental accuracy.

Most scattering cross sections of other Raman bands were measured against the nitrogen Q -branch as standard. Therefore the 'relative normalized differential Raman scattering cross section'

$$\begin{aligned} \Sigma_k &= \frac{d\sigma_k/d\Omega}{(d\sigma/d\Omega)_{Q,N_2}} \cdot \frac{(\tilde{\nu}_0 - \tilde{\nu}_k)^4}{(\tilde{\nu}_0 - \tilde{\nu}_{N_2})^4} \cdot \left(1 - \exp\left(-\frac{hc\tilde{\nu}_k}{kT}\right) \right) \\ &= \frac{\tilde{\nu}_{N_2}}{\tilde{\nu}_k} \cdot \frac{g_k(45\alpha'_k^2 + 7\chi_k\gamma'_k^2)}{45\alpha'_{N_2}^2 + 7\chi_{N_2}\gamma'_{N_2}^2} \end{aligned}$$

was defined, where χ_k denotes the fraction of the anisotropic scattering which contributes to the Q -branch of the Raman band. In most cases only the scattering cross sections of Q -branches were determined, because it is difficult to measure the intensity of the extended rotational wings with reasonable accuracy.

Averages of experimentally determined relative normalized differential Raman scattering cross sections for selected gases are given in Table 4.3-7. New values for carbon disulfide CS_2 (Montero et al., 1984), ethane C_2H_2 (Martín and Montero, 1984; Gough and Murphy, 1986), propane C_3H_8 (Gough et al., 1987), acetylene C_2H_2 (Domingo et al., 1982; Orduna et al., 1982), benzene C_6H_6 (Fernández-Sánchez and Montero, 1989), and dimethylacetylene C_4H_6 (Meßler et al., 1994) have been included to update the last published compilation (Schrötter, 1982). The data from which the averages in Table 4.3-7 were calculated agree with one another to within $\pm 20 \%$ with few exceptions.

Table 4.3-7 Average relative normalized differential Raman scattering cross sections Σ_k for Q -branches of vibrational bands

Molecule	$\tilde{\nu}_k/\text{cm}^{-1}$	Σ_k
N ₂	2331	1
O ₂	1555	1.04
H ₂	4156	3.86
D ₂	2986	2.53
F ₂	893	0.32
Cl ₂	554	2.25
HF	3062	1.34
HCl	2886	3.10
HBr	2558	4.42
HI	2230	5.80
CO	2143	0.93
NO	1877	0.38
CO ₂	1388	1.13
	1285	0.75
CS ₂	658	7.3 #
	802	1.3 #
N ₂ O	2224	0.50
	1285	1.98
ONF	1844	0.66
H ₂ O	3652	3.51
	1595	0.008
H ₂ S	2611	6.80
O ₃	1103	3*
SO ₂	1151	3.99*
C ₂ H ₂	3374	1.39
	1973	6.36
C ₂ D ₂	1765	6.28
C ₂ N ₂	2330	11.9 #
NH ₃	3334	5.83
ND ₃	2420	3.06
CH ₄	2917	8.55
CCl ₄	459	6.45*
SiCl ₄	423	9.8
GeCl ₄	397	16.3
SnCl ₄	369	22.2
TiCl ₄	389	32.6
CH ₂ Cl ₂	713	3.94
CHCl ₃	773	1.73*
	674	2.71*
CH ₃ Cl	2965	6.55
SF ₆	774	3.60
SeF ₆	708	6.96
TeF ₆	698	6.40

Table 4.3-7 continued

Molecule	$\tilde{\nu}_k/\text{cm}^{-1}$	Σ_k
UF ₆	665	12.6
C ₂ H ₄	3020	6.4
	1623	2.12
	1342	2.8
C ₂ H ₃ Cl	1632	1.65*
CH ₃ OH	2846	4.7
C ₂ H ₆	2914	20.6**
		15.0
	993	2.10**
		1.17
C ₃ H ₈	2908	19.6
	870	1.6
C ₆ H ₆	3070	15.4
	992	12.4
C ₆ H ₁₂	802	4.03
C ₄ H ₆	2937	26.2
	2251	7.7
	694	1.5

* Average taken only for visible exciting lines

** Cross section for total band

4.3.2.4 Conclusion

In this section mainly results of linear Raman spectroscopy of gases and vapours have been considered and selected examples of the results of nonlinear techniques were included, e.g. CARS or stimulated and inverse Raman spectroscopy, by which much higher resolution can be achieved. Further such investigations have been reviewed elsewhere (Esherick and Owyong, 1982; Schrötter et al., 1988a, 1988b, 1990; Lavorel et al., 1992).

4.4 Matrix-isolated molecules*

4.4.1 Introduction

The matrix isolation technique is based on the principle of trapping chemical species, such as atoms, molecules, or ions in high dilution in the lattice sites of an inert, rigid solid host. The term “high dilution” indicates that statistically every third to tenth lattice

* Section 4.4 is contributed by H. Schnöckel, Karlsruhe and H. Willner, Hannover

site in each direction is occupied by trapped species; hence its density is comparable to that of the gaseous state under standard conditions. In the solid state, diffusion is considerably hindered, so that interactions between the isolated species are prevented and short-lived species can be preserved indefinitely. Nature provides several examples of matrix isolation. Traces of H_2O_2 , for instance, formed photolytically in the atmosphere, are trapped in Greenland's glaciers. The variation of the H_2O_2 concentration with the depth makes it possible to draw conclusions about the activity of the sun over the past 20000 years. Another interesting case of a prehistoric matrix is *Lapis lazuli*. The blue color of this mineral is due to S_3^- radical anions, isolated in a lattice of aluminosilicate. In solution, the S_3^- ion is short-lived.

However, science has extended nature's possibilities in stabilizing especially short-lived species by using frozen noble gases at low temperature as host materials. In this text, the term "matrix isolation" is used only to refer to this special technique. The application of solid noble gases makes it possible to investigate trapped species by different spectroscopic methods, since this material is highly transparent over a wide spectral range. From its inception (Pimentel et al., 1954; Porter and Norman, 1954), this technique has been applied to an ever-increasing range of chemical and physical problems, and the number of publications in this area has increased rapidly each year (now amounting to a total of approximately 5000). Nearly 150 review articles and books dealing with this subject as well as the very recent contributions and references therein (Almond and Downs, 1989; Andrews and Moskovits, 1989) are recommended for further study.

4.4.2 Vibrational spectra of matrix-isolated molecules

Molecules which are isolated in a noble gas matrix can be characterized by a wide range of spectroscopic techniques. However, the most common and most powerful tool is vibrational spectroscopy, on which this chapter focuses.

Although there is little interaction between host and matrix, environmental effects shift the IR absorptions of trapped species relative to those of unperturbed molecules in the gas phase (in general, $\Delta\nu/\nu$ is on the order of 0.005). The environmental effect on the IR absorption has been extensively studied in terms of inductive, dispersive, and repulsive contributions (Barnes, 1973). A more qualitative interpretation of matrix shifts has been suggested by Pimentel and Charles (1963): The matrix cage affects the vibrational coordinates of the trapped molecule, with the low force-constant coordinates experiencing a stronger influence than the high force-constant coordinates. Thus, a negative shift is observed for high-frequency stretching vibrations, while low-frequency stretching vibrations, bending, and rocking motions cause a positive shift ($\nu_{(\text{matrix})} > \nu_{(\text{gas})}$). In comparison with bands in the gas or the liquid phase, the half-widths of infrared absorptions of matrix-isolated molecules are small (0.1 to 2 cm^{-1}), because molecular rotations, intermolecular interactions, and hot transitions are prevented. Hence it is possible to resolve nearly degenerate vibrations — vibrations of isotopically substituted molecules, conformers, and isomers — and to study weakly bound molecular complexes which are dissociated under normal temperature and pressure conditions.

Over the past few years, sophisticated techniques have been developed to investigate reactive, unstable species even in the gas phase, e.g., molecular beam experiments, monitored by laser spectroscopy. As a specific example, the vibrational frequency of the high-temperature Na^{35}Cl molecule was measured at $364.6985(25) \text{ cm}^{-1}$ (Horiai et al., 1988). Although this value is not very different from the frequency of 335.9 cm^{-1} found for the argon matrix-isolated molecule (Ismail et al., 1975), the higher accuracy and knowledge of the exact absolute wave number of the unperturbed molecule are sometimes essential in order to elucidate its molecular physics. On the other hand, more chemically related problems (e.g., reactions of NaCl in solid noble gases) can be solved in a much simpler and more economical way by the matrix technique. This is demonstrated in this chapter.

Up until now, Raman spectra of matrix-isolated species have rarely been recorded, due to the low scattering cross-section inherent to the technique. If the progress in FT-Raman spectroscopy which has been observed over the last years continues (Cutler, 1990), there will be a renaissance of matrix applications.

4.4.3 Basic experimental details

The basic procedure of a matrix experiment is quite simple, as shown by Fig. 4.4-1. In a high-vacuum system and under controlled conditions, the investigated species are deposited onto a cold surface, together with a large excess (ca. 1:1000) of inert gas. Subsequently, the infrared spectrum is measured in transmission if a CsI or silicon window is used as matrix support, or in reflectance if the matrix is deposited on a metal mirror. A high-quality metal mirror made of diamond-cut and Al-plated copper is preferred over a CsI or silicon support because in the former case light passes twice through the matrix and a wide spectral range from 50000 to 10 cm^{-1} can be covered. Besides, in Raman measurements it is crucial to use a metal mirror as matrix support.

The thickness of the matrix during deposition can be monitored by laser interference. For infrared measurements, 0.05 to 0.5 mm are sufficient. Due to the low density of matrix-isolated species, a matrix for Raman study must be a few mm thick in order to maximize the Raman scattering of the incident laser radiation. The production of a good matrix is dependent on several parameters, such as the rate of deposition, the nature of the matrix gas and the trapped species, the temperature and purity of the cold surface, and the composition and after-treatment of the matrix. A matrix is referred to be good if it contains no impurities besides the trapped monomeric species of interest, if it shows no matrix effects on distinct vibrational bands, and if it is highly transparent (nearly invisible). In order to exclude impurities (especially water), an appropriate gas handling system and synthetic device have to be used, and a clean high vacuum is essential. The cold matrix support acts as an efficient cryopump, which collects a large amount of air from leaks and desorbed vapors (water, oil, etc.) from the warm inner surface of the matrix-isolation assembly. Assuming that there is only a minor source of impurities of $10^{-5} \text{ mbar} \cdot \text{L} \cdot \text{s}^{-1}$ near the matrix support, a quantity of $4 \cdot 10^{-2} \text{ mbar} \cdot \text{L}$ ($2 \cdot 10^{-3} \text{ mmol}$) is collected in one hour. If, during the same period of time, 4 mmol of a matrix

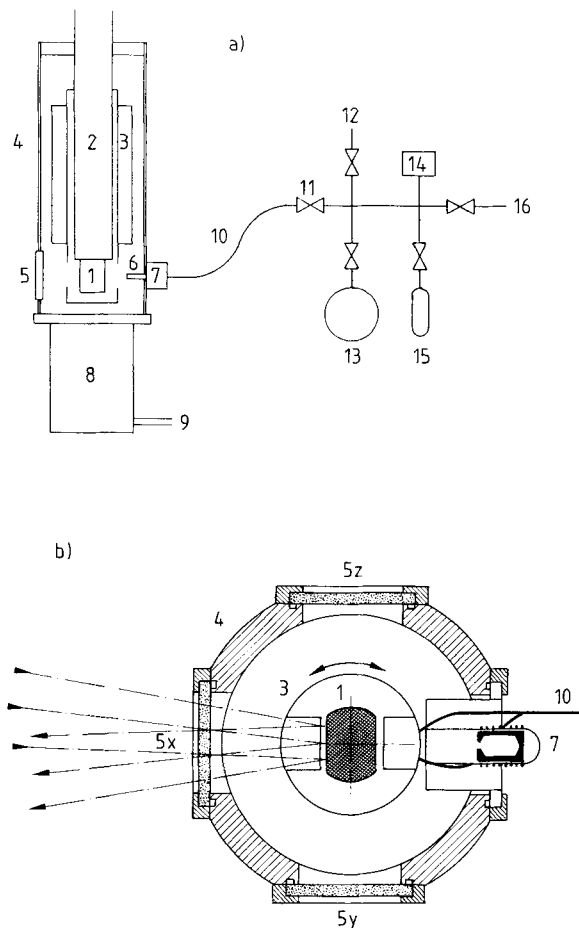


Figure 4.4-1 Basic composition of an apparatus for matrix-isolation experiments a) Rotatable cryostat with gas-handling system, b) Sectional view in the level of the matrix support, (1) matrix support, (2) refrigerator, 4-40 K, (3) radiation shield, 77 K, (4) vacuum shroud, (5) infrared window, x KBr, y PE, z quartz glass, (6) spray-on nozzle, (7) synthetic device, e.g., Knudsen cell, (8) turbomolecular pump, $p < 10^{-7}$ mbar, (9) to backing pump, (10) transfer line, quartz or stainless steel capillary, (11) needle valve, (12) inert gas inlet, Ne, Ar, N₂, ..., (13) bulb for gas mixtures, (14) capacity manometer, (15) sample, (16) to high-vacuum system.

mixture (1:1000) are deposited, then the quantity of the isolated species is $4 \cdot 10^{-3}$ mmol. In this unfavorable case, one particle of impurity is trapped with each isolated molecule, which may lead to a serious misinterpretation of the spectrum of the studied molecule. Therefore, the overall leak rate of the matrix-isolation assembly should be less than 10^{-6} mbar · L · s⁻¹; a turbomolecular pump (located as closely as possible to the matrix support) must provide clean vacuum conditions on the order of 10^{-6} mbar in the warm

system. In order to minimize cryopumping vapors (water, oil, etc.), a 77 K radiation shield surrounding the matrix support is strongly recommended.

A matrix is a nonequilibrium solution of trapped species in a solid noble gas. In order to minimize the chances of aggregation among the trapped species, the heat of condensation of the matrix gas must be transferred as fast as possible to the refrigerant, and the mobile layer between the solid matrix and the gas phase must be very small. Thus, the matrix support is usually connected to the refrigerator using indium foil as a very efficient thermal conductor. However, the cold surface may, if it is not entirely clean, offer some resistance to the heat transfer. Furthermore, the thermal conductivity of a solid noble gas is considerably temperature dependent; e.g., argon shows maximum conductivity at 10 K. At this temperature, an argon matrix should therefore be formed by continuous deposition. The deposition rate (0.5-5 mmol argon h⁻¹) is dependent on the geometry of the matrix assembly (spray-on nozzle, matrix support, distance to pump) and on the concentration, size, and intermolecular forces of the matrix-isolated species. The optimum conditions for minimizing aggregation and obtaining a transparent matrix can be found only by trial and error. If the temperature of the matrix support and the cooling power of the refrigerator are insufficient, aggregation problems can be overcome by applying the pulsed deposition technique (Perutz and Turner, 1973). For cooling, a great variety of closed-cycle refrigerators and continuous-flow helium cryostats are commercially available. Closed-cycle refrigerators based on the Sterling principle (Gifford and McMahon, 1960) operate at about 10-12 K, with enough cooling power for most matrix applications. In addition, three-stage closed-cycle refrigeration systems capable of 1 W at 4.2 K are available for neon matrix experiments. These devices combine a two-stage closed cycle cooler with a Joule-Thompson expansion cycle. The advantages of a continuous-flow helium cryostat are apparent only where higher cooling power and faster cooling down/warming up cycles are desired.

Even under optimal conditions of matrix deposition, yielding exclusively monomeric species of interest in a transparent matrix, distinct absorptions in the infrared spectrum often appear as multiplets spread over a few wavenumbers. This complicates the interpretation of matrix spectra and is known as the "matrix effect". The matrix effect is due to the fact that isolated particles occupy different substitutional lattice sites (which differ slightly in energy). Since this effect is connected with the geometry of guest and host species, the impact of a matrix effect depends on the matrix material (Ne, Ar, Kr, N₂, etc.). Energetically unfavored matrix sites can be removed by annealing the matrix. An argon matrix, for instance, softens at temperatures above 20 K, and argon atoms can rearrange around the trapping sites. On the other hand, the isolated species start to diffuse and to form aggregates. Since diffusion requires more time than rearrangement, the matrix should be warmed up as much as possible for a short period. With a xenon "overcoat" (Swanson and Jones 1981), an argon matrix can be warmed to 42 K without showing significant evaporation. Precise temperature control is achieved with calibrated silicon diodes (4-320 K), which can be checked with a vapor-pressure thermometer.

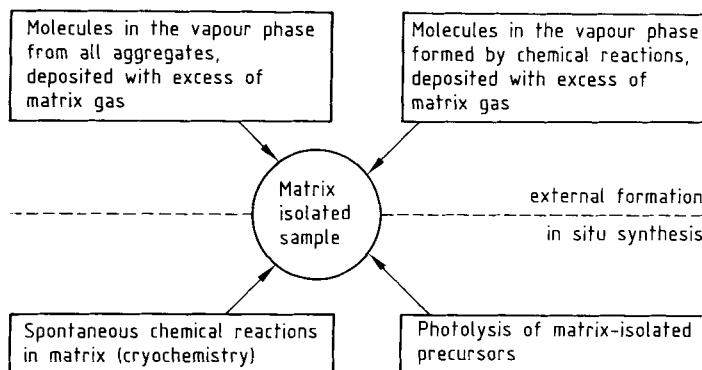
Besides the assembly around the matrix support, the other components of a matrix-isolation instrument also require some comment. Great emphasis is placed on the appropriate design of the gas handling system and on the devices for sample preparation. Precursor substances or matrix samples with a vapor pressure of more than 1 mbar at

room temperature can be mixed with matrix gases in a bulb (volume 0.5–1 L) which is connected to a high vacuum apparatus. Since not all chemicals can be handled in glass, a stainless steel apparatus should also be available. Precise pressure measurement is possible with capacity manometers, which are resistant against any gas. Since only a few mg of the matrix sample are introduced into the high-vacuum apparatus, its inner surface and that of the transfer tube to the matrix support must be pretreated, so that no decomposition or hydrolysis of the matrix sample can occur before the latter reaches the cold surface. The inner surface is conditioned best by removing adsorbed moisture with ClF_3 or with SOCl_2 , and by finally flushing the apparatus with a large excess of the matrix sample. Noble gases are available in high purity (>99.9999%) and can be used for this purpose. For transfer tubes between the gas handling system and the cold matrix support, flexible stainless-steel or polyamide-coated fused silica capillaries, usually used for gas chromatography, are recommended. It is the chemist's task to construct ingenious devices for sample generation (on a mg scale) in front of the matrix support.

Apart from innovative ideas in chemistry, progress in the field of matrix isolation is closely coupled with the development of new instruments and devices. Fourier-transform infrared instruments have enormously increased the amount of information which is obtained from matrix-isolation experiments. With new helium-cooled infrared detectors and faster Fourier-transform processors, less time is required to obtain high-quality spectra over a large spectral range. Unusual species at low concentrations and isotopic molecules with a low natural abundance can therefore now be detected. Additionally, hidden data are easily accessible by spectra subtraction (e.g., of the spectra before and after photolysis).

4.4.4 Methods of matrix preparation and formation of guest species

In this section, methods of synthesizing matrix-isolated molecules are discussed. In principle, there are two strategies, as represented in Scheme 4.4-1.



Scheme 4.4-1

In the first case, the species of interest is formed *externally* before matrix isolation takes place, and in the second case it is generated *in situ* from an already trapped precursor. The scheme illustrates the methods of sample preparation with the help of various examples.

4.4.5 Molecules in the vapor phase

It is easy to mix a volatile compound with a large excess of matrix gas in a bulb and to deposit this mixture at low temperature. The advantage of the resulting infrared spectrum of a matrix-isolated species over corresponding spectra obtained in the gaseous or the solid state is demonstrated by the spectra of perchloric acid, HClO_4 , shown in Fig. 4.4-2.

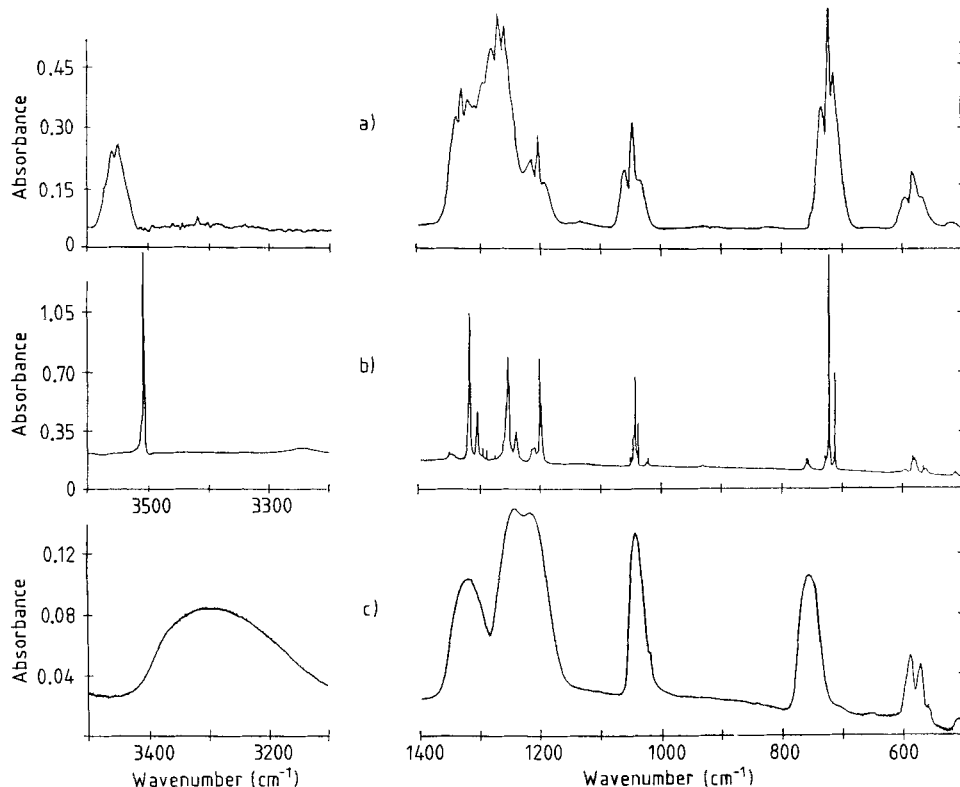


Figure 4.4-2 Infrared spectra of perchloric acid, HClO_4 : a) in the gas phase at 295 K, 2 mbar in a 20 cm cell equipped with silicon windows; b) isolated in an argon matrix at 11 K, 0.7 mmol, molar ratio 1:500. c) as a solid film at 50 K after slow evaporation of the argon from the matrix-isolated sample b). Note the changes in the band positions, band shapes, and absorbances between b and c.

In the gase phase, the infrared bands are broad (50 cm^{-1}), due to the rotational structure, overlapping vibrations, and hot transitions. In the solid state, the rotational motions are quenched, but due to intermolecular (hydrogen bond) and correlation field interactions, the band positions are shifted and the bands are even broader. The infrared absorptions of matrix-isolated molecules are close to the gas-phase frequencies and exhibit a sharp line-like character (half-widths 0.1 to 2 cm^{-1}). Hence the spectra of matrix-isolated molecules are less complicated, and, in comparison to gas phase or solid state spectra, the sensitivity and selectivity of detection increase by a factor of about 10 to 100. Closely spaced vibrations attributed to mixtures of similar molecules, such as conformers, rotamers, molecular complexes, or isotopic species, e.g., $\text{H}^{35}\text{ClO}_4$ and $\text{H}^{37}\text{ClO}_4$, are easily distinguished.

Molecules which are capable of undergoing conversion to an isomer of similar thermodynamic stability via a low activation barrier ($>10 \text{ kJ mol}^{-1}$) may be quenched in a matrix which has the composition of the vapor prior to deposition. The distribution of isomers in a matrix can be influenced by changing the temperature of a heated nozzle. By analyzing the intensities of relevant infrared absorptions, the molar ratio between two conformers can be determined as a function of the gas temperature. On this basis, the enthalpy difference between the two forms can be obtained by a van't Hoff plot. On the basis of matrix studies for the conversion of the *s-cis* to the *s-gauche* form of methyl vinyl ether, a value of $\Delta H = 6.62 \text{ kJ mol}^{-1}$ was found (Gunde et al., 1985).

Co-deposition of two different species from the gas phase under suitable conditions affords a small number of molecular complexes in the matrix. The weak intermolecular interaction can be measured by determining the vibrational perturbation of the complex submolecules relative to that of the free matrix-isolated molecules. Hydrogen bonding is by far the strongest intermolecular force which plays a central role in a wide range of fundamental chemical and physical phenomena. Hydrogen fluoride, HF, is an excellent proton-donor molecule which allows to study the intrinsic properties of hydrogen bonding with various proton-acceptor molecules, isolated in a matrix (Andrews, 1984). In comparison to other proton donating molecules, HF has two advantages: i) it forms the strongest hydrogen bonds, and ii) it produces simple infrared spectra for HF complexes. HF complexes are characterized by frequency shifts of $\nu(\text{HF})$ and $\delta(\text{HF})$ in comparison to free matrix-isolated HF (for an argon matrix $\nu(\text{HF}) = 3920 \text{ cm}^{-1}$ and $\delta(\text{HF}) = 40 \text{ cm}^{-1}$. The frequency shifts of complexes isolated in an argon matrix (e.g., $\text{N}_2 \cdots \text{HF}$ $3881/262 \text{ cm}^{-1}$, $\text{OC} \cdots \text{HF}$ $3790/389 \text{ cm}^{-1}$, $\text{HCN} \cdots \text{HF}$ $3626/586 \text{ cm}^{-1}$) can be correlated with the strength of the hydrogen bond and the proton affinity of the base.

Isotopic effects of matrix-isolated species measured at a high accuracy ($< 0.1 \text{ cm}^{-1}$) can be exploited to maximum advantage. The composition and symmetry of a new matrix molecule (see following section) is frequently determined by performing experiments with enriched isotopes and model calculations. Since isotopic substitution has no influence on the potential function and the geometry of a molecule, exact unperturbed isotopic vibrational frequencies are useful input data for a force field calculation, such as OCCl_2 (Schnoeckel, 1975), SCCl_2 (Hauswirth and Willner, 1979). The number of internal force constants z (of the general valence force field, GVFF) for a molecule with C_1 -symmetry and N fundamentals equals $z = N \cdot (N + 1)/2$. The number of experimental

data which are needed to determine the internal force constants increases enormously with the size of the molecule.

The molecular geometry can also be estimated from isotopic data, if the molecule exhibits only one or two fundamentals in one symmetry class, BrNCO (Gerke et al., 1989).

Besides the above-mentioned application for volatile, stable compounds, the technique of matrix isolation is superior to gas-phase investigation of compounds with a low vapor pressure. The vapor pressure of molybdenum hexacarbonyl, Mo(CO)₆, for instance, is only 10⁻¹ mbar at room temperature, which is insufficient for ordinary gas-phase infrared measurements. However, if Mo(CO)₆ is flushed with a stream of matrix gas and if the final mixture is deposited as a matrix, then the density of the Mo(CO)₆ molecules increases considerably. This integration effect (the deposition time varies from 5 minutes to several hours) is very important for high-temperature species and has interesting analytical applications.

High-temperature species may be generated by a hot Knudsen cell, placed a few centimeters in front of the matrix support (see Fig. 4-1b). An excess of matrix gas is then introduced into the molecular stream and quenched as a matrix. The amount of sample is determined by quantitatively condensing the material onto a quartz microbalance for a certain test period. The amount of matrix gas is measured manometrically or with an electronic gas flow controller. The ratio sample/matrix gas is then calculated. Besides evaporation of a solid – assuming the molecules in the vapor phase exhibit the same stoichiometric composition as the solid – high-temperature species can also be generated from precursors by thermal fragmentation and chemical reactions (see following section).

During the past few years there has been an increasing interest in high-temperature species, because they are important for many high-temperature chemical and technological processes, such as modern light sources, chemical vapor deposition, and combustion processes.

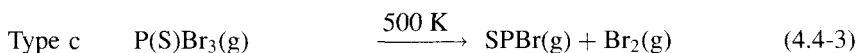
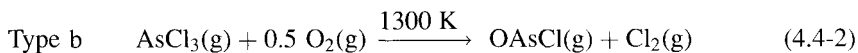
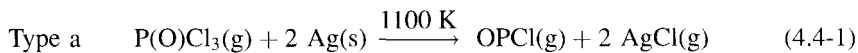
High-temperature species are not only identified by their vibrational spectra; entropies, force fields, and molecular geometries can also be determined, particularly for small molecules (e.g., transition-metal halides MX₂,...).

Finally, matrix isolation, coupled with high-resolution gas chromatography, provides a powerful tool for infrared trace analysis. Modern GC/FTIR (gas chromatography/Fourier transform infrared) systems use gold-coated light pipes for “in-flight” measurements. Dead volume, light throughput, and the measuring time limit the sensitivity of the light pipe technique to the ng range. As discussed earlier, matrix isolation exceeds the sensitivity and selectivity of gas-phase measurements by a factor of 10 to 100. Additional advantages of matrix isolation are: i) there is no restriction to the scanning time, and ii) microscope optics with a better light throughput can be attached; an overall sensitivity increase by three to four orders of magnitude is thus possible (pg range). A complete matrix isolation/GC/FTIR system, known as “Cryolect”, is marketed by Mattson (Reedy et al., 1985). The cold surface in this system is a polished metal cylinder, which moves along its axis as it rotates to produce a small helical matrix band; the band is then sampled by the highly focused beam of an FTIR spectrometer. With a narrow-band, highly sensitive MCT detector, the optimal diameter of the matrix is 0.3 mm. Further progress is possible by using improved infrared detectors with smaller active areas.

4.4.5.1 Molecules in the vapor phase, formed by chemical reaction

The fact that an ultra-high vacuum is essential in order to protect the matrix support from impurities and that an excess of an inert matrix gas must be used is of great advantage for the synthesis of short-lived species in the gas phase. Such syntheses, including solid/gas reactions at high and at low temperatures, flash pyrolysis, and reactions between two different vapors, all at low pressure, are described below.

The recent trend has been to investigate molecules containing multiple bonds between atoms of the second and higher period (e.g., $\text{Si}=\text{C}$, $-\text{P}=\text{C}$, etc.). While several such molecules – synthesized on a preparative scale – are protected from polymerization at room temperature by bulky organic substituents, the simple basic examples (such as $\text{H}_2\text{Si}=\text{CH}_2$) can be stabilized only under matrix conditions. Molecules of the types $\text{O}=\text{E}-\text{X}$ and $\text{S}=\text{E}-\text{X}$ ($\text{E} = \text{P}, \text{As}, \text{Sb}; \text{X} = \text{F}, \text{Cl}, \text{Br}$) also belong to this class of compounds, which have been studied extensively by matrix isolation and by several other techniques (Binnewies and Schnoeckel, 1990). These species were formed prior to matrix isolation by (a) solid/precursor, (b) gas/precursor or (c) precursor bond cleavage reactions:



All of the reactions mentioned above are appreciably endothermic, but the entropy change is positive. With increasing temperature and decreasing pressure, the position of the equilibrium is therefore shifted to the right. The choice of the reaction type (a, b, or c) and of the temperature was made for thermodynamic reasons and in order to exclude side reactions as far as possible.

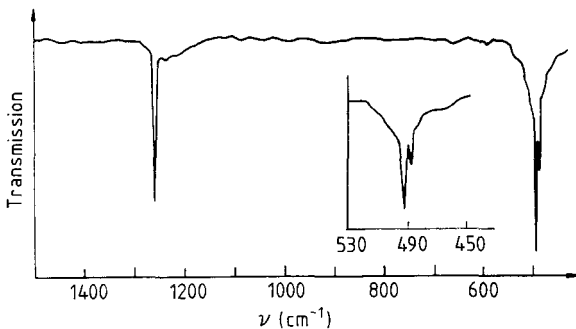
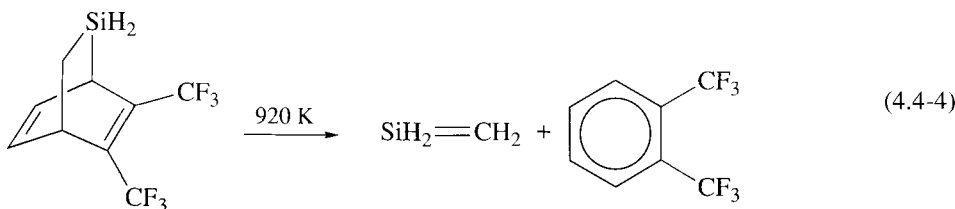


Figure 4.4-3 Infrared spectrum of the high-temperature $\text{O}=\text{P}-\text{Cl}$ molecule, isolated in solid argon.

The procedure of interpreting data concerning the molecule OPCl is described as an example. Fig. 4.4-3 shows the infrared spectrum of matrix-isolated OPCl with the two stretching vibrations at 1237.7 ($\nu(\text{PO})$) and at 489.4 cm^{-1} ($\nu(\text{PCl})$). The deformation mode, of much lower intensity, lies at 308.0 cm^{-1} . By using the precursor $\text{P}^{18}\text{OCl}_3$, the absorptions are shifted to 1211.8, 484.7, and 298.0 cm^{-1} , respectively. These data confirmed the assignment of vibrations and the assumed sequence of the atoms O–P–Cl. Furthermore, by means of a normal coordinate analysis it was possible to limit the bond angle to a value of 105°, which is in accordance with the results of quantum-mechanical calculations.

The following example demonstrates the strategy adopted for pyrolysis reactions. The precursor molecule has to decompose by cleaving the weakest bonds in order to form the species of interest and a stable byproduct. In this manner the above-mentioned silaethene, SiH_2CH_2 , was first formed according to:



and subsequently isolated in an argon matrix (Maier et al., 1984). If the argon matrix containing silaethene is irradiated with light of a wavelength of $\lambda > 320 \text{ nm}$, isomerization to methylsilylene, CH_3SiH , occurs. This isomerization can be reversed by photolysis of methylsilylene at a shorter wavelength ($\lambda = 254 \text{ nm}$); whereas annealing of the matrix favors dimerization. The changes in the infrared spectrum accompanying the production of methylsilylene are illustrated in Fig. 4.4-4. This example demonstrates the potential of

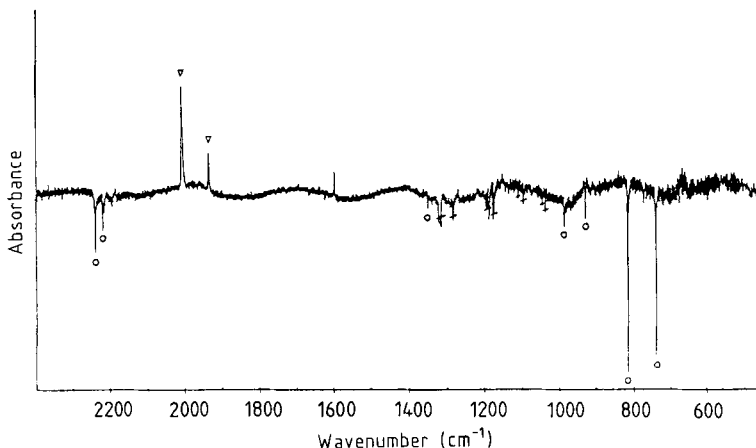
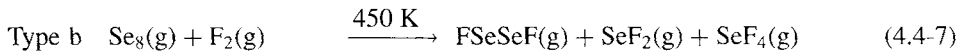


Figure 4.4-4 Difference IR spectrum of matrix-isolated pyrolysis products according to Eq. 4.4-4 in Ar at 10 K before and after UV photolysis for 10 minutes. Photolysis isomerizes silaethene (o) to methylsilylene (▽). The bands marked by a dash are due to hexafluoroxylene which has not been completely eliminated. (Reproduced with permission from Chem. Ber. (1984) 117: 2369).

the photolytic technique in producing new species, in distinguishing between species of different photostability, and in simplifying infrared spectra (see following section).

However, high temperatures are not essential to produce unstable, reactive species in the gas phase under matrix conditions. This is exemplified by investigations of the lower sulfur and selenium fluorides. These can be prepared near room temperature and at low pressure by fast reactions between a solid and a precursor (type a) or between a gas and a precursor (type b):



All reactions are exothermic with little change in entropy, and product formation is kinetically controlled. With increasing temperature, in Eqs. (4.4-5, 4.4-6) SF₄ or in Eq. (4.4-7) more SeF₄ is formed. The isomers of S₂F₂ have been investigated in order to improve the vibrational assignment and to calculate the general valence force fields, including data from isotopically enriched ³⁴S₂F₂ (Haas and Willner, 1979 a). The metathesis reactions were carried out by passing mixtures of S₂Cl₂ and argon (1:500) through 5 mm thick layers of metal fluoride powder. While AgF leaves the CISSCl skeleton unchanged, HgF₂ acts as an efficient catalyst for the isomerization of FSSF to the more stable SSF₂.

The formation and infrared detection of lower selenium fluorides was achieved as follows (Haas and Willner, 1979 b): A 6 · 1 mm quartz glass tube was used to conduct the matrix gas stream onto the cold CsI-support. The inner surface of this tube was covered with a thin layer of an equimolar mixture of highly enriched ⁷⁶Se and ⁸²Se. While warming the tube to about 450 K, which causes slow evaporation of selenium, a mixture of fluorine and argon (1:500) was passed through the tube, and the primary products were quenched in a matrix onto the CsI-support at 12 K. The resulting infrared spectrum is presented in Fig. 4.4-5. SeF₄ absorptions, known from a reference spectrum, are labeled *x*. Variation of the reaction conditions caused changes in the product distribution, and the remaining bands were assigned to two new species a and b. The presence of SeF₂ (a) and FSeSeF (b) was proven by analysis of the isotopic pattern and by comparison with the spectra of SF₂ and FSSF. UV-photolysis of the matrix caused a decrease in the bands (b) and the appearance of new bands (c), which were assigned to SeSeF₂. Three new binary compounds were thus produced in a single experiment. Force constants and a bond angle of 94° for SeF₂ were derived from the vibrational data.

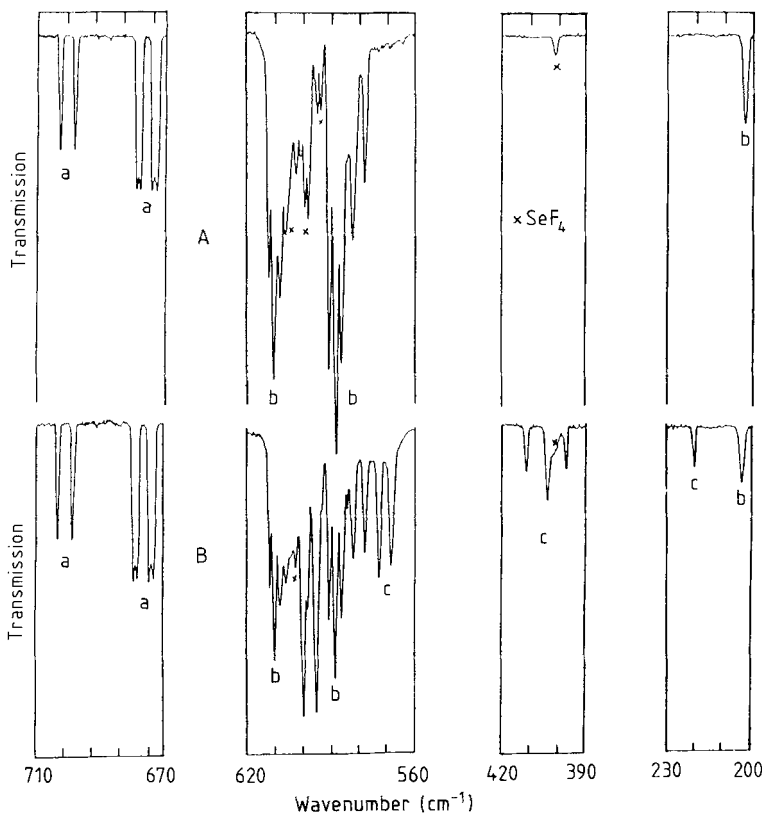


Figure 4.4-5 IR spectra of matrix-isolated reaction products according to equation (4.4-7), using a highly enriched mixture of ^{76}Se and ^{82}Se in Ar at 10 K before (A) and after (B) UV photolysis. (a) represents SeF_2 , photolysis isomerizes FSeSeF (b) to SeSeF_2 (c) (Reproduced with permission from Z. Anorg. Allg. Chem. (1979) 454: 17).

4.4.6 Spontaneous chemical reactions in a matrix (Cryochemistry)

A homogeneous chemical reaction proceeds via transport processes (convection, diffusion); approach of the reactants due to intermolecular forces in the 100 pm range leads to molecular complexes; and finally, after activation of the complex, charge and bond redistribution takes place. Matrix techniques offer the possibility of studying individual stages in a reaction process between isolated species. The efficiency of a reaction in a matrix depends on the mobility of the matrix-isolated species, the strength of the intermolecular interaction, and the height of the activation barrier. The mobility of a species which is isolated in a matrix is related to its size; electrons and atoms are far more mobile

than molecules. Atoms are produced in the gas phase prior to matrix deposition by electrical discharge in gases (e.g., H, O, N, F, ...), or by high-temperature sources (e.g., metal atoms, Si, Se,...); alternatively, they may be formed *in situ* by photolysis of precursor molecules ($\text{HI} \rightarrow \text{H}$, $\text{F}_2 \rightarrow \text{F}$, $\text{O}_3 \rightarrow \text{O}$, $\text{N}_3\text{CN} \rightarrow \text{C}$, etc). The strength of intermolecular interaction is reflected by the dipole moment of a molecule or by the ability of electron tunneling of species with loosely bound electrons. Hence it is difficult to isolate monomeric NaCl molecules and metal atoms. Besides, the height of the activation barrier must be very small for spontaneous matrix reactions to occur. This is true for reactants with open electron shells, such as atoms, radicals, and unsaturated molecules; e.g., SiO , AlF , OPCl , $\text{Cr}(\text{CO})_5$, etc. Such species are suitable for "cryochemical" reactions.

If the concentration, support temperature, and deposition rate are higher than in monomeric isolation, aggregates are formed during the deposition of reactive species. In this way, stepwise polymerization of reactive molecules (e.g., $\text{SiO} \rightarrow (\text{SiO})_{2,3}$ (Schnoeckel et al., 1989), formation of metal aggregates from metal atoms (Moskovits, 1989), or the growth of a crystal lattice ($\text{NaCl} \rightarrow (\text{NaCl})_x$ (Martin, 1977)) can be observed. The structures of "metal molecules" are often determined by Raman spectroscopy. A similarly interesting example is the formation of Se_3 molecules from Se_2 and Se atoms (Schnoeckel et al., 1982). The effusing molecular beam of a Knudsen cell, containing only Se_2 molecules and Se atoms, was mixed with an excess of nitrogen and trapped at 14 K. After annealing the matrix up to 25 K for a few minutes, a resonance Raman spectrum of Se_3 molecules was measured (Fig. 4.4-6). The spectrum shows a progression in the symmetric stretching vibration. Force constants and the bond angle were obtained by the use of isotopic data. These Se_3 species are also present in high-temperature equilibria of selenium vapor, but their concentration in the Se_x mixture is much lower than in the mixture resulting from matrix reaction.

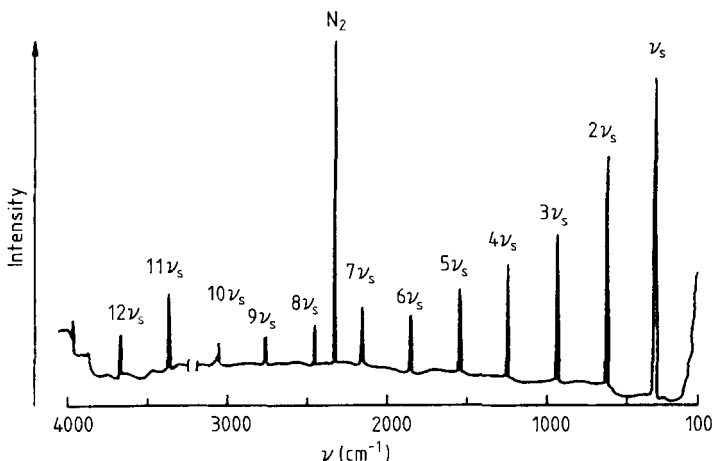
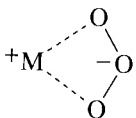


Figure 4.4-6 Resonance Raman spectrum of $^{80}\text{Se}_3$ in solid N_2 . Excitation line: 514 nm (Ar+).

Most matrix reactions are performed by co-deposition of two different reactants. This method is the preferred technique of introducing metal atoms as reactive species, an application of the matrix technique which has been reviewed extensively (Moskovits and Ozin, 1976). In general, metal atoms react spontaneously with small molecules such as H₂, O₂, N₂, CO, CH₄, H₂O, etc. at 10 K, if the activation barrier is less than a few kJ mol⁻¹. Under these conditions unusual species are formed. While strontium or nickel metal reacts with oxygen at high temperature to give the stable oxides SrO(s) or NiO(s), strontium or nickel atoms react in a matrix to form M⁺O₂⁻, with the O₂⁻ unit bound "side-on". The O₂ frequencies in SrO₂ of 1120 and in NiO₂ of 966 cm⁻¹ reflect a certain difference in the bonding. With an excess of O₂, only Ni is able to form a complex with two O₂ ligands. No stable complexes of nickel with O₂ or N₂ are known to exist at room temperature, but under matrix conditions Ni atoms and N₂ form Ni(N₂)₄, in analogy to the stable isoelectronic nickel tetracarbonyl. By conducting similar experiments with CO/N₂ mixtures, it was possible to identify all species in the series Ni(CO)_x(N₂)_{4-x}. These few examples of reactions of nickel atoms are representative of the broad chemistry of transition metal atoms.

Many free radicals (e.g., CX₃), have been stabilized in an argon matrix after the halogen atom Y was abstracted from CX₃Y by lithium or by one of the heavier group I metals (Andrews, 1976). Group I metal atoms also undergo charge transfer reactions with O₂, O₃, NO₂,... and lithium forms more covalently bonded complexes with C₂H₂, C₂H₄, etc. Cryochemical reaction of group I metal atoms with O₃ led to the first extensive characterization of the ozonide ion (Andrews and Spiker, 1973). Different lasers (450–530 nm) were used to excite the symmetric stretching vibration $\nu_1 = 1016 \text{ cm}^{-1}$ in the resonance Raman spectrum. From this frequency and the infrared spectrum ($\nu_2 = 601$, $\nu_3 = 802 \text{ cm}^{-1}$ of the natural and the ¹⁸O-enriched species), a complete force field and a geometry with $r = 138 \text{ pm}$ and $\alpha = 108 \pm 5^\circ$ was derived. Since the ion pairs in the matrix are arranged as follows:



the bond angle was assumed to be larger in the free ion. The preparation of KO₃ single crystals allowed an improvement of these data by an X-ray diffraction study ($r = 135 \text{ pm}$, $\alpha = 113.5 \pm 1^\circ$ by Hesse et al., 1989).

The synthetic principle described above for reactions in matrices is also employed in preparative work. For this purpose, highly reactive species, such as metal atoms, SiF₂, SiO, BF, BCl, etc. are co-condensed with a substrate at -196 °C. After warming up and separation from excess substrate and by-products, numerous new compounds have been synthesized on a gram scale (Timms, 1976). If the substrate cannot be condensed at -196 °C (e.g., CO), a closed-cycle helium refrigerator can be used to maintain a temperature of 30 K on the cold surface. In this way, Ru(CO)₅ has for the first time been prepared on a gram scale (Godber et al., 1986).

4.4.7 Photochemical reactions in a matrix

Photolysis of matrix-isolated molecules is a particularly effective route to unstable molecules and ions (Perutz, 1985). In order to activate molecular complexes and molecules, knowledge about the UV/VIS absorption spectrum of the photolabile precursor and the use of light of the appropriate energy are essential. Light sources are available over the entire spectral range, such as metal vapor (Hg, Cd, Na,...), Xe, or D₂ arc lamps in connection with cut-off, band-pass, or interference filters or monochromators, lasers, or windowless discharge lamps. Molecular complexes with energy barriers which are too high for cryochemical reactions at 15 K can be activated by photolysis. Two of the early examples are the formation of HOF and KrF₂ by photolysis of matrix-isolated H₂O/F₂ and Kr/F₂ complexes (Noble and Pimentel, 1968; Turner and Pimentel, 1963). Both compounds are now available on a preparative scale (Studier and Appleman, 1971; Slivnic et al., 1975).

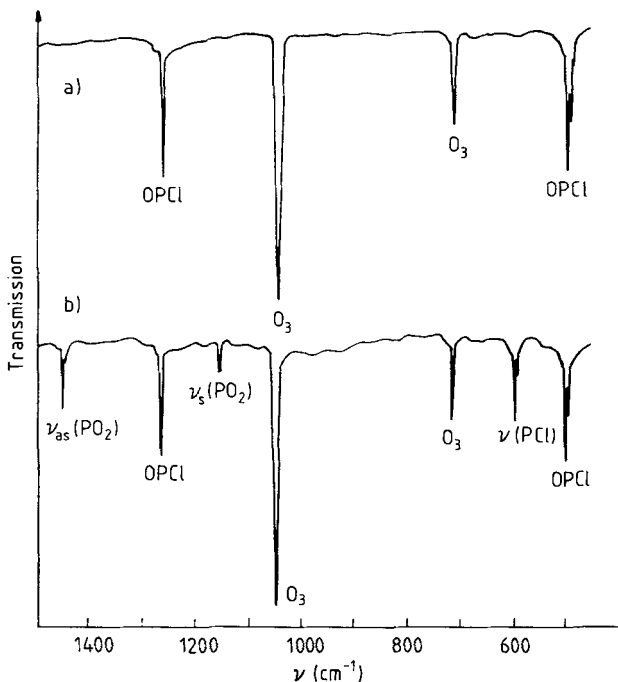


Figure 4.4-7 a) Infrared spectrum of the high-temperature OPCl molecule, co-condensed with O₃ in an Ar matrix. b) Infrared spectrum of the same sample after photolysis with a high-pressure Hg lamp for 15 min.

This principle has also been applied to several other photochemically induced redox reactions, especially with ozone as an oxidant. A good example is the oxidation of the high-temperature species OPCl. The infrared spectrum of a matrix-isolated mixture of

OPCl and O_3 is shown in Fig. 4.4-7a. After photolysis by a mercury arc lamp with light of the wavelength $\lambda > 310$ nm, the spectrum changed drastically (Fig. 4.4-7b). New bands appeared at 1448, 1147, and 581 cm^{-1} and were assigned to the O_2PCl molecule. With additional $^{16/18}\text{O}$ and $^{35/37}\text{Cl}$ isotopic data, the molecular structure and a force field were derived, which are in good agreement with the results of *ab initio* calculations. This triply coordinated phosphorus (V) compound polymerizes on annealing the matrix and pumping off the excess of argon. Finally, an O_2PCl film with P–O–P linkages was left (Ahrlrichs et al., 1986).

Apart from oxidation reactions using O atoms from O_3 as precursor molecules, several oxidation processes in matrices have been performed with S atoms which were generated photochemically from OCS (Hawkins et al., 1985). A very simple but instructive example is the reaction of the high-temperature SiS molecule with OCS. After photolysis, the CO_2 analogue molecule SiS_2 is formed. The linear structure was deduced from the isotopic shifts ($^{32}\text{S}/^{34}\text{S}$ and $^{28}\text{Si}/^{29}\text{Si}$) of the antisymmetric stretching vibration (Schnoeckel and Koepe, 1989).

When alkali metal atoms are co-condensed with strong electron acceptors in matrices, electron transfer occurs spontaneously, as discussed above in the case of $\text{K} + \text{O}_3$. If not spontaneous, electron transfer can easily be activated by photolysis. Irradiation by the Na_D line (583 nm; cf. ionization energy corresponding to 243 kJ mol^{-1}) is sufficient to transfer the sodium valence electron to several molecular substrates; e.g., $\text{Cl}_2 \rightarrow \text{Cl}_2^-$, $\text{B}_2\text{H}_6 \rightarrow \text{B}_2\text{H}_6^-$, $\text{HI} \rightarrow \text{H} + \text{I}^-$.

Photochemically produced small atoms (H, C, N, O, F), co-deposited with matrix-isolated substrates, led to a wide variety of unstable molecules and radicals. This synthetic route is very efficient if the substrate itself acts as a matrix material (O_2 , CO, CH_4). Apart from these reactions, photo-induced decomposition and isomerization processes of matrix-isolated molecules can be studied by vibrational spectroscopy. Photoelimination of small, thermodynamically stable molecules (N_2 , CO_2 , CF_4 , HF,...) from a precursor is the most important photoprocess for generating unstable molecules in low-temperature matrices. Photochemical loss of dinitrogen from azido and diazo compounds is frequently observed in matrices. One example is that of azido halides (Milligan and Jacox, 1964).



These nitrenes, which are very short-lived in the gas phase, were characterized unambiguously by their vibrational frequencies, including data of ^{15}N -isotopically enriched precursor molecules NF: 1115, N^{35}Cl : 825, NBr: 691 cm^{-1} (argon matrix).

Laser photolysis (488 nm) of Cl_2O affords the ClCIO isomer in addition to ClO . Both IR and Raman spectra of eight isotopomers were used to establish the identity of ClCIO and to estimate a bond angle of 120° (Chi and Andrews, 1973). The primary products of the photolysis of a matrix-isolated molecule are very often not identical with the finally observed species. The matrix cage holds the primary products together, so that they can recombine to form a secondary product, which may be photolyzed further. In the gas phase, Cl_2O photodissociates into $\text{Cl} + \text{ClO}$. At low temperature, ClO dimerizes to form ClOOCl . This species is a key compound for understanding the chemical processes leading to the antarctic “ozone hole” (Birk et al., 1989).

4.5 Crystals*

4.5.1 Vibration of an unidimensional diatomic chain

We consider a chain of unit cells containing two masses m and M , connected by an elastic bond with a force constant f , and separated by a distance a . The masses are numbered $2i-1$ and $2i$ for the cell i . Displacements during motion are noted x_{2i-1} and x_{2i} .

The equations describing the motion of the masses in the unit i are:

$$\begin{aligned} m \frac{d^2x_{2i-1}}{dt^2} &= f(x_{2i+1} + x_{2i-1} - 2x_{2i}) \\ M \frac{d^2x_{2i}}{dt^2} &= f(x_{2i} + x_{2i-2} - 2x_{2i-1}) \end{aligned} \quad (4.5-1)$$

We are looking for a harmonic solution with frequency ν which also shows spatial periodicity corresponding to the lattice. This can be introduced through a wavelength λ , defining unit cells of the chain with the same motion. Therefore we can write:

$$\begin{aligned} x_{2i-1} &= A_m \cos(2\pi(\nu t - (2i-1)a/\lambda)) \\ x_{2i} &= A_M \cos(2\pi(\nu t - 2ia/\lambda)) \end{aligned} \quad (4.5-2)$$

It follows that

$$\begin{aligned} (2f - 4\pi^2\nu^2m)A_m - 2f \cos(2\pi a/\lambda)A_M &= 0 \\ -2f \cos(2\pi a/\lambda)A_m + (2f - 4\pi^2\nu^2M)A_M &= 0 \end{aligned} \quad (4.5-3)$$

Non-trivial solutions of this set of equations with variables A_m , A_M , and ν exist if

$$\text{Det} \begin{vmatrix} 2f - 4\pi^2\nu^2m & -2f \cos(2\pi a/\lambda) \\ -2f \cos(2\pi a/\lambda) & 2f - 4\pi^2\nu^2M \end{vmatrix} = 0 \quad (4.5-4)$$

One obtains two solutions:

$$\nu^2 = \frac{f}{4\pi^2mM} \left[m + M \pm \sqrt{m^2 + M^2 + 2mM \cos(4\pi a/\lambda)} \right] \quad (4.5-5)$$

* Section 4.5 is contributed D. Bougeard, Lille

Obviously, the two waves have frequencies which depend on the wavelength λ , the distance between atoms with identical motions, or the distance between unit cells which vibrate in phase. Due to the periodicity of the cosine function, the two frequencies show the same variation of $1/\lambda$ in the regions $0 \dots 1/(2a)$, $1/(2a) \dots 1/(4a)$, etc. At both ends, $\lambda = \infty$ and $\lambda = 2a$, all unit cells vibrate in phase; in the center, at $\lambda = 4a$, two consecutive cells vibrate in opposition. All cases between in-phase and out-of-phase vibrations of consecutive cells are contained in the region $1/\lambda = 0 \dots 1/4a$, which is referred to as the *first Brillouin zone*. The vector k , oriented in the direction of wave propagation with a modulus $2\pi/\lambda$, is called wave vector. If both masses are identical, the two branches of the monoatomic chain coalesce at $\lambda = 4a$ with a frequency of $(1/2\pi)(2f/m)^{1/2}$. If the masses are different, a frequency gap exists between $(1/2\pi)(2f/m)^{1/2}$ and $(1/2\pi)(2f/M)^{1/2}$ (Fig. 4.5-1). The low frequency branch tends to zero as k approaches zero. According to the low frequency region covered by this mode, the branch is referred to as *acoustic*. In contrast, the high frequency branch is called *optical*. Unit cell parameters are usually on the order of several Ångströms, while the radiation used for infrared and Raman studies is in the range of several thousands of Ångströms. $1/\lambda$ will always be very small compared to $1/a$ and only vibrations corresponding to k around zero will be observed. Equation 4.5-5 thus becomes

$$\nu^+ = \frac{1}{2\pi} \sqrt{\frac{2f(m+M)}{mM}} \quad \text{and} \quad \nu^- = 0 \quad (4.5-6)$$

With $\nu^- = 0$, we can extract $A_m = A_M$ and conclude that the motion is an overall translation of the chain. The same operation with ν^+ leads to $mA_m = -MA_M$. In this case, the amplitude varies with the mass ratio, but the negative sign indicates that the sublattice m vibrates against the sublattice M .

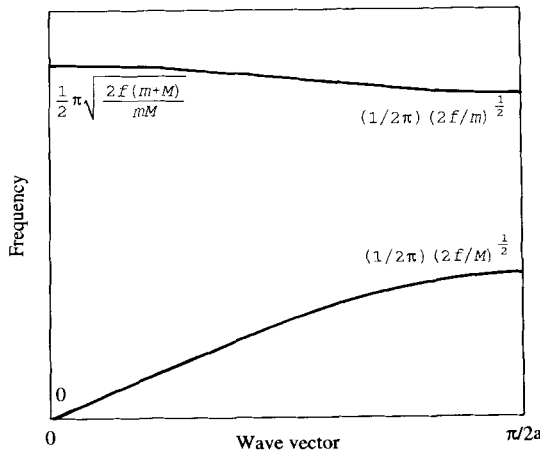


Figure 4.5-1 Dispersion curve for unidimensional diatomic chain. The ratio of the masses is $M/m = 5$. Note that a is the interatomic distance while the lattice periodicity is $2a$.

4.5.2 Qualitative extension to a three-dimensional lattice

In the previous discussion we have been concerned with only one degree of freedom of each atom, i.e., only one direction of motion. It could have been represented as a longitudinal motion in the direction of the chain and of the wave. However, the same formalism can also be applied to calculate motions which are transversal to the chain and to the direction of propagation. In order to differentiate between these different cases, one distinguishes between *transversal* (*T*) and *longitudinal* (*L*), *optical* (*O*) and *acoustic* (*A*) modes. We have seen that the only motions which are spectroscopically active are those in which all unit cells vibrate in phase. For such motions, the energy of the system is a multiple of the energy of one unit cell, and the investigation can focus on one primitive unit cell. Such a cell with N atoms has $3N$ degrees of freedom, which combine to $3N$ normal modes. Three of these can be assigned to the three overall translations of the unit cell (one in each direction in space). They correspond to the acoustic branch of the unidimensional model and are also called *acoustic*. The remaining $3N - 3$ modes with non-zero frequencies are referred to as *optical modes*.

This approach describes motions of particles without considering their physical nature, and it particularly neglects the charge associated with each atom. For so-called polar vibrations, which change the dipole moment of the sample, this description is too simple, particularly in the case of ionic crystals. The polar vibrations of the ions create long-range electromagnetic waves which interact with the mechanical motions defined previously. If we assume a diatomic cubic lattice ($N = 2$), we expect three optic and three acoustic modes. Group theory shows that each set of three modes should be degenerate, so that only one band can be expected in the infrared spectrum. In fact, interaction of these three modes with the induced field causes splitting into two degenerate transverse motions at lower frequency and one longitudinal mode at higher frequency. Two bands can therefore be expected. As for infrared absorption, where resonance of the crystal modes with the infrared wave is necessary, only the transverse modes which can interact with the transverse electric field are observed as one band. The frequency of the longitudinal band can be calculated by the Lyddane-Sachs-Teller equation (Lyddane et al., 1941). This behavior is known as longitudinal-transversal splitting and is often referred to as *LO - TO splitting*. It is not limited to this simple example, but is generally observed for all polar vibrations in the entire Brillouin zone.

Another approach to the dynamics of a crystal lattice considers the relative magnitude of the forces in the solid state in the presence of different entities (ions, molecules). The bond energies of such entities usually exceed the energy of intermolecular interactions (van der Waals or electrostatic forces) by several orders of magnitude. Hydrogen bonds are also weaker than the discussed bond energies, although this difference is less important. Experience confirms the validity of this approach and shows that solid state spectra can in part be interpreted with the help of the spectra of isolated molecules. Z molecules with N atoms in a primitive unit cell have $3NZ$ degrees of freedom. Each molecule has $3N - 6$ degrees of freedom, the activity of which depends on the symmetry of the molecule in the crystal, the site symmetry. In going from the gas phase (isolated molecule) to the solid state, different effects can be observed:

- static effects: frequency shift due to changes in the geometry (bond length or angle), appearance of forbidden bands, splitting of degenerate modes due to the disappearance of symmetry elements at the crystal site and finally appearance of new bands in the low frequency region, corresponding to the restoring forces in the solid phase acting on the rotational degrees of freedom. One molecule in the unit cell gives rise to $3N - 6$ internal modes, 3 rotational modes, called librations, and 3 translational modes with zero frequency,
- dynamic effects: these changes are caused by several entities in a unit cell leading to coupling of the corresponding molecular modes. Each internal mode gives rise to Z components appearing in the spectra as a splitting, referred to as correlation field or factor group splitting. Further in the low frequency region one expects $3Z$ librations, $3Z - 3$ translational, and 3 acoustic modes.

In short, a spectrum contains $Z(3N - 6)$ internal modes and $6Z - 3$ lattice modes, divided into $3Z$ librations and $3Z - 3$ translations. This model is useful for the qualitative study of a spectrum. However, classification according to internal-lattice and librational-translational modes is not always useful. If the molecules are flexible or contain heavy atoms or functions, then the lowest internal modes reach the low frequency region, where the lattice modes are expected. In this case, and particularly in the presence of strong intermolecular forces (hydrogen bonds), internal and external degrees of freedom belonging to the same symmetry species can couple, and the first approximation loses validity. Similarly, distinction between librational and translational lattice modes is only possible if the site symmetry group contains a center of symmetry which causes $g - u$ exclusion. In the absence of such a center, both types of motion can couple. In favorable cases, the extent of this coupling can be experimentally determined by isotopic substitution, in other cases by calculating the crystal dynamics. The spectroscopic activity, such as that of a free molecule, can be determined by symmetry considerations. In this case, if $k = 0$, the symmetry is that of the factor group which is isomorphic with the space group (see Secs. 2.6 and 2.7.5).

4.5.3 Single crystal spectroscopy

The techniques are basically similar to those discussed for liquid samples. In this context, we shall only discuss some points which are specific of the solid state. Since crystal spectra are more complicated than pure vibrational spectra of isolated molecules, we have to look for experimental possibilities of simplifying the assignment of the bands and their interpretation. The most obvious approach involves using single crystals, which makes it possible to divide the spectra into sets of bands with the same symmetry properties. Two quantities are important for studying the crystalline phase: refractive index and polarizability. Both can be represented by ellipsoids, the axes of which are parallel. These ellipsoids also have the symmetry properties of the crystal lattice. In a cubic crystal, all physical properties are isotropic, and the ellipsoid becomes a sphere. Space groups with at least one symmetry axis C_n of the order of three or higher ($n > 2$) correspond to so-called uniaxial crystals which belong to the trigonal, tetragonal, and

hexagonal systems. The ellipsoids show rotational symmetry around the C_n axis. All other space groups correspond to biaxial crystals, where the ellipsoids have three different axes. All three are fixed parallel to the crystal axes in the orthorhombic system; one out of the three axes is fixed parallel to the C_2 axis in the monoclinic space groups; all three ellipsoid axes are freely oriented relative to the crystal axes in the triclinic system. Thus, from the cubic to the orthorhombic system, the ellipsoid axes are or can be chosen parallel to the crystal axes. Birefringence is a consequence of the existence of two or three main refractive indices in a crystal, dividing the radiation into an ordinary and an extraordinary wave. In spectroscopic investigations it is desirable to avoid this effect. It can be circumvented by using linearly polarized light in which the plane of polarization coincides with the direction of one of the main axes of the ellipsoid of the refractive indices. It is therefore important to study the solid state using single crystals which are carefully cut and oriented.

4.5.3.1 Infrared spectra

Uniaxial crystals have two refractive indices. Two measurements with linearly polarized light on one slice containing the high symmetry axis provide all possible information. One measurement is obtained in which the direction of polarization is parallel to the main axis; the second one is taken after rotating the polarization or the sample by 90° .

To investigate biaxial crystals, two slices are necessary, each containing two of the ellipsoid axes. The presence of one common axis permits a correlation between both measurements. If the polarization of the bands in the reference system of the crystal ellipsoids and the position of the ellipsoids in the crystal are known, it is possible to determine the polarization of the crystal-fixed axes and to assign the bands to symmetry species on the basis of the character tables for the factor groups. In cases where the growth rate of the crystals is very anisotropic it is difficult to grow a crystal from which two slices can be obtained. In this case, it may be useful to investigate one slice and to compare the resulting spectra with powder spectra in order to obtain the remaining bands by evaluating the difference (see Sec. 2.7.6.4).

The arguments raised in the discussion of absorption spectra obviously also apply to reflection spectra, which are frequently obtained of samples with high absorption coefficients. A method of obtaining optical constants by using the Kramers-Kronig relation is discussed in Sec. 6.4.

4.5.3.2 Raman spectra

The polarizability α being a symmetric tensor, six components can be separated by using a suitable experimental set-up. By definition,

$$\begin{pmatrix} \mu_x \\ \mu_y \\ \mu_z \end{pmatrix} = \begin{pmatrix} \alpha_{xx} & \alpha_{xy} & \alpha_{xz} \\ \alpha_{yx} & \alpha_{yy} & \alpha_{yz} \\ \alpha_{zx} & \alpha_{zy} & \alpha_{zz} \end{pmatrix} \begin{pmatrix} E_x \\ E_y \\ E_z \end{pmatrix} \quad (4.5-7)$$

where μ is the dipole moment induced by the electric field E . In order to isolate one single component of the tensor, it is necessary to study one component of the induced dipole moment created by one single component of the electric field; for example, $\mu_y = \alpha_{yz}E_z$. In order to work without birefringence splitting, the incoming light must be linearly polarized parallel to the z axis of the index ellipsoid (which is also the z axis of the polarizability tensor). Only Raman light polarized parallel to the y axis is analyzed by the spectrometer. Such a measurement is performed on a single crystal, cut according to the optical axis or axes; from the cubic to the orthorhombic system, the relation between these axes and the crystal axes are evident. For the monoclinic and triclinic systems, coordinate transformation between both axis systems is necessary. The incoming laser light is linearly polarized and its electrical vector can be rotated by 90° with the help of a $\lambda/2$ plate. The Raman light is analyzed by a polarization film which can be turned by 90° . After leaving this film, the light passes through a $\lambda/4$ plate or a scrambler, which transforms linearly polarized light into circularly polarized light in order to compensate for the polarization behavior of the spectrometer itself. Such experiments are often presented in terms of the so-called Porto symbolism $a(bc)d$ (Damen et al., 1966), in which

a is the direction of the incoming radiation,

b stands for the orientation of the polarization vector of incoming laser light,

c is the orientation of the analyzed direction of the Raman signal, and

d represents the direction of observation.

As a consequence, an experiment $a(bc)d$ will show the component α_{bc} of the polarizability tensor. In a final step, knowing the spectrum, the symmetry species are assigned in a straightforward manner using the tables of the factor group. In the example discussed above, obtaining the yz component requires an experimental $u(yz)v$ or $u(zy)v$ set-up. The six solutions $x(yz)$, $x(zy)z$, $y(yz)z$, $y(zy)x$, $z(yz)x$, and $z(zy)y$ are possible with a 90° geometry. With a 90° geometry, one experimental set-up leads to four different spectra (two orientations of polarization of the incoming light, multiplied by the two possible orientations of the analyzer), which can be shown to give access to the three off-diagonal terms and one diagonal term of the polarizability tensor.

4.5.4 An investigated example: calcium carbonate

We shall study two forms of calcium carbonate CaCO_3 : calcite and aragonite. Thus, it is possible to see the behavior of identical chemical entities in different crystalline environments. Both crystals are of an ionic nature and contain CO_3^{2-} groups as covalent entities with their own internal modes.

4.5.4.1 Calcite

The space group is $R\bar{3}c$ (D_{3d}^6) with two CaCO_3 entities in the unit cell. The Ca^{2+} ions are located at Wyckoff sites (a) (Hahn, 1987) with symmetry 32, the carbon atoms are found at (b) sites (symmetry $\bar{3}$), and the oxygen atoms are at (c) sites. The structure

consists of ...Ca²⁺...CO₃²⁻...Ca²⁺... chains along the C₃ axis. The interesting feature is the conservation in the solid state of the C₃ and the three binary axes of the isolated CO₃²⁻ group. The four atoms give rise to 6 internal modes, which can be classified as 1A₁ + 1A₂ + 2E. The A₁ mode is the in-phase stretching of all C=O bonds. The A₂ mode is the out-of-plane angle deformation. The vibrations of the E species are degenerate; one is the C=O stretching mode, the other is planar deformation. In the solid state, the two carbonate ions couple and produce two modes: an in-phase and an out-of-phase mode, according to the following scheme:

$$A_1 \rightarrow A_{1g} + A_{1u}$$

$$A_2 \rightarrow A_{2g} + A_{2u}$$

$$E \rightarrow E_g + E_u$$

Due to the mutual exclusion rule, g modes (except A_{2g}) are Raman active, while u modes (except A_{1u}) are infrared active. We thus expect the internal modes to give rise to three bands in the Raman spectrum and to three bands in the infrared. In order to determine the lattice modes, we have to consider the carbonate anions with 6 degrees of freedom each and two calcium cations with three degrees of freedom. One obtains $2 \times 6 + 2 \times 3 - 3 = 15$ lattice vibrations and 3 acoustic modes. These can be classified as 2A_{2g} + 1A_{1u} + 2A_{2u} + 2E_g + 3E_u, and one can expect 2 Raman (E_g) and 5 IR (A_{2u} and E_u) bands. Table 4.5-1 shows that all are observed. The influence of dynamic coupling on the internal modes (frequency difference between corresponding g and u modes) in the unit cell is on the order of some cm⁻¹ and therefore very small.

4.5.4.2 Aragonite

CaCO₃ as aragonite crystallizes in the space group Pnma (D_{2h}^{16}). The carbonate anions lose their C₃ axes, and the structure consists of columns of carbonate ions arranged parallel to lines of calcium cations. The site symmetry of the anions is σ, the carbon and one oxygen atom lying in this plane. The orthorhombic unit cell contains four CaCO₃ units. Due to the disappearance of the C₃ axes, no degeneracy exists and the E modes of the isolated carbonate ions split into two components. As a consequence of the unit cell coupling, each of these components can give rise to four bands, i.e., two g type and two u type bands. The internal modes are classified as

$$4A_g + 2B_{1g} + 4B_{2g} + 2B_{3g} + 2A_u + 4B_{1u} + 2B_{2u} + 4B_{3u},$$

and their activity is governed by the factor group 2/m 2/m 2/m (D_{2h}). Table 4.5-1 shows the observed spectra. The ν₄ band around 700 cm⁻¹ demonstrates that 6 out of the 8 components are observed in the 20 cm⁻¹ range, showing the power of this single crystal technique. In the lattice mode region, four CaCO₃ units are expected to give rise to $6 \times 4 + 3 \times 4 - 3 = 33$ vibrations, which in Raman spectroscopy are classified as

Table 4.5-1 Observed spectra of calcite and aragonite (Bhagavantam, 1939; Hellwege, 1970; Frech, 1980)

CALCITE				ARAGONITE			
Raman	Infrared			Raman	Infrared		
	Transv.	Longit.			Transv.	Longit.	
ν_3	1434 E_g			1574 1462	B_{1g} A_g		
		1407	1549 E_u			1466 1443	1588 B_{1u} 1561 B_{2u}
ν_1	1086 A_{1g}	inact.	A_{1u}	1085	A_g	1085 1083	1085 B_{1u} 1083 B_{3u} Internal modes
ν_2	inact. A_{2g}	872	890 A_{2u}	907 853	B_{2g} A_g	853	877 B_{3u}
ν_4	712 E_g	712	715 E_u	721 717 705 701	B_{1g} B_{2g} A_g B_{3g}	713 699	716 B_{1u} 701 B_{2u}
		303 297	387 A_{2u} 381 E_u				
	284 E_g			284	A_g	294 B_{1u}	
				272	B_{3g}	274 B_{2u}	
		223	239 E_u	248	B_{2g}	274 B_{3u}	
				214	A_g		Lattice modes
				206	B_{2g}	200 B_{1u}	
				193	A_g	200 B_{2u}	
				190	B_{3g}	200 B_{3u}	
				180	B_{2g}		
				(177)	B_{3g}		
	156 E_g			161	A_g		
				152	B_{1g}		
				142	A_g		
		92	136 A_{2u}	123	B_{3g}	118 B_{3u}	
		102	123 E_u	112	B_{1g}	114 B_{1u}	
						100 B_{2u}	

$5A_g + 5B_{2g} + 4B_{1g} + 4B_{3g}$ and in infrared as $4B_{1u} + 3B_{2u} + 4B_{3u}$. Table 4.5-1 shows that a large number of these lattice modes are observed. In this context we cannot discuss the intensities in detail, but it might be interesting to mention that some unusual patterns have remained unexplained for a long time. Ismail et al. were able to show that minor displacements within the unit cell would transform the symmetry of the structure

from *Pnma* to *P3m1* (D_{3d}^3), with only two CaCO_3 units in the cell (Ismail, 1982). The consequence would be that nearly all bands which are forbidden in this structure appear in the spectra as low-intensity bands. This, in fact, resembles the extinction rules in radiocrystallography.

Table 4.5-1 finally provides some information concerning the *LO-TO* behavior of the bands. It ranges from as little as several cm^{-1} in the case of nearly non-polar modes such as ν_4 to about 150 cm^{-1} in the case of the highly polar ν_1 mode in both crystalline phases.

4.5.5 Applications

Since a spectrum is determined by the structure of the sample, which in turn is a consequence of the forces (and particularly the intermolecular forces in the solid state), this technique is able to provide two-fold information. An introduction to the application of the discussed methods towards the investigation of intermolecular forces is provided in Sec. 5.2, including a short review of the quality which can be obtained. Another obvious application is the identification of samples. Table 4.5-1 demonstrates clearly that, if the formula is known, the spectra provide an indication of the phase of a sample. By using micro-techniques it is possible to identify samples or parts of samples in fields ranging as widely as geology, medicine (kidney stones), pharmacy, electronics, painting (mineral pigments), and materials research.

Another field of application is the investigation of phase transitions. One makes use of the fact that structural modification changes the spectra, which can be interpreted either in terms of a new structure or a change of some of its patterns, or as an aid to understand the microscopic mechanism of the transition. The described method is suited to examining transitions involving conformational change, because usually only a few bands show a change of frequency and/or intensity in going from one conformation to the other. By concentrating on these few bands it is possible to monitor the transition. This technique can be very important for pharmaceutical products, whose conformation may change after pressure treatment and which may thus arrive at a medically less active modification.

Order-disorder phase transitions have also been studied extensively, and in this case spectroscopy complements crystallographic methods. The internal modes, which depend essentially on the intramolecular forces, represent the local symmetry; the lattice modes, which ‘feel’ long-range effects (up to 100 \AA in the case of electrostatic forces), show the influence of the overall symmetry. As an example, squaric acid undergoes a phase transition at 100°C , corresponding to the disorder of the protons in the potential double well of a hydrogen bond. The structure changes from monoclinic to tetragonal. The internal modes show that the molecule retains its symmetry during phase transition. During these vibrations ($\tilde{\nu} > 300 \text{ cm}^{-1}$), the protons remain long enough in each potential well to vibrate. The lattice modes, on the contrary, show the expected selection rules for protons disordered and delocalized in the center of the hydrogen bonds (Bougeard, 1978).

The typical and much discussed effect of phase transitions is a so-called soft mode. A soft mode is a vibration, the frequency of which nears zero as the physical parameter (mostly the temperature but sometimes also the pressure or the external electric field) approaches its critical point. One of the first soft modes was observed by Raman et al. in the $\alpha \rightarrow \beta$ quartz transition (Raman and Nedungadi, 1940). The theory of these modes was proposed by Cochran (Cochran, 1960, 1961). It turns out that the soft mode is simply the vibration that, due to its form, allows the transformation from one phase to the other. At the transition point, the restoring forces disappear and the frequency approaches zero. Extensive reviews of the application of spectroscopy in connection with the investigation of phase transitions have been provided by Rao and Iqbal (Rao and Rao, 1978; Iqbal, 1986).

4.6 Liquid crystals: orientational order and optical anisotropy*

4.6.1 Introduction to liquid crystals

Long-range order of the molecular orientation is the basis of liquid crystalline behaviour and the accompanying extraordinary optical phenomena of these phases; the complete or partial absence of positional order grants fluidity and, thus, experimental flexibility. Compared to a perfect crystal, such a liquid crystal is just partially ordered as also are e.g. stretched polymeric (e.g. Michl and Thulstrup, 1986), rheologic and tribologic samples (Biresaw, 1990) when the molecules are aligned by an outer mechanical strain. An alternative denomination is 'mesophase' stressing the occurrence of such states intermediate to well known phases, namely above the temperature range of the crystalline solid but below the one of the isotropic liquid.

The acquisition of orientational order before abandoning the positional disorder during a transition out of isotropy reveals processes and mechanisms which otherwise are obscured. With decreasing temperature, the three-dimensional crystal lattice is often approached through several liquid crystalline phases such as *smectic* ones, with increasingly higher positional order. Changing ambient pressure can result in further order principles so that over all a variety of states exists. Interestingly enough, an external electric or magnetic field does not so much influence the individual behaviour of the molecules but their collective properties: A comparably small force can give rise to a macroscopic reorientation of the sample. This in turn changes the optical appearance and thus, opens the way to outstanding technical applications such as displays, modulators, shutters, optical data storages, and 'smart' devices (e.g. Schadt, 1993a and 1993b; Johnson et al., 1993). Presently interest focusses on ferroelectric and nonlinear optical properties

* Section 4.6 is contributed by E.-H. Korte, Berlin

(Janossy, 1991; Kremer, 1992; Zentel et al., 1992; Eich, 1993). Since the liquid crystalline order is sensitive to temperature changes, this is used to visualize temperature differences of a substrate (e.g. Grabmaier, 1975). For special display effects but even more in science, liquid crystals are employed as anisotropic solvents for aligning solute or probe molecules. Just to mention one applicational field different from optics, liquid crystals are used as high-performance stationary phases in both, gas and liquid chromatography (Pesek and Williamsen, 1992).

Virtually everything what was known about liquid crystals and their applications in engineering and science at that time was summarized by Kelker and Hatz (1980) with comprehensive bibliography. Since then, the development of liquid crystalline polymers widened considerably the scope of applications (Ciferri, 1991; Collyer, 1992; Plate, 1993; especially for investigations by IR spectroscopy see Volchek and Purkina, 1992). Numerous meetings are devoted to advances in understanding and applying the liquid crystalline state, their proceedings indicate present tendencies (Palfy-Muhoray and Soileau, 1992; Chiellini and Veracini, 1993; Finkelman et al., 1993).

Very generally, the physical and chemical properties of almost all molecular species are anisotropic, including the shape how soever defined. Because of averaging, this does not become obvious either when the individual molecules rotate through wide angles within the sampling time of the experiment or when an ensemble of differently oriented molecules contributes to the measured signal. However, if the molecules within a sample are aligned, the macroscopic properties of the sample are anisotropic as well. Studies of these anisotropic quantities show the molecular structure in more detail, however, for revealing them usually somewhat more elaborate experiments are required. For instance, the spectroscopist has to deal with optical anisotropy, i.e., must work with polarized radiation and account for linear birefringence as well as linear dichroism (e.g. Szivessy, 1928), Sec. 3.2.1.2C. It must be kept in mind, that with the changes of type and degree of order usually also the density and furthermore the underlying optical properties change. The often neglected linear birefringence might turn out to be both, sensitive to the variations and relevant for the observations. At least for experiments under oblique incidence (with respect to the optical axis of the sample), the reliable interpretation of results demands for careful consideration of anisotropy.

In each of the states whether the material is crystalline, somehow partially ordered, or isotropic, an individual molecule experiences a different vicinity. Therefore, interactions and next-neighbour effects such as hydrogen bondings will vary upon changing from one state to the adjacent one with the consequence, that bands in the vibrational spectra might be shifted, change their intensities and widths to such an extend that even bands may disappear or new ones appear. In this way the reorganization processes related to phase transitions can be monitored. Basically most of these changes are observable with conventional spectra, i.e. those taken without polarizer. The knowledge on the influence of intermolecular interactions on vibrational spectra as available in the literature can be applied here in order to interprete the spectral changes in terms of changes in the structure of the mesophase, the mutual orientations of the molecules, or their distances and conformational changes. Such studies were reviewed by Bulkin (1976 and 1981) and are included in the book by Kirov and Simova (1984). Improved time resolution has facilitated the access to reorientation kinetics and dynamics of monomeric (e.g. Gregoriou

et al., 1991; Fontana, 1992; Urano and Hamaguchi, 1992; Nakano et al., 1993; Palmer, 1993) as well as polymeric liquid crystals (e.g. Braeuchler et al., 1991; Wiesner et al., 1991 and 1992).

The adequate sensor for the orientational order on a molecular scale is a dipole transition moment and thus, polarized absorption spectroscopy is usually first choice for observing and investigating order related phenomena. Among the different spectral ranges the infrared one grants particularly detailed information. In this context Raman spectroscopy appears to be less straightforward, however, it provides us with knowledge which is not attainable from measurements based on one absorption process (e.g. Pershan, 1979; Kirov and Simova, 1984). In this contribution some basic relations between the orientational order of liquid crystals and features in their infrared spectra will be outlined. Leaving positional order out of consideration we confine ourselves to nematic and cholesteric liquid crystals and furthermore, basically rigid monomers with thermotropic behaviour are assumed.

4.6.2 Degree of order and optical anisotropy of nematics

Nematic liquid crystals are the type of mesophase the structure of which differs least from the one of an isotropic liquid: The only but essential difference is that on the average all the molecules are ordered parallel with one of their axes. This is schematically shown in Fig. 4.6-1 where the bars represent rod-like, i.e., cylindrically symmetric molecules. Such molecules rotate freely around their preferred axis which for energetical reasons will be the 'long' one. However, it might differ from the precise geometrically longest diameter of the molecule (Kuball et al., 1987). The vector pointing into common direction is called *director*, it coincides with the optical axis of the uniaxial structure. A bulk nematic sample appears opaque and turbid due to macroscopically non-uniform orientation. In a thin layer the macroscopic alignment can be stabilized by the influence of the walls, e.g. the cell windows. By different pre-treatments of the surfaces (e.g. Schadt, 1993a), the nematogenic molecules can be caused either to align parallel (*planar* or *homogeneous* sample structure) or perpendicular to the wall (*homeotropic*).

Fig. 4.6-1 conveys an impression on the alignment of the molecules which by no means is realistic. The apparent parallel alignment of the long axes results from averaging over orientational fluctuations for each individual molecule which are due to thermal excitation along with the repellent force by the surrounding phase. The probability of a molecule to adopt a certain orientation is given by the distribution function which

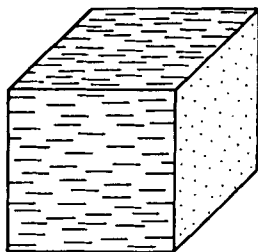


Figure 4.6-1 The nematic molecular arrangement.

advantageously is expanded on the basis of Legendre polynomials P_i (de Gennes, 1974; Luckhurst, 1993). Due to the symmetry of the phase uneven terms vanish, and the first essential contribution comes from the second-order term P_2 . It is based on the projection of the preferred molecular axis on the director and consequently related to the momentary angle ϑ formed by these two directions. Averaging over all the molecules of the sample yields a specification of the degree of order in terms of the Maier-Saupe *order parameter* S

$$S \equiv \left(1 - \frac{3}{2} \langle \sin^2 \vartheta \rangle \right) = \bar{P}_2(\cos \vartheta) \quad (4.6-1)$$

where the angular brackets and the upper bar, respectively, indicate averaging. This quantity is defined to adopt values between unity characterizing perfect alignment and zero indicating random orientation (Maier and Saupe, 1958, 1959 and 1960). Typical values of S for nematic liquid crystals are in the range from 0.3 to 0.8.

It should be noted that the distribution over a sphere, i.e. in space rather than over a plane, has to be considered. Referring to a globe, the angle ϑ states just the latitude, the length of the related parallel and thus the relevant weight within the distribution increases with $\sin \vartheta$. Consequently equal probability of all possible orientations leads to $\langle \sin^2 \vartheta \rangle = 2/3$ so that the order parameter S vanish for an isotropic sample. Larger values of $\langle \sin^2 \vartheta \rangle$ would lead to a negative value of the order parameter S , however, this indicates primarily an inappropriate assignment of the molecular axes or the director.

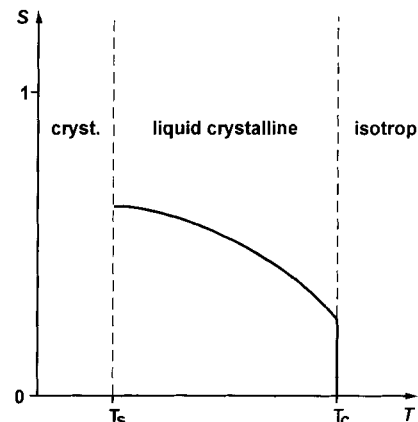


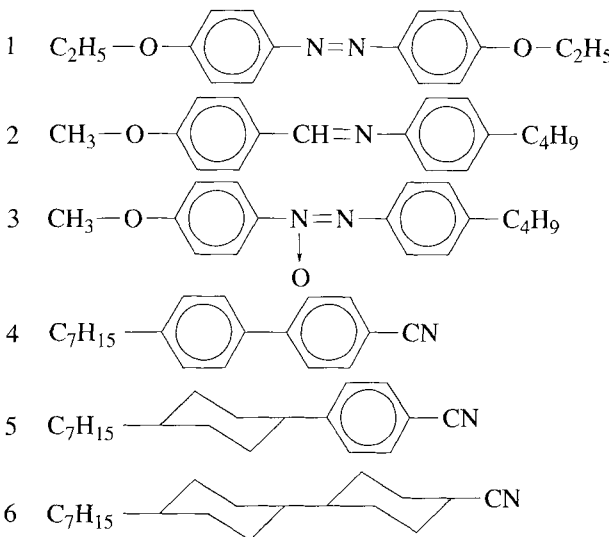
Figure 4.6-2 Schematic plot of the temperature dependence of the order parameter S of a rod-like molecule in a nematic phase; T_s indicates the solid-nematic transition temperature, T_c the nematic-isotropic one (clearing point).

From what was said before it should be clear that the degree of order and thus, the value of the order parameter depend on temperature. It is theoretically explained and experimentally verified that after the transition from the crystalline state into the nematic one, with increasing temperature S decreases first slowly then with increasing gradient; this is sketched in Fig. 4.6-2. However it does not vanish by approaching zero but collapses when a certain value is reached. The related temperature of the order-disorder transition is called *clearing point* T_c giving credit to the sudden change from opacity of a bulk sample to the full transparency it exhibits in the isotropic state. This behaviour

is explained by the *mean-field approach* (Luckhurst et al., 1975): According to this model, a given molecule does not experience the presence of all the other molecules but by a force field acting like a cylindrically symmetric cage. Assuming realistic thermodynamical conditions the orientational order of a probe molecule is calculated and the order parameters are attributed to all the other molecules, thus characterizing the bulk mesophase itself. The theory explains that self-consistency in the sense that the molecules mutually stabilize their orientation, is possible only above a certain degree of order.

It must be kept in mind, that S represents just a first-order approximation of the distribution function, and this under the additional premise of complete cylindrical symmetry only. It might be an acceptable measure when comparing cases for which a mean-field model applies. However, comparing the order parameters of liquid crystals with those of other partially ordered phases, such as stretched polymers or tribological samples can be misleading due to possibly different types of distribution functions.

Table 4.6-1 Structures of nematogenic molecules



The next refinement of the model takes into account that the shape of most molecular species differs from being rod-like; typical nematogenic molecules are given in Table 4.6-1. The resulting behaviour of such a bi-axial molecule is often associated with hindered rotation, however it can also be understood from a rigid-body model where different moments of inertia lead to oscillations of different angular amplitudes in spite of identical (thermal) excitation and identical repulsive forces (Korte, 1983). This can be summarized by order parameters defined as above but referring to one of the two shorter,

transverse axes each. Actually their difference can be expressed as an order parameter (Alben et al., 1972)

$$D = \frac{3}{2} < \sin^2 \vartheta \cos 2\varphi > \quad (4.6-2)$$

where φ denotes the Eulerian angle of pure rotation while the Eulerian angle of nutation comes into play only for biaxial phases (compare Fig. 4.6-3).

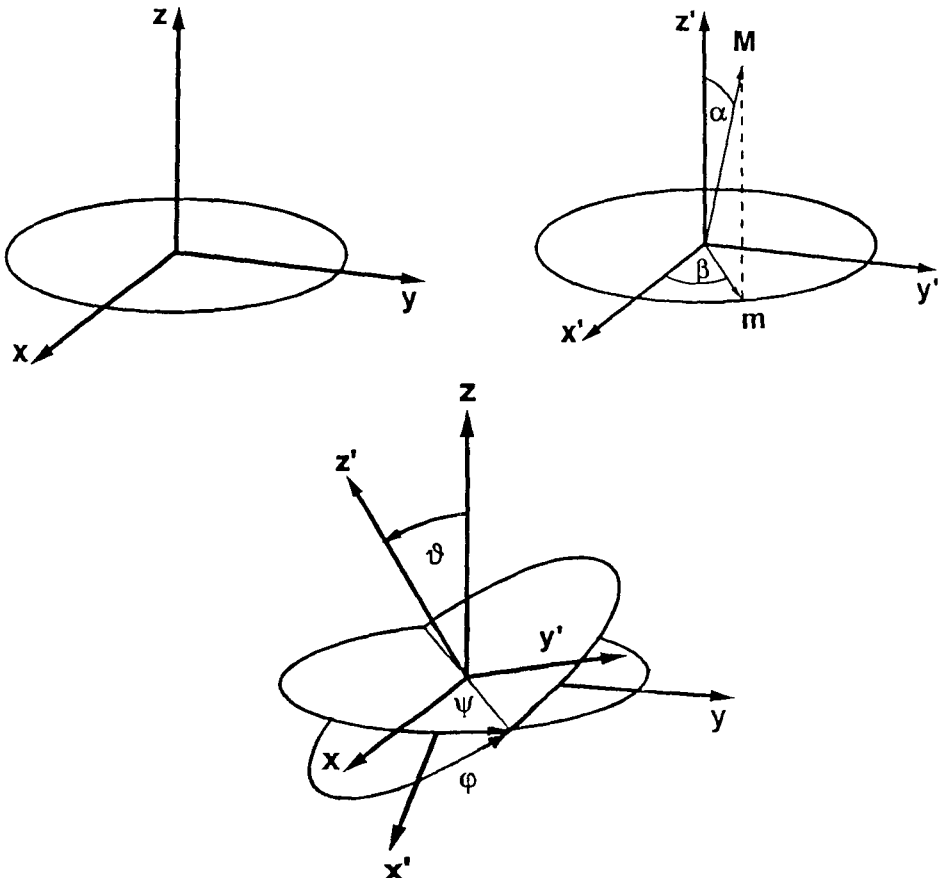


Figure 4.6-3 Eulerian angles ϑ , φ , and ψ the molecular frame z' (long axis), y' , and x' (short axis) forms with the laboratory frame z , y , x of which z agrees with the director and the optical axis of the macroscopic sample; also given are the angles α and β specifying within the molecular frame the orientation of a transition moment M and its projection m onto the x' , y' -plane.

As shown in Fig. 4.6-4, D is related to S by a unique function for any given value of a parameter

$$\lambda = \left(\frac{3}{2}\right)^{\frac{1}{2}} \frac{\sigma_{y'} - \sigma_{x'}}{2\sigma_z - \sigma_{y'} - \sigma_{x'}} \quad (4.6-3)$$

where σ_i denotes the relevant dimension of the molecule along its axis i (van der Meer and Vertogen, 1976); $i = x'$ refers to the short axis, y' to the intermediate and z' to the long one. This parameter λ quantifies how much the molecular shape deviates from cylindrical symmetry; for nematicogenic molecules it is often smaller than 0.2 and therefore, the order parameter D is in the order of 0.1.

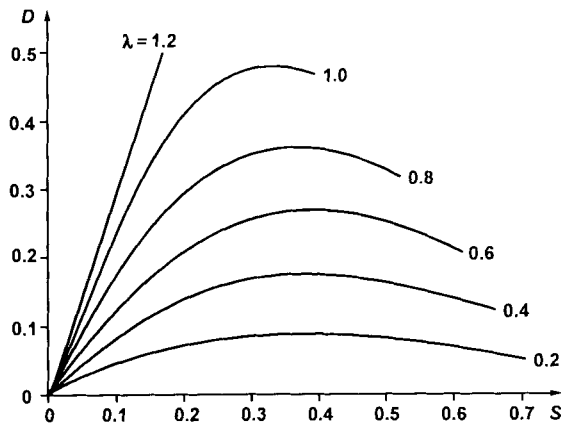


Figure 4.6-4 Dependence of the transverse-axes order parameter D on the long-axis order parameter S , parameter is λ (see text).

The order parameters S for all three molecular axes or alternatively, the combination S plus D describe on the level of the first relevant polynomial term the orientational distribution of a rigid, non-cylindrical molecule in the uniaxial nematic phase. Additional order parameters come into play for biaxial phases (Straley, 1974). A concise overview on the concepts from statistical mechanics relevant to order parameters was given by Zannoni (1979).

Most experiments do not depend on order parameters of higher rank, e.g. the influence of orientational order on an absorption band is completely described in terms of S and D (Luckhurst, 1993). On the other hand, Raman-spectra being based on a two-photon effect are influenced additionally by the order parameters of the next level, such as the Legendre polynomial \bar{P}_4 (Pershan, 1979). This is of considerable theoretical interest, however, up to now of less importance for practical applications. There are some further experimental techniques for gathering information on the orientational order, among these are fluorescence, neutron and electron scattering. Probably the most reliable method is NMR (Emsley, 1985), however this usually means deuteration of all hydrogen atoms but one.

As to infrared spectroscopy – and the same holds good for other spectral ranges – the orientational order is readily observable in form of dichroism: Being related to the molecular shape, the molecular polarizability is anisotropic as well. By the alignment of the molecules this anisotropy is transferred to the sample, however damped due to the imperfect order as described by the order parameters. As a consequence, the dielectric function and furthermore the (complex) refractive index are anisotropic, so that eventually (linear) dichroism and birefringence occur.

Considering in this frame a certain transition moment parallel to the preferred molecular axis, it is evident that radiation with the electric vector oscillating parallel to the optical axis experiences stronger absorbance (A_{\parallel}) than perpendicularly polarized radiation (absorbance A_{\perp}). Closer inspection shows (Maier and Saupe, 1959) that A_{\parallel} increases with increasing degree of order and thus, increasing order parameter S , while A_{\perp} decreases:

$$\begin{aligned} A_{\parallel} &= \frac{A_0}{3}(1 + 2S) \\ A_{\perp} &= \frac{A_0}{3}(1 - S) \end{aligned} \quad (4.6-4)$$

where A_0 denotes the total absorbance. Provided the transition moment forms an angle α with the preferred molecular axis the equations must be completed with respect to the order parameter D (Korte, 1983)

$$\begin{aligned} A_{\parallel} &= \frac{A_0}{3}[1 + 2S(1 - \frac{3}{2}\sin^2\alpha) + D\sin^2\alpha\cos 2\beta] \\ A_{\perp} &= \frac{A_0}{3}[1 - S(1 - \frac{3}{2}\sin^2\alpha) - \frac{1}{2}D\sin^2\alpha\cos 2\beta] \end{aligned} \quad (4.6-5)$$

where β refers to the angle between the projection of the transition moment on the transverse plane and the shortest axis of the molecule (see Fig. 4.6-3).

If the mesophase consists of cylindrically symmetric molecules, D vanishes because of the equivalence of the two transverse axes and so do the last terms in both expressions of Eqs. 4.6-5. However even then, the dichroism of a given absorption band depends on the orientation of the related transition moment within the molecular frame. Taking the dichroism to be defined as $(A_{\parallel} - A_{\perp})$, it is always negative for a 'perpendicular band' for which $\alpha = 90^\circ$, as opposed to a 'parallel band' discussed before with Eqs. 4.6-4. When the condition $\sin^2\alpha = 2/3$ is fulfilled, i.e. $\alpha \approx 54.7^\circ$ what is sometimes called the *magic angle*, all the influence of the order parameter S on the absorbance vanishes. As a consequence of the different orientations of the various transition moments within the molecular skeleton, an infrared spectrum usually comprises both, positive as well as negative dichroism bands. An example is shown in Fig. 4.6-5 with a compound containing para-substituted phenyl rings (see caption): the pronounced dichroic bands above 1000 cm^{-1} are mostly due to $\nu(\text{ring})$, i.e.

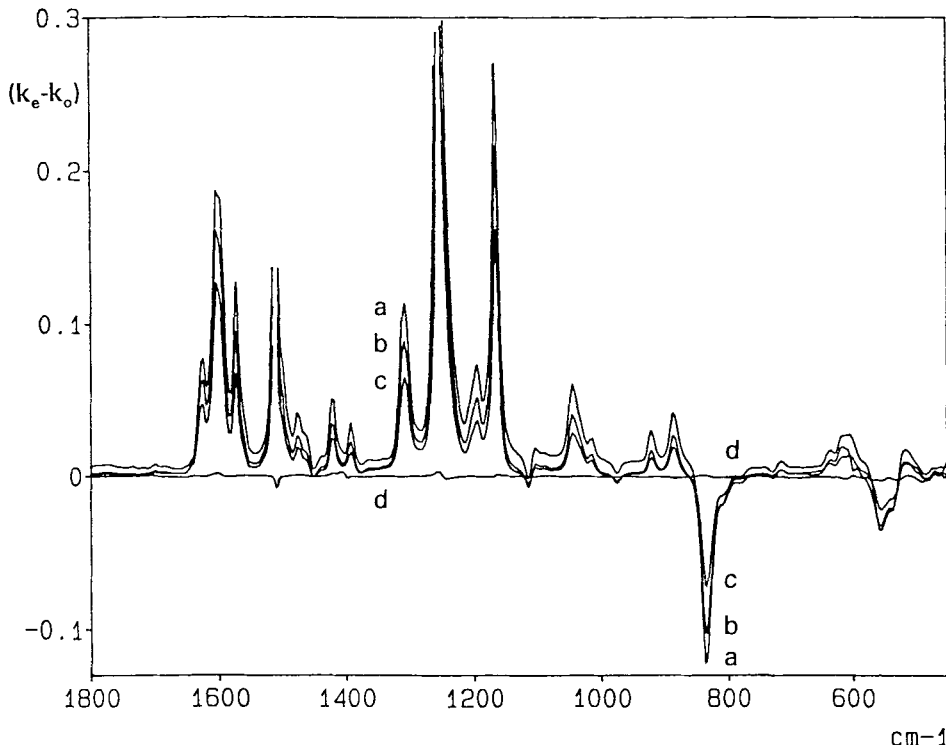


Figure 4.6-5 Infrared linear dichroism of a nematic sample (EBBA/MBBA: equimolar mixture of N-(*p*-ethoxybenzylidene)-*p'*-*n*-butylaniline and its methoxy analogue **2** of Table 4.6-1; Riedel-de Haën) expressed as the difference of the absorption indices k_o and k_e (imaginary part of the complex refractive index) for the ordinary and the extraordinary beam, resp.; the temperature increases and thus, the degree of order decreases from spectrum a to spectrum d, the latter was taken close to the clearing point T_c where the order and consequently the anisotropy vanishes (Reins et al., 1993).

in-plane vibrations parallel to the para axis while the pronounced negative band is caused by a $\gamma(\text{C}-\text{H})$ vibration of the ring perpendicular to its plane.

For oblate molecules the dichroism is further influenced by the transverse-axis order parameter D . Its influence is the larger the more the orientation of the transition moment differs from the preferred molecular axis. Largest contributions should be found for perpendicular bands ($\alpha = 90^\circ$), in any case the sign of the contribution depends on whether the transition moment projects primarily on the shortest or the intermediate molecular axis. For a transition moment under the magic angle the dichroism is governed by D alone due to the vanishing contribution from S .

Absorption is one consequence of a (vibrational) transition, the spectral behaviour of the refractive index reflects the same phenomenon. Within the spectral interval of an absorption band the refractive index follows a dispersion curve. Kramers-Kronig integral equations (for applications in optics see Caldwell and Eyring, 1971; Hopfe et al., 1981;

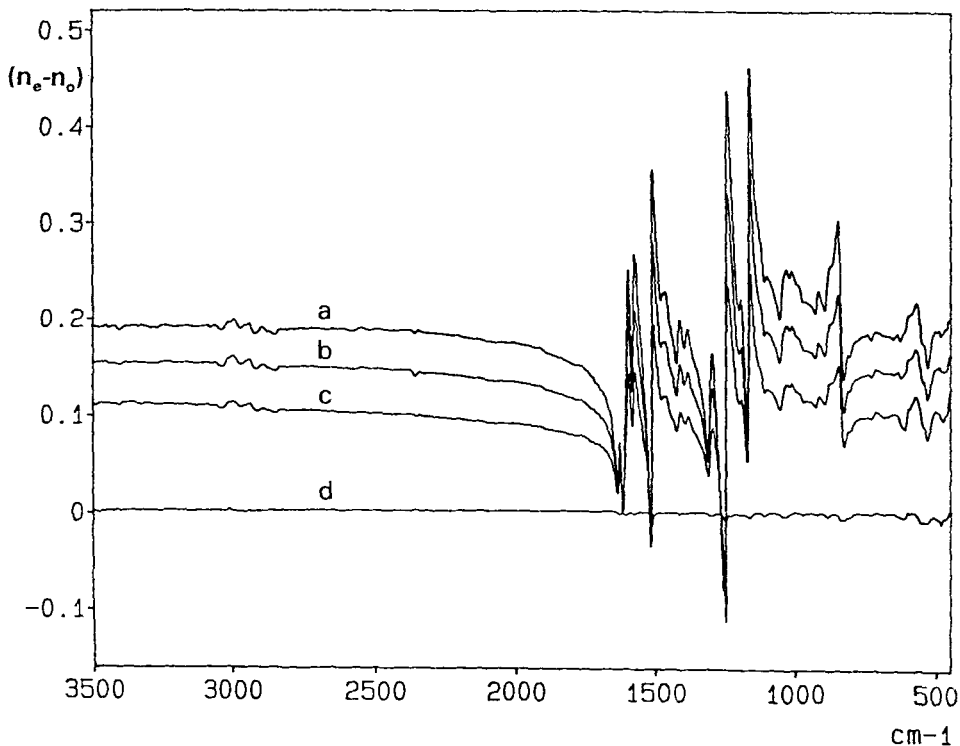


Figure 4.6-6 Infrared linear birefringence $n_e - n_o$; same sample and same parameters as for Fig. 4.6-5 (Reins et al., 1993).

for more general information see Bode, 1950) correlate absorption index and refractive index. In a similar way dichroism and birefringence depend on each other, so that from the entire spectrum of the one quantity the value of the other at each spectral point can be calculated. The individual values of the refractive indices for the ordinary (n_o) and the extraordinary (n_e) beams as well as the birefringence ($n_e - n_o$), depend on the degree of order in a correspondent way as the absorbances and the dichroism do (Maier and Saupe, 1958, 1959, and 1960; Saupe and Maier, 1961).

Little is known about infrared refractive indices of organic compounds, and only very few such studies related to liquid crystals are reported. To some extend this is due to the fact that special techniques and even dedicated equipment are required. On the other hand birefringence can be derived from the polarization pattern produced by the phase difference between the ordinary and the extraordinary beam. This experiment had been outlined by Born and Wolf (1980) and was applied to liquid crystals by Wu et al. (1984). The procedure is primarily suitable in transparent regions, for a more comprehensive optical characterization it should be extended to complete ellipsometry (Reins et al., 1993). Results obtained by infrared-spectroscopic ellipsometry are shown in Figs. 4.6-5 and 4.6-6.

4.6.3 Evaluation of order and orientation

In order to evaluate order parameters from absorption measurements, it is advantageous to employ the dichroic ratio $R \equiv A_{\parallel}/A_{\perp}$ so that the total absorption A_0 and experimental factors such as the thickness are cancelled out. With this quantity, Eq. 4.6-2 can be rewritten as (Clark and Saunders, 1982; Korte, 1983)

$$(R - 1)/(R + 2) = S (1 - \frac{3}{2} \sin^2 \alpha) - \frac{1}{2} D \sin^2 \alpha \cos 2\beta \quad (4.6-6)$$

On the left side of the equation experimental results are reduced to one number which by the expression on the right side is interpreted in terms of the order parameters and the orientation of the related transition moment. On first glance it seems that S and D can be evaluated from the bands due to any two transitions of different, but well known orientations within a rigid molecule. However, this is possible only with quite limited accuracy due to the anisotropy of the internal field. This field originates from the dipole moments being induced in the individual molecules by the external radiation field. Its anisotropy is a consequence of the molecular alignment and impedes the comparison of different bands. Several approaches how to evaluate and to eliminate the influence were proposed (Neugebauer, 1954; Vuks, 1966; Haller et al., 1973; de Jeu and Bordewijk, 1978), however at least for the infrared range convincing results for practical applications have not been reported yet.

The influence could be minimized by evaluating the dichroic ratios related to two spectrally neighboured bands the transition moments of which are parallel to one of the molecular transverse axes each: Due to the uniaxiality of the phase these bands should be similarly influenced, so that reliable information on D results (Korte, 1983; Lampen, 1991). To be sure about the transition moments being strictly parallel to one of the three molecular axes, the symmetry of the molecules should be C_{2v} or D_{2h} (Michl and Thulstrup, 1986), what in strict sense is hardly found with mesogenic molecules.

On the other hand, just the fact that a dichroism band is negative - leading to $R < 1$ and a negative value on the left side of Eq. 4.6-3 - indicates that the transition moment forms a large angle with the molecular long axis. A positive dichroism band is related with a transition moment which primarily projects on the long axis. Already such qualitative hints can be helpful when molecular vibrations are to be assigned.

More often than for mesogenic molecules, such assignments are useful with respect to the great number of molecules which do not form a liquid crystalline phase on their own. Such assignments can be obtained equivalently when the molecules are dissolved in a nematic liquid crystal (Belkhakem and Jordanov, 1990, 1991a, 1991b, 1992; with respect to chiral molecules see Kuball et al., 1979). The attainable concentration is limited, since the non-mesogenic molecules disturb the mesomorphic order and reduce the temperature range of its existence primarily by lowering the clearing temperature. The solute molecules experience an equivalent cage as the mesogenic molecules do and are aligned therein according to their anisotropy. As for all studies of diluted solutions, the bands of the solvent might obscure the relevant bands of the solute. Fortunately enough the choice of nematics is nowadays quite wide and some types such as bi-cyclohexyl

derivatives lack in strong absorption bands. The dichroic ratios observed for the solute bands are then interpreted in the same way as for neat liquid crystals. However it should be kept in mind that the order parameters of solvent and solute do not agree in general (Altschuh et al., 1984). On the other hand the degree of order of the solute molecules will reflect changes of the one of the solvent and thus, solute molecules can serve as probe.

A favourably competing, in principle very closely related technique is the orientation of guest molecules in stretched polymer foils; inherent advantages are the apparently negligible internal field, and the poor spectrum of the matrix (Michl and Thulstrup, 1986). The three orientation coefficients evaluated from such measurements are graphically represented by one position in an orientation triangle. This is being used for nematic liquid crystals also (Schönhofer et al., 1990) and the coefficients are easily transformed into the order parameters S and D along with the parameter λ as defined by Eq. 4.6-3.

Details of the reliable determination of the dichroic ratio - by referring to maximum or integral values, separation of overlapping bands - have been discussed by Maier and Saupe (1958, 1959, 1960) as well as Thulstrup and Michl (1982). An experimental alternative for determining the dichroic ratio has been proposed by Kelker, Hatz and Wirzing (1973): The sample is prepared once in homogeneous alignment and a second time in homeotropic alignment. Therefore in the first case the average of A_{\parallel} and A_{\perp} is measured, while in the second just A_{\perp} is determined. This alternative offers the advantage that no polarizer is necessary at all, however on the expenses of accuracy since two samples have to be prepared whose macroscopic alignment might differ.

4.6.4 The cholesteric helical structure: analysis and application

Twisting a nematic structure around an axis perpendicular to the average orientation of the preferred molecular axes, one arrives at the molecular arrangement commonly called *cholesteric* (Kelker and Hatz, 1980). The *twisted nematic* phase is optically uniaxial, however with the axis perpendicular to the (rotating) director. Such a mesophase combines the basic properties of nematics with the implications of chirality: The structure itself is chiral and as a consequence, a non-identical mirror image exists as it is shown schematically in Fig. 4.6-7. Besides the order parameters mentioned before, the essential characteristics of a cholesteric mesophase are the *pitch*, i.e., the period of the helical structure as measured along the twist axis, and its *handedness*, i.e., whether the phase is twisted clockwise or anticlockwise.

Cholestogenic compounds (i.e. such which produce cholesteric phases) are optically active, i.e. their molecules are chiral; under equivalent conditions the enantiomers form countercurrent, but otherwise identical helical structures. The close relationship of cholesteric and nematic phases is emphasized by the fact that a racemic mixture of cholestogenic compounds does not form a mesophase but a nematic one (Leclercq et al., 1969). A nematic phase can also be formed by mixtures of non-enantiomeric cholestogens which tend to form oppositely coiled structures on their own. However, the ratio

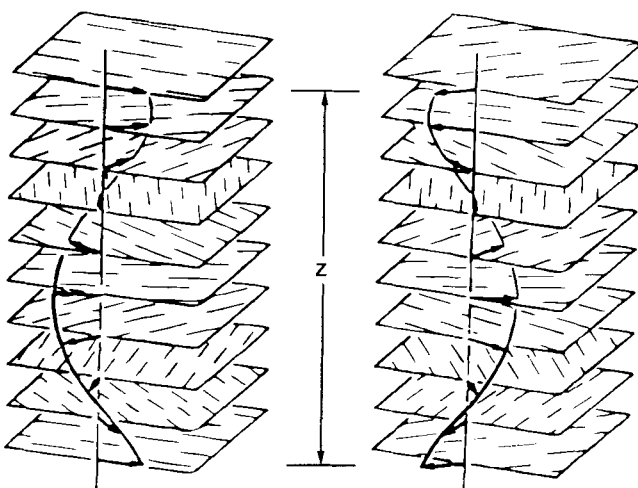


Figure 4.6-7 Antipodal cholesteric molecular arrangements (one period z each).

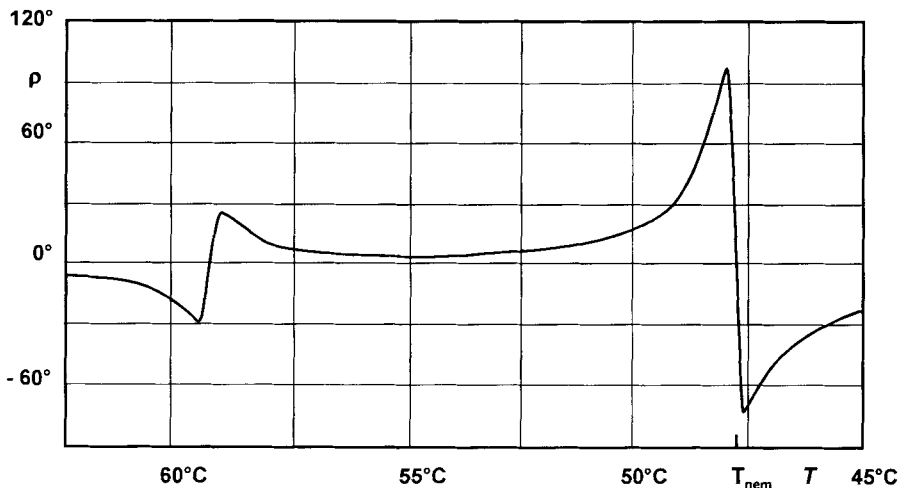


Figure 4.6-8 Optical rotation exhibited by a 0.2 mm thick sample of a mixture of cholesteryl chloride and cholestrylo myristate (molar ratio 1.67) at 1900 cm^{-1} : Scanning the temperature changes the pitch. At 59.5°C the pitch corresponds to 1900 cm^{-1} , at about 48°C the twisting influences of the mixture components are mutually compensated so that the sample is nematic, at lower temperatures the structure is countercurrent. Above and below T_{nem} the rotatory dispersion follows a curve as derived by de Vries (1951).

at which they mutually compensate their twisting tendencies depends on temperature (compare Fig. 4.6-8). On the other hand as reported by Friedel (1922), a cholesteric structure can be induced in a nematic liquid crystal by doping it with chiral (not necessarily cholestogenic) molecules. Also in this case a racemic solute does not cause a twist at all.

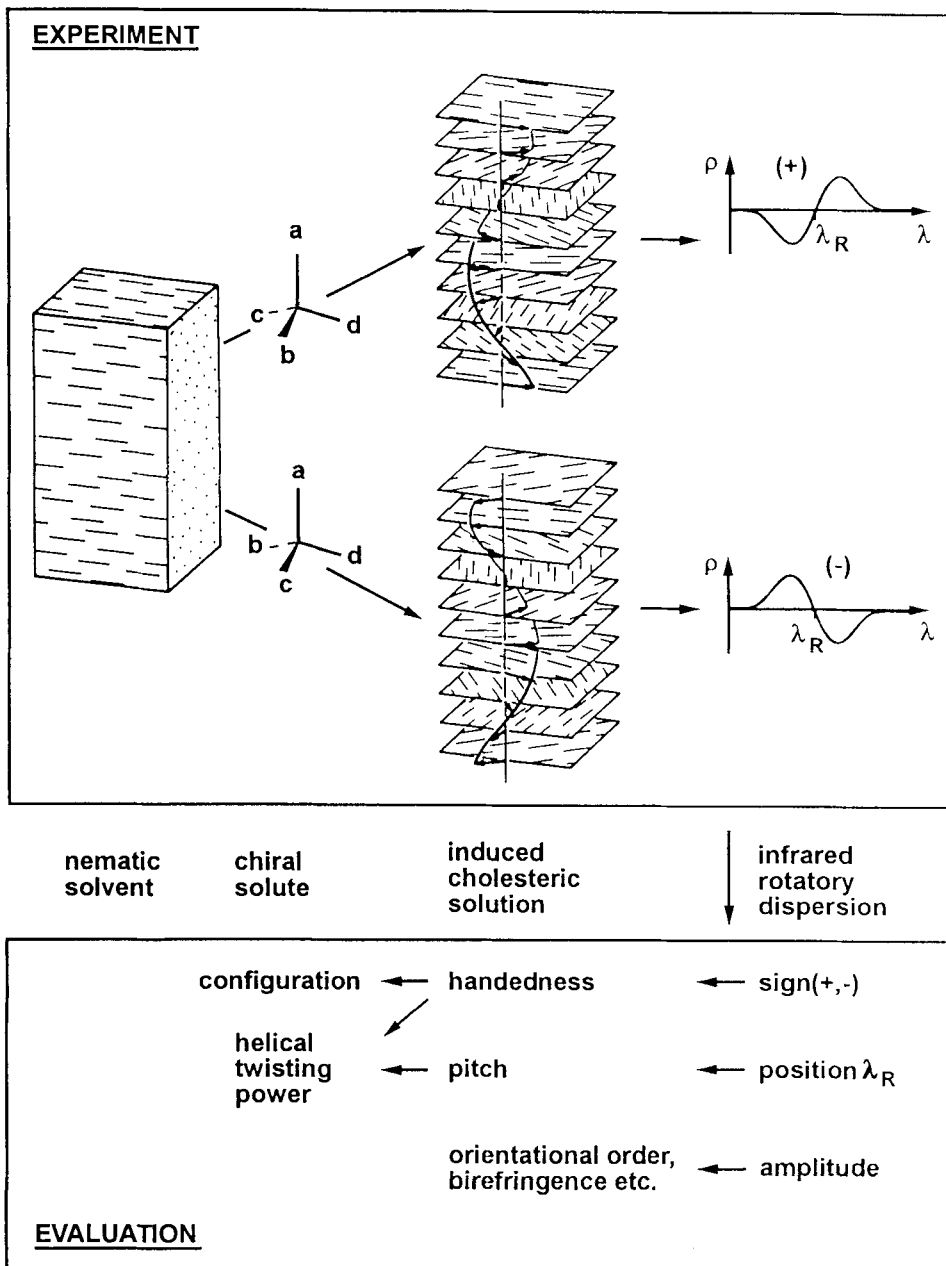


Figure 4.6-9 Induced cholesteric solutions: Schematic outline of experiment and evaluation of the optical rotation $\rho(\lambda)$ related to the selective reflection band (reflection Cotton effect, RCE, centred at the wavelength λ_R) in order to characterize the chirality of the solute molecules by the helical twisting power.

Such twisted nematic phases are called *induced cholesteric solutions* and - as schematically outlined in Fig. 4.6-9 - enantiomers cause countercurrently twisted structures. As discussed by Korte and Schrader (1981) this effect offers the potential of sensitively characterizing the chirality of small amounts of optically active compounds. There are no restrictions as to the type of chirality, and the experiments can advantageously be based on infrared spectroscopy. The application of induced cholesteric solutions was later reviewed again by Solladié and Zimmermann (1984). The host phase is the more twisted the more of the optically active guest compound is dissolved. Quantifying the twist by the inverse pitch z^{-1} and the concentration by the molar fraction x , the ability of a chiral solute to twist a given nematic host phase is characterized by the helical twisting power (HTP; Baessler and Labes, 1970). For small values of x this quantity P is defined by the relation

$$z^{-1} = xP \quad (4.6-7)$$

The induced handedness can be specified on the basis of a suitable convention (see below) by attributing a sign to P (and formally to z). Since the HTP of enantiomers does not differ but for the sign, the non-twisting action of a racemic mixture is evident, and generally the twisting power of a compound is reduced according its enantiomeric purity. On the whole the helical twisting power fulfills the requirements of a chirality observation (Korte and Schrader, 1981) as defined by Ruch (1977).

Therefore, when the helical twisting power is determined experimentally, its sign distinguishes enantiomers, its absolute value is compound specific. The information on the solute conveyed by the helical twisting power is on an equivalent level as the one from specific rotation $[\alpha]_D^T$ (where the superscript T specifies the temperature and the subscript D denotes the frequency of the Na-D line), for instance

- the validity of both quantities is restricted to the particular solvent and the temperature;
- for quantitative purposes the enantiomeric purity of the sample used must be included;
- the correlation with the absolute configuration of the molecule is not straightforward.

As to the latter fact, correlations between the handedness induced by a certain enantiomer and its absolute configuration have been reported (Saeva, 1973; Gottarelli et al., 1975, 1976; Richter and Korte, 1978; Richter et al., 1980; Korte et al., 1980; Korte and Schrader, 1981). They are based on specific guest-host interactions, on priority sequences in empirical analogy to the Cahn-Ingold-Prelog nomenclature (e.g. Cahn et al., 1966) or on chirality functions (e.g. Ruch and Schönhofer, 1968, 1970). Furthermore, induced cholesteric solutions can be employed to prove optical activity and chirality, and to determine enantiomeric purity or concentration of one chiral constituent in a mixture (Korte, 1985). However, the discrimination of enantiomers seems to be the most valuable and appropriate application.

Experimentally, the cholesteric structure parameters, i.e., pitch and handedness, can be derived from the optical properties of the phase and very specially from its so-called *selective reflection*. This most striking phenomenon is the reflection of one component of circular polarized radiation in a spectral interval around that wavelength λ_R which within the medium matches the cholesteric pitch, i.e. $\lambda_R/n = z$ when n denotes the

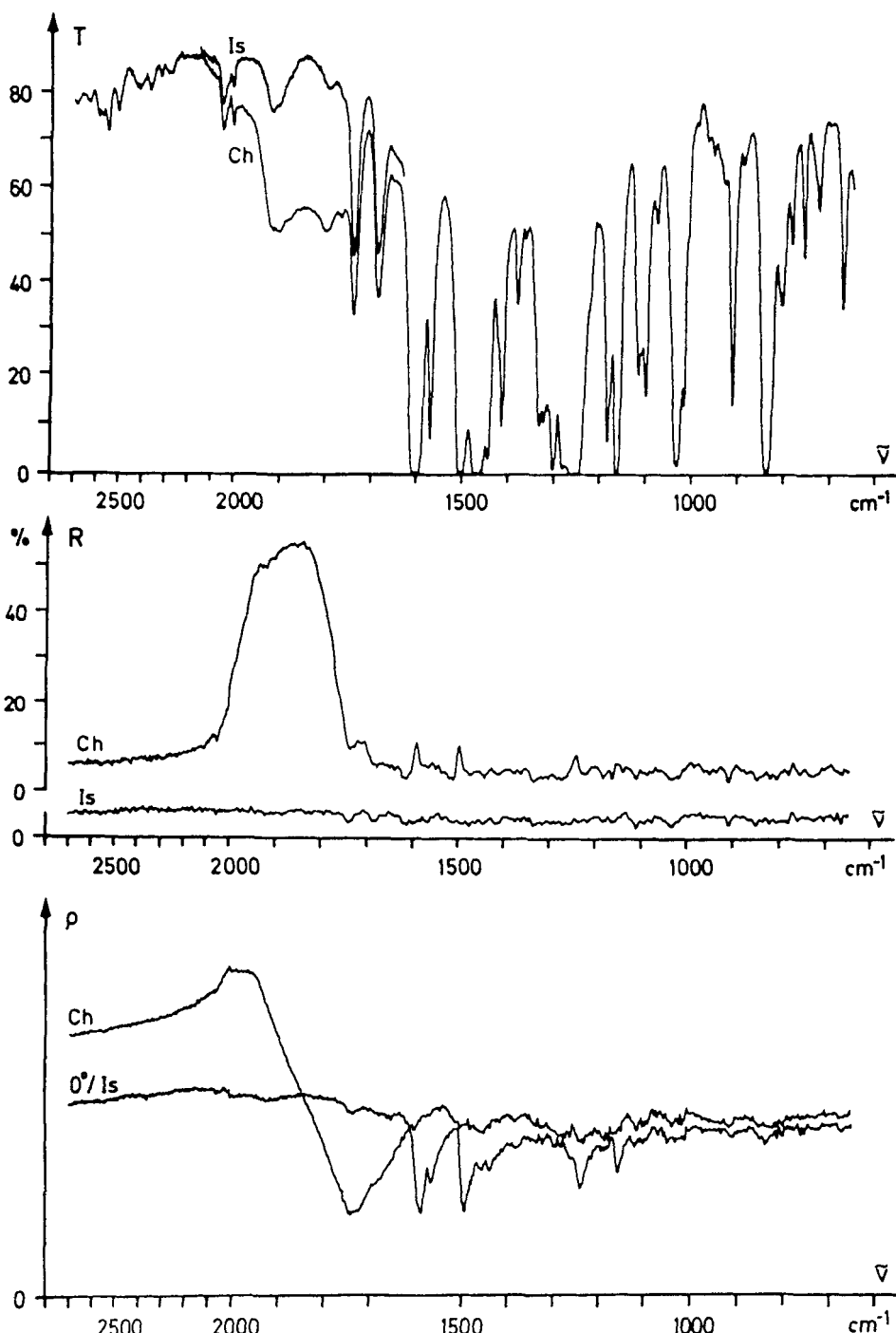


Figure 4.6-10 Infrared spectra of transmittance T , reflectance R , and optical rotation ρ of an induced cholesteric solution at 22 °C (Ch) and as isotropic liquid at 63 °C (Is). Solvent: eutectic mixture of the isomeric N-oxides of *p*-methoxy-*p'*-*n*-butylazobenzene, see 3 of Table 4.6-1 (Nematic Phase IV Lierystal; E. Merck); solute: 17- β -acetoxy-5- β -androst-1-en-3-one; molar fraction $x = 0.055$ (Korte and Schrader, 1981).

average refractive index $(n_e + n_o)/2$; the sign of its circular polarization (left-handed or right-handed) depends on the handedness of the structure (Mathieu, 1939; Elser and Ennulat, 1976; Schadt, 1993a). The other component is transmitted unaffectedly except for absorption. As a consequence its polarity is opposite to the one of the reflected component but equally indicative. Equivalent but opposite results are obtained for the helical counterpart. In this way the selective reflection band or the related spectral band of reduced transmittance (compare Fig. 4.6-10) reveal the parameters of the cholesteric structure under study.

In most cases, a non-mesogenic solute can be dissolved in a nematic host up to a comparably small concentration only; as obvious from Eq. 4.6-4, this means a weak twist and thus, a large pitch. Usually it matches infrared or even far infrared wavelengths (with some non-cholestogenic solutes a selective reflection in the visible spectrum can be attained as shown by Stegemeyer and Mainusch, 1971). Fortunately enough, with an infrared spectrometer a wide range of wavelengths and thus, pitches is readily accessible. The spectra - some of which are shown in Fig. 4.6-10 - can be recorded (Korte and Schrader, 1981)

- with unpolarized radiation:

The pitch is indicated by the spectral position of the selective-reflection or reduced-transmittance band;

- with circular polarized radiation (Jordanov et al., 1988):

Additionally the handedness can be determined;

- with linear polarized radiation:

Around the selective-reflection band the plane of polarization of incident radiation is strongly rotated, the spectral dependence of this optical rotation resembles a dispersion curve; as outlined below, position and shape give indication of both structure parameters.

Furthermore, non-spectroscopic techniques are applicable which mostly are based on visual observations with wedged sample layers (e.g. summarized by Korte and Schrader, 1981). The background is the competition of invariant orientation of the molecules at and by the surfaces of the cell windows rendering possible only helices with e.g. a full number of halfperiods versus the tendency of the cholesteric material to stabilize the inherent pitch. As a consequence, texture defects occur where the number of halfperiods change abruptly, thus separating areas of different numbers. Results from a similar, but infrared-spectroscopic experiment are shown in Fig. 4.6-11. Compression and dilatation of the pitch in order to match the geometrical width of the wedge are clearly seen from the wavenumber shift of the bands which were recorded close to one of the separating lines using a reflection microscope. The band of highest reflectance refers to the position where the gap can be filled adequately by equilibrium periods, i.e. the least distorted case.

For the infrared circular polarization devices and techniques are not as readily available as e.g. in the visible range. Suitable retarders exist which exhibit virtually achromatic quarterwave behaviour from well above 4000 cm^{-1} to about 700 cm^{-1} (Korte et al., 1988), Sec. 3.2.3. Being based on internal total reflection they deviate the beam, nevertheless they render possible to take Fourier-transform spectra of a sample irradiated with circular polarized radiation as well as to analyze the polarization state of radiation

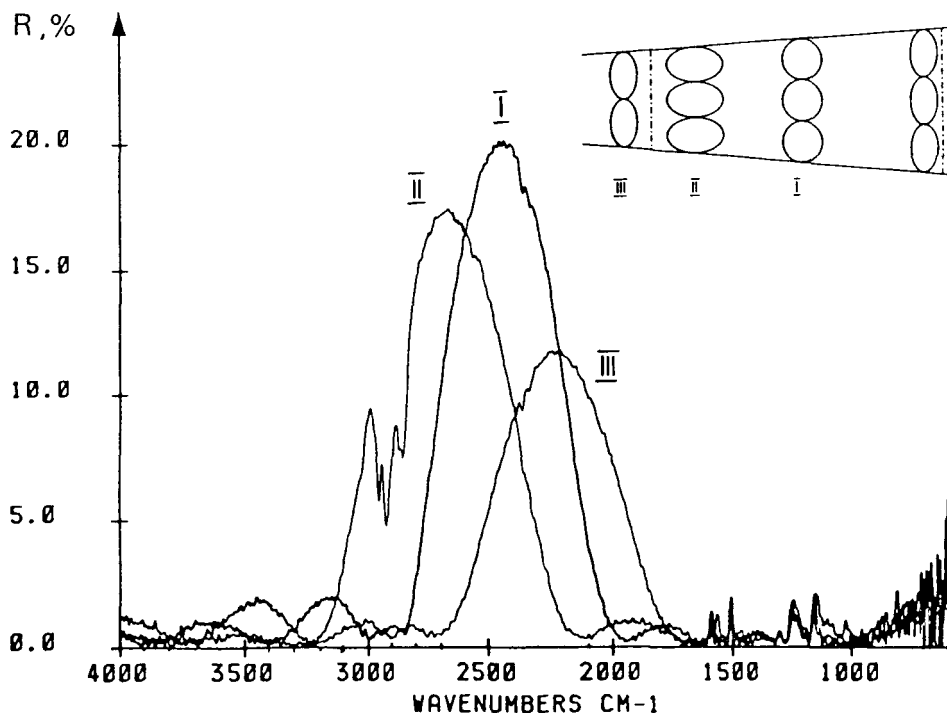
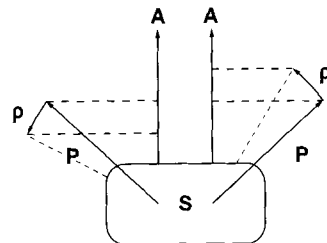


Figure 4.6-11 Selective reflection observed with an infrared microscope at different positions in a wedged sample as schematically outlined by the insert (see text), Zachmann and Korte, unpublished.

after interaction with a sample. Alternatively cholesteric samples in the range of their selective reflection are used to produce circular polarized infrared radiation (Jordanov and Tsankov, 1984), similarly this effect is used in the visible range for projection devices (Schadt, 1993a).

The experimentally most simple procedure of determining both structure parameters is to measure how the plane of polarization of transmitted radiation is rotated in dependence on the wavelength. This polarimetric experiment is easily performed with any infrared spectrometer (Korte, 1978; Belz et al., 1981; Bualek et al. 1986) using a polarizer before and one as analyzer behind the sample as given in Fig. 4.6-12. When spectra are taken with the vectors of the polarizers forming angles of $\pm 45^\circ$, in their ratio the transmittance of the sample is compensated, so that just a spectrum of the angle ρ of optical rotation is obtained (the case of superimposed linear dichroism was analyzed by Tsankov et al., 1984). As obvious from the results presented in Fig. 4.6-13, this technique grants sufficient angular resolution since for samples of convenient thickness the amplitudes of the relevant features are usually in the order of ten degrees. In this way the cholesteric structure parameters are easily determined - the pitch from the spectral position of the centre of the dispersion-like feature, the handedness from the sign of the rotation gradient

Figure 4.6-12 Schematic representation of the experiment for recording the optical rotation of the sample S: P vector of polarizer, i.e. direction of the electric vector of transmitted radiation, A vector of analyzer; the sample rotates the electric vector of the radiation through an angle φ leading (as indicated by the broken lines) to different intensities in the two experimental configurations to be realized readily with a double-beam spectrometer or sequentially with a single-beam instrument.



right there. The sign conventions used to describe the optical activity of isotropic media can be adopted so that

- a clockwise rotation of the plane of polarization as seen from the detector is taken to be positive,
- the dispersion-like feature in the rotation spectrum is named *Cotton effect*,
- such a Cotton effect is called positive if in between the extrema (traditionally referred to as anomalous) the rotation angle increases with increasing wavelength.

Because of its correlation with the selective reflection we refer to this feature as reflection Cotton effect or, in short, *RCE* (Korte and Schrader, 1981). All together, a positive *RCE* indicates a left-handed cholesteric helical structure also called *M* helix and, vice versa, a negative *RCE* indicates a right-handed *P* helix. The evaluation is summarized in Fig. 4.6-9.

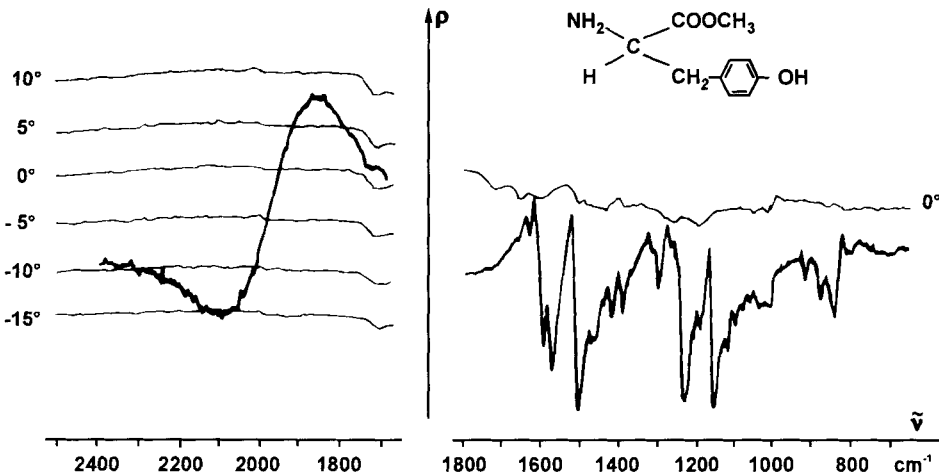


Figure 4.6-13 Optical rotation φ recorded as outlined in Fig. 4.6-12: Spectra of two differently concentrated solutions of S-tyrosine-methylester in the nematic mixture EBBA/MBBA (equimolar mixture of N-(*p*-ethoxybenzylidene)-*p'*-*n*-butylaniline and its methoxy analogue 2 of Table 4.6-1; Riedel-de Haën), left: *RCE* (molar fraction $x \approx 0.024$) related to the selective reflection band indicating pitch and handedness of the structure, thus characterizing the chirality of the solute molecules by the helical twisting power; right: Sequence of *ACE* ($x \approx 0.0024$, therefore the *RCE* should occur around 200 cm^{-1}) each of which indicates the induced handedness and therefore, discriminates enantiomers (Korte, 1978).

Besides possibly one RCE (i.e., provided the selective reflection occurs in the spectral range addressed), the infrared spectrum of the optical rotation comprises several Cotton effects which usually are spectrally narrower and often of smaller amplitudes; examples are given in the two subspectra of Fig. 4.6-13. The secondary effects occur at the spectral positions of absorption bands, primarily those of the solvent rather than of the highly diluted solute whose spectral contributions are more or less buried in the ones of the solvent. The sign of any of these *absorption Cotton effects (ACE)* depends on whether or not the angle the related transition moment forms with the preferred molecular axis is smaller than the magic angle (see Sec. 4.6.2), and whether or not the selective reflection occurs at shorter wavelengths. On these premises the observed sign reflects the handedness of the cholesteric phase (Korte and Schrader, 1981).

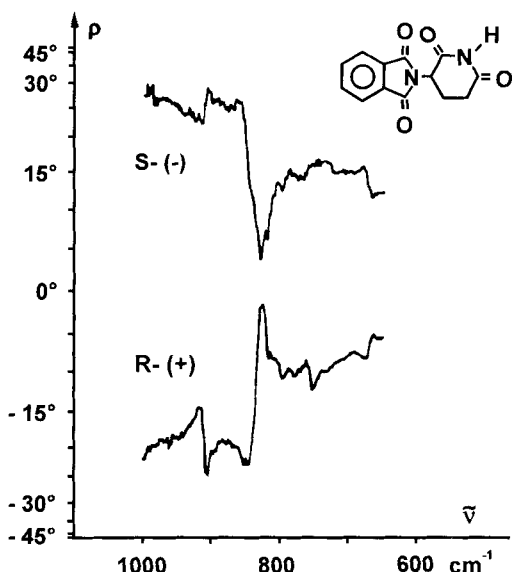


Figure 4.6-14 Part of the rotatory spectra of the enantiomers of Thalidomide in Nematic Phase IV Lixristal (eutectic mixture of the isomeric N-oxides of *p*-methoxy-*p'*-*n*-butylazobenzene, see 3 of Table 4.6-1; E. Merck).

In any case however, antipodal helices cause countercurrent spectra of the optical rotation, so that the observation of just a single Cotton effect is sufficient to discriminate the antipodes and, in case, enantiomeric solutes. For such an experiment the choice of the infrared spectral range is no longer dictated by the structure period but by the presence of suitable transition moments. The low demand for the chiral solute to be characterized (Korte, 1978) is exemplified by Fig. 4.6-14. In the 20 μm wide sample cell an area of 3 mm times 3 mm was filled with approximately 200 μg solution containing circa 0.2 μg of either S-(-) or R-(+) Thalidomide (Contergan) in a nematic solvent. In the spectral interval shown, at least three oppositely shaped ACE are found, the pronounced one around 836 cm^{-1} is related to the γ (C-H), phenyl-H out-of-plane vibration of the

solvent molecules - the same vibration giving rise to the negative (linear) dichroism band of the neat solvent in the nematic state (compare Fig. 4.6-5). Each of these Cotton effects alone allows to distinguish among the enantiomers of the solute. The demand for just microamounts of the chiral solute renders possible to employ this experimentally simple procedure for instance to discriminate metabolites after (thin-layer) chromatographic separation.

4.6.5 From nematic anisotropy to cholesteric optical activity

The chirality of the cholesteric structure and the dispersion-like rotation spectrum similar to a Cotton effect, suggest that this should be called optical activity, especially optical rotation. This latter can be considered as circular birefringence, i.e., different refractive indices for left and right circular polarized radiation. However, already the term optical rotatory dispersion might be misleading since in conventional interpretation this would demand for an accompanying circular-dichroism band. Leaving reflection completely out of consideration, transmittance spectra could be mistaken to support this assumption. However, the intensity missing in the transmission spectrum was reflected, absorption might totally be absent, and all phenomena disappear upon transition of the sample into the isotropic state as also shown in Fig. 4.6-10. This indicates that selective reflection is based on the cholesteric order and thus, on the structure of this phase, so that some type of interference might be responsible. In any case, the phenomena stated here are *not* related to VCD and VORD (e.g. Nafie, 1984), the vibrational-transition based analogues to circular dichroism (CD) and optical rotatory dispersion of optically active compounds in the ultraviolet and visible range which all are observed in isotropic state (e.g. Mason, 1982). There should be closer similarities to the optical activity of helical polymers as far as models such as copper wire helices are applicable (Tinoco and Freeman, 1975).

The cholesteric selective reflection is often associated with Bragg reflection (Elser and Ennulat, 1976; Schadt, 1993a). However, an effect which is quite similar from a different point of view, is exploited in high-power laser applications: The dielectric mirror consisting of a stack of thin, transparent layers of basically two materials in alternating sequence. Such a stratified medium (Born and Wolf, 1980) acts as a highly efficient mirror in a certain spectral interval only. Compiling it from suitably birefringent materials a linear analogue of the cholesteric behaviour can be formulated (Korte et al., 1994).

As early as in 1951 de Vries showed that a twisted stack of birefringent layers is an adequate model for a cholesteric structure in order to reproduce a principally correct spectral dependence of the optical rotation also around the selective reflection band as it was recorded in a different way for Fig. 4.6-8. Even if the layer thickness is formally reduced to zero the optical rotation and its spectral dependence is preserved. Several other approaches were reported to describe particular effects of the cholesteric structure such as the selective reflectance or the rotatory anomaly (e.g. Chandrasekhar and Prasad, 1971; Chandrasekhar and Ranganath, 1974; Schönhofer et al., 1983; Eidner et al., 1989).

The ACE and the dependence of its sign were explained by Holzwarth et al. by considering the layers to be linear dichroic due to vibrational transitions of the molecules aligned therein (Holzwarth et al., 1973; Holzwarth and Holzwarth, 1973). In spite of being due to a linear transition moment, the resulting circular dichroism band seems to indicate an optically active transition (Chabay, 1972; Dudley et al., 1972, 1975).

The transfer of the nomenclature of isotropic optical activity is surely acceptable where it evidently yields a descriptive picture of the experimental observations. However, precautions are necessary as to apparently self-evident implications, this is all the more important since the anisotropic nature of the sample is by no means obvious when observing parallel to the optical and thus helical axis. An unbiased and complete record of how a cholesteric sample acts on the measuring radiation can be obtained by ellipsometry. This method (compare Sec. 6.4) yields a comprehensive description of the state of polarization including the degree of polarization (Röseler, 1990). An adequate simulation can be based on the Berreman formalism (1972) rendering possible a study of particularities observed, such as pronounced depolarization related to the selective reflection band (Reins et al., 1994).

Several models were proposed to explain the twisting influence of the chiral molecules (Goossens, 1971; Stegemeyer and Finkelmann, 1973; Finkelmann and Stegemeyer, 1974). It might be not too surprising that the orientational order in the vicinity of a dissymmetric molecule experiences a small twist, however, the tendency of keeping neighboured molecules as parallel as possible, causes a long-range collective reorientation by which new macroscopic properties appear.

The phenomenon of induced cholesteric solutions can be considered as an amplification of chirality by transforming it from the intramolecular level into macroscopic order. Induced cholesteric solutions proved to be an often very sensitive tool to reveal and to characterize molecular chirality, the experimental data can be achieved from simple infrared spectra. For a detailed interpretation of the cholesteric optical activity, the optical model used must account for the often masked anisotropy.

4.7 Infrared and Raman spectroscopy of biomolecules*

Introduction

Investigating biomolecules by vibrational spectroscopy has a number of advantages over other techniques. These advantages, as is readily recalled, include minimum or no damage to the sample, small amounts of sample material, a wide range of variable parameters (ionic strength, concentration, pH, temperature, hydration in the case of films and fibers), little interference of the main biological solvent (water) in the case of Raman spectroscopy, and the possibility of meeting this difficulty in FTIR spectroscopy by ex-

* Section 4.7 is contributed by A. Cao, J. Liquier, and E. Taillandier, Paris

changing H₂O by D₂O or by using ATR technology. One of the main advantages of vibrational spectroscopy is its ability to afford information about samples in different physical states: dilute solutions, concentrated solutions or gels, hydrated fibers or films, and crystals. Many new results in the field of biomolecules have been obtained as a result of the fantastic development of computer facilities and of new technologies (multichannel and CCD detectors, near infrared Fourier transform Raman, hyper Raman spectroscopy, transient pico and femtosecond spectroscopy, SERS, etc.).

This chapter is divided into three main parts, the first of which deals with nucleic acids, while the second part is dedicated to the investigation of proteins and pigments. The third part finally focuses on biomembranes.

4.7.1 Nucleic acids

4.7.1.1 Experimental methods: IR and classical Raman spectroscopy

4.7.1.1.1 Solutions

In order to investigate nucleic acids by vibrational spectroscopy, concentrations of 10-30 mg/ml are required.

This apparently high figure is explained by a number of arguments. A high DNA concentration is commonly found in native systems (cell nuclei). Model investigations of short oligomers show that duplex conformations of helices, which tend to dissociate at a lower concentration, are stable at a high concentration. Only small amounts of DNA or RNA are required, since FTIR and Raman spectra may be obtained from a sample volume around 5 microliters. Solution spectra may be recorded either in H₂O or in D₂O solution. Due to the H → D isotopic shift, several distinct "windows" can be used to detect the spectrum of a nucleic acid in solution. These are discussed in detail in a different section (Sec. 4.7.1.2). Dilute solutions (0.02 M for nucleotides) are successfully studied by FTIR, particularly in the spectral region between 2000 and 1300 cm⁻¹. To this end, D₂O solutions and cells with a path length of 10-20 μm are used.

4.7.1.1.2 Films and fibers

Native DNAs and polynucleotides can be stretched out as films or fibers. Sealed inside cells with IR transparent windows or in glass capillaries for Raman studies, films and fibers may be exposed to an atmosphere with a controlled relative humidity. This is achieved by simply placing small vessels with known saturated salt solutions at the bottom of the cell or by bringing them in contact with the capillary. Changing the relative humidity induces conformational transitions in the sample (Secs. 4.7.1.3.1 and 4.7.1.3.2). Raman studies of polynucleotides have thus been correlated with X-ray diffraction results obtained from the same fibers (Erfurth et al., 1975; Goodwin and Brahms, 1978).

Another interesting method of investigating oriented films involves using polarized infrared radiation. Two different FTIR spectra are obtained of such samples if the electric field of the incident IR beam is polarized parallelly or perpendicularly to the primary axis of orientation of the sample. Such dichroic spectra may provide information concerning the orientation of subgroups in a biopolymer, for example of the phosphate groups of nucleic acids, with respect to the helical axis (Sec. 4.7.1.3.4).

4.7.1.1.3 Crystals

New developments in spectroscopic techniques have made it possible to obtain Raman spectra and more recently also FTIR spectra of oligomer crystals. The crystal area used for FTIR studies with all reflecting Cassegrain type microscopes is about $30 \times 30 \mu\text{m}$, while the laser beam focused through the microscope covers about $5 \mu\text{m}$ in diameter. Several examples of IR and Raman crystal studies, some of them correlating with X-ray crystal diffraction studies, are listed in Sec. 4.7.1.3.5.

4.7.1.2 What does the vibrational spectrum of a nucleic acid look like?

Different spectral domains reflect motions of individual subgroups of a molecule. Assignments can be made by comparison with the IR and Raman spectra of simple bases, nucleosides, nucleotides, and polymers (Tsuboi, 1969). Isotopic substitution by ^{15}N or ^{18}O , which causes selective absorption shifts, has also been employed (Miles, 1964; Tsuboi et al., 1968).

We shall briefly discuss the principal spectral domains, starting with the highest wavenumbers. The bands between 1800 and 1450 cm^{-1} are mainly attributed to double bond stretching vibrations of the residual bases. The intense Raman line around 1489 cm^{-1} in particular reflects motions of the N7 atom of purines. This region is successfully studied by FTIR investigation of D_2O solutions, which shift the strong water absorption around 1650 cm^{-1} towards lower wavenumbers around 1230 cm^{-1} . The IR absorptions in this region are extremely sensitive both to base pairing and base stacking interactions. Their shifts or relative intensity changes may be used to study interactions at the level of nucleic acid bases, in particular interactions with the carbonyl groups (Sec. 4.7.1.4 and 4.7.1.5).

The second spectral region between 1450 and 1250 cm^{-1} might be designated as the base “fingerprint” region. It shows infrared and Raman peaks caused by vibrations of the bases coupled through the glycosidic C1'-N1 or C1'-N9 linkage to vibrations of the sugar molecules. The peak positions are sensitive both to sugar puckering (north type, C3'endo, A family form or south type, C2'endo, B family form, sugars) and to the relative orientation of the bases with respect to the sugar molecules (*syn* and *anti* conformations).

Located between 1250 and 1000 cm^{-1} are vibrational modes of the phosphate groups and of the sugar units. There is an important difference between the FTIR and the Raman spectra: the two strong IR bands located around 1230 and 1089 cm^{-1} are attributed to the antisymmetric and symmetric stretching vibrations of the PO_2^- groups, respectively. The former band is extremely sensitive to the conformation, while the latter changes very

little with the conformation. In the corresponding Raman spectrum, only the symmetric stretching vibration of the phosphate groups is active.

The bands between 1000 and 800 cm⁻¹ are mainly attributed to the vibrational modes of the sugar moieties and of the phosphodiester backbone. Some of the most important IR marker bands and Raman marker lines which make it possible to characterize the helical type of nucleic acids are found in this region (Sec. 4.7.1.3).

The peaks between 800 and 600 cm⁻¹ are caused by vibrations of the bases which are coupled to sugar vibrations and out-of-plane carbonyl bending vibrations. A mode attributed to a guanine imidazole ring vibration coupled via the C1'-N9 linkage to a sugar vibration in particular is extremely sensitive to the conformation. It therefore gives evidence of transitions between the different helical families of nucleic acids (Secs. 4.7.1.3.1, 4.7.1.3.2).

The low wavenumber region was studied more recently, both by FTIR and by Raman (Urabe et al., 1985; Powell et al., 1987; Weidlich et al., 1990). Several conformationally sensitive modes were detected below 250 cm⁻¹.

4.7.1.3 The three main families of nucleic acid double helix conformations

Despite the extremely variable geometry of nucleic acids, they may be classified according to three main families of conformations. There are two right-handed helices (A and B

Table 4.7-1 IR bands and Raman lines “markers” of A, B and Z conformations

RAMAN			INFRARED		
A	B	Z	A	B	Z
1320 dG	1375 dA 1363 dG	1362 dA 1354 dG 1315 dGdA	1705	1715	1434 1408 d
			1418 d	1425 d	1355 dGdA
			1375 dGdA	1375 dGdA	
			1335 dT	1344 dT	
			1335 dA	1328 dA	
	1264 dC	1275 T 1240 P 1188 d			1320 dG
			1275 T	1281 T	1264
			1240 P	1225 P	1215 P
			1188 d		1065 d
807 Bk	832 Bk	815 Bk	882 d		929
780 Bk	788 Bk		864 d		
		746 Bk		840 d	
	682 dG		806 d		
662 dG	669 dA, dT	622 dG, dA			

d: deoxyribose P: Phosphate Bk: Backbone

form families) and one left-handed one (Z form family). Members of the B family include C and D type DNAs which are observed in particular conditions concerning counterions and relative humidity, while the A' RNA helices are variants of the A group (for a review concerning the helical geometries of nucleic acids, see Saenger, 1988). These three families are easily distinguished by vibrational spectroscopy; and conformational transitions between them may be monitored either by IR or by Raman spectroscopy. Signs of A, B and Z conformations have been obtained for various polynucleotides and oligomers. Table 4.7-1 lists a set of infrared and Raman markers of different geometries. This table is not an exhaustive list of all IR and Raman peaks of nucleic acid spectra but presents a selection of the main marker peaks and is intended to help characterize the conformational families of oligo and polynucleotides. Wavenumbers may slightly vary within one family, depending particularly on the nucleic acid sequence.

4.7.1.3.1 The B → A conformational transition

Most native DNAs and certain synthetic polynucleotides are able to undergo a B → A conformational transition. In films and fibers, this transition may be induced by decreasing the relative humidity to which the sample is exposed. This is demonstrated by the Raman spectra of fibers (Erfurth et al., 1975; Martin and Wartell, 1982; Prescott et al., 1984) and by the IR spectra of films (Pilet and Brahms, 1973; Taillandier et al., 1985) made of native DNAs. In the case of polynucleotides, the decrease of relative humidity affords different results, depending on the sequence of the polymer. Thus, poly d(A-T) and poly d(A-C), poly d(G-T) – double stranded DNA with one strand adenine and cytosine and in the other guanine and thymine – show a classical B → A transition (IR: Brahms et al., 1976; Taillandier et al., 1984a; Adam et al., 1987. Raman: Thomas and Benevides, 1985; Jenkins et al., 1986).

The IR spectra exhibit the following modifications (these are shown, for example, in Figure 4.7-1 a,b, which presents the FTIR spectra of a poly d(A-T) film at 100% (top) and at 58% (center) relative humidity (the bottom spectrum will be discussed later). A band characteristic of base pairing (this band is not exhibited by denatured DNA) involving the *in-plane* C=O and C=N stretching vibrations is shown by the B form above 1710 cm⁻¹ and by the A form below 1710 cm⁻¹ (at 1717 and 1706 cm⁻¹, respectively). The B form deoxyribose vibration at 1425 cm⁻¹ is shifted to a lower wavenumber at 1418 cm⁻¹ in the spectrum of the A form. In the case of A-T base pairs, two B form absorptions at 1344 and 1328 cm⁻¹, respectively, attributed to dA and dT residual vibrations, shift in opposite directions and are superimposed at 1335 cm⁻¹ in the A form spectrum (Liquier et al., 1991). Similarly, the thymine N-H vibrational band shifts from 1281 cm⁻¹ in the spectrum of the B form to 1275 cm⁻¹ in that of the A form. The antisymmetric stretching vibration of phosphates shows considerable displacement to higher wavenumbers from 1225 to 1243 cm⁻¹. The A form spectrum exhibits a sharp intense band around 1188 cm⁻¹, attributed to a C-C vibration of deoxyriboses. The sugar units undergo a south type → north type reorientation, which is reflected by the replacement of the 843 cm⁻¹ band by a pattern of three absorptions at 806, 864, and 882 cm⁻¹.

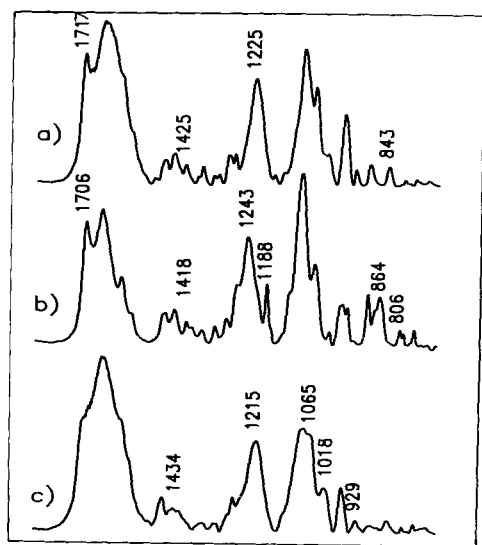


Figure 4.7-1 FTIR spectra of poly d(A-T). poly d(A-T) films. a) 100% RH, B form; b) 58% RH, A form; c) 58% RH in the presence of nickel ions, Z form.

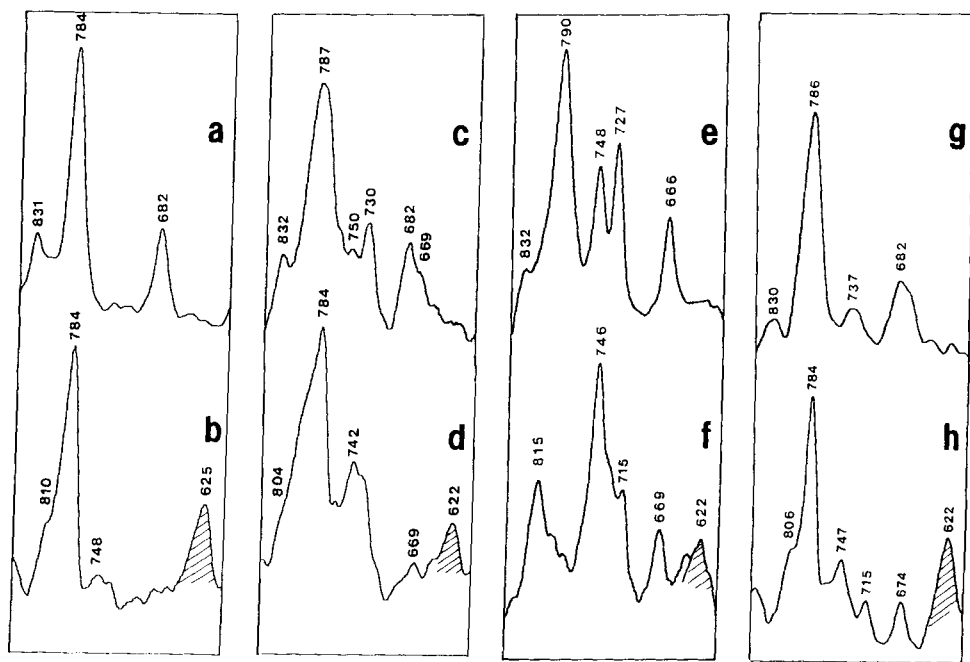


Figure 4.7-2 Raman spectra between 600 and 850 cm^{-1} of: a) poly d(G-C), B form; b) poly d(G-C), Z form; c) poly d(A-C), poly d(G-T), B form; d) poly d(A-C), poly d(G-T), Z form; e) poly d(A-T), B form; f) poly d(A-T), Z form; g) d(CACGTG), B form; h) d(CACGTG), Z form. The line characteristic of purines in *syn* conformation is hatched.

Raman spectra show the same B → A transition in fibers. This is particularly prominent in a number of lines in the 800-600 cm⁻¹ region. The north and south conformers of the sugars correlate with Raman lines around 807 cm⁻¹ in the spectrum of the former geometry and around 832 and 788 cm⁻¹ in that of the latter one. It should be mentioned that in polyribonucleotide spectra the 807 cm⁻¹ line is observed at a slightly higher wavenumber (815 cm⁻¹ for poly rG, poly rC), which may indicate a small but significant difference in the geometry of the two types of A structures (DNA and RNA). This spectral region also features a guanosine vibrational mode which is extremely conformationally sensitive. This guanine imidazole ring vibration, coupled through the glycosidic linkage to a deoxyribose vibration, is observed around 682 cm⁻¹ in the spectrum of the B form (Fig. 4.7-2a), at 672 cm⁻¹ in that of the A form, and at 625 cm⁻¹ in that of the Z form (Fig. 4.7-2b), see following section.

The B → A conformational transition can be induced in solution, for example by increasing the ionic strength (poly dG, poly dC exhibits the B form in 0.1 M NaCl and shows the A form in 4 M NaCl (Nishimura et al., 1986)). Another option is to work in aqueous ethanolic solution containing more than 80% alcohol (native DNA, Martin and Wartell, 1982). In all of these cases, the conformation is characterized by the previously discussed marker lines in the respective Raman spectra.

These spectral markers make it possible to determine the relative content of each geometry in mixtures of A and B conformations. The ratio of the integrated intensities of the IR absorptions around 860 and 835 cm⁻¹, $\bar{A}835/(\bar{A}835+\bar{A}860)$ for example, provides an estimate of the amount of B form in a sample (Liquier et al., 1990). Similarly, the percentage of furanose rings in the north type geometry may be measured by Raman spectroscopy using the relative intensities of the 807 cm⁻¹ line and the band at 1100 cm⁻¹ (Brown et al., 1972; Thomas and Hartman, 1973).

4.7.1.3.2 The B → Z conformational transition

The left-handed Z conformation of the d(C-G)₃ oligomer discovered by X-ray crystal diffraction (Wang et al., 1979) was studied by Raman spectroscopy (Thamann et al., 1981). The Raman spectra of the d(C-G)₃ crystal and of the poly d(G-C) solution, which contains large amounts of salt, unambiguously demonstrate the presence of the left-handed Z structure of the short oligomer in the crystal and of the long polynucleotide in solution at a high salt level. In contrast, the Raman spectrum of poly d(G-C) at a low salt level reflects the B form (Pohl et al., 1973). The Z conformation of poly d(G-C) has also been characterized by IR spectroscopy of films (Taillandier et al., 1981; Pilet and Leng, 1982; Taboury et al., 1985) and in solution.

The putative biological importance of the left-handed conformation and the rarity of G-C alternating sequences in the genome have stimulated the search for other sequences which are able to undergo a B → Z transition. Incorporating A-T base pairs in a regularly alternating G-C sequence makes it more difficult to induce reorientation from right to left. However, experimental conditions have been found at which oligomers and polymers containing all four types of bases and polymers containing regularly alternating A-T bases adopt a left-handed geometry. Their conformation in hydrated films was characterized by

IR spectroscopy (Taillandier et al., 1984a, 1985; Adam et al., 1986a,b,c) and in solution by Raman spectroscopy (McIntosh et al., 1983; Ridoux et al., 1987, 1988).

The main IR markers of the Z conformation are summarized below (the IR spectrum presented in Fig. 4.7-1c, for instance, is that of Z form poly d(A-T)). Starting with high wavenumbers, polymers containing A-T base pairs absorb at 1434 cm^{-1} , while this peak is not observed in the spectra of the right-handed A and B forms of poly d(A-C), poly d(G-T) and poly d(A-T). The B form deoxyribose vibration at 1425 cm^{-1} and that of the A form at 1418 cm^{-1} are shifted still further by the Z form, which absorbs around 1408 cm^{-1} . The purine base-sugar vibration of the *anti* conformation at 1375 cm^{-1} is shifted to 1355 cm^{-1} by the *syn* geometry. Sequences containing G-C base pairs exhibit strong bands at 1320 and 1264 cm^{-1} . $B \rightarrow Z$ transition shifts the antisymmetric stretching vibration of phosphates to lower wavenumbers ($1225 \rightarrow 1215\text{ cm}^{-1}$), while $B \rightarrow A$ transition shifts this peak to higher wavenumbers. The intensity profile of the symmetric phosphate stretching vibration is modified and the relative intensities of the bands at 1065 and 1018 cm^{-1} increase. Finally, a new band emerges at 929 cm^{-1} , i.e., in the region of the sugar vibrations below 1000 cm^{-1} , whereas the intensity of the 890 cm^{-1} band, which is characteristic of right-handed helices, decreases. Deuterated samples containing G-C base pairs show splitting of the sharp B form band at 778 cm^{-1} into two components at 784 - 778 cm^{-1} . Investigation of methylated poly d(G-C) on the C5 site of cytosines has shown that these bands may be assigned, respectively, to guanine and cytosine vibrational modes (Taboury et al. 1985).

Fig. 4.7-2 exhibits characteristic Raman lines of Z form helices. It shows the Raman spectra of right-handed (top row) and left-handed (bottom row) conformations of the three polymers poly d(G-C), poly d(A-C), poly d(G-T), poly d(A-T), and of an oligomer d(CACGTG). Particularly noticeable features of the bottom row spectra (Z conformation) are the characteristic sugar-backbone lines around 815 and 746 cm^{-1} , as well as the purine line of the *syn* conformation around 622 cm^{-1} . Other important spectral changes reflecting a $B \rightarrow Z$ transition are the emergence of an intense dG line at 1320 cm^{-1} , the shift of a purine line (dA from 1375 to 1362 cm^{-1} , dG from 1363 to 1354 cm^{-1}), and the appearance of a dC line at 1264 cm^{-1} (see Table 4.7-1).

4.7.1.3.3 Hydrogen - deuterium exchange

Isotopic exchange of hydrogen in DNA was studied a long time ago (Bradbury et al., 1961). The exchangeable hydrogens can be divided into three categories. OH and NH hydrogens which are not involved in interstrand base pairing by hydrogen bonding exchange instantaneously. The NH hydrogens of bases which are engaged in interstrand hydrogen bonds exchange fast, but the kinetics of this exchange can be measured (Englander, 1963). Hydrogens attached to the C8 of purines exchange slowly and require elevated temperature. This selective C8-H exchange is caused by incubating the DNA at high temperature and, in addition to the guidance it affords in assigning IR and Raman bands, makes it possible to detect interactions at the N7 site, which is extremely reactive. Demonstration of the fact that transition metal ions are bound to this purine N7 site of regularly alternating purine-pyrimidine polymers explains the stabilization of the *syn*

conformation of guanosines and/or adenosines and therefore also the fact that nickel ions are responsible for the left-handed Z conformation of poly d(A-C).poly d(G-T) and poly d(A-T) (Taboury et al., 1984; Adam et al., 1986a). H-D exchange may also be employed as a dynamic indicator of the conformation of the nucleic acid. Raman spectroscopy has been used to define a retardation factor, which is the ratio of the deuterium exchange rate of polymers and monomers. Extremely different values were obtained for the A, B, and Z geometries, as well as for multiple helical structures (Benevides and Thomas, 1985).

4.7.1.3.4 Infrared linear dichroism

Infrared linear dichroism measurements may be performed on unidirectionally oriented samples. In the case of DNA, the favored axis of orientation is the axis of the double helix. Films are prepared by unidirectional stroking while the sample is gently dried. Two spectra are recorded with the electric field of the incident light oriented parallelly

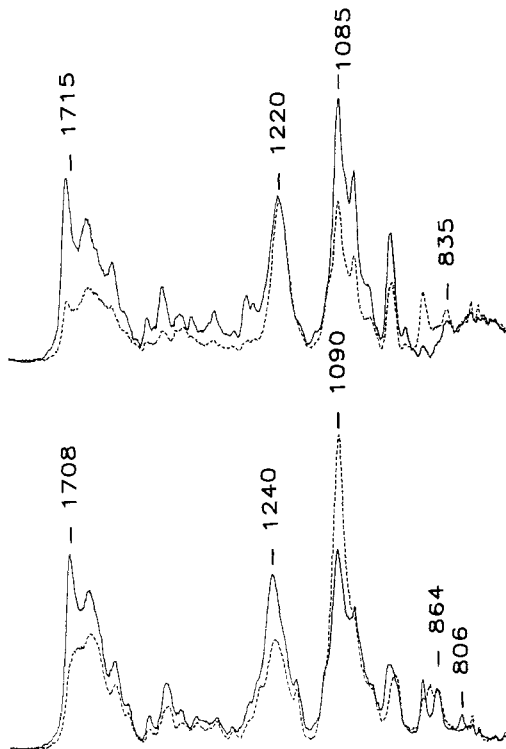


Figure 4.7-3 Polarized infrared spectra of salmon sperm DNA films. Top 98% RH, B form; bottom 58% RH, A form. Electric field of incident radiation directed perpendicularly (full line) or parallelly (dotted line) to the preferential orientation of the sample.

and, respectively, perpendicularly to the axis of orientation of the polynucleotide. The absorption ratio measured at the maximum of an IR band if the electric field is oriented perpendicularly versus parallelly to the axis of orientation $R = A_{\perp}/A_{\parallel}$ is referred to as the dichroic ratio of this band. It correlates with the orientation angle between the transition moment of the band and the higher symmetry axis of the polymer (Hill, 1972).

This technique was employed to monitor the B → A transition of DNA as a function of the relative humidity (Pilet and Brahms, 1973; Pohle et al., 1984). The investigated bands are those which reflect the vibrations of the phosphate groups. As shown by Fig. 4.7-3, which presents the polarized infrared spectra of a salmon sperm DNA hydrated film with 93% RH (top, B form) and 58% RH (bottom, A form), the dichroism of the two phosphate bands changes. The B form of the antisymmetric PO_2 stretching vibration around 1230 cm^{-1} is non-dichroic, while that of the A form is perpendicular. The B form of the symmetric PO_2 stretching vibration around 1090 cm^{-1} is perpendicular, while that of the A form is parallel. A simple computation, for instance for the latter band, shows that the value of the angle between the transition dipole moment of this vibration and the double helical axis varies between 68° (B form) and 49° (A form). This parameter is an extremely sensitive indicator of a B → A transition and may also be employed to show the inhibition of a B → A transition by various classes of molecules, such as proteins (Liquier et al., 1977; Taillandier et al., 1979) or drugs (Fritzsche and Rupprecht, 1990).

4.7.1.3.5 Crystal studies

Since the first Raman spectrum of a DNA crystal was published (Thamann et al., 1981), micro Raman spectroscopy has been used extensively to study oligomer conformations in the solid state. Crystallization of short oligonucleotides often causes conformational transitions. The d(C-G)₃ Z form crystal, for instance, was grown from a solution of the B type hexamer (Wang et al., 1979). Fig. 4.7-2 presents a similar transition of the d(CACGTG) sequence. The Raman spectra clearly indicate the presence of the B form in solution (Fig. 4.7-2 g, lines at 830 and 682 cm^{-1}) and the occurrence of the Z form in the crystalline phase (Fig. 4.7-2 h, lines at 806 , 747 and 622 cm^{-1}). Comparing Raman spectra of crystals with spectra of aqueous solutions, which vary in terms of ionic strength and counterion conditions, affords information concerning the relative ease with which certain B geometry sequences convert to their A or Z forms (Wang et al., 1987).

Very recently the first micro FTIR investigations of DNA crystals were published (Urpi et al., 1989; Liquier et al., 1990). The use of Cassegrain type microscopes coupled to spectrophotometers equipped with high sensitivity detectors made it possible to obtain IR spectra of d(GGTATACC) and d(CCCCCGGGGG) crystals. The previously discussed IR marker bands show that two conformations with north and south type sugars coexist in the former crystal (bands at 861 and 834 cm^{-1}). This is in good agreement with a model proposed by Doucet et al., 1989, on the basis of X-ray diffuse scattering results, according to which B form octamers are trapped in a tunnel formed by six A form octamers (Doucet et al., 1989). The A type form shown by FTIR spectroscopy is slightly different from the canonical fiber A form, which is reflected in particular by the in-

plane double bond vibrations of the bases (band observed at 1694 cm^{-1} instead of 1705 cm^{-1}) and of the phosphates (low wavenumber of the antisymmetric stretching vibration band and splitting of the symmetric stretching vibration band). The crystal spectrum of d(CCCCCGGGGGG), in contrast, exhibits only the characteristic pattern of north type sugars (bands at 864 and 806 cm^{-1}) and reflects an A conformation similar to that observed in fibers with a classical base pairing absorption located at 1705 cm^{-1} . Recent investigation of this crystal by X-ray diffraction indeed demonstrates that this complete helical turn of A DNA shows average structural parameters, similar to those determined in fibers (Verdaguer et al., 1991).

4.7.1.4 Triple helices

The increasing interest in the formation of triple helices is a result of the assumed existence of *in-vivo* intramolecular triple helical structures which may be formed by homopurine-homopyrimidine sequences. Such sequences are often found in the eukaryotic genome, especially in putative regulatory regions of genes and hot spots of recombination (for review see Wells et al., 1988). The fact that oligonucleotides can form bonds specifically to complementary homopurine-homopyrimidine duplexes via formation of triple stranded structures has opened up new fields in the understanding of DNA binding reagents (Moser and Dervan, 1987; Perrouault et al., 1990). Early IR studies concerning base triplets focused on base pairing problems (Miles, 1964; Howard et al., 1971). Triple stranded structures formed by homopolymers containing only A, T, or U bases and either riboses or deoxyriboses have been systematically investigated. Triplexes formed by adding a dT or an rU single strand to duplexes in A family form (poly rA. poly rU), in B family form (poly dA. poly dT), or in a heteronomous conformation (poly rA. poly dT) present identical FTIR spectra in the region of base double bond vibrations. This shows that base interactions are similar, irrespective of the triplex. The sugar conformations showed a different result. The IR spectra only exhibit the characteristic bands of exclusively north type sugars (868 and 815 cm^{-1}) for poly rU. poly rA. poly rU and of exclusively south type sugars (band at 840 cm^{-1}) for poly dT. poly dA. poly dT. (Liquier et al. 1991).

The characterization of the formation of triple helices by C⁺GC triplets, combined with the set of marker bands shown by the TAT triplet, made it possible to study triple helical structures containing both isomorphous TAT and C⁺GC bases (Akhebat et al., 1992; Ouali et al., 1993).

4.7.1.5 DNA-drug interactions

There are two different classes of drugs which play a role in drug-DNA interactions: intercalating drugs and groove binding drugs. The family of non-intercalating minor groove binding drugs has been studied extensively, particularly because of their specificity with regard to the DNA sequence. Netropsin, distamycin, and Hoechst 33258, for instance, bind preferentially to A-T base pairs, while a number of derivatives, espe-

cially thiazole-lexitropsins, have been synthesized in an attempt to obtain a certain G-C specificity.

The interaction between netropsin and polymers containing A-T base pairs, poly d(A-T) and poly dA, poly dT, was studied by FTIR (Liquier et al., 1989). Possible interaction sites include the phosphate groups, the sugars, and the bases. Both the antisymmetric and symmetric vibrations of the phosphate groups of the polymers remain unaffected as netropsin is successively added to the DNA until a ratio of one drug molecule per three A-T base pairs is reached. This rules out any possibility of interaction with the phosphate groups. On the contrary, the spectral region in which the carbonyl vibrations of the bases are found is modified by addition of netropsin: the shift of the $C_2=O_2$ carbonyl stretching vibration band of poly d(A-T) at 1696 cm^{-1} reflects an interaction between the drug and the carbonyl group of the thymine located in the narrow groove of the double-stranded DNA.

UV resonance Raman studies on poly dA, poly dT and poly d(A-T) distamycin complexes have suggested that the conformational flexibility of poly d(A-T) decreases by binding a drug (Grygon and Spiro, 1989).

Thiazole derivatives of lexitropsins and modified Hoechst 33258 have been synthesized (Bathini et al., 1990). FTIR spectra of complexes of poly d(A-T) or poly dG, poly dC and a derivative of Hoechst 33258, obtained by substituting pyridine for the benzene ring of the benzimidazole moiety and replacing one benzimidazole unit by benzoxazole with the oxygen oriented towards the minor groove, show that the poly d(A-T) spectrum is not significantly affected. The two carbonyl bands ($C_2=O_2$ of guanines and $C_6=O_6$ of cytosines), on the other hand, are shifted upon addition of the drug, which has acquired G-C recognition properties (Adnet et al., 1992).

The second class of drugs (intercalating drugs) involves interaction of the two anthracycline derivatives aclacinomycin A and violamycin B1 with DNA, which has recently been investigated by infrared linear dichroism (Fritzsche and Rupprecht, 1990). The restriction of the $B \rightarrow A$ transition as a consequence of drug binding turns out to be only slightly dependent on the DNA base composition.

Coulombic interactions between water soluble porphyrins and nucleic acids have also been studied by ATR FTIR and UV Raman (Nonaka et al., 1990). It was found that the N-methylpyridil group interacts preferentially with one of the two oxygens of the PO_2 groups of the DNA duplex.

The interaction of anticarcinogenic substances, such as cis-platinum, with nucleic acid constituents was studied by Raman spectroscopy (Bertoluzza et al., 1988).

4.7.2 Proteins – pigments

Proteins constitute the largest portion of living matter in all types of cells. They serve as structural elements in cells and tissues, show specific catalytic activity, function as enzymes, and are found in cell membranes. Most IR and classical Raman studies focus on the characterization of protein secondary structures by using sets of absorption bands and diffusion Raman lines reflecting especially the motions of peptide groups (Sec.

4.7.2.1). A number of recently developed techniques, such as time resolved resonance Raman, surface enhanced Raman spectroscopy, and near IR Fourier transform Raman, are described in Section 4.7.2.2.

4.7.2.1 IR and classical Raman spectroscopy

4.7.2.1.1 Band assignment and protein conformation

Infrared spectra of proteins may be obtained either in the solid state (KBr pellets, crystals, or by diffuse reflectance techniques (Yang et al., 1985)) or in solution (D_2O solutions, ATR techniques, as in the case of protein adsorption studies (Gendreau et al., 1982; Sec. 6.4)). Raman spectra of proteins are usually obtained in solution.

The vibrational spectra of proteins exhibit several relatively intense peaks which change but little in wavenumber and intensity from one sample to another. These bands are associated with the CONH moiety, which is common to all molecules of this type. The slight variations which are, in fact, observed, particularly in terms of position, may afford information regarding the structure and conformation of the investigated molecule. There are nine prominent bands, which, in order of decreasing wavenumber, are referred to as amide A, amide B, and amide I to VII (Miyazawa, 1962). N-methylacetamide was used as a model molecule for the investigation of the CONH group vibrations (Fillaux, 1981; Fillaux and Baron, 1981). The remaining lines in the vibrational spectra of polypeptides and proteins, whose intensity is usually weaker, have been attributed to amino acid side chain vibrations (Lord and Yu, 1970; Van Wart and Sheraga, 1976; Fasman et al., 1978; Kitagawa et al., 1979; Harada et al., 1982).

Three of the amide bands are of particular interest for the study of polypeptide and protein conformations: amide I, between 1680 and 1600 cm^{-1} , is mainly associated with the stretching vibration of the C=O bond, while amide II, found between 1580 and 1480 cm^{-1} , and amide III, observed between 1300 and 1230 cm^{-1} , are both associated with coupled C–N stretching and N–H bending vibrations of the peptide groups (Susi, 1969). These peaks are conformationally sensitive, and the observed positions may be attributed to α helices, parallel and antiparallel β sheets, β turns, or random coils (Krimm, 1962; Chen and Lord, 1974; Lord, 1977; Krimm and Bandeker, 1980). Assignment of these lines has become much easier through the understanding of the coupling between normal modes of amide groups in oligopeptides (Krimm, 1986).

4.7.2.1.2 Treatment of data

The widths of the amide I bands which are associated with the different structures are large compared to the separation of their peak maxima, which is why the amide I absorption of a complex protein consists of several overlapping bands. Deconvolution and derivative techniques have been employed to detect the individual components (Kauppinen et al., 1981; Susi and Byler, 1983; Mantsch et al., 1986). Quantitative estimates for different conformations have been obtained by ulterior curve fitting procedures (Byler

and Susi, 1986). Deconvolution and second derivative spectra of the broad amide I band of photosynthetic bacterial reaction centers, for instance, revealed a remarkable agreement between the α helical content of membrane proteins determined by X-ray diffraction on RC crystals and the values obtained by FTIR spectroscopy (Nabedryk et al., 1991).

A method based on factor analysis followed by correlation of the factor loadings with structural composition has recently been proposed. This technique involves constructing a calibration set from infrared spectra of proteins whose secondary structure has been determined by X-ray. Factor analysis creates series of abstract spectra, which are combined to generate the original spectrum (Lee et al., 1990). This procedure was employed to estimate the secondary structures of membrane proteins (Lee et al., 1991).

Difference spectroscopy is another method which has been applied to the resolution enhancement of infrared and Raman spectra of proteins. A difference spectrum may be obtained, for example, by subtracting the spectrum of the same sample before and after an external agent has been applied. If the sample is slightly sensitive, the spectrum obtained after irradiation is subtracted from that obtained before irradiation. The spectra are thus simplified: the difference spectrum shows only those absorptions which are associated with the groups which are actually involved in a particular change (Rothschild and Marrero, 1982). Raman difference spectroscopy was employed to study small ligands bound to active sites in proteins, such as NaDH and NaD⁺ bound to lactate dehydrogenase (Deng et al., 1989). FTIR spectroscopy was used to investigate atomic interactions in enzyme substrate intermediates (Wharton et al., 1988).

4.7.2.1.3 Membrane proteins

Investigation of amide vibrations by vibrational spectroscopy may show changes of the protein conformation induced by common biological preparative techniques which are believed to be mild, such as sonication or addition of non-denaturing detergents. An increase in the β and disordered structure at the expense of the α helical conformation, for instance, was observed during the IR spectroscopic investigation of brain proteolipid *apoprotein* which had undergone such treatment (Carmona et al., 1988).

The Ca^{++} -ATPase activity of sarcoplasmic reticulum from rabbit and winter flounder was investigated (Vrbjar et al., 1990). While lipids from both sources turned out to be disordered, the activity of the protein showed a different temperature dependence. The secondary structure of *lipophilin* in DMPC or DMPG, a hydrophobic myelin protein, was studied by Surewicz et al. (1987d). Monitoring the amide I band showed that the protein adopts a highly ordered secondary structure. At room temperature, this structure consists predominantly of an α -helix (55%) and β -sheet conformations (36%). This secondary structure is not affected by transition from the lipid gel-like phase to the liquid crystalline phase. Atrial natriuretic peptide atriopeptin III, which exhibits a random structure in aqueous solution, adopts a highly ordered structure in the complex with DMPG, where it is arranged predominantly in β -sheets (Surewicz et al., 1987a).

Nicotinic *acetylcholine receptors* which are reconstituted with mixtures of phospholipids containing negatively charged PA and cholesterol were shown to be stabilized by

the latter (Fong and McNamee, 1987). It was suggested that the protein-sterol interactions enhance the helical structure and that the negatively charged lipid enhances the β conformation of the receptor. This is consistent with functional studies which demonstrate that the ion channel activity requires the presence of both sterol and negatively charged phospholipids in the membranes. Purified acetylcholine receptor membranes from *Torpedo californica* show the predominance of the β -sheet conformation over the α -helical one (Naumann et al., 1990).

The β sheet orientation in *porin*, a trimeric integral protein which forms channels across *E.coli* outer membranes, was determined by analyzing the amide I band and its shoulders around 1631 cm^{-1} and the amide II band around 1530 cm^{-1} . The results showed that the β sheets are oriented perpendicularly to the membrane (Nabedryk et al., 1988).

4.7.2.2 Recent techniques

4.7.2.2.1 Resonance Raman spectroscopy

UV resonance Raman spectroscopy (UVRR), Sec. 6.1, has been used to determine the secondary structure of proteins. The strong conformational frequency and cross section dependence of the amide bands indicate that they are sensitive monitors of protein secondary structure. Excitation of the amide bands below 210 nm makes it possible to selectively study the secondary structure, while excitation between 210 and 240 nm selectively enhances aromatic amino acid bands (investigation of tyrosine and tryptophan environments) (Song and Asher, 1989; Wang et al., 1989, Su et al., 1991). Quantitative analysis of the UVRR spectra of a range of proteins showed a linear relation between the non-helical content and a newly characterized amide vibration referred to as amide S, which is found at 1385 cm^{-1} (Wang et al., 1991).

UV resonance Raman saturation spectroscopy (Sec. 6.1) proved to be a useful approach to monitoring photophysical relaxation processes in complex systems and environments (Asher, 1988; Teraoka et al., 1990). The value of this technique of determining tyrosine, phenylalanine, and tryptophan residue excited state relaxation rates is demonstrated by investigations of lysozyme, myoglobin, and glucagon (Harmon et al., 1990). The application of UV resonance Raman saturation spectroscopy to monitor protein conformations and dynamics is in the process of being developed. The R \rightarrow T structural change in hemoglobin has been followed by time resolved UVRR. Deconvolution and difference spectroscopy have been used to distinguish changes in individual aromatic amino acid signals (Rodgers et al., *in the press*). Time resolved resonance Raman spectroscopy also made it possible to study carbomonooxyhemoglobin photolysis (Kaminaka et al., 1990).

Resonance Raman spectroscopy (RR), Sec. 6.1, is a powerful technique in the field of enzymology. An extremely accurate structure-reactivity correlation was obtained by observing the wavenumber of the carbonyl group during catalytic attack by acyl serin proteases (Tong and Carey, 1990). Evidence of bonds formed with substrates at more

than one location near the active site was supplied by RR, which was used to study acyl groups in papains (Tonge et al., 1991). These findings have important implications for enzymology and drug design. The investigation of enzyme-substrate complexes at low temperature (5K) has made it possible to monitor the effects of freezing out protein motions and to understand the role of protein dynamics in catalysis (Kim and Carey, 1991).

Bacteriorhodopsin : the retinal binding protein bacteriorhodopsin (BR), which is found in the cell membrane of halobacteria, is able to transport protons across the membrane upon illumination. The resulting proton gradient is used by the cell as an energy source to drive metabolic processes under anaerobic conditions. Light absorption initiates a cyclic process during which the parent chromophore BR570 passes through various intermediate states and finally returns to its original state within a few milliseconds. The different intermediates of the BR photocycle have been studied by time resolved resonance Raman spectroscopy (Stockburger and Alshuth, 1986; Diller and Stockburger, 1988; Fig. 4.7-4) and ultrafast FTIR (Diller et al., 1991; Nolker and Siebert, 1991). The role of electrostatics in the primary conversion of rhodopsin to bathorhodopsin was elucidated by investigating isotopically labeled retinal chromophores by resonance Raman spectroscopy (Deng and Callender, 1987; Deng et al., 1991), see also Sec. 6.6.3.

Carotenoids : carotenoids have the dual function of light harvesting and photoprotection. The carotenoid configurations are naturally selected to fulfill these functions: the all-trans configuration serves as light harvesting complex, while the 15 *cis* configuration has a photoprotective function (Lutz et al., 1987; Koyama, 1990). Raman spectroscopy has demonstrated that free and bound carotenoids, which exhibit the same Raman frequencies, have essentially the same 15 *cis* configuration, but that the polyene backbone is somewhat twisted. Key bands which make it possible to distinguish central bent configurations have been found (Koyama et al., 1988). Transient Raman spectroscopy was applied to determine the T1 state structure of *trans* β carotenoids (Hashimoto and Koyama, 1989; Hashimoto et al., 1991). Picosecond and femtosecond Raman spectroscopy was used to study vibrational relaxation in carotenoids (Hayashi et al., 1991; Okamoto et al., 1991; Noguchi et al., 1991; Koyama, 1991). Similarly, the transfer of energy from carotenoids to bacteriochlorophyll in photosynthetic light harvesting complexes was also investigated by RR spectroscopy (Hayashi et al., 1989; Noguchi et al., 1990).

Chlorophylls: chlorophylls have a variety of functions in photosynthetic systems, including collection of photons, transfer of excitation energy, operation of the primary photoinduced charge separation, and transfer of the resulting photoelectrons. Resonance Raman spectroscopy offers the possibility of selectively observing chlorophylls in their native structures (Lutz, 1984; Koyama et al., 1986; Tasumi and Fujiwara, 1987; Lutz and Robert, 1988; Nozawa et al., 1990; Lutz and Mantele, 1991). Transient Raman spectroscopy is a unique method of revealing the excited state structures of chlorophylls. The T1 and S1 states were revealed by nanosecond Raman spectroscopy (Nishizawa et al., 1989; Nishizawa et al., 1991; Nishizawa and Koyama, 1991).

Bacterial reaction centers have also been studied extensively by resonance Raman spectroscopy, Fig. 4.7-4 (for a review, see Robert, 1990; Mattioli et al., 1991a).

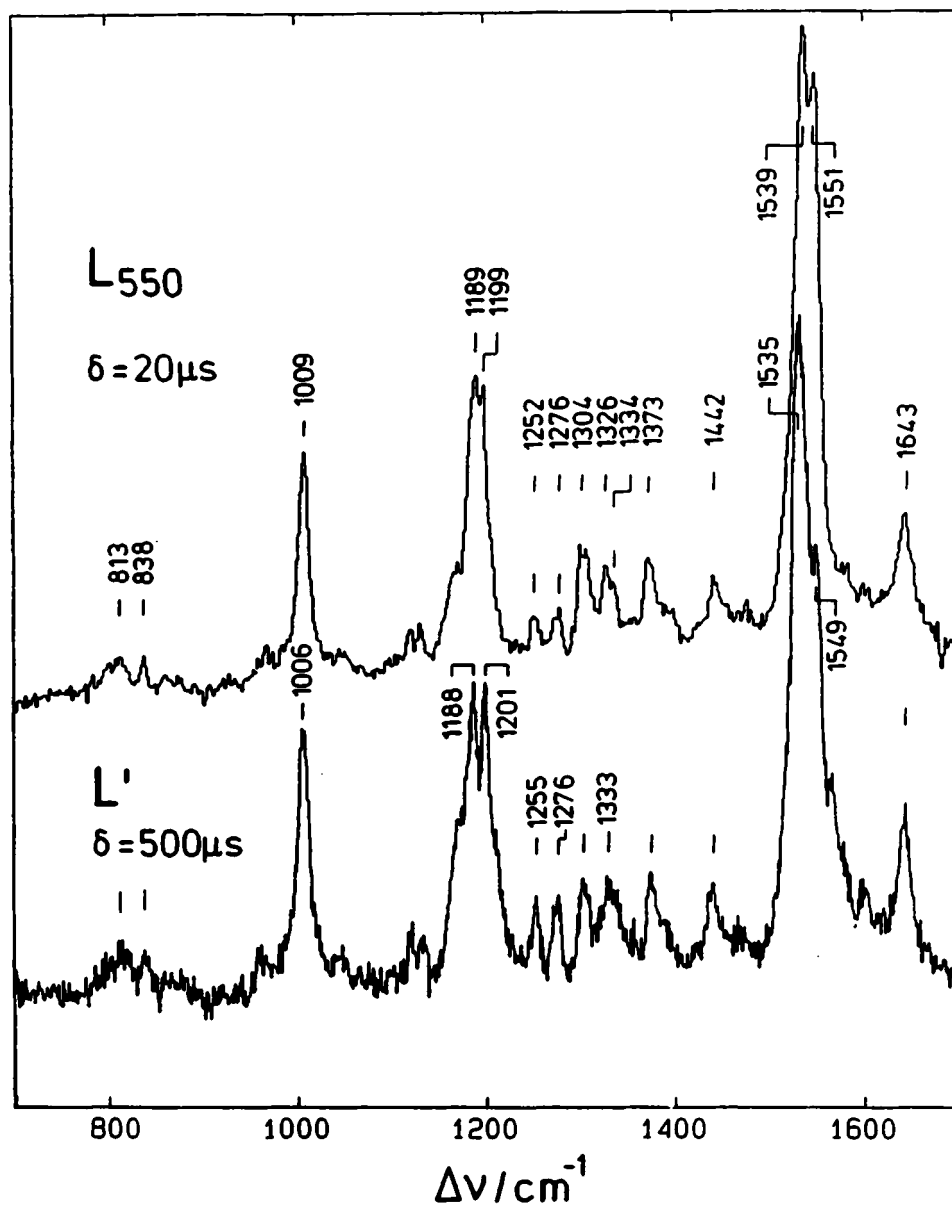


Figure 4.7-4 RR spectra of L intermediates of bacteriorhodopsin at delay times of 20 and 500 ms (from ref. Diller and Stockburger, 1988).

4.7.2.2.2 Surface enhanced Raman spectroscopy

Since the pioneering work by Cotton et al. on heme proteins (Cotton et al., 1980), surface enhanced resonance Raman spectroscopy (SERRS), Sec. 6.1, has been used to study a large variety of biomolecules, such as retinal proteins (Nabiev et al., 1985), flavoproteins (Coperland et al., 1984; Holt and Cotton, 1987), chlorophylls (Cotton and Van Duyne, 1982; Hildebrandt and Spiro, 1988), and oxyhemoglobins (de Groot and Hesters, 1987). The advantages of this technique include low sample concentration and fluorescence quenching. The main question is whether or not the native structure and function of the molecule is preserved on the metal surface.

SERS may be employed to analyze highly complex biomedical samples. Extracts obtained by homogenizing human lenses, for instance, have been investigated by SERS to selectively probe for certain biological components, such as adenine containing molecules (5'Amp), aromatic acids (tyrosine and tryptophan) (Sokolov et al., 1991), or lens pigments (Nie et al., 1990).

Surface enhanced hyper Raman (SEHRS), Sec. 6.1, is capable of providing new vibrational information, due to its peculiar selection rules: vibrational modes which are inactive in both IR and Raman may be active in hyper Raman scattering. The inherently weak signal of hyper Raman scattering may be enhanced by a factor of 10^{13} via a surface process which is similar to SERS. Recent efforts to apply SEHRS to biomolecules include the investigation of 3-hydroxykynurenone, which is a near-UV absorbing chromophore in the human eye lense, and copper chlorophyllin, both of which were studied at a concentration of $2\cdot10^{-5}$ M (Yu and Nie, 1990). Since 3-hydroxykynurenone has low symmetry, all hyper-Raman active modes are also Raman active, which is why the SERS and SEHRS spectra of this compound resemble each other. The SERS and SEHRS spectra of chlorophyllin, on the other hand, differ considerably, which proves that SEHRS makes it possible to extract new vibrational hence structural information from biomolecules.

4.7.2.2.3 Near IR FT Raman spectroscopy

Near infrared Fourier transform Raman with laser excitation at $1.06\text{ }\mu\text{m}$ precludes electronic absorption, almost completely eliminating photolytic sample decomposition and fluorescence interference. It has been applied to the study of photolabile biomolecules, i.e., *cobalamins* (Nie et al., 1991), *bacteriorhodopsin* (Gerwert et al., 1990), Sec. 6.6.3, *chlorophylls* (Mattioli et al., 1990, 1991b), *cytochrome c*, and model *metalloporphyrins*. Other investigations concern complex biological materials, such as pigmented squirrel eye lenses, normal and cataractous human eye lenses, bones, teeth, blood vessels, liver tissue, and muscles. Characteristic Raman lines of the major components of these materials have been identified. For example, research on the human lens by near IR FT Raman spectroscopy has shown that aging and the formation of senile cataract in the human lens are accompanied by a number of processes, including conversion of SH to disulfide, decrease of the tryptophan concentration, and changes in the protein conformations (Nie et al., 1990). Combination of FT Raman with fiber optics technology might lead to developments such as FT Raman fibroscopes. Two dimensional IR FT Raman

spectra of human cataractous crystalline lenses have been obtained under a microscope with a spatial resolution in the range of 10 µm (Hoffman et al., 1990).

4.7.2.3 The cytochrome *c* system

Cytochrome c is an essential component of the mitochondrial respiratory chain. O₂ reduction during cell respiration is catalyzed by a family of hem-copper proteins, the cytochrome oxydases (*cytochrome c* oxydase in eukaryotes). In the course of cell respiration, electrons originating from the oxydation of food to CO₂ reduce O₂ to water molecules. Electrons are transferred to the metallic center of cytochrome oxydase, where catalysis occurs. The structure and electronic transfer properties of *cytochrome c* adsorbed on silver electrodes have been studied by surface enhanced resonance Raman spectroscopy (SERR). It was shown that the protein envelope prevents the heme group from coming in direct contact with the metal surface. Cytochrome *c* on the metal surface may thus be used to study the electron donor and acceptor functions of its heme group (Hildebrandt and Stockburger, 1984). It has been proposed that biological electron transfer reactions are controlled by electron field induced conformational transitions of *cytochrome c* upon complex formation with its physiological redox partners (Hildebrandt and Stockburger, 1989 a,b). SERR spectroscopy may help to elucidate the electron transfer reactions of adsorbed species and thus provide complementary information in addition to conventional electrochemical methods. Resonance Raman spectroscopy was used in conjunction with site directed mutagenesis and X-ray crystallography to provide important information concerning chemical interactions at the enzyme active site of *cytochrome c oxydase* (Smulevitch et al., 1988a, b, 1989, 1990a, b). Transient absorption and resonance Raman spectra of the intermediates of the reaction of cytochrome oxydase with oxygen were obtained (Ogura et al., 1989; Egawa et al., 1991). Studies involving resonance Raman spectra excited at 441.6 nm demonstrate the feasibility of monitoring the structures of oxidized flavins as well as ferrihemes of the enzyme (Desbois et al., 1989). Early intermediates of the reduction of O₂ by cytochrome oxydase are reflected by a Fe-O stretching vibration in the respective time resolved resonance Raman spectra (Varotsis et al., 1989). A dioxygen adduct of cytochrome a3 was detected during the mixed valence cytochrome oxydase/dioxygen reaction (Varotsis et al., 1990). Very recently, the Cu A-ligand stretching resonance Raman band of *cytochrome c oxydase* was observed with a new CCD Raman device with 840 nm excitation (Takahashi et al., 1991).

4.7.2.4 Nucleoproteins

4.7.2.4.1 Chromatin

Chromatin, the main constituent of chromosomes, is composed of high molecular weight double stranded DNA comprising two classes of proteins, i.e., five histones (H1, H2a,

H2b, H3 and H4, in some cases H1 is replaced by another protein H5) and a considerable number of non-histone proteins, all in very small amounts. A repetitive structural subunit, the nucleosome, was isolated, crystallized, and investigated by X-ray diffraction (Finch et al., 1977) and neutron scattering (Pardon et al., 1977) (for a review see Felsenfeld, 1978).

Vibrational spectroscopy was used to study native chromatin as well as reconstituted DNA-histone complexes. IR (Liquier et al., 1979) and Raman spectra (Goodwin and Brahms, 1978; Savoie et al., 1985) show that the DNA in chromatin adopts a B type conformation. The important role adopted by the α helical parts of the histones in stabilizing the B conformation of histone-DNA complexes was demonstrated by IR (Taillandier et al., 1984b). Raman spectra of chromatin have made it possible to localize histone-DNA interactions in the minor groove and non-histone protein-DNA interactions in the major groove (Goodwin and Brahms, 1978).

UV resonance Raman spectra of model histone-DNA complexes show that H2A and H2B preferentially bind to G-C base pairs, while H3 and H4 bind to A-T base pairs (Laigle et al., 1982).

Recent progress in confocal micro Raman spectroscopy has made it possible to investigate chromosomes and whole single living cells (Puppels et al., 1990, 1991). A spatial resolution of less than $1 \mu\text{m}^3$ was obtained. Different Raman spectra have been recorded of the cytoplasm and the cell nucleus. The spectrum of the nucleus consists of lines attributed to DNA and protein vibrations, strongly resembling the spectra of isolated chromatin. The search for left-handed Z form DNA in metaphase chromosomes is in progress.

Raman spectroscopy may be used to study complex biological systems, such as intact lenses, which can be investigated *in vivo* (Bertoluzza and Fagnano, 1989).

4.7.2.4.2 Viruses

Viruses contain a nucleic acid molecule (single stranded RNA, single or double stranded DNA), encapsulated in a protein coating. One or more classes of protein molecules may be present, but their arrangement in the capsid is usually extremely symmetrical. Viral capsids contain several hundreds of proteic subunits (for a review of virus structures, see Jurnak et al., 1984). The Raman spectrum of a virus contains lines which, on the one hand, are characteristic of the nucleic acid and on the other hand characterize the proteins. In the spectra of solutions of equivalent molar concentrations, the relative intensity of the protein lines is usually three to four times weaker than the lines of nucleic acids. Thus, depending on the composition of the virus, the Raman spectrum will be dominated either by bands of the nucleic acid (Sec. 4.7.1.3) or by protein bands (Sec. 4.7.2.1). Both the nucleic acid conformation and the protein geometry of a wide variety of viruses have been elucidated by Raman spectroscopy. The list includes RNA viruses, such as bacteriophages R17 (Hartman et al., 1973), MS2 (Thomas et al., 1976), and plant viruses, including TMV (Shie et al., 1978), single stranded DNA viruses from filamentous bacteriophages, such as Pf1 and fd (Thomas and Murphy, 1975), and double stranded DNA viruses, such as T7 and P22 bacteriophages.

4.7.3 Biomembranes

Since Chapman and coworkers (Chapman et al., 1966) first attempted to investigate the membrane structure by vibrational spectroscopy, there has been considerable technical improvement. Infrared and Raman spectroscopy are now routine tools for structural investigations in membranes (Fringeli and Gunthard, 1981 for ATR-IR; Casal and Mantsch, 1984 and Mendelsohn and Mantsch, 1986 for FTIR; Verma and Wallach, 1983; Levin, 1984 for classical Raman spectroscopy and Levin and Neil Lewis, 1990 for FT-Raman spectroscopy).

A cell membrane consists mainly of a lipid matrix, which serves as a cell permeability barrier, and a skeleton containing proteins and other constituents. The lipid content depends on the type of cell; there are two main classes of lipids, i.e., phospholipids and glycolipids. Most mammalian membranes also contain another important lipid, cholesterol. Unlike nucleic acids and proteins, the primary features of lipids are rarely reflected by the properties of individual molecules, but rather through a combination of several molecules. The best known membrane structure is the lamellar one, in which phospholipids are arranged in bilayers with two hydrocarbon arrays in the internal hydrophobic region and the polar groups exposed to the external aqueous interfaces. Peripheral proteins are attached to these groups, and intrinsic proteins are embedded in the hydrophobic region. The proteins are responsible for most of the activity of biological membranes. Their conformational changes and structural reorganization is believed to depend on the interaction with the lipid bilayer. In this context, vibrational spectroscopy may help to elucidate their interactions and conformational changes of the protein or the lipid molecules.

4.7.3.1 Characteristic wavenumbers and spectral regions usually used for membrane studies

Polar phospholipids are investigated best in the spectral region between 3100 and 700 cm^{-1} . The infrared and Raman spectra of lipids may be divided into bands which originate from molecular vibrations of the acyl chains, of the head group, and of the interfacial region. The characteristic wavenumbers of different groups are tabulated in the references listed above. The IR and Raman bands of specifically deuterated fatty acids and completely deuterated acyl chains have also been characterized (Mendelsohn and Maisano, 1978; Lee et al., 1984; Devlin and Levin, 1990).

4.7.3.1.1 Infrared absorption bands

Acyl chain modes. The two strongest bands around 2850 cm^{-1} and 2920 cm^{-1} , corresponding to the symmetric and antisymmetric stretching modes of CH_2 groups are conformationally sensitive and their change is indicative of modification of the *trans/gauche* ratio. They are shifted towards higher wavenumbers if either the content of *gauche* conformer or the disorder of the chains increases. Their bandwidths, which are related to the mobility of the chains, are also diagnostic parameters (Amey and Chapman, 1983;

Mendelsohn and Mantsch, 1986). The less intense band at 1470 cm^{-1} , which corresponds to the scissoring mode of CH_2 groups, is in some cases useful. Mendelsohn used the rocking mode wavenumbers of selectively deuterated methylene groups to monitor the conformational disorder in bilayers (Mendelsohn, 1991).

Head group and interfacial region modes. The strongest band corresponds to the stretching vibrations associated with the double bond C=O stretching mode around 1735 cm^{-1} . This band is easily observed by using deuterated water. Self-deconvolution showed that in the spectra of diacyl lipids this broad band consists of two components. These components, at 1742 cm^{-1} and 1727 cm^{-1} , had previously been assigned to the stretching vibrations of the non-equivalent sn1-C=O and sn2-C=O groups of the phospholipid molecules. However, more detailed studies involving $^{13}\text{C}=\text{O}$ labeled lipids have recently demonstrated that the band at 1742 cm^{-1} corresponds to non-hydrogen-bonded C=O stretching, while the one at 1727 cm^{-1} corresponds to hydrogen-bonded C=O stretching (Mantsch and Hubner, 1991). Two other strong bands are associated with the PO_2^- symmetric stretching vibration (around 1088 cm^{-1}) and with the antisymmetric stretching vibration (around 1232 cm^{-1}).

4.7.3.1.2 Characteristic Raman bands

The region of CH stretching vibrations ($3000\text{-}2800\text{ cm}^{-1}$). The strongest bands in the spectra of saturated acyl chains around 2850 cm^{-1} and 2880 cm^{-1} are attributed to the symmetric and antisymmetric stretching vibrations of the CH_2 groups. Other Raman bands around 2932 cm^{-1} , 2952 cm^{-1} , and 2964 cm^{-1} are attributed to the motions of the terminal CH_3 groups of the acyl chains. An important feature of the CH_2 stretching bands around 2850 cm^{-1} and 2880 cm^{-1} is their intensity ratio $I(2850)/I(2880)$, which is very sensitive to the chain packing. This ratio and that of $I(2932)/I(2880)$ can be used to determine relative bilayer order/disorder parameters. The $I(2850)/I(2880)$ ratio in particular reflects interchain interactions, whereas the $I(2932)/I(2880)$ ratio indicates effects originating from changes through intrachain *trans/gauche* isomerization which are superimposed on the chain-chain interactions (Levin and Neil Lewis, 1990).

The region of C-C stretching vibrations ($1150\text{-}1050\text{ cm}^{-1}$). Other useful Raman bands are found in the $1150\text{-}1050\text{ cm}^{-1}$ range, corresponding to the skeletal optical region (C-C stretching vibrations). The sharp bands around 1060 cm^{-1} and 1130 cm^{-1} have been assigned to all-*trans* chain segments, and the broad band at 1090 cm^{-1} is attributed to chains with *gauche* configurations (Gaber et al., 1978; Pink et al., 1980). The intensity ratio $I(1060)/I(1090)$ or $I(1130)/I(1090)$ and the wavenumber difference $\Delta\nu(1090\text{-}1060\text{ cm}^{-1})$ or $\Delta\nu(1130\text{-}1060\text{ cm}^{-1})$ have been used to monitor the chain order or the membrane fluidity. The sizes of units jointly undergoing chain melting can also be evaluated.

4.7.3.2 Phospholipid model membranes

Phospholipid assemblies may exist in many physical states, depending on their molecular structure, temperature, and environment (Marsh, 1991). The bilayer is the major structure of biological membranes, and the investigated model membranes were often in the gel-

like state, i.e., L β or P β' , or in the liquid crystalline state L α , in which the chain melts at the transition temperature T_m . Since lipid thermotropic behavior is directly relevant for the structure and function of natural membranes, most studies by vibrational spectroscopy deal with this transition.

4.7.3.2.1 Phase transitions investigated by vibrational spectroscopy

The gel-like to liquid crystalline phase transition is clearly reflected by the relatively sudden *increase* in wavenumber of the CH₂ stretching band around 2850 cm⁻¹ in the IR absorption spectrum or by the *decrease* in wavenumber of the C=O stretching band contour around 1735 cm⁻¹. The *increasing* wavenumber of the CH₂ stretching band reflects a *decrease* in the chain order. Besides, the bandwidth suddenly changes as a result of the mobility change when the acyl chains undergo phase transition. The Raman spectra show other consistent changes, in particular the increasing intensity ratios I(2850)/I(2880) and I(2932)/I(2880) (Snyder et al., 1980; Litman et al., 1991).

The C=O stretching band in the IR absorption spectrum is equally useful. Phase transition shifts this band from 1738 cm⁻¹ towards lower wavenumbers; it is found around 1733 cm⁻¹ as phospholipid vesicles undergo a gel to liquid crystalline phase transition T_m . Mantsch interpreted the shift towards lower wavenumbers of the overall band contour peak as resulting from the intensity increase of the component at 1727 cm⁻¹ upon a change in hydration (by hydrogen bonding) during the transition (Mantsch and Mc Elhaney, 1991).

Finally, it should be mentioned that the temperature profile may indicate the possible existence of heterogeneities or microdomains. Raman spectra have shown such phase separations in bilayers prepared with DHPG/DPPC mixtures and in lipids containing highly unsaturated sn2-acyl and completely saturated sn1-acyl, such as POPC, PAPC, and PDPC (Litman et al., 1991).

4.7.3.2.2 The interdigitated phase

There are special conditions in which the gel-like phase of a phospholipid appears in a particular form, i.e., the interdigitated phase. This phase may be induced by a number of proteins (Boggs and Moscarello, 1982), cations (Cunningham and Lis, 1986), or other amphiphilic agents, such as chlorpromazine or tetracaine (Mc Intosch et al., 1983). These amphiphilic agents typically interact with the polar aqueous interface of one layer of the phospholipid bilayer and penetrate into the hydrophobic region, but not deeply, creating vacancies for the penetration of the acyl chains of the opposite layer. The interdigitated phase may also be induced by dissymmetry of the acyl chains (Huang et al., 1983; Levin et al., 1985). In this case, vacancies are created by a mismatch in the length of the acyl chains. The thickness of bilayers undergoing transition to the interdigitated phase is reduced, the average sectional area per polar head increases, whereas the arrangement of the chains generally becomes more compact.

O'Leary and Levin (Raman spectroscopy) and Siminovitch et al. (FTIR) were the first to employ vibrational spectroscopy to explore this phase (O'Leary and Levin, 1984;

Siminovitch et al., 1987). By comparing DPPC dispersed in water (which does not exist in an interdigitated phase) and DPPC dispersed in perdeuterated glycerol (which was known to be in an interdigitated phase at low temperature), Levin and collaborators showed that the interdigitated phase can be monitored by studying the Raman intensity ratios I(2850)/I(2880) and I(2932)/I(2880) (Levin et al., 1985).

Concerning IR spectroscopy, it was demonstrated by high-pressure FTIR that the spectra of the non-interdigitated and those of the interdigitated phase exhibit marked differences in terms of splitting of the methylene scissoring band δCH_2 around 1468 cm^{-1} and its correlation field component $\delta^*\text{CH}_2$.

4.7.3.2.3 Effect of drugs on phospholipid model membranes

It is well known that there is a relationship between the response to drug action and the lipophilic character of a drug (Hansch and Clayton, 1973). When a drug molecule diffuses into a cell and provokes a certain cellular response, it first encounters the cell membrane. The effect of various drugs on phospholipid model membranes was investigated by vibrational spectroscopy. The ultimate goal of these studies is to locate interactions in different regions of the bilayer. These interactions must *a priori* be reflected by physical properties involving the behavior of the bilayer. Physical parameters which are changed by the presence of drugs may play an important role in the activity of proteins and thus in the response to drug action.

Drugs may interact with a phospholipid bilayer in the hydrophobic region or/and at the polar heads. In the hydrophobic region, some drugs fluidize the bilayer by shifting the liquid crystalline to gel-like phase transition towards a lower temperature and thus extend the temperature range in which the bilayer exists in the liquid crystalline phase. This is revealed by the high wavenumber of the CH_2 stretching mode. In general, the presence of drugs does not affect the wavenumber of this mode at temperatures far from the transition temperature. Drugs do alter the profile of the transition curve in that they change the transition point and the transition width (Hantz et al., 1989, 1992). This behavior is illustrated in Fig. 4.7-5, which shows the effect of the amphiphilic drug *loperamide* (which belongs to the opiate family and shows an antidiarrheal effect). The liquid crystalline to gel-like phase transition is split. This may be due to a rearrangement of the bilayer in the liquid crystalline state prior to transition to the gel phase. A second example is *halothane*, a volatile general anesthetic (Tsai et al., 1990). It seems that halothane interacts with the polar interface and decreases the fluidity of the outer face of the bilayer, while it increases the fluidity of the inner region. Monitoring the intensity ratio I(2932)/I(2880), showed that in the gel phase halothane is excluded from the hydrophobic region but not from the polar head outer face (Craig et al., 1987). Interesting examples are those of local anesthetics, such as *tetracaine*, and membrane stabilizing agents, such as *D-propranolol*, which induce interdigitation (Auger et al., 1988; Cao et al., 1991).

The effect of *adriamycin*, an anti-tumor chemical, on cardiolipin (CL), a phospholipid specific to the inner mitochondrial membrane, was studied by ATR-IR spectroscopy. It was shown that in the very stable complex the structures of both adriamycin and cardiolipin are different from those of the pure substances (Goormaghtigh et al., 1987).

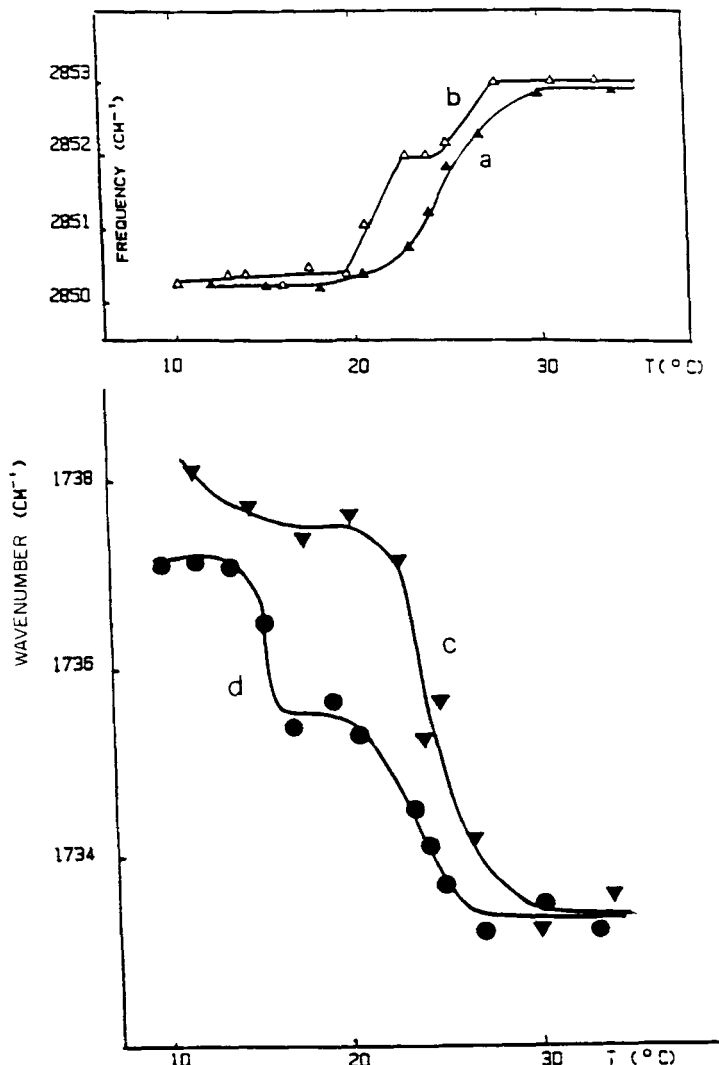


Figure 4.7-5 Temperature dependence of the wavenumbers characteristic of a) and b) CH_2 symmetric stretching and c) and d) $\text{C}=\text{O}$ stretching in DMPC LUV. a) and c) in the absence of loperamide, b) and d) in the presence of loperamide. This is to emphasize that the low-temperature transitions of $\nu(\text{CH}_2)$ and $\nu(\text{C}=\text{O})$ occur at two different temperatures (Hantz et al., 1989).

4.7.3.2.4 Interactions with ionophores

Some peptide antibiotics act as trans-membrane ion channels. Vibrational spectroscopy shows that ionophores, such as *gramicidin A*, *valinomycin*, *nystatin*, and *amphotericins*, interact with phospholipid bilayers (Susi et al., 1979).

Gramicidin A is a linear pentadecapeptide which has frequently served as a model for an internal protein. IR spectroscopy shows that above the transition temperature

T_m and at low concentration, gramicidin A slightly decreases the lipid gauche isomers and increases the chain motion. This effect is more pronounced below T_m . Moreover, gramicidin A broadens the transition (Lee et al., 1984). Raman spectroscopy also reveals an increase in the fluidity of the gel phase of DPPC (Susi et al., 1979).

Vibrational spectroscopy also shows interactions of polyene antibiotic ion channels *nystatin* and *amphotericin B* with phospholipid bilayers (Bunow and Lewin, 1977a; Iqbal and Weidekamm, 1979; Van de Ven et al., 1984). In particular, Fourier Transform Raman spectroscopy demonstrates that at high temperature, the amphotericin A complex of DPPC/cholesterol is more ordered, whereas the amphotericin B complex is as ordered as the pure lipid/cholesterol system. In the low temperature phase and in the presence of the sterol-antibiotic complex, the bilayers were suggested to be in the interdigitated state (Levin and Neil Lewis, 1990).

4.7.3.2.5 Effect of polycations on charged lipids

These polycations are known to interact with negatively charged phospholipids and can induce the fusion of PS and PA vesicles (Kouaouci et al., 1985; Bicknell-Brown et al., 1986; Casal et al., 1987a, b; Laroche et al., 1990 and 1991). By using FTIR, Casal et al. showed that with fully hydrated saturated PS bilayers, divalent cations Ca^{++} bind to the PO_2^- groups of DMPS, resulting in the loss of hydration, a changing conformation of the glycerol backbone, and a more ordered packing of the acyl chain. For poly-L-lysine (PLL), it was shown that the effect on DMPA depends on the degree of polymerization of the peptide.

4.7.3.3 Phospholipid bilayers in the presence of cholesterol, membrane proteins, and peptides

Cholesterol and membrane proteins, including structural ones such as *glycophorin* and *myelin basic protein* and functional ones such as $\text{Ca}^{2+}-\text{ATPase}$, *bacteriorhodopsin*, and *cytochrome c*, are important components of biological membranes. Cholesterol-lipid and a number of protein-lipid interactions have therefore been extensively investigated by vibrational spectroscopy. Interactions of hormones and toxins with phospholipid bilayers were also investigated.

4.7.3.3.1 Effect of cholesterol

Vibrational spectroscopy shows that inclusion of cholesterol in phospholipid bilayers tends to decrease the fluidity of the hydrophobic region above the main transition point T_m and to increase it below T_m . The presence of cholesterol in DPPC or DMPC multilayered vesicles does not affect the transition point but simply broadens the transition by decreasing the CH_2 -stretching wavenumber in the liquid crystalline phase and by increasing it in the gel-like phase (Lippert and Peticolas, 1971; Spiker and Levin, 1976; Casal and Mantsch, 1984). There is also evidence that lipid-cholesterol interaction increases the amount of bound water in the headgroups (Levin et al., 1985).

4.7.3.3.2 Interactions with membrane proteins

Interactions with lipid bilayers may be illustrated by some typical membrane proteins.

Glycophorin : The effect of glycophorin, an integral protein from the human erythrocyte membrane, on individual phospholipids or mixtures of these was investigated by FTIR (Dluhy et al., 1983; Mendelsohn et al., 1986) and by Raman spectroscopy (Taraschi and Mendelsohn, 1980; Pink et al., 1980). Glycophorin lowers the gel-like to liquid crystalline phase transition. The *gauche* conformer content is increased in the gel phase, whereas there is a little effect on the liquid crystalline phase. The decrease of the transition point indicates disruption of the chain packing in the presence of this protein in the hydrophobic region of the bilayer. However, no evidence was found of an immobilized lipid component. FTIR indicates that glycophorin interacts preferentially with negatively charged lipid PS and that there is no neutral DPPC in the bilayer of the ternary DPPC/PS/glycophorin system. Other proteins, such as *myelin basic protein* (from the central nervous system myelin) and Ca^{2+} -ATPase (from sarcoplasmic reticulum), also increase the *gauche* content in the gel-like phase (Surewicz et al., 1987c; Amey and Chapman 1983). *Bacteriorhodopsin* (from the purple membrane of *Halobacterium halobium*) shows the same increase below T_m but has no effect on DMPC bilayers above T_m (Lee et al., 1984).

Cytochrome c, on the other hand, interacts with phospholipid vesicles, causing significant conformational changes in the protein and lipid systems. Resonance Raman spectroscopy made it possible to establish a correlation between structural changes in the protein and in the charged lipids DMPG and DOPG upon complex formation. Moreover, a marked narrowing of IR absorption bands involving C=O group vibrations and correlation field splitting of the CH₂ scissoring band were observed if DMPG/cytochrome c complexes were incubated at low temperature. This points to a highly ordered and tightly packed lipid gel phase, caused by electrostatic interaction with the head groups of the lipids (Muga et al., 1990). The effect of ferricytochrome c on DPPC, cardiolipin, and DMPA/DMPCd₅₄ was studied by Raman spectroscopy (Vincent and Levin, 1981, 1988 and 1991).

Live and deproteinated plasma membranes of *Acholeplasma laidlawii* were investigated by FTIR (Casal et al., 1980; Cameron et al., 1985). The temperature profiles of the gel to liquid crystalline phase transition of intact and deproteinated membranes, monitored by $\nu_{as}(CD_2)$, differ considerably. In intact membranes, the transition is broad and at temperatures within the range of the phase transition the live mycoplasma is able to keep the fluidity of its plasma membranes at a much higher level than that of the isolated plasma membrane. Native and reconstituted *sarcoplasmic reticulum* were investigated by Mendelsohn et al. (Mendelsohn et al., 1984). It appears that the protein Ca^{2+} -ATPase interacts preferentially with the DOPC component of the membrane. A survey of these studies is available (Mantsch and McElhaney, 1991).

4.7.3.3.3 Interaction with hormones

Interaction with phospholipid bilayers of a number of hormones, such as *atriopeptin III*, an atrial natriuretic peptide, and of *calcitonin* was investigated by Surewicz et al.

(Surewicz et al., 1987a, b). FTIR shows that below T_m , calcitonin decreases the conformational order of the acyl chains of DMPG and DMPA. However, the interaction with DMPA is weaker, due to the difference in the degree of intermolecular interaction between the headgroups of the two lipids.

4.7.3.3.4 Effect of toxins

The effect of toxins such as *melittin* (from the honey-bee venom), *myotoxin a*, and *cardiotoxin* (from the snake venom) was investigated by vibrational spectroscopy (Pézolet et al., 1982; Faucon et al., 1983; Liddle and Tu, 1985; Lafleur et al., 1987). Monitoring the Raman intensity ratio $I(1060)/I(1080)$ indicated that the lipid/melittin assemblies in DPPC are characterized by a high conformational order, little intermolecular chain-chain interaction, and a low cooperativity of the gel-like liquid crystalline phase transition. The effect of *ricin*, a toxic lectin, on DPPC and DPPC-cerebroside mixtures was studied by Raman and IR spectroscopy. It was suggested that ricin mainly interacts with the interfacial domains of the bilayers (Picquart et al., 1989).

4.7.3.4 Glycolipids

Glycolipids constitute the second class of biomembranes. Like phospholipids, they possess acyl chains, but they have different polar heads containing at least one sugar unit. Heading the list are glycosphingolipids, divided into cerebrosides and gangliosides. Gangliosides are abundant in the central nervous system. In *Escherichia coli* and *Salmonella minnesota*, the outer leaflet of the outer membrane is made up of lipopolysaccharides, consisting of a poly or oligosaccharide linked to a lipid component known as *lipid A*.

The constitutions of gangliosides are complex, since their head groups contain oligosaccharide chains with varying amounts of derivatives of a negatively charged sugar, i.e., neuraminic acid. Their thermotropic behavior depends on the number and position of the charges in the head group (Bach, 1983). In contrast to phospholipids, gangliosides associate in aqueous solution to form micelles instead of bilayers. *Gangliosides GM1*, which are miscible with egg lecithin, were studied by FTIR as a mixture with DMPC as host lipid. The amide I and II bands were compared with those of sphingomyelin and the packing investigated. Addition of GM1 seems to stabilize the DMPC bilayer, reflected by a shift of the DMPC transition point towards a higher temperature (Muller et al., 1991).

Lipid A was investigated by FTIR, X-ray diffraction, and fluorescence techniques (Naumann et al., 1987). Analysis of the CH_2 scissoring vibrations showed that lamellar structures exist at temperatures below 30 °C, but that no stable closed vesicles are formed. Orientation measurements of lipopolysaccharides prepared from *E. coli* and *Salmonella minnesota* by ATR-FTIR also showed a highly ordered gel phase. Besides, the transition from the gel phase α to the liquid crystalline phase β was also studied (Brandenburg and Seydel, 1988).

Conclusion

Vibrational spectroscopy has proven to be a powerful method of studying biological molecules. Continued technical improvement (FT spectroscopy, time resolved spectroscopy, etc.) open up new domains of investigation which help solve fundamental problems of structure-function correlation at the molecular level. Many domains are beginning to be explored, and results are expected in the fields of compatible biomaterials, intelligent drug development, and in vivo spectroscopic measurement.

Acknowledgments

The authors would like to thank all colleagues who have kindly provided their recent and valuable results, and apologize for not having been able to quote all of the material sent to us and the excellent literature in the field.

Abbreviations

The nomenclature of lipids is according to IUPAC (IUPAC-IUB 1976)

CL: cardiolipin

DMPC: dimyristoyl phosphatidylcholine

DOPC: dioleoyl phosphatidylcholine

DPPC: dipalmitoylphosphatidylcholine

DMPG: dimyristoyl phosphatidylglycerol

PA: phosphatidic acid

PE: phosphatidylethanolamine

PS: phosphatidylserine

POPC: 1-palmitoyl, 2-oleoyl phosphatidylcholine

SM: sphingomyelin

4.8 Conducting polymers, semiconductors, metals, and superconductors*

This section discusses applications of IR and Raman spectroscopy to materials with reasonable or even very high conductivity. These systems generally present special problems in addition to those described in earlier sections. Incident radiation interacts not only with the vibrational excitations of the material but also with the free carriers and with its electronic structure. These interactions may create phenomena such as free carrier absorption, excitation across the energy gap, exciton transitions, or light scattering by free electrons. Excitations are very often in the IR spectral range, particularly in the

* Section 4.8 is contributed by H. Kuzmany, Wien

case of inorganic semiconductors. However, since this book is dedicated to vibrational spectra, electronic effects are only considered inasmuch as they are directly coupled to vibrational excitations. Nevertheless, it seems appropriate to devote the introductory paragraph to the contribution of free carriers and resonance transitions in infrared and Raman spectroscopy.

Of the materials listed in the headline, conducting polymers are probably most attractive to chemists, since the material design and material preparation of these systems definitely falls within their area of interest. Thus, after an introductory section discussing special aspects of the Raman scattering and IR spectroscopy of free carriers, it appears convenient to start with a description of the application of Raman and IR spectroscopy to these systems. From a chemical point of view, conducting charge transfer crystals are closely related to conducting polymers. However, research on the former is in general less intense, which is also true of vibrational spectroscopy. We will review the most important results in subsection 4.8.3. Vibrational spectroscopy is traditionally applied to investigate semiconducting materials which undergo phase transitions, such as many of the IV-VI compounds, or to study systems with free carriers where the latter distort phonon lines. However, classical semiconductors generally have only very few atoms per unit cell and thus exhibit comparatively simple vibrational spectra. They are discussed in subsection 4.8.4. On the other hand, the application of vibrational spectroscopy to novel oxidic superconductors has recently gained considerable interest and is summarized in subsection 4.8.5. Finally, most recently a new phase of carbon was discovered which forms a molecular crystal from soccer ball shaped molecules. These materials were named fullerenes and are particular attractive to vibrational spectroscopy as it will be discussed in subsection 4.8.6.

- There is no appropriate summary which reviews the above mentioned field. Thus, we consider it a challenge to collect the most interesting data and to report on the state of the art and on the success of vibrational spectroscopy in this field. However, there are several excellent review articles which discuss some of the aspects. The following publications are most closely related to our topic: Resonance Raman spectroscopy of conjugated polymers (Kuzmany and Bartonek, 1990a); Raman spectroscopy of oxidic superconductors (Thomsen and Cardona, 1989); Dynamic properties of II-VI semiconductors (Jantsch et al., 1983); Raman scattering of semiconductors (Richter, 1976). Raman scattering of solid state material is extensively discussed by a number of review articles edited by Cardona, and Cardona and Guentherodt in a five volume series on the “Light Scattering of Solids” (Cardona, 1975), (Cardona and Guentherodt, 1982, 1983, 1984, 1989).

4.8.1 Infrared and Raman spectroscopy of systems with free carriers and resonance transitions

As described in previous sections of this book, Raman and IR intensities are determined by the square of the derivative of the polarizability or of the dipole moment with respect

to the normal coordinate of a vibration. Thus, it is necessary to know the contributions of free carriers and resonance transitions. These contributions can only be derived by laborious quantum mechanical calculations which are beyond the scope of this book. However, there are a number of very simple but very useful approximations which are summarized here.

In order to investigate solids or polymer systems with free carriers by IR spectroscopy, it is very convenient to measure the reflectivity instead of absorbance or transmittance. Thus, the problems to be discussed in this context are usually described by a linear response formalism. In its simplest form, this means that the response function (dielectric function) $\varepsilon(\omega)$ of a damped harmonic oscillator is used to describe the interaction between light and matter. The complex form of this function is

$$\varepsilon(\omega) = \varepsilon_\infty - \frac{\omega_p^2}{\omega^2 + i\omega\gamma} + \sum_j \frac{\omega_{pj}^2}{\omega_j^2 - \omega^2 - i\omega\gamma_j}, \quad (4.8-1)$$

where ε_∞ is the contribution of the core electrons. The second part of this equation describes the contribution of the free carriers; while the third part, in which the sum extends over all vibronic oscillations, quantifies the contribution of the latter. Note that the sign of the imaginary part in the denominator of this term depends on the phase angle chosen for the incident wave. γ is the inverse free carrier lifetime, and ω_p equals the plasma frequency of the free carriers:

$$\omega_p^2 = \frac{ne^2}{\varepsilon_0 m},$$

where n , m , and ε_0 are, respectively, the carrier concentration, the carrier mass, and the dielectric constant in the vacuum. In the third part of Eq. 4.8-1, ω_j , γ_j , and ω_{pj} represent, respectively, the frequencies, the damping constants, and the strengths of the vibronic oscillations. Very often, ω_{pj} is replaced by the dimensionless oscillator strength S_j :

$$S_j = \omega_{pj}^2 / \omega_j^2$$

In a generalized oscillator model, the oscillator strength includes the quantum mechanical description of the interaction problem, including the number of oscillators available for interaction.

Maxwell's relation between ε and the complex index of refraction N

$$N = n + i\kappa = \sqrt{\varepsilon}$$

affords the complex amplitude reflection coefficient R for perpendicular incidence:

$$R(\omega) = \rho(\omega)e^{i\phi(\omega)} = \frac{n + i\kappa - 1}{n + i\kappa + 1}, \quad (4.8-2)$$

from which the reflectivity for the intensity

$$r = R(\omega)R^*(\omega) = \frac{(n+1)^2 + \kappa^2}{(n+1)^2 + \kappa^2} \quad (4.8-3)$$

is obtained. Since $\ln(\rho(\omega)) = \ln(\sqrt{r(\omega)})$ and the phase $\phi(\omega)$ of the complex reflection coefficient obey the Kramers-Kronig relation, the full dielectric function may be determined by measuring r . In order to discuss experimental results it is often convenient to use the complex high frequency conductivity $\sigma(\omega)$ instead of r or ε . σ and ε are related according to the Maxwell equations:

$$\varepsilon = \varepsilon_\infty + \frac{i\sigma}{\omega\varepsilon_0} \quad (4.8-4)$$

The real part σ_1 of σ divided by ε_0 is the fraction of energy absorbed per second. All above mentioned relations are valid for the free carrier part as well as for the vibronic part of the dielectric function. In cases where the absorption process dominates the interaction, the latter may be described by the imaginary part of the dielectric function or by the real part of the optical conductivity in the form

$$\alpha = 4\pi\kappa/\lambda = \sigma_1(\omega)/c_0\varepsilon_0 n \quad (4.8-5)$$

Details of the derivation of the harmonic oscillator dielectric function and of the Kramers-Kronig transformation are described in standard textbooks, such as (Kuzmany, 1990b; Kittel, 1976). Eq. 4.8-1 is also well known as the Kramers-Heisenberg dielectric function. The integrated absorption coefficient in Eq. 4.8-5 is very often used in conventional vibronic IR spectroscopy to characterize the concentration of the absorbing species.

The line shape of a single harmonic oscillator transition is Lorentzian, as shown by Eq. 4.8-1. In solids with free carriers, the single phonon oscillator transition is often coupled to a continuum of free carrier transitions. If this is the case, then the resulting line shape is determined by interference of the individual transitions and is given by

$$\alpha(\omega) = \alpha_0 \frac{(Q + \zeta)^2}{1 + \zeta^2}, \quad (4.8-6)$$

where Q is an asymmetry parameter and

$$\zeta = 2(\omega - \omega')/\gamma$$

determines the resonance position with the damping parameter γ . Line shapes obeying Eq. 4.8-6 are referred to as Fano line shapes (Fano, 1961).

Free carrier contributions to Raman scattering are represented by the free carrier term in the perturbation Hamiltonian for the propagation of light in matter. The resulting relation between Raman cross section and response function $\chi(q, \omega) = \varepsilon(q, \omega) - \varepsilon_\infty$ for of a nondegenerate electron gas is

$$\frac{\partial^2 \sigma}{\partial \Omega \partial \omega} = r_0^2 \left(\frac{\omega_i}{\omega_r} \right)^2 V^2 S(q, \omega), \quad (4.8-7)$$

where $r_0 = e^2/4\pi\varepsilon_0 mc_0^2$ is the classical radius of the free electron, and $S(q, \omega)$ equals

$$S(q, \omega) = \frac{\varepsilon_0 \varepsilon_\infty^2 \hbar q^2}{V \pi e^2} (1 - e^{-\hbar \omega / K_B T})^{-1} \text{Im} \left\{ \frac{1}{\varepsilon(q, \omega)} \right\}.$$

In the limit of a dilute electron gas ($\chi(q, \omega) \ll \varepsilon_\infty \text{Im}\{1/\varepsilon(q, \omega)\}$) becomes $(1/\varepsilon_\infty^2) \text{Im}\{\chi(q, \omega)\}$ where $\chi(q, \omega)$ is derived from the Lindhard dielectric function for the degenerate free electron gas. For a nondegenerate electron gas like in semiconductors the dynamical structure factor is obtained with

$$\text{Im}\{\chi(q, \omega)\} = \frac{\pi \varepsilon_\infty \omega}{\lambda_D^2 q^3} \left(\frac{m}{2\pi K_B T} \right)^{1/2} \exp \left(-\frac{m\omega^2}{2q^2 K_B T} \right).$$

λ_D is the Debye screening length for a nondegenerate electron gas. The wave vector q is determined from the scattering geometry. Since $2K_B T/m = v_{th}^2$ the free carrier scattering extends approximately to qv_{th}/c_0 (in wavenumbers). For a degenerate electron gas this limit is qv_F/c_0 . Abstreiter et al. have described the Raman scattering of free electrons in detail (Abstreiter et al., 1984).

Electronic Raman scattering originates not only from free electron excitations, but also from collective electron excitations in the form of plasmons. So far, these two types of excitation have been observed only in conventional semiconductors and to some extent in high temperature superconductors, as discussed in subsections 4.8.4 and 4.8.5. However, doped polymers with not too high carrier concentrations or charge transfer systems are possible candidates, and the search for electronic Raman scattering in such systems is one of the challenges in this field.

As discussed in connection with IR absorption, Raman lines from a discrete transition may also assume Fano type shapes if the transition is coupled to a continuum of scattering states. This continuum may originate from various sources like, for example, electronic or two phonon excitations. In general, Raman scattering makes it even easier to observe Fano lines, since the free carrier response very often covers up details of the line shape in IR reflection. Similarly, such line shapes have so far only been shown by classical semiconductors and most recently by superconductors, and it is a challenge to search for them in other conducting organic systems.

Resonance enhancement of Raman intensities is discussed in Sec. 6.1. Since we are focusing on molecular and quasi-molecular systems, resonance enhancement may be described by Albrecht's theory, using in particular the A term and the B term of the Herzberg-Teller expansion of the interaction term (Tang and Albrecht, 1970). In small molecules, the A term plays a leading role. With increasing molecular size, the A term decreases and finally, as chains become very long, the B term dominates and converges to

the solid state description of the resonance Raman process (Kuerti and Kuzmany, 1991). The magnitude of the A term is determined within the Franck-Condon approximation. Thus, for a single electronic transition and for an optically quasi-onedimensional system, the cross section of a first order Raman process is

$$\frac{\partial^2 \sigma}{\partial \Omega \partial \omega} = \frac{2\omega_s^4}{9c_0^4 \hbar} |\alpha_{12}|^2 \quad (4.8-8)$$

where α_{12} is the transition polarizability between states 1 and 2:

$$\alpha_{12} = M_{12}^2 \sum_v \frac{\langle 0|v\rangle \langle v|1\rangle}{\epsilon_v - \hbar\omega_i + \gamma/2}$$

$\langle 0|v\rangle \langle v|1\rangle$ is the expectation value of a one-phonon transition (Franck-Condon integral); γ stands for the width of the electronic level, M_{12} represents the electron transition matrix element, and ϵ_v stands for the overall transition energy, consisting of the pure electronic transition ϵ_{12} and the infinite manifold of vibronic transitions:

$$\epsilon_v = \epsilon_{12} + \sum_j v_j \omega_j \hbar$$

The sum in Eq. 4.8-8 covers all vectors v determined by the vibronic occupation numbers v_j . This result has frequently been used to describe the resonance Raman intensities of conjugated molecules.

4.8.2 Infrared and Raman spectroscopy of conjugated polymers

Conjugated polymers (CP) are highly chromophoric systems, which makes Raman spectroscopy and in particular its resonance excitation version a very attractive tool to investigate vibronic properties and electronic structures. IR spectroscopy has been used mainly to study the doping process and structural phase transitions.

Conjugated polymers

Over the past twenty years, conjugated polymers have stimulated considerable interest as a new class of organic solid materials. Molecular as well as solid state concepts are not only appropriate but required to describe these systems. This is one reason why they have gained appreciable scientific recognition. Vibrational and to some extent also spectroscopic properties are adequately described by a molecular model, but transport phenomena and many thermodynamic properties require a solid state interpretation. According to the solid state concept, conjugated polymers range from very good insulators

to highly metallic materials; their conductivity reaches values which are typical of transition metals. This is certainly another sound reason for the increasing scientific attraction of these materials. Finally, the very well known high application potential of the polymers has stimulated many industrial laboratories, particularly throughout the chemical industry, to promote research and to extend the applicability of them.

Conjugated polymers are basically characterized by an alternating single bond - double bond structure which can be quantitatively described by a bond order parameter p . There are a number of special cases where triple bonds are included, so that p may vary between 0 and 2. Besides, interruptions of the backbone by heteroatoms, such as nitrogen in polyaniline, are possible and even systems where conjugation is based on overlapping σ bonds between nearest neighbors, such as polysilanes are included. Except for σ -conjugated systems, all polymers possess a backbone in which the carbon atoms are sp^2 hybridized and the extra p_z electron is in a π orbital.

The standard example of a CP is poly(acetylene) (PA), whose chemical structure is characterized by alternating single and double bonds in a triangular (*trans* transoid form) or in a trapezoidal (*cis* transoid form) carbon backbone. This bond alternation structure has been experimentally established (Fincher et al., 1982) and has been confirmed by *ab initio* quantum chemical calculations (Karpfen and Petkov, 1979). As a consequence, the electronic spectrum exhibits a gap in the center of the $2p_z$ band, which explains the insulating (semiconducting) properties of the system. Chemically speaking, this means that the HOMO-LUMO transition energy remains finite even for infinitely long chains. Physicists tend to attribute the existence of this gap to electron-phonon interaction, and they consider it a consequence of a Peierls distortion or a spontaneous symmetry breaking. This is a very useful description for PA, but the consideration of the electron-phonon interaction as an exclusive source for the formation of the gap has not really been confirmed. Electron correlation may as well contribute considerably to it.

The physical properties of other CPs are very similar to those of PA, even though one may distinguish between two types of systems: those with a degenerate and those with a non-degenerate ground state. A polymer has a degenerate ground state when a phase shift by one bond yields an energetically equivalent ground state. It has a nondegenerate ground state, on the other hand, when the phase shift results in an energetically higher state. Examples of systems with a non-degenerate ground state include poly(paraphenylenes) and poly(thiophene), which have a (lower) aromatic and a (higher) quinoid configuration.

The features shared by all CPs originate from the common nature of their π -electron system. Three important properties are most characteristic.

- i. chromophoric character in the visible and near infrared region
- ii. high conductivity in the oxidized or in the reduced state
- iii. reversible redox activation in a suitable electrolyte

The doping process of a single isolated chain resembles that of semiconductors. Electron acceptors or electron donors change the electron population in the valence or in the conduction band or, vice versa, electrons or holes from the polymer bands ionize the doping molecules, which are intercalated between the chains. Chemically speaking, this process equals an oxidation or reduction of the chains. The redox character of the doping process is reflected even more clearly by the fact that electrochemical oxidation and

reduction are excellent means of transforming a polymer from its insulating to its metallic state. To date, more than 100 different conjugated polymers have been prepared and characterized. Tab. 4.8-1 lists a number of particularly interesting systems, together with their chemical structure and some physical data, such as HOMO-LUMO transition energy (energy gap, ϵ_g) and maximum room temperature conductivity after doping σ_{\max} . Each of the listed structures represents an entire family of CPs. Review articles on CPs are available from Heeger et al. (1988) and from Skotheim (1986).

In detail the doping process of the polymers is more complicated than described above, because oxidation or reduction of the backbone severely distorts the chain (Heeger et al., 1988). Again, in analogy to the behavior of carriers in polar semiconductors, these distortions, together with their charge, are referred to as polarons. A chemist may regard them simply as radical cations or radical anions on the chain. However, an important

Table 4.8-1 Conjugated polymers

Polymer ^a	Symbol	Chemical structure	ϵ_g	σ_{\max}	Reference
p(acetylene),					
<i>trans</i>	trans-PA		1.6	10^5	Naarmann, 1987
<i>cis</i>	cis-PA		1.9	—	Chiang et al., 1977
p(paraphenylene-vinylene)	PPV		2.5	3×10^3	Hoerhold et al., 1987
p(pyrrrol)	PPy		3.2	1000	Ogasawara et al., 1986
p(thiophene)	PT		2.2	200	Akimoto et al., 1986
p(alkylthiophene)	PAT		2.5	95	Sato et al., 1987
p(isothianaphthene)	PITN		1	0.4	Kobayashi et al., 1985
p(heteroarylene methines)	PHAM		1	0.1	Becker et al., 1989
p(aniline)	PANI		3.8	100	Epstein et al., 1989
p(diacetylene)	PDA		2.5	—	Bloor et al., 1985
p(di-n-alkyl silane)	PDNAS		3.8	0.5	Zeigler, 1989

^a p stands for poly

characteristic of these polarons is their ability to pull electronic states from the valence band and from the conduction band into the gap and thus to dramatically change the optical properties. Referring to polarons rather than radicals implies that particular attention is being paid to this change in the density of states. For the sake of clarity, the electronic structures of polarons created by holes and electron polarons, together with the corresponding chemical structure, are shown in Fig. 4.8-1a. Polaron states may interact to form bipolarons or, in the case of a backbone with a degenerate ground state, to form charged solitons. Both features are also illustrated in Fig. 4.8-1. The chemical structure is shown only for hole polarons and hole bipolarons, since electron polarons and electron bipolarons have not yet been observed in aromatic systems. Also, the geometry of the

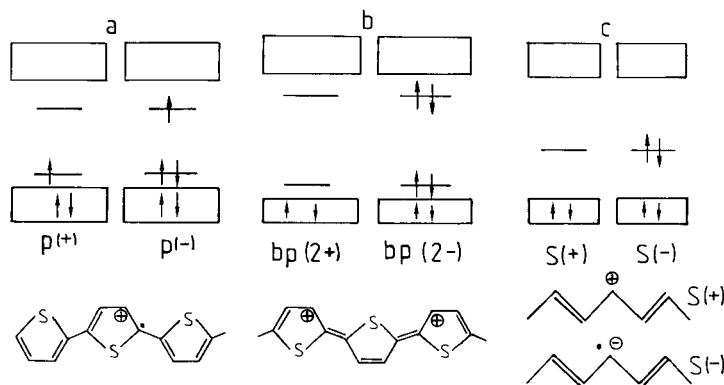


Figure 4.8-1 Electronic structure and chemical structure of hole and electron polarons (a), hole and electron bipolarons (b), and hole and electron solitons (c). Examples of chemical structures refer to poly(thiophene) and poly(acetylene), respectively.

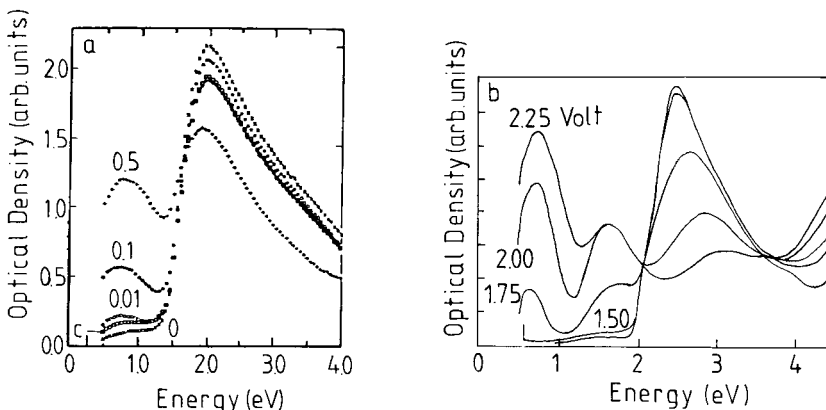


Figure 4.8-2 Optical absorption of conjugated polymers with a degenerate ground state (trans-poly(acetylene)) (a), according to Suzuki et al., 1980 and a non-degenerate ground state (poly(thiophene)) (b), according to Danno et al., 1993 in various doping states. Doping concentrations are indicated in % in (a) and by the applied potential in (b).

charge defects is certainly more relaxed than shown in the figure, and at higher doping levels we may consider them as polaron, bipolaron, or soliton bands. In any case, it is important to keep in mind that these new species are not really mobile quasiparticles like polarons in semiconductors, but that they characterize the density of states of a system. Since optical transitions are possible from fully or partially occupied states to empty or singly occupied states, different structures afford different optical absorption patterns and in turn different conditions for resonant Raman excitation. Fig. 4.8-2 exemplifies by two instances how doping changes optical absorption from an intrinsic band to band transition to a transition between states within a gap.

At a first glance, σ bonded polymers may be considered as being characteristically different from π bonded polymers. However, there are several systems which truly behave very much like π polymers. Characteristic examples include polysilanes, whose backbone is a σ bonded silicon zig-zag chain with alkylic side groups (Rabolt et al., 1986). The similarity to the π -systems results from the fact that there is an efficient overlap of adjacent orbitals leading to conjugated σ bonds.

In the described sense, conjugated polymers represent a new class of solid materials. There is no question that infrared and Raman spectroscopy are valuable tools to analyze these systems.

Raman scattering

The extensive literature on Raman scattering of conjugated polymers confirms the suitability of this technique for the analysis of conjugated systems. Due to the generally chromophoric nature of such materials, resonance type scattering may be expected. If we summarize the applicability of Raman scattering to CPs, we may distinguish between the following topics:

- A Analysis of chemical structure for CPs, in particular with respect to the difference between the doped and the undoped state. This is a conventional approach for analyzing organic systems and reveals important details about the doping process.
- B Structural analysis of configurations along the chain. This application is unconventional and capable of pointing out defects along the backbone. It leads to the important conjugation length concept for these polymers (Kuzmany, 1980).
- C Characterization of dynamic processes, such as cis-trans isomerization, order-disorder transitions (thermodynamic phase transitions), doping dynamics, and polymerization features. It certainly involves correlation of vibrational characteristics with other features, such as spin, during the doping process.
- D Theoretical models

A Chemical structure and Raman lines

It is convenient to discuss Raman investigations starting with item A. Tab. 4.8-2 lists prominent Raman lines for a number of CPs. The numbers in parentheses are the relative intensities on a scale of 1 to 5. Lines may be assigned to special vibrations according to the general rules outlined in earlier chapters of this book. Isotopic substitution in particular has been applied frequently and very successfully to these materials. In addition

Table 4.8-2 Raman lines of various conjugated polymers

Polymer ^a	Wavenumber cm ⁻¹				Reference
p(acetylene), <i>trans</i> - <i>cis</i> - <i>n</i> -doped	1450(5)	1290(1)	1050(5)	1010(2)	Harada et al., 1980
	1540(4)	1250(5)	910(3)		Lichtmann et al., 1984
	1560(5)	1260(5)	1120(2)	1140(2)	Eckhardt et al., 1985
p(3Me-thiophene), <i>p</i> -doped	1470(5)	986(<1)	722(<1)	550(<1)	Steigmeier et al., 1987
	1559(5)	1318(1)	1050(3)	990(3)	Furukawa et al., 1988
p(isothianaphthene)	1470(5)	1307(3)	1173(3)	447(3)	Wallnoefer et al., 1989
p(p-phenylene) p(p-phenylene- vinylene)	1595(5)	1280(1)	1220(3)		Lefrant et al., 1990
	1586(5)	1550(1)	1330(1)	1174(2)	Lefrant et al., 1989a
p(octylthiophene),	1475(5)	1373(<1)	1200(<1)	728(<1)	Danno et al., 1991
p(aniline), EM-salt EM-base	1622(5)	1196(5)	881(1)		Kuzmany et al., 1985
	1495(5)	1169(5)	775(1)		Bartonek et al., 1990
p(di-n-hexylsilane)	1175(1)	690(5)	494(1)	372(1)	Kuzmany et al., 1986
p(diacetylene)	2086(2)	1485(5)	1203(1)	952(1)	Batchelder et al., 1982

^a p stands for poly

comparison of spectra with those of known oligomers and investigation of the polarization properties of stretch-aligned polymers has turned out to be very useful. Vibronic frequencies have been calculated either by conventional force field programs, as outlined in Secs. 2.5 and 5.2 of this book, or by renormalization techniques. In the latter case, the vibrational frequencies of the σ -bonded system are calculated first, and renormalization is then performed by switching on electron-phonon interaction with the π -electrons (Horovitz, 1982; Ehrenfreund et al., 1987). The lines of *trans*-PA listed in Tab. 4.8-2 are excited with a red laser and have been attributed to C=C stretching: 1450 cm⁻¹, C–H in-plane bending with considerable contribution from C–C and C=C stretching: 1050 cm⁻¹, and C–H out-of-plane bending: 1010 cm⁻¹. The intensities of the lines correlate directly with the C=C stretching contribution of the respective normal coordinate (Schuegerl and Kuzmany, 1981). The shapes and positions of the lines at 1450 and 1050 cm⁻¹ change drastically with the energy of the exciting laser. This phenomenon is discussed below. After doping, particularly after p-doping, the spectrum appears considerably bleached and broadened (Kuzmany, 1980), mainly because the resonance conditions are changed, as shown in Fig. 4.8-2. In many cases it cannot be excluded that, at least in the *p*-doped state, only the portion of the sample which remains undoped is observed. The *n*-doped samples show new lines at 1260 cm⁻¹ and 1560 cm⁻¹, which have been attributed to localized chain vibrations. Their frequencies and intensities are modified by perturbation of the doping atom (Mulazzi and Lefrant, 1989). The main Raman lines of *cis*-PA have been attributed to C=C stretching: 1540 cm⁻¹, C–C + C=C stretch: 1250 cm⁻¹, CH in-plane bending: 910 cm⁻¹. Doped *cis*-PA does not exist, since doping automatically induces *cis-trans* isomerization, as demonstrated below. In interpreting Raman spectra of PA, care must be taken because the resonance response plays many games. A typical

example is shown in Fig. 4.8-3, which displays Raman spectra of what is almost exclusively *cis*-PA, as characterized by the three strong lines at 1540, 1250, and 910 cm⁻¹ in the upper part of the figure. The weak lines at 1130 and 1500 cm⁻¹ originate from 5 to 10% *trans*-PA contamination of the *cis*-polymer. If the spectrum is excited with a red laser, the lines from the contamination are dominant, even though the concentration does not exceed 10%. This surprising result is due to the fact that the red laser is just below the resonance of the *cis*-polymer but coincides with the resonance of the *trans*-polymer; whereas the blue laser is beyond the resonance of both polymers.

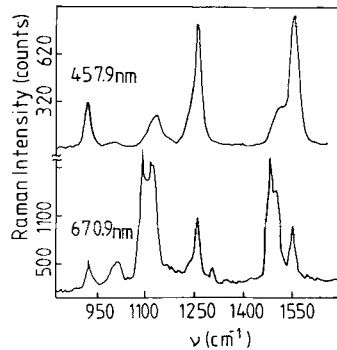


Figure 4.8-3 Anomalous Raman scattering of *cis*-poly(acetylene). The upper spectrum is excited with a blue laser, the lower spectrum with a red laser, as described in Kuzmany et al., 1981.

PMET is a more common object of investigation than the structurally simpler PT, because the extra methyl group guarantees α - α coupling and thus affords a more defined polymer. Interpretation of the lines as C=C stretching: 1470 cm⁻¹ and as thiophene ring deformation: 722 cm⁻¹ is based on comparison with PT (Furukawa et al., 1987) and on force field calculations (Faulques et al., 1989). The ground state of the neutral polymer was found to be aromatic, whereas the doped state is quinoid. This is a simple consequence of the formation of bipolarons, since the structure between two bipolarons is quinoid. PPy behaves very much like PT and PMET, but has a slightly larger energy gap.

PITN has attracted considerable attention because of its strongly reduced gap even in the neutral state (Bredas, 1985). Since doping shifts absorption to a lower energy level, this polymer becomes highly transparent in the doped state. Assignment to vibrational modes is based on comparison to PT and benzene and on a force field analysis (Faulques et al., 1989; Wallnoefer et al., 1989a). Two types of Raman lines have been observed: a set of resonance-enhanced lines, which have been attributed to the neutral polymer, and another set of non-resonant-enhanced modes, attributed to the doped polymer. Interestingly, it was concluded from Raman experiments that the ground state of PITN is quinoid, whereas the doped state is aromatic. This experimental result was confirmed by a quantum chemical calculation (Lee and Kertesz, 1988). Thus, with respect to the ring structure, PITN behaves contrary to PT. PPV is attractive because it can be prepared as a stretch-oriented material with considerable anisotropic properties. Stretch orientation is introduced via a precursor of the polymer. The lines at 1330 and 1628 cm⁻¹ have been

attributed to the vinyl group, while those at 1550, 1586, and 1174 cm^{-1} represent the benzene ring.

PANI has been known for more than a century but has remained poorly characterized up until very recently. However, over the past few years it has become one of the best characterized CPs on the market. Raman lines of two PANI species are listed in Tab. 4.8-2. The lines were interpreted on the basis of isotopic substitution and comparison with smaller molecules (Furukawa et al., 1988). The line at 1433 cm^{-1} in particular was identified as originating from smeared-out double bonds between the nitrogen and the phenyl rings, with the phenyl rings equidistant from the nitrogen atom. The lines listed for the PEM base form (polyemeraldine base form) appear in addition to those of the PEM salt form (polyemeraldine salt form). The Raman lines of PDNHS can be divided into two groups. One group reflects backbone vibrations (C-Si stretching: 690 cm^{-1} , Si-Si stretching: 372 cm^{-1} , Si-Si non-*trans* conformer: 494 cm^{-1}), while the second group of lines is caused by vibrations of the side chains (CH_2 rocking: 1175 cm^{-1}). The former group exhibits a strong resonance enhancement in the blue spectral range, and all lines are very anisotropic for oriented samples.

Finally, PDA is of particular scientific interest since macroscopic single crystals can be grown from it. The lines have been interpreted as follows: $\text{C}\equiv\text{C}$ stretching: 2086 cm^{-1} , $\text{C}=\text{C}$ stretching: 1485 cm^{-1} , C-C stretching: 1203 cm^{-1} , and $\text{C}\equiv\text{C}$ bending: 952 cm^{-1} .

B Structural analysis of the backbone

Even more important than structural analysis is the analysis of configurational defects along the backbone. Results of such investigations can be considered most typical of CPs; in the experiment, this is reflected as a shift of the Raman line position as the energy of the exciting laser changes. This phenomenon has been referred to as a dispersion of Raman lines, since lasers with different quantum energies scatter with different momentum transfers of phonons. Thus, the observed shift of phonons formally defines the dependence of the phonon energy on the momentum. An experiment demonstrating this effect is shown in Fig. 4.8-4a, which exhibits Raman spectra of *trans*-PA excited by different laser lines. The Raman line of the C=C stretching mode at 1500 cm^{-1} is split into a primary line at 1450 cm^{-1} and a satellite line, which shifts by about 60 cm^{-1} as the laser excitation shifts from red to green. It turns out that this phenomenon is not a dispersion effect but a consequence of a photoselective resonance process. The backbone of the polymer is viewed as consisting of properly conjugated regions, which are interrupted by defects destroying the conjugation, such as sp^3 hybridization. The vibrational and optical properties of these regions depend on their size, i.e., on the conjugation length. A phenomenological description is found in Fig. 4.8-4b. The red and the blue laser, respectively, excite different portions of the polymer in resonance across a precisely defined energy gap ϵ_g which, consequently, defines the conjugation length N . N finally determines the vibrational frequency and thus the obtained spectrum. The details are somewhat more complicated, since not all defects always entirely interrupt conjugation (Kuerti and Kuzmany, 1987). Besides, each laser energy excites all conjugated segments, but with different resonance enhancement. Nevertheless, this model is

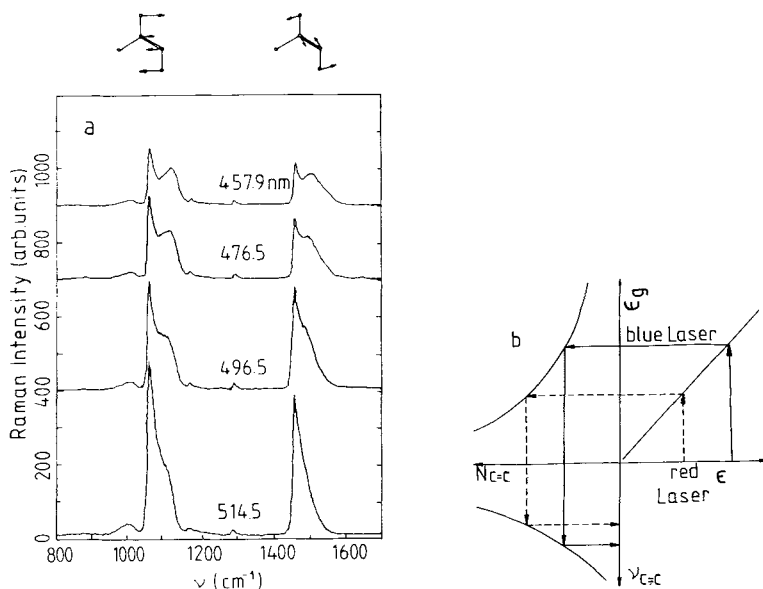


Figure 4.8-4 Raman spectra of trans-poly(acetylene) excited by different laser lines, according to (Imhoff, 1983) (a), and a schematic representation of the dispersion effect in conjugated polymers. The continuous and the dashed arrows, respectively, refer to a red and a blue laser (b).

Table 4.8-3 Dispersion of Raman lines of various undoped and doped conjugated polymers

Polymer ^a	Line (cm^{-1})	Dispersion (cm^{-1}/eV)	Reference
p(acetylene), <i>cis</i>	1540	7	Lichtmann et al., 1984
<i>trans</i>	1500	76	Kuzmany, 1985
p(heptadiene)	1500	60	Zemach et al., 1985
p(diacetylene)	1500	55	Kuerti et al., 1987
p(pyrrrole)	1569	7	Furukawa et al., 1988
p(thiophene)	1500	18	Vardeny et al., 1987
p(3-Me-thiophene)			
p-doped	1470	24	Steigmeier et al., 1987
p(3-octylthiophene)	1460	40	Danno et al., 1991
p(isothianaphthene)	1500	40	Wallnoefer et al., 1989b
p(p-furylenevinylene)	1432	32	Lefrant et al., 1989a
p(di-n-hexylsilane)	689	6	Kuzmany et al., 1986
p(paraphenylene)	1598	0	Lefrant et al., 1989b

^a p stands for poly

useful to describe the dispersion behavior of *trans*-PA quantitatively, as demonstrated below. The dispersion effect is not limited to *trans*-PA but is shown by most CPs. Tab. 4.8-3 lists dispersion data of selected polymers, shown as wave number shift per energy shift for the exciting laser. Dispersion is typically between 10 and 40 cm^{-1}/eV , although in exceptional cases, such as *trans*-PA or PDA, it can become as large as 70 cm^{-1}/eV . The effect of disturbing the backbone conjugation by defects can be demonstrated by using systematically degraded samples. This is exemplified in Fig. 4.8-5a, which shows Raman spectra of *trans*-PA after exposure to ambient conditions. Oxygen reacts with the unsaturated backbone to form carbonyl groups, which interrupt the conjugation. Thus, the high frequency portion of the Raman lines continuously increases relative to the low frequency portion. The line position hardly changes, because it is determined by the resonance condition. Dispersion is restricted to modes with a strong bond alternation amplitude in their normal coordinate.

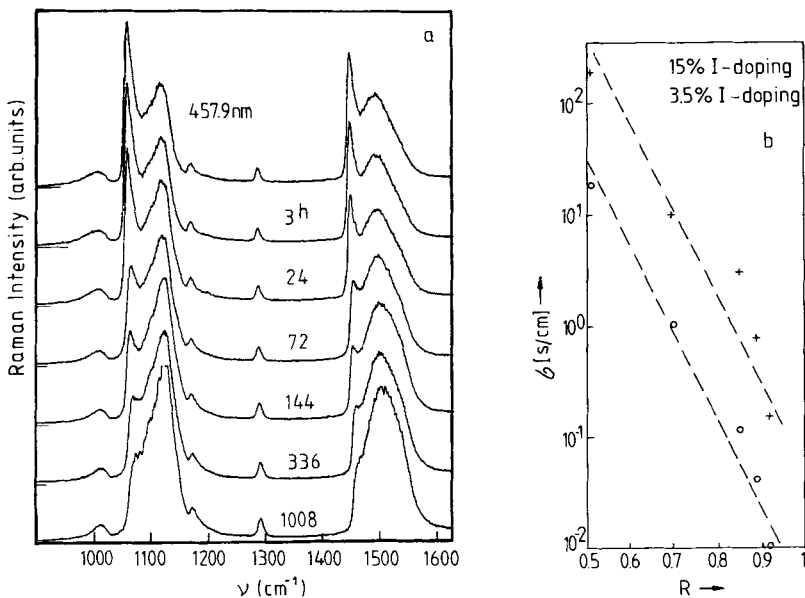


Figure 4.8-5 Raman spectra of poly(acetylene), degraded by exposure to ambient conditions. The numbers refer to the exposure time in hours, according to Knoll and Kuzmany, 1984 (a), and to the conductivity of the samples after iodine doping with different concentrations of defects, characterized by the ratio R of the satellite peak intensity to the primary peak intensity of the $\text{C}=\text{C}$ stretching mode, according to Schaefer-Siebert et al. 1987 (b).

An outline of a quantitative description of the dispersion phenomenon is given below. This theory provides a description of the backbone structure of a polymer insofar as it evaluates a distribution function for conjugation lengths on the chains. In certain cases this was found to correlate with the conductivity of the polymer after doping and thus provided important information concerning the conduction mechanism. Fig. 4.8-5b

exemplifies this by showing the relation between the concentration of defects in *trans*-PA, obtained from the Raman spectrum, and the conductivity of the material after iodine doping at two different doping levels.

C Dynamic processes

A very promising application of Raman scattering is the investigation of dynamic processes, such as isomerization, doping, and order-disorder phase transitions. Many of these experiments can be performed *in situ*, which guarantees very high resolution with respect to time and sensitivity. Fig. 4.8-6a shows Raman spectra excited with a 457.9 nm laser line which reflect *cis-trans* isomerization of PA. From the normalized integrated line intensities obtained at different temperatures for the amplitude mode of the *cis* and the *trans* isomer two different activation energies, i.e., 15 kcal/mol and 35 kcal/mol were evaluated. The lower and the higher energy, respectively, corresponds to the isomerization of disordered and ordered parts of the polymer.

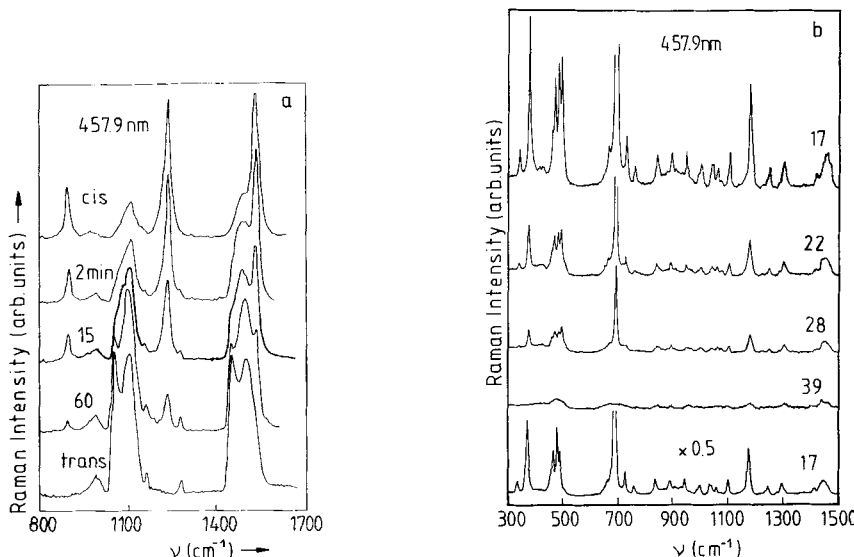


Figure 4.8-6 Isomerization of poly(acetylene). The numbers indicate the exposure time in minutes at 130 °C, according to Kuzmany, 1985 (a). A representation of Raman spectra of poly(di-n-hexylsilane), excited at different temperatures (in degrees Celsius)(b). The bottom spectrum demonstrates the reversibility of the phase transition, according to Kuzmany et al., 1986.

Another dynamic phenomenon has been observed in systems which undergo thermochromic phase transitions, such as σ -conjugated poly(alkylsilanes) and π -conjugated poly(alkylthiophenes). As a result of this transition, the highly ordered crystalline portion of the polymer experiences disorder, due to side chain melting. The conjugation length consequently decreases and the optical absorption shifts to higher values. This may have

a dramatic influence on the Raman intensities, as shown in Fig. 4.8-6b for PDNHS. At temperatures above the phase transition at 35 °C, the very strong room temperature spectrum becomes completely bleached. This is due to the fact that the energy gap of PDNHS is 3.8 eV at room temperature and increases considerably during the phase transition. Thus, the transition energy is shifted away from the laser line, and the resonance excitation is quenched. A dispersion effect is difficult to observe, since the laser line is on the low frequency side of the resonance, and the longest segments are therefore always closest to resonance.

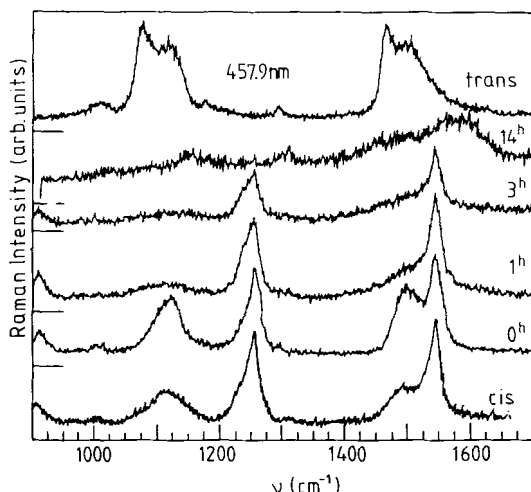


Figure 4.8-7 Raman spectra obtained *in situ* during electrochemical doping of cis-poly(acetylene) in acetonitrile/LiClO₄ at 3.8 V vs. Li. Doping times are indicated in hours, according to Meisterle et al., 1984.

The process of doping reduces the Raman intensities, since the accumulation of densities of states at the band edges is generally flattened. If, as with PA, the resonance of the neutral state is in the visible, it is particularly strongly bleached, since most of the oscillator strength of the optical excitation shifts to the infrared region (see, e.g., Fig. 4.8-2). Changes in the Raman spectra during doping can be studied very conveniently by an *in situ* electrochemical doping experiment, as demonstrated in Fig. 4.8-7. Doping proceeds with time at a redox potential of 3.8 V vs. Li. The first lines disappearing are from the trans contamination in the cis polymer, which indicates that this part of the polymer is doped first. The lines attributed to *cis*-PA disappear next, until the spectrum finally appears completely bleached and very much resembles the spectrum of a doped polymer in the gas phase. Reducing the applied potential to zero (top spectrum) reverses the doping process. Comparison with the spectra in Fig. 4.8-4 shows that the undoped state is now purely in its trans form. Thus, these experiments provide clear evidence of *cis-trans* isomerization during the doping process. In polymers whose energy gap is in the ultraviolet region, the resonance excitation is not necessarily quenched by the doping

process, but characteristic line shifts may be observed. A good example is PANI, which is most stable in its semioxidized PEM form. PEM is neutral in an environment with a pH above 3.7 and forms a salt in an acidic medium with pH below 2. In the base form, one out of four phenyl rings is quinoid (Fig. 4.8-8a), whereas in the salt form every second nitrogen is protonated and the nitrogen-phenyl bonds become equal. This has been confirmed by an internal redox reaction of the protonated imine nitrogens in PEM base (MacDiarmid et al., 1987), as shown in Fig. 4.8-8a. Raman spectra make it possible

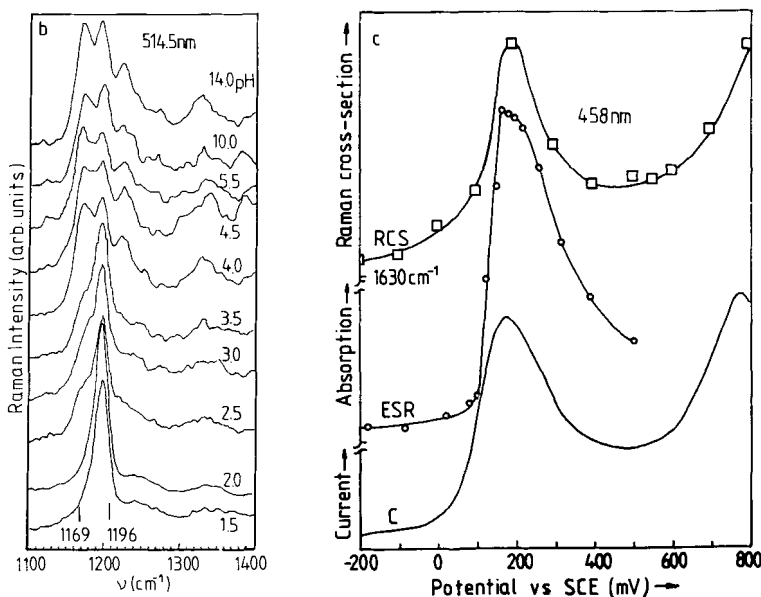
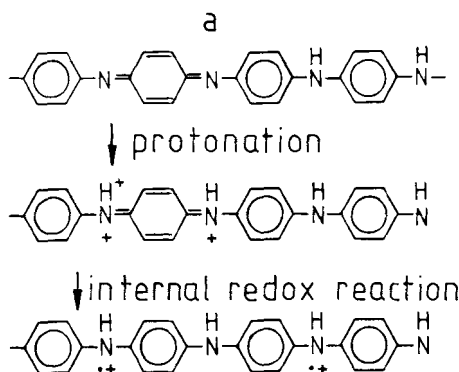


Figure 4.8-8 Internal redox reaction and chemical structure of PANI (a), change of δ_{CH} Raman lines as a result of protonation (b), according to (Bartonek et al., 1990). Redox current (C), spin concentration (ESR), and Raman cross section of the polaron type ring mode at 1630 cm^{-1} (RCS) vs. oxidation potential (c), according to Kuzmany and Bartonek, 1990a.

to monitor the vibrational changes during transition from the quinoid ring structure in its base form, which is observed at 1169 cm^{-1} , to the aromatic polaron type form of the salt, represented by the same type of vibration at 1196 cm^{-1} , in detail, as demonstrated by Fig. 4.8-8b. Similar results have been obtained for the C=C ring vibrations (Bartonek and Kuzmany, 1991). During oxidation, particularly in an acidic electrolyte, the intensity of the Raman line of the polaron at 1630 cm^{-1} was found to be directly related to the spin concentration measured by an ESR experiment. This is shown in Fig. 4.8-8c, which compares the intensity of the polaron Raman line to the observed ESR signal intensity and to the current in the first oxidation wave. The initial increase of the polaron Raman line is consistent with the generation of spin carrying polarons. At a certain concentration, the polarons start to interact and to form first bipolarons and then a PEM salt, which no longer contains single polarons.

D Theoretical models

The dispersion phenomenon has been quantitatively approached by three models. Initially, Albrecht's theory (Tang and Albrecht, 1970) was applied to the finite segments of the polymer. Then, in the case of materials such as *trans*-PA, use of an empirical distribution function $P(N)$ for the conjugation length made it possible to exactly reproduce the line shapes and line intensities resulting from excitation with different laser lines:

$$I(\omega, \omega_j, \omega_L) = \text{const.} \sum_N P(N) |\alpha_{12}(N, \omega, \omega_L)|^2 \omega_s^4 L(\omega, \omega_j(N)) \quad (4.8-9)$$

where $L(\omega, \omega_j(N))$ is the Lorentzian line from Eq. 4.8-8 and α_{12} is the transition polarizability of all vibrational frequencies ω_j , given by Eq. 4.8-8 (Kuzmany, 1985). In Eq. 4.8-8 and Eq. 4.8-9, the transition energies, transition matrix elements, and vibrational

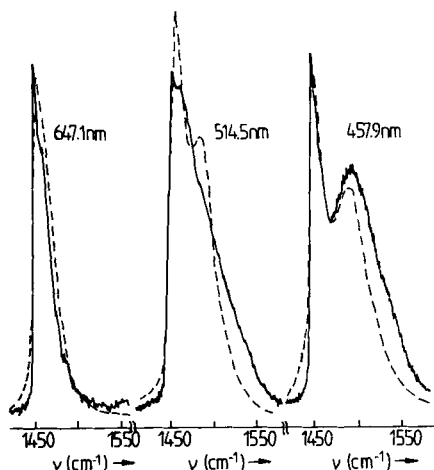


Figure 4.8-9 Comparison between observed and calculated Raman lines of the C=C stretching mode in *trans*-poly(acetylene) for three different laser excitations, according to Kuzmany et al., 1985.

frequencies must be considered to be functions of the conjugation length N and must be determined by a suitable quantum chemical approximation. It is particularly important to remember that the matrix elements are highly dependent on the HOMO-LUMO transition energy and thus on the number of double bonds in the finite chain (Kuzmany et al., 1983). Fig. 4.8-9 shows a comparison between measured and calculated Raman lines for the amplitude mode of *trans*-PA. There is only one scaling factor between calculation and experiment which applies to all three lines.

More recently the amplitude mode model, which is a solid state approach to the problem, has been developed. Chains are assumed to be infinitely long, but each chain is thought to have a different overall electron-phonon coupling constant $\tilde{\lambda}$. More precisely, $\tilde{\lambda}$ may even include other interaction processes which renormalize the phonon frequencies. The latter and the Raman intensities are obtained from

$$D_0(\omega) = -(1 - 2\tilde{\lambda})^{-1} \quad (4.8-10)$$

where

$$D_0(\omega) = \sum_j \lambda_j \frac{\omega_{0j}^2}{\omega^2 - \omega_{0j}^2 - i\omega\gamma_j}$$

and from

$$\frac{\partial^2 \sigma}{\partial \Omega \partial \omega} \propto |f(\hbar\omega_L)/\epsilon_g| \text{Im} \frac{D_0(\omega)}{1 + (1 - 2\tilde{\lambda})D_0(\omega)}, \quad (4.8-11)$$

respectively. ω_{0j} are the nonrenormalized phonon frequencies, and λ_j are the individual normalized coupling constants. $f(\hbar\omega_L)$ is a function describing the resonance behavior of $\hbar\omega_L = \epsilon_g$, and γ_j stands for phonon damping. Eqs. 4.8-10 and 4.8-11 afford the intensity of a Raman line by summation over the distribution of all electron-phonon coupling constants $P(\tilde{\lambda})$. In Fig. 4.8-10 $D_0(\omega)$ is plotted for vanishing γ_i . Renormalized phonon frequencies are obtained by the intersection of horizontal lines with this function according to Eq. 4.8-10. P and S in the figure stands for the primary and the satellite line, respectively. The amplitude mode model is an elegant way to approach Raman line dispersion. However, it needs a large number of input parameters, such as bare phonon frequencies and individual coupling constants. Due to normalization, $3n - 1$ input parameters are required for n modes. On the other hand, the bare phonon frequencies and the coupling constants directly afford the energy gap and the shift of vibrational frequencies resulting from interaction with the π -electrons for any value of $\tilde{\lambda}$. A conceptual difficulty arises from the comparatively sophisticated assumption that chains are infinitely long and perfect, but still renormalized by a distributed electron-phonon coupling constant $P(\tilde{\lambda})$. Very recently, the amplitude mode model has been extended to chains with a finite length. The concept of distributed coupling constants is thus no longer unreasonable (Kuerti and Kuzmany, 1991). Since the electronic transition matrix elements are not

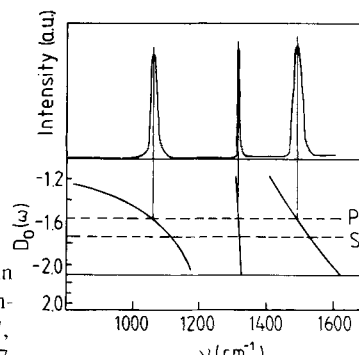


Figure 4.8-10 Renormalized Raman line positions and Raman intensities of *trans*-poly(acetylene), with bare phonon frequencies and coupling constants $1235, 1309, 2040\text{ cm}^{-1}$ and $0.07, 0.02, 0.91$, respectively, according to Ehrenfreund et al., 1987.

explicitly determined, the distribution functions $P(\tilde{\lambda})$ obtained from a fit to experimental results are not very reliable and cannot be compared with the solutions of Eq. 4.8-9.

A most recently developed description of the problem interprets the amplitude mode model in terms of a molecular concept of chains with cyclic boundary conditions (Zerbi et al., 1989). An effective conjugation coordinate Q_{ja} with a corresponding force constant f_{ja} is defined. The vibrational frequencies are calculated as a function of f_{ja} , which plays the same role as $\tilde{\lambda}$ in the amplitude mode model. Accordingly, the Raman intensity is obtained from the respective ja components of individual modes. This new concept, like the amplitude mode model, properly describes the relative intensities of different modes, but the correct line shapes and line intensities for excitation with different laser lines can not be obtained, since transition matrix elements are not evaluated explicitly.

Interestingly, in some of the systems showing no dispersion of Raman lines, such as PPP, the conjugation length was found to determine the intensity ratio of the ring breathing mode at 1280 cm^{-1} and the δ_{CH} -mode at 1220 cm^{-1} (Lefrant and Buisson, 1991).

Infrared spectroscopy of conjugated polymers

Infrared spectroscopy may be used to investigate conjugated polymers in much the same way as Raman spectroscopy. Both methods make it possible to analyze chemical structures, to study dynamical processes such as *cis-trans* isomerization, or to investigate the doping process. However, because of the missing correlation between electronic and vibronic transitions, the infrared scenario is less colorful. For instance, no shift of IR active modes indicating particular structural defects of the polymer backbone has yet been observed.

As in Raman scattering conventional spectroscopic techniques, as well as *in situ* geometries have been used to investigate polymers. Among the latter methods, external and internal reflection spectroscopy have proven particularly successful for these materials (Neugebauer et al., 1983), (Neckel, 1987). Figure 4.8-11 demonstrates the respective beam and sample geometries for the two methods. In the case of external reflection, the polymer is grown as a thin film on a highly reflecting metallic sheet; the IR radiation passes through twice. The transmitted radiation is measured relative to the portion of

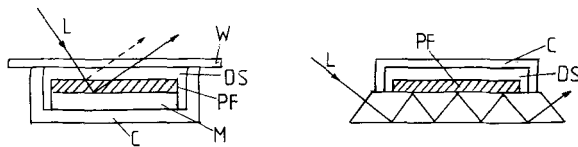


Figure 4.8-11 Experimental arrangements for *in situ* external and internal reflection spectroscopy. C: cup, M: metal sheet, PF: polymer film, DS: doping solution, W: window, L: IR beam.

radiation which is reflected by the pure metal sheet. The portion of radiation reflected by the surface of the film is usually neglected. Evaluation of the difference spectra makes this technique a useful tool for detailed investigations of changes in a sample which accompany processes such as doping in an electrochemical cell or change of the doping solution. Unfortunately, absolute spectra can not be obtained, since the IR absorption lines of the surrounding solution usually cover the spectrum of the polymer completely. This difficulty is avoided by the geometry of internal reflection spectroscopy, which involves an IR beam guided along the surface of a semiconducting crystal by internal total reflection. The polymer is grown as a thin film on the electrode surface, and penetration of the propagating electric field provides interaction with the vibrational modes. Since the solution is far enough away from the beam, it no longer interacts with the radiation, and undisturbed spectra are obtained. These two geometries have very frequently been employed in electrochemical modulation spectroscopy, where the metal sheet or the semiconductor is used as a working electrode in a three-electrode electrochemical cell (Beden and Lamy, 1988), (Christensen and Hamnett, 1989).

A Structure and doping

As in Raman spectroscopy, we may draw up a list of absorption frequencies which are typical of particular polymers in the neutral and in the doped state. Table 4.8-4 provides such a list for some of the most extensively studied compounds. As in Tab. 4.8-2,

Table 4.8-4 Characteristic IR absorption lines of conjugated polymers

Polymer, p = poly		Wavenumber cm ⁻¹			Reference
p(acetylene), <i>trans</i>	3013(2)	1292(1)	1015(5)	528	Shirakawa et al., 1971
p(acetylene), <i>cis</i>	3050(1)	1329(5)	740(5)	446(5)	Shirakawa et al., 1971
p(acetylene), <i>n</i> -doped		1385(5)	1259(1)	832(3)	Rabolt et al., 1979
p(octylthiophene)	2900(>5)	1510(1)	1460(5)	824(2)	Gustafsson, 1990
p(thiophene)	1499(1)	1417(3)	≈820(3)	700(5)	Akimoto et al., 1986
p(aniline), PEM-base	1594(5)	1501(5)	1304(3)	828(2)	Harada et al., 1989
PEM-salt	1576(4)	1497(4)	1301(5)	1141(5)	Sariciftci et al., 1990
p(phenylenevinylene)		1518(5)	960(5)	830(4)	Lefrant et al., 1989
p(pyrrrol)	3400(4)	3100(1)	1550(4)	720(5)	Nazzal et al., 1985

relative line intensities are set in parentheses. The considerable difference between the IR absorption lines of the *trans* and of the *cis* form of PA makes it possible to analyze the isomerization process as successfully as by Raman experiments. The out-of-plane deformation of *cis*-PA at 740 cm^{-1} and that of *trans*-PA at 1015 cm^{-1} are particularly useful indicators of the isomerization process. Again, a thermodynamic analysis reveals two activation energies of 15 and 30 kcal/mol, respectively, for the isomerization process (Shirakawa and Ikeda, 1971). Lines are generally interpreted in a straightforward manner: lines around 3000 cm^{-1} correspond to ν_{CH} (or ν_{NH} at 3400 cm^{-1} in PPy), lines around 1500 cm^{-1} are attributed to ring stretching or C=C stretching modes, and lines around 800 cm^{-1} are associated with out-of-plane CH deformation.

Interestingly, very often new and very strong lines which are close to the known Raman lines of totally symmetric modes in the respective neutral polymer emerge in the IR spectra as a consequence of doping. Similar results have been obtained with charge transfer systems, such as TEA (TCNQ_2) (Rice et al., 1977), as discussed in the following subsection. Fig. 4.8-12 exemplifies this by the spectra of *trans*-PA, in which this phenomenon was observed for the first time. The doping-induced modes are found at 1385 , 1259 , and 832 cm^{-1} . Recently, similar effects have been observed in other polymers, such as PANI (MacCall et al., 1989). From a more detailed investigation of the new modes in *trans*-PA it was suggested that they originate from the doping-induced distortion of the backbone (soliton), as a consequence of its coupling to the doping ion.

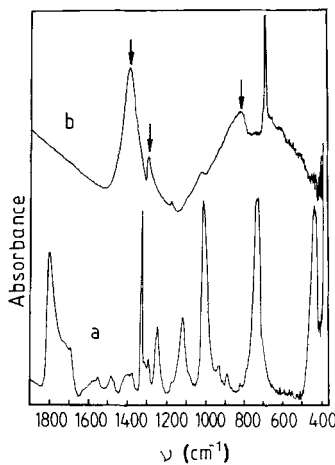


Figure 4.8-12 IR absorption spectra of neutral (a) and AsF_5 -doped poly(acetylene) (b), according to Rabolt et al., 1979.

Each resonance-enhanced Raman mode has a counterpart in the IR spectrum, due to the pinning of charge oscillations. The amplitude mode model can be used to derive the doping-induced modes if a pinning constant α for the renormalization of the bare phonons is employed instead of the renormalization constant $\tilde{\lambda}$ for π -electron interaction (Ehrenfreund et al., 1987). This procedure is very similar to the evaluation of Raman modes by Eq. 4.8-10, as indicated in Fig. 4.8-10. The high frequency conductivity $\sigma(\omega)$ is obtained from

$$\sigma(\omega) = i\omega C \frac{-D_0(\omega)}{1 + (1 - \alpha)D_0(\omega)}, \quad (4.8-12)$$

where C is a constant describing the average charge density and the formal mass of the charge defect. α defines the pinning potential for the charge distribution of the defect. Thus, this model only requires one additional parameter in order to explain the doping-induced modes. As shown in the following section, this formalism even applies to the pinning of photo-induced charges. In addition to pinning-induced modes, absorptions due to shape vibrations of the charge-carrying configuration have been reported (Heeger et al., 1988).

Interesting results have been obtained from *in situ* electrochemical doping experiments with PMeT and PANI, as shown in Fig. 4.8-13a and b. In both cases, the background absorption increases considerably during oxidation (doping), which indicates an appreciable free carrier contribution to the absorption spectrum. For PANI, this contribution was calculated for an effective medium (Maxwell-Garnet) dielectric response function (Kuzmany et al., 1988). Further increase of the oxidation potential decreases the free carrier contribution in this polymer, and a different insulating form of PANI is obtained. Reports on reflection spectra analyzed as outlined in subsection 4.8.1 are not very frequent (Kamiya and Tanaka, 1988). The surface of the polymer is usually not smooth enough to guarantee a minimum of diffuse light scattering.

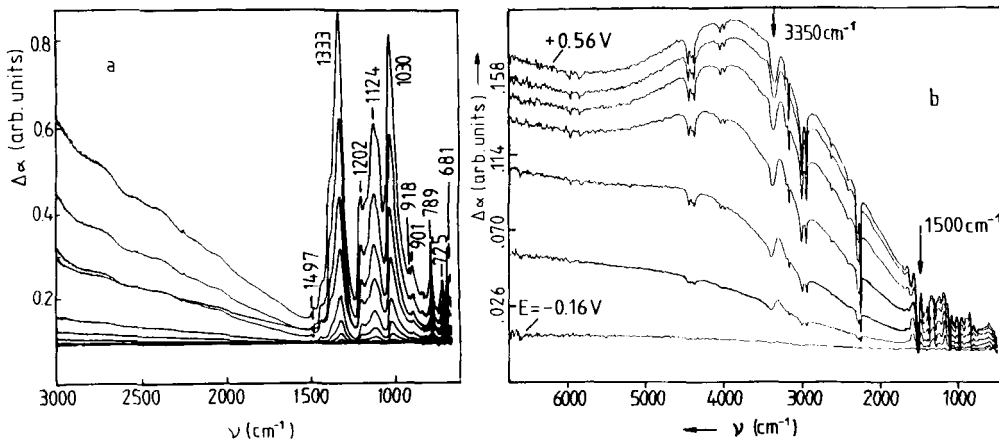


Figure 4.8-13 Absorbance differences $\Delta\alpha$ during electrochemical oxidation of poly(methylthiophene) in an organic electrolyte (a), measured *in situ*, according to Neugebauer et al., 1983, and corresponding values for the oxidation of poly(aniline) in an acidic electrolyte (b), according to Kuzmany et al., 1988. The indicated potential is vs. SCE.

B Photo-induced absorption

Photo-induced IR absorption spectra in the spectral range of vibrational modes have been studied extensively, and a strong correlation with doping-induced IR absorption

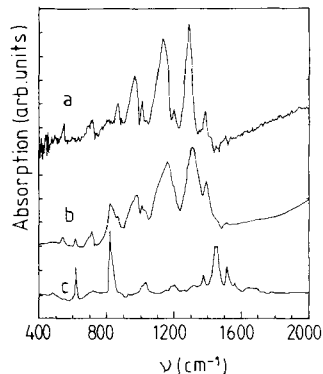


Figure 4.8-14 Comparison of photoinduced vibrational absorption (a) with doping-induced vibrational absorption (b) and an undoped sample (c) of poly(3-methylthiophene), according to Kim et al., 1987.

was observed. This is exemplified by PMeT, shown in Fig. 4.8-14. The top spectrum is the photoinduced absorption measured after exciting a KBr pellet sample of PMeT with an argon laser. Spectrum b is obtained after doping the polymer with 4% PF_6^- , and the bottom spectrum is that of the neutral polymer. The one-to-one correspondence between the photoinduced spectrum and the spectrum of the doped sample is striking. This is explained by the argument that photoinduced charges create a similar distortion on the chains as charges resulting from chemical doping. Even though the larger part of the excited carriers will immediately recombine, a small fraction excited on different chains will form polaron or bipolaron states, as discussed above. These electronic excitations are pinned to local defects and thus couple to the A_g modes. This is a symmetry disrupting process which gives rise to A_g modes in the IR spectrum. Again, the amplitude mode model described in Section 4.8.2D yields the correct IR frequencies if a single coupling constant is used as a parameter. This constant is similar to but not necessarily identical with the coupling constant of the doping-induced IR vibrational modes.

4.8.3 Infrared and Raman spectroscopy of organic charge-transfer crystals

Organic charge-transfer crystals are another class of novel organic materials which may exhibit very high, metallic conductivity or even become superconducting. These crystals are, like polymers, highly anisotropic, since they consist of stapled large planar molecules; conduction is caused by π -bands overlapping only in the direction of stapling. Band filling is established by charge-transfer between a donor stack and an acceptor stack. Incomplete charge-transfer results in fractionally filled bands and thus creates metallic systems. In order to obtain superconductivity, considerable interstack interaction at least in one direction is required, so that these systems very often become quasi two-dimensional (Schweitzer et al., 1987). The best known representatives of this class of materials are TTF-TCNQ (tetrathiofulvalene (acceptor)-tetracyanoquinodimethane (donor)) and $(\text{BEDT-TTF})_2[\text{Cu}(\text{CNS})_2]$ (bis(ethylenedithio)tetrathiofulvalene (donor)-copperthiocyanate (acceptor)). The Cu-complex can be replaced by several other groups. The high-

est transition temperature to superconductivity, a value of 12.8 K, was reported for a halogenated BEDT-TTF-Cu-complex (Williams and Beno, 1990). Molecular and crystal structures are shown in Fig. 4.8-15. Raman spectroscopy has appreciably promoted the understanding of these systems, since it demonstrates that any type of charge-transfer leads to a considerable line shift of molecular vibrational modes (Bozio et al., 1975). In TTF, shifts by as much as 80 cm^{-1} have been observed during charge-transfer between zero and 0.7 (Kuzmany and Kundu, 1979). Similarly, a charge-transfer of 1 in TCNQ resulted in a downshift of the $A_g\nu_4$ mode ($\text{C}=\text{C}$ stretching) by up to 65 cm^{-1} . Assuming a linear relation between charge-transfer and frequency shift of TTF-TCNQ, the charge-transfer was determined to be 0.55, which yields band filling up to $2 k_F = 0.275$ in reciprocal lattice units (Kuzmany et al., 1978). This is in very good agreement with neutron scattering experiments. The linear relation between charge-transfer and mode shift is confirmed by investigations of mixed crystal systems, such as $\text{NMP}_x\text{Phen}_{1-x}\text{TCNQ}$. In this system, the charge-transfer is expected to increase linearly with x , since phenazin always remains neutral. This is demonstrated in Fig. 4.8-16, in which the line position of the $\text{C}=\text{C}$ stretching mode is plotted versus the NMP concentration in the mixed crystal. Again, the charge-transfer affords the position of the Fermi level.

In the resonance Raman spectra of BEDT-TTF, an interesting line was observed around 100 cm^{-1} which could be associated with the symmetric stretch mode of the I_3^- molecule shown in Fig. 4.8-15. At low temperature, the mode splits into three components, a behavior which has been attributed to crystal field interaction (Swietlik et al., 1987).

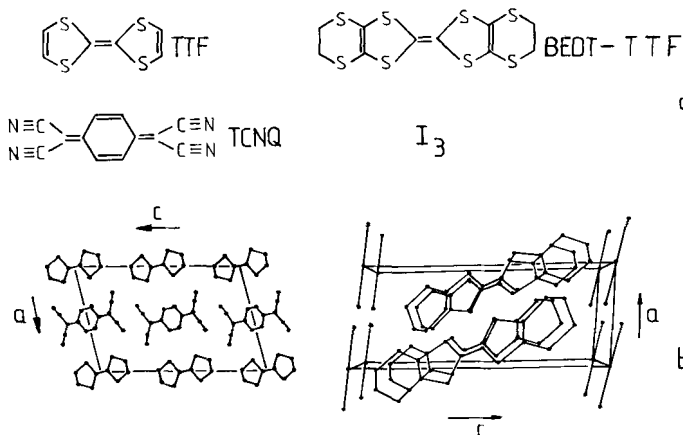


Figure 4.8-15 Molecular (a) and crystal structures (b) of the charge-transfer systems TTF-TCNQ and β -(BEDT-TTF)₂J₃, according to Schweitzer et al., 1987.

A frequently discussed phenomenon of IR vibrational spectroscopy is the electron - molecular vibration coupling of totally symmetric in-plane molecular modes. As a consequence of coupling to the free carriers, these modes become visible in the IR absorption if the light is polarized parallel to the stacking direction. This effect was first observed in TEA(TCNQ)₂ (triethylammonium (TCNQ)₂), as shown in Fig. 4.8-17a, b.

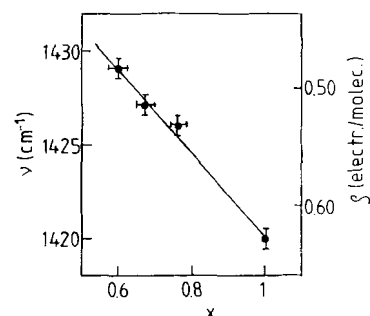


Figure 4.8-16 Position of the C=C stretching mode and charge-transfer for $\text{NMP}_x\text{Phen}_{1-x}\text{TCNQ}$ vs. NMP concentration, according to Kuzmany et al., 1980.

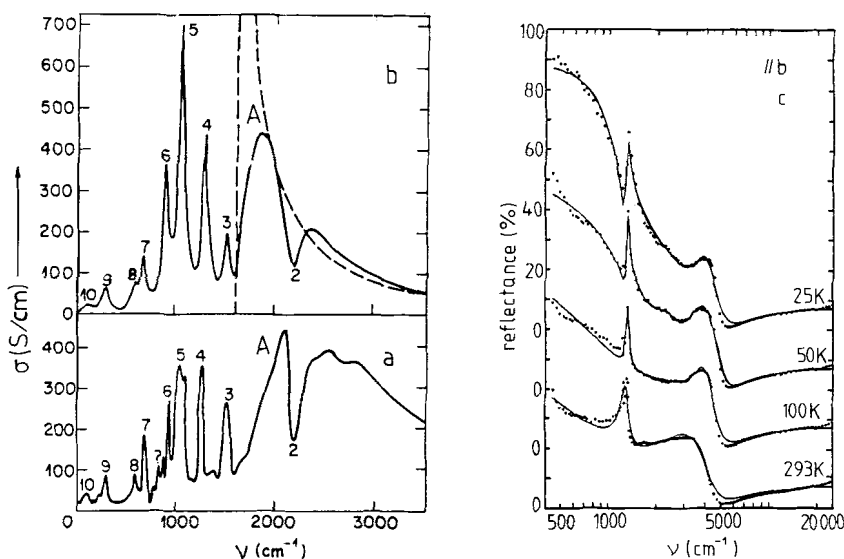


Figure 4.8-17 Infrared conductivity σ of $\text{TEA}(\text{TCNQ})_2$, experimentally determined (a), and calculated (b), according to Rice et al., 1977, and IR reflectance of $(\text{BEDT-TTF})_2[\text{Cu}(\text{SCN})_2]$ at different temperatures (c), according to Ugawa et al., 1988. The numbers in (a) and (b) refer to structures corresponding to 9 of the 10 A_g modes of TCNQ. A is the single particle electronic transition. The zeros of reflectance in (c) correspond to the four consecutive spectra.

It was quantitatively interpreted (Rice et al., 1977) as originating from bond alternation phase oscillations (in contrast to the bond alternation amplitude oscillations mentioned in subsection 4.8.2D). The vibrational absorption lines labeled 2 to 10 are directly related to the A_g Raman lines of TCNQ. The broad peak above 1600 cm^{-1} originates from the single electron transition across the gap, and the indented line shape of mode 2 is a consequence of Fano interference between the single electron continuum and the phonon mode. The line intensities are determined by the respective electron - vibration coupling constants.

IR reflection spectra have been used to study the free carrier concentration and the free carrier lifetime in superconducting systems. As an example, Fig. 4.8-17c shows the

IR reflectance of (BEDT-TTF)₂[Cu(SCN)₂] at various temperatures. The strong increase of the reflectance with decreasing temperature is due to the decreasing carrier scattering rate. The continuous line is a fit of Eqs. 4.8-1 and 4.8-2. The two peaks at 1200 cm⁻¹ and 3000 cm⁻¹, respectively, are attributed to a vibronic and to an interband transition.

Numerous other examples of the application of Raman and IR spectroscopy have been reported. For complete information, the proceedings of the biannual International Winter School on Electronic Properties of Polymers (IWEPP) and the International Conferences on Synthetic Metals (ICSM) may be considered.

4.8.4 Infrared and Raman spectroscopy of semiconductors

Both infrared and Raman spectroscopy have been used extensively to analyze semiconductors. In the case of IR spectroscopy, this appears quite natural, since the gap energies and consequently all donor or acceptor states of most of the important semiconductors are in the infrared region. In addition, the free carrier response in the presence or absence of a magnetic field is typically in the IR spectral range. Since this type of spectroscopy is purely electronic, it is not reviewed here. Instead, we will concentrate on phonon mediated spectroscopy. Similarly, Raman spectroscopy has frequently been used to study electronic transitions by resonance excitation of characteristic points in the band structure. Again, this is not reviewed here. Instead, an example is given of how free carriers can modify phonon spectra. Both IR and Raman spectroscopy of semiconductors are excellently reviewed in the following articles, IR: (Ramdas and Rodriguez, 1981; Petrou and McCombe, 1991), Raman: (Richter, 1976), and in the series on "Light Scattering in Solids" by Cardona, as mentioned in the introduction. A good example of phonon mediated IR spectroscopy of semiconductors is the soft mode behavior of IV-VI compounds. These compounds have a high temperature cubic phase with the point group O_h and NaCl crystal structure, and quite a few of them undergo a structural phase transition at low temperature to form a rhombohedral phase with point group C_{3v} . This transition is driven by an optic mode, for which the TO component softens while approaching the transition temperature. The optic modes in the cubic structure have F_{1u} symmetry and are only IR active. In the rhombohedral phase, the F_{1u} mode splits into $E + A_1$, both of which are Raman as well as IR active. The transition temperature depends on the composition of the crystal. SnTe, for instance, is cubic at room temperature, whereas GeTe is already rhombohedral and has a T_c far above 300 K. Pb_{1-x}Ge_xTe is a convenient system to study, because the carrier concentration is only on the order of 10¹⁸ cm⁻³. The TO and the LO mode frequencies are observed around 15 and 110 cm⁻¹, respectively (Jantsch, 1983). The plasma edge for 10¹⁸ cm⁻³ is around 200 cm⁻¹ and thus beyond the LO frequency. Fig. 4.8-18a shows the reflectivity of a Pb_{1-x}Ge_xTe crystal with $x = 0.0056$ in the spectral range between 5 and 30 cm⁻¹. The onset of the decrease in reflectivity is the TO component frequency. The high reflectivity above this value is due to plasma reflection. The circles are calculated from Eqs. 4.8-3b and 4.8-1. Fig. 4.8-18b shows the dependence of this frequency on the temperature and the carrier concentration. The linear relation between the square frequency and T corresponds to the Curie-Weiss

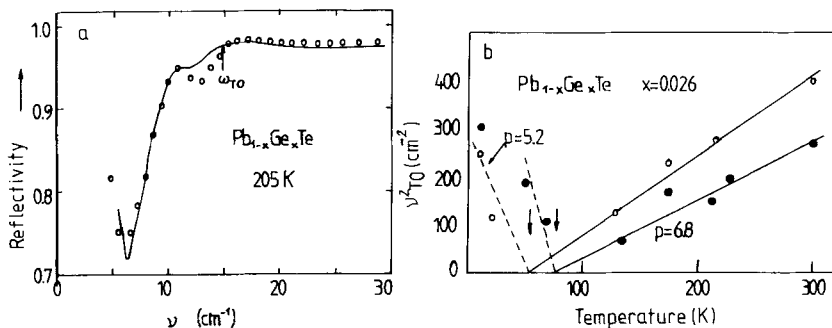


Figure 4.8-18 Soft modes of $\text{Pb}_{1-x}\text{Ge}_x\text{Te}$. Reflectivity, experimentally determined (full line) and calculated (circles), for $x = 0.0056$ (a) and square TO frequency vs. temperature for two different carrier concentrations $p = 5.2 \cdot 10^{17}$ and $6.8 \cdot 10^{17} \text{ cm}^{-3}$, respectively, as indicated in (b), according to Jantsch, 1983.

law concerning phase transition. The increase of T_c with increasing carrier concentration is due to a difference in the defect concentration and is not caused by direct interaction of the carriers with the core atoms.

Free carriers change Raman spectra, either by single particle contribution to the spectrum, or by phonon-plasmon interaction. In addition, interference of electronic transition continua with single phonon excitations may lead to Fano line shapes, as mentioned in the introduction. The Fano effect is encountered in p-doped Si crystals, as shown in Fig. 4.8-19. The shown lines correspond to the respective Raman active F_{2g} mode at 520 cm^{-1} for crystals with 4 different carrier concentrations, excited with a red laser. The continuous line is calculated according to Eq. 4.8-6. Antiresonance on the low frequency side and line enhancement on the high frequency side are a consequence of the positive value of Q . A reverse type of behavior is possible in the case of a negative Q .

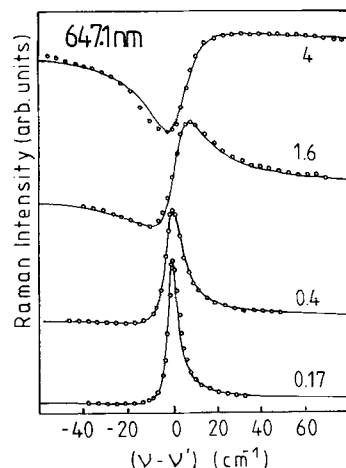


Figure 4.8-19 Raman spectrum of p-doped Si excited with a red laser, according to Cerdeira et al., 1973. The carrier concentration is indicated in units of 10^{20} cm^{-3} .

Raman scattering from free carriers in GaAs is shown in Fig. 4.8-20a for two polarization directions. With (yz) scattering, the LO and TO components of the threefold degenerate mode and a free carrier contribution around a Raman shift of zero are observed. In the case of (zz) scattering geometry, the phonon is considerably suppressed as a result of the F symmetry of the mode, but a line due to the excited plasmon appears at 130 cm^{-1} . With increasing carrier concentration, this line shifts upwards until it meets that of the phonon. Interaction with the LO component splits the mode into an ω_p^+ and an ω_p^- branch. This is shown in Fig. 4.8-20b, again for GaAs. With increasing carrier concentration, the ω_p^- branch approaches the TO phonon line, whereas the ω_p^+ branch continues to increase with the square root of the carrier concentration. The continuous lines in this figure are calculated from the coupled mode equation

$$\omega_p^{\pm 2} = \{(\omega_p^2 + \omega_{LO}^2) \pm [(\omega_p^2 + \omega_{LO}^2)^2 - 4\omega_p^2\omega_{TO}^2]^{1/2}\}/2 \quad (4.8-13)$$

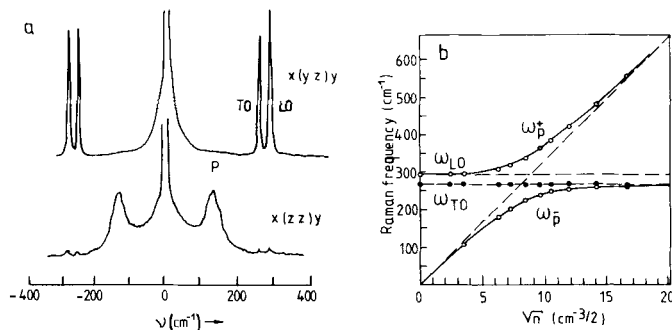


Figure 4.8-20 Raman scattering of GaAs with free carriers. $n = 1.75 \cdot 10^{17} \text{ cm}^{-3}$ and two different scattering geometries, according to Mooradian 1972, (a) and phonon-plasmon interaction vs. square root of carrier concentration, according to Mooradian and McWorther, 1967, (b).

4.8.5 Infrared and Raman spectroscopy of metals and superconductors

Infrared spectra of vibronic excitations in metals are not observed because of the strong shielding effect of free carriers. Raman spectra of conventional two-atomic or multi-atomic metals, such as Zn (Fraas and Porto, 1970) and V₃Si (Klein and Dierker, 1984), have been reported, but failed to gain importance.

Superconducting materials have been known since the discovery of the phenomenon of superconductivity in 1911 by Kamerlingh Onnes. They are characterized by the absence of any measurable resistivity and by their perfect diamagnetic behavior below

a characteristic temperature T_c . Thus, in the superconducting state a current can flow without loss. In the early days of superconductivity, transition temperatures were in the range of 10 to 20 K or lower. However, since 1986, superconductors with much higher transition temperatures have been available (Bednorz and Mueller, 1986). Latest generally accepted records in T_c are as high as 153 K (Chu et al., 1993). The high T_c materials are complicated oxidic compounds and very attractive candidates for IR and Raman spectroscopy.

A satisfactory theoretical description of the conventional superconductors, commonly known as the BCS theory, was published in 1957 by Bardeen, Cooper, and Schrieffer. The basic principles of this theory involve pairing of electrons by interaction with a lattice distortion (phonon). As a consequence the originally continuous distribution of excited electronic states is now interrupted by a gap of 2Δ between the occupied states below and empty states above it. The BCS theory claims that this energy is related to the transition temperature by $2\Delta = 2.53K_B T_c$. Formally, the gap resembles the energy gap of a semiconductor. However, its response to electromagnetic radiation is completely different. Incident radiation with a frequency below the gap energy is not transmitted but totally reflected, since the impedance is a pure inductance for a lossless current. For a radiation with a quantum energy larger than 2Δ single electrons can be excited and the radiation is absorbed. Thus, the change of reflectivity from a value of exactly 1 to less than one as a function of the frequency determines the gap energy, which is one of the most important parameters of a superconductor. Since gap energies of classical superconductors are in the range of several wavenumbers and those of oxidic superconductors are expected to be on the order of several ten to hundred wavenumbers, far-IR spectroscopy is very useful for such investigations. Superconducting energy gaps of In, Sn, and Pb have thus been determined (Richards and Tinkam, 1960).

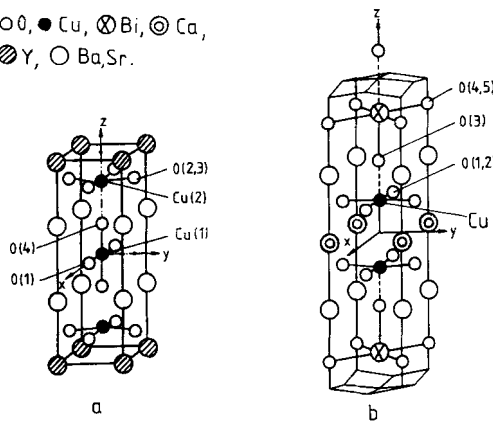
IR and Raman spectroscopy have proven to be particularly useful tools for the investigation of oxidic systems, since these materials can be prepared at a wide range of carrier concentrations, even below metallic values. They show very pronounced phonon spectra which exhibit a number of unique features concerning the transition to the metallic state and the transition to the superconducting state. Thus, the following discussion focuses exclusively on oxidic systems.

The superconductor originally discovered by Bednorz and Mueller was $\text{La}_{2-x}\text{Ba}_x\text{CuO}_4$ ($x = 0.75$), with a T_c of 35 K. The bivalent Ba atom acts as a doping species as it replaces the trivalent La atom in the insulator La_2CuO_4 . The La-system was shortly later outdated by $\text{YBa}_2\text{Cu}_3\text{O}_7$, which has an even higher T_c of 92 K. The structures of all presently known oxidic superconductors are perovskite-related, with a characteristic CuO_2 plane as the most important structural element. Superconductivity is thought to be located in these planes. Fig. 4.8-21 shows two representative structures of oxidic superconductors. Both of these systems have two CuO_2 -planes per unit cell. In the Y compound, these planes are formed by the atoms labeled O(2,3) and Cu(2), while in the Bi compound they are defined by the atoms labeled O(1,2) and Cu. Almost all systems either belong to the point group D_{2h} or D_{4h} . Thus, factor group analysis of vibrational modes affords straightforward results. Tab. 4.8-5 lists some of the most important superconducting compounds, together with their Raman and IR lines. Column 2 shows the conventional symbol for each superconductor. Considerable effort has been dedicated to the assignment

Table 4.8-5 Raman and IR lines of oxidic superconductors

Superconductor	Symbol		Wavenumber cm ⁻¹	Raman active	Reference
La ₂ CuO ₄	214	426(4)	276(2) 229(>5)	154(2)	Sugai et al., 1990
YBa ₂ Cu ₃ O ₇	123	502(5)	440(2) 340(4)	150(3)	Kuzmany et al., 1989
Bi ₂ Ca ₁ Sr ₂ Cu ₂ O ₈	2122	630(5)	470(2) 290(1)	120	Kuzmany et al., 1989
Nd _{2-x} Ce _x CuO ₄		581(5)	480(2) 328(3)	228(3)	Heyen et al., 1990
IR active					
La ₂ CuO ₄ E ,TO	214	645(1)	504(5) 352(3)	244(1)	Sugai et al., 1990
YBa ₂ Cu ₃ O ₇	123	610(5)	570(2) 320(4)	195(2)	Kuzmany et al., 1989
Bi ₂ Ca ₁ Sr ₂ Cu ₂ O ₈	2122	590(5)	480(3) 370		Forro et al., 1990
Nd _{2-x} Ce _x CuO ₄ ,E _u	NdCe	512(2)	353(5) 304(5)	132(3)	Heyen et al., 1990

○ O, ● Cu, ⊗ Bi, @ Ca,
⊗ Y, ○ Ba, Sr.

**Figure 4.8-21** Crystal structure of oxidic superconductors: YBa₂Cu₃O₇ (a) and Bi₂Ca₁Sr₂Cu₂O₈ (b).

of the lines; as a consequence, these lines are now reasonably well interpreted. As a general rule, the strong lines in the spectral range between 300 and 500 cm⁻¹ correspond to the motion of various oxygen atoms. Low frequency modes around 150 cm⁻¹ and below are caused by copper, rare earth, or alkali metals. The lines listed in Tab. 4.8-5 are to some extent average values of results reported by several authors, as discussed in a recent review article (Kuzmany et al., 1989; Thomson and Cardona, 1989). More recent data on single crystals may be obtained from (McCarty et al., 1990), who describes the 123 system, and from (Boekholt et al., 1990a), who focuses on the 2122 system. The frequencies in the spectra of 214 and NdCe are selected single crystal data. Of the many known oxidic superconductors, YBa₂Cu₃O₇ is the most extensively investigated and thus also the best analyzed system. The most important vibrations are those which are closest

to the superconducting CuO plane. In 123 compounds, these include the asymmetric out-of-plane oxygen motion at 340 cm^{-1} (*as*-O(2,3) mode), the symmetric out-of-plane oxygen motion at 440 cm^{-1} (*s*-O(2,3) mode), and the apex oxygen (O4) motion parallel *c* at 502 cm^{-1} in the Raman spectra and related modes in the IR spectra. Factor group analysis shows that the apex oxygen atom has only Raman-active modes, whereas the oxygen in the CuO chain (Cu(1),O(1)) exhibits only infrared-active modes.

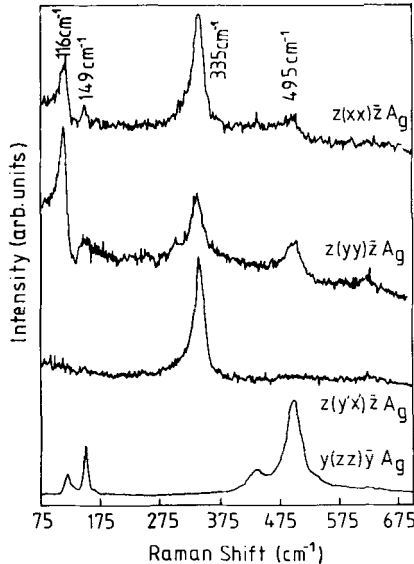


Figure 4.8-22 Polarized Raman spectra of twin free single crystals of $\text{YBa}_2\text{Cu}_3\text{O}_7$, according to McCarty et al., 1990.

Single crystal Raman spectra of 123 compounds have defined selection rules and prove that in unpolarized spectra A_g modes dominate. Fig. 4.8-22 shows polarized Raman spectra of these compounds. The strongest spectra are obtained with a (zz) scattering geometry, except for the *as*-O(2,3) mode at 340 cm^{-1} , which has a nearly zero Raman tensor component in this direction. It is therefore occasionally referred to as quasi B_{1g} .

The quasi B_{1g} mode exhibits a strong asymmetric line shape which originates from an interaction of the mode with the electron continuum (Coopper et al., 1988; Friedl et al., 1990). The asymmetry, the line width and the line position are characteristic functions of the temperature. This is demonstrated in Fig. 4.8-23a where the Raman lines for the modes as measured above and below T_c are shown for $\text{ErBa}_2\text{Cu}_3\text{O}_7$. The full drawn lines are fitted from Eq. 4.8-6. For temperatures below T_c the line is clearly downshifted and broadened in contrast to what one would expect from a conventional behavior of vibrational modes. The broadening and the softening of the line starts exactly at the transition temperature to superconductivity and thus demonstrates a strong interaction of the phonons with the charge carriers. In contrast to the results for the Er-compound the Eu-compound with the same structure and the same value for T_c does not show the broadening. Since in the Eu-compound the quasi B_{1g} mode has a 10% lower frequency it is concluded that the broadening mechanism originates from a breaking of electron pairs and the vibrational quanta in the Eu-compound do just not have enough energy for

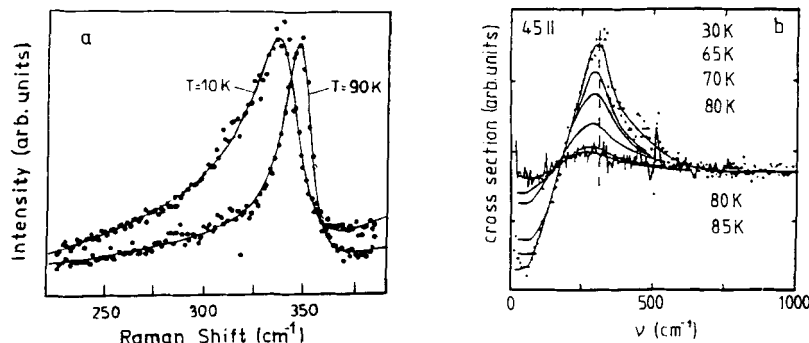


Figure 4.8-23 Raman lines for the *as*-O(2,3) mode of $\text{ErBa}_2\text{Cu}_3\text{O}_7$ as measured above and below T_c , according to Friedl et al., 1990 (a) and electronic Raman scattering of single crystal $\text{YBa}_2\text{Cu}_3\text{O}_7$ at various temperatures and after subtraction of phonon lines, according to Hackel, 1990, (b).

this process. This yields a very accurate value of $5k_B T_c$ for the gap energy in the 123 superconductors.

Theoretical models to explain the observed change in line width and line position as a result of transition to superconductivity quantitatively are based on strong electron-phonon interaction (Zeyher and Zwicknagel, 1990).

Raman scattering from the electronic continuum is another possibility to obtain information on the superconducting energy gap. According to Eq. 4.8-7, electronic Raman scattering provides a spectrum with a broad continuum. The opening up of a gap is reflected in the scattering continuum as a bleaching of the low energy part and an increase of the Raman intensities just above the gap energy. This behavior has been observed in single crystal spectra of $\text{YBa}_2\text{Cu}_3\text{O}_7$ (Cooper et al., 1988; Hackl et al., 1990), as shown in Fig. 4.8-23b, and in those of $\text{Bi}_2\text{Ca}_1\text{Sr}_2\text{Cu}_2\text{O}_8$ (Boekhold and Guentherodt, 1990b). The spectra shown in Fig. 4.8-23b are obtained at various temperatures after subtracting the phonon lines. The gap in the electronic spectrum starts to open up at T_c and becomes more and more pronounced as T approaches zero. The observed shape of the Raman intensity is a good measure of the electronic density of states in the superconductor. The continuous line has been calculated by a theoretical model, as described by Klein and Dierker (1984).

At T_c , infrared spectra also exhibit various phonon anomalies. Fig. 4.8-24 demonstrates this for a Cu/Ga substituted 123-superconductor (a) and a Tl-based superconductor (b). The Y compound clearly shows spontaneous softening of the mode at T_c , whereas in the spectrum of the Tl superconductor the mode at 305 cm^{-1} bleaches below T_c (110 K), while another mode at lower energy gains oscillator strength. Interestingly, IR-active phonons do not only soften but may also harden as a consequence of phase transition. This led to the conclusion that there are two different gap energies, one around 30 meV ($\approx 5k_B T_c$) for electrons in the *a*, *b* plane, and one around 10 meV ($\approx 1.7k_B T_c$) in *c*-direction.

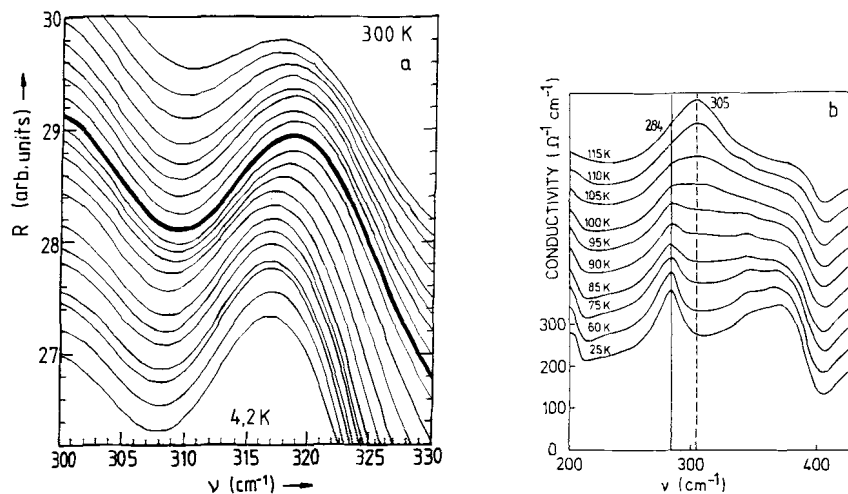


Figure 4.8-24 Phonon anomalies from IR-reflectance on $\text{YBa}_2\text{Cu}_3\text{O}_7$ (a), according to Kuzmany et al., 1990b, and from IR-conductivity in $\text{Tl}_2\text{Ba}_2\text{Sr}_2\text{Cu}_3\text{O}_{10}$ (b), according to Zetterer et al. 1990. The bold line in part (a) labels the transition temperature.

Direct measurement of the superconducting energy gap by an IR reflectivity experiment below and above T_c turned out to be difficult if the electric field vector was polarized in the a, b plane, due to the so-called clean limit condition of oxidic superconductors. Clean limit means the gap energy is larger than \hbar/γ . γ is the reciprocal electron life time in Eq. 4.8-1. According to the clean limit condition, the response of the IR reflectivity to the opening of the superconducting gap is very small (Timusk and Tanner, 1989). Electrons in substituted samples usually have a shorter mean free path, so that the gap is observed more easily. However, it is important to keep in mind that in polycrystalline samples the change in reflectivity of the polarization of the light along the c axis dominates and that therefore only the gap in this direction is observed. Fig. 4.8-25 shows values of the reduced energy gap $\epsilon_g(T)/\epsilon_g(0)$, derived from the onset of the reflectivity change as a function of frequency versus reduced temperature T/T_c in two samples of a 123 compound with different transition temperatures.

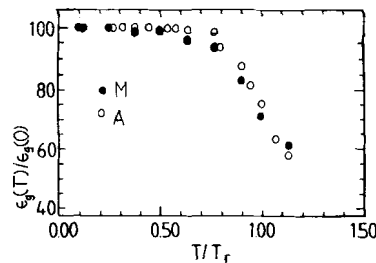


Figure 4.8-25 Reduced energy gap versus reduced temperature for two substituted $\text{YBa}_2\text{Cu}_3\text{O}_7$ superconductors with transition temperatures of 80 K (\bullet) and 60 K (\circ), respectively, according to Kuzmany et al., 1990b.

Another interesting phenomenon in such compounds shown by IR spectroscopy is the decrease of oscillator strength with increasing carrier concentration. This effect has been demonstrated clearly by the LaSr system, where the carrier concentration can be changed continuously by changing the Sr concentration. The response of the IR absorption lines to a changing carrier concentration depends considerably on the polarization of the mode. In Fig. 4.8-26, this is demonstrated for the spectral range between 400 and 800 cm⁻¹. The two absorption lines at 677 cm⁻¹ and 517 cm⁻¹ correspond to an in-plane oxygen motion and to an out-of-plane Cu motion, respectively. The in-plane mode response decreases with increasing carrier concentration and is completely shielded in the metallic state. However, it reappears if the system is counterdoped by Cu/Zn substitution.

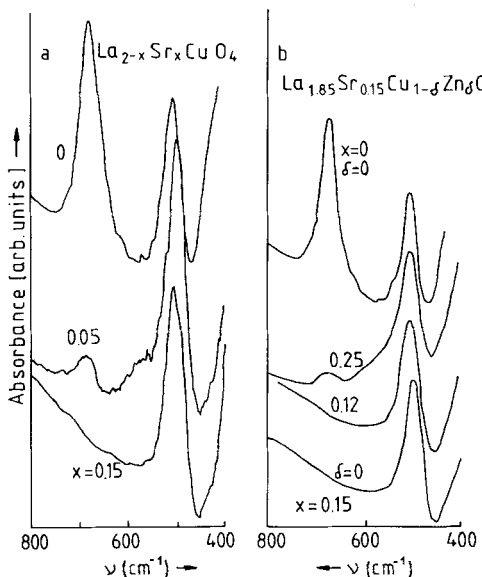


Figure 4.8-26 Absorption of IR-active vibrational modes in $\text{La}_{2-x}\text{Sr}_x\text{CuO}_4$ at different doping concentrations; Sr doping (a) and Cu/Zn substitution (b).

4.8.6 Infrared and Raman spectroscopy of fullerenes

Fullerenes are definitely beautiful materials and particular useful to demonstrate the potentialities of Raman and infrared spectroscopy. They represent a new form of carbon first discovered by Kroto and Smally in laser evaporated graphite (Kroto et al., 1985). However, access to material science was only after Krätschmer and Huffman discovered a technique to prepare large quantities of these compounds by burning graphite in an arc discharge (Krätschmer et al., 1990). The most famous and the most intensively studied fullerene is the soccerball shaped C_{60} consisting of 20 carbon hexagons and 12 carbon pentagons entangled in a way to give I_h point symmetry. The C_{60} molecule is

shown in Fig. 4.8-27a. At room temperature these molecules form the molecular crystal fullerite which has an *fcc* Bravais lattice (Fig. 4.8-27b). The *fcc* lattice is not immediately compatible with the I_h symmetry of the molecule but requires free rotation of the latter on its crystal site. This gives rise to several interesting phase transitions on cooling the fullerite to low temperatures.

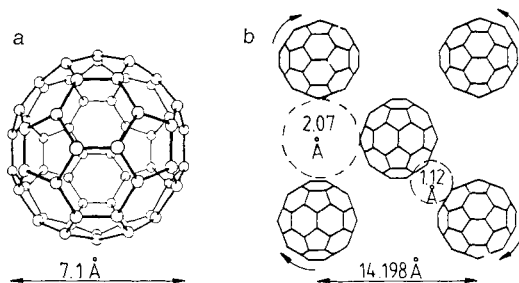


Figure 4.8-27 C_{60} fullerene molecule (a) and C_{60} fullerite crystal (b). The dashed circles in b represent the octahedral and tetrahedral interstitial sites at $(1/2, 1/2, 1/2)$ and $(1/4, 1/4, 1/4)$, respectively.

The carbon atoms are in a nearly sp^2 hybridized state which relates these compounds strongly to the conjugated polymers and guarantees the same colorful vibrational spectroscopy as described in the above subsections. Also, the fullerenes can be doped to a metallic state which in some cases even goes superconducting with a rather high transition temperature (Rosseinsky et al., 1991). The state of the art in fullerene research up to 1993 is well described in (Dresselhaus et al., 1993).

Undoped fullerenes

The I_h symmetry of the 60-atoms molecule allows $2A_g$ and $8H_g$ modes to be Raman active and $4T_{1u}$ modes to be IR active. The four IR active modes are at 1430, 1185, 580 and 528 cm^{-1} , respectively. The most important Raman modes are at 1469 (tangential bond alternation or pinch mode, A_g), 495 (radial breathing mode, A_g) and 271 (squashing mode, H_g) cm^{-1} , respectively. In the low temperature phase degenerate modes split from a crystal field and Davidov interaction. Good reviews on the group theoretical analysis and on the line positions are given in (Dresselhaus et al., 1992; Matus and Kuzmany, 1993).

Doped fullerenes

Doping of fullerenes proceeds similar to the doping of polymers. Electron donors are intercalated to the rather large octahedral and tetrahedral interstitial sites of the *fcc* lattice and fill the originally LUMO derived band of the semiconducting pristine compound with electrons. The resulting materials are fullerides, salts of the fullerites. Basic information on the structure and properties of fullerites and fullerides can be obtained from the special

issue in J. Chim. Phys. Solids edited by Fischer and Cox (1992). Partial filling of the LUMO band can lead to a metallic state. This is for example the case when doping with the alkali metals potassium or rubidium to the stoichiometry M_3C_{60} where M is the alkali metal. As in the case of the CT-systems vibrational modes are characteristically shifted by this process and the measurement of the line positions allows to determine the charge transfer. This works particularly well for the A_g -pinch mode as shown in Fig. 4.8-28a. As a matter of fact the phase K_1C_{60} was first discovered by its characteristic Raman spectrum (Winter and Kuzmany, 1992) and was found to undergo a phase separation into two other compounds with $x = 0$ and $x = 3$ below a characteristic temperature of 420 K. This is demonstrated in Fig. 4.8-28b. Good summaries representing the state of the art in Raman spectroscopy of the fullerene derived materials can be found in (Eklund et al., 1993; Kuzmany et al., 1994).

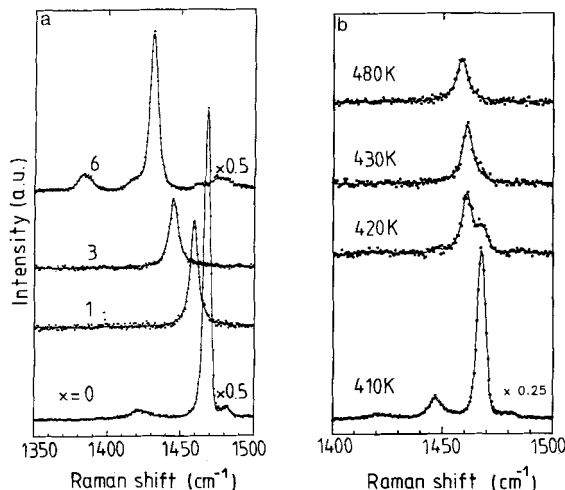


Figure 4.8-28 Position and line shape of the A_g -pinch mode in K_xC_{60} for various doping states x in single crystal C_{60} (a) and temperature dependence of the spectra in the corresponding spectral range for $x=1$, Winter and Kuzmany (1994), unpublished; (b), according to Winter and Kuzmany (1994).

Similar results were obtained for the T_{1u} modes from IR spectroscopy. The highest mode was found to shift as much as 15 cm^{-1} per charge on the molecule between $x = 0$ and $x = 6$. Coupling of the vibrations to the charge on the molecule leads in some cases to a dramatic increase of the infrared activity (Pichler et al., 1994). Figure 4.8-29 shows the near IR reflectivity for three phases of the fullerene as obtained from a thin film sample. Undoped C_{60} and K_6C_{60} are semiconductors with a high IR transmission off the vibronic resonances and thus exhibit interference fringes. K_3C_{60} is a metal with a Drude like reflectivity and no interferences.

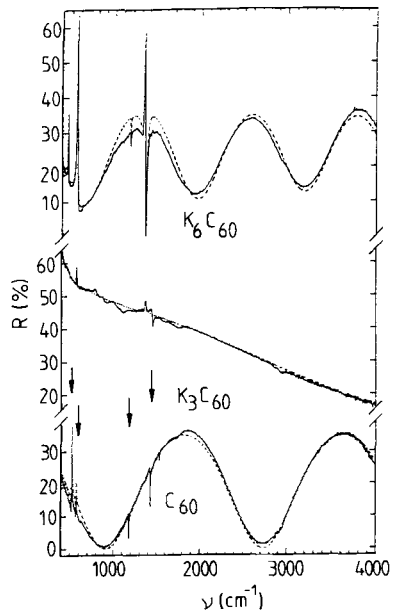


Figure 4.8-29 Near infrared reflectivity of a thin fullerite film and fulleride films doped with potassium to $x=3$ and 6 . The dashed line is as calculated from Eq. 4.8-1 to 4.8-3 including multiple reflection, according to Pichler et al., 1994. The four F_{1u} modes in the undoped film ($x=0$) are marked with arrows.

4.8.7 Summary and conclusion

This section demonstrates that both Raman and IR spectroscopy can be employed advantageously to investigate systems with free carriers. The response of the carriers may either be direct, in the sense that they contribute immediately to the interaction of the exciting laser light or the exciting IR radiation with the system, or it may be indirect, i.e., via interaction with the phonons. In addition, vibrational scattering or vibrational absorption also yield information on important parameters of such systems.

The section focuses on conducting polymers whose Raman spectrum is always resonance-enhanced and thus yields information not only on the vibronic structure but also directly on the electronic system. IR spectroscopy may be employed to study the doping process and to analyze phase transitions. In the case of organic charge transfer systems, Raman scattering and IR spectroscopy were shown, among others, to provide information on band filling, free carrier concentration, and mobility. Electronic Raman scattering and free carrier effects of classical semiconductors have been extensively investigated and are thoroughly understood. Finally, high temperature superconductors and fullerenes are a new and promising field of application of Raman and IR spectroscopy, even though in IR spectroscopy the clean limit conditions of cuprat superconductors give at present a problem to straightforward analyses.

5 Evaluation procedures

5.1 Quantitative analysis, automatic quality control*

5.1.1 General

The integrated intensity of an infrared absorption band is given by

$$A = \frac{N \cdot \pi}{3 c} \left(\frac{d\mu}{dQ} \right)_0^2, \quad (5.1-1)$$

it is proportional to the change of the molecular dipole moment μ with the normal coordinate Q (describing the vibration, see Sec. 2.3).

The intensity of the radiation scattered by the Raman effect, I_R , excited with radiation of a frequency $\tilde{\nu}_0$ is proportional to I_0 , the radiant power of the exciting radiation:

$$I_R \sim N \cdot I_0 (\tilde{\nu}_0 \pm \tilde{\nu}_k)^4 \sum (\alpha'_{\rho\sigma})_k^2 \quad (5.1-2)$$

$\tilde{\nu}_k$ is the frequency of the normal vibration k and $\alpha'_{\rho\sigma}$ the change of the components of the molecular polarizability with the normal coordinate (see Secs. 2.4, 3.4.5 and 3.5.4). In both cases, N is the number of molecules per unit volume involved in the process. IR as well as Raman spectroscopy can therefore be applied in quantitative analysis.

Information concerning the identity and the quantity of a compound is encoded in the spectral features of the bands: their position, intensity, and shape. The overall information which is contained in a spectrum, according to information theory amounts to $10^4 \dots 10^7$ bit (see Secs. 3.3.4 and 3.3.5).

Out of this content, only 10 bit of information are needed to quantify one compound in a sample with an accuracy of about 0.1 %. For quantitative determination, one intensity measurement has to be carried out for each investigated analyte. The number of significantly different intensity intervals S , and, based on these, the information content of the spectrum $I = \text{ld } S$ increases with decreasing noise power Φ_N :

$$S = \frac{\Phi_2 - \Phi_1}{\Phi_N} \quad (5.1-3)$$

Here, $\Phi_2 - \Phi_1$ is the range of the intensity scale.

* Section 5.1 is contributed by M. Spickermann, Lübeck

The same equation applies to trace analysis; however, due to the fact that in this case the concentrations are near those given by the detection limit, the number of intensity intervals is smaller than in quantitative analysis, which is performed in an optimum concentration range (see Fig. 5.1-1). Detection limits in trace analysis as well as some general considerations concerning this issue are discussed in Secs. 3.3.4, 3.3.5 and 3.4.4 (Schrader, 1980; Schrader et al., 1981).

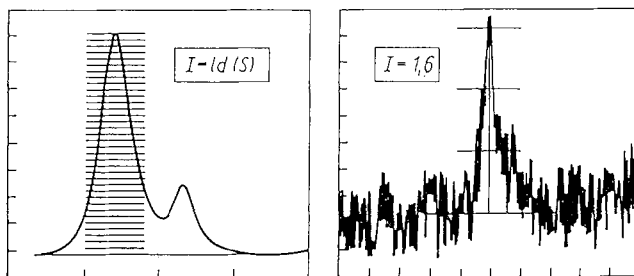


Figure 5.1-1 Information contents of vibrational spectra. The number of intensity intervals and therefore the information which is available for quantitative analysis depends on the noise in the spectra.

Quantitative analyses are usually carried out by comparing the measured quantities of test samples with those of standards with known concentrations. Due to the uniqueness of the vibrational spectrum of a compound, individual bands can often be found which make it possible to carry out multicomponent analyses, even with mixtures of ten or more constituents. Another advantage is the extremely wide variety of samples which can be analyzed by vibrational spectroscopy. The prerequisites and the evaluation procedures for single as well as for multicomponent analyses have been described extensively by Weitkamp and Barth (1976). Several optimization procedures have been published by Junker and Bergmann (1974, 1976).

Multicomponent analyses must occasionally be performed without external calibration if the pure components are not available (as for conformational equilibria or problems in polymer chemistry). Adequate methods to solve these problems are discussed by Koenig et al. (1977, 1979).

In principle, it is possible to determine compounds in the concentration range from ppm up to 100%, with a standard deviation of about 1% or less. In multicomponent analysis, the lowest concentration of each investigated component must be of the order of about 1%. The amount of substance which is needed for IR as well as for Raman experiments is in general in the range of a few milligrams. For both methods, microtechniques are available, which reduce the necessary amount by several orders of magnitude (see Secs. 3.4.4 and 3.5.3.3).

In quantitative analysis usually calibration functions are needed which reflects the relation between the measured quantity (for instance, the radiant flux) and the concentration. The S/N ratio should be as high as possible in order to afford the maximum number of distinguishable intensity intervals. As a consequence, the spectral band width should

be rather wide (Schrader et al., 1981). Systematic distortions of the band profiles in the spectra may be corrected by either including them in the calibration or by correcting them by one of the methods described in Sec. 5.1.3.2.

If modern equipment with *online* computers is available, the sensitivity of IR and Raman spectroscopy can be enhanced by techniques such as spectral smoothing, deconvolution of overlapping bands, difference spectroscopy, derivative spectroscopy, or integration of band areas. A relative accuracy of approximately $\pm 10\%$ requires only a small number of standards (possibly only one); whereas analyses with an accuracy of $\pm 1\%$ often require preparation of a number of standards, as well as certain precautions concerning the instrumental parameters and the sample itself. Since the precision of an analysis cannot be better than that of the analyzed sample, sampling and sample preparation have to be carried out very carefully. With nearly all methods of quantitative analysis, it is basically necessary to prepare standards which are as similar as possible to the sample itself in order to include non-linearities due to interactions between the constituents in the calibration. It is assumed generally that the overall signal is a linear combination of that of the analyte as well as that of the non-analyte components. It is useful to eliminate or to minimize the effect of the non-analyte signals on the quantitative analysis. The first step in a quantification procedure is therefore the identification of at least the main components of a sample.

There are several textbooks which discuss basic considerations concerning quantitative analysis by vibrational spectroscopy. Only a few of them present a realistic discussion of practical aspects, including an estimate of errors related to particular steps of the methods, for instance, the textbooks by Weitkamp and Barth (1976), Volkmann (1972), Smith (1979, 1986), Günzler and Böck (1975) on IR spectroscopy; and Otting (1952), Schrötter and Klöckner (1979), and Grasselli and Bulkin (1991) on Raman spectroscopy.

Vibrational spectroscopy is best suited for the identification and subsequent quantification of compounds in connection with quality control. A simple but very impressive method of automatic identity control has been described by Weitkamp and Wortig (1977) (see Sec. 5.1.6, 3).

5.1.2 Relation between measured quantities and concentration

In absorption spectroscopy, including IR, the fundamental equation which governs the relation between the intensities of the incident and the transmitted radiation (I_0 and I) and the concentration c is referred to as the Lambert-Beer law, expressed as

$$\log \frac{I_0}{I} = \log \frac{1}{\tau} = A = a c d \quad (5.1-4)$$

A = absorbance

a = absorption coefficient

d = cell thickness

c = concentration of the sample

τ = transmittance

Certain requirements are assumed to be met in the derivation of this law. Some of the major ones are:

- monochromatic light with parallel rays
- no stray light
- parallel entrance and exit planes
- homogeneously distributed sample with infinitesimal small particle size (no scattering)
- no molecular interaction

It is difficult to meet all of these requirements. Deviations from the Lambert-Beer law may be due to the spectrometer, to the reflection at the cell windows (Staat et al., 1983), to cell imperfections, or to effects caused by the sample itself. If these are recognized and taken into account in the calibration, they do not affect the quantitative accuracy. Since Eq. 5.1-4 holds only for monochromatic radiation, the finite slit width of the spectrometer is an important factor causing deviation from the law while using grating spectrometers. This slit width, together with the particular slit function, makes polychromatic radiation with a small wavenumber interval reach the detector instead of monochromatic radiation. The wavenumber interval increases if the slit is opened in order to reduce the noise. This results in a shift of the maximum absorbance from the true to an apparent value, unless the slit width is much smaller than the band width. Based on the assumption of Lorentzian band shapes, ratios of true to apparent maxima for various slit widths and absorbance values have been listed by Ramsay (1952). A more detailed description of the spectrometer function has been provided by Volkmann (1972). In quantitative analysis, the described errors affects the linearity and the slope of the calibration curve, but only if the maximum absorbance is taken into account. As the maximum of a band decreases, the band itself broadens. The integrated intensity is thus practically unaffected and can be considered as a better quantity for quantitative analysis. This holds also in situations when the width or the shape of the analyte band changes with increasing concentration of the analyte or when the appearance of the band is influenced by molecular interactions from the matrix.

The relation which describes the intensity of a Raman band is determined by the number of scattering molecules per unit volume N , the differential scattering cross section $d\sigma/d\Omega$, and the intensity of the incident laser beam I_0 :

$$I \sim N I_0 \cdot \left(\frac{d\sigma}{d\Omega} \right) \quad (5.1-5)$$

(Eq. 5.1-2, Secs. 2.4, 3.5.4). Hence, if the scattering cross section $\left(\frac{d\sigma}{d\Omega} \right)$ is independent of the concentration and if the intensity of the incident laser beam I_0 remains constant, then the intensity of a band is directly proportional to the sample concentration. This concentration can be derived from the spectrum of an unknown

- directly, if the value of the scattering cross section is known,
- by comparison with standards of known concentrations, as in the case of IR spectroscopy.

It is often possible to use the height of a line as a measure of the intensity. Nevertheless, as in the case of IR, it seems to be better to also employ band areas for quantitative de-

termination. It should be emphasized that Raman spectra may be masked by fluorescence of impurities in a sample, as well as by stray light resulting from elastically scattered radiation. Interference due to fluorescence may be discovered by changing the excitation wavelength. If the wavelength of the exciting radiation is increased, the disturbing fluorescence is reduced or even eliminated, as for NIR FT Raman spectroscopy (see Sec. 3.5.5).

In IR as well as in Raman spectroscopy, effects resulting from the sample itself appear mainly at higher concentrations and may be due, for example, to intermolecular interactions (hydrogen bonding, formation of associates, micelles, etc.). The resulting deviations from the Lambert-Beer law or their influence on the measured Raman band positions or intensities can be used to study these intermolecular interactions.

5.1.3 Quantitative analysis by IR spectroscopy

According to the Lambert-Beer law, the absorbance can be related directly to the concentration of a compound in a sample. However, IR spectrometers usually record and present data in terms of percent transmission rather than in absorbance units. In these cases, the absorbance values, which are proportional to the logarithms of the respective transmission values (see Eq. 5.1-4), have to be calculated from the spectra. Absorbance measurements should be taken exactly for the band maximum. Even small errors in the reproducibility of the wavenumber setting causes considerable variations of the measured absorbance. In order to avoid errors due to the influence of the spectrometer function, it

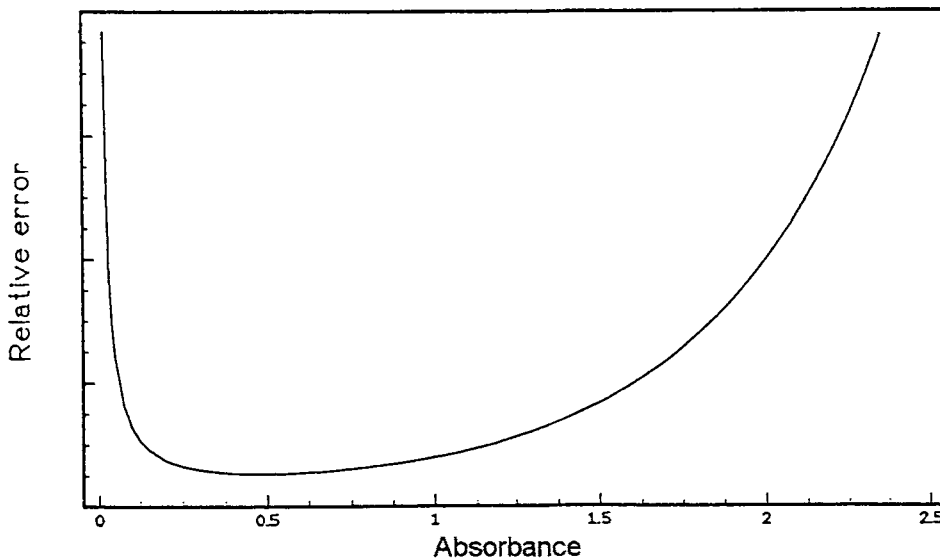


Figure 5.1-2 Error function for absorbance measurements.

has already been pointed out that evaluation should be based on the integrated absorbance of a band rather than on the absorbance at a single wavenumber. There is no limitation to the type of band which can be used for analysis if the absorbance is in the optimum range of $0,2 < A < 0,7$ equivalent to a transmission of about $60\% > \tau > 20\%$. This can be ensured by adjusting the sample concentration or the cell thickness. In this range, the absorbance reading shows a minimum error (see, Fig. 5.1-2). A characteristic feature of quantitative analysis, the detection limit, is discussed in Sec. 3.3.5. Stevenson and Winefordner (1991) discuss the procedure to determine the detection limit of ultratrace analyses.

5.1.3.1 Calibration methods based on band maxima

Absorbance values can be calculated in different ways, depending on the available spectrometer:

- a) in cases where data have to be treated manually, the procedure involves using a millimeter scale and calculating $\log(I_0 / I)$ as shown in Fig. 5.1-3a.

The absorbance calculation itself makes it necessary to determine the transmittance of the band maximum (I) as well as that of the 'band minimum' (I_0), which equals the transmission of the so-called background. Despite the fact that I_0 may be difficult to determine accurately, satisfactory baselines can in many cases be constructed, as shown in Fig. 5.1-3b. This method is known as the 'baseline method'.

- b) if the spectrum is presented on an absorbance scale, the value can be derived directly from the difference between the maximum and the minimum absorbance at the wavenumber of the maximum of the band with various baseline options as shown in Fig. 5.1-4.

There are applications, where best results can be obtained without using a baseline (McClure, 1987). If solvent and sample bands overlap, the solvent bands can be compensated for by placing a matching cell in the reference beam, filled with pure solvent only. Using modern computer assisted instrumentation, this compensation can also be performed mathematically by subtracting the solvent spectrum from that of the dissolved sample.

There are several methods of obtaining more accurate quantitative results:

- 1) The first method involves preparing standard analyte solutions at concentrations that are, respectively, slightly lower and slightly higher than that of the analyte in the unknown sample, but are always similar to the sample concentration. By placing the unknown in the sample beam and each of the standards successively in the reference beam of a double beam spectrometer, a series of curves can be obtained which reflect only the difference between the unknown and the standards. The differences can be magnified by employing ordinate expansion methods. Even small differences in composition between unknown and standards are thus reflected as large differences in the spectrum (Smith, 1979, 1986).
- 2) There is a variation of this method, which is particularly suited to samples which contain only a small amount of a substance whose bands, to add to the problem, overlap with those of a main component. In this case, the first scan is obtained as outlined

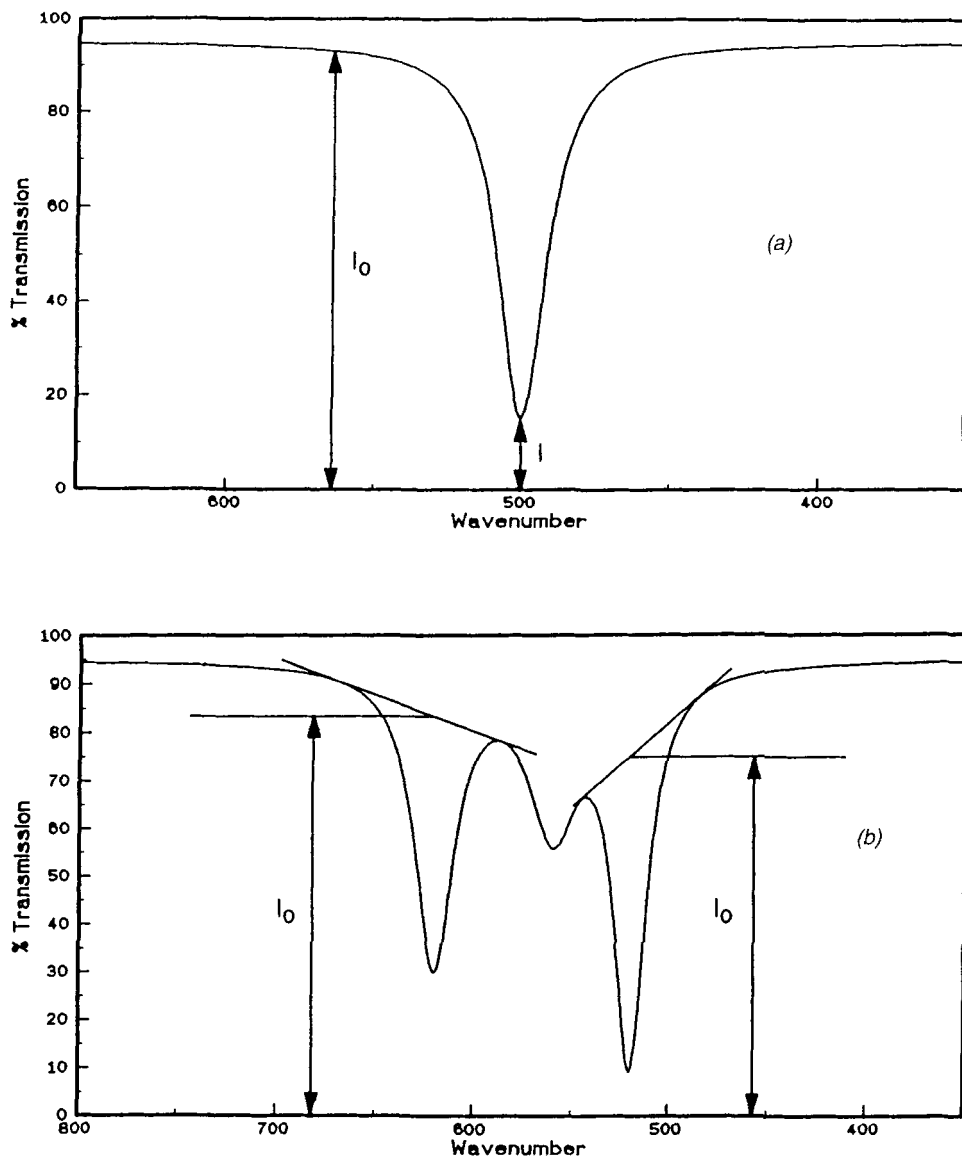


Figure 5.1-3a/b Definition of I_0 and I for the determination of absorbance values from transmittance spectra.

above. The contents of the sample and the reference cell are then exchanged (not the cells themselves!) and a second scan is recorded. The resulting difference is now twice as high as that obtained with a single scan, so that the accuracy also increases by a factor of two. Another advantage of this method is that cell mismatch is automatically encountered (Smith, 1979, 1986).

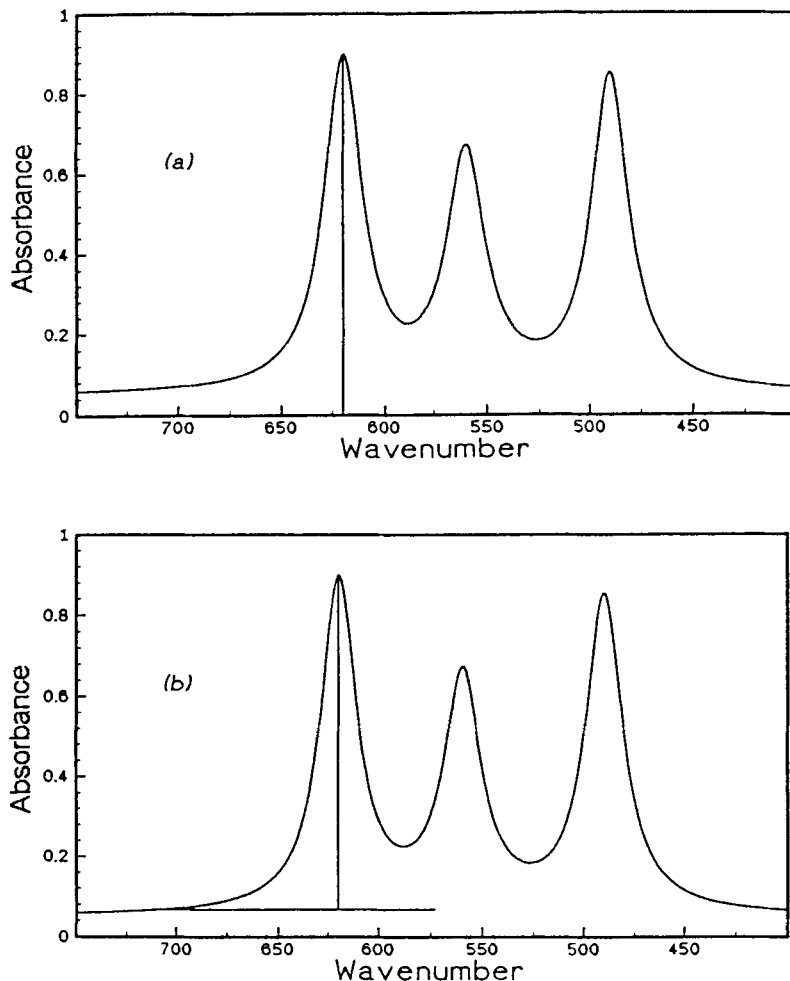


Figure 5.1-4 Illustration of various baseline options in spectral evaluation by peak height measurements (a) no baseline; (b) horizontal single-point base-line; (c) two-point baseline; (d) common tangent baseline.

3) In general, difference spectroscopy is capable of providing an accuracy on the order of 0.1% or even better, particularly if the noise is reduced by accumulating spectra. This is not very time-consuming with FT-IR spectrometers. A general procedure for setting up analyses by difference spectroscopy has been described by Smith (1979, 1986).

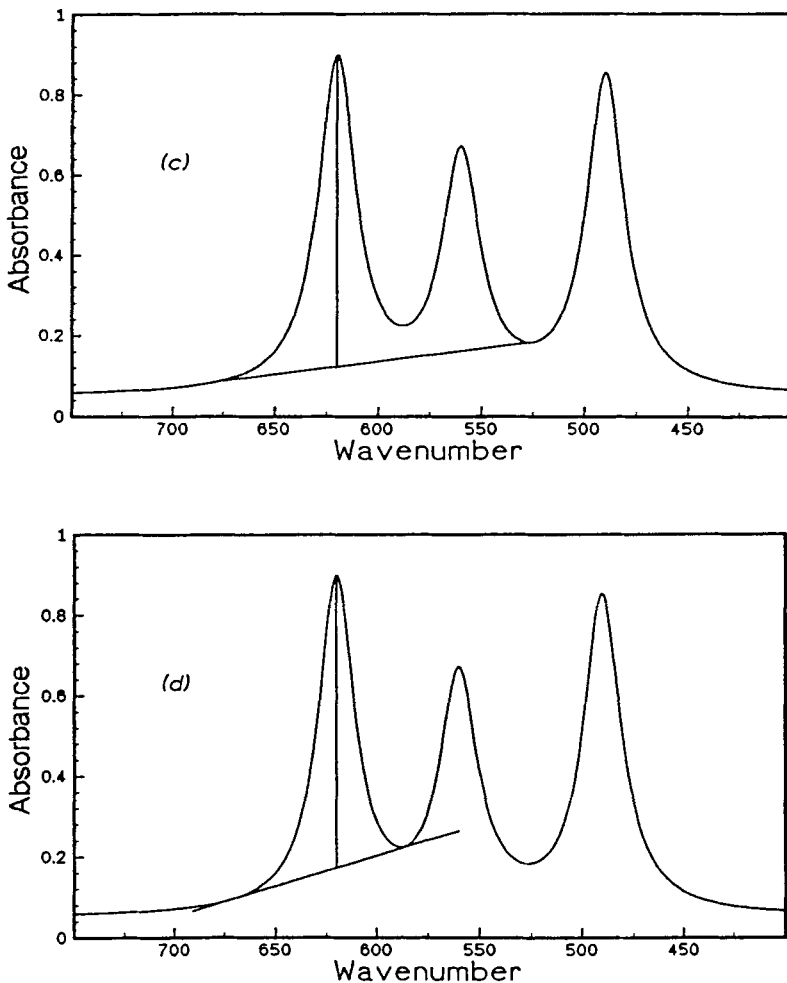


Figure 5.1-4 continued

5.1.3.2 Calibration methods based on integrated intensities

As mentioned above, calculated absorbance values derived from peak height measurements are sensitive to matrix effects as well as changes in instrument properties. The integrated intensity defined as

$$\bar{A} = \int a_{\tilde{\nu}} d\tilde{\nu} = \frac{1}{cd} \int \ln\left(\frac{I_0}{I}\right)_{\tilde{\nu}} d\tilde{\nu} \quad (5.1-6)$$

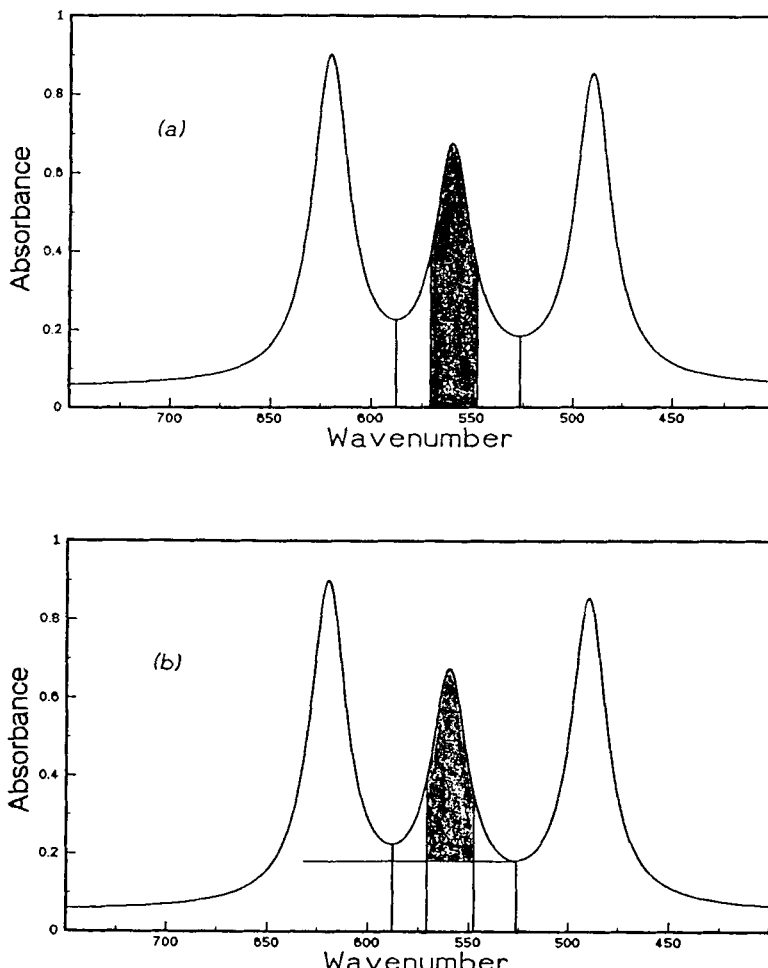


Figure 5.1-5 Illustration of various baseline options in spectral evaluation by peak area measurements (a) no baseline; (b) horizontal single-point base-line; (c) two-point baseline; (d) common tangent baseline.

shows much less sensitivity to the properties of the instrument. In cases where bandwidth or shape changes with increasing concentration of the analyte, evaluation of band area is especially advantageous rather than peak height measurements.

Theoretically, the function in Eq. 5.1-6 must be integrated between $-\infty$ and $+\infty$. In practical IR spectroscopy, the integration can be carried out between $\tilde{\nu}_0 - 5 \Delta\tilde{\nu}_{1/2}$ and $\tilde{\nu}_0 + 5 \Delta\tilde{\nu}_{1/2}$. Here, $\Delta\tilde{\nu}$ is the halfwidth of the band. With modern equipment, the integrated intensities can be derived directly from the absorbance versus wavenumber spectrum. In general a peak area evaluation represents a summation of all absorbance values over the wavenumber range in which the band appears. Therefore the number of points in practical measurements depends on the wavenumber interval of the data and

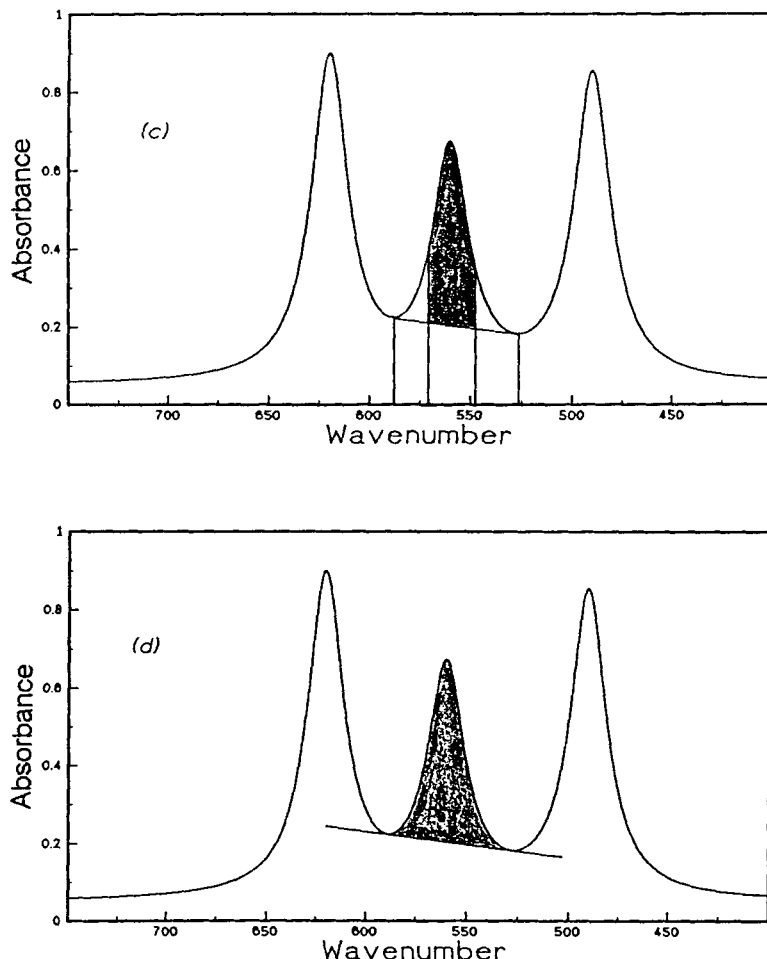


Figure 5.1-5 continued

the upper and lower wavenumber limits of the band. If the results obtained from the summation of absorbances over the designated interval are multiplied by the value of the interval, absorbance area measurements are independent of the data interval and the values have the correct units.

A useful variation in the band area evaluation is referred to as 'slice area'. This technique excludes the wings of the band from the summation and builds the sum of absorbances from the portion of the bands where the S/N ratio is largest. Fig. 5.1-5 show the various possibilities of the evaluation of band areas.

Three other methods are mentioned in detail:

a) The Ramsay method of direct integration

If the band shape of an IR absorption band can be assumed to be Lorentzian, then

$$\ln \left(\frac{I_0}{I} \right) = \frac{a}{(\tilde{\nu} - \tilde{\nu}_0)^2 + b^2} \quad (5.1-7)$$

It follows from Eq. 5.1-6 that the integrated intensity can be expressed as

$$\begin{aligned} \bar{A} &= \frac{1}{c d} \int_{-\infty}^{+\infty} \frac{a}{(\tilde{\nu} - \tilde{\nu}_0)^2 + b^2} d\tilde{\nu} \\ &= \frac{1}{c d} \cdot \frac{a}{b} \arctan \left[\frac{\tilde{\nu} - \tilde{\nu}_0}{b} \right]_{-\infty}^{+\infty} = \frac{1}{c d} \cdot \frac{\pi a}{b} \end{aligned} \quad (5.1-8)$$

and with respect to

$$\ln \left(\frac{I_0}{I} \right)_{\tilde{\nu}_0} = \frac{a}{b^2} \quad \text{and} \quad \Delta\tilde{\nu}_{1/2} = 2b \quad (5.1-9)$$

it follows that

$$\bar{A} = \frac{1}{c d} \cdot \frac{\pi}{2} \ln \left(\frac{I_0}{I} \right)_{\tilde{\nu}_0} \Delta\tilde{\nu}_{1/2} \quad (5.1-10)$$

Thus, the integrated intensity is derived from the absorbance at the maximum and the halfwidth of a band. The value of \bar{A} must be corrected by a factor K , which depends on the maximum absorbance and on the slit width of the spectrometer. K values are listed in the original paper by Ramsay (1952) as well as in the textbook of Brügel (1969).

b) Extrapolation method according to Wilson and Wells

According to Wilson and Wells (1946), the true integrated intensity \bar{A} can be determined from the apparent integrated intensity \bar{A}' , measured at different concentrations or different cell thicknesses. The measured values of the apparent integrated intensity are plotted against the respective concentration or cell thickness. The true integrated intensity is obtained by extrapolating the straight line to zero concentration or zero path length of the cell. Based on the assumption of a Lorentzian band profile, the relation between the apparent integrated intensity (\bar{A}') and the true integrated intensity (\bar{A}) can be expressed as

$$\bar{A}' = \bar{A} + \bar{A} \cdot \tan \delta \cdot \ln \left(\frac{\tau_0}{\tau} \right)_{\tilde{\nu}_0} \quad (5.1-11)$$

in which τ is the measured transmittance. The factor $\tan \delta$ depends on the relation between the spectral slitwidth s and the true halfwidth $\Delta\tilde{\nu}_{1/2}$. Values have been listed by Ramsay (1952) and Brügel (1969).

c) Extrapolation method according to Bourgin (1927)

This method of determining the true integrated intensity is based on integration:

$$\bar{A}' = \int (1 - \tau_{\tilde{\nu}}) d\tilde{\nu} = \int (1 - (I/I_0)_{\tilde{\nu}}) d\tilde{\nu} \quad (5.1-12)$$

in which $\tau_{\tilde{\nu}}$ is the transmittance at a given wavenumber. Due to the fact that the band area is practically independent of the spectral resolution (Dennison, 1928; Nielsen et al., 1944), it is justified to use the true values I and I_0 . Inserting the Lambert-Beer law in the form

$$\frac{I}{I_0} = e^{-a c d} \quad (5.1-13)$$

and expanding the exponential function into a power series yields

$$\frac{\bar{A}'}{c d} = \int [a_{\tilde{\nu}} - \left(\frac{a_{\tilde{\nu}}^2}{2!}\right) c d + \left(\frac{a_{\tilde{\nu}}^3}{3!}\right) (c d)^2 - \dots] d\tilde{\nu}. \quad (5.1-14)$$

Extrapolation of the absorbance to zero leads to the true integrated intensity \bar{A} of the absorption band:

$$\lim_{cd \rightarrow 0} \left(\frac{\bar{A}'}{c d} \right) = \int a_{\tilde{\nu}} d\tilde{\nu} = \bar{A} \quad (5.1-15)$$

The main advantage of this method lies in its independence of the spectral resolution and of the band profile (Dennison, 1928). A comparison of the approximation methods shows that the three methods give integrated intensity values within a 95% agreement.

5.1.3.3 Quantitative analysis based on derivative spectroscopy

It follows from the Lambert-Beer law that the derivative of the absorbance versus wavenumber (wavelength) plot is also directly proportional to the concentration:

$$A = a c d \quad \frac{dA}{d\lambda} = \frac{da}{d\lambda} c d$$

$$\frac{d^n A}{d\lambda^n} = \frac{d^n a}{d\lambda^n} c d \quad (5.1-16)$$

Derivative techniques are at present performed by computer; they are advantageous in situations where

- the analytical bands suffer overlap,
- due to difficulties in the choice of baseline points calibration by peak heights is not satisfactory.

The increase of resolution in the derivative spectra is accompanied by an increase in noise with each derivation. Furthermore, derivative spectra are influenced by the halfwidths of the bands. Broad bands in the original spectrum are poorly recognizable in the second and higher derivatives. Derivative spectra are therefore best suited to eliminate broad band background absorptions. The decrease in the signal-to-noise-ratio upon generating a derivative spectrum may be offset by smoothing the original spectra. The use of derivatives in quantitative analysis is discussed by Williams and Spragg (1982).

5.1.3.4 Single component analysis

The initial step involves choosing the analytical band according to the following rules:

- the band should not overlap with bands of other constituents, of the sample or the solvent. In certain cases, the solvent bands have to be compensated for by reference beam compensation or by spectrum subtraction techniques
- the absorbance of the chosen band should over the entire selected concentration range not drop below 0.2 or exceed 0.7.

Quantitative analysis can be carried out by different techniques:

1) Determination based on external standards

1a) Single standard method

A standard sample of exactly known concentration of the analyte is used to determine the absorption coefficient a of the analyte according to Eq.5.1-4. Its value can be used afterwards to calculate the concentration of the analyte in unknown samples.

If, for example, in the standard sample the analyte is dissolved to give a 0.57% solution, and the absorbance A of the analytical band equals 0.394 at a cell thickness of $d = 0.5$ mm, the calculation of the absorption coefficient yields

$$a = A/(c \cdot c' \cdot d) = 0.394/(100 \cdot 0.57 \cdot 0.5) = 0.01382$$

Using this value the concentration of the analyte in a 0.38% solution of an unknown sample which shows an absorbance of $A = 0.250$, measured in a cell of the same thickness as the standard sample, can be calculated to

$$c = A/(a \cdot c' \cdot d) = 0.250/(0.01382 \cdot 0.38 \cdot 0.5) = 95.2\%$$

If there are no deviations from the Lambert-Beer law, the accuracy of the results is limited only by measuring errors. An analysis of the random and systematic errors that occur during the determination of the IR absorption coefficient of liquids and their influence on the precision and accuracy of the results has been provided by Staat et al.

(1983). Resolution errors occurring in FT-IR measurements of peak absorbances have been investigated experimentally by Jalsovský (1984) for unapodized spectra as well as for triangular and Happ-Genzel apodization.

1b) Calibration using multiple standards

Apart from the problems discussed above, deviations from the Lambert-Beer law have to be expected in many analyses, because, due to differences in the interactions between molecules in the standard and the unknown sample, the law loses validity over a larger concentration range. In these cases it is therefore necessary to prepare a number of standards at concentrations covering the entire expected range, and to calculate the absorption coefficient of the analyte at the given wavenumber. The plot of the measured absorbance values against the known concentrations of the analyte yields the so-called calibration function. If the Lambert-Beer law applies, the calibration function will be linear. The slope of the straight line can be related to the sensitivity of the analysis (see Sec. 3.3.5). It is worthwhile calculating the functional relation between absorbance and concentration of the calibration function by the least squares fit method and then to calculate the concentrations of the unknown samples on the basis of this relation, rather than through readings from the graph.

For statistical analysis it is necessary to prepare and to measure each standard at least twice. In routine analysis, carried out according to carefully prepared guidelines, confidence limits are $P = 0.95$, based on the standard distribution. In all other cases, especially in solving discrepancies between analytical results or for preparing instructions, confidence limits of $P = 0.95$ or $P = 0.99$, based on the t distribution, are used. The confidence intervals decrease somewhat more as the number of measurements increases, up to about 6. Above this number the effect is negligible. It can be shown that at a given number of measurements the confidence limit of the final result will be at its minimum if the number of calibration standards equals the number of sample measurements (Weitkamp and Barth, 1976).

2) Standard addition method

Ideally, the standards used for calibration should have approximately the same composition as the unknown sample. This is true not only for the analyte concentration, but also for the other species which are contained in the sample matrix, in order to minimize the effect on the measured absorbance values. An advantage of this method is the option of including even small absorbance values in the range of minimum error. The method is therefore well suited to the determination of small quantities of unknowns.

The standard addition method, mostly chosen for spectrometric analysis, involves adding different increments of a standard solution containing the analyte to aliquots of the same size of the sample. Each solution is then diluted to a fixed volume before measuring the absorbance values.

Let V_x be the volume of the identical aliquots of the sample with the unknown concentration c_x . To each of the flasks a variable volume V_s of the standard is added with known concentration c_s , and the different flasks are then filled up to the volume V_e . If the Lambert-Beer law applies, the absorbances of the solutions are

$$A = \left(\frac{aV_x c_x d}{V_e} \right) + \left(\frac{aV_s c_s d}{V_e} \right)$$

Plotting the different values of A versus the added volume of the standard V_s yields a straight line: $A = \alpha + \beta V_s$. The equation of the straight line can be derived by least squares analysis. The slope and the intercept of the straight line gives the unknown concentration:

$$\alpha/\beta = V_x c_x / c_s \quad c_x = \alpha c_s / \beta V_x$$

A method based on systems of linear equations, including overdetermination and determination of the standard deviation of the result, has been described by Weitkamp and Barth (1976).

3) Internal standard method

Using internal standards in quantitative analysis is advantageous, for instance, in cases where the sample thickness cannot be determined exactly, or in gaseous samples whose total pressure is unknown. The compound which serves as an internal standard should have a simple spectrum which does not interfere with the bands of the analyte. It should be a stable substance, readily available, and non-toxic. The following substances have been recommended as internal standards by Colthup et al. (1975)

- in nujol mulls: calcium carbonate, naphthalene, or *D*-alanine
- in KBr pellets: sodium azide or potassium thiocyanate.

According to the Lambert-Beer law, the absorbance of the analyte at wavenumber $\tilde{\nu}_S$ is given by $A_S = a_S \cdot d \cdot c_S$, and the absorbance of the internal standard at $\tilde{\nu}_R$ is $A_R = a_R \cdot d \cdot c_R$. Dividing the two equations yields A_S / A_R . The quotient of the values of the absorption coefficient remains constant at the used wavenumbers. If the concentration of the internal standard c_R is constant, an overall constant K

$$A_S / A_R = [a_S / (a_R \cdot c_R)] \cdot c_S = K \cdot c_S$$

can be determined, which is the slope of the straight line formed by plotting A_S / A_R versus c_S . If K is known, the analyte concentration in the unknown sample is thus obtained.

5.1.3.5 Multicomponent analysis

Vibrational spectroscopy is particularly suited for multicomponent analysis. At least one analytical band must be selected for each component to be quantified. However, if several components are present, some of the analytical bands usually interfere with those of the other constituents. In performing the analysis, it is worthwhile to choose only those bands which show minimum interference. If intermolecular interaction between compounds can be excluded over the entire interesting concentration range, the absorbance at any given wavenumber equals the sum of the absorbances of all constituents of the sample:

$$A_i = a_{i1}c_1d + a_{i2}c_2d + a_{i3}c_3d + \dots + a_{ij}c_jd$$

where a_{ij} is the absorption coefficient of compound j at wavenumber $\tilde{\nu}_i$.

In order to determine the concentrations c_j of n components, it is obviously necessary to carry out measurements at a minimum of n wavenumbers. Care must be taken to ensure that these measurements are mathematically independent in order to set up the system of linear equations:

$$\begin{aligned} A_1 &= (a_{11}c_1 + a_{12}c_2 + \dots + a_{1n}c_n)d = d \sum_{j=1}^n a_{1j}c_j \\ A_2 &= (a_{21}c_1 + a_{22}c_2 + \dots + a_{2n}c_n)d = d \sum_{j=1}^n a_{2j}c_j \\ &\vdots \\ A_n &= (a_{n1}c_1 + a_{n2}c_2 + \dots + a_{nn}c_n)d = d \sum_{j=1}^n a_{nj}c_j \end{aligned} \quad (5.1-17)$$

Defining a value k_{ij} such that

$$k_{ij} = a_{ij}d \quad \text{and} \quad A_i = \sum_{j=1}^n k_{ij}c_j \quad (5.1-18)$$

the system of linear equations (Eq. 5.1-17) can be written as

$$\begin{bmatrix} A_1 \\ A_2 \\ \vdots \\ A_n \end{bmatrix} = \begin{bmatrix} k_{11} & k_{12} & \dots & k_{1n} \\ k_{21} & k_{22} & \dots & k_{2n} \\ \vdots & & \dots & \vdots \\ k_{n1} & k_{n2} & \dots & k_{nn} \end{bmatrix} \begin{bmatrix} c_1 \\ c_2 \\ \vdots \\ c_n \end{bmatrix} \quad (5.1-19)$$

or in shorthand matrix notation

$$\mathbf{A} = \mathbf{K} \cdot \mathbf{C} \quad (5.1-20)$$

Each diagonal term k_{ii} of each row in Eq. 5.1-19 represents the absorption coefficient of the component i for which the respective band with wavenumber $\tilde{\nu}_i$ with the absorbance A_i was chosen. If the bands have been selected appropriately (none or negligible overlapping from bands of other constituents of the sample), this diagonal term is large, whereas the off-diagonal elements (which represent the fraction of A_i from the other constituents) are small or even zero. Nevertheless, these off-diagonal coefficients represent absorptions of the other components which contribute to the chosen band. If the absorption coefficients at the chosen wavenumber positions have been determined for each constituent of the sample, the concentrations c_i of these constituents may be determined by solving the linear equations using standard methods of matrix algebra.

If there are only two compounds in a sample, then

$$\begin{aligned} c_1 &= [A_1 a_{22} - A_2 a_{12}] / [(a_{22} a_{11} - a_{12} a_{21})d] \\ c_2 &= [A_2 a_{11} - A_1 a_{21}] / [(a_{22} a_{11} - a_{12} a_{21})d] \end{aligned} \quad (5.1-21)$$

For samples of three constituents, one may use Cramers rule to solve the linear equations. If more components are involved, it is convenient to carry out the calculations with the inverted matrix \mathbf{K}^{-1} . It follows from Eq. 5.1-20 that

$$\mathbf{K}^{-1} \cdot \mathbf{A} = \mathbf{K}^{-1} \cdot \mathbf{K} \cdot \mathbf{C} = \mathbf{C} \quad (5.1-22)$$

if \mathbf{K} is a square matrix.

If the number of elements in matrix \mathbf{A} equals that in matrix \mathbf{C} , the linear equations have a unique solution. However, any error in one of the A_i values introduces an error into the \mathbf{C} matrix and therefore into the concentrations which have to be determined. In order to minimize the experimental error, it is useful to overdetermine the system of linear equations and then to minimize the sum of squares of the deviations between calculated and measured absorbances.

For two unknowns the overdetermined system contains at least three equations, in matrix notation

$$\begin{bmatrix} A_1 \\ A_2 \\ A_3 \end{bmatrix} = \begin{bmatrix} k_{11} & k_{12} \\ k_{21} & k_{22} \\ k_{31} & k_{32} \end{bmatrix} \begin{bmatrix} c_1 \\ c_2 \end{bmatrix} \quad (5.1-23)$$

or, according to Eq. 5.1-20:

$$\mathbf{A} = \mathbf{K} \cdot \mathbf{C} \quad (5.1-23a)$$

The 'best' solution by the least squares criterion is found by multiplication of the matrix of the absorption coefficients \mathbf{K} with its transpose \mathbf{K}^T

$$\mathbf{K}' = \mathbf{K}^T \cdot \mathbf{K} \quad (5.1-24)$$

By the same route we get \mathbf{A}'

$$\mathbf{A}' = \mathbf{K}^T \cdot \mathbf{A} \quad (5.1-24a)$$

This gives two equations for two unknowns, the solution of these two equations is the optimum solution to the three (or even more) original equations. With Eq. 5.1-23a and multiplication from the left hand side by the matrix \mathbf{K}'^{-1}

$$\mathbf{K}'^{-1} \cdot \mathbf{A}' = \mathbf{K}'^{-1} \cdot \mathbf{K}' \cdot \mathbf{C} \quad (5.1-25)$$

the concentration of the unknown sample is

$$\mathbf{C} = \mathbf{K}'^{-1} \cdot \mathbf{A}' \quad (5.1-26)$$

In the case of non-ideal systems, where overlapping of bands is combined with more pronounced deviations from the Lambert-Beer law, the procedures of quantitative analysis are considerably more complex. An introduction into these problems has been provided by Baumann (1962), Perkampus (1992) and Massart et al. (1988). Nonlinear multicomponent analysis by IR spectrophotometry has been described by Maris and Brown (1983).

Software packages for quantitative analysis by computer assisted IR spectroscopy include routine operations for quantitative single or multicomponent analysis. Efficient software programs are designed such that only the concentrations of the standards and the wavenumber positions of the bands are required as input data. The accuracy of quantitative analysis by IR spectroscopy depends on a number of factors, with band intensities and the possible presence of interference heading the list. In a favorable situation, the accuracy may be very high. However, if weak absorptions and overlapping bands are employed, large errors may occur.

Although in principle there is no limitation to the number of compounds, multicomponent analysis of more than three or four constituents of a sample should be avoided. In this case it seems to be better to separate the compounds prior to analysis. Nevertheless, quantitative analysis by vibrational spectroscopy is extremely powerful in situations where other methods prove very difficult or impossible, e.g., in the investigation of mixtures of isomers. General rules for carrying out multicomponent analyses of normal and higher precision have been described by Perry (1970), see also Perkampus (1992).

5.1.3.6 Analysis of binary mixtures without external calibration

A general spectroscopic method of quantitatively analyzing binary mixtures, which does not require external calibration, has been developed by Diem and Krimm (1981). It is based on a technique introduced by Hirschfeld (1976), which makes it possible to resolve a spectrum of a mixture of a small number of components whose proportions are unknown into the spectra of the constituents without isolating them. If the components are recognized, traditional methods of quantitative analysis can be applied. If the components are not known, a spectrum of the original mixture and a spectrum obtained after partial

fractionation are needed. The method is based on the scaling factors required to null the components, one at a time, by successively subtracting the absorbance in the two spectra. The effect of errors in the scaling factors on the analytical result is taken into consideration. The results show that quantitative analysis by this technique can have a high accuracy, even if the intensity of the index band is only modest. In most cases it should be possible to obtain an accuracy of 1% absolute.

5.1.3.7 Quantitative reflection spectroscopy

ATR or diffuse reflection techniques are widely used for materials which are difficult to analyze by absorption methods, such as thin layers on nontransparent substrates, substances with very high absorption which are difficult to prepare in thin layers, or substances with a special consistency. Some basic considerations concerning quantitative ATR spectroscopy have been described by Müller et al. (1981). This publication emphasizes the fact that the functional behavior of the ATR spectrum of an absorbing sample must be evaluated with regard to the refractive index as well as to the absorption index of the sample. It is shown that, as a consequence, reflection measurements can be used to determine concentrations of nonabsorbing samples. Further information on reflection spectroscopy is presented in Sec. 6.4.

5.1.4 Quantitative analysis by Raman spectroscopy

From Eqs. 5.1-2 and 5.1-5 it follows that the intensity of a Raman line is proportional to the number of molecules per unit volume which are involved in the scattering process. The measured intensities can therefore be used to determine concentrations of compounds. The evaluation procedures for single as well as for multicomponent analysis are in principle identical to those used in IR spectroscopy. Nevertheless, it must be emphasized that Raman intensities are affected by many experimental factors.

A comprehensive review of the available Raman scattering cross section data of gases and a discussion of the problems associated with the determination of Raman scattering cross sections in liquids has been published by Schrötter and Klöckner (1979). A publication by Abe et al. (1977) deals with absolute Raman intensities of liquids. There are also methods of measuring absolute scattering cross sections in crystal powders (Lopez and Montero, 1977; D'Orazio and Schrader, 1976) and in crystals (Gorelik and Sushchinskij, 1970).

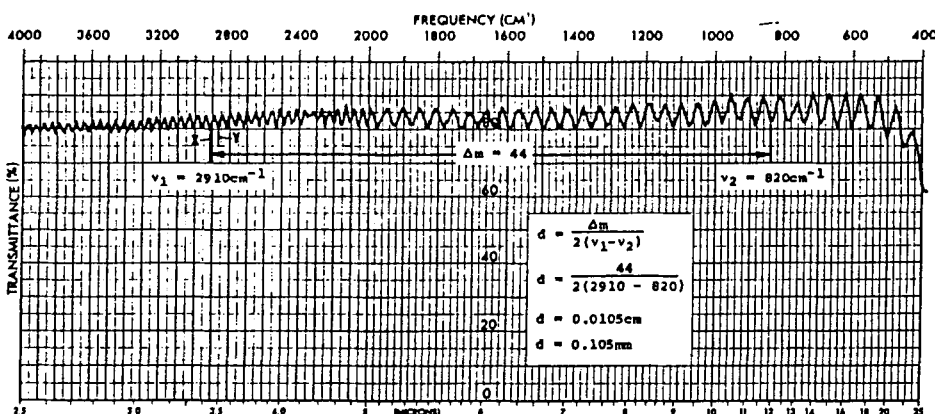
Better analytical results can be expected if relative instead of absolute intensities are used for quantitative analysis! The determination of relative intensities of liquids has been discussed by Bernstein and Allen (1955). Relative scattering cross sections of gases have been described by Schrötter and Klöckner (1979). There are certain cases in which the solvent can be used as an internal standard. Otherwise, the standard must be added to the investigated sample. In this case, the relation between the intensity of the standard and that of the compound to be determined must be known.

5.1.5 Examples

5.1.5.1 Quantitative analysis of liquid solutions

In order to avoid effects caused by the sample itself, quantitative analyses should be carried out of dilute solutions. The bands which are selected for analysis should be isolated and preferably be free of interference with the solvent or other components. If overlapping cannot be avoided, the bands of the solvent can be compensated for by placing a matching solvent-filled cell into the reference beam, or by subtracting the solvent spectrum by computer. In recording a spectrum of the empty cell, interferences occur due to the reflection of radiation at the surface of the window material inside the cell. The number and wavenumbers of the maxima and minima of the interference fringes in the spectrum (see Fig. 5.1-6) gives the cell thickness:

$$d = n / 2(\tilde{\nu}_1 - \tilde{\nu}_2) \text{ [cm]} \quad (5.1-27)$$



Interference fringes of an empty sealed sample cell $(d = 0,1 \text{ mm})$

Figure 5.1-6 Determination of cell thickness by the method of interference fringes.

Determination of hydrocarbons in water by IR spectroscopy

This method is standardized and described in the 'German standard methods of examining of water, waste water, and sludge' (DIN 38409-H18). The hydrocarbons are extracted from the water by use of 1,1,2-trifluoroethane. The characteristic bands at 2958 cm^{-1} (CH_3 group), 2924 cm^{-1} (CH_2 group) and 3030 cm^{-1} (CH of aromatic compounds) are

used for the quantitative determination. If the hydrocarbons which are responsible for the contamination are known, special reference mixtures of these substances can be used for calibration. The mass concentration of an aqueous sample for automobile fuels or mineral oils can be determined according to equations and by employing the values of the absorption coefficients listed in DIN 38409-H18.

The multicomponent determination of the three xylene isomers and ethylbenzene in a cyclohexane solution has been described by Baumann (1962). The bands at 795.2, 768, 741.2, and 696.3 cm^{-1} were selected as analytical bands. Table 5.1-1 lists the absorption coefficients of the pure compounds, measured in cyclohexane solution, as well as the absorbance values of the 'unknown' at the chosen wavenumbers. With the procedure of Sec. 5.1.3.5 the concentrations of the components can be calculated. The actual concentrations in $\text{mol}\cdot\text{L}^{-1}$ were: ethylbenzene 0.07912, o-xylene 0.07661, m-xylene 0.05105, p-xylene 0.04672.

Table 5.1-1 Values of the absorption coefficients of the four pure compounds as measured in cyclohexane solution at several different concentrations in cm^2/mol together with the absorbance values of the 'unknown mixture'

Wavenumber	Ethyl-benzene	o-Xylene	m-Xylene	p-Xylene	Absorbance x 10 Unknown
696.3	0.87769	0.0	0.06843	0.03403	0.7386
741.2	0.29324	2.53158	0.03546	0.03424	2.2036
768.0	0.08196	0.0	1.51512	0.02612	0.8676
795.2	0.04077	0.0	0.05139	1.50164	0.7721

An IR spectrophotometric determination of trace amounts of water in selected organic solvents has been reported by Barbutta and Edgell (1978). It is based on the O-H stretching vibration of isolated water molecules at 3571 cm^{-1} .

Trace analysis by IR spectroscopy, involving pre-concentration, separation, and computer techniques has been reported by Hannah et al. (1978). The term trace analysis is used to refer to concentrations in the ppm range up to 1%. In instances where interference is at its minimum, analysis may be performed in a straightforward manner by using difference techniques. However, there are many cases in which analysis may be complicated by the fact that the trace material is structurally similar to the matrix material. Moreover, the presence of other trace compounds is intolerable if their spectra interfere with that of the compound under investigation. In this case it is often necessary to use pre-concentration or separation techniques. This method is illustrated by analyses of aromatic isomers, gasoline additives, drugs, and polymer additives. The different aspects of trace analyses by infrared spectroscopy are discussed by Smith (1986).

A method of quantitatively determining mole fractions of stereoisomers by IR differential absorbance measurements has been described by Gendreau and Griffiths (1976). Absorbance spectra of the pure isomers at a certain concentration are subtracted from the absorbance spectrum of the mixture at the same concentration. The method is claimed to be accurate even if the analytical bands of the isomers have different absorption coefficients or half-widths.

The detection and measurement of dimethylnitrosamine by laser Raman spectroscopy has been reported by Thomas (1977). This compound is carcinogenic. Raman spectroscopy was chosen for several reasons:

- the compound is highly water soluble, and Raman scattering caused by water is quite weak,
- there are two intense Raman active vibrational modes which can be used for quantification,
- with high power lasers it is possible to study highly diluted samples.

The lowest concentration which could be detected by the authors was 10 mg L^{-1} .

Application of laser Raman multichannel spectroscopy to a kinetic investigation in the liquid phase has been reported by Crunelle-Cras and Merlin (1977). A multichannel spectrometer with photoelectric image devices, interfaced with a data acquisition and handling system, permits the study of fast processes, exemplified by the fast oxidation of the sulfite ion by the bromate ion in an acidic medium.

The use of laser Raman spectrometry in order to quantitatively investigate the urea synthesis under process conditions has been reported by Van Eck et al. (1983). Only Raman spectroscopy seems to suit the problem, since the visible radiation which is used to excite and detect Raman transitions can easily be directed to a measuring cell. Furthermore, water, which is an acceptable solvent, and all compounds involved in the synthesis show characteristic Raman bands. In order to compensate for many of the instrumental factors relative intensities were used instead of absolute intensities. Reproducible window mountings are a necessity. The effect of pressure and temperature on the Raman intensity have to be taken into account if measurements are to be carried out *in situ* (Sec. 6.8). The effect of the temperature is moderated by using an internal standard.

5.1.5.2 Gases

Vibrational spectroscopy is successfully employed to quantitative analysis of gases, especially if real time and on-line analyses are needed. In order to compensate the effects of pressure broadening, it is worthwhile to carry out all measurements at the same total pressure. To this end, the sample is placed in an inert gas, such as nitrogen or a noble gas, and the pressure raised to a defined value. The partial pressure instead of the concentration is used in the Lambert-Beer law. The calibration curve is valid only at the calibration temperature. If the temperature of the sample deviates from this temperature, the partial pressure has to be corrected by the Gay-Lussac law.

The quantitative determination of small concentrations of organic solvents in a working place atmosphere by IR spectroscopy has been reported by Schäcke et al. (1972). The measurements were carried out using a multipass gas cell with a maximum pathlength of 10 m. Such cells allow the determination of compounds in the ppm or even ppb region.

Quantitative IR spectroscopic measurements for environmental analysis are often carried out by using simple non-dispersive instruments.

Michaelis and Weitkamp (1984) describe sensitive remote and *in situ* detection of air pollutants by laser absorption measurements. The application of laser absorption in

connection with pulsed narrow-band sources allows remote range-resolved detection of gaseous air pollutants with sensitivities down to 30 ppb and ranges up to several km. According to the authors, the long path absorption method and the DAS (differential absorption and scattering) LIDAR (light detecting and ranging) offer the most attractive potential for remote sensing applications.

The determination of carbon dioxide concentrations in flames by Raman spectroscopy has been described by Blint et al. (1979). The mole fraction of CO₂ is obtained by calculating the ratio of the intensity of the Raman lines to the intensity of the N₂ band. It is pointed out that the calculation for each spectrum must include the respective partition function. The theoretical fitting of computer processed laser Raman spectra of methane and propane air flames has been discussed by Stephenson and Blint (1979).

The use of Raman spectroscopy for environmental analysis has been discussed by Schrötter et al. (1979). The sensitivity and the accuracy of Raman intensities of gases make it possible to determine gas traces in the atmosphere. The main advantage is the fact that the analytical bands are neatly separated and show no interference (see Fig. 5.1-7), so that different components can be determined simultaneously.

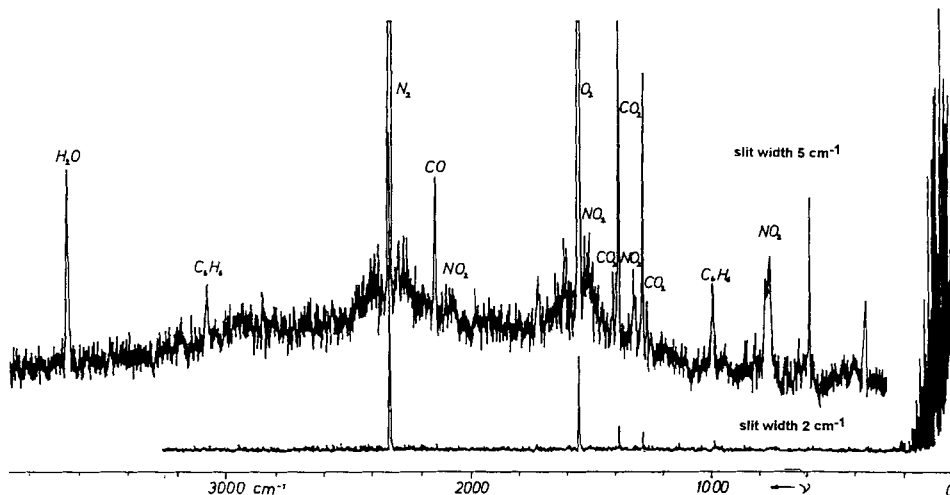


Figure 5.1-7 Raman spectrum of automobile exhaust gases for the simultaneous determination of different components.

A multichannel Raman spectrometer for the study of dynamic processes in analytical chemistry has been described by D'Orazio and Hirschberger (1983), they recorded the Raman spectra of automobile exhaust gases (Figs. 5.1-8a — 5.1-8c).

5.1.5.3 Solids

Vickers et al. (1984) have shown that quantitative analysis of acetaminophene and phenylpropanoleamine hydrochloride, which are used in a variety of pharmaceutical prepara-

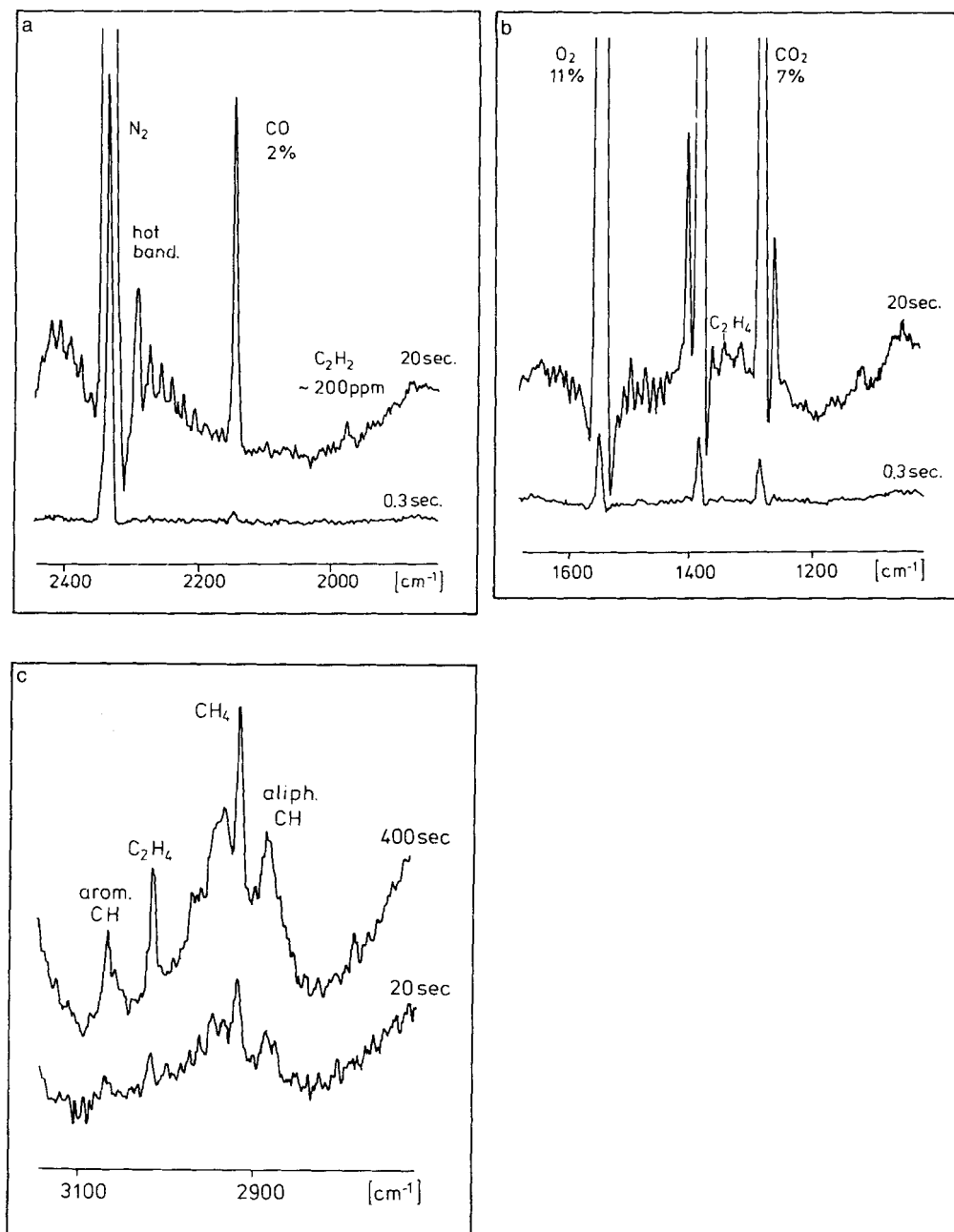


Figure 5.1-8a-c Raman spectra of automobile exhaust gases, **a** range of N₂, CO, C₂H₂; **b** range of O₂, CO₂, C₂H₄; **c** range of CH stretching vibrations.

tions, can be analyzed by Raman measurements of solid samples with an accuracy and precision of more than 1% in the case of acetaminophene and more than 3% in the case of phenylpropanoleamine hydrochloride.

IR measurements of solids are notoriously difficult to quantify. Quantitative analysis of solids by KBr pelleting should be avoided whenever possible. Several aspects may make KBr or other pellets inadequate for this purpose:

- The surface structures of standards and investigated sample may not be identical, measurements based on an external standard may be subject to errors,
- inhomogeneities in the sample distribution throughout the pellet and
- differences in the particle sizes of the different pellets do not allow employing the Lambert-Beer law.

If the necessary results cannot be obtained by other methods, very careful sample preparation may give results with a standard deviation of approximately $\pm 10\%$. In some cases, internal standards, such as bands of naphthalene (780 cm^{-1}) or KSCN (2100 cm^{-1}) can be used for semiquantitative measurements.

Quantitative analysis of fiber mixtures in polyester-wool textures by KBr pelleting has been described by Hannah et al. (1975). Deviations from the real values were approximately 1%.

A method of quantitatively determining 0.2% polyvinyl acetate in polystyrene has been described by Peitscher (1979) by using difference spectroscopy. Quantitative single component analysis of polymer films has been described by Chalmers et al. (1982). All samples were prepared by hot compression molding. This treatment produces a mat film surface, which suppresses interference fringes in the IR spectrum. For quantitative analysis it is essential that the thus produced films are homogeneous, of uniform thickness, and free of bubbles and irregularities. A clear section of each was chosen for the measurements.

A comprehensive treatment of the analysis of polymers has been published by Hummel and Scholl (1991).

5.1.6 Quality control

Vibrational spectroscopy is excellently suited to quality control. This is demonstrated by some examples:

1) Semiconductor technology

The silicon raw material can be analyzed by FT-IR spectroscopy. The oxygen and carbon content is determined by comparing the ratios of the oxygen and carbon bands with those of the characteristic phonon absorptions of the silicon lattice (see Fig. 5.1-9; Zachmann, 1987). The measurements are calibrated by a reference wafer of similar thickness and surface condition in order to avoid complicated correction calculations. In a special manufacturing process for integrated circuits, Si wafers are coated with very thin films

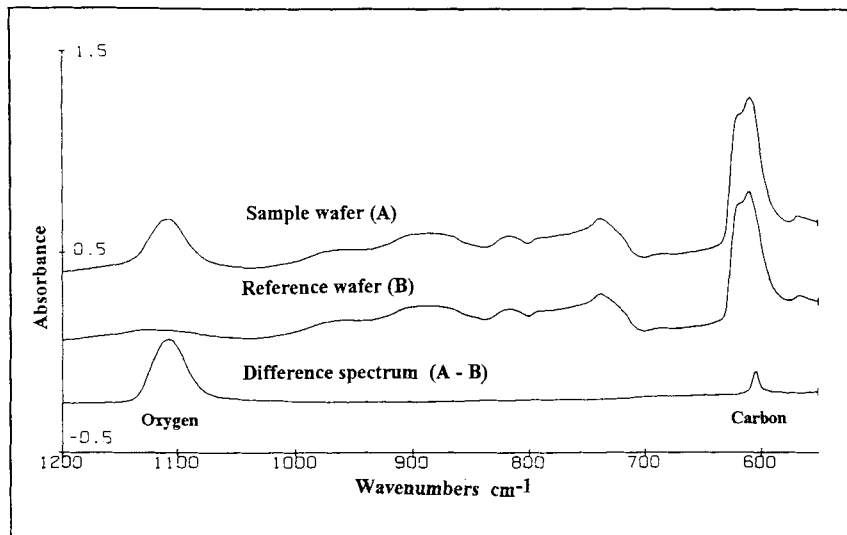


Figure 5.1-9 Infrared transmittance spectra for the determination of impurities of oxygen and carbon in Si wafers (sample thickness 0.5 mm, resolution 4 cm⁻¹).

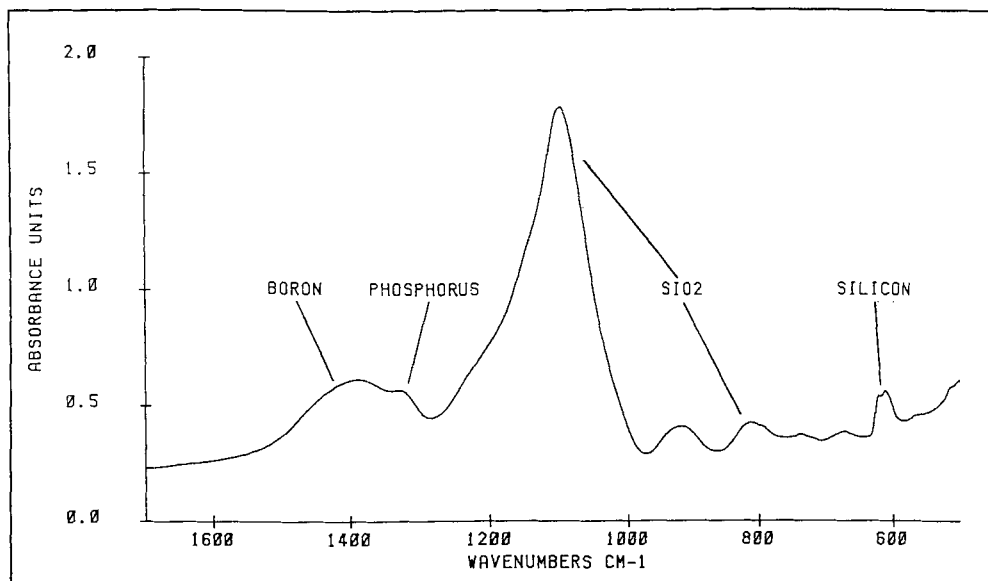


Figure 5.1-10 IR absorption spectrum of a boron-phosphorous-silicate glass coated wafer for the determination of the boron and phosphorous content of the SiO₂ coating (sample thickness less than 1 μm, resolution 4 cm⁻¹).

of boron-phosphorus-silicate glass (BPSG). The absolute boron and phosphorus content and their relative concentrations determine the chemical and physical property of the film. Boron and phosphorus can be determined quantitatively by FT-IR spectroscopy (Fig. 5.1-10; Zachmann, 1987).

2) Polymer industry

The possibilities of quality control in polymer industry have been considerably enhanced by the introduction of computer assisted IR and FT-IR spectrometers. One of the most frequently used techniques in this field is the difference spectroscopy. Difference spectroscopy involves subtracting the digitally stored spectrum of a standard from, for ex-

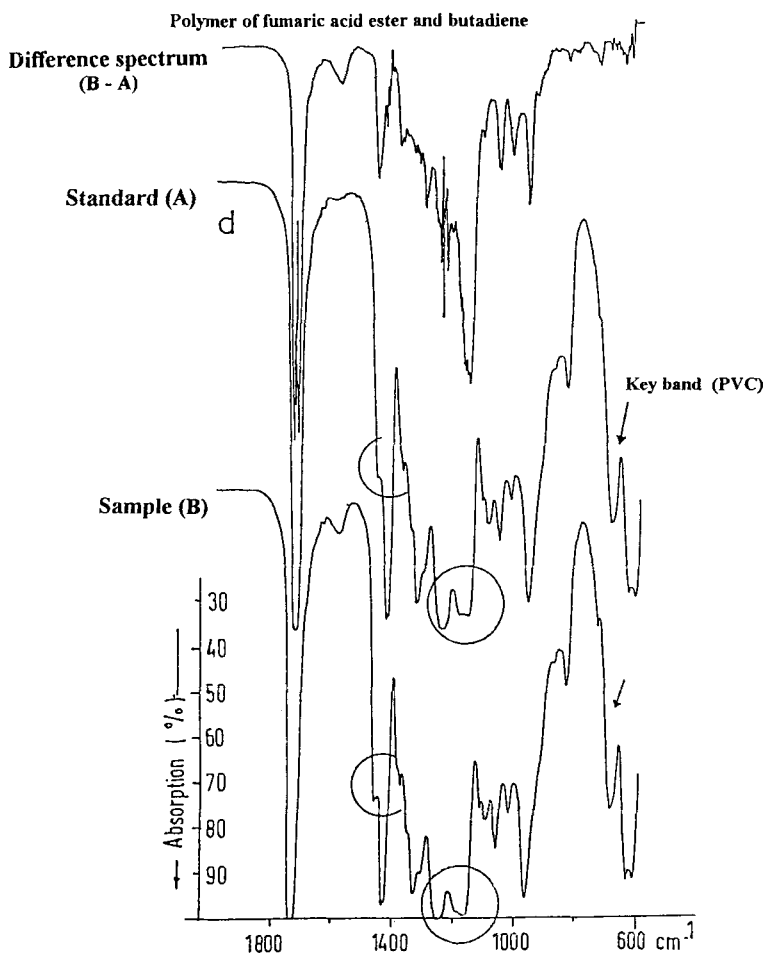


Figure 5.1-11 IR difference spectroscopy for quality control of impact resistant PVC (see text).

ample, an actually measured spectrum, using an adequate factor or a key band to fit the spectra to the same sample thickness. The manipulations are carried out on the absorbance spectra. Impact resistant PVC contains a polymer derived from fumaric acid ester and butadiene as impact resistant component. Without using difference spectroscopy there are practically no variations to be seen in the spectra of two production batches. Difference spectroscopy however, shows that sample *B* contains an overdose of impact resistant component amounting to approximately 25% (see Fig. 5.1-11; Peitscher, 1979).

The determination of the microstructure of polybutadiene, i.e., the distribution of *cis* and *trans*-1,4-polybutadiene, as well as that of *trans*-1,4- and 1,2-polybutadiene in polystyrene presents an analytical challenge. Fig. 5.1-12 shows the spectrum of a mixture of polystyrene and polybutadiene, obtained in CS₂ solution. Difference spectroscopy with pure polystyrene as a standard affords the spectrum of the polybutadiene fraction, from which the microstructure can easily be determined (Peitscher, 1979).

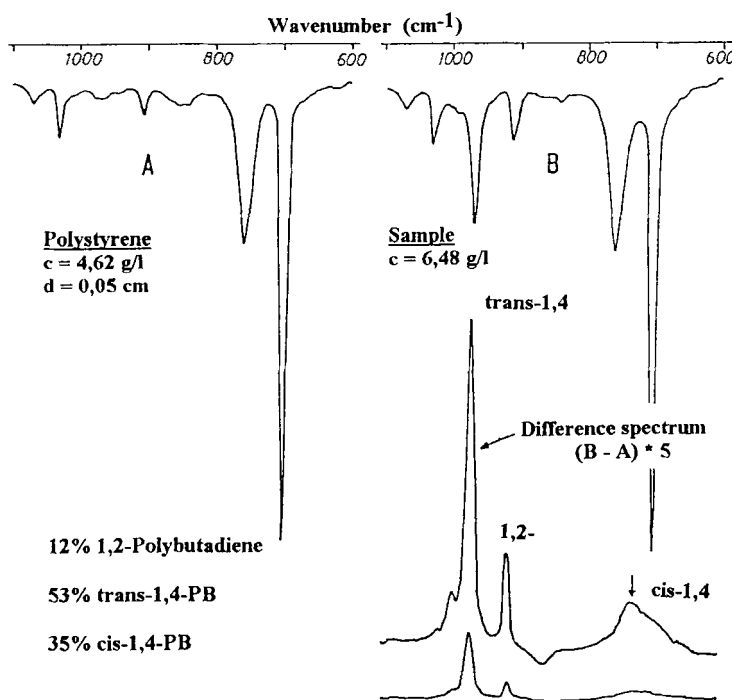


Figure 5.1-12 IR difference spectroscopy for the determination of the microstructure of polybutadiene in the presence of polystyrene.

Even materials with a high filler content (e.g. dental fillings) can be identified quite reliably by difference spectroscopy, as long as the filler is mainly monodispers. Organically filled construction materials with a low binder concentration can be identified if the characteristic absorption of the binder does not coincide with strong bands of the filler.

Difference spectroscopy has its limits. The basic source of errors is the lack of reproducibility of the wavenumber and intensity scale of a spectrum. This is a special problem if dispersive spectrometers are used. Fig. 5.1-13 shows the spectrum of polyacrylonitrile (with interferences), together with two difference spectra (ordinate expanded by a factor of 4). Apparently, due to very slight differences in the two consecutive spectra, the sharp bands of the original spectrum are converted to derivative bands in the difference spectrum (Hummel and Votteler, 1983; for dispersive Raman spectroscopy these effects have been discussed by Laane, 1981). A more 'dangerous' effect is the inhomogeneous sample distribution in the beam. The latter decreases the absorbance, compared to spectra obtained at homogeneous sample thickness and distribution (for example, distribution of a sample in KBr pellets). The effect is negligible in weak bands but considerable in strong ones. Such samples will produce erroneous results if examined by difference spectroscopy. Mixing of different polymers usually yields multiphase systems. If the components of a polymer blend are non-crystalline, the spectrum of the blend approximately equals a superposition of the spectra of the pure components. If the refractive indices of the individual phases in the mixture differ considerably, the resulting spectra will exhibit band shapes similar to those produced by the Christiansen effect. In this case, difference spectroscopy produces erroneous results, too. More detailed information about computer assisted IR spectroscopy of multicomponent polymeric systems has been provided by Hummel et al. (1983).

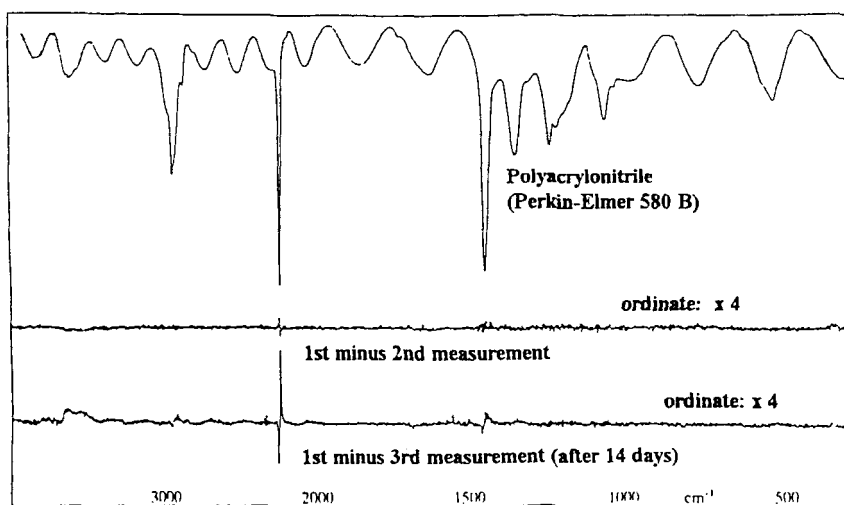


Figure 5.1-13 Effect of irreproducibility of wavenumbers on difference spectroscopy with grating spectrometers.

Polymers with very low light transmission properties give highly inadequate spectra, which are difficult to evaluate. The lower curve in Fig. 5.1-14, for instance, shows the spectrum of polyethylene, including 2% soot. The upper portion of Fig. 5.1-14 shows that the scale expansion considerably enhances the accessible information content of the spectrum (Peitscher, 1979).

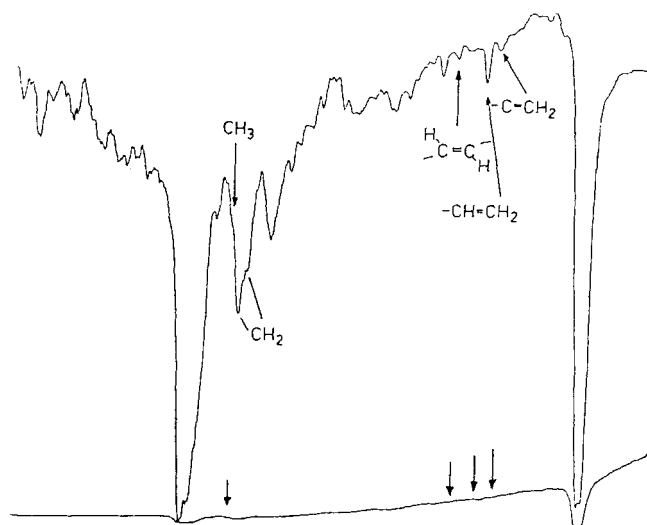


Figure 5.1-14 Enhancing the information content of the IR spectrum of a polymer with very poor light transmission properties using difference spectroscopy and ordinate scale expansion: Spectrum of polyethylene containing 2% soot $d = 140 \mu\text{m}$.

3) Automatic identity control by computer assisted IR spectroscopy

The identity test is a very useful tool of quality control, for example in the pharmaceutical industry. The identity of two samples may be unequivocally established by a method described by Weitkamp and Wortig (1983).

The absorbance values at each wavenumber interval ($\Delta\tilde{\nu}_i$) of a sample spectrum (S) and a reference spectrum (R) should be the same or, due to slight differences in sample preparation, proportional to each other:

$$A(R)_i = a + b \cdot A(S)_i \quad (5.1-28)$$

This equation of a straight line takes into account a slight difference of the base lines by the constant a . By applying least-squares regression the constants a and b are determined. The variance of $A(R)$ indicates the degree of conformity between the two spectra. If sample and reference spectrum differ only slightly, the spectra should be compared blockwise, and the standard deviations of the different blocks should be used. This method is useful for spectra which show a sufficient number of sharp bands. It may fail if there are broad bands, in which case it is necessary to compare the second derivatives of the spectra. The algorithm is shown in Fig. 5.1-15.

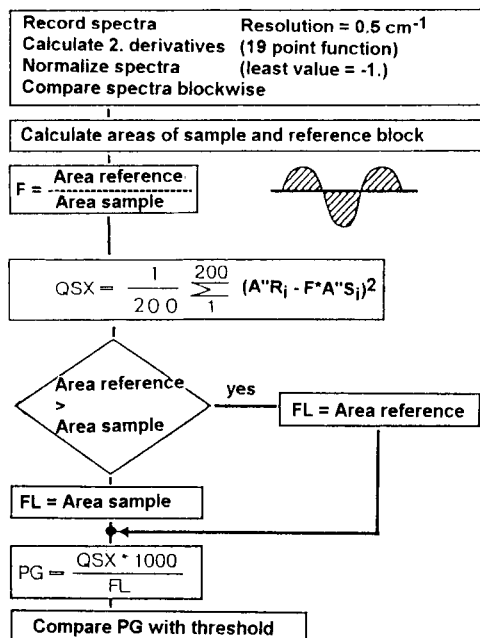


Figure 5.1-15 Algorithm for the comparison of higher-order spectra for automatic identity control of pharmaceuticals.

4) Analysis of fabric additives

IR spectroscopy is a common analytical technique in the textile industry. IR is capable of identifying fibers and their additives, as well as showing quantitative blend ratios and additive contents. The ATR (attenuated total reflection) technique, especially in its multiple form, MIR (multiple internal reflection) is of special importance in this field. The sample preparation is simple and fast: the cut out swatches with appropriate surface areas are placed against each side of the MIR crystal, ensuring sufficient and uniform contact across the crystal surface. The internal reflection methods are non-destructive, so that the sample may be saved for other types of analysis, they are, further, methods of surface analysis. This is advantageous in all cases where the finish resides primarily on the fiber surface. In this case, a very strong spectrum of the finish is obtained, with minimal interference from the base fiber (Hannah et al., 1975).

Finishes that soak the fiber may be extracted and the solution deposited directly onto the MIR crystal. After evaporation of the solvent, thin films remain, to which MIR is very sensitive; intense spectra of the solute can be obtained from microgram quantities. Fibers and textiles can be identified either by using at least 10 µg of substance to prepare micro KBr pellets, or by using about 500 mg and applying MIR techniques.

Of special importance are the methods of investigating single fibers by infrared or Raman microscopes (Schrader, 1990).

5) Gas analysis

Economical spectrometers for quality control by quantitative analysis of gases, liquids, and solids, but especially of gases has been devised by introducing microprocessor techniques to simple filter spectrophotometers using tunable interference filters (Gilby et al., 1980). Gases can be analyzed using multiple pass cells up to an effective sample thickness of 20 m. Possible impurities in the breathing oxygen for pilots together with their detection limits, are listed in Table 5.1-2. The analytical wavelengths and absorbance values per ppm of several contaminants are shown in Table 5.1-3. Table 5.1-4 shows the results of the analysis which was performed at 9.1 bar to increase the concentration by a factor of nine (Truett and Bayliss, 1983). A laser Raman sensor for the measurement of traces of hydrogen gas was described by Adler-Golden et al. (1992).

Table 5.1-2 List of possible contaminants in breathing oxygen for pilots

Contaminant	Use limit (ppm)	Wavelength (mm)	Detection limit (ppm)
CO ₂	10	4.25	2
N ₂ O	1	4.50	0.5
CO	2	4.70	2
CH ₄	50	3.24	5
C ₂ H ₂	0.1	13.75	0.05
C ₂ H ₄	0.4	10.58	0.4
C ₂ + H-C's	6	3.35	1
Refrigerants	2		0.1
Solvents	0.2		0.1
Other	0.2		

Table 5.1-3 Analytical wavelengths and absorbance per ppm for several contaminants in pilot's breathing oxygen

Table 5.1-4 Printout of an analysis of synthetic gas mixture in oxygen at 9.1 bar and 20 - 25 m pathlength

Nominal value	20ppm	8ppm	5ppm	10ppm	2ppm	5ppm	3ppm	5ppm	5ppm C ₂ H ₆
	CH ₄	C ₂ H ₆	C ₂ H ₄	C ₄ H ₁₀	C ₂ H ₂	CO ₂	N ₂ O	CO	5ppm C ₄ H ₁₀
CH ₄	<u>19.7</u>	.1	.3	.8	.7	.6	.4	1.3	.1
C ₂ H ₆	.2	<u>8.2</u>	.1	-.4		-.1		-.1	<u>5.3</u>
C ₂ H ₄	.1	.2	<u>4.7</u>	.3	.2	.1		.1	
C ₄ H ₁₀	.3	-.1	.2	<u>10.3</u>		.1			<u>4.3</u>
C ₂ H ₂					<u>1.6</u>	.1			
CO ₂	.1	.3		2.1	.1	<u>4.9</u>	.1	.1	1.1
N ₂ O					-.1		-.1	<u>3.2</u>	-.2
CO	.1	.1	.2	.4	.2	.2	-.1	<u>5.3</u>	

5.1.7 Chemometrics

In the preceding paragraphs a multitude of mathematical procedures has been mentioned. These procedures have been carried out in the past first by using simple calculating machines as well as slide rules. With the advent of process computers integrated into the spectrometers the classical procedures can be performed much faster and with higher precision. Moreover, methods too complex and expensive to be applied with simple tools can now be employed: Statistical and other mathematical methods to design or select optimal measurement procedures and experiment, and to provide maximum relevant chemical information by analyzing chemical data. These methods became known as chemometrics (Kowalski, 1975).

Since its appropriate discussion would exceed the limits of this book a few citations of current comprehensive books are given here: Massart et al. (1988) and McClure (1987). Martens and Naes (1989) describe multivariate calibrations, Malinowski (1991) the factor analysis.

Fredericks et al. (1985) describe 'materials characterization by factor analysis of IR spectra', Wold et al. (1987) the 'principal component analysis', and Haaland and Thomas (1988) 'materials characterization using factor analyses of FT-IR spectra'. Of special importance are the procedures using 'fuzzy logic' and 'neural networks' (Harrington, 1991; Zupan and Gasteiger, 1993).

5.2 Calculation of frequencies and intensities of vibrations of molecules and crystals*

Vibrational spectra depend on structural parameters and are therefore suitable sources of information about microscopic properties of the vibrating units (molecules, polymers, crystals). Since the relation between structural parameters and spectra is not a direct one, it is necessary to develop model calculation methods. They are presented in this chapter. A more detailed discussion of this subject has been provided by Wilson et al. (1955) and Califano (1976).

5.2.1 General formulation

A molecule with n atoms can be described by a Cartesian system whose origin is at the center of mass and whose axes correspond to the inertia axes. An atom i with mass m_i performing a motion is characterized by its equilibrium coordinates $\sigma_{i0}(\sigma = x, y, z)$ and its general coordinates σ_i . Displacement from the equilibrium position is described by $\Delta\sigma_i = \sigma_i - \sigma_{i0}$. The column vector x_1, \dots, z_n is noted X , the corresponding row vector is the transposed vector noted X^T . The kinetic energy T of the molecule can be expressed by

$$2T = \sum_{i=1}^{3n} m_i \left(\frac{d\Delta\sigma_i}{dt} \right)^2 \quad (5.2-1)$$

Using the mass-weighted Cartesian coordinates σ_M defined as

$$\sigma_{M_{3i-2}} = x_i m_i^{1/2} \quad \sigma_{M_{3i-1}} = y_i m_i^{1/2} \quad \sigma_{M_{3i}} = z_i m_i^{1/2} \quad (5.2-2)$$

this expression simplifies to

$$2T = \sum_{i=1}^{3n} \left(\frac{d\Delta\sigma_{Mi}}{dt} \right)^2 = X'^T M' X' \quad (5.2-3)$$

in which the primes indicate the derivation with respect to the time t . Assuming that the motions have small amplitudes, the potential energy V can be expanded into a series around the equilibrium position

* Section 5.2 is contributed by D. Bougeard, Lille

$$2V = 2V_0 + 2 \sum_{i=1}^{3n} \left(\frac{dV}{d\Delta\sigma_{Mi}} \right)_0 \Delta\sigma_{Mi} + \\ + \sum_{i=1}^{3n} \sum_{j=1}^{3n} \left(\frac{d^2V}{d\Delta\sigma_{Mi} d\Delta\sigma_{Mj}} \right)_0 \Delta\sigma_{Mi} \Delta\sigma_{Mj} + \dots \quad (5.2-4)$$

If the origin of the potential energy is set for the equilibrium geometry, then $V_0 = 0$. At the equilibrium position the molecule should be at the minimum of the potential energy hypersurface; therefore all first order derivatives are zero. The following term containing the second derivatives is called the harmonic term. These derivatives are noted f_{Mij} and are referred to as force constants:

$$f_{Mij} = \left(\frac{d^2V}{d\Delta\sigma_{Mi} d\Delta\sigma_{Mj}} \right)_0 \quad (5.2-5)$$

If higher terms are neglected, the calculations are said to be performed according to the harmonic approximation, and the potential energy can be written as

$$2V = \sum_{i=1}^{3n} \sum_{j=1}^{3n} f_{Mij} \Delta\sigma_{Mi} \Delta\sigma_{Mj} = \mathbf{X}^T \mathbf{F}_{\mathbf{XM}} \mathbf{X} \quad (5.2-6)$$

The resulting values for T and V can be introduced into Newton's equation of motion

$$\frac{d}{dT} \left[\frac{dt}{d \left(\frac{d\Delta\sigma_{Mi}}{dt} \right)} \right] + \frac{dV}{d\Delta\sigma_{Mi}} = 0 \quad (5.2-7)$$

If follows that

$$\frac{d^2\Delta\sigma_{Mi}}{dt^2} + \sum_{j=1}^{3n} f_{Mij} \Delta\sigma_{Mj} = 0 \quad \text{for } i = 1, 2, 3, \dots, 3n \quad (5.2-8)$$

This set of second order differential equations can be solved by using a solution of the form

$$\Delta\sigma_{Mi} = K_i \cos(\lambda^{1/2}t + \varphi) \quad (5.2-9)$$

which affords

$$-K_i\lambda + \sum_{j=1}^{3n} f_{Mij} K_j = 0 \quad \text{for } i = 1, 2, 3, \dots, 3n \quad (5.2-10)$$

If \mathbf{E} represents the unit matrix and \mathbf{K} stands for the column vector containing the K_i values, then the linearized system of equations can be written in matrix form:

$$(\mathbf{F}_{\mathbf{XM}} - \lambda \mathbf{E}) \mathbf{K} = 0 \quad (5.2-11)$$

The trivial solution $\mathbf{K} = 0$ represents a vibration without amplitude and is not interesting in terms of physics. Further solutions are obtained from the secular equation

$$\det(\mathbf{F}_{\mathbf{XM}} - \lambda \mathbf{E}) = 0 \quad (5.2-12)$$

i.e., the values λ are eigenvalues of the $\mathbf{F}_{\mathbf{XM}}$ matrix, while the corresponding amplitudes \mathbf{K} are eigenvectors. The frequencies can be derived from $\lambda = c/\nu$. It should be noted that \mathbf{K} has the dimension of massweighted Cartesian coordinates. As eigenvectors of a secular equation, the amplitudes are not uniquely defined; only the ratios of amplitudes are determined. These new vectors are orthogonal and form a basis in the $3n$ -dimensional space. They are called normal coordinates. Each frequency with its eigenvector defines a normal mode. The relation between mass-weighted $X_{\mathbf{M}}$ and normal coordinate \mathbf{Q} is

$$X_{\mathbf{M}} = L_{\mathbf{XM}} \mathbf{Q} \quad \text{or} \quad \mathbf{Q} = L_{\mathbf{XM}}^{-1} X_{\mathbf{M}} \quad (5.2.13)$$

On this basis we can write T and V as

$$\begin{aligned} 2T &= \mathbf{Q}^T L_{\mathbf{XM}}^{-1} L_{\mathbf{XM}} \mathbf{Q}' \quad \text{or as} \quad L_{\mathbf{XM}}^T L_{\mathbf{XM}} = \mathbf{E} \\ 2T &= \mathbf{Q}'^T \mathbf{Q}' \\ 2V &= \mathbf{Q}^T L_{\mathbf{XM}}^{-1} \mathbf{F}_{\mathbf{XM}} L_{\mathbf{XM}} \mathbf{Q} \end{aligned} \quad (5.2-14)$$

however, since $L_{\mathbf{XM}}^{-1} \mathbf{F}_{\mathbf{XM}} L_{\mathbf{XM}}$ is a diagonal matrix \mathbf{A} , one can write

$$2V = \mathbf{Q}^T \mathbf{A} \mathbf{Q} \quad (5.1-15)$$

The normal coordinates thus transform both kinetic and potential energies into quadratic forms and are orthonormal. Each of them can therefore be treated as an harmonic oscillator. As a result of using a Cartesian system, six of the eigenvalues are zero, because they correspond to overall motions of the undeformed molecule in the absence of restoring forces.

At this point it is obvious that there are two different approaches to this formalism. In the first approach, the structure and the force field are known (or supposed to be known), and it is possible to calculate and interpret the spectra. The second approach makes it possible to gain information about the molecular structure and/or force field on the basis of known spectra.

5.2.2 Internal coordinates

The described treatment has the disadvantage of being based on Cartesian coordinates, which depend on the system of axes used to localize the molecule. As an example, a methyl group can have different coordinates (CH_3 in toluene or ethane), while the chemical and spectroscopic properties of both are very similar. In order to take advantage of this chemical information, internal coordinates were introduced, which refer to chemically relevant quantities. A molecule with n atoms has $3n$ degrees of freedom, six of which correspond to the overall translations and rotations of the molecule. Only $3n - 6$ coordinates are necessary to describe the vibrational motions of the system. Five types of coordinates can be defined:

- bond stretching: variation of the bond length
- valence angle bending: variation of the angle between two chemical bonds with a common atom (HCH angle in a CH_3 group)
- out-of-plane bending: Variation of the angle between a plane, defined by two bonds with a common atom, and a third bond between the common atom and a fourth one (out-of-plane motion of C=O in formaldehyde)
- torsion: Variation of the dihedral angle between two planes (for example in hydrogen peroxide)
- linear bending: extension of the valence angle bending in case the bonds are colinear, in order to take the degeneracy into account (example CO_2)

The advantage of this coordinate system is that it corresponds to a chemist's thinking and that the obtained parameters can easily be correlated to other properties, such as bond length, ionic character, activation or formation energy, etc. The problem of defining a complete set of internal coordinates has been treated by Decius (Decius, 1949). The transformation from Cartesian \mathbf{X} to internal \mathbf{R} coordinates proceeds via the \mathbf{B} matrix.

$$\mathbf{R} = \mathbf{BX} \quad (5.2-16)$$

The coefficients of the \mathbf{B} matrix have been developed by Wilson and Califano (Wilson, 1955; Califano, 1976). The corresponding formulas are included in all available normal coordinate packages. In the system of internal coordinates the force constants are defined as the second derivatives of the potential energy with respect to two coordinates. In order to obtain the $\mathbf{F}_\mathbf{X}$ matrix, the $\mathbf{F}_\mathbf{R}$ matrix with internal coordinates has to be transformed according to

$$\mathbf{F}_\mathbf{X} = \mathbf{B}^{-1} \mathbf{F}_\mathbf{R} \mathbf{B} \quad (5.2-17)$$

As this point it is important to note that the \mathbf{B} matrix is usually not square and therefore cannot be inverted. In fact, it transforms from Cartesian (dimension $3n$) to internal coordinates (dimension $3n - 6$). In simple cases, six dummy coordinates ($T_x, T_y, T_z, R_x, R_y, R_z$) may be added to the $3n - 6$ internal ones in order to obtain an invertible square matrix. However, in some cases the symmetry of the problem makes it necessary to introduce redundant non-linearly independent coordinates (6 CCC angles for benzene or 6 HCH angles for CH_4). Gussoni et al. (1975) has shown that it is possible to use the transposed matrix instead of the inverse one and that this choice is the only one which ensures invariance of the potential energy upon coordinate transformation. We can therefore write

$$\mathbf{F}_X = \mathbf{B}^T \mathbf{F}_R \mathbf{B} \quad (5.2-18)$$

In order to calculate the \mathbf{F}_{XM} matrix, we define the \mathbf{M}^{-1} matrix, which is a $3n \times 3n$ matrix with n triplets of values $1/m_i$ on the diagonal. Thus,

$$\mathbf{F}_{XM} = \mathbf{M}^{-1} \mathbf{F}_X \quad (5.2-19)$$

$$\mathbf{F}_{XM} = \mathbf{M}^{-1} \mathbf{B}^T \mathbf{F}_R \mathbf{B} \quad (5.2-20)$$

This leads to the secular equation

$$(\mathbf{M}^{-1} \mathbf{B}^T \mathbf{F}_R \mathbf{B} - \lambda \mathbf{E}) \mathbf{K} = 0 \quad (5.2.21)$$

The left term can be multiplied by \mathbf{B} :

$$(\mathbf{B} \mathbf{M}^{-1} \mathbf{B}^T \mathbf{F}_R - \lambda \mathbf{E}) \mathbf{B} \mathbf{K} = 0 \quad (5.2-22)$$

Writing

$$\mathbf{B} \mathbf{M}^{-1} \mathbf{B}^T = \mathbf{G} \quad (5.2-23)$$

results in

$$(\mathbf{G} \mathbf{F}_R - \lambda \mathbf{E}) \mathbf{B} \mathbf{K} = 0 \quad (5.2-24)$$

This is recognized as a secular equation which gives the solution to the problem in internal coordinates. This is the original formulation proposed by Wilson, leading to the term “GF matrix method” which is often encountered in the literature. The relation between internal and normal coordinates is given by

$$\mathbf{R} = \mathbf{L}_Q \mathbf{Q} \quad \text{or} \quad \mathbf{Q} = \mathbf{L}_Q^{-1} \mathbf{R} \quad (5.2-25)$$

5.2.3 Symmetry coordinates

In normal coordinate treatment the molecular symmetry can be used for two complementary purposes. On the one hand, it can afford a block-diagonalization of the secular equation, leading to smaller independent blocks which can more quickly be treated separately. Unfortunately, due to the speed of modern computers, the work which is necessary to take the symmetry into account is often as extensive as the computer time which is saved. The second aspect is more interesting in connection with the treatment of large molecules, because in this case block-diagonalization leads to a symmetry selection of the calculated normal modes, which can be related to experimental information (infrared and/or Raman intensity, polarization of bands, gas phase band contours). This method has the disadvantage that, as a result of the low symmetry of many chemically interesting large molecules, these symmetry criteria are insufficient. If used, the symmetry coordinates are defined according to

$$\mathbf{S} = \mathbf{U}\mathbf{X} \quad (5.2-26)$$

The \mathbf{U} matrix elements are obtained by the projection operator technique

$$S_{\Delta\sigma_i}^{(\gamma)} = N \sum_R \chi_R^{(\gamma)} R_{(\Delta\sigma_i)} \quad (5.2-27)$$

where γ defines a symmetry species,

σ_i is a generator coordinate ($\Delta x_1, \dots$) for a set of equivalent atoms,

$\chi_R^{(\gamma)}$ is the character of the operation R for the species γ ,

$R(\Delta\sigma_i)$ is the result of the transformation of $\Delta\sigma_i$ by R ,

N is a normalization factor.

A similar treatment is obviously possible for internal coordinates. The use of symmetry coordinates leads to a new matrix \mathbf{F}_{XSM}

$$\mathbf{F}_{\text{XSM}} = \mathbf{U}\mathbf{F}_{\text{XM}}\mathbf{U}^T = \mathbf{U}\mathbf{M}^{-1/2}\mathbf{B}^T\mathbf{F}_{\text{R}}\mathbf{B}\mathbf{M}^{-1/2}\mathbf{U}^T \quad (5.2-28)$$

5.2.4 Summary of the coordinate systems

$$\begin{array}{ccc}
 S & \xrightarrow{\mathbf{U}_R} & R \\
 & & \downarrow \mathbf{B} \\
 Q & \xrightarrow{\mathbf{L}_X} & X \\
 & & \downarrow \mathbf{M}^{1/2} \\
 S & \xrightarrow{\mathbf{U}_X} & X_M
 \end{array}
 \quad R \xrightarrow{\mathbf{B}} X \quad \text{means } R = BX$$

5.2.5 Program packages for normal coordinate treatment

With the development of computer techniques, a large number of programs have become available which make it possible to calculate normal modes (Schachtschneider, 1964; Shimanouchi, 1968; McIntosh and Peterson, 1977; Gwinn, 1971; Sellers et al., 1977; Jones, 1970). This list does not include all existing packages, but it comprises the most frequently cited and most easily available ones (QCPE, Quantum Chemistry Program Exchange, University of Bloomington). All these programs perform the same types of calculations based on Cartesian or internal coordinates, and the derivatives in question are computed analytically or numerically. These programs initially afford frequencies which can be directly compared to the observed ones. It is important to remember that the calculated values are harmonic, while the experimental ones are essentially anharmonic. The eigenvectors have to be treated further in order to be comparable with the assignment of experimentally determined characteristic frequencies. This calculation affords the PED (Potential Energy Distribution), which allows a partition of the potential energy over the different defined force constants and thus localizes it in a certain portion of the molecule. This information is completed by the L_X matrix, which describes the normal coordinate in the Cartesian system. The Jacobian matrix J , which contains the terms $J_{ij} = d\nu_i/df_j$, describes the correlation between the frequency i and the force constant j . It is used in other programs which, starting from a trial set of force constants, calculate the corresponding spectra and, after comparing these with known ones, fit or refine the force constants. The programs mostly use the least squares method to minimize the difference between calculation and measurement. Such an optimization process may be enhanced by investigating not only one molecule but a series of isotopically labeled species, which provides supplementary experimental data without introducing new parameters and thus improves the quality of the mathematical treatment. There are other molecular properties which may supplement vibrational frequencies in order to enlarge the experimental data base which is necessary to fit the potential function of molecules which are not too large: Coriolis coupling constants (Kivelson and Wilson, 1953), centrifugal distortion constants, and mean square amplitudes of vibrations (Morino et al., 1952).

5.2.6 Potential energy functions

$3n - 6$ internal coordinates are needed to study a molecule with n atoms; the symmetric force constant matrix therefore contains $(3n - 5)(3n - 6)/2$ force constants. The corresponding force field is referred to as General Valence Force Field (GVFF). The symmetry and the topology of large molecules with a ring structure involving three-coordinated, four-coordinated, or higher coordinated atoms lead to the definition of more than $3n - 6$ internal coordinates, thus giving rise to a basis of non-independent coordinates and to an Internal Valence Force Field. Since a maximum of $3n - 6$ frequencies is observed, it is impossible to determine all previously defined parameters, and it is necessary to introduce a number of assumptions to reduce the number of variables. This leads to a Simplified General Valence Force Field. Shimanouchi and his group have extensively

investigated another type of simplified force field, the Urey-Bradley Force Field (UBFF). In the case of a triatomic molecule XYZ , this approach is based on the valence coordinates XY and YZ , the angle XYZ , and the non-bonded distance $X...Z$. The model assumes that the off-diagonal parameters are caused by interactions between non-bonded atoms. A review of this field and the obtained results has been provided by Shimanouchi (1970). It seems that in general the UBFF works nicely for vibrations of heavy atoms without electron delocalization. In case of discrepancy, the UBFF is improved by including a number of off-diagonal terms which lead to a Modified UBFF (MUBFF). Finally, there is a somewhat different approach which involves treating chemical functions as local subunits with their respective idealized symmetries. CH_3 , for instance, is considered a group with C_{3v} symmetry, CH_2 possesses C_{2v} symmetry, and so on. The corresponding force field is referred to as Local Symmetry Force Field. It permits the transfer of force constants which have been determined on small molecules to larger molecules which do not possess overall symmetry but which have local symmetrical groups. This very useful method has been presented in a series of papers by Shimanouchi et al. (1978 and papers cited therein). This discussion shows that almost all operations starting from the exactly defined GVFF afford an approximate intermediate force field which reflects important molecular properties: symmetry, steric effects, electron delocalization, bending of bonds, etc. The practical approach to calculating large molecules involves

- 1) defining the potential function,
- 2) transferring the unchanged force field from known molecular subunits,
- 3) if possible, deriving force constants by extrapolating known parameters to undetermined subunits,
- 4) estimating, on the basis of chemical experience, whether extrapolation is possible or not,
- 5) calculating the normal modes,
- 6) comparing the results with known parameters (frequencies, symmetry and assignment or characteristic frequencies, for example by isotopic substitution),
- 7) starting a refinement cycle involving force constants until convergence is reached, but being careful to keep the problem mathematically defined; the numbers of observed frequencies and parameters must be in correct relation in order to perform a least squares refinement.

A large number of reliable force fields have been described in the literature which may be transferred to similar molecules. The best known example is that of aliphatic hydrocarbons, where a single force field is able to reproduce the spectra of alkanes from ethane to polyethylene, including branched and cyclic systems (Schachtschneider and Snyder, 1963, 1965). Based on these results, several investigations have been performed concerning alkane derivatives and alkenes. An extensive collection of existing force fields has been discussed by Califano (1976). In fact, it is impossible to list all existing force fields. Before starting a new treatment, it is necessary to perform a literature search and to analyze the existing information carefully. It is important to transfer the parameters under conditions which are compatible with those under which they were determined. A clear definition of the geometry is a prime concern, because some investigations are based on the experimentally determined geometry, while others use standard geometrical parameters.

Before closing this discussion, two IUPAC recommendations should be cited. The first one concerns the definition and notation of force constants (IUPAC, 1977). The second recommendation lists test data and results of normal coordinate calculations, which make it possible to check new programmes or new installed packages (IUPAC, 1985). Finally a last remark concerns the units encountered in publications. Numerical values of force constants are usually given in mdyn/Å, mdyn, or mdyn·Å for stretching, stretching-bending and bending force constants, respectively. The conversion factors to the SI system are

$$1 \text{ mdyn}/\text{\AA} = 10^2 \text{ N/m},$$

$$1 \text{ mdyn} = 10^{-8} \text{ N},$$

$$1 \text{ mdyn}\cdot\text{\AA} = 10^{-18} \text{ J}.$$

Another type of units is sometimes encountered in the Russian literature, where the mass unit is the mass of the hydrogen atom ($m_H = 1.088$), and the length unit equals the length of a CH bond ($R_{CH} = 1.09 \text{ \AA}$). The corresponding parameters can hardly be compared to those that are common in the West, and special care must be taken to make sure which type of units is used in a publication.

5.2.7 Physical significance of force constants

The physical interpretation of force constants is the object of a large number of publications, not all of which are cited here. A number of characteristic examples demonstrate the type of information which can be obtained from these parameters, see also Secs. 2.5 and 4.2.2.3.6.

5.2.7.1 Valence stretching

Table 5.2-1 Correlation between force constant, bond length and hybridization for some hydrocarbons

	sp ³	sp ²	sp
$X = H$	CX_4	C_2X_4	C_2X_2
	4.90 1.09	5.10 1.06	5.80 mdyn/Å 1.06 Å
$X = Cl$	3.20 1.76	3.80 1.72	5.20 mdyn/Å 1.64 Å
	C_2H_6	$CH_3-C_6H_5$	$(CH_3)_3C \equiv C(CH_3)_3$
C—C	4.40 1.56	4.80 1.50	5.30 mdyn/Å —

Obviously, there is a correlation between the force constant, the bond length, and the hybridization of an atom, as shown in Table 5.2-1. One can verify that these data confirm the relation proposed by Badger (1934)

$$K = 1.86 \cdot 10^5 / (R_{ij} - a_{ij}) \quad (5.2-29)$$

in which K is the force constant in mdyn/Å, R_{ij} is the interatomic distance, and a_{ij} is a parameter depending only on the nature of the atoms i and j . Gordy proposed a similar relation, which includes the bond order N and the electronegativity χ (Gordy and Orville-Thomas, 1956)

$$K = 1.67 N \left(\frac{\chi_i \chi_j}{R_{ij}} \right)^{3/4} + 0.3 \quad (5.2-30)$$

This relation can provide a first estimation of the bond order of a given bond in a molecule, particularly if the molecule is large.

5.2.7.2 Interaction force constants

In a somewhat older paper, Coulson et al. provide an analysis of the cross terms in triatomic XY_2 molecules (Coulson, 1948). The potential function was defined as

$$2V = f_1 \Delta r_1^2 + f_2 \Delta r_2^2 + 2f_{12} \Delta r_1 \Delta r_2 + r_1 r_2 f_\theta \Delta \theta^2 + 2gr_1(\Delta r_1 + \Delta r_2)\Delta\theta \quad (5.2-31)$$

The authors were able to show that resonance, rehybridization, and interatomic non-bonded repulsion cause a positive f_{12} parameter, while interatomic attraction leads to a negative f_{12} . The same behavior is expected for g , except in the case of resonance, where the situation is not simple enough to afford a result. The principle of this analysis is an interesting one. If only the bonding part is included, the following terms are retained:

$$2V = f_1(\Delta r_1^2 + \Delta r_2^2) + 2f_{12}\Delta r_1 \Delta r_2 \quad (5.2-32)$$

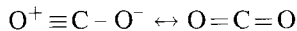
If we suppose that a displacement Δr_1 is performed around the equilibrium, this will cause a modification Δr_2 of r_2 . At equilibrium, the first derivatives should be zero, and therefore

$$dV/d\Delta r_1 = 2f_1\Delta r_1 + 2f_{12}\Delta r_2 = 0 \quad (5.2-33)$$

This simplifies that

$$\Delta r_2 = - (f_{12}/f_1) \Delta r_1 \quad (5.2-34)$$

Thus, f_1 being positive, Δr_1 and Δr_2 have opposite signs if f_{12} is positive, and vice versa. This is exactly what is expected of resonance between different structures. Two resonance structures of CO_2 , for instance,



show that a decrease of the left $\text{C}=\text{O}$ bond length ($\Delta r_1 < 0$) enhances the single bond character of the right bond, increasing its length and therefore yielding a positive Δr_2 . This rule becomes most evident as a result of the necessity to introduce so-called Kekulé interactions in order to calculate aromatic rings, which are interactions between CC bonds in ortho ($f_{12} > 0$), meta ($f_{13} < 0$), and para ($f_{14} > 0$) position.

The angle bending interactions of ethylene and ethane in *cis* or *trans* position with a common bond have been analyzed by Shimanouchi as an evidence of the flexibility of the C–C and C=C bonds. He used this investigation to obtain an estimation of Young's modulus of bonds (Shimanouchi, 1957).

In fact, a different approach has recently been explored which utilizes the increased calculation capacity offered by computers. Most of the newly designed semi-empirical and ab initio quantum-chemical programs have an option to perform a normal coordinate analysis at the end of an SCF geometry optimization. The force constants are usually obtained by analytical or numerical derivation of the energy at the minimum of the hypersurface. Such options are provided, for instance, by CADPAC (Amos and Rice, 1987) or GAUSSIAN (Frisch et al., 1988, 1993) at the ab initio level or by MOPAC (Stewart, 1989) at the semi-empirical level. This approach has the great advantage that it suppresses all the hypotheses which are required for a usual force field, because all derivatives are systematically calculated by the potential function. On the other hand, the treatment of large and interesting chemical systems is limited by the size of the computer and the computation time (and costs) of such a treatment. Besides, unlike hypotheses for the empirical force field, these methods introduce either systematic errors resulting from the approximation used for the semi-empirical approach, or a dependence on the basis set used for the ab initio calculations. Some of these effects are well known and can be corrected by renormalization (bonding coordinates) (Allouche and Pourcin, 1993; Zhou et al., 1993). Since different types of coordinates are affected differently by computational errors, the coupling patterns in the spectra can be modified considerably. This leads to calculated spectra and assignments which can hardly be compared to the quality of a well-conducted normal coordinate analysis. In the recent years rapid developments of the local density techniques have led to alternatives enabling the calculation of middle-sized molecules with reasonable computer capacities (time and memory) (Stave and Nicholas, 1993; March, 1992; Ziegler, 1991).

5.2.8 Vibrational frequencies of crystals

The transition from the isolated molecule to a crystal has two important consequences for the calculation of vibrational spectra. On the one hand, different types of interactions, including van der Waals forces, electrostatic interactions, and hydrogen bonds, now contribute to the potential; these must be taken into account. Depending on the nature of the crystal, all or some of its components contribute, although by different orders of magnitude and different radii of influence. On the other hand, the complication resulting from the crystal size is partly countered by the three-dimensional translation symmetry, which reduces the size of the numerical problem.

5.2.8.1 General treatment

Since there are several monographs providing a detailed description of the basic development, this is not repeated in this context. The list includes, for instance, Born and Huang (1954), Maradudin et al. (1971), and Califano et al. (1981). The vibrational frequencies are obtained by diagonalization of the dynamical matrix D , which contains elements of the form

$$D_{\mu l}^{\nu m}(k) = \sum_{\beta} \exp(-2\pi i k \cdot r_{\beta}) (\frac{d^2 V}{d Q_{1\mu l} d Q_{\beta \nu m}})_0 \quad (5.2-35)$$

in which μ and ν stand for the particles (ions or molecules), l and m are the coordinates of these particles, and β is the unit cell, located at a distance r_{β} from the reference unit cell. The wave vector k is a measure of the phase shift between two neighboring unit cells (Sec. 4.5). With a modulus of $2\pi/\lambda$ (λ is the wavelength), k is practically zero in infrared and Raman spectra. Accordingly, the exponential term equals one, i.e., only motions in which the primitive unit cells vibrate in phase are observed. This was recognized early by Shimanouchi, who proposed an extension of the *GF* matrix method in order to calculate diamond, CaF₂, and perovskite fluorides (Shimanouchi et al., 1961; Nakagawa et al., 1967). In the case of molecular crystals the problem may be simplified by treating the molecules as entities, since intermolecular and intramolecular potentials usually differ by several orders of magnitude. There are thus two possibilities. The first option, known as rigid-body approximation, operates only on the so-called lattice modes which are usually observed between 0 and 250 cm⁻¹ and which consist of translations and/or rotations (librations) of molecules around their equilibrium positions. Coupling of these degrees of freedom with internal motion is neglected. The second possibility is based on the assumption that molecules in a crystal remain unchanged. This option, on the one hand, utilizes the normal modes of the isolated molecule, on the other hand it employs the translations and vibrations as a basis for a complete treatment of the unit cell. This alternative allows coupling between internal and external degrees of freedom. The corresponding formalism has been developed by Califano, who also reviews some examples (Califano, 1976).

In investigating crystal spectra, such as those of isolated molecules, supplementary information may be used apart from the frequencies in order to improve the determination of the potential. The elastic constants (Shiro, 1972; Walmsley, 1968), the mean square amplitudes, and several thermodynamic functions (Pertsin and Kitaigorodsky, 1987) have been calculated for several crystals. By using inelastic neutron diffusion it is also possible to obtain vibrations involving *out-of-phase* vibrations of the unit cells and to measure the dispersion curves over the entire *Brillouin zone*. It is thus possible to test the validity of the potential model for a larger number of experimental points. Another test technique involves measuring the velocity of sound by ultrasonic measurement or by the slope of the acoustic modes at the center of the Brillouin zone. For this application it is necessary to calculate the vibration far from the center of the zone, using programs which can operate with an exponential term which no longer equals one.

5.2.8.2 Potential function

In order to obtain the dynamic matrix, a good representation of the potential is needed. Supposing that the internal field is known from the investigation of the isolated molecule, the components of the above-mentioned intermolecular potential must be described.

5.2.8.2.1 Van der Waals interactions

Van der Waals forces comprise an attractive part, the induction or London forces, and repulsion between the atoms at short distance. For short contacts, these forces are usually treated according to the atom-atom method, which has recently been extensively reviewed by Pertsin and Kitaigorodsky (1987). This approach is based on empirical parameters. The interaction between two molecules is represented as the sum of all the interactions of all atoms of one molecule with all atoms of the other one. The atom-atom interactions are added as long as the summation converges, usually between 6 and 10 Å. Two different analytical forms are usually assumed:

$$V_{ij} = -A_{ij} / r_{ij}^6 + B_{ij} / r_{ij}^m \quad 8 < m < 14 \quad \text{Lennard-Jones type} \quad (5.2-36)$$

$$V_{ij} = -A_{ij} / r_{ij}^6 + B_{ij} \exp(-C_{ij}r_{ij}) \quad \text{Buckingham type} \quad (5.2-37)$$

in which A_{ij} , B_{ij} , and C_{ij} are parameters depending only on the chemical nature of the atoms i and j . r_{ij} is the distance between the atoms. In order to reduce the number of parameters, combination rules are sometimes used for the cross terms:

$$A_{ij} = (A_{ii}A_{jj})^{1/2}, \quad B_{ij} = (B_{ii}B_{jj})^{1/2}, \quad C_{ij} = (C_{ii} + C_{jj})/2 \quad (5.2-38)$$

The study of several simple crystals has shown that these rules are somewhat too simple and that they may afford results which are far from the real values. They can be very

useful as initial values at the beginning of an optimization process. The investigations frequently aimed at determining transferable parameters. This was realized for the atoms C and H. The process seems to be much more difficult for systems containing heteroatoms. Pertsin gives a review of actually available parameters (1987), see also Sec. 2.5.4, Eqs. 2.5-16...18.

5.2.8.2.2 Hydrogen bond

The nature of the hydrogen bond is still the object of numerous publications. In the lattice-dynamic treatment, these interactions are mostly treated according to a phenomenological approach, which tends to use the built-in possibilities of the programs or which taylors a special potential function to reflect the features of the hydrogen bond (energy, distance and force constant); several examples have been cited by Bougeard (1988).

5.2.8.2.3 Electrostatic interaction

For this section two formalisms can be defined which represent the limit of all treatment. The first method of introducing the Coulomb forces is a straightforward application of the atom-atom method, in which a partial charge is assigned to each atom, leading to a potential term $q_i q_j / r_{ij}$. This approach suffers from two difficulties: the need for values for the partial charges in the solid state, and the very slow convergence of the $1/r_{ij}$ series compared to the other terms ($1/r^6$ or exp). The former problem can be met by quantum chemical determination of the charges. This usually involves performing the calculation for an isolated molecule, which can be quite different from a molecule in a crystal. The slow convergence of the $1/r$ series is treated by using a summation in the reciprocal space, proposed by Ewald (1921). The second approach by rigid-body approximation involves assigning a set of molecular multipoles to each molecule and using multipole expansion to calculate the contribution of the electrostatic forces to the crystal dynamics. This formalism has been developed by Califano et al. (1981). It has the advantage of employing experimentally determined molecular values (dipole, quadrupole). The primary problem arises from multipole expansion, which theoretically only applies if the distance between molecules are much larger than the molecular size, a condition which in large molecules is not always rigorously fulfilled. An intermediate solution has been proposed, based on the distributed multipole method (Stone, 1990). The multipole distribution can be adapted to ensure satisfactory convergence of the series; it also affords a better description of the anisotropy of the crystal field. The major drawback is that the distribution of atom and bond multipoles is not unique. Several approaches may be proposed. New parameters are introduced to improve the agreement between calculation and experience. However, quantifying the personal experience of the author is always very difficult.

5.2.8.3 Concluding remarks on solid state calculations

No computer program for the calculation of the frequencies in solids has been developed into a standard, as with the calculation of isolated molecules; and no such program is available from exchange organizations. Various research groups have developed their own software, which is often designed for the solution of particular problems, limiting its usefulness in general (symmetry, size). A pioneer in this field, Shimanouchi produced a package which offers the possibility to consider the translational symmetry (Shimanouchi, 1968). Compared to more recent developments, which directly incorporate the potential, he introduces only the force constants, i.e., the second derivative of the potential function. This only yields the normal modes, while recent programs offer simultaneous determination of lattice energy, equilibrium conditions, and lattice dynamics. Although this is not the topic of this section, it should finally be mentioned that similar results can be obtained by applying molecular dynamics techniques (MD). A sample containing a large number of interacting molecules is studied classically over a long time. The density of state and the IR and Raman band profiles can be deduced from the corresponding correlation functions. A large computer memory and time are obviously required for such investigations, which are still far from being routine techniques.

5.2.9 Vibrational intensities

Different definitions of intensities have been given (Sec. 2.3, 2.4). It has been shown that the band absorption coefficient A_k of the normal mode k is related to the molecular quantities by the relation

$$A_k = \frac{\pi N}{3c^2} g_k ((d\mu_x/dQ_k)_0^2 + (d\mu_y/dQ_k)_0^2 + (d\mu_z/dQ_k)_0^2) \quad (5.2-39)$$

in which A_k is estimated in a spectrum in which cm^{-1} is the unit of the frequency scale. N and c are Avogadro's number and the speed of light, g_k is the degeneracy of the vibration k , $\mu_{x,y,z}$ are the components of the dipole moment, Q_k stands for the k th normal mode, and 0 indicates that derivation is performed near the equilibrium position. For the Raman intensity we will concentrate on off-resonance spectroscopy, and we suppose that the excitation wavelength is far enough from the absorption bands of the sample. For the 90° experimental design with freely moving molecules (gas), the Raman intensity I_k of the k th normal mode is given by

$$I_k = I_0 \frac{2\pi^2 h}{c} F(\tilde{\nu}_k) g_k (\alpha_k^2 + \frac{2}{9} \gamma_k^2) \quad (5.2-40)$$

in which the symbols are the same as for the infrared intensity. Further, h is Planck's constant.

$$F(\nu_\kappa) = \frac{(\tilde{\nu}_0 - \tilde{\nu}_k)^4}{\tilde{\nu}_k(1 - \exp(-hc\tilde{\nu}_k/kT))} \quad (5.2-41)$$

contains all temperature and excitation factors, and

$$\alpha_k = (\mathrm{d}\alpha_{xx}/\mathrm{d}Q_k + \mathrm{d}\alpha_{yy}/\mathrm{d}Q_k + \mathrm{d}\alpha_{zz}/\mathrm{d}Q_k)/3 \quad (5.2-42)$$

$$\begin{aligned} \gamma_k^2 = & ((\mathrm{d}\alpha_{xx}/\mathrm{d}Q_k - \mathrm{d}\alpha_{yy}/\mathrm{d}Q_k)^2 + \\ & + (\mathrm{d}\alpha_{yy}/\mathrm{d}Q_k - \mathrm{d}\alpha_{zz}/\mathrm{d}Q_k)^2 + (\mathrm{d}\alpha_{zz}/\mathrm{d}Q_k - \mathrm{d}\alpha_{xx}/\mathrm{d}Q_k)^2 + \\ & + 6 [(\mathrm{d}\alpha_{xy}/\mathrm{d}Q_k)^2 + (\mathrm{d}\alpha_{yz}/\mathrm{d}Q_k)^2 + (\mathrm{d}\alpha_{zx}/\mathrm{d}Q_k)^2]) / 2 \end{aligned} \quad (5.2-43)$$

These equations show that the spectra contain information concerning microscopic molecular quantities, such as dipole moment and polarizability. It is therefore very useful to consider using the second dimension of the spectra and to develop calculation methods for the intensities. Thus, knowing the normal coordinate Q_k , we have to calculate the variation of the dipole moment and of the polarizability with Q_k , i.e., determine both quantities for geometries of the deformed molecule according to the normal mode. Both quantities, μ and α , can be obtained by classical and quantum chemical methods.

An efficient method to visualize the properties of the normal coordinates is to calculate *activity measurements, AM*. They show which components of the dipole moment vector and the polarizability tensor are modulated by the vibration, and the relative sign of the infrared and Raman optical activity (Schrader et al., 1984; Schrader, 1988). The necessary transformation of the eigenvectors (Eq. 5.2-13) needs only seconds of computer time. The *AMs* are useful to assign vibrations to symmetry species and to check the input of the frequency calculation: the symmetry of the Cartesian coordinates of the atoms as well as of the force constant matrix. This program is part of the *SPSIM* program package (Fischer et al., 1989).

5.2.9.1 Classical methods

The purpose of classical methods is to obtain transferable molecular intensity parameters, to calculate reliable intensities within reasonable computation times, and to investigate large interesting molecules.

5.2.9.1.1 Electro-optical theory

This method is based on a proposition by Wolkenstein (1941) and has been developed further and used extensively in the last few years (Gussoni, 1979). This approach involves writing the molecular dipole moment and the polarizability as sums over all bonds of the molecule:

$$\mu = \sum_{l=1}^L m_l \quad \text{and} \quad \alpha = \sum_{l=1}^L \alpha_\lambda \quad (5.2-44)$$

In this context the case of the infrared intensity is outlined. The somewhat more complex treatment of the Raman intensity can be derived analogously, as shown by Gussoni (1979). Each vector \mathbf{m}_l can be written

$$\mathbf{m}_l = m_l \mathbf{e}_l \quad (5.2-45)$$

\mathbf{e}_l being a unit vector in the direction of the l th bond. The derivation with respect to Q_k leads to

$$(d\mu/dQ_k)_0 = \sum_{l=1}^L ((dm_l/dQ_k)_0 \mathbf{e}_l + m_l (de_l/dQ_k)_0) \quad (5.2-46)$$

The L matrix permits the transition between internal and normal coordinates

$$dm_l/dQ_k = \sum_{j=1}^K (dm_l/dR_j)(dR_j/dQ_k) = \sum_{j=1}^K (dm_l/dR_j)L_{jk} \quad (5.2-47)$$

$$de_l/dQ_k = \sum_{j=1}^K (de_l/dR_j)(dR_j/dQ_k) = \sum_{j=1}^K (de_l/dR_j)L_{jk} \quad (5.2-48)$$

in which j labels one of the K internal coordinates of the molecule. It follows that

$$(d\mu/dQ_k)_0 = \sum_{l=1}^L \left(\left(\sum_{j=1}^K (dm_l/dR_k)L_{jk} \right) \mathbf{e}_l + m_l \left(\sum_{j=1}^K (de_l/dR_j)L_{jk} \right) \right) \quad (5.2-49)$$

Two types of parameters appear in this expression. m_l represents bond dipole moments, while dm_l/dR_k represents derivatives of the bond dipole moment with respect to the internal coordinates (bond stretching, angle deformation, out-of-plane deformation, and torsion). These parameters are referred to as electro-optical parameters (*eop*). All other quantities are derived from the structure or from the normal coordinate calculation. The electro-optical parameters can be derived from measured intensities, like force constants are derived from measured frequencies. Compared to the determination of force constants, the problem in this case is that the number of parameters is much higher.

Besides, the intensity only yields the square of $d\mu/dQ$, and the sign has to be determined by plausibility reflection or through quantum chemical methods. Gussoni et al. have found an elegant route to determining the electro-optical parameters of a series of small alkanes and were able to apply these values to calculations of the vibrational intensities of cyclohexane on the one hand and polyethylene on the other hand (Gussoni et al., 1977; Abbate et al., 1977). Another application is the physical interpretation of electro-optical parameters which were shown to correlate nicely with other quantities. The charge flux in hydrogen atoms, for example, shows the disposition of the atoms to form a hydrogen bond (Gussoni et al., 1984).

5.2.9.1.2 Polar tensors

This method was proposed by Biarge et al. (1961). Assuming a linear dependence between displacement r_α and variation of the dipole moment and the additivity of the effects on different nuclei, one can write

$$\Delta\mu = \sum_{i=1}^N \mathbf{D}_i r_i \quad (5.2-50)$$

N being the number of atoms and \mathbf{D}_i defined by

$$\mathbf{D}_i = \begin{pmatrix} d\mu_x/dx_i & d\mu_x/dy_i & d\mu_x/dz_i \\ d\mu_y/dx_i & d\mu_y/dy_i & d\mu_y/dz_i \\ d\mu_z/dx_i & d\mu_z/dy_i & d\mu_z/dz_i \end{pmatrix} \quad (5.2-51)$$

r_α is expressed in Cartesian coordinates. These polar tensors \mathbf{D}_i can be derived from experimental intensities by elementary coordinate transformation. If the axes x , y , and z are chosen such that the bonds are oriented along one of the axes, then the derivatives can be used to interpret the changes of the electron clouds during a vibration. Besides, considering the definitions of the axes, it is possible to transfer atomic polar tensors between similar molecules and to estimate their intensities (Person and Newton, 1974; Person and Overend, 1977).

5.2.9.2 Quantum chemical methods

Since the intensity calculation can be reduced to calculating α and μ for deformed molecules, the availability of quantum chemical methods immediately led to attempts to employ them to determine vibrational intensities (Segal and Klein, 1967). The polarizability is the proportionality factor between the induced dipole moment and the inducing electric field. It is therefore necessary to use a perturbation treatment which takes the electric field into account. Two different approaches were explored: the Finite

field Perturbation Theory (FPT), and the classical second order perturbation method, sometimes referred to as SOS-method (Sum Over States), because of the form of the expressions used. The former technique introduces the perturbation directly into the Fock matrix through two additional terms, which correct the diagonal elements and those non-diagonal elements which correspond to *s* and *p* orbitals of one atom (Hush and Williams, 1970). The perturbational method is derived from the expression of the energy of the induced dipole moment in an electric field and leads to the expression

$$\alpha_{ij} = 2 \sum_{k=1}^{\text{occ}} \sum_{I=1}^{\text{virt}} \frac{\langle \varphi_I | \mu_i | \varphi_k \rangle \langle \varphi_k | \mu_j | \varphi_I \rangle}{E_I - E_k} \quad (5.2-52)$$

where *I* and *k* label the molecular orbitals, μ is the dipole moment operator, and *E* is the energy of the molecular orbitals (Blom, 1977).

The necessary derivations with respect to the small displacements can be performed either numerically, or, more recently, also analytically. These analytical methods have developed very rapidly in the past few years, allowing complete *ab initio* calculation of the spectra (frequencies and intensities) of medium sized molecules, such as furan, pyrrole, and thiophene (Simandiras et al., 1988); however, with this approach the method has reached its present limit. Similar calculations are obviously possible at the semi-empirical level and can be applied to larger systems. Different comparative studies have shown that the precise calculation of infrared and Raman intensities makes it necessary to consider a large number of excited states (Voisin et al., 1992). The complete quantum chemical calculation of a spectrum will therefore remain an exercise which can only be performed for relatively small molecule. For larger systems, the classical electro-optical parameters or polar tensors which are calibrated by quantum chemical methods applied to small molecules, will remain an attractive alternative. For intensity calculations the local density method is also increasing their capabilities and yield accurate results with comparatively reduced computer performance (Dobbs and Dixon, 1994).

A special field of application of these techniques is the determination of molecular conformations in cases where X-ray and neutron techniques are not applicable, in solution or in the liquid phase. It is known that conformers afford essentially the same spectra; the intensities of some bands may vary. It is sufficient to investigate some bands in order to determine the conformation, and quantum chemical methods can be applied (Oelichmann et al., 1981a, b, 1982; Grunenberg and Bougeard, 1987).

6 Special techniques and applications

6.1 Applications of non-classical Raman spectroscopy: resonance Raman, surface enhanced Raman, and nonlinear coherent Raman spectroscopy*

6.1.1 Introduction**

The principle and applications of classical Raman scattering are discussed in previous chapters. Using this technique there are, however, some serious problems to deal with:

- (i) The poor efficiency of the Raman effect, where even in favorable cases the conversion of the incident laser photons into the Raman signal is only of the order of 10^{-8} , makes it very difficult to record Raman spectra from poor scatterers or from materials with very low concentration values.
- (ii) In molecules belonging to specific point groups (e. g. C_6 , D_6 , C_{6v} , C_{4h} , D_{2h} , D_{3h} , D_{6h} , etc.) there exist silent vibrational modes which are neither Raman nor IR active.
- (iii) Certain molecular systems exhibit high fluorescence quantum yield and even weak fluorescence signals may be strong enough to totally obscure the Raman signal.
- (iv) In classical Raman spectroscopy the spectral resolution of the observed bands is often limited by the resolution of the monochromator, whereas the laser line width in most cases is small enough and does not contribute appreciably to the observed Raman band width.

There are several techniques to avoid or overcome one or the other problem. Resonance Raman scattering, for instance, is able to enhance the Raman scattering cross section by orders of magnitude. The resonance Raman effect can be observed when the exciting frequency is close to (pre-resonance Raman effect) or even coincides (rigorous resonance Raman effect) with dipole allowed electronic transitions in the molecule un-

* Section 6.1 is contributed by W. Kiefer, Würzburg

** Section 6.1.1 is contributed by W. Kiefer, Würzburg and M. Spiekermann, Lübeck

der investigation. Due to special surface effects, molecules adsorbed on metal surfaces undergo much higher scattering efficiencies. This so-called surface enhanced Raman scattering (SERS) has gained much interest in recent years and has been applied to many studies particularly in the investigation of organic and biological molecules. Although hyper Raman spectroscopy, which in principle allows to observe most of the vibrations which are forbidden both in Raman and in infrared spectra, is a very inefficient method and at the time of its first realization was very difficult to perform, it has been developed meanwhile to a high standard. Due to the development of highly efficient detectors (optical multichannel analyzers) and favourable lasers (acousto-optically Q-switched Nd:YAG lasers, $\sim 5\text{kHz}$ repetition rate) hyper Raman spectroscopy has become a useful spectroscopic technique (see Sec. 3.6.2.1) by now. The possibility of fluorescence suppression and increasing the spectral resolution considerably by means of nonlinear coherent Raman techniques has already been discussed in Secs. 3.6.1 and 3.6.2.

In this section we first discuss the principles of resonance Raman and surface-enhanced Raman scattering and give some specific examples. Since the hyper Raman effect and the coherent nonlinear Raman effects have been described in Sec. 3.6, we only add some typical applications of the methods.

6.1.2 Resonance Raman spectroscopy (RRS)

As mentioned above, resonance occurs in Raman spectroscopy when the photon energy of the exciting laser beam is approximately equal to the energy of an electric dipole allowed transition of the material under investigation. Two broad types of resonance effect can be identified: the preresonance Raman effect (pre-RRE) and the rigorous resonance Raman effect (RRE). Typically the pre-RRE is observed when the exciting radiation frequency comes within the high or low frequency wings but not under the observable vibrational structure of the electronic absorption band involved in the Raman scattering process. When the exciting radiation frequency actually falls within the observable vibrational structure, then the RRE is observed. The intensities of Raman bands associated with totally symmetric vibrational modes which are strongly coupled to the electronic excited state may be enhanced by as much as a factor of 10^6 . This enhancement makes RRS attractive to chemists, biochemists, biologists as well as to physicists. The technique has been used to study the vibrational and electronic properties of such diverse materials as iodine vapor, GaAs single crystals, heme proteins in solution and conjugated macromolecules to mention only very few materials. The enhancement of the Raman bands does not only make the recording of the spectra easier than in its absence, it also permits isolation of the Raman bands of a chromophore – the molecule or part of a molecule which gives rise to the electronic transition – in situations where it would be impossible to make such assignments using classical Raman spectroscopy. This selectivity is particularly apparent in complex biological molecules, where resonance Raman spectra have been extensively studied. Because biological chromophores are often at sites of biological activity, the technique is considered to hold promise as a probe of

biological structure. Also, resonance Raman studies of the use of dyes as labels involving biologically important molecules, have been successfully performed. The concentrations at which RR spectra were obtained are sufficiently low (10^{-3} to 10^{-5} M) so as to eliminate intermolecular interactions other than those with the solvent. This makes the data very relevant to the usual physical situation. RRS also holds promise as a technique for the detection of small amounts of atmospheric pollutants like NO_2 , O_3 , etc. A further area which is attracting an increasing amount of attention is that of the RR spectra of structurally simple inorganic molecules.

Information about the properties of a molecule in an electronic excited state can also be obtained from RRS. An important quantity in this regard is the excitation profile (EP) which is obtained by measuring the Raman intensity of a vibrational mode as a function of incident laser photon energy. From the EP, the strength of the interaction between the electronic excited state and the vibrational mode can be estimated and, in certain cases, so can the frequency of the vibrational mode in the excited state. With additional information it may also be possible to determine the atomic displacements between the ground and the excited states. The EP, which must be corrected for spectral response of the spectrometer and for the ν^4 law, preferably using an internal standard, essentially duplicates the absorption band profiles. In this way valuable information relating the assignment and vibrational structure of electronic absorption spectra can be derived.

In principle, no special Raman instrumentation is needed to perform RRS because RR spectra can be obtained with conventional Raman spectrometers, if the suitable excitation wavelength is applied. However, a number of difficulties arise in attempting to measure quantitatively RR intensities. These include those associated with (i) making allowance for the competition between scattering and absorption processes, (ii) eliminating the so-called thermal lens effect and the thermal decomposition of the sample and (iii) eliminating eventual simultaneous fluorescence or photolysis. Some of the experimental problems involved in this type of light scattering have been solved by the introduction of devices which permit relative motion between the sample and the focused laser beam. By means of these techniques localized overheating of the sample or its decomposition is avoided.

There have been several important reviews of RRS and its applications: Behringer (1967, observed resonance Raman spectra); Tang and Albrecht (1970, developments in the theories of vibrational Raman intensities); Behringer (1974, theories of resonance Raman scattering), Behringer (1975, experimental resonance Raman spectroscopy); Spiro and Loehr (1975, RR spectra of heme proteins and other biological systems); Clark (1975, RR spectra of inorganic molecules and ions); Martin and Falicov (1975, resonant Raman scattering); Richter (1976, resonant Raman scattering in semiconductors); Kiefer (1977, recent techniques in Raman spectroscopy); Nishimura et al., (1978, RRS of nucleic acids); Siebrand and Zgierski (1979, RRS - a key to vibronic coupling); Rousseau et al., (1979, the resonance Raman effect); Mortensen and Hassing (1980, polarization and interference phenomena in resonance Raman scattering); Carey (1980, Raman and RR studies of biological systems); Carey (1982, biochemical applications of Raman and RR spectroscopies); Clark (1984, Raman and RRS of linear chain complexes); Batchelder and Bloor (1984, RRS of conjugated macromolecules); Lutz (1984, RR studies in photosynthesis); Lee and Albrecht (1985, a unified view of Raman, resonance Raman, and

fluorescence spectroscopy); Hamaguchi (1985, the RR effect and depolarization in vibrational Raman scattering); Harada and Takeuchi (1986, Raman and ultraviolet RR spectra of proteins and related compounds); Morris and Bienstock (1986, RR of flavins and flavoproteins); Kitagawa (1986, RR spectra of reaction intermediates of heme enzymes); Stockburger et al., (1986, RRS of bacteriorhodopsin: structure and function); Spiro (1987, RR spectra of polyenes and aromatics); Myers and Mathies (1987, RR intensities: a probe of excited-state structure and dynamics); Asher (1988, UV resonance Raman studies of molecular structure and dynamics).

6.1.2.1 Resonance Raman theories

In this chapter we shortly summarize two theories developed to describe the resonance Raman effect, starting with the traditional approach to resonance Raman intensities (see Sec. 6.1.2.1.1) which begins with the dispersion expressions originally derived by Kramers and Heisenberg (1925) and Dirac (1927) from second-order time-dependent perturbation theory and which is known in the literature as the Albrecht theory (Albrecht, 1961). Then, in Sec. 6.1.2.1.2, we focus on a new and more intuitively appealing picture of the resonance Raman process, which has been pioneered by Lee and Heller (1979) and which is now called the time-dependent theory. We will not describe in detail here the transform theory as developed by Page and Tonks (1981) which starts from the time-correlator formalism of Hyzhnyakov and Tehver (1967). While the Albrecht and the Lee-Heller theories express the Raman cross section directly in terms of molecular parameters, the transform theory relies on exploiting the relationship between the optical absorption cross section and the resonance Raman amplitude to obtain an expression for the theoretical Raman excitation profile in terms of the measured absorption spectrum. All three approaches to resonance Raman intensities have been described comprehensively in an excellent review by Myers and Mathies (1987). Only the sum-over-states and the time-dependent picture will be discussed in the following.

6.1.2.1.1 The sum-over-states picture*

The traditional approach to evaluating RR intensities involves a summation over all unperturbed eigenstates of the resonant electronic state. This is a direct consequence of the quantum-mechanical derivation of the polarizability tensor components employing second order perturbation theory as given by the Kramers-Heisenberg-Dirac (KHD) relation for the transition polarizability tensor:

$$(\alpha_{\rho\sigma})_{fi} = \sum_r \left\{ \frac{\langle f|\mu_\rho|r\rangle\langle r|\mu_\sigma|i\rangle}{\hbar\omega_{ri} - \hbar\omega_0 - i\Gamma_r} + \frac{\langle f|\mu_\sigma|r\rangle\langle r|\mu_\rho|i\rangle}{\hbar\omega_{rf} + \hbar\omega_0 - i\Gamma_r} \right\} \quad (6.1-1)$$

Here, $\langle f|\mu_\rho|r\rangle$ is the ρ th component of the transition dipole moment associated with the transition $f \leftarrow r$, μ_ρ being the dipole moment operator in the ρ direction. ω_0 and ω_{ri}

* Section 6.1.2.1.1 is contributed by W. Kiefer, Würzburg and M. Spiekermann, Lübeck

are the angular frequencies of the incident radiation and the angular frequency associated with a transition from the initial state i of the Raman transition to any state r of the unperturbed molecule, respectively. Γ_r is a damping factor related to the lifetime of the state r . $\hbar = h/2\pi$ with h being the Planck constant. Note, that the summation is over all states r of the unperturbed system, with the exclusion of i and f , the states between which the Raman transition takes place. The coordinate suffixes ρ and σ refer to the molecule-fixed cartesian vectors x , y and z .

The interpretation of Eq. (6.1-1) is that Raman scattering is a two-photon process involving virtual absorption from the initial state i to the entire manifold of eigenstates of the unperturbed molecule, followed by virtual emission to the final state f .

In the semiclassical approach, the molecule is described quantum mechanically, i. e. the polarizability tensor is calculated according to Eq. (6.1-1), whereas the electric field, the induction of the dipole moment via the polarizability of the molecule as well as the dipole scattering itself are described using classical electrodynamics. The scattering of the induced dipole moment is therefore treated as that arising from an oscillating Hertzian dipole. Such approaches have been worked out in detail in several texts by Placzek (1934), Behringer and Brandmüller (1956), Behringer (1958), and by Albrecht (1961). Thus, the total intensity scattered into the solid angle 4π at angular frequency $\omega_{sc} = \omega_0 \pm \omega_{fi}$ (plus for anti-Stokes, minus for Stokes, ω_{fi} = angular frequency for Raman transition from state i to state f) on the average by one freely orientable molecule is given by (Behringer and Brandmüller, 1956)

$$I_{fi} = CI_0\omega_{sc}^4 \sum_{\rho,\sigma} |(\alpha_{\rho\sigma})_{fi}|^2, \quad (6.1-2)$$

where I_0 is the incident intensity at angular frequency ω_0 and C is a constant which depends on the unit system used. Note, that when the Raman scattering process is treated completely by quantum mechanics (quantization also of the electric field) then ω_{sc}^4 is replaced by $\omega_0\omega_{sc}^3$.

When the angular frequency of the exciting light (ω_0) becomes close to the transition angular frequency for an absorption band of the molecule (ω_{ri}) the first term of Eq. (6.1-1) begins to dominate, and the resonant excited state dominates the sum over states of the Raman polarizability expression. Thus, for excitation into an absorption band ($\omega_0 \approx \omega_{ri}$) Eq.(6.1-1) may now be rewritten as

$$(\alpha_{\rho\sigma})_{fi} = \sum_r \left\{ \frac{\langle f|\mu_\rho|r\rangle \langle r|\mu_\sigma|i\rangle}{\hbar\omega_{ri} - \hbar\omega_0 - i\Gamma_r} \right\} \quad (6.1-3)$$

In the adiabatic Born-Oppenheimer approximation, the eigenstates of the unperturbed molecule, i. e. $|i\rangle$, $|f\rangle$, and $|r\rangle$, may be expressed as products of electronic, vibrational, and rotational states. In the following we restrict our discussion to the vibrational resonance Raman effect and hence, assuming that the molecule is initially in the vibrational state $|v_i\rangle$ and that the Raman transition starts and terminates in the ground electronic state $|g\rangle$, we may write

$$\begin{aligned}|i> &= |gv_i> = |g>|v_i> \\|f> &= |gv_f> = |g>|v_f> \\|r> &= |ev_e> = |e>|v_e>\end{aligned}\tag{6.1-4}$$

where $|e>$ is a resonant excited electronic state and $|v_f>$ and $|v_e>$ represent the vibrational final states of the Raman process and the vibrational states in the excited electronic state, respectively.

Using Eq. (6.1-4) the dipole transition moments in the numerator of Eq. (6.1-3) now become

$$\begin{aligned}< f|\mu_\rho|r> &= < v_f|M_\rho^e|v_e> \\< r|\mu_\sigma|i> &= < v_e|M_\sigma^e|v_i>\end{aligned}\tag{6.1-5}$$

The expressions on the right sides of Eq. (6.1-5) now involve only vibrational wavefunctions (v_i , v_f , v_e) whereas the electronic wave functions appear in M^e , which is the pure electronic transition moment connecting the ground with the excited electronic state e . M^e is a function of nuclear coordinate and can be expanded into a Taylor series about the equilibrium position (Herzberg-Teller expansion):

$$M^e = M_0^e + \left(\frac{\partial M^e}{\partial Q} \right)_0 Q + \dots\tag{6.1-6}$$

Similar expressions are valid for each of the $3N-6$ possible normal coordinates. If we introduce Eqs. (6.1-5) and (6.1-6) in Eq. (6.1-3) we obtain

$$(\alpha_{\rho\sigma})_{fi} = A + B + \dots\tag{6.1-7}$$

where

$$A = \sum_{e,v_e} \frac{M_{0\rho}^e M_{0\sigma}^e}{\hbar\omega_{ri} - \hbar\omega_0 - i\Gamma_{ev}} < v_f|v_e>< v_e|v_i>\tag{6.1-8}$$

$$\begin{aligned}B &= \sum_{e,v_e} \frac{M_{0\rho}^e \left(\frac{\partial M_\sigma^e}{\partial Q} \right)_0}{\hbar\omega_{ri} - \hbar\omega_0 - i\Gamma_{ev}} < v_f|v_e>< v_e|Q|v_i> \\&+ \sum_{e,v_e} \frac{\left(\frac{\partial M_\rho^e}{\partial Q} \right)_0 M_{0\sigma}^e}{\hbar\omega_{ri} - \hbar\omega_0 - i\Gamma_{ev}} < v_f|Q|v_e>< v_e|v_i>\end{aligned}\tag{6.1-9}$$

A and B are the well-known Albrecht's A - and B -terms, respectively. Note that in Eq. (6.1-7) higher order terms which contain products of derivatives of M^e have been neglected which would lead to additional terms (C , etc.).

The electronic transition moment, M^e , is much larger than its derivative in respect to the normal coordinate, $\left(\frac{\partial M^e}{\partial Q}\right)$. Thus the A term is the dominant contributor to the resonance Raman intensity as long as the product of the vibrational overlap integrals (Franck-Condon (FC-) factors), $\langle v_f | v_e \rangle \langle v_e | v_i \rangle$, do not vanish. However, if a vibration along Q is not totally symmetric, but is antisymmetric with respect to a symmetry element, then this product and hence the A -term is always equal to zero. Therefore only totally symmetric vibrations give rise to resonance enhancement via the Albrecht A -term. Another criterium determines whether or not there will be RR scattering via the A -term, since the Franck-Condon factors will differ from zero only if the excited state geometry is displaced along a symmetric mode coordinate relative to the ground state. This assumes identical orthonormal vibrational wavefunctions in the ground and excited states as is the case for two identical harmonic oscillators. This is illustrated in Fig. 6.1-1 where the potential function of a harmonic oscillator represents both states. If the excited electronic state is not displaced in respect to the ground electronic state, i. e. $\Delta = 0$, then the product of the two FC-factors vanishes. As examples, two cases are illustrated for a RR excitation of the fundamental transition between vibrational states $v_f = 1 \leftarrow v_i = 0$.

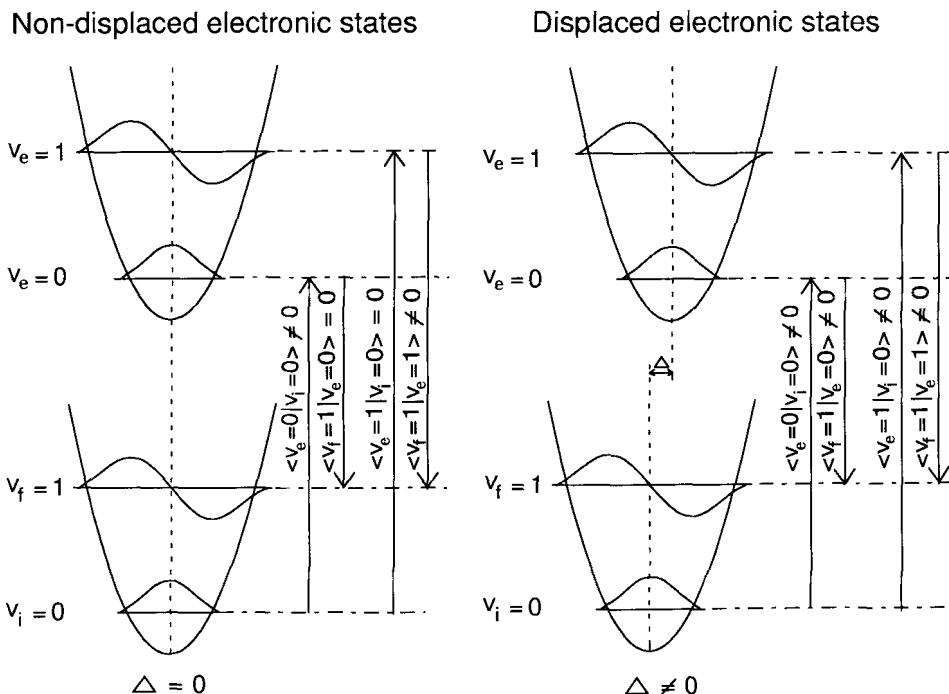


Figure 6.1-1 Resonance Raman scattering via the A -term as given in Eq. 6.1-8. For a non-displaced electronic state (harmonic oscillator model) there is always one vanishing Franck-Condon factor which brings the A -term contribution to zero. A displacement (Δ) of the excited electronic state in respect to the ground state allows nonvanishing vibrational overlaps for both, the upward and downward transitions (Adapted from Asher, 1988).

If the vibrational state $v_e = 0$ is the resonant state in the electronic excited state, then the *FC* factor $\langle v_f = 1 | v_e = 0 \rangle$ vanishes, whereas for $v_e = 1$ being the intermediate state the *FC* factor $\langle v_e = 1 | v_i = 0 \rangle$ reduces the transition polarizability (Eq. 6.1-8, A-term) and hence the RR intensity to zero. The same holds for all vibrational levels $v_e \geq 2$. However, for $\Delta \neq 0$ all the relevant *FC* factors for upward and downward transitions are unequal to zero as indicated schematically in the right panel of Fig. 6.1-1. It has been shown by Myers and Mathies (1987) that for small displacements of the excited state potential surface along the Raman active normal coordinate (small Δ), the resonance Raman intensity is approximately proportional to Δ^2 . For very small displacements only the fundamental vibrational transition shows significant enhancement while large displacements result in lengthy overtone progressions. Thus, excited state geometry changes can be directly deduced from the pattern of internal coordinates active in the enhanced vibrations (Myers and Mathies, 1987).

The approximation adapted for the *A*-term is equivalent to assuming that the value of the electronic transition moment remains equal to that at $Q = 0$, and is independent of which vibrational transition is accompanying the electronic transition. This is called the Condon approximation.

Enhancement via Albrecht's *B*-term derives from the non-Condon dependence of the electronic transition moment upon the vibrational coordinate. Unlike the *A*-term, the *B*-term arises from the vibronic mixing of two excited states and it is non-zero for scattering due to both totally symmetric and non-totally symmetric fundamentals, provided that they are responsible for vibronic coupling of the states. The latter only takes place for a vibrational fundamental whose irreducible representation is contained in the direct product of the irreducible representations of the two states. Thus, *B*-term activity for a totally symmetric mode requires that the latter must vibronically couple two states of the same symmetry. As a consequence of the non-crossing rule this holds only for few excited states which are lying very close together.

The relative contributions of *A*-and *B*-term scattering under resonance conditions is a subject of considerable interest and different conclusions have been found for different systems. For example the *A*-term predominates for π -electron systems, e. g. polyenes, especially for their main intense absorption band (Warshel 1977). Vibrational wavefunctions of non-totally symmetric modes are more nearly orthogonal. Thus, vibrations may only derive their intensities from the *B*-term. *A*-term and *B*-term enhancement can be distinguished experimentally by their excitation profiles. For *A*-term scattering a peak in the excitation profile is expected at the origin of the resonant electronic transition and subsidiary peaks at successive excited state vibrational levels. The amplitudes of the peaks depend on the successive Frank-Condon factors. For *B*-term scattering excitation profile maxima are expected at the $0 \leftarrow 0$ and $1 \leftarrow 0$ positions for each of the mixing modes, since the products $\langle v_f | v_e \rangle \langle v_e | Q | v_i \rangle$ and $\langle v_f | Q | v_e \rangle \langle v_e | v_i \rangle$ are largest for these levels.

In general, *B*-type enhancement is significantly smaller than *A*-type. For excitation far from resonance the *A*-term approaches zero and only the *B*-term contributes to the scattered intensity.

Finally we mention, that the *B*-term contribution to the transition polarizability may give rise to an asymmetric scattering tensor, i. e. $\alpha_{\rho\sigma} \neq \alpha_{\sigma\rho}$, leading to the phenomenon

of "anomalous" polarization. For further details on this subject we refer to the review by Mortensen and Hassing (1980).

6.1.2.1.2 The time-dependent picture

The theory discussed until now is based on the Kramers-Heisenberg-Dirac dispersion relation for the transition polarizability tensor as given in Eq. (6.1-1). The expression shown in this equation describes a steady state scattering process and contains no explicit reference to time. Therefore, the resonance Raman theory which is based on the KHD dispersion relation is sometimes also termed as "time-independent theory" (Ganz et al., 1990).

In order to facilitate deduction of excited-state properties (Johnson and Peticolas, 1976; Warshel, 1977) considerable activity ensued in the analysis of resonance Raman spectra and excitation profiles. However, progress was limited by the conceptual and computational clumsiness of Eq. (6.1-1). Only for small molecules it has been possible to calculate resonance Raman spectra numerically by means of Eq. (6.1-1) (see for example Strempl and Kiefer, 1991 a-c and references therein). The main problem arises through the summation over many states which for large polyatomic molecules is nearly impossible to perform.

The time-dependent formulation of Raman (and particularly resonance Raman) scattering has been introduced by Hizhnnyakov and Tehver (1967), Lee and Heller (1979), Heller et al. (1982), Tannor and Heller (1982), and Myers et al. (1982). Its derivation is strikingly simple. Through a straightforward mathematical transformation (see for instance Myers et al., 1982), the KHD relation can be transformed into an integral over time which we will show here for the vibronic part of the polarizability in the Condon approximation. First we rewrite the A-term as given in Eq. (6.1-8) to be

$$A = \sum_e M_{op}^e M_{0\sigma}^e \sum_{v_e} \frac{\langle v_f | v_e \rangle \langle v_e | v_i \rangle}{\hbar\omega_{ri} - \hbar\omega_0 - i\Gamma_{ev_e}} \quad (6.1-10)$$

and consider only the vibronic expression for the polarizability tensor (summation over v_e). Using $\hbar\omega_{ri} = E_v - E_i$; $\hbar\omega_0 = E_\ell$, $\Gamma_{ev_e} = \Gamma$, and $v_f = f$, $v_e = v$, $v_i = i$, we arrive at the following expression which is identical to Eq. (12) of Myers et al. (1982):

$$\alpha_{fi} = \sum_v \frac{\langle f | v \rangle \langle v | i \rangle}{E_v - E_i - E_\ell - i\Gamma} \quad (6.1-11)$$

The denominator $s = E_v - E_i - E_\ell - i\Gamma$ in the expression of Eq. (6.1-11) can now be transformed into a time-dependent expression using the mathematical relation

$$\frac{1}{s} = \frac{i}{\hbar} \int_0^\infty e^{-\frac{i}{\hbar} st} dt \quad (6.1-12)$$

α_{fi} then results in

$$\alpha_{fi} = \frac{i}{\hbar} \int_0^\infty \sum_v \langle f|v \rangle \langle v|i \rangle \exp \{ -i(E_v - E_i - E_\ell - iI)t/\hbar \} dt \quad (6.1-13)$$

Then, since

$$\langle v|e^{-iE_v t/\hbar} = \langle v|e^{-iHt/\hbar} \quad (6.1-14)$$

where H is the excited-state vibrational Hamiltonian, Eq. (6.1-13) can be written as

$$\alpha_{fi} = \frac{i}{\hbar} \int_0^\infty \sum_v \langle f|v \rangle \langle v|e^{-iHt/\hbar}|i \rangle \exp \{ i(E_i + E_\ell + iI)t/\hbar \} dt \quad (6.1-15)$$

If the propagator $e^{-iHt/\hbar}$ is considered to operate on the right hand side, then

$$e^{-iHt/\hbar}|i \rangle = |i(t) \rangle \quad (6.1-16)$$

and one obtains the final result for α_{fi} by using closure to remove the sum over states v :

$$\alpha_{fi} = \frac{i}{\hbar} \int_0^\infty \langle f|i(t) \rangle e^{-I_t/\hbar} \exp \{ i(E_i + E_\ell)t/\hbar \} dt \quad (6.1-17)$$

The resonance Raman intensity is then obtained by inserting α_{fi} of Eq. (6.1-17) into Eq. (6.1-2).

The quantity $|\langle f|i(t) \rangle| e^{-I_t/\hbar}$ has been termed Raman overlap (Myers and Mathies, 1987). It is the product of the modulus of a time-dependent Franck-Condon factor between the final state and the initial wavefunction propagated on the electronic surface, i. e. $|\langle f|i(t) \rangle|$ and a damping function $e^{-I_t/\hbar}$ which decreases exponentially with time.

The expression for α_{fi} (Eq. 6.1-17) and I_{fi} (Eq. 6.1-2) have the intuitively appealing interpretation of resonance Raman scattering schematically shown in Fig. 6.1-2. The latter has been adapted from Fig. 4 of the Myers and Mathies review (1987). The resonance Raman scattering process starts from state $|i\rangle$, which is a vibrational eigenstate of the ground electronic surface, represented by a harmonic potential function. At time zero, the interaction of the electronic transition moment with the incident radiation causes a vertical transition to the excited electronic surface. The vibrational state $|i\rangle$, now finding itself under the influence of a Hamiltonian (H) begins to evolve with time. If the ground and excited surfaces are significantly displaced, the wavepacket $|i(t)\rangle$ quickly moves away from its initial position and reaches the right side of the excited state potential function (dashed line in Fig. 6.1-2, panel A). There it is reflected and moves back to

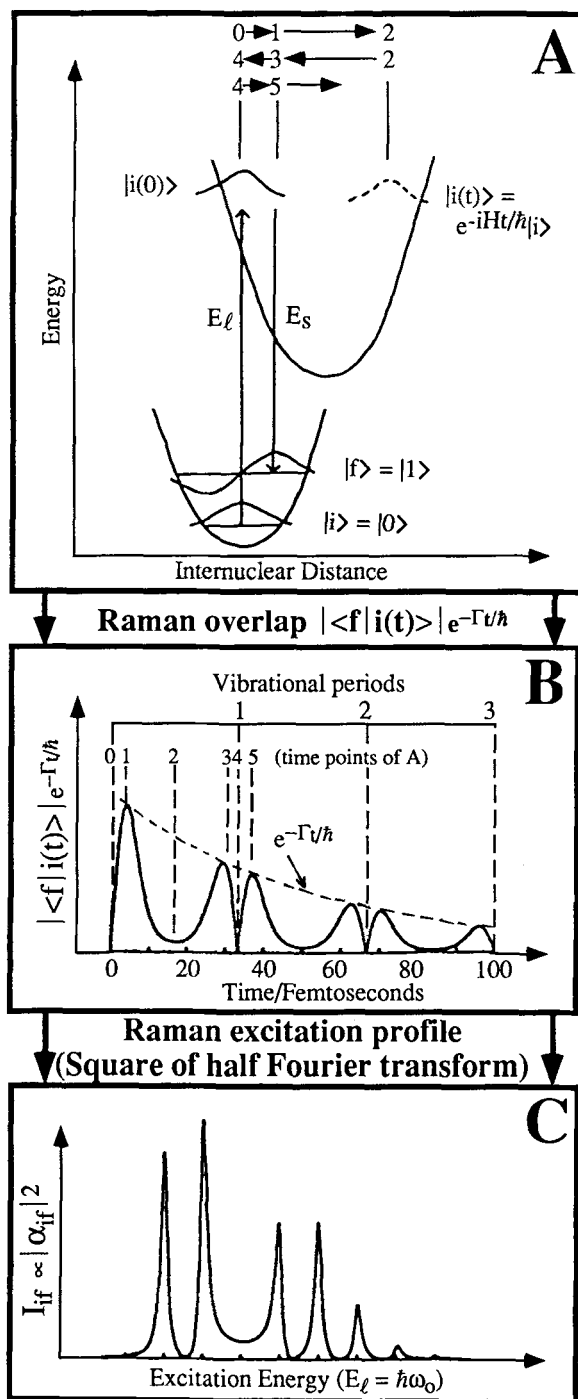


Figure 6.1-2 The time-dependent picture of resonance Raman scattering; panel A: interaction of the incident photon with the electronic transition moment sends the initial vibrational state $|i\rangle$ to the excited electronic surface, where it is propagated by the excited-state vibrational Hamiltonian; panel B: the Raman overlap $\langle f | i(t) \rangle e^{-\Gamma t / \hbar}$ as a function of time; panel C: the excitation profile as a function of the incident photon energy E_ℓ is given by the square of the half Fourier transform of the overlap between $|i(t)\rangle$ and the final vibrational level $|f\rangle$ (Adapted from Myers and Mathies, 1987).

positions of shorter internuclear distances. In the further process it oscillates between the inner and outer classical turning points until the wavefunction is damped out by the function $e^{-I\tau/\hbar}$. During propagation, the $|i(t)\rangle$ wave packet crosses regions with high overlap with the wavefunction $|f\rangle$ in the electronic ground state. For the case illustrated in Fig. 6.1-2 a maximum overlap is reached soon (a few fs) after initial propagation (point 1 in panel A). Hence the Raman overlap function $|\langle f|i(t)\rangle|e^{I\tau/\hbar}$ has a maximum at this timepoint (see panel B, where the Raman overlap is plotted as a function of time). It then decreases as $|i(t)\rangle$ moves far away from $|f\rangle$ (point 2), increases to another maximum (point 3) on the return trip with less amplitude because of small damping, and goes to zero at the end of one full cycle (point 4), where $|i(t)\rangle$ is orthogonal to $|f\rangle$. Reflection at the left side of the excited state potential function causes further peaks in the Raman overlaps. This continues until $|i(t)\rangle$ is damped out. Only three vibrational periods are depicted in panel B of Fig. 6.1-2.

Since the Raman intensity I_{fi} (Eq. 6.1-2) is proportional to the modulus square of α_{fi} and the latter is obtained by integration over the Raman overlap function (Eq. 6.1-17) the Raman excitation profile ($I_{fi} = I_{fi}(\omega_0)$) can be directly calculated by a half Fourier transformation of the Raman overlap. This has been done in panel C of Fig. 6.1-2, where for the case discussed in panels B and C the Raman intensity is plotted as a function of excitation energy ($E_\ell = \hbar\omega_0$).

After the discovery of the so-called continuum resonance Raman scattering in halogen molecules by Holzer et al. (1970) much interest has arisen for this type of resonance Raman scattering both experimentally and theoretically. Here, the intermediate, i. e. resonant Raman state is that of a repulsive excited electronic state or of the repulsive part of a bound excited electronic state. Figure 6.1-3 shows the situation of continuum resonance Raman scattering for the Br₂ molecule when excited with the blue $\lambda_o = 457.9$ nm argon ion laser line. Since the intermediate state is above the dissociation limit of the bound B(³ Π_{o+u}) state, the continuum of the repulsive part of this state as well as the continuum of the pure repulsive ¹ Π_{1u} state both contribute to the continuum resonance Raman scattering intensity. Furthermore one may assume the limit of infinitely narrow states and it is therefore not necessary to include the damping term in the relevant expression for α_{fi} . However, it is necessary to accommodate the pole which occurs for those continuum states at exact resonance. Eq. (6.1-11) may be rewritten to accommodate the singularity as (Rousseau and Williams, 1976):

$$\alpha_{fi} = \frac{1}{\hbar} \left\{ \mathcal{P} \int_0^\infty \frac{\langle f|v\rangle \langle v|i\rangle}{\omega_{ri} - \omega_o} \rho(\omega_{ri}) d\omega_{ri} - i\pi \langle f|v\rangle \langle v|i\rangle \rho(\omega_{ri}) \Big|_{\omega_{ri}=\omega_0} \right\} \quad (6.1-18)$$

where $\rho(\omega_{ri})$ is the density of continuum states and and \mathcal{P} is the principal part of the integral.

In the time-dependent picture, since $\Gamma = 0$, Eq. (6.1-17) then reduces to

$$\alpha_{fi} = \frac{i}{\hbar_o} \int_0^\infty \langle f|i(t)\rangle \exp\{i(E_i + E_\ell)t/\hbar\} dt \quad (6.1-19)$$

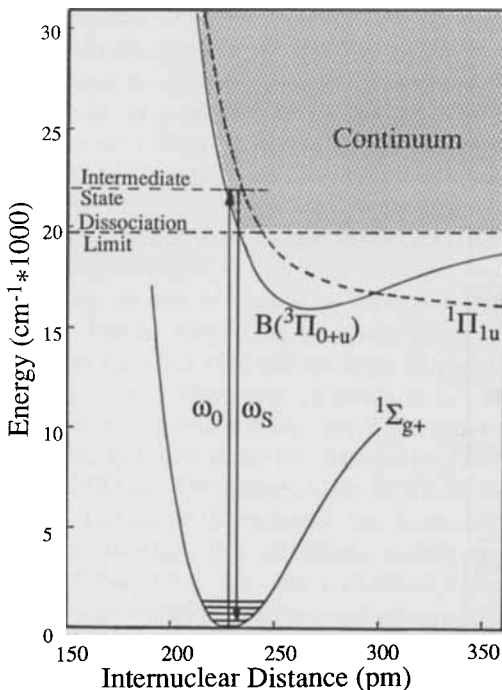


Figure 6.1-3 Schematic representation of continuum resonance Raman scattering for the Br_2 molecule. The incident laser frequency (ω_0) is in resonance with the continuous states of the repulsive $^1\Pi_{1u}$ excited state and the repulsive part of the bound $B(^3\Pi_{0+u})$ state, which is above the dissociation limit at around $20\ 000\ \text{cm}^{-1}$ (Baierl and Kiefer, 1981).

Both expressions for α_{fi} (Eqs. 6.1-18 and 6.1-19) have been used to numerically calculate the resonance Raman intensities of halogen and interhalogen molecules and their dependence on the incident laser energy $E_\ell = \hbar\omega_0$ (Rousseau and Williams, 1976; Baierl and Kiefer, 1980, 1981; Ganz et al., 1990, 1992; Ganz and Kiefer, 1993a, 1994).

In the time dependent calculations the wavepacket propagation ($|i(t)\rangle$) is numerically evaluated by fast Fourier transform propagation of vibrational states (Bisseling et al., 1985; Kosloff, 1985). The time-dependent description also allows to nicely discuss the continuum resonance Raman scattering process in an instructive wavepacket picture. This is illustrated in Fig. 6.1-4 for a diatomic molecule, (Ganz et al., 1990). Here, a vibrational $|i\rangle = |1\rangle$ to $|f\rangle = |2\rangle$ (first hot band) transition in $^{79}\text{Br}_2$ at $\lambda_0 = 457.9\ \text{nm}$ laser excitation is considered. The continuum resonance Raman scattering process is described by the initial ($t = 0$) transition from $|i\rangle$ to the electronic excited state (panel A). Then the wavepacket $|i(t)\rangle$ propagates on mainly the repulsive $^1\Pi_{1u}$ electronic state until delay times t (B: $t = 20\ \text{fs}$, C: $t = 40\ \text{fs}$). Only during a short propagation time the wavepacket $|i(t)\rangle$ overlaps with the final state $|f\rangle$. Hence only during this time the $|i(t)\rangle$ function has non-vanishing overlap with the final vibrational $|f\rangle = |2\rangle$ state in the electronic ground state and therefore gives rise to continuum resonance Raman

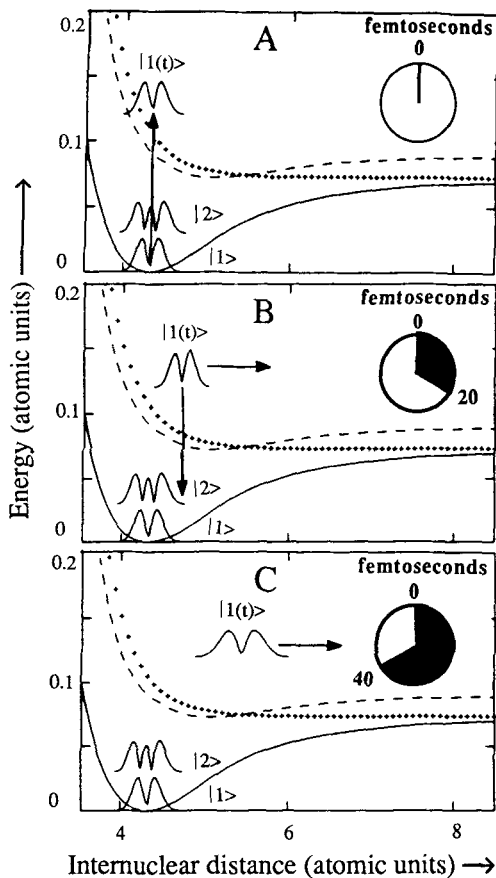


Figure 6.1-4 Illustration of Eq. 6.1-19, the time-dependent approach to continuum resonance Raman scattering. Shown is a $|2\rangle \leftarrow |1\rangle$ vibrational Raman transition in $^{79}\text{Br}_2$ for $\lambda_0 = 457.9$ nm excitation. As examples, (A), (B) and (C) show the potential curves of the relevant ground ($X = 1\Sigma_g^+$, continuous line) and excited ($B = 3\Pi_{0+u}$, dashed line, and $\Pi = 3\Pi_{1u}$, dotted line) electronic states, together with the absolute values of the coordinate representations of the initial state $|i\rangle = |1\rangle$, final state $|f\rangle = |2\rangle$, and the time-dependent state $|i(t)\rangle$ at times $t = 0, 20$ and 40 fs, respectively. The excitation and de-excitation processes and the related unimolecular dissociations are indicated schematically by vertical and horizontal arrows. For clarity of presentation, the energy gap between state $|i\rangle$ and $|f\rangle$ is expanded (Ganz et al., 1990).

scattering. From the sequence of snap-shots in Fig. 6.1-4, it is obvious that the most efficient resonance Raman transitions occur within ultrashort times, corresponding to an average delay time of appr. 14 fs (Ganz et al., 1990) for this particular vibrational transition ($|f\rangle = |2\rangle \leftarrow |i\rangle = |1\rangle$). Marginal interfering transitions via electronic state $B(3\Pi_{0+u})$ (Baierl and Kiefer, 1980, 1981) are not shown in Fig. 6.1-4 for clarity of presentation.

In contrast to bound excited electronic states, where the wavepacket $|i(t)\rangle$ oscillates (with damping) within the classical turning points of the potential surface (see Fig. 6.1-2) in continuum resonance Raman scattering the molecule either dissociates or it returns to the electronic ground state via Raman scattering. Therefore only the accelerated propagation away from the repulsive functions must be considered for the overlap function $\langle f|i(t)\rangle$. Because nonvanishing vibrational overlaps occur within ultrashort times of the order of $t \approx 10 - 20$ fs, damping plays no role at all, i. e. $e^{\Gamma t/\hbar} \approx 1$. This is why the damping function is neglected in Eq. 6.1-19 for the description of continuum resonance Raman scattering.

It may be also of interest to show how the *FC*-overlap integral $\langle f|i(t)\rangle$ for a resonance Raman vibrational transition ($f \leftarrow i$) in a diatomic molecule depends on time in a real case. As example we show in panel A of Fig. 6.1-5 the absolute value of the overlap for the vibrational transition $|f\rangle = |6\rangle \leftarrow |i\rangle = |0\rangle$ for the iodine molecule ($|\langle 6|0(t)\rangle|$) which gives rise to the fifth overtone in the resonance Raman spectrum of I_2 when excited above the dissociation limit of the $B(^3\pi_{0+})$ electronic state (Ganz and Kiefer, 1993a). The highest value of the time-dependent *FC*-overlap integral is reached around 16 fs after the molecule has been excited into the dissociation continuum of the B state. Although this vibrational transition corresponds to an overtone, the function $f(t) = |\langle 6|0(t)\rangle|$ is nearly identical to the wavefunction of the initial state ($|i\rangle = |0\rangle$) from which the resonance Raman scattering process takes place. This "reflection principle" has been first shown by Kolba et al. (1992). Figure 6.1-5 also shows how simply the excitation profile of a Raman transition can be obtained (see also Fig. 6.1-2):

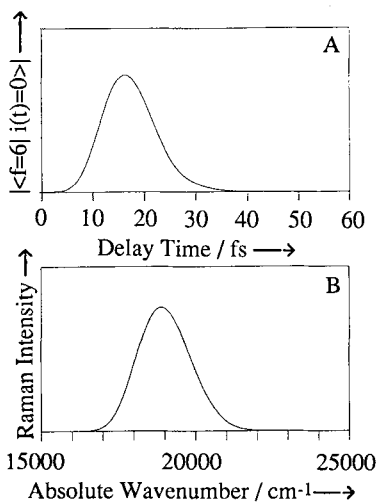
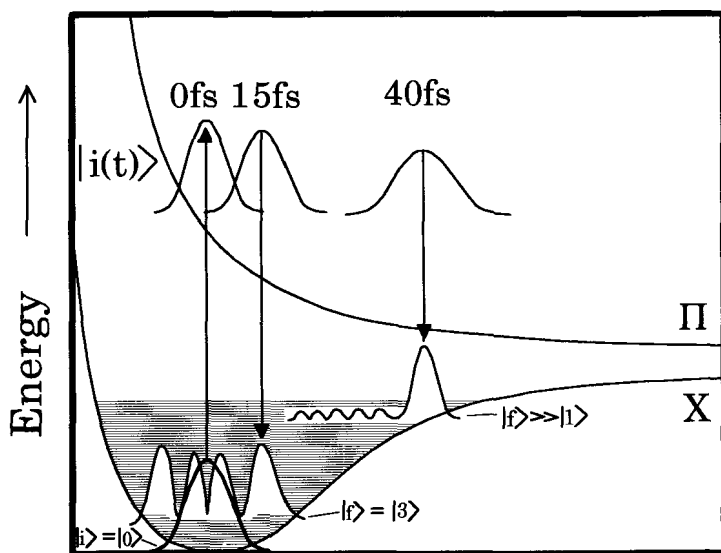


Figure 6.1-5 Stokes transition for continuum resonance Raman scattering in $^{127}I_2$ from the initial vibrational state $|i\rangle = |0\rangle$ to the final state $|f\rangle = |6\rangle$ via electronic state $B(^3\Pi_{0+})$. (A) Absolute value of the time overlap $|\langle 6|0(t)\rangle|$ as a function of time, (B) excitation profile of this transition [square of the half Fourier transform of $\langle f|i(t)\rangle$ as a function of energy] (Ganz and Kiefer, 1993 a).

one just has to half Fourier transform the time-dependent FC factor $\langle f|i(t) \rangle$ and plot this quantity as a function of energy. This has been done for the $6 \leftarrow 0$ vibrational transition for the iodine molecule in panel B of Fig. 6.1-5 (Ganz and Kiefer, 1993a).

The time-dependent picture also allows to explain why so many overtones appear in continuum resonance Raman scattering in diatomic molecules. During propagation of $|i(t)\rangle$ the wavepacket moves across regions also having large overlaps with the higher vibrational levels $|f\rangle$ in the electronic ground state. As is well known, the wavefunctions at these levels have large values around the classical turning points and in particular at the outer classical turning point of an anharmonic oscillator. Fig. 6.1-6 shows schematically the generation of the overtone pattern while the wavepacket $|i(t)\rangle$ quickly moves away from its initial position after the interaction of the electronic transition moment with the incident radiation has caused the vertical transition from the ground to the excited electronic surface.



Internuclear Distance →

Figure 6.1-6 Generation of the overtone pattern in continuum resonance Raman scattering of a diatomic molecule. The propagating wavepacket brought up from the initial vibrational level in the electronic ground state into the excited electronic state evolves rapidly with time. While passing over regions with high vibrational overlaps the molecule can deexcite to the various vibrational levels of the electronic ground state. Such overtone transitions are schematically shown for $\Delta v = 3$ (second overtone) and an overtone with high vibrational quantum number change ($\Delta v \gg 1$). Note that the energy gap between state $|3\rangle$ and state $|0\rangle$ is expanded for clarity of presentation.

Based on the two approaches to continuum resonance Raman theory, many spectra of diatomic molecules could be successfully simulated (Hartke, 1989, 1991; Ganz and Kiefer, 1993a, 1994). Besides the good simulations of continuum resonance Raman band

shapes, scattering delay times (Hartke et al., 1992), the already mentioned reflection principle (Kolba et al., 1992) as well as a symmetry principle (Ganz et al., 1992) could be derived for this Raman scattering where resonance takes place with the continuous energy levels of dissociative excited state potential functions.

Finally, we like to mention that equivalent to the conventional energy frame KHD formulation, the time-dependent theory of Raman scattering is free from any approximations except the usual second order perturbation method used to derive the KHD expression. When applied to resonance and near resonance Raman scattering, the time-dependent formulation has shown advantages over the static KHD formulation. Apparently, the time-dependent formulation lends itself to an interpretation where localized wave packets follow classical-like paths. As an example of the numerical calculation of continuum resonance Raman spectra we show in Fig. 6.1-7 the simulation of the $\Delta_v = 4$ transitions (third overtone) of I_2 excited with $\lambda_0 = 488.0$ nm. Both, the KHD (Eqs. 6.1-2 and 6.1-18) as well as the time-dependent approach (Eqs. 6.1-2 and 6.1-19) very nicely simulate the experimental spectrum which consists mainly of Q - and S -branch transitions (Ganz and Kiefer, 1993b).

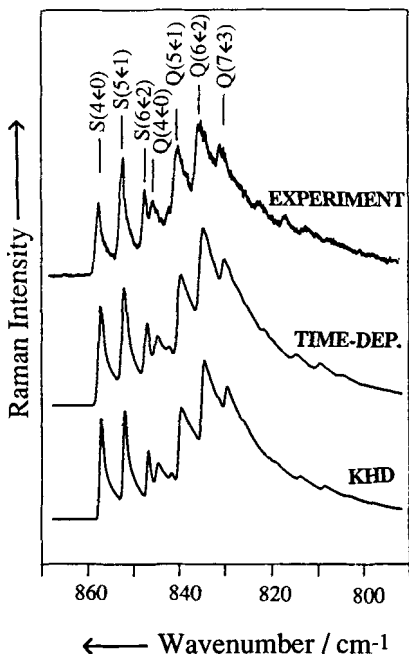


Figure 6.1-7 Experimentally observed continuum resonance Raman spectrum for the $\Delta_v = 4$ transitions in $^{127}I_2$ together with a simulation of the spectrum applying the time-dependent as well as the Kramers-Heisenberg-Dirac (KHD) approaches as indicated. Excitation wavelength $\lambda_0 = 488.0$ nm (Ganz and Kiefer, 1993 b).

6.1.2.2 Applications of resonance Raman spectroscopy*

In this section we review some selected applications of resonance Raman scattering. For further examples we refer to the many reviews which appeared on the subject (see chapter 6.1.2)

6.1.2.2.1 Anharmonicity constants from overtone progressions

One of the features in ordinary Raman spectra is the more or less absence of overtones and combination bands. In resonance Raman spectra long, well defined progressions of overtones occur corresponding to totally symmetric vibrations or combinations with them. For example Kiefer and Bernstein (1972) observed about 15 overtones in the gas phase spectrum of I_2 and about the same number of overtones of the iodine molecule dissolved in various organic liquids (Kiefer and Bernstein, 1973). The same authors reported 7 overtones in the permanganate and 9 overtones in the chromate ions (Kiefer and Bernstein, 1972b). Also Clark and Mitchell (1973) observed 9 overtones in the resonance Raman spectrum of TiI_4 in solution. Using the overtone progression it is possible to calculate harmonic frequencies and anharmonicity constants of the appropriate vibrations. For example, for a diatomic molecule, these parameters may be obtained from the relationship

$$\nu(n)/n = \omega_e - \omega_e x_e(n + 1) + \dots \quad (6.1-20)$$

where $\nu(n)$ is the observed wavenumber of any overtone, ω_e is the harmonic frequency of the vibration, $\omega_e x_e$ is the first anharmonicity constant and n is the vibrational quantum number. A plot of $\nu(n)/n$ against n yields approximately a straight line with a slope equal to $\omega_e x_e$ and an intercept $\omega_e - \omega_e x_e$.

From the overtone progressions of molecules in solution it may be possible to obtain the effect of intermolecular interaction on the ground state properties of the molecule under investigation, since a frequency change with the used solvent can be observed (Kiefer and Bernstein, 1973b).

6.1.2.2.2 Accurate determination of excited state repulsive potential functions of diatomic molecules in the gaseous phase

As discussed above, continuum resonance occurs when the excitation laser energy is higher than the dissociation limit of an excited, bound electronic state or directly with purely repulsive states. Continuum resonance Raman spectra of gaseous molecules are very sensitive to the position and shape of the potential functions involved in this type of light scattering as well as to the electronic transition moments between ground and excited states. Since it is possible to calculate the relevant spectra using both the KHD

* Section 6.1.2.2 is contributed by W. Kiefer, Würzburg and M. Spiekermann, Lübeck

approach as well as the time-dependent theory (see Sec. 6.1.2.1), the simulation of continuum resonance Raman spectra of fundamentals and overtones allows a precise determination of the shape and position of excited state potential functions. This has been shown in extensive studies in halogen and interhalogen molecules (see for example Ganz and Kiefer, 1994 and references therein), where the observed spectra of fundamental and overtone transitions could be simulated very accurately with both kinds of theoretical approaches. In order to elucidate the very high sensitivity of the continuum resonance Raman intensity of rovibrational transitions in diatomic molecules we show how the shape of the spectra changes when the potential curves are altered slightly. This is demonstrated in Figures 6.1-8 and 6.1-9 for the case of continuum resonance Raman excitation ($\lambda_0 = 363.8$ nm) of the isotopically pure $^{35}\text{Cl}_2$ molecule. In Figure 6.1-8 three curves for the $^1\Pi_{1u}$ potential of the chlorine molecule are displayed, which is responsible for the resonance scattering. Potential 1 turns out to be the exact one, i.e. which yields the right spectral profile whereas potentials 2 and 3 are shifted by only about 1% (= 2 pm) with respect to potential 1 to smaller and larger internuclear separation, respectively. In Fig. 6.1-9 the experimental (spectrum A) and three calculated spectra (spectra B-D) of the fourth overtone ($\Delta v = 5$) excited with $\lambda_0 = 363.8$ nm using the different $^1\Pi_{1u}$ potential curves are shown. Spectrum B is calculated using potential 1 as given in Fig. 6.1-8, spectra C and D with potentials 2 and 3, respectively. The very different band shapes of calculated spectra C and D with respect to the observed spectrum A is obvious. In spectrum C the $Q(6 \leftarrow 1)$ band (hot band) is too large and in spectrum D it is too small compared to the $Q(5 \leftarrow 0)$ band. Since there is a large

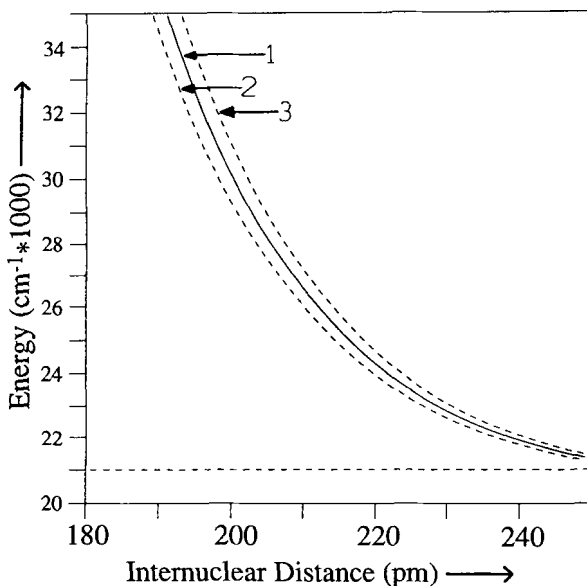


Figure 6.1-8 Different potential curves for the $^1\Pi_{1u}$ state of $^{35}\text{Cl}_2$. Potential 1 is the correct one, potentials 2 and 3 are the same as 1 but shifted by 2 pm to smaller and larger internuclear separation, respectively (Stremmel and Kiefer, 1991).

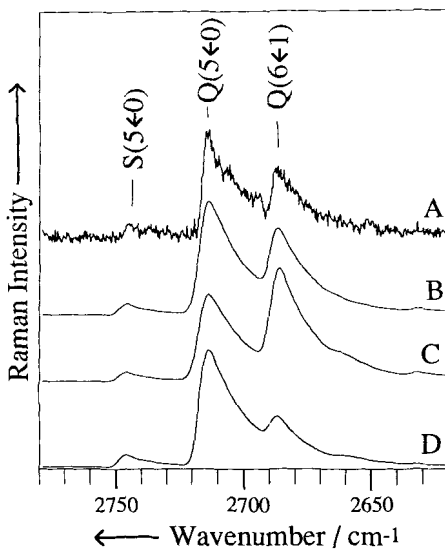


Figure 6.1-9 Continuum resonance Raman spectra of the fourth overtone ($\Delta v = 5$) of $^{35}\text{Cl}_2$ excited with $\lambda_0 = 363.8$ nm. A: experiment; B, C, D: calculated (KHD-approach) with potentials 1, 2, and 3 as shown in Figure 6.1-8, respectively (Stremmel and Kiefer, 1992).

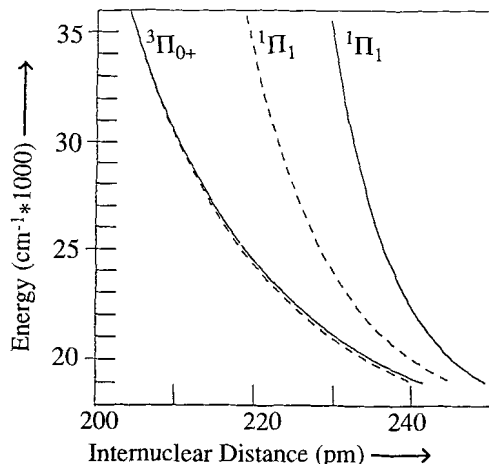


Figure 6.1-10 Repulsive excited state potential curves $^1\Pi_1$ and $^3\Pi_{0+}$ of $^{127}\text{I}^{35}\text{Cl}$ as indicated in the figure. Solid line: derived from continuum resonance Raman studies (Ganz and Kiefer, 1994); dotted lines: data reported from one-photon absorption studies (Child and Bernstein, 1973).

amount of information from fundamental, hot band and overtone transitions derived from the comparison of experimentally observed and theoretically simulated spectra, excited with various laser frequencies, it turns out that this kind of study is able to

derive potential functions from excited repulsive states, which are more accurate than those derived from continuous absorption spectra, where only one experimental spectrum serves for the derivation of spectral parameters. This is particularly the case when more than one excited state contribute to the continuous absorption spectrum. In continuum resonance Raman spectroscopy interference effects between the states drastically change the intensity pattern in the observed spectra. These changes again can serve for the precise determination of repulsive state functions. In Fig. 6.1-10 we show for the $^{127}\text{I}^{35}\text{Cl}$ molecule the optimized potential functions for the $^1\Pi_1$ and $^1\Pi_{0+}$ states as derived from simulations of continuum resonance Raman spectra (solid lines) (Ganz et al., 1993; Ganz and Kiefer, 1994) and compare them to those derived from one-photon absorption spectra (dashed lines) (Child and Bernstein, 1973).

6.1.2.2.3 Determination of excited state structure of polyatomic molecules

Similarly to the procedure developed for diatomic molecules which has been discussed in Sec. 6.1.2.2, experimental resonance Raman intensity data from polyatomic molecules can be analyzed in order to derive structural information on excited electronic states. Two fundamentally different approaches are described in the literature (for a detailed

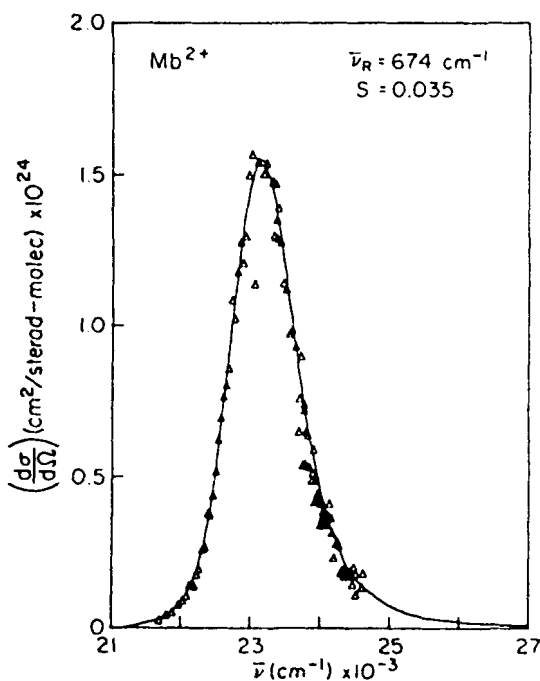


Figure 6.1-11 Observed (Δ points) and calculated (solid line) excitation profile of the 674 cm^{-1} porphyrin ring mode of deoxymyoglobin. The data are plotted on an absolute Raman cross section scale by reference to an internal sulfate standard at 980 cm^{-1} (Bangcharoenpaurpong et al., 1984).

review see Myers and Mathies, 1987). The direct modeling approach involves searching for the complete set of excited-state parameters that generate the best fit to the experimental absorption and resonance Raman data. The calculations may be carried out by using either the sum-over-states or the time-dependent method, whichever is more efficient for the specific problem. In the alternative transform method (for a review see Page, 1991), the experimental absorption spectrum is used to directly generate a theoretical excitation profile for each observed mode, and the excited-state displacement in each mode is chosen to give the best fit between the calculated and experimental intensities. Both approaches have been comprehensively described by Myers and Mathies, 1987.

As an example of the application of the transform method we show in Fig. 6.1-11 the observed and calculated excitation profile of the 674 cm^{-1} porphyrin ring mode of deoxymyoglobin (Bangcharoenpaupong et al., 1984). Notice that the data are placed on an absolute cross-section scale by comparison to the sulfate internal standard. The solid line represents a transform fit to the data with use of the Soret band into which excitation has been performed. The excellent agreement between the calculated and experimental bandshapes allows the displacement of the excited electronic state in respect to the ground state to be determined very precisely through a computationally straight forward procedure. It should be noted that only one parameter has been utilized in this calculation to achieve an essentially perfect fit to the experimental data. For further details we refer to Bangcharoenpaupong et al. (1984).

6.1.2.2.4 Resonance Raman spectroscopy of biochemical and biological systems

Water, the ubiquitous biological medium, is an excellent absorber of infrared radiation, leaving only restricted windows for IR spectroscopy. However, since water is a poor Raman scatterer, Raman spectroscopy does not suffer as much from this limitation. Therefore resonance Raman spectroscopy is an effective probe of the local environment of biological chromophores *in situ* and in aqueous solutions at biologically interesting concentrations. Since vibrational frequencies are sensitive to geometric and bonding arrangement of localized groups of atoms in a molecule the method is applicable in the central challenge of modern biochemistry to elucidate biological function in terms of molecular structure. Key aspects of many biochemical interactions occur when a relatively small molecule is in contact with a highly specialized local environment. Elucidation in chemical terms of these ligand-active-site interactions represents some of the crucial problems of molecular biochemistry. Resonance Raman labels, the technique of which has been pioneered by Carey et al. (1972), provide a precise indicator or reporter technique to study the nature of events produced by biologically active sites on the bond ligand. The basis of the method, which is reviewed by Carey and Schneider (1978), is the use of resonance Raman labels which, while yielding vibrational and electronic spectral data, are at the same time biologically active molecules.

There has been tremendous work performed in molecular spectroscopy of biochemical and biological spectroscopy applying resonance Raman scattering. Several aspects have been discussed in detail by experts in the field. Spiro and Loehr (1975) have been one of the first researchers to summarize achievements made in the observation of res-

onance Raman spectra of biological materials such as metal containing enzymes and proteins, heme proteins, and other delocalized π -systems such as chlorophyll, vitamins, carotenoids, visual pigments, nucleotide bases, and aromatic protein side chains. This work could be performed with excitation by means of argon and krypton ion lasers available at that time because these molecules have their strong absorption bands where these lasers emit. The absorption band of nucleic acids are beyond these spectral regions and only after the development of UV laser sources (around 260 nm) resonance Raman studies on nucleic acids became a very active field. Nishimura et al. (1978) have reviewed resonance Raman studies on this subject with particular emphasis of the uracil, adenine and guanine residue. Effects of isotopic substitutions, calculation of normal vibrations as well as the Duschinsky effect (Duschinsky, 1937) were discussed as well.

In 1980-1982 comprehensive reviews on Raman and resonance Raman studies of biological and biochemical systems appeared in the literature (Carey and Solares, 1980; Carey, 1982). Particularly work on protein conformation, natural, protein-bound chromophores, resonance Raman labels (as already mentioned above), nucleic acids and nucleic acid-protein complexes as well as on lipids, membranes, and carbohydrates were reviewed.

A special review is devoted to resonance Raman studies in systems involved in the photosynthetic process (Lutz, 1984). Resonance Raman spectroscopy has proved to be a powerful tool in studying these systems. As a vibrational spectroscopy method, it yields the type of information needed on ground electronic states of molecules, with a sub-molecular resolution. By making use of low-energy photons, which are those powering the photosynthetic machinery, it constitutes a mildly perturbing method. As a resonance method, it can be extremely selective: for example (Lutz, 1984), most photosynthetic organisms contain sets of light-harvesting pigments, the electronic spectra of which are largely complementary in the visible and near UV regions so that the organism absorbs solar photons over a wide spectral range. These pigments, i.e. chlorophylls, carotenoids and phycobilins, thus constitute independent and selectively observable probes of the membrane and of its subunits. Lutz (1984) has shown how wide, although very specific, the applicability range of resonance Raman spectroscopy can be in photosynthesis.

An updated guide for interpreting resonance Raman spectra of proteins and related compounds has been presented by Harada and Takeuchi (1986). Another report on this type of molecular spectroscopy on flavins and flavo-proteins appeared in the same year (Morris and Bienstock, 1986). Other specialized reviews on biological and biochemical subjects have been published by Kitagawa (1986) on the resonance Raman spectra of reaction intermediates of heme enzymes and on the retinal-binding protein, the bacteriorhodopsin (Stockburger et al., 1986), whose unique function as a light-driven proton pump was first elucidated by Oesterhelt and Stoeckenius (1973). This membrane protein has been found to be of much interest and several reviews have appeared in the past (Ottolenghi, 1980; Birge, 1981; Stoeckenius and Bogomoliu, 1982; Lanyi, 1984).

The great interest in resonance Raman spectroscopy as probe for studying biological systems still continues. Very recent results can be extracted from the biannual proceedings of the international Raman conferences (Durig and Sullivan, 1990; Kiefer et al., 1992; Yu and Li, 1994) and from the conferences on the spectroscopy of biological molecules (Bertoluzza et al., 1989; Hester and Gerling, 1991; Theophanides et al., 1993).

6.1.2.2.5 Various applications of resonance Raman spectroscopy

One of the most useful advantages of resonance Raman spectroscopy is its ability to record spectra at very low concentrations. For example, Thibeau et al. (1978) have shown that this type of spectroscopy is able to detect hazardous chemicals in water. Nitrophenol-based pesticides or fungicides could be detected at concentrations below 1 ppm.

The use of resonance Raman spectroscopy for the study of transient species, including free radicals, has been reviewed by Hester (1978). Provided only that excitation may be achieved within an intense absorption band specific to the intermediate species, selective resonance enhancement permits the detection and characterization of such species at concentrations in the 10^{-4} – 10^{-5} molar range without serious interference from spectra of other dissolved species such as excess reactant and product molecules.

A further area which had attracted an increasing amount of attention is that of the resonance Raman spectra of structurally simple inorganic molecules, particularly those possessing allowed electronic transitions in the visible region. Clark (1975) and Clark and Dines (1986) have reviewed the application of resonance Raman excitation in inorganic chemistry.

The technique of resonance Raman spectroscopy is also attractive to the study of conjugated macromolecules. By tuning the laser wavelength to that of the maximum of the absorption band of the conjugated backbone, the vibrational modes of the backbone atoms are strongly enhanced relative to those of the sidegroups. Batchelder and Bloor (1984) have reviewed this area of research, in which resonance Raman spectroscopy has played a significant role. For example, polydiacetylenes form a class of polymers which in some cases can be prepared as large single crystals by solid state polymerization of the monomer (Wegner, 1971).

Extensive studies on the absorption, resonance Raman and resonance CARS spectroscopy (see also Sec. 6.1.4.2.3) on partially polymerized substituted diacetylene single crystals have been performed recently by Materny et al. (1992a-c), Materny and Kiefer (1992a-e), and by Engert et al. (1992). Resonance Raman spectroscopy has helped in the analysis of a wide range of properties of polydiacetylenes such as the polymerization process, backbone and electronic structure. There is also considerable interest in the simplest conjugated macromolecules, polyacetylene, since doping with donor and acceptor molecules has produced electrical conductivity typical of metals (MacDiarmid and Heeger, 1979). The structure and the doping mechanisms have been studied using resonance Raman spectroscopy (see also Sec. 4.9.2).

Also linear chain complexes such as $\text{Pt}(\text{etn})_4\text{Cl}_3$ which is known colloquially as Wolffram's red (etn being an abbreviation for ethylamine) have been studied successfully by resonance Raman spectroscopy (Clark, 1984). As example, we show in Fig. 6.1-12 the resonance Raman spectrum of a related halogen-bridged linear-chain species, $[\text{Pt}(\text{pn})_2][\text{Pt}(\text{pn})_2\text{Br}_2][\text{Cu}_3\text{Br}_5]_2$ (Clark et al., 1980). Although this species contains a complicated copper bromine chain, the resonance Raman spectrum (Fig. 6.1-12) is completely dominated by bands attributed to the ν_1 fundamental and its overtones $n \cdot \nu_1$ of the platinum-bromine chain.

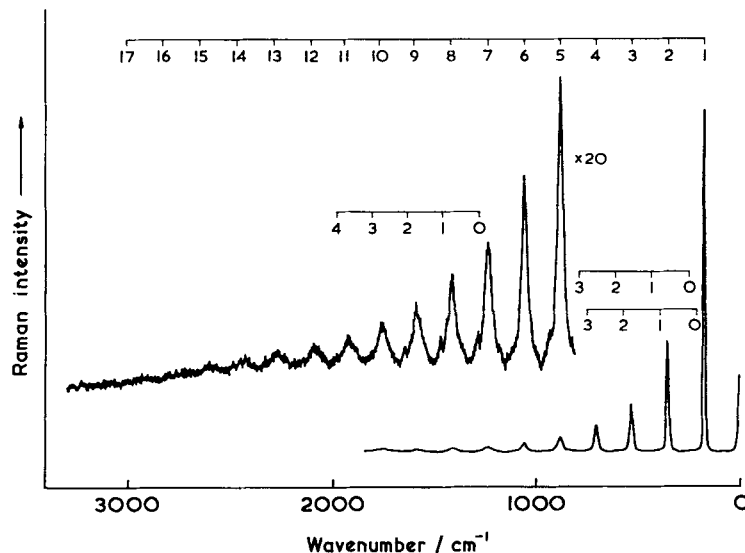


Figure 6.1-12 The resonance Raman spectrum of $[\text{Pt}(\text{pn})_2] [\text{Pt}(\text{pn})_2 \text{Br}_2] [\text{Cu}_3\text{Br}_5]_2$ at 80 K with $\lambda_0 = 568.2$ nm excitation (Clark et al., 1980).

6.1.3 Surface enhanced Raman scattering (SERS)

The study of vibrational spectra of adsorbed molecules on surfaces is one of the most interesting chapters in vibrational spectroscopy. Although there is a number of powerful techniques that use probes other than electromagnetic radiation, the basic and complementary infrared and Raman spectroscopy have become two of the most incisive methods for the study of structure and reactivity on surfaces. Infrared spectroscopy of adsorbates was developed first and has improved considerably since then (Yates and Madey, 1987). Although this technique is proving to be an invaluable tool for the study of vibrational spectra of adsorbed species, it suffers from a lack of sensitivity to submonlayer coverages and from the relative difficulties of probing solution-solid interfaces or polymer-modified surfaces when the bulk phase (e.g., solution or polymer) is strongly absorbing in the IR region. Normal Raman spectroscopy is suitable for the study of aqueous solution-solid interfaces, but the inherent weakness of the Raman scattering process makes probing thin layers or even submonolayers on surfaces extremely difficult. In the 1970s some novel results led to the discovery of surface enhanced Raman scattering (SERS). Fleischmann et al. (1974) observed large Raman signals from pyridine adsorbed onto electrochemically roughened silver electrodes and attributed this effect to an increased surface area. Careful qualitative investigations by Jeanmaire and Van Duyne (1977) as well as independently by Albrecht and Creighton (1977) showed that the Raman scattering cross section *per molecule* was enhanced by four to six orders of magnitude relative to that of the pyridine molecule in pure liquid. This enormous

enhancement factors are the basis of the powerful SERS method for studying adsorbed molecules. Most of the SERS studies published so far have been performed with silver, but other metals, e. g. copper or gold, also showed enhanced Raman spectra under certain conditions.

In this section we will shortly discuss the theoretical mechanisms which lead to the large enhancement factors. Then we will review the basis for the technique and its experimental requirements, and finally we describe a few selected examples of problems to which SERS has been applied. An incredibly wide variety of adsorbates has been studied by SERS and over 3000 original papers have been published to date including several reviews (Van Duyne, 1979; Furtak and Rayes, 1980; Otto, 1980; Yamada, 1981; Birke and Lombardi, 1982; Chang and Furtak, 1982; Dormhaus, 1982; Ueba et al., 1982; Ausseneegg et al., 1983; Otto, 1983, 1984; Pockrand, 1984; Wokaun, 1984; Efrima, 1985; Moskovits, 1985; Koglin and Séquaris, 1986; Seki, 1986; Weitz et al., 1986; Barlett and Cooney, 1987; Cotton, 1988; Creighton, 1988, 1990; Kneipp, 1990; Aroca and Kovacs, 1991; Otto, 1991; Otto et al., 1992).

6.1.3.1 SERS theories

The theoretical understanding of the mechanisms for surface enhancement is not yet complete. However, it is generally agreed that in any given adsorbate-substrate system several enhancement mechanisms may be operating (Moskovits, 1985). As is well known, the intensity of normal Raman scattering from free molecules is determined by the first order transition electric dipole, p , which depends on the transition polarizability of the molecule α and the electric field E incident on the molecule ($p = \alpha E$). The origin of SERS must therefore be sought in enhancement either of the transition polarizability α or of the electric field E . The theories for surface enhancement are therefore divided into two classes: the "electromagnetic field" enhancement mechanism, in which the field experienced by the adsorbate molecule is larger than it would experience far from the surface, and the "molecular" enhancement mechanism, in which α is perturbed by interactions of the adsorbate with the surface.

Classical electromagnetic theory indicates that molecules at metal surfaces will experience an electromagnetic field which is larger than that of the incident radiation. The extent of the enhancement depends on a number of factors, including the electric properties of the metal, the distance of the molecule from the surface, the orientation of the molecule in respect to the normal of the surface, the energy of the incident radiation, the morphology of the surface, and the size and geometry of surface roughness. Of particular importance is surface roughness or curvature, which can be obtained electrochemically or by the use of sols or island films (see Sec. 6.1.3.2). Calculations showed that the interaction of a light field with a flat (smooth) metal surface can produce about sixfold enhancement of the adsorbate molecule's Raman scattered intensity (Moskovits, 1985). By contrast, roughened surfaces can provide enhancements of 10^4 to 10^7 . The most effective substrates for SERS consist of small metal particles or rough surfaces of conductive materials. Light incident on such surfaces can excite conduction electrons in the metal, generating a plasma resonance. The particle then becomes polarized, and the

electromagnetic field in the interior of the particle becomes significantly larger than the applied field; this field falls off as $1/r^3$ away from the surface. The magnitude of the enhancement is given by the Lorenz-Mie theory (Kerker, 1969) and has been calculated for model SERS substrates such as isolated spherical and ellipsoidal particles.

In order to see how the electric field may be enhanced at a rough or particulate metal surface we take as a model a metallic sphere which is small compared to the incident optical wavelength. This simple model has been discussed in detail by Creighton (1988). On irradiating the sphere with light the incident field induces a displacement in the conduction electrons of the sphere. Hence an oscillating dipole is generated in the sphere, which in turn radiates a secondary field as shown in Fig. 6.1-13. The oscillating field E at the surface is then the sum of the incident and the secondary fields. However, since the conduction electrons are spatially confined, they have a characteristic frequency known as the plasma frequency and a quantized energy called a plasmon. Thus, if the incident frequency coincides with the plasma frequency, there is a resonant response to the field which yields a large induced dipole and therefore an enhanced secondary field at the surface. The plasma frequency depends on the metal and on the shape and size of the particle, and for roughened or particulate silver, gold or copper surfaces these resonances are in the visible or near infrared spectral region. It is this increase in the surface electromagnetic field if the incident wave is close to the resonance plasma frequency that is one of the main contributions to SERS enhancement.

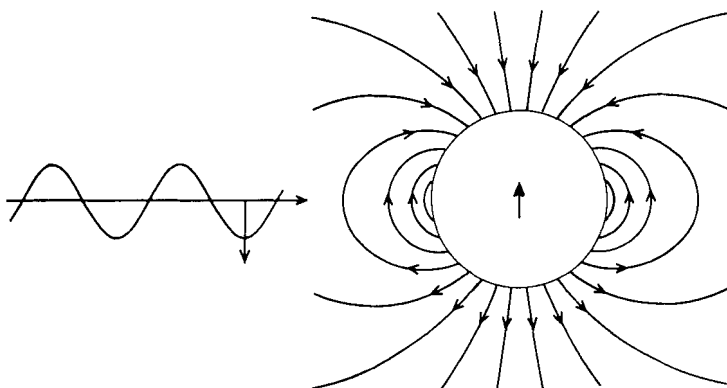


Figure 6.1-13 To illustrate the "electromagnetic" (EM) enhancement of SERS a simple model of a small metal sphere (radius is much less than the wavelength) experienced by an electromagnetic oscillating field is considered. If the sphere is illuminated at the plasma resonance frequency of the metal electrons a high electric field on the metal surface is generated, whose electric field lines are shown (Creighton, 1988).

The transition polarizability α can also be enhanced as a result of electronic interaction between the adsorbate and the metal. The most significant mechanism that produces an increase in the apparent value of α involves charge transfer between the metal and the adsorbate. Creighton (1986) has given a very illustrative example how charge transfer may occur from the metal to the adsorbate, which we will describe in the following.

Figure 6.1-14 shows on the left-hand side filled π and empty π^* orbitals of the free pyridine molecule from semi-empirical LCAO-SCF calculations (Mataga and Nishimoto, 1957). On the right-hand side the energy level diagram showing the metallic density of states near the Fermi level E_F of adsorbate-free copper (calculated 4s-, 4p- and 3d-band energies, Lasser et al., 1981) is displayed, taking the work function of adsorbate-free copper to be 4.1 eV. Comparing the energy levels of the molecule with those of the metal one recognizes that one-electron charge transfer transitions from the Fermi or from lower levels of the metal to the adsorbate's empty π^* orbital correspond to visible-range photons. These transitions have indeed been confirmed by optical spectroscopy (Pettinger et al., 1978; Yamada et al., 1987) or by electron energy loss spectroscopy (Avouris et al., 1981; Dinardo et al., 1984). Such charge transfer transitions have large oscillator strengths and they are therefore expected to result in a large increase in the polarizability of the molecule at the surface when they are subject to optical fields with frequencies inside the charge transfer band. As a result the adsorbate-metal-surface complex becomes a resonance Raman scatterer at these frequencies.

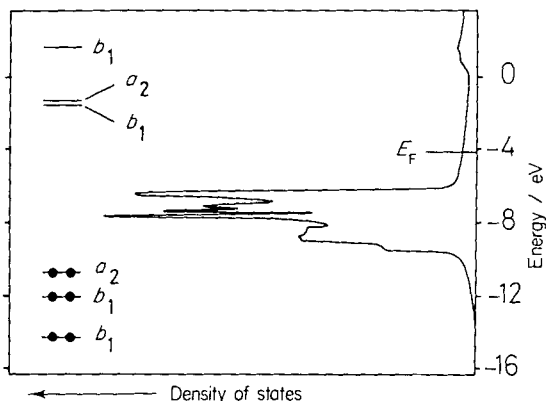


Figure 6.1-14 To illustrate the "molecular" (α) enhancement of SERS due to resonance Raman scattering for excitation into a charge transfer band of the adsorbate-metal-surface-complex the filled π and empty π^* orbital levels of pyridine and the metallic density of states of copper are shown on the left- and right-hand side, respectively; for details see text (Creighton, 1986).

A third way (Creighton, 1988) in which the surface may modify the intensity of Raman scattering by molecules adsorbed at the surface is by perturbing the molecules as a result of the bonding interaction with the surface. However, it turned out that this "chemical effect" on the Raman spectra is relatively small, and it is not normally considered to be a part of SERS, though it is inseparable from it. Several other SERS mechanisms have also been proposed (see for instance the discussion by Moskovits, 1985) which by now are widely thought to make at most only minor contributions to the enhancements observed in SERS.

By the two strong-enhancement mechanisms as discussed above a number of features inherent in SERS can now be understood. They have been summarized by Creighton (1990). Finally, we notice that the selection rules for SERS are fundamentally the same

as those for conventional Raman spectroscopy. However, because the local field at the surface is highest in the direction normal to the surface, vibrational modes involving changes in the adsorbate polarizability perpendicular to the surface are preferentially enhanced. A detailed summary of the selection rules for SERS has been given by Creighton (1988). The normal direction of the electric field plus the fact that the electromagnetic field amplitude falls off rapidly with distance from the surface allow one to determine the adsorbate orientation with respect to the average surface normal as well as the proximity of adsorbate functional groups to the surface.

6.1.3.2 Techniques for SERS

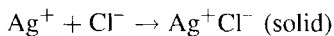
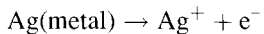
Most SERS studies employ the same instrumentation as is used for conventional Raman spectroscopy, i. e. a laser light source, sample area, collection optics, and double or triple monochromators with either photomultiplier or optical multichannel (diode array or CCD) detectors. To maximize the observed enhancement, the incident wavelength must be appropriate for the substrate material. Typically, the blue and green lines of an argon ion laser and the red lines of a krypton ion laser are used for silver. The krypton ion as well as dye lasers operating in the red region are mostly employed for copper and gold. Recently also excitation has been performed in the near IR region (Roth et al., 1993; Kneipp et al., 1993; Liang et al., 1993 a, b).

To obtain surface enhanced Raman spectra from adsorbates, special sample techniques are required to produce surface roughness or small clusters either isolated in solution or as powders at surfaces. Several techniques have been described in detail in the literature (see for example Cooney et al., 1982; Cotton, 1988).

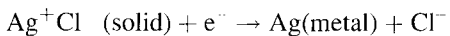
In the following we discuss shortly only a few of the most common types of substrates. For details we refer to the reviews cited above or to original papers published in journals.

In order to investigate molecules adsorbed at the solid-liquid interface roughened electrode surfaces or metal colloids in solution (sols) are prepared. For investigations of the solid-gas or solid-vapour interface several methods are available to produce metal island films on SERS-active substrates.

Electrodes. The first observations of SERS were made from species on silver electrodes. An essential prerequisite for a strong SERS signal from molecules adsorbed on the electrode, surface roughness, is obtained by running electrochemical oxidation-reduction cycles (ORC) (Chang and Laube, 1984; Koglin and Séquaris, 1986; Roth et al., 1993). During the oxidation half cycle a metal salt, usually a halide, is formed at the electrode surface:



When reduced, the liberated metal does not redeposit uniformly over the electrode surface, but instead forms clusters of the metal at the surface:



The average size of these small clusters is on the scale of 1...500 nm. One of the principal advantages of the use of electrodes is that it is possible to control the surface potential of the SERS substrate. In this way SERS becomes nearly an ideal structurally sensitive tool for *in situ* investigations of potential dependent effects on surfaces. For an overview of SERS on electrodes see also Chang, 1987.

Sols. A very frequently utilized substrate for SERS is the metal sol. Such metal colloids are prepared by reducing a dissolved metal salt in aqueous or a variety of non-aqueous solvents (Creighton et al., 1979) such as acetonitrile (Guzonas et al., 1984, Irish et al., 1985), dimethylformamide (Hutchinson et al., 1983), ethanol (Siiman et al., 1983), and propylene carbonate (Virdee and Hester, 1984). For example silver nitrate solution may be reduced with sodium borohydride. This produces sols consisting of spherical silver particles with a diameter of a few ten nm and a rather narrow size distribution. The most intense SERS signals are obtained, however, from aggregated metal sols, consisting of large assemblies of individual colloidal particles each about several ten nm in size.

The sols are easy to prepare (see also Lee and Meisel, 1982) and the molecules whose SERS spectra are to be obtained are added to the sol in very small concentrations ($10^{-4} \dots 10^{-14}$ mol/l). Recently a new method for preparing SERS active colloids has been pioneered by Neddersen et. al. (1993). By means of laser ablation of metals with a Nd:YAG laser operating at 1064 nm, stable Ag, Au, Pt, Pd, and Cu colloids were directly prepared in water and organic solvents. An important advantage of this method over conventional chemical procedures is that the colloids are free of organic or ionic species. Consequently, the chemical and physical effects of ions or other adsorbates can be studied under carefully controlled conditions. The authors report that the SERS activity of colloidal metals prepared by this laser ablation method is comparable or even superior to that of chemically prepared colloids.

The plasma frequency which is the important property for obtaining electromagnetic enhancement can be easily characterized by the absorption spectrum of the colloidal solution.

Metal films. A third, also very popular, substrate for SERS are vacuum-deposited island films, which are more stable than sols, but they are more difficult to prepare and require a vacuum deposition apparatus (Wood and Klein, 1979; Chen et al., 1979). If the substrate in the vacuum is not cooled the temperature increases metal atom mobility, causing nuclei to grow into islands, i. e. small clusters of 3 nm up to a few ten nm in diameter. Metal vapour deposited on a cold substrate (usually below 120 K) forms a rough film as a result of the reduced mobility of the metal atoms on the cold substrate (Liao et al., 1981; Meier et al., 1985; Vo-Dinh et al., 1986; Pettenkofer et al., 1987; Otto, 1988).

Other SERS-active substrate techniques include mechanical polishing polycrystalline silver (Vo-Dinh et al., 1988) or ion bombardment in vacuo (Wood and Zwemer, 1981; Davies et al., 1986). A chemical procedure to prepare silver island films using Tollen's reagent was developed by Ni and Cotton (1986) which turned out to be simple, rapid and highly reproducible. In addition, the surface roughness and hence the enhancement

factor can be controlled with this technique. A comprehensive description for the surface preparation in electrochemical and colloidal systems and for UHV studies has been published by Efrima (1985).

6.1.3.3 Some applications of SERS

Because SERS provides both rich spectroscopic information and high sensitivity as a result of the large enhancement effect it is an ideal tool for trace analysis as well as for in-situ investigations of various interfacial processes. The method has been applied for the study of a variety of molecules from diatomic to molecules of biological importance. The many reviews (see introduction to Sec. 6.1.3) published on this molecular spectroscopy technique give numerous examples of the wide range to which this method can be applied. In the following we give a small selection of some important features.

The high intensity associated with SERS makes it possible to obtain vibrational spectra of molecules from very dilute solutions. Kneipp (1988) has demonstrated that a complete SERS spectrum of rhodamine 6G on silver sol can be recorded from a $4 \cdot 10^{-12}$ mol/l concentration of the dye (Fig. 6.1-15). The strongest band could even be found in a concentration of $7 \cdot 10^{-14}$ mol/l from a sample which contains about 0,2 fg rhodamine 6G corresponding to about 250 000 molecules. Since the actual scattering volume within the laser focus is smaller than about 10 pl it can be estimated that the number of molecules contributing to the SERS signal is of the order of 100. Since a single molecule can undergo several scattering events within a particular time interval, the SERS technique allows detection limits for favorable systems that can compete with

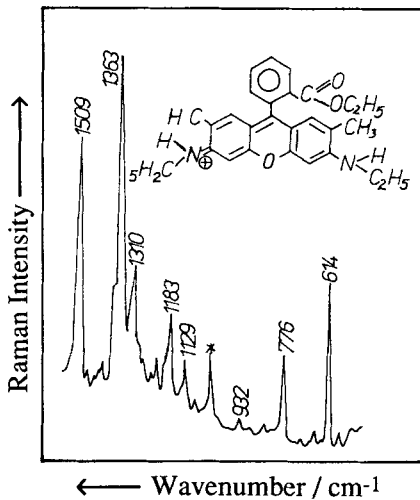


Figure 6.1-15 SERS spectrum of rhodamine 6G in silver sol; concentration of Rh6G = $4 \cdot 10^{-12}$ mol/l; excitation $\lambda_0 = 514.5$ nm (Adapted from Kneipp, 1988).

those of high-sensitive fluorescence spectroscopy. However, SERS has the additional advantage of high *structural* sensitivity. Even so the rhodamine 6G/Ag sol is one of the best SERS systems, other systems which normally have enhancement factors of the order 10^6 provide structurally sensitive detection limits at the subnanogram level (Kneipp, 1990).

A number of investigations have explored the possibility of using SERS for the direct analysis of species separated by thin-layer chromatography (TLC), high performance liquid chromatography (HPLC), and gas chromatography (GC). As example Tran (1984a) reported the subnanogram detection of dyes on filter paper by SERS, whereas Freeman et al. (1988) described the successful combination of SERS with HPLC and Roth and Kiefer (1994) the one with GC. Bello et al. (1990) utilized SERS as an *in situ* technique with silver-coated alumina for identification of components in a mixture of structurally similar components. Ni et al. (1990) have reported the coupling of SERS to flow-injection analysis (FIA) and collected real-time spectra of RNA bases on silver sols and Pothier and Forcé (1990, 1992) directed their research towards the use of SERS on a silver electrode as a detection method for flowing streams. By making use of an efficient charge-coupled device detection (CCD) system they were able to record SERS spectra at the silver electrode with short integration times which allowed a rapid time response to adsorption/desorption by appropriate potential modulation. Fig. 6.1-16 shows as example SERS

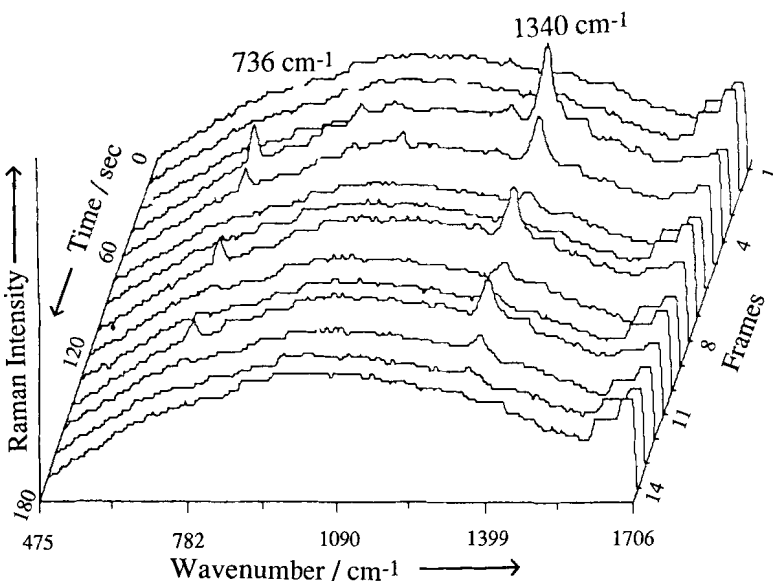


Figure 6.1-16 SERS at the silver electrode as a detection method for flowing streams. Shown are SERS spectra with 4 s integration times (= frame). 400 nanomole repeat injections of adenine were injected at frames 4, 8, and 11 into phosphate buffered 0.1 M KCl flowing at 1.0 ml/min. Peaks at 736 and 1340 cm⁻¹ are characteristic vibrational modes of adenine (Pothier and Forcé, 1992).

spectra of adenine taken at different times (frames) after three 400 nmol injections of adenine (at frames 4, 8, and 11) were injected into a phosphate buffered mobile phase flowing at 1.0 ml/min. The 736 and 1340 cm⁻¹ bands are characteristic vibrational modes of adenine (Pothier and Force, 1992).

For further reading on the coupling of SERS with chromatographic methods see Tran (1984b), Berthold et al. (1987), Séquaris and Koglin (1987), Force (1988), Garrell (1989), and Soper et al. (1990).

Besides its application to trace analytical problems SERS has also been successfully applied for surface analysis. The large enhancement factors allow the detection of mono- or even submonolayers adsorbed on various metal surfaces. SERS does, in principle, not require surface-vacuum boundaries in contrast to most other surface spectroscopic techniques and it is therefore an ideal tool for *in-situ* investigations of various interfacial processes. As example, SERS spectra of adsorbates on the surface of a technical copper catalyst under reaction conditions (Wokaun and Baiker, 1986) have been recorded. Another example, which nicely illustrates the high surface sensitivity of SERS, was reported by Ishida and Ishitani (1983) who used a Raman microprobe instrument in combination with Auger electron spectroscopy for the investigation of thin films formed on the surface of polycrystalline silver relay contacts. From the observed enhanced Raman scattering, carbon and sulfur compounds such as silver sulfate have been identified in the thin films formed on Ag contacts operated repeatedly under several kinds of controlled gas flows, while the Auger electron spectra taken from the same samples could only indicate the presence of silver, carbon, sulfur and oxygen. SERS, apparently yields more *structural* information.

Optical waveguides can also be used to produce strong Raman scattering from thin surface films (Rabolt and Swalen, 1988). The authors illustrate their method with applications to thin films of organic polymers and other molecular species at the surface, including organized molecular monolayers formed by the Langmuir-Blodgett technique or by self-assembly through adsorption at a solid surface. Information on surface orientation is obtained by polarization of both the incident laser illumination and the collected radiation, making this a most subtle technique for characterization of molecular thin films.

The normal Raman spectra of many biomolecules in aqueous solution cannot be observed because of their very low solubility in water. SERS has proved to be able to provide excellent vibrational spectra of biomolecules with concentrations of 10⁻⁶ M and smaller (Cotton, 1988). The adsorbed biomolecules can be studied by using either electrodes or colloid particles. The advantage of colloid SERS is the simple experimental pretreatment procedure and the possibility of measuring the Raman spectra in conventional cells or in capillaries. Moreover, compared with electrode SERS spectroscopy, the molecular structure is not influenced through the oxidation-reduction cycle or applied voltage during pretreatment. Since SERS of biomolecules has been reviewed already in Sec. 4.7.2.2 including a short discussion of surface enhanced hyper Raman scattering (Yu and Nie, 1990) we simply mention that also SERS with coherent nonlinear techniques such as SECARS (surface enhanced coherent anti-Stokes Raman scattering) has been reported recently by Liang et al. (1994).

6.1.4 Applications of nonlinear Raman spectroscopy

The methods of nonlinear Raman spectroscopy, i. e. spontaneous hyper Raman scattering (based on the hyperpolarizability) and coherent nonlinear Raman scattering (based on the third-order-nonlinear susceptibilities) are discussed in detail in Sec. 3.6.1. In Sec. 3.6.2 the instrumentation needed for these types of nonlinear spectroscopy is described. In this section we present some selected, typical examples of hyper Raman scattering (Sec. 6.1.4.1), coherent anti-Stokes Raman scattering (Sec. 6.1.4.2), stimulated Raman gain and inverse Raman spectroscopy (Sec. 6.1.4.3), photoacoustic Raman spectroscopy (Sec. 6.1.4.4) and ionization detected stimulated Raman spectroscopy (Sec. 6.1.4.5).

6.1.4.1 Hyper Raman spectroscopy

The importance of the hyper Raman effect as a spectroscopic tool results from the fact that it allows the observation of modes, which are accessible neither by infrared nor by linear Raman spectroscopy. Since its discovery by Terhune et al. (1965), hyper Raman spectra have been observed in all three states of aggregate. However, reasonable signal-to-noise ratios could only be obtained for a not too long measurement time after the development of high repetitive, high power lasers and highly sensitive detectors (multichannel diode arrays or charge-coupled devices (CCDs)). Before that time only a few gases have been studied which include ethane, ethene and methane (Verdieck et al., 1979). Only vibrational spectra of modest resolution have been obtained in these studies. A number of group IV tetrahalides have been studied in the liquid phase by Dines et al. (1976). Semi-quantitative intensities and depolarization ratios were measured and discussed. Other liquids whose Raman spectra have been reported include water (French and Long, 1975; Terhune et al., 1965) and tetrachloroethene (Schmid and Schrötter, 1977). Probably most hyper Raman work was performed in crystals: NH₄Cl, and NH₄Br (Long, 1979), calcite (Polivanov and Sayakhov, 1978 and 1981) NaNO₂ (Vogt, 1973; Weimann and Vogt, 1974), NaNO₃ (Ortmann and Vogt, 1976; Vogt and Neumann, 1978; Long, 1979), LiNbO₃ (Denisov et al., 1978), SrTiO₃ (Vogt and Rossbroich, 1981, Inoue et al., 1981), caesium and rubidium halides (Vogt and Neumann, 1976, 1979), rutile (Denisov et al., 1980), PbI₂ (Yu and Levy, 1981), CuBr (Honerlage et al., 1980), diamond (Yu and Alfano, 1975), and quartz (Denisov et al., 1980). Stimulated hyper Raman scattering has been observed from sodium vapor (Cotter et al., 1977), resonance hyper Raman scattering from CdS (Polivanov et al., 1979), and surface enhanced hyper Raman scattering from SO₃²⁻ ions adsorbed on silver powder (Murphy et al., 1982).

Technological advances, i. e. cw pumped acousto-optically Q-switched Nd:YAG lasers with repetition rates of up to 5 kHz combined with multichannel detection systems have increased the ease of obtaining hyper Raman signals. By making use of this advanced technology, hyper Raman spectra of benzene and pyridine could be obtained by Nederdansen et al. (1989). Spectra from benzene, deuterated benzene and carbon tetrachloride have been obtained with high signal-to-noise ratios by Acker et al. (1989). As example, we show in Fig. 6.1-17 the hyper-Raman spectra of benzene and deuterated benzene.

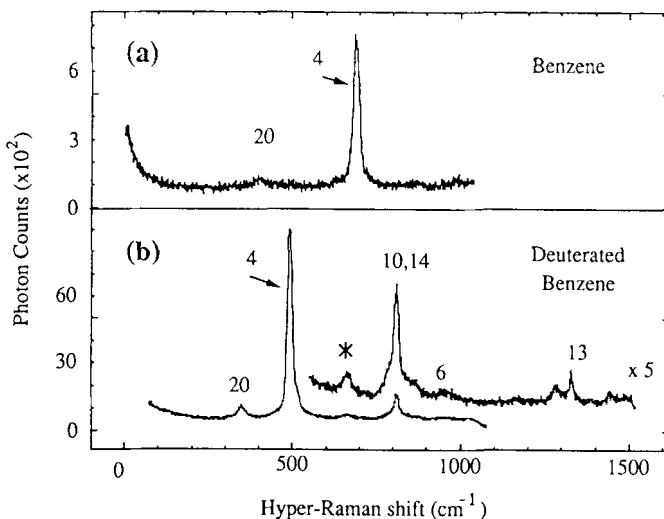


Figure 6.1-17 Hyper-Raman spectra of C_6H_6 excited with a Nd:YAG laser ($\lambda_0 = 1.064$ nm) Q -switched at 1 kHz (a) and of C_6D_6 in the lower spectrum with the laser Q -switched at 6 kHz (b) (Acker et al., 1989).

The observed hyper Raman bands are labeled by numbers (4, 6, 10, 13, 14, 20) and correspond to the $\nu_4(A_{2u})$, $\nu_6(B_{1u})$, $\nu_{10}(B_{2u})$, $\nu_{13}(E_{1u})$, $\nu_{14}(E_{1u})$, and $\nu_{20}(E_{2u})$ vibrations of C_6D_6 , respectively. The notation used is that of Herzberg (1964). Figure 6.1-18 shows the low-lying vibrational energy levels for C_6D_6 grouped by their activity involving transition from the ground state, i. e. Raman, IR, hyper-Raman (HR), and none of the above which are grouped as silent. Note that in the third column four modes with energy below 1500 cm^{-1} are only hyper Raman active and three modes of symmetry A_{1u} and E_{1u} are both IR and hyper-Raman active. Except for the $\nu_{19}(E_{2u})$ mode all hyper-Raman active modes could be found in the spectrum displayed in Fig. 6.1-17. Note, that there are modes which are still silent in the one-, two-, and three-photon processes schematically shown in the lower part of Fig. 6.1-18, i.e. the modes $\nu_3(A_{2g})$, $\nu_7(B_{2g})$, and $\nu_8(B_{2g})$. It is interesting to mention that an antisymmetric polarizability tensor component belongs to class A_{2g} , so that for conditions under which the α tensor becomes non-symmetric this A_{2g} mode which is otherwise inaccessible would be active. The modes of class B_{2g} are active in the second hyper Raman effect which is controlled by the fourth rank second hyperpolarizability tensor γ (Long, 1982).

Ziegler and coworkers (Ziegler et al., 1987; Chung and Ziegler, 1988; Ziegler, 1990; Campbell and Ziegler, 1993) pioneered hyper Raman scattering under resonance conditions for molecules in the gas phase. High quality rotational resonance hyper Raman spectra of NH_3 were obtained using blue incident radiation at half the $\tilde{X} \rightarrow \tilde{A}$ transition energy (Ziegler et al., 1987). Recently the same laboratory reported hyper-Raman scattering of methyl iodide for excitation with a laser line which has been tuned through the two-photon resonance with the absorption band of a predissociative Rydberg transition in the VUV (175 - 183 nm) (Campbell and Ziegler, 1993). Their result demonstrates the

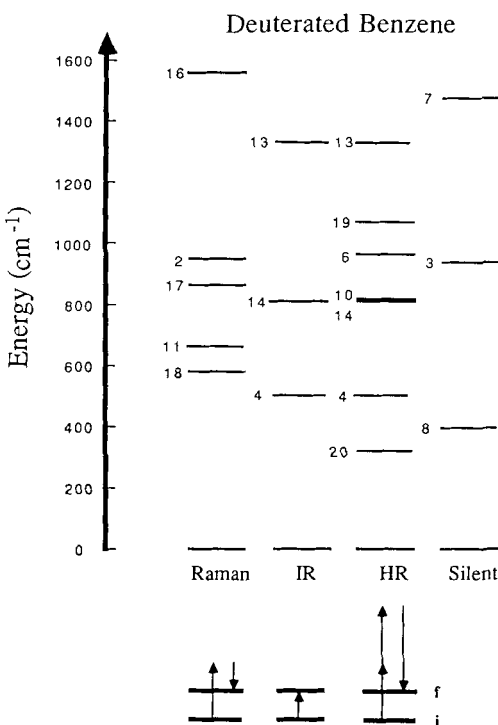


Figure 6.1-18 Vibrational energy levels of C₆D₆ (energy < 1600 cm⁻¹) grouped by their activity from the ground state, i.e. Raman, IR, or hyper-Raman (HR). Mode labeling follows Herzberg's notation (Herzberg, 1964). Modes which are not active in Raman, IR, or hyper-Raman are grouped as silent (Acker et al., 1989).

ability of this nonlinear Raman technique to probe the ultrafast dynamics of molecular levels in the VUV. Due to this two-photon resonance with molecular levels via resonant hyper Raman spectroscopy, only the viewing region must be evacuated or purged in order to observe scattering due to resonance with these high-lying electronic levels. Similarly to linear resonance Raman scattering, overtones or combination bands can also be observed for resonantly excited hyper Raman scattering. An example is given in Fig. 6.1-19 where several higher order modes of methyl iodide can be observed.

Ziegler et al. (1989, 1990) have recently reviewed hyper Raman spectroscopic studies including hyper Raman scattering in liquids and crystals, surface enhanced hyper Raman scattering (Golab et al., 1988) as well as the vibronic and rotational theory for resonance enhanced hyper Raman scattering.

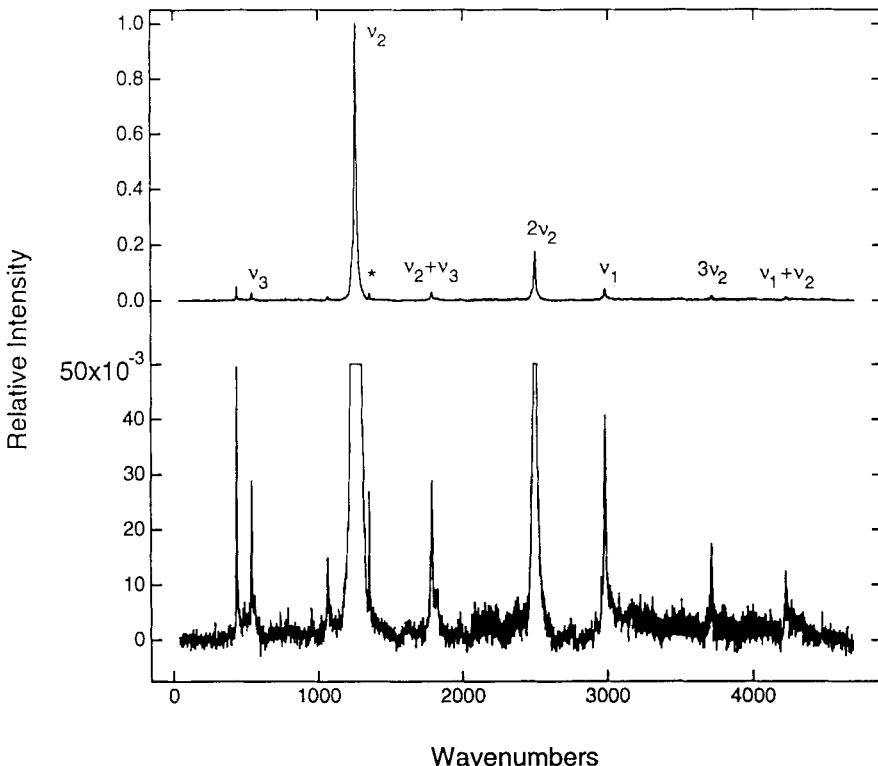


Figure 6.1-19 Resonance hyper Raman spectrum of CH_3I vapor excited at 365.95 nm (Campbell and Ziegler, 1993).

6.1.4.2 Coherent anti-Stokes Raman spectroscopy (CARS)

The advantages of CARS, i. e. high signal strength, very high spectral or temporal resolution, discrimination against fluorescence, etc., have opened new ways to the study of molecular structure and dynamics. As mentioned already in Sec. 3.6 several reviews have appeared which deal with the various different aspects. In the following some selected examples will be given to demonstrate the capability of this nonlinear coherent technique: spectroscopy of gas-phase molecules with applications to high resolution and combustion studies, femtosecond time resolved spectroscopy in the liquid state, and resonance CARS of the solid state. For further information or applications we refer to the reviews compiled in Sec. 3.6.

6.1.4.2.1 Spectroscopy of gas-phase molecules*

After the first observation of CARS by Maker and Terhune (1965) applications to gas phase studies followed shortly thereafter (Rado, 1967), but the real impetus for practical applications only came with the pioneering experiments of Taran and coworkers (1973) on combustion systems and with the subsequent commercial development of pulsed Nd:YAG and tunable dye lasers of high power and narrow spectral bandwidth. The last ca. 15 years have seen a remarkable growth in the number of CARS applications to molecular and physical properties, particularly in the field of gas phase systems. The latter are challenging because of low sample densities and the narrow transition linewidths make them attractive for high resolution studies. Gas phase CARS spectra have been obtained so far at pressures down to a few Pascal, at temperatures ranging from a few K to 3600 K, and at a resolution better than about 10^3 cm^{-1} . Applications of high resolution CARS have been reviewed by Schrötter et al. (1988), Schrötter and Boquillon (1988, 1989) and recently by Lavorel et al. (1992) and by Berger et al. (1992). With cw lasers as well as with injection-locked flashlamp-pumped dye laser systems effective instrumental resolutions of 0.001 cm^{-1} and 0.0004 cm^{-1} , respectively, have

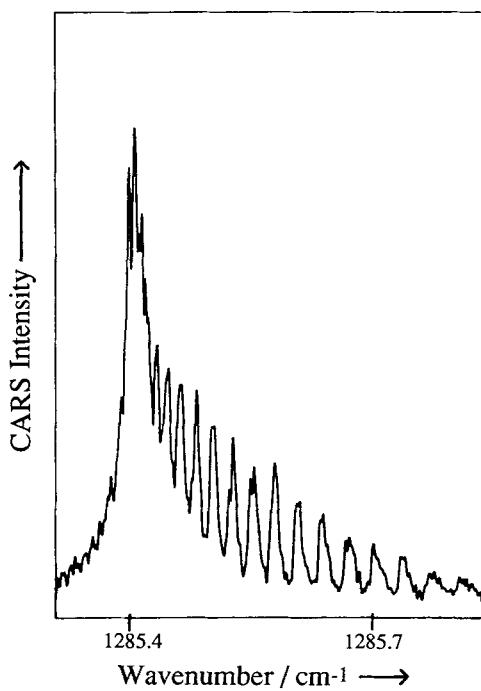


Figure 6.1-20 Example of a high-resolution ($\sim 0.0004 \text{ cm}^{-1}$) CARS spectrum. The Q-branch of the lower component of the Fermi resonance diad of CO_2 at room temperature and at a pressure of 5 kPa (37.5 Torr) in the vicinity of 1285 cm^{-1} is shown (Ouazzany et al., 1988).

* Section 6.1.4.2.1 is contributed by W. Kiefer, Würzburg and A. Leipertz, Erlangen

been obtained and the Q -branches of many di-, tri-, and four-atomic as well as spherical XY_4 top molecules have been studied. As an example we show in Fig. 6.1-20 the Q -branch of the lower component of the Fermi resonance diad in CO_2 at room temperature and at a pressure of 5 kPa (35.5 Torr) in the vicinity of 1285 cm^{-1} (Ouazzany et al., 1988). Note that the whole spectral range displayed is only about 0.5 cm^{-1} . The rotational structure seen there has been resolved for the first time and could be simulated by the authors in very good agreement with the experiment. From the same group investigations of collisional effects applying CARS have been reported (Lavorel et al., 1992) which is of particular importance as a basis for the determination of temperatures and pressures. The high accuracy of the determination of line positions and widths has allowed the measurement of self-density frequency shifts of nitrogen (Lavorel et al., 1987; Bonamy et al., 1988).

One very active area of the gas phase CARS technique has been the remote sensing of temperature and species in hostile environments such as gas discharges, plasmas, flames, internal combustion engines, and the exhaust from jet engines. The high signal intensity and the excellent temporal and spectral resolution of CARS make it a favorite method for such studies. For example, Péalat et al. (1985) have used CARS to measure state populations and changes in discharges of H_2 , N_2 and O_2 at pressure ranging from a few kPa down to 0.6 Pa. Hata et al. (1986) employed gas phase CARS in monitoring SiH_2 intermediates in their investigation of silane plasmas commonly used in amorphous silicon deposition processes. Many laboratories are engaged in combustion research. Developments in this important diagnostic area have been reviewed by Eckbreth (1988), Greenhalgh (1988), Leipertz (1989), and Stricker and Meier (1994). Combustion studies in engines include thermometry in a diesel engine (Kajiyama et al., 1982), in a production petrol engine (Greenhalgh et al., 1985), and thermometry and species measurements in a fully afterburning jet engine (Eckbreth et al., 1984). Investigations on turbulent flames were performed by Eckbreth and Hall (1979) and on sooting flames by Hall and Boedecker (1984) as well as by Bengtsson et al. (1992).

Temperature information from CARS spectra derives from spectral shapes either of the Q -branches or of the pure rotational CARS spectra of the molecular constituents. In combustion research it is most common to perform thermometry from nitrogen since it is the dominant constituent and present everywhere in large concentration despite the extent of chemical reaction. The Q -branch of nitrogen changes its shape due to the increased contribution of higher rotational levels which become more populated when the temperature increases. Figure 6.1-21 displays a calculated temperature dependence of the N_2 CARS spectrum for experimental parameters typically used in CARS thermometry (Hall and Eckbreth, 1984). Note that the wavenumber scale corresponds to the absolute wavenumber value for the $\sim 2320 \text{ cm}^{-1}$ Q -branch of N_2 when excited with the frequency doubled Nd:YAG laser at 532 nm ($\simeq 18796 \text{ cm}^{-1}$), i. e. $\tilde{\nu}_{as} = 18796 + 2320 = 21116 \text{ cm}^{-1}$. The bands lower than about 21100 cm^{-1} are due to the rotational structure of the first vibrational hot band.

For the case that there are not too many constituents in the gas under investigation the use of the pure rotational CARS technique (Zheng et al., 1984; Alden et al., 1986) may be superior to vibrational CARS thermometry since the spectra are easily resolvable (for N_2 the adjacent rotational peaks have a spacing of appr. 8 cm^{-1}) compared with the

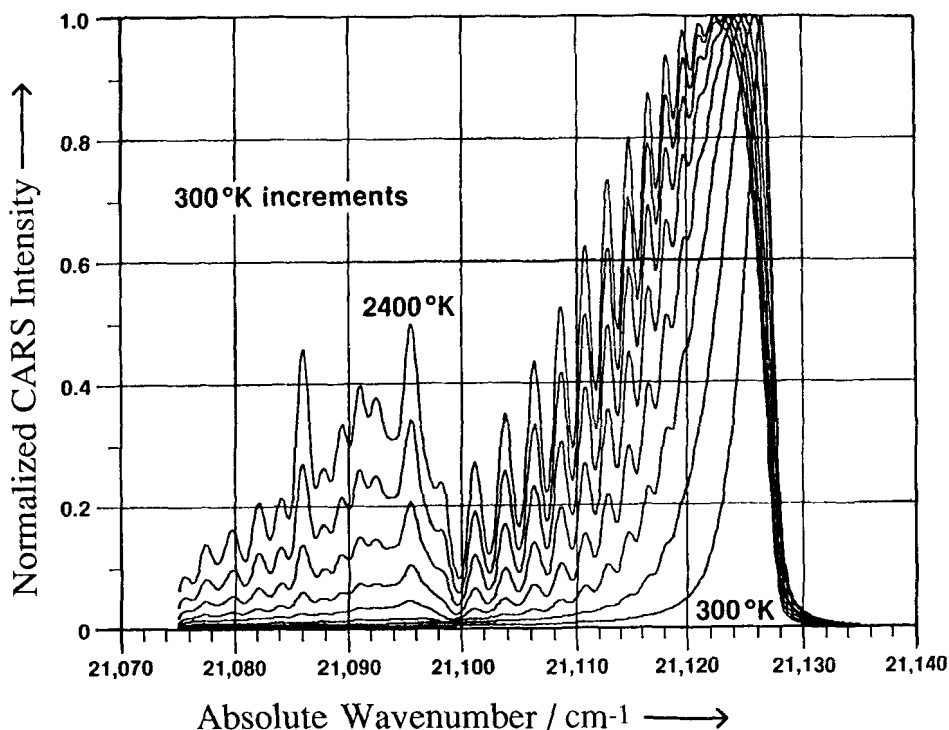


Figure 6.1-21 Temperature dependence of N_2 CARS spectrum from 300 to 2400 K in 300 K increments (Hall and Eckbreth, 1984).

congestion of the rotational lines in the vibrational bands of the Q-branch spectra (see Fig. 6.1-21). An experimental comparison of rotational and vibrational CARS techniques, under similar conditions have been made (Zheng et al., 1984) that demonstrates that rotational CARS may be viable for flame-temperature measurements up to 2000 K. Of course, the pure rotational approach can not be applied for spherical molecules which have no pure rotational CARS spectrum. An elegant method, using Fourier analysis based on the periodicity of pure rotational CARS spectra has been introduced by Lasser et al. (1985).

In addition to temperature measurements, the gas-phase CARS technique also provides information on the fluctuating properties occurring for instance in turbulent combustion systems. However, concentration measurements are more difficult to perform than temperature ones because the absolute intensity is required, while temperature measurements are only based on the shape of the spectrum. Simultaneous information on the relative concentrations between several species are easier to obtain. For such investigations the technique called dual broadband CARS has been introduced by Eckbreth and Anderson (1985) which allowed the researchers to simultaneously generate CARS spectra of CO_2 , N_2 and H_2O in the postflame zone of a premixed C_2H_4 -air flame.

Quantitative gas-phase CARS spectroscopy has also been applied to probing species in a laboratory chemical reactor (England et al., 1984, 1986) and to temperature measurements inside incandescent lamps (Devonshire et al., 1986). Another interesting area is that of CARS applied to free expansion jets. The key benefits of this technique are the spectral simplification of cold molecules and the increased concentrations of small van der Waals complexes obtained under the non-equilibrium jet conditions (Nibler and Pubanz, 1988). CARS probing in supersonic molecular beams was shown to be feasible by Huber-Wälchli and Nibler, 1982). König et al. (1982) reported the first direct observation of the Raman spectra of molecular clusters using CARS in a pulsed molecular beam. In their experiment, complexes of ethylene and argon were evidenced by a peak red-shifted 4.8 cm^{-1} from the ethylene ν_2 vibration at 1623 cm^{-1} . The spectra of small hydrogen-bonded dimers, trimers and polymers have been examined subsequently by CARS and other techniques (Maroncelli et al., 1985; Hopkins et al., 1985). The even weaker van der Waals bonds could also be studied with the CARS technique, e. g. the CO_2 dimer in expansions of CO_2/He mixtures (Pubanz et al., 1985).

Besides the initial object of CARS as a tool for the determination of molecular energy levels and its application to combustion studies and related areas, there are several other scientific applications of academic interests. These include spectral lineshape studies, collisional effects, Dicke narrowing, nonadditivity effects, and motional narrowing. CARS turned out to be an excellent method for these studies (Berger et al., 1992 and references therein).

6.1.4.2.2 Femtosecond time-resolved studies in liquids and solutions

Time resolved coherent anti-Stokes Raman spectroscopy of condensed matter has been recently extended to the femtosecond domain allowing direct and detailed studies of the fast relaxation processes of molecular vibrations in liquids. The vibrational phase relaxation (dephasing) is a fundamental physical process of molecular dynamics and has attracted considerable attention. Both experimental and theoretical studies have been performed to understand microscopic processes of vibrational dephasing. Developments in ultrafast coherent spectroscopy enables one now to obtain direct time-domain information on molecular vibrational dynamics. Femtosecond time-resolved coherent anti-Stokes Raman scattering measuring systems have been constructed (see Sec. 3.6.2.2.3) with an overall time resolution of less than 100 fs (10^{-13} s). Pioneering work has been performed by Leonhardt et al., 1987; Zinth et al., 1988; Aechtner et al., 1990; Joo et al., 1991; Okamoto and Yoshihara, 1991; Fickenscher et al., 1992; Inaba et al., 1992, 1993; Okamoto et al., 1993 a, b).

Since the pulse time is so short (see Sec. 3.6.2.2.3) one can coherently excite many vibrational modes at a time and monitor relaxation processes in real time. The first reported femtosecond time-resolved CARS experiments (Leonhardt et al., 1987; Zinth et al., 1988) showed beautiful beating patterns and fast decays of the coherent signal for several molecular liquids. The existence of an intermolecular coherence transfer effect was suggested from the analysis of the beating patterns (Rosker et al., 1986). Subsequent studies by Okamoto and Yoshihara (1990) include the vibrational dephasing of the 992 cm^{-1} benzene mode. A fast dephasing process was found that is possibly related to

rotation of the molecule in the liquid. Also time-resolved *resonance CARS* studies for a benzene solution of β -carotene and a methanol solution of a dye have been reported by the same authors. They observed expected rise and decay signals in β -carotene, but only a decay signal in the dye solution, which is probably due to inhomogeneous broadening.

Using a three-colour femtosecond CARS apparatus, Fickenscher et al. (1992) were able to measure very precisely the dependence of the dephasing time T_2 of the ν_2 mode of acetone for isotopic dilution and the solvent CCl_4 . The measured isotopic dilution effect could be explained by a resonant transfer of vibrational quanta to nearest neighbours via the repulsive part of the internuclear potential.

Another example of the observation of femtosecond time-resolved CARS is that of Inaba et al. (1993a) who studied the $\text{C}\equiv\text{C}$ stretching vibration of alkynes (monoalkyl-

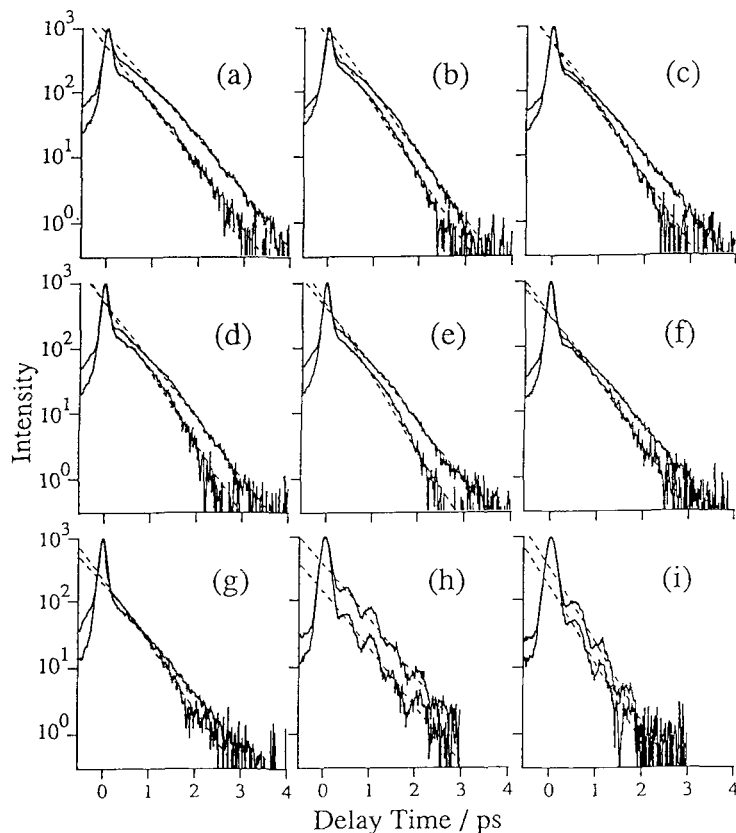


Figure 6.1-22 Time resolved CARS for the $\text{C}\equiv\text{C}$ stretching of alkynes in the neat state (upper trace in each panel) and in mixtures with dimethylformamide (lower trace); (a) $\text{C}_3\text{H}_7\text{C}\equiv\text{CH}$; (b) $\text{C}_4\text{H}_9\text{C}\equiv\text{CH}$; (c) $\text{C}_5\text{H}_{11}\text{C}\equiv\text{CH}$; (d) $\text{C}_6\text{H}_{13}\text{C}\equiv\text{CH}$; (e) $\text{C}_7\text{H}_{15}\text{C}\equiv\text{CH}$; (f) $\text{C}_8\text{H}_{17}\text{C}\equiv\text{CH}$; (g) $\text{C}_{10}\text{H}_{21}\text{C}\equiv\text{CH}$; (h) $\text{CH}_3\text{C}\equiv\text{CC}_2\text{H}_5$; (i) $\text{C}_3\text{H}_7\text{C}\equiv\text{CC}_3\text{H}_7$. The mole fraction is 50 % in each mixture (Inaba et al., 1993a).

acetylenes and dialkylacetylenes) as shown in Fig. 6.1-22. It was found by these studies that the dephasing of the $\text{C}\equiv\text{C}$ stretching of $\text{C}_3\text{H}_7\text{C}\equiv\text{CH}$ is accelerated in mixtures with either proton-donors or proton-acceptors. The dephasing rates of the $\text{C}\equiv\text{C}$ stretching of monoalkylacetylenes ($\text{C}_n\text{H}_{2n+1}\text{C}\equiv\text{CH}$) with relatively long alkyl chains ($n \geq 4$) are nearly the same, and are accelerated in mixtures with dimethylformamide regardless of the length of the alkyl chain. On the other hand, the authors reported that the dephasing in dialkylacetylenes is not accelerated in mixtures with dimethylformamide, reflecting the absence of hydrogen bonding between dialkylacetylenes and dimethylformamide.

In another study using femtosecond time-resolved CARS the same research group investigated the $\text{C}\equiv\text{N}$ stretching vibration of alkanenitriles ($\text{C}_n\text{H}_{2n+1}\text{CN}$, $n = 1 - 17$) (Okamoto et al., 1993a). It was found that the vibrational dephasing rates ($1/T_2$) observed for the neat alkanenitriles are proportional to the square root of the number of carbon atoms (n) in the alkyl chain.

A number of other interesting studies in a variety of systems can be expected in the future for this sophisticated ultrashort technique, which also includes Raman echo measurements (Inaba et al., 1993 b).

6.1.4.2.3 Resonance CARS of the solid state

As discussed in Sec. 6.1.2 resonance Raman spectroscopy is a valuable tool to investigate structural as well as electronic properties of absorbing substances. However, many organic, inorganic or biological materials may not be accessible to resonance Raman spectroscopy. This is due to strong luminescence when excited by laser radiation in the absorption region. Hence, in many cases it is not possible to obtain spectroscopic information from linear Stokes or anti-Stokes Raman spectroscopy. On the other hand, many, particularly organic substances show considerable third-order nonlinear susceptibilities $\chi^{(3)}$ as for example polyacetylenes, polydiacetylenes or chlorophyll. For such systems resonance CARS spectroscopy is a suitable tool to obtain resonance Raman information via the anti-Stokes, coherent spectroscopical method. However, in performing resonance CARS spectroscopy in solids one must realize that this technique results in a fairly complicated arrangement between the sample and the coherent beams. First, the phase-matching condition (Eq. 3.6-5, Fig. 3.6-3) has to be obeyed, where the momentum vectors depend also on the refractive index of the solid media (Eq. 3.6-6). Therefore a continuous adjustment of the crossing angle between the incident laser beams (\vec{k}_L , \vec{k}_S) as well as of the angle between the pump laser beam and the CARS beam (\vec{k}_L , \vec{k}_{AS}) is required during the scan of the CARS spectrum. Second, in order to excite particular phonons in the crystals, the difference between the pump and the Stokes beam wave vectors must coincide with the wave vector of the coherently excited phonon in the solid ($\vec{k}_L - \vec{k}_S = \vec{k}_{\text{phonon}}$). Depending on the strength of absorption and sample thickness CARS in solids is either performed in transmission or in reflection (backscattering CARS, see Sec. 3.6.2.2.1).

As an example of resonance CARS studies in solids, for which a linear resonance Raman study has been impossible to perform because of simultaneous strong luminescence, we consider here investigations on colour zones in substituted diacetylene crystals

originating from partial polymerization. Such studies (Materny and Kiefer, 1992 a, b) have been performed with a CARS apparatus described in Fig. 3.6-8 (see Sec. 3.6.2.2.1). The authors showed that it is possible to obtain CARS signals with fairly good signal to noise ratio despite strong luminescence.

For a long time it has been known that diacetylene monomer single crystals (Wegner, 1969) undergo, upon thermal annealing or exposure to high-energy radiation, topochemical solid-state polymerization. From this reaction polymer chains are formed, which have a substantial p-electron delocalization, forming a pseudo-one-dimensional electronic system. Colour zones occur in such crystals due to different chain lengths and

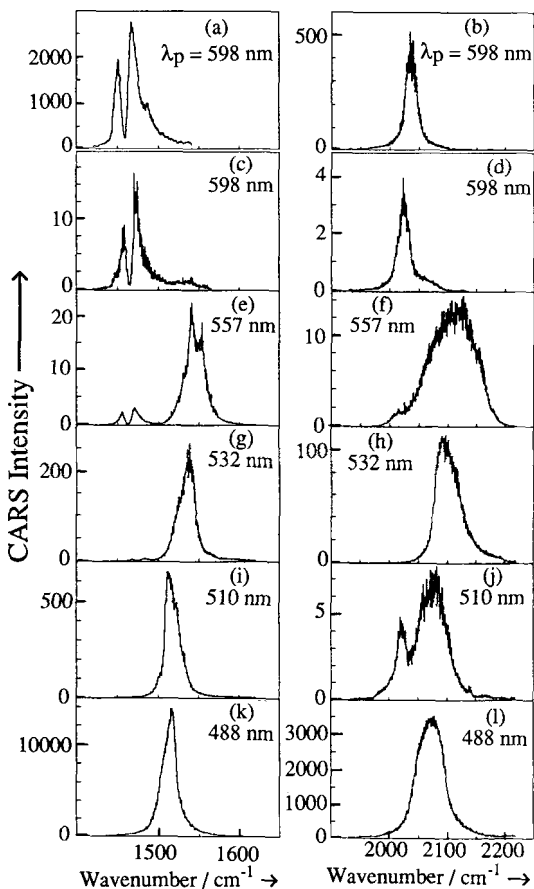
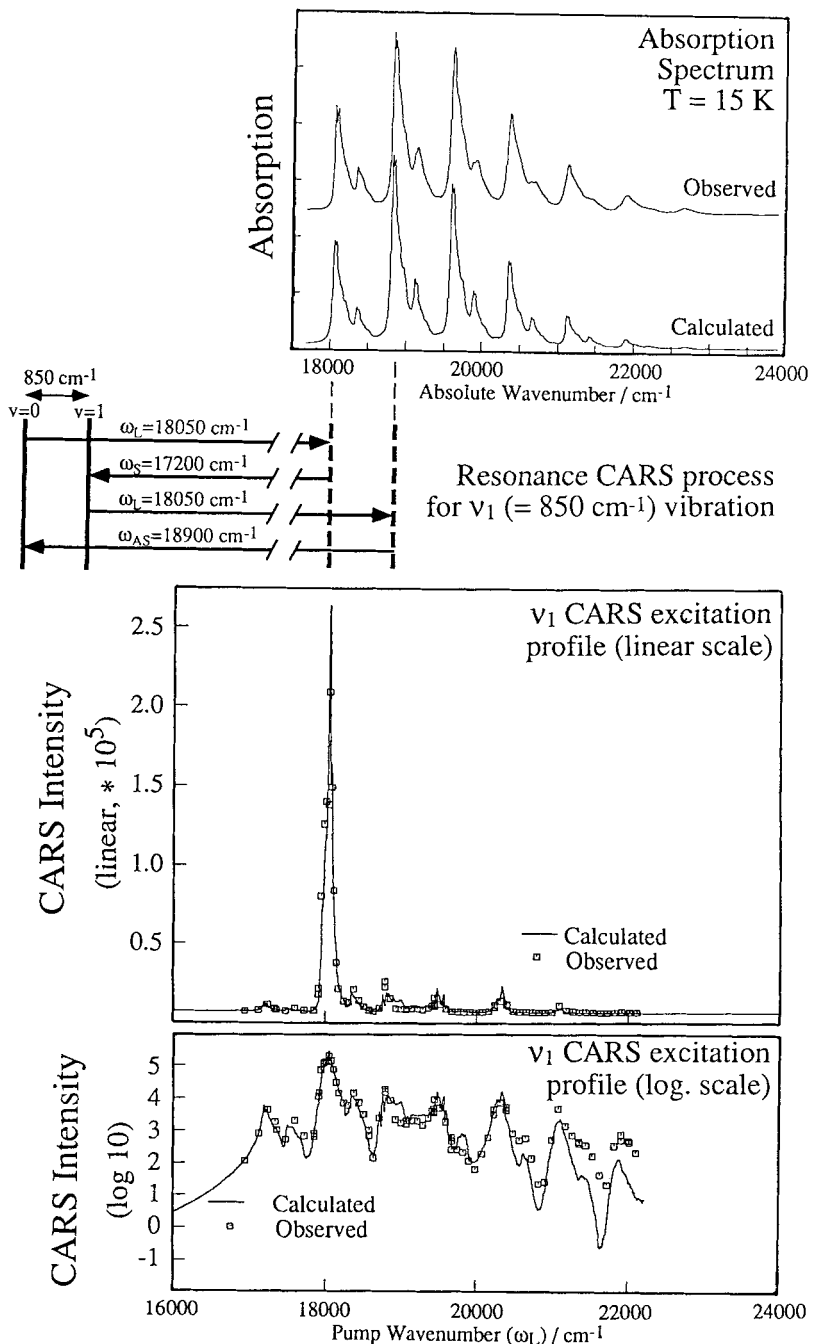


Figure 6.1-23 Resonance CARS spectra of a substituted diacetylene single crystal (FBS-DA) at 10 K. The pump wavelength λ_p used is labeled for each spectrum. (a) and (b) show CARS spectra of the P-colour zone, and (c)-(l) those for the Y-colour zone. Spectra on the left side correspond to the C=C stretching region, and those on the right side to the C≡C stretching region. For further details, see text (Materny and Kiefer, 1992b).

CARS studies were performed on these zones in crystals with low polymer content, where the polymer chains were embedded in the monomer matrix. As mentioned, resonance Raman excitation within the strong absorption of the polymer chains, i. e. within the absorption of the colour zone, produced high luminescence levels which obscured the bands in linear Raman spectroscopy. In contrast, luminescence free resonance CARS spectra could be obtained as shown in Fig. 6.1-23 for the case of an FBS DA crystal at 10 K temperature (FBS = 2,4-hexadiynylene-di-p-fluorobenzene sulfonate, DA = diacetylene). On the left and right panels of Fig. 6.1-23 CARS spectra are displayed for the region of the C=C and C≡C stretching region around 1500 cm^{-1} and 2100 cm^{-1} , respectively. Spectra (a) and (b) are those of the P-colour zone (P = principal) and (c) - (l) those of the Y-colour zone (Y=yellow). Note the very different CARS intensities as well as bandshapes for the various excitation wavelengths of the pump laser (λ_p , which corresponds to ω_L of the CARS process as outlined in Sec. 3.6.2.2) which are due to different resonant enhancements. Comparing spectrum (k) with (c), for example, shows in addition the very high dynamic range (at least four orders of magnitude) inherent in this type of spectroscopy. Analyzing the CARS spectra together with the absorption spectra of several substituted DA crystals, the authors were able to derive important structural as well as electronic properties of this type of crystal. For details on resonance CARS studies on various types of diacetylene single crystals we refer to the original literature (Materny and Kiefer, 1992 a-e, 1993; Materny et al., 1992 a-c; Ganz et al., 1993).

Another, instructive example for resonance CARS in a solid model system has been reported by Leuchs and Kiefer (1993 a). Polarized resonance CARS experiments on the ν_1 vibration of the permanganate ion doped in a KClO_4 crystal at low temperature were performed. At a temperature of 15 K the vibronic structure of the resonant, excited electronic state is well resolved as revealed by a low temperature absorption spectrum of the single crystal (see upper spectrum in Fig. 6.1-24). The experimentally observed absorption spectrum could be simulated in good agreement with the experiment by making use of the time-correlator formulation for the optical absorption in the dipole approximation (Page, 1991). By tuning the pump wavelength ($\hat{=}$ angular frequency ω_L) across the vibronically resolved absorption region, whose main peaks correspond to the ν_1 progression of the permanganate ion in the excited electronic state, the ν_1 CARS excitation profile can be obtained as shown in the lower part of Fig. 6.1-24 in a linear as well as a logarithmic (\log_{10}) vertical scale. On the linear scale one can particularly recognize a strong and sharp peak at angular frequency $\omega_L < 18050\text{ cm}^{-1}$, which can be explained by the fact that both intermediate states of the CARS process are in resonance with vibrational ν_1 states in the excited electronic state (see the CARS energy level diagram in Fig. 6.1-24 which has been rotated by 90° from the usual presentation to fit to a horizontal energy scale in order to coincide with the wavenumber scale for absorption and excitation profile). Because of anharmonicity of the ν_1 vibration and a small but not negligible difference between the wavenumber of the ν_1 vibration in the ground and excited electronic states the pronounced double resonance feature occurs only at excitation with angular frequency ω_L around 18050 cm^{-1} . However, weaker resonance features can be seen particularly in the log scale CARS excitation profile presentation in the lower part of Fig. 6.1-24. The latter could also be calculated numerically by a theory



which is essentially the transform theory developed by Page (1991) with extension to a four-photon (CARS) process by Leuchs and Kiefer (1993 a).

6.1.4.3 Stimulated Raman gain and inverse Raman spectroscopy (SRGS, IRS)

The advantages of the two coherent Raman techniques, stimulated Raman gain (SRGS) and inverse Raman spectroscopy (IRS), have been described in detail in Secs. 3.6.1.3 and 3.6.2.3. Here, we present an instructive example for each technique emphasizing the high resolution capability of these methods.

Stimulated Raman gain spectroscopy with tunable lasers was first demonstrated in liquids (Görner et al., 1974; Owyoung, 1977; Owyoung and Jones, 1977). By using a multipass optical gas cell, a high enough sensitivity was achieved by Owyoung et al. (1978, 1979) for nearly Doppler-limited resolution in the spectrum of the ν_1 band of methane at a pressure of 4.6 kPa by the cw SRGS technique. These works marked the breakthrough of non-linear Raman spectroscopy to the detailed analysis of resolved Q-branches of rotational-vibrational bands of polyatomic molecules (see also Sec. 4.3.2).

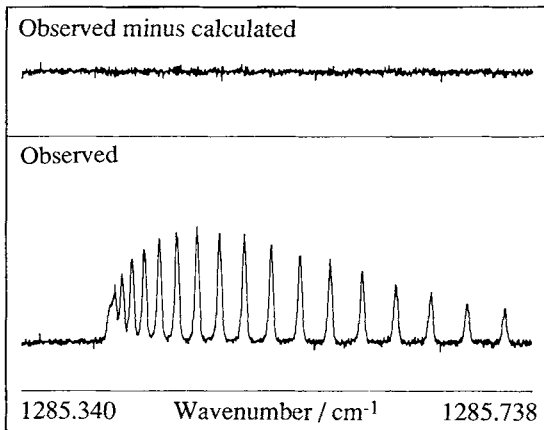


Figure 6.1-25 High resolution multi-pass stimulated Raman gain spectrum (SRGS) of the Q-branch of the lower component of the Fermi resonance diad of $^{12}\text{C}^{16}\text{O}_2$ at a pressure of 200 Pa (1.5 Torr) (Saint-Loup et al., 1990).



Figure 6.1-24 Resonance CARS excitation of the ν_1 ($= 850 \text{ cm}^{-1}$) vibration of the permanganate ion doped in a KClO_4 single crystal. The absorption spectrum at $T = 15 \text{ K}$ shows the vibronic structure of the MnO_4^- -ion. CARS excitation with $\omega_L = 18\,050 \text{ cm}^{-1}$ and $\omega_S = 17\,200 \text{ cm}^{-1}$ gives rise to a twofold resonance since the intermediate states of the CARS process coincide with the sharp electronic transitions. The CARS ν_1 excitation profile peaks particularly for this double resonance (see linear scale). Further resonances can be seen in the CARS excitation profile plotted on a \log_{10} scale (Adapted from Leuchs and Kiefer, 1993a, b).

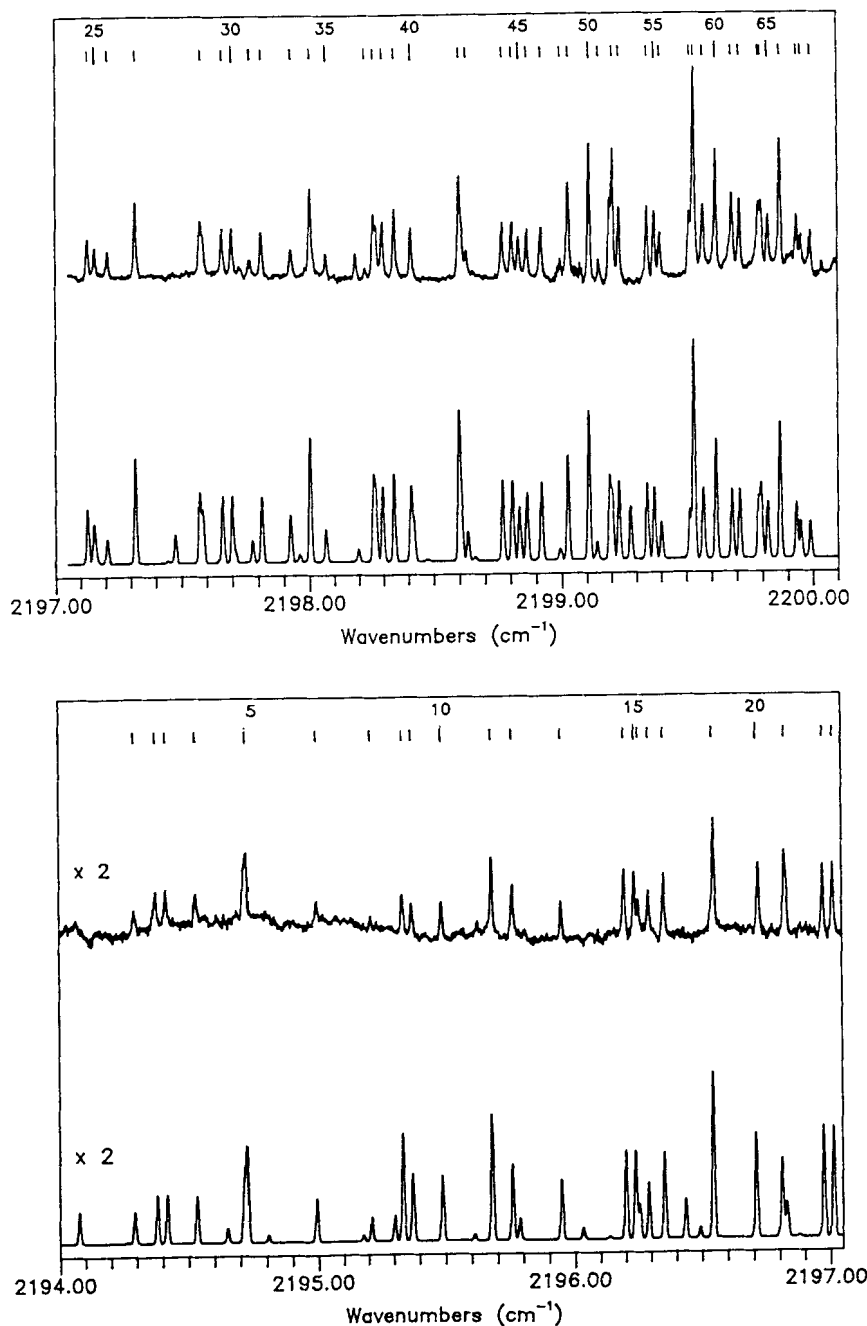


Figure 6.1-26 High resolution inverse Raman spectrum of the ν_2 Q-branch of CH_3D between 2194 and 2200 cm^{-1} . Upper traces: observed, lower traces: calculated spectra (Bermejo et al., 1990).

The Q-branches of numerous molecules, particularly of linear and spherical top molecules have been analyzed by means of SRGS and IRS (for a review see Schrötter et al., 1990). As an example of a recent high resolution SRGS spectrum we show in Fig. 6.1-25 the spectrum of the Q -branch of the lower component of the Fermi resonance diad of $^{12}\text{C}^{16}\text{O}_2$ at 1285 cm^{-1} . The spectrum has been recorded at a pressure of 200 Pa (1.5 Torr) using a multiple reflection cell (Saint-Loup et al., 1988). It can be compared to the CARS spectrum shown in Fig. 6.1-20 which has been taken at much higher pressure (37.5 Torr). The improvement in resolution and sensitivity over the CARS spectrum is considerable. The excellent agreement with a calculation assuming Voigt line profiles is demonstrated by the residual spectrum in the upper trace.

An example for high-resolution IRS is given in Fig. 6.1-26, where the ν_2 Q -branch of CH_3D is displayed. This spectrum has been recorded with the quasi-cw inverse Raman spectrometer developed by Bermejo et al. (1990) whose schematic arrangement is shown in Fig. 3.6-15 and described in Sec. 3.6.2.3. It represents a Doppler-limited spectrum of the C-D stretching band. The authors were able to assign the observed transitions by performing a theoretical fit to the observed data which allowed them to refine some of the rotational-vibrational constants.

For further examples of SRGS and IRS spectra we refer to the various reviews which dealt with these subjects (Schrötter et al., 1990, and references therein).

6.1.4.4 Photoacoustic Raman spectroscopy (PARS)

As discussed in Secs. 3.6.1.3 and 3.6.2.4 in photoacoustic Raman spectroscopy (PARS) the energy deposited in the sample by excitation of e. g. a vibration by the stimulated Raman process leads to pressure increases through relaxation to translational energy and can therefore be detected by a sensitive microphone.

When the pump (ω_L) and Stokes (ω_S) beams have only small frequency differences, as can be achieved for example by using a frequency-doubled Nd:YAG laser for ω_L and a dye laser with amplifier pumped by the third harmonic of the same Nd:YAG laser for ω_S (Barrett, 1981), the recording of pure rotational PARS spectra becomes possible. Such a spectrum at medium resolution is shown in Fig. 6.1-27. The striking feature of this spectrum is the absence of a strong Rayleigh component at the pump wavelength (532 nm) because at that wavelength no energy is deposited in the sample. For other Raman methods such as spontaneous Raman scattering, CARS or SRGS, the presence of intense Rayleigh scattering makes it difficult to observe pure rotational Raman transitions, especially if the Raman shifts are very small. This absence of the Rayleigh component makes the PARS technique particularly well suited for studying pure rotational Raman transitions.

The PARS technique has been recently extended to study vibrational-rotational transitions with high resolution ($\sim 0.005\text{ cm}^{-1}$). The apparatus for this is displayed in Fig. 3.6-16 (Rotger et al., 1992). A high resolution PARS spectrum of the lower component of the Fermi resonance diad of CO_2 at a pressure of 1.6 kPa (= 11 Torr) is shown in Fig. 6.1-28. This is the same spectral region as already displayed in Fig. 6.1-20 by the high

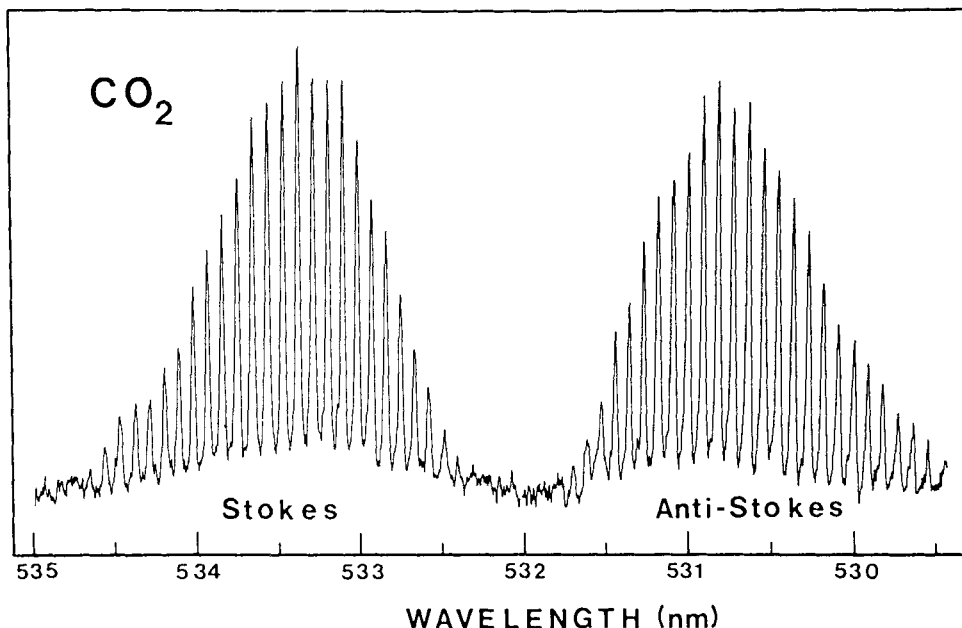


Figure 6.1-27 The pure rotational photoacoustic Raman (PARS) spectrum of CO_2 gas at a pressure of 80 kPa (600 Torr); pump laser wavelength at 532 nm. Note the complete absence of any acoustical signal due to Rayleigh scattering (at 532 nm) (Barrett, 1981).

resolution CARS spectrum and by the multi-pass stimulated Raman gain (SRGS) spectrum shown in Fig. 6.1-25. The authors (Rotger et al., 1992) report that the comparison between single-pass and multi-pass stimulated Raman spectrum of this vibrational band shows that the PARS technique leads to a better signal-to-noise ratio than the single-pass SRGS technique by about one order of magnitude at 1.3 kPa pressure. However, one must take into consideration that low pressure ($< 1.3 \text{ kPa}$) is not favourable for detection of a PARS signal. The multi-pass SRGS method gives a larger enhancement of sensitivity at very low pressure (Rotger et al., 1992).

There have been some other studies where the PARS technique has been applied, e.g. in a medium-resolution experiment, in which a direct comparison between CARS and PARS spectra of the ν_1 bands of glyoxal and of methane at pressures of 4 and 6.7 kPa, respectively, excited under similar conditions could be made (Duval et al., 1986). The CARS profiles showed a broader appearance which the authors attribute to contributions of the real part of the nonlinear susceptibility, however, this assumption should be proved by calculation of both profiles.

In another PARS study (Hopkins et al., 1985) it was shown that photoacoustic Raman spectroscopy is a sensitive technique for obtaining Raman spectra of hydrogen-bonded complexes in the gas phase. PARS spectra of the CN stretching ν_1 region of HCN as a function of pressure revealed bands which could be assigned to HCN dimers and trimers.

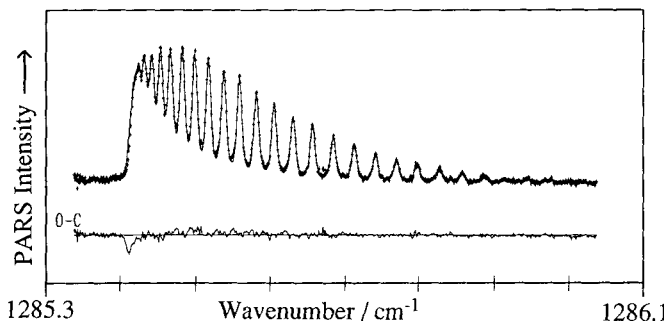


Figure 6.1-28 High resolution photoacoustic Raman (PARS) spectrum of the lower component of the Fermi resonance diad of CO_2 at a pressure of 1.6 kPa (11 Torr). Solid line: calculated spectrum; +: experimental (Rotger et al., 1992).

6.1.4.5 Ionization detected stimulated Raman spectroscopy (IDSRS)

In Secs. 3.6.1.3 and 3.6.2.5 we have discussed how the sensitivity in determining Raman transitions can be enormously increased by employing nonlinear Raman schemes in which the shifts in vibrational state populations due to stimulated Raman transitions are probed by resonance-enhanced multiphoton ionization (Esherick and Owyong, 1983; Esherick et al., 1985). As ions can be detected with much higher sensitivity than photons, the signal-to-noise ratio in the non-linear Raman spectrum of (e. g.) NO could be improved by a factor of 10^3 by this method (Esherick and Owyong, 1983). In fact, one can obtain sufficient sensitivity to characterize the Raman transitions of species even in molecular beams. The high sensitivity of IDSRS made it for instance possible to investigate the degenerate Fermi doublet ν_{16} and $\nu_2 + \nu_{18}$ of benzene in such a molecular beam experiment (Esherick et al., 1985). The two Fermi sub-bands could be recorded separately by selectively tuning the UV laser into resonance with electronic transitions from one of the two states. When the Stokes laser is tuned, then the rovibrational structure of only one Raman transition is recorded. Figure 6.1-29 shows in the upper part the lines belonging to ν_{16} and in the lower part those assigned to $\nu_2 + \nu_{18}$ in the same spectral region.

By mass-analyzing the ions created in this ionization detected stimulated Raman spectroscopy scheme one is also able to obtain the Raman spectra of *minority* species in the molecular beam, e. g. weakly bound complexes and clusters, without interference from the spectral features due to majority species, e. g. bare molecules. Felker's group has used IDSRS and the Fourier transform IDSRS technique (see Sec. 3.6.2.5) with mass-selective detection to obtain Raman spectra of a number of molecular complexes and clusters (Hartland et al., 1988, 1990, 1992; Henson et al., 1989, 1993; Felker et al., 1992). Figure 6.1-30 shows example spectra corresponding to benzene/deutero-benzene dimers in the region of the ν_2 (A_{1g}) (Herzberg's notation; Herzberg, 1964) totally symmetric stretch fundamental of benzene-d₆ (Hartland et al., 1990). The spectra were obtained employing the Fourier transform version of IDSRS. Spectrum (a) represents the ν_2 fundamental of benzene-d₆, whereas spectra (b) and (c) show the high resolution

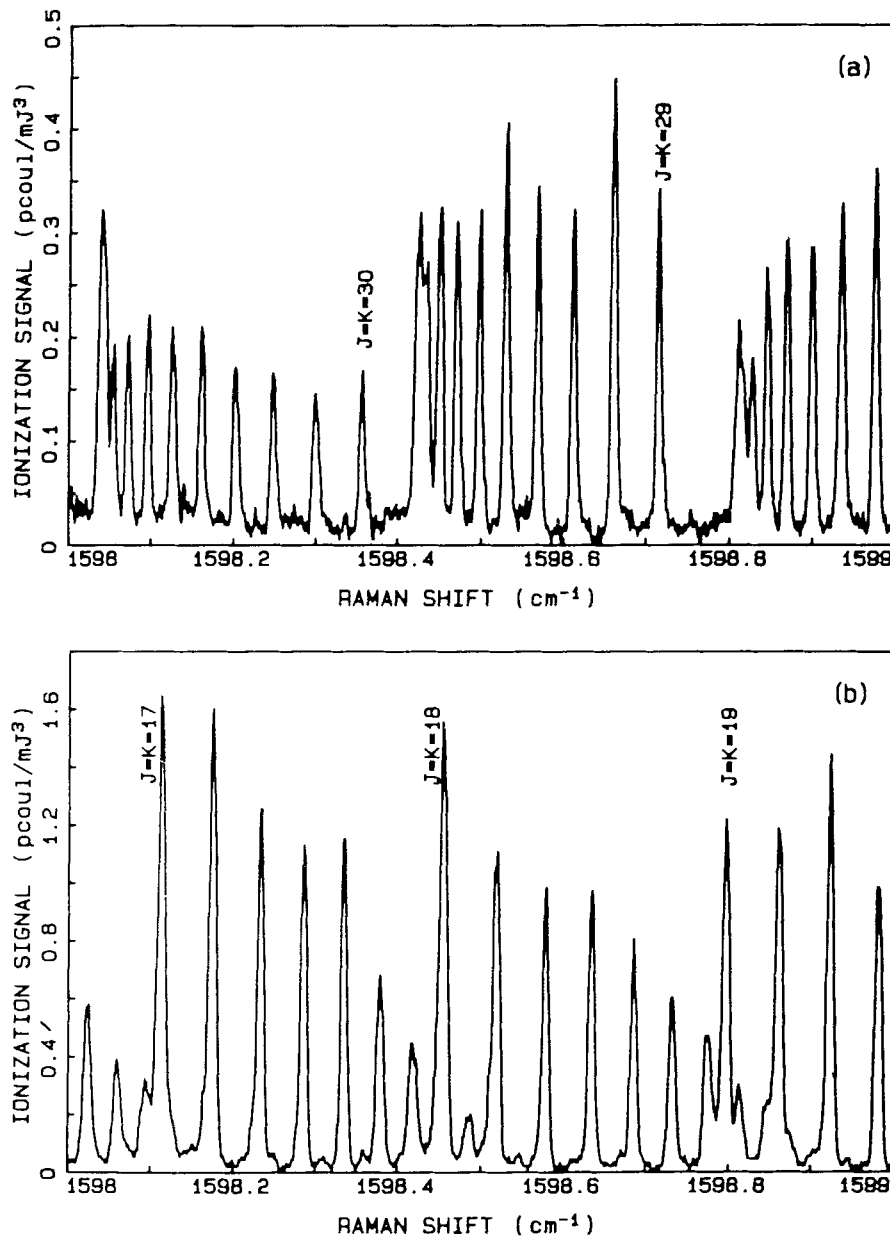


Figure 6.1-29 Ionization detected stimulated Raman (IDSRS) spectra of benzene in the region of overlap between the ⁶O-branch transitions of ν_{16} and the ³S-branch transitions of $\nu_2 + \nu_{18}$. (a) UV laser tuned to $36\ 467\text{ cm}^{-1}$; (b) UV laser tuned to $36\ 496\text{ cm}^{-1}$ (Esherick et al., 1985).

IDSRS spectra of the benzene dimers $C_6H_6 - C_6D_6$ (which are denoted $d_0 - d_6$) and $C_6D_6 - C_6D_6$ ($d_6 - d_6$), respectively. From measurements of a number of isotopomers of the species in several spectral regions of the benzene monomer, several significant results relating to structure have been obtained (Felker et al., 1992).

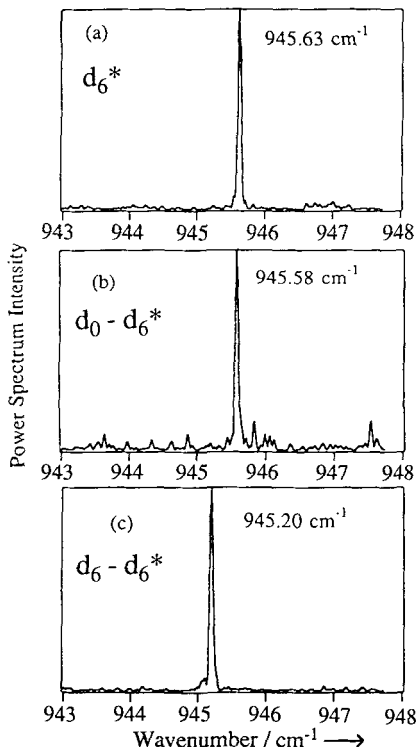


Figure 6.1-30 Fourier transform ionization detected stimulated Raman spectra in the region corresponding to the totally symmetric C-C-stretch fundamental of benzene-d₆: (a) benzene-d₆ monomer, (b) d₀-d₆ benzene dimer, (c) d₆-d₆ benzene dimer (Hartland et al., 1990).

From the sophisticated measurements performed in Felker's laboratory it seems that the various versions of ionization-detected stimulated Raman techniques (with mass analysis) have great capabilities in the high resolution vibrational spectroscopy of weakly bound complexes and clusters. One expects that IDSRS will become increasingly productive in the studies of cluster ground-state structure and dynamics.

6.2 Principles and application of near-infrared spectroscopy*

6.2.1 Introduction

The near-infrared (NIR) spectral range extends from about 4000 cm^{-1} to $12\,500\text{ cm}^{-1}$ between the infrared and visible regions. With the exception of the R-branch of the hydrogen fluoride fundamental, the near-infrared vibrations of all common materials are overtone and combination modes, which become active as a consequence of either mechanical or electrical anharmonicity. The analysis of these bands follows the same principles as those underlying the study of overtones and combination modes in the classical infrared (see Sec. 2.3). Thus, there is no special theory of near-infrared spectroscopy. Review articles on NIR spectroscopy have been published by Kaye (1954), Wheeler (1959), Goddu (1960), Whetsel (1968), and Weyer (1985). A Colthup-type chart showing the positions, the ranges, and the intensities of the absorption of characteristic functional groups has been provided by Goddu and Delker (1960).

The fact that NIR is used to a lesser extent than IR spectroscopy is partly due to the late development of appropriate instrumentation. Early NIR work was performed using UV-VIS spectrometers with extension units for low wavenumbers or, vice versa, on IR spectrometers with high wavenumber accessories. The NIR spectra obtained by these methods were of low quality. Instrumental restrictions of this type no longer exist, and high-quality NIR spectra are provided by improved conventional and also by Fourier-transform (FT) spectrometers. A FT-NIR atlas comprising the spectra of approximately 2000 substances in the wavenumber range 3800 to $10\,500\text{ cm}^{-1}$ has been edited (Buback and Vögele, 1993). The corresponding digital spectra are available from Chemical Concepts (Weinheim, F.R.G.).

The application of NIR spectroscopy has been further stimulated by the development of NIR diffuse reflectance techniques which are widely used in the analysis of agricultural, pharmaceutical, biochemical and synthetic polymer materials (Siesler, 1991). The rapidly increasing use of NIR spectroscopy is illustrated in the book "Making Light Work: Advances in Near infrared spectroscopy", edited by Murray and Cowe (1992) as well as in the Handbook of Near-Infrared Analysis by Burns and Ciureak (1992).

Considering the enormously large number of combination and overtone transitions that is calculated for polyatomic molecules, one might expect that the near-infrared spectrum consists of too many absorption components to be of any practical value for qualitative and quantitative analysis. Inspection of measured NIR spectra, however, shows that even larger molecules exhibit only relatively few bands. This finding is explained by a transition to "local modes" at higher energy (Mills, 1992). The remarkable simplicity of NIR spectra is somewhat reduced when Fermi resonance coupling gives rise to additional absorption components (see Figs. 6.2-8 and 6.2-9). The occurrence of relatively few bands

* Section 6.2 is contributed by M. Buback, Göttingen

at high NIR wavenumbers may also be understood as a consequence of vibrational intensity being strongly diminished toward higher order combination and overtone modes. In this context, the term "higher order combination mode" refers to an increased number of fundamentals contributing to a particular combination mode. As a crude rule of thumb, the vibrational intensity (see Eq. 6.2-3) and also the molar absorption coefficient (see Eq. 6.2-1), e.g., that of the band maximum, decrease by about one order of magnitude for each additional fundamental species contributing to an overtone or combination mode. A significant decrease in vibrational intensity by about one order of magnitude between the v -th and the $(v+1)$ -th overtone has already been described by Lippert and Mecke (1951) in their pioneering article on band positions and vibrational intensities in the second and third C–H stretching overtone regions of a wide variety of organic materials. The consequences of such changes are easily visualized by considering near-infrared absorption around 9000 cm^{-1} as an example. Vibrational motions with fundamental frequencies at $\nu_{01} = 1500\text{ cm}^{-1}$ contribute as fifth overtones, $(6\nu_{01})$; whereas vibrations with $\nu_{02} = 3000\text{ cm}^{-1}$ contribute as second overtones $3(\nu_{02})$. Assuming that the fundamentals are of equal intensity and that each order of overtone reduces the intensity to the same extent, e.g., by one order of magnitude, it is readily understandable why, around 9000 cm^{-1} , the overtone absorption due to $(6\nu_{01})$ is negligible compared to the absorption caused by $(3\nu_{02})$. It is understood that fundamentals and overtones which are discussed in this simple example are symmetry-allowed and that the influence of anharmonicity on band positions is neglected. If the qualitative argumentation used in the 9000 cm^{-1} region is applied to near-infrared bands around 6000 cm^{-1} , it becomes obvious that the latter essentially result from first overtones and binary combination modes of vibrations with fundamental frequencies around 3000 cm^{-1} . Thus, the absorption bands of organic materials in the 6000 cm^{-1} region largely consist of first overtone and binary combination mode absorption associated with C–H stretching fundamentals.

Near-infrared absorption is therefore essentially due to combination and overtone modes of higher energy fundamentals, such as C–H, N–H, and O–H stretches, which appear as lower overtones and lower order combination modes. Since the NIR absorption of polyatomic molecules thus mainly reflects vibrational contributions from very few functional groups, NIR spectroscopy is less suitable for detailed qualitative analysis than IR, which shows all (active) fundamentals and the overtones and combination modes of low-energy vibrations. On the other hand, since the vibrational intensities of near-infrared bands are considerably lower than those of corresponding infrared bands, optical layers of "reasonable" size (millimeters, centimeters) may be transmitted in the NIR, even in the case of liquid samples, compared to the layers of μm size which are detected in the infrared. This has important consequences for the direct quantitative study of chemical reactions, chemical equilibria, and phase equilibria via NIR spectroscopy.

The advantages of NIR diffuse reflectance techniques which rapidly develop are due to the direct analysis of solids without any necessity for special sample preparation (Weyer, 1985; Stark et al., 1986; Murray and Cowe, 1992). In NIR absorption and reflectance techniques fibre optics may be used which allow analysis remote from the spectrometer.

Combination modes of intramolecular vibrations cannot occur in diatomic molecules. The near infrared spectra of heteronuclear diatomics only consist of overtone components and, if measured at an appropriate optical path length, these spectra appear like

corresponding fundamental modes, e.g., in terms of band shape. In this text, examples of the NIR absorption of small molecules are presented, followed by NIR spectra of polyatomic molecules. The chapter closes by describing a number of examples of how NIR spectroscopy is applied in quantitative analysis.

6.2.2 Near-infrared spectra of small molecules

The near-infrared absorption of simple diatomic molecules is exemplified by carbon monoxide (Buback et al., 1985). The pure vibrational transitions of the first and second overtone in the gas phase are at 4260 cm^{-1} and at 6350 cm^{-1} , respectively. Fig. 6.2-1 shows the molar absorption coefficient ε at $127\text{ }^{\circ}\text{C}$ and at various densities ϱ between 0.10 and 0.65 g cm^{-3} . ε is defined as

$$\varepsilon = A \cdot (c \cdot l)^{-1} \quad (6.2-1)$$

in which A is the decadic absorbance, c is the actual density (in moles per unit volume), and l is the optical path length. At this supercritical temperature ($T_c = -141\text{ }^{\circ}\text{C}$) the density may be varied continuously between gaseous and liquidlike states. Individual rotational-vibrational lines cannot be detected, since all the spectra in Fig. 6.2-1 are completely pressure-broadened. The pressure values which correspond to the limiting spectra at 0.1 and 0.65 g cm^{-3} are 124 and 2116 bar , respectively. The curves are slightly shifted in vertical direction in order to avoid too much overlap between them. The envelope of the gaseous P and R branches is clearly observed at lower densities. The gap between the two branches becomes less pronounced as the density increases.

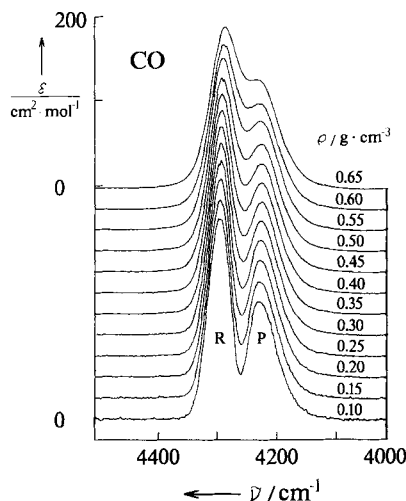


Figure 6.2-1 Molar absorption coefficient ε of the stretching first overtone of pure carbon monoxide at $127\text{ }^{\circ}\text{C}$ and various densities ϱ between 0.10 g cm^{-3} (124 bar) and 0.65 g cm^{-3} (2116 bar).

In Fig. 6.2-2, the molar absorption coefficient ε of pure CO in the second overtone region at 127 °C is plotted for densities ρ between 0.15 and 0.65 g cm⁻³ corresponding to pressure values between 193 and 2116 bar. The signal-to-noise ratio of these spectra is lower than in the first overtone spectra. This is because the optical path length has not been increased enough to compensate for the enormous reduction of vibrational intensity from the first to the second overtone, where ε changes by about two orders of magnitude. For optical path lengths of about 20 mm, the absorbance of CO at a density of 0.15 g cm⁻³ and a temperature of 127 °C, corresponding to 193 bar, (see the bottom curve in Fig. 6.2-2) is below 0.02. High-resolution, low-pressure NIR spectra therefore require fairly long optical paths.

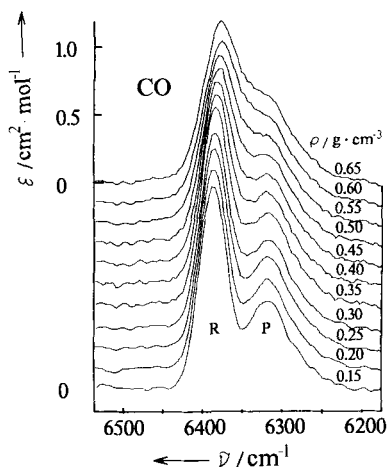


Figure 6.2-2 Molar absorption coefficient ε of the stretching second overtone of pure carbon monoxide at 127 °C and various densities ρ between 0.15 g cm⁻³ (193 bar) and 0.65 g cm⁻³ (2116 bar).

The positions of individual rotational-vibrational lines, which are known for both the first and the second overtone of gaseous CO, may be used to describe the vibrational bandshape at high density. According to a model developed by Bouanich et al. (1981, 1983), the band contour, expressed as the reduced molar absorption coefficient ε_n , is calculated as the sum of the individual lines in the gas phase spectrum.

$$\varepsilon_n(\tilde{\nu}) = \varepsilon(\tilde{\nu}) / B(0 \rightarrow v) \quad (6.2-2)$$

where $B(0 \rightarrow v)$ is the vibrational intensity of the $(v-1)$ th overtone, and the vibrational intensity B of a given mode is defined as:

$$B = \int \varepsilon(\tilde{\nu}) d\tilde{\nu} \quad (6.2-3)$$

The half-widths of the lines in the gas phase spectrum are assumed to be proportional to the density. The model contains only one adjustable parameter, by which the band shape of individual lines can be varied between a Lorentzian and a nearly Gaussian shape. Fig. 6.2-3 (Buback et al., 1985) shows that spectra calculated according to this model (data points in Fig. 6.2-3) are in good agreement with the experimental spectra (solid curves). A CO density of 0.2 g cm^{-3} at 227°C corresponds to a pressure of 355 bar. In other words, this model, which, apart from a single adjustable parameter, is based only on spectroscopic data derived from the gas phase spectrum, can be applied over an extended region of states. The success of this simple model in describing spectra of compressed carbon monoxide is certainly due to the absence of important intermolecular interactions. Additivity of modified gas phase rotational-vibrational lines to yield the band contour in the compressed state can not be expected with strongly polar materials.

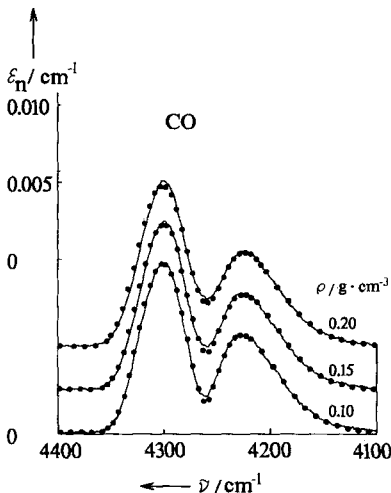


Figure 6.2-3 Comparison of observed line shapes (solid curves) with those calculated (data points) according to the model by Bouanich et al. (1981, 1983) for the first overtone absorption of pure carbon monoxide at 227°C and various densities ρ .

The pronounced *P* and *R* branch contours in the first and second overtone spectra of CO (Figures 6.2-1 and 6.2-2) clearly indicate appreciable rotational freedom in dense carbon monoxide. The wavenumbers of maximum absorption in the *P* and in the *R* branch, $\tilde{\nu}_P(\max)$ and $\tilde{\nu}_R(\max)$, of the first overtone (Fig. 6.2-4) and of the second overtone (Fig. 6.2-5) at various temperatures are plotted as a function of the pure carbon monoxide density. As is to be expected, the separation between these two maxima increases with the temperature. In all experimental spectra, the solid line in both figures indicates the arithmetic mean, $\tilde{\nu}_m$, of the maximum positions of the *P* and the *R* branch. $\tilde{\nu}_m$ slightly decreases with the density but is independent of the temperature. The straight line formed by $\tilde{\nu}_m$ in Fig. 6.2-4 can be extrapolated to $\tilde{\nu}_m^0 = 4261.9 \text{ cm}^{-1}$, which is very close to the literature value $\tilde{\nu}^0 = 4260.1 \text{ cm}^{-1}$ for the pure vibrational transition in the gas phase (Bouanich et al., 1981). Similarly, extrapolation of the second overtone data in Fig. 6.2-5

yields $\tilde{\nu}_m^0 = 6351.4 \text{ cm}^{-1}$, which is in good agreement with the value reported for the pure vibrational transition in the gas phase: $\tilde{\nu}^0 = 6350.8 \text{ cm}^{-1}$. (Burch and Gryvnak, 1967). Extrapolation of $\tilde{\nu}_m$ to higher densities (Figures 6.2-4 and 6.2-5) yields values (see Buback et al., 1985) which are very close to the maximum wavenumbers observed in bands with a single maximum (without *P* and *R* branch contour) in the spectra of liquid and solid carbon monoxide.

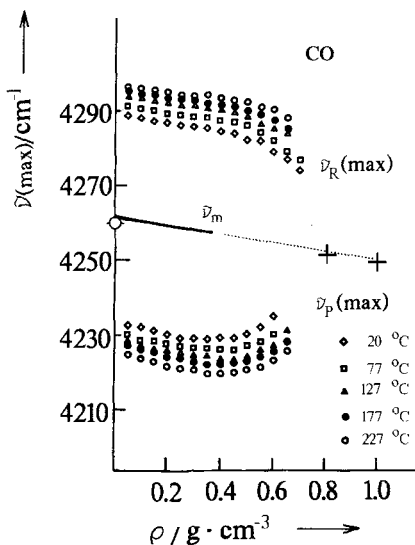


Figure 6.2-4 Density dependence of the wavenumber at the *P* and *R* branch first overtone absorption maxima, $\tilde{\nu}_P(\text{max})$ and $\tilde{\nu}_R(\text{max})$, of pure CO at temperatures between 20 and 227 °C; $\tilde{\nu}_m$ is the arithmetic mean of $\tilde{\nu}_P(\text{max})$ and $\tilde{\nu}_R(\text{max})$; + is quoted from Vu et al. (1963) and -o- from Bouanich et al. (1981).

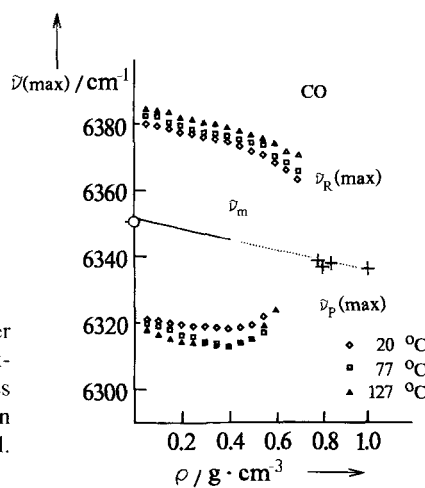


Figure 6.2-5 Density dependence of the wavenumber at the *P* and *R* branch second overtone absorption maxima, $\tilde{\nu}_P(\text{max})$ and $\tilde{\nu}_R(\text{max})$, of pure CO at temperatures between 20 and 127 °C; $\tilde{\nu}_m$ is the arithmetic mean of $\tilde{\nu}_P(\text{max})$ and $\tilde{\nu}_R(\text{max})$; + is quoted from Vu et al. (1963) and -o- from Burch and Gryvnak (1967).

Inspection of the density and the temperature dependence of the vibrational intensity B (see Eq. 6.2-3) provides further evidence of the weakness of intermolecular interactions in compressed carbon monoxide. Thus, the spectroscopic properties in the dense fluid phase are either quite similar to the corresponding gas phase values or are closely related to these values and may be derived from data of the gas phase spectrum. Fig. 6.2-6 shows the density dependence of the reduced vibrational intensity for the first and second overtones of CO.

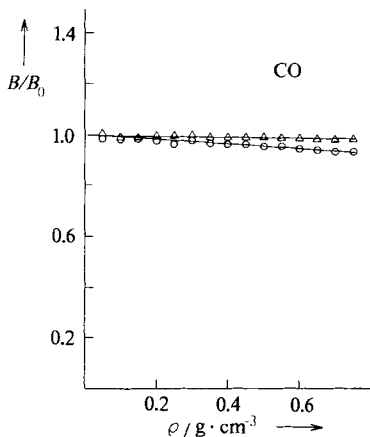


Figure 6.2-6 Density dependence of the reduced vibrational intensity B/B_0 of the first overtone (triangles) and second overtone (circles) of pure CO; B_0 is the respective vibrational intensity in the gas phase.

B_0 is the vibrational intensity in the gaseous state. The B/B_0 values are independent of the temperature, at least between 25 and 227 °C, and decrease only slightly with increasing density (Buback et al., 1985). The vibrational intensity of the first overtone is reduced by less than 2 per cent in the experimental density range. An (almost) constant value of B is important for a quantitative spectroscopic analysis covering an extended region of states, because at a known optical path length l , the concentration c can unambiguously be determined from the measured integrated absorbance (see Eqs. 6.2-1 and 6.2-3):

$$c = (B \cdot l)^{-1} \int A(\tilde{\nu}) d\tilde{\nu} \quad (6.2-4)$$

It has been found that the near-infrared spectra of even polar materials show little variation with the density and the temperature (Luck, 1965; Luck and Ditter, 1968; Buback, 1991). This is in contrast to the IR spectra, e.g., those of oxygen-hydrogen stretching fundamentals (Franck and Roth, 1967) and of pure hydrogen chloride (Buback and Franck, 1971), in which changes of B by several hundred per cent are observed between gaseous and liquid states (see Section 6.7.3). The additional advantages of NIR for quantitative

purposes result from the fact that the molar absorption coefficient ε decreases by several orders of magnitude toward higher overtones and combination modes. In Fig. 6.2-7, the CO absorption at a density of 0.15 g cm^{-3} and at 127°C is shown in the fundamental and the first and second stretching overtone regions. A logarithmic scale was chosen for the ordinate in order to plot the spectra, whose vibrational intensities differ considerably, in one coordinate system.

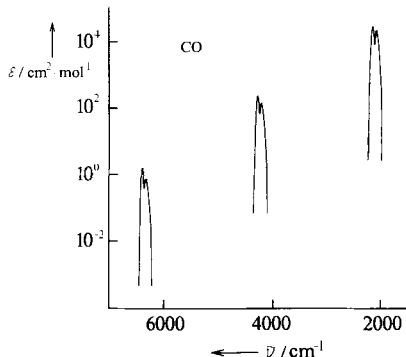


Figure 6.2-7 Molar absorption coefficient ε of pure CO (density 0.15 g cm^{-3} , 127°C) in the fundamental as well as the first and second stretching overtone regions.

There are several ways of taking advantage of this appreciable variation of ε .

I. If CO concentrations are to be measured spectroscopically during a chemical process or in chemical equilibrium or phase equilibrium studies, quite different optical path lengths l and thus reactor dimensions may be used. As an example, l is calculated for a system where the CO concentration is 0.15 g cm^{-3} . In order to ensure the good quality of the spectra, the absorbance at the band maxima should not exceed $A_{max} = 1$. With this limiting absorbance, the optical path lengths calculated from the ε values in the band maxima (Fig. 6.2-7) are 0.066 mm, 7.9 mm, and 1120 mm, respectively, in the fundamental, first, and second overtone region.

II. If a Fourier transform interferometer is available, which scans the entire wavenumber range depicted in Fig. 6.2-7, the dynamic range for quantitative analysis can be considerably increased. Low concentrations, e.g., of products during the initial period of a reaction, are measured in the fundamental or first overtone region; whereas high concentrations, e.g., of starting materials in the beginning and products at the end of reactions, are detected via the second overtone spectrum. In the case of CO, absorbance at the band maxima of $A_{max} = 1$, at an arbitrarily chosen path length of 250 mm, is brought about by CO concentrations of $3.9 \cdot 10^{-5} \text{ g cm}^{-3}$, $4.7 \cdot 10^{-3} \text{ g cm}^{-3}$, and 0.67 g cm^{-3} in the fundamental, first, and second overtone mode, respectively. The same type of arguments (I and II) applies to almost all materials (see also Section 6.7.4), which demonstrates the extended applicability of near-infrared spectroscopy in quantitative *on-line* analysis.

The vibrational intensities $B(0 \rightarrow v)$ of fundamental and overtone modes may be related to the electric dipole moment function $M(r)$ around the equilibrium internuclear distance r_e of the diatomic molecule (Chackerian, 1976) via rotationless matrix elements

$R(0 \rightarrow v)$. The dipole moment function is usually expressed as a power series in terms of the reduced displacement $x = (r - r_e)/r_e$:

$$M(x) = \sum_i M_i x^i.$$

There are equations which relate the rotationless matrix elements to the dipole moment derivatives (Singh and Luck, 1981a, 1981b). Analysis of the vibrational intensities of the first and second overtone of gaseous carbon monoxide, together with the B -value of the fundamental mode according to Chackerian and Tipping (1983), yields the following expression (Buback et al., 1985) for the dipole moment function:

$$M(x) = M_o + 3.653x - 0.255x^2 - 3.340x^3.$$

These data are in reasonable agreement with dipole moment derivatives obtained by ab initio calculations (Werner, 1981): $M_1 = 3.587$ D, $M_2 = -0.120$ D, and $M_3 = -3.760$ D, where the dipole moment is given in Debye units (1 D = $3.338 \cdot 10^{-30}$ C m).

Fig. 6.2-8 shows the NIR absorbance around 5000 cm^{-1} of pure CO_2 at 77°C (Buback et al., 1986a) for several densities varying between 0.1 g cm^{-3} (54 bar) and 1.2 g cm^{-3} (2300 bar) from bottom to top in steps of 0.1 g cm^{-3} . The pressure-broadened bands are slightly shifted in vertical direction and arranged so as to avoid too much overlap. The band system in Fig. 6.2-8, which consists of three main components, has been assigned to the $2\nu_1 + \nu_3$, $\nu_1 + 2\nu_2^0 + 2\nu_3$, and $4\nu_2^0 + \nu_3$ combination modes, which are coupled via Fermi resonance. The sequence of spectra reveals a transition from bands with P and R type contours at lower density to single bands at higher density. Additional weak bands or shoulders occur at the highest densities. The components at 4808 cm^{-1} and 5123 cm^{-1} have been assigned to hot-band transitions (Herzberg, 1945).

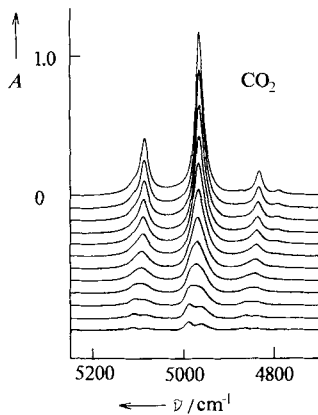


Figure 6.2-8 Near-infrared absorbance of pure CO_2 at 77°C and at densities varying - from bottom to top - in steps of 0.1 g cm^{-3} between 0.1 g cm^{-3} (54 bar) and 1.2 g cm^{-3} (2300 bar).

Fig. 6.2-9 shows corresponding NIR spectra of pure CO₂ at 127 °C in the wavenumber range from 6000 to 6600 cm⁻¹ (Buback et al., 1986b). From bottom to top, the density varies between 0.1 g cm⁻³ (66 bar) and 1.2 g cm⁻³ (3100 bar). The band system has been assigned to $3\nu_1 + \nu_3$, $2\nu_1 + 2\nu_2^0 + \nu_3$, $\nu_1 + 4\nu_2^0 + \nu_3$, and $6\nu_2^0 + \nu_3$ coupled via Fermi resonance. Toward higher density, the contour of each of the main bands is gradually transformed from a *P* and *R* branch envelope into a single, fairly symmetric component. Additional weak bands are observed at the highest densities. The bands at 6190 cm⁻¹ and 6530 cm⁻¹ have been assigned to hot-band transitions (Rothman and Young, 1981). The spectra in Figures 6.2-8 and 6.2-9 demonstrate that higher order bending overtones contribute significantly to the absorption of (lower order) stretching combination modes when vibrational intensity is exchanged by Fermi resonance.

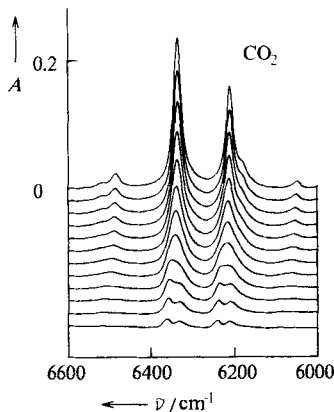


Figure 6.2-9 Near-infrared absorbance of pure CO₂ at 127 °C and at densities varying - from bottom to top - in steps of 0.1 g cm⁻³ between 0.1 g cm⁻³ (66 bar) and 1.2 g cm⁻³ (3100 bar).

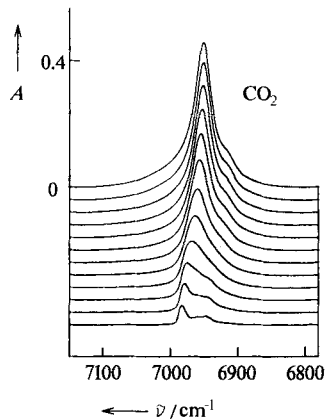


Figure 6.2-10 Near-infrared absorbance of the stretching second overtone $3\nu_3$ of pure CO₂ at 77 °C and at densities varying - from bottom to top - in steps of 0.1 g cm⁻³ between 0.1 g cm⁻³ (54 bar) and 1.2 g cm⁻³ (2300 bar).

Fig. 6.2-10 shows the absorbance of the second overtone stretching mode $3\nu_3$ of CO₂ at 77 °C at densities varying from bottom to top, in steps of 0.1 g cm⁻³ between 0.1 g cm⁻³ and 1.2 g cm⁻³. As the density increases, the band contour with a pronounced R branch at 6980 cm⁻¹ is gradually transformed into an intense band with a low wavenumber shoulder. Closer inspection of the band shape at different temperatures and pressures reveals that, in addition to the (00⁰3) - (00⁰0) Σ - Σ transition, a Π - Π hot-band transition, (00¹3) - (00¹0), with P and R branches at around 6920 cm⁻¹ and 6950 cm⁻¹, respectively, contributes to the absorption (Buback et al., 1986b).

The vibrational intensities and their dependence on the temperature and the pressure are of special interest to quantitative analysis covering an extended region of states. Fig. 6.2-11 shows the vibrational intensity of the $3\nu_3$ second overtone, B (6700-7300), which has been determined by integration of the experimental absorbance spectra in the wavenumber region between 6700 cm⁻¹ and 7300 cm⁻¹. The data points are mean values for the temperature range from 25 °C to 227 °C. A temperature dependence of the vibrational intensity at constant density cannot be detected.

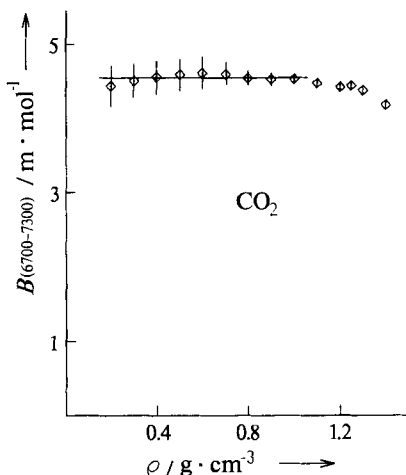


Figure 6.2-11 Density dependence of the vibrational intensity of pure CO₂ in the wavenumber range from 6700 cm⁻¹ to 7300 cm⁻¹. The data points are mean values for the temperature range between 25 °C and 227 °C.

Up to a density of about 1.0 g cm⁻³, the vibrational intensity is found to be independent of the temperature and the density (or pressure). At the highest densities, B (6700-7300) slightly decreases. This behavior, which is also observed in several other near-infrared bands of CO₂ (Buback et al., 1986a, 1986b), seems to indicate that repulsive interactions are becoming important in highly compressed fluid CO₂. This assumption is supported by an inspection of the density dependence of the band maximum positions. In Fig. 6.2-12, the wavenumbers of maximum absorption in the P and the R branch, $\tilde{\nu}_P(\max)$ and $\tilde{\nu}_R(\max)$, of the component around 4980 cm⁻¹ (see Fig. 6.2-8) are plotted versus the density. The arithmetic mean values of the P and R branch maxima, $\tilde{\nu}_m$, which are shown as full circles in the lower density spectra, linearly decrease with the density. They can be

extrapolated to the experimental band maximum positions at densities above 0.4 g cm⁻³, where the *P* and *R* branch contour has turned into a single maximum. At densities above 1.0 g cm⁻³, $\tilde{\nu}(\text{max})$ becomes independent of the density and may even return to higher wavenumbers at the highest densities. The $\tilde{\nu}(\text{max})$ vs. density plots of the other CO₂ modes shown in Figures 6.2-9 and 6.2-10 exhibit the same type of behavior. A blue shift of vibrational modes with increasing pressure (density) has been attributed to essential contributions of repulsive interactions (Benson and Drickamer, 1957; Wiederkehr and Drickamer, 1958).

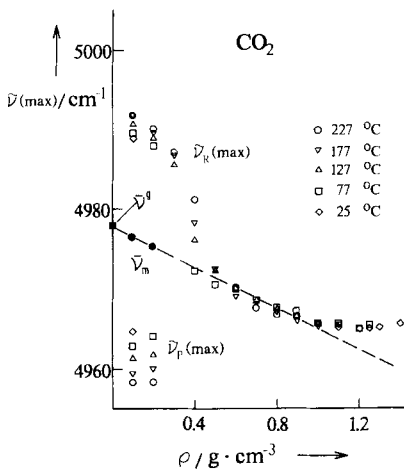


Figure 6.2-12 Density dependence of the band maximum position, $\tilde{\nu}(\text{max})$, of the Fermi triad component with wavenumber $\tilde{\nu}^g = 4977.8 \text{ cm}^{-1}$ in the gas phase spectrum of pure CO₂ at temperatures between 25 and 227 °C; $\tilde{\nu}_m$ is the arithmetic mean of the corresponding *P* and *R* branch maxima, $\tilde{\nu}_P(\text{max})$ and $\tilde{\nu}_R(\text{max})$.

As an example of near-infrared spectra of polar molecules, Fig. 6.2-13 shows the absorbance of pure ammonia in the wavenumber region from 3900 cm⁻¹ to 5600 cm⁻¹ at 250 °C and at various densities, increasing in steps of 0.025 g cm⁻³ from 0.025 g cm⁻³ (lowest curve) to 0.525 g cm⁻³ (Rohde, 1989; Buback, 1991). The band with an absorption maximum around 4400 cm⁻¹ has been assigned to the combination mode $\nu_2 + \nu_3$; the band around 5000 cm⁻¹ has been assigned to $\nu_3 + \nu_4$ (Herzberg, 1945). Integration of the curves in Fig. 6.2-13 and reduction to a unit path length and a unit concentration (or density) yields a vibrational intensity for the sum of both combination modes which, at an experimental accuracy of a few per cent, is independent of the density. In contrast, the vibrational intensity of the N–H stretching fundamentals around 3200 cm⁻¹ changes by about 300 per cent between the gaseous and the liquid like state.

Vibrations with *B* values that are independent of or only slightly dependent on the state of the system, e.g., on the temperature, pressure, concentration, and solvent properties, extend the usefulness of these modes for quantitative analysis. The experimental data which are presently available indicate that a large number of NIR vibrations show this kind of behavior. Whether or to which extent *B* of a certain vibration is constant, however,

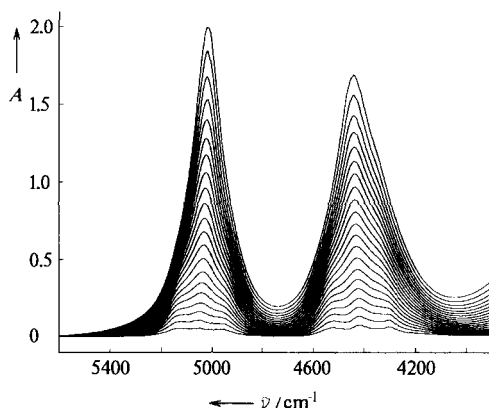


Figure 6.2-13 Near-infrared absorbance of the $\nu_2 + \nu_3$ and $\nu_3 + \nu_4$ modes of pure ammonia at 250 °C at densities varying - from bottom to top - in steps of 0.025 g cm⁻³ between 0.025 g cm⁻³ (58 bar) and 0.525 g cm⁻³ (1810 bar).

has to be studied in individual experiments. The accuracy of quantitative analysis via NIR spectroscopy obviously depends on the quality of the procedure applied in determining B .

The near-infrared spectra of even larger molecules consist of relatively few components. Problems may arise in connection with the correct assignment of the observed bands. Figures 6.2-14 and 6.2-15 show the absorbance of the dense fluid ethene around 6000 cm⁻¹ and around 8800 cm⁻¹ at 2500 bar and 220 °C. It is very helpful to measure spectra over an extended pressure range, since bands in the dense state are easily correlated with gaseous absorption components which, in general, are well assigned. In addition, bands which are symmetry-forbidden in the gaseous state can be detected in a sequence of spectra recorded at increasing density. This information, combined with

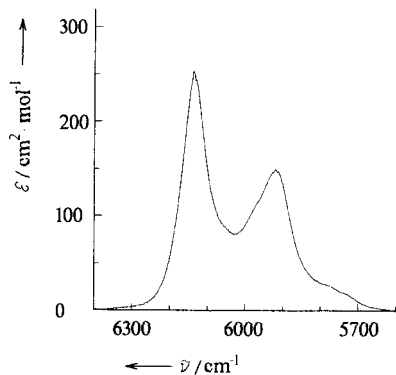


Figure 6.2-14 Molar absorption coefficient ε of pure ethene $\nu(\text{CH})$ first overtone at 220 °C and 2500 bar.

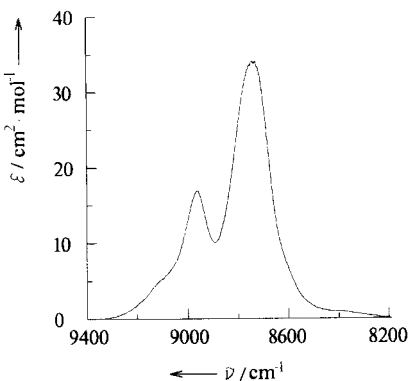


Figure 6.2-15 Molar absorption coefficient ε of pure ethene $\nu(\text{CH})$ second overtone at 220 °C and 2500 bar.

the well-established arguments of group theory, facilitates the assignment of NIR modes in cases such as ethene, where twelve fundamentals have to be considered.

The intense band at 6140 cm^{-1} (Fig. 6.2-14) has been assigned to the combination mode $\nu_5 + \nu_9$ (B_{3u}), with perhaps some minor contribution from $\nu_1 + \nu_9$ (B_{2u}). The band at 5920 cm^{-1} is caused by the $\nu_2 + \nu_3 + \nu_{11}$ and $\nu_2 + \nu_6 + \nu_9$ vibrations. The 8970 cm^{-1} band in Fig. 6.2-15 is attributed to the absorption of $2\nu_1 + \nu_{11}$ (B_{3u}), with contributions from the $3\nu_9$ (B_{2u}) second overtone. The absorption around 8740 cm^{-1} is explained by an overlap of (B_{3u})-species: $2\nu_{11} + \nu_3 + \nu_{12}$ and $3\nu_{11}$ with (B_{1u})-species: $2\nu_5 + \nu_2 + \nu_7$ and $2\nu_9 + \nu_2 + \nu_7$ (Nees and Buback, 1976).

6.2.3 Near-infrared spectra of selected organic compounds

The advantages of using NIR for quantitative spectroscopic analysis have been outlined in Sections 6.2.1 and 6.2.2. For this application the detailed assignment of overtone and combination modes is less important than precise knowledge of the molar absorption coefficients and of the vibrational intensities of a large number of chemical compounds over an extended NIR range. The NIR library comprising digital spectra of approximately 2000 organic materials (mostly pure liquids at ambient temperature and pressure) is available in digital form from Chemical Concepts (Weinheim, F.R.G) and as a hardcopy (Buback and Vögele, 1993). The spectra were compiled from twice as many Fourier-transform NIR spectra. The spectrum of each substance was measured at two optical path lengths, 0.5 mm and 20 mm. The library contains spectra of each substance, covering the overlapping regions between 3800 cm^{-1} and 7200 cm^{-1} and from 6300 cm^{-1} to 10500 cm^{-1} . The spectral resolution is 2 cm^{-1} , and zero filling of 2 during Fourier transformation provides a digital resolution of 1 cm^{-1} . The spectra are stored as absorbance versus wavenumber data. Molar absorption coefficients and vibrational intensities are easily and directly obtained from the precisely known optical path length and from the

known densities of the pure liquids. In addition, the NIR library also contains a peak table showing the relative intensities of the absorption components in each spectrum, as well as an info file and a structure file for each substance.

This text presents NIR spectra of a few common organic materials. In order to facilitate the assignment of bands, spectra of compounds belonging to homologous series are plotted together (Hitzeroth-Halfbrodt, 1988). A detailed discussion of near-infrared absorption due to C–H vibrations has been presented by Goddu (1960).

Fig. 6.2-16a shows a series of near-infrared spectra of n-alkanes in the region of the first overtone of the C–H stretching modes. The substances (from bottom to top) are C_5H_{12} , C_6H_{14} , C_7H_{16} , C_8H_{18} , C_9H_{20} , $C_{10}H_{22}$, $C_{11}H_{24}$, $C_{12}H_{26}$, and $C_{15}H_{32}$. All the spectra were obtained using pure liquids at ambient pressure and temperature, with an optical path length of 0.5 mm. The absorption components at 5785 cm^{-1} and 5672 cm^{-1} have been assigned, respectively, to the first overtone of antisymmetric and symmetric C–H stretches of CH_2 groups. The spectra of smaller n-alkane molecules are more complex. $n-C_5H_{12}$ (lowest curve) shows additional absorption, caused by terminal CH_3 groups.

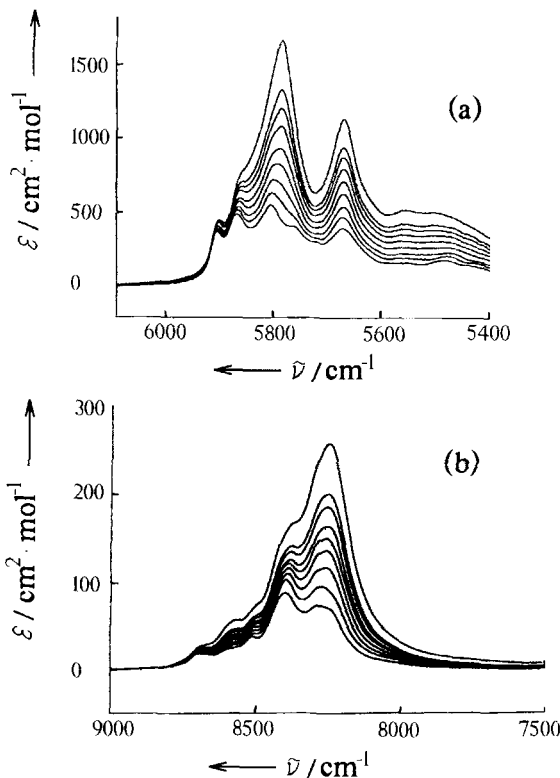


Figure 6.2-16 Molar absorption coefficient ε of the n-alkanes C_5H_{12} (lowest curve), C_6H_{14} , C_7H_{16} , C_8H_{18} , C_9H_{20} , $C_{10}H_{22}$, $C_{11}H_{24}$, $C_{12}H_{26}$ and $C_{15}H_{32}$ (highest curve) (a) wavenumber range of the C–H stretching first overtones, (b) wavenumber range of the C–H stretching second overtones.

Fig. 6.2-16b shows the molar absorption coefficients of the n-alkanes depicted in Fig. 6.2-16a in the region of the second overtone of the C–H stretching modes. The optical path length is 20 mm. The absorption of the 2nd overtone of the C–H stretches of CH₂ groups at 8250 cm⁻¹ becomes increasingly dominant as the chain length increases. The absorptions at high wavenumbers shown in Fig. 6.2-16b may be interpreted as second overtones of C–H absorptions of CH₃ groups and as combination modes, including C–H stretches of CH₃ units.

Fig. 6.2-17 shows the absorption in the regions of the first and second overtones of C–H stretches in a number of 1-alkenes: C₅H₁₀, (lowest curve), C₆H₁₂, C₇H₁₄, C₈H₁₆, C₁₀H₂₀, C₁₂H₂₄, C₁₄H₂₈, and C₁₈H₃₆, (highest curve). In those wavenumber regions where C–H stretching overtone and combination modes of CH groups in saturated CH₂ and CH₃ entities are observed, the alkene spectra are very similar to the corresponding alkane curves shown in Fig. 6.2-16. Additional absorption components, associated with C–H stretching modes involving unsaturated (sp²) carbon atoms, are observed in the first overtone region of C–H stretches (Fig. 6.2-17a) around 6115 cm⁻¹ and in the

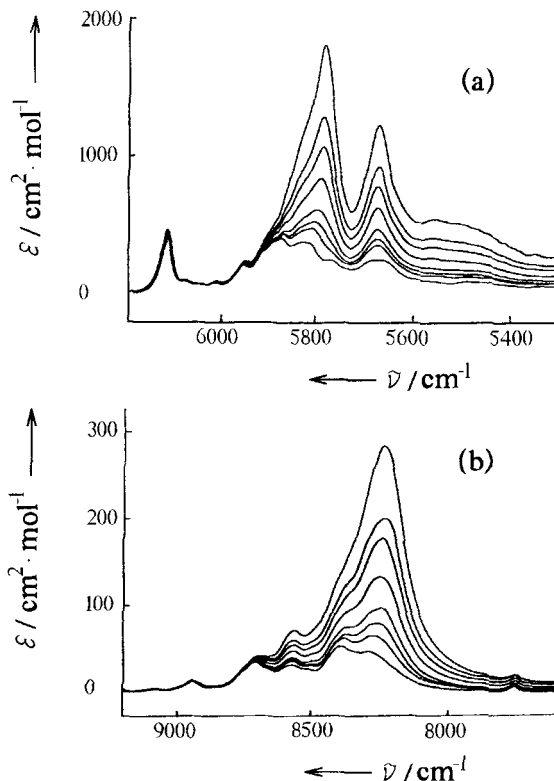


Figure 6.2-17 Molar absorption coefficient ε of various 1-alkenes: C₅H₁₀, (lowest curve), C₆H₁₂, C₇H₁₄, C₈H₁₆, C₁₀H₂₀, C₁₂H₂₄, C₁₄H₂₈, and C₁₈H₃₆, (highest curve) (a) wavenumber range of the C–H stretching first overtones, (b) wavenumber range of the C–H stretching second overtones.

second overtone region (Fig. 6.2-17b) around 8950 cm^{-1} . These two absorptions are well separated from bands assigned to saturated hydrocarbons and clearly characterize double bonds through the absorption of the attached C-H groups.

Fig. 6.2-18 shows the first and second overtone regions of C-H stretching modes in the near-infrared spectra of three 1-alkynes (C_5H_8 , C_6H_{10} , C_7H_{12} , from bottom to top). The C-H stretching modes of triply bound C-H groups are shifted to still higher wavenumbers. The first overtone is observed around 6525 cm^{-1} (Fig. 6.2-18a), and the second overtone is found around 9637 cm^{-1} (Fig. 6.2-18b). These absorptions are thus distinctly set off from those of C-H groups whose carbon atom is involved in single or double bonds.

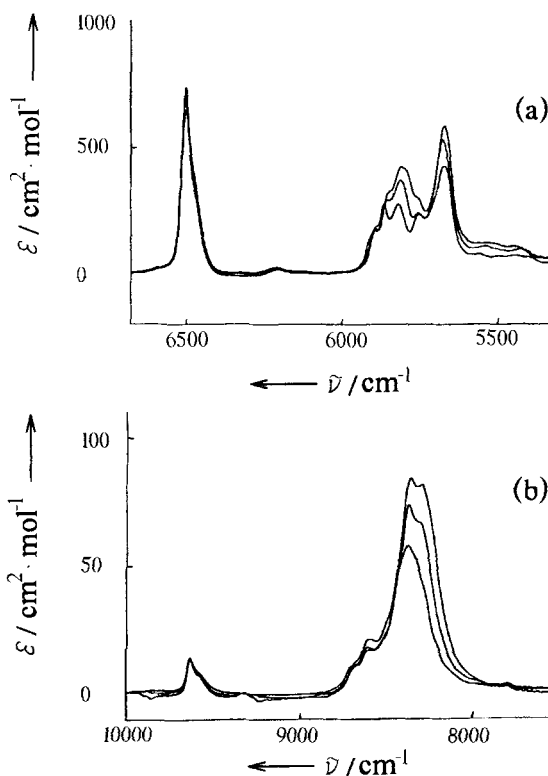


Figure 6.2-18 Molar absorption coefficient ε of various 1-alkynes: C_5H_8 , C_6H_{10} , C_7H_{12} from bottom to top (a) wavenumber range of the C-H stretching first overtones, (b) wavenumber range of the C-H stretching second overtones.

The characteristic near-infrared absorption associated with the first and second overtone of C-H stretches in phenyl groups (Ph) around 5950 cm^{-1} and around 8760 cm^{-1} , respectively, is shown in Figures 6.2-19a and 6.2-19b. The curves reflect the absorbance of several n-alkyl benzenes: $\text{C}_2\text{H}_5\text{Ph}$ (lowest curve), $\text{C}_3\text{H}_7\text{Ph}$, $\text{C}_4\text{H}_9\text{Ph}$, $\text{C}_5\text{H}_{11}\text{Ph}$, $\text{C}_6\text{H}_{13}\text{Ph}$, $\text{C}_7\text{H}_{15}\text{Ph}$, $\text{C}_8\text{H}_{17}\text{Ph}$, $\text{C}_{10}\text{H}_{21}\text{Ph}$, and $\text{C}_{12}\text{H}_{25}\text{Ph}$, (highest curve).

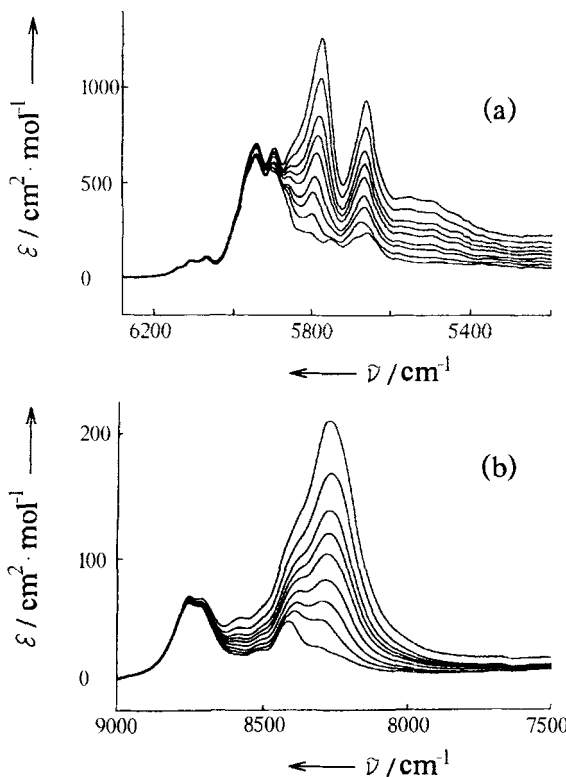


Figure 6.2-19 Molar absorption coefficient ε of various n-alkyl benzenes: $\text{C}_2\text{H}_5\text{Ph}$ (lowest curve), $\text{C}_3\text{H}_7\text{Ph}$, $\text{C}_4\text{H}_9\text{Ph}$, $\text{C}_5\text{H}_{11}\text{Ph}$, $\text{C}_6\text{H}_{13}\text{Ph}$, $\text{C}_7\text{H}_{15}\text{Ph}$, $\text{C}_8\text{H}_{17}\text{Ph}$, $\text{C}_{10}\text{H}_{21}\text{Ph}$, and $\text{C}_{12}\text{H}_{25}\text{Ph}$ (highest curve); Ph = C_6H_5 (a) wavenumber range of the C-H stretching first overtones, (b) wavenumber range of the C-H stretching second overtones.

The first and second overtone regions of C-H stretching modes in the NIR absorption spectra of several 1,ω-dibromoalkanes are shown in Figures 6.2-20a and 6.2-20b. The compounds are: $\text{BrC}_4\text{H}_8\text{Br}$ (lowest curve), $\text{BrC}_5\text{H}_{10}\text{Br}$, $\text{BrC}_6\text{H}_{12}\text{Br}$, $\text{BrC}_8\text{H}_{16}\text{Br}$, and $\text{BrC}_9\text{H}_{18}\text{Br}$ (highest curve). In these spectra, a C-H absorption which is characteristic of CH_2Br units is found in both absorption regions.

Knowledge of the vibrational intensity B is of primary importance to quantitative analysis. For the first and second overtones of C-H stretches, this quantity has been studied on saturated carbon atoms in several homologous series (Buback and Vögele, 1988; Hitzeroth-Halfbrodt, 1988). Fig. 6.2-21 shows B as a function of the number of (saturated) C-H bonds, n , for the series of n-alkanes which is presented in Fig. 6.2-16. The first overtone region (Fig. 6.2-21a) is integrated between 5300 and 6100 cm^{-1} against a horizontal base-line through the spectral data points around 6100 cm^{-1} . The linear B versus n relation passing through the origin of the coordinate system demonstrates that the vibrational intensity $B^{\text{C}-\text{H}}$ per C-H bond is constant. (A quantity corresponding to

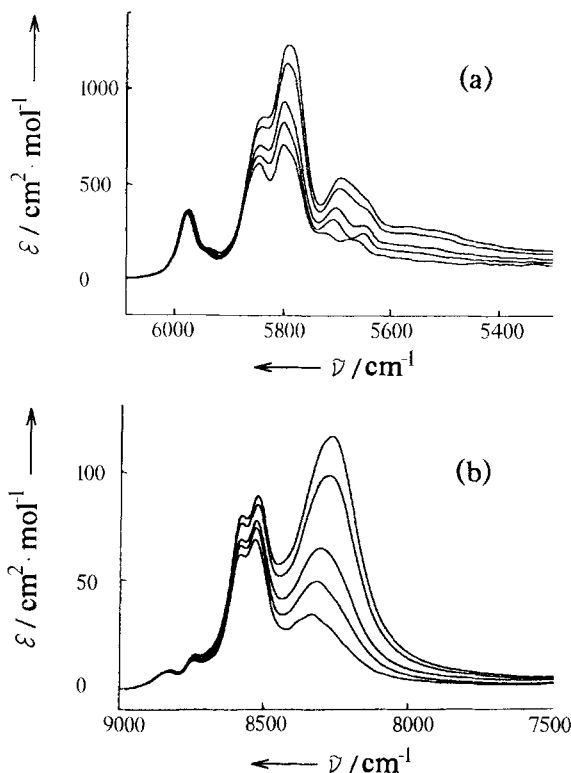


Figure 6.2-20 Molar absorption coefficient ε of various 1, ω -dibromoalkanes: BrC₄H₈Br (lowest curve), BrC₅H₁₀Br, BrC₆H₁₂Br, BrC₈H₁₆Br, and BrC₉H₁₈Br (highest curve) (a) wavenumber range of the C–H stretching first overtones, (b) wavenumber range of the C–H stretching second overtones.

$B^{\text{C}-\text{H}}$ has already been introduced and discussed by Lippert and Mecke (1951)). The same result is obtained from the B versus n plot for the second overtone regions of C–H stretches between 7500 and 9000 cm^{-1} , as shown by Fig. 6.2-21b.

Corresponding B versus n plots have been obtained for several homologous series of substituted alkanes, e.g., alkyl nitriles (Fig. 6.2-22) and alkyl carboxylic acid chlorides (Fig. 6.2-23). The first overtones of saturated C–H stretching in alkyl nitriles are integrated between 5320 and 6100 cm^{-1} (Fig. 6.2-22a) and those of alkyl carboxylic acid chlorides are integrated between 5200 and 6200 cm^{-1} (Fig. 6.2-23a). In the second overtone region (Figures 6.2-22b and 6.2-23b), the absorbance of saturated C–H stretches of all substances is integrated between 7500 and 9000 cm^{-1} . As with n-alkanes, the linear relation between B and n indicates that one $B^{\text{C}-\text{H}}$ value adequately represents the vibrational intensity B associated with the absorption of C–H bonds in which C is a saturated carbon atom. The $B^{\text{C}-\text{H}}$ values for the same overtone do not significantly change upon substitution. In the second overtone region between 7500 and 9000 cm^{-1} of very

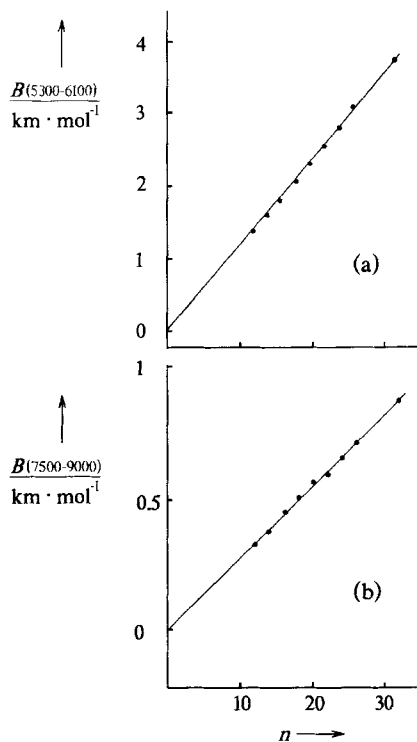


Figure 6.2-21 Vibrational intensity B of C-H modes of n-alkanes, plotted as a function of the number of C-H bonds n (a) C-H stretching first overtone region between 5300 and 6100 cm^{-1} (b) C-H stretching second overtone region between 7500 and 9000 cm^{-1} .

different materials, such as alkanes, alkenes, alkynes, nitriles, ketones, acid chlorides, amines, and alkanols, the vibrational intensity $B_{\text{C-H}}$ per C-H bond involving a saturated carbon atom (as plotted in Figures 6.2-21b, 6.2-22b, and 6.2-23b) is found to vary by no more than ± 10 per cent. This opens up interesting applications in quantitative analysis.

6.2.4 Quantitative analysis via near-infrared spectroscopy

Since the vibrational intensities B of characteristic near-infrared bands are independent or only slightly dependent on the state of the system, e.g., gaseous or liquid like density (see Section 6.2.2), NIR is well suited to quantitative analysis up to high pressures and temperatures. Moreover, in spectroscopic measurements covering an extended NIR wavenumber range, overtone and combination modes with very different molar absorption coefficients can be recorded simultaneously. This makes it possible to determine concentrations differing by several orders of magnitude in a single experiment (see Figs.

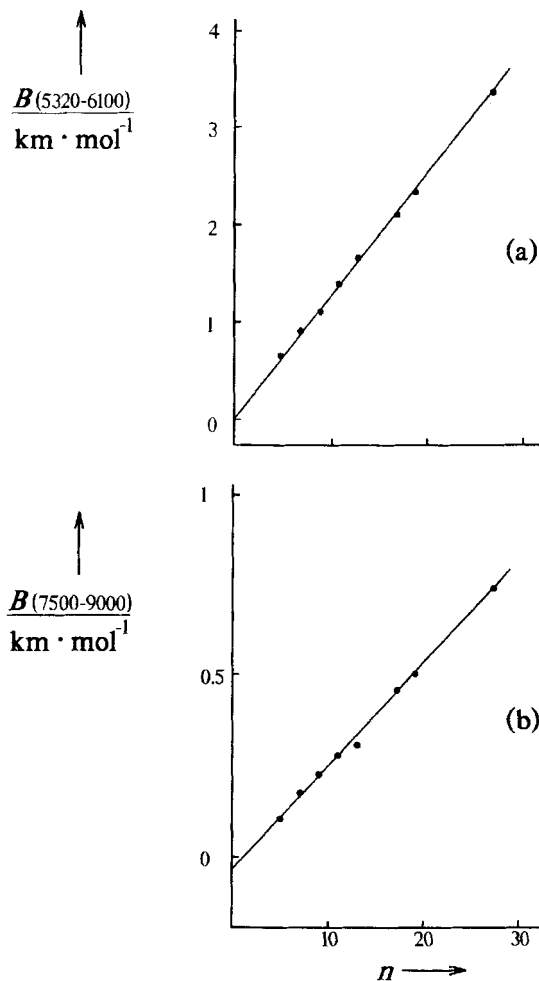


Figure 6.2-22 Vibrational intensity B of C-H modes of alkyl nitriles, plotted as a function of the number of C-H bonds n (a) C-H stretching first overtone region between 5320 and 6100 cm^{-1} (b) C-H stretching second overtone region between 7500 and 9000 cm^{-1} .

6.2-7 and 6.7-23). In addition, reasonable optical path lengths of millimeter or centimeter size may be used in NIR spectroscopy, as compared to the layers of micrometer size which are required in infrared analysis of liquid or compressed gaseous materials. Since almost all substances which are practically relevant have characteristic NIR absorption bands, quantitative analysis via near-infrared spectroscopy is generally applicable to *on-line* concentration measurements in connection with chemical reactions, chemical equilibria, and phase equilibria. Inspection of the reference NIR spectral data for the relevant chemical species shows which NIR range provides special advantages for the quantitative analysis of a particular system.

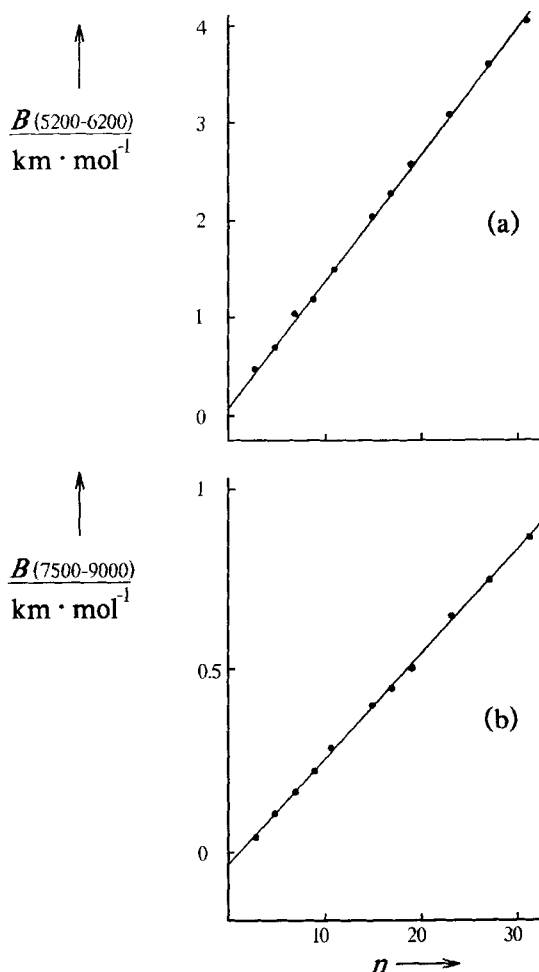


Figure 6.2-23 Vibrational intensity B of C-H modes of alkyl carboxylic acid chlorides, plotted as a function of the number of C-H bonds n (a) C-H stretching first overtone region between 5200 and 6200 cm^{-1} (b) C-H stretching second overtone region between 7500 and 9000 cm^{-1} .

The scope of this method is by far too broad to be presented in detail. The *on-line* NIR technique is especially valuable for studies under unusual or extreme conditions. The fluid phase equilibrium in the ethene-polyethylene system has been studied by Nees (1978) up to 300 °C and 3000 bar; the solubility of adamantane, of octacosane, and of squalane in fluid CO_2 up to 1000 bar has been determined NIR-spectroscopically by Swaid et al. (1985).

The potential of the NIR method for the investigation of chemical transformations is demonstrated by a few examples of polymerization reactions. Fig. 6.2-24 shows a series of NIR spectra, measured in the second overtone region of the C-H stretching modes

during an ethene homopolymerization at 190 °C and an initial pressure of 2630 bar (Brackemann et al., 1986). During the reaction, the ethene absorbance at 8740 and 8970 cm⁻¹ (see Fig. 6.2-15) decreases and the polyethylene absorbance around 8260 cm⁻¹ (see Fig. 6.2-16) increases. Starting from pure ethene, the spectra in Fig. 6.2-24 cover a conversion range up to about 80 per cent.

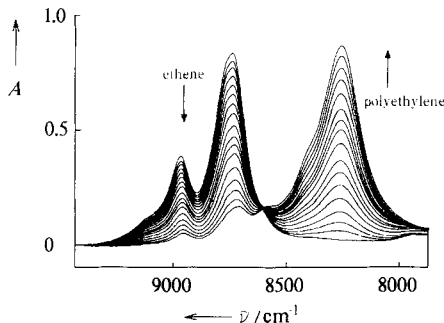


Figure 6.2-24 Near-infrared absorbance spectra, recorded during free-radical polymerization of ethene at 190 °C and 2630 bar initial pressure (the arrows indicate the direction of the absorbance change with the reaction time).

The appearance of the spectra of the reacting mixture is clear and simple, especially since the educt (ethene) contains only one type of C–H bond (C H on sp^2 -hybridized carbon atoms), which are transformed into C H involving “saturated” carbon atoms. The situation is different in polymerizations where the monomer already contains C H groups of the alkane type. This is illustrated in Fig. 6.2-25 by a series of NIR spectra, measured in the first overtone region of the C–H stretching modes during butyl acrylate homopolymerization at 70 °C (Huckestein, 1991). The initial spectrum of pure butyl acrylate, with the highest absorbance in the region of C–H modes of unsaturated carbon

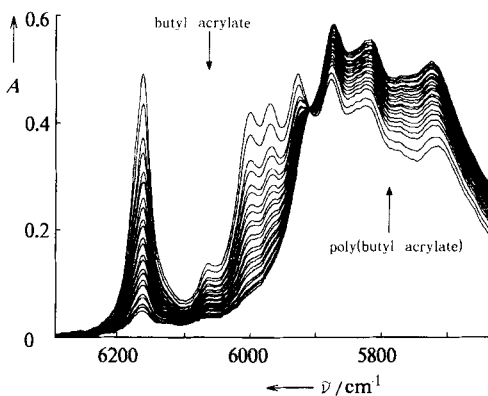


Figure 6.2-25 Near-infrared absorbance spectra, recorded during free-radical polymerization of butyl acrylate at 70 °C and one atmosphere (the arrows indicate the direction of the absorbance change with the reaction time).

atoms above 5900 cm^{-1} , already exhibits appreciable absorption in the 5700 to 5800 cm^{-1} range, where the first overtone of C-H in butyl groups is observed (see Fig. 6.2-16). The increase in absorbance around 5800 cm^{-1} is due to the formation of alkane type C-H modes during polymerization.

Fig. 6.2-26 shows NIR spectra covering the first overtone region of C-H stretching modes, measured during styrene homopolymerization at $40\text{ }^{\circ}\text{C}$ and 2000 bar. The absorption of the monomer between 6100 and 6200 cm^{-1} decreases and the bands in the region of alkane type C-H stretching modes around 5700 cm^{-1} increase during the reaction. In the 5900 to 6000 cm^{-1} range, where the first overtones of aromatic C-H stretches of monomer and polymer absorb, only minor spectral changes are observed during polymerization.

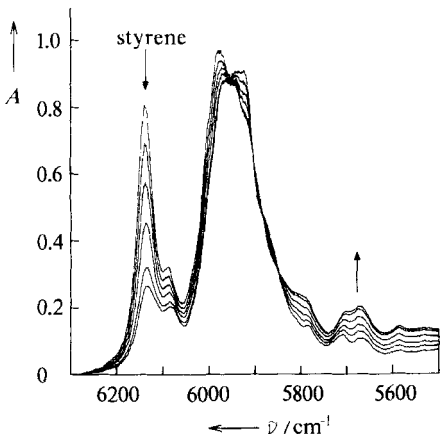


Figure 6.2-26 Near-infrared absorbance spectra, recorded during free-radical polymerization of styrene at $40\text{ }^{\circ}\text{C}$ and 2000 bar (the arrows indicate the direction of the absorbance change with the reaction time).

6.2.5 Concluding remarks

Near-infrared spectroscopy is a widely applicable analytical technique for the quantitative study of liquid and compressed gaseous systems, including fluid states, up to high pressures and temperatures. The experiments are performed with optical path lengths of at least millimeter and centimeter size. The NIR wavenumber range which can be recorded simultaneously is fairly large. This makes it possible to scan overtone and combination modes, whose vibrational intensities differ by several orders of magnitude, in one spectroscopic experiment. This provides a large dynamic range for concentration measurement. The described options are extended by recording both IR and NIR at the same time, e.g., by using a Fourier-transform instrument. Trace amounts may thus be analyzed together with the respective primary components. One example of this type of investigation is the study of chemically initiated styrene polymerization (Huckestein,

1991). By carrying out one experiment, changes of monomer and polymer and also of the initiator (azobisisobutyronitrile) are reflected in the NIR and the IR, respectively. Quantitative analysis is largely facilitated by the appearance of characteristic non-overlapping bands. On the other hand, computer programs for band separation are available. In addition, the integration of molar absorption coefficients to yield concentrations need not extend over entire bands, but may be performed over half bands or even over suitable band sections.

The assignment of NIR bands and the analysis of the NIR bandshape, band maximum positions, and vibrational intensities is equivalent to the procedures applied to study overtone and combination modes in the classical mid-infrared region.

Apart from the absorption techniques illustrated in Sections 6.2.2 - 6.2.4, NIR spectroscopy is also extensively used for reflectance measurements (Murray and Cowe, 1992). It goes without saying that advanced techniques, such as time resolved experiments, may also be performed in the NIR. This is illustrated by another example of polymerization studies. Fig. 6.2-27 shows the conversion U , induced by a single KrF (248 nm) excimer laser pulse (of about 20 ns width), during ethene-polyethylene polymerization at 190 °C and 2550 bar (Buback and Schweer, 1989). The production of radicals by the laser pulse occurs almost instantaneously at the time $t = 0$ and is much faster than even the first radical-monomer propagation step. The comparatively small conversion per pulse is measured with a time resolution of 10 µs by the NIR absorbance of polyethylene at a fixed wavenumber in the region around $8258 \pm 5 \text{ cm}^{-1}$ (see Fig. 6.2-24). The experimental assembly essentially consists of a halogen lamp, a grating monochromator, and an InSb detector (Buback et al., 1986d).

Single pulse experiments, as shown in Fig. 6.2-27, may be performed at different stages of conversion during a polymerization reaction. Analysis of the measured U versus t curves provides a very detailed picture of the polymerization kinetics, e.g., of rate coefficients as a function of monomer conversion (Buback, 1991).

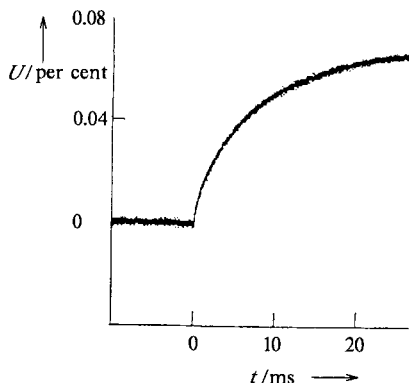


Figure 6.2-27 Time resolved near-infrared measurement (at $8258 \pm 5 \text{ cm}^{-1}$) of monomer conversion, induced by a single pulse from a KrF excimer laser (248 nm), during ethene polymerization at 190 °C and at 2550 bar (reaction mixture already containing 9.5% polyethylene before this particular pulse was applied).

6.3 Vibrational optical activity (VOA)*

The most important biological and pharmaceutical substances are chiral. Since the Contergan® tragedy it is well known that the two enantiomers of a chiral substance have profoundly different effects on organisms: only one enantiomer of Thalidomide induces fetal abnormalities. It is now commonly regarded as a professional blunder not to separate the enantiomers of a chiral medicament and test them separately for desirable and malicious effects. Unfortunately the methods for determining the absolute configuration of chiral substances are limited in both scope and number. The most accurate of the rivalling techniques, X-ray crystallography in its variety sensitive to chirality, namely the measurement of anomalous dispersion (Bijvoet et al., 1951), is tedious and needs perfect single crystals. The much less accurate method of measuring the circular dichroism (CD) in the visible and normal ultraviolet range (e.g. Snatzke, 1967; Ciardelli and Salvadori, 1973), is well suitable for the measurement of solutes, but depends on the availability of a chromophore, such as the C=O- and C=C-group. Unfortunately the electrons in the most important organic groupings, the C-C- and C H-groups, are only excited at higher energies. The transitions occur in the vacuum UV region, where they are technically less accessible and the bands overlap with each other.

The measurement of vibrational optical activity (VOA) lacks some of the severe disadvantages mentioned. Vibrational spectral bands are less likely to overlap and can be measured using two complementary techniques: namely infrared and Raman spectroscopy. They can be measured as well in the crystalline as in the liquid or gaseous state, and the techniques are applicable to solutions while nearly reaching (complemented with the appropriate theoretical models) the accurateness of the X-ray method. VOA has drawbacks too: the effects are quite small and tend to be obscured by artifacts. They are about 10^4 times weaker than the optical rotatory dispersion (ORD) and the circular dichroism (CD) in the UV-VIS range. However, this apparent disadvantage is more and more relieved by instrumental advances.

6.3.1 Vibrational circular dichroism (VCD)

6.3.1.1 Introduction

Vibrational circular dichroism (VCD) is formally an extension of the long known method of circular dichroism (Cotton, 1895), now termed electronic circular dichroism (ECD). Sometimes it is also termed infrared circular dichroism (IR-CD), though also low-lying electronic transitions occur in the infrared. That is why the first measurements of CD in the infrared spectral regions examined these transitions. The measurement of VCD began in the near infrared region and slowly advanced to longer wavelengths, until VCD was

* Section 6.3 is contributed by G. G. Hoffmann, Essen

really an infrared method. Thus it was complementary to its related technique, the measurement of Raman circular intensity difference (CID), which was first only applicable to low-wavenumber transitions and then slowly proceeded to higher-energy transitions. Though Raman CID was the first of the two types of measurement of vibrational optical activity, it was not as sensitive as VCD. Consequently applications of VCD to stereochemical problems are much longer possible than utilisations of Raman optical activity, ROA.

The supplementation of experimental VCD by *ab initio* - calculations is considerably advanced. For small molecules it is possible to calculate the theoretical VCD with sufficient precision, so that for these molecules the absolute configuration can be deduced reliably.

6.3.1.2 Instrumental techniques

As a first step towards the measurement of single molecule effects, Schrader and Korte (1972) reported the measurement of the infrared rotatory dispersion of carvone in liquid crystalline solution. They used a modified commercial spectrometer. They observed a huge effect which is not the result of the carvone itself but of the liquid crystal in which a helical arrangement (cholesteric state) is induced by the chiral solute (Sec. 4.6.4). In this case the liquid crystal acts as a kind of molecular amplifier which allows the absolute configuration of tiny amounts of solutes to be determined reliably. At about the same time Dudley et al., (1972) measured the infrared circular dichroism of (-)-menthol in a liquid crystal. Their equipment consisted of a normal infrared spectrometer supplemented by a Fresnel rhomb made from sodium chloride.

In the years to follow the key to the measurement of vibrational circular dichroism was the development of photoelastic modulators suitable for work in the infrared spectral region. The first successful measurements of circular dichroism originating from vibrational transitions in the infrared were done by Hsu and Holzwarth (1973) on thin slices of monocrystalline $\alpha\text{-NiSO}_4 \cdot 6 \text{ H}_2\text{O}$ and $\alpha\text{-ZnSeO}_4 \cdot 6 \text{ H}_2\text{O}$. For this measurements the authors used a normal dispersive IR spectrometer supplemented by a linear polarizer and a photoelastic modulator made from Germanium.

To produce circularly polarized light, it is common practice to use a linear polarizer followed by a quarter wave plate at an angle of 45° to the polarization axis of the polarizer (Sec. 3.2.3). A photoelastic modulator (PEM) is a device in which an optically isotropic element is compressed periodically to become a phase plate with an optical retardation of $\pm\pi/2$, respectively (or, using equivalent nomenclature, a wave plate with an optical retardation of $\pm\lambda/4$). The polarization is altered with the operating frequency of the PEM this way. The polarization states occurring during a modulation cycle of the PEM are shown in Fig. 6.3-1. The sine-shaped curve pictures the relative stress on the modulator element ("crystal") during two periods of vibration, the polarizations shown are valid for one wavelength only (i.e. the tuning wavelength). The radiation changes from linearly polarized light at zero phase retardation to right elliptically polarized light, and reaches right circularly polarized light at a phase retardation of exactly

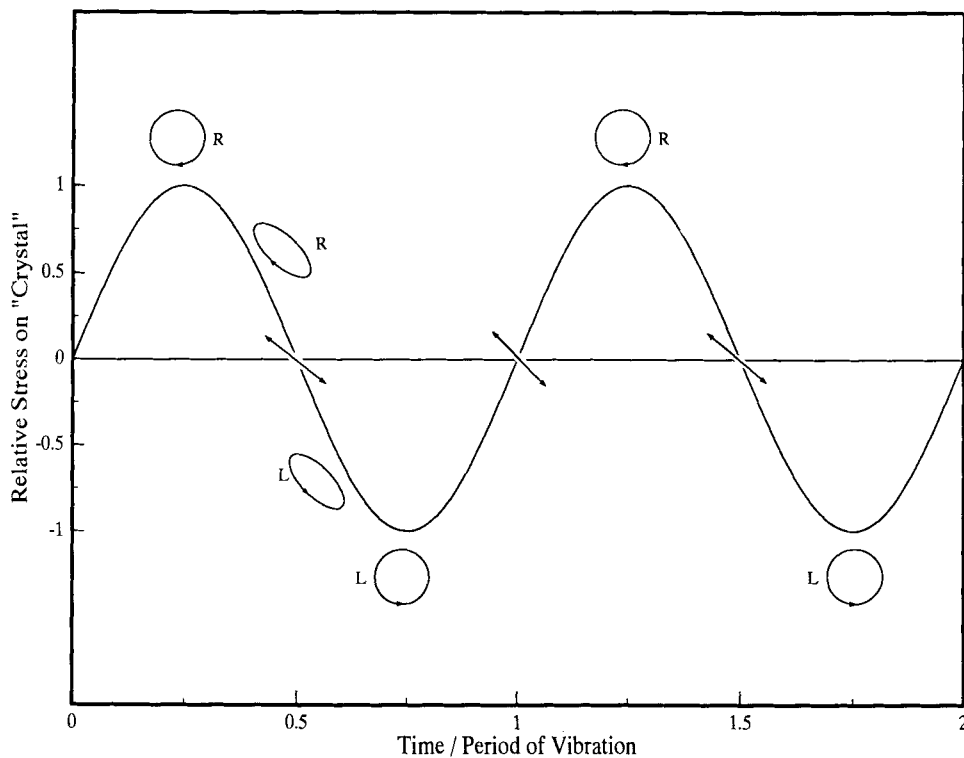


Figure 6.3-1 States of polarization produced by a linear polarizer followed by a PEM.

$\pi/2$ (maximum of sine wave). Moving through right elliptically, linearly, and left elliptically polarized states, the light becomes left circularly polarized at a phase retardation of $-\pi/2$ (minimum of sine wave).

Since a phase plate is only designed for one wavelength, a PEM is only capable of producing pure circularly polarized radiation at exactly one wavelength, and even that only at the positive and negative peaks of its sinusoidal modulation cycle. Accordingly, one has to adjust the voltage at the piezoelectric transducers driving the PEM as one scans the wavelengths of the infrared region.

In an infrared spectrometer equipped with a linear polarizer and a PEM the CD of the sample is then extracted from the detector signal by means of a lock-in amplifier tuned to the operating frequency of the photoelastic modulator.

Nafie et al., (1979) measured the VCD of a solution of (+)-camphor in CCl_4 with a Michelson interferometer using a wire grid linear polarizer on a BaF_2 support and a ZnSe modulator. The interferometers reached a much better signal to noise ratio than the dispersive instruments had shown before. Nowadays the dispersive VCD instruments are used mainly for work in the C–H and N–H stretching frequency region, as there is a sharp decrease in sensitivity at high Fourier frequencies (these approach the modulator

frequency and cannot be easily separated). The optical components in the sample compartment of a VCD spectrometer are shown in Fig. 6.3-2. Into the sample compartment one puts a linear polarizer (e.g. an aluminium grid on a KRS5 support) and a photoelastic modulator followed by the sample. After the sample the beam is focused on a detector (usually mercury cadmium telluride, MCT). To avoid overload, the detector is protected by an optical low-pass filter, which removes the unwanted light of higher frequency.

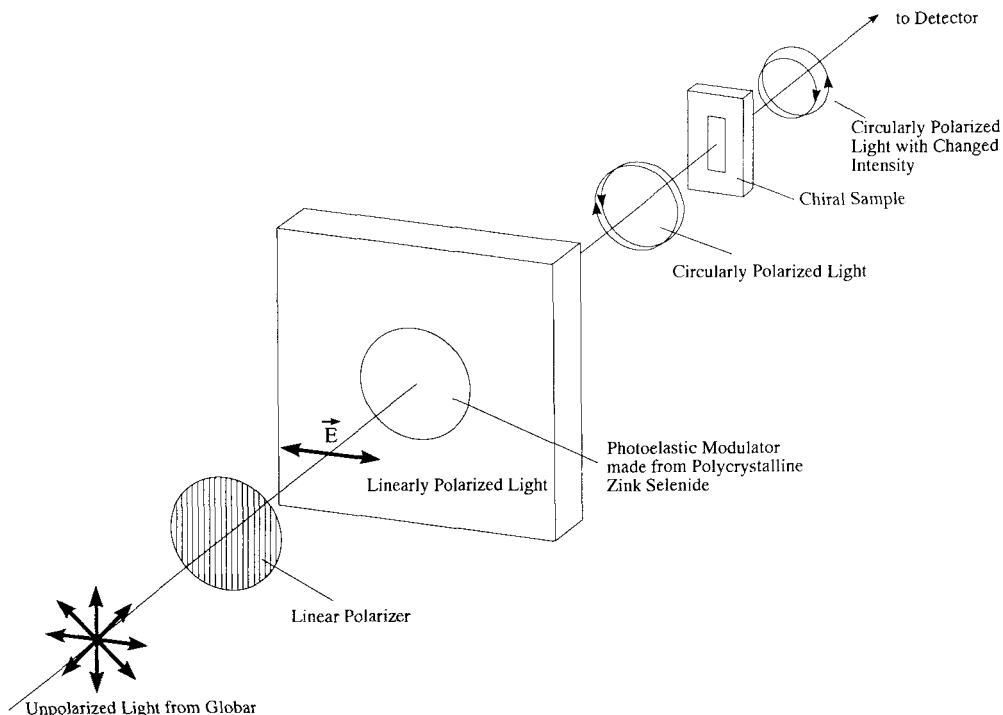


Figure 6.3-2 Sample compartment of a PEM-based VCD spectrometer.

In the process of obtaining a VCD spectrum from the suitably equipped interferometer, some electronic processing and numerical calculations are involved. This is illustrated in Fig. 6.3-3. The signal at the output of the detector's preamplifier consists of a conventional interferogram on which the CD is imprinted as a tiny modulation. As in dispersive VCD work this modulation is extracted with a lock-in amplifier tuned to the modulation frequency by the PEM's synchronization output. The procedure results in a small interferogram termed "AC". The detector signal is also fed into a low-pass filter where the modulation is "stripped" off. The conventional interferogram obtained by this treatment is called "DC". The two interferograms measured this way are then converted from analog to digital and fed into a computer. Here they are Fourier-transformed and the AC part is divided by the DC part (taking into account, of course, the amplification by the

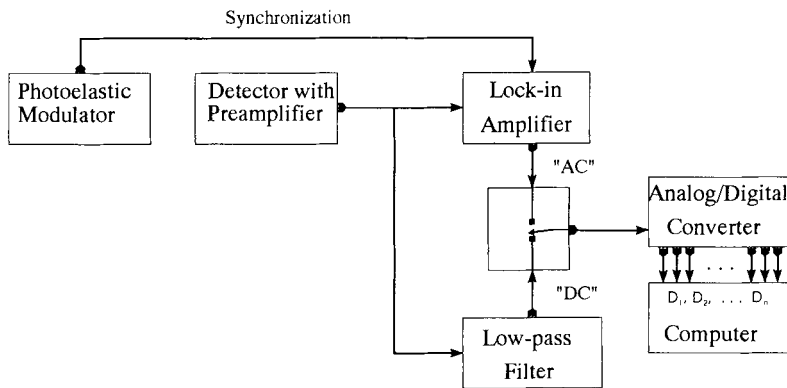


Figure 6.3-3 Scheme of signal flow in a VCD spectrometer.

lock-in). The computer can now also be used to compensate for the Bessel dependence of the modulation process as determined by a calibration experiment.

In Fourier-transform spectrometers using a PEM, it is very important to calibrate the instrument's overall response to circularly polarized radiation, because, as one measures a whole range of frequencies at once, the effectivity of a PEM is dependent from the wavelength in form of a Bessel function. Calibration is done by placing a multiple quarter wave plate (i.e. a "thick" phase plate with a retardation of $n \cdot \lambda + \lambda/4$) followed by a second polarizer in the optical path behind the photoelastic modulator. The polarizers should only be parallel or crossed, PEM and quarter wave plate are placed at 45° to their axes of polarization. Fig. 6.3-4 shows the principal orientations which are possible for the calibration equipment. Following the first polarizer (and the PEM, not shown in the figure for clarity) designated as a circle, the square of the quarter wave plate is placed. In the figure the 'fast' axis of the calibration plate is shown as arrow. The plate

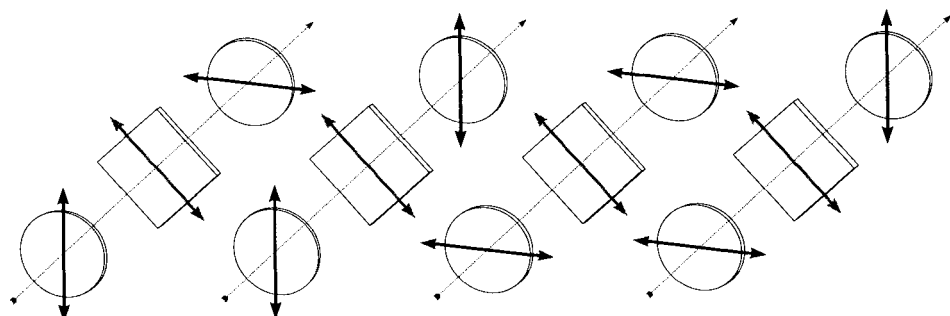


Figure 6.3-4 Orientation of calibration plate and polarizers in a calibration experiment.

is then followed by the second polarizer. If circularly polarized light, whose wavelength is such that one linear component is retarded by $\lambda/4$, is sent through the arrangement, linearly polarized light results. This the second polarizer can be either transmittant or blocking, depending on its orientation. For a more detailed description of the calibration process, the reader is referred to the article of Polavarapu (1985).

Fig. 6.3-5 shows the spectra taken with a CdSe calibration plate on a Bruker IFS-66 FT-IR spectrometer. Theoretically four curves should result. For calibration purposes, however, it is only necessary to record two curves, as the two other curves are mirror images of the latter. The curves shown in the figure were taken with only a single orientation of the CdSe calibration plate, but one with parallel and another with crossed polarizers. They are the results of 32 coadded interferograms transformed without apodization. As result we chose a power spectrum, since this is less noisy. A further advantage is that we do not need to use the (in the case of calibration spectra) complicated phase correction. The curves cross at certain points. Interpolating between those crossings, we get a curve with which we can multiply our spectra for the correction of Bessel function dependence. We also clearly can identify the node of the Bessel function at about 2450 cm^{-1} . The modulator was tuned to quarter wave retardation at 1111 cm^{-1} .

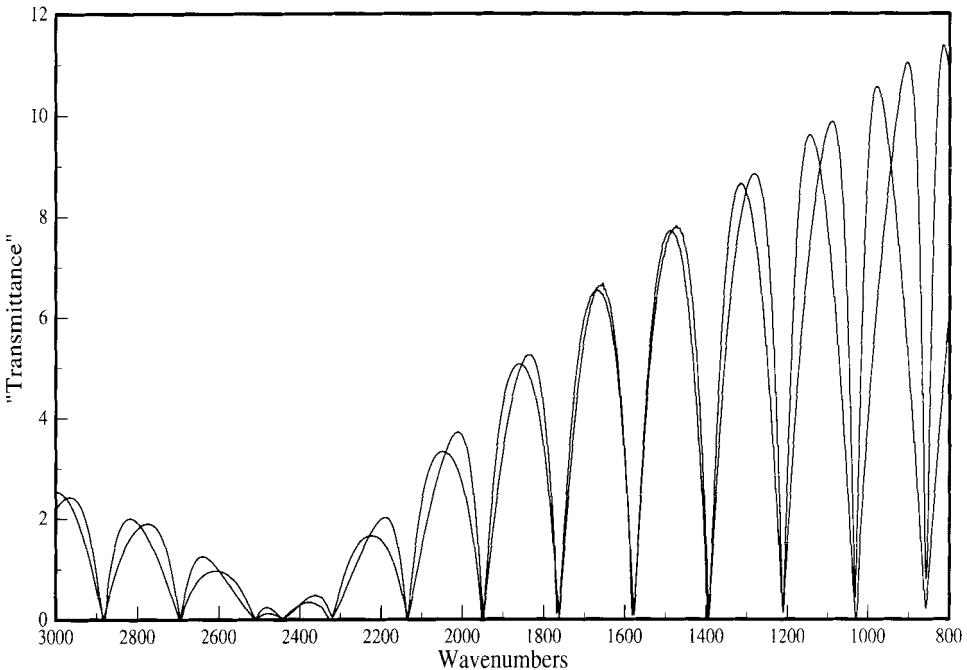


Figure 6.3-5 Calibration spectra.

Commercial FT-instruments use many optical elements which may produce artifacts. Therefore a dedicated VCD interferometer was built (Hoffmann and Hochkamp, 1992a) which consists only of the minimal amount of optical elements necessary for a photoelectric modulator based VCD instrument (Fig. 6.3-6). Interferograms taken for a CdSe

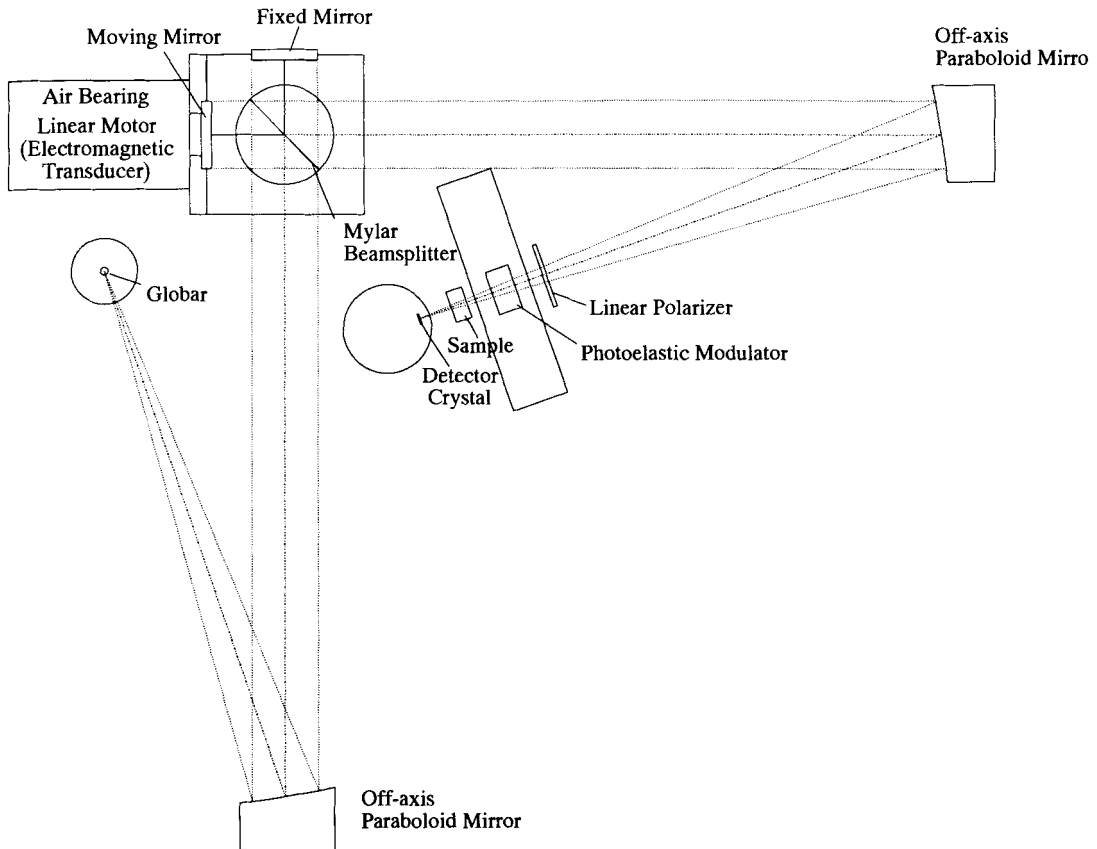


Figure 6.3-6 Optical layout of a dedicated VCD interferometer.

calibration plate with this instrument can be seen in Fig. 6.3-7. For the measurement of the interferograms a simultaneous technique (Hoffmann and Hochkamp, 1992b) is used. Instead of recording the “AC” and the “DC” part one after the other, the two signals are sampled nearly simultaneously using an input multiplexer in front of the analog-to-digital converter. As the “AC” part is always delayed by the passage through the lock-in amplifier, this can be done without introducing an error. The result of this procedure is that each slight change in the baseline of the interferometer has the same effect on both interferograms and should be canceled out this way.

A very promising technique is the measurement of circular dichroism (and linear dichroism) by means of a polarizing interferometer (Martin and Puplett, 1969). The Martin-Puplett-interferometer uses a linear polarizer as beamsplitter. If the interferogram produced at the detector is Fourier transformed, the sine FT gives directly the circular

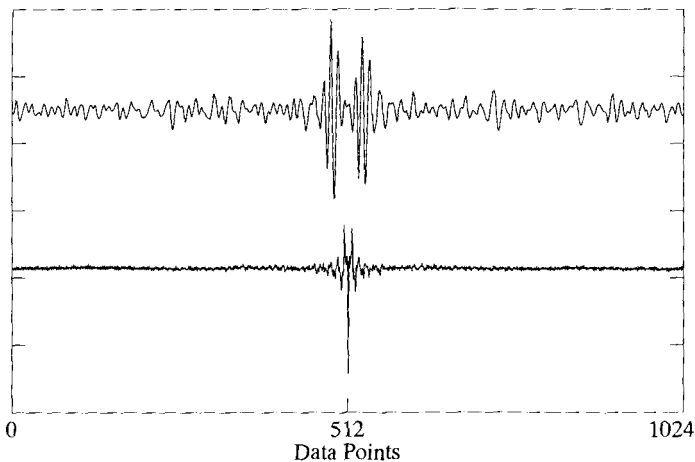


Figure 6.3-7 “AC” and “DC” Interferograms of a calibration experiment.

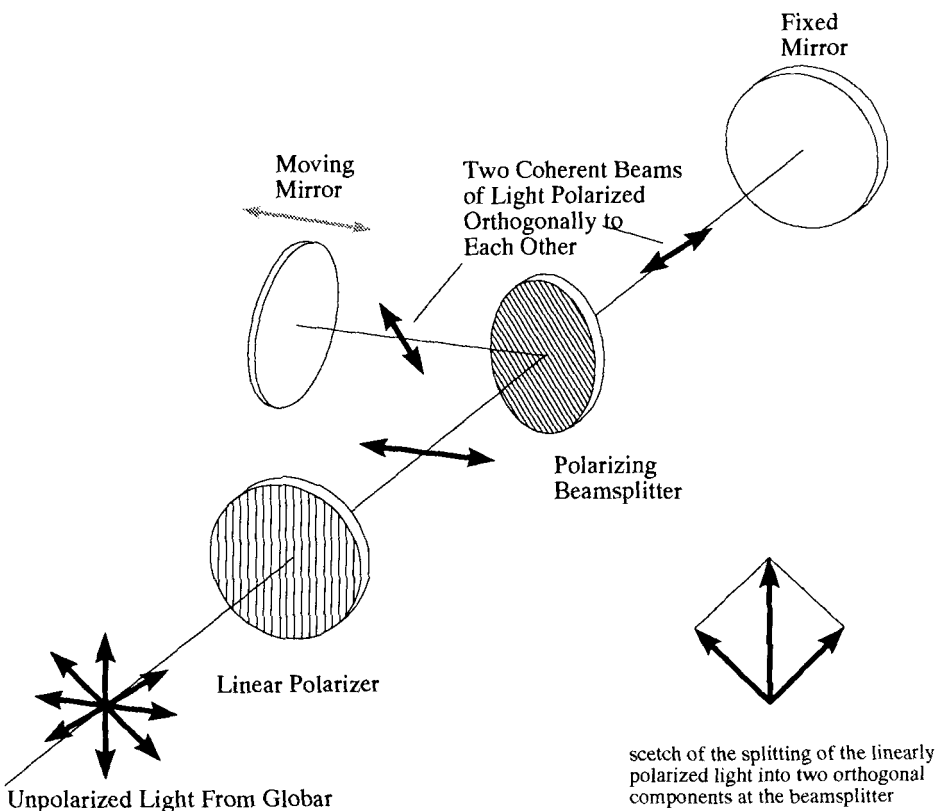


Figure 6.3-8 Optical layout of a Martin-Puplett interferometer.

dichroism, whereas the cosine FT directly produces the linear dichroism of the sample. Its performance has been analysed by Dignam and Baker (1981). The commercial realization by Bomem (1987) is shown in Fig. 6.3-8. But it was not before 1990, that Ragunathan et al. were able to report the first real VCD measurements with a polarizing instrument. Their results will be detailed in section 6.3.1.4.

6.3.1.3 Theoretical models

In accordance with the convention in infrared spectroscopy, where the experimental dipole strength of the vibrational transition is proportional to the area under the band, in VCD spectroscopy one likewise defines an experimental quantity proportional to the area under the band. This quantity, called rotatory strength, can also be calculated theoretically. The theoretical rotatory strength R_{01}^a (see e.g. Caldwell and Eyring, 1971) of a molecular state transition is given as the imaginary part of the vector product of the electrical dipole moment and the magnetic transition moment (here a denotes the a^{th} normal mode). In this formalism, adapted to vibrational transitions, the electrical dipole transition moment will be created by the dipole moment operator μ_r acting on the wavefunction of the vibrational ground state ψ_{g0}^a and the excited state wavefunction ψ_{g1}^a , whereas the magnetic transition moment is produced by the magnetic moment operator \mathbf{m} acting on the wave function ψ_{g1}^a of the first excited state and the wave function ψ_{g0}^a of the vibrational ground state (note the reversed order).

$$R_{01}^a = \text{Im} [\langle \psi_{g0}^a | \mu_r | \psi_{g1}^a \rangle \langle \psi_{g1}^a | \mathbf{m} | \psi_{g0}^a \rangle] \quad (6.3-1)$$

Several simple models have been devised for the understanding of VCD and the calculation of vibrational rotatory strengths. They will be described shortly in the following.

6.3.1.3.1 The degenerate coupled oscillator (DCO) model

Coupled oscillator models are extensions to the simple models developed for electronic circular dichroism. They are well known under the name “exciton theory” (see e.g. Harada and Nakanishi, 1972). These models, extended to vibrational transitions, describe the coupling of pairs of electric dipole transition moments. They predict equal amounts of positive and negative VCD intensity:

$$R^\pm(\text{DCO}) = \mp \left\{ \frac{\pi\nu}{2c} \right\} T_{ab} \cdot \{ \mu_a \times \mu_b \} \quad (6.3-2)$$

When two identical achiral chromophors a and b are present in the same molecule and form a chiral arrangement, they can interact with each other and alleviate the degeneracy of the transition. In this way the VCD shows a so-called couplet: a positive effect closely followed (going to longer wavelength) by a negative one (a positive couplet) or vice versa (a negative couplet). In the equation above ν is the transition frequency, T_{ab} the separation of the dipoles, and μ the dipole moment.

The applicability of the model have been studied using steroids with two C=O - functionalities located in six-membered rings (Narayanan and Keiderling, 1983). The DCO model proves to be satisfactory for all six but one cases.

6.3.1.3.2 The fixed partial charge (FPC) model

The fixed partial charge (FPC) model was first introduced by Deutsche and Moscowitz (1968) for polymers. Later on it was modified by Schellman (1973) to be used to predict the VCD of small molecules.

If nuclear charges are shielded statically by electronic charges, one can assign so-called fixed partial charges to the nuclei. It is assumed that the charges don't alter during the vibration of the molecule. The rotatory strength of the transition is then given by Eq. 6.3-3, where n is the number of the nuclei, ξ_n is the fixed partial charge, $R_{n,0}$ the equilibrium rest position of nucleus n , and Q_p the p^{th} normal mode.

$$R_{10}^p(FPC) = \frac{\hbar}{4c} \left[\sum_n e\xi_n \left(\frac{\partial R_n}{\partial Q_p} \right)_0 \right] \cdot \left[\sum_n R_{n,0} \times e\xi_n \left(\frac{\partial R_n}{\partial Q_p} \right)_0 \right] \quad (6.3-3)$$

6.3.1.3.3 The charge flow (CF) model

The charge flow (CF) model, which is essentially a refinement of the FPC model, was introduced by Abbate et al. (1981). It consists of the FPC terms already described and new terms describing the contribution of the charge flow.

$$R_{10}^p(CF) = \frac{\hbar}{4c} \left[\sum_n e\xi_n \left(\frac{\partial R_n}{\partial Q_p} \right)_0 + \sum_\alpha l_\alpha^0 e_\alpha^0 \left(\frac{\partial ez_\alpha}{\partial Q_p} \right)_0 \right] \cdot \left[\sum_n R_{n,0} \times e\xi_n \left(\frac{\partial R_n}{\partial Q_p} \right)_0 + \sum_\alpha n_\alpha^0 \times l_\alpha^0 e_\alpha^0 \left(\frac{\partial ez_\alpha}{\partial Q_p} \right)_0 \right] \quad (6.3-4)$$

Here e_α denotes the unit vector along the of equilibrium direction of the α^{th} bond and l_α the equilibrium length of that bond, n_α is the vector which crosses e_α . Lone pair electrons are not taken into account.

6.3.1.3.4 The localized molecular orbital (LMO) model

The localized molecular orbital (LMO) model was first proposed by Nafie and Walnut (1977). In the context of this model the rotatory strength of a vibrational transition is evaluated by separate contributions of each orbital and each nucleus.

$$R_{10}^p(LMO) = \frac{\hbar}{4c} \left[\sum_n eZ_n S_{np} \sum_k e(-2)\sigma_{kp} \right] \cdot \left[\sum_n R_{n,0} \times eZ_n S_{np} + \sum_k r_{k,0} \times e(-2)\sigma_{kp} \right] \quad (6.3-5)$$

Here, e denotes the charge of the electron, which has to be multiplied by (-2) for two-fold occupied orbitals. The full nuclear charge, Z_n is retained. S_{np} is the vector of motion by the harmonic normal vibration Q_p , the derivative of the position vector $\partial R / \partial Q_p$ as in Eqs. 6.3-3 and 6.3-4.

6.3.1.3.5 The dynamic polarization (DP) model

This model again is the extension of a similar model for electronic CD, the dynamic coupling model. It was formulated by Barnett et al. (1980) and is only valid for vibrational transitions that can be simplified as localized, e.g. a group mode. The rotatory strength of the transition can then be thought as arising from the vector product of the zero-order electric dipole transition moment μ_{0v} with a first-order magnetic dipole transition moment \mathbf{m}_{v0} :

$$R_{0v} = \text{Im}(\mu_{0v} \cdot \mathbf{m}_{v0}) \quad (6.3-6)$$

This magnetic moment can be pictured as arising from the induction of electric dipoles in the rest of the molecule (consisting of “substituents”), which have component vectors forming a vector product with the position vector from the chromophore origin to that of the substituent.

The authors applied the model to the VCD of the aliphatic C-H stretching modes of 9,10-dihydrodibenzo[c,g]phenanthrene. The agreement of the experimental spectrum with the calculated one is only good if one takes Fermi resonance into account.

6.3.1.3.6 The inertial motion (IM) model

The inertial motion model is a specialized model formulated by Barron and Buckingham (1979) for the torsional modes of the CH₃-groups. As it has no general applicability, it will not be detailed here.

6.3.1.3.7 The bond moment (BM) model

The bond moment model, first formulated by Barron (1979), was reformulated by Polavarapu (1983) to compare it to the charge flow model. His expression for the rotatory strength of a vibrational transition is then:

$$\begin{aligned}
R_l = & \frac{\hbar}{8\pi} \left[\sum_A \sum_k \left(q_k \Delta_{kA} \delta_{\alpha\lambda} + \frac{\partial q_k}{\partial x_{A\lambda}} e_{k\alpha} r_k \right) S'_{A\lambda} \right] \\
& \times \left[\sum_A \sum_k \varepsilon_{\alpha\beta\gamma} \left(R_{k\beta} q_k \Delta_{kA} \delta_{\gamma\lambda} + \delta_{R_{k\beta}, R_{A\lambda}} q_k e_{k\gamma} r_k \right. \right. \\
& \left. \left. + R_{k\beta} \frac{\partial q_k}{\partial x_{A\lambda}} e_{k\gamma} r_k \right) S'_{A\lambda} \right]
\end{aligned} \tag{6.3-7}$$

where q_k is the charge, e_k the unit vector, and r_k the length of the bond k . Δ_{kA} can be +1, -1, and 0, depending on whether the atom A is origin atom, end atom or not contained in the bond k . $S'_{A\lambda}$ is the partial derivative of $x_{A\lambda}$ with the normal coordinate Q_l , and $\delta_{R_{k\beta}, R_{A\lambda}}$ is equal to 1 if $R_{k\beta} = R_{A\lambda}$, and zero in all other cases. Polavarapu concludes that the bond moment model and the charge flow model are equivalent but require different parametrization taken from experimental results.

6.3.1.3.8 The atomic polar tensor (APT) model

Polar tensors have been developed by Biarge et al. (1961) to aid in the calculation of vibrational intensities (see also Sec. 5.2.9.1.2). They are derived for each atom by displacing the atom in small increments along the cartesian coordinates and noting the change in dipole moment.

$$\mu(\alpha) = \begin{pmatrix} \partial\mu_x/\partial x_\alpha & \partial\mu_x/\partial y_\alpha & \partial\mu_x/\partial z_\alpha \\ \partial\mu_y/\partial x_\alpha & \partial\mu_y/\partial y_\alpha & \partial\mu_y/\partial z_\alpha \\ \partial\mu_z/\partial x_\alpha & \partial\mu_z/\partial y_\alpha & \partial\mu_z/\partial z_\alpha \end{pmatrix} \tag{6.3-8}$$

Here $\mu(\alpha)$ is the change in the dipole moment of the molecule for the displacement of the α^{th} atom.

Nafie and Friedman (1983) have used this formalism to arrive at a simple expression for the rotatory strength of a vibrational transition:

$$R_{10}^p(APT) = \frac{\hbar}{4c} \left[\sum_n \left(\frac{\partial \mu}{\partial R_n} \right) S_{np} \right] \left[\sum_n \left(R_{n,0} \times \frac{\partial \mu}{\partial R_n} \right) S_{np} \right] \tag{6.3-9}$$

Here the components of $(\partial\mu/\partial R_n)$ are the elements of the atomic polar tensor for the n^{th} atom in the molecule.

As the method readily lends itself to implementation into a quantum chemical program, the authors also give the appropriate formulation for the CNDO method and report calculations on L-alanine and (+)-(3*R*)-methylcyclohexanone, which, as they state, compare favorably with experiment and simpler theories.

6.3.1.3.9 The ring current mechanism

Nafie and Freedman (1986) introduced this new elementary mechanism to account for the amplification of the VCD signal in some molecules containing an intramolecular ring. One observes for example large monosignate signals in some sugars which are known to exist in the pyranose form (Paterlini et al., 1986). Here $\Delta\epsilon$ is about 1 to 3 times 10^{-3} . The occurrence of these large signals is attributed to an electron flow which is introduced when a molecular vibration alters the partition of charge in the molecule. The intramolecular ring which is needed for this current needs not to be a covalently bounded one, a ring formed by hydrogen bonding, as in alanine derivatives (Oboodi et al., 1985) is sufficient. Calculations show that a very small charge is sufficient to generate a large rotatory strength if it moves nearly circular on a plane orthogonal to the path of motion associated to the vibration which generates the charge.

$$\mu_v = I_b r_b + \sum_i I_i r \quad (6.3-10)$$

$$m = \frac{1}{2c} (R_b \times I_b r + \sum_i R_i \times I_i r) \quad (6.3-11)$$

An extreme example of the generation of a ring current is the azide stretch band at 2025 cm^{-1} in the VCD spectrum of azidomethemoglobin A (Marcott et al., 1979). With an anisotropy ratio of 0.02 it shows the largest single molecule effect observed today.

6.3.1.3.10 The magnetic field perturbation method (MFP)

This theory was first formulated by Stephens (1985). In his approach to go beyond the Born-Oppenheimer approximation, Stephens mixed excited electronic states with the ground state. Though that approach seemed to call for the difficult calculation of excited electronic states, he finally arrived at expressions, that only involve ground state properties. As an example to the application of the theory Jalkanen et al. (1989b) report nuclear shielding tensors, atomic polar and axial tensors, as well as IR and VCD intensities of the ammonia isotopomer $\text{N}^1\text{H}^2\text{H}^3\text{H}$ (NHDT) using different basis sets.

The electric dipole transition moment of the i^{th} vibrational mode at frequency ω_i is calculated as:

$$\langle 0 | (\mu_{el})_\beta | 1 \rangle_i = \left(\frac{\hbar}{2\omega_i} \right)^{\frac{1}{2}} \sum_{\lambda,\alpha} P_{\alpha\beta}^\lambda S_{\lambda\alpha,i} \quad (6.3-12)$$

here $P_{\alpha\beta}^\lambda$ is the atomic polar tensor of the λ^{th} atom with its components:

$$P_{\alpha\beta}^\lambda = E_{\alpha\beta}^\lambda + N_{\alpha\beta}^\lambda \quad (6.3-13)$$

$E_{\alpha\beta}^\lambda$ is the electronic part,

$$E_{\alpha\beta}^\lambda = \left[\frac{\partial}{\partial X_{\lambda\alpha}} \langle \psi_G(R) | (\boldsymbol{\mu}_{el})_\beta | \psi_G(R) \rangle \right]_{R_0} \quad (6.3-14)$$

and $N_{\alpha\beta}^\lambda$ the nuclear part of the tensor.

$$N_{\alpha\beta}^\lambda = Z_\lambda e \delta_{\alpha\beta} \quad (6.3-15)$$

The magnetic dipole transition moment on the other hand formulates as:

$$\langle 0 | (\boldsymbol{\mu}_{mag})_\beta | 1 \rangle_i = -(2\hbar^3 \omega_i)^{1/2} \sum_{\lambda,\alpha} M_{\alpha\beta}^\lambda S_{\lambda\alpha,i} \quad (6.3-16)$$

where $M_{\alpha\beta}^\lambda$ is the atomic axial tensor:

$$M_{\alpha\beta}^\lambda = I_{\alpha\beta}^\lambda + J_{\alpha\beta}^\lambda \quad (6.3-17)$$

with the electronic contribution $I_{\alpha\beta}^\lambda$ to the atomic axial tensor given as:

$$I_{\alpha\beta}^\lambda = \left\langle \left(\frac{\partial \psi_G(R)}{\partial X_{\lambda\alpha}} \right)_{R_0} \middle| \left(\frac{\partial \psi_G(R_0, H_\beta)}{\partial H_\beta} \right)_{H_\beta=0} \right\rangle \quad (6.3-18)$$

with the nuclear contribution $J_{\alpha\beta}^\lambda$ to the atomic axial tensor given as:

$$J_{\alpha\beta}^\lambda = \frac{i}{4\hbar c} \sum_\gamma \varepsilon_{\alpha\beta\gamma} (Z_\lambda e) R_{\lambda\gamma}^0 \quad (6.3-19)$$

The two transition moments can now be combined in the common way to give the vibrational rotatory strength:

$$R(0 \rightarrow 1)_i = \text{Im}(\langle 0 | \vec{\mu}_{el} | 1 \rangle_i \cdot \langle 1 | \vec{\mu}_{mag} | 0 \rangle_i) \quad (6.3-20)$$

In the expressions above $\psi_G(R_0, H_\beta)$ is the ground state electronic wave function at the equilibrium nuclear position R_0 , $X_{\lambda\alpha}$ are the Cartesian displacement coordinates of nucleus λ ($\alpha = x, y, z$), related to the normal coordinates by $S_{\lambda\alpha i}$.

The MFP theory has been implemented into the CADPAC (Amos and Rice, 1990) series of *ab initio* programs. The program is capable of calculating the necessary derivatives *analytically*, thereby increasing the attainable precision considerably. As the expressions are not origin independent, the program calculates two different rotatory strengths: one with common origin gauge and the second with distributed origin (origin at nuclei gauge). The latter seems to give more reliable results, but it is not necessarily the best choice.

6.3.1.3.11 The sum-over-states vibronic coupling (VC) method

Nafie and Freedman (1983) derived the vibronic coupling theory of infrared transition intensities using only ground state wave functions. According to this theory the rotatory strength can be given as:

$$\begin{aligned} R_{gf,gi} &= \text{Im} \sum_j \sum_k \frac{e_j e_k}{2m_k c} (\mathbf{r}_j)_{gi, gf} \cdot (\mathbf{r}_k \times \mathbf{p}_k)_{gf, gi} \\ &= \sum_j \sum_k \frac{e_j e_k}{2m_j m_k c \omega} (\mathbf{p}_j)_{gi, gf} \cdot (\mathbf{r}_k \times \mathbf{p}_k)_{gf, gi} \end{aligned} \quad (6.3-21)$$

This equation can readily be expressed in terms of LCAO-MO wave functions (which are quite lengthy and shall not be given here) and can be readily implemented into computer programs. Dutler and Rauk (1989) wrote an extension to the GAUSSIAN 82 series of programs and applied the theory to oxirane and its deuterated analogues. Later Rauk et al., (1990) calculated infrared and VCD intensities of CH₃OH, CH₃NH₂, NH₂NH₂, and HOOH and some deuterated derivatives. Unfortunately, comparable experimental results will never become available, as chiral conformers of these substances are not amenable to isolation.

6.3.1.4 Experimental results

As already some excellent reviews have appeared (e. g. Nafie, 1984; Stephens and Lowe, 1985), emphasis is placed on the achievements of the last five years. Freedman et al. (1991) give a detailed analysis of the VCD spectra of (*S,S*)-[2,3-²H₂]oxirane both in solution and in the gaseous phase. The analysis is based on an *ab initio* calculation using the 4-21G basis set and the experimental geometry.

Eggiman et al. (1991) measured the VCD spectrum of 6,8-dioxabicyclo[3.2.1]octane as solution in CCl₄ and CS₂ from 800 to 1500 cm⁻¹. They compare the experimental absorption and VCD spectra with calculations using the FPC, CF and APT models. They found moderate agreement.

The measurement of vibrational circular dichroism was confined to the region below 15 μm resulting from the transmittance characteristics of the photoelastic modulator made from zink selenide (ZnSe). This was changed by the employment of a photoelastic modulator made from cadmium telluride (CdTe) with sufficient transparency down to about 300 cm⁻¹.

Using this modulator in a dedicated VCD interferometer, the VCD spectrum of (+)-(*R*)-3-methylcyclohexanone in the spectral region of 700 to 300 cm⁻¹ could be measured for the first time (Hoffmann and Hochkamp, 1992a). The sign of the bands corresponds well to the rotatory strengths calculated with distributed origin, however in the two lowest frequency transitions the signs are reversed. The comparison of the spectral bands measured at the low resolution of 32 cm⁻¹ to the rotatory strengths calculated with CADPAC 4.2 at the 3-21G and the 6-31G level is shown in Table 6.3-1. A single scaling factor of 0.9 is used for the frequencies.

Table 6.3-1 Experimental and calculated VCD of (*R*)-(+)-3-methylcyclohexanone below 600 cm⁻¹

Experimental Wavenumbers and VCD		Calculated Wavenumbers and Rotatory Strengths			
		BasisSet 3-21G		Basis Set 6-31G	
$\tilde{\nu}$ /cm ⁻¹	sign	$\tilde{\nu}$ /cm ⁻¹	debye ²	$\tilde{\nu}$ /cm ⁻¹	debye ²
386	-	387.2	+7.1 · 10 ⁻⁸	391.7	+5.9 · 10 ⁻⁸
398	+	395.8	-4.2 · 10 ⁻⁸	401.5	-4.2 · 10 ⁻⁸
440	±	428.8	+1.4 · 10 ⁻⁸	429.0	+2.1 · 10 ⁻⁸
491	-	445.7	-4.8 · 10 ⁻⁸	457.3	-2.4 · 10 ⁻⁸
515	+	515.5	+21.5 · 10 ⁻⁸	521.3	+17.0 · 10 ⁻⁸
540	-	529.7	-14.6 · 10 ⁻⁸	533.8	-14.8 · 10 ⁻⁸

The first successful VCD measurements with a polarizing Michelson interferometer were done on pinene (Ragunathan et al. 1990). They used a wire grid polarizer on a BaF₂ substrate as the beamsplitter, limiting the measurement to 11 μ on the long wavelength side and an optical long-pass filter (to prevent saturation of the detector) putting a limit of 6 μ to the short wavelength side.

The spectrum of (-)-α-pinene as a 50 μm film of neat liquid using a Bomem spectrometer with a polarizing interferometer attachment is a composite of 60 000 VCD scans and 12 000 transmission scans and took 19.5 hours to be measured. A spectrum with comparable signal to noise ratio is shown in Fig. 6.3-9. This was measured in our laboratory with a PEM-based VCD spectrometer and is a composite of only 5000 scans (five blocks of 1024 scans each). The noise estimate shown as the upper trace is the difference between two 5000 scan VCD spectra.

The synthesis, normal mode analysis and the comparison of experimental and calculated VCD spectra report Malon et al. (1992) on dideuteriobutyrolactone. For the calculations they use the 6-31G** basis set. The spectra of Oxiran and its deuterated analogues have been calculated by Dutler and Rauk (1989) and compared to the results of unpublished measurements of Spenzer et al.

The Raman, infrared, and VCD spectra of the steroid precursor (+)-5,6,7,8-tetrahydro-8-methylindan-1,5-dione were calculated on the 6-31G level of theory (Hoffmann, 1993) and compared to the experimental spectra.

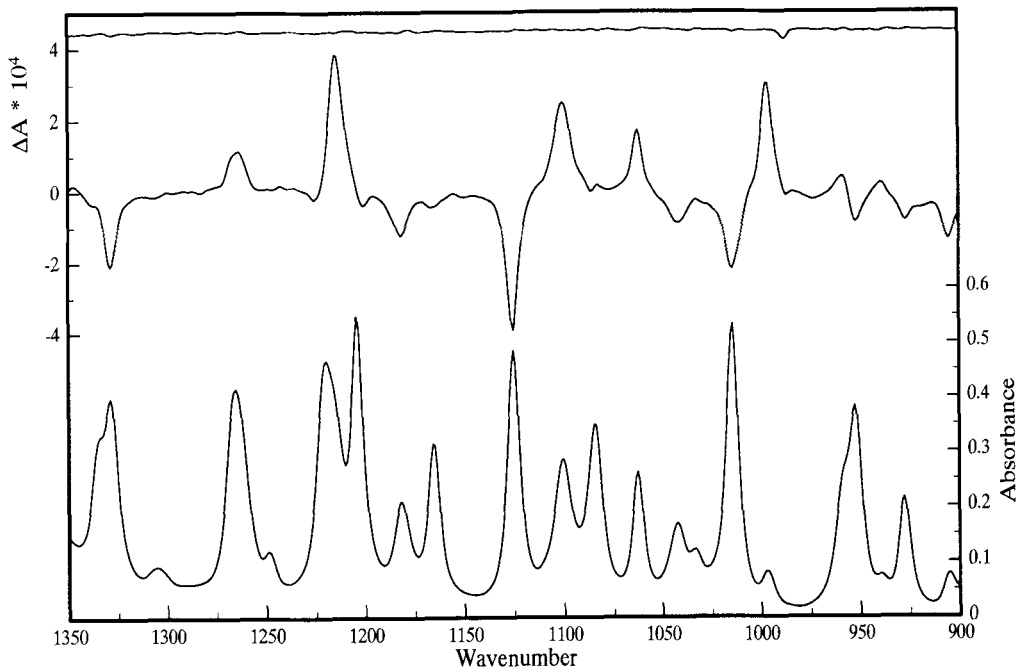


Figure 6.3-9 VCD spectrum of (-)- α -pinene (neat, 50 μm).

The spectrum of crystalline $\alpha\text{-NiSO}_4 \cdot 6 \text{ H}_2\text{O}$ has recently been reinvestigated by Hoffmann. It is shown in Fig. 6.3-10. Unlike the original spectrum of Hsu and Holzwarth (Sec. 6.3.1.2), it was measured on a modified Nicolet 7199 FT-IR spectrometer using a ZnSe photoelastic modulator.

Bour and Keiderling (1993) report *ab initio* simulation of the vibrational circular dichroism of coupled peptides in the amide I and II region. Using the MFP model and the 4-31G basis set they were able to reproduce the VCD sign pattern and the relative intensities of spectra of proteins in the α -helical, β -sheet 3_{10} -helical and polyproline II conformations.

The measurement of IR spectra in aqueous solution is often very difficult, because the broad bands of water tend to obscure important features of the solute. Therefore most VCD spectra reported today were measured in organic solvents, as a pure liquid or, in the case of biological substances, where the conformations in an aqueous medium were important, in D_2O solution. This technique has the drawback that the solute tends to become partially deuterated, creating ambiguities in the interpretation of spectra. Recently Baumruk and Keiderling (1993) reported the vibrational circular dichroism in the amide I and II bands of proteins in H_2O solution. For comparison the spectra of the proteins in D_2O are also given. Their examination of myoglobin, hemoglobin, α -chymotrypsin, albumin, concanavalin A, cytochrome c, triose phosphate isomerase, ribonuclease S, β -lactoglobulin A, and poly-L-lysine allows them to draw conclusions upon the secondary structures of the proteins in agreement with the results from other methods.

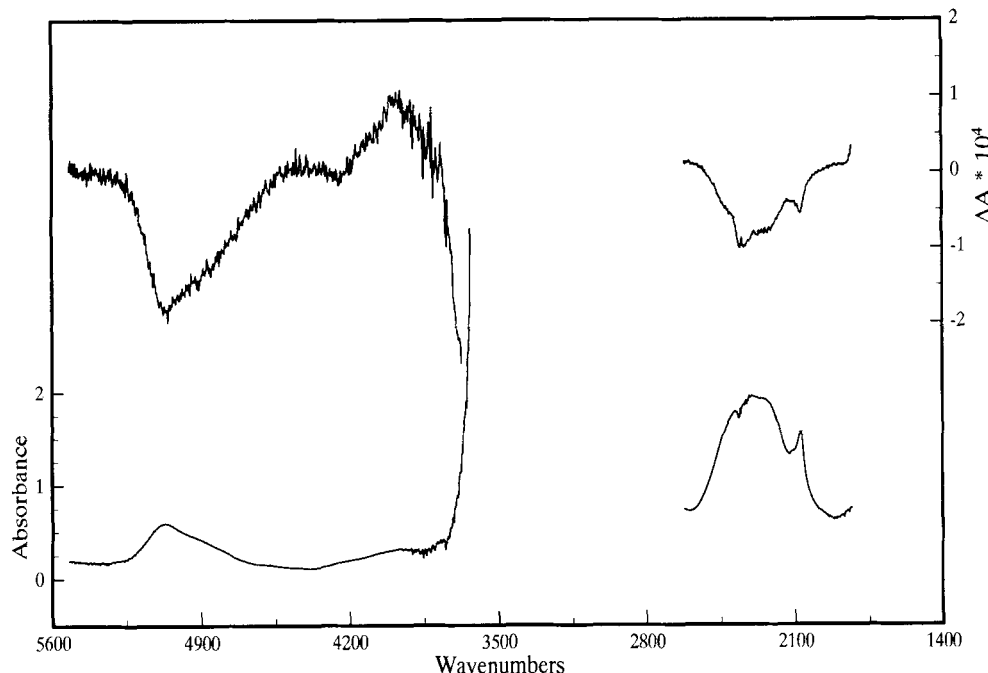


Figure 6.3-10 VCD spectrum of a NiSO_4 single crystal slice ($d = 63 \mu\text{m}$).

A review on VCD of biological macromolecules has been given by Keiderling and Pancoska (1993). Using a test set of 13 proteins and comparing electronic circular dichroism (ECD) and VCD to the results of the X-ray structures, VCD proved to be slightly more reliable for the prediction of α -helix content, but clearly better for the determination of β -sheet content. The authors arrive at the conclusion that the different spectroscopic methods of deriving protein structure should be viewed as complementary and used together.

VCD on achiral molecules becomes feasible when an achiral sample is put into a strong magnetic field. The magnetic field vector can in this case be parallel or antiparallel to a component of the dipole transition moment and this way positive and negative signals become possible. The method is consequently termed magnetic VCD, MVCD.

Rotational Zeeman effect in carbon monoxide reported Wang and Keiderling (1993). From the same group the MVCD of methane (Wang et al., 1991) and ammonia (Wang et al., 1992) was communicated. Rotationally resolved MVCD of HCl and DCl was reported by Tam and Keiderling (1993). The MVCD method is well suited to investigate rotational g values, while being not as complicated as microwave or molecular beam magnetic resonance experiments.

6.3.2 Raman optical activity (ROA)

6.3.2.1 Introduction

Compared to the measurement of VCD the measurement of optical activity in the Raman spectrum offers all the well known advantages that Raman spectroscopy has over infrared spectroscopy: the use of the inexpensive glass as the sample cell, and the occurrence of fewer bands, overtones and combination bands are reduced in intensity, thereby diminishing the possibility of overlap. Very important also is the fact that water is usable as solvent.

The first genuine ROA effects were measured by Barron et al. in 1973, following some earlier claims which proved to be artifacts. Two years later, the first review of Raman optical activity (and on Rayleigh OA) by Barron and Buckingham (1975) appeared. The theory of ROA is explained in the book of Barron (1982), which also details other types of optical activity.

The measurement of optical activity in Raman spectra is most often done by measuring the circular intensity difference (CID) and the circular intensity sum (CIS). Using this technique the linearly polarized laser beam used for excitation is modulated with a KDP electrooptical modulator resulting in an exciting beam which changes its state of polarization from left to right circularly polarized at a frequency of about 1/3 Hz. The Raman intensities are then collected separately and the dimensionless Raman CID calculated using:

$$\Delta = \frac{(I^R - I^L)}{(I^R + I^L)} \quad (6.3-22)$$

Here I^R and I^L are the Raman intensities measured with right and left circularly polarized excitation light, respectively.

As there could be some confusion between the circular intensity difference and the dimensionless circular intensity difference (which is only occasionally given in the literature), the latter should be given a different name, e.g. DCID.

6.3.2.2 Instrumental techniques

In the early years of ROA measurements the only detectors of sufficient sensitivity were photomultipliers. Later Boucher et al. (1977) pioneered the work with multichannel detectors using an intensified vidicon and reduced the measurement time to one tenth, while Hug and Surbeck (1979) were able to get rid of nearly all artifacts with a new instrumental design and using a self-scanning diode array coupled to an image intensifier. Thus they were able to improve the measuring speed by about a factor of 200 to the disadvantage of scanning instruments. Barron et al. (1987) reported about a new ROA instrument using an intensified diode array detector system. The sensitivity of ROA measurements could be further enhanced impressively by the use of cooled charge coupled

devices (CCDs) as the detector (Barron et al., 1989). A *backthinned* CCD has about twice the quantum efficiency as the normal CCD, it is already very close to an ideal detector.

Another big step ahead was the employment of the 180° configuration (see Sec. 6.3.3.2.2), enhancing sensitivity and therefore even allowing weakly scattering substances in aqueous solution to be measured (Hecht et al., 1989) Fig. 6.3-11 shows the optical arrangement of a ROA instrument employed for backscattering measurements (redrawn from Barron et al., 1992).

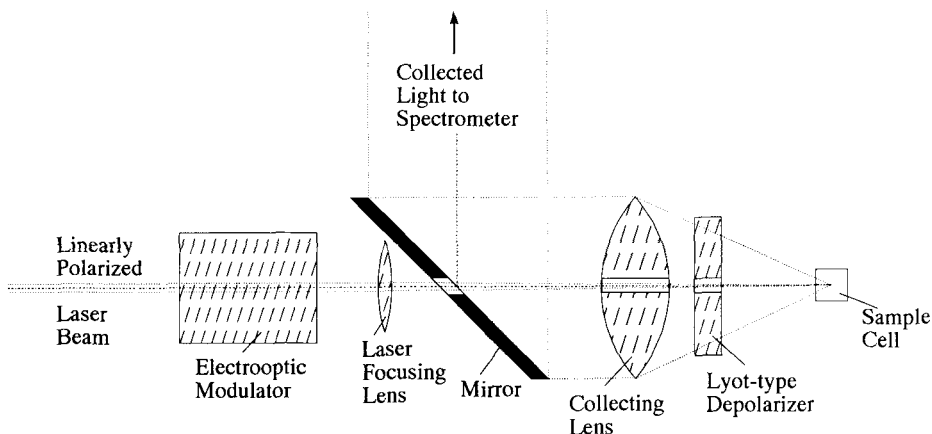


Figure 6.3-11 180° ROA arrangement (redrawn from Barron et al., 1992b).

Nafie (1992) has given a review about the latest VOA instrumentation. Until 1988, the only measured form of ROA was incident circular polarisation (ICP) ROA, but as the process observed in Raman spectroscopy is a two-photon process, there are four possibilities for measuring Raman optical activity. ICP ROA is the unpolarized measurement of the Raman radiation emitted upon excitation with alternating right and left circularly polarized light. It is shown in Fig. 6.3-12, following the sketches of Nafie. As the first of the other possibilities scattered circular polarisation (SCP) ROA was measured. This

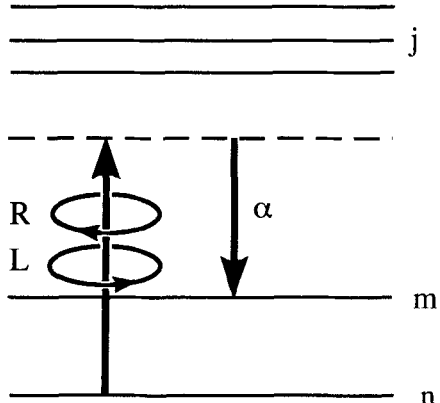


Figure 6.3-12 ICP ROA (redrawn from Nafie, 1992).

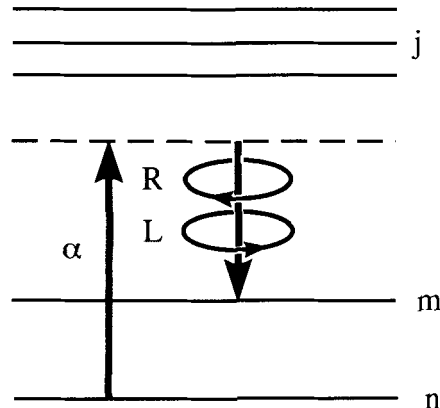


Figure 6.3-13 SCP ROA.

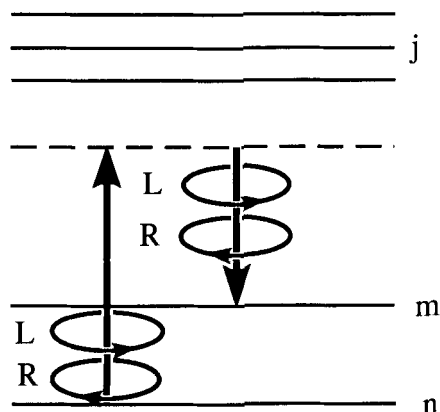


Figure 6.3-14 DCP_I ROA.

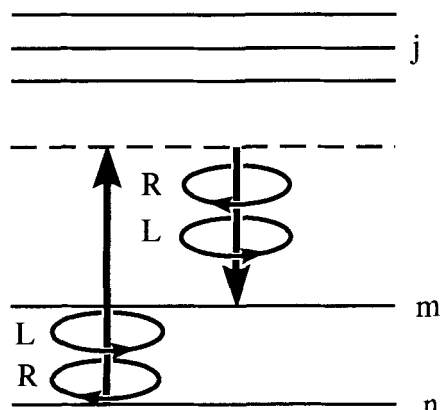


Figure 6.3-15 DCP_{II} ROA.

is done by exciting a Raman spectrum with unpolarized light and then measuring the amount of right and left circularly polarized light in the emitted radiation (Fig. 6.3-13). Finally dual circular polarization (DCP) ROA could be measured, which in turn can be splitted further into the in-phase form (DCP_I ROA) and the out-of-phase form (DCP_{II} ROA). In these measurements the exciting radiation is left and right circularly polarized and the detection of the emitted Raman radiation is sensitive to the amount of right and left circularly polarized light contained in it. As shown in Figs. 6.3-14 and 6.3-15, the two sub-forms of measurement differ only in the synchronicity of excitation and detection. Nafie (1992) has designed an instrument that can measure all these forms of ROA one after the other. It is shown in Fig. 6.3-16.

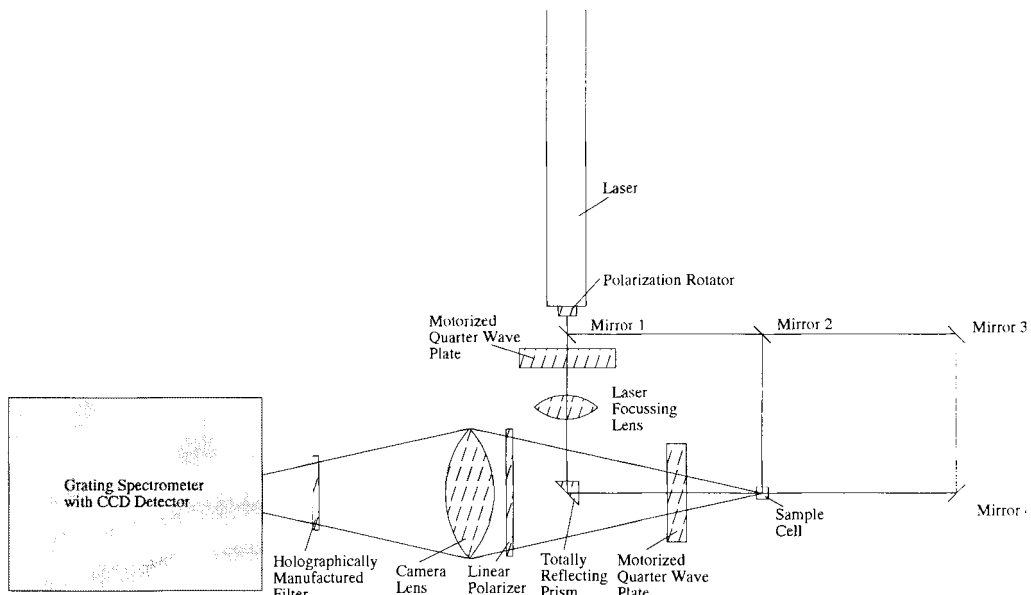


Figure 6.3-16 Multi-ROA instrument (redrawn from Nafie, 1992).

The versatile instrument is not only capable of measuring the four forms of ROA, but also of using different scattering geometries. This latter feature is implemented with the aid of four mirrors and a totally reflecting prism. Using only the prism, a backward scattering (180°) geometry is used. A 90° geometry is produced by using mirror 1 and 2, whereas using mirrors 1, 3 and 4 allows to employ forward scattering. Two zeroth-order quarter wave plates in mounts, which can be rotated with stepping motors, are used to control the polarization of the excitation light or the polarization of the detected light. Using either one or both of the plates decides the type of ROA measurement employed.

Analogous to the measurement of VCD, Polavarapu (1988) has proposed a polarizing interferometer for the measurement of ROA.

6.3.2.3 Theoretical models

Theoretical models of different complexity are available for Raman CID. They can be used to calculate the Raman optical activity with quantum chemical programs. Though some good results have been reported using semiempirical calculations, the most reliable are the results obtained with *ab initio* methods, pioneered by Polavarapu (1990).

Hecht and Nafie (1991) have published their first part of a complete circular polarization formalism of the theory of natural Raman optical activity.

6.3.2.3.1 The molecular polarizability and optical activity tensors

The occurrence of Raman scattering is connected to the change in polarizability during the transition of the molecule from one vibrational state to the other. Circular polarization ROA arises from interference of the electric dipole – electric dipole polarizability tensor with the electric dipole – magnetic dipole and the electric dipole – electric quadrupole optical activity tensors. Due to limited space, no rigorous derivation of the theory will be given here, but only the most important results shall be shown.

The following common conventions are used: complex entities have been noted by a tilde and can be decomposed into a real and an imaginary part, e.g. in the case of the polarizability tensor:

$$\tilde{\alpha}_{\alpha\beta} = \alpha_{\alpha\beta} - i\alpha'_{\alpha\beta} \quad (6.3-23)$$

In the discussion of Raman and ROA theory an important concept is that of the invariants. The values of invariants, the simplest example of which is the mean polarizability α , do not alter if the principal axes of the molecule are rotated.

Ordinary Raman scattering intensity (far from resonance) can be expressed in terms of two invariants: the isotropic transition polarizability α^2 , and the anisotropic transition polarizability $\beta(\alpha)^2$.

$$\alpha^2 = \frac{1}{9}\alpha_{\alpha\alpha}\alpha_{\beta\beta} = \frac{1}{9}(\alpha_{XX} + \alpha_{YY} + \alpha_{ZZ})^2 \quad (6.3-24)$$

$$\begin{aligned} \beta(\alpha)^2 &= \frac{1}{2}(3\alpha_{\alpha\beta}\alpha_{\alpha\beta} - \alpha_{\alpha\alpha}\alpha_{\beta\beta}) \\ &= \frac{1}{2}[(\alpha_{XX} - \alpha_{YY})^2 + (\alpha_{XX} - \alpha_{ZZ})^2 + (\alpha_{YY} - \alpha_{ZZ})^2 + \\ &\quad + 6(\alpha_{XY}^2 + \alpha_{XZ}^2 + \alpha_{YZ}^2)] \end{aligned} \quad (6.3-25)$$

where α denotes the molecular polarizability tensor, and X , Y , and Z are the principal axes of the molecule. If a greek subscript is used we look at a vector or tensor component and the subscript can be equal to X , Y , or Z . A repeated subscript has the meaning of a summation over all three cartesian components.

In Raman optical activity one encounters three additional invariants: the isotropic part of the magnetic dipole optical activity tensor $\alpha G'$, and its anisotropic part, $\beta(G')^2$, and the anisotropic part involving the electric quadrupole optical activity tensor, $\beta(A)^2$.

$$G' = \frac{1}{3}G'_{\alpha\alpha} = \frac{1}{3}(G'_{XX} + G'_{YY} + G'_{ZZ}) \quad (6.3-26)$$

$$\begin{aligned} \beta(G')^2 &= \frac{1}{2}(3\alpha_{\alpha\beta}G'_{\alpha\beta} - \alpha_{\alpha\alpha}G'_{\beta\beta}) \\ &= \frac{1}{2}[(\alpha_{XX} - \alpha_{YY})(G'_{XX} - G'_{YY}) + (\alpha_{XX} - \alpha_{ZZ})(G'_{XX} - G'_{ZZ}) + \\ &\quad + (\alpha_{YY} - \alpha_{ZZ})(G'_{YY} - G'_{ZZ}) + 6(\alpha_{XY}G'_{XY} + \alpha_{XZ}G'_{XZ} + \alpha_{YZ}G'_{YZ})] \end{aligned} \quad (6.3-27)$$

$$\begin{aligned} \beta(A)^2 &= \frac{1}{2}\omega\alpha_{\alpha\beta}\varepsilon_{\alpha\gamma\delta}A_{\gamma,\delta\beta} \\ &= \frac{1}{2}\omega[(\alpha_{YY} - \alpha_{XX})A_{Z,XY} + (\alpha_{XX} - \alpha_{ZZ})A_{Y,ZX} + (\alpha_{ZZ} - \alpha_{YY})A_{X,YZ}] \end{aligned} \quad (6.3-28)$$

Che and Nafie (1992) report the isolation of ROA invariants and illustrate the technique using the spectra of (+)-*trans*-pinane and (-)-*α*-pinene as examples. Later the same year, Hecht (1992) challenges their results and proposes variable scaling factors for the different ROA bands depending on their depolarization ratio. To reach this results, he emphasizes the importance of the inclusion of the cone of collection into the procedure for the isolation of Raman optical activity invariants.

The dimensionless CIDs (Barron and Buckingham, 1971) for right angle scattering can then be expressed using these invariants as:

$$\Delta_x(90^\circ) = \frac{2[45\alpha G' + 7\beta(G')^2 + \beta(A)^2]}{c[45\alpha^2 + 7\beta(\alpha)^2]} \quad (6.3-29)$$

for the polarized measurement, and as:

$$\Delta_z(90^\circ) = \frac{12[\beta(G')^2 - \frac{1}{3}\beta(A)^2]}{6c\beta(\alpha)^2} \quad (6.3-30)$$

for the depolarized measurement.

The dimensionless CIDs at the two other possible scattering geometries can then be given as (Barron, 1982):

$$\Delta(0^\circ) = \frac{8[45\alpha G' + \beta(G')^2 - \beta(A)^2]}{2c[45\alpha^2 + 7\beta(\alpha)^2]} \quad (6.3-31)$$

$$\Delta(180^\circ) = \frac{48[\beta(G')^2 + \frac{1}{3}\beta(A)^2]}{2c[45\alpha^2 + 7\beta(\alpha)^2]} \quad (6.3-32)$$

Andrews (1980) discussed the dependance of ROA on the scattering angle *en detail*.

6.3.2.3.2 The bond polarizability model

In accordance with Placzek's theory (1934) we can write the real part of the complex transition polarizability as the dynamic vibrational polarizability operator (which is a function of a static configuration Q of nuclei) acting on the vibrational state functions ν_m and ν_n :

$$(\alpha_{\alpha\beta})_{\nu_m\nu_n} = \langle \nu_m | \alpha_{\alpha\beta}(Q) | \nu_n \rangle \quad (6.3-33)$$

Both the initial vibrational state ν_n and the final vibrational state ν_m belong to the electronic ground state.

Similarly to the transition polarizability the vibrational transition optical activity tensors are written as:

$$(G'_{\alpha\beta})_{\nu_m\nu_n} = \langle \nu_m | G'_{\alpha\beta}(Q) | \nu_n \rangle \quad (6.3-34)$$

$$(A_{\alpha,\beta\gamma})_{\nu_m\nu_n} = \langle \nu_m | A_{\alpha,\beta\gamma}(Q) | \nu_n \rangle \quad (6.3-35)$$

We can now expand the operators in a Taylor series in the normal coordinates and replace the p^{th} normal vibrational coordinates Q_p by the local internal vibrational coordinates s_q :

$$s_q = \sum_{p=1}^{3N-6} L_{qp} Q_p \quad (6.3-36)$$

where L_{qp} are the elements of the transformation matrix from cartesian to normal coordinates.

Looking at the expressions for Δ (Eqs. 6.3-23 to 6.3-26) we see that we need five different products of the tensors $\alpha_{\alpha\beta}$, $G'_{\alpha\beta}$ and $A_{\alpha,\beta\lambda}$ to calculate the optical activity of a fundamental transition associated with the vibrational normal coordinates Q_p :

$$\begin{aligned} & \langle 0 | \alpha_{\alpha\beta} | 1_p \rangle \langle 1_p | \alpha_{\alpha\beta} | 0 \rangle = \\ & \frac{\hbar}{2\omega_p} \left[\sum_i \sum_q \left(\frac{\partial \alpha_{i\alpha\beta}}{\partial s_q} \right)_0 L_{qp} \right] \left[\sum_j \sum_r \left(\frac{\partial \alpha_{j\alpha\beta}}{\partial s_r} \right)_0 L_{rp} \right] \end{aligned} \quad (6.3-37)$$

$$\begin{aligned} & \langle 0 | \alpha_{\alpha\beta} | 1_p \rangle \langle 1_p | G'_{\alpha\beta} | 0 \rangle = \\ & - \frac{\hbar\omega}{4\omega_p} \varepsilon_{\beta\gamma\delta} \left\{ \sum_{i < j} (R_{ji\gamma})_0 \left[\sum_q \left(\frac{\partial \alpha_{i\alpha\beta}}{\partial s_q} \right)_0 L_{qp} \right] \left[\sum_r \left(\frac{\partial \alpha_{j\delta\alpha}}{\partial s_r} \right)_0 L_{rp} \right] + \right. \\ & + \left[\sum_i \sum_q \left(\frac{\partial \alpha_{i\alpha\beta}}{\partial s_q} \right)_0 L_{qp} \right] \left[\sum_j (\alpha_{j\delta\alpha})_0 \sum_r \left(\frac{\partial r_{j\gamma}}{\partial s_r} \right)_0 L_{rp} \right] \left. \right\} + \\ & + \frac{\hbar}{2\omega_p} \left[\sum_i \sum_q \left(\frac{\partial \alpha_{i\alpha\beta}}{\partial s_q} \right)_0 L_{qp} \right] \left[\sum_j \sum_r \left(\frac{\partial G'_{j\alpha\beta}}{\partial s_r} \right)_0 L_{rp} \right] \end{aligned} \quad (6.3-38)$$

$$\begin{aligned} \frac{1}{3}\omega\langle 0|\alpha_{\alpha\beta}|1_p\rangle\langle q_p|\varepsilon_{\alpha\gamma\delta}A_{\gamma,\delta\beta}|0\rangle = \\ \frac{\hbar\omega}{4\omega_p}\varepsilon_{\beta\gamma\delta}\left\{\sum_{i<j}(R_{ji\gamma})_0\left[\sum_q\left(\frac{\partial\alpha_{i_{\alpha\beta}}}{\partial s_q}\right)_0L_{qp}\right]\left[\sum_r\left(\frac{\partial\alpha_{j_{\beta\alpha}}}{\partial s_r}\right)_0L_{rp}\right] + \right. \\ \left. + \left[\sum_i\sum_q\left(\frac{\partial\alpha_{i_{\alpha\beta}}}{\partial s_q}\right)_0L_{qp}\right]\left[\sum_j(\alpha_{j_{\beta\alpha}})_0\sum_r\left(\frac{\partial r_{j\gamma}}{\partial s_r}\right)_0L_{rp}\right]\right\} + \\ + \frac{\hbar\omega}{6\omega_p}\left[\sum_i\sum_q\left(\frac{\partial\alpha_{i_{\alpha\beta}}}{\partial s_q}\right)_0L_{qp}\right]\left[\varepsilon_{\alpha\gamma\delta}\sum_j\sum_r\left(\frac{\partial A_{j_{\gamma,\delta\beta}}}{\partial s_r}\right)_0L_{rp}\right] \end{aligned} \quad (6.3-39)$$

$$\begin{aligned} \langle 0|\alpha_{\alpha\alpha}|1_p\rangle\langle 1_p|\alpha_{\beta\beta}|0\rangle = \\ \frac{\hbar}{2\omega_p}\left[\sum_i\sum_q\left(\frac{\partial\alpha_{i_{\alpha\alpha}}}{\partial s_q}\right)_0L_{qp}\right]\left[\sum_j\sum_r\left(\frac{\partial\alpha_{j_{\beta\beta}}}{\partial s_r}\right)_0L_{rp}\right] \end{aligned} \quad (6.3-40)$$

$$\begin{aligned} \langle 0|\alpha_{\alpha\alpha}|1_p\rangle\langle 1_p|G'_{\beta\beta}|0\rangle = \\ \frac{\hbar}{2\omega_p}\left[\sum_i\sum_q\left(\frac{\partial\alpha_{i_{\alpha\alpha}}}{\partial s_q}\right)_0L_{qp}\right]\left[\sum_j\sum_r\left(\frac{\partial G'_{j_{\beta\beta}}}{\partial s_r}\right)_0L_{rp}\right] \end{aligned} \quad (6.3-41)$$

It can then be shown (Barron and Buckingham, 1974) that for a molecule consisting of only ideally axially symmetric bonds $\beta(G)^2 = \beta(A)^2$ and $\alpha G = 0$. Using this equations, one can reduce the dimensionless CIDs for the different measurements to:

$$\Delta(0^\circ) = 0 \quad (6.3-42)$$

$$\Delta(180^\circ) = \frac{64\beta(G')^2}{2c[45\alpha^2 + 7\beta(\alpha)^2]} \quad (6.3-43)$$

$$\Delta_x(90^\circ) = \frac{16\beta(G')^2}{c[45\alpha^2 + 7\beta(\alpha)^2]} \quad (6.3-44)$$

$$\Delta_z(90^\circ) = \frac{8(G')^2}{6c\beta(\alpha)^2} \quad (6.3-45)$$

It can be seen from these equations that it is clearly preferable to use the 180° configuration for the measurement of ROA, since the CID in backscattering is four times more intense. Together with a two-fold increase in Raman intensity the improved signal-to-noise ratio allows for an eight-fold reduction of the measurement time. The first measurements with this geometry have been published by Hecht et al. (1989).

Hecht and Barron (1993) discuss the time reversal and Hermiticity characteristics of optical activity operators. They formulate the Raman optical activity observables for the four different forms of ROA in terms of matrix elements of the absorptive and dispersive parts of these operators. Rupprecht (1989) applied a matrix formalism for Raman optical activity to intensity sum rules.

6.3.2.4 Experimental results

As in the discussion on experimental VCD, this section will focus on the achievements of the last five years, even though some older results shall be given, where they seem to be in place.

Even more than fourteen years ago Hansen et al. (1979) used ROA to determine the absolute configuration of (+)-(R)-1-methyldane.

In the series of *R*-(+)-1-phenylethylamine, *R*-(+)-1-phenylethanol and *R*-(+)-1-phenylethylthiol Barron et al. (1989) examine the influence of heteroatom Rydberg p-orbitals on the ratio of polarized to depolarized ROA spectra. They explain the intensities of the methyl antisymmetric deformation band as injection of a large electric quadrupole contribution from the Rydberg orbitals, which are, as a crude calculation shows, of sufficient extension.

Ab initio and experimental Raman optical activity in (+)-(R)-Methyloxirane were reported by Bose et al. (1990). The measured spectra include depolarized, polarized, and "magic angle" Raman and ROA spectra. Magic angle (i.e. transmission axis of the analyser set at $\pm 35.26^\circ$ to the vertical) ROA spectra contain only contributions arising from the electric dipole - magnetic dipole polarizability. All three kinds of spectra were calculated with two basis sets and compared to experiments. All spectral features could be reproduced correctly in sign but only moderately in intensity.

Hecht et al. (1992) published the ROA spectra of pinanes and pinenes. They reported the SCP and ICP Raman optical intensities for right angle scattering in the four naturally occurring substances. The intensities for both experimental techniques in each case were identical within the noise level of the experiments, well in agreement with theory for far from resonance conditions.

Backscattered dual circular polarization results on ephedrine and its stereoisomers are reported by Yu et al. (1993). All four stereoisomers examined show very similar Raman spectra, but their ROA spectra nicely show the sensitivity of ROA to the configurations and conformations of the molecules. As the features observed seem to be connected to the *local* stereochemistry, it seems to be possible that in the near future, with some more experimental data at hand, to deduce the absolute configuration of molecules of unknown stereochemistry directly from the ROA spectra.

Polavarapu et al. (1993) reported recently the experimental and *ab initio* - theoretical results on (*R*)-(+)-3-methylcyclohexanone. They were able to reproduce the Raman and ROA spectra of the compound under study using the 6-31G and the 6-31G* basis sets. Since the reported depolarized ROA spectrum concerning signal-to-noise ratio shows the state of the art, it is reproduced in Fig. 6.3-17. The depolarized spectrum was taken of

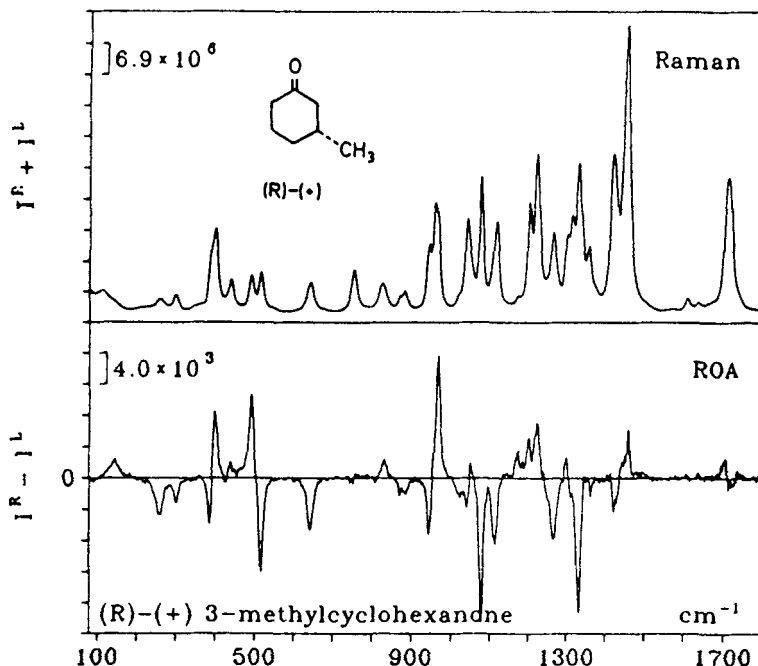


Figure 6.3-17 ROA spectrum of (+)-3-methylcyclohexanone (Reprinted with permission from Polavarapu et al., 1993, copyright 1993 American Chemical Society.) ~800 mW of 488 nm excitation light, pathlength 5 mm, 2.4 cm^{-1} resolution.

the neat liquid at right-angle scattering geometry using the 488 nm Argon ion laser line at a power of 800 mW.

The analysis of the ROA spectrum of alanine supported by *ab initio* calculations was presented by Barron et al. (1991). Later on, Gargaro et al. (1993) reported the ROA spectra of L-serine, L-cysteine, L-valine, L-threonine and L-isoleucine in aqueous solution.

A very interesting area is the measurement of ROA in natural substances of high molecular weight. Hecht et al. (1992) showed spectra of nucleosides thymidine and 2'-desoxycytidine. Barron et al. (1992a) reported the ROA of enzymes. The same year Barron et al. (1992b) published the ROA of proteins. The L-alanine trimer, ribonuclease A, lysozyme and bovine serum albumin spectra were discussed.

Bell et al. (1993) showed vibrational Raman optical activity of the carbohydrates D-galactose, D-maltose and laminarin at low wavenumbers. The authors observed a ROA couplet at $427 \pm 10 \text{ cm}^{-1}$ which, according to their opinion, reflects the configuration of the glycosidic links in complex carbohydrates.

Wen et al. (1993) showed the ROA spectra of 15 monosaccharides in aqueous solution. They found three main regions of interest, where ROA spectra should provide insights into local stereochemistry. The first is the region of 750 to 950 cm^{-1} reflecting anomeric configuration, the second at 950 to 1200 cm^{-1} gives information about ring structure and

patterns of substituents and the third above 1200 cm^{-1} answers the question about the conformation of an exocyclic hydroxymethyl group.

Recently, Barron and Hecht (1993) wrote a review of the latest ROA studies on biomolecules. They summarized the work published in this field to date and emphasized the point that ROA should provide more insight into protein structure than VCD. This conclusion is drawn on the fact that it is easily possible to replace N–H by N–D and to note the spectral changes, thereby often simplifying the spectrum by the reduction of overlap. VCD is not that easily possible in H_2O solution as normal water tends to obscure important parts of the IR spectrum, and there only the D_2O results are more readily available.

Wen et al. (1994) investigated the Raman optical activity of poly-L-lysine both as the random coil and the α -helix. They compared these spectra to the spectra of bovine serum albumin and insulin and arrived at the conclusion that tertiary structure of proteins can be readily deduced from the ROA spectra.

Raman optical activity can not only be measured in liquids or in solution, but also in crystals. As an example, the Raman CID spectra of both enantiomeric forms of sodium chlorate single crystals (Lindner, 1994) together with their sum spectra are shown in Fig. 6.3-18. Here a broken line represents the (-)-form. The transitions examined belong to the triply degenerate polar F phonons split into transverse and longitudinal modes.

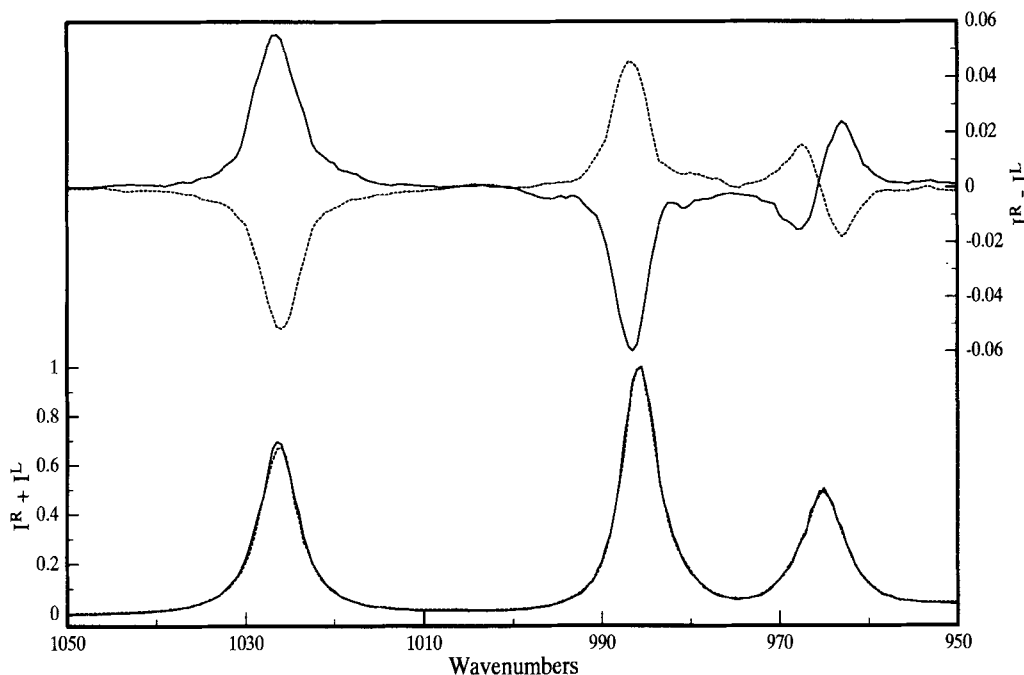


Figure 6.3-18 ROA spectrum of sodium chlorate single crystal taken with 1 W of 488 nm excitation light; $d = 0.85\text{ mm}$ for (+)-, and $d = 2.70\text{ mm}$ for (-)- NaClO_3 . Spectra are normalized to the strongest band.

The depolarized spectra were taken employing a 90 ° scattering geometry on a Ramanor HG.2S (Jobin-Yvon) scanning Raman spectrometer using a KD*P electrooptic modulator and 1 Watt of the 488 nm Argon ion laser line.

The measurement of Raman optical activity of achiral molecules in magnetic fields is also possible. An example of this technique is the magnetic ROA spectrum of the iridium (IV) hexachloride dianion published by Barron et al. (1987). The researchers used a magnetic field of 1 Tesla.

6.3.3 Conclusions

The measurement of vibrational optical activity has already proven to be a valuable tool in determining the structures of chiral compounds. Even relatively complicated natural compounds of medium size and the large biopolymers can reveal some of their structural secrets upon analysis of the VOA spectra. A bundle of theoretical models has been developed. Together with the fact that chiral substances become increasingly important for the chemical and pharmaceutical industry and have to be analysed somehow, the importance of vibrational optical activity, considered as a laboratory curiosity only some ten years ago, is to be expected to grow rapidly.

6.4 Foundations and features of infrared reflection techniques*

6.4.1 Introduction

Reflection is a ubiquitous phenomenon, dominating most visual impressions. Even the complementary effect, namely transmission, can virtually not be observed without being influenced by reflection. Wherever optical properties change, reflection occurs - very particular at the surface of a sample and at any boundary between two optically different media. Actually it is the step in the parameters rather than the thickness of uniform material, what governs this response.

Quite early in the history of infrared spectroscopy, reflections in form of reststrahlen bands were observed indicating strong absorption. Nowadays infrared spectroscopy is widely applied to organic compounds which are comparably weak absorbers. For their studies such reflection methods are favoured, whose results are interpretable in almost the same way as transmittance spectra are. However, there is an increasing interest in applying other reflection techniques also to such samples. Advantageous aspects are:

- sample preparation can be avoided, simplifying routine work and enabling us to address delicate samples;
- the optical properties can be determined completely and without reference to a special technique; from such data the optical response under any condition is exactly predictable;

* Section 6.4 is contributed by E.-H. Korte, Berlin and A. Röseler, Berlin

- the selectivity can be improved, e.g. by varying the angle of incidence and the polarization azimuth; information from different depths within the sample are discriminated;
- a sensitivity can be reached rendering possible the study of monolayers or even less, on substrates.

However when comparing to transmission, for reflection additional physical quantities and more experimental parameters are relevant. As a consequence a large variety of results is possible. These can be interpreted reliably only if the experiment is well defined and well understood; spectra simulations and model calculations are often instructive and necessary to discriminate optical effects from sample properties.

6.4.2 Physical background

If matter is exposed to an electric field E , an electric displacement D results which formally is given by

$$D = \varepsilon E \quad (6.4-1)$$

where ε is called permittivity or dielectric constant. For an oscillating field ε varies with frequency and is usually called dielectric function. From ultraviolet to infrared frequencies and beyond this range, the optical response can be specified in this way. The refractive index n is related to the dielectric function by

$$n = \sqrt{\varepsilon} \quad (6.4-2)$$

and grants an equivalent, sometimes more illustrative description. For instance it is used in the well-known formulation of Snell's law

$$n_1 \sin \varphi_1 = n_2 \sin \varphi_2 \quad (6.4-3)$$

(see Fig. 6.4-1) which describes the *refraction* of an electromagnetic wave at the interface between two media; φ denotes the angle the propagation direction forms with the normal of the interface.

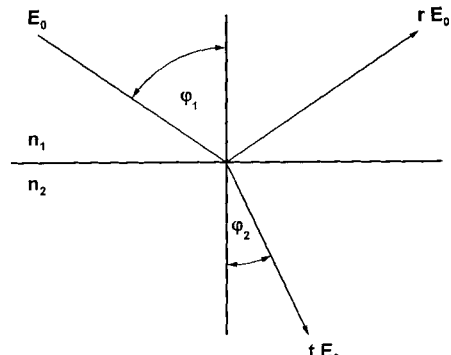


Figure 6.4-1 Notation used for Snell's law. The amplitude of the electric vector of the incident wave is E_0 , r and t are the amplitude coefficients for reflection and transmission, respectively. The electric vector of s-polarized radiation is perpendicular to the plane shown.

On the basis of Maxwell's theory, the reflected and the refracted waves are explicitly stated by Fresnel's equations. The coefficient r correlates the amplitude E of the reflected wave with the amplitude E_0 of the incident one (Born, 1933; Born and Wolf, 1980; Bennett and Bennett, 1978):

$$\begin{aligned} r_s &= (n_1 \cos\varphi_1 - n_2 \cos\varphi_2)/(n_1 \cos\varphi_1 + n_2 \cos\varphi_2) \\ &= -\sin(\varphi_1 - \varphi_2)/\sin(\varphi_1 + \varphi_2) \\ r_p &= (n_2 \cos\varphi_1 - n_1 \cos\varphi_2)/(n_2 \cos\varphi_1 + n_1 \cos\varphi_2) \\ &= \tan(\varphi_1 - \varphi_2)/\tan(\varphi_1 + \varphi_2) \end{aligned} \quad (6.4-4)$$

The polarization is specified by the plane in which the electric vector oscillates: the index s stands for perpendicular to the plane of reflection, and the index p stands for parallel to it (note: the traditional definition of the plane of polarization is perpendicular to the plane of the vector oscillations!). The condensed expressions on the very right side of these equations result from applying Snell's law. For optically active media and incident circularly polarized radiation see Sec. 6.3; compare also Secs. 3.2, 4.6.4 and 4.6.5. The square of an electric field strength E is measured as intensity; the quotient of the reflected intensity and the incident one is the *reflectance* R

$$R = r^2 \quad (6.4-5)$$

provided no absorption is involved. As a consequence, R depends on the polarization azimuth. The amplitude coefficients for the refracted components are found to be

$$\begin{aligned} t_s &= 2n_1 \cos\varphi_1/(n_1 \cos\varphi_1 + n_2 \cos\varphi_2) \\ t_p &= 2n_1 \cos\varphi_1/(n_2 \cos\varphi_1 + n_1 \cos\varphi_2) \end{aligned} \quad (6.4-6)$$

The refracted intensity is $\tau = (1 - R)$, however, this is not just t^2 . Since this radiation component is now travelling in a different medium, the energy density has to be taken into account. From considering the Poynting vector it follows

$$\tau = |t|^2(n_2 \cos\varphi_2)/(n_1 \cos\varphi_1) \quad (6.4-7)$$

It gives the intensity just behind the interface. It is further reduced by absorption when travelling through the medium. This attenuation is usually specified by the term ('inner') *transmittance* T .

The reflectance at a boundary between air ($n = 1$) and a non-absorbing medium of $n = 1.5$ is shown in Fig. 6.4-2 for both polarizations in dependence on the angle of incidence. Identical results are obtained for the same ratio n_1/n_2 even if the individual values differ. For grazing incidence, i.e. $\varphi_1 = 90^\circ$ and thus $\cos\varphi_1 = 0$, reflectance

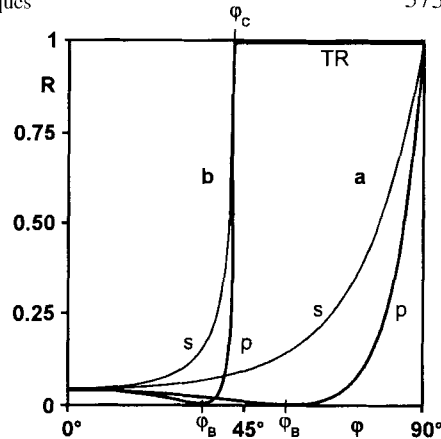


Figure 6.4-2 Reflectance R versus angle of incidence φ for s and p polarization. On an interface between a medium ($n = 1.50$) and air ($n = 1$) radiation is incident (a) from air, (b) from medium. φ_B denotes the Brewster angles, φ_C the critical angle; TR marks the range of total reflection.

approaches unity independent of polarization and material. The angle at which no p-polarized radiation is reflected at all, is called *Brewster angle* φ_B or polarizing angle. The latter denomination refers to the fact that radiation having been reflected under this angle is totally s polarized. The situation arises when the direction of the refracted beam and the one of the reflected beam are mutually perpendicular; from Snell's law one finds

$$\varphi_B = \tan^{-1}(n_2/n_1) \quad (6.4-8)$$

Provided $n_1 > n_2$, there is one angle of incidence for which $\sin\varphi_2$ equals unity. Beyond this so-called critical angle

$$\varphi_C = \sin^{-1}(n_2/n_1) \quad (6.4-9)$$

Snell's law cannot be fulfilled with real angles of refraction. Provided the refractive index of the rarer medium n_2 is real, one finds

$$\cos\varphi_2 = (1 - n_1^2 \sin^2\varphi_1/n_2^2)^{1/2} = i(n_1^2 \sin^2\varphi_1/n_2^2 - 1)^{1/2} \quad (6.4-10)$$

with $i^2 = -1$. Inserting this expression into Eqs. 6.4-4 makes clear that total reflectance occurs (see Fig. 6.4-2): the reflection coefficients for both, p-polarized and s-polarized radiation components equal unity since they are ratios of complex conjugates with consequently identical moduli (absolute values). As dictated by Snell's law, the angle of reflection agrees with the one of incidence, however the reflected beam is slightly displaced (see insert in Fig. 6.4-3). This is known as Goos-Hänchen effect (Goos and Hänchen, 1943, 1947; Goos and Lindberg-Hänchen, 1949) and related to the fact that the energy travels along the boundary without penetrating the rarer medium, still it causes an evanescent field therein. This is the case of an extremely inhomogeneous wave (Born and Wolf, 1980), where the planes of constant phase and the planes of constant amplitude do not coincide, actually they are perpendicular to each other.

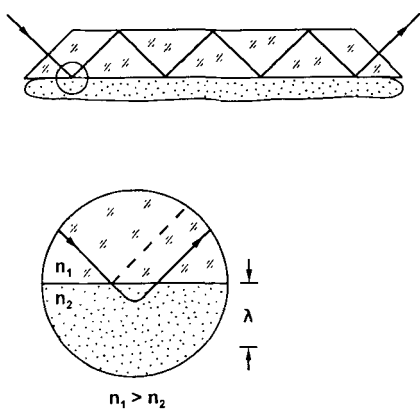


Figure 6.4-3 Attenuated total reflection (ATR): multiple reflections element.

If the rarer medium absorbs, the reflection is no longer without loss: the evanescent field is weakened and the reflected wave cannot be reconstructed with full amplitude. As a consequence, the spectrally almost constant reflectance is modulated with a sort of absorption spectrum of the rarer medium. The related experimental technique ATR is discussed in Sec. 6.4.4.3.

The considerations before refer to the non-absorbing case when ε and n are real quantities. In order to characterize the optical properties completely absorption must be included. This can be achieved by taking the optical and dielectric functions to be complex quantities comprising two real figures each. The (real) refractive index n is complemented by the real absorption index k to constitute the complex refractive index

$$\hat{n} = n + ik \quad (6.4-11)$$

Other specifications of absorption such as transmittance T , absorbance A , (decadic molar) absorptivity ϵ [$\text{L mol}^{-1} \text{cm}^{-1}$], absorption coefficient a [cm^{-1}] are interrelated with the absorption index k by

$$a = 4\pi\tilde{\nu}k = \epsilon c / (\ln 10)$$

$$T = e^{-ad} = 10^{-ecd} \quad (6.4-12)$$

$$A = ecd$$

where c denotes concentration [mol/L], d thickness [cm] and $\tilde{\nu}$ wavenumber [cm^{-1}]; it should be seen that in Eqs. 6.4-12 ϵ does not denote a dielectric property (ε).

For the complex quantities the quadratic relation $\hat{n}^2 = \hat{\varepsilon}$ (cf. Eq. 6.4-2) is still valid. Consequently, the parts of $\hat{\varepsilon} = \varepsilon' + i\varepsilon''$ are found to be

$$\varepsilon' = n^2 - k^2 \quad \varepsilon'' = 2nk \quad (6.4-13)$$

Reflectance must be identified now with the square of the modulus of the reflection coefficients Eqs. 6.4-4

$$R = |r|^2 = rr^* \quad (6.4-14)$$

with r^* being the complex conjugate. Closer inspection proves that some intensity is reflected even from an interface between two media which do not differ but in the absorption index k . This is obvious from the explicit expression for the reflectance against air at normal incidence

$$R_s(0^\circ) = R_p(0^\circ) = [(1 - n)^2 + k^2] / [(1 + n)^2 + k^2] \quad (6.4-15)$$

As any complex figure, the reflection coefficients r can be written in the general form

$$r = |r|\exp(i\delta) \quad (6.4-16)$$

where δ states a phase angle. The phase shift introduced by the process of reflection depends on the same parameters as the amplitude coefficients do, and it depends on polarization.

The superposition of two coherent but phase-shifted waves oscillating in mutually perpendicular planes causes the tip of the electric vector to travel on a helical path with elliptical cross-section. The ellipse represents the most general polarization state. Depending on the parameters it might degenerate into a straight line or a circle characterizing linear or circular polarization, respectively (cf. Sec. 3.2). In any case, the polarization (excluding total intensity) is completely characterized by two parameters which are the proportion of the rectangle circumscribing the ellipse (see Fig. 6.4-4)

$$|E_p| / |E_s| = |r_p| / |r_s| \equiv \tan\psi \quad (6.4-17)$$

and the mutual phase difference Δ of the p and s components. The two angles ψ (stating the slope of the diagonal) and Δ are called ellipsometric parameters, their use is outlined in Sec. 6.4.4.2.

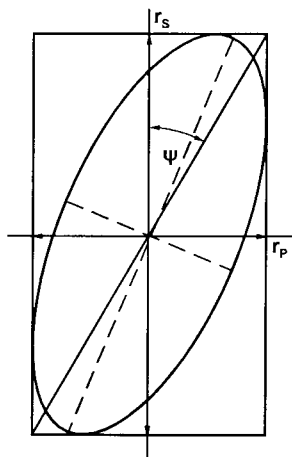


Figure 6.4-4 Elliptical polarization: The path of the tip of the electric vector as projected into a plane perpendicular to the direction of propagation. The ellipse is generated by mutually perpendicular oscillations with amplitudes r_s and r_p , resp., which are phase shifted by an angle Δ . It is fully defined by the ellipsometric parameters Δ and $\psi = \tan^{-1}(|r_s| / |r_p|)$.

All deviations from a monotonous spectral behaviour in the infrared range can be traced back to vibrational resonances. Their direct consequences are the absorption bands and the related dispersion anomalies in the n spectrum. Traditionally the term anomaly refers to the interval where the refractive index increases with decreasing wavenumbers, it is used here to define a somewhat wider range. Whole spectra can be simulated on the basis of sets of suitably selected oscillators, some of which might be outside the spectral range under consideration. Typical features are often modelled with one or two oscillators while the remaining influence by all the others is taken into account by a background. Assuming a Lorentzian oscillator of strength f and damping constant Γ , with resonance at the wavenumber $\tilde{\nu}_0$, the dielectric function varies with wavenumber $\tilde{\nu}$ as

$$\begin{aligned}\varepsilon'(\tilde{\nu}) &= \varepsilon_\infty + (\tilde{\nu}_0^2 - \tilde{\nu}^2)f / [(\tilde{\nu}_0^2 - \tilde{\nu}^2)^2 + \Gamma^2\tilde{\nu}^2] \\ \varepsilon''(\tilde{\nu}) &= \Gamma\tilde{\nu}f / [(\tilde{\nu}_0^2 - \tilde{\nu}^2)^2 + \Gamma^2\tilde{\nu}^2]\end{aligned}\quad (6.4-18)$$

where ε_∞ denotes the dielectric constant at infinitely large frequency. For two oscillators, differing in strength, spectra of ε' and ε'' as well as n and k were simulated on this basis:

- the parameters of the strong oscillator ($\tilde{\nu}_0 = 1000 \text{ cm}^{-1}$, $f = 0.2 \cdot 10^6 \text{ cm}^{-2}$, $\Gamma = 15 \text{ cm}^{-2}$, $\varepsilon_\infty = 2.1$) were chosen for similarity with the pronounced infrared resonance of quartz glass; the absorption index exceeds 2.5 so that for best transmittance measurements (at $T = e^{-1}$) a thickness of about 0.3 μm would be required; results including the ellipsometric parameters are shown in Fig. 6.4-5;
- the weak oscillator ($\tilde{\nu}_0 = 1000 \text{ cm}^{-1}$, $f = 800 \text{ cm}^{-2}$, $\Gamma = 10 \text{ cm}^{-1}$, $\varepsilon_\infty = 1.8$) is typical for many bands of organic compounds; the maximum absorption index is about 0.03, and 30 μm would be an appropriate thickness; results are shown in Fig. 6.4-6.

Strong oscillator

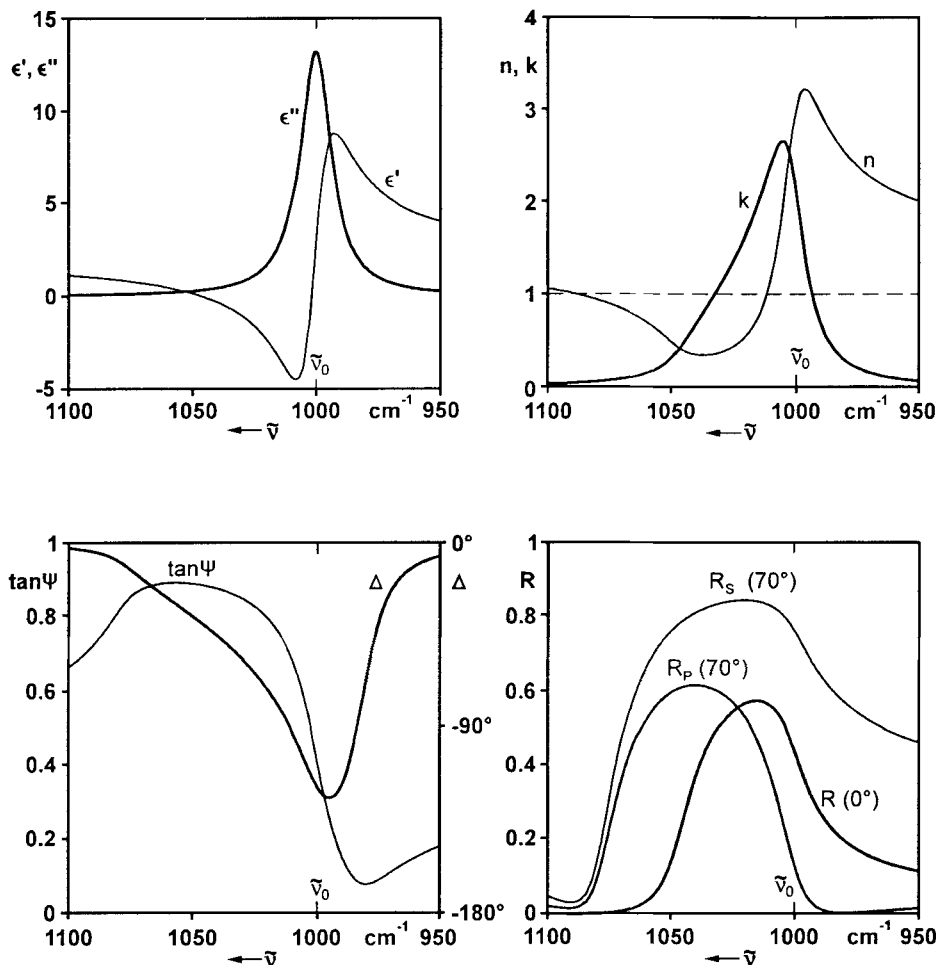


Figure 6.4-5 Simulated spectra of a strong oscillator (strength $f = 200 \cdot 10^3 \text{ cm}^{-2}$) with resonance at $\tilde{\nu}$: real and imaginary part of the dielectric function $\hat{\epsilon} = \epsilon' + i\epsilon''$, refractive index n and absorption index k , ellipsometric parameters Δ and ψ , as well as reflectance R for the angles of incidence and the polarization states stated.

For the weak oscillator the shapes of all graphs related to \hat{n} and $\hat{\epsilon}$ are symmetrical with respect to the resonance frequency, pairwise similar, and no distinctive wavenumber shift is found. The reflectance spectrum resembles closely the dispersion anomaly of the (real) refractive index. The spectral variations of the components of the dielectric function are

Weak oscillator

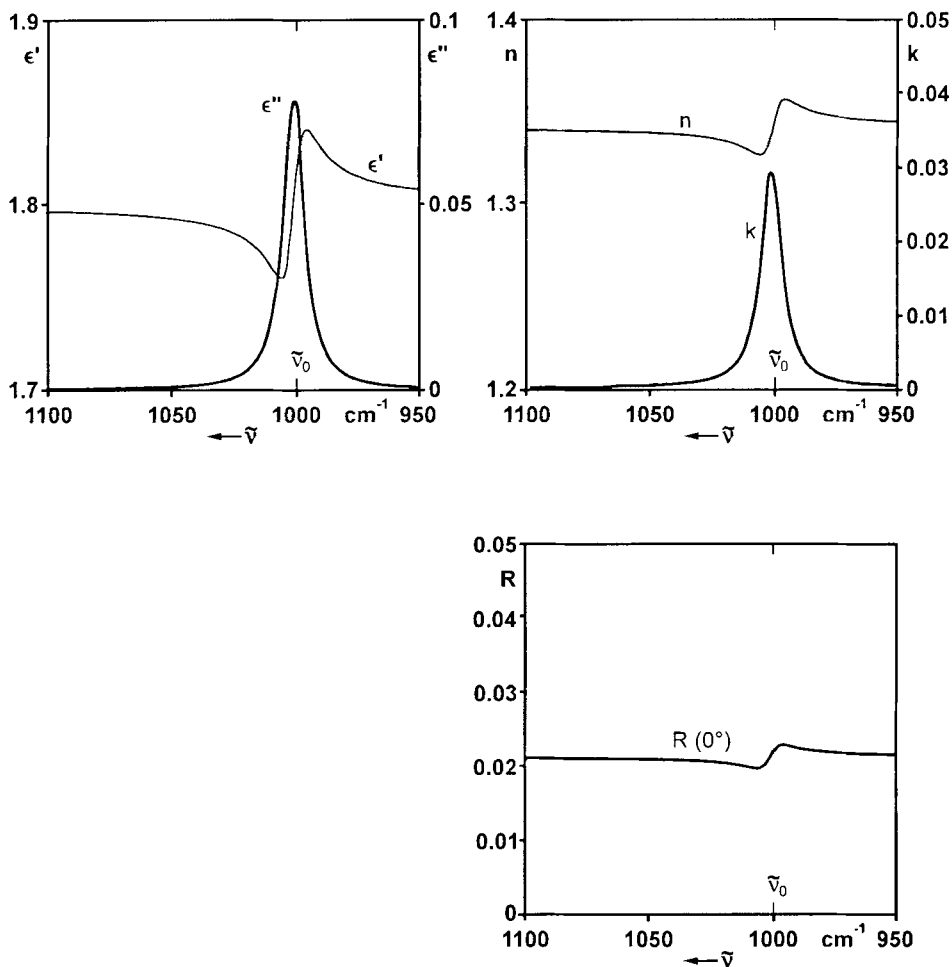


Figure 6.4-6 Simulated spectra of a weak oscillator ($f = 0.8 \cdot 10^3 \text{ cm}^{-2}$). Same notations as for Fig. 6.4-5.

principally similar for both model oscillators but in scale. In solid state spectroscopy the band in the ϵ'' is often referred to as *transversal optical mode* or in short, TO mode.

For the strong oscillator the n and k spectra are asymmetric. The shift of the k maximum away from the resonance frequency is particularly obvious. In such a case a reliable representation of the vibrational structure cannot be derived from transmittance spectra and thus, from the absorption index k alone. Another peculiarity of the strong oscillator is the spectral range where the (real) refractive index is below unity. This renders

possible total reflection against air at appropriate angles of incidence. For such effects observed with minerals and inorganic glasses, the term *reststrahlen* was coined. The strong influence of this range on the reflectance spectra is obvious from Fig. 6.4-5 where simulations for normal and oblique incidence are presented. Reflectance at 0° incidence (Eq. 6.4-15) is primarily determined by the absorption band (k) accomplished on the low-wavenumber side by the contribution from the refractive index. The spectral shape is similar to a band rather than to a dispersion feature. Also at large angles of incidence, the reflectance spectra for s-polarized and p-polarized radiation are characterized by bands. These are definitely shifted away from the resonance frequency and into the reststrahlen range, and they are correspondingly broadened.

The high-wavenumber limit of such a reflectance band is clearly defined by the point where n equals unity ($\tilde{\nu} \approx 1090 \text{ cm}^{-1}$), i.e. the refractive index of ambient air. The other occurrence of $n = 1$ close to $\tilde{\nu}_0$ is accompanied by such high absorption, that considerable reflectance is observed at least for the s-polarized component. The reflectance band for p-polarized radiation is limited to short wavenumbers where the condition for the Brewster angle is met. This condition is met a second time within the reflection band. This does not become evident in the reflectance spectrum due to the related high value of k .

To some extend the existence of a reststrahlen range ($n < 1$) defines a strong oscillator. Within this range another remarkable situation is found where $\epsilon' = 0$. According to Eq. 6.4-13 this means $n = k$. This condition refers to the so-called *longitudinal optical (LO) mode* and cannot be observed with bulk material. Its excitation by a transversal electromagnetic wave should be forbidden. However, when a thin film of a reststrahlen material is deposited on a highly reflecting substrate such as metal, a guided wave can be excited at this particular wavenumber. This phenomenon is known as Berreman effect (Berreman, 1963) and renders possible to identify and quantify surface layers of some nanometers thickness - roughly ten thousand times thinner than the infrared wavelength used (Weidner and Röseler, 1992). The outstanding gain in sensitivity is reached since radiation is travelling a long distance within the film rather than just traversing it. An experimental example is given in Fig. 6.4-7.

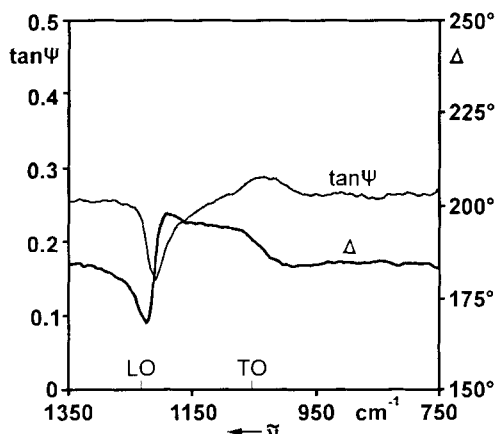


Figure 6.4-7 Berreman effect observed with a ca. 22 nm thick layer of SiO_2 on Si substrate.

Considering a spectral range, the total agreement of the optical functions of two media is an exception even if their properties are similar. At an interface between such media, reflection occurs but for that point where the optical functions agree: the interface becomes invisible. The effect enhanced by multiple occurrence, is used for the so-called Christiansen filter (Geffcken, 1939), consisting of particles immersed in a liquid, both components are selected for appropriate dispersion. As a consequence, incident radiation is scattered except for a narrow spectral transmission window. An equivalent effect occurs with pellets, i.e. particulates embedded in e.g. KBr: as long as the individual particles are large enough to cause considerable scattering, the recorded bands of a transmission spectrum are distorted with a dispersion-like contribution (Christiansen effect).

Vibrations are the origin of the optical properties described by the complex functions $\hat{\varepsilon}$ or \hat{n} . In both cases the real and imaginary parts show two different aspects of just the same phenomenon, therefore it is not too surprising, that they carry the same information. In such an instance, a general relation exists which correlates the two parts by integral equations (Kramers, 1929; Kronig, 1926). In the context of spectroscopy, these *Kramers-Kronig transformations* are to be applied to the full spectrum from zero to infinitely large wavenumbers of one (real or imaginary) part in order to obtain the value of the other part at any chosen wavenumber ($\tilde{\nu}_0$). The spectrum of the latter can be calculated point by point. In the most general case, Hilbert transformations of the type

$$\begin{aligned} F'(\tilde{\nu}_0) &= 1 / \pi \mathcal{P} \int_{-\infty}^{+\infty} d\tilde{\nu} F''(\tilde{\nu}) / (\tilde{\nu} - \tilde{\nu}_0) \\ F''(\tilde{\nu}_0) &= -1 / \pi \mathcal{P} \int_{-\infty}^{+\infty} d\tilde{\nu} F'(\tilde{\nu}) / (\tilde{\nu} - \tilde{\nu}_0) \end{aligned} \quad (6.4-19)$$

(\mathcal{P} indicates the principal value) are applied to a function $F = F' + iF''$ (Bode, 1950; Smith, 1985; Hopfe et al., 1981). Such so-called dispersion relations exist between the (real) refractive index and the absorption index. Dedicated software programs are available, also specially for (infrared) spectroscopic purposes (Hopfe, 1989), a generalization for oblique incidence on layered systems was given by Grosse and Offermann (1991).

As it is easily derived from Eqs. 6.4-18, the relations are valid also for birefringence and dichroism. As far as optical activity in the UV/VIS range is concerned transformations on this basis have already been widely used for decades to correlate circular-dichroism bands and Cotton effects, i.e. anomalies of the optical rotatory dispersion (Moffit and Moscowitz, 1959; Blout et al., 1967). Another relation is mentioned in the following section.

6.4.3 Modelling and evaluation

Using Fresnel's equations (Eqs. 6.4-4) the reflectance at an interface between two homogeneous media can be calculated for all angles of incidence and azimuths of the plane of polarization. As a prerequisite, the compound specific optical functions $\hat{\varepsilon}$ or \hat{n} or

the parameters of an equivalent set of oscillators must be known for both media. With anisotropic samples, i.e. those exhibiting birefringence and dichroism, additionally the orientation of the axes with respect to the probing radiation must be taken into account (cf. Sec. 3.2).

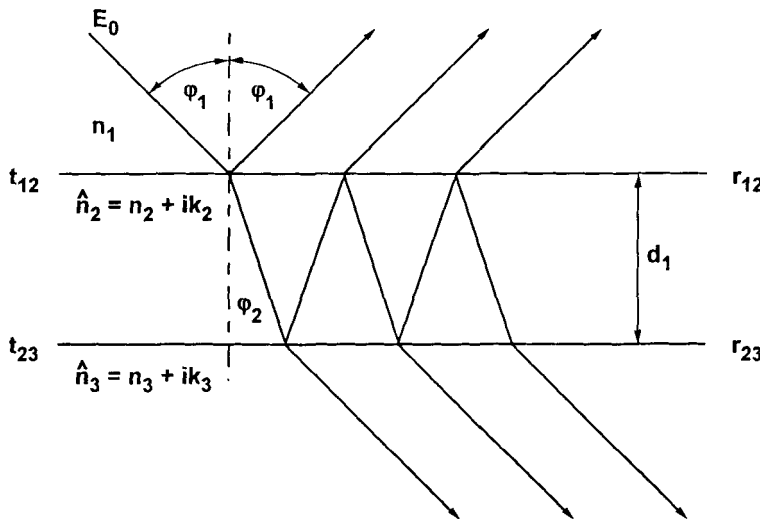


Figure 6.4-8 Multibeam interference from a planoparallel slab (notation for the three media problem).

The refracted component is further attenuated according to Beer's law when travelling through the second medium. In a slab of limited thickness d , radiation reflected at the back surface returns to the front surface where it is refracted out of the slab. This radiation might interfere with externally reflected radiation (see Fig. 6.4-8). Including further reflections results in a multibeam interference pattern which is described by the general Airy equation

$$r_{\text{Airy}} = (r_{1,2} + r_{2,3}e^{i\zeta}) / (1 + r_{1,2}r_{2,3}e^{i\zeta}) \quad (6.4-20)$$

where $r_{i,j}$ denotes the reflection coefficients at the interface from medium i to medium j , and

$$\zeta = 4\pi\nu d(\hat{n}_2^2 - \hat{n}_1^2 \cos^2\varphi_1)^{1/2} = 4\pi\nu d(\hat{n}_2 \cos\varphi_2)$$

quantifies the phase shift and the attenuation resulting from a dual passage through the slab. While reflection basically does not depend on thickness, geometry comes into play here: except for the first one, all other contributions depend on the pathlength.

For the calculation of the optical response of stratified media, i.e. piles of planoparallel layers, several algorithms have been proposed which render possible an easy handling even without computer. Abelès (1963) introduced a characteristic 2×2 matrix for an individual film. The matrix elements are functions of $\hat{\epsilon}$ or \hat{n} , and the thickness, as well as of the angle of incidence and the azimuth of polarization. Multiplication of the matrices for all the layers grants the characteristic matrix of the pile as a whole, from which reflectance and transmittance is easily derived (Born and Wolf, 1980). Wolter (1956) proposed a convenient algorithm for calculating sequentially the response of the pile. Further calculatory simplifications are possible for periodically structured media (Born and Wolf, 1980). An example is the so-called *dielectric mirror* which consists of bi-layers made up from non-absorbing materials. Depending on the refractive indices and the thicknesses, such a stack exhibits 'selective reflection', i.e. high reflectance within a limited spectral interval. A similar effect occurs with cholesteric liquid crystals for circular polarized radiation (cf. Sec. 4.6.3).

Simplified evaluations are possible when for instance interference patterns in a non-absorbing spectral range reveal the thickness of a particular layer. Such analyses e.g. of semiconductor multilayers by simulating and fitting spectra reveal astonishing details (Grosse, 1989, 1992; Grosse et al., 1990; Weidner and Röseler, 1992).

Since multilayered structures can be treated conveniently, they can be applied to model continuous changes of optical properties, such as concentration gradients. This requires the optical functions for many neighboured concentrations throughout the mixing range. As long as structural details of a mixture are small compared to the wavelength and no specific interactions among the constituents occur, a uniform optical function can be derived from the polarizabilities of the neat components and their volume fractions. From the *effective-medium approximations* (Aspnes, 1985) the best suited one must be chosen by considering the microstructure of the mixture. The Maxwell-Garnett variety refers to

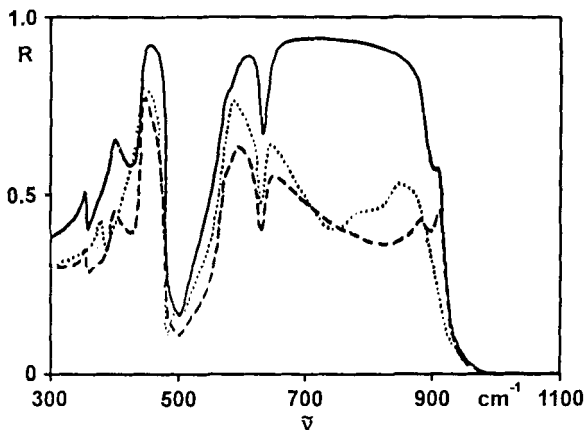


Figure 6.4-9 Modelling of a rough surface on Al_2O_3 ceramics. Solid line: spectrum simulated for smooth surface; broken line: simulated with gradient layer; dotted line: measured at 20° incidence (Hopfe et al., 1993c).

the case where the particles of one component are completely surrounded by the matrix medium (Garnett, 1904, 1906). The Bruggeman model applies to random or aggregate configurations (Bruggeman, 1935). Effective medium approximations also allow to model rough surfaces or interfaces, which tend to influence the spectra considerably (see Fig. 6.4-9): each layer is considered to be made up from the bulk material and vacuum, and the dilution with vacuum decreases from the outer surface to the compact substrate (Hopfe et al., 1993a-c). In such a case some radiation should be diffusely reflected (cf. Sec. 6.4.4.5) with an essentially different spectral pattern; however this radiant flux is spread all over the entire hemisphere above the sample so that it does not contribute substantially to what is detected in the comparably narrow cone of specular reflection.

Generally, transmittance and reflectance of a sample as well as the related polarization states can be calculated as far as the optical functions of the different components and the geometry of the sample are reliably known. The optical behaviour of neat metals and other inorganic solids are well documented even for the infrared range (e.g. Palik, 1985 and 1991). For organic compounds mostly just transmission spectra are known qualitatively. Independent of this, the inverse problem of evaluating the optical data from measured spectra is usually more difficult. In most cases the algorithms mentioned above cannot simply be inverted. Furthermore, two relevant quantities give the full information only in the case of a thick sample, but would not be sufficient to characterize e.g. a layer on an exactly known substrate, since the layer thickness is a third independent parameter. Fitting calculated and measured results within a broader spectral range rather than for just one resolution element is advantageous. Measurements at different angles of incidence can be employed to obtain more results, however this usually implies that differently large areas are addressed.

Ellipsometry grants the independent determination of two results per resolution element without changing the experimental geometry; this technique is described in Sec. 6.4.4.2. More often however, the information on the phase shift is abandoned and just the reflectance is determined. Usually it is measured by comparing the signal caused by the reflected intensity with the one obtained when the sample is replaced by a mirror. Even without correcting for its reflectance such results can often be used for further mathematical evaluation. The Fresnel reflection coefficient r in the form given by Eq. 6.4-16 can be rewritten as

$$\ln r = \ln|r| + i\delta = \frac{1}{2} \ln R + i\delta \quad (6.4-21)$$

(cf. Eq. 6.4-14). Again the real part and the complex one are correlated by a dispersion relation, and therefore the phase δ can be reconstructed from the measured reflectance spectrum by a Kramers-Kronig transformation (Hopfe, 1989). Both quantities together allow e.g. to calculate the components of the dielectric function of a thick sample. For more complicated sample structures, careful consideration of possible pitfalls is recommended (Grosse and Offermann, 1991).

A difficulty in reconstructing the phase arises from the range of particularly low reflectance around the high-wavenumber occurrence of $n = 1$ as discussed with Fig. 6.4-5. The resulting large absolute value of the logarithm dominates the integral while

the measurement might be particularly susceptible to errors due to poor signal-to-noise ratio or imperfect polarization discrimination. The general concern with regard to the application of Kramers-Kronig relations are the usually limited ranges of measured data. Anyway for practical applications often spectral patterns rather than absolute data are important, as e.g. for identification of compounds via library search. For such purposes a Kramers-Kronig transformation is a ready-to-use tool also for weakly absorbing, for instance organic materials (Hopfe, 1989).

The two components of each of the compound-specific complex functions $\hat{\varepsilon}$ or \hat{n} define the optical properties of a medium completely. The availability of both of the related components renders possible to derive the underlying oscillatory structure as well as to calculate the spectra of the medium to be expected with any well-defined experimental technique.

6.4.4 Experimental techniques

In the preceding sections some peculiarities of strongly absorbing materials were sketched. Because of the difficulties to measure transmission spectra of such materials and to interpret these adequately, reflection spectroscopy always was a necessary analytical tool. Its experimental application is facilitated by strong spectral features, and the detailed interpretation by the small number of resonances. The usually large number of neighboured, often overlapping yet less pronounced features of molecular compounds lead to a different type of spectra. An illustrative comparison of the spectra of strongly and weakly absorbing model compounds simulated for different spectroscopic techniques, has been given by Grosse (1990).

The possibility to obtain detailed vibrational spectra of surface structures with increased sensitivity, is utilized to study adsorption, chemical modification, catalytic processes etc. (e.g. Chabal, 1988; Allara, 1993; Chabal et al., 1993). Several authors review and compare the potentials of the different techniques (Leyden and Murthy, 1987; Leyden, 1990; Grosse, 1991; Roberts, 1992; Yarwood, 1993). In what follows, the basic reflection techniques are outlined with particular emphasis on weak absorbers.

6.4.4.1 Specular reflection spectra

Different features are stressed to specify the most basic type of reflection when referring to it as

- *specular reflection*: the angles of incidence and reflection agree,
- *external reflection*: radiation does not penetrate the medium prior to being reflected, or
- *Fresnel reflection*: Eqs. 6.4-4 apply directly in their most simple version.

The last denomination implies that the sample is thick enough so that virtually no radiation having been reflected on a deeper interface or even the back surface of the sample, interferes with the one reflected at the front surface. This is quantified by the penetration

depth (Born, 1933) on the basis of the amplitude decrease to e^{-1} by absorption. For weakly absorbing samples it amounts to the order of hundred micrometers even within bands. However the penetration depth does not state a thickness necessary e.g. to provide the full information, considerably thinner films can actually be studied in reflection.

Inspecting once again in Fig. 6.4-5 the optical functions of the strong oscillator shows that n and k are presented with equal scale and that their variation ranges are quite similar. Therefore they both influence strongly the reflectance and its spectral dependence. For a weakly absorbing medium, the spectral variation of the product nk is determined primarily by k alone; the relative variation of n can almost be neglected since the anomalies' amplitudes are small compared to their high background (see Fig. 6.4-6). The spectrum of the difference $n^2 - k^2 = \epsilon'$ closely follows the real refractive index, since the small values of k do not contribute substantially. As a consequence, it is the (real) refractive index which governs the reflectance of a weak-oscillator medium. Since the background level of the refractive index does not show much structure, for many organic compounds the resulting reflectance spectra are comparably flat.

A set of s-polarized spectra of a polymer slab obtained with different angles of incidence is shown in Fig. 6.4-10: the small dispersion-like features are centred at the oscillator frequencies and follow the shape of the refractive index. With closely neighboured or even overlapping resonances, the anomalies are difficult to resolve since a dispersion curve extends over a wider spectral interval than the related absorption band does. This impedes e.g. the compilation of band tables to be used for searching in conventional spectral libraries. By no means an automatic peak-locating routine designed for absorption bands in transmission spectra must be applied: the bands would appear to be shifted. In order to convert reflectance spectra into absorption-proportional ones,

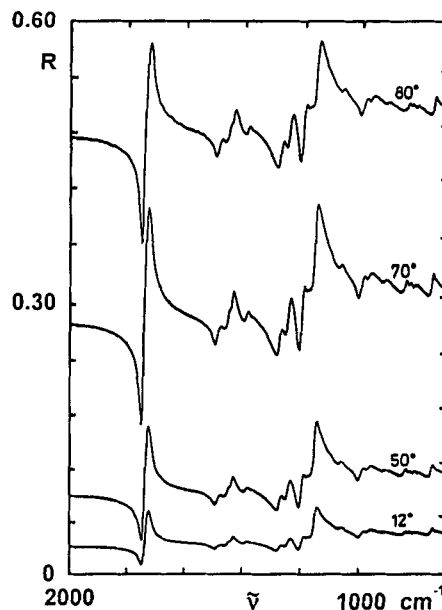


Figure 6.4-10 Reflectance spectra of poly(methyl methacrylate), PMMA, for s-polarized radiation. Angles of incidence indicated.

a Kramers-Kronig transformation should be employed what is easily possible nowadays owing to readily available software (such as FSOS; Hopfe, 1989) and computerized spectrometers.

From Fig. 6.4-10 it is obvious, that the background level increases with increasing angle of incidence as long as s-polarized radiation is used. This agrees with Fig. 6.4-2. The amplitudes of the anomalies increase also, however they reach a maximum where the background reflectance is about 0.4 (Korte, 1990a). This behaviour can be derived from dR/dn , i.e. the sensitivity of reflectance (cf. Eqs. 6.4-4 and 6.4-5) to changes of the refractive index. The calculated graph is presented in Fig. 6.4-11. In this way the spectroscopist can control the fraction which is refracted into the sample and thus, influence the strength of the – wanted or unwanted – response due to reflection at interfaces within the material.

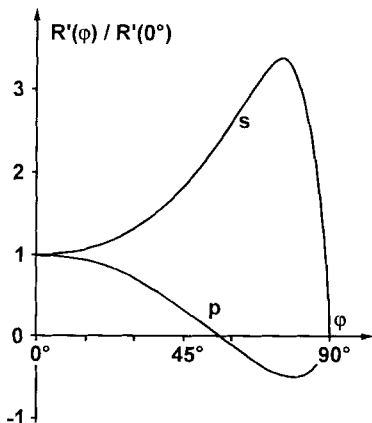


Figure 6.4-11 $R' = dR/dn$ as indicator of the amplitude of reflectance anomalies of a medium of $n = 1.5$ and $k \approx 0$, for both polarizations and all angles of incidence φ . Note the negative range beyond the Brewster angle ($R' = 0$) indicating inverted anomalies.

The condition of largest anomalies is met at larger angles, the use of a polarizer is obligatory. In a particular case it might be advantageous to measure without polarizer, i.e. at normal incidence. This implies smaller features but improved signal-to-noise ratio due to omitting the polarizer. With not too high quality demands, the use of a polarizer can also be avoided with an angle of incidence close to the Brewster angle of the sample: predominantly s-polarized radiation is reflected (Jansen et al. 1992).

Basically the reflectance spectra recorded with p-polarized radiation are less pronounced, still they show some interesting details. The background (real) refractive index defines a Brewster angle where vanishing reflectance is to be expected; however, due to the dependence of the reflectance on absorption a weak but observable spectrum occurs (Korte and Staat, 1989; Ishino and Ichida, 1992). This reflection spectrum does not consist of dispersion-like anomalies but of bands similar to emission signals; an example is shown in Fig. 6.4-12. Such spectra are approximately proportional to k^2 . With larger angles of incidence one observes spectra with inverted anomalies, as indicated by the negative range of the graph for p polarization in Fig. 6.4-11. This inversion can be used to identify unwanted contributions to the detected radiation (Korte and Staat, 1989).

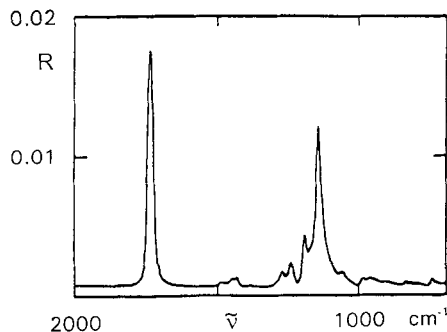


Figure 6.4-12 Measured reflectance of p-polarized radiation close to the Brewster angle of poly(methyl methacrylate).

Specular reflection can favourably be employed to avoid or reduce sample preparation in routine analyses, continuous process control or where sampling is not permitted. As an example for the latter case, studies of the surfaces of *objets d'art* shall be mentioned, for instance varnishes on historical violins (Korte and Staat, 1993). The comparison of diffuse-reflectance spectra being possibly due to scattering by the wooden substrate or inhomogeneous layers of the varnish, and of specular-reflectance spectra under different angles of incidence and different azimuths of polarization, renders possible a detailed comparison with reference spectra recorded under similar conditions. The conversion of such specular reflection spectra into absorption ones is routinely performed, taking the reflectance of an aluminium mirror to be unity does not constitute a relevant deficit.

6.4.4.2 Spectroscopic ellipsometry

With ellipsometry the polarization state of reflected radiation rather than just its intensity, is experimentally determined. Ellipsometry is not so much another experimental technique but a more thorough variety of the traditional ones, whether external or internal reflection. Two results per resolution element, namely the ellipsometric parameters ψ (cf. Eq. 6.4-17) and Δ , are derived independently from the measurements. These can further be evaluated for the two optical functions of the medium behind the reflecting surface or other two data of a more complex sample. In any case there is no information necessary from other spectral ranges as it is for Kramers-Kronig relations. In comparison to the conventional reflection experiment, ellipsometry grants more information with a more reliable basis, e.g. since no standards are needed.

Ellipsometry is routinely applied in the visible spectral range (Azzam and Bashara, 1977), even in industrial practice. A typical task is to monitor the thickness and the real structure of an epitaxial layer on a semiconductor substrate during wafer production, where the optical properties of both media are well known. Often one wavelength is addressed only, this renders possible to apply a so-called nulling procedure: the phase difference is measured by compensating it with an adjustable retarder. In the infrared range, ellipsometry should be performed in combination with a Fourier-transform spectrometer in order to take advantage from the improved signal-to-noise ratio (Röseler,

1990; Röseler et al., 1993). However the spectrally multiplexing procedure requires a photometric technique to be applied. To circumvent an absolute calibration of the intensity scale and to avoid experimental errors due to different optical paths and particularly, different irradiated areas, the evaluation should be based on quotients of intensities which were obtained under identical conditions except the polarization states.

One possible ellipsometric procedure (Röseler, 1990) is outlined with Fig. 6.4-13. A set of four spectra is taken with the polarization azimuths (α) parallel and perpendicular to the plane of reflection plus the intermediate ones at 45° with the former. The analyzer in the reflected beam is kept on the constant azimuth of 45° . Step-scan interferometers or scanning spectrometers might be combined with a continuously rotating analyzer (or polarizer). Alternatively a Photo Elastic Modulator (PEM) can be employed to produce a sinusoidally varying phase shift, so that the information of interest can be extracted as certain frequency components of the resulting signal (Benferhat and Drevilllion, 1987). In all cases the individual spectra are taken with identical experimental geometry. The results are as accurate as the intensity scale of the spectrometer is reliably linear, what to a high degree can be assumed for Fourier interferometers.

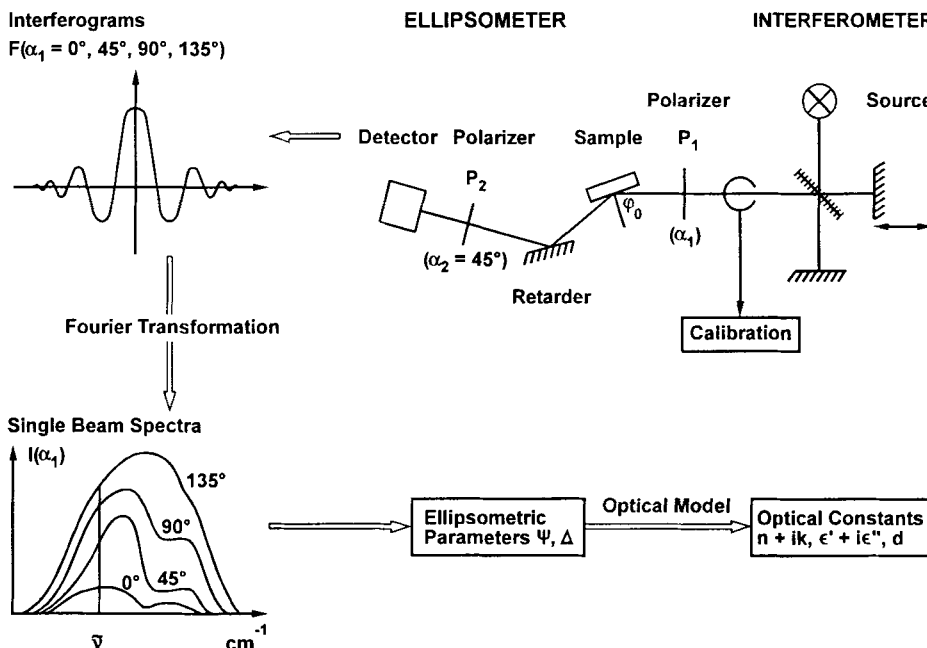


Figure 6.4-13 Procedure of photometric infrared-spectroscopic ellipsometry.

Starting with radiation of equal field strength for all the four measurements, the coefficients r_p and r_s can be taken as (half) the side lengths of the box which circumscribes the ellipse in the reflected beam (see Fig. 6.4-4). Since intensities $I = EE^*$ are measured, one has

$$\tan^2 \psi = I(0^\circ) / I(90^\circ) \equiv Q_1 \quad (6.4-22a)$$

where the index notation has been replaced by the polarization azimuth (0° refers to p). Due to the use of trigonometric functions, this primary result is easily transformed into

$$(1 - Q_1) / (1 + Q_1) = \cos 2\psi \quad (6.4-22b)$$

The wave components in the 0° plane and in the 90° one are phase shifted by δ_p and δ_s , respectively. The resulting difference $\delta_p - \delta_s = \Delta$ acts on the quotient $Q_2 \equiv I(45^\circ) / I(135^\circ)$ whose components are the intensities measured at the intermediate polarization azimuths

$$(1 - Q_2) / (1 + Q_2) = \sin 2\psi \cos \Delta \quad (6.4-23)$$

In order to improve the evaluation in the range where the cosine function is quite insensitive, an additional phase shift is introduced by placing a retarder in the reflected beam. Usually an internal-reflection prism is employed to produce a phase shift somewhere in the range from 30° up to 150° . Since the refractive index does not change much within the transparent spectral range, the phase shift produced by such a retarder is almost achromatic (Korte et al., 1988). For limited spectral ranges multilayer devices are also suitable (Röseler and Molgedey, 1984). Provided a phase retardation of exact 90° is applied, one finds with the quotient Q'_2 of $I'(45^\circ)$ and $I'(135^\circ)$

$$(1 - Q'_2) / (1 + Q'_2) = \sin 2\psi \sin \Delta \quad (6.4-24)$$

Now the state of polarization of the reflected radiation can be determined completely and specified by the coordinates on a Poincaré sphere or by the full set of four Stokes parameters s (cf. Sec. 3.2); the latter are related to the ellipsometric parameters by

$$s_1 / s_0 = \cos 2\psi j \quad s_2 / s_0 = \sin 2\psi \cos \Delta j \quad s_3 / s_0 = \sin 2\psi \sin \Delta \quad (6.4-25)$$

The sum of their squares equals unity provided no depolarization occurs (see below).

The ellipsometric parameters ψ and Δ experimentally determined with a homogeneous thick sample, are algebraically related with the components of the dielectric function, which in turn define the refractive index and the absorption index (Born and Wolf, 1980). The parameters for the strong oscillator used to simulate the spectra shown in Fig. 6.4-5 were chosen to resemble the strong infrared resonance of quartz glass. Radiation reflected from such a sample was measured ellipsometrically; the evaluation led to the results presented in Fig. 6.4-14. For weaker absorbers such as many molecular compounds,

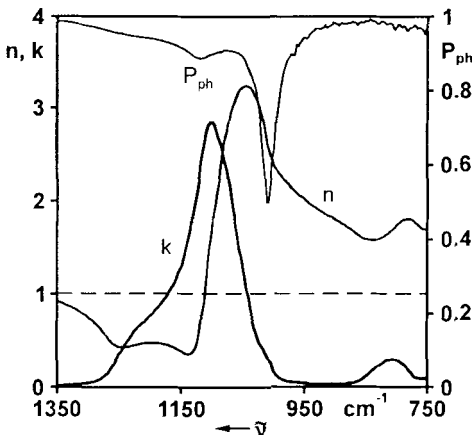


Figure 6.4-14 Spectra of the refractive index n , the absorption index k , and the degree of (phase) polarization P_{ph} of quartz glass as derived from ellipsometric measurements.

ellipsometric measurements under ATR conditions seem to be more appropriate. An experimental example is given in the following section.

The outstanding advantage of determining all four Stokes parameters is that they define the state of polarization completely. As a consequence, the spectrum of the degree of polarization P as commonly defined as well as the spectrum of a similar quantity P_{ph} referring to the phase Δ can be derived. The latter is closely related to the degree of coherence as introduced by Born and Wolf (1980). It is reduced when the detected radiation comprises components with different values of Δ , since due to averaging one has

$$\langle \sin\Delta \rangle^2 + \langle \cos\Delta \rangle^2 \leq 1 \quad (6.4-26)$$

A dip in a limited spectral interval or a generally low level of these quantities indicate deviations from the ideal experiment such as shortcomings in spectral or lateral resolution, hidden imperfections, or an unexpected contribution of radiation reflected from the back surface of the sample; in any case the origin should be clarified carefully. As an example the P_{ph} spectrum derived from the quartz measurements is included in Fig. 6.4-14: the sharp decrease just below 1000 cm^{-1} is due to the opening angle of the cone of detected radiation, namely $70^\circ \pm 4^\circ$. Without better angular discrimination, the abrupt phase change through almost 180° at the Brewster angle cannot properly be resolved (Röseler, 1992).

Ellipsometry can also be applied to transmission measurements: linear birefringence and dichroism of an anisotropic sample cause differences in amplitudes and phase shifts for waves of different polarization azimuths. Such experiments seem to be of considerable interest for partially ordered systems such as liquid crystals (cf. Sec. 4.6), here the degrees of polarization P and P_{ph} reveal information related to order and reorientation processes (Korte et al., 1993; Reins et al., 1993).

6.4.4.3 Attenuated total reflection

To obtain a spectrum by means of attenuated total reflection - usually abbreviated by ATR - the sample is brought into optical contact with an auxiliary medium. The measuring beam is directed through the latter to be reflected internally at the interface to the sample; for this reason the technique is also referred to as *internal reflection*. The auxiliary-medium element might have the form of a prism, a semi-cylinder, or a hemisphere. For multiple reflections a rod and slab with oblique facets as optical inlet and outlet (see Fig. 6.4-3) are used. Necessarily the material of such an element must be infrared transparent and of high refractive index. Commonly used are KRS-5 (TlI/TIBr, $n \approx 2.4$), ZnSe ($n \approx 2.4$), or Ge ($n \approx 4$), less frequently Si ($n \approx 3.5$), in the near infrared range even glass (Nishio et al., 1990). The ATR technique has proved to be versatile and convenient for routine studies. Typical samples range from viscous liquids to soft solids such as oil, paste, plastic, also skin and tissue even *in-vivo*. Everything what is brought easily into contact with the surface of the internal reflection element while it is difficult to prepare as thin film, can advantageously be studied by ATR. A comprehensive survey was given by Mirabella (1985).

The sample absorbs the evanescent field so that the totally reflected wave is attenuated accordingly: the reflectance spectrum closely resembles a transmission spectrum. Usually such spectra can actually be interpreted and evaluated as transmittance, and commercially available accessories are designed to support this. With angles of reflection well above the critical one, some sensitivity is lost which however is regained by multiple internal reflections. How pronounced the actual spectrum is, can be adjusted by the number of reflections used, i.e. the sample-coated area of the slab: whether both surfaces, one surface, or just a fraction. In any case the area of a given reflection should fully be covered to avoid spectral dilution.

An illustrative description of the implicit parameters was given by Harrick (1967) on the basis of a low-absorption approximation. This applies well for most organic materials, for materials of stronger absorption the Fresnel equations or the thereupon based layer algorithms mentioned in Sec. 6.4.3 should be applied. The depth from which analytical information can be gathered is conveniently characterized by the penetration depth d_p . This is the distance in which the amplitude of an electric field decays to a fraction e^{-1} of its initial value. For the evanescent field one finds

$$d_p = \lambda_1 / [2\pi(\sin^2 \varphi_1 - n_2^2 / n_1^2)^{1/2}] \quad (6.4-27)$$

where $\lambda_1 = \lambda / n_1$ denotes the effective wavelength in the denser medium (index 1). The difference in this expression states a sort of angular distance since the quotient n_2 / n_1 defines the sine of the actual critical angle. With constant experimental geometry this distance can be adjusted by changing the denser medium. At large angles of incidence, d_p is less than the used wavelength *in vacuo*, for high-refracting elements even in the order of a few tenths of it. The penetration depth increases strongly when approaching the critical angle where total reflection converts into refraction. The angular dependence opens access to depth profiling (Urban and Koenig, 1990); the contributions from different depths are superimposed and the exact cancellation of individual components can

be a difficult task (Chalmers and Mackenzie, 1988). On the whole, d_p gives an estimate how thick the film or surface layer is which actually contributes to the resulting spectrum or in how far a poor spectrum can be attributed to unsufficient sample thickness. From Fig. 6.4-15 it is obvious that the signal increases with increasing sample thickness only up to a certain value which is related to the penetration depth.

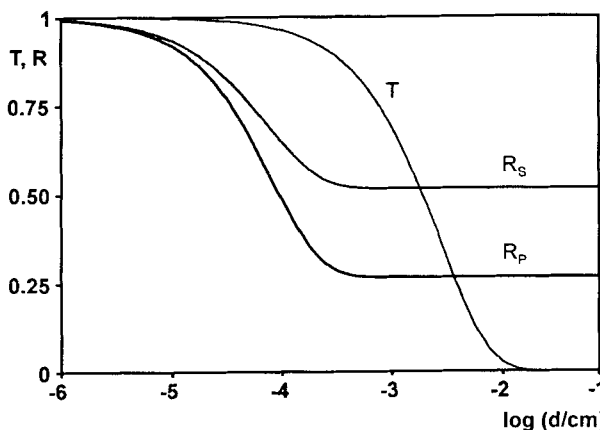


Figure 6.4-15 ATR response R calculated for ten internal reflections *versus* sample thickness for both polarizations. Transmittance is given for comparison. Parameters: $n_1 = 2.4$; $\varphi_1 = 45^\circ$; $n_2 = 1.35$; $k_2 = 0.03$.

The actual strength of the analytical signal can be characterized by the equivalent thickness d_e ; this is the sample thickness necessary to produce an equally pronounced transmission spectrum (Harrick, 1967). In the calculation for the ATR case, the increased field strength at the interface in the rarer medium along with its exponential decay are taken into account. The increase of field strength is different for the s-polarized and p-polarized components and thus, their effective thicknesses differ. The p-polarized component is always related to a larger equivalent thickness and thus to a more pronounced absorption signal. As the penetration depth, also the effective thicknesses are proportional to the wavelength, so that bands are relatively more pronounced at low wavenumbers.

For large angles of incidence, the penetration depth is greater than the effective thickness, so that transmission through a d_p -thick layer would yield a more pronounced spectrum than ATR does (see Fig. 6.4-15). Close to the critical angle d_e exceeds d_p : the increase of the field strength at the interface makes ATR more sensitive than a transmission measurement would be. However ATR is often applied to make very thin layers effective, e.g. when dealing with aqueous solutions. The effective thickness varies strongly upon approaching the critical angle, so that the dispersion of the refractive index through an absorption band causes considerable effect on the spectra: bands appear to be distorted particularly by tailing at their longer-wavelength sides and maxima are shifted rendering questionable traditional evaluation schemes.

Remedial measures are increasing the angle of reflection or choosing a denser medium of higher refractive index. Alternatively the experiment could be complemented to yield

ellipsometric parameters from which the optical functions and subsequently correct spectra of any type can be derived. An example of ellipsometric ATR measurements is given in Fig. 6.4-16 where the two absorption bands shown are quite strong for a liquid. The different band-intensity ratios in the k and ϵ'' spectra, respectively, indicate that a transmittance or k spectrum alone does not represent completely the vibrational structure, but the dispersion (n) has to be included. In this example the condition of total reflection is not met throughout the infrared spectrum, however, Fresnel's equations apply for both cases without modification.

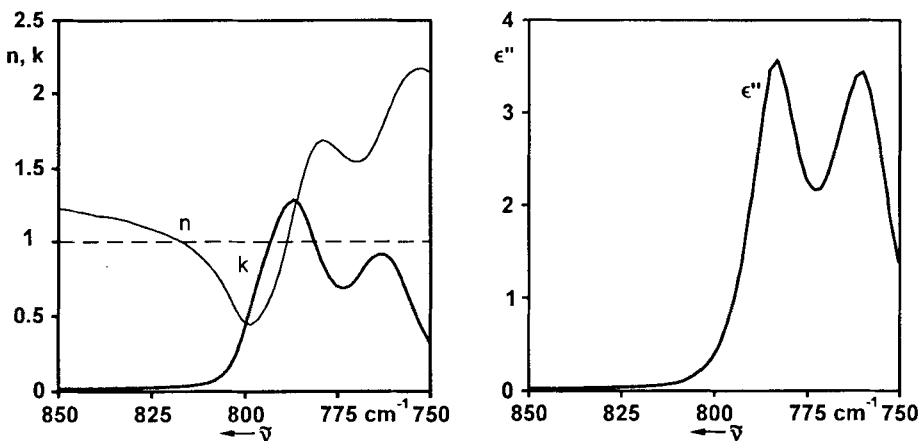


Figure 6.4-16 The components n and k of the complex refractive index, and the imaginary part ϵ'' of the dielectric function of CCl_4 as derived from ellipsometric ATR measurements.

The optical functions can precisely and accurately be derived from ATR experiments also without polarized radiation but measuring at two angles of incidence and employing Kramers-Kronig transformations (Crawford et al., 1978). Alternative methods are primarily based on transmission measurements along with some values of the refractive index obtained from ATR experiments (Jones and Hawrenek, 1976; Hawrenek et al. 1976).

Polarized incident radiation is necessary also when anisotropic samples such as stretched polymers (Flournoy and Schaffers, 1966) are studied. Crystals may require immersion in order to assure the necessary optical contact. Plastic selenium has proved to be useful (Gottlieb, 1968). In this way the three different infrared spectra of an orthorhombic single crystal were obtained which are shown in Fig. 2.7-10 (cf. Sec. 2.7.6.4; Schrader et al., 1971). The orientation of the optical axis or axes with respect to the experimental frame is crucial. For the evaluation the field components have to be considered separately in order to interpret the response of the oriented transitions correctly. Addressing different components equivalently is achieved by rotating the sample together with the internal reflexion element with respect to the beam (Hobbs et al., 1983; Palm, 1994).

Different from the case when of a refracted wave travels through a medium and thus no field occurs in direction of propagation, the evanescent field consists of (generally

different) components in each direction. Since the three principal components experience different phase shifts, also circular polarization effects can be observed by ATR (Jordanov and Schrader, 1986).

The increased field amplitudes at the interface can advantageously be employed to study surface treatments (Chalmers and Mackenzie, 1988; Parry and Harris, 1990) and ultrathin films including Langmuir-Blodgett structures (Yarwood, 1990). For such samples the effective thickness as defined before, will exceed the actual thickness several times. In such a case no spectral distortions such as band tailing, or band shift occur, and the critical angle does not depend on the refractive index of the film but on the one of the medium beyond the film (Harrick, 1967). When this is air, the angular range of total reflection is wider than for bulk organic samples. Particular attention has been paid to passivation layers, adsorbed molecules, and polymer coatings (e.g. Kellner, 1986; Weigel and Kellner, 1989). Spectral changes in a film deposited on an ATR crystal can be monitored, when e.g. the film selectively collects certain components from atmosphere or out of a passing fluid (cf. Sec. 6.5).

6.4.4.4 Reflection absorption

The term *reflection absorption* classes a group of experiments where the sample to be analyzed is placed on a mirror so that the absorption of the sample reduces the reflectance, and a sort of transmission spectrum of the sample results. The sample thickness ranges from many times the wavelength down to fractions of a monolayer. At either end of this scale special experimental modifications provide improved sensitivity with respect to the actual thickness.

In a simple version, the measuring beam is reflected within a sample cell at its bottom. Provided this bottom is metallic and the angle of incidence is not too large, the incident and the reflected beams superimpose to form a standing wave with a node on the reflector (Born and Wolf, 1980). As long as the sample layer in the cell is thick as compared to the wavelength the intuitive argument of applying the absorption twice is correct. Such configurations are mostly used in near infrared spectroscopy, often with a diffusely reflecting bottom (cf. Sec. 6.2).

With layers the thickness of which is in the order of the wavelength, some curious dependences are observed. At the metal substrate a node is located, normal to its surface the field amplitude of the standing wave varies regularly. Therefore the absorption does not increase monotonously with increasing thickness but displays some modulation (Pacansky et al., 1987). The calibration, reflectance *versus* thickness might be ambiguous. With different angles of incidence and choosing substrates with optical properties somewhere between metals and dielectrics, a multitude of spectral manifestations can be produced (Yen and Wong, 1989). For reliable evaluations a larger spectral range or at least two different angles must be used.

With a thickness below quarterwave, the response decays not only with the thickness but additionally with the field amplitude approaching the node. Thus zero sensitivity is to be expected at the very surface on the metal substrate. Advantageously another ex-

perimental configuration can be employed to increase the sensitivity to surface species. As mentioned above the reflection is associated with different phase shifts for the differently orientated components of the electric vector. With a metallic surface the shift of the s-polarized component (the electric vector $E_s = E_y$ oscillates perpendicular to the plane of reflection and parallel to the surface) is close to 180° for all angles of incidence. For the p-polarized component E_p , the shift is small for the larger part of the angular range before it increases sharply to 180° when approaching grazing incidence. As outlined in Fig. 6.4-17, this component can be split further into the components parallel (E_x) and perpendicular (E_z) to the surface. Near grazing incidence the former component is close to zero due to geometrical reasons, so that only the contribution E_z normal to the surface remains. These contributions from the incoming and the reflected wave, respectively, interfere constructively since the reflection introduces a phase shift of 180° : provided the reflectance of the substrate is close to unity, one gains a factor of 2 in field strength (Greenler, 1965).

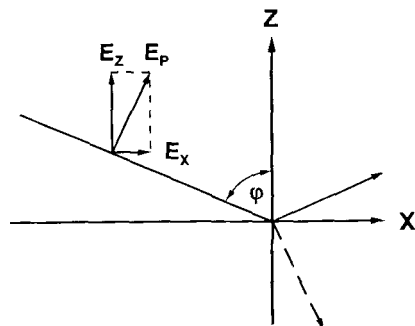


Figure 6.4-17 Notation used to discuss the field enhancement at grazing incidence. The y axis is perpendicular to the plane shown and parallel to the electric vector of s-polarized radiation.

Depending on intensity, i.e. the square of the field strength, the absorption signal caused by the molecules on the surface is fourfold increased. With an approximately collimated beam, the irradiated area is increased proportional to the secant of the angle of incidence, and due to the larger area the radiation interacts with accordingly more molecules. In comparison to transmittance, a sensitivity increase by a factor in the order of 20 is to be expected (Greenler, 1965). Smaller, but still remarkable benefits are obtained with less brightly reflecting substrates such as water or glassy carbon, which are of particular interest for practical applications (Porter, 1988; Mitchell and Dluhy, 1988; Udagawa et al., 1989).

In the extreme case of grazing incidence, a field component exists only normal to the surface. Therefore an interaction is possible exclusively with transition moments or components thereof, orientated perpendicular to the surface. This anisotropy of interaction can also be explained by selection rules, which are based on symmetry consideration and include the mirror image of the analyte produced by the metallic surface.

The resulting spectral features are comparable to absorption bands, their amplitude being very small in comparison to the reflected intensity. Therefore it is essential for the measurements, that due to destructive interference the perpendicular component of incident radiation shows hardly any interaction with the absorbing surface species. Therefore

just by changing the polarization azimuth a reference intensity is measured. With polarization modulation, in particular with such a high frequency as offered e.g. by photo elastic modulators, advantageous conditions can be realized (Golden et al., 1981).

These experimental techniques might be classified with external reflection. More specifically they are known under one of the acronyms IRRAS, IRAS or RAIRS, referring to both, reflection-absorption and infrared spectroscopy. To make clear whether a bulky sample or just surface adsorbates are addressed, often the terms transflexion or grazing incidence spectroscopy (GIS), respectively, are used. However, when the same effect is exploited for an analyte on a less brightly reflecting substrate, smaller angles than grazing incidence constitute the optimum. It seems that a clear nomenclature is still missing.

Reflection-absorption techniques at grazing incidence or other appropriate angles have found widest interest (Golden, 1985) due to the potential for studying sub-monolayer coverage. Preferred fields of application are the characterization of adsorbates on metal surfaces, their transformations and kinetics (Hollins and Pritchard, 1985; Chesters, 1986; Hayden, 1987; Bradshaw and Schweizer, 1988), of the electrode / electrolyte interface (Porter et al., 1984; Beden and Lamy, 1988), and Langmuir-Blodgett or other ultrathin organic films (Yarwood, 1990; Swalen and Rabolt, 1985). Besides characterization and identification, the method grants information on kinetics (Hoffmann and Weisel, 1992), and on orientation and order in the surface layer on the basis of its directional selectivity (Swalen and Rabolt, 1985). It compares favourably with the competing vibrational-spectroscopic method of electron energy-loss spectroscopy (EELS; Chesters and Sheppard, 1988) since the latter must be used in vacuum and suffers from low resolution. Alternative detection schemes for surface species include thermal and calorimetric measurements as well as emission spectroscopy (Richards and Tobin, 1987).

The underlying optical phenomena are quite complex and the experimental results cannot be anticipated straightforwardly. Therefore simulations are generally necessary to discriminate shifts and distortions of spectral band shapes caused by optical effects from those caused by surface-induced changes in structure or chemical bonding (Allara et al., 1978; Porter, 1988).

6.4.4.5 Diffuse reflection

Diffuse-reflection spectroscopy is a widely used experimental technique which, different from the previously mentioned techniques, is not only based on reflection and refraction but additionally on diffraction. The exact description, e.g. assuming Mie scattering, and quantitative simulation of the spectra is at least difficult (Grosse, 1990). The most comprehensive overview on all related aspects was given by Kortüm (1969). Experimental examples refer mostly to the visible spectral range, more recent reviews deal with near infrared (Osborne and Fearn, 1986), infrared (Korte, 1990b), and far infrared spectroscopy (Ferraro and Rein, 1985).

Scattering of radiation within the sample is one essential of the effect, therefore the sample must be inhomogeneous. Typical are particulates while the well-known equation was derived by Kubelka and Munk (1931) to describe the visual impression of paint

layers, i.e. a uniform matrix with pigment particles or other scattering inclusions. The model which leads to this equation refers exclusively to energy transport within the sample back and forth along the coordinate perpendicular to the surface. The nature of the phenomena causing loss and changing the propagation direction of radiation is not considered. The fundamental differential equations are defined and solved in Sec. 3.5.3.1 (Eqs. 3.5-6 and 3.5-7). This results in

$$F(R) = (1 - R)^2 / (2R) = K / S \quad (6.4-28)$$

where K specifies the absorbing and S the scattering ability per length of the sample material. The reflectance R must be measured with a sample which is thick enough that no radiation reaches the back surface; it seems that in infrared this thickness does not exceed a few millimeters. To indicate that this condition is met the notation R_∞ is used.

Generally, the assumption is made that scattering does not depend on the wavenumber so that the conversion of the measured reflectance spectrum R by means of the Kubelka-Munk function $F(R)$, results in an absorption-proportional representation. As for ATR and reflection-absorption spectroscopy, also the diffuse-reflectance spectrum does not consist of dispersion features but band-like structures. For changes in low absorption, the sensitivity of diffuse reflectance is greater than the one of transmittance, while strong absorption bands are less pronounced in the diffuse-reflection (see Fig. 6.4-18). Therefore, diffuse-reflectance spectra resemble poorly resolved transmittance spectra. For diffuse reflectance spectra where R is in the order of 0.01 or below, the function $-\log R$ or just $1/R$ is equally well suited for conversion (Olinger and Griffiths, 1988). Such levels are found with compact samples such as polymer foams or varnishes with filler (Otto, 1987; Korte and Otto, 1988).

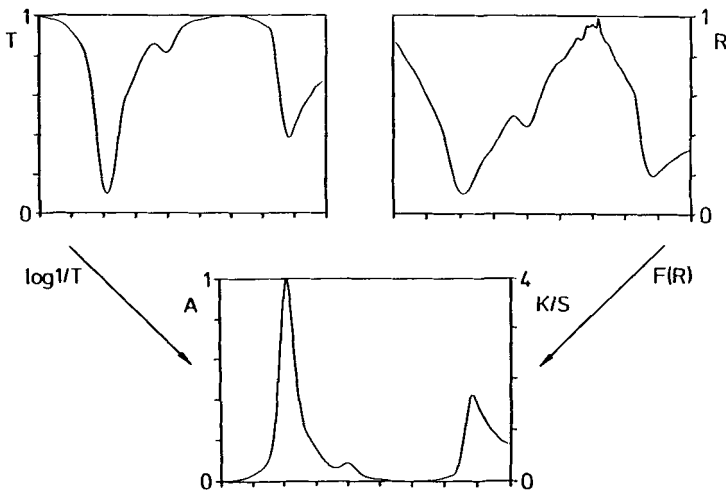


Figure 6.4-18 Transmittance T and diffuse reflectance R spectra related to the same compound specified by its absorbance spectrum $A \sim K/S$.

With a strongly scattering sample, the reflected radiation is spread over the entire hemisphere above the sample. With the same optical throughput the spectrometer provides, only a small fraction of the scattered radiation would be collected; therefore losses are inevitable. The adequate detection system is the integrating sphere ('Ulbricht Kugel'), which in its ideal form would reflect each ray without loss again and again until it happens to fall onto the detector. In infrared however, the ideal situation is by no means given, and instead mirrors covering large solid-angle are used. Efficiency is in the order of 0.1 only (Hirschfeld, 1986; Korte, 1988).

For particulate samples, and even more for compact samples exhibiting a smooth surface, it is crucial to prevent specularly reflected radiation from being detected together with the diffusely reflected component. To avoid this, the solid angle into which the incident radiation is specularly reflected should be excluded. Advantageously, irradiation normal to the surface (Korte and Otto, 1988) or out-of-plane configurations are used (see Fig. 6.4-19). As an alternative, a razor blade is vertically positioned on the surface as a blocker for surface-reflected radiation (Messerschmidt, 1985).

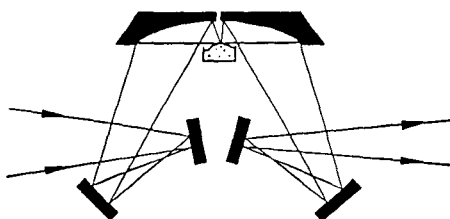
For qualitative spectra sample preparation is usually unnecessary. Reproducible sample preparation of particulates is difficult, since reflection depends on particle size, shape, packing density as well as on the texture of the macroscopic surface. Almost all powdered samples should be diluted with a non-absorbing particulate matrix such as KBr. This contributes to meeting the prerequisites of the Kubelka-Munk model such as sufficient penetration depth and a homogeneous radiation field. For the latter reason, it was recommended to use an overlayer of KBr powder for compact samples (McKenzie et al., 1984). Dissolved analytes can be deposited on the matrix powder by evaporating the solvent. This has been used for sensitive infrared detection of liquid-chromatographic fractions (Kuehl and Griffiths, 1980; Conroy et al., 1985). Similarly high sensitivity is reached for other surface deposits.

With diffuse-reflection optics a reference signal cannot be measured without a standard. With reference to diluted samples, the matrix particulate is best suited. In this way, contaminations of the matrix which are virtually inevitable due to the large specific surface, are compensated for. For undiluted, specially compact samples, gold covered erasive paper has proved to be an excellent ready-to-use standard (Otto, 1987).

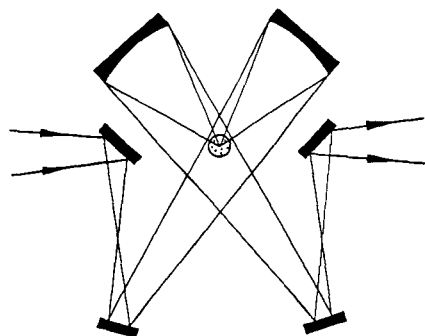
For KBr powder (Uvasol, E. Merck) a reflectance of 0.873 at 1724 cm^{-1} was reported (Reinecke et al., 1988). At such a level, the matrix absorption must be included in a quantitative evaluation. Similarly, the scattering properties of the analyte material must be taken into account at higher concentrations. Several approaches have been proposed (cf. review by Korte, 1990b)

The particular sensitivity of diffuse-reflection spectroscopy to surface structures, is due to the usually multiple reflection and diffraction of radiation at the surfaces of the scattering particles. Therefore catalytic processes and chemically modified surfaces are frequently studied this way.

a



b



c

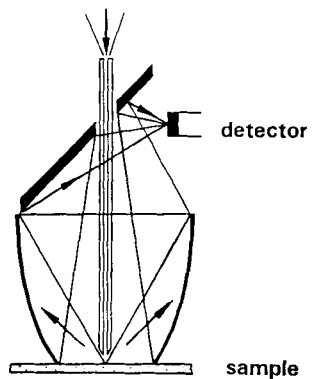


Figure 6.4-19 Optical schemes of different diffuse-reflection accessories. (a) in-plane configuration, usable with blocker; (b) out-of-plane configuration; (c) attachment for large samples (Korte and Otto, 1988).

6.4.4.6 Competing techniques

Infrared emission spectroscopy shall be mentioned first. The physical background basing on Planck's and Kirchhoff's laws, and experimental aspects are treated in Sec. 3.3.1. The frequently encountered problem of self-absorption in thick samples is avoidable by transient heating or cooling (Jones and McClelland, 1989). As Sullivan et al. (1992) point out, emission can be utilized as a surface analytical tool competing well with the related infrared techniques. Generally, information is gathered from a front layer of about 0.01 μm and 5 μm thickness (Urban and Koenig, 1990). Submonolayer coverage of adsorbates on single-crystal metal substrates were analyzed using a liquid-helium cooled spectrometer (Richards and Tobin, 1987).

The feasibility of thermic and calorimetric detection of the absorbed radiation has been mentioned in the context of grazing-incidence experiments. This is quite close to the class of photothermal techniques with which a number of different detection schemes is employed (Coufal, 1986). Out of these, photoacoustic spectroscopy (PAS) is frequently used in infrared spectroscopy (Graham et al., 1985; Urban et al., 1990; McClelland, 1992) while inspite of its potential, thermal beam deflection has not yet found as many applications as in other spectral ranges, possibly due to the lower availability of suitable lasers (Low and Morterra, 1985).

The photoacoustic effect was discovered by Bell (1880, 1881): by absorption of radiation heat is generated within a sample, and is used to warm up the gas surrounding the sample in a (nearly closed) volume; its thermal expansion is detected by a microphone. Since the heat reaches the surface by heat diffusion, the response depend not only on the optical properties of the sample but also on its thermal ones (Rosencwaig and Gershoff, 1975, 1976). The depth from which the heat can reach the surface and thus contribute to the detected signal, depends on the modulation frequency of radiation intensity. Depth profiling in the range of 0.02 μm to 50 μm , approximately, is easily performed, and no restrictions as to the surface shape exist (Urban and Koenig, 1990). Special aspects of data treatment are considered by Michaelian (1990).

A different, possibly promising effect of increased infrared sensitivity are surface electromagnetic waves (SEW). Employing these extremely low coverages of organic molecules e.g. on metals can be studied (Zhizhin and Yakovlev, 1990a, 1990b). Also the effect of surface enhanced infrared spectroscopy due to metal-island films has been analyzed (Osawa et al., 1993) as well as the general diagnostical prospects of microrough metal surfaces (Brodsy and Urbakh, 1990).

6.5 Continuous extraction technique*

6.5.1 Introduction

Trace analysis is usually a discontinuous process comprising several procedures in sequence: sampling, enrichment, separation, and measurement. In this section a technique is described which intends to integrate all necessary procedures in order to facilitate continuous measurements. It combines reversible extraction of the analyte by membranes with the measurement of the absorption of its infrared bands.

The usual method for the spectrometric determination of hydrophobic substances in water is to extract it with a hydrophobic solvent and to evaluate its infrared spectrum (see Sec. 5.1.5.1). This *discontinuous* procedure cannot be applied in *real time* and *on-line*.

The new method described in this section allows *continuous* spectrometric control of hydrophobic analytes in gases or water, for example in waste water or the atmosphere at work areas. It can be miniaturized to construct a *sensor for real time and on-line control*.

Water exhibits very strong absorption bands in the mid-IR region, which generally precludes its use as a solvent for IR spectroscopy. Aqueous samples can be analyzed by so-called ATR-spectroscopy (Fahrenfort, 1961; Harrick, 1979), see Sec. 6.4. However, ATR detection limits are often too large. Therefore further effort is necessary to exclude water and to enrich the organic compound in the area where the evanescent wave is penetrating the sample.

This is achieved by a polymer film covering the internal reflection element (IRE); it acts continuously as a *reversibly extracting* medium. This effect may be used for a quantitative determination of organic samples. Because the polymer material is hydrophobic, only weak absorption bands due to water appear in the spectra.

6.5.2 The ATR membrane technique

This section describes the membrane ATR technique in detail; the general theory of ATR has been previously introduced in Sec. 6.4. For more information about the normal ATR spectroscopy – theory, application, further literature – the books of Harrick (1979) and Mirabella (1985) are recommended.

6.5.2.1 ATR membrane cell

Fig. 6.5-1 shows a sample cell in which the polymer covering the IRE is in direct contact with the sample stream to be analyzed. The sample – either an aqueous solution or a gas – is continuously drawn through the sample cell. The sample temperature should

* Section 6.5 is contributed by E. Lentz, Essen

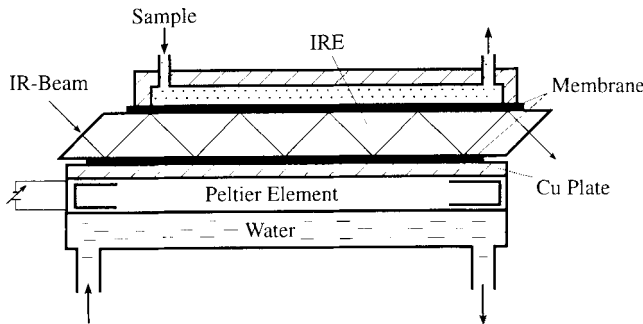


Figure 6.5-1 Example of an ATR cell with temperature control (Wyzgol, 1989).

be constant and deviate by no more than $\pm 1^\circ\text{C}$, because the extraction of the organic compounds strongly depends on the temperature.

Either one side or both sides of the IRE may be covered with a polymer layer.

Especially for aqueous samples the flow velocity should be selected carefully. On one hand it should be sufficiently large to decrease the Nernst diffusion layer (see Sec. 6.5.3.3). On the other hand the flow velocity is not allowed to exceed a certain limit in order to avoid damaging the membranes.

6.5.2.2 Basic aspects of ATR theory

As shown in Sec. 6.4 radiation is totally reflected at the boundary between a medium with a refractive index n_1 and a medium with lower refractive index n_2 if it hits this boundary with an incident angle greater than the critical angle $\Theta_c = \arcsin(n_2/n_1)$. The reflected radiation energy penetrates the boundary as a so-called evanescent wave. The penetration depth d_p is the thickness within which the intensity decreases to $1/e$ of the intensity at the boundary (see Fig. 6.5-2). It is a function of the refractive indices n_1 and n_2 , the incident angle Θ , and the wavelength λ (in vacuum). With $n_{21} = n_2/n_1$:

$$d_p = \frac{\lambda}{2\pi n_1 \sqrt{\sin^2 \theta - n_{21}^2}} \quad (6.5-1)$$

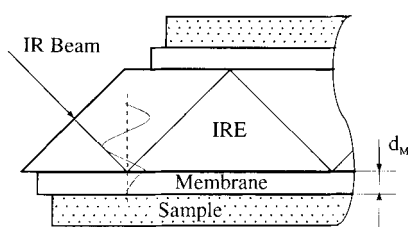


Figure 6.5-2 Principle of the membrane ATR arrangement (Wyzgol, 1989).

The penetration depth should be discussed separately from the effective thickness d_e . The latter is the thickness needed in normal transmission measurements to achieve the same absorbance as measured with one internal reflection. The effective thickness can be calculated theoretically (Harrick, 1979). The results show for randomly polarized radiation and for sample thicknesses greater than d_p that the effective thickness is proportional to the penetration depth. The wavelength dependence of the refractive indices can usually be neglected. So we arrive at:

$$d_e = \frac{n_{21} \cos \theta}{1 - n_{21}^2} \left(1 + \frac{2 \sin^2 \theta \cdot n_{21}^2}{(1 + n_{21}^2) \sin^2 \theta - n_{21}^2} \right) d_p \quad (6.5-2)$$

Regarding Eq. 6.5-1 it is obvious that the absorbance is proportional to the wavelength. This is different from normal transmission spectroscopy. For an incident angle of 45° Eq. 6.5-2 can be simplified to:

$$d_e = \frac{3}{\sqrt{2}} \frac{n_{21}}{1 - n_{21}^2} d_p \quad (\text{for } \theta = 45^\circ) \quad (6.5-3)$$

The angle of incidence to the surface of total reflection should be somewhat (more than 5°) greater than the critical angle. Otherwise nonlinearity of the absorbance, band shifts and other difficulties may occur.

6.5.2.3 Selection of the internal reflection element

The IRE material must show transparent regions in the infrared and it should have a proper refractive index to allow internal reflection. It must be insoluble in the usual solvents and chemical inert to all components in the sample. However, from the list of IR-transparent materials in Table 3.4-1 only a few are recommended for IRE's. Table 6.5-1 lists most of these materials.

For our purpose ZnSe seems to be an optimal material. Its refractive index is high enough to allow internal reflection with suitable incident angles and is not so high to give great reflection losses. The transmission region allows the detection of most organic compounds and the mechanical properties are quite good.

Of the large number of possible IRE shapes (Harrick, 1979) only few are usually used for the membrane method. Their shapes are like a trapezoid or parallelepiped. Cylindrical IRE with conical ends (Tunnel Cell^R, Circle Cell^R (Doyle, 1990)) and even optical fibers are also possible.

6.5.2.4 Selection and preparation of membranes

The choice of a suitable polymer material is a prerequisite for the success of the enrichment process. In general, all polymers with a low degree of crystallinity and low glass temperature show good enrichment capacities (Table 6.5-2).

Table 6.5-1 Materials suitable for IRE's

		Refractive index, mean value	Transmission region ^a in μm	Remarks
Silver chloride	AgCl	2.0	0.45-16	Sensitive to UV and VIS, very soft, react with many metals
Silver bromide	AgBr	2.2	0.5-22	Sensitive to UV and VIS, very soft, react with many metals
Germanium KRS-5	Ge TlBr/I	4.0 2.35	2.0-11.4 0.7-30	High refractive index Very toxic, soft, attacked by warm water, acids and bases
Zinc sulfide	ZnS	2.24	0.7-10	
Zinc selenide	ZnSe	2.42	0.5-14.3	May react with acids to H ₂ Se
Silicon	Si	3.42	1.1-6.7 30-FIR	Very hard, high refractive index

^a The transmission range is reduced relative to Table 3.4-1 because of the longer light path (ca. 80 mm) through the IRE.

Table 6.5-2 Glass temperature of some polymers (Vollmert, 1979)

Polymer	Glass temperature in °C
Poly(dimethylsiloxane)	-120
Poly(tetrafluoroethylene)	- 85
Poly(ethylene)	- 78
Poly(isoprene)	- 70
Poly(isobutylene)	- 60
Poly(vinylacetate)	33
Poly(vinylchloride)	80
Poly(styrene) (atactic)	100

The membrane should

- exhibit a simple IR spectrum. In particular, it should have no or only weak absorption bands in the region where the analyte absorbs,
- not solvate in water or react with the crystal surface and provide sufficient long-term mechanical stability,
- have a high capacity to extract organic compounds,
- be easy to produce and to reproduce.

During all measurements the enrichment of the organic compounds should be completely reversible and their concentration in the membrane should be proportional to the concentration in the sample. Irreversible enrichment is discussed later (see Sec. 6.5.4.1)

Polyethylene (PE) has a very simple IR spectrum (Fig. 6.5-3) and is therefore one of the favored materials. Analytes may belong to nearly all classes of organic substances,

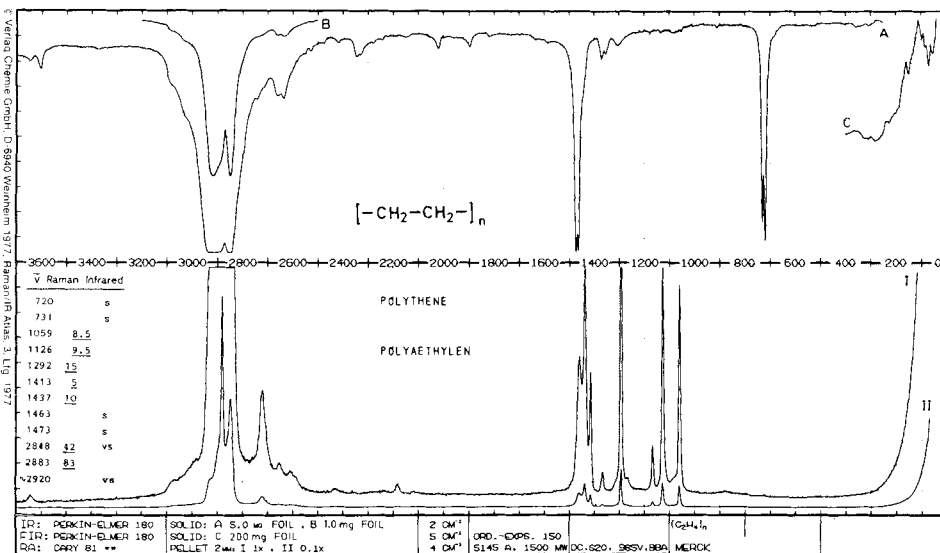


Figure 6.5-3 IR- and Raman-spectra of polyethylene (Schrader, 1989).

with the exception of simple aliphatic hydrocarbons. The absorption bands of these compounds overlap with those of the polymer – a difficulty which may be obviated by using completely deuterated PE. In enrichment experiments, the low density form ($\rho = 0.89 \text{ g cm}^{-3}$) shows the smallest time constant of the enrichment process and a relatively high enrichment factor compared to higher density PE. The degree of crystallinity is reflected in the broad band between 1300 and 1400 cm⁻¹. A description and an assignment of PE bands has been provided by Koenig (1980).

Poly(dimethylsiloxane) (PDMS) is generally known for its great ability to reversibly dissolve organic hydrophobic solvents as well as a number of other substances. It is easily permeated by a variety of gaseous compounds, e.g. CO₂, H₂O (g) (Elias, 1972). This advantage is reduced by its relatively complicated IR spectrum (Schrader, 1989), see Fig. 6.5-4. The strong absorption bands in the region below 1100 cm⁻¹ obscure the bands of halogenated hydrocarbons. However, aromatic compounds may be detected by their ring vibrations between 1260 and 1420 cm⁻¹ and above 1500 cm⁻¹. Detectable compounds also include hydrocarbons with carbonyl groups, compounds such as CS₂ or CO, and others.

Poly(octadecylsiloxane) is often used in chromatography to prepare reversed phase column material. The process which takes place during a chromatographic run is closely related to the enrichment process described here; i.e., materials which are employed to provide stationary phases for chromatography may also be used for preparing enriching membranes. This material gives rise to fewer absorption bands than PDMS but more than PE.

Poly(etheresteramide) is also useful, especially to investigate molecules with a certain dipole moment. Poly(etheresteramide) is an example of a relatively polar membrane. The absorption bands allow the detection of several different classes of compounds, because

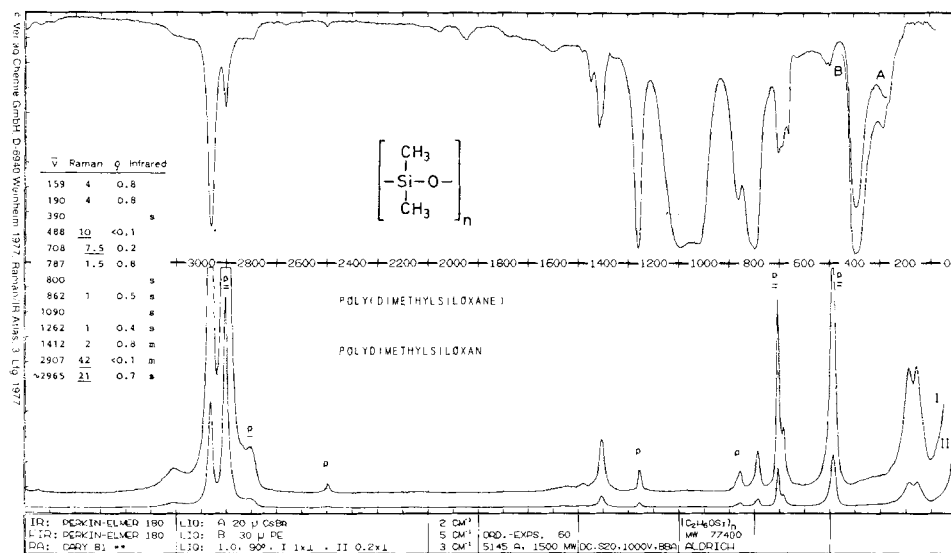


Figure 6.5-4 IR- and Raman-spectra of poly(dimethylsiloxane) (Schrader, 1989).

the polymer does not absorb strongly in the regions between 1400 and 1100 cm⁻¹ and between 1000 and 600 cm⁻¹.

Plasticizers usually increase the extraction capability with the great disadvantages of many additional bands and slowly-changing properties because of the continuous loss of the plasticizers.

There are some other polymers suitable in principle for membrane materials, like polystyrene, polytetrafluoroethylene, polyvinylchloride etc.. Unfortunately, these polymers have great disadvantages: they show poor enrichment factors, they do not adhere strongly enough to the crystal surface, or they form poor membranes, etc.

The thickness of the membrane should exceed the penetration depth of the IR radiation in order to suppress the absorption bands of water. The optimum thickness is about 10 to 20 μm. The stability of such a membrane is satisfactory and the resulting time constant for the enrichment process is not too large.

To ensure optimum contact, the polymer membrane should be produced directly on the surface of the internal reflection element. These membranes are usually made:

1. by placing several drops of polymer solution on the crystal (e.g. PE as 1% solution in o-Xylene at boiling temperature). Care must be taken to evenly distribute this solution and to let it dry slowly to avoid cracks. It may be useful to repeat this step several times with a dilute solution.

2. by syntheses directly from the oligomer or the monomer. For instance, PDMS is made by mixing two liquid poly(dimethylsiloxanes): one with Si-H groups and the other with vinyl groups. Poly(octadecylsiloxane) is made from trichlorooctadecylsilane, which is heated to vaporize and then condensed on the crystal surface where it reacts with water vapor to form the polymer (Heinrich, 1987).

6.5.3 Membrane processes

The enrichment process in a membrane is characterized by the enrichment factor and the time constant. The first parameter describes a thermodynamic property, the latter a kinetic property. Both are discussed in this section with the limitation to low concentrations of the analyte ($\leq 1\%$ in the membrane). Otherwise changing of the refractive index and swelling of the polymer membrane will severely complicate the situation.

6.5.3.1 Enrichment factor

The enrichment or partition factor $f_{M/S}$ is the relation between the concentrations of an analyte in two phases: in our case between the membrane polymer on the one hand and the solvent, gas or aqueous solution, on the other:

$$f_{M/S} = \frac{c_{Memb}}{c_{Solv}} \quad (6.5-4)$$

It is evident that the enrichment factor depends on the nature of the analytes, the solvent, the polymer, and the temperature.

Table 6.5-3 Enrichment factor $f_{M/G}$, boiling point and time constant τ of some organic compounds as gaseous samples (Wyzgol, 1989)

Substance		Enrichment factor ^a $f_{M/G}$	Boiling point ^b in °C	Time constant ^c in s	Increasing factor ^d b_g
Nitrous oxide	N ₂ O	5	- 88.5	-	3.5
Carbon disulfide	CS ₂	90	46.2	3	2.6
Halothane	CF ₃ -CHBrCl	100	50.2	3	1.5
Acetone	CH ₃ -CO-CH ₃	120	56.2	3.5	3.3
Benzene	C ₆ H ₆	230	80.1	-	≈2
Toluene	C ₇ H ₈	750	110.6	4	2.8
Chlorobenzene	C ₆ H ₅ Cl	2400	132.0	10	2.9
Tetrachloroethene	C ₂ Cl ₄	2600	121.0	9	-
o-Xylene	C ₈ H ₁₀	4700	144.4	9	2.8
Dichlorobenzene	C ₆ H ₄ Cl ₂	18300	173.0	25	2.0
Nitrobenzene	C ₆ H ₅ NO ₂	75000	210.8	-	≈2
Trichlorobenzene	C ₆ H ₃ Cl ₃	89500	213.5	115	2.0

a) at 29 °C in poly(dimethylsiloxane)

b) (Weast, 1977)

c) τ for a poly(dimethylsiloxane) membrane 90 µm in thickness, transmission measurement, 29 °C

d) b_g is introduced later (see 6.5.3.4 Improvement of the detection limit)

For gaseous samples the enrichment is determined by the free enthalpies of condensation and mixing. The free enthalpy of mixing is mainly a function of the polymer. Thus for some polymers very useful relations exists which derive the enrichment factors of various substances from their boiling points (Table 6.5-3).

Wyzgol has found such relations for poly(dimethylsiloxane)/poly(diethylsiloxane) (PDS) and low density polyethylene (PE, $\rho = 0.92 \text{ g cm}^{-3}$):

$$\lg(f_{PDS/G}) = 4.29T_b/T - 2.54 \quad r = 0.993 \quad (6.5-5)$$

$$\lg(f_{PE/G}) = 4.78T_b/T - 3.46 \quad r = 0.986 \quad (6.5-6)$$

where T_b is the boiling point and T is the temperature both in K, r are the correlation coefficients. These relations are only valid for hydrophobic organic substances.

Table 6.5-4 Enrichment factor $f_{M/W}$, water solubility and time constant τ of some organic compounds as aqueous solutions (Wyzgol, 1989)

Substance	Enrichment factor ^a $f_{M/W}$	Water solubility ^b in mg/L	Time constant ^c in s
Aniline	1.0	36000	≈ 10
Benzaldehyde	3.6	3300	≈ 10
Benzonitrile	11	10000 (100 °C)	≈ 10
2,4-Dichlorophenol	15	4500	<10
Nitrobenzene	24	1847	20
Carbon disulfide	66	1794	47
4-Chloronitrobenzene	68	-	55
3-Nitrotoluene	70	496 (30 °C)	56
Benzene	100	1736	56
1,1-Dichloroethene	110	-	60
Toluene	300	470	210
Chlorobenzene	460	308	170
1,3-Dichlorobenzene	960	106	510
Iodobenzene	1030	214	412
p-Xylene	1070	196	452
1,2,4-Trichlorobenzene	1100	33	810
2-Chlorotoluene	1170	-	580
Diphenyl ether	1930	16	≈ 1600
2-Chlorobiphenyl	5130	4,1	3650
Hexachlorobutadiene	6800	4,4	>2600

a) at 29 °C in poly(dimethylsiloxane)

b) at 20 °C (Kertes, 1985; Sorensen and Arlt, 1979; Horvath, 1982; Weil et al., 1974; Windholz, 1983)

c) τ for a poly(dimethylsiloxane) membrane 25 µm in thickness, ATR, flow velocity 15 cm s⁻¹, 25 °C

Similar free enthalpy relationships are found for aqueous solutions. Here the enrichment factor is deduced from other known partition coefficients like the solubility in water or the octanol-water partition coefficient $f_{Oct/W}$.

For polydimethylsiloxane (PDMS) Wyzgol gives the following relations (20 °C, see also Table 6.5-4):

$$\ln(f_{PDMS/W}) = -\ln s - 0.015 t_b + 1.96 \quad r = 0.969 \quad (6.5-7)$$

$$\lg(f_{PDMS/W}) = 1.25 \lg f_{Oct/W} - 1.05 \quad r = 0.984 \quad (6.5-8)$$

where s is the solubility in water in mol/L, t_b is the boiling point now in °C. It is also possible to determine enrichment factors from chromatographic data (Schantz and Martire, 1987).

For gaseous samples in the temperature region from 0 to 40 °C the partition coefficient normally increases by a factor 2 - 4 if the temperature decreases about 20 °C. Generally, aqueous samples show much weaker dependence on temperature and the sign is often not predictable.

6.5.3.2 Time constant of the extraction process

The time constant is mainly determined by diffusion processes towards and inside the membrane. The time constant τ is the time which is needed to reach 1-1/e of the final concentration. The solution of Fick's law with suitable boundary conditions gives a relation for the time constant:

$$\tau = \frac{d_M^2}{2D} \quad (6.5-9)$$

where d_M is the thickness of the membrane, and D is the diffusion coefficient.

In most polymers the diffusion coefficients have magnitudes from $10^{-9} \text{ cm}^2 \text{ s}^{-1}$ to $10^{-5} \text{ cm}^2 \text{ s}^{-1}$ at 20 °C. For a membrane thickness of 25 µm the resulting time constants are between 3000 and 0.3 seconds. For PDMS the diffusion coefficients are between 10^{-5} and $10^{-6} \text{ cm}^2 \text{ s}^{-1}$ at 20 °C for most organic substances. The time constants experimentally determined for gaseous samples are of the order 1 to 100 s (Table 6.5-3). Because the diffusion is greatly affected by temperature it is necessary to control the temperature of the membrane to have reproducible results.

6.5.3.3 The Nernst diffusion layer

For gaseous samples the quadratic relation of the time constant to the membrane thickness can be verified by experiment. For aqueous solutions the measured relation is often only directly proportional to the membrane thickness and sometimes up to 50 times larger than

expected (Table 6.5-4). This is a result of the Nernst diffusion layer which describes the slope of the concentration from the fluid sample to the solid membrane. The concentration decreases within this layer to a very small value in front of the membrane. This value is only controlled by diffusion because no convection occurs inside this layer. In general the flow is laminar, then the average thickness of the Nernst diffusion layer $\bar{\delta}_N$ is:

$$\bar{\delta}_N = 2 \left(\frac{l\nu}{v} \right)^{1/2} \left(\frac{D_W}{\nu} \right)^{1/3} \quad (6.5-10)$$

where l is the length of the IRE in contact to the sample, ν is the kinematic viscosity, v is the flow velocity and D_W is the diffusion coefficient of the analyte in water.

The kinematic viscosity of dilute aqueous solutions is ca. $0.01 \text{ cm}^2 \text{ s}^{-1}$. So Nernst diffusion layers $\bar{\delta}_N$ between 200 and 30 μm result at flow velocities between 5 and 100 cm s^{-1} . For small molecules like benzene, tetrachloroethene, etc. the diffusion coefficients in water and in the PDMS membrane are of the same order. Then the time constant is approximately:

$$\tau_W \approx \frac{(d_M + \bar{\delta}_N)^2}{2D'} \quad (6.5-11)$$

where D' is now the average value of the diffusion coefficients in water and in the polymer.

Therefore, altering d_M effects the time constant less than expected without the Nernst diffusion layer. The time constants τ for the enrichment from aqueous samples in a PDMS membrane are of the order of 10 to 600 s for small molecules like benzene derivatives and up to e.g. 3600 s for 2-chlorobiphenyl (Table 6.5-4).

6.5.3.4 Improvement of the detection limit

In Sec. 3.3.4 the detection limit and related analytical quantities are described in detail. In this section we define the detection limit as the concentration c we get from a signal which is three times as high as the standard deviation of the background (Kaiser, 1965). The signal should be the absorbance which is proportional to the concentration. The mean value of the noise amplitude will be approximately 5 times the standard deviation (Doerffel, 1988). With this assumption we get

$$c \approx \frac{3\Phi_N}{5d\varepsilon} \quad (6.5-12)$$

where Φ_N is the noise amplitude, d is the thickness of the sample and ε is the integral molar decadic absorption coefficient.

It is common to use the peak absorption coefficient instead of the integral absorption coefficient. In most cases only small errors are introduced by this simplification. It is evident that the detection limit decreases with the membrane method as $1/f_{M/S}$. For gases extracted by the membrane the usual rotational vibrational bands vanish if the compound is dissolved in a polymer, since the molecule is no longer able to rotate freely. As a result, one relatively sharp absorption band is observed which has the same integral absorption coefficient as the rotational vibrational absorption band. So, for gases the detection limit is decreased by an additional factor b_g (see Table 6.5-3). For the ATR-method the thickness of the sample is the effective thickness multiplied by the number of reflections N . So we get as detection limit for the membrane method

$$c_M = \frac{0.6\Phi_N}{Nd_e\varepsilon_{max}f_{M/S}b_g} \quad (6.5-13)$$

In practice this relation is only an approximation because of the uncertainty of all of the parameters. Nevertheless it is still an useful estimation. For example: CS_2 in water should be measured. The ZnSe-IRE with a length of 50 mm, a thickness of 3 mm, and windows with an angle of 45° , allow 12 reflections in the sample area. It is coated with a PDMS membrane ($n \approx 1.4$) of $20 \mu\text{m}$ thickness. The band at 1521 cm^{-1} ($= 6.575 \mu\text{m}$) with a peak absorption coefficient of $3100 \text{ L mol}^{-1} \text{ cm}^{-1}$ is evaluated. With Eq. 6.5-1 and 6.5-3 the pathlength is calculated to be $N \cdot 0.31 \cdot \lambda = 24.5 \mu\text{m}$. Within this spectral range the noise amplitude Φ_N is measured as 0.001 absorbance units. The enrichment factor $f_{M/W}$ is 66.

Therefore the detection limit is calculated to be $1.2 \cdot 10^{-6} \text{ mol/L}$, or to 0.090 mg/L ($M = 76.13 \text{ g/mol}$). Wyzgol found experimentally 0.1 mg/L which is in sufficient agreement with our estimation.

6.5.4 Alternative membrane procedures

6.5.4.1 Non-reversible enrichment

Another sampling technique (resembling a chemical sensor) involves an irreversible chemical reaction between the membrane material and one of the components of the sample; after "loading" such a material for a defined time the content of the organic compound in the membrane is measured, resulting in an integral concentration over a longer period of time.

6.5.4.2 Optical fibers covered with membranes

The membrane method (Sec. 6.5.2) has been described by Opitz et al. (1983) and in other publications (Wyzgol et al., 1989; Heinrich et al., 1990). Already in the first patent

application (Opitz et al., 1983) a useful variant of the ATR technique has been described: the cladding of optical fibers can be used as membrane for the extraction. This technique is used in our laboratory (Wyzgol et al., 1991) as well as in others (Taga et al., 1993; Conzen et al., 1993; Paiss et al., 1993). They reach detection limits between 1 and 50 ppm for six common chlorinated hydrocarbons by using a sensing part only 10 cm in length (silver halide fiber) with time constants in the range of some minutes (Krska et al., 1993).

Such fibers should have the same properties as good IRE, e.g. sufficient transmission for IR radiation, insolubility in solvents, and chemical inertness. Further, they should have good mechanical properties (e.g. flexibility), they must be step index fibers, and it must be possible to remove the original cladding and to apply the sensitive one without any damage to the fiber.

There are at this time no IR-fibers which fulfill all of these demands. The mainly used fibers are made of poly-crystalline silver halide (refractive index 2.2 at 10.6 μm) with very good transmission over the whole MIR (2 to 16 μm , see Fig. 6.5-5), and good mechanical properties. The disadvantages are that they react with many commonly used metals and that they are sensitive to visible radiation, especially to UV radiation (Ceram optec, 1991).

Other possible types of fibers are the chalcogenide glass fibers (e.g. Ge-As-Se) or heavy-metal fluoride fibers. Their transmission region is limited (2 to 10 μm , Fig. 6.5-5) and they are very fragile if the original cladding is removed.

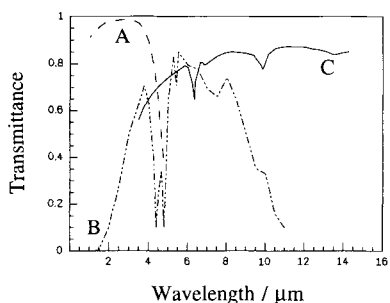


Figure 6.5-5 Transmission for some IR-fibers (1m in length). (A): Zirconium fluoride (Fiber System, 1991), (B): chalcogenide (Fiber Systems, 1991), (C): silver halide (Ceram Optec, 1991).

The covering of the fibers with an enriching membrane is more complicated but also possible with the same procedures as used for normal IRE.

There are still two ways of using IR-fibers. First, a little part of the fiber is cut and used as an cylindrical IRE. The second way is to cover a little part of a long fiber where the other parts have the function to transport the light from the source to the sensitive part and to forward it to the detector or spectrometer. Since these fibers have a thickness of several hundred μm up to 1 mm, the number of reflections may be greater, making the detection limit smaller than in the described ATR experiments.

Besides the poor chemical or mechanical properties of presently available IR fibers have some additionally inherent disadvantages which limit their usage considerably. From Eq. 6.5-1 and 6.5-2 it can be seen that the effective thickness, the number of reflections

and as a result also the absorbance are strongly related to the angle of total reflection. Unfortunately this angle is influenced by

- the shape of the fiber ends. A fiber cut perpendicular to its axis (as for the communication technique) has the smallest number of reflections. Conical or oblique cut fibers show many more reflections. It is very difficult to reproduce the desired ends of the possible IR transparent fibers. However, in recent literature Jonas and Braiman (1993) and in part Lowry et al. (1993) tried interesting ways to overcome this problem.
- the optical arrangement of coupling to the light source and to the detector. For normal "large" IRE's the arrangement is much more reproducible (Jonas and Braiman, 1993).
- the topography of the fiber itself. For instance the absorbance of an analyte depends on whether the fiber is linearly or curved. The resulting signal is additionally modulated by all mechanical movements of the fiber (e.g. vibrations).

Further disadvantages:

- up to now the number of reflections and the effective thickness are only calculated for meridional rays, which cross the axis of the fiber. Unfortunately, these rays are a small minority in optical fibers.
- a temperature control of a fiber cell is necessary but more complicated.

Nevertheless, fibers may become a reasonable alternative to "normal" IRE's for e.g. applications without any change of the sample arrangement after calibration.

6.5.4.3 Combination of continuous distillation and head space analysis

To avoid the influence of mechanical contaminations of waste water on the membrane a head space variant can be used. In this variant the covered IRE is not in direct contact with the liquid water but with the vapor above this water. To improve the detection limit the waste water can be heated and the IRE can be cooled (see Fig. 6.5-6).

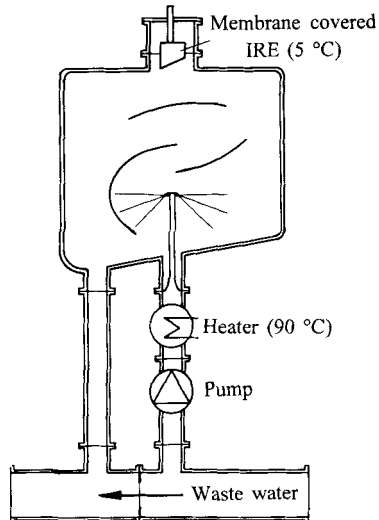


Figure 6.5-6 Combination of distillation with head space analysis for the continuous control of hydrophobic contaminations in waste water (Schrader, 1993).

The vapor phase from heated waste water often enriches the organic compound. This “enriched” vapor partly condenses at the membrane on the IRE. Additionally, the enrichment factor increases because of the lower temperature of the membrane. Therefore the head space method has mainly two advantages: first, protecting the IRE from contamination and second, improving the detection limit.

For instance, the large solubility of dichloromethane in water causes a relatively low enrichment factor of ca. 80 (PDMS, 30 °C). As a result the detection limit for direct measurements of aqueous solutions with membrane covered IRE's is ca. $1.9 \cdot 10^{-3}$ mol/L. Using the head space variant with heated aqueous sample (90 °C) and cooled IRE (5 °C) the detection limit is improved by a factor of 30 to $6.2 \cdot 10^{-5}$ mol/L.

6.5.4.4 Measurement of the transmission of the membrane

For gaseous samples it is often recommendable to use extracting membranes in “normal transmission” measurements (Schrader et al., 1990a). The membrane is deposited on a window or freely attached without any support in the sample chamber.

This technique allows a larger thickness of the membrane (up to 200 µm). To reduce the time constant it is sometimes better to combine several thinner membranes. With this technique the light path through the gaseous sample can be minimized to a few millimeters reducing the influence of water absorption.

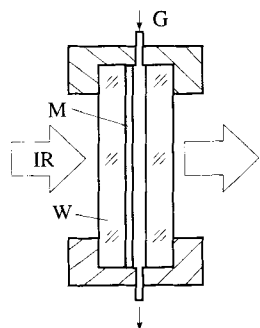


Figure 6.5-7 Principle of the membrane transmission method. G: Gas inlet, M: Membrane, W: Window.

To demonstrate the capability of the membrane transmission technique an equivalent length l_{trans} is defined. This length gives the necessary length of a common gas cell within which the same absorbance is measured as using enriching membranes for equivalent concentration of the analyte (for b_g see Eq. 6.5-13 and Table 6.5-3):

$$l_{trans} = f_{M/G} b_g d_M \quad (6.5-14)$$

For a membrane thickness d_M (PDMS) of 200 µm the following equivalent lengths were calculated:

carbon disulfide	47 mm	
benzene	92 mm	
toluene	420 mm	(0,4 m)
tetrachloroethene	505 mm	(0,5 m)
o-xylene	2632 mm	(2,6 m)
1,2,4 trichlorobenzene	35800 mm	(35,8 m)

Based on this we have developed a small IR-photometer (Fig. 6.5-8) to detect aromatic compounds in gaseous samples (Lentz et al., 1994).

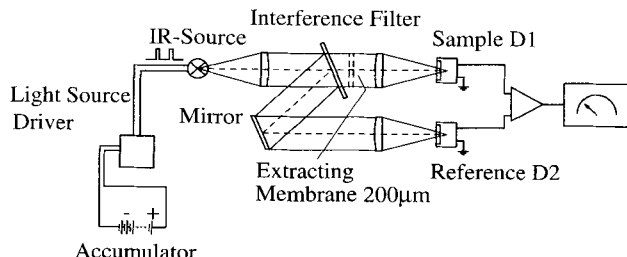


Figure 6.5-8 Principle of a small IR-photometer based on the membrane transmission method.

IR radiation is emitted from the electrically modulated light source. The analytically relevant spectral range is transmitted through an interference filter, the sample chamber, and the membrane. This radiation is focused on a thermal detector (D1), pyroelectrical or thermopile. The reflected radiation from the filter is used as a reference (D2). A comparison of the ATR-, the fiber-, and the transmission-method, Secs. 6.5.2.1, 6.5.4.2, and 6.5.4.4, shows that the ATR method is most versatile for all applications and that the transmission method allows the lowest limit of detection for gases (Hadziladzaru, 1994). The properties of the ATR method by employing wavelength selection with tunable interference filters has been studied by Lebioda (1994).

6.6 Investigation of fast reactions and intermediates*

6.6.1 Introduction

Although infrared spectroscopy is a classical method of analytical and structural investigations (Colthup et al., 1990), it can also provide valuable insight into the mechanisms of chemical reactions (Lau et al., 1993). Especially timeresolved Fourier-Transform-Infrared-difference-spectroscopy has recently proved itself as a powerful new method for studies of molecular reaction mechanisms of large proteins up to 120000 Dalton

* Section 6.6 is contributed by K. Gerwert, Bochum

and time resolution up to nanoseconds. Here the application to proteins is given as an example.

The infrared spectrum of a protein is dominated by its peptide backbone amide I ($\text{C}=\text{O}$) and amide II ($\text{C}-\text{N}$, NH) vibrations. Fig. 6.6-1 shows a typical IR absorption spectrum of a hydrated protein film, in this case bacteriorhodopsin. In addition to the strong amide I (1658 cm^{-1}) and amide II (1546 cm^{-1}) bands water also contributes largely to the absorption (3379 cm^{-1} , 1650 cm^{-1}).

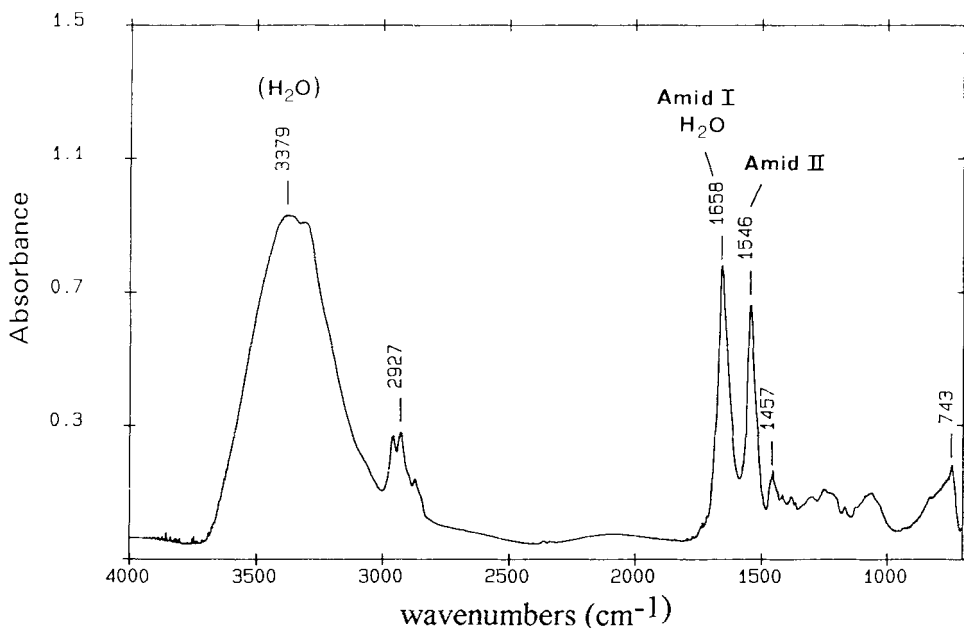


Figure 6.6-1 Typical absorption spectrum of a hydrated protein film (bacteriorhodopsin).

The major problem in measuring reactions consists in selecting small absorption bands of molecular groups which undergo reactions from the large background absorption of water and of the entire protein. This difficulty is met by obtaining difference spectra between spectra of the protein in its ground state and in an activated state. Such measurements require highly sensitive instrumentation. FTIR has two advantages over conventional dispersive IR spectroscopy, i.e., the multiplex and the Jaquinot advantage. This makes it possible to reliably detect such small absorption changes with a time resolution of a few nanoseconds. Alternatively, if it is sufficient to measure only absorption changes within a bandwidth of a few wavenumbers, photolysis setups with dispersive elements providing a time resolution down to picoseconds can be used. Instead of presenting a comprehensive literature review, this section develops the basic ideas of FTIR reaction mechanism studies. Examples include the light-induced proton-pump mechanism of the membrane protein bacteriorhodopsin and the light-induced electron transfer reactions of bacterial photosynthetic reaction centers. For detailed reviews, see (Braiman and Rothschild, 1988; Kitagawa and Maeda, 1989; Gerwert, 1993).

6.6.2 Methods

6.6.2.1 Principles of FTIR

The relative absorbance changes $\Delta A/A$ in the infrared as a result of protein activity are on the order of 10^{-3} to 10^{-4} underneath a high background absorbance of up to 1. FT instruments have a number of distinct advantages over dispersive instruments. Dispersive instruments such as those shown in Fig. 6.6-2, which measure wavenumbers sequentially are not sufficiently stable during the entire measuring time to provide complete, high quality difference spectra.

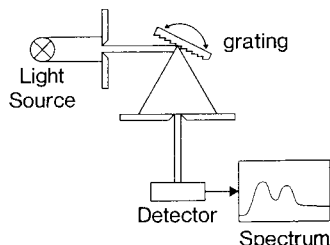


Figure 6.6-2 Diagram of a dispersive instrument.

In contrast, the Michelson interferometric FTIR technique drastically reduces the measuring time by the multiplex advantage. Measuring n spectral elements, each within a time period Δt , requires a total time of $T = n \cdot \Delta t$ with a dispersive instrument and $T = \Delta t$ with an FTIR instrument (Griffiths and de Haseth, 1986). The second advantage of FTIR instruments is the so-called Jaquinot advantage which increases the light throughput as compared to dispersive instruments. A linear increase in the light intensity increases the signal-to-noise ratio quadratically.

In principle, an FTIR instrument consists of a Michelson interferometric arrangement (see Fig. 6.6-3) with a light source G (globar), a beam splitter BS, a fixed mirror FM, a movable mirror MM, and a detector (MCT). The very sensitive MCT detectors

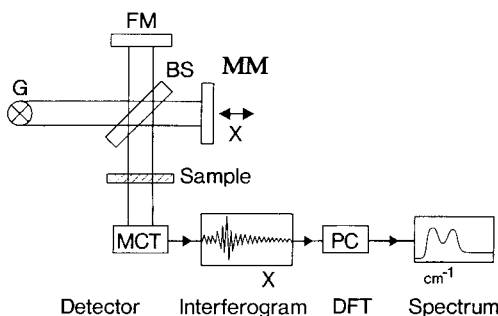


Figure 6.6-3 Diagram of an FTIR apparatus.

($D^* > 10^{11} \text{ cm}^{-1} \text{ Hz}^{1/2} \text{ W}^{-1}$) generally operate best in the mid-IR region. The resulting interferogram is a function of the intensity versus the distance x of MM. This scan distance x determines the spectral resolution $\Delta\tilde{\nu}$:

$$\Delta\tilde{\nu} \propto \frac{1}{x} \quad (6.6-1)$$

The digitized (ADC) discrete interferogram is Fourier transformed (DFT) by a PC to yield a wavenumber dependent spectrum. Sampling points are determined by the interference pattern of a monochromatic HeNe laser beam which is transferred collinearly with the IR beam. The resulting high wavenumber accuracy constitutes the third advantage of FTIR.

This section very briefly outlines some of the problems connected with the Fourier transformation. For details, textbooks such as Griffiths and de Haset (1986) can be recommended. Problems arise primarily because digital computers perform discrete rather than continuous FT of the interferogram $I(x)$, an approximation which requires care to avoid errors. As a result of DFT, the continuous variables, i.e., the scan length x and the frequency $\tilde{\nu}$, become the discrete variables $n \cdot \Delta x$ and $k \cdot \Delta\tilde{\nu}$:

$$S(k \cdot \Delta\tilde{\nu}) = \sum_{n=0}^{N-1} I(n \cdot \Delta x) e^{i2\pi n \cdot \frac{k}{N}} \quad (6.6-2)$$

In practice, one uses a less redundant fast Fourier transform algorithm, e.g., the Cooley-Tukey algorithm rather than the expression shown above. Possible problems connected with discrete Fourier transformation (DFT) include

1. Zero filling, which avoids the so-called “picket fence effect” by adding zeroes to the interferogram and thereby causing spectral interpolation between the measured points.
2. Aliasing, which is caused by overlap of intensities in the spectrum and its mirror image automatically generated by the DFT. Care must be taken to avoid overlap of intensities with the mirror symmetrical replicate (alias) above a certain frequency (Nyquist frequency). As a result, only $N/2$ points in the calculated spectrum can be used. FT routines are usually ‘dealaised’.

However, aliasing can actually reduce the number of sampling points without loss of spectral information; intensity depression beyond a certain wavenumber allows increased sampling point spacing and thereby decreased sampling rate. In our time-resolved investigations for the spectral range between 1800 and 800 cm^{-1} , an optical filter is used to extinguish the IR intensity above the folding wavenumber, 1975 cm^{-1} . Therefore data acquisition is required only at every 8th sampling point determined by the HeNe laser interference pattern.

3. Leakage, i.e., truncation of the interferogram at maximum optical path difference, resulting in the convolution of the true interferogram with a boxcar function, which causes “leakage” of the band intensities into side lobes. Leakage can be avoided by employing an appropriate apodization function instead of the boxcar function. With dispersive

instruments, one has to deal with the instrumental line shape, while FT instruments offer a free choice of its apodization function and thus make it possible to optimize the apodization for a specific application. For our purposes, the Blackman Harris apodization function appears to be most useful. For more details concerning apodization functions, see Griffiths and de Haset (1986).

4. Phase correction: in contrast to the theoretical expectation, the measured interferogram is typically not symmetric about the centerburst ($x = 0$). This is a consequence of experimental errors, e.g., frequency-dependent optical and electronic phase delays. One remedy is to measure a small part of the interferogram doublesided. Since the phase is a weak function of the wavenumber, one can easily interpolate the low resolution phase function and use the result later for phase correction. If there is considerable background absorption, phase errors may falsify the intensities of bands in the difference spectra. To avoid such phase errors for difference spectroscopy, the background absorbance should therefore be less than one.

Fourier transformation of the interferogram affords a single channel background spectrum including the spectral characteristics of the mirrors, the globar and the detector detectivity. The IR spectrum of a sample, such as the one shown in Fig.6.6-1, is obtained by subtracting from the sample spectrum the background sample-free spectrum.

6.6.2.2 Time-resolved FTIR techniques

This section describes the state of the art of fast time-resolved FTIR techniques, together with the advantages and limitations of each method. Sec. 6.6.3 discusses the application of the described techniques to actual problems.

6.6.2.2.1 Static FTIR

In the *static FTIR mode*, the simplest technique to realize, data acquisition takes several seconds. At such low time resolution, it is necessary in order to record spectra of the activated protein states to stabilize the transient intermediates for several minutes, for instance by cooling, by pH variation, or by photo stationary accumulation. It must be possible to vary these external parameters without removing the sample from the apparatus or changing the sample, since any disturbance even in the sample position causes larger absorption changes than those induced by protein activity. We will return in Sec. 6.6.3.3 to an example of the static technique allowing to monitor reactions taking place at room temperature in femtoseconds. The reaction is decelerated to minutes by cooling down to 77 K.

6.6.2.2.2 Rapid scan

The principle of the *rapid scan mode* is simple: after taking a reference spectrum of the sample in its ground state, one activates the reaction (e.g., by a laser flash) and obtains an interferogram in a much shorter time than the half life time of the reaction (e.g., the photocycle).

The time pattern of such an experiment, as shown in Fig. 6.6-4, shows an upper trace (IR) with a “Take DATA” signal indicating in its “high” state interferogram recording, and a lower trace (VIS) showing an typical absorption change in the visible spectral range, which indicates the photocyclic reaction of the protein. The first two reference (R) interferograms reflect the ground state and the succeeding 28 are photocyclic reaction interferograms.

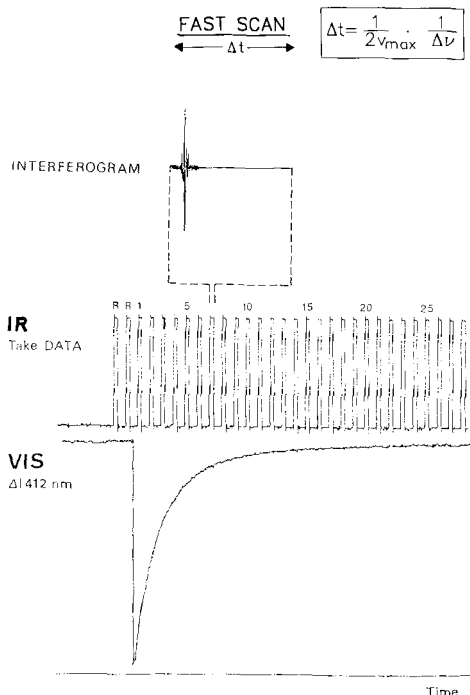


Figure 6.6-4 Diagram of Rapid Scan methode.

The velocity of the scanner V_{max} and the desired spectral resolution $\Delta\tilde{\nu}$ determine the scan duration Δt and thereby the time resolution:

$$\Delta t = \frac{1}{2V_{max}} \cdot \frac{1}{\Delta\tilde{\nu}} \quad (6.6-3)$$

State of the art spectrometers today yield typically a time resolution of 7 ms at 4 cm^{-1} spectral resolution. As we have shown, Fourier transformation makes it possible to even resolve processes whose half life times are of the order of the scan time (Gerwert et al., 1990). If the half life of the observed process is shorter than the duration of the scan, then the intensity of the interferogram is convoluted by the absorption change due to the chemical reaction in the sample. Thus, the absorption changes during the bacteriorhodopsin photocycle can be described by sums of exponentials. This leads to

convolution of the interferogram by exponential functions, resulting in Lorentzian line shape broadening only.

Significant improvements of state of the art spectrometers yielding increased scanner velocity are unlikely to occur. This has practical reasons, e.g., the acceleration at the turning points is already on the order of several g. Without a radical change of design, rapid scan time resolution is limited to the millisecond range.

Fig. 6.6.5 shows an time resolved FTIR apparatus based on the Bruker IFS 88 model, in which an excimer pumped dye laser system (EMG102, FL 105, Lambda Physik) initiates protein activity by a laser flash. The home-made counter, trigger, and opto-delay units are used to initiate the laser flash at the correct scanner position. The controller which regulates the scanner is the crucial unit for time resolved measurements. Fourier transformation is performed on Sun workstations. It is possible to monitor not only absorbance changes in the infrared, but simultaneously those in the visible region. The conventional, home-made photolysis apparatus consists of a halogen lamp as a light source (VIS), interference filters to select the wavelength, and germanium windows to orient the visible beam so that it is collinear to the IR beam and to reflect it after the sample out of the FTIR apparatus onto a photodiode. The coated germanium windows are

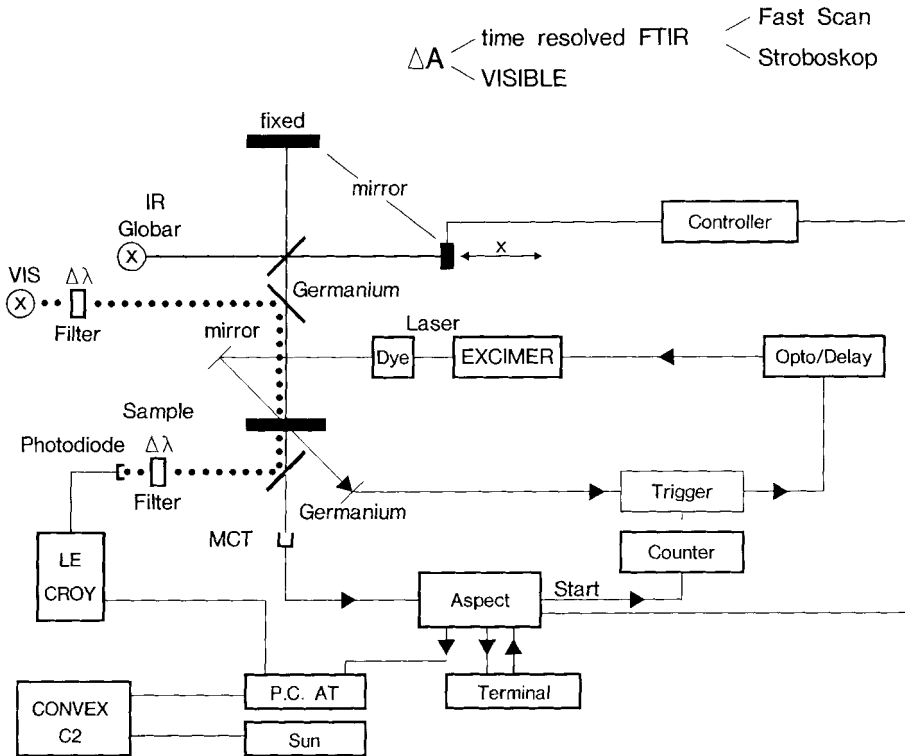


Figure 6.6-5 Diagram of experimental setup.

transparent in the IR but reflect visible light. A digital oscilloscope (Le Croy) monitors absorbance changes in the visible region. The visible and IR data are transferred to a PC and then, via ethernet, passed on to a workstation (SUN) network. Data analysis is performed on a convex C2 supercomputer.

Fourier transformation produces a time-dependent series of difference spectra. The absorbance changes at a specific wavenumber are simply obtained by reordering the data in dependence of time. Examples are discussed in section 6.6.3.

6.6.2.2.3 Stroboscope technique

Merely as a result of software changes, the *stroboscope method* with our experimental setup afforded a time resolution of a few microseconds (Souvignier and Gerwert, 1992).

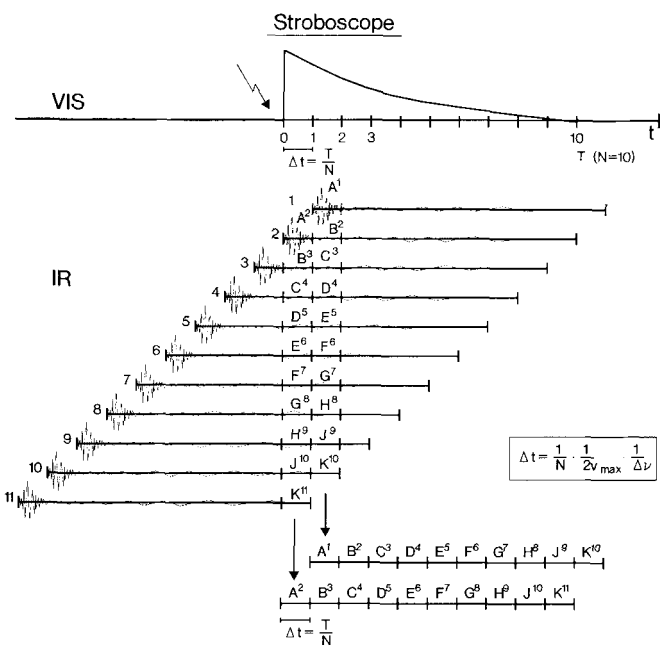


Figure 6.6-6 Diagram of stroboscope technique.

The idea is this: If it takes a time period T to monitor a complete interferogram with the length X , then it only requires a time period T/N to record a segment X/N of the interferogram. In successive experiments, all N segments of the interferogram are recorded. The software sorts and combines these segments to a new interferogram with an increased time resolution of T/N . Fig. 6.6-6 illustrates: a typical absorption change in the visible (VIS) spectral region indicates protein activity. Recording of succeeding interferograms (1...11) is differently delayed with respect to the reaction. The n th interferogram relative to the excitation starts at the time

$$\frac{n \cdot x}{10}, \quad n = 1, 2, \dots \quad (6.6-4)$$

The rearranged new interferograms ($A^2 B^3 \dots K^{11}$) have a time resolution which is ten times higher than the original interferograms (in this example). Since each interferogram contains several useful segments (e.g., including $A^1 B^2 C^3 \dots K^{10}$), the multiplex advantage persists partially although to a less degree as N increases. This is the main reason why the described method is so time consuming. Experimental details are found below in section 6.6.3.5. A time resolution of 20 microseconds is realised with this technique. Typical measuring times are 10-15 hours. The important point is that there is still the Jaquinot advantage, which is why this instrumentation requires less averages than dispersive instruments.

6.6.2.2.4 Step scan

In the *step scan mode*, the scanner stops at a sampling position, protein activity is initiated, and the apparatus measures the time dependence at a sampling point of the interferogram (Griffiths, 1975; Palmer et al., 1989; Uhmann et al., 1991; Weidlich and Siebert, 1993). This is repeated at each sampling point of the interferogram. The position of the scanner must be accurate down to a few nanometers while the intensity change during the reaction is measured, which makes this method very sensitive to external disturbances (e.g., noise!). It is recommended to use a vacuum instrument on a vibrationally isolated table. The time resolution, in principle determined by the response time of the detector (10 ns), is recently improved to 500 nanoseconds (Weidlich and Siebert, 1993).

6.6.2.3 Time-resolved conventional IR techniques

By focusing on the absorption changes at a few wavenumbers only, one can realize an apparatus for time resolved measurements by analogy to conventional visible photolysis apparatus. A conventional Perkin Elmer grating spectrometer upgraded with an MCT detector achieves a time resolution of 400 ns (Gerwert et al., 1985). Replacing the globar light source with photodiodes (Hermann et al., 1982) yields higher light intensities and thus increases the signal-to-noise ratio.

Further improvement is achieved using a picosecond-pulsed laser light source in contrast to a continuous one. Time resolution thus is determined by the lifetime of the probe beam instead of the response time of the detector in analogy to picosecond time resolved experiments in the visible spectral range (for a recent review see Stoutland et al., 1992).

Conclusion

The static technique able to resolve reactions on the second-time scale is easiest to perform and a good point to start with. The reaction can be slowed down by variation of external parameters. The rapid scan technique can resolve already millisecond reactions and has the broadest applicability. A time resolution of microseconds is most easily

achieved by the stroboscope technique because data acquisition is performed in the rapid scan mode and improvement of the time resolution is gained by software treatment of the data. A time resolution on the nanosecond time scale can be obtained by the step scan technique. The stroboscope and the step-scan techniques rely on the ability to repeatedly initiate the investigated process. As a result, their scope is largely limited to cyclic processes. If the sample can be renewed between measurements, e.g., by flow or by two-dimensional scanning of the sample, it may be possible to also apply these techniques to noncyclic processes. In contrast, the fast scan technique is broadest in scope, because it is not inherently limited to cyclic reactions. Using pulsed light sources picoseconds time resolution is obtained but only for small spectral segments; it is therefore useful for specific questions only.

6.6.3 Application to bacteriorhodopsin

6.6.3.1 Introduction

Bacteriorhodopsin, a light-driven proton pump, is a large (27000 Dalton) membrane protein, located in the purple membrane of *halobacterium halobium* (for a recent review see Lanyi, 1993). It spans the membrane by seven- α -helices (see Fig 6.6-7). The chromophore retinal is embedded inside the protein, shielded by the helices. Retinal connects to the Lys 216 of the protein via a protonated Schiff's base (Fig. 6.6-7).

Light-excitation of ground-state BR₅₇₀ (the subscripts refer to the absorption maxima) initiates a photocycle with the intermediates J₆₁₀, K₅₉₀, L₅₅₀, M₄₁₂, N₅₃₀, and O₆₆₀ (Fig. 6.6-8).

Upon light excitation, the chromophore retinal undergoes an all-trans to 13-cis isomerization in 450 femtoseconds (Fig. 6.6-8). The Schiff's base is deprotonated during the L to M reaction and is reprotonated again in the course of the M to N conversion. M is generally believed to be the key intermediate in the proton pumping mechanism. During the L to M reaction, the protein releases protons to the extra-cellular side and takes them up from the cytoplasmic side during the M to BR reaction (Fig 6.6-8).

6.6.3.2 Sample preparation

Due to the considerable absorption of water in the mid infrared spectral region, meaningful spectra of hydrated proteins are obtained by transmission measurements through very thin (2-10 micrometer) films. This involves placing a drop of a protein suspension or solution on an IR window and then carefully concentrating it on this window by drying it under a nitrogen stream. The protein film on the window is then left to equilibrate in a hydration chamber at 100% humidity for at least 10 hours. Alternatively the protein suspension is centrifuged and the pellet is squeezed between two IR windows. A typical

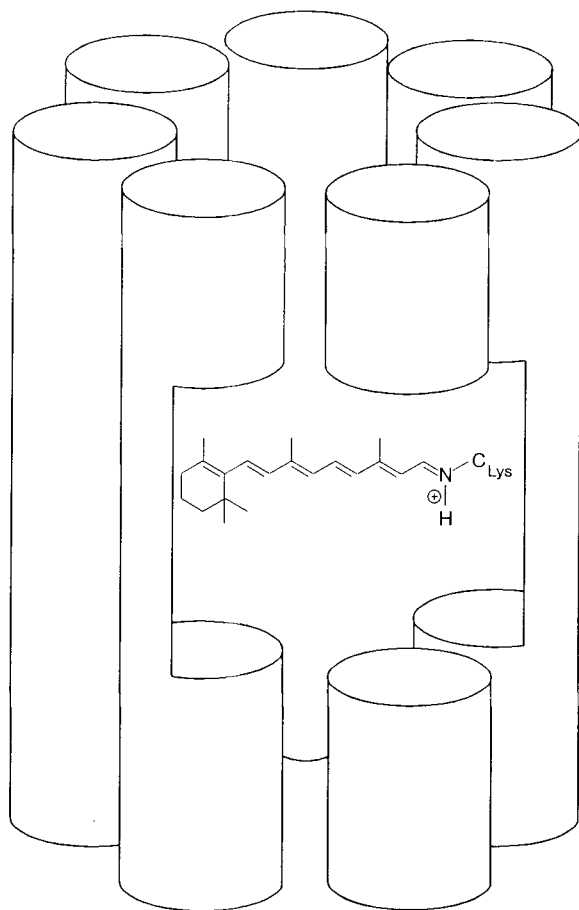


Figure 6.6-7 Scheme of bacteriorhodopsin structure.

measurement requires about 100 to 150 μg of protein. The initial concentration is a few $\mu\text{mol} \cdot \text{L}^{-1}$ and the final concentration in the $\text{mmol} \cdot \text{L}^{-1}$ range.

The sample chamber is supplemented by a second IR window, which is separated from the basic IR window by a thin spacer of several micrometers. Fig. 6.6-9 shows an outline of the IR sample chamber.

In the case of bacteriorhodopsin, it was explicitly shown that such carefully hydrated thin protein film afford the same rate constants as suspensions (Gerwert et al., 1990).

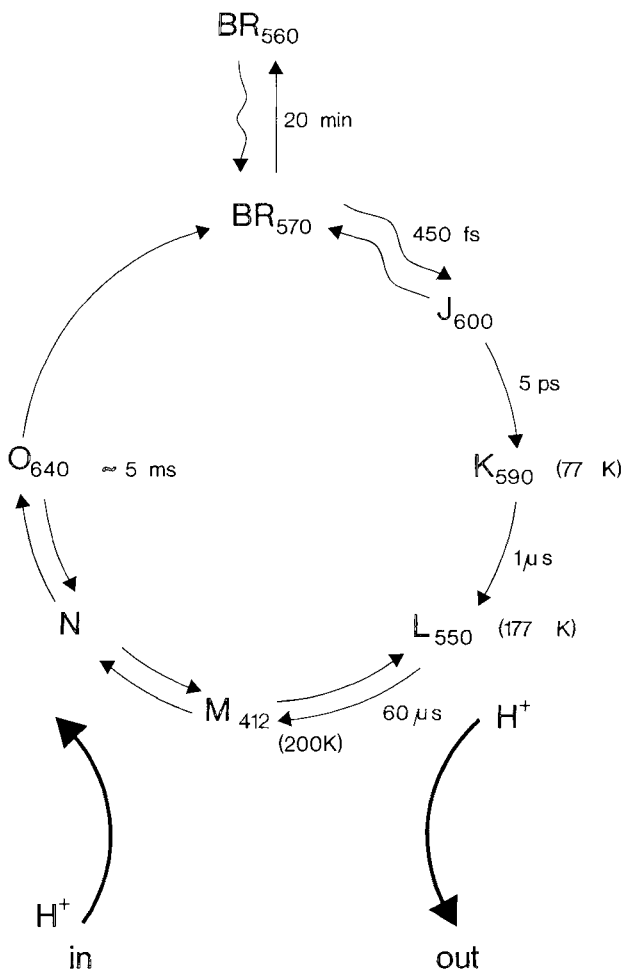


Figure 6.6-8 Photocycle model of bacteriorhodopsin.



Figure 6.6-9 Diagram of the sample chamber.

6.6.3.3 An example of a static (low-temperature) FTIR measurement, the *BR* to *K* transition

At 77 K, the *K* intermediate is stable for several minutes. A static *BR-K* difference spectrum is obtained as follows: 1) in the dark, cool the sample to 77 K; 2) obtain

a spectrum of the *BR* ground state; 3) for several minutes, irradiate the sample at a wavelength shorter than 550 nm in order to generate a mixture of *BR* and *K*; 4) record a spectrum of the mixture of *BR* and *K*; 5) subtract the spectrum obtained according to (2) from that recorded in step (4). A *BR-K* difference spectrum (like the one shown in Fig. 6.6-10) results in which positive bands are caused by *K* and negative bands by *BR*. All bands in the difference spectra represent absorption changes of the protein and are highly reproducible.

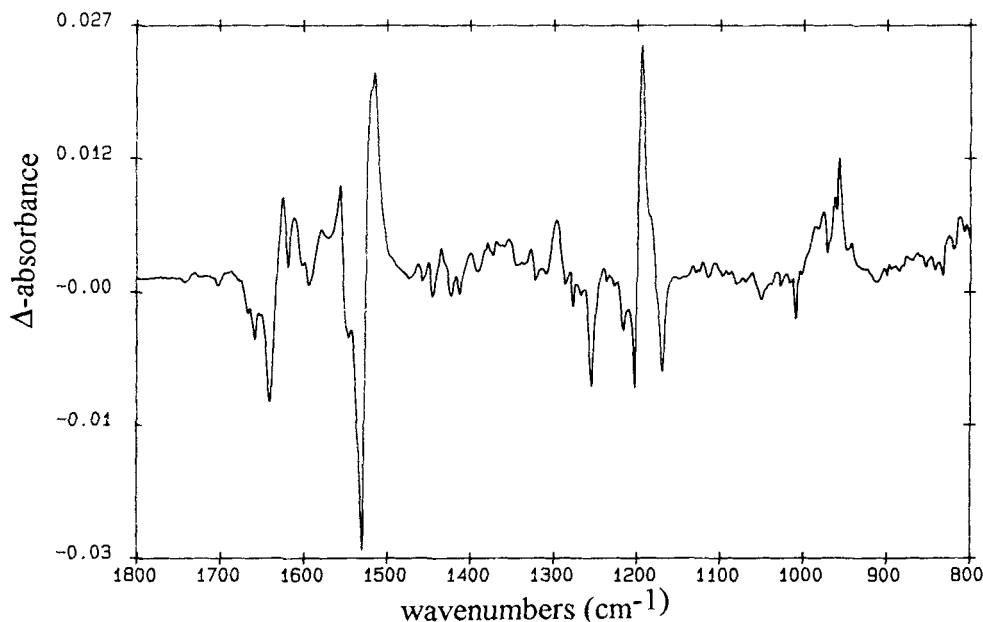


Figure 6.6-10 *BR-K* difference spectrum.

What information does the difference spectrum provide concerning the intramolecular mechanism of the *BR* to *K* transition? The frequency shifts observed (Fig 6.6-10) between 1300 and 1100 cm⁻¹ characterize an all-trans to 13-cis isomerization of retinal. The unusually strong out-of-plane vibrations at 960 cm⁻¹ and 814 cm⁻¹ indicate considerable distortion of the terminal part of the chromophore. In summary, the *BR-K* difference spectrum shows that isomerization forces the chromophore and the protein backbone into a strained conformation, generating tension in the protein, which in turn drives the ensuing reactions.

6.6.3.4 An example for band assignment, the *BR* to *L* transition

As in the case of *K* the *L* intermediate is also stabilized at low temperature (170 K). The *BR-L* difference spectrum is given as an example for band assignments. Bands

are assigned by using isotopically labeled proteins or by amino acid exchange via site directed mutagenesis (Engelhard et al., 1985; Gerwert and Siebert, 1986; Gerwert et al., 1989). Isotopical labeling shifts the frequency at which the labeled group absorbs. Site directed exchange of an amino acid eliminates its corresponding absorption band but such substitution may change the structure of the protein. Isotopic labeling has the advantage of marking the molecular group noninvasively but it is not site-specific. Reviews of band assignments in bacteriorhodopsin difference spectra are discussed by Braiman and Rothschild (1988) and Kitagawa and Maeda (1989).

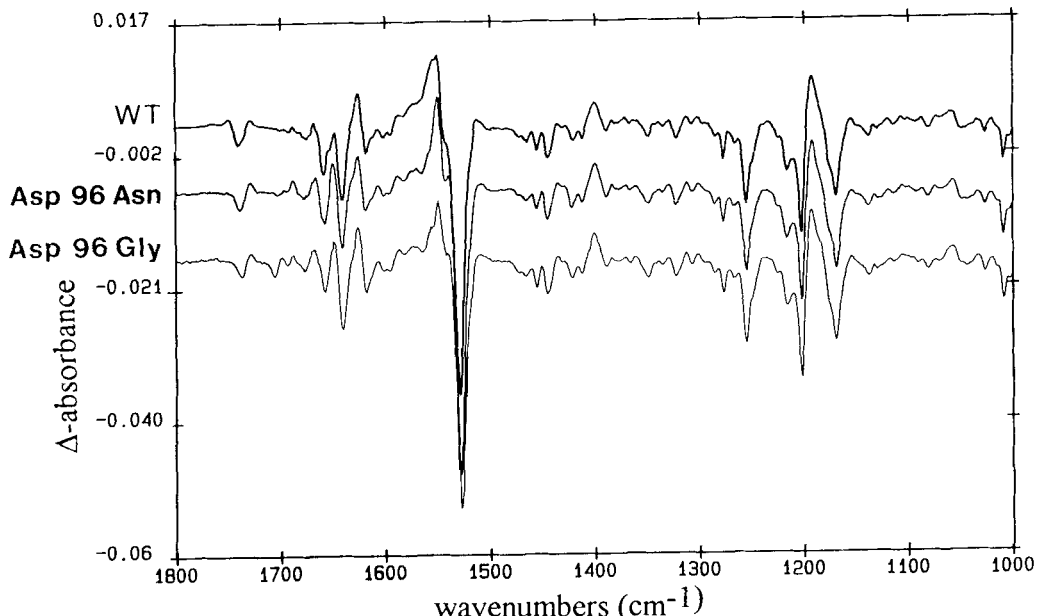


Figure 6.6-11 *BR-L* difference spectrum of a) Wild Type b) Asp 96 Asn and Asp 96 Gly mutant.

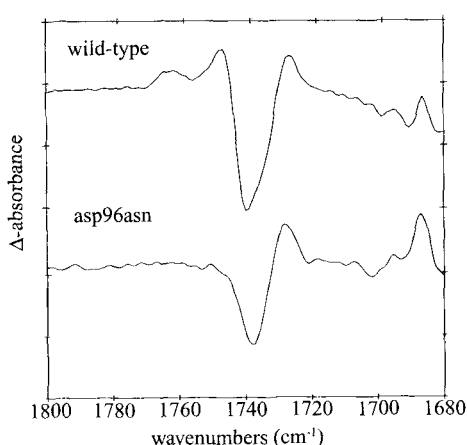


Figure 6.6-12 Expanded carbonyl region of Fig. 6.6-11 a) Wild Type b) Asp 96 Gly mutant.

Fig. 6.6-11 shows the *BR-L* difference spectra of the wild type and the Asp-96-Asn and Asp-96-Gly mutants (Gerwert et al., 1989). Absorption changes in the spectral range between 1500 cm^{-1} and 1000 cm^{-1} are highly reproducible. Carbonyl band shifts from 1742 cm^{-1} to 1748 cm^{-1} are absent in the spectrum of the mutant, as shown on an enlarged scale in Fig. 6.6-12. Thus, the missing difference band is caused by the 4-carbonyl vibration of exchanged Asp 96 (Gerwert et al., 1989).

6.6.3.5 An example of the stroboscope technique: the *L* to *M* transition

The *L* to *M* transition lends itself to modern $20\text{ }\mu\text{s}$ resolution stroboscopic investigation (Gerwert and Souvignier, 1993). Fig. 6.6-13 shows a 3-D plot of the difference spectra obtained by stroboscopic FTIR during the *L* to *M* to *N/O* to *BR* transitions. It shows the smoothed curve fits instead of the original data. Fig. 6.6-14 shows one of this series as example one difference spectrum recorded 70 microseconds after the laser flash, which represent primarily the “room temperature” *BR-L* difference spectrum (compare also Fig. 6.6-11).

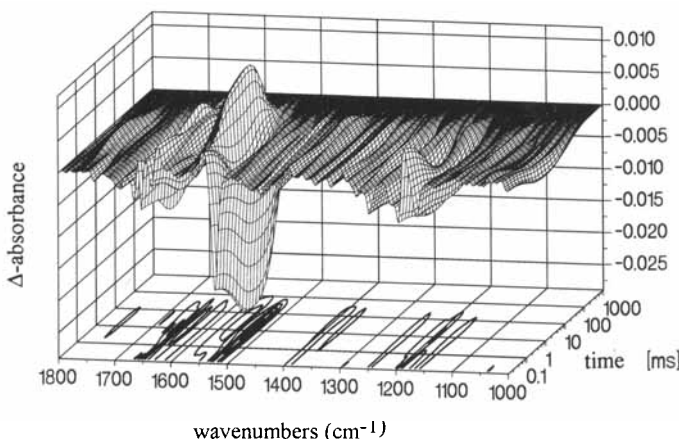


Figure 6.6-13 3-D Plot of IR absorbance changes between 1800 cm^{-1} and 1000 cm^{-1} .

Fig. 6.6-15a exhibits as example the absorbance change at 1186 cm^{-1} (from Fig. 6.6-13) on a logarithmic time scale. The changes in this band represent deprotonation of the Schiff's base during the conversion of *L* to *M* (disappearance) and its reprotonation and reisomerization (reappearance) during the conversion of *M* to *BR* via *N/O*. Fig. 6.6-15b shows the absorbance change at 1762 cm^{-1} , indicating transient protonation of Asp 85. Transient protonation of Asp 85 and deprotonation of the Schiff's base have the same rate constant (compare Figs. 6.6-15a and 6.6-15b). We conclude therefore that Asp 85 is the internal proton acceptor of the Schiff's base proton (Gerwert et al., 1989).

For the interpretation of time resolved data the adequate kinetic analysis plays a key role. A so-called global fit analysis affords the apparent rate constants of these

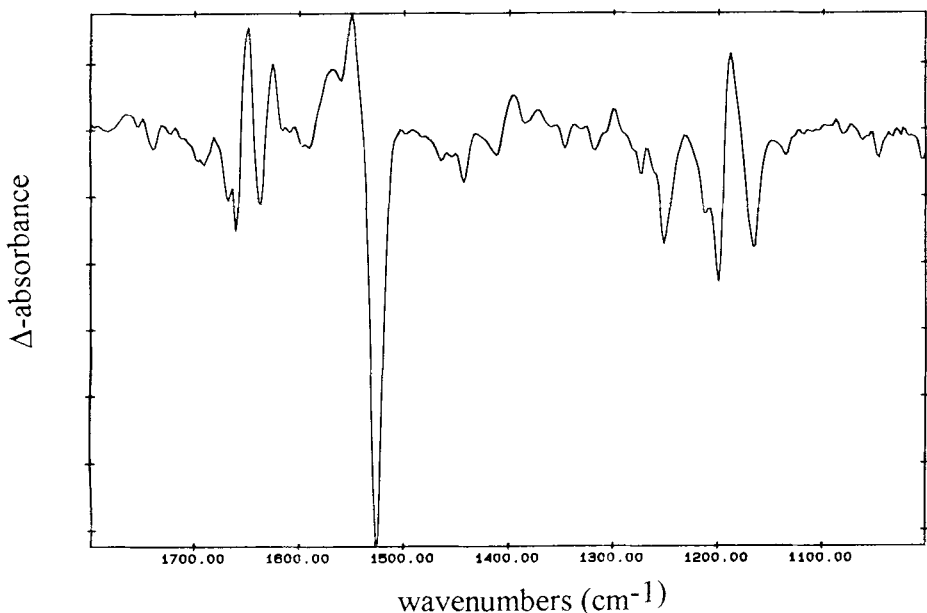


Figure 6.6-14 BR-L Difference spectrum (room temperature).

processes. This includes fitting not only the absorbance change at a specific wavenumber, but changes at up to 250 wavenumbers simultaneously (Souvignier and Gerwert, 1992). All reactions are assumed to be first-order and can therefore be described by a sum of exponentials. The fit procedure minimizes the difference between the measured data $\Delta A_{\text{measured}}$ and the theoretical description ΔA , weighted according to the noise w_{ij} at the respective wavenumbers, and summarized not only over the time (t) but also over the wavenumbers ($\tilde{\nu}$). In global fit analysis the absorbance changes ΔA in the visible and infrared are analyzed with sums of n_r exponentials with apparent rate constants k_l and amplitudes a_l .

$$\Delta A(\tilde{\nu}, t) = \sum_{l=1}^{n_r} a_l(\tilde{\nu}) e^{-k_l t} + a_o(\tilde{\nu}) \quad (6.6-5)$$

In this analysis, the weighted sum of squared differences f between the fit with n rate constants k_l and data points at n_w measured wavelengths $\tilde{\nu}_i$ and n_t time t_j is minimized:

$$f = \sum_{i=1}^{n_w} \sum_{j=1}^{n_t} (w_{ij})^2 (\Delta A_{\text{measured}}(\tilde{\nu}_i, t_j) - \sum_{l=1}^{n_r} a_l(\tilde{\nu}_i) e^{-k_l t_j} + a_o(\tilde{\nu}_i))^2 \quad (6.6-6)$$

Recently, a novel kinetic analysis, singular value decomposition, is performed allowing the assignment of intramolecular reactions independent of specific kinetic models to intermediates (Heßling et al., 1993)

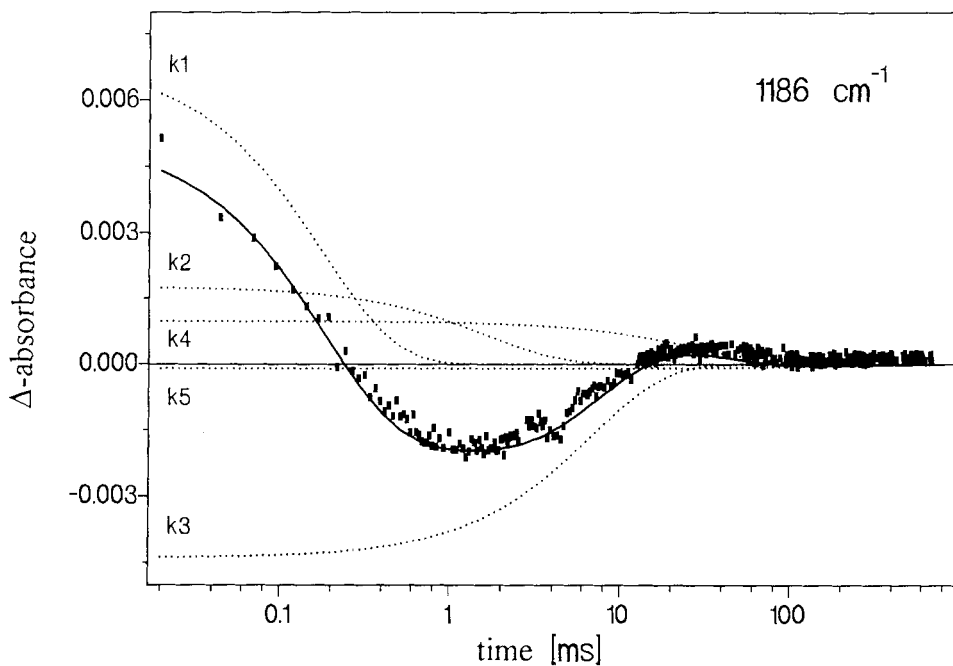


Figure 6.6-15a Absorbance change at 1186 cm^{-1} .

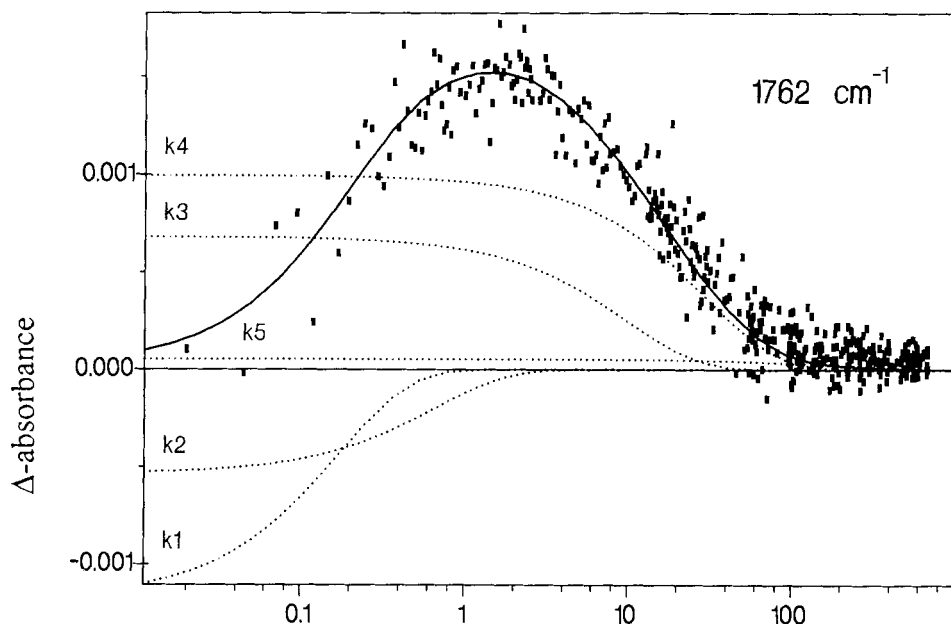


Figure 6.6-15b Absorbance change at 1762 cm^{-1} .

6.6.3.6 An example of the rapid scan method: the *M* to *BR* conversion

A time resolution of about 7 ms makes the rapid scan technique an ideal tool to monitor the *M* to *BR* backreaction. Fig. 6.6-16 exhibits a 3-D plot of the time evolution curve fits of the absorbance changes during the *M* to *BR* conversion. This represents the later part of Fig 6.6-13 measured with stroboscopic FTIR technique. The result of the time resolved FTIR measurements led to a detailed model of the proton-pump-mechanism and are summarized in Fig 6.6-17: after light induced $C_{13}=C_{14}$ double bond isomerization and twist around the $C_{14}-C_{15}$ single bond of retinal, the pK of the protonated Schiff base is reduced. In the *L* to *M* transition a proton is transferred from $C=NH^+$ to asp 85. Because a proton is released in the *L* to *M* transition another proton donor group has to be involved in the proton-release mechanism (AH^+). After relaxation around the light induced twist of the $C_{14}-C_{15}$ single bond and a structural change, of the peptide H-bonds, in the *M* to *N* transition, the Schiff base is reprotonated in the *M* to *N* transition from asp 96. Bound water molecules may be involved in the reprotonation pathway. Asp 96 is already reprotonated in the *N* to *O* transition.

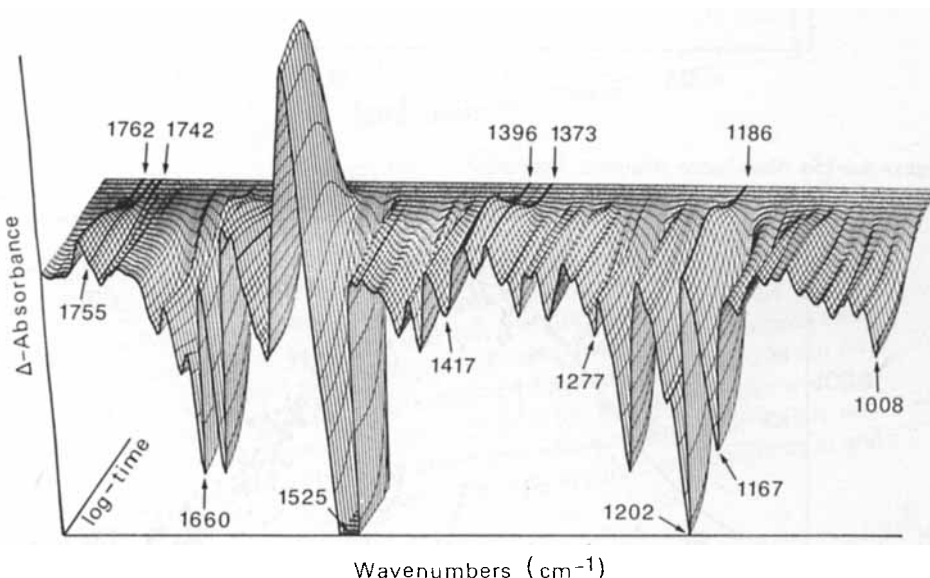


Figure 6.6-16 Absorbance change between 1800 cm^{-1} and 1000 cm^{-1} , measured by rapid scan technique.

Conclusion

As demonstrated, different time-resolved FTIR techniques allow to study the complete photocycle of bacteriorhodopsin in the entire range from picoseconds to several milliseconds. Infrared difference spectra trace reactions which take place in different parts of the protein molecule. Isotopically labeled proteins or proteins with mutations at specific sites

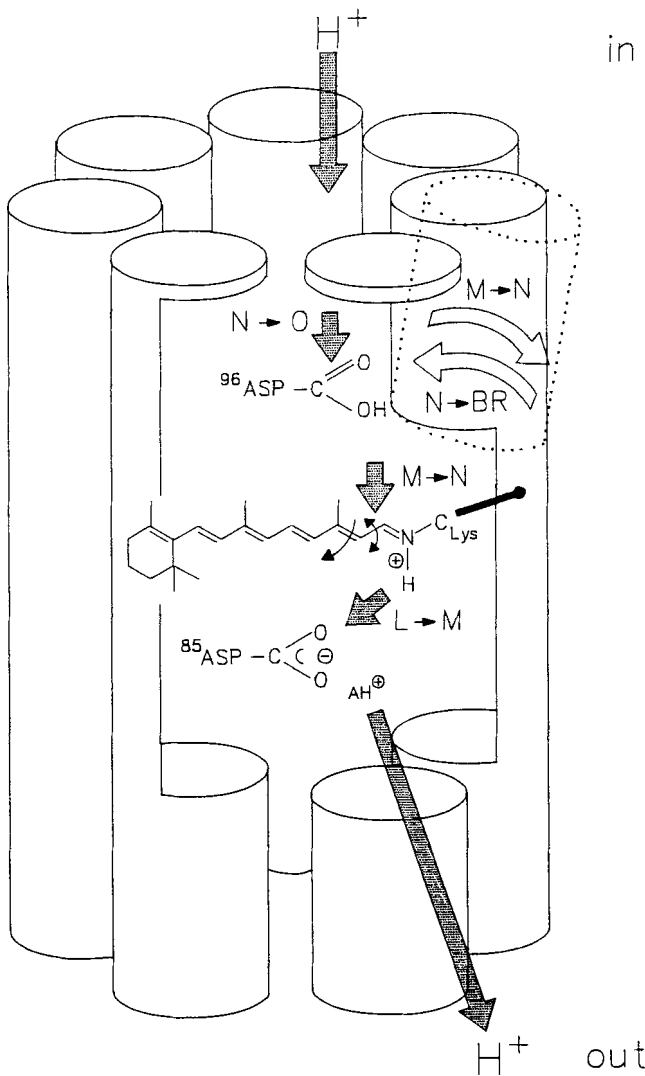


Figure 6.6-17 Model of proton pump mechanism of bacteriorhodopsin.

are used to assign the absorption bands in the difference spectra to specific molecular groups. As in the case of bacteriorhodopsin, a combination of physical and molecular-biology methods will contribute significantly to an understanding of the structure-function relationship in proteins at the atomic level.

6.6.4 Application to bacterial photosynthetic reaction centers

FTIR difference spectroscopy is not restricted to bacteriorhodopsin. Recent work has focused on different bacterial photosynthetic reaction centers with molecular weights of about 100 000 Daltons (for a review, see Deisenhofer and Michel, 1989). Absorption changes during the electron transfer steps, starting at the primary donor P (Bchl) and proceeding via the intermediate acceptor I (bacteriopheophytin BPh) and the quinone Q_A and ending at the quinone Q_B are characterised by FTIR spectroscopy (see Fig. 6.6-18) (Buchanan et al., 1992). The role of the protein environment in electron transfer can thus be determined. As an example, Fig. 6.6-19 shows the P⁺Q_B – PQ_B difference spectra of *Rps. viridis*.

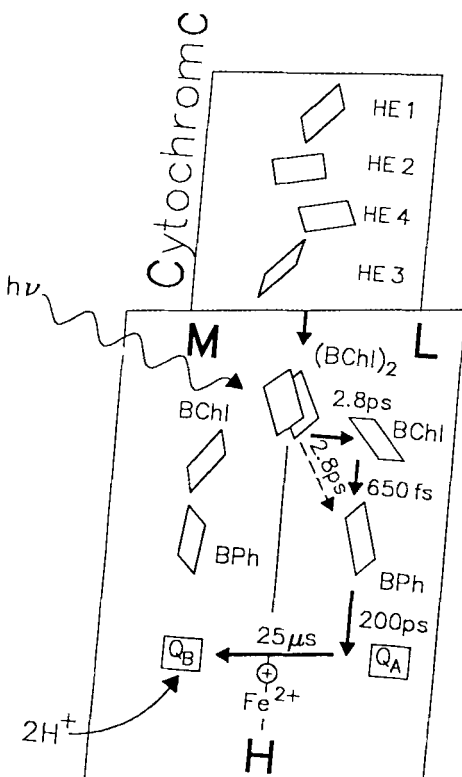


Figure 6.6-18 Scheme of the photosynthetic reaction center structure.

The difference spectra of the different charge separated states are dominated by the absorption changes of the chromophores and the quinones (Buchanan et al., 1992). Band shifts from 1743 cm^{-1} to 1755 cm^{-1} and from 1672 cm^{-1} to 1712 cm^{-1} are characteristic of the oxidation of bacteriochlorophyll b in an aprotic environment. They correspond to the absorbance changes of the 10-c-ester- and 9-keto-carbonyl groups of the primary

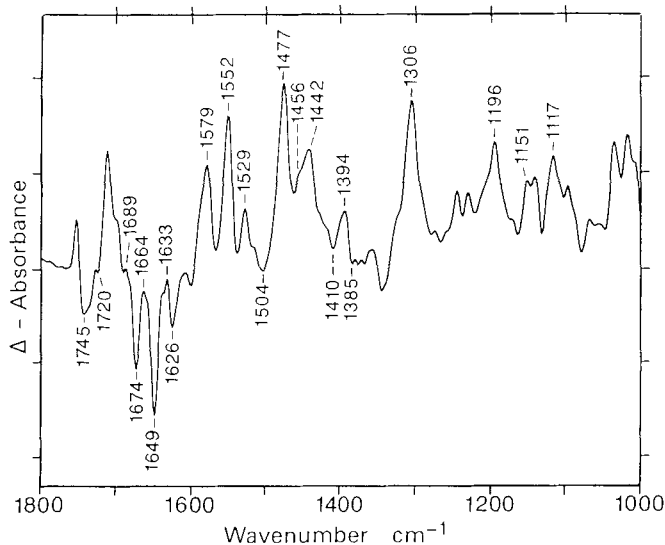


Figure 6.6-19 Difference spektrum of $P^+Q_B - PQ_B$.

donor (Gerwert et al., 1989). The bands at 1477 cm^{-1} , 1440 cm^{-1} , and 1394 cm^{-1} represent semiquinone carbonyl vibrations in a protic environment (Buchanan et al., 1992).

Conclusion and perspektives

The described studies of bacterial reaction centers indicate that FTIR it is a powerful analytical method, even useful for large proteins over 100 000 Dalton.

Recent research focus now on applying FTIR methods to proteins without an intrinsic chromophore. In investigating oncogenic hras p21, for instance, protein activity is stimulated with a photolabile substance such as “caged GTP” (Fig 6.6-21). A UV laser flash, which separates the head group and releases GTP, triggers the GTPase activity of p21. This new experimental approach offers now a very broad applicability to study chemical reactions by time-resolved FTIR.

6.6.5 FT-Raman spectroscopy

Near-infrared excited FT-Raman spectroscopy has recently begun to show promise (Schrader, 1990), because the fluorescence is drastically reduced. It has the Jaquinot advantage over classical Raman spectroscopy, which affords a better signal-to-noise ratio. FT-Raman is an excellent technique to supplement FTIR difference spectroscopy in investigations of intramolecular protein reactions because Raman spectra have the

advantage that they are not affected by water; they may therefore be employed to study protein solutions or suspensions.

It was used to investigate bacteriorhodopsin as well as the activity of bacterial reaction centers. As example a *BR-K*-FT-Raman difference spectrum is given. A procedure similar to FTIR is employed to monitor the *BR* to *K* transition by FT-Raman spectroscopy. In the dark, the sample is cooled to 77 K. The resulting FT-Raman spectra agree very well with the corresponding RR spectra (Fig. 6.6-20). This indicates that a preresonant Raman state is excited and only the retinal vibrations of the chromophore protein complex are detected. After subtracting the spectrum of *BR*, a *BR-K* difference spectrum (Fig. 6.6-22) is obtained. The chromophore vibrations between 1300 cm⁻¹ and 1100 cm⁻¹ in this spectrum agree nicely with those in the FTIR *BR-K* difference spectrum (compare with Fig. 6.6-10). The 1640/1650 cm⁻¹ and 1550/1540 cm⁻¹ difference bands do not appear in the FT-Raman difference spectrum, which points to the fact that these bands are caused by protein backbone vibrations. The spectrum of bacteriorhodopsin only shows chromophore vibrations of the protein. In contrast, rhodopsin also seems to exhibit protein vibrations (Sawatzki et al., 1990).

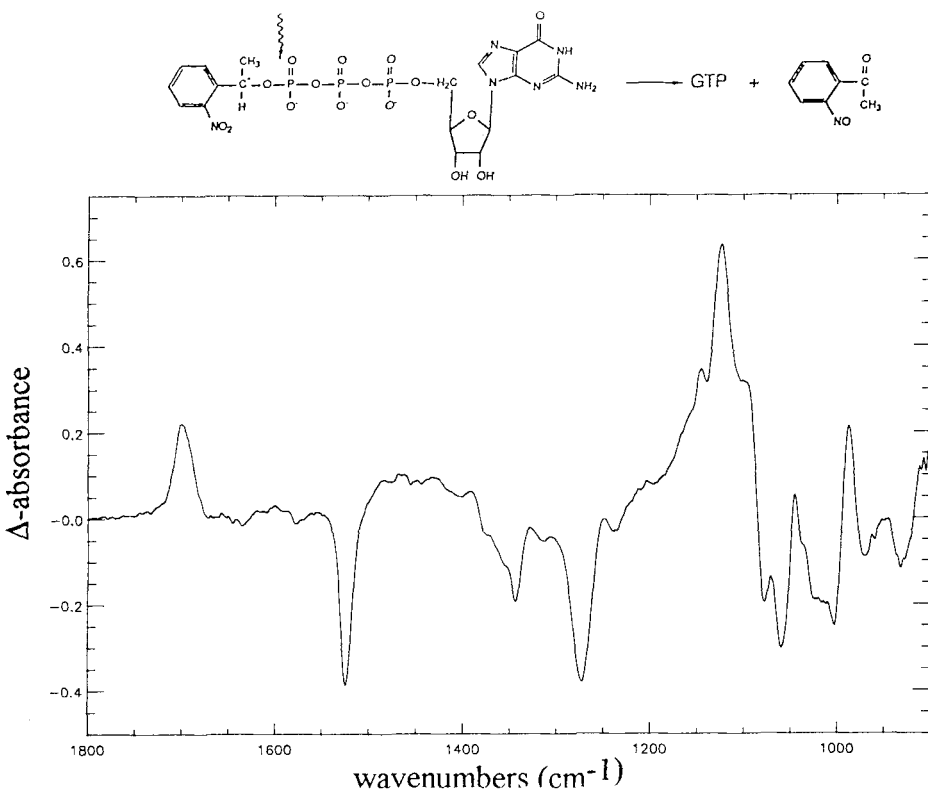


Figure 6.6-20 FTIR-difference spectra of caged GTP-photolysis.

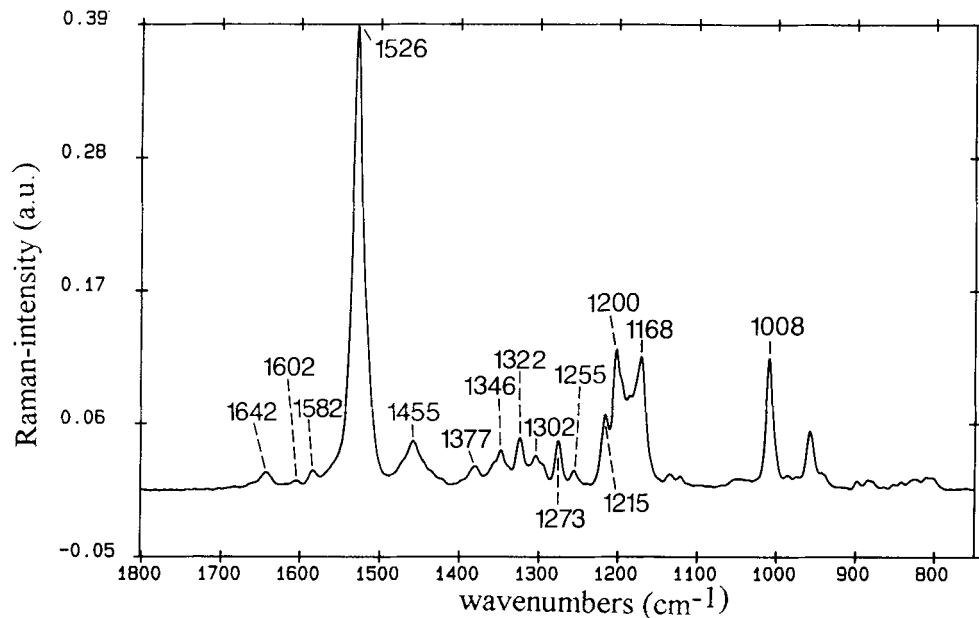


Figure 6.6-21 FT-Raman spectrum of a *BR-K* mixture.

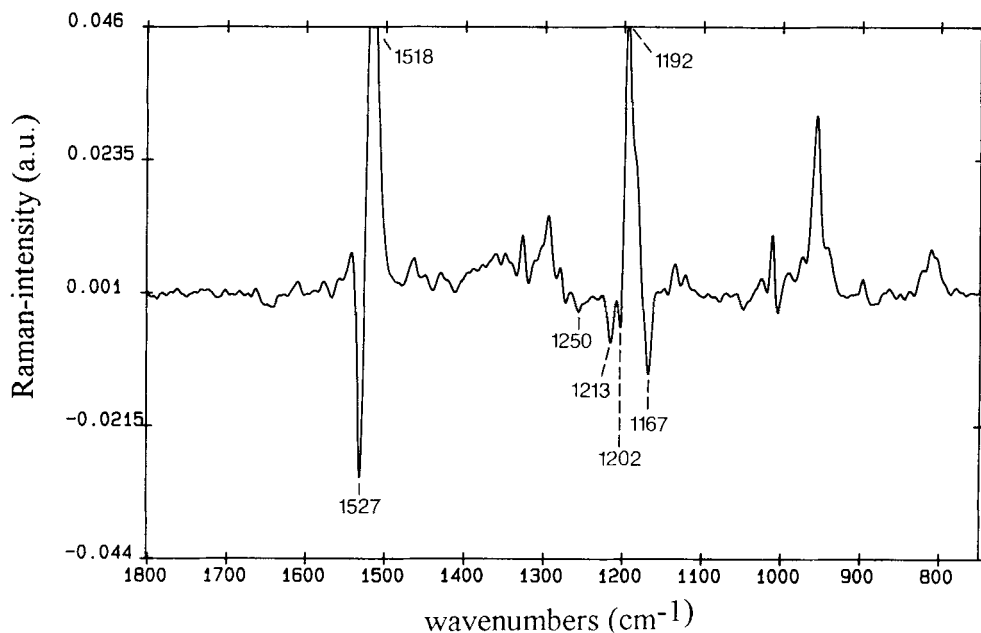


Figure 6.6-22 FT-Raman *BR-K* difference spectrum.

Conclusion

FT techniques have greatly broadened the scope of both IR and Raman spectroscopy. In the near future, these methods are expected to provide a considerable stimulant to studies of time dependent phenomena in complex systems. The stroboscope and step-scan technique are probably also useful for FT-Raman. This would be very convenient, since it is relatively easy to back up an FTIR instrument with an FT-Raman module.

6.7 Application of high-pressure techniques*

6.7.1 Introduction

Modern high-pressure research encompasses a plethora of fields and has extended applications in physics, chemistry, the geosciences, planetary science, biochemistry, biology, material science, and in engineering, including chemical engineering. The term “high pressure” in this context refers to pressures of at least a few hundred bars and mostly in excess of one kbar (0.1 GPa).

Infrared and Raman studies at very high pressure (up to several hundred kbar) are carried out fairly routinely with diamond anvil cells (DAC). The DAC, which was first developed for high-pressure infrared absorption measurements by Weir et al. (1959) and for X-ray studies by Jamieson et al. (1959), has become a very powerful tool for a wide variety of ultra-high pressure investigations, with particularly important applications in solid state physics. The potential of the method has increased enormously with the introduction of gaskets into the DAC by Van Valkenburg (see Jayaraman, 1983) and with the possibility of pressure calibration by the ruby fluorescence method (Forman et al., 1972).

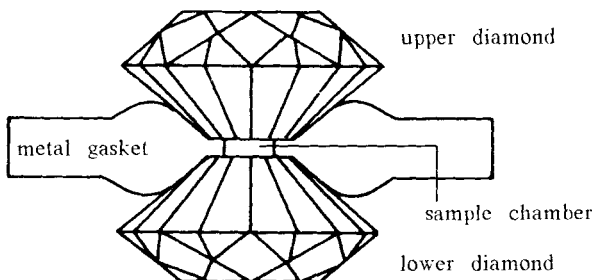


Figure 6.7-1 Diamond anvil cell - basic components.

* Section 6.7 is contributed by M. Buback, Göttingen

The basic principle of a DAC is illustrated in Fig. 6.7-1. The sample chamber is formed by the flat parallel faces of two opposed anvils and the hole in a metal gasket. The flat octagonal surface of the diamond anvils can have an area of approximately 0.2 mm^2 . The sample chamber also contains a pressure transmitting medium to provide hydrostatic conditions and a small ruby chip of the size of a few μm for pressure measurement. The thrust for compressing the anvils may be generated by a thread-and-knee mechanism (Huber et al., 1977), but several other techniques have also been developed. Together with many examples of high-pressure physical investigations, these methods are described in a comprehensive review by Jayaraman (1983). Applications of diamond anvil IR techniques in medical science have been presented by Wong et al. (1993). The authors report that normal connective tissue may be unambiguously differentiated from malignant tissue by pressure-tuning FT-IR spectroscopy. Further information about diamond anvil cells is found in the book by Sherman and Stadtmuller (1987) and in the literature cited in it. Optical studies of solids at high pressure are also performed in several types of piston-cylinder apparatus and also in non-cylindrical optical cells, which have also been described by Sherman and Stadtmuller (1987).

For chemical applications, vibrational spectroscopy of high-pressure fluid phases, including liquids and compressed gases, is of special importance (Buback, 1991). The fluid, i.e., the non-solid region of a substance, is illustrated in Fig. 6.7-2. The packing density of the circles is approximately proportional to the density of a substance. The bottom left part of Fig. 6.7-2 shows the vapor pressure curve which, up to the critical point, separates the liquid phase from the gas phase. Above the critical temperature (T_c), the density of a substance may change continuously between gaseous and liquid like states; vibrational spectroscopic methods make it possible to study the structure and dynamics

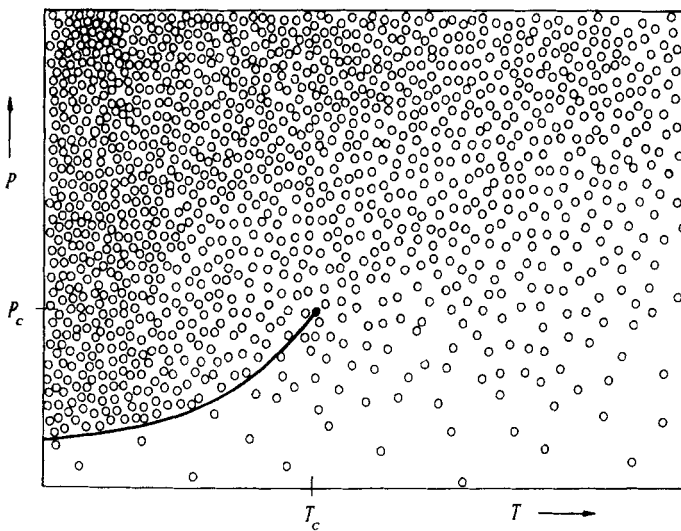


Figure 6.7-2 Pressure-temperature diagram representing the density of a simple substance; (P_c) critical pressure, (T_c) critical temperature.

of the fluid state over a wide range of densities (see also Sec. 6.2.2). Along with the density, several other physical properties, such as the viscosity, the dielectric constant, and the heat transfer coefficients vary considerably with the pressure and the temperature. Thus, phase equilibria and chemical equilibria may be considerably affected, and it is possible to carry out chemical reactions by exploiting the special properties of dense fluid phases.

High pressure is used extensively in chemical transformations because of its preparative and diagnostic value (Asano and le Noble, 1978; van Eldik et al., 1989). Research on high-pressure fluid phase kinetics is directed both toward the detailed study of existing technical processes and toward the development of novel processes in which the application of high pressure, for instance, induces or improves the selectivity.

Infrared, near-infrared (see Sec. 6.2), and Raman high-pressure techniques are very suitable tools for the characterization of fluid states and especially for the quantitative analysis of fluids. Sec. 6.7.2 shows a few cells which are used for the vibrational spectroscopy of fluids at pressures up to a maximum of 7 kbar and at temperatures up to 650 °C, although the maximum conditions of both pressure and temperature are not simultaneously applied (see also Buback, 1991). Sec. 6.7.3 describes changes in the vibrational spectra of polar substances and of aqueous solutions, and Sec. 6.7.4 presents a few applications of high-pressure spectroscopy in the investigation of chemical transformations.

6.7.2 Optical cells for vibrational spectroscopy of fluids at high pressures and temperatures

Even if the focus is exclusively on optical cells, it is impossible to review the large number of published experimental arrangements in a chapter of limited size. Since the field has already been treated by Sherman and Stadtmuller (1987), this text is only concerned with optical cells for vibrational spectroscopic studies (IR, NIR, Raman) of fluid phases under conditions involving high pressure and high temperature up to a maximum of about 650 °C and 7 kbar. This is the area of the authors greatest personal experience (Buback, 1981; Buback et al., 1987).

Cells for fluid phase spectroscopy require windows which can withstand high pressure and high temperature and can be used over as wide a spectral range as possible. For IR and NIR studies, the window material must necessarily be transparent in the wavenumber range which is being investigated; whereas vibrational modes in Raman experiments are recorded as wavenumber differences with respect to the laser line, which is usually in the visible region (and partly in the NIR). Raman spectra may thus be obtained in cells equipped with the same type of windows as those which are used for absorption spectroscopy in the visible (and NIR) range. This is mostly sapphire or quartz. For IR experiments in an extended range of wavenumbers, different types of window materials must be used, depending on the wavelength. This creates special problems for high-pressure studies, because only a very limited number of window materials is available.

For measurements in the range from 2000 to 50 000 cm⁻¹ at pressures up to 10 kbar, sapphire is unrivalled as a high-pressure, high-temperature window material, especially since it is also very resistant to chemical attack. In the wavenumber region below 2000 cm⁻¹, windows made of polycrystalline silicon (down to 1450 cm⁻¹) and of CaF₂ single crystals (down to 1000 cm⁻¹) can be used. With these materials, the maximum working pressure must be reduced to 3 kbar and 2 kbar, respectively. At still lower wavenumbers, windows made of diamond (type IIa), and in some cases those made of quartz and silicon may be used. Further information about high-pressure window materials is given by Ferraro and Basile (1974) and by Sherman and Stadtmuller (1987).

The optical windows are easily sealed by applying Poulter's principle (Poulter, 1932) which is a modification of Bridgman's unsupported area principle. A detailed view of this window seal is given in Fig. 6.7-3. The window (3) rests on the optically flat polished surface of a steel plug (5) with a cylindrical bore. In order to compensate for surface imperfections, a sealing ring (4) of approximately 10 µm thick gold foil is placed between window and plug. In experiments below 200 °C, spacers made of poly(tetrafluoroethylene) of about the same thickness can be used. The pressure at the seating face exceeds the internal high pressure by a factor of $d_1^2/(d_1^2 - d_2^2)$, which is the ratio of the total surface area (d_1 : window diameter) to the unsupported surface area (d_2 : diameter of the bore in the steel plug). The high-pressure window is held under compression by a steel cap (2) which ensures effective sealing even at lower pressures. Sealing problems may arise in high temperature - moderate pressure investigations, due to the difference in the thermal expansion of steel and sapphire. Caps made of stainless steel perform satisfactorily up to 400 °C. Above this temperature, special care should be taken to use materials for the cap whose thermal expansion coefficient matches that of the window material. For use with sapphire windows, niobium is a suitable cap material to ensure that sufficient compressional stress is maintained on the window, even at high temperature and low pressure.

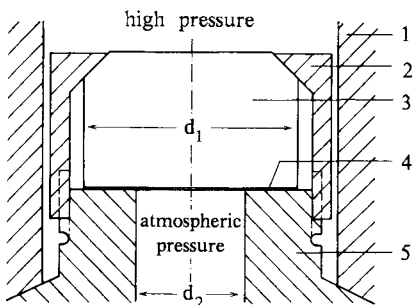


Figure 6.7-3 Sealing of high-pressure optical windows according to Poulter (1932); 1 cylindrical wall of the autoclave, 2 cap, 3 window, 4 sealing ring, positioned on the polished surface of a steel plug, 5 stainless steel plug.

Fig. 6.7-4 shows an optical cell for absorption studies up to 3500 bar and 300 °C. The two windows (1) are sealed according to the principle illustrated in Fig. 6.7-3. The steel plugs (5) are pressed against the body of the stainless steel cell by a flange (3) which is secured by several screws (2) on each side. The optical path length is determined by the distance between the internal surfaces of the high-pressure windows. Holes are drilled

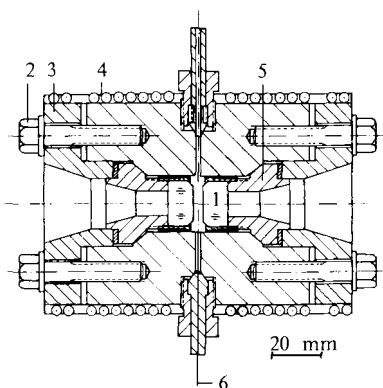


Figure 6.7-4 Optical high-pressure cell; 1 window, 2 screw, 3 flange, 4 heating, 5 stainless steel plug, 6 sheathed thermocouple.

into the cell body perpendicularly to the axis of the cylindrical cell in order to allow the sample to be introduced and one or more sheathed thermocouples (6) to be inserted. The cell is heated from the outside with a resistance heater (4), which is mounted on a brass support. By increasing the ratio of outer to inner cell diameter, autoclaves of the type shown in Fig. 6.7-4 have been used up to 7 kbar (see also Fig. 6.7-8).

In studying chemical transformations, the internal walls of the high-pressure cell, which are made of stainless steel containing significant amounts of nickel, cobalt, molybdenum, and other constituents with potentially catalytic activity, may substantially influence the course of a reaction. This problem can be avoided by using a procedure which was introduced by le Noble and Schlott (1976), in which the investigated system is contained in an inner cell made of quartz and equipped with a movable piston, which closely fits into the cylindrical bore of the quartz cell. A recently introduced alternative method of high-pressure IR investigation of fluids (Tost, 1988; Buback et al., 1988) uses a poly(tetrafluoroethylene) (PTFE) container, into which the reaction mixture is sealed by welding. This PTFE cell has a wall thickness of about 0.1 mm; the analyzing IR beam penetrates the cell, which is fitted into the autoclave, in such a way that it is in direct contact with the inner faces of the two high-pressure windows.

Since the investigated fluid is usually unable to also act as a pressurizing medium, the internal volume of the high-pressure cell is separated from the fluid in the pressure generating system by a steel bellows, as shown in Fig. 6.7-5. The bellows (7) shuts off potentially corrosive reaction systems from sensitive parts of the pressurizing system, e.g., gauges and pressure generators, and it also prevents solid species in the reaction mixture from precipitating in the colder parts of the apparatus, e.g., in the capillary tubes. The position of the bellows is monitored from the outside by means of an inductive detector (3) (Buback and Lendle, 1981a).

Special problems arise in quantitative IR spectroscopic investigations of pure fluids at high pressure. In this case, the optical path length should usually be as short as several μm . These distances are of about the same size as the changes of path length induced by applying pressure and temperature in cells of the type shown in Figures 6.7-4 and 6.7-5. Moreover, it is extremely difficult to join the parts of such a cell in a way which affords a

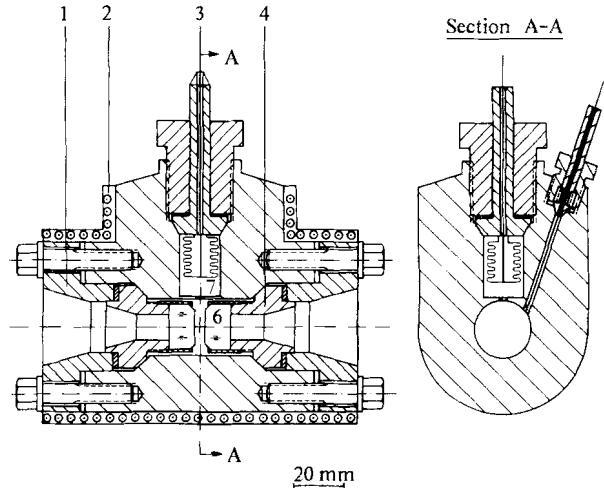


Figure 6.7-5 Optical high-pressure cell with a bellows; 1 flange, 2 heating, 3 to inductive detector, 4 stainless steel plug, 5 sheathed thermocouple, 6 window, 7 bellows.

path length of less than 0.1 mm. These difficulties may be overcome by using the device shown in Fig. 6.7-6, which makes it possible to change the optical path length from the outside while the cell is under pressure (Buback, 1977; Bohn and Franck, 1988).

One of the windows (1) is sealed to a fixed steel plug (5). The second window (2) is attached to a movable piston (12), which is sealed to a packing (7) by means of a screw (10). The screw (11), between (10) and the piston (12), has different threads on the inner and the outer diameter. In the special cell shown in Fig. 6.7-6, which may be operated up to 2.5 kbar and 200 °C, the pitch of the screws is 1.50 mm and 1.25 mm. Due to this difference, the turning screw (11), while (10) and (12) are mounted in counter-rotatory direction (by auxiliary equipment not shown in Fig. 6.7-6), moves

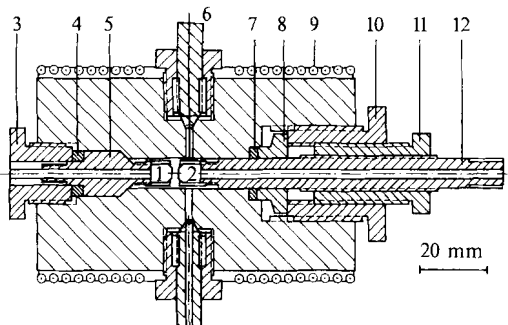


Figure 6.7-6 High-pressure cell with variable optical path length; 1 and 2 window, 3 screw, 4 stainless steel ring, 5 stainless steel plug, 6 sheathed thermocouple, 7 packing, 8 stainless steel ring, 9 heating, 10 and 11 screw, 12 movable piston.

the piston (12) in the direction of the optical cylindrical axis. In this case, a full turn of the screw (11) corresponds to a displacement of (12) by 250 µm (1.50 mm - 1.25 mm). Absorbance spectra are obtained by the following procedure: The optical path length, which initially, after all parts have been fitted, is rather large, is reduced by turning the screw (11), until an absorption spectrum is recorded in which the absorbance in the interesting wavenumber range does not or not significantly exceed $A = 1$. The optical path length is then decreased further by turning (11) by a precisely measured angle, which corresponds to the accurately known optical path length difference Δl . A second spectrum is then recorded in the new position. If the concentration is known, the molar absorption coefficient is directly obtained via the precisely measured optical path length $l = \Delta l$ by using the first spectrum as a sample and the second one as a reference spectrum (Eq. 6.2-1). There is an additional advantage to this technique, which measures test sample and reference sample at identical pressure and temperature: the absence of uncertainties, due to a bending of the high-pressure windows and due to the difference between the refractive indices of test sample and reference sample (Buback, 1981).

The difficulty of obtaining precise IR measurements at short optical path lengths, e.g., below 0.5 mm, may also be overcome by using high-pressure cells with a single optical window. The cell in Fig. 6.7-7 was designed by Franck and Roth (1967). A metal spring (7) presses an optically flat stainless steel (or Pt-Ir) mirror (6) against the optical window (4), from which it is separated by a spacer made of gold foil (5), which determines the optical path length. Actually, several pieces of gold foil are used as a spacer in order

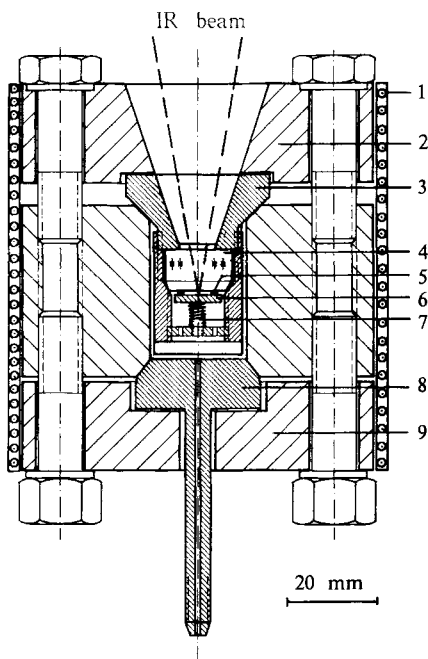


Figure 6.7-7 Optical high-pressure cell; 1 heating, 2 flange, 3 stainless steel plug, 4 window, 5 spacer made of gold foil, 6 mirror, 7 metal spring, 8 stainless steel plug with capillary boring for the introduction of the sample fluid, 9 flange.

to provide free access of the fluid to the sample space between window and mirror. The IR beam, which should be diverted from the normal spectrometer direction by a micro reflectance accessory so as to focus on the mirror surface, passes through the sample layer twice; namely, before and after being reflected at the mirror. The mirror is surrounded by the fluid on all sides. The optical path length is thus independent of the pressure, if one neglects a certain bending of the sapphire window. Cells of the type shown in Fig. 6.7-7 have been used by Franck and Roth (1967) up to 5 kbar and 500 °C.

Following the same principles as those which govern the designing of cells for absorption experiments, Raman cells for high-pressure, high-temperature studies have also been constructed by Lindner and Franck (see Tödheide, 1972). A Raman cell for use up to 7 kbar and 250 °C (Eckel et al., 1981) is shown in Fig. 6.7-8.

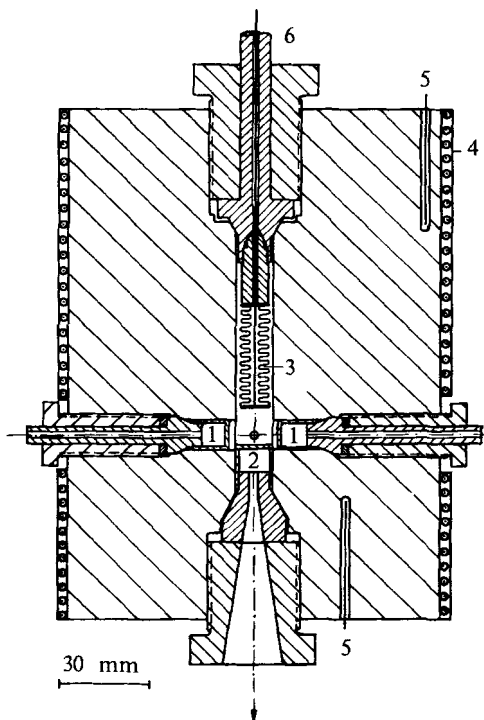


Figure 6.7-8 High-pressure Raman cell; 1 window for the passage of the laser beam, 2 window for the detection of Raman scattered light, 3 bellows, 4 heating, 5 thermocouple, 6 to inductive detector.

Two smaller sapphire windows (1) for the passage of the laser beam are sealed onto conical steel plugs, which are fitted into opposite cross-bores in the cylindrical stainless steel autoclave. The Raman-scattered light is observed through a larger sapphire window (2) at a right angle to the laser beam. The sample is separated from the pressurizing system by means of a steel bellows (3) in the bore through the cylindrical axis of the high-pressure vessel. Additional capillary cross-bores at a right angle to the cylindrical axis make it possible to charge the cell and to introduce sheathed thermocouples into

the investigated fluid. The temperature is also controlled via thermocouples (5), which are fitted into the cell body.

It goes without saying that by combining the principles sketched in Figures 6.7-8, a wide variety of cells for the optical investigation of fluids at high pressure and high temperature may be constructed. Such cells have primarily been developed by the Franck group at the University of Karlsruhe (see Buback, 1981). Cells of this type, together with many other arrangements for the optical investigation of fluids, have been reviewed by Sherman and Stadtmuller (1987).

6.7.3 Vibrational spectra of polar fluids

High-pressure, high-temperature optical cells may be used to study the differences between the vibrational spectra of low and high density states. Thus, the spectrum of the gaseous state, which is generally well characterized, changes into that of a liquidlike state through a sequence of spectra measured at supercritical temperature and increasing pressure. These data can provide information about the structure and dynamics of fluids. As shown in Sec. 6.2.2, the near-infrared spectroscopic properties of dense fluids are either rather similar to the corresponding gas phase values or are closely related to these data. In the infrared region, the spectroscopic properties of gaseous and liquid phases can be quite different. Particularly pronounced changes are observed in the A–H stretching modes of pure polar materials (A = oxygen, nitrogen, halogen).

Fig. 6.7-9 shows the molar absorption coefficient ϵ of the O–D stretching fundamental of HDO (5 mol % HDO in H_2O with a minor D_2O concentration) at $400\text{ }^\circ\text{C}$ at densities ρ between 0.01 g cm^{-3} and 0.9 g cm^{-3} (Franck and Roth, 1967). The experimental

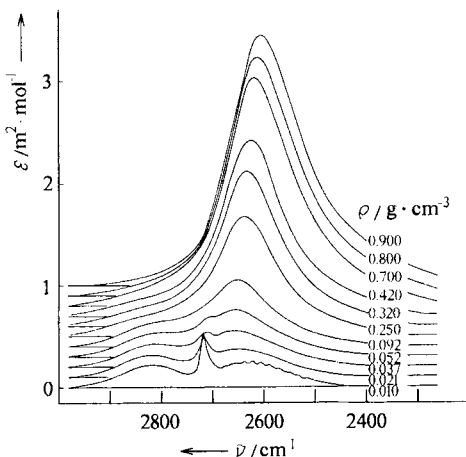


Figure 6.7-9 Molar absorption coefficient ϵ of the O–D stretching mode of HDO at $400\text{ }^\circ\text{C}$ and at various densities ρ .

temperature is slightly above the critical point ($T_c = 374^\circ\text{C}$). The highest density in Fig. 6.7-9 corresponds to a pressure of 3900 bar. Working with HDO/H₂O mixtures rather than with pure H₂O has the advantage of facilitating the interpretation of the spectra. The band contour is gradually transformed from a *P*, *Q*, and *R* type absorption band at the lowest densities (Fig. 6.7-9) into a single broad band without any shoulders at high density. The integrated molar absorption coefficient (vibrational intensity) *B* (see Eq. 6.2-3) is considerably enhanced as the density increases (note, however, that the base lines are slightly shifted), and the wavenumber at maximum absorbance, $\tilde{\nu}_{max}$, is lowered by about 120 cm⁻¹ in going from the gaseous to the liquidlike state.

Considerable changes of *B* and $\tilde{\nu}_{max}$ are also observed (Fig. 6.7-10) in the vibrational fundamental of pure hydrogen chloride, measured at various densities ϱ and at 100 °C, which is above the critical temperature ($T_c = 51^\circ\text{C}$). At the lowest density, the familiar spectrum with *P* and *R*-branches is obtained. The rotational structure is lost with increasing density, and at the highest density there is a single, nearly symmetrical band.

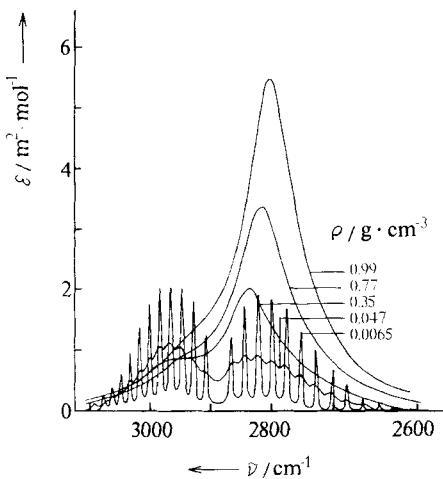


Figure 6.7-10 Molar absorption coefficient ϵ of pure hydrogen chloride at 100 °C and at various densities ϱ .

The influence of the density on the vibrational absorption of HDO (Fig. 6.2-9) and of HCl (Fig. 6.2-10) is qualitatively rather similar. Hydrogen bonds, which are known to considerably influence the absorption of the stretching fundamentals, should play a major role in water; whereas specific interactions of this type are not expected to be dominant in fluid hydrogen chloride. The two substances are compared in Fig. 6.7-11, which shows a $\Delta\tilde{\nu}$ versus ϱ/ϱ_c diagram. $\Delta\tilde{\nu} = \tilde{\nu}_{gas} - \tilde{\nu}_{max}$ is the shift of the wavenumber at the absorption maximum relative to its position in the gas phase spectrum; and ϱ/ϱ_c is the density, reduced by the corresponding critical density. The band maximum position in the spectra of both substances clearly depends on the density at a given constant temperature. At constant density, the band maximum position in the spectrum of HCl is only slightly temperature dependent, whereas in the case of HDO the band shifts considerably with the temperature. However, above 400 °C the O-D stretching mode shows a tendency similar to that of the HCl mode. The behavior of HCl (Fig. 6.7-11) can be regarded as being

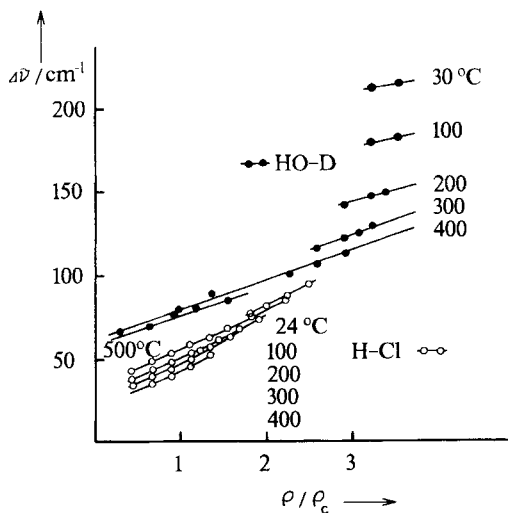


Figure 6.7-11 Wavenumber shift $\Delta\tilde{\nu} = \tilde{\nu}_{gas} - \tilde{\nu}_{max}$ of the O-D mode of HDO and of the H-Cl vibration as a function of the reduced density ρ/ρ_c at various temperatures.

typical of a dipolar liquid; whereas the strong temperature dependence shown by the O-D mode in HDO below 400 °C is an indication of significant hydrogen bonding (Buback and Franck, 1971). According to this criterion, water at supercritical temperature, even in a highly condensed phase, behaves like a normal dipolar fluid.

The position of the O-D band maximum has also been used to indicate the structure of fluid electrolyte solutions. Fig. 6.7-12 shows the wavenumber of the O-D band maximum, $\tilde{\nu}_{max}$, in aqueous (HDO/H₂O) lithium chloride solutions at 2800 bar and various temperatures as a function of the LiCl content x (in mol %) (Valyashko et al., 1980). The 25 °C isotherm is measured at 20 bar. If x is small, $\tilde{\nu}_{max}$ is considerably dependent

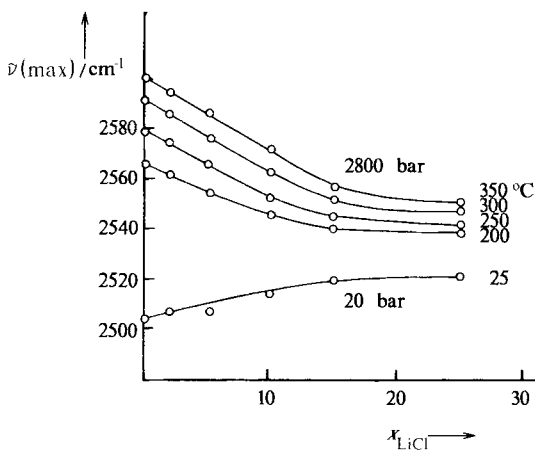


Figure 6.7-12 Concentration dependence of the O-D band maximum position, $\tilde{\nu}_{max}$, in aqueous (HDO/H₂O) LiCl solution; x_{LiCl} : concentration of lithium chloride in mol %.

on both the temperature and the salt concentration. This behavior is characteristic of a water-like medium with hydrogen bonds. If lower values of $\tilde{\nu}_{max}$ are equivalent to a high degree of hydrogen bonding, then the data shown in Fig. 6.7-12 indicate that at 25 °C and at a low salt concentration, addition of LiCl destroys the structure. At temperatures of 200 °C and higher, however, pure water has much less of a structure and added LiCl enhances what structure there is. At more than 15 mol % LiCl, the concentration dependence of $\tilde{\nu}_{max}$ almost disappears, and the temperature dependence becomes small. Regions showing this type of behavior are referred to as “melt-like” (Valyashko, 1977). IR experiments have also been performed on aqueous (HDO/H_2O) sodium perchlorate solutions up to high pressures and temperatures. The resulting spectra clearly show that there is no continuous distribution of the states of the water molecules. Moreover, a close similarity between the band contours of the O-D infrared spectra of aqueous perchlorate solutions and the O-D Raman spectra of water and of aqueous salt solutions is observed (Valyashko et al., 1981).

Raman experiments are particularly useful for the study of fluid aqueous electrolyte solutions because of the relative ease with which spectra may be obtained at low wavenumbers (see Sec. 6.7-1). Apart from intramolecular hydrogen-oxygen stretching modes, intermolecular modes may therefore also be investigated. Moreover, low-lying intramolecular vibrations of complex species dissolved in the aqueous phase can be studied. Schulz (1974) measured the Raman scattering of aqueous $ZnCl_2$ solutions (0.1 to 13 molar) in the Zn–Cl stretching region around 300 cm^{-1} up to pressures of 4 kbar and 500 °C. Fig. 6.7-13 shows the molar integrated Raman scattering intensity (MIRSI) of the Zn–Cl stretching mode in the dense fluid system (in arbitrary units) as a function of temperature. The $ZnCl_2$ concentrations are between 0.5 and 13 mol L⁻¹. At the highest concentration, the

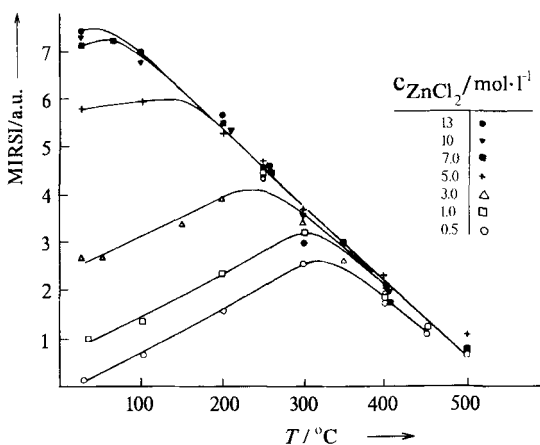


Figure 6.7-13 Molar integrated Raman scattering intensity (MIRSI) in the Zn–Cl stretching region of zinc chloride solutions with a very different salt content in the compressed fluid state as a function of the temperature.

scattering intensity steadily decreases as the temperature increases from the ambient level up to 500 °C; whereas at low and moderate concentrations, the molar scattering intensity goes through a maximum. The pronounced effect is a result of the dependence of the Raman intensity on the character of the investigated bond. In purely ionic systems Raman scattering is negligible. The decrease of the scattering intensity with temperature which is pronounced at high salt concentrations has been attributed to the conversion of ZnCl_4^2- complexes to $\text{ZnCl}_2 + 2 \text{Cl}^-$ ions, which reduces the Zn–Cl Raman intensity. In moderately concentrated solutions, increasing temperature lowers the static dielectric constant, thus favoring the formation of non-polar species. These are responsible for increasing the scattering intensity. The intermediate maximum appears at the point at which, toward the highest temperatures, simple ions are formed. Extrapolation of the data in Fig. 6.7-13 suggests that dense aqueous ZnCl_2 solutions above 550 °C constitute simple ionic fluids.

6.7.4 Chemical transformations in the dense fluid phase studied by high-pressure spectroscopy

Sec. 6.2.4 outlines the application of NIR spectroscopy in quantitative analysis and provides a few examples of high-pressure NIR studies. Thus, the present section is primarily concerned with high-pressure IR investigations. The advantages of the combined use of IR and NIR high-pressure spectroscopy for kinetic investigations of fluids are exemplified by high-pressure ethene polymerization. General surveys on chemical reactions at high pressure are given by Asano and Le Noble, 1978; Isaacs, 1981; and Matsumoto and Acheson, 1991.

Figure 6.7-14 shows IR spectra between 3500 and 3700 cm^{-1} , measured during the thermal decomposition of di-*tert* butyl peroxide in *n*-heptane at 160 °C and 100 bar

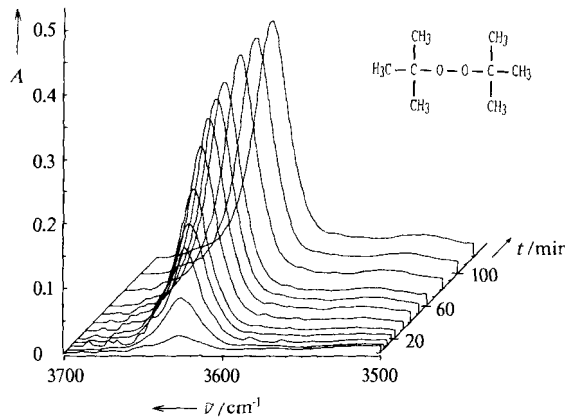


Figure 6.7-14 Infrared absorbance spectra, recorded during the thermal decomposition of di-*tert* butyl peroxide in *n*-heptane at 160 °C and 100 bar; *t*: reaction time. The initial peroxide concentration is 0.1 mol · L⁻¹.

(Buback and Lendle, 1979). The band around 3620 cm^{-1} is attributed to the O-H stretching mode of *tert*-butanol, which is produced by reaction of the primary radical species $\text{OC}(\text{CH}_3)_3$ with hydrogen atoms of the solvent. A similar application of quantitative IR high-pressure spectroscopy is shown in Fig. 6.7-15. The IR spectra in the carbonyl stretching region are measured during the decomposition of *tert*-butyl peroxy pivalate in *n*-heptane at 80°C and 2000 bar (Buback and Lendle, 1981). The peroxide band at 1775 cm^{-1} decays, and the absorption at 2340 cm^{-1} , due to formed CO_2 , increases. The weak absorption at 1725 cm^{-1} is attributed to acetone. Measurements in the 3500 to 3700 cm^{-1} region (not included in Fig. 6.7-15) also show the formation of *tert*-butanol and of small amounts of pivalic acid. Measurements like the ones shown in Figures 6.7-14 and 6.7-15 provide direct access to a detailed investigation of the decomposition kinetics in an extended temperature and pressure range. They also allow the direct observation of several reaction pathways.

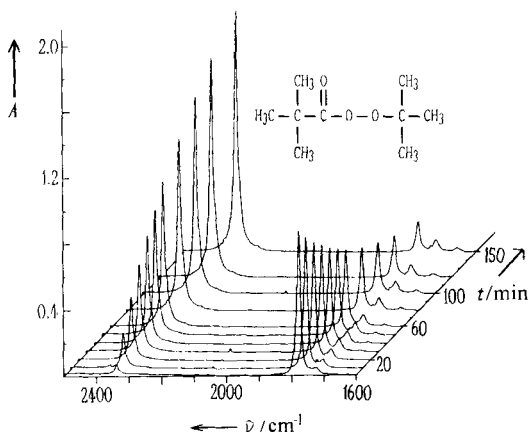


Figure 6.7-15 Infrared absorbance spectra, recorded during the thermal decomposition of *tert*-butyl peroxy pivalate in *n*-heptane at 80°C and 2000 bar; t : reaction time. The initial perester concentration is $0.01\text{ mol} \cdot \text{L}^{-1}$.

High-pressure absorption spectroscopy is widely applicable for studying the reactivity and the selectivity of chemical transformations. Some results are shown concerning the investigation of the *hetero*-Diels-Alder reactions between the enamine carbaldehyde **1** and enamino ketones **2** with ethyl vinyl ether **3**, which lead to the diastereomeric dihydropyrans **4 + 5** and **6 + 7**, respectively, Scheme 6.7-1 (Buback et al., 1988; Buback et al., 1989).

Experimental IR absorbance spectra, measured during the cycloaddition of **1** and **3** in CH_2Cl_2 solution at 60°C and 1500 bar, are shown in Fig. 6.7-16. Absorptions attributed to the solvent and to vibrational modes, which do not change during the reaction, are easily eliminated by subtracting the first spectrum, which is recorded after the system has reached the experimental temperature and pressure, from all subsequently measured spectra. The spectra shown in Fig. 6.7-16 are thus transformed into the spectroscopic data

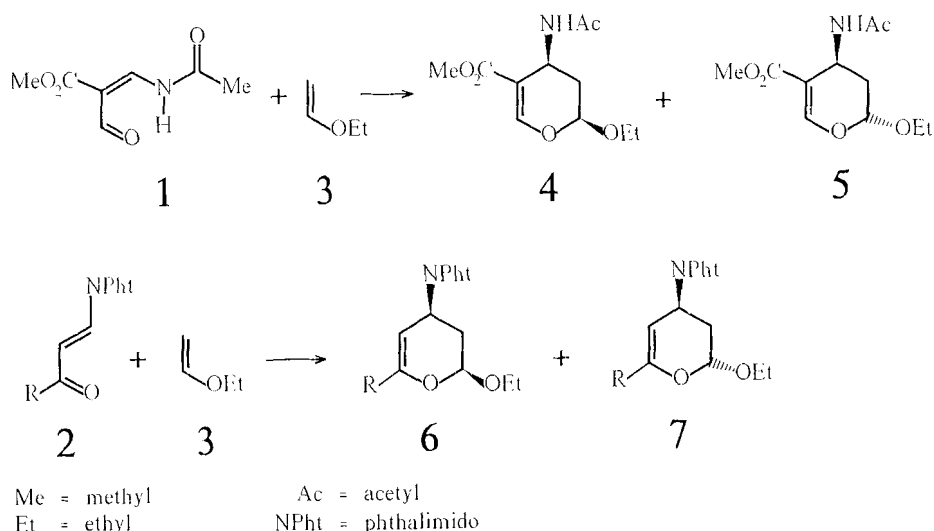
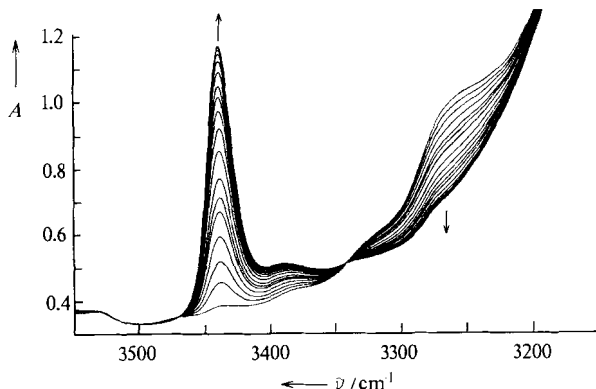
**Scheme 6.7-1**

Figure 6.7-16 Infrared absorbance spectra, recorded during cycloaddition of **1** and **3** in a CH_2Cl_2 solution at 60°C and 1500 bar. The series of spectra covers a reaction time of 4 hours. Each spectrum has been recorded within 1 minute. The initial concentrations are 0.04 mol of **1** and one mol of **3** per kg solution in CH_2Cl_2 .

plotted in Fig. 6.7-17. The positive absorbance around 3440 cm^{-1} is due to the increasing absorption of N-H stretching modes in the products **4** and **5**, whereas the negative absorbance around 3260 cm^{-1} illustrates the disappearance of the diene component during the reaction. The small arrows show the direction of the change of absorbance with the reaction time.

Diels-Alder reactions have also been studied via the fundamental and the first overtone absorptions of carbonyl stretching modes. Absorbance spectra measured during the cycloaddition of **2** (with $\text{R} = \text{CCl}_3$) and **3** in CH_2Cl_2 solution at 1000 bar and 95°C are shown in Fig. 6.7-18.

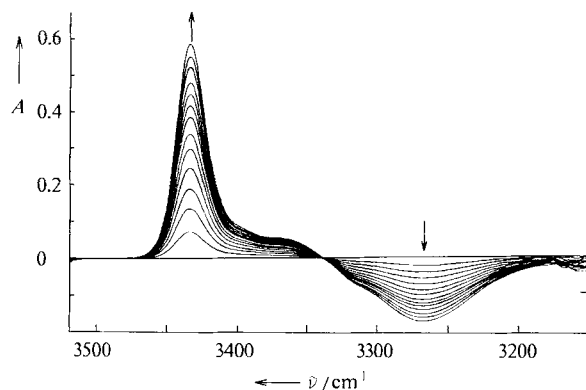


Figure 6.7-17 Difference infrared absorbance spectra, recorded during cycloaddition of **1** and **3** in a CH_2Cl_2 solution at 60°C and 1500 bar (same experiment as in Fig. 6.7-16, see text). The arrows indicate the direction of the change in absorbance during the reaction.

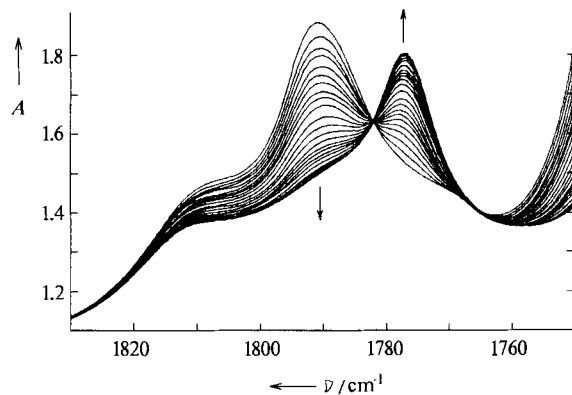


Figure 6.7-18 Infrared absorbance spectra, recorded during cycloaddition of **2** (with $\text{R} = \text{CCl}_3$) and **3** in an CH_2Cl_2 solution at 95°C and 1000 bar. The series of spectra covers a reaction time of 12 hours. The initial concentrations are 0.01 mol of **2** and one mol of **3** per kg solution in CH_2Cl_2 .

If the reaction mixture is contained in an internal poly(tetrafluoroethylene) cell transmitting IR radiation (see Sec. 6.7.2), quantitative analysis via high-pressure spectroscopy (Figures 6.7-16 to 6.7-18)) yields precise values of the rate coefficients of these Diels-Alder reactions. As an example, the pressure dependence of the rate coefficient k of the cycloaddition of **2** (with $\text{R} = \text{CF}_3$) and **3** in CH_2Cl_2 solution at 45°C (Buback et al., 1989) is shown in Fig. 6.7-19.

In addition to time-dependent experiments, the ratio at which the diastereomeric products **6** and **7** are formed as a function of the reaction pressure and temperature has been studied by high-pressure liquid chromatography. The chromatographic analysis was per-

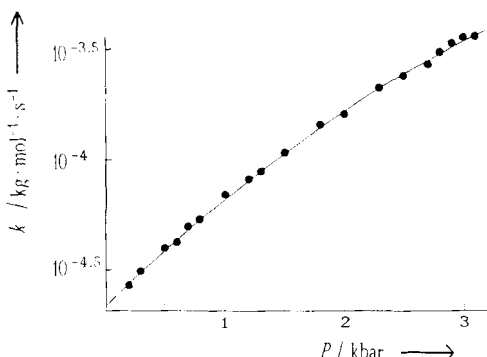


Figure 6.7-19 Dependence of the rate coefficient k on the pressure during cycloaddition of **2** (with $R = CF_3$) and **3** in a CH_2Cl_2 solution at $45\text{ }^\circ C$.

formed after removing the reaction mixture out of the optical high-pressure cell. In the studied pressure and temperature range, changes in the ratio of the product concentrations **6/7** by almost one order of magnitude are observed (Tietze et al., 1988). Combining the reactivity and selectivity data provides quantitative information about the total amount and about the diastereomer ratio of products obtained at specified temperature, pressure, and concentration within a given time.

Application of high-pressure vibrational spectroscopy in order to study and to monitor technically relevant fluid phase processes under extreme conditions is exemplified by high-pressure ethene polymerization. Several vibrational bands in the IR and the NIR may be used to detect concentrations directly in the ethene/polyethylene system (Buback, 1984). Some of these are plotted in Fig. 6.7-20. The conversion of unsaturated (ethylenic)

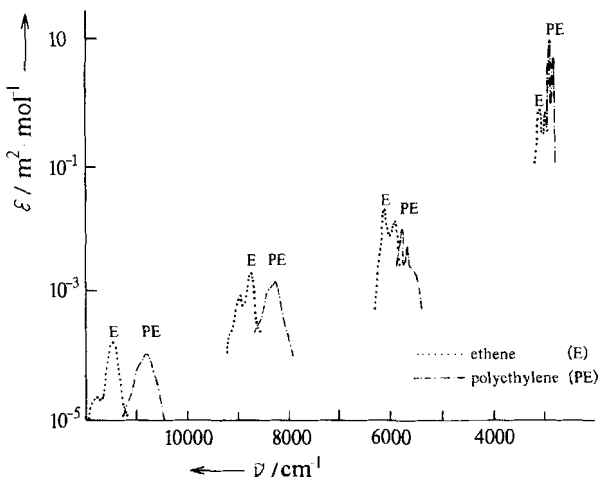


Figure 6.7-20 Molar absorption coefficient ϵ of selected bands of dense fluid ethene (E) and of liquid polyethylene (PE) in the IR/NIR range between 2000 cm^{-1} and $12\,000\text{ cm}^{-1}$.

C-H stretching modes to saturated (hydrocarbon) C-H is accompanied by a pronounced change of the fundamental, overtone, and combination modes (see also Sec. 6.2.4). The change of ϵ by several orders of magnitude in an extended IR-NIR range can be used to obtain measurements at quite different optical path lengths (reactor dimensions) or to quantitatively determine, within a single cell, species that occur at extremely different concentrations. For the case of CO, this is illustrated in Sec. 6.2.2. The same arguments apply to ethene (E) and polyethylene (PE) and to other materials. The E and PE bands are sufficiently separated to allow small concentrations of PE to be detected in the presence of very high amounts of E. In Fig. 6.7-21, this is demonstrated by a sequence of spectra measured during the polymerization of pure ethene up to 0.2 % conversion. The trace amounts of polymeric material during the initial period of the reaction are easily detected by IR spectroscopy in the C-H fundamental region.

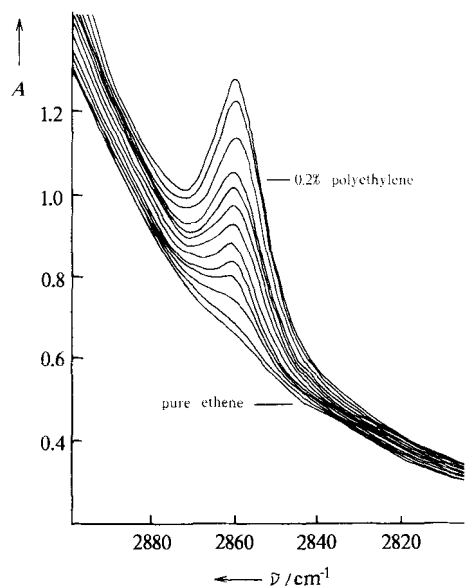


Figure 6.7-21 Infrared absorbance in the region of the C-H stretching fundamentals during the initial period of a high-pressure ethene polymerization up to 0.2 % conversion. For reaction time compare Fig. 6.7-22.

The polymerization of ethene may be followed up to high conversion by monitoring the first overtone of the C-H stretching vibration around 6000 cm^{-1} and the second overtone around 8600 cm^{-1} at optical path lengths of about 1 mm and 10 mm, respectively. The C-H second overtone region is presented in Fig. 6.2-24. Fig. 6.7-22 shows the near-infrared absorbance spectra in the C H first overtone region, recorded during an ethene polymerization at $200\text{ }^{\circ}\text{C}$ and at an initial pressure of 2500 bar. Ethene absorption (at higher wavenumbers) decreases and polyethylene absorption increases during the reaction. This technique has also been used to study several other free-radical polymerizations, with special interest in the understanding of polymerization up to high conversion (Buback, 1991).

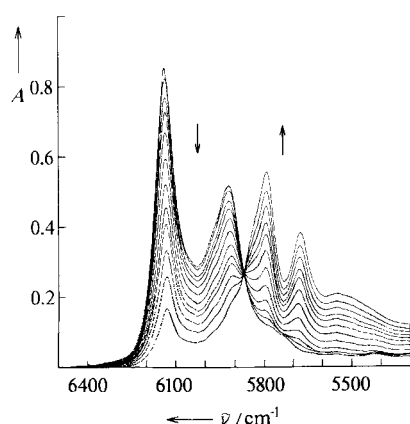


Figure 6.7-22 Near-infrared absorbance spectra, recorded during a free-radical polymerization of ethene at 200 °C and 2500 bar initial pressure (the arrows indicate the direction of the change of absorbance with the reaction time.)

The time to measure spectra of this quality under high-pressure conditions has been about 1 min. The absolute time scale of the experiment depends on the method of initiation. In thermally initiated (spontaneous) polymerizations reaction time can be several hours or even days. In contrast, in excimer laser-initiated free radical polymerizations application of a few laser pulses each of about 20 ns duration can induce changes between subsequent spectra as on this figure.

The examples presented in Figures 6.7-14 to 6.7-22 demonstrate that quantitative IR/NIR high-pressure spectroscopy allows *on-line* investigation of high-pressure processes. The technique is widely applicable toward studies on the reactivity and the selectivity of chemical transformations in an extended region of states.

6.8 Low- and high-temperature techniques, spectrometric determination of sample temperature*

6.8.1 General

The observation, evaluation, and interpretation of rotational and vibrational spectra at low or high temperature yields additional information in different fields of physical chemistry, as described by Herzberg (1945, 1950); Wilson, Decius and Cross (1955); Colthup, Daly and Wiberley (1975); Brandmüller and Moser (1962); Volkmann (1972); Long (1977); Schrader (1980); Günzler and Böck (1975); Orville-Thomas (1974); Irvin (1976) and Sherwood (1972).

This technique has been successfully applied to investigate, among others, the following:

- a) chemical reactions and kinetics, mixing and combustion processes,
- b) phase transitions,
- c) rotational isomerism,
- d) macromolecules,
- e) intermolecular interactions,
- f) chemical equilibria,

* Section 6.8 is contributed by A. Leipertz, Erlangen and M. Spickermann, Lübeck

- g) unstable substances,
- h) absorption band profiles.

Additionally, high pressure experiments, which are in some respects equivalent to low temperature investigations, provide information concerning, for example, lattice anharmonicity. The desired sample temperature is almost always maintained by using appropriate sample cells.

In order to reach a low temperature, the sample may be placed inside a metal block which is flushed with a cooling medium. Such devices reach approximately -78 °C. Even lower temperatures are achieved if the sample holder is in thermal contact with a heat exchanger. Liquid nitrogen is usually vaporized in the heat exchanger to cool the sample. To maintain the desired temperature, most sample holders can be heated electrically. Vaporization of liquid helium, typically in a closed cycle, also has a cooling effect. To avoid heat loss and to protect the cell windows from condensed water, the cells are surrounded by a vacuum chamber or a chamber containing a dry gas at atmospheric pressure.

To afford moderate temperatures, the sample holders themselves are heated electrically.

Peltier elements are sometimes used to generate either high or low temperature. Temperature control is mostly achieved by thermocouples.

Thermostated sample cells for all physical states are commercially available. To obtain vapor phase spectra of materials with low vapor pressure, heatable gas cells with a standard length or multiple reflection cells are needed.

Fig. 6.8-1 shows a photograph of such a gas cell designed for IR spectroscopy. The cell can be heated up to 250 °C. It may be used for gases, vapors, and samples which



Figure 6.8-1 Heatable cell for recording IR spectra of vapors and gases up to 250 °C. The cell can also be used to record spectra of compounds which are liquid or solid at ambient temperature.

at ambient temperature are still in the liquid or solid state. The temperature is measured by a thermocouple and can be controlled with a precision of $\pm 1^\circ\text{C}$. Fig. 6.8-2 shows a variable temperature cell which may be used in the range from -180°C to 250°C with a precision of more than 0.1°C . This cell can be employed in nearly all commercially available IR spectrometers. Liquid nitrogen is the cooling medium, and an electric heater sets the desired temperature. The sample cell has AgCl windows and is placed in a vacuum chamber with NaCl windows. The outer windows can be heated to prevent condensed water from precipitating. This cell may also be used to measure absorption bands at low temperature in order to investigate crystallinity, polymerizations, phase transitions, or reaction kinetics.

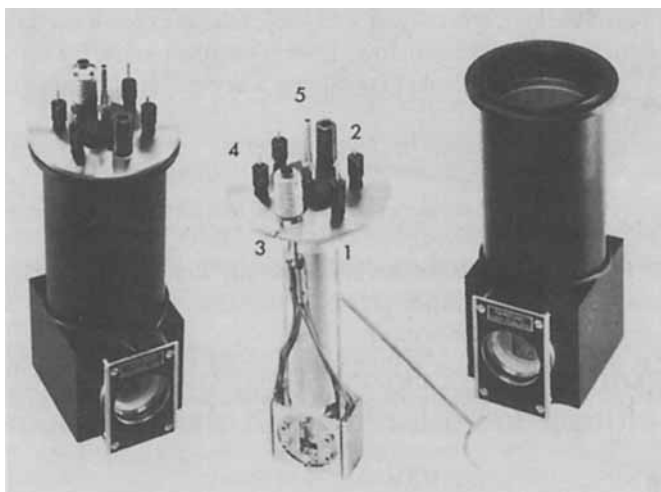


Figure 6.8-2 IR cell for liquids and solids to record spectra in the temperature range -180°C to $+250^\circ\text{C}$. 1) Contact for thermocouple 2) Vacuum connection 3) Connection for the window heating 4) Flow through tube 5) attenuation assembly for the cooling performance.

A high pressure cell with a variable path length for quantitative absorption measurements up to 2.5 kilobar and 250°C has been described by Buback (1977). This cell makes it possible to determine absorption band intensities with an error of less than $\pm 2\%$. A high pressure cell for absorption studies in the far-infrared region up to 10 kilobar at temperatures between 300 K and 10 K has been described by Medina (1980). The advantages and disadvantages of different window materials are discussed in detail (see Sec. 6.7).

The design and efficiency of a heatable far-infrared gas cell of the light pipe type with a long path length has been investigated by Lykke Hansen and Nicolaisen (1979). According to these authors, this cell has been used for the study of formamide, naphthalene, and 4-fluoro-aniline. The authors concluded that the combination of a long path length and a heatable cell is a powerful tool for obtaining vibrational spectra of materials with a low vapor pressure at room temperature. The cell can be cleaned easily if it is attacked by corrosive samples.

An alternative approach involving commercial non-thermostated cells and pellet holders to thermostat the appropriate cell mount has been proposed by Cameron and Jones (1981). Thermostating the mount by flushing the cell body with a liquid or a gas enabled the authors to maintain a sample temperature which varied only by ± 0.05 °C.

Raman measurements can in principle be obtained with sample holders which are heated and cooled by the same technique. A large variety of transparent window materials is available through which the incident laser beam and the scattered light can pass. Raman spectroscopy is thus highly suited to studies at high or low temperature. To record spectra in the usual 90° manner, it is necessary for the windows to be adequately arranged. The sample holder itself may be built as shown in Fig. 6.8-3. A glass tube containing the sample is placed in a metal holder with four boreholes. Two of these holes are designed for the laser beam to pass through the sample onto the reflecting mirror and back through

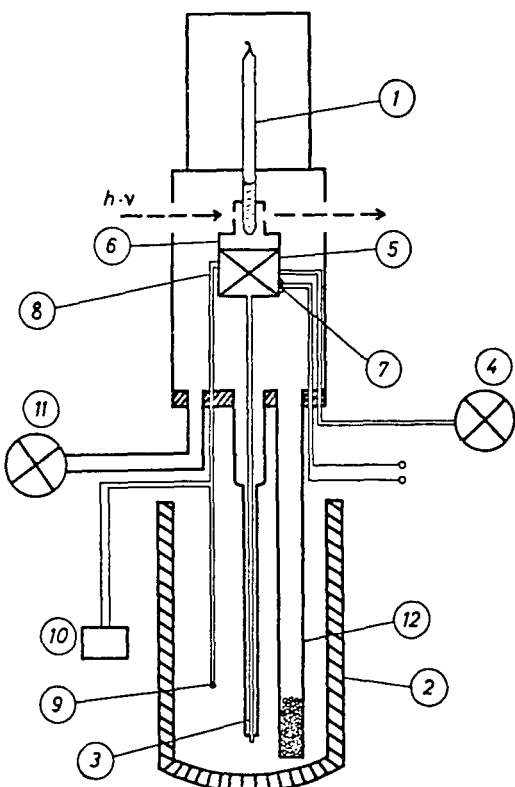


Figure 6.8-3 Variable temperature Raman cell (77 K-400 K)

- 1) sample cell 2) Dewar for liquid N₂ 3) flow through tube 4) suction pump 5) heat exchanger 6) sample holder 7) heating assembly 8) thermocouple 9) reference for thermocouple 10) assembly for temperature reading and control 11) vacuum pump for evacuation of the cell 12) cooling trap for remainders of moisture.

the sample. The Rayleigh and Raman light is collected through the two other holes. These should have a somewhat larger diameter in order to increase the intensity of the signal.

Homborg and Preetz (1976) have described a technique of recording laser Raman spectra of rotating solid samples at the temperature of liquid nitrogen in an evacuated cell. The sample is rotated so as to prevent it from being heated too much by the incident laser beam. The authors show that the surface of a pellet with a thickness of about 1 mm will warm up by only 3 degrees. Jodl and Holzapfel (1979) have described an optical cell which is suitable for Raman studies and absorption measurements of gases, liquids, and solids at pressures up to 10^9 Pa and temperatures down to 4.2 K. The main body of the high pressure cell is connected to a commercial two-stage gas compressor by a standard high pressure capillary and is clamped to the bottom of a liquid helium tank of a specially constructed helium cryostat. The capability of the cell was demonstrated by recording impurity induced Raman spectra of a sample of KI with 1 mol% NO₂ at 4.2 K at a pressure of $6.6 \cdot 10^8$ Pa.

Abdullah and Sherman (1980) have described a variable temperature one-window high pressure cell. Raman spectra of four different phases of NH₄Br illustrate the applicability of this cell for 180° Raman scattering studies.

A cryostatic cell for polarized Raman studies has been described by Halac and Gutierrez (1983). This cell facilitates the growing of single crystals from the liquid as well as the determination of the sample orientation by X-ray diffraction. It consists of two coaxial tubes. The innermost one is made of stainless steel and contains liquid nitrogen as a cooling fluid. Its lower end is in thermal contact with a goniometer head. A sealed glass capillary tube contains the sample and is placed in the specimen holder of the goniometer head. After evacuating the cell, the growth of a single crystal is initiated by gradually cooling the sample holder. The cell is mounted on the Raman spectrometer in such a way that each of crystal axes is successively perpendicular to the laser beam. This requires the cell to be operated in horizontal and vertical positions. The publication exemplifies this approach by the Raman spectra of crystalline bromine.

All of the discussed investigations basically make it necessary to determine the temperature of the investigated sample. Measuring the temperature by spectroscopic methods has a number of advantages if:

- 1) the sample temperature cannot be measured by traditional techniques, e.g., by thermometer or thermocouple (remote sensing, astronomic measurements)
- 2) the use of mechanical probes results in more or less strong perturbation of the system and in practice produces erroneous results (heating by laser beam; determining the temperature of a flame or another reacting system; evaluating thermodynamic functions)
- 3) the temperature is too high to be measured by mechanical probes (determining the temperature of a plasma)
- 4) techniques are needed for the time-resolved determination of the temperature in very small selected sections of a turbulent flow system. (This also applies to the determination of concentrations by these methods. The resulting data therefore make it possible to study fast chemical reactions in turbulent flow systems as well as turbulent mixing mechanisms and to determine flow structures).

5) it is necessary to discriminate between the rotational/vibrational and the transitional temperature, which some of the described techniques allow.

Temperature is usually defined as a thermodynamic quantity arising from the macroscopic properties of a system which can be described by equations of state, such as the Ideal Gas Law. This must be distinguished from the atomistic definition, which deals with the population at different energy levels and which is the basis of the spectroscopic definition of temperature. In the case of IR and Raman spectroscopy, only the vibrational and the rotational states are of interest usually. According to the Boltzmann distribution law, the population of a distinct level of energy E_i is proportional to

$$g \cdot e^{-E_i/kT} \quad (6.8-1)$$

in which g = degeneracy of the state

k = Boltzmann constant

T = absolute temperature

In this expression, the population is characterized by the temperature, and vice versa. In the case of vibrational states, this temperature is referred to as *vibrational temperature* and in the case of rotational states as *rotational temperature*. If the system is in equilibrium, the thus defined temperature is identical with the *thermodynamic temperature*. At the equilibrium position, the population of each energy level can be calculated by the Boltzmann law by using *one* temperature only. Comparing IR and Raman methods reveals a characteristic difference between the two: Raman light is generated by focusing a laser beam and therefore affects a very small area of the sample; whereas an IR signal can be considered as the sum of the absorptions of all layers through which the radiation emitted by the source passes. Homogenous samples always afford the same results, irrespective of the method. Raman methods applied to inhomogenous samples, on the other hand, afford only local information, independently of the rest of the sample. This is due to gradients in the particle concentration or the sample temperature (flames, exhausts, chemical reaction zones in flow reactors, etc.). This may be advantageous. However, a large number of experiments are needed to obtain comprehensive information. The influence of the inhomogeneity of a sample on its IR spectrum is very complex. If local information is required, it is often impossible to draw simple conclusions from the measured overall signal.

Tourin (1966) has provided an overview over spectroscopic measurements of the temperature of gases; and Drake et al. (1979) have published a comparison of different spectroscopic methods of determining flame temperatures.

The following sections describe the determination of temperature by IR and Raman spectroscopy and exemplify the application of these techniques.

6.8.2 Temperature determination by IR spectroscopy

6.8.2.1 Determining the rotational temperature from the rotational structure of vibrational-rotational bands

6.8.2.1.1 Determination of the rotational temperature of C=O

As an example let us consider a linear heteronuclear molecule of the point group $C_{\infty v}$, such as CO. For this molecule, the degeneracy of states at the higher rotational levels ($J \neq 0$) is $2J + 1$. The Boltzmann distribution function therefore leads to

$$n_J/N = (1/Q_r)(2J + 1)e^{-J(J+1)Bhc/kT} \quad (6.8-2)$$

in which n_J/N = fraction of molecules in the state J with energy E_J

Q_r = rotational partition function

J = rotational quantum number

B = rotational constant ($B = h/8\pi^2 c I$)

I = moment of inertia

If the levels are close to each other and the temperature is not too low, the rotational partition function Q_r can be expressed by

$$Q_r = \int_0^\infty (2J + 1)e^{-J(J+1)Bhc/kT} dJ = kT/hcB \quad (6.8-3)$$

Hence the number of molecules in a particular level E_J depends on the absolute temperature, the value of the moment of inertia, and the actual value of J . The value of n_J increases with increasing temperature and decreases with increasing J . Fig. 6.8-4

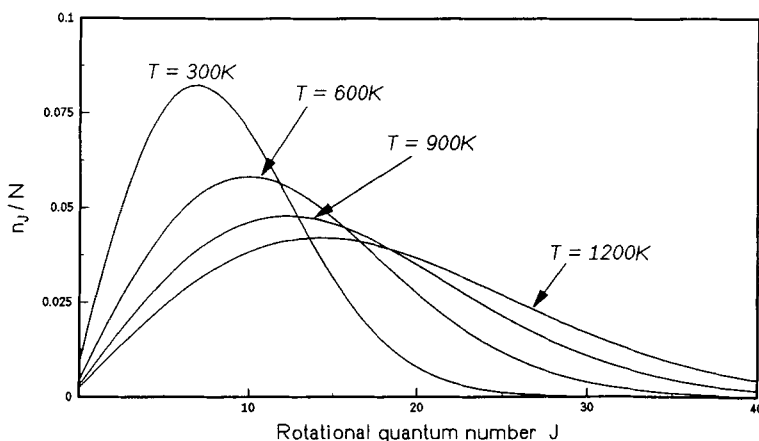


Figure 6.8-4 n_J/N as a function of J calculated for four different temperatures.

shows the graph of equation (6.8-2) for CO, plotted at four different temperatures. The population of the individual levels passes through maxima which may be located by differentiating equation (6.8-2), defining $d\eta_J/dJ = 0$, and solving for J , which yields

$$J_{max} = (kT/2Bhc)^{1/2} - 1/2 \quad (6.8-4)$$

In the case of CO ($B = 1.922 \text{ cm}^{-1}$), we get

$$J_{max}(300\text{K}) = 7(6.865)$$

$$J_{max}(600\text{K}) = 10(9.916)$$

$$J_{max}(900\text{K}) = 12(12.256)$$

$$J_{max}(1200\text{K}) = 14(14.230)$$

These results are in accordance with the maxima of the thermal population of the rotational states shown in Fig. 6.8-4. This method, of course, can only be applied if the rotational lines can be obtained from the spectra. Due to the fact that the J_{max} values are integers, temperature determination by equation (6.8-4) yields uncertain values, especially at higher temperatures. In principle it is possible to obtain the temperature of a sample from the intensities of distinct rotational lines or from the intensity ratio of two consecutive lines. This will be exemplified later by rotational Raman lines.

6.8.2.1.2 Making use of the distance between the maxima of *P* and *R* branch

According to the reasons discussed in Section 6.8.2.1.1, the distance between the maxima of the *R* and *P* branches $\Delta\tilde{\nu}_{PR}^{max}$ also depends on the temperature. If the distinct rotational lines cannot be resolved, the temperature may be derived from

$$\Delta\tilde{\nu}_{PR}^{max} = (8BkT/hc)^{1/2} = 2.358(T \cdot B)^{1/2} \quad (6.8-5)$$

This relation applies to linear molecules. Gerhard and Dennison (1933) have shown that the spacing between successive maxima of the *P* and *R* branches in a parallel band of a symmetrical top molecule can in certain cases be expressed by

$$\Delta\tilde{\nu} = S(\beta)/\pi c(kT/I_B)^{1/2} \quad (6.8-5a)$$

with $\beta = (I_B/I_A) - 1$. $S(\beta)$ is related to β , which is in the range between 1/2 and 100 given by the empirical formula

$$\log S(\beta) = 0.721/(\beta + 4)^{1.13} \quad (6.8-5b)$$

Equations for the calculation of the band contours of different shaped molecules have been provided by Herzberg (1945), Badger and Zumwalt (1938), as well as by Seth-Paul (1969). The sample temperature can be derived from the respective infrared spectra by using these equations.

Fig. 6.8-5 shows part of a spectrum of C_2H_2 ($B = 1.177 \text{ cm}^{-1}$). A $\Delta\tilde{\nu}_{PR}^{\max}$ of 45 cm^{-1} is obtained from this spectrum. The resulting sample temperature is $T = 309 \text{ K}$, a value which is to be expected for a sample in a gas cell inside the closed sample compartment of an IR spectrometer.

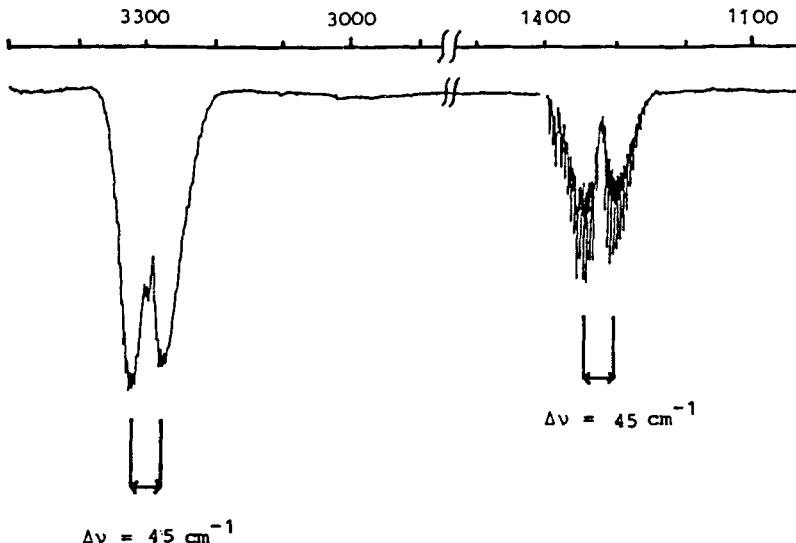


Figure 6.8-5 IR absorption bands of C_2H_2 . The sample temperature can be derived from the PR separation.

6.8.2.2 Deriving the vibrational temperature from the intensities of overtones and combination bands (Breeze et al., 1964)

The temperature dependence $\Phi(T)$ of the integrated band intensities $\alpha(T)$ at constant pressure can be expressed as

$$\Phi(T) = [\alpha(T)/\alpha(T_0)] \cdot (T/T_0) \quad (6.8-6)$$

It can be shown that $\Phi(T) = 1$ applies to the band intensities of fundamental vibrations, so that these bands cannot be used for temperature determination.

Nevertheless, the integrated band intensities of overtones and combination bands show a characteristic temperature dependence. As a result of the anharmonicity of the vibrations, these bands are observed in vibrational spectra. For overtones ($\Delta\nu = n, n > 1$), the band intensity function of the temperature is expressed as

$$\Phi(T)_{\text{overtone}} = [1 - \exp(-h\nu_0 c/kT)]^n [1 - \exp(-nh\nu_0 c/kT)] \quad (6.8-7)$$

For combination bands ($n_1\tilde{\nu}_1 + n_2\tilde{\nu}_2 + \dots$), this expression becomes

$$\Phi(T)_{\text{combi}} = [1 - \exp(-hc\tilde{\nu}_1/kT)]^{-n_1} \cdot [1 - \exp(-hc\tilde{\nu}_2/kT)]^{-n_2} \cdot \dots \cdot \{1 - \exp[-(n_1hc\tilde{\nu}_1 + n_2hc\tilde{\nu}_2 + \dots)/kT]\} \quad (6.8-8)$$

Fig. 6.8-6a shows the calculated temperature function for the fundamental vibration and the first overtone of NO. Fig. 6.8-6b shows the respective temperature dependence of the two combination bands $\tilde{\nu}_1 + \tilde{\nu}_3$ and $2\tilde{\nu}_1 + \tilde{\nu}_3$ of the antisymmetric stretching vibration $\tilde{\nu}_3$ of CO_2 with the symmetric stretching vibration $\tilde{\nu}_1$, which in itself is IR forbidden.

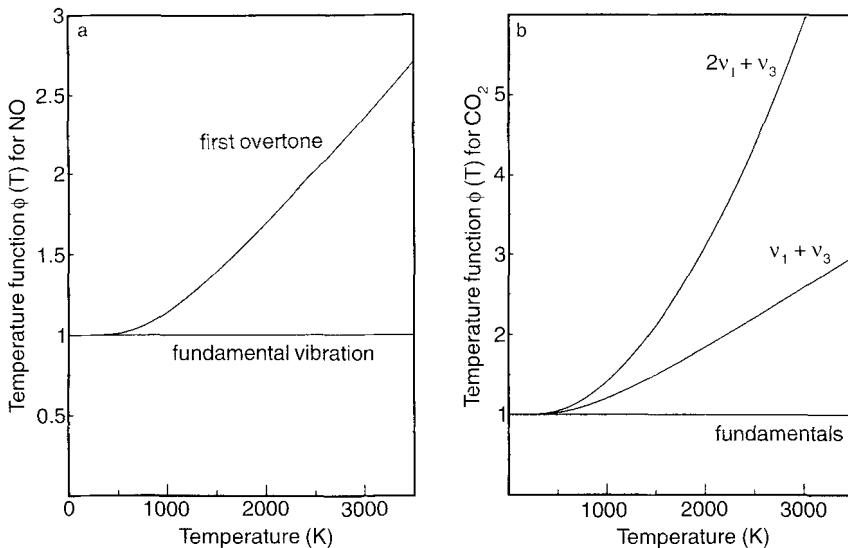


Figure 6.8-6 Calculated temperature function $\Phi(T)$ for (a) the fundamental vibration and the first overtone of NO, (b) the $\tilde{\nu}_1 + \tilde{\nu}_3$ well as the $2\tilde{\nu}_1 + \tilde{\nu}_3$ combination bands of CO_2 .

6.8.2.3 Temperature determination by simulating band contours

Due to the rotational structure as well as the so-called *hot band* absorptions (Sec. 2.5.3), the contour of a rovibrational band depends on the temperature. Today it is possible to determine molecular constants such as moments of inertia, Coriolis coupling constants, centrifugal distortion constants, and anharmonicity coefficients by FTIR as precisely as possible in order to calculate the intensity and shape of an absorption band. In such a simulation process the temperature may be used as a parameter. The results can be compared to the experimental spectra and the temperature may be deduced by fitting the calculated to the observed bands. This is possible with IR as well as with Raman bands. A review of curve fitting procedures and their limitations has been given by Maddams (1980).

6.8.2.4 The procedure of line reversal

The signal observed by the detector can be divided into two parts: 1. the portion of light emitted by the source which is absorbed by the sample, and 2. the light which is emitted by the heated sample itself (Sec. 3.3.1 and 3.5.4). If the sample temperature is higher than the detector temperature, self-emission of the sample leads to apparent transmission. In absorption measurements the source is hot compared to the sample and behaves as a black body radiator, while in emission experiments the detector 'faces' a hot sample against a cold background. Absorption and emission spectroscopy meet at the point where the sample temperature equals the source (background) temperature. In this case, sample and background are in thermal equilibrium and therefore in an equilibrium of radiation, i.e., absorption and emission of radiation by the sample are exactly equal. If the temperature of the background (source) radiator can be changed systematically, it is possible to find the point at which the lines change from absorption to emission or vice versa (reversal of the lines). At this point, sample and background (source) must have the same temperature if the source can be treated as a black body radiator.

If the temperature distribution is homogeneous throughout the sample, any of the lines may be used to determine the temperature. It is in any case advantageous to use strong lines in order to reduce the error of the measurements. This method is thus useless if, due to a low sample concentration or lack of sample thickness, all lines show little absorbance.

6.8.3 IR emission spectra

According to the Planck and Kirchhoff law, the spectral radiance of an emitting sample at a given wavenumber and a given temperature equals the product of its absorption factor $a(\tilde{\nu})$ and the spectral radiance of a black body radiator at equal conditions (see Eqs. 3.3-4 ... 3.3-8). For butadiene-1,3 the influence of the factor due to the black body radiator can easily be observed. Strong absorption bands in the region of 11 μm for example ($\gamma\text{-CH}$ vibrations), correlate with bands of relatively weak intensity in the emission spectrum. Weak absorption bands in the spectral region at 3 to 4 μm , on the other hand, have strong counterparts in the emission spectrum (for comparison see Sec. 3.4, Fig. 3.4-2). The temperature dependence of the spectral radiance of the black body radiator shows that at 800 K the maximum is expected to be at a wavelength of about 4 μm (Fig. 3.3-1) (Belz et al., 1987).

According to the Kirchhoff law, the capability of spectral emission equals the capability of spectral absorption. If the spectral absorptivities are known, it is therefore possible to determine vibrational temperatures from emission spectra. It is important to remember that the absorption coefficient throughout a band in a spectrum often varies considerably with the temperature. Temperatures are usually determined by fitting the calculated to the observed intensities.

In contrast to the method of line reversal described in the preceding section, the discussed technique can be applied even if the emission bands are very weak.

It should be noted that the spectral emission is influenced by the self-absorption of the emitted radiation by the sample. If the temperature distribution is homogeneous, this effect is already included in the determination of the absorptivity. In inhomogeneous samples, the self-absorption may be neglected if the absorptivity is below 5%. In this case, the overall emission can be treated as the sum of the emission of all infinitely thin layers into which the sample can be divided (Pepperhoff and Grasz, 1955). Otherwise, the emission of all inner layers must be corrected by transmission factors before summation. For practical calculations, the sample volume can be divided into different layers, each of which is assumed to be in thermal equilibrium.

If the vibrational temperature is determined by using the intensities of different bands, a distinct value is obtained for each band. These values do not represent the arithmetic mean of all temperatures. Due to the nonlinear increase of the spectral radiance by the black body radiator, the hot zones appear more pronounced than the cold ones. On the other hand, the influence of the more distant zones with respect to the observer is reduced by stronger self-absorption. The vibrational temperatures deduced from bands with high absorption coefficient are therefore lower than those derived from bands with smaller absorption coefficient. Nevertheless, all thus obtained temperature values are between the lowest and the highest temperature of the sample. The method of fitting calculated spectral profiles to the observed ones has been successfully applied in these cases, too.

The determination of vibrational and rotational temperatures by using emission spectra may be exemplified by vinyl chloride, which can be treated with good approximation

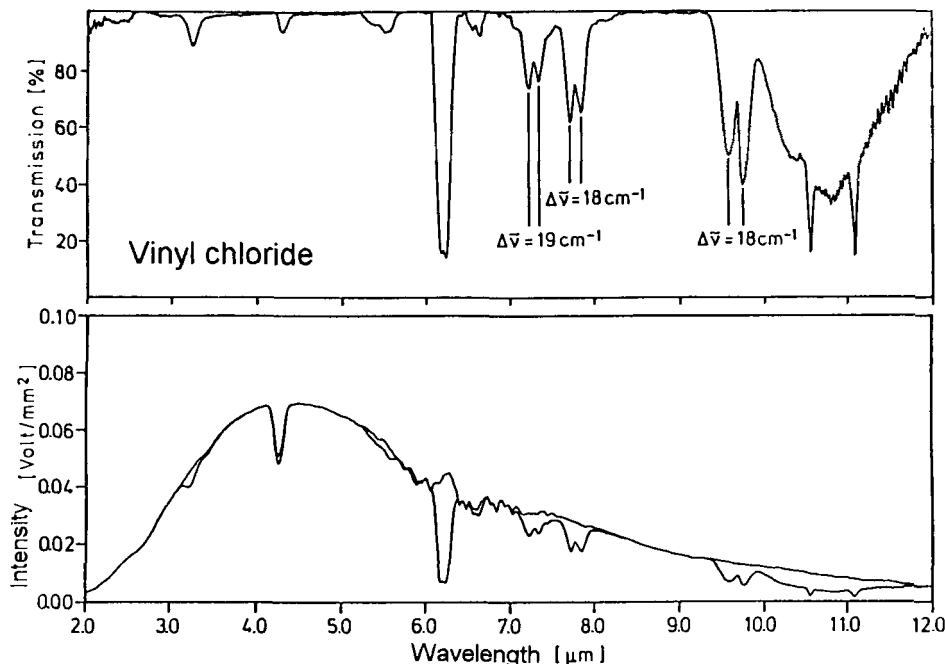


Figure 6.8-7 PR separation of parallel bands of vinyl chloride at room temperature $p = 5.332 \cdot 10^3$ Pa, path length = 10 cm, slit width = 0.5 mm.

as a prolate symmetric top (Gutberlet, 1978). Its spectra are shown in Fig. 6.8-7. The temperature of the sample may be determined by comparison of calculated with experimental data, which yields values between 815 K and 930 K. In the emission spectrum of vinyl chloride shown in Fig. 6.8-8, the PR separation of the bands $\tilde{\nu}_5$, $\tilde{\nu}_6$, and $\tilde{\nu}_7$ is well represented. The rotational temperature can therefore be determined by using the approximation $\Delta\tilde{\nu}_{PR}^{max} \sim T^{\frac{1}{2}}$. This applies to parallel bands of symmetric tops with selection rules $\Delta J = 0, \pm 1$ and $\Delta K = 0$. Table 6.8-1 shows the resulting rotational temperatures, which are within the range of temperatures derived from band intensities (Gutberlet, 1978).

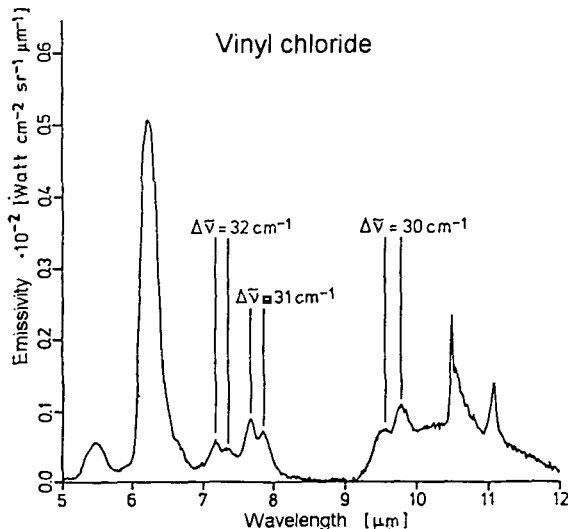


Figure 6.8-8 PR separation of parallel bands in the IR emission spectrum of vinyl chloride, $p = 9.331 \cdot 10^3$ Pa, slit width = 0.8 cm.

Table 6.8-1 Rotational temperature from PR separation of bands in the emission spectrum of vinyl chloride

$\Delta\tilde{\nu}_{PR}^{max}$ (300K)	$\Delta\tilde{\nu}_{PR}^{max}$ (T)	T_{Rot}
$\tilde{\nu}_5$	19	32
$\tilde{\nu}_6$	18	31
$\tilde{\nu}_7$	18	30

6.8.4 Temperature determination by linear Raman spectroscopy

(Brandmüller and Moser (1962); Long (1977); Schrader (1980); Placzek and Teller (1933); Stricker and Just (1979); Leipertz (1981a,1981b); Leipertz (1984))

6.8.4.1 Rotational temperature from the intensity distribution in purely rotational Raman spectra

The intensity of the Stokes (s) and anti-Stokes (as) lines in a purely rotational Raman spectrum can be expressed as a function of the rotational quantum number J

$$I_s(J) = k_1 \cdot (\tilde{\nu}_0 - \tilde{\nu}_R)^4 \cdot N \cdot I_0 \cdot \{ [g_j(J+1)(J+2)] / [(2J+3) \cdot Q_r] \} \cdot \exp[-hcBJ(J+1)/kT] \quad (6.8-9a)$$

$$I_{as}(J) = k_1 \cdot (\tilde{\nu}_0 + \tilde{\nu}_R)^4 \cdot N \cdot I_0 \cdot \{ [g_j(J-1)] / [(2J-1) \cdot Q_r] \} \cdot \exp[-hcBJ(J-1)/kT] \quad (6.8-9b),$$

in which $\tilde{\nu}_0$ denotes the radiated laser frequency, $\tilde{\nu}_R$ is the Raman shift of the respective Raman transition in the molecule, N stands for the density of the investigated gas molecules of the sample, I_0 represents the radiated laser intensity, and g_j is the statistical weight of the molecular state. The first line in the Stokes wing is attributed to $J = 0$, while the first line in the anti-Stokes wing is attributed to $J = 2$.

Fig. 6.8-9 exemplifies this by showing the temperature dependence of the relative intensities of the distinct lines and of the overall band contour calculated for N_2 ($T_1 \ll T_2 \ll T_3$) (Leipertz, 1981a; 1981b). In principle, either one of these quantities - relative intensities of single lines or band contours - may be used to determine the rotational temperature.

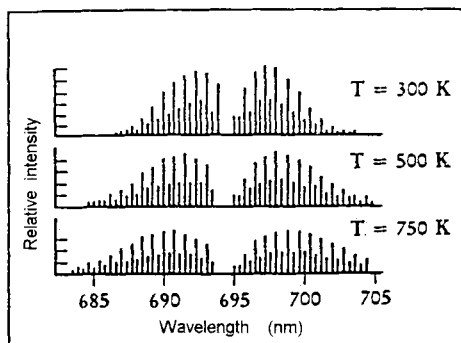


Figure 6.8-9 Schematic representation of the Stokes-/anti-Stokes rotational line intensities of N_2 at different temperatures generated by radiating a ruby laser with $\lambda_0 = 694.3$ nm.

6.8.4.1.1 Intensity ratio of two lines in the Stokes wing

If the rotational quantum numbers of the two investigated lines are J and J' , then the temperature may be determined according to

$$T_s = [J'(J' + 1) - J(J + 1)](hcB/k)/[\ln(X \cdot Y \cdot Z)]^{-1} \quad (6.8-10)$$

$$X = I_s(J)/I_s(J')$$

$$Y = [g_{J''}(2J + 3)(J' + 1)(J' + 2)]/[g_J(2J' + 3)(J + 1)(J + 2)]$$

$$Z = \{[\tilde{\nu}_0 - 4B(2J + 3/2)]/[\tilde{\nu}_0 - 4B(2J' + 3/2)]\}^4$$

6.8.4.1.2 Taking into account all rotational lines of the Stokes and the anti-Stokes wing

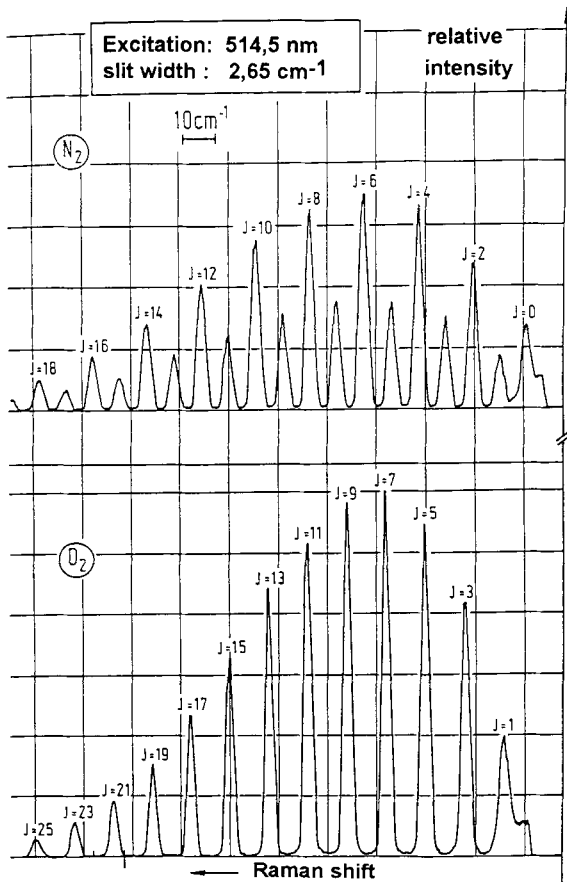


Figure 6.8-10 Stokes wings of the collected rotational Raman spectra of N_2 and O_2 at room temperature using an argon ion laser.

For the Stokes wing, we can develop Eq. (6.8-9a) to give

$$[hcB/k]J(J+1)T^{-1} = \ln\{[I_s(J)(2J+3)]/[k_2g_J(J+1)(J+2) \cdot A]\} \quad (6.8-11)$$

with $A = [\tilde{\nu}_0 - B(4J+6)]^4$

Dividing the right-hand side of Eq. (6.8-11) by hcB/k and plotting the resulting values of J against $J(J+1)$ yields a straight line whose slope represents the temperature. This approach is advantageous wherever high precision is required. Mathematical evaluation, after all, involves a large number of individual lines, while only two lines are employed by the method described in Sec. 6.8.4.1.1. Figs. 6.8-10 and 6.8-11 exemplify the use of this evaluation technique at room temperature.

Fig. 6.8-10 shows the Stokes wings of the collected rotational Raman spectra of N_2 and O_2 .

Fig. 6.8-11 exhibits the data and the evaluation plot described above. From the slope of both lines a temperature of 292 K can be deduced for N_2 and also for O_2 (Leipertz; 1981a).

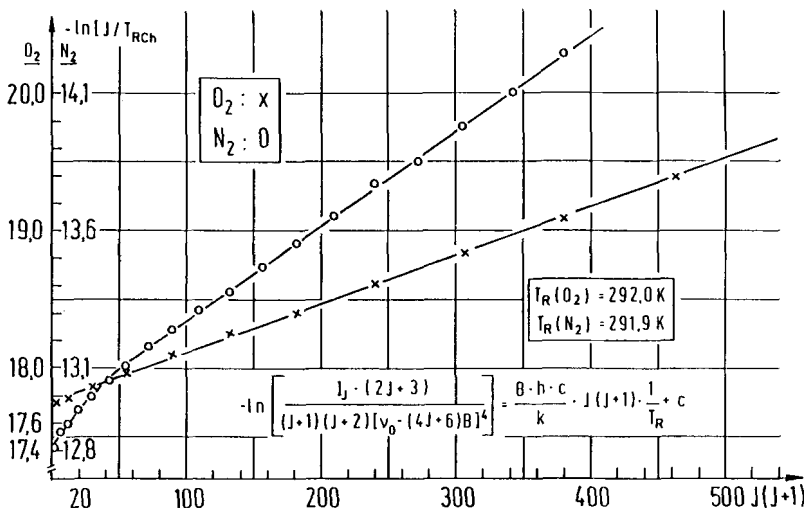


Figure 6.8-11 Temperature determination from the evaluation plot by taking into account all rotational lines from the spectra in Fig. 6.8-10.

It is basically possible to determine the temperature from the purely rotational wings over a wide temperature range. The best results are obtained in the temperature range much below 1000 K. In this region, the intensity differences between the lines are remarkable. As the temperature increases, the intensity differences gradually even out (see also Fig. 6.8-9), so that the good resolution of the temperature determination is lost (Leipertz, 1981b). However, this technique has been used successfully even at flame temperature (Drake and Rosenblatt, 1978; Stricker and Just, 1979; Kreutner et al., 1983).

6.8.4.2 Determining the vibrational temperature from the intensity distribution of vibrational-rotational Raman bands

The temperature dependence of the Q branch in the Stokes region of a vibrational-rotational Raman band is described by

$$I(v, J) = k_3(\tilde{\nu}_0 - \tilde{\nu}_R)^4 \cdot N \cdot I_0 \{ [g_J(v+1)(2J+1)(J+1)J]/[(2J+1)(2J+3)Q_v Q_r]\} \cdot \exp\{-hc[\tilde{\nu}_R v + J(J+1)B]/kT\} \quad (6.8-12)$$

The exponent may be divided into a vibrational part

$$\{-hc\tilde{\nu}_R v/kT_{vib}\}$$

and a rotational part

$$\{-hcBJ(J+1)/kT_{rot}\},$$

where T_{vib} is the vibrational and T_{rot} is the rotational temperature. If the sample is in thermal equilibrium, both temperatures are identical and Eq. (6.8-12) may be applied without change.

Fig. 6.8-12 shows the change of the contour of the vibrational-rotational N_2 band with the temperature (Stricker et al., 1979; Leipertz, 1981a, 1981b).

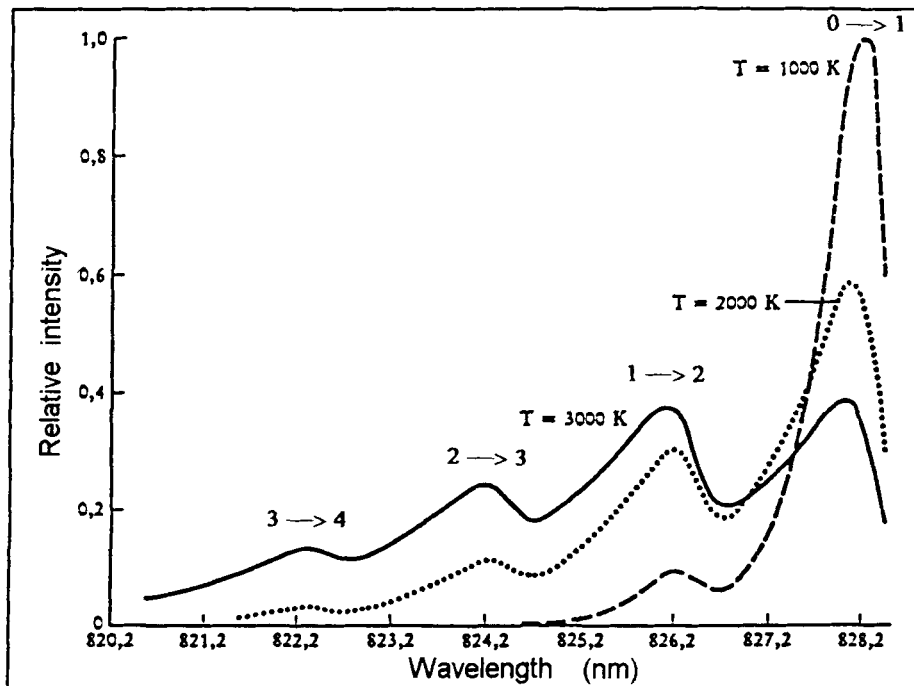


Figure 6.8-12 Calculated Stokes Q -branch intensities for N_2 at different temperatures.

If, outside the thermal equilibrium, such as in supersonic flows, the two temperatures differ, then the two temperatures can be derived separately. Fig. 6.8-13 shows the appearance of the O₂ Stokes *Q* branch at a fixed rotational temperature of 300 K and at three different vibrational temperatures.

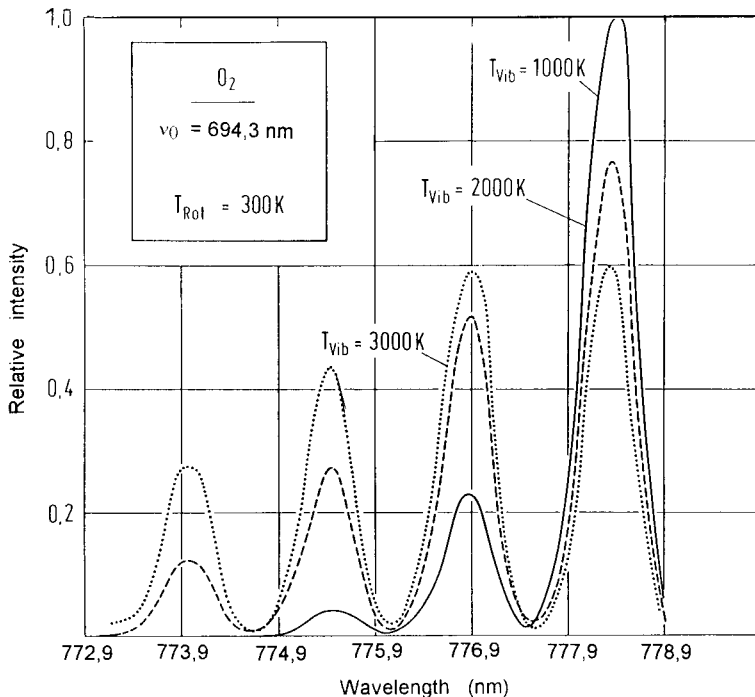


Figure 6.8-13 Vibrational-rotational Raman spectra of O₂ for fixed rotational temperature (300 K) and different vibrational temperatures (1000 K, 2000 K, 3000 K).

6.8.4.2.1 Temperature determination by simulating band profiles

This method can be applied at any temperature, especially above 500 K. The band profile at different temperatures is simulated by a computer program and the results are fitted against the experimental spectrum. This method benefits from the advancement of computers and computer graphics (Stricker and Just, 1979; Leipertz, 1981a, 1981b; Altmann et al., 1972; Hickman and Liang, 1972).

Fig. 6.8-14 exemplifies the measurement of the O₂ temperature at 1250 K in a flame position where the O₂ concentration is 9,9% (Leipertz et al., 1987). Both the temperature and the concentration of the species are obtained simultaneously by using a computer fit.

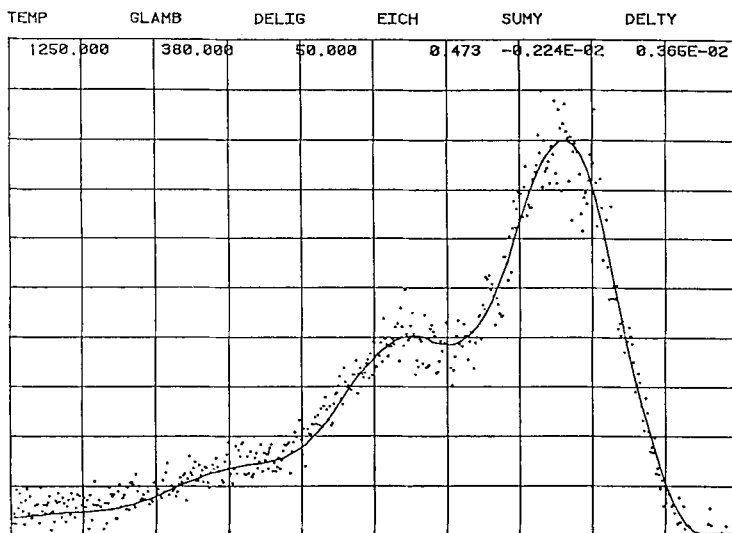


Figure 6.8-14 Temperature and O₂ concentration determination using a computer fit between measured (dotted) and calculated (continuous line) spectra.

6.8.4.2.2 Intensity ratios of vicinal maxima of vibrational transition bands ('hot bands')

The vibrational temperature is obtained from the equation

$$T = h\tilde{\nu}_R/k \cdot \left\{ \ln(I_v/I_{v+1}) + \ln[(v+2)/(v+1)] \right\}^{-1} \quad (6.8-13)$$

Fig. 6.8-15 shows the intensity ratio $I_{v+1}/I_v(v = 0)$ for N₂ as a function of the temperature (Leipertz, 1981a, 1981b). This method may be applied to higher temperatures; in the case of N₂, for instance, it may be used for temperatures above 600 K.

6.8.4.2.3 Ratios of integrated intensities of Stokes and anti-Stokes vibrational Raman bands

The intensity ratio of the corresponding bands is given by

$$I_s/I_{as} = (\tilde{\nu}_0 - \tilde{\nu}_R)^4 / (\tilde{\nu}_0 + \tilde{\nu}_R)^4 \cdot \exp(hc\tilde{\nu}_R/kT) \quad (6.8-14)$$

According to this equation, the vibrational temperature can be derived from

$$T = h\tilde{\nu}_R/k \cdot \left\{ \ln(I_s/I_{as}) - 4\ln[(\tilde{\nu}_0 - \tilde{\nu}_R)/(\tilde{\nu}_0 + \tilde{\nu}_R)] \right\}^{-1} \quad (6.8-15)$$

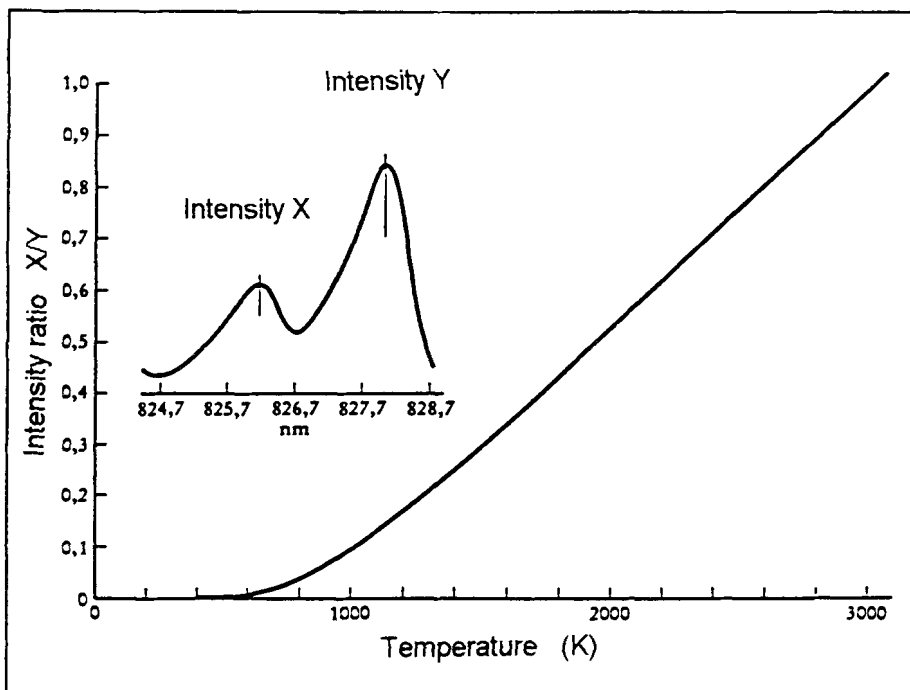


Figure 6.8-15 Calculated intensity ratio for different neighboured maxima in the spectrum of nitrogen. Peak X: 826.2 nm Peak Y: 828.1 nm Band profile for $T = 2000$ K using an interference filter with half band width of 0.5 nm.

This method may be applied to solid, liquid, or gaseous samples. Considering the fact that the difference in wavenumbers between the Stokes and the anti-Stokes signals is frequently large, the spectral sensitivity of the detector should be taken into account. A calibration curve may be obtained, as proposed by D'Orazio and Schrader (1974). A typical example is shown in Fig. 6.8-16; see also Sec. 2.4 and Fig. 2.4-2.

According to Malyj and Griffiths (1983), determining the equilibrium rotational or vibrational temperature by the Stokes/anti-Stokes ratio is not as simple and straightforward as the equations imply. The authors discuss the problems which evolve as a result of using standard lamps and show how to meet these difficulties by using reference materials to measure the temperature as well as to determine the instrumental spectral response function. The list of suitable materials includes vitreous silica and liquid cyclohexane, which are easy to handle and available in most laboratories. The publication includes a detailed statistical analysis of systematic errors and also describes tests with a number of transparent materials.

Table 6.8-2 shows experimental and calculated intensity ratios of Raman bands of CCl_4 , measured by Bernstein and Allen (1955). It seems to be possible to measure the temperatures of liquid samples over a wide temperature range. Fig. 6.8-17 shows the temperature dependence of the I_s/I_{as} ratio of a number of gases between 500 K

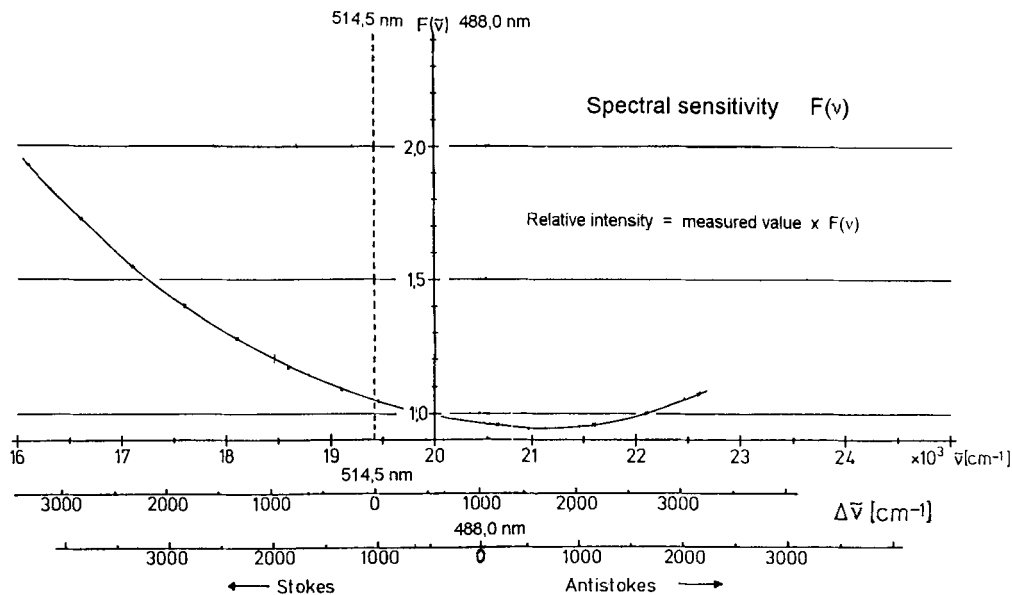


Figure 6.8-16 Calibration curve for the spectral sensitivity of a detector tube.

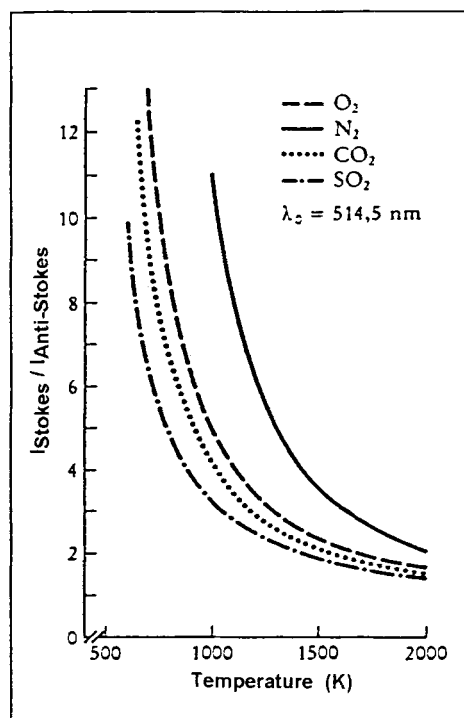


Figure 6.8-17 Calculated Stokes/anti-Stokes intensity ratios for some molecules at different temperatures.

Table 6.8-2 Experimental (exp.) and calculated (calc.) intensity ratios of Raman band of carbon tetrachloride (Bernstein and Allen, 1955)

$\tilde{\nu}/\text{cm}^{-1}$	exp. (40 °C)	$I_{\text{Stokes}}/I_{\text{anti-Stokes}}$	calc. (40 °C)
218	0.40 ± 0.02		0.3963
314	0.26 ± 0.01		0.2636
458	0.13 ± 0.01		0.143

and 2000 K ($\lambda_0 = 514.5$ nm argon ion laser, Stricker and Just, 1979; Leipertz, 1981a, 1981b). The slopes of the curves show that in these cases the method works well at temperatures below 1500 K. At temperatures up to 2000 K and higher, the results are more or less uncertain, due to the small changes in the intensity ratios.

6.8.5 Applications

6.8.5.1 Reaction kinetics

There are two ways of obtaining information about kinetic data of chemical reactions

- 1) measuring the entire spectra or some portion of them at distinct time intervals
- 2) time-resolved measurements at a given wavenumber.

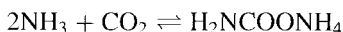
These techniques yield information concerning the rates and the rate coefficients of chemical reactions. If the experiments are carried out at different temperatures, additional data concerning the activation energy E_A may be obtained from

$$\frac{d \ln k}{dT} = E_A / (RT^2) \quad (6.8-16)$$

Due to the development of fast observation methods in vibrational spectroscopy, even faster reactions can now be investigated. It is possible to record an IR spectrum in a fraction of a second. For Raman spectroscopy pulsed lasers and multichannel spectrometers are used (for further information see Sec. 6.6).

Raman spectroscopy is a powerful tool in situations where chemical reactions have to be examined under process conditions. This is especially true where other spectroscopic techniques fail, possibly due to the fact that one of the components cannot be observed or that major portions of a spectrum are obscured by the signals of one component. Many industrial chemical processes proceed at elevated temperature and pressure. The development and optimization of process conditions benefit from knowledge of the exact composition of the reaction mixture.

In cases where sampling and off-line analysis fails, *in situ* measurements must be carried out. Van Eck et al. (1983) have exemplified this by the synthesis of urea. The reaction proceeds in two steps:



The temperature range is between 170 and 210 °C and the pressure may vary between 15 and 25 MPa. Altering these conditions will considerably change the composition of the reaction mixture. The authors were able to show that Raman spectroscopy is a very suitable method for quantitative *in situ* analysis of the synthesis of this substance.

One of the most promising energy saving tasks is the improvement of technical combustion processes. In order to investigate the very complex technical combustion phenomena, these are usually separated into simpler portions. This is why laboratory experiments are carried out with model flames and the experimental results are compared with sophisticated mathematical models. Due to the high temperatures in the flames, spectroscopic methods are preferred. Since oxygen itself is directly involved in the combustion process, it may be used as an indicator for combustion control. Like other homonuclear diatomic molecules, oxygen gives rise to a Raman signal. This is why Raman techniques are widely used for this purpose. A large number of publications describe the measurement of the concentration of particular species and of the temperature in flames (Stricker and Just, 1979; Leipertz, 1981a, 1981b, 1983, 1984, 1989; Schallert, 1982;

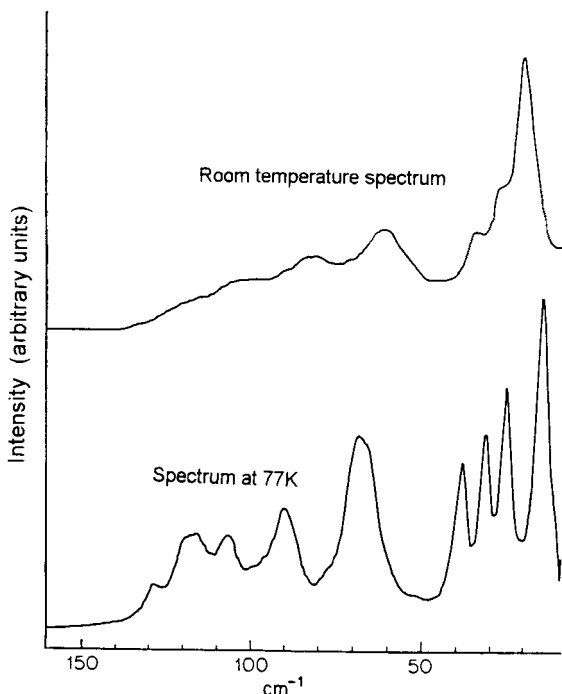


Figure 6.8-18 The Raman phonon spectra of 2-benzyl-5-benziliden-cyclopentanone at room temperature (top) and at 77K.

Kreutner et al., 1983, 1987; Stephenson and Blint, 1979). A review of recent progress in this field has been provided by Eckbreth (1988) and Laurendeau (1988). Spontaneous Raman scattering lends itself to the measurement of concentrations of species above a few percent and to the determination of temperature. It can therefore also be used to investigate mixing processes (Leipertz, 1981b, 1981c).

Prasad et al. (1982) have described Raman investigations of solid state reactions. They show that it is advantageous to obtain the spectra at lower temperature, typically at 120 K. Lower frequency phonon spectra show considerable broadening at room temperature, so that details of spectral features are lost. Raman phonon spectra of 2-benzyl-5-benzilidene cyclopentanone at room temperature and at 77 K (see Fig. 6.8-18) indicate that lower temperature improves the resolution of the spectral features. This phenomenon can be used for a detailed analysis in order to elucidate the reactivity of a compound at room temperature. However, it is necessary to make sure that neither the reactant nor the product undergoes a structural phase transition between room temperature and the low temperature at which the spectrum is recorded. This is confirmed by studying the phonon spectra as a function of the temperature.

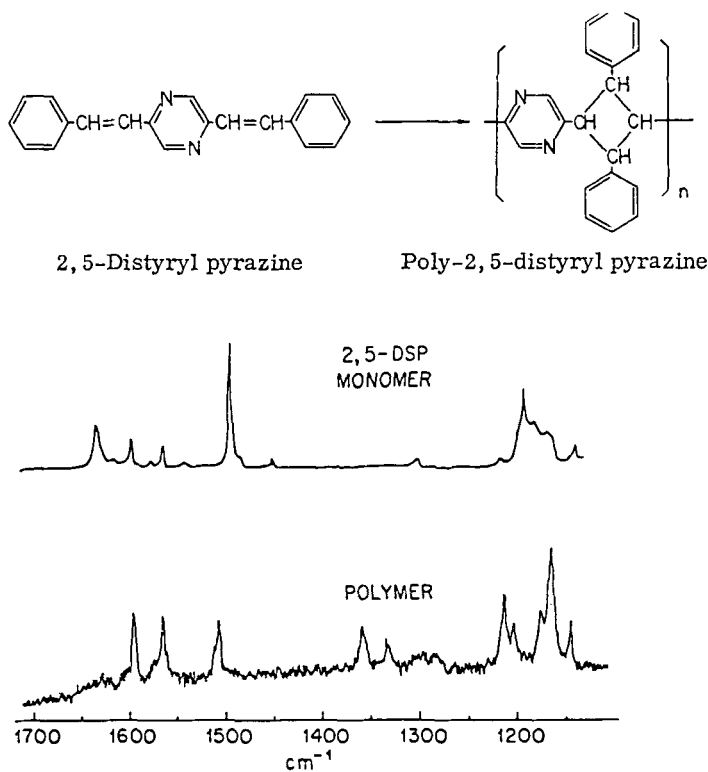


Figure 6.8-19 Reaction scheme for the 'four-center-type' polymerization of 2,5-distyryl pyrazine as well as part of the Raman spectra of the α -DSP monomer and its polymer at 100 K.

The same publication also describes the investigation of the photopolymerization of 2,5-distyryl pyrazine (DSP) as an example of the four-center type polymerization of diolefines. This reaction produces a highly crystalline polymer.

Fig. 6.8-19 shows the reaction scheme as well as the Raman spectra of the α -DSP monomer and its polymer at 100 K in the spectral region between 1100 and 1700 cm^{-1} . The significant difference between the spectra leads to the conclusion that α -DSP has undergone a chemical transformation. Fig. 6.8-20 exhibits phonon spectra of α -DSP, recorded during polymerization. Clearly, the phonon spectrum of the partially polymerized material results from superposition of monomer and polymer bands. As the reaction proceeds, the intensity of the monomer peaks decreases while the intensity of the polymer bands increases. The authors concluded that the solid state polymerization of α -DSP proceeds by a heterogeneous mechanism throughout the entire conversion.

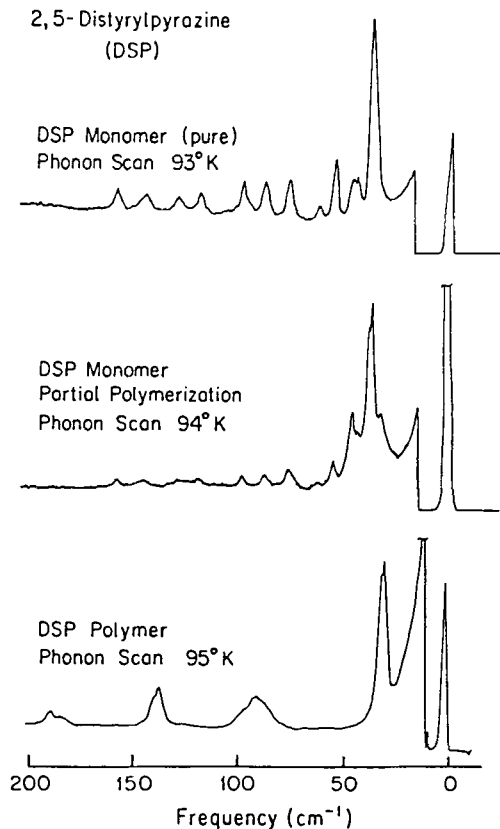


Figure 6.8-20 Raman phonon spectra of α -DSP at 95 K obtained as a function of the grade of polymerization.

6.8.5.2 Phase transitions

Vibrational spectroscopic investigations are very useful for the examination of phase transition phenomena, which are of importance, for example, in connection with ferroelectric substances, piezoelectric properties, and plastic crystals. Low temperature techniques are often required to investigate plastic crystals, which possess considerable power of sublimation. Investigations at different temperatures, including sample techniques and measurement of sample temperatures, have been reported by Woost (1983). Fig. 6.8-21 shows portions of the Raman spectra of hexachloroethane in the temperature region of the second phase transition at about 71 °C. During the transition to the plastic phase, some of the vibrations showed an interesting variation in their relative intensities. In the transition phase, the $\bar{\nu}_8/\bar{\nu}_2$ ratio was determined to be $(0.65 \pm 0.05):1$, whereas in the plastic phase it is $(0.45 \pm 0.05):1$. Furthermore, it was shown that the phase transition itself follows a hysteresis curve, a phenomenon which is often observed in first order phase transitions (Woost, 1983). Colombo (1976) reported Raman spectroscopic studies of the phase transition of a phenanthrene crystal. Polarized Raman spectra of phenanthrene single crystals were studied at temperatures between -190 °C and 90 °C. The observed changes in the spectra were associated with intramolecular regrouping. The symmetry of the molecule can change from C_2 at room temperature to C_s above the transition temperature. The observed results indicate that the phase transition of the phenanthrene

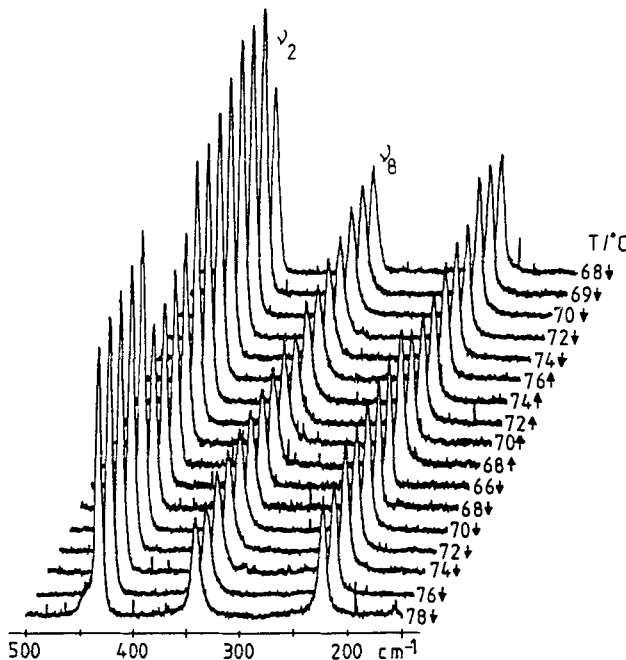


Figure 6.8-21 Raman spectra of hexachloroethane in the region of the second phase transition at 71 °C.

crystal is due only to rapid weakening of intermolecular forces resulting from anomalous dilatation of the lattice. A more detailed discussion of vibrational spectroscopy of crystals and phase transition phenomena is found in Secs. 2.7.5, 4.5 and 4.8.

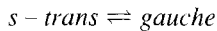
6.8.5.3 Rotational isomerism

In molecules in which two carbon atoms are connected by a single bond, the substituents of the carbon atoms may assume an infinite number of dihedral angles. The molecule itself can assume various shapes by rotating about the C-C single bond. However, depending on the substituents, one or more of these conformations correspond to a minimum in the potential energy curve of the system. Molecules with conformations corresponding to the minima in the potential energy curve are called *conformers*. The potential energy of the ethane molecule goes through two minima as the molecule assumes a so-called *staggered* or *eclipsed* conformation. The infinite number of conformations between these two extremes are referred to as *skew* or *gauche* conformations.

Since the energy barriers between the conformers at room temperature are small compared to the product kT , the respective molecules exist as an equilibrium mixture of different conformers.

Different conformations of a molecule are usually represented by different spectroscopic signals, so that the respective concentrations can easily be derived from the intensities of the respective signals. The temperature dependence of the equilibrium constant of the conformational equilibrium affords the enthalpy and entropy of rotation about the single bond, as shown in this text.

Consider the following equilibrium:



of conformational isomers with an equilibrium constant K , which depends on the temperature and can be expressed as

$$K = c_{\text{s trans}} / c_{\text{gauche}} \quad (6.8-17)$$

where $c_{\text{s trans}}$ and c_{gauche} are the concentrations of the *trans* and the *gauche* isomer, respectively. It should be noted that c_{gauche} is the sum of the concentrations of the two *gauche* isomers, which cannot be distinguished by vibrational spectroscopic methods. The relation between the equilibrium constant and the differences in enthalpy ΔH and entropy ΔS of the conformers is obtained from

$$-RT \ln K = \Delta H - T\Delta S \quad (6.8-18)$$

which affords

$$\ln K = -1/T(\Delta H/R) + \Delta S/R \quad (6.8-19)$$

Assuming that ΔH and ΔS are constant within a limited temperature range, these quantities are accessible if K can be determined at least at two temperature values.

IR spectroscopy

According to the Lambert-Beer law, the concentrations of the conformers are

$$A_{\text{trans}} = a_{\text{trans}} \cdot c_{\text{trans}} \cdot d \quad (6.8-20\text{a})$$

$$A_{\text{gauche}} = a_{\text{gauche}} \cdot c_{\text{gauche}} \cdot d \quad (6.8-20\text{b})$$

Substituting the respective concentrations in Eq. (6.8-17) yields

$$K = (a_{\text{trans}}/a_{\text{gauche}}) \cdot (A_{\text{gauche}}/A_{\text{trans}}) \quad (6.8-21)$$

and combination with Eq. (6.8-19) affords

$$\ln[A_{\text{gauche}}/A_{\text{trans}}] + \ln[a_{\text{trans}}/a_{\text{gauche}}] = -1/T(\Delta H/R) + \Delta S/R \quad (6.8-22)$$

If $\ln K$ is plotted against $1/T$, ΔH and ΔS may be obtained from the slope and the intercept of the straight line with the ordinate

$$\ln K = -a \cdot 1/T + b \quad (6.8-23)$$

The exact determination of ΔH and ΔS by this general approach requires knowledge of the temperature dependence of $A_{\text{gauche}}/A_{\text{trans}}$ as well as that of $a_{\text{gauche}}/a_{\text{trans}}$; the latter value can only be determined indirectly (de Meijere et al., 1974; Braun and Lüttke, 1975).

The situation is simplified by employing the following restrictions:

$$\begin{aligned} a_{\text{gauche}}(T)/a_{\text{trans}}(T) &= \text{const.} \\ da_{\text{gauche}}(T)/dT &\neq 0 \\ da_{\text{trans}}(T)/dT &\neq 0 \end{aligned} \quad (6.8-24)$$

Since $\ln [a_{\text{gauche}}/a_{\text{trans}}]$ is assumed to be constant at a given temperature, Eq. (6.8-22) can be rewritten:

$$\ln[A_{\text{gauche}}/A_{\text{trans}}] = -1/T(\Delta H/R) + \Delta S/R + \ln[a_{\text{gauche}}/a_{\text{trans}}] \quad (6.8-25)$$

Plotting $\ln[A_{\text{gauche}}/A_{\text{trans}}]$ against $1/T$ yields a straight line, analogous to Eq. (6.8-23):

$$\ln[A_{\text{gauche}}/A_{\text{trans}}] = -a \cdot 1/T + b$$

by virtue of which ΔH and ΔS may be defined as

$$\Delta H = -R \cdot a = -R \cdot [\text{d} \ln(A_{\text{gauche}}/A_{\text{trans}})/\text{d}(1/T)] \quad (6.8-26)$$

and

$$\Delta S = +R[b - \ln(a_{\text{gauche}}/a_{\text{trans}})] \quad (6.8-27)$$

ΔH is now very easy to determine by simply measuring the integrated band intensities A_{gauche} and A_{trans} at two temperatures. Assuming that the temperature dependence of the absorption coefficients is linear, the constant ratio $a_{\text{gauche}}/a_{\text{trans}}$ (see Eq. 6.8-27) can be obtained by linear least squares fit procedures using the 'normalized' integrated intensities \bar{A}_{gauche} and \bar{A}_{trans} (Braun and Lüttke, 1975).

$$\bar{A}_{\text{gauche}}(T) = A_{\text{gauche}}(T)/[c_{\text{ges}}(T) \cdot d(T)] \quad (6.8-28a)$$

$$\bar{A}_{\text{trans}}(T) = A_{\text{trans}}(T)/[c_{\text{ges}}(T) \cdot d(T)] \quad (6.8-28b)$$

The structure of 1,3-difluoropropane has been investigated by Klaboe et al. (1982). IR spectra were obtained of the compound as a vapor, in solution, and of the unannealed and annealed solid between 4000 and 30 cm^{-1} . Raman spectra were recorded of the liquid and of the unannealed and the annealed solid. The authors show that in the vapor phase the compound exists in at least three conformations. The ratios of the conformational abundance are given in brackets GG(63), AG(27) and GG''(10). The dominant GG conformer is the one which persists in the crystalline state, too.

Durig and Little (1981) determined the conformational barriers to internal rotation of methyl vinyl ketone by IR and Raman spectroscopy. They recorded IR spectra of the gaseous and the solid states and the Raman spectrum of the liquid state. They also determined the potential function for internal rotation of the asymmetric top and obtained the following potential constants: $V1 = 180 \pm 9$, $V2 = 827 \pm 107$, $V3 = 113 \pm 8$, and $V4 = 150 \pm 34 \text{ cm}^{-1}$. According to these data, the *s-trans* conformer is the predominant form at ambient temperature, and the enthalpy difference between the *s-trans* and the *s-cis* conformer in the gas phase is 280 cm^{-1} . The relative intensities of the Raman bands as a function of the temperature afford an enthalpy difference of 172 cm^{-1} for the liquid.

Raman spectroscopy

The determination of ΔH and ΔS from Raman intensities is analogous to the corresponding method used in IR spectroscopy, which is described in more detail in the preceding section.

Instead of measuring the absorption A_k of a vibrational band k , the Raman intensity I_k is determined. Using the restrictions (see preceding section)

$$S_{\text{gauche}}(T)/S_{\text{trans}}(T) = \text{const.}; \quad dS_{\text{gauche}}(T)/dT \neq 0; \quad dS_{\text{trans}}(T)/dT \neq 0 \quad (6.8-29)$$

where S_{gauche} and S_{trans} are the Raman scattering coefficients of the *gauche* and the *trans* isomer, respectively, we obtain

$$\ln [I_{\text{gauche}}/I_{\text{trans}}] = -\Delta H/R \cdot 1/T + \Delta S/R + \ln [S_{\text{gauche}}/S_{\text{trans}}] \quad (6.8-30)$$

Plotting the left-hand side of this equation against $1/T$, the slope a and the ordinate intercept b of the resulting straight line may be used to calculate ΔH and ΔS :

$$\Delta H = -R \cdot a = -R[d \ln (I_{\text{gauche}}/I_{\text{trans}})/d(1/T)] \quad (6.8-31)$$

$$\Delta S = +R \cdot [b - \ln (S_{\text{gauche}}/S_{\text{trans}})] \quad (6.8-32)$$

By evaluating the integrated intensities of the Raman bands at 551 and 659 cm^{-1} , attributed to the C-Br stretching vibrations of the *gauche* and the *trans* isomer of 1,2-dibromoethane, Spiekermann et al. (1976) obtained the following values for ΔH and ΔS :

$$\Delta H = 2.75 \pm 0.15 \text{ kJ/mol}$$

$$\Delta S = 8.03 \pm 0.84 \text{ J/(mole} \cdot \text{K)}$$

The ΔS value was determined on the assumption that the Raman scattering coefficients S_{gauche} and S_{trans} are independent of the temperature.

Scherer and Snyder (1980) investigated the low-frequency Raman spectra of liquid n-alkanes. The highly temperature dependent intensities of the longitudinal acoustic modes of the n-alkanes ($n = 11 \dots 14$) were measured at different temperatures and were used to determine an average energy difference of $2125 \pm 209 \text{ kJ/mol}$ between the *trans* and *gauche* conformation of the C-C bond.

These results show that Raman spectroscopy may be used to quantify the thermodynamic properties of molecules with at least the same accuracy as IR spectroscopy. However, the main advantage of Raman spectroscopy lies in the possibility of determining the sample temperature of precisely those molecules which are excited by the laser beam from Stokes/anti-Stokes intensity ratios. Furthermore, investigations of aqueous solutions (such as biological samples) are expected to create less technical problems than IR window materials.

6.8.5.4 Unstable substances

Highly reactive molecules, which are transient or nonexistent under normal conditions, must be studied at low temperature. The technique of trapping species as isolated entities

in an inert solid and subsequently investigating them by vibrational spectroscopy is described in Sec. 4.4. The present section deals with substances that can be handled in liquid solutions at moderately low temperature. An interesting aspect is the possibility of observing the vibrational spectra of carbocations or protonated compounds in order to obtain structural information or to gain deeper insight into the basic steps of acid catalyzed reactions.

A couple of years ago, mixtures of $\text{HSO}_3\text{F-SbF}_5$ and related systems, so-called *magic acids*, attracted interest in their role as solvent systems capable of stabilizing carbocations and conjugated acids of very weak organic bases (for a review see Olah, 1973). Spectroscopic methods, i.e., NMR spectroscopy, are widely used to investigate such compounds. Due to the fact that considerable overlapping with solvent bands is to be expected, vibrational spectroscopy is less commonly used. However, it can be useful on occasion, as shown below. Since most of the window materials used in IR spectroscopy are damaged by magic acids, only Raman spectroscopy has met with success.

6.8.5.4.1 Carbocations

Olah et al. (1971) reported the vibrational spectrum of the t-butyl cation, which is stable in magic acid at low temperature. They assigned the vibrational frequencies by com-

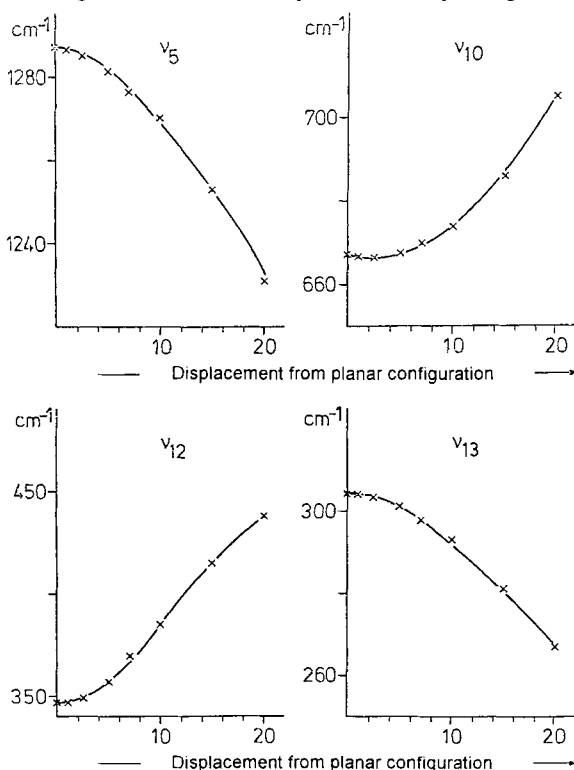


Figure 6.8-22 Calculated frequency dependence of some skeleton vibrations of the $\text{C}(\text{CH}_3)_3$ cation on the displacements of the methyl groups from the 'planar' configuration.

paring them to those of the $\text{B}(\text{CH}_3)_3$ molecule. Based on this comparison, the authors arrived at a planar configuration of the t-butyl-cation. This assumption was confirmed by Spiekermann (1975), who determined the dependence of the skeleton vibrations of $\text{C}(\text{CH}_3)_3$ from the displacement of the methyl groups from the planar configuration by a normal coordinate calculation. The expected frequency variations in this calculation are shown in Fig. 6.8-22. There is no evidence of such variations in the vibrational spectrum of the t-butyl-cation obtained by Olah, which suggests a planar configuration and therefore confirms the 'classical' nature of the ion.

6.8.5.4.2 Protonated organic compounds

These molecules are known as intermediates in acid catalyzed reactions. To understand the mechanism of these reactions, both the position of the acid-base equilibrium and the location of the proton in the first step of the reaction must be known. Dimethyl sulfoxide (DMSO) contains two potentially basic centers in the S=O group. Consequently, either the oxygen atom or the sulfur atom may be protonated. Investigations of the actual location of the proton in protonated DMSO by NMR spectroscopy led to contradictory results. Analysis of the vibrational spectra ought to clarify the problem. IR spectroscopy is better suited to the detection of OH groups, while Raman spectroscopy is used to advantage to detect SH groups (Schrader, 1973). As mentioned above, recording the IR spectra of superacids creates considerable experimental difficulties. Besides, superacids themselves also contain OH groups. Spiekermann and Schrader (1977) investigated the Raman spectra of approx. 30 mol% solutions of DMSO and of dimethyl sulfide (DMS) in 100% magic acid ($\text{HSO}_3\text{F-SbF}_5$, 1:1). The spectra of the respective protonated species show new bands and/or band shifts relative to those of the pure compounds DMSO and DMS and those of the pure superacid (Fig. 6.8-23). The region of the skeletal vibrations below 1500 cm^{-1} is difficult to interpret, since the signals of the protonated species in this region are superimposed by bands of the pure superacid and of the complex ions which are present in solutions of this type. For compounds with SH groups, the signal of the S-H stretching vibration appears at 2550 to 2600 cm^{-1} . In the spectrum of protonated DMS, the band is observed quite clearly at 2550 cm^{-1} (Fig. 6.8-23c), while the spectrum of protonated DMSO shows no bands in this region (Fig. 6.8-23e). This is a definite indication of the absence of SH groups in the protonated dimethyl sulfoxide and thus a proof that the protonation occurs at the oxygen atom. Bertoluzza et al. (1981) supported this result by suggesting that the oxygen atom in DMSO is the basic center of the molecule.

It is known that nucleophilic substitution of alcohols in strong acids leads to cleavage of the C–O bond, while the OH group is protonated to form an oxonium ion which can easily be displaced by a nucleophile. The first spectroscopic evidence of a protonated alcohol was reported in 1961. It was detected by NMR spectroscopic investigation of a solution of $\text{C}_2\text{H}_5\text{OH}$ in $\text{BF}_3\text{-HF}$ (McLean and Mackor, 1961). This paper, together with a corresponding publication by Olah et al. (1967), shows that aliphatic alcohols are protonated at the oxygen atom. At low temperature, the protonated compounds are stable enough for spectroscopic investigation. Fig. 6.8-24 shows the Raman spectra of pure CH_3OH and CH_3OH in magic acid ($\text{HSO}_3\text{F-SbF}_5$, 1:1) at 193 K. The band at 970 cm^{-1} in

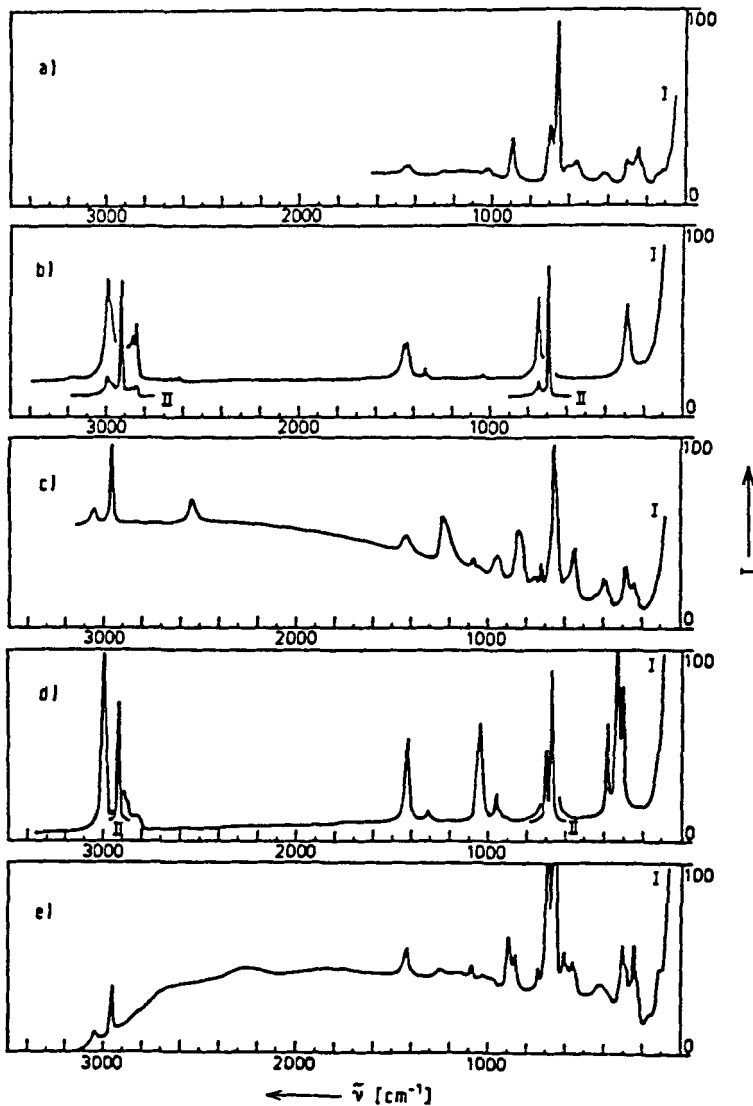


Figure 6.8-23 Raman spectra of a) Magic acid (MA) b) CH_3S (2) c) 30mol% (2) in MA d) $\text{CH}_3=\text{SO}$ (1) e) 30mol% (1) in MA.

the spectrum of the protonated compound is attributed to the $\text{C}-\text{OH}_2^+$ stretching vibration. The shift of the C-H stretching vibrations toward higher wavenumbers can be explained by a change in the hybridization of the carbon atom from sp^3 to sp^2 , which increases the force constant of the C-H bond relative to that of pure methanol (Spiekermann, 1975).

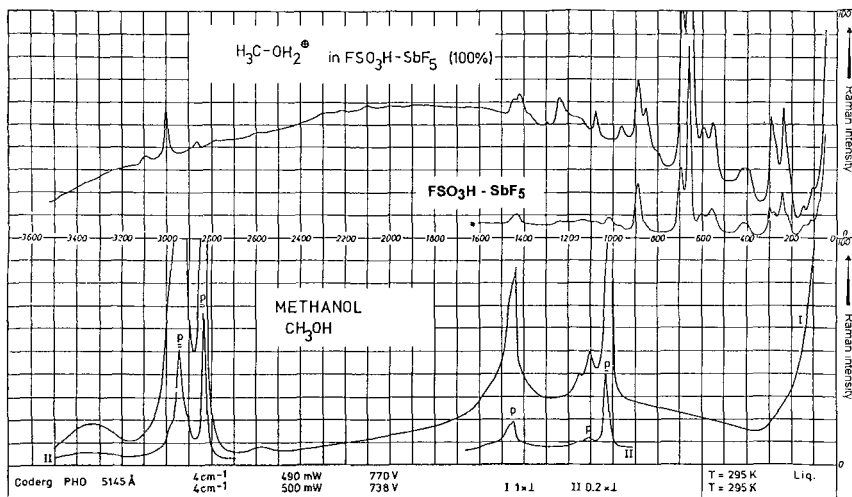
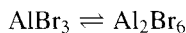


Figure 6.8-24 Raman spectra of pure CH_3OH and CH_3OH in Magic acid.

6.8.5.5 Intermolecular and intramolecular interactions

AlBr_3 is an example of a molecule which exists as a monomer at 880°C and dimerizes at low temperature:



The amount of dimer increases as the temperature decreases. There is a large number of other molecules which undergo similar structural changes. Since vibrational spectra are governed by the symmetry of the investigated compounds, IR and Raman spectroscopy are powerful tools for the study of structural changes. In the case of AlBr_3 it was possible to calculate the equilibrium constant for the dissociation reaction and hence the enthalpy of dissociation. The obtained value was

$$\Delta H = -96 \pm 1.5 \text{ kJ/mol}$$

(Long, 1977; Beattie and Horder, 1969).

Comparing the vapor phase Raman spectra of phosphorus(V)chloride with the spectrum of the solid compound, which is obtained by rapidly cooling the vapor to the temperature of liquid N_2 , shows that in the vapor phase and in the metastable solid phase the compound exists in the molecular form PCl_5 . The stable solid phase, on the other hand, has the ionic structure $\text{PCl}_4^+\text{PCl}_6^-$ (Long, 1977; Ozin, 1971).

In the solid state, SnCl_2 exhibits a polymeric structure. The spectrum of the compound in the vapor phase at 650°C can be attributed to a monomeric non-linear structure (Long, 1977, Perry, 1969).

In the case of organic substances, phenomena such as the formation of hydrogen bonds are reflected in the respective IR and Raman spectra. The most frequent partners in hydrogen bonding are oxygen, nitrogen, and halogens. In acetic acid, two molecules of the same species are self-associated through intermolecular hydrogen bonds. In the IR spectrum of acetic acid in the gaseous state at 430 K, the 'free' OH stretching frequency is observed at 3583 cm^{-1} . In the acetic acid crystal near 90 K, its frequency shifts to 2875 cm^{-1} . These frequency shifts can be attributed to kinematic effects and to changes of force constants due to electronic effects of hydrogen bonding (Novak, 1979).

Kirchner and Richter (1972) examined a series of phenyl substituted aliphatic alcohols whose OH stretching vibrational band splits in non-polar solvents. They also investigated the gaseous state, where two band maxima appeared in the spectral range of the OH fundamentals. The temperature dependence of the relative intensities of the double band, investigated in the range from 100 to 200 °C, in connection with the results obtained in non-polar solvents lead to the conclusion that intramolecular hydrogen bonds are formed. The bond energies of the hydrogen bonds of 2-phenylethanol and 2-phenylpropanol were found to be 11 and $12 \pm 1.5\text{ kJ/mol}$, respectively.

It is generally possible to study the effects of changes of state on the intramolecular and intermolecular forces in inorganic and organic compounds by investigating the variations in the vibrational spectra with decreasing temperature as the gas phase changes to the liquid and then to the solid state.

6.8.5.6 Macromolecules

Vibrational spectroscopy provides information on the chemical composition of polymers, the geometric arrangement of their atoms in space, and the interatomic forces which result from valence bonding and intermolecular interactions.

Sears et al. (1981) obtained the Raman spectrum of thermally polymerizing styrene as a function of time in the temperature range between 70 and 100 °C. The intensities of the C=C stretching vibration at 1631 cm^{-1} and of the C-H bending vibration of the vinyl groups at 1415 cm^{-1} indicate the proceeding conversion from monomer to polymer. The authors suggest that during polymerization the polymer is uniformly distributed throughout the sample and that the rate of polymerization at 100 °C is about four times as high as that at 70 °C.

Petcavich et al. (1978) employed IR subtraction techniques to elucidate the mechanism of the oxidative degradation of polychloroprenes at 60 °C. The spectra were taken at $60 \pm 2\text{ }^{\circ}\text{C}$. The results lead to the conclusion that 1,2- and 3,4-structural irregularities are involved in the initial stage of the thermal oxidation of these compounds at 60 °C. In addition, a simple free radical mechanism seems to be consistent with the experimental results. The observed results suggest that polychloroprenes may be stabilized towards oxidative degradation by eliminating the 1,2- and 3,4-structures by chemical modification of the polymer after synthesis.

6.8.5.7 Coupling of thermogravimetric analysis with IR spectroscopy

Thermogravimetric analysis (TGA) is a successful and widely employed technique of measuring the change of weight of a sample as a function of the temperature; whereas IR spectroscopy has been successfully employed to identify gaseous samples. Recent publications (Wieboldt et al. (1988); Belz (1989) demonstrate that a combination of these two techniques allows complete characterization of materials in terms of thermal stability and decomposition mechanisms.

As in a GC-IR experiment, all spectral information is displayed during the run (Fig. 6.8-25) and all spectra are stored on the hard disc for post running processing. The Gram Schmidt reconstruction of the spectral data can be analyzed in order to obtain the components which are cleaved during decomposition of the sample. Library search may fail in the case of technical products due to the more complex composition of the evolving gases, which, for example, contain monomers as well as additional compounds, such as plasticizers, etc. The use of special TGA/FT-IR libraries should be very helpful and is recommended therefore.

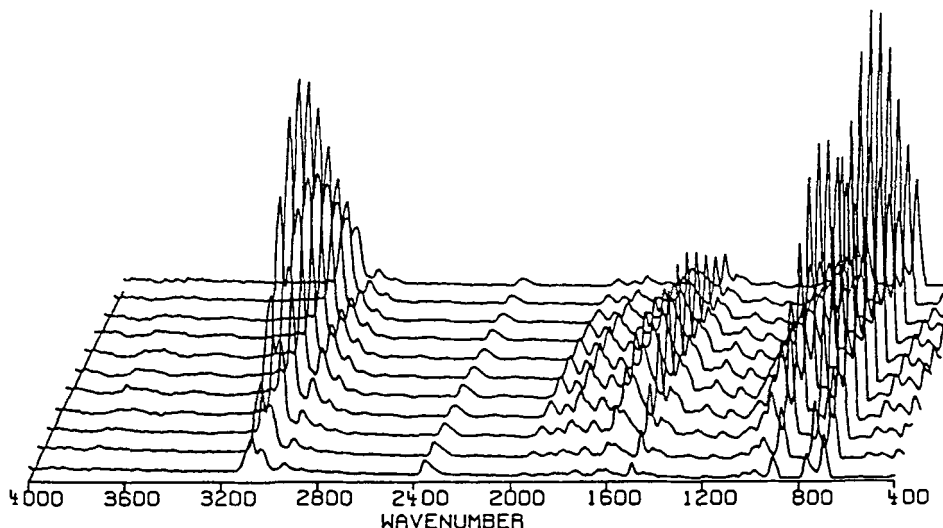


Figure 6.8-25 Spectral information displayed during the run of the TA-IR experiment.

Appendix

7 Character tables

Applications of symmetry properties of molecules and crystals are discussed at several places in this book. In the introduction (Sec. 2.7) basic literature has been mentioned. In this Section the most important tool, the character tables are reproduced – with some additions – from a booklet by Atkins, Child and Phillips (1970) *Tables for Group Theory* by permission of Oxford University Press.

In addition the reader may find tables with selection rules for the Resonance Raman and Hyper Raman Effect in the book of Weidlein et al. (1982). Special discussions about the basics of the application of group theory to molecular vibrations are given in the books of Herzberg (1945), Michl and Thulstrup (1986), Colthup et al. (1990) and Ferraro and Nakamoto (1994). Herzberg (1945) and Brandmüller and Moser (1962) describe the calculation of thermodynamical functions (see also textbooks of physical chemistry). For the calculation of the rotational contribution of the partition function a symmetry number has to be taken into account. The following tables give this number in \bigcirc .

Schoenflies symbols are given for all point groups. Hermann/Mauguin symbols are given for the 32 crystallographic point groups.

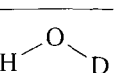
For some point groups of planar molecules, C_{2v} , D_{2h} , D_{4h} , and D_{6h} , it is necessary in order to avoid ambiguity to standardize the definition of the Cartesian coordinate axes (Mulliken, 1955):

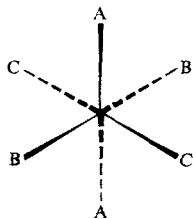
For planar molecules of the point group C_{2v} the z -axis is the axis of symmetry, the x -axis is always chosen perpendicular to the plane of the molecule.

For planar D_{2h} molecules the x -axis is to be chosen perpendicular to the plane of the molecule and the z -axis so that it passes through the greatest number of atoms or, if this rule is not decisive, so that it cuts the greatest number of bonds.

For planar D_{4h} and D_{6h} molecules the C_2 and the C'_2 axes as well as the σ_v and σ_d planes are chosen as follows: (a) the C_2 axes shall pass through the greater number of atoms or, (b), in case specification (a) is not decisive, shall intersect the greater number of bonds. The σ_v and σ_d classes of operations should be distinguished by the specification that, (a), the σ_v planes shall pass through the greater number of those atoms which are in the square or hexagonal (or similar) array, or, (b), in case specification (a) is not decisive, shall intersect the greater number of bonds among such atoms. The location of the σ_v planes are thus similar to those of the C_2 axes.

1. The Groups C_1 , C_s , C_i

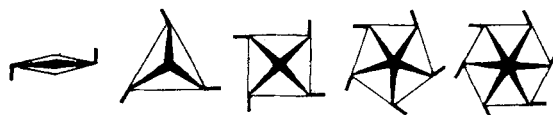
C_1	E	CFClBrI	①
(1)			
<hr/>			
A	1		
<hr/>			
			
$C_s = C_h$	E	σ_h	①
(m)			
			
A'	1	1	x, y, R_z
			$x^2, y^2,$
			z^2, xy
A''	1	-1	z, R_x, R_y
			yz, xz
<hr/>			



$C_i = S_2$	E	i	HClFC-CHClF	①
(I)				
<hr/>				
A_g	1	1	R_x, R_y, R_z	$x^2, y^2, z^2,$
				xy, xz, yz
A_u	1	-1	x, y, z	
<hr/>				

2. The Groups C_n ($n = 2, 3, \dots, 8$)

C_2	E	C_2	H_2O_2	②
(2)				
<hr/>				
A	1	1	z, R_z	x^2, y^2, z^2, xy
B	1	-1	x, y, R_x, R_y	yz, xz
<hr/>				



C_3	E	C_3	C_3^2	$\varepsilon = \exp(2\pi i/3)$			(3)
(3)				z, R_z		$x^2 + y^2, z^2$	
A	1	1	1				
E	$\begin{cases} 1 & \varepsilon \\ 1 & \varepsilon^* \end{cases}$	$\begin{cases} \varepsilon^* \\ \varepsilon \end{cases}$		$(x, y)(R_x, R_y)$		$(x^2 - y^2, xy)(yz, xz)$	

C_4	E	C_4	C_2	C_4^3				(4)
(4)					z, R_z		$x^2 + y^2, z^2$	
A	1	1	1	1				
B	1	-1	1	-1			$x^2 - y^2, xy$	
E	$\begin{cases} 1 & i \\ 1 & -i \end{cases}$	$\begin{cases} -1 & -i \\ -1 & i \end{cases}$			$(x, y)(R_x, R_y)$		(yz, xz)	

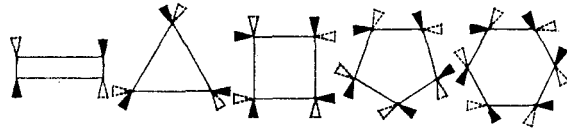
C_5	E	C_5	C_5^2	C_5^3	C_5^4	$\varepsilon = \exp(2\pi i/5)$			(5)
A	1	1	1	1	1	z, R_z		$x^2 + y^2, z^2$	
E_1	$\begin{cases} 1 & \varepsilon \\ 1 & \varepsilon^* \end{cases}$	$\begin{cases} \varepsilon^2 & \varepsilon^{*2} \\ \varepsilon^{*2} & \varepsilon^2 \end{cases}$	$\begin{cases} \varepsilon^* & \varepsilon \\ \varepsilon & \varepsilon^* \end{cases}$			$(x, y)(R_x, R_y)$		(yz, xz)	
E_2	$\begin{cases} 1 & \varepsilon^2 \\ 1 & \varepsilon^{*2} \end{cases}$	$\begin{cases} \varepsilon^* & \varepsilon \\ \varepsilon & \varepsilon^* \end{cases}$	$\begin{cases} \varepsilon & \varepsilon^{*2} \\ \varepsilon^{*2} & \varepsilon \end{cases}$					$(x^2 - y^2, xy)$	

C_6	E	C_6	C_3	C_2	C_3^2	C_6^5	$\varepsilon = \exp(2\pi i/6)$			(6)
A	1	1	1	1	1	1	z, R_z		$x^2 + y^2, z^2$	
B	1	-1	1	-1	1	-1				
E_1	$\begin{cases} 1 & \varepsilon \\ 1 & \varepsilon^* \end{cases}$	$\begin{cases} -\varepsilon^* & -1 \\ -\varepsilon & -1 \end{cases}$	$\begin{cases} -\varepsilon & \varepsilon^* \\ -\varepsilon^* & \varepsilon \end{cases}$				(x, y)		(xz, yz)	
E_2	$\begin{cases} 1 & -\varepsilon^* \\ 1 & -\varepsilon \end{cases}$	$\begin{cases} -\varepsilon & 1 \\ -\varepsilon^* & 1 \end{cases}$	$\begin{cases} -\varepsilon^* & -\varepsilon \\ -\varepsilon & -\varepsilon^* \end{cases}$						$(x^2 - y^2, xy)$	

C_7	E	C_7	C_7^2	C_7^3	C_7^4	C_7^5	C_7^6	$\varepsilon = \exp(2\pi i/7)$			(7)
A	1	1	1	1	1	1	1	z, R_z		$x^2 + y^2, z^2$	
E_1	$\begin{cases} 1 & \varepsilon \\ 1 & \varepsilon^* \end{cases}$	$\begin{cases} \varepsilon^2 & \varepsilon^3 \\ \varepsilon^{*2} & \varepsilon^{*3} \end{cases}$	$\begin{cases} \varepsilon^3 & \varepsilon^{*3} \\ \varepsilon^2 & \varepsilon \end{cases}$	$\begin{cases} \varepsilon^{*3} & \varepsilon^{*2} \\ \varepsilon^3 & \varepsilon^2 \end{cases}$	$\begin{cases} \varepsilon^{*2} & \varepsilon^* \\ \varepsilon^2 & \varepsilon \end{cases}$	$\begin{cases} \varepsilon^* & \varepsilon \\ \varepsilon & \varepsilon^* \end{cases}$		(x, y)		(xz, yz)	
E_2	$\begin{cases} 1 & \varepsilon^2 \\ 1 & \varepsilon^{*2} \end{cases}$	$\begin{cases} \varepsilon^{*3} & \varepsilon^* \\ \varepsilon^3 & \varepsilon \end{cases}$	$\begin{cases} \varepsilon^* & \varepsilon \\ \varepsilon & \varepsilon^* \end{cases}$	$\begin{cases} \varepsilon & \varepsilon^3 \\ \varepsilon^3 & \varepsilon^2 \end{cases}$	$\begin{cases} \varepsilon^3 & \varepsilon^{*3} \\ \varepsilon^{*3} & \varepsilon^2 \end{cases}$	$\begin{cases} \varepsilon^{*3} & \varepsilon^2 \\ \varepsilon^2 & \varepsilon \end{cases}$				$(x^2 - y^2, xy)$	
E_3	$\begin{cases} 1 & \varepsilon^3 \\ 1 & \varepsilon^{*3} \end{cases}$	$\begin{cases} \varepsilon^3 & \varepsilon \\ \varepsilon & \varepsilon^{*2} \end{cases}$	$\begin{cases} \varepsilon^* & \varepsilon^2 \\ \varepsilon^2 & \varepsilon \end{cases}$	$\begin{cases} \varepsilon^2 & \varepsilon^{*2} \\ \varepsilon^{*2} & \varepsilon \end{cases}$	$\begin{cases} \varepsilon^{*2} & \varepsilon \\ \varepsilon & \varepsilon^3 \end{cases}$	$\begin{cases} \varepsilon & \varepsilon^3 \\ \varepsilon^3 & \varepsilon \end{cases}$					

C_8	E	C_8	C_4	C_2	C_4^3	C_8^3	C_8^5	C_8^7	$\varepsilon = \exp(2\pi i/8)$	$\textcircled{8}$
A	1	1	1	1	1	1	1	1	z, R_z	$x^2 + y^2, z^2$
B	1	-1	1	1	1	-1	-1	-1		
E_1	$\begin{cases} 1 & \varepsilon \\ 1 & \varepsilon^* \end{cases}$	$\begin{cases} i \\ -i \end{cases}$	$\begin{cases} -1 \\ -1 \end{cases}$	$\begin{cases} -1 \\ i \end{cases}$	$\begin{cases} -\varepsilon^* \\ -\varepsilon \end{cases}$	$\begin{cases} -\varepsilon \\ -\varepsilon^* \end{cases}$	$\begin{cases} \varepsilon^* \\ \varepsilon \end{cases}$		(x, y) (R_x, R_y)	(xz, yz)
E_2	$\begin{cases} 1 & i \\ 1 & -i \end{cases}$	$\begin{cases} -1 \\ -1 \end{cases}$	$\begin{cases} 1 \\ 1 \end{cases}$	$\begin{cases} -1 \\ -1 \end{cases}$	$\begin{cases} -i \\ i \end{cases}$	$\begin{cases} i \\ -i \end{cases}$	$\begin{cases} -i \\ i \end{cases}$			$(x^2 - y^2, xy)$
E_3	$\begin{cases} 1 & -\varepsilon \\ 1 & -\varepsilon^* \end{cases}$	$\begin{cases} i \\ -i \end{cases}$	$\begin{cases} -1 \\ -1 \end{cases}$	$\begin{cases} -i \\ i \end{cases}$	$\begin{cases} \varepsilon^* \\ \varepsilon \end{cases}$	$\begin{cases} \varepsilon \\ \varepsilon^* \end{cases}$	$\begin{cases} -\varepsilon^* \\ -\varepsilon \end{cases}$			

3. The Groups D_n ($n = 2, 3, 4, 5, 6$)



D_2 (222)	E	$C_2(z)$	$C_2(y)$	$C_2(x)$	Twisted Ethene	$\textcircled{4}$
A	1	1		1		x^2, y^2, z^2
B_1	1	1	-1	-1	z, R_z	xy
B_2	1	-1	1	-1	y, R_y	xz
B_3	1	-1	-1	1	x, R_x	yz

D_3 (32)	E	$2C_3$	$3C_2$	Twisted Ethane	$\textcircled{6}$
A_1	1	1	1		$x^2 + y^2, z^2$
A_2	1	1	-1	z, R_z	
E	2	-1	0	$(x, y)(R_x, R_y)$	$(x^2 - y^2, xy)(xz, yz)$

D_4 (422)	E	$2C_4$	$C_2 (= C_4^2)$	$2C'_2$	$2C''_2$	$\textcircled{8}$
A_1	1	1	1	1	1	$x^2 + y^2, z^2$
A_2	1	1	1	-1	-1	z, R_z
B_1	1	-1	1	1	-1	$x^2 - y^2$
B_2	1	-1	1	-1	1	xy
E	2	0	-2	0	0	$(x, y)(R_x, R_y)$ (xz, yz)

D_5	E	$2C_5$	$2C_5^2$	$5C_2$		(10)
-------	-----	--------	----------	--------	--	------

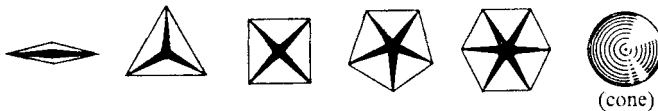
A_1	1	1	1	1		$x^2 + y^2, z^2$
A_2	1	1	1	-1	z, R_z	
E_1	2	$2 \cos 72^\circ$	$2 \cos 144^\circ$	0	$(x, y)(R_x, R_y)$	(xz, yz)
E_2	2	$2 \cos 144^\circ$	$2 \cos 72^\circ$	0		$(x^2 - y^2, xy)$

D_6	E	$2C_6$	$2C_3$	C_2	$3C'_2$	$3C''_2$		(12)
-------	-----	--------	--------	-------	---------	----------	--	------

(622)

A_1	1	1	1	1	1	1		$x^2 + y^2, z^2$
A_2	1	1	1	1	-1	-1	z, R_z	
B_1	1	-1	1	-1	1	-1		
B_2	1	-1	1	-1	-1	1		
E_1	2	1	-1	-2	0	0	$(x, y)(R_x, R_y)$	(xz, yz)
E_2	2	-1	-1	2	0	0		$(x^2 - y^2, xy)$

4. The Groups C_{nv} ($n = 2, 3, 4, 5, 6$)



(pyramid)

C_{2v}	E	C_2	$\sigma_v(xz)$	$\sigma'_v(yz)$	H_2O		(2)
	(2mm)						
A_1	1	1	1	1	z	x^2, y^2, z^2	
A_2	1	1	-1	-1	R_z	xy	
B_1	1	-1	1	-1	x, R_y	xz	
B_2	1	-1	-1	1	y, R_x	yz	

C_{3v}	E	$2C_3$	$3\sigma_v$	NH_3		(3)
----------	-----	--------	-------------	--------	--	-----

(3m)

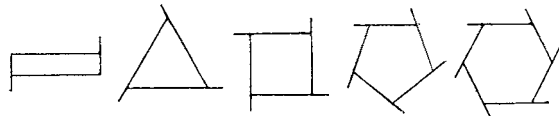
A_1	1	1	1	z		$x^2 + y^2, z^2$
A_2	1	1	-1	R_z		
E	2	-1	0	$(x, y)(R_x, R_y)$	$(x^2 - y^2, xy)(xz, yz)$	

C_{4v} (4mm)	E	$2C_4$	C_2	$2\sigma_v$	$2\sigma_d$	XeOF ₄	④
A_1	1	1	1	1	1	z	$x^2 + y^2, z^2$
A_2	1	1	1	-1	-1	R_z	
B_1	1	-1	1	1	-1		$x^2 - y^2$
B_2	1	-1	1	-1	1		xy
E	2	0	-2	0	0	$(x, y)(R_x, R_y)$	(xz, yz)

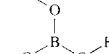
C_{5v}	E	$2C_5$	$2C_5^2$	$5\sigma_v$			⑤
A_1	1	1		1	1	z	$x^2 + y^2, z^2$
A_2	1	1		1	-1	R_z	
E_1	2	$2 \cos 72^\circ$	$2 \cos 144^\circ$	0	$(x, y)(R_x, R_y)$	(xz, yz)	
E_2	2	$2 \cos 144^\circ$	$2 \cos 72^\circ$	0			$(x^2 - y^2, xy)$

C_{6v} (6mm)	E	$2C_6$	$2C_3$	C_2	$3\sigma_v$	$3\sigma_d$		⑥
A_1	1	1		1	1	1	z	$x^2 + y^2, z^2$
A_2	1	1		1	-1	-1	R_z	
B_1	1	-1		-1	1	-1		
B_2	1	-1		-1	-1	1		
E_1	2	1	-1	-2	0	0	$(x, y)(R_x, R_y)$	(xz, yz)
E_2	2	-1	-1	2	0	0		$(x^2 - y^2, xy)$

5. The Groups C_{nh} ($n = 2, 3, 4, 5, 6$)



C_{2h} (2/m)	E	C_2	i	σ_h	H-C=C-F	②
A_g	1	1	1	1	R_z	x^2, y^2, z^2, xy
B_g	1	-1	1	-1	R_x, R_y	xz, yz
A_u	1	1	-1	-1	z	
B_u	1	-1	-1	1	x, y	

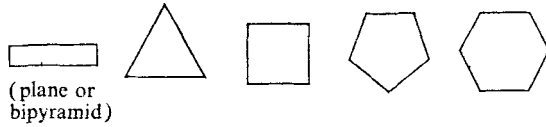
C_{3h}	E	C_3	C_3^2	σ_h	S_3	S_3^5	$\varepsilon = \exp(2\pi i/3)$
(6)							
A'	1	1	1	1	1	1	$x^2 + y^2, z^2$
E'	$\begin{cases} 1 & \varepsilon & \varepsilon^* \\ 1 & \varepsilon^* & \varepsilon \end{cases}$	$\begin{cases} 1 & \varepsilon & \varepsilon^* \\ 1 & \varepsilon^* & \varepsilon \end{cases}$	$\begin{cases} 1 & \varepsilon & \varepsilon^* \\ 1 & \varepsilon^* & \varepsilon \end{cases}$	$\begin{cases} 1 & \varepsilon & \varepsilon^* \\ 1 & \varepsilon^* & \varepsilon \end{cases}$	(x, y)	$(x^2 - y^2, xy)$	
A''	1	1	1	-1	-1	-1	z
E''	$\begin{cases} 1 & \varepsilon & \varepsilon^* \\ 1 & \varepsilon^* & \varepsilon \end{cases}$	$\begin{cases} -1 & -\varepsilon & -\varepsilon^* \\ -1 & -\varepsilon^* & -\varepsilon \end{cases}$	$\begin{cases} -1 & -\varepsilon & -\varepsilon^* \\ -1 & -\varepsilon^* & -\varepsilon \end{cases}$	$\begin{cases} -1 & -\varepsilon & -\varepsilon^* \\ -1 & -\varepsilon^* & -\varepsilon \end{cases}$	(R_x, R_y)	(xz, yz)	

C_{4h} (4/m)	E	C_4	C_2	C_4^3	i	S_4^3	σ_h	S_4	(4)
A_g	1	1	1	1	1	1	1	R_z	$x^2 + y^2, z^2$
B_g	1	-1	1	-1	1	-1	1	$-R_z$	$x^2 - y^2, xy$
E_g	{ 1 1 } -i -1 -i i 1 -i -1 i }	{ 1 1 } i -1 i -i -1 -i -1 i }	{ 1 1 } -1 -1 1 -i -1 -1 -1 i }	{ 1 1 } -1 -1 -1 1 -i -1 -1 i }	(R_x, R_y)	(xz, yz)			
A_u	1	1	1	1	-1	-1	-1	-1	z
B_u	1	-1	1	-1	-1	1	-1	1	
E_u	{ 1 1 } i -1 -i -1 -i -1 1 i }	{ 1 1 } i -1 -i -1 -i -1 1 i }	{ 1 1 } -1 -1 1 -i -1 -1 -1 i }	{ 1 1 } -1 -1 -1 1 -i -1 -1 i }	(x, y)				

C_{5h}	E	C_5	C_5^2	C_5^3	C_5^4	σ_h	S_5	S_5^7	S_5^3	S_5^9	$\varepsilon = \exp(2\pi i/5)$	(5)
A'	1	1	1	1	1	1	1	1	1	1	R_z	$x^2 + y^2, z^2$
E'_1	$\begin{cases} 1 & \varepsilon \\ 1 & \varepsilon^* \end{cases}$	$\begin{cases} \varepsilon^2 & \varepsilon^{*2} \\ \varepsilon^{*2} & \varepsilon^2 \end{cases}$	$\begin{cases} \varepsilon^* & \varepsilon \\ \varepsilon & \varepsilon^* \end{cases}$	$\begin{cases} 1 & 1 \\ 1 & 1 \end{cases}$	$\begin{cases} \varepsilon & \varepsilon^* \\ \varepsilon^* & \varepsilon \end{cases}$	$\begin{cases} \varepsilon^2 & \varepsilon^{*2} \\ \varepsilon^{*2} & \varepsilon^2 \end{cases}$	$\begin{cases} \varepsilon^2 & \varepsilon \\ \varepsilon & \varepsilon^2 \end{cases}$	$\begin{cases} -\varepsilon^* & \varepsilon \\ \varepsilon & -\varepsilon^* \end{cases}$	$\begin{cases} 1 & 1 \\ 1 & 1 \end{cases}$	$\begin{cases} R_z & (x, y) \\ (x, y) & (x^2 - y^2, xy) \end{cases}$		
E'_2	$\begin{cases} 1 & \varepsilon^2 \\ 1 & \varepsilon^{*2} \end{cases}$	$\begin{cases} \varepsilon^* & \varepsilon \\ \varepsilon & \varepsilon^* \end{cases}$	$\begin{cases} \varepsilon & \varepsilon^2 \\ \varepsilon^2 & \varepsilon \end{cases}$	$\begin{cases} \varepsilon^{*2} & 1 \\ 1 & \varepsilon^{*2} \end{cases}$	$\begin{cases} \varepsilon^2 & \varepsilon^* \\ \varepsilon^* & \varepsilon \end{cases}$	$\begin{cases} \varepsilon & \varepsilon^* \\ \varepsilon^* & \varepsilon \end{cases}$	$\begin{cases} \varepsilon & \varepsilon^* \\ \varepsilon^* & \varepsilon^2 \end{cases}$	$\begin{cases} 1 & 1 \\ 1 & 1 \end{cases}$	$\begin{cases} x^2 - y^2 & (x^2 - y^2, xy) \\ (x^2 - y^2, xy) & (xz, yz) \end{cases}$			
A''	1	1	1	1	1	-1	-1	-1	-1	-1	z	
E''_1	$\begin{cases} 1 & \varepsilon \\ 1 & \varepsilon^* \end{cases}$	$\begin{cases} \varepsilon^2 & \varepsilon^{*2} \\ \varepsilon^{*2} & \varepsilon^2 \end{cases}$	$\begin{cases} \varepsilon^{*2} & \varepsilon^* \\ \varepsilon^2 & \varepsilon \end{cases}$	$\begin{cases} \varepsilon^* & -1 \\ \varepsilon & -1 \end{cases}$	$\begin{cases} \varepsilon & -\varepsilon \\ -\varepsilon & -\varepsilon^* \end{cases}$	$\begin{cases} -\varepsilon^2 & -\varepsilon^{*2} \\ -\varepsilon^{*2} & -\varepsilon^2 \end{cases}$	$\begin{cases} -\varepsilon^{*2} & -\varepsilon^* \\ -\varepsilon^2 & -\varepsilon \end{cases}$	$\begin{cases} -\varepsilon^* & -\varepsilon \\ -\varepsilon & -\varepsilon^2 \end{cases}$	$\begin{cases} 1 & 1 \\ 1 & 1 \end{cases}$	$\begin{cases} (R_x, R_y) & (R_x, R_y) \\ (R_x, R_y) & (xz, yz) \end{cases}$		
E''_2	$\begin{cases} 1 & \varepsilon^2 \\ 1 & \varepsilon^{*2} \end{cases}$	$\begin{cases} \varepsilon^* & \varepsilon \\ \varepsilon & \varepsilon^* \end{cases}$	$\begin{cases} \varepsilon & \varepsilon^2 \\ \varepsilon^2 & \varepsilon \end{cases}$	$\begin{cases} \varepsilon^{*2} & -1 \\ -1 & \varepsilon^{*2} \end{cases}$	$\begin{cases} -\varepsilon^2 & -\varepsilon^* \\ -\varepsilon^* & -\varepsilon \end{cases}$	$\begin{cases} -\varepsilon & -\varepsilon^* \\ -\varepsilon^* & -\varepsilon^2 \end{cases}$	$\begin{cases} -\varepsilon & -\varepsilon^2 \\ -\varepsilon^2 & -\varepsilon \end{cases}$	$\begin{cases} 1 & 1 \\ 1 & 1 \end{cases}$	$\begin{cases} (xz, yz) & (xz, yz) \\ (xz, yz) & (xz, yz) \end{cases}$			

C_{6h} (6/m)	E	C_6	C_3	C_2	C_3^2	C_6^5	i	S_3^5	S_6^5	σ_h	S_6	S_3	$\varepsilon = \exp(2\pi i/6)$	⑥
A_g	1	1	1	1	1	1	1	1	1	1	1	1	R_z	$x^2 + y^2, z^2$
B_g	1	-1	1	-1	1	-1	1	-1	1	-1	1	-1		
E_{1g}	1	ε	$-\varepsilon^*$	-1	$-\varepsilon$	ε^*	1	ε	$-\varepsilon^*$	-1	$-\varepsilon$	ε^*	(R_x, R_y)	(xz, yz)
E_{1g}	1	ε^*	$-\varepsilon$	-1	$-\varepsilon^*$	ε	1	ε^*	$-\varepsilon$	-1	$-\varepsilon^*$	ε		
E_{2g}	1	$-\varepsilon$	$-\varepsilon^*$	1	$-\varepsilon$	$-\varepsilon^*$	1	$-\varepsilon$	$-\varepsilon^*$	1	$-\varepsilon$	$-\varepsilon^*$		$(x^2 - y^2, xy)$
A_u	1	1	1	1	1	1	-1	-1	-1	-1	-1	-1	z	
B_u	1	-1	1	-1	1	-1	-1	1	-1	1	-1	1		
E_{1u}	1	ε	$-\varepsilon^*$	-1	$-\varepsilon$	ε^*	-1	$-\varepsilon$	ε^*	1	ε	$-\varepsilon^*$	(x, y)	
E_{1u}	1	ε^*	$-\varepsilon$	-1	$-\varepsilon^*$	ε	-1	$-\varepsilon^*$	ε	1	ε^*	$-\varepsilon$		
E_{2u}	1	$-\varepsilon$	$-\varepsilon^*$	1	$-\varepsilon$	$-\varepsilon^*$	-1	ε	ε^*	-1	ε	ε^*		

6. The Groups D_{nh} ($n = 2, 3, 4, 5, 6$)



D_{2h} (mmm)	E	$C_2(z)$	$C_2(y)$	$C_2(x)$	i	$\sigma(xy)$	$\sigma(xz)$	$\sigma(yz)$	B_2H_6	C_2H_4	④
A_g	1	1	1	1	1	1	1	1	x^2, y^2, z^2		
B_{1g}	1	1	-1	-1	1	1	-1	-1	R_z	xy	
B_{2g}	1	-1	1	-1	1	-1	1	-1	R_y	xz	
B_{3g}	1	-1	-1	1	1	-1	-1	1	R_x	yz	
A_u	1	1	1	1	-1	-1	-1	-1			
B_{1u}	1	1	-1	-1	-1	-1	1	1	z		
B_{2u}	1	-1	1	-1	-1	1	-1	1	y		
B_{3u}	1	-1	-1	1	-1	1	1	-1	x		

D_{3h}	E	$2C_3$	$3C_2$	σ_h	$2S_3$	$3\sigma_v$	1, 3, 5 Benzene, Cyclopropane	(6m2)
----------	-----	--------	--------	------------	--------	-------------	-------------------------------------	-------

A'_1	1	1	1	1	1	1	$x^2 + y^2, z^2$	
A'_2	1	1	-1	1	1	-1	R_z	
E'	2	-1	0	2	-1	0	(x, y)	$(x^2 - y^2, xy)$
A''_1	1	1	1	-1	-1	-1		
A''_2	1	1	-1	-1	-1	1	z	
E''	2	-1	0	-2	1	0	(R_x, R_y)	(xz, yz)

D_{4h}	E	$2C_4$	C_2	$2C'_2$	$2C''_2$	i	$2S_4$	σ_h	$2\sigma_v$	$2\sigma_d$	Cyclobutane	(4/mmm)
----------	-----	--------	-------	---------	----------	-----	--------	------------	-------------	-------------	-------------	---------

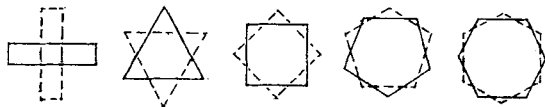
A_{1g}	1	1	1	1	1	1	1	1	1	1	$x^2 + y^2, z^2$	
A_{2g}	1	1	1	-1	-1	1	1	1	-1	-1	R_z	
B_{1g}	1	-1	1	1	-1	1	-1	1	1	-1		$x^2 - y^2$
B_{2g}	1	-1	1	-1	1	1	-1	1	-1	1		xy
E_g	2	0	-2	0	0	2	0	-2	0	0	(R_x, R_y)	(xz, yz)
A_{1u}	1	1	1	1	1	-1	-1	-1	-1	-1		
A_{2u}	1	1	1	-1	-1	-1	-1	-1	1	1	z	
B_{1u}	1	-1	1	1	-1	-1	1	-1	-1	1		
B_{2u}	1	-1	1	-1	1	-1	1	-1	1	-1		
E_u	2	0	-2	0	0	-2	0	2	0	0	(x, y)	

$D_{5h} E 2C_5$	$2C_5^2$	$5C_2 \sigma_h 2S_5$	$2S_5^3$	$5\sigma_v$	Cyclopentadienyl- anion, IF_7	(10)
-----------------	----------	----------------------	----------	-------------	---	------

A'_1	1 1	1	1 1 1	1	1	$x^2 + y^2, z^2$	
A'_2	1 1	1	-1 1 1	1	-1	R_z	
E'_1	2 2cos72 °	2cos144 ° 0	2 2cos72 °	2cos144 ° 0	(x, y)		
E'_2	2 2cos144 °	2cos72 ° 0	2 2cos144 °	2cos72 ° 0		$(x^2 - y^2, xy)$	
A''_1	1 1	1	1 -1 -1	-1	-1		
A''_2	1 1	1	-1 -1 -1	-1	1	z	
E'_1	2 2cos72 °	2cos144 ° 0	-2 -2cos72 °	-2cos144 ° 0	$(R_x, R_y)(xz, yz)$		
E''_2	2 2cos144 °	2cos72 ° 0	-2 -2cos144 °	2cos72 ° 0			

D_{6h}	E	$2C_6$	$2C_3$	C_2	$3C'_2$	$3C''_2$	i	$2S_3$	$2S_6$	σ_h	$3\sigma_d$	$3\sigma_v$	Benzene	(12)
$(6/mmm)$														
A_{1g}	1	1	1	1	1	1	1	1	1	1	1	1	$x^2 + y^2, z^2$	
A_{2g}	1	1	1	1	-1	-1	1	1	1	1	-1	-1	R_z	
B_{1g}	1	-1	1	-1	1	-1	1	-1	1	-1	1	-1		
B_{2g}	1	-1	1	-1	-1	1	1	-1	1	-1	-1	1		
E_{1g}	2	1	-1	-2	0	0	2	1	-1	-2	0	0	(R_x, R_y)	
E_{2g}	2	-1	-1	2	0	0	2	-1	-1	2	0	0	$(x^2 - y^2, xy)$	
A_{1u}	1	1	1	1	1	1	-1	-1	-1	-1	-1	-1		
A_{2u}	1	1	1	1	-1	-1	-1	-1	-1	-1	1	1	z	
B_{1u}	1	-1	1	-1	1	-1	-1	1	-1	1	-1	1		
B_{2u}	1	-1	1	-1	-1	1	-1	1	-1	1	1	-1		
E_{1u}	2	1	-1	-2	0	0	-2	-1	1	2	0	0	(x, y)	
E_{2u}	2	-1	-1	2	0	0	-2	1	1	-2	0	0		

7. The Groups D_{nd} ($n = 2, 3, 4, 5, 6$)



$D_{2d} = V_d$	E	$2S_4$	C_2	$2C'_2$	$2\sigma_d$	Allene	(6)
$(42m)$							
A_1	1	1	1	1	1	$x^2 + y^2, z^2$	
A_2	1	1	1	-1	-1	R_z	
B_1	1	-1	1	1	-1	$x^2 - y^2$	
B_2	1	-1	1	-1	1	xy	
E	2	0	-2	0	0	(x, y) (R_x, R_y)	(xz, yz)

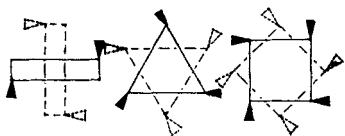
D_{3d}	E	$2C_3$	$3C_2$	i	$2S_6$	$3\sigma_d$	Ethane	Cyclohexane	(6)
$(3m)$									
A_{1g}	1	1	1	1	1	1	$x^2 + y^2, z^2$		
A_{2g}	1	1	-1	1	1	-1	R_z		
E_g	2	-1	0	2	-1	0	(R_x, R_y)	$(x^2 - y^2, xy)$ (xz, yz)	
A_{1u}	1	1	1	-1	-1	-1			
A_{2u}	1	1	-1	-1	-1	1	z		
E_u	2	-1	0	-2	1	0	(x, y)		

D_{4d}	E	$2S_8$	$2C_4$	$2S_8^3$	C_2	$4C'_2$	$4\sigma_d$	S_8	(8)
A_1	1	1	1	1	1	1	1		$x^2 + y^2, z^2$
A_2	1	1	1	1	1	-1	-1	R_z	
B_1	1	-1	1	-1	1	1	-1		
B_2	1	-1	1	-1	1	-1	1	z	
E_1	2	$\sqrt{2}$	0	$-\sqrt{2}$	-2	0	0	(x, y)	
E_2	2	0	-2	0	2	0	0		$(x^2 - y^2, xy)$
E_3	2	$-\sqrt{2}$	0	$\sqrt{2}$	-2	0	0	(R_x, R_y)	(xz, yz)

D_{5d}	E	$2C_5$	$2C_5^2$	$5C_2$	i	$2S_{10}^3$	$2S_{10}$	$5\sigma_d$	Ferrocene	(10)
A_{1g}	1	1		1	1	1	1	1	$x^2 + y^2, z^2$	
A_{2g}	1	1	1	-1	1	1	1	-1	R_z	
E_{1g}	2	$2\cos 72^\circ$	$2\cos 144^\circ$	0	2	$2\cos 72^\circ$	$2\cos 144^\circ$	0	(R_x, R_y)	(xz, yz)
E_{2g}	2	$2\cos 144^\circ$	$2\cos 72^\circ$	0	2	$2\cos 144^\circ$	$2\cos 72^\circ$	0		$(x^2 - y^2, xy)$
A_{1u}	1	1		1	-1	-1	-1	-1		
A_{2u}	1	1	1	-1	-1	-1	-1	1	z	
E_{1u}	2	$2\cos 72^\circ$	$2\cos 144^\circ$	0	-2	$-2\cos 72^\circ$	$-2\cos 144^\circ$	0	(x, y)	
E_{2u}	2	$2\cos 144^\circ$	$2\cos 72^\circ$	0	-2	$-2\cos 144^\circ$	$-2\cos 72^\circ$	0		

D_{6d}	E	$2S_{12}$	$2C_6$	$2S_4$	$2C_3$	$2S_{12}^5$	C_2	$6C'_2$	$6\sigma_d$	(12)
A_1	1	1	1	1	1	1	1	1	1	$x^2 + y^2, z^2$
A_2	1	1	1	1	1	1	1	-1	-1	R_z
B_1	1	-1	1	-1	1	-1	1	1	-1	
B_2	1	-1	1	-1	1	-1	1	-1	1	z
E_1	2	$\sqrt{3}$	1	0	-1	$-\sqrt{3}$	-2	0	0	(x, y)
E_2	2	1	-1	-2	-1	1	2	0	0	
E_3	2	0	-2	0	2	0	-2	0	0	
E_4	2	-1	-1	2	-1	-1	2	0	0	
E_5	2	$-\sqrt{3}$	1	0	-1	$\sqrt{3}$	-2	0	0	(R_x, R_y)
										(xz, yz)

8. The Groups S_n ($n = 4, 6, 8$)



S_4	E	S_4	C_2	S_4^3	Tetraphenyl-methane	(2)
(4)						
A	1	1	1	1	R_z	$x^2 + y^2, z^2$
B	1	-1	1	-1	z	$x^2 - y^2, xy$

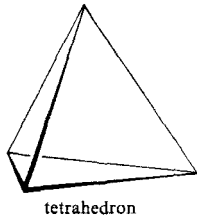
$$E \left\{ \begin{matrix} 1 & i & -1 & -i \\ 1 & -i & -1 & i \end{matrix} \right\} (x, y)(R_x, R_y) (xz, yz)$$

S_6	E	C_3	C_3^2	i	S_6^5	S_6	$\varepsilon = \exp(2\pi i/3)$	(3)
(3)								
A_g	1	1	1	1	1	R_z	$x^2 + y^2, z^2$	
E_g	1	ε	ε^*	1	ε	ε^*	(R_x, R_y)	$(x^2 - y^2, xy)$
	1	ε^*	ε	1	ε^*	ε		(xz, yz)
A_u	1	1	1	-1	-1	-1	z	
E_u	1	ε	ε^*	-1	$-\varepsilon$	$-\varepsilon^*$	(x, y)	
	1	ε^*	ε	-1	$-\varepsilon^*$	$-\varepsilon$		

S_8	E	S_8	C_4	S_8^3	C_2	S_8^5	C_4^3	S_8^7	$\varepsilon = \exp(2\pi i/8)$	(4)
A	1	1	1	1	1	1	1	R_z	$x^2 + y^2, z^2$	
B	1	-1	1	-1	1	-1	1	-1	z	
E_1	1	ε	i	$-\varepsilon^*$	-1	$-\varepsilon$	$-i$	ε^*	(x, y)	
	1	ε^*	$-i$	$-\varepsilon$	-1	$-\varepsilon^*$	i	ε	(R_x, R_y)	
E_2	1	i	-1	$-i$	1	i	-1	$-i$		$(x^2 - y^2, xy)$
	1	$-i$	-1	i	1	$-i$	-1	i		
E_3	1	$-\varepsilon^*$	$-i$	ε	-1	ε^*	i	$-\varepsilon$		(xz, yz)
	1	$-\varepsilon$	i	ε^*	-1	ε	$-i$	$-\varepsilon^*$		

9. The Cubic Groups

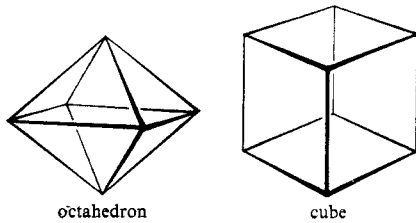
T	E	$4C_3$	$4C_3^2$	$3C_2$		$\varepsilon = \exp(2\pi i/3)$	(12)
(23)							
A	1	1	1	1		$x^2 + y^2 + z^2$	
E	$\begin{Bmatrix} 1 & \varepsilon & \varepsilon^* & 1 \\ 1 & \varepsilon^* & \varepsilon & 1 \end{Bmatrix}$					$(x^2 - y^2, 2z^2 - x^2 - y^2)$	
T	3	0	0	-1	(x, y, z) (R_x, R_y, R_z)	(xy, xz, yz)	



T_d	E	$8C_3$	$3C_2$	$6S_4$	$6\sigma_d$		CCl_4	(12)
(43m)								
A_1	1	1	1	1	1		$x^2 + y^2 + z^2$	
A_2	1	1	1	-1	-1			
E	2	-1	2	0	0		$(2z^2 - x^2 - y^2,$ $x^2 - y^2)$	
T_1	3	0	-1	1	-1	(R_x, R_y, R_z)		
T_2	3	0	-1	-1	1	(x, y, z)	(xy, xz, yz)	

T_h	E	$4C_3$	$4C_3^2$	$3C_2$	i	$4S_6$	$4S_6^2$	$3\sigma_d$		$\varepsilon = \exp(2\pi i/3)$	(12)
(m3)											
A_g	1	1	1	1	1	1	1	1		$x^2 + y^2 + z^2$	
E_g	$\begin{Bmatrix} 1 & \varepsilon & \varepsilon^* & 1 & 1 & \varepsilon & \varepsilon^* & 1 \\ 1 & \varepsilon^* & \varepsilon & 1 & 1 & \varepsilon^* & \varepsilon & 1 \end{Bmatrix}$									$(2z^2 - x^2 - y^2,$ $x^2 - y^2)$	
T_g	3	0	0	-1	3	0	0	-1	(R_x, R_y, R_z)	(xy, yz, xz)	
A_u	1	1	1	1	-1	-1	-1	-1			
E_u	$\begin{Bmatrix} 1 & \varepsilon & \varepsilon^* & 1 & -1 & -\varepsilon & -\varepsilon^* & -1 \\ 1 & \varepsilon^* & \varepsilon & 1 & -1 & -\varepsilon^* & -\varepsilon & -1 \end{Bmatrix}$										
T_u	3	0	0	-1	-3	0	0	1	(x, y, z)		

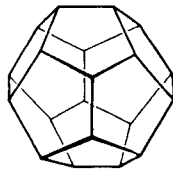
O	E	$8C_3$	$3C_2$	$6C_4$	$6C'_2$		(432)	(24)
A_1	1	1	1	1	1			$x^2 + y^2 + z^2$
A_2	1	1	1	-1	-1			
E	2	-1	2	0	0			$(2z^2 - x^2 - y^2,$ $x^2 - y^2)$
T_1	3	0	-1	1	-1	(x, y, z)		
						(R_x, R_y, R_z)		
T_2	3	0	-1	-1	1			(xy, xz, yz)



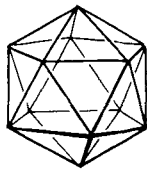
O_h	E	$8C_3$	$6C_2$	$6C_4$	$3C_2$	i	$6S_4$	$8S_6$	$3\sigma_h$	$6\sigma_d$	SF ₆	(24)
$(m3m)$					$(= C_4^2)$							
A_{1g}	1	1	1	1	1	1	1	1	1	1	$x^2 + y^2 + z^2$	
A_{2g}	1	1	-1	-1	1	1	-1	1	1	-1		
E_g	2	-1	0	0	2	2	0	-1	2	0	$(2z^2 - x^2 - y^2,$ $x^2 - y^2)$	
T_{1g}	3	0	-1	1	-1	3	1	0	-1	-1	(R_x, R_y, R_z)	
T_{2g}	3	0	1	-1	-1	3	-1	0	-1	1	(xz, yz, xy)	
A_{1u}	1	1	1	1	1	-1	-1	-1	-1	-1		
A_{2u}	1	1	-1	-1	1	-1	1	-1	-1	1		
E_u	2	-1	0	0	2	-2	0	1	-2	0		
T_{1u}	3	0	-1	1	-1	-3	-1	0	1	1	(x, y, z)	
T_{2u}	3	0	1	-1	-1	-3	1	0	1	-1		

10. The Groups I, I_h

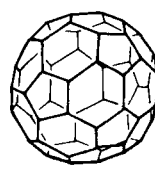
I	E	$12C_5$	$12C_5^2$	$20C_3$	$15C_2$	$\eta^\pm = \frac{1}{2}(1 \pm 5^{\frac{1}{2}})$	$\textcircled{60}$
A	1	1	1	1	1	$x^2 + y^2 + z^2$	
T_1	3	η^+	η^-	0	-1	(x, y, z) (R_x, R_y, R_z)	
T_2	3	η^-	η^+	0	-1		
G	4	-1	-1	1	0		
H	5	0	0	-1	1	$(2z^2 - x^2 - y^2,$ $x^2 - y^2,$ $xy, yz, zx)$	



dodecahedron



isosahedron



fullerene

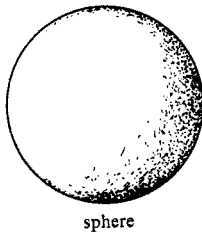
I_h	E	$12C_5$	$12C_5^2$	$20C_3$	$15C_2$	i	$12S_{10}$	$12S_{10}^3$	$20S_6$	15σ	$\eta^\pm = \frac{1}{2}(1 \pm 5^{\frac{1}{2}})$	$\textcircled{60}$
A_g	1	1	1	1	1	1	1	1	1	1	$x^2 + y^2 + z^2$	
T_{1g}	3	η^+	η^-	0	-1	3	η	η^+	0	-1	(R_x, R_y, R_z)	
T_{2g}	3	η^-	η^+	0	-1	3	η^+	η^-	0	-1		
G_g	4	-1	-1	1	0	4	-1	-1	1	0		
H_g	5	0	0	-1	1	5	0	0	-1	1	$(2z^2 - x^2 - y^2,$ $x^2 - y^2,$ $xy, yz, zx)$	
A_u	1	1	1	1	1	-1	-1	-1	-1	-1		
T_{1u}	3	η^+	η^-	0	-1	-3	$-\eta^-$	$-\eta^+$	0	1	(x, y, z)	
T_{2u}	3	η^-	η^+	0	-1	-3	$-\eta^+$	$-\eta^-$	0	1		
G_u	4	-1	-1	1	0	-4	1	1	-1	0		
H_u	5	0	0	-1	1	-5	0	0	1	-1		

11. The groups $C_{\infty v}$ and $D_{\infty h}$

$C_{\infty v}$	E	$2C_{\infty}^{\phi}$...	$\infty\sigma_v$		HCN	①
$A_1 \equiv \Sigma^+$	1	1	...	1	z	$x^2 + y^2, z^2$	
$A_2 \equiv \Sigma^-$	1	1	...	-1	R_z		
$E_1 \equiv \Pi$	2	$2\cos\phi$...	0	$(x, y)(R_x, R_y)$	(xz, yz)	
$E_2 \equiv \Delta$	2	$2\cos 2\phi$...	0		$(x^2 - y^2, xy)$	
$E_3 \equiv \Phi$	2	$2\cos 3\phi$...	0			
...			

$D_{\infty h}$	E	$2C_{\infty}^{\phi}$...	$\infty\sigma_i$	i	$2S_{\infty}^{\phi}$...	∞C_2	HC \equiv CH	②
Σ_g^+	1	1	...	1	1	1	...	1	$x^2 + y^2,$ z^2	
Σ_g^-	1	1	...	-1	1	1	...	-1	R_z	
Π_g	2	$2\cos\phi$...	0	2	$-2\cos\phi$...	0	(R_x, R_y)	(xz, yz)
Δ_g	2	$2\cos 2\phi$...	0	2	$2\cos 2\phi$...	0		$(x^2 - y^2,$ $xy)$
...	
Σ_u^+	1	1	...	1	-1	-1	...	-1	z	
Σ_u^-	1	1	...	-1	-1	-1	...	1		
Π_u	2	$2\cos\phi$...	0	-2	$2\cos\phi$...	0	(x, y)	
Δ_u	2	$2\cos 2\phi$...	0	-2	$-2\cos 2\phi$...	0		
...	

12. The Full Rotation Group (SU_2 and R_3)



$$\chi^{(j)}(\phi) = \begin{cases} \frac{\sin(j + \frac{1}{2})\phi}{\sin \frac{1}{2}\phi} & \phi \neq 0 \\ 2j + 1 & \phi = 0 \end{cases}$$

Notation: Representations labelled $I^{(j)}$ with $j = 0, \frac{1}{2}, 1, \frac{3}{2}, \dots \infty$. For R_3 j is confined to integral values (and written l or L) and the labels $S \equiv I^{(0)}$, $P \equiv I^{(1)}$, $D \equiv I^{(2)}$, etc. are used.

References

- Abate S, Gussoni M, Masetti G, Zerbi G (1977) J Chem Phys 67:1519
- Abbas MM, Kunde VG, Mumma MM (1979) J Geophys Res 84:2681
- Abbate S, Laux L, Overend J, Moscowitz A (1981) J Chem Phys 75:3161
- Abbe E (1871) Jenaer Z f Med u Naturw VI:263
- Abdullah AH, Sherman WJ (1980) J Phys E Sci Instrum 13:1155
- Abe N, Wakayama M, Ito M (1977) J Raman Spectrosc 6:38
- Abelès F (1963) Progr Opt 2:249
- Abney W, Festing RE (1881) Phil Trans 172:887
- Abraham JC, Etz ES (1979) Science 206:716
- Abstreiter G, Cardona M, Pinczuk (1984) Topics in Appl Phys 54:5. In: Cardona M, Guentherodt G (eds) Light scattering in Solids IV. Springer, Berlin Heidelberg New York London
- Acker WP, Leach DH, Chang RK (1989) Chem Phys Lett 155:491
- Ackermann M, Trimout D, Müller C, Wueffles DJ (1979) Pure Appl Geophys 117:367
- Adam S, Bourtyre P, Liquier J, Taboury JA, Taillandier E (1987) Biopolymers 26:251
- Adam S, Bourtyre P, Liquier J, Taillandier E (1986) Nucleic Acids Res 14:3501
- Adam S, Liquier J, Taboury JA, Taillandier E (1986) Biochemistry 25:3220
- Adam S, Taboury JA, Taillandier E, Popinel A, Huynh Dinh T, Igolen J (1986) J Biomol Struct Dyn 3:873
- Adler-Golden SM, Goldstein N, Bien F, Matthew MW, Gersh ME, Cheng WK, Adams FW (1992) Appl Opt 31:831
- Adnet F, Liquier J, Taillandier E, Singh MP, Rao KE, Lown JW (1992) J Biomol Struct Dyn 10:565
- Aechtner P, Fickenscher M, Laubereau A (1990) Ber Bunsenges Phys Chem 94:399
- Ahlrichs R, Ehrhardt C, Lakenbrink M, Schunk S, Schnoeckel H (1986) J Am Chem Soc 10:3596
- Ahmajian M, Brown CW (1973) Environ Sci Technol 7:452
- Akhebat A, Dagneaux C, Liquier J, Taillandier E (1992) J Biomol Struct Dyn 10:577
- Akhmanov SA, Koroteev NI, Magintskii SA, Morozov VB, Tarasevich AP, Tunkin VG (1985) J Opt Soc Am B2:640
- Akimoto M, Furukawa Y, Takeuchi H, Harada I, Soma Y, Soma M (1986) Synth Met 15:353-360
- Alben R, McColl JR, Shih CS (1972) Solid State Commun 11:1081
- Albrecht AC (1961) J Chem Phys 34:1476
- Albrecht H, Müller G, Schaldach M (1977) Biomed Technik E 22:361
- Albrecht H, Müller G, Schaldach M (1978) Proceedings 6th Int Conf on Raman Spectroscopy, Bangalore, Heyden, London
- Albrecht MG, Creighton JA (1977) J Am Chem Soc 99:5215
- Alden M, Bengtsson PE, Edner H (1986) Appl Opt 25:4493
- Alkemade CTJ, Snelleman W, Boutilier GD, Pollard BD, Winefordner JD, Chester TL, Omenetto N (1978) Spectrochim Acta 33B:383
- Alkemade CTJ, Snelleman W, Boutilier GD, Winefordner JD (1980) Spectrochim Acta 35B:261
- Allara DL (1993) Crit Rev Surf Chem 2:91
- Allara DL, Baca A, Pryde CA (1978) Macromolecules 11:1215
- Allen jr HC, Cross PC (1963) Molecular Vib-Rotors, The Theory and Interpretation of High Resolution Infrared Spectra. John Wiley, New York
- Allin EJ, May AD, Stoicheff BP, Stryland JC, Welsh HL (1967) Appl Opt 6:1597
- Allouche A, Pourcin J (1993) Spectrochim Acta 49A:571
- Almond MJ, Downs AJ (1989) Spectroscopy of Matrix Isolated Species. In: Clark RJH, Hester RE (eds) Advances in Spectroscopy, vol 17. John Wiley, Chichester

- Altmann K, Klöckner W, Strey G (1976) Z Naturforsch 31a:1311
- Altmann K, Strey G, Hochenbleicher JG, Brandmüller J (1972) Z Naturforsch 27a:56
- Altmann K, Strey G (1972) Z Naturforsch 27a:65
- Altschuh J, Weiland R, Kosack JV, Schulze H, Strauss A, Kappus M, Kau P, Kuball HG (1984) Mol Cryst Liq Cryst 113:321
- Amat G, Nielsen HH, Tarrago G (1971) *Rotation-Vibration of Polyatomic Molecules*. Marcel Dekker, New York
- Ambartzumian RV, Cetokhov VS (1977) Acc Chem Res 10:61
- Amberger HD, Fischer RD, Rosenbauer GG (1975) Ber Bunsenges Phys Chem 79:1226
- Amey RL, Chapman D (1983) In: Chapman D (ed) *Biomembranes Structure and Functions*. McMillan Press, London, Chap 4, p 199
- Amos RD, Rice JE (1987) *The Cambridge Analytic Derivatives Package*, Cambridge
- Amos RD, Rice JE (1990) CADPAC: *The Cambridge Analytic Derivatives Package*. Issue 4.2, Cambridge, 1990
- Anderson DH, Wilson TE (1975) Anal Chem 47:2482
- Anderson RJ, Griffiths PR (1975) Anal Chem 47:2339
- Anderson RJM, Esherick P (1980) J Opt Soc Am 70:663
- Andreev GN, Stratmann AW, Schrader B (1989) Mol Cryst Liq Cryst 167:27
- Andreev GN, Stratmann AW, Schrader B (1989) Mol Cryst Liq Cryst 167:33
- Andrews DL (1980) J Chem Phys 72:4141
- Andrews L (1976) *Infrared and Raman Spectroscopic Studies of Alkali-Metal-Atom Matrix-Reaktion Products*. In: Moskovits M, Ozin GA (eds) *Cryochemistry*. John Wiley, New York, p 195
- Andrews L (1979) Appl Spectrosc 33:199
- Andrews L (1984) J Phys Chem 88:2940
- Andrews L, Moskovits M (eds) (1989) *Chemistry and Physics of Matrix-Isolated Species*. North-Holland, Amsterdam
- Andrews L, Spiker RC (1973) J Chem Phys 59:1851
- Angeloni L, Righini R, Castellucci E, Foggi P, Califano S (1988) J Phys Chem 92:983
- Angstl R, Finsterhölzl H, Frunder H, Illig D, Papousek D, Pracna P, Rao KN, Schrötter HW, Urban S (1985) J Mol Spectrosc 114:454
- Angström AJ (1868) *Recherches sur le spectre solaire*, Paris
- Angström AJ (1889) *Öfversigt Af Kongl Vetenskaps Akadem Förhandl*, Stockholm, p 549
- Angström AJ (1890) *Öfversigt Af Kongl Vetenskaps Akadem Förhandl*, Stockholm, p 331
- Ansmann A (1974) Dissertation, Universität Dortmund
- Ansmann A, Schrader B (1976) J Raman Spectrosc 5:281
- Antoon MK, D'Esposito L, Koenig JL (1979) Appl Spectrosc 33:351
- Argade PV, Rothschild KJ, Kawamoto AH, Herzfeld J, Herlihy WC (1981) Proc Natl Acad Sci USA 78:1643
- Arlinghaus RT, Andrews L (1984) J Chem Phys 81:4341
- Aroca R, Kovacs GJ (1991) In: *Vibrational Spectra and Structure*. Durig JR (ed) vol 19. Elsevier, Amsterdam, p 55
- Asano T, Le Noble WJ (1978) Chem Rev 78:407
- Asher SA (1988) In: Ann Rev Phys Chem, vol 39, Strauss HL, Babcock GT, Moore CB (eds) Annual Reviews Inc, Palo Alto, p 537
- Aspnes DE (1985) The Accurate Determination of Optical Properties by Ellipsometry. In: Palik ED (ed) *Handbook of Optical Constants of Solids*. Academic, Orlando, p 89
- Asthana BP, Kiefer W (1993) in *Vibrational Spectra and Structure*, vol 20, Durig JR (ed) chapter 2
- ASTM (1977) American Society for Testing and Materials. Annual Book of ASTM Standards, Part 42, Philadelphia
- Atkins PW (1983) *Molecular Quantum Mechanics*. University Press, Oxford
- Atkins PW, Child MS, Phillips CSG (1970) *Tables for Group Theory*, Oxford University Press
- Auger H, Jarrell HC, Smith ICP, Siminovitch DJ, Mantsch HH, Wong PTT (1987) Biochemistry 27:6086
- Aussenegg FR, Leitner A, Lippitsch ME (eds) (1983) *Surface Studies with Lasers*. Springer, Berlin
- Avouris P, Demuth JE (1981) J Chem Phys 75:4783

- Avram M, Mateescu GD (1972) Infrared Spectroscopy, Applications in Organic Chemistry. Wiley-Intersc, New York
- Azzam RMA, Bashara NM (1977) Ellipsometry and Polarized Light. North-Holland, Amsterdam
- Babikov YuL, Tashkun SA, Tyuterev VG, Champion JP, Pierre G, Wenger C (1993) Atmospheric Spectroscopy Applications Workshop, Reims, France; Spectrochimica Acta Electronica (to be published)
- Bach D (1983) In: Chapman D (ed) Biomembrane Structure and Function. Verlag Chemie, Chapt 1, p 1
- Badger RM (1934) J Chem Phys 2:128
- Badger RM (1934) J Chem Phys 3:710
- Badger RM, Zumwalt LR (1938) J Chem Phys 6:711
- Baessler H, Labes MM (1970) J Chem Phys 52:631
- Baijerl P, Kiefer W (1980) J Raman Spectrosc 10:197
- Baijerl P, Kiefer W (1981) J Raman Spectrosc 11: 393
- Bakshi V, Kearney RJ (1989) J Quant Spectrosc Radiat Transfer 42:111
- Bandermann F (1980) Auswertung von Meßdaten. In: Ullmanns Encyklopädie der technischen Chemie, 4th edn. Verlag Chemie, Weinheim, pp 41-50
- Bandy AR, Hillard ME, Emery LE (1973) Appl Spectrosc 27:421
- Bangcharoenpauppong O, Schomaker KT, Champion PM (1984) J Am Chem Soc 106:5688
- Baranska H, Labudzinska A (1980) Chemia Aalityczana 25:607
- Barbe A, Marche P, Secroun C, Jouve P (1979) Geophys Res Lett 6:463
- Barbetta A, Edgell W (1978) Appl Spectrosc 32:93
- Bardeen J, Cooper LN, Schrieffer JR (1957) Phys Rev 108:1175
- Bardorff W, Heydtmann H (1978) Ber Bunsenges Phys Chem 82:649
- Barnes AJ (1973) Theoretical treatment of matrix effects. In: Hallam HE (ed) Vibrational Spectroscopy of Trapped Species. J Wiley, London, p 133
- Barnes AJ, Orville-Thomas WJ (eds) (1977) Vibrational Spectroscopy - Modern Trends. Elsevier, Amsterdam New York
- Barnett CJ, Drake AF, Kuroda R, Mason SF (1980) Mol Phys 41:455
- Barrett JJ (1981) In: Chemical Applications of Nonlinear Raman Spectroscopy, Harvey AB (ed). Academic Press, New York, chapter 3
- Barrett JJ, Adams NI (1968) J Opt Soc Am 58:311
- Barrett JJ, Begley RF (1975) Appl Phys Lett 27:129
- Barrett JJ, Berry MJ (1979) Appl Phys Lett 34:144
- Barrett JJ, Heller DF (1982) In: Nonlinear Raman Spectroscopy and its Chemical Applications, Kiefer W, Long DA, (eds). Reidel, Dordrecht, p 563
- Barrett JJ, Siebert DR, West GA (1982) In: Nonlinear Raman Spectroscopy and its Chemical Applications, Kiefer W, Long DA, (eds). Reidel, Dordrecht, p 585
- Barron LD (1976) Raman Optical Activity, Proceedings Vth International Raman Conference, vol 4, no 44, Freiburg, p 677.
- Barron LD (1978) In: Clark RJH, Hester RE (eds) Advances in Infrared and Raman Spectroscopy. Heyden & Son, London
- Barron LD (1979) Raman Optical Activity. In: Mason SF (ed) Optical activity and chiral discrimination. Reidel, Dordrecht, p 219
- Barron LD (1982) Molecular Light Scattering and Optical Activity, Cambridge University Press, Cambridge
- Barron LD, Bogaard MP, Buckingham AD (1973) J Am Chem Soc 95:604
- Barron LD, Bogaard MP, Buckingham AD (1973) Nature 241:113
- Barron LD, Buckingham AD (1971) Mol Phys 20:1111
- Barron LD, Buckingham AD (1974) J Am Chem Soc 96:4769
- Barron LD, Buckingham AD (1975) Ann Rev Phys Chem 26:381
- Barron LD, Buckingham AD (1979) J Am Chem Soc 101:1979
- Barron LD, Cooper A, Ford SJ, Hecht L, Wen ZQ (1992b) Faraday Discuss 93:259
- Barron LD, Gargaro AR, Hecht L, Polavarapu PL (1991) Spectrochim Acta 47A:1001
- Barron LD, Hecht L (1993) Biomolecular conformational studies with vibrational Raman optical activity. In: Clark RJH, Hester RE (eds) Biomolecular spectroscopy, part B, Advances in spectroscopy. Wiley, 20:235
- Barron LD, Hecht L, Hug W, MacIntosh MJ (1989) J Am Chem Soc 111:8731

- Barron LD, Torrance JF, Cutler DJ (1987) *J Raman Spectrosc* 18:281
- Barron LD, Vrbancich J (1984) *Topics Current Chem* 123:151
- Barron LD, Wen ZQ, Hecht L (1992a) *J Am Chem Soc* 114:784
- Barrow GM (1962) *Introduction to Molecular Spectroscopy*. McGraw Hill, New York
- Barrow RF, Long DA, Millen DJ (1973) *Molecular Spectroscopy, A Specialist Periodical Report*. The Chemical Society, London
- Barthelemy JP, Copin A, Deleu R, Closset JL (1979) *Talanta* 26:885
- Bartlett JR, Cooney RP (1987) In: *Spectroscopy of Inorganic-Based Materials*, Clark RJH, Hester RE (eds). Wiley, Chichester p 187
- Bartonek M, Kuzmany H (1991) *Synth Met* 41:607
- Bartonek M, Sariciftci NS, Kuzmany H (1990) *Synth Met* 36:83-93
- Batchelder DN, Bloor D (1982) *J Phys C: Solid State Phys* 15:3005
- Batchelder DN, Bloor D (1984) In: *Advances in Infrared and Raman Spectroscopy*, vol 11, Clark RJH, Hester RE (eds). Heyden, London, p 133
- Bates JB, Boyd GE (1973) *Appl Spectrosc* 27:204
- Bathini Y, Rao KE, Shea RG, Lown JW (1990) *Chem Res Toxicol* 3:268
- Baumann RP (1962) *Absorption Spectroscopy*. John Wiley, London
- Baumgarten E (1977) *Fresenius Z Anal Chem* 287:118
- Baumruk V, Keiderling TA (1993) *J Am Chem Soc* 115:6939
- Beattie IR, Horder JR (1969) *J Chem Soc A* 2656
- Becher HJ (1968) *Kraftkonstantenrechnungen aus den Schwingungsspektren einfacher organischer Moleküle*. In: Davison A et al (eds) *Fortschritte der chemischen Forschung*. Springer, Berlin, 10:155
- Becher HJ (1972) *Angew Chem Int Ed Engl* 11:26
- Becher HJ, Adrian A (1970) *J Mol Struct* 6:479
- Becher HJ, Brockmeyer HJ, Prigge U (1978) *J Chem Res (S)*:117
- Becher HJ, Fenske D (1978) *J Chem Res (S)*:167
- Becher HJ, Friedrich F, Willner H (1973) *Z Anorg Allg Chem* 395:134
- Becher HJ, Friedrich F, Willner H (1976) *Z Anorg Allg Chem* 426:15
- Becher HJ, Schnoeckel H, Willner H (1974) *Z Phys Chem N F* 92:33
- Beck J, Straehle J (1987) *Z Anorg Allg Chem* 554:50
- Becker R, Bloechl G, Braeunling H (1989) In: Kuzmany H, Mehring M, Roth S (eds) *Electronic Properties of Polymers III*. Springer Series Solid State Sciences 91:465-469. Springer, Berlin
- Beckmann A, Fietz H, Kiefer W, Laane J (1981) *Phys Rev A* 24:2518
- Beden B, Lamy C (1988) *Infrared Reflectance Spectroscopy*. In: Gale RJ (ed) *Spectroelectrochemistry, Theory and Practice*. Plenum, New York. p 189
- Bednorz JG, Mueller KA (1986) *Z Phys B-Condensed Matter* 64:189
- Beebe KR, Kowalski BR (1987) *Anal Chem* 59:1007A
- Behringer J (1958) *Z Elektrochem* 62:906
- Behringer J (1967) In: *Raman Spectroscopy: Theory and Practice*, vol 1, Szymanski HA (ed) Plenum, New York, p 168
- Behringer J (1973) *Factor Group Analysis Revisited and Unified*, Springer Tracts in Modern Physics, vol 68. Springer, Berlin, p 161
- Behringer J (1974) In: *Molecular Spectroscopy*, vol 2, Barrow RF, Long DA, Millen DJ (eds) The Chemical Society, London, p 100
- Behringer J (1975) In: *Molecular Spectroscopy*, vol 3, Barrow RF, Long DA, Millen DJ (eds) The Chemical Society, London, p 163
- Behringer J, Brandmüller J (1956) *Z Elektrochem* 60:643
- Belkhakem M, Jordanov B (1990) *J Mol Struct* 218:309
- Belkhakem M, Jordanov B (1991a) *J Mol Struct* 245:195
- Belkhakem M, Jordanov B (1991b) *J Mol Struct* 245:29
- Belkhakem M, Jordanov B (1992) *J Mol Liq* 53:161
- Bell AF, Hecht L, Barron LD (1993) *J Raman Spectrosc* 24:633
- Bell AG (1880) *Am J Sci* 20:305
- Bell AG (1881) *Phil Mag* 11:510
- Bell RJ (1972) *Introductory Fourier Transform Spectroscopy*. Academic Press, New York
- Bellamy LJ (1975) *The Infrared Spectra of Complex Molecules*, 3rd edn. Chapman & Hall, London
- Bellamy LJ (1980) *Advances in Infrared Group Frequencies*, 2nd edn. Chapman & Hall, London

- Bellanato J, Juarez M, Ramos M (1978) Rev Agroquim Tecnl Aliment 18:353
- Bello JM, Stokes DL, Vo-Dinh T (1990) Anal Chem 62:1349
- Belz HH (1980) Dissertation, Universität Essen
- Belz HH (1989) Labor Praxis, April
- Belz HH, Gutberlet H, Schallert B, Schrader B (1987) Appl Spectrosc 41:1009
- Belz HH, Jede F, Schrader B (1981) Appl Spectrosc 35:279
- Belz HH, Niggemann W (1975) Diplomarbeit, Dortmund
- Bendtsen J (1974) J Raman Spectrosc 2:133
- Benevides JM, Thomas GJ Jr (1985) Biopolymers 24:667
- Benferhat R, Drevillon B (1987) Ann Chim (Paris) 12:385
- Bengtsson B, Martinsson M, Alden M, Kröll S (1992) Combust Sci Technol 81:129
- Bennett JM, Bennett HE (1978) Polarization. In: Driscoll W G, Vaughan W (eds) Handbook of Optics. McGraw Hill, New York.
- Benson AM, Drickamer HG (1957) J Chem Phys 27:1164
- Bentham PB, Romak CG, Shurvell HF (1985) Can J Chem 63:2303
- Berger H, Lavorel B, Millot G (1992) In: Applied Laser Spectroscopy. Andrews DL (ed). VCH Verlagsgesellschaft, Weinheim, p 267
- Bergert U (1990) Diplomarbeit, Göttingen
- Bergin FJ, Shurvell HF (1989) Appl Spectrosc 43:516
- Bergmann G, Thimm G (1958) Naturwiss 45:359
- Berjot M, Mansait M, Theophanides TM (1979) Experimental techniques of resonance Raman spectroscopy applied to biological molecules. In: Theophanides TM (ed) Infrared Raman spectroscopy of biological molecules. Nato advanced study institute series. Series C, vol 43. D Reidel publishing company, Dordrecht
- Berman JM, Goodman L (1987) J Chem Phys 87:1479
- Bermejo D, Santos J, Cancio P (1992) J Mol Spectrosc 156:15
- Bermejo D, Santos J, Cancio P, Doménech JL, Domingo C, Orza JM, Ortigoso J, Escribano R (1990) J Raman Spectrosc 21:197
- Bermejo D, Santos J, Cancio P, Fernandez-Sanchez JM, Montero S (1992) J Chem Phys 97:7055
- Bernstein HJ (1967) J Mol Spectrosc 22:122
- Bernstein HJ (1973) Resonance Raman spectra. In: Mathieu JP (ed) Advances in Raman spectroscopy, vol 1. Heyden and Sons, London
- Bernstein HJ, Allen G (1955) J Opt Soc Am 45:237
- Bernstein HJ, Sunder S (1977) Resonance Raman Spectroscopy and Normal Coordinate Analysis of some Model Compounds of Heme Proteins, chapt 26. In: Barnes AJ, Orville-Thomas WJ (eds) Vibrational Spectroscopy - Modern Trends. Elsevier, Amsterdam New York, p 413
- Berreman DW (1963) Phys Rev 130:2193
- Berreman DW (1972) J Opt Soc Amer 62:502
- Berthold A, Laserna JL, Winefordner JD (1987) Appl Spectrosc 41:1137
- Bertie JE, Jones RN, Behnam V (1986) Appl Spectrosc 40:427
- Bertie JE, Keefe CD, Jones RN, Mantsch HH, Moffat DJ (1991) Appl Spectrosc 45:1233
- Bertolini JC, Rousseau J (1979) Surf Sci 83:531
- Bertoluzza A, Bonora S, Fini G, Battaglia MA, Monti P (1981) J Raman Spectrosc 11:430
- Bertoluzza A, Fagnano C (1989) J Mol Struct 214:111
- Bertoluzza A, Fagnano C, Monti P (1989) Spectroscopy of Biological Molecules - State of the Art, Societa Editrice Esculapio, Bologna
- Bertoluzza A, Fagnano C, Tosi MR, Tugnoli V (1987) In: Schmid ED, Schneider FM, Siebert F (eds) Spectroscopy of biological molecules. John Wiley and Sons, New York, p 41
- Bertoluzza A, Fagnano C, Tosi MR, Tugnoli V, Morelli MA, Barbarella G (1988) In: Schmid ED, Schneider FM, Siebert F (eds) Spectroscopy of Biological Molecules, John Wiley & Sons, New York, p. 411
- Beuermann S (1990) Diplomarbeit, Göttingen
- Bhagavantam S, Venkatarayudu T (1939) Proc Indian Acad Sciences A 9:224
- Bhagavantam S, Venkatarayudu T (1969) Theory of Groups and its Application to Physical Problems. Academic Press, New York
- Biarge JF, Herranz J, Morcillo J (1961) J An R Soc Esp Fis Quim A57:81
- Bicknell-Brown E, Brown KG, Borchman D (1986) Biochim Biophys Acta 862:134
- Bidleman TF, Olney CE (1974) Bull Environ Contam Toxicol 11:442

- Bielefeld D, Willner H (1980) Spectrochim Acta 36A:989
- Bijvoet JM, Peerdeman AF, Van Bommel AJ (1951) Nature 168:271
- Binnewies M, Schnecke H (1990) Chem Rev 90:321
- Biresaw G (ed) (1990) ACS Symposium Series 441: Tribology and the Liquid-Crystalline State. American Chemical Society, Washington, DC
- Birge RR (1981) Ann Rev Biophys Bioeng 10:315
- Birk M, Friedl RR, Cohen EA, Picket HM, Sander SP (1989) J Chem Phys 91:6588
- Birk M, Winnewisser M (1976) Chem Phys Lett 123:386
- Birke RL, Lombardi JR (1982) In: Advances in Laser Spectroscopy, vol 1, Garetz B, Lombardi JR (eds). Heyden, Philadelphia, p 143
- Bisseling RH, Kosloff R, Manz J, Schor HHR (1985) Ber Bunsenges Phys Chem 89:270
- Blaha JJ, Rosasco GJ (1978) Anal Chem 50:892
- Blaha JJ, Rosasco GJ, Etz ES (1978) Appl Spectrosc 32:292
- Blank RE, Wakefield T (1979) Anal Chem 51:50
- Bleckmann P (1974) Z Naturf A29:1485
- Bleckmann P, Schrader B, Meier W, Takahashi H (1971) Ber Bunsenges Phys Chem 75:1279
- Bleckmann P, Wiegeler W (1977) J Mol Struct 42:227
- Blint RJ, Stephenson DA, Bechtel JH (1979) Western States Section/Combustion Institute Spring Meeting, Provo, Utah
- Bloembergen N (1963) Proc IEEE 51:124
- Bloembergen N (1967) Am J Phys 35:989
- Bloembergen N (1978) In: Proceedings of the Sixth Int Conf Raman Spectrosc, vol 1, Schmid ED, Krishnan RS, Kiefer W, Schröter HW (eds). Heyden, London, p 335
- Bloembergen N (1982) Science 216:1057
- Blom CE, Altona C (1977) Mol Phys 33:875
- Blom CE, Altona C (1977) Mol Phys 34:177
- Bloor D, Chance RR (1985) Polydiacetylenes, Martinus Nijhoff Publishers, Dordrecht Boston Lancaster
- Blout ER, Carver JP, Shechter E (1967) ORD of Polypeptides and Proteins. In: Snatzke G (ed) Optical Rotatory Dispersion and Circular Dichroism in Organic Chemistry. Heyden, London, p 224
- Bode HW (1950) Network analysis and feedback amplifier design. Academic, New York
- Boekholt M, Erle A, Splitgerber-Huennikes PC, Guentherodt G (1990a) Solid State Commun 74:1107-1112
- Boekholt M, Guentherodt G (1990b) Physica C 169:436-440
- Boggs JM, Moscarello MA (1982) Biophys J 37:57
- Bohdansky J (1957) Z Phys 149:383
- Bohn MA, Franck EU (1988) Ber Bunsenges Phys Chem 92:850
- Boiteau HL (1979) Toxicol Eur Res 1979:59
- Bonem Inc. (1987) Application note number DA3-8701
- Bonamy L, Bonamy J, Robert D, Lavorel B, Saint-Loup R, Chaux R, Santos J, Berger H (1988) J Chem Phys 89:5568
- Borman SA (1982) Anal Chem 54:1024A
- Born M (1933) Optik. Springer, Berlin
- Born M (1972) Optik. Springer, Berlin Heidelberg New York
- Born M, Huang K (1954) Dynamical theory of crystal lattices, Clarendon Press, Oxford
- Born M, Wolf E (1980) Principles of optics, 6th edn. Pergamon, Oxford
- Bose PK, Polavarapu PL, Barron LD, Hecht L (1990) J Phys Chem 94:1734
- Bouanich JP, Nguyen Van Thanh, Rossi I (1983) J Quant Spectrosc Radiat Transfer 30:9
- Bouanich JP, Nguyen Van Thanh, Strapalias H (1981) J Quant Spectrosc Radiat Transfer 26:53
- Boucher H, Brocki TR, Moscovits M, Bosnich B (1977) J Am Chem Soc 99:6870
- Bougeard D (1988) Croat Chem Acta 61:243
- Bougeard D, Bleckmann P, Schrader B (1973) Ber Bunsenges Phys Chem 77:1059
- Bougeard D, Brüggenthies S, Schrader B (1980) J Mol Struct 60:155
- Bougeard D, Le Calve N, Novak A, Chanh NB (1978) Mol Cryst Liq Cryst 44:113
- Bougeard D, Novak A (1978) Solid State Com 27:453
- Bougeard D, Righini R, Califano S (1979) Chem Phys 40:19
- Bour P, Keiderling TA (1993) J Am Chem Soc 115:9602

- Bourgin DG (1927) *Phys Rev* 29:794
Bouttier GD, Pollard BD, Winefordner JD, Chester TL, Omenetto N (1978) *Spectrochim Acta* 33B:401
Bouwman R, Freriks ILC (1980) *Appl Surf Science* 4:11, 21
Bozio R, Girlando A, Pecile C (1975) *J Phys Chem* 33:1237
Brackemann H, Buback M, Vögele HP (1986) *Makromol Chem* 187:1977
Bradbury EH, Price WC, Wilkinson GR (1961) *J Mol Biol* 3:301
Bradshaw AM, Schweizer E (1988) Infrared Reflection-Absorption Spectroscopy of Adsorbed Molecules. In: Clark RJH, Hester RE (eds) *Spectroscopy of Surfaces*. Wiley, Chichester. p 413
Braechler M, Boeffel C, Spiess HW (1991) *Makromol Chem* 192:1153
Brahms S, Brahms J, van Holde KE (1976) *Proc Natl Acad Sci USA* 73:3453
Braiman MS, Rothschild KJ (1988) *Ann Rev Biophys Chem* 17:541
Brakel R, Schneider FW (1988) In: *Advances in Nonlinear Spectroscopy*, vol 15, Clark RJH, Hester RE (eds). Wiley, Chichester, chapter 4
Brandenburg K, Seydel U (1988) *Eur Biophys J* 16:83
Brandmüller J (1980) Zum Symmetriebegriff und seine Bedeutung für Naturwissenschaft und Künste. In: Preisinger A (ed) *Symmetrie*. Springer, Wien
Brandmüller J (1986) *Comp & Maths* 12B:97
Brandmüller J, Claus R (1988) *Croat Chem Acta* 61:267
Brandmüller J, Kiefer W (1978) *Physicists View Fifty Years of Raman Spectroscopy*, Raman Anniversary Issue, The Spex Speaker, Metuchen NJ
Brandmüller J, Moser H (1962) *Einführung in die Ramanspektroskopie*. Steinkopff Verlag, Darmstadt, p 286
Brandmüller J, Winter FX (1985) *Z Kristallogr* 172:291
Brandrup J, Immergut EH (eds) (1975) *Polymer Handbook* John Wiley & Sons, New York
Braterman PS (1976) Spectra and Bonding in Metal Carbonyls B: Interpretation. In *Structure and Bonding*, vol 26. Springer, Berlin, p1
Braun H, Lüttke W (1975) *J Mol Struct* 28:391, 415
Braund DB, Cole ARH, Cugley JA, Honey FR, Pulfrey RE, Reece GD (1980) *Appl Opt* 19:2146
Bredas JL (1985) *J Chem Phys* 82:3808
Breeze JC, Ferriso CC, Ludwig CB, Malkmus W (1964) *J Chem Phys* 42:402
Brester CJ (1923) *Kristallsymmetrie und Reststrahlen*, Dissertation Rijks-Universiteit, Utrecht
Bribes JL, Gaufres R, Monan M, Lapp M, Penney CM (1976) *Appl Phys Lett* 28:336
Bridoux M et al (1978) *C R Acad Sci Paris C* 286:573
Brodersen S (1979) High-Resolution Rotation-Vibrational Raman Spectroscopy. In: Weber A (ed) *Raman Spectroscopy of Gases and Liquids*, Topics in Current Physics, vol 11. Springer, Berlin, p 7
Brodersen S, Langseth A (1956) *Math Fys Skr Dan Vid Selsk* 1:1
Brodnikowskii AM, Zharov VP, Koroteev NI (1985) *Sov J Quantum Electron* 15:12, 1600
Brodsky AM, Urbakh MI (1990) *Prog Surf Sci* 33:91
Bron WE, Juhasz T, Mehta S (1989) *Phys Rev Lett* 62:1655
Brown CW, Lynch PF, Ahmadjian M (1974) *Anal Chem* 46:183
Brown KG, Kiser EJ, Peticolas WL (1972) *Biopolymers* 11:1855
Brown PJ (1982) *J R Statist Soc B* 44:287
Browning J, Goggin PL, Goodfellow RJ, Norton MJ, Rattray AJM, Taylor BF, Mink J (1977) *J Chem Soc Dalton*:2061
Brügel W (1950) *Z Phys* 127:400
Brügel W (1964) Ultrarot-Betriebskontrollgeräte. In: Hengsterberg J, Sturm B, Winkler O (eds) *Messen und Regeln in der chem Technik*. Springer, Berlin
Brügel W (1969) *Einführung in die Ultrarotspektroskopie*. Steinkopff, Darmstadt
Bruker (1993) personal communication
Bualek S, Chingduang P, Bunsawansong P, Phaoivibul O, Korte EH, Schrader B (1986) *Appl Spectrosc* 40:109
Buback M (1977) *Z Naturforsch* 32a:1295
Buback M (1981) *Phys Chem Earth* 13/14:345
Buback M (1984) *Z Naturforsch* 39a:399
Buback M (1991) *Angew Chem* 103:658, *Angew Chem Int Ed Engl* 30:641

- Buback M, Crerar DA, Vogel-Koplitz LM (1987) Vibrational and Electronic Spectroscopy of Hydrothermal Systems, Chap 14. In: Ulmer GC, Barnes HL (eds) *Hydrothermal Experimental Techniques*. Wiley Interscience, New York
- Buback M, Franck ÉU (1971) *Ber Bunsenges Phys Chem* 75:33
- Buback M, Hipppler H, Schweer J, Vögele HP (1986d) *Makromol Chem Rapid Commun* 7:261
- Buback M, Lendle H (1979) *Z Naturforsch* 34a:1482
- Buback M, Lendle H (1981a) *Makromol Chem* 184:193
- Buback M, Lendle H (1981b) *Z Naturforsch* 36a:1371
- Buback M, Nees FW (1976) *Ber Bunsenges Phys Chem* 80:650, 1017
- Buback M, Schweer J (1989) *Z Phys Chem (Munich)* 161:153
- Buback M, Schweer J, Tups H (1985) *Ber Bunsenges Phys Chem* 89:545
- Buback M, Schweer J, Tups H (1986a) *Z Naturforsch* 41a:505
- Buback M, Schweer J, Tups H (1986b) *Z Naturforsch* 41a:512
- Buback M, Tost W, Hübsch T, Voß E, Tietze LF (1989) *Chem Ber* 122:1179
- Buback M, Tost W, Tietze LF, Voß E (1988) *Chem Ber* 121:781
- Buback M, Vögele HP (1988) Library of Fourier transform near infrared spectra. Research project of the Bundesminister für Forschung und Technologie. Data are becoming available from Chemical Concepts, P.O. Box 100202, 6940 Weinheim, FRG
- Buback M, Vögele HP (1993) FT-NIR Atlas. VCH, Weinheim
- Buback M, Vögele HP, Winkels HJ (1986c) *Makromol Chem Makromol Symp* 5:69
- Buchanan S, Michel H, Gerwert K (1992) *Biochem* 31:1314
- Buchholz N, Mattes R (1986) *Angew Chem Int Ed Engl* 25:1104
- Buker JF, Sample JD (1976) Tunable Diode Laser Instruments, ISA Reprint. Pittsburg, pp 76-613
- Bulkin BJ (1976) Vibrational spectroscopy of liquid crystals. In: Brown GH (ed) *Advances in liquid crystals*, vol 2. Academic, New York, p 199
- Bulkin BJ (1981) Vibrational spectra of liquid crystals. In: Clark RJH, Hester RE (eds) *Advances in infrared and Raman spectroscopy*, vol 8. Heyden, London, p 151
- Bunker PR (1979) *Molecular Symmetry and Spectroscopy*. Academic Press, New York
- Bunow MR, Levin IW (1977a) *Biochim Biophys Acta* 464:202
- Burch DE, Gryvnak DA (1967) *J Chem Phys* 47:4930
- Burdett JK, Poliakoff M, Turner JJ (1978) Vibrational Energy Levels in Matrix Isolated Species. In: Clark RJH, Hester RE (eds) *Advances in Infrared and Raman Spectroscopy*, vol 2. Heyden, London, p 1
- Bürger H, Burczyk K, Bielefeldt D, Willner H, Ruoff A, Molt K (1979) *Spectrochim Acta* 35A:875
- Bürger H, Eujen R (1974) Low-valent silicon. In: Davison A et al (eds) *Topics in current chemistry*, vol 50. Springer, Berlin, p 1
- Bürger H, Willner H (1988) *Mol Spectrosc* 128:221
- Burns DA, Ciurcak EW (eds) (1992) *Handbook of Near-Infrared Analysis*, Marcel Dekker Inc, New York
- Bush SF, Adamo RG, Levin IW (1980) *Biochemistry* 19:4429
- Butler LRP, Laqua K (1993) IUPAC Recommendation V.4 IX. Pure Appl Chem (to be published)
- Butler M, Salem N, Hoss W (1979) *Chem Phys Lipids* 29:99
- Byer RL, Duncan M, Gustafson E, Oesterlin P, Konig F (1981) Pulsed and CW Molecular Beam CARS Spectroscopy. In: McKellar ARW, Oka T, Stoicheff BP (eds) *Laser Spectroscopy* V, Springer, Berlin, p 233
- Byler DM, Susi H (1986) *Biopolymers* 25:469
- Cabana A, Bachand J, Giguere J (1974) *Can J Phys* 52:1949
- Cabannes J (1928) *Compt Rend Acad Sc (Paris)* 186:1201
- Cahn RS, Ingold CK, Prelog V (1966) *Angew Chem* 78:413
- Caldwell DJ, Eyring H (1971) *The theory of optical activity*. Wiley, New York London Sydney Toronto
- Califano S (1976) *Vibrational States*. John Wiley & Sons, New York London
- Califano S, Schettino V, Neto N (1981) *Lattice dynamics of molecular crystals*, Springer, Berlin
- Callomon JH, Dunn TM, Mills IM (1966) *Phil Trans Roy Soc London* 259:499
- Cameron D, Jones RN (1981) *Appl Spectrosc* 35:448
- Cameron DC, Casal HL, Mantsch HH (1979) *J Biochem Biophys Methods* 1:21
- Cameron DG, Martin A, Moffatt DT, Mantsch HH (1985) *Biochemistry* 24:4355
- Campbell DJ, Ziegler LD (1993) *Chem Phys Lett* 201:159

- Cao A, Hantz-Brachet E, Azize B, Taillandier E, Perret G (1991) *Chem Phys Lipids* 58:225
- Cardona M (1975) Light Scattering in Solids I, *Topics in Appl Phys* 8, Springer, Berlin Heidelberg New York London
- Cardona M, Guentherodt G (1982) Light Scattering in Solids II, *Topics in Appl Phys* 50, Springer, Berlin Heidelberg New York London
- Cardona M, Guentherodt G (1983) Light Scattering in Solids III, *Topics in Appl Phys* 51, Springer, Berlin Heidelberg New York London
- Cardona M, Guentherodt G (1984) Light Scattering in Solids IV, *Topics in Appl Phys* 54, Springer, Berlin Heidelberg New York London
- Carey P, Schneider H (1978) *Acc Chem Res* 11:122
- Carey P, Schneider H, Bernstein HJ (1972) *Biochem Biophys Res Commun* 47:588
- Carey PR (1981) *Can J Spectrosc* 26:134
- Carey PR (1982) Biochemical Applications of Raman and Resonance Raman Spectroscopies. Academic, New York
- Carey PR, King RW (1979) *Biochemistry* 18:2834
- Carey PR, Salares VR (1980) Raman and resonance Raman studies of biological systems. In: Clark RJH, Hester RE (eds) *Advances in Infrared and Raman spectroscopy*, vol 7. p 1 Heyden and Sons, London
- Carey PR, Schneider H (1978) *Acc Chem Res* 11:122
- Carmona P, De Cozar M, Garcia-Segura LM, Monreal J (1988) *Eur Biophys J* 16:169
- Carus TL (60 B.C.) *De rerum natura* V, 610; Citation of Tyndall J (1871) *Fragment on Science for Unscientific People*. Longway, Greens & Co, London
- Casal HL, Cameron DG, Smith ICP, Mantsch HH (1980) *Biochemistry* 19:444
- Casal HL, Mantsch HH (1984) *Biochim Biophys Acta* 779:381
- Casal HL, Mantsch HH, Hauser H (1987a) *Biochemistry* 26:4408
- Casal HL, Martin A, Mantsch HH, Paltauf F, Hauser H (1987b) *Biochemistry* 26:7395
- Castellucci E, Jonuscheit J, Lehner U, Schröter HW (1993) (unpublished)
- Ceram Optec (1991) Product Information. Bonn, Germany
- Cerdeira F, Fjeldly TA, Cardona M (1973) *Phys Rev B* 8:4734
- Chabal YJ (1988) *Surf Sci Rep* 8:211
- Chabal YJ, Harris AL, Raghavachari K, Tully JC (1993) *Int J Mod Phys B* 7:1031
- Chabay I (1972) *Chem Phys Lett* 17:283
- Chackerian C (1976) *J Chem Phys* 65:4228
- Chackerian C, Tipping RH (1983) *J Mol Spectrosc* 99:431
- Chalmers JM, Mackenzie MW (1988) Solid Sample Techniques. In: Mackenzie MW (ed) *Advances in Applied Fourier Transform Infrared Spectroscopy*. Wiley, Chichester. p 105
- Chalmers JM, Willis HA, Cowell GM, Spragg RA (1982) *Perkin Elmer Infrared Bulletin* 99
- Champion JP (1977) *Can J Phys* 55:1802
- Champion JP, Loete M, Pierre G (1992) Spherical Top Spectra. In: Rao KN and Weber A (eds) *Spectroscopy of the Earth's Atmosphere and Interstellar Medium*. Academic Press, New York, p 339
- Chandrasekhar S, Prasad JS (1971) *Mol Cryst Liq Cryst* 14:115
- Chandrasekhar S, Ranganath GS (1974) *Mol Cryst Liq Cryst* 25:195
- Chang IC (1981) *Optical Engineering* 20:824
- Chang RK (1987) *Ber Bunsen Phys Chem* 91:296
- Chang RK, Furtak TS (1982) (eds) *Surface Enhanced Raman Scattering*. Plenum, New York
- Chang RK, Laube BL (1984) *CRC Crit Rev Solid State Mater Sci* 12:1
- Chantry GW (1978) *J Mol Struct* 45:307
- Chantry GW, Plane TJ (1960) *J Chem Phys* 32:319
- Chantry GW, Plane TJ (1961) *J Chem Phys* 34:1268
- Chapman D, Byrne P, Shippley GG (1966) *Proc Roy Soc London* 290:215
- Chapman D, Williams RM, Ladbrook BD (1967) *Chem Phys Lipids* 1:445
- Chase DB, Parkinson BA (1988) *Appl Spectrosc* 42:1186
- Che D, Nafie LA (1992) *Chem Phys Lett* 189:35
- Chen CY, Burstein E, Lundquist E (1979) *Solid State Commun* 32:63
- Chen MC, Lord RC (1974) *J Am Chem Soc* 96:4750
- Cheng CP, Ludowise JD, Schrader GC (1980) *Appl Spectrosc* 34:146
- Chesters MA (1986) *J Electron Spectrosc Relat Phenom* 38:123

- Chesters MA, Sheppard N (1988) Electron Energy-Loss Spectroscopy. In: Clark RJH, Hester RE (eds) *Spectroscopy of Surfaces*. Wiley, Chichester, p 377
- Chi FK, Andrews L (1973) *J Phys Chem* 77:3062
- Chiang CK, Fincher CR, Park YW, Heeger AJ, Shirakawa H, Louis EJ, Gau SC, MacDiarmid AG (1977) *Phys Rev Lett* 39:1098
- Chiellini E, Veracini CA (eds) (1993) *Proceedings of the Fourteenth International Liquid Crystal Conference*. In: *Liq Cryst*, vol 14
- Child MS, Bernstein RB (1973) *J Chem Phys* 57:5916
- Chingduang P (1981) Dissertation, Universität Essen
- Christensen PA, Hamnett A (1989) In-situ infrared studies of the electrode-electrolyte interface. In: Compton RG, Hamnett A (eds) *New Techniques for the Study of Electrodes and their Reactions*. Elsevier, Amsterdam Oxford New York, p 1
- Christie DA, McCreery RL (1990) *Appl Spectrosc* 44:1229
- Chu CW, Gao L, Chen F, Huang ZJ, Meng RL (1993) *Nature* 365:326
- Chu HT et al (1979) *Adv Chem Ser* 174:87
- Chung Y, Ziegler LD (1988) *J Chem Phys* 88:7287
- Ciardelli F, Salvadori P (eds) (1973) *Fundamental aspects and recent developments in ORD and CD*. Heyden, London
- Ciferri A (ed) (1991) *Liquid crystallinity in polymers: Principles and fundamental properties*. VCH, New York
- Claassen HH, Goodman GL, Kim H (1972) *J Chem Phys* 56:5042
- Clark FRS, Moffatt DM (1978) *Appl Spectrosc* 32:547
- Clark MG, Saunders FC (1982) *Mol Cryst Liq Cryst (Letters)* 82:267
- Clark RJH (1975) In: *Advances in Infrared and Raman Spectroscopy*, vol 1, Clark RJH, Hester RE (eds). Heyden, London, p 143
- Clark RJH (1984) In: *Advances in Infrared and Raman Spectroscopy*, vol 11, Clark RJH, Hester RE (eds) Heyden, London, p 95
- Clark RJH, Dines TJ (1986) *Angew Chem Int Ed Engl* 25:131
- Clark RJH, Franks ML (1975) *J Am Chem Soc* 92:2691
- Clark RJH, Hester RE (1975) *Advances in Infrared and Raman Spectroscopy*. Heyden & Son, London
- Clark RJH, Kurnov M, Keller HJ, Keppler B, Traeger U (1980) *J Chem Soc (Dalton)* 2498
- Clark RJH, Mitchell PD (1973) *J Am Chem Soc* 95:8300
- Clark RJH, Stead MJ (1981) *Inorg Chem* 20:2759
- Clarke EGC (ed) (1969) *Isolation and Identification of Drugs*. The Pharmaceutical Press, London
- Claus R (1980) *Symmetrie in der Musik*. In: Preisinger A (ed) *Symmetrie*. Springer Wien
- Cleij P, Dijkstra A (1979) *Fresenius Z Anal Chem* 298:97
- Cloppenburg B, Manczak K, Prockl H, Schröter HW, Strey G (1979) *Z Naturforsch* 34a:1160
- Coates JP (1974) *Proc Inst Petr Symp chapt 2, Laser Raman Spectroscopy in the Oil Industry* 1974:13, John Wiley, New York
- Coates JP, Setti LC (1983) SAE Technical Paper Series, paper 831681 presented at: Fuels and Lubricants Meeting, San Francisco, California
- Coblentz WW (1905) *Investigations of Infrared Spectra*, Carnegie Institution, Washington. Republication (1962): The Coblentz Society, Norwalk
- Cochran W (1960) *Adv Phys* 9:387
- Cochran W (1961) *Adv Phys* 10:401
- Cole ARH (1977) *IUPAC-Tables of Wavenumbers for the Calibration of Infrared Spectrometers*, 2nd edn. Pergamon Press, Oxford
- Colles MJ, Pidgeon CR (1975) *Rep Progr Phys* 38:329
- Collins DW, Fitchen DB, Lewis A (1973) *J Chem Phys* 59:5714
- Collyer AA (ed) (1992) *Liquid crystal polymers: From structures to applications*. Elsevier, London
- Colombo L (1976) *Proceedings of the 5th International Conference on Raman Spectroscopy*, Freiburg, p 532
- Colthup NB (1980) *Appl Spectrosc* 34:1
- Colthup NB, Daly LH, Wiberley SE (1975) *Introduction to Infrared and Raman Spectroscopy*, 2nd edn. Academic Press, New York
- Colthup NB, Daly LH, Wiberley SE (1990) *Introduction to Infrared and Raman Spectroscopy*, 3rd edn. Academic Press, Boston

- Compaan A (1977) *Appl Spectrosc Rev* 13:295
Connes P, Michel G (1975) *Appl Opt* 14:2067
Conroy CM, Griffiths PR, Jinno K (1985) *Anal Chem* 52:1394
Conzen JP, Brück J, Ache HJ (1993) *Appl Spectrosc* 47:753
Cook BW, Louden JD (1979) *J Raman Spectrosc* 8:249
Cook R, Paterson MD (1978) *Forensic Sci Internat* 12:237
Cooney RP, Boutilier GO, Winefordner JD (1977) *Anal Chem* 49:1048
Cooney RP, Tsai P (1980) *J Raman Spectrosc* 9:33
Cooper SL, Klein MV, Pazol BG, Rice JP, Ginsberg DM (1988) *Phys Rev B* 37:5920-5923
Coperland RA, Fodor SPA, Spiro TG (1984) *J Am Chem Soc* 106:3872
Coron JM, Ghidaglia JM, Helein F (eds) (1991) Proceedings of the NATO advanced research workshop on defects, singularities, and patterns in nematic liquid crystals: Mathematical and physical aspects. *NATO ASI Ser C*, vol 332. Kluwer Academic, Dordrecht, p 428
Cossé C, Fouassier M, Mejean T, Tranquille M, DiLella DP, Moskovits M (1980) *J Chem Phys* 73:6076
Cotter D, Hanna DC, Tuttlebee WHW, Yuratich MA (1977) *Opt Commun* 22:190
Cotton A (1895) *C R H Acad Sci* 120:989
Cotton FA (1990) Chemical Applications of Group Theory, 3rd edn. Wiley-Intersci, New York
Cotton FA, Hunter DL (1974) *Inorg Chim Acta* 11:L9
Cotton FA, Kraihanzel CS (1962) *J Am Chem Soc* 84:4432
Cotton FA, Kraihanzel CS (1963) *Inorg Chem* 2:533
Cotton FA, Kraihanzel CS (1964) *Inorg Chem* 3:702
Cotton FA, Musco M, Jagupsky G (1967) *Inorg Chem* 6:1357
Cotton TM (1988) In: *Spectroscopy of Surfaces*, Clark RJH, Hester RE (eds). Wiley, p 91
Cotton TM, Schultz SG, van Duyne RP (1980) *J Am Chem Soc* 102:7960
Cotton TM, van Duyne RP (1982) *FEBS Lett* 147:81
Coufal H (1986) *Fresenius Z Anal Chem* 324:456
Coulson CA, Duchesne J, Manneback C (1948) Contribution a l'étude de la structure moléculaire, Desoer, Liege
Courmayer R, Shearer JC, Anderson DM (1977) *Anal Chem* 49:2275
Cowie IA, McNicol JW (1985) *Appl Spectrosc* 39:257
Crabtree RH (1990) *Acc Chem Res* 23:95
Craig NC, Bryant GJ, Levin IW (1987) *Biochemistry* 26:2449
Craig RC, Levin IW (1979) *Appl Spectrosc* 33:475
Crawford B Jr, Goplen TG, Swanson D (1978) The Measurement of Optical Constants in the Infrared by Attenuated Total Reflection. In: Clark RJH, Hester RE, *Advances in Infrared and Raman Spectroscopy*, vol 4, Heyden London, p 47
Creighton JA (1980) *Springer Series in Chemical Physics*, vol 15, Springer, Berlin, p 145
Creighton JA (1986) *Surf Sci* 173:665
Creighton JA (1988) In: *Spectroscopy of Surfaces*, Clark RJH, Hester RE (eds). Wiley, p 37
Creighton JA (1990) In: *Spec Rep Roy Soc Chem*, vol 84, *Surface Analysis Techniques and Applications*. Roy Soc, London, p 13
Creighton JA, Blatchford CG, Albrecht MG (1979) *J Chem Soc Faraday Trans II* 75:790
Crookell A, Fleischmann M, Hanniet M, Hendra PJ (1988) *Chem Phys Lett* 149:123
Crookell A, Hendra PJ, Mould HM, Turner AJ (1990) *J Raman Spectrosc* 21:85
Crunelle-Cras M, Merlin JC (1977) *J Raman Spectrosc* 6:261
Cunningham T, Lis LJ (1986) *Biochim Biophys Acta* 861:237
Cutler DJ (1990) *Spectrochim Acta* 46A:123
Cutler DJ, Petty CJ (1991) *Spectrochim Acta* 47A:1159
Cyvin SJ, Cyvin BN, Mogstad T (1986) *Spectrochim Acta* 42A:985
D'Orazio M, Hirschberger R (1983) *Optical Engineering* 22:308
D'Orazio M, Schrader B (1974) *J Raman Spectrosc* 2:585
D'Orazio M, Schrader B (1976) *J Raman Spectrosc* 4:253
Dai Y, Swinnea JS, Steinfink H, Goodenough JB, Campion A (1987) *J Am Chem Soc* 109:5291
Damen TC, Porto SPS, Tell B (1966) *Phys Rev* 142:570
Danno T, Kuerti J, Kuzmany H (1991) *Phys Rev B* 43:4809
Danno T, Kuzmany H (1993) *Synth Met* 58:257
Danzer K (1978) *Z Chem* 18:104

- Danzer K, Eckschlager K, Wienke D (1987a) Fresenius Z Anal Chem 327:312
- Danzer K, Than E, Molch D, Küchler L (1987b) Analytik. Wissenschaftliche Verlagsgesellschaft, Stuttgart
- Darling JH, Ogden JS (1972) J Chem Soc Dalton:2496
- Darling JH, Ogden JS (1973) J Chem Soc Dalton:1079
- Davidson G (1989) Vibrational spectra of transition-element compounds. In: Davidson G, Ebsworth EAV (eds) Spectroscopic properties of inorganic and organometallic compounds, vol 22. The Royal Society of Chemistry, Cambridge, p 278
- Davies B, Poliakoff M, Smith KP, Turner JJ (1978) J Photochem 1978:2
- Davies JP, Pachuta SJ, Cooks RG, Weaver MJ (1986) J Anal Chem 58:1290
- Davies PB, Morton-Jones AJ (1987) Appl Phys B 42:35
- de Abney W, Festing RE (1881) Phil Trans Royal Soc (London) 172:887
- Decius JC (1949) J Chem Phys 17:1315
- Decius JC, Hexter RM (1977) Molecular Vibrations in Crystals. McGraw-Hill, New York
- de Groot J, Hester RE (1987) J Phys Chem 91:1963
- Deisenhofer J, Michel H (1989) Science 245:1463
- Delank HW, Fischer R, Kaiser H, Schrader B, Spicker H (1964) Deutsche Z Nervenheilkunde 185:664
- Delhaye M, Dhamelein court P (1975) J Raman Spectrosc 3:33
- De Martino A, Frey R, Drodere F, Ducuing F (1979) Infrared Phys 19:247
- de Meijere A, Lüttke W, Heinrich F (1974) Liebigs Ann Chem 1974:306
- Demröder W (1991) Laserspektroskopie. Springer Verlag, Berlin
- de Mul FFM, van Welie AGM, Otto C, Mud J, Greve J (1984) J Raman Spectrosc 15:268
- Deng H, Callender RH (1987) Biochemistry 26:7418
- Deng H, Manor D, Weng G, Rath P, Koutalos Y, Ebrey T, Gebhard R, Lugtenburg J, Tsuda M, Callender RH (1991) Biochemistry 30:4495
- Deng H, Zheng J, Sloan D, Burgner J, Callender RH (1989) Biochemistry 28:1525
- Denisov VN, Mavrin BN, Podobedov VB, Sterin KE (1978) Opt Commun 26:372
- Denisov VN, Mavrin BN, Podobedov VB, Sterin KE (1980) JETP Lett 32:316
- Denisov VN, Mavrin BN, Podobedov VB, Sterin KE, Varshai BG (1980) Opt Spectrosc USSR 49:221
- Dennison DM (1928) Phys Rev 31:503
- Desbois A, Lutz M, Banerjee R (1979) Biochemistry 18:1510
- Desbois A, Tegoni M, Gervais M, Lutz M (1989) Biochemistry 28:8011
- Deutscher CW, Moscovitz A (1968) 49:3257
- Devlin MT, Levin IW (1990) J Raman Spectrosc 21:441
- Devonshire R, Dring IS, Hoey G, Porter FM, Williams DR, Greenhalgh DA (1986) Chem Phys Lett 129:191
- De Vos JC (1954) Physica XX:690
- Dhamelein court P (1979) Raman Molecular Microprobe, These. L'Universite de Lille; Raman Molecular Microprobe, MOLE. Instruments SA, München
- Diem HE, Krimm S (1981) Appl Spectrosc 35:421
- Diem M, Gothin PJ, Kupfer JM, Tindall AG, Nafie LA (1977) J Am Chem Soc 99:8103
- Dignam MJ, Baker DM (1981) Appl Spectrosc 35:186
- DiLella DP, Limm W, Lipson RH, Moskovits M, Taylor KV (1982) J Chem Phys 77:5263
- Dill B, Heydtmann H (1978) Chem Phys 35:161
- Diller R, Iannone M, Cowen B, Maiti S, Bogomolni R, Hochstrasser RM (1991) In: Hester RE, Girling RB (eds) Spectroscopy of Biological Molecules. Royal Society of Chemistry, p 125
- Diller R, Stockburger M (1988) Biochemistry 27:7641
- DIN Deutsches Institut für Normung (ed) (1982) German Standard Methods for the examination of water, waste water and sludge, DIN 38409-H18, Beuth Verlag, Berlin
- Dinardo NJ, Avouris P, Demuth JE (1984) J Chem Phys 81:2169
- Dines TJ, French MJ, Hall RJB, Long DA (1976) in Proc Vth Int Conf Raman Spectrosc, Schmid ED, Brandmüller J, Schrader B, Schröter HW (eds). Schulz Verlag, Freiburg, p 707
- Dippel B, Keller S, Schrader B (1992) XIII International Conference on Raman Spectroscopy. John Wiley & Sons, Chichester, p 478
- Dirac PAM (1927) Proc Roy Soc London A 114:710
- Dluhy RA, Mendelsohn R, Casal HL, Mantsch HH (1983) Biochemistry 22:1170

- Dobbs KD, Dixon DA (1994) *J Phys Chem* 98:4489
- Doerffel K (1988) *Fresenius Z Anal Chem* 330:24
- Doerffel K, Eckschlager K (1981) *Optimale Strategien in der Analytik*. Harry Deutsch Verlag, Frankfurt (M)
- Doerffel K, Hildebrandt W (1969) *Wiss Z TH Chem Carl Schorlemmer Leuna-Merseburg* 11:30
- Dollish FR, Fateley WG, Bentley FF (1974) *Characteristic Raman Frequencies of Organic Compounds*. Wiley-Intersc, New York
- Domingo C, Escribano R, Murphy WF, Montero S (1982) *J Chem Phys* 77:4353
- Domingo C, Montero S (1987) *J Chem Phys* 86:6046
- Dornhaus R (1982) In: *Springer Tracts in Modern Physics*, vol 22. Springer, Berlin, p 201
- Doucet J, Benoit JP, Cruse WBT, Prange T, Kennard O (1989) *Nature* 337:190
- Dowling JM, Stoicheff BP (1959) *Can J Phys* 37:703
- Downs AJ, Goode MJ, Pulham CR (1989) *J Am Chem Soc* 111:1936
- Doyle WM (1990) *Appl Spectrosc* 44, 1:50
- Drake MC, Grabner LH, Hastie JW (1979) *National Bureau of Standards Special Publ* 561:1105
- Drake MC, Rosenblatt GM (1976) *Chem Phys Lett* 44:313
- Drake MC, Rosenblatt GM (1978) *Combust Flame* 33:179
- Draper NR, Smith H (1966) *Applied Regression Analysis*. Wiley, New York
- Dresselhaus G, Dresselhaus MS, Eklund PC (1992) *Phys Rev* B45:6923
- Dresselhaus G, Dresselhaus MS, Eklund PC (1993) *J Mater Res* 8:2054
- Drushel HV, Iddings FA (1963) *Anal Chem* 35:28
- Dubois P, Lelieur JP, Lepoutre G (1988) *Inorg Chem* 27:3032
- Dudley RJ, Mason SF, Peacock RD (1972) *JCS Chem Comm* 1084
- Dudley RJ, Mason SF, Peacock RD (1975) *J Chem Soc Faraday Trans II* 71:997
- Duncan JL, Harper J, Hamilton E, Nivellini GD (1983) *J Mol Spectrosc* 102:416
- Duppen K, Weitekamp DP, Wiersma DA (1983) *J Chem Phys* 79:5835
- Dupuis PF, Dijkstra A (1978a) *Fresenius Z Anal Chem* 290:357
- Dupuis PF, Dijkstra A, van der Maas JH (1978b) *Fresenius Z Anal Chem* 291:27
- Durana JF (1979) *Polymer* 20:1306
- Durig J (ed) (1972) *Vibrational Spectra and Structure, A Series of Advances*. Elsevier, Amsterdam
- Durig JR, Carter RO, Carreira LA (1974) *J Chem Phys* 60:3098
- Durig JR, Little TS (1981) *J Chem Phys* 75:3360
- Durig JR, Sullivan JF (1990) (eds) *Proc. XIIth Int Conf Raman Spectrosc.* Wiley, London
- Dutler R, Rauk A (1989) *J Am Chem Soc* 111:6957
- Duval AB, King DA, Haines R, Isenor NR, Orr BJ (1986) *J Raman Spectrosc* 17:177
- Dyer CD, Hendra PJ (1992) *Analyst* 117:1393
- Earl GJ, Gans P, Gill JB (1985) *J Chem Soc Dalton*:663
- Ebel HF, Bliefert C (1990) *Schreiben und Publizieren in den Naturwissenschaften*. VCH Weinheim
- Ebel S, Hocke J (1979) *Fresenius Z Anal Chem* 299:23
- Ebsworth EAV, Rankin DWH, Cradock S (1987) *Structural Methods in Inorganic Chemistry*. Blackwell, Oxford
- Eckardt H, Shacklette LW, Szobota JS, Baughman RH (1985) *Mol Cryst Liq Cryst* 117:401
- Eckbreth AC (1978) *Appl Phys Lett* 32:421
- Eckbreth AC (1988) *Laser Diagnostics for Combustion Temperature and Species*. Abacus Press, Turnbridge Wells, Cambridge, Mass
- Eckbreth AC, Anderson TJ (1985) *Appl Opt* 24:2731
- Eckbreth AC, Dobbs GM, Stufflebeam JH, Tellex PA (1984) *Appl Opt* 23:1328
- Eckbreth AC, Hall RJ (1979) *Combustion and Flame* 36:87
- Eckel R, Buback M, Strobl GR (1981) *Coll Polym Sci* 259:326
- Eckert K (1977) *Biopolymers* 16:2549
- Eckhardt G, Wagner WG (1966) *J Mol Spectrosc* 19:407
- Eckschlager K (1969) *Errors, Measurement and Results in Chemical Analysis*. Van Nostrand, London
- Eckschlager K (1977) *Fresenius Z Anal Chem* 277:1; (1977) *Anal Chem* 49:1265
- Edwards HGM, Farwell DW, Goryn AC, Long DA (1986) *J Raman Spectrosc* 17:129
- Edwards HGM, Good EAM, Long DA (1976) *J Chem Soc Faraday Trans II* 72:984
- Edwards HGM, Long DA, Mansour HR, Najm KAB (1979) *J Raman Spectrosc* 8:251
- Edwards HGM, Long DA, Najm KAB, Thomsen M (1981) *J Raman Spectrosc* 10:60

- Eesley GL (1981) Coherent Raman Spectroscopy, Pergamon Press, Oxford
- Efrima S (1985) In: Modern Aspects of Electrochemistry, vol 16, Conway BE, White RE, Bockris OM (eds). Plenum, New York, p 253
- Egawa T, Ogura T, Makino R, Ishimura Y, Kitagawa T (1991) J Biol Chem 266:10246
- Eggiman T, Shaw RA, Wieser H (1991) J Phys Chem 95:95
- Ehrenfreund E, Vardeny Z, Brafman O, Horovitz B (1987) Phys Rev B36:1535
- Ehrlich G, Scholze H, Gerbatsch R (1969) Spectrochim Acta 24B:641
- Eich M (1993) Ber Bunsenges Phys Chem 97:1261
- Eidner K, Mayer G, Schmidt M, Schmiedel H (1989) Mol Cryst Liq Cryst 172:191
- Eklund PC, Zhou P, Wang KA, Dresselhaus G, Dresselhaus MS (1992) J Phys Chem Solids 53:1391
- Elias GH (1972) Makromoleküle, 2nd edn. Hüthig & Wepf Verlag, Basel Heidelberg
- Elser W, Ennulat RD (1976) Selective reflection of cholesteric liquid crystals. In: Brown GH (ed) Advances in liquid crystals, vol 2. Academic, New York, p 73
- Emsley JW (1985) Nuclear magnetic resonance of liquid crystals. Reidel, Dordrecht
- Engelhard M, Gerwert K, Hess B, Kreutz W, Siebert F (1985) Biochemistry 24:400
- Engert C, Materny A, Kiefer W (1992) Chem Phys Lett 198:395
- England WA, Glass DHW, Brennan G, Greenhalgh DA (1986) J Catal 100:163
- England WA, Milne JM, Jenny SN, Greenhalgh DA (1984) Appl Spectrosc 38:867
- England SW (1963) Biochemistry 2:798
- Eppinger S, Rabold A, Misra TN, Nandy SK, Schrötter HW (1991) Verhandl DPG (VI) 26, in press
- Eppinger S, Rabold A, Misra TK, Nandy SK, Schrötter HW (1992) J Mol Struct 266:389
- Epstein AJ, MacDiarmid AG (1989) Springer Series Solid State Sciences 91:282. In: Kuzmany H, Mehring M, Roth S (eds) Electronic Properties of Polymers III Springer, Berlin Heidelberg New York London
- Erfurth SC, Bond PJ, Petricolas WL (1975) Biopolymers 14:1245
- Erlenmaier H, Adrian P (1974) CZ Chemie Technik 1974:191
- Escribano JR, Barron LD (1988) Mol Phys 65:327
- Esherick P, Anderson RJM (1980) Chem Phys Lett 70:621
- Esherick P, Owyong A (1982) High Resolution Stimulated Raman Spectroscopy. In: Clark RJH, Hester RE (eds) Advances in Infrared and Raman Spectroscopy, vol 9. Heyden, London, p 130
- Esherick P, Owyong A (1983) Chem Phys Lett 103:235
- Esherick P, Owyong A, Patterson C (1983) J Phys Chem 87:602
- Esherick P, Owyong A, Plíva J (1985) J Chem Phys 83:3311
- Etz ES, Rosasco GJ, Blaha JJ (1978) Observation of the Raman Effect from small single particles: Use in the chemical identification of airborne particulates. In: Toribara TY et al (eds) Environmental Pollutants. Plenum Press, New York, p 413
- Evans PA (1991) Spectrochim Acta 47A:1441
- Everall NJ, Howard J (1989) Appl Spectrosc 43:778
- Ewald PP (1921) Ann Phys 64:253
- Eyring H, Henderson D, Jost W (eds) (1970) Physical Chemistry An Advanced Treatise. vol IV, Molecular Properties. Academic Press, New York London
- Eysel HH, Bertie JE (1988) J Raman Spectrosc 19:59
- Fabelinsky VI, Krynetsky BB, Kulevsky LA, Mishin VA, Prokhorov AM, Savel'ev AD, Smirnov VV (1977) Opt Commun 20:389
- Fadini A (1976) Molekülkraftkonstanten. Steinkopff, Darmstadt
- Fadini A, Schnepel FM (1985) Schwingungsspektroskopie, Methoden, Anwendungen. Thieme, Stuttgart
- Fahr E, Mitschke M (1979) Spektren und Strukturen Organischer Verbindungen. Verlag Chemie, Weinheim
- Fahrenfort J (1961) Spectrochim Acta 17:698
- Fano U (1961) Phys Rev 124:1866
- Fantoni R, van Helvoort K, Knoppers W, Reuss J (1986) Chem Phys 110:1
- Fasman GD, Itoh K, Liu CS, Lord RC (1978) Biopolymers 17:125
- Fassel VA (1972) Pure Appl Chem 30:653
- Fassel VA (1974) Appl Spectrosc 28:398
- Fast H, Welsh HL, Lepard DW (1969) Can J Phys 47:2879
- Fast JD, Stumpers FLHM (1956) Philips Techn Rundsch 18:164

- Faucon JF, Dufourcq J, Bernard E, Duchesneau L, Pezolet M (1983) Biochemistry 22:2179
- Faulques E, Wallnofer W, Kuzmany H (1989) J Chem Phys 90:7585-7593
- Favrot J et al (1979) Photochem Photobiol 29:99
- Feldman T, Romanko J, Welsh HL (1955) Can J Phys 33:138
- Feldman T, Shepherd GG, Welsh HL (1956) Can J Phys 34:1425
- Feilker PM, Henson BF, Venturo VA, Hartland GV (1992) In: Proc XIIth Int Conf Raman Spectrosc, Kiefer W, Cardona M, Schaack G, Schneider FW, Schröter HW (eds) Wiley, Chichester, p 230
- Feilgett P (1958) J Phys Radium (Paris) 19:187
- Felsenfeld G (1978) Nature 271:115
- Fermi E (1931) Z Phys 71:250
- Fernandez-Sanchez JM, Montero S (1989) J Chem Phys 90:2909
- Fernandez-Sanchez JM, Montero S (1991) J Chem Phys 94:7788
- Fernandez-Sanchez JM, Valdenebro AG, Montero S (1989) J Chem Phys 91:3327
- Ferraro JR, Basile LJ (1974) Appl Spectrosc 28:505
- Ferraro JR, Basile LJ (1980) Appl Spectrosc 34:216
- Ferraro JR, Nakamoto K (1994) Introductory Raman Spectroscopy, Academic Press, New York
- Ferraro JR, Rein AJ (1985) Applications of Diffuse Reflectance Spectroscopy in the Far-Infrared Region. In: Ferraro JR, Basile LJ (eds) Fourier Transform Infrared Spectroscopy, vol 4. Academic, Orlando
- Ferraro JR, Ziomek JS (1975) Introductory Group Theory. Plenum Press, New York
- Fiber Systems (1991) Product Information. Silver Springs, USA
- Fickenscher M, Laubereau A (1990) J Raman Spectrosc 21:857
- Fickenscher M, Purucker HG, Laubereau A (1992) Chem Phys Lett 191:182
- Fillaux F, Baron MH (1981) Chem Phys 62:275
- Finch A, Gates PN, Radcliffe K, Dickson FN, Bentley FF (1970) Chemical Applications of Far Infrared Spectroscopy. Academic Press, London
- Finch JT, Lutter LC, Rhodes D, Brown RS, Rushton B, Levitt M, Klug A (1977) Nature 269:29
- Fincher jr CR, Chen CE, Heeger AJ, Macdiarmid AG, Hastings JB (1982) Phys Rev Lett 48:100
- Finkelmann H, Pohl L, Rubner R, Sackmann H, Stegemeyer H (eds) (1993) Berichtsheft Hauptversammlung 1993 Neue Eigenschaften und Anwendungen von Flüssigkristallen, Ber Bunsenges Phys Chem 97:1169
- Finkelmann H, Stegemeyer H (1974) Ber Bunsenges Physik Chem 78:869
- Finsterhölzl H (1982) Ber Bunsenges Phys Chem 86:797
- Finsterhölzl H, Hochenbleicher JG, Strey G (1977) J Raman Spectrosc 6:13
- Finsterhölzl H, Klöckner HW, Srinivasan K, Schröter HW, Brandmüller J (1978) Indian J Pure Appl Phys 16:370
- Finsterhölzl H, Schröter HW, Strey G (1981) J Raman Spectrosc 11:375
- Firth S, Klotzbuecher WE, Poliakoff M, Turner JJ (1987) Inorg Chem 26:3370
- Fischer JE, Cox DE (1992) J Phys Chem Solids 53:
- Fischer M, Schmid R (1985) Chemie und Physik. In: Polymere Werkstoffe, vol 1. Georg Thieme Verlag, Stuttgart New York, p 363
- Fischer P, Bougeard D, Schrader B (1989) Simulation der Schwingungsspektren (SPSIM). In: Gauglitz G (ed), Software-Entwicklung in der Chemie. Springer, Berlin
- Fleischmann M, Hendra PJ, McQuillan AJ (1974) Chem Phys Lett 26:163
- Fleischmann M, Hendra PJ, McQuillan AJ, Paul RL, Reid ES (1975) J Raman Spectrosc 3:153
- Flick K (1965) Arbeitsschutz 7:161
- Flory JP (1953) Principles of Polymer Chemistry. Cornell University Press, Ithaca New York, p 576
- Flournoy PA, Schaffers WJ (1966) Spectrochim Acta 22:5
- Flournoy PA, Schaffers WJ (1966) Spectrochim Acta 22:15
- Flytzanis C (1975) In: Quantum Electronics: A Treatise, vol I, part A, Rabin AH, Tang LC (eds). Academic Press, New York, p 9
- Fong TM, McNamee MG (1987) Biochemistry 26:3871
- Fontana MP (1992) Molecular dynamics in nematic phases: Raman and infrared spectroscopy. In: Phase transitions in liquid crystals. NATO ASI Ser B 290:259
- Forcé RK (1988) Anal Chem 60:1989
- Forman RA, Piermarini GJ, Barnett JD, Block S (1972) Science 176:284

- Forro L, Carr GL, Williams GP, Mandrus D, Mihaly L (1990) Phys Rev Lett 65:1941-1944
- Foster RB, Hills GW, Jones WJ (1977) Mol Phys 33:1589
- Fraas LM, Porto SPS (1970) Solid State Commun 8:803
- Franck EU, Roth K (1967) Discuss Faraday Soc 43:108
- Frankiss SG, Harrison DJ (1975) Spectrochim Acta 31A:161
- Fraser GV, Keller A, Pastor JM, De Saha JA, Martuscelli E (1979) Polymer 20:780
- Frassa KA, Sarkis AB (1968) SAE Transactions 77:sect 4, paper 680759
- Frassa KA, Siegfriedt RK, Houston CA (1966) SAE Transactions 74:591
- Fraunhofer J (1821) In: Lommel E (ed) (1888) Fraunhofer's gesammelte Schriften, München
- Frech R, Wang EC, Bates JB (1980) Spectrochim Acta 36A:915
- Fredericks PM, Lee JB, Osborn PR, Swinkels DAJ (1985) Appl Spectrosc 39:303, 311
- Freedman TB, Spencer KM, Ragunathan N, Nafie LA, Moore JA, Schwaab JM (1991) Can J Chem 69:1619
- Freeman RD, Hammaker RM, Meloan CE, Fateley WG (1988) Appl Spectrosc 42:456
- Freeman SK (1974) Applications of Laser Raman Spectroscopy, Wiley-Intersc, John Wiley & Sons, New York London Sydney Toronto
- Frei K, Günthard HH (1963) J Opt Soc Am 51:83
- French MJ, Long DA (1975) J Raman Spectrosc 3: 391
- Freund SM, Maier II WB, Holland RF, Beattie WH (1978) Anal Chem 50:1260
- Friedel G (1922) Ann Phys (Paris) 18:273
- Friedl B, Thomson C, Cardona M (1990) Phys Rev Lett 65:915
- Friedrich HB, Jung-Pin Yu (1987) Appl Spectrosc 41:227
- Fringeli VP, Gunthard HH (1981) In: Grell E (ed) Membrane Spectroscopy. Springer Verlag, New York, p 270
- Frisch MJ, Head-Gordon M, Schlegel HB, Raghavachari K, Binkley JS, Gonzales C, Defrees DJ, Fox DJ, Whiteside RA, Seeger R, Melius CF, Baker J, Martin RL, Kahn LR, Stewart JJP, Fluder EM, Topiol S, Pople JA (1988) GAUSSIAN 88, Gaussian Inc, Pittsburgh, PA
- Frisch MJ, Trucks GW, Schlegel HB, Gill PMW, Johnson BG, Wong MW, Foresman JP, Robb MA, Head-Gordon M, Replogle ES, Gomperts R, Andres JL, Raghavachari K, Bingley JS, Gonzales C, Martin RL, Fox DJ, De Frees DJ, Baker J, Stewart JJP, Pople JA (1993) GAUSSIAN 92, Gaussian Inc, Pittsburgh, PA
- Fritzsche H, Rupprecht A (1990) J Biomol Struct Dyn 7:1135
- Fritzsche H, Rupprecht A, Rupprecht M (1984) Nucleic Acids Res 12:9165
- Frunder H, Angstl R, Illig D, Schröter HW, Lechuga-Fossat L, Flaud JM, Camy-Peyret C, Murphy WF (1985) Can J Phys 63:1189
- Frunder H, Illig D, Finsterhözl H, Schröter HW, Lavorel B, Roussel G, Hilico JC, Champion JP, Pierre G, Poussigne G, Pascand E (1983) Chem Phys Lett 100:110
- Frunder H, Matziol L, Finsterhözl H, Beckmann A, Schröter HW (1986) J Raman Spectrosc 17:143
- Fuller MP, Griffiths P (1978) Anal Chem 50:1906
- Fuller MP, Ritter GL, Draper CS (1988) Appl Spectrosc 42:217
- Furic K, Durig JR (1988) Appl Spectrosc 42:175
- Furtak TE, Reyes J (1980) Surf Sci 93:351
- Furukawa Y, Akimoto M, Harada I (1987) Synth Met 18:151-156
- Furukawa Y, Tazawa S, Fujii Y, Harada I (1988a) Synth Met 24:329-341
- Furukawa Y, Ueda F, Hyodo Y, Harada I, Nakajima T, Kawagoe T (1988b) Macromolecules 21:1297-1305
- Gaber BP, Petricolas WL (1977) Biochim Biophys Acta 465:260
- Gaber BP, Yager P, Petricolas WL (1978) Biophys J 21:161
- Gadd GE, Poliakoff M, Turner JJ (1987) Organometallics 6:391
- Gans P (1975) Vibrating Molecules. Chapman and Hall, London
- Ganz M, Hartke B, Kiefer W, Kolba E, Manz J, Strempel J (1990) Vibrat Spectrosc 1:119
- Ganz M, Kiefer W (1993a) J Raman Spectrosc 24:463
- Ganz M, Kiefer W (1993b), unpublished results
- Ganz M, Kiefer W (1994) Mol Phys 81:69
- Ganz M, Kiefer W, Kolba E, Manz J, Vogt P (1992) Chem Phys 164: 99
- Ganz M, Kiefer W, Leuchs M, Materny A, Strempel J, Vogt P (1993) Vibrat Spectrosc 5:1
- Ganz M, Strempel J, Kiefer W (1993) Chem Phys Lett 207:110

- Gargaro AR, Barron LD, Hecht L (1993) *J Raman Spectrosc* 24:91
- Garnett JCM (1904) *Philos Trans Roy Soc (London)* 203:385
- Garnett JCM (1906) *Philos Trans Roy Soc (London)* A205:237
- Garrell RL (1989) *Anal Chem* 61:401 A
- Geffcken W (1939) *Kolloid-Z* 86:55
- Geick R (1977) *Fresenius Z Anal Chem* 288:1
- Geladi P (1988) *J Chemometrics* 2:231
- Geladi P, Kowalski BR (1986) *Anal Chim Acta* 185:19
- Gemperline PJ (1989) *J Chemometrics* 3:549
- Gendreau RM, Griffiths PR (1976) *Anal Chem* 48:1907
- Gendreau RM, Griffiths PR (1976) *Anal Chem* 48:1910
- Gendreau RM, Leininger RJ, Winters S, Jakobsen RJ (1982) Biomaterials. In: Cooper SL, Peppas NA (eds) *Interfacial Phenomena and Applications*, American Chemical Society, Washington, Ser 199:371
- Gennes PG de (1974) *The physics of liquid crystals*. Clarendon, Oxford
- Genzel L, Kuhl J (1978) *Infrared Phys* 18:113
- Gerard A, Burch JM (1975) *Introduction to Matrix Methods in Optics*. John Wiley & Sons, London New York Sydney Toronto
- Gerhard SL, Dennison DM (1933) *Phys Rev* 43:197
- Gerke M, Schatte G, Willner H (1989) *J Mol Spectrosc* 135:359
- Gerrard DL (1991) *Organic and Petrochemical Applications of Raman Spectroscopy*. In: Grasselli JG, Bulkin BJ (eds) *Analytical Raman Spectroscopy*, chapt 9. John Wiley & Sons, New York
- Gerry MCL, Levis-Bevan W, Merer AJ, Westwood NPC (1985) *J Mol Spectrosc* 119:153
- Gershikov AG, Spiridonov VP (1981) *J Mol Struct* 75:291
- Gerwert K (1992) *Biochim et Biophys Acta* 1101:147
- Gerwert K (1993) *Current Opinion Structural Biology* 3:769
- Gerwert K, Cepus V, Scheidig A, Goody RS (1993) *Proc Time-Resolved Vibrational Spectroscopy VI*, Lau A, Siebert F, Werncke W (eds), Springer, p 185
- Gerwert K, Hess B, Engelhard M (1990) *FEBS Lett* 261:449
- Gerwert K, Hess B, Soppa J, Oesterhelt D (1989) *Proc Natl Acad Sci USA* 86:4943
- Gerwert K, Hoffmann A, Schrader B (1990) In: Durig JR, Sullivan JF (eds). *Proceedings of the XII international conference on Raman spectroscopy*. ICORS, p 852
- Gerwert K, Hoffmann A, Schrader B (1992) In: Kiefer W, Cardona M, Schaack G, Schneider FW, Schröter HW (eds). *Proceedings of the XIII International Conference on Raman Spectroscopy*. John Wiley & Sons, Chichester, p 490
- Gerwert K, Rodriguez-Gonzales R, Siebert F (1985) In: Laubereau A, Stockburger M (eds) *Time Resolved Vibrational Spectroscopy*. Springer Verlag, Berlin Heidelberg New York Tokyo, p 259
- Gerwert K, Siebert F (1986) *EMBO Journal* 5:805
- Gerwert K, Souvignier G (1993) *Nachr Chem Techn Lab* 41:950
- Giachetti A, Stanley RW, Zalubas R (1970) *J Opt Soc Am* 60:474
- Gifford WE, McMahon HO (1960) *Adv Cryogenic Engineering* 5:354
- Gilbert BP, Williams SD, Mamantov G (1988) *Inorg Chem* 27:2359
- Gilby AC, Syrjala RJ, Schlichti G (1980) *Chemie Technik* 9:189
- Gilette PC, Koenig JL (1982) *Appl Spectrosc* 36:535
- Gilson TR, Evans J (1984) *J Chem Soc Dalton Trans*:155
- Gilson TR, Purnell MR (1982) *J Raman Spectrosc* 12:222
- Gobrecht H, Seek S, Klose T (1965) *CR Acad Sci Paris* 261:373
- Godber J, Huber HX, Ozin GA (1986) *Inorg Chem* 25:2909
- Goddu R (1960) *Adv Anal Chem Instrum* 1:347
- Goddu R, Delker D (1960) *Anal Chem* 32:140
- Görner H, Maier M, Kaiser W (1974) *J Raman Spectrosc* 2:363
- Golab JT, Sprague JR, Carron KT, Schatz GC, Van Duyne RP (1988) *J Chem Phys* 88:7942
- Golay MJE (1949) *Rev Sci Instr* 20:816
- Golden WG (1985) *Fourier Transform Infrared Reflection-Absorption Spectroscopy*. In: Ferraro J R, Basile LJ (eds) *Fourier Transform Infrared Spectroscopy, Applications to Chemical Systems*, vol 4. Academic, Orlando. pp 315 - 344
- Golden WG, Dunn DS, Overend J (1981) *J Catalysis* 71:395
- Goldman A, Saunders RS (1979) *J Quant Spectrosc Rad Transfer* 21:155

- Goodwin DD, Brahms J (1978) Nucleic Acids Res 5:835
- Goormaghtigh E, Brasseur R, Huart P, Ruyschaert JM (1987) Biochemistry 26:1789
- Goos F, Hänchen H (1943) Ann Physik 43:383
- Goos F, Hänchen H (1947) Ann Physik 1:333
- Goos F, Hänchen H (1974) Ann Physik 6:87, 333
- Goos F, Lindberg-Hänchen H (1949) Ann Physik 5:251
- Goossens WJA (1971) Mol Cryst Liq Cryst 12:237
- Gordiets BF, Markov MN, Shelepin LA (1978) Planet Space Sci 26:933
- Gordy W (1946) J Chem Phys 14:305
- Gordy W, Orville-Thomas WJ (1956) J Chem Phys 24:439
- Gore RG, Hannah RW (1973) Angew IR Spektroskopie, Perkin Elmer Heft 7. Perkin Elmer, Überlingen
- Gorelik VS, Sushchinskij (1970) Sov Phys Solid State 12:1157
- Gottarelli G, Samori B, Marzocchi S, Stremmenos C (1975) Tetrahedron Lett 24:1981
- Gottarelli G, Samori B, Stremmenos C (1976) Chem Phys Lett 40:308
- Gottlieb K (1967) Z Instr 75:125
- Gottlieb K (1968) Dissertation, Universität Dortmund
- Gottlieb K, Schrader B (1966) Fresenius Z Anal Chem 216:307
- Gough KM, Murphy WF (1986) J Chem Phys 85:4290
- Gough KM, Murphy WF, Stroyer-Hansen T, Svendsen EN (1987) J Chem Phys 87:3341
- Grabmaier JG (1975) Medical and technical applications of liquid crystals. In: Meier G, Sackmann E, Grabmaier JG (eds) Applications of liquid crystals. Springer, Berlin Heidelberg New York, p 83
- Graham JA, Grim WM III, Fateley WG (1985) Fourier Transform Infrared Photoacoustic Spectroscopy of Condensed-Phase Sample. In: Ferraro JR, Basile LJ (eds) Fourier Transform Infrared Spectroscopy, Applications to Chemical Systems, vol 4. Academic, Orlando, p 345
- Grambow L, Grosskreutz R, Kempin F (1979) Draegerheft 314:1
- Gramlich V, Herbeck R, Schlenker P, Schmid ED (1978) J Raman Spectrosc 7:101
- Graner G (1981) J Mol Spectrosc 90:394
- Grasiuk AZ, Zubarer IG (1978) Appl Phys 17:211
- Grasselli JG, Bulkin BJ (eds) (1991) Analytical Raman Spectroscopy. John Wiley & Sons, New York
- Grasselli JG, Hazle MAS, Wolfram LE (1977) Applications of Raman Spectroscopy in the Petroleum Industry, Mol Spectrosc Proc Conf 6th 77:200
- Grasselli JG, Snavely MK, Bulkin BJ (1981) Chemical Applications of Raman Spectroscopy, John Wiley & Sons, New York
- Greenhalgh DA (1988) In: Advances in Nonlinear Spectroscopy, Clark RJH, Hester RE (eds). Wiley, p 193
- Greenhalgh DA, Rahn LA (1990) J Raman Spectrosc 21:847
- Greenhalgh DA, Williams DA (1986) AERE-Harwell Report AERE-R 12222
- Greenhalgh DA, Williams DA, Baker CA (1985) Proc Autotech Conf I Mech E
- Greenler RG (1965) J Chem Phys 44:310
- Gregoriou VG, Chao JL, Toriumi H, Palmer RA (1991) Chem Phys Lett 179:491
- Griffith DWT, Schuster G (1987) J Atmospheric Chem 5:59
- Griffiths PR (1972) Anal Chem 44:1909
- Griffiths PR (1975) Chemical Infrared Fourier Transform Spectroscopy. John Wiley & Sons, New York
- Griffiths PR (1977) Appl Spectrosc 31:284
- Griffiths PR, Azarraga LV, de Haseth JA, Hannah RW, Jakobsen RJ, Ennis MM (1979) Appl Spectrosc 33:543
- Griffiths PR, de Haseth JA (1986) Fourier Transform Infrared Spectroscopy, John Wiley & Sons, New York
- Grisar R, Preier H, Schmidtke G, Restelli G (eds) (1987) Monitoring gaseous pollutants by tunable diode lasers. D Reidel, Dordrecht
- Grosse P (1989) Trends Anal Chem 8:222
- Grosse P (1990) Vibrat Spectrosc 1:187
- Grosse P (1991) Microchim Acta 2:309
- Grosse P, Harbecke B, Heinz B, Jantz W, Maier M (1990) Appl Phys A50:7

- Grosse P, Offermann V (1991) *Appl Phys A* 52:138
- Grunenberg A, Bougeard D (1987) *J Mol Struct* 160:27
- Grygon CA, Spiro TG (1989) *Biochemistry* 28:4397
- Güell OA, Holcombe JA (1990) *Anal Chem* 62:529
- Gunde TBR, Felder P, Günthard H (1985) *Spectrochim Acta* 41A:319
- Günzler H, Böck H (1975) IR-Spektroskopie, eine Einführung. Verlag Chemie, Weinheim
- Gussoni M (1979) Advances in Infrared and Raman Spectroscopy. In: Clark RJ, Hester R (eds), chapter 2, Heyden, London
- Gussoni M, Abbate S (1976) *J Chem Phys* 65:3439
- Gussoni M, Abbate S, Zerbi G (1977) *J Raman Spectrosc* 6:289
- Gussoni M, Castiglione, Zerbi G (1984) *J Phys Chem* 88:600
- Gussoni M, Dellepiane G, Abbate S (1975) *J Mol Spectrosc* 57:323
- Gustafsson G (1990) Spectroscopic and electrical studies of some conjugated polyheterocycles, Linköping University Linköping, Dissertations Nr 229
- Gutberlet H (1978) Dissertation, Universität Dortmund
- Guzonas DA, Atkinson GF, Irish DE (1984) *Chem Phys Lett* 107:193
- Gwinn WD (1971) *QCPE* 11:176, 177
- Haaland DM, Easterling RG, Vopicka DA (1985) *Appl Spectrosc* 39:73
- Haaland DM, Thomas EV (1988) *Anal Chem* 60:1193
- Haarmann T, Köser HJK (1979) *Fresenius Z Anal Chem* 296:18,97,105
- Haas A, Willner H (1978) *Spectrochim Acta* 34A:541
- Haas A, Willner H (1979a) *Spectrochim Acta* 35A:953
- Haas A, Willner H (1979b) *Z Anorg Allg Chem* 454:17
- Hackl R (1990) Springer Series Solid State Sciences 99:312. In: Kuzmany H, Mehring M, Fink J (eds) Electronic Properties of High Tc-Superconductors. Springer, Berlin Heidelberg New York London
- Hahn T (1987) International Tables for Crystallography, vol A, 2nd edn. D Reidel, Dordrecht
- Halac E, Gutierrez N (1983) *J Phys E Sci Instrum* 16:471
- Hall RJ, Boedeker LR (1984) *Appl Opt* 23:1340
- Hall RJ, Eckbreth A (1984) In: Laser Applications, Ready F, Erf RK (eds). Academic, New York
- Hallam HE (ed) (1973) Vibrational Spectroscopy of Trapped Species. John Wiley, London
- Haller I, Huggins HA, Lilienthal HR, McGuire TR (1973) *J Phys Chem* 77:950
- Hamaguchi H (1985) In: Advances in Infrared and Raman Spectroscopy, vol 12, Clark RJH, Hester RE (eds). Heyden, London, p 273
- Hamaguchi H, Harada I, Shimanouchi T (1974) *Chem Lett* 1974:1405
- Hamaguchi H, Tasumi M, Yoshifuji M, Inamoto N (1984) *J Am Chem Soc* 106:508
- Hanna DA et al (1979) *J Chromatogr Sci* 17: 423, 434
- Hannah RW, Pattacini SC (1973) Angewandte Infrarotspektroskopie Heft 4, 9. Bodenseewerk Perkin Elmer, Überlingen
- Hannah RW, Pattacini SC, Grasselli JG, Mocadlo SE (1978) *Appl Spectrosc* 32:69
- Hannah RW, Zeller MV, Pattacini SC (1975) Angewandte Infrarot-Spektroskopie, Perkin Elmer Heft 14
- Hansch C, Clayton J (1973) *J Pharmaceutical Sc* 62:1
- Hansen G (1949) *Optik* 1:227, 269
- Hansen G (1950) *Optik* 6:337
- Hansen HJ, Sliwka HR, Hug W (1979) *Helv Chim Act* 62:1120
- Hansma PK, Kirtley J (1978) *Acc Chem Res* 11:440
- Hanst PL (1976) *Opt Quantum Electron* 8:87
- Hanst PL (1978) *Appl Opt* 17:1360
- Hanst PL et al (1975) *J Air Pollut Control Assoc* 25:1220
- Hanst PL, Lefohn AS, Gay BW (1973) *Appl Spectrosc* 27:188
- Hantz E, Cao A, Perret G, Lewin G, Schatz F, Rolland Y (1992) *J Lip Res* 2:185
- Hantz E, Cao A, Phadke RS, Taillandier E (1989) *Chem Phys Lipids* 51:75
- Harada I, Furukawa Y, Tasumi M, Shirakawa H, Ikeda S (1980) *J Chem Phys* 73:4746
- Harada I, Furukawa Y, Ueda F (1989) *Synth Met* 29:E303-E312
- Harada I, Shimanouchi T (1966) *J Chem Phys* 46:2708
- Harada I, Takamatsu T, Tasumi M, Lord RC (1982) *Biochemistry* 21:3674

- Harada I, Takeuchi H (1986) In: Advances in Infrared and Raman Spectroscopy, vol 13, Clark RJH, Hester RE (eds). Heyden, London, p 113
- Harada N, Nakanishi K (1972) Acc Chem Res 5:257
- Harmon PA, Teraoka J, Asher SA (1990) J Am Chem Soc 112:8789
- Harrick NJ (1967) Internal Reflection Spectroscopy. Wiley-Interscience, New York
- Harrick NJ (1979) Internal reflection spectroscopy 2nd edn. Harrick Scientific corporation, New York
- Harrington BP (1991) J Chemometrics 5:467
- Harris DC, Bertolucci MD (1978) Symmetry and Spectroscopy. Oxford University Press, New York
- Harris SE, Wallace RW (1969) J Opt Soc Amer 59:744
- Hartig W, Schmidt W (1979) Appl Phys 18:235
- Hartke B (1989) Chem Phys Lett 160:538
- Hartke B (1991) J Raman Spectrosc 22:131
- Hartke B, Kiefer W, Kolba E, Manz J, Strempel J (1992) J Chem Phys 96:5636
- Hartland GV, Henson BF, Connell LL, Corcoran TC, Felker PM (1988) J Phys Chem 92:6877
- Hartland GV, Henson BF, Venturo VA, Hertz RA, Felker PM (1990) J Opt Soc Am B7:1950
- Hartland GV, Joireman PW, Connell LL, Felker (1992) J Chem Phys 96:179
- Hartman KA, Clayton NW, Thomas GJ Jr (1973) Biochem Biophys Res Comm 50:942
- Harvey AB (1981) Chemical Applications of Nonlinear Raman Spectroscopy, Academic Press, New York
- Harvey PD, Butler IS (1985) Can J Chem 63:1510
- Hashimoto M, Koyama Y (1989) Chem Phys Lett 163:251
- Hashimoto M, Koyama Y, Hirata Y, Mataga N (1991) J Phys Chem 95:3072
- Hata N, Matsuda A, Tanaka K (1986) J Appl Phys 59:1872
- Hatzilazaru A (1994) Dissertation, Universität Essen
- Hausdorff HH (1977) J Chromatogr 134:131; American Laboratory, May 1978
- Hauswirth W, Willner H (1979) Spectrochim Acta 35A:263
- Hawkins M, Almond MY, Downs AJ (1985) J Phys Chem 89:3326
- Hawrenek JP, Neelakantan P, Young RP, Jones RN (1976) Spectrochim Acta 32A:75, 32A:85
- Hayashi H, Brack TL, Nogushi T, Tasumi M, Atkinson GH (1991) J Phys Chem 95:6797
- Hayashi H, Noguchi T, Tasumi M (1989) Photochem Photobiol 49:337
- Hayden BE (1987) Reflection Absorption Infrared Spectroscopy. In: Yates JT Jr, Madey TE (eds) Vibrational Spectroscopy of Molecules on Surfaces. Plenum New York, p 267
- Hecht L (1992) Chem Phys Lett 195:518
- Hecht L, Barron LD (1993) Mol Phys 80:601
- Hecht L, Barron LD, Hug W (1989) Chem Phys Lett 158:341
- Hecht L, Barron LD, Wen ZQ, Ford SJ (1992) In: Kiefer W et al (eds), Proceedings of the Thirteenth International Conference on Raman Spectroscopy (ICORS) Würzburg, Wiley, Chichester
- Hecht L, Che D, Nafie LA (1992) J Phys Chem 96:4266
- Hecht L, Nafie LA (1991) Mol Phys 72:441
- Heeger AJ, Kivelson S, Schrieffer JR, Su WP (1988) Review of Mod Phys 60:781-850
- Heidberg J, Hussla I, Hoefs E, Stein H, Nestmann A (1978) Rev Sci Instr 49:1571
- Heidberg J, Singh RD, Chen CF (1978) Z Phys Chem NF 110:135, 159
- Heidberg J, Singh RD, Stein H (1978) Ber Bunsenges Phys Chem 82:54
- Heidberg J, Stein H, Hussla I (1978) Ber Bunsenges Phys Chem 82:1238
- Heinrich P (1987) Dissertation, Universität Essen
- Heinrich P, Wyzgol R, Hatzilazaru A, Schrader B, Lübbbers DW (1990) Appl Spectrosc 44:1641
- Heinrich P, Wyzgol R, Opitz N, Lübbbers DW, Schrader B (1985) Pflügers Archiv Eur J Physiol 405:2 R 64
- Heise HM, Winther F, Lutz H (1981) J Mol Spectrosc 90:531
- Heitler W, Herzberg G (1929) Naturwiss 17:673
- Heitner-Wirguin C, Hall D (1979) J Membr Sci 5:1
- Heller EJ, Sundberg RL, Tannor D (1982) J Phys Chem 86:1822
- Hellmann H (1978) Vom Wasser 50:231
- Hellwege KH, Lesch W, Plihal M, Schaack C (1970) Z Phys 232:61
- Helm D, Labischinski H, Schallehn G, Naumann D (1991) J General Microbiology 137:69
- Helmholtz H (1874) Pogg Annal Jubelband:557

- Hendra PJ (1968) *Spectrochim Acta* 24A:125
Hendra PJ (ed) (1990) Applications of Fourier Transform Raman Spectroscopy, *Spectrochim Acta A* 64:2, pp 121-338 (special issue)
Hendra PJ, Ellis G, Cutler DJ (1988) *J Raman Spectrosc* 19:413
Hendra PJ, Jones C, Warnes G (1991) Fourier Transform Raman Spectroscopy. Ellis Horwood, New York
Hendra PJ, Le Barazer P, Crookell A (1989) *J Raman Spectrosc* 20:35
Henesian MA, Kulevskii L, Byer RL (1976) *J Chem Phys* 65:5530
Henson BF, Hartland GV, Venturo VA, Felker PM (1989) *J Chem Phys* 91:2751
Henson BF, Hartland GV, Venturo VA, Hertz RA, Felker PM (1991) *Chem Phys Lett* 176:91
Henson BF, Venturo VA, Hartland GV, Felker PM (1993) *J Chem Phys* 98:8361
Hermann C (1928) *Z Kristallogr* 68:257
Hermann H, Grevels FW, Henne A, Schaffner K (1982) *J Phys Chem* 86:515
Herschel W (1800) *Phil Trans Roy Soc (London)* 90:284
Herzberg G (1945) Molecular Spectra and Molecular Structure, II. Infrared- and Raman Spectra of Polyatomic Molecules. Van Nostrand, New York
Herzberg G (1950) Molecular Spectra and Molecular Structure, I. Spectra of Diatomic Molecules. Van Nostrand, New York
Hesse M, Meier H, Zech B (1979) Spektroskopische Methoden in der Organischen Chemie. Thieme, Stuttgart
Hesse W, Jansen M, Schnick W (1989) *Prog Solid St Chem* 19:47
Heßling B, Souvignier G, Gerwert K (1993) *J Biophys* 65:1929
Hester RE (1978) In: Clark RJH, Hester RE (eds) Advances in Infrared and Raman Spectroscopy, vol 4, chapt 1. Heyden & Son, London
Hester RE (1978) *J Raman Spectrosc* 7:74
Hester RE, Girling RB (1991) Spectroscopy of Biological Molecules. Royal Society of Chemistry, London
Heyen ET, Kliche G, Kress W, König W, Cardona M, Rampf E, Prade J, Schröder U, Kulkarni AD, de Wette FW, Pinol S, Paul DMCK, Moran E, Alario-Franco MA (1990) *Solid State Commun* 74:1299-1304
Hickman RS, Liang HL (1972) *Rev Sci Instrum* 43:796
Hildebrandt P, Spiro TG (1988) *J Phys Chem* 92:3355
Hildebrandt P, Stockburger M (1984) *J Phys Chem* 90:6017
Hildebrandt P, Stockburger M (1989a) *Biochemistry* 28:6710
Hildebrandt P, Stockburger M (1989b) *Biochemistry* 28:6722
Hill RA, Eshierick P, Owyong A (1983) *J Mol Spectrosc* 100:119
Hill RL (1972) *Biopolymers* 11:1929
Hills GW, Foster RB, Jones WJ (1977) *Mol Phys* 33:1571
Hills GW, Jones WJ (1975) *Trans Faraday Soc II* 71:812
Hinkley ED (ed) (1976) Laser Monitoring of the Atmosphere, Topics in Applied Physics, vol 14. Springer, Berlin
Hinkley ED, Nill KW, Blum FA (1976) Infrared Spectroscopy with tunable Lasers. In: Walther H (ed) Topics in Applied Physics, vol 2. Springer, Berlin
Hirakawa AY, Tsuboi M (1975) *Science* 188:359
Hirano S, Kanamatsu T (1979) *Anal Biochem* 96:64
Hirota E (1979) *J Mol Spectrosc* 74:209
Hirschfeld T (1976a) *Anal Chem* 48:721
Hirschfeld T (1976b) *Appl Spectrosc* 30:68
Hirschfeld T (1976c) *Appl Spectrosc* 30:234
Hirschfeld T (1977a) *Appl Spectrosc* 31:289
Hirschfeld T (1977b) *Appl Spectrosc* 31:471
Hirschfeld T (1986) *Appl Spectrosc* 40:1082
Hirschfeld T, Chase B (1986) *Appl Spectrosc* 40:133
Hisatsune IC, Delvin JP, Wada J (1962) *Spectrochim Acta* 18:1641
Hitzeroth-Halfbrodt G (1988) Diplomthesis, Göttingen
Hizhnjakov V, Tehver I (1967) *Phys Stat Solidi* 21:755
Hobbs JP, Sung SCP, Krishnan K, Hill SL (1983) *Macromolecules* 16:193
Hochenbleicher G, Schröter HW (1971) *Appl Spectrosc* 25:360

- Hoerhold HH, Helbig M, Raabe D, Opfermann J, Scherf U, Stockmann R, Weiss D (1987) *Z Chem* 27:126-138
- Höfert HJ (1960) Zeiss-Informationen 60. Carl Zeiss, Oberkochen, Sonderdruck 550-659 d
- Hoffer H, Szklendar G (1979) *Dtsch Molk Ztg* 100:634
- Hoffmann A, Keller S, Schrader B, Ferwerda R, van der Maas JH (1991) *J Raman Spectrosc* 22:497
- Hoffmann A, Schrader W, Schrader B (1990) In: Durig JR, Sullivan JF (eds). Proceedings of the XII international conference on Raman spectroscopy. ICORS, p 860
- Hoffmann FM, Weisel MD (1992) *ACS Symp Ser* 482:202
- Hoffmann GG (1993) *SPIE* 2089:140
- Hoffmann GG, Hochkamp HJ (1992a) *SPIE* 1575:400
- Hoffmann GG, Hochkamp HJ (1992b) *Fresenius J Anal Chem* 344:227
- Hoffmann GG, Kollek A, Schrader B (1992) In: Kremer M (ed), Höchstleistungsrechenzentrum - Wissenschaftliche Projekte 1991, HLRZ, Jülich, p 149
- Hoffmann GG, Menzebach HU, Oelichmann B, Schrader B (1992) *Appl Spectrosc* 46:568
- Hoffmann GG, Schrader B, Snatzke G (1987b) *Rev Sci Instrum* 58:1675
- Holland F, Winnewisser M, Maier G, Reisenauer HP, Ulrich A (1988) *J Mol Spectrosc* 130:470
- Holland-Moritz K, Sausen E, Djudovic P, Coleman MM, Painter PC (1979) *J Polym Sci Phys Ed* 17:1, 25
- Hollas JM (1972) Symmetry in Molecules. Chapman and Hall, London
- Hollas JM (1982) High Resolution Spectroscopy. Butterworth, London
- Hollinger AB, Welsh HL (1978) *Can J Phys* 56:974,1513
- Hollinger AB, Welsh HL, Jammu KS (1979) *Can J Phys* 57:767
- Hollins P, Pritchard J (1985) *Prog Surf Sci* 19:275
- Holt RE, Cotton TM (1987) *J Am Chem Soc* 109:1841
- Holzer W (1968a) *J Mol Spectrosc* 25:123
- Holzer W (1968b) *J Mol Spectrosc* 27:522
- Holzer W, Moser H (1964) *J Mol Spectrosc* 13:430
- Holzer W, Moser H (1966) *J Mol Spectrosc* 20:188
- Holzer W, Murphy WF, Bernstein HJ (1970) *J Chem Phys* 52:399
- Holzwarth G, Chabay I, Holzwarth NAW (1973) *J Chem Phys* 58:4816
- Holzwarth G, Holzwarth NAW (1973) *J Opt Soc Amer* 63:324
- Holzwarth G, Hsu EC, Mosher HS, Faulkner TR, Moscowitz A (1974) *J Am Chem Soc* 96:251
- Homborg H (1980) *Z Anorg Allg Chem* 460:17
- Homborg H, Preetz W (1976) *Spectrochim Acta* 32A:709
- Honerlage B, Rossler U, Phach VD, Bivas A, Grun JB (1980) *Phys Rev B* 22:797
- Honigs DE, Freelin JM, Hietfje GM, Hirschfeld TB (1983) *Appl Spectrosc* 37:491
- Hooker RH, Rest AJ, Whitwell (1984) *J Organomet Chem* 266:C27
- Hopfe V (1989) FSOS: Software package for IR-VIS-UV Spectroscopy on solids, Interfaces and layered Systems, Preprint No. 122, Technische Universität Karl-Marx-Stadt, Chemnitz
- Hopfe V, Grählert W, Brennfleck K, Korte EH, Theiß W (1993b) *Fresenius J Anal Chem* 346:99
- Hopfe V, Klobes P, Marx G (1981) Berechnung der dielektrischen Funktion von Festkörpern aus optischen Reflexionsspektren mittels Kramers-Kronig-Analyse; *Wiss Z d.Techn. Hochschule Karl-Marx-Stadt* 23:211
- Hopfe V, Korte EH, Klobes P, Grählert W (1993a) *Appl Spectrosc* 47:423
- Hopfe V, Korte EH, Klobes P, Grählert W (1993b) *J Mol Struct* 293:245
- Hopkins GA, Maroncelli M, Nibler JW, Dyke TR (1985) *Chem Phys Lett* 114:97
- Horiai K, Fujimoto T, Nakagawa K, Uetiara H (1988) *Chem Phys Lett* 147:133
- Hornischer R, Moser H (1972) *Spectrochim Acta* 28A:81
- Horovitz B (1982) *Solid State Commun* 41:729-734
- Horvath AL (1982) Halogenated Hydrocarbons, Solubility-Miscibility with Water. Marcel Dekker, New York
- Hoskins LC, Alexander U (1977) *Anal Chem* 49:695
- Höskuldsson A (1988) *J Chemometrics* 2:211
- Howard FB, Frazier J, Miles HT (1971) *J Biol Chem* 246:7073
- Howard WF, Nelson WH, Sperry JF (1980) *Appl Spectrosc* 34:72
- Hsu EC, Holzwarth G (1973) *J Chem Phys* 59:4678
- Huang C, Mason JT, Levin IW (1983) *Biochemistry* 22:2775

- Hub W, Schneider S, Doerr F (1979) *Angew Chem* 91:348
- Huber G, Syassen K, Holzapfel WB (1977) *Phys Rev B* 15:5123
- Huber KP, Herzberg G (1979) *Molecular Spectra and Molecular Structure IV. Constants of Diatomic Molecules*. Van Nostrand, New York
- Huber-Wälchli P, Günthard HH (1978) *Chem Phys Lett* 59:186
- Huber-Wälchli P, Guthals DM, Nibler JW (1979) *Chem Phys Lett* 67:233
- Huber-Wälchli P, Nibler JW (1982) *J Chem Phys* 76:273
- Huckestein B (1991) Thesis, Göttingen
- Hug W, Surbeck H (1979) *Chem Phys Lett* 60:186
- Hummel DO (ed) (1974) *Polymer Spectroscopy*. Verlag Chemie, Weinheim
- Hummel DO, Scholl F (1991) *Atlas of Polymer and Plastics Analysis*, 3 volumes. VCH Publishers, Weinheim
- Hummel DO, Votteler Chr (1982) *Kemia-Kemi* 9:10:660
- Hummel DO, Votteler Chr (1983) *Angew Makromol Chem* 117:171
- Hummel DO, Votteler Chr, Winter M (1983) *Kunststoffe* 73:193
- Huong PV (1978) *Adv Infrared Raman Spectrosc* 4:85
- Hush NS, Williams ML (1970) *Chem Phys Lett* 5:507
- Hutchinson K, McQuillan AJ, Hester RE (1983) *Chem Phys Lett* 98:27
- Ibach H, Lehwald S (eds) (1978) *Vibrations in adsorbed Layers*. Kernforschungsanstalt Jülich
- Imhoff EA (1983) Thesis, Mat Science Center, Cornell Univ Ithaca, New York
- Inaba R, Okamoto H, Yoshihara K, Tasumi M (1991) *Chem Phys Lett* 185:56
- Inaba R, Okamoto H, Yoshihara K, Tasumi M (1992) *J Phys Chem* 96:8385
- Inaba R, Okamoto H, Yoshihara K, Tasumi M (1993a) *J Phys Chem* 97:7815
- Inaba R, Tominaga K, Tasumi M, Nelson KA, Yoshihara K (1993b) *Chem Phys Lett* 211:183
- Indralingam R, Simeonson JB, Petrucci GA, Smith BW, Winefordner JD (1992) *Anal Chem* 64:964
- Inoue K, Asai N, Sameshima T (1981) *J Phys Soc Japan* 50:1291
- International Tables see Hahn T (1983)
- Iqbal Z, Owens FJ (1986) *Vibrational spectroscopy of phase transitions*, Academic Press, Orlando
- Iqbal Z, Weidekamm E (1979) *Biochim Biophys Acta* 555:426
- Irish DE, Hill IR, Archambault P, Atkinson GF (1985) *J Solution Chem* 14:221
- Irvin KJ (1976) *Structural Studies of Macromolecules by Spectroscopic Methods*. Wiley & Sons, London
- Irwin RM, Cooke JM, Laane J (1977) *J Am Chem Soc* 99:3273
- Isaacs NS (1981) *Liquid Phase High Pressure Chemistry*. J Wiley & Sons
- Ishida H, Ishitani A (1983) *Appl Spectr* 37:450
- Ishida H, Koenig JL, Kenney ME (1979) *Proc Ann Conf Reinf Plast* 1979:34H, 17B
- Ishino Y, Ichida H (1992) *Appl Spectrosc* 46:504
- Ismail MA, Jayasoorya VA, Kettle SFA (1982) *J Mol Struct* 79:349
- Ismail ZK, Hauge RH, Margrave JL (1975) *J Mol Spectrosc* 54:402
- IUPAC (1955) *J Chem Phys* 23:1997
- IUPAC (1976) *Pure Appl Chem* 45:99
- IUPAC (1977) *Appl Spectrosc* 31:569
- IUPAC (1985) *Pure Appl Chem* 57:121
- Jacob E (1989) *Fresenius Z Anal Chem* 333:761
- Jacquinot P (1954) *J Opt Soc Am* 44:761
- Jain MK, Zakim D (1987) *Biochim Biophys Acta* 906:33
- Jalkanen KJ, Stephens PJ, Amos RD, Handy NC (1987) *Chem Phys Lett* 142:153
- Jalkanen KJ, Stephens PJ, Lazzaretti P, Zanasi R (1989a) *J Phys Chem* 93:6583
- Jalkanen KJ, Stephens PJ, Lazzaretti P, Zanasi R (1989b) *J Chem Phys* 90:3204
- Jalsovszky G (1984) *J Mol Struct* 114:127
- Jamieson JC, Lawson AW, Nachtrieb ND (1959) *Rev Sci Instrum* 30:1016
- Jammu KS, St John GE, Welsh HL (1966) *Can J Phys* 44:797
- Janatuinen T, Byckling E (1985) International Laboratory, September
- Janossy I (ed) (1991) *Perspectives in Condensed Matter Physics*, vol 5: *Optical Effects in Liquid Crystals*. Kluwer Academic, Dordrecht
- Jansen JAJ, Posthumus de Boer A, van der Maas J (1992) *Appl Spectrosc* 46:88
- Jansen K, Schmitte J, Dehncke K, Fenske D (1987) *Z Anorg Allg Chem* 552:201
- Jansen M (1977) *Angew Chem Int Ed Engl* 16:534

- Jansen M (1979) *Angew Chem Int Ed Engl* 18:698
- Jansen M, Pebler J, Dehnicke K (1982) *Z Anorg Allg Chem* 495:120
- Jansen M, Schatte G, Tobias KM, Willner H (1988) *Inorg Chem* 27:1703
- Jansen M, Tobias KM, Willner H (1986) *Naturwiss* 73:734
- Jantsch W (1983) Springer Tracts in Mod Phys 99:1
- Jantsch W, Bussmann-Holder, Biltz H, Vogl P (1983) Springer Tracts in Mod Phys 99. Springer, Berlin Heidelberg New York London
- Jayaraman A (1983) *Rev Mod Phys* 55:65
- Jeanmaire DL, VanDuyne RP (1976) *J Amer Chem Soc* 98:4029
- Jeanmaire DL, VanDuyne RP (1976) *J Amer Chem Soc* 98:4034
- Jeanmaire DL, VanDuyne RP (1977) *J Electroanal Chem* 84:1
- Jenkins BG, Wartell RM, Alderfer JL (1986) *Biopolymers* 25:823
- Jennings DE, Weber A, Brault JW (1986) *Appl Opt* 25:284
- Jennings DE, Weber A, Brault JW (1987) *J Mol Spectrosc* 126:19
- Jensen HB, Brodersen S (1979) *J Raman Spectrosc* 8:103
- Jensen HP, Schellman JA, Troxel T (1978) *Appl Spectrosc* 32:192
- Jensovsky L (1962) *Z Chem* 2:334
- Jensovsky L (1962) *Z Chem* 3:453
- Jeu WH de (1992) Microscopic aspects of the nematic phases. In: Phase transitions in liquid crystals. NATO ASI Ser B 290:17
- Jeu WH de, Bordewijk P (1978) *J Chem Phys* 68:109
- Jia W, Yen WM (1989) *J Raman Spectrosc* 20:785
- Jodl HJ, Holzapfel WB (1979) *Rev Sci Instrum* 50:340
- Johansson J, Martinsson BG, Eng ST (1978) *IEEE Trans Instrum Meas IM* 27:358
- Johnson BB, Petricolas WL (1976) *Ann Rev Phys Chem* 27:465
- Johnson KM, McKnight DJ, Underwood I (1993) *IEEE J Quantum Electron* 29:699
- Jonas RE, Braiman MS (1993) *Appl Spectrosc* 47:1751
- Jones H (1978) *Comments At Mol. Phys* 8:51
- Jones H, Lindenmeyer J (1987) *Chem Phys Lett* 135:189
- Jones LH (1971) Inorganic Vibrational Spectroscopy. M Dekker Inc, New York
- Jones RN (1970) NRC Canada Report
- Jones RN (ed) (1976)-(1977) Computer Programs for Infrared Spectrophotometry, 2nd edn, Bulletin 11-17. National Research Council Canada, Ottawa
- Jones RN (1981) *Can J Spectrosc* 26:1
- Jones RN (1985) Analytical Applications of Vibrational Spectroscopy - A Historical Review. In: Durig JR (ed) Chemical, Biological and Industrial Applications of Infrared Spectroscopy. John Wiley & Sons, pp 1 - 50
- Jones RN, Hawrenek JP (1976) *Spectrochim Acta* 32A:111
- Jones RN, Sandorfy C (1956) The Application of Infrared and Raman Spectrometry to the Elucidation of Molecular Structure. In: Weissberger A (ed) Technique of Organic Chemistry, vol IX Chemical Applications of Spectroscopy, p 247
- Jones RW, McClelland JF (1989) *Anal Chem* 61:650, 1810
- Jones WJ, Stoicheff BP (1964) *Phys Rev Lett* 13:657
- Jonuscheit J, Lehner U, Schrötter HW (1994) (unpublished)
- Joo T, Dugen MA, Albrecht AC (1991) *Chem Phys Lett* 177:4
- Jordanov B, Korte EH, Schrader B (1988) *J Mol Struct* 174:147
- Jordanov B, Korte EH, Schrader B (1988) *Microchim Acta Wien II*:275
- Jordanov B, Schrader B (1986) *J Mol Struct* 141:297
- Jordanov B, Tsankov D (1984) *J Mol Struct* 115:457; 117:261
- Jouvard JM, Lavorel B, Champion JP, Brown LR (1991) *J Mol Spectrosc* 150:201
- Julius WH (1892) Verhandl Konikl Akad Amsterdam, Deel 1, No 1
- Junker A, Bergmann G (1974) *Fresenius Z Anal Chem* 272:267
- Junker A, Bergmann G (1976) *Fresenius Z Anal Chem* 278:191, 273
- Jurnak FA, MacPherson A (1984) Virus structures. In: Biological Macromolecules and Assemblies, vol 1. Wiley Pub Co, New York
- Jurs PC (1970) *Anal Chem* 42:1633; (1971) 43:22, 1812
- Kaiser H (1965) *Z Anal Chem* 209:1
- Kaiser H (1970) *Anal Chem* 42(2): 24 A, (4):26 A

- Kaiser H (1972) *Fresenius Z Anal Chem* 260:252
- Kaiser H (1973) In: *Methodicum Chimicum I* 1, p 1. G Thieme Verlag Stuttgart, (1974) engl ed vol I A, p 1. Academic Press, New York
- Kaiser R, Gottschalk G (1972) Elementare Tests zur Beurteilung von Meßdaten, BI Hochschul Taschenbücher 774, Mannheim
- Kajiyama K, Sajiki S, Kataoka H, Maeda S, Hirose C (1982), SAE Technical Paper 821036
- Kaldor A, Porter RF (1971) *J Am Chem Soc* 93:2140
- Kaminaka S, Ogura T, Kitagawa T (1990) *J Am Chem Soc* 112:23
- Kamiya K, Tanaka J (1988) *Synth Met* 25:59-70
- Karger AM, English RP, Smith RJD (1973) *Appl Opt* 12:2083
- Karpfen A, Petkov J (1979) *Solid State Commun* 29:251
- Kastler A, Rousset A (1941) *J Phys* 2:49
- Katsuyama T, Matsumura H (1989) *Infrared Optical Fibers*. Adam Hilger, Bristol
- Kauppinen J (1979) *Infrared Phys* 19:191
- Kauppinen JK, Moffat DJ, Mantsch HH, Cameron DG (1981) *Appl Spectrosc* 35:271
- Kawaguchi K, Butler JE, Yamada C, Bauer SH, Minowa T, Kanamori H, Hirota E (1987) *J Chem Phys* 87:2438
- Kawaguchi K, Hirota E (1987) *J Chem Phys* 87:6838
- Kawashima Y, Kawaguchi K, Hirota E (1987) *J Chem Phys* 87:6331
- Kaye W (1954) *Spectrochim Acta* 6:257
- Keck Z, Bernstein HJ (1965) *J Mol Spectrosc* 15:378
- Keiderling TA, Pancoska P (1993) Structural studies of biological macromolecules using vibrational circular dichroism. In: Clark RJH, Hester RE (eds) *Biomolecular spectroscopy*, part B, *Advances in spectroscopy*, vol 20, Wiley, p 267
- Kelker H, Hatz R (1980) *Handbook of liquid crystals*. Verlag Chemie, Weinheim
- Kelker H, Hatz R, Wirz G (1973) *Fresenius Z Anal Chem* 267:161
- Keller S (1991) Diplomarbeit, Universität Essen
- Keller S, Löchte T, Dippel B, Schrader B (1993) *Fresenius J Anal Chem* 346:863
- Keller S, Schrader B, Hoffmann A, Schrader W, Metz K, Rehlaender A, Pahnke J, Ruwe M, Budach W (1994) *J Raman Spectrosc*, in print
- Kellner R (1986) *Teubner-Texte Phys* 9:272
- Ken WE (1977) *Fortschr Urol Nephrol* 9:234
- Kerker M (1969) *The Scattering of Light and Other Electromagnetic Radiation*, Academic Press, New York
- Kerkhof FPJM et al (1979) *Stud Surf Sci Catal* 3:77
- Kertes AS (1985) *Solubility Data Series*, vol 20. Pergamon Press, Oxford
- Kettle SFA (1977) *The Vibrational Spectra of Metal Carbonyls*. In *Topics*. Springer, Berlin, p 111
- Kiefer W (1973) *Appl Spectrosc* 27:253
- Kiefer W (1974) *Appl Spectrosc* 28:115
- Kiefer W (1977) Recent Techniques in Raman Spectroscopy. In: *Advances in Infrared and Raman Spectroscopy*, vol 3, Clark RJH, Hester RE (eds). Heyden, London, p 1
- Kiefer W (1980) Active Raman Spectroscopy in Spectroscopy. In: Comes FJ, Müller A, Orville-Thomas WJ (eds) *Chemistry and Physics, Modern Trends*. Elsevier, Amsterdam; *J Mol Struct* 59:305
- Kiefer W (1988) *Croat Chem Acta* 61:473
- Kiefer W (1989) *Nachr Chem Tech Lab, Sonderheft Spektroskopie*, 37:184
- Kiefer W, Bernstein HJ (1972a) *J Mol Spectrosc* 43:366
- Kiefer W, Bernstein HJ (1972b) *Mol Phys* 23:835
- Kiefer W, Bernstein HJ (1973) *J Raman Spectrosc* 1:417
- Kiefer W, Cardona M, Schaack G, Schneider FW, Schröter HW (eds) *Proc. XIIIth Int Conf Raman Spectrosc*, Wiley, London
- Kiefer W, Long DA (1982) *Nonlinear Raman Spectroscopy and its Chemical Applications*, Reidel, Dordrecht
- Kiefer W, Schmid WJ, Topp JA (1975) *Appl Spectrosc* 29:434
- Kiefer W, Topp JA (1974) *Appl Spectrosc* 28:26
- Kienitz H (1958) *Fresenius Z Anal Chem* 164:80
- Kienitz H (1961) *Ultrarot und Raman Spektroskopie*. In: *Ullmanns Encyklopädie der technischen Chemie* 2nd edn, chapt 2/1. Verlag Chemie, Weinheim, p 236

- Killian JA, van den Berg CW, Tournous H, Keur S, Slotboom AJ, van Scharenberg GJM, de Kruijff B (1986) *Biochim Biophys Acta* 857:13
- Kim KC, Griggs E, Person WB (1978) *Appl Opt* 17:2511
- Kim KC, Holland RF, Filip H (1978) *Appl Spectrosc* 32:287
- Kim M, Carey PR (1991) *J Mol Struc* 242:421
- Kim YH, Hotta S, Heeger AJ (1987) *Phys Rev B* 36:7486-7490
- Kimel S, Speiser S (1977) *Chem Rev* 77:437
- King FW, Schatz GC (1979) *Chem Phys* 38:245
- Kirchhoff R (1859) Untersuchungen über das Sonnenspektrum und die Spektren chemischer Elemente, Abhandlungen der Berliner Akademie (1861-63)
- Kirchner HH, Richter W (1972) *Z Phys Chem Neue Folge* 81:274
- Kirov N, Simova P (1984) Vibrational spectroscopy of liquid crystals. Publishing House of the Bulgarian Academy of Sciences, Sofia
- Kitagawa T (1986) In: *Advances in Infrared and Raman Spectroscopy*, vol 13, Clark RJH, Hester RE (eds). Heyden, London, p 443
- Kitagawa T, Azuma T, Hamagushi K (1979) *Biopolymers* 18:451
- Kitagawa T, Maeda A (1989) *Photochem Photobiol* 50:883
- Kitaigorodsky AI (1973) *Molecular Crystals and Molecules*. Academic Press, New York
- Kittel C (1976) *Introduction to Solid State Physics*, 5th edn. Wiley Eastern Limited, New Delhi
- Kivelson D, Wilson EB (1953) *J Chem Phys* 21:1229
- Klaebroeck P, Bougeard D, Schrader B, Paetzold P, von Pllotho C (1985) *Spectrochim Acta* 41A:53
- Klaebroeck P, Kloster-Jensen E, Christensen DH, Jonsen I (1970) *Spectrochim Acta* 26A: 1567
- Klaebroeck P, Lothe JJ, Lunde K (1957) *Acta Chem Scand* 11:1677
- Klaebroeck P, Nielsen JR (1960) *J Chem Phys* 32:899; 33:1764
- Klaebroeck P, Powell DL, Stolevik R, Vorren O (1982) *Acta Chem Scand A* 36:471
- Klaunig W (1953) *Feingerätetechnik* 2:179
- Kleber W (1961) *Einführung in die Kristallographie*. VEB Verlag Technik, Berlin
- Klein MV, Dierker SB (1984) *Phys Rev B* 29:4976:4991
- Kliche G, Schwarz M, von Schnerring HG (1987) *Angew Chem Int Ed Engl* 26:349
- Klocek P, Sigel GH (1989) *Infrared Fiber Optics*. SPIE Optical Engineering Press, Bellingham, Washington
- Klöckner HW, Finsterhölzl H, Srinivasan K, Schröter HW (1978) *Appl Spectrosc* 32:401
- Kłosowski J, Steger E (1979) *J Raman Spectrosc* 8:169
- Kneipp K (1988) *Exp Tech Phys* 36:161
- Kneipp K (1990) *Exp Techn Phys* 38:1
- Kneipp K, Roth E, Engert C, Kiefer W (1993) *Chem Phys Lett* 207:450
- Knippers W, van Helvoort K, Stolte S, Reuss J (1985) *Chem Phys* 98:1
- Knoll P, Kuzmany H (1984) *Mol Cryst Liq Cryst* 106:317-329
- Knoll P, Singer R, Kiefer W (1990) *Appl Spectrosc* 44:776
- Kobayashi N, Colaneri M, Boysel F, Widl F, Heeger AJ (1985) *J Chem Phys* 82:5717
- Koenig JK (1980) *Microstructure of Polymer chains*, John Wiley & Sons, New York Chichester Brisbane Toronto
- Koenig JK, D'Esposito L, Antoon MK (1977) *Appl Spectrosc* 31:292
- Koenig JL, Kormos D (1979) *Appl Spectrosc* 33:349
- Koeniger F, Mueller A (1975) *J Mol Spectrosc* 56:200
- Koeniger F, Mueller A, Nakamoto K (1975) *Z Naturforsch* 30b:456
- Koenigstein JA, Mortensen OS (1973) chapt 8. In: *The Raman Effect*, vol 2. M Dekker, New York
- Koga O, Onishi T, Tanaru K (1974) *Chem Comm* 1974:464
- Koglin E, Séquaris JM (1986) *Top Curr Chem* 134:1
- Kohles N, Laubereau A (1987) *Chem Phys Lett* 138:365
- Kohlrausch KWF (1931) *Der Smekal-Raman-Effekt*. Springer, Berlin
- Kohlrausch KWF (1938) *Der Smekal-Raman-Effekt. Ergänzungsband 1931-1937*, Springer, Berlin
- Kohlrausch KWF (1943) *Ramanspektren*. Akademische Verlagsgesellschaft Leipzig, (1972) reprint: Heyden & Son, London
- Kolba E, Manz J, Schreier HJ, Trisca I (1992) *Chem Phys Lett* 189:505
- Kompa KL (1979) *Laser Separation of Isotopes*. In: SIPRI Year Book, Taylor Francis, London, p 73
- König F, Oesterlin P, Byer RL (1982) *Chem Phys Lett* 88:477

- Konjevic N, Jovicevic S (1979) Spectrosc Lett 12:259
- Korte EH (1978) Appl Spectrosc 32:568
- Korte EH (1983) Mol Cryst Liq Cryst 100:127
- Korte EH (1985) The characterization of enantiomers by induced cholesteric solutions; principles and experimental techniques. In: Proceedings of the International Conference on Circular Dichroism, vol 6. Bulgarian Academy of Sciences, Sofia, p 145
- Korte EH (1988) Appl Spectrosc 42:428
- Korte EH (1990a) Vibrat Spectrosc 1:179
- Korte EH (1990b) Infrarot-Spektroskopie diffus reflektierender Proben. In: Günzler H, Borsdorf R, Fresenius W, Huber W, Kelker H, Lüderwald I, Tölg G, Wisser H (eds) Analytiker Taschenbuch, vol 9. Springer Berlin, p 91
- Korte EH, Jordanov B, Kolev D, Tsankov D (1988) Appl Spectrosc 42:1394
- Korte EH, Otto A (1988) Appl Spectrosc 42:38
- Korte EH, Richter WJ, Chingduang P (1980) Ber Bunsenges Phys Chem 84:45
- Korte EH, Röseler A, Reins J (1993) SPIE 2089:482
- Korte EH, Schrader B (1981) A new chiroptical method: Infrared rotatory dispersion of induced cholesteric solutions. In: Clark RJH, Hester RE (eds) Advances in infrared and Raman spectroscopy, vol 8. Heyden, London, p 226
- Korte EH, Schrader B, Bualek S (1978) J Chem Res M 1978:3001
- Korte EH, Staat H (1989) SPIE 1145:296
- Korte EH, Staat H (1993) Fresenius J Anal Chem 347:454
- Kortüm G (1969) Reflexionsspektroskopie, Springer, Berlin
- Kortüm G, Delfs H (1964) Spectrochim Acta 20:405
- Kosloff R (1988) J Chem Phys 92:2087
- Kostyk E, Welsh HL (1980) Can J Phys 58:534
- Kouaoui R, Silvins JR, Graham I, Pezolet M (1985) Biochemistry 24:7132
- Kowalski BR (1975) Anal Chem 47:1152A
- Koyama Y (1990) In: Carotenoids: Chemistry and Biology. Krinsky NI, Mathews-Roth MM, Taylor RF (eds). Plenum Pub Co, p 207
- Koyama Y (1991) J Photochem Photobiol B 9:265
- Koyama Y, Takatsuka I, Nakata M, Tasumi M (1988) J Raman Spectrosc 19:37
- Koyama Y, Umemoto Y, Akamatsu A, Uehara K, Tanaka M (1986) J Mol Struct 146:273
- Kozlov DN, Prokhorov AN, Smirnov V (1979) J Mol Spectrosc 77:21
- Krabbe HJ, Hegemeier H, Schrader B, Korte EH (1978) J Chem Res M 1978:3020
- Krahn W, Stursberg K (1978) Gasdyn Chem Lasers Proc Int Symp 1976:224
- Kramers HA (1929) Phys Z 30:522
- Kramers HA, Heisenberg W (1925) Z Physik 31:681
- Krasser W, Renouprez AJ (1977) J Raman Spectrosc 8:92
- Krasser W, Renouprez AJ, Koglin E (1979) J Raman Spectrosc 6:209
- Krätschmer W, Lamb LD, Fostiropoulos K, Huffman DR (1990) Nature 347:354
- Kraus HJ (1989) Diplomarbeit, Universität Lübeck
- Kremer F (ed) (1992) Ferroelectric liquid crystal polymers. In: Polym Adv Technol, vol 3(5). Wiley, Chichester
- Kress J (1975) J Organomet Chem 99:23, 199
- Kreutner W, Stricker W, Just T (1983) Ber Bunsenges Phys Chem 87:1045
- Kreutner W, Stricker W, Just T (1987) Appl Spectrosc 41:98
- Kreuzer LB (1978) Anal Chem A 50:597
- Krimm S (1962) J Mol Biol 4:528
- Krimm S (1986) In: Spiro TG (ed) Biological Applications of Raman Spectroscopy, vol 1. Wiley Pub Co, New York
- Krimm S, Bandeker J (1980) Biopolymers 19:1
- Krishan K, Bulkin BJ (1978) Appl Spectrosc 32:338
- Kronig R (1926) J Opt Soc Am 12:547
- Kroto H, Heath JR, O'Brien SG, Curl RF, Smalley RE (1985) Nature 318:162
- Krska R, Taga K, Kellner R (1993) Appl Spectrosc 47:1484
- Kuball HG, Acimis M, Altschuh J (1979) J Am Chem Soc 101:20
- Kuball HG, Strauss A, Kappus M, Fechter-Rink E, Schönhofen A, Scherowsky G (1987) Ber Bunsenges Phys Chem 91:1266

- Kubelka P (1948) *J Opt Soc Am* 38:448
- Kubelka P, Munk F (1931) *Z Techn Techn Physik* 12:593
- Kuehl D, Griffiths PR (1979) *J Chromatogr Sci* 17:471
- Kuehl DT, Griffiths PR (1980) *Anal Chem* 52:1394
- Kuerti J, Kuzmany H (1987) Springer Series Solid State Sciences 76:43. In: Kuzmany H, Mehring M, Roth S (eds) *Electronic Properties of Polymers*. Springer, Berlin Heidelberg New York London
- Kuerti J, Kuzmany H (1991) *Phys Rev B* 44:597-613
- Kumer JB (1977) *J Geophys Res* 82:2195
- Kunkel E, Peitscher G, Peter KS (1977) *Tenside* 14:199
- Kupecek P, Le Person H, Comte M (1979) *Infrared Phys* 19:263
- Kutzelnigg W, Mecke R, Schrader B, Nerdel F, Kresze G (1961) *Ber Bunsenges Phys Chem* 65:109
- Kuzmany H (1980) *Phys Stat Sol (b)* 97:521-531
- Kuzmany H (1985) *Pure and Applied Chem* 57:235
- Kuzmany H (1988) unpublished
- Kuzmany H (1990a) *Macromol Chem, Macromol Symp* 37:81-97
- Kuzmany H (1990b) *Festkörperspektroskopie*. Springer, Berlin Heidelberg New York
- Kuzmany H, Bartonek M (1990a) *Europhys Lett* 12:167-172
- Kuzmany H, Elbert M (1980) *Solid State Commun* 35:597
- Kuzmany H, Farmer JL, Miller RD, Rabolt J (1986) *J Chem Phys* 85:7413
- Kuzmany H, Genies EM, Syed A (1985) Springer Series Solid State Sciences 63:223. In: Kuzmany H, Mehring M, Roth S (eds) *Electronic Properties of Polymers*. Springer, Berlin Heidelberg New York London
- Kuzmany H, Imhoff EA, Fitchen DB, Sarhangi A (1981) *Mol Cryst Liq Cryst* 77:97
- Kuzmany H, Kundu B (1979) *Acta Physica Austriaca* 20:213
- Kuzmany H, Kundu B, Stolz J (1978) *Proc Int Conf Lattice Dynamics*. Balkanski M (ed) Famarion, Paris, p 584
- Kuzmany H, Matus M, Burger B, Winter J (1994) *Advanced Materials*, in press
- Kuzmany H, Matus M, Faulques E, Pekker S (1989) Vibrational spectra and transport properties of high temperature superconductors. In: Narlikar A (ed) *Studies of High Temperature Superconductors*. Nova Science Pub, New York, p 299
- Kuzmany H, Sariciftci NS, Neugebauer H, Neckel A (1988) *Phys Rev Lett* 60:212-215
- Kuzmany H, Sumetsberger B, Matus M, Zachmann G (1990b) *Europhys Lett* 12:703-708
- Kuzmany H, Surjan PR, Kertesz M (1983) *Sol State Communic* 48:243-247
- Laane J (1981) *J Chem Phys* 75:2539
- Lafleur M, Dasseux JL, Pigeon M, Dufourc J, Pezolet M (1987) *Biochemistry* 26:1173
- Laigle A, Chinsky L, Turpin PY, Hartmann B, Thuong NT, Leng M (1986) *Nucleic Acids Res* 14:3425
- Laigle A, Chinsky L, Turpin PY, Liquier J, TAILLANDIER J (1982) *Nucleic Acids Res* 10:7395
- Lampen P (1991) Dissertation, Universitaet, Essen
- Landolt-Börnstein (1951) *Molekeln I and II*, 6th edn, vols I/2 and I/3. Springer
- Landolt-Börnstein (1955) *Kristalle*, 6th edn, vol I/4. Springer
- Landsberg G, Mandelstam L (1928) *Naturwiss* 16: 557, 772
- Langley SP (1881) *Am J Arts & Sci* 21:187
- Langley SP (1883) *Phil Mag* 15:153
- Langley SP (1884) *Phil Mag* 17:194
- Lanyi J (1993) *Biochim et Biophys Acta* 1183:241
- Lanyi JK (1984) In: *Bacteriorhodopsin and Related Light-Energy Converters in Bioenergetics*, Ernster L (ed). Elsevier, p 315
- Lapp M, Penney CM (eds) (1974) *Laser Raman Gas Diagnostics, Proceedings of the Project SQUIO Laser Raman Workshop on the Measurement of Gas Properties*. Plenum Press, New York
- Lapp M, Penney CM (1977) Raman Measurements on Flames. In: Clark RJH, Hester RE (eds) *Advances in Infrared and Raman Spectroscopy*, vol 3, p 204
- Laqua K (1980) *Emissionsspektroskopie*. In: Ullmanns Encyklopädie der technischen Chemie, Verlag Chemie 5:441
- Laqua K, Hagenah WD, Waechter H (1967) *Fresenius Z Anal Chem* 225:142

- Laqua K, Melhuish WH, Zander M (1988) IUPAC Recommendation V.4 VII Pure Appl Chem 60:1449
- Laroche G, Dufourc EJ, Dufourcq J, Pezolet M (1991) Biochemistry 30:3105
- Laroche G, Dufourc EJ, Pezolet M, Dufourcq J (1990) Biochemistry 26:6460
- Larson EM, Brown TM, van Dreele RB (1986) Acta Crystallogr B42:533
- Lasser R, Smith NV, Benbow RL (1981) Phys Rev B24:1895
- Lasser T, Magros E, Leipertz A (1985) Opt Lett 10:535
- Lau A, Siebert S, Wernke W (eds) (1993) Time resolved vibrational spectroscopy, vol 6. Springer, Berlin
- Laubereau A, Kaiser W (1978) Rev Mod Phys 50:607
- Laubereau A, Purucker HG (1992) Il Nuovo Cimento 14D:979
- Laubereau A, Wochner G, Kaiser W (1978) Chem Phys 28:363
- Lauer JJ, King VW (1979) Infrared Phys 19:395
- Laurendeau NM (1988) Prog Energy Combust Sci 14:147
- Lavorel B, Chaux R, Saint-Loup R, Berger H (1987) Opt Commun 62:25
- Lavorel B, Millot G, Kou QL, Guelachvili G, Bouzouba K, Lepage P, Tyuterev VG, Pierre G (1990) J Mol Spectrosc 143:35
- Lavorel B, Millot G, Rotger M, Rouillé G, Berger H, Schrötter HW (1992) J Mol Struct 273:49
- Lavorel B, Pykhow R, Millot G (1993) J Quant Spectrosc Rad Transf 49:579
- Lebioda K (1994) Dissertation, Universität Essen
- Lechuga-Fossat L, Flaud JM, Camy-Peyret C, Johns JWC (1984) Can J Phys 62:1889
- Leclercq M, Billard J, Jacques J (1969) Mol Cryst Liq Cryst 8:367
- Lee D, Albrecht AC (1985) In: Advances in Infrared and Raman Spectroscopy, vol 12, Clark RJH, Hester RE (eds). Heyden, London, p 179
- Lee DC, Durrani AA, Chapman A (1984) Biochim Biophys Acta 769:49
- Lee DC, Haris PI, Chapman D, Mitchell RC (1990) Biochemistry 29:9185
- Lee DC, Haris PI, Chapman D, Mitchell RC (1991) In: Hester RE, Girling RB (eds) Spectroscopy of Biological Molecules. Royal Society of Chemistry, p 7
- Lee PC, Meisel D (1982) J Phys Chem 86:3391
- Lee SY, Heller EJ (1979) J Chem Phys 71:4777
- Lee YS, Kertesz M (1988) J Chem Phys 88:2609-2617
- Lefrant S, Buisson JP (1991) NATO ASI series p.313 In: G. Messier (ed) Organic molecules for nonlinear optics and photonics, Kluwer Academic Publication
- Lefrant S, Buisson JP, Eckhardt H (1990) Synth Met 37:91-98
- Lefrant S, Mevellec JY, Buisson JP, Perrin E, Eckhardt H, Han CC, Jen KY (1989a) Springer Series Solid State Sciences 91:123. In: Kuzmany H, Mehring M, Roth S (eds) Electronic Properties of Polymers III. Springer, Berlin Heidelberg New York London
- Lefrant S, Perrin E, Buisson JP, Eckhardt H, Han CC (1989b) Synth Met 29:E91-E96
- Lehrer E (1937) Z techn Physik 18:393
- Lehrer E (1942) Z techn Physik 23:169
- Leimkuehler M, Mattes R (1986) J Sol State Chem 65:260
- Leipertz A (1981) Optics Laser Technol 13:21
- Leipertz A (1981) Phys Unserer Zeit 12:107
- Leipertz A (1981) Wärme 87:10
- Leipertz A (1983) Appl Opt 22:901
- Leipertz A (1984) Habilitationsschrift, Bochum
- Leipertz A (1989) Chem Ing Tech 61:39
- Leipertz A (1989) In: Instrumentation for Combustion and Flow Engines, Durao DFG, Witze EP, Whitelaw JH (eds). Kluwer Academic, Dordrecht, p 107
- Leipertz A, Fiebig M (1979) Appl Opt 18:357
- Leipertz A, Haumann J, Fiebig M (1987) Chem Eng Technol 10:190
- Lemmon DH, Swartz JC (1994) J Mol Struct, to be published
- Le Noble WJ, Schlott R (1976) Rev Sci Instrum 47:770
- Lentz E, Hatzilazarou A, Lebioda K, Schrader B (1994) Mobiles IR-Photometer zum Nachweis organischer Verbindungen mit Hilfe extrahierender Membranen. In: Tagungsband zur InCom '94, GIT Verlag, Düsseldorf
- Leonard DA (1975) Opt Quant Electron 7:197
- Leonhardt R, Holzapfel W, Zinth W, Kaiser W (1987) Chem Phys Lett 133:373

- Leonhardt R, Holzapfel W, Zinth W, Kaiser W (1987) *Rev Phys Appl* 22:1735
- Lepard DW (1970) *Can J Phys* 48:1664
- Lephardt JO, Fennier RA (1980) *Appl Spectrosc* 34:174
- Lesicki L, Nibler JW (1976) *J Chem Phys* 65:871
- Leuchs M, Kiefer W (1993a) *J Chem Phys* 99:6302
- Leuchs M, Kiefer W (1993b) *Phys Rev* 48B:15690
- Leupold WR (1978) Dissertation, Universität Dortmund
- Leupold WR, Domingo C, Niggemann W, Schrader B (1980) *Fresenius Z Anal Chem* 303:337
- Levenson MD (1982) *Introduction to Nonlinear Laser Spectroscopy*, Academic Press, New York
- Levin IR (1984) In: Clark RJM, Hester RE (eds) *Advances in IR and Raman Spectroscopy*. Wiley Heyden, New York, p 1
- Levin IW (1991) In: Hester RE, Girling RB (eds) *Spectroscopy of Biological Molecules*. Royal Society of Chemistry, p 155
- Levin IW, Neil Lewis E (1990) *Anal Chem* 62:1101A
- Levin IW, Thompson TE, Barenholz Y, Huang C (1985) *Biochemistry* 24:6282
- Levy Y, Dupeyrat R (1977) *J Phys Colloq C5 Sup no 11*, T38:253
- Levy Y, Imbert C, Cipriani J, Racine S, Dupeyrat R (1974) *Opt Commun* 11:66
- Lewis A (1976) *The Spex Speaker* 21, no 2
- Leyden DE (1990) *Chem Modif Surf* 3:1
- Leyden DE, Murthy RSS (1987) *Spectroscopy* 2:28
- Li W, Purucker HG, Laubereau A (1992) *Opt Commun* 94:300
- Liang EJ, Engert C, Kiefer W (1993a) *J Raman Spectrosc* 24:775
- Liang EJ, Engert C, Kiefer W (1993b) *Vibr Spectrosc* 6:79
- Liang EJ, Weippert A, Funk JM, Materny A, Kiefer W (1994) *Chem Phys Lett*, in press
- Liao PF, Bergmann JG, Chemla DS, Wokaun A, Melugailis J, Hawryluk AM, Economou NP (1981) *Chem Phys Lett* 82:355
- Licht K, Reich P (1971) *Literature Data for IR, Raman, NMR Spectroscopy of Si, Ge, Sn and Pb Organic Compounds*. VEB Deutscher Verlag der Wissenschaften, Berlin
- Lichtermann LS, Imhoff EA, Sarhangi A, Fitchen B (1984) *J Chem Phys* 81:168-184
- Liddle WK, Tu AT (1985) *Biochemistry* 24:7635
- Liebrecht F, Finsterhözl H, Schröter HW, Montero S (1988) *Indian J Pure Appl Phys* 26:51
- Lieneweg F (ed) (1976) *Handbuch der Technischen Temperaturmessung*. Vieweg, Braunschweig
- Lindenmayer J, Magg U, Jones H (1988) *J Mol Spectrosc* 128:172
- Lindner M (1994) Untersuchung der optischen Aktivität enantiomorpher Einkristalle mit Hilfe der Raman-Spektroskopie. Dissertation, Universität Essen
- Linton HR, Nixon ER (1958) *J Chem Phys* 28:990
- Lin-Vien D, Colthup NB, Fateley WG, Grasselli JG (1991) *The Handbook of Infrared and Raman Characteristic Frequencies of Organic Molecules*. Academic Press, New York
- Lippert E, Mecke R (1951) *Z Elektrochem Ber Bunsenges* 55:366
- Lippert JL, Petricolas WL (1971) *Proc Natl Acad Sc USA* 68:1572
- Liquier J, Akhebat A, Taillandier E, Ceolin F, Huynh Dinh T, Igolen J (1991) *Spectrochim Acta* 47A:177
- Liquier J, Gadenne MC, Taillandier E, Defer N, Favatier F, Kruh J (1979) *Nucleic Acids Res* 6:1479
- Liquier J, Mchami A, Taillandier E (1989) *J Biomol Struct Dyn* 7:119
- Liquier J, Taboury J, Taillandier E, Brahms J (1977) *Biochemistry* 16:3262
- Liquier J, Taillandier E, Petricolas WL, Thomas GA (1990) *J Biomol Struct Dyn* 8:295
- Liteanu C, Rica I (1979) *Anal Chem* 51:1986
- Litman BJ, Lewis EN, Levin IW (1991) *Biochemistry* 30:313
- Loëte M, Berger H (1977) *J Mol Spectrosc* 68:317
- Lolck JE, Owyong A, Eshierick P (1985a) *J Raman Spectrosc* 16:163
- Lolck JE, Poussigue G, Pascaud E, Guelachvili G (1985b) *J Mol Spectrosc* 111:235
- Lolck JE, Robiette AG, Brown LR, Hunt RH (1982) *J Mol Spectrosc* 92:229
- Lommel E (1878) *Wiedemanns Ann d Phys* 3:251
- Long DA (1971) In: Stavely L (ed) *Characterization of Chemical Purity, Organic Compounds*. Butterworths, London
- Long DA (1977) *Raman Spectroscopy*. McGraw Hill, London

- Long DA (1979) In: Nonlinear Behaviour of Molecules, Atoms & Ions in Electric, Magnetic or Electromagnetic Fields, Neel C, (ed). Elsevier, Amsterdam, p 153
- Long DA (1982) The polarizability and hyperpolarizability tensors. In: Kiefer W, Long DA (eds) Non-linear Raman spectroscopy and its chemical applications. Nato advanced study institute series, C, vol 93. D Reidel Publishing Company, Dordrecht, p 174
- Long DA (1988) Internat Rev in Phys Chem 7:317
- Long GJ, Basile LJ, Ferraro JR (1974) Appl Spectrosc 28:73
- Lopez MA, Montero S (1977) Appl Spectrosc 31:469
- Lorber A, Kowalski BR (1988) J Chemometrics 2:93
- Lorber A, Wangen LE, Kowalski BR (1987) J Chemometrics 1:19
- Lord RC (1977) Appl Spectrosc 31:187
- Lord RC, Yu NT (1970) J Mol Biol 50:509
- Low MJD, Morterra C (1985) Adsorpt Sci Technol 2:131
- Lowry SR, May TE, Bornstein A (1993) Appl Spectrosc 47:30
- Luck WAP (1963) Ber Bunsenges Phys Chem 67:186
- Luck WAP (1965) Ber Bunsenges Phys Chem 69:626
- Luck WAP, Ditter W (1968) Ber Bunsenges Phys Chem 72:365
- Luckhurst GR (1993) Ber Bunsenges Phys Chem 97:1169
- Luckhurst GR, Zannoni C, Nordio PL, Segre U (1975) Molec Phys 30:1345
- Ludernitz T, Brandenburg K, Seydel U, Roths A, Galanos C, Rieschel ET (1989) Eur Biochem 179:11
- Luft KF (1943) Z Techn Phys 24:97
- Luft KF (1947) Angew Chemie 19:2
- Luft KF (1975) Ann Occup Hyg 18:45
- Luongo JP (1964) J Polymer Sci Polym Lett B2:75
- Lutz M (1984) In: Clark RJM, Hester RE (eds) Advances in IR and Raman Spectroscopy. Wiley, Heyden, New York, 11:211
- Lutz M, Kleo J, Reiss-Husson F (1976) Biochem Biophys Res Comm 69:711
- Lutz M, Mantele W (1991) In: Scheer H (ed) Chlorophylls. CRC Press, p 855
- Lutz M, Robert B (1988) In: Spiro TG (ed) Biological applications of Raman spectroscopy 3:347
- Lutz M, Szponarski W, Berger G, Robert B, Neumann JM (1987) Biochim Biophys Acta 894:423
- Lyddane RH, Sachs RG, Teller E (1941) Phys Rev 59:673
- Lykke Hansen E, Nicolaisen FM (1979) Infrared Phys 19:225
- MacDiarmid AG, Chiang JC, Richter AF, Epstein AJ (1987) Synth Met 18:285
- MacDiarmid AG, Heeger AJ (1979) Synthetic Metals 1:101
- MacLean C, Mackor EL (1961) J Chem Phys 34:2207
- Maddams WF (1980) Appl Spectrosc 34:245
- Maier G, Mihm G, Reisenauer HP, Littmann D (1984) Chem Ber 117:2369
- Maier G, Reisenauer HP, Hu J, Schaad LJ, Hess Jr BA (1990) J Am Chem Soc 112:5117
- Maier G, Reisenauer HP, Schafer U, Balli H (1988) Angew Chem Int Ed Engl 27:566
- Maier W, Saupe A (1958) Z Naturforsch 13A:564
- Maier W, Saupe A (1959) Z Naturforsch 14A:882
- Maier W, Saupe A (1960) Z Naturforsch 15A:287
- Maiman TH (1960) Nature 187:433
- Maker PD, Terhune RW (1965) Phys Rev A137:801
- Malinowski ER (1977) Anal Chem 49:606, 612
- Malinowski ER (1991) Factor Analysis in Chemistry, 2nd edn. John Wiley & Sons, New York & Sons
- Malinowski ER, Howery DG (1980) Factor Analysis in Chemistry. Wiley, New York
- Malon P, Mickley LJ, Sluis KM, Tam CN, Keiderling TA, Kamath S, Uang J, Chickos JS (1992) J Phys Chem 96:10139
- Malyi M, Griffiths JE (1983) Appl Spectrosc 37:315
- Manne R (1987) Chemometrics and Intelligent Laboratory Systems 2:187
- Mantsch HH, Casal HL, Jones RN (1986) In: Clark RJH, Hester RE (eds) Advances in Spectroscopy, John Wiley Pub Co, vol 13:1
- Mantsch HH, Hubner W (1991) In: Hester RE, Girling RB (eds) Spectroscopy of Biological Molecules. Royal Society of Chemistry, p 147
- Mantsch HH, McElhaney (1991) Chem Phys Lipids 57:213

- Mantsch HH, Yang PW, Martin A, Cameron DG (1988) *Eur J Biochem* 178:335
- Mantz AW (1978) *Appl Opt* 17:1347
- Maradudin AA, Montroll EW, Weiss GH, Ipatava P (1971) Theory of lattice dynamics in the harmonic approximation, Academic Press, New York
- March N (1992) Electro Density Theory of atoms and molecules. Academic Press
- Marcott C, Havel HA, Hedlund B, Overend J, Moscowitz A (1979) A vibrational rotational strength of extraordinary intensity. Azidomethemoglobin A. In: Mason SF (ed) Optical activity and chiral discrimination, Reidel, Dordrecht, p 289
- Margenau H, Murphy GM (1955) The Mathematics of Physics and Chemistry. D Van Nostrand, New York
- Mariotte E (1686) Traite de la Nature des Couleurs, Paris
- Maris MA, Brown CW (1983) *Anal Chem* 55:1694
- Marko KA, Rimai L (1979) *Opt Lett* 4:211
- Maroncelli M, Hopkins GA, Nibler JW, Dyke TR (1985) *J Chem Phys* 83:2129
- Marsh D (1991) *Chem Phys Lipids* 57:109
- Martens H, Karstang T, Naes T (1987) *J Chemometrics* 1:201
- Martens H, Naes T (1984) *Trends Anal Chem* 3:204, 266
- Martens H, Naes T (1989) Multivariate Calibration. John Wiley & Sons, Chichester New York
Brisbane Toronto Singapur
- Martin DR, Puplett E (1969) *Infrared Phys* 10:105
- Martin J, Montero S (1984) *J Chem Phys* 80:4610
- Martin JC, Wartel RM (1982) *Biopolymers* 21:499
- Martin RM, Falicov LM (1975) In: Light Scattering in Solids, Cardona M (ed) Topics in Applied Physics, vol 8. Springer, Berlin, p 80
- Martin TP (1977) *J Chem Phys* 67:5207
- Martinez RZ, Santos J, Cancio P, Bermejo D (1993) XXIIth European CARS Workshop, Villigen, Switzerland, poster P27, and private communication
- Mason SF (1982) Molecular optical activity and the chiral discriminations. Cambridge University Press, Cambridge
- Massart DL, Vandeginste BGM, Deming SN, Michotte Y, Kaufmann L (1988) Data Handling in Science and Technology, vol 2, Chemometrics: a textbook. Elsevier, Amsterdam
- Mataga N, Nishimoto K (1957) *Z Phys Chem NF* 13:140
- Materny A, Kiefer W (1992a) *J Chem Phys* 97:841
- Materny A, Kiefer W (1992b) *J Raman Spectrosc* 23:595
- Materny A, Kiefer W (1992c) *J Raman Spectrosc* 23:605
- Materny A, Kiefer W (1992d) *Phys Rev B* 46:2704
- Materny A, Kiefer W (1992e) *Macromol* 25:5074
- Materny A, Kiefer W (1993) in Coherent Raman Spectroscopy: Applications and New Developments, Castellucci R, Righini R, Foggi P, eds, World Scientific, Singapore, p 235
- Materny A, Kiefer W, Schwoerer M (1992b) *J Chem Phys* 97:2237
- Materny A, Leuchs M, Kiefer W (1992c) *Il Nuovo Cimento* 14D:989
- Materny A, Leuchs M, Michelis T, Schaschek K, Kiefer W (1992a) *J Raman Spectrosc* 23:99
- Mathai PM, Shepherd GG, Welsh HL (1956) *Can J Phys* 34:1448
- Mathies R (1979) *Chem Biochem Appl Lasers* 4:55. Academic Press New York
- Mathies R, Yu NT (1978) *J Raman Spectrosc* 7:349
- Mathieu JP (1939) *Bull Soc France Min Cryst* 62:174
- Matsui T et al (1978) *J Bioeng* 2:539
- Mattioli TA, Gray KA, Lutz M, Oesterhelt D, Robert B (1991a) *Biochemistry* 30:1715
- Mattioli TA, Hoffmann A, Lutz M, Schrader B (1990) *CR Acad Sci Paris*, 310 serie III:441
- Mattioli TA, Hoffmann A, Robert B, Schrader B, Lutz M (1991b) *Biochemistry* 30:4648
- Mattioli TA, Hoffmann A, Robert B, Schrader B, Lutz M (1991c) In: Spectroscopy of Biological Molecules, Hester RE, Girling RB (eds), The Royal Society of Chemistry, p 47
- Matus M, Kuzmany H (1993) *Appl Phys A* 56:241
- Matz G (1978) personal communication, Die BASF 5:13
- Mauguin C (1931) *Z Kristallogr* 76:542
- Mayer H, Sajonz D (1983) *Siemens Energietechnik* 5:6
- Mayer LD, Nelsetnen GL (1981) *Biochemistry* 20:2457

- McCall RP, Roe MG, Ginder JM, Kusumoto T, Epstein AJ, Asturias GE, Scherr EM, MacDiarmid AG (1989) *Synth Met* 29:E433-E438
- McCarty KF, Liu JZ, Shelton RN, Radousky HB (1990) *Phys Rev B* 41:8792-8797
- McCarty RP, Radousky HB, Liu JZ, Shelton RN (1991) *Phys Rev B* 44:13751-13754
- McClelland JF, Luo S, Jones RW, Seaverson LM (1992) *Springer Ser Opt Sci* 69:113
- McClure GL (1981) *Perkin Elmer Infrared Bulletin* 89
- McClure GL (1987) In: Willis HA, van der Maas JH, Miller RGJ (eds) *Laboratory Methods in Vibrational Spectroscopy*. John Wiley, London
- McDaniel RV, McLaughlin (1985) *Biochim Biophys Acta* 819:153
- McDonald RS, Wilks PA (1989) *Appl Spectrosc Rev* 22:335
- McDowell RS, Patterson CW, Owyong A (1980) *J Chem Phys* 72:1071
- McIntosh TJ, McDaniel RV, Simon SA (1983) *Biochim Biophys Acta* 731:109
- McIntosh D, Ozin GA (1977) *Inorg Chem* 16:51
- McIntosh DF, Peterson MR (1977) *QCPE* 11:342
- McIntosh JP, Grieger I, Eckstein F, Zarling DA, van de Sande JH, Jovin TM (1983) *Nature* 304:83
- McKenzie MT, Culler SR, Koenig JL (1984) *Appl Spectrosc* 38:786
- McLean C, Mackor EL (1961) *J Chem Phys* 34:2207
- Mead DG (1980) *Appl Spectrosc* 34:171
- Mecke R (1932) *Z Physik Chem* B16:409, 421; B17:1
- Medina FD (1980) *Infrared Phys* 20:297
- Meer BW van der, Vertogen G (1976) *Phys Letters A* 59:279
- Mehner T, Goecke HJ, Schunck S, Schnoeckel H (1990) *Z Anorg Allg Chem* 580:121
- Meier M, Wokaun A, Vo-Dinh T (1985) *J Phys Chem* 89:1843
- Meier W, Schrader B, Pisarcik M (1972) *Meßtechnik* 5:119
- Meisterle P, Kuzmany H, Nauer G (1984) *Phys Rev B* 29:6008
- Mellier A, Diaf A (1988) *Chem Phys Lipids* 46:51
- Melloni M (1833) *Ann Chimie Physique* 53:5
- Melloni M (1835) *Ann Chimie Physique* 55:337
- Melloni M (1835) *Ann Phys Chem* 35:112
- Memon MI, Wilkinson GR, Sherman WF (1982) *J Mol Struct* 80:113
- Mendelsohn R (1991) In: Hester RE, Girling RB (eds) *Spectroscopy of Biological Molecules*. The Royal Society of Chemistry, p 151
- Mendelsohn R, Anderle G, Jaworsky M, Mantsch HH, Dluhy RA (1984) *Biochim Biophys Acta* 775:215
- Mendelsohn R, Dluhy R, Taraschi T, Cameron DG, Mantsch HH (1986) *Biochemistry* 20:6699
- Mendelsohn R, Dluhy RA, Crawford T, Mantsch HH (1984) *Biochemistry* 23:149
- Mendelsohn R, Maisano J (1978) *Biochim Biophys Acta* 506:192
- Mendelsohn R, Mantsch HH (1986) In: Watts A, de Pont JJH (eds) *Progress in Protein-Lipid Interaction* 2. Elsevier Sci Publishers, Chapter 4, p 103
- Menges G, Schwesig H (1979) *Kautsch Gummi Kunstst* 32:643
- Merlin JC, Lorriaux JL, Hester RE (1981) *J Raman Spectrosc* 11:384
- Messerschmidt RG (1985) *Appl Spectrosc* 39:737
- Messerschmidt RG, Chase DB (1989) *Appl Spectrosc* 43:11
- Meßler P, Schrötter HW (1992) (unpublished)
- Meßler P, Schrötter HW, Sarka K (1994) *J Raman Spectrosc* 25, in press
- Michaelian KH (1990) *Vibr Spectra Struct* 18:81
- Michaelis W, Weitkamp C (1984) *Fresenius Z Anal Chem* 317:286
- Michel G, Cahay R (1986) *J Raman Spectrosc* 17:79
- Michelson AA (1890) *Am J Sci* 39:115
- Michl J, Thulstrup EW (1986) *Spectroscopy with polarized light*. VCH Publishers Inc, New York
- Mierzecki R (1979) *Acta Phys Pol A* 56:261
- Miles HT (1964) *Proc Natl Acad Sci USA* 51:1104
- Miller RGJ, Stace BC (1972) *Laboratory Methods in Infrared Spectroscopy*. Heyden & Son, London
- Milligan DE, Jacox ME (1964) *J Chem Phys* 40:2461
- Millot G, Boutahar A, Lavorel B, Wenger C, Saint-Loup R, Berger H (1990) *J Raman Spectrosc* 21:803

- Millot G, Lavorel B, Chaux R, Saint-Loup R, Pierre G, Berger H, Steinfeld JI, Foy B (1988) *J Mol Spectrosc* 127:156
- Millot G, Lavorel B, Steinfeld JI (1991) *J Chem Phys* 95:7938
- Millot G, Lavorel B, Steinfeld JI (1992) *J Quant Spectrosc Rad Transfer* 47:81
- Mills IM (ed) (1988) Quantities, Units and Symbols in Physical Chemistry, IUPAC, Blackwell Scientific Publications, Oxford
- Mills IM (1963) *Spectrochim Acta* 19:1585
- Mills IM (1965) *Pure Appl Chem* 11:325
- Mills IM (1992) Understanding spectra of highly excited vibrational states. In: Murray I, Cowe IA (eds) *Making Light Work: Advances in Near Infrared Spectroscopy*. VCH, Weinheim
- Mink J, Kereszty G (1988) *Croat Chem Acta* 61:731
- Minkin VI, Osipov OA, Zhdanov YA (1970) *Dipole moments in Organic Chemistry*. Plenum Press, New York
- Mirabella FM Jr (1985) *Appl Spectrosc Rev* 21:45
- Mirabella FM, Harrick NJ (ed) (1985) *Internal Reflection Spectroscopy: Review and Supplement*. Harrick Scientific Corporation, New York
- Mitchell ML, Dluhy RA (1988) *J Am Chem Soc* 110:712
- Miyazawa T (1962) In: Stahmann MA (ed) *Polyamino acids, polypeptides and proteins*. University Wisconsin Press Madison
- Miyazawa T, Shimanouchi T, Mizushima SI (1956) *J Chem Phys* 24:408
- Mizushima SI, Shimanouchi T, Nakamura K, Hayashi M, Tsuji S (1956) *J Chem Phys* 26:970
- Moffit W, Moscowitz A (1959) *J Chem Phys* 30:648
- Mohan N, Müller A, Nakamoto K (1975) The Metal Isotope Effect on Molecular Vibrations. In: Clark RJH, Hester RE (eds) *Advances in Infrared and Raman Spectroscopy*, vol 1. Heyden, London, p 173
- Möller KD, Rothschild WG (1971) *Far Infrared Spectroscopy*, Wiley Interscience, New York
- Montero S, Domingo C, Wetzel F, Finsterhölzl H, Schröter HW (1984) *J Raman Spectrosc* 15:380
- Mooradian A (1972) *Laser Handbook*. In: Arecchi FT, Schulz du Bois EO (eds). North Holland Amsterdam, p 1309
- Mooradian A, McWorther AL (1967) *Phys Rev Lett* 19:849
- Moore DS, VoDinh T, Schrader B (1993) Draft of Document XV of IUPAC Commission V.4
- Morino Y, Kuchitsu K, Shimanouchi T (1952) *J Chem Phys* 20:726
- Morris MD, Bienstock R (1986) In: *Advances in Infrared and Raman Spectroscopy*, vol 13, Clark RJH, Hester RE (eds). Heyden, London, p 395
- Morse PM (1929) *Physic Rev* 34:57
- Mortensen A, Christensen DH, Faurskov Nielsen O, Pedersen E (1991) *J Raman Spectrosc* 22:47
- Mortensen OS, Hassing S (1980) In: *Advances in Infrared and Raman Spectroscopy*, vol 6, Clark RJH, Hester RE (eds). Heyden, London, p 1
- Moser HE, Dervan PB (1987) *Science* 238:645
- Moskovits M (1985) *Rev Mod Phys* 57:783
- Moskovits M (1986) *Metal Clusters*. In: Moskovits M (ed) *Metal Clusters*. Wiley, New York, p 185
- Moskovits M (1989) *Matrix-Isolated Metal Clusters*. In: Andrews L, Moskovits M (eds) *Chemistry and Physics of Matrix-Isolated Species*. North-Holland Amsterdam, p 49
- Moskovits M, DiLella DP (1980) *J Chem Phys* 73:4917
- Moskovits M, Ozin GA (eds) (1976) *Cryochemistry*. John Wiley, New York
- Moskovits M, Ozin GA (1976) *J Mol Struct* 32:71
- Muga A, Mantsch HH, Surewicz WK (1990) In: *Biophysics for the 90's*, Tenth International Biophysics Congress, p 218
- Mulazzi E, Lefrant S (1989) *Synth Met* 28:D323-D329
- Muller E, Kopf E, Blume A (1991) In: Hester RE, Girling RB (eds) *Spectroscopy of Biomolecules*. The Royal Society of Chemistry, p 189
- Müller A, Koeniger F, Weinstock N (1974) *Spectrochim Acta* 30A:641
- Müller G (1978) Proceedings of the Sixth International Conference on Raman spectroscopy, vol. 2. Bangalore, G Heyden, London, p 524, 526
- Müller G, Abraham K, Schaldach M (1981) *Appl Opt* 20:1182
- Mulliken RS (1955) *J Chem Phys* 23:1997
- Murphy DV, von Raben KU, Chang RK, Dorain PB (1982) *Chem Phys Lett* 85:43

- Murphy RE, Cook FH, Sakai H (1975) *J Opt Soc Am* 65:600
Murphy WF (1977a) *J Chem Phys* 67:5877
Murphy WF (1977b) *Mol Phys* 33:1701
Murphy WF (1978) *Mol Phys* 36:727
Murphy WF (1991) Chemical Applications of Gas-Phase Raman Spectroscopy: In: Grasselli JG, Buikin BJ (eds) *Analytical Spectroscopy*. Wiley, Chichester, p 425
Murphy WF, Holzer W, Bernstein HJ (1969) *Appl Spectrosc* 23:211
Murphy WF, Montero S (1981) *Mol Phys* 44:187
Murray CA, Greytak TJ (1979) *J Chem Phys* 71:3355
Murray I, Cowe IA (1992) *Making Light Work: Advances in Near Infrared Spectroscopy*. VCH, Weinheim
Musty PR, Nickless G (1974) *J Chromatogr* 100:83
Myers AB (1990) *J Opt Soc Am B* 7:1665
Myers AB, Mathies RA (1987) In: *Biological Applications of Raman Spectroscopy*, vol 2. Wiley, New York, p 1
Myers AB, Mathies RA, Tannor DJ, Heller EJ (1982) *J Chem Phys* 77:3857
Naarmann H (1987) Springer Series Solid State Sciences 76:12. In: Kuzmany H, Mehring M, Roth S (eds) *Electronic Properties of Polymers*. Springer, Berlin Heidelberg New York London
Nabedryk E, Bardin AM, Breton J (1985) *Biophys J* 48:873
Nabedryk E, Breton J, Thibodeau DL (1991) In: Hester RE, Girling RB (eds) *Spectroscopy of Biological Molecules*. The Royal Society of Chemistry, p 67
Nabedryk E, Garavito RM, Breton J (1988) *Biophys J* 53:671
Nabiev IR, Esrimov RG, Chumanov GD, Kuriatov AB (1985) *Biol Membr* 2:1003
Naes T, Irgens C, Martens H (1986) *Appl Statist* 35:195
Naes T, Martens H (1988) *J Chemometrics* 2:155
Nafie LA (1984) Vibrational Optical Activity. In: Clark RJH, Hester RE (eds) *Advances in Infrared and Raman Spectroscopy*, vol 11. Wiley-Heyden, Chichester, pp 49
Nafie LA (1992) SPIE 1681:29
Nafie LA, Diem M, Vidrine DW (1979) *J Amer Chem Soc* 101:496
Nafie LA, Freedman TB (1983) *J Chem Phys* 78:7108
Nafie LA, Freedman TB (1986) *J Chem Phys* 90:763
Nafie LA, Keiderling TA, Stephens PJ (1976) *J Am Chem Soc* 89:2715
Nafie LA, Walnut TH (1977) *Chem Phys Lett* 49:441
Nagaso T, Yamada K (1975) *J Raman Spectrosc* 3:153
Nakagawa I, Tsuchida A, Shiranouchi T (1967) *J Chem Phys* 47:982
Nakamizo M et al (1978) *Carbon* 16:281
Nakamoto K (1978) *Infrared Spectra of Inorganic and Coordination Compounds*, 3rd edn. Wiley Intersc John Wiley & Sons, New York London Sydney Toronto
Nakano T, Yokoyama T, Toriumi H (1993) *Appl Spectrosc* 47:1354
Narayanan U, Keiderling TA (1983) *J Amer Chem Soc* 105:6406
Naumann D, Schultz C, Born J, Labischinski H, Brandenburg K, von Busse G, Brade H, Seydel U (1987) *Eur J Biochem* 164:159
Naumann D, Schultz C, Hucho F (1990) Biophysics for 90's, Tenth International Biophysics Congress, p 390
Naylor T de V (1989) Comprehensive Polymer Science. In: Allen G, Bevington JC (eds) *The synthesis, characterization, reactions and applications of polymers*, vol 2. C. Pergamon Press, Oxford New York, p 650
Nazzal AI, Street GB, Wynne KJ (1985) Characterization of polypyrrole. In: Labes MM (ed) *Molecular crystals and liquid crystals*. Gordon and Breach Science Publishers, New York London Paris Montreux Tokyo, p 303
Neckel A (1987) *Microchim Acta [Wien]* 3:263-280
Neddersen J, Chumanov G, Cotton TM (1993) *Appl Spectrosc* 47:1959
Neddersen JP, Mounter SA, Bostick JM, Johnson OK (1989) *J Chem Phys* 90:4719
Nees F (1978) Thesis, Karlsruhe
Nees FW, Buback M (1976) *Z Naturforsch* 31a:1960
Neppe A, Butler IS, Eisenberg A (1979) *Macromolecules* 12:948
Nestor JR, Lippincott ER (1973) *J Raman Spectrosc* 1:305

- Neugebauer H, Neckel A, Nauer G, Brinda-Konopik N, Garnier F, Tourillon G (1983) *Journal de Physique* 12:C10-517
- Neugebauer HEJ (1954) *Can J Phys* 32:1
- Ni F, Cotton TM (1986) *Anal Chem* 58:3159
- Ni F, Sheng R, Cotton TM (1990) *Anal Chem* 62:1958
- Nibler JW, Knighten GV (1978) In: *Raman Spectroscopy of Gases and Liquids*, Weber A (ed) Springer, Berlin, p 253
- Nibler JW, Schaub WM, MacDonald JR, Harvey AB (1977) In: *Vibrational Spectra and Structure*, vol 6, Durig JR (ed) New York, chapter 3
- Nibler JW, Pubanz GA (1988) in *Advances in Spectroscopy*, vol 15, Clark RHE, Hester RE (eds) Wiley, Chichester, chapter 1
- Nie S, Bergbauer KL, Ho JH, Kuck jr JFR, Yu NT (1991) *Spectroscopy* 5:24
- Nie S, Bergbauer KL, Kuck jr JFR, Yu NT (1990) *Exp Eye Res* 51:619
- Nie S, Lipscomb LA, Feng S, Yu NT (1990) *Chem Phys Lett* 167:35
- Nielsen JR, Thormpton U, Dale EB (1944) *Rev d Phys* 16:307
- Niggemann W (1980) Dissertation, Universität Essen
- Nishimura Y, Hirakawa AY, Tsuboi M (1978) In: *Advances in Infrared and Raman Spectroscopy*, vol 5, Clark RJH, Hester RE (eds), Heyden, London, p 217
- Nishimura Y, Hirakawa AY, Tsuboi M (1978) *Resonance Raman Spectroscopy of Nucleic Acids*. In: Barnes AJ, Orville-Thomas WJ (eds) (1977) *Vibrational Spectroscopy - Modern Trends* vol 5. Elsevier, Amsterdam New York
- Nishimura Y, Torigoe C, Tsuboi T (1986) *Nucleic Acids Res* 14:2737
- Nishio E, Ikuta N, Okabayashi H, Hannah RW (1990) *Appl Spectrosc* 44:614
- Nishizawa E, Hashimoto H, Koyama Y (1989) *Chem Phys Lett* 164:155
- Nishizawa E, Hashimoto H, Koyama Y (1991) *Chem Phys Lett* 181:387
- Nishizawa E, Koyama Y (1991) *Chem Phys Lett* 176:390
- Nitsch W, Kiefer W (1977) *Opt Commun* 23:240
- Nobili L (1830) *Sci & Arts* (Bibliotheque Universelle Geneve) 44:225
- Nobili L (1834) *Sci & Arts* (Bibliotheque Universelle Geneve) 57:1
- Nobili L, Melloni M (1831) *Ann Chimie Physique* 48:187
- Noble PN, Pimentel GC (1968) *Spectrochim Acta* 24A:797
- Noggle JH (1976) *J Chem Ed* 53:190
- Noguchi T, Hayashi H, Tasumi M (1990) *Biochim Biophys Acta* 1017:280
- Noguchi T, Hayashi H, Tasumi M, Atkinson GH (1991) *J Phys Chem* 95:3168
- Nolker K, Siebert F (1991) In: Hester RE, Girling RB (eds) *Spectroscopy of Biological Molecules*. Royal Society of Chemistry, p 205
- Nonaka Y, Lu DS, Dwivedi A, Strommen DP, Nakamoto K (1990) *Biopolymers* 29:999
- Nonnenmacher G (1961) *Die Normalschwingungen einfacher Benzolderivate*. Dissertation, Universität Freiburg
- Novak A (1979) *Vibrational Spectroscopy in Hydrogen Bonding Systems*. In: Theophanides TM (ed) *Infrared and Raman Spectroscopy of Biological Molecules*, NATO Advanced Study Institute Series. D Reidel, Dordrecht
- Nozawa T, Noguchi T, Tasumi M (1990) *J Biochem* 108:737
- Nyquist RA, Kagel RO (1971) *Infrared Spectra of Inorganic Compounds (3800-45 cm⁻¹)*. Academic Press, New York London
- Oboodi MR, Lal BB, Young DA, Freedman TB, Nafie LA (1985) *J Am Chem Soc* 107:1547
- Oelichmann HJ (1979) Dissertation, Universität Dortmund
- Oelichmann HJ, Bougeard D, Schrader B (1981a) *J Mol Struct* 77:149
- Oelichmann HJ, Bougeard D, Schrader B (1981b) *J Mol Struct* 77:179
- Oelichmann HJ, Bougeard D, Schrader B (1982) *Angew Chem internat Edit engl* 21:639
- Oertel RP, Myhre DV (1972) *Anal Chem* 44:1589
- Oesterhelt D, Stoeckenius W (1973) *Proc Natl Acad Sci USA* 70:2853
- Ogasawara M, Funahashi K, Demura T, Hagiwara T, Iwata K (1986) *Synth Met* 14:61-69
- Ogura T, Yoshikawa S, Kitagawa T (1989) *Biochemistry* 28:8022
- Ohono K, Matsura H, McNaughton, Kroto HW (1987) *J Mol Spectrosc* 126:245
- Ohta N, Ito M (1976) *J Mol Spectrosc* 59:396
- Okamoto H, Hayashi H, Yoshihara K, Tasumi M (1991) *Chem Phys Lett* 182:96
- Okamoto H, Inaba R, Tasumi M, Yoshihara K (1993a) *Chem Phys Lett* 206:388

- Okamoto H, Inaba R, Yoshihara K, Tasumi M (1993b) *Chem Phys Lett* 202:161
- Okamoto H, Yoshihara K (1990) *J Opt Soc Am B* 7:1702
- Okamoto H, Yoshihara K (1991) *Chem Phys Lett* 177:568
- Olah GA (1973) *Angew Chem Int Ed Engl* 12:173
- Olah GA, DeMember JR, Commeyras A, Bribes JL (1971) *J Am Chem Soc* 93:459
- Olah GA, Sommer J, Namanworth E (1967) *J Am Chem Soc* 89:3576
- Olah GA, White AM, DeMember JR, Commeyras A, Lui CY (1970) *J Am Chem Soc* 92:4627
- O'Leary TT, Levin IW (1984) *Biochem Biophys Acta* 776:185
- Olinger JM, Griffiths PR (1988) *Anal Chem* 60:2427
- Opitz N, Lübbbers DW, Schrader B (1983) *Europ Patent EP 0144 713 B1*, US Patent 5 059 396
- Orduna F, Domingo C, Montero S, Murphy WF (1982) *Mol Phys* 45:65
- Ortmann L, Vogt H (1976) *Opt Commun* 16:234
- Orville-Thomas WJ (1974) *Internal Rotation in Molecules*. Wiley & Sons, London
- Osawa M, Ataka KI, Yoshii K, Nishikawa Y (1993) *Appl Spectrosc* 47:1497
- Osborne BG, Fearn T (1986) *Near Infrared Spectroscopy in Food Analysis*. Wiley, New York
- Oseroff AR, Callender RH (1974) *Biochemistry* 13:4243
- Osten DW (1988) *J Chemometrics* 2:39
- Ottensen DK, Gray HB, Jones LH, Goldblatt M (1973) *Inorg Chem* 12:1051
- Otting W (1952) *Der Raman-Effekt und seine analytische Anwendung*. Springer Verlag, Berlin Göttingen Heidelberg
- Otto A (1980) *Appl Surf Sci* 6:309
- Otto A (1983) In: *Light Scattering in Solids*, vol IV, Cardona M, Güntherodt G (eds). Springer, Berlin
- Otto A (1984) In: *Topics Appl Phys*, vol 54. Springer, Berlin, p 243
- Otto A (1987) *Infrarotspektroskopie mit diffus reflektierter Strahlung: in-situ-Messungen an schwach streuenden Proben*. VDI-Verlag, Düsseldorf
- Otto A (1988) *Ind J Pure Appl Phys* 26:141
- Otto A (1991) *J Raman Spectrosc* 22:743
- Otto A, Mrozek I, Grabhorn H, Akemann W (1992) *J Phys Condens Matt* 4:1143
- Ottolenghi M (1980) *Adv Photochem* 12:97
- Ouali M, Letellier R, Adnet F, Liquier J, Sun JS, Lavery R, Taillandier E (1993) *Biochemistry* 32:2098
- Ouazzany Y, Boquillon JP, Lavorel B (1987) *Can J Phys* 65:1588
- Ouazzany Y, Boquillon JP, Schröter HW (1988) *Mol Phys* 63:769
- Ovander LN (1960) *Opt Spektrosk* 9:302
- Ovander LN (1964) *Opt Spektrosk* 16:401
- Overend J (1975) *Rotation Vibration Spectroscopy in the Infrared*. In: Durig JR (ed) *Vibrational Spectra and Structure*. Elsevier, Amsterdam
- Owyong A (1977) *Opt Commun* 22:323
- Owyong A (1979) In: *Laser Spectroscopy IV*, Walther H, Rothe KW (eds) Springer Series Opt Sci, vol 21. Springer, Berlin, p 175
- Owyong A (1981) In: *Chemical Applications of Nonlinear Raman Spectroscopy*, Harvey AB (ed) Academic Press, New York, chapter 7
- Owyong A, Jones ED (1977) *Opt Lett* 1:152
- Owyong A, Patterson CW, MacDowell RS (1978) *Chem Phys Lett* 59:156
- Owyong A, Patterson CW, MacDowell RS (1979) *Chem Phys Lett* 61:636
- Ozaki Y, Cho R, Ikegaya S, Muraishi S, Kawauchi K (1992) *Appl Spectrosc* 46:1503
- Ozin GA (1971) *Prog Inorg Chem* 14:173
- Pacansky J, England C, Waltman RJ (1987) *J Polymer Sci: Part B: Polymer Physics* 25:901
- Paetzold P, Eleftheriadis E, Minkwitz R, Woelfel V, Gleiter R, Bischof P, Friedrich G (1988) *Chem Ber* 121:61
- Page JB (1991) In: *Light Scattering in Solids VI*, Cardona M, Güntherodt G (eds). Springer, Berlin, p 17
- Page JB, Tonks DL (1981) *J Chem Phys* 75: 5694
- Pagsberg P, Wilbrandt R, Hansen KB, Weisberg KV (1976) *Chem Phys Lett* 39:538
- Paiss I, Bunimovich D, Katzir A (1993) *Appl Opt* 32:5867

- Palfy-Muhoray P, Soileau MJ (eds) (1992) Proceedings of the 4th International Topical Meeting of the Optics of Liquid Crystals. In: Mol Cryst Liq Cryst Sci Technol, Sect A 1992(222/223). Gordon & Breach, Reading, p 276
- Palik ED (ed) (1985) Handbook of Optical Constants of Solids. Academic, Orlando
- Palik ED (ed) (1991) Handbook of Optical Constants of Solids II. Academic, Boston
- Palm K (1994) Vibrat Spectrosc 6:185
- Palmer RA (1993) Spectroscopy (Eugene, Oreg) 8:26
- Palmer RA, Manning CJ, Rzepiela JA, Widder JM, Chao JL (1989) Appl Spectrosc 43:193
- Papousek D, Aliev MR (1982) Molecular Vibrational Rotational Spectra. Elsevier Scientific Publ Comp, Amsterdam
- Pardon JF, Worcester DL, Wooley JC, Cotter RI, Lilley DHJ, Richards BM (1977) Nucleic Acids Res 4:3199
- Park JM (1977) NASA Contractor Report 2925. National Techn. Information Service, Springfield, Virginia
- Parker FS (1971) Applications of Infrared Spectroscopy in Biochemistry, Biology and Medicine. A Hilger, London
- Parker FS (1973) In: Ciaccio EL (ed) Water and Water Pollution Handbook vol 4. M Dekker, New York
- Parry DB, Harris JM (1990) Chem Modif Surf 3:127
- Patel CKN (1978) Science 202:157
- Paterlini MG, Freedman TB, Nafie LA (1986) J Am Chem Soc 108:1389
- Pattacini SC (1982) Perkin Elmer INFRARED Bulletin 93
- Péalat M, Taran JPE, Bacal M, Hillion F (1985) J Chem Phys 82:4943
- Peitscher G (1979) Chemie Anlagen + Verfahren 7:86
- Peitscher G, Holtrup G (1975) Angew Makromol Chem 47:111 (1975)
- Pelletier MJ, Reeder RC (1991) Appl Spectrosc 45:765
- Pepperhoff W, Graß G (1955) Archiv für das Eisenhüttenwesen 26:1
- Perkampus HH (1992) UV-VIS Atlas of Organic Compounds, VCH Publishers, Weinheim
- Perkampus HH, Schönberger E (1976) Chem Phys Lett 44:348
- Perrouault L, Asseline U, Rivalle C, Thuong NT, Bisagni E, Giovannangeli C, Le Doan T, Helene C (1990) Nature 344:358
- Perry JA (1970) Appl Spectrosc Rev 3:229
- Perry RO (1969) J Chem Soc D 886
- Pershan PS (1979) Raman studies of orientational order in liquid crystals. In: Luckhurst GR, Gray GW (eds) The molecular physics of liquid crystals. Academic, London, p 385
- Person WB, Newton JH (1974) J Chem Phys 61:1040
- Person WB, Overend J (1977) J Chem Phys 66:1442
- Pertsin AJ, Kitaigorodsky AI (1987) The atom-atom potential method. Springer, Berlin
- Perutz RN (1985) Chem Rev 85:97
- Perutz RN, Turner JJ (1973) J Chem Soc Faraday Trans II 69:452
- Perzl F, Moser H (1968) J Mol Spectrosc 26:237
- Pesek JJ, Williamsen EJ (1992) Trends Anal Chem 11:259
- Petcavich RJ, Painter PC, Coleman MM (1978) Polymer 19:1249
- Peticolas WL, Tsuboi M (1979) The Raman spectroscopy of nucleic acids. In: Theophanides TM (ed) Infrared and Raman spectroscopy of biological molecules. Nato advanced study institute series, Series C, vol 43. D Reidel Publishing Company, Dordrecht
- Petrou A, McCombe BD (1991) Magnetospectroscopy of confined semiconductor systems. In: Landwehr G, Rashba EI (ed) Landau Level Spectroscopy. vol 27/1, North Holland Amsterdam Oxford New York Tokyo
- Pettenkofer C, Mrozek I, Bornemann T, Otto A (1987) Surf Sci 188:519
- Pettinger B, Wening U, Kolb DM (1978) Ber Bunsen Phys Chem 82:1326
- Pezolet M, Duchesneau L, Bougis P, Faucon JF, Dufourcq J (1982) Biochim Biophys Acta 704:515
- Pfeiffer M, Lau A, Werncke W (1990) J Raman Spectrosc 21:835
- Pflung HD, Jaeschke-Boyer H, Sattler EL (1979) Nachr Chem Tech Lab 27:548
- Pichler T, Winkler R, Kuzmany H (1994) Phys Rev B, in press
- Pickett HM, Strauss HL (1977) Anal Chem 44:265
- Picquart M, Nicolas E, Lavialle E (1989) Eur Biophys J 17:143
- Pidgeon CR, Smith SD (1977) Infrared Physics 17:515

- Pilet J, Brahms J (1973) *Biopolymers* 12:387
- Pilet J, Leng M (1982) *Proc Nat Acad Sci USA* 79:26
- Pilz W, Kriegsmann H (1987) *Z Phys Chem (Leipzig)* 268:215
- Pimentel GC (1977) Techniques for Studying Highly Reactive and Unstable Species Chap 8. In: Barnes AJ, Orville-Thomas WJ (eds) *Vibrational Spectroscopy - Modern Trends*. Elsevier, Amsterdam New York p 79
- Pimentel GC, Charles SW (1963) *Pure Appl Chem* 7:111
- Pimentel GC, Dows DA, Whittle E (1954) *J Chem Phys* 22:1943
- Pink DA, Green TJ, Chapman D (1980) *Biochemistry* 19:349
- Piva AC, Pascal JL, Potier ACR (1971) *R Séances Acad Sci Ser C* 272:1495
- Placzek G (1934) In: *Handbuch der Radiologie*, vol 6, Akadem Verlagsges Leipzig, part 2, p 209
- Placzek G (1934) Rayleigh-Streuung und Raman-Effekt. In: Marx E (ed), *Handbuch der Radiologie*, Band VI, Teil II. Akademische Verlagsgesellschaft, Leipzig, p 205
- Placzek G, Teller E (1933) *Z Phys* 81:209
- Planck M (1900) *Verh D Phys Ges* 2:237
- Plate NA (ed) (1993) *Liquid-crystal polymers*. Plenum, New York
- Pliva J, Esherick P, Owyong A (1987) *J Mol Spectrosc* 125:393
- Pliva J, Johns JWC (1983) *Can J Phys* 61:269
- Pliva J, Johns JWC (1984) *J Mol Spectrosc* 107:318
- Pliva J, Johns JWC, Goodman L (1990) *J Mol Spectrosc* 140:240
- Pliva J, Pine AS (1982) *J Mol Spectrosc* 93:209
- Pliva J, Valentín A, Chazelas J, Henry L (1989) *J Mol Spectrosc* 134:220
- Pockrand I (1984) In: *Springer Tracts in Modern Physics*, vol 104. Springer, Berlin, p 1
- Pohl FM, Ranade A, Stockburger M (1973) *Biochim Biophys Acta* 335:85
- Pohle W, Zhurkin VB, Fritzsche H (1984) *Biopolymers* 23:2603
- Polavarapu PL (1983) *Mol Phys* 49:645
- Polavarapu PL (1985) Fourier Transform Infrared Vibrational Circular Dichroism. In: Ferraro JR, Basile LJ (eds) *Fourier Transform Infrared Spectroscopy*, vol 4, p 68
- Polavarapu PL (1988a) In: Clark RJH, Long DA (ed) *Proceedings of the Eleventh International Conference on Raman Spectroscopy*, p 949
- Polavarapu PL (1988b) *Chem Phys Lett* 148:21
- Polavarapu PL (1990) *J Phys Chem* 94:8106
- Polavarapu PL, Black TM, Barron LD, Hecht L (1993) *J Am Chem Soc* 115:7736
- Polivanov YN, Sayakhov RS (1978) *Sov Phys Solid State* 20:1564
- Polivanov YN, Sayakhov RS (1979) *JETP Lett* 30:580
- Polivanov YN, Sayakhov RS (1981) *Phys Stat Solid b103:89*
- Polland HJ, Elsaesser T, Seilmeyer A, Kaiser W, Kussler M, Marx MJ, Sens B, Drexhage KH (1983) *Appl Phys B32:53*
- Porcher JP, Günthard HH (1970) *J Phys E Sci Instr* 3:261
- Porro TJ (1971) *J Assoc Off Anal Chem* 54:1040
- Porter G, Norman I (1954) *Nature* 174:508
- Porter MD (1988) *Anal Chem* 60:1143A
- Porter MD, Karweik D, Kuwana T, Theis W, Norris GB, Thiernan TO (1984) *Appl Spectrosc* 38:11
- Porterfield DR, Campion A (1988) *J Am Chem Soc* 110:408
- Porto SPS, Giordmaine JA, Damen TC (1966) *Phys Rev* 147:608
- Porto SPS, Krishnan RS (1967) *J Chem Phys* 47:1009
- Pothier NJ, Forcé RK (1990) *Anal Chem* 62:678
- Pothier NJ, Forcé RK (1992) *Appl Spectrosc* 46:147
- Poulet H, Mathieu JP (1970) *Spectres de Vibration et Symétrie des Cristaux*. Gordon & Breach, Paris
- Poulter TC (1932) *Phys Rev* 40:860
- Poussigue G, Pascaud E, Champion JP, Pierre G (1982) *J Mol Spectrosc* 93:351
- Powell HM, Jones JH, Williams WD, McGuire RL, (1978) *ISA Transactions* 17:69
- Powell JW, Edwards GS, Genzel L, Kremer F, Wittlin A, Kubasek W, Peticolas WL (1987) *Phys Rev A* 35A:3929
- Prandtl L (1965) *Führer durch die Strömungslehre*, 6th edn. Vieweg, Braunschweig
- Prasad PN, Swiatkiewicz J, Eisenhardt G (1982) *Appl Spectrosc Rev* 18:59

- Preier H (1977) Ber Phys Techn Bundesanst Braunschweig, PTB-Me-13, 45
- Prescott B, Steinmetz W, Thomas jr GJ (1984) Biopolymers 23:235
- Prior Y (1984) IEEE J Quantum Electron QE-20:37
- Prockaska FT, Andrees L (1978) J Chem Phys 68:5568
- Pubanz GA, Maroncelli M, Nibler JW (1985) Chem Phys Lett 120:313
- Pugh LA, Rao KN (1976) Intensities from Infrared Spectra. In: Rao KN (ed) Molecular Spectroscopy, Modern Research, vol 2. Academic Press, New York
- Pulay P (1969) Mol Phys 17:197
- Pulay P, Fogarasi G, Boggs JE (1981) J Chem Phys 74:3999
- Pulay P, Fogarasi G, Pang F, Boggs J (1979) J Am Chem Soc 110:2550
- Pulham CR, Downs AJ, Goode MJ, Rankin DWH, Robertson HE (1991) J Am Chem Soc 113:5149
- Puppels GJ, de Mul FFM, Otto C, Greve J, Robert-Nicoud M, Arndt-Jovin DJ, Jovin TM (1990) Nature 347:301
- Puppels GJ, Olminkhof JHF, Segers-Nolten GMJ, Otto C, de Mul FFM, Greve J (1991) Exp Cell Res 195:361
- Purucker HG, Tunkin V, Laubereau A (1993) J Raman Spectrosc 24:453
- Rabold A, Eppinger S, Gerry MCL, Nandy SK, Schröter HW (1990) Raman Spectra of Some Vapors: Benzene, t-Glyoxal, Methanol and Osmium Tetroxide. In: Durig JR, Sullivan JF (eds). Proceedings of the 12th International Conference on Raman Spectroscopy. Wiley, Chichester, p 170
- Rabolt JF, Clarke TC, Street GB (1979) J Chem Phys 71(11):4614
- Rabolt JF, Hofer D, Miller RD, Fickes GN (1986) Macromolecular 19:611
- Rabolt JF, Swalen OJ (1988) In: Spectroscopy of Surfaces, Clark RJH, Hester RE (eds). Wiley, Chichester, p 1
- Ragunathan N, Lee NS, Freedman TB, Nafie LA, Tripp C, Buijs H (1990) Appl Spectrosc 44:5
- Rahn LA, Greenhalgh DA (1986) J Mol Spectrosc 119:11
- Rahn LA, Rosasco GJ (1990) Phys Rev A41:3698
- Raman CV (1928) Indian J Phys 2:387
- Raman CV (1928) Nature (London) 121:619
- Raman CV (1930) The Molecular Scattering of Light, Nobel Lecture delivered at Stockholm, Dec 11th. (1953) Proceedings of the Indian Academy of Sciences 37:343
- Raman CV, Krishnan KS (1928) Nature (London) 121:501
- Raman CV, Krishnan KS (1928) Nature 121:711
- Raman CV, Nedungadi TMK (1939) Nature 143:679
- Raman CV, Nedungadi TMK (1940) Nature 145:147
- Ramdas AK, Rodriguez S (1981) Rep Prog Phys 44:1297-1387
- Ramdas LA (1928) Ind J Phys 3:131
- Ramsay DA (1952) J Am Chem Soc 74:72
- Rann CS (1972) Anal Chem 44:1669
- Rao CNR, Rao KJ (1978) Phase transitions in solids. McGraw Hill, New York
- Rasetti F (1929) Nature (London) 123:205, 757
- Rasetti F (1929) Phys Rev 34:367
- Rasetti F (1929) Proc Natl Acad Sci USA 15:234, 515
- Rasetti F (1930) Z Phys 61:598
- Rasetti F (1930) Z Phys 66:646
- Rasmussen GT et al (1978) Anal Chim Acta 103:2-3
- Rauk A, Dutler R, Young D (1990) Can J Chem 68:258
- Reddy SP, Devi VM, Baldacci A, Ivancic W, Rao KN (1979) J Mol Spectrosc 74:217
- Reedy GT, Bourne S, Cunningham PT (1979) Anal Chem 51:1535
- Reedy GT, Ettinger DG, Schneider JF, Bourne S (1985) Anal Chem 57:1602
- Reinecke D, Jansen A, Fister F, Schernau U (1988) Anal Chem 60:1221
- Reins J, Korte EH, Röseler A (1993) Thin Solid Films 234:486
- Reins J, Korte EH, Röseler A (1994) to be published
- Reitz AW (1940) Z physik Chem B 46:181
- Renschler DL, Hunt JL, McCubin TK, Polo SR (1969) J Mol Spectrosc 31:173
- Rice MJ, Pietronero L, Bruesch P (1977) Solid State Commun 21:757-760
- Rich NH, Lepard DW (1971) J Mol Spectrosc 38:549
- Rich NH, Welsh HL (1971) J Opt Soc Amer 61:977

- Richards PL, Tinkam M (1960) *Phys Rev* 119:575
- Richards PL, Tobin RG (1987) Infrared Spectroscopy of Adsorbates on Metals: Direct Absorption and Emission. In: Yates JT Jr, Madey TE (eds) *Vibrational Spectroscopy of Molecules on Surfaces*. Plenum New York, p 417
- Richter W (1976) In: *Solid State Physics*, Höhler G (ed), Springer Tracts in Modern Physics, vol 78. Springer, Berlin, p 121
- Richter WJ, Heggemeier H, Krabbe HJ, Korte EH, Schrader B (1980) *Ber Bunsenges Phys Chem* 84:200
- Richter WJ, Korte EH (1978) *Ber Bunsenges Phys Chem* 82:812
- Ridoux JP, Liquier J, Taillandier E (1987) *Nucleic Acids Res* 15:5813
- Ridoux JP, Liquier J, Taillandier E (1988) *Biochemistry* 27:3874
- Rimai L, Hyde ME, Gill G (1973) *J Am Chem Soc* 95:4493
- Robert B (1989) *Biochim Biophys Acta* 1017:99
- Roberts NK (1992) *Springer Ser Surf Sci* 23:187
- Robertson JM, Woodward I (1938) *Proc Roy Soc A* 164:436
- Rocard Y (1928) *Compt Rend Acad Sc (Paris)* 186:1107
- Rodgers KR, Su C, Subramaniam S, Spiro TG (1992) *(J Am Chem Soc* 114:3697)
- Rogers CE, Stannett V, Szwarc M (1959) *J Phys Chem* 63:1406
- Rohde S (1989) Diplomthesis, Göttingen
- Romanko J, Feldman T, Welsh HL (1955) *Can J Phys* 33:588
- Rosasco GJ, Blaha JJ (1980) *Appl Spectrosc* 34:140
- Röseler A (1990) *Infrared Spectroscopic Ellipsometry*. Akademie-Verlag, Berlin
- Röseler A (1990) *Infrared Spectroscopic Polarimetry*. Akademie Verlag, Berlin
- Röseler A (1992) *J Opt Soc Amer A* 9:1124
- Röseler A, Korte EH, Reins J (1993) *Vibrat Spectrosc* 5:275
- Röseler A, Molgedey W (1984) *Infrared Phys* 24:1
- Rosencaig A, Gersho A (1975) *Science* 190:556
- Rosencaig A, Gersho A (1976) *J Appl Phys* 47:64
- Rosenthal JE, Murphy GM (1936) *Rev Mod Phys* 8:317
- Rosker MJ, Wise FW, Tang LC (1986) *Phys Rev Lett* 57:321
- Rosseinsky MJ, Ramirez AP, Glarum SH, Murphy DW, Haddon RC, Hebard AF, Palstra TTM, Kortan AR, Zahurak SM, Makhija AV (1991) *Phys Rev Lett* 66:2830
- Rotger M, Lavorel B, Chaux R (1992) *J Raman Spectrosc* 23:303
- Roth E, Hope GA, Schweinsberg DP, Kiefer W, Fredericks PM (1993) *Appl Spectrosc* 47:1794
- Roth E, Kiefer W (1994) *Appl Spectrosc* 48: October issue
- Rothman LS, Gamache RR, Goldman A, Brown LR, Toth RA, Pickett HM, Poynter RL, Flaud JM, Camy-Peyret C, Barbe A, Husson N, Rinsland CP, Smith MAH (1987) *Appl Opt* 26:4058
- Rothman LS, Young LDG (1981) *J Quant Spectrosc Radiat Transfer* 25:505
- Rothschild KJ, Clark NA, Rosen KM, Sanches R, Hsiao TL (1980) *Biochem Biophys Res Comm* 92:1266
- Rothschild KJ, de Grip WJ, Sanches R (1980) *Biochim Biophys Acta* 596:338
- Rothschild KJ, Marrero M (1982) *Proc Natl Acad Sci USA* 79:4045
- Rouillé G, Millot G, Saint-Loup R, Berger H (1992) *J Mol Spectrosc* 154:372
- Rouse GB (1979) *J Polym Sci Polym Phys Ed* 17:81
- Rousseau DL, Bauman RP, Porto SPS (1981) *J Raman Spectrosc* 10:253
- Rousseau DL, Friedman JM, Williams PF (1979) In: *Raman Spectroscopy of Gases and Liquids*, Weber A (ed) Topics in Current Physics, vol 11. Springer, Berlin, p 203
- Rousseau DL, Williams PF (1976) *J Chem Phys* 64: 3519
- Rubens H, Aschkinass E (1898) *Astrophys Jour* 8:181
- Ruch E (1977) *Angew Chem* 89:67
- Ruch E, Schönhofer A (1968) *Theor Chim Acta* 10:91
- Ruch E, Schönhofer A (1970) *Theor Chim Acta* 19:225
- Rupprecht A (1989) *Acta Chem Scand* 43:207
- Rutgers GAW, de Vos JC (1954) *Physica* XX:715
- Rutgers GAW, de Vos JC (1973) Absolute Spectroradiometric Measurements, National Bureau of Standards Special Publication, Gaitersburg, 378:53
- Rutherford NM, Olmstead MM, Balch AL (1984) *Inorg Chem* 23:2833

- Sadeghi-Jorabchi H, Wilson RH, Belton PS, Edwards-Webb JD, Coxon TD (1991) Spectrochim Acta 47A:1449
- Saenger W (1988) Cantor CR (ed) Principles of Nucleic Acid Structure. Springer Verlag Pub Co, New York
- Saeva FD (1973) Mol Cryst Liq Cryst 23:171
- Saint-Loup R, Lavorel B, Millot G, Wenger C, Berger H (1990) J Raman Spectrosc 21:77
- Salares VR et al (1979) Biochim Biophys Acta 576:176
- Salares VR, Young NM, Carey PR, Bernstein HJ (1976) In: Schmid ED, Brandmüller J, Kiefer W, Schrader B, Schröter W (eds) Proceedings of the Vth International Conference on Raman Spectroscopy. HF Schulz Verlag, Freiburg, p 210
- Salzer R, Steinberg KH, Klaeboe P, Hoffmann A, Schrader B (1991) Zeolites 11:694
- Santos J, Cancio P, Domenech JL, Rodriguez J, Bermejo D (1992) Laser Chem 12:53
- Santos J, Domenech JL, Cancio P, Bermejo D (1993) Poster D42 at 13th Colloquium on High Resolution Molecular Spectroscopy, Riccione, Italy
- Saricifci NS, Kuzmany H, Neugebauer H, Neckel A (1990) J Chem Phys 92:4530
- Sato M, Tanaka S, Kaeriyama K (1987) Synth Met 18:228
- Saupe A, Maier W (1961) Z Naturforsch 16A:816
- Savage CM, Maker PD (1971) Appl Opt 10:965
- Savitzky A, Golay MJE (1964) Anal Chem 36:1627; (1972) Correction Anal Chem 44:1906
- Savoie R, Jutier JJ, Alex S, Nadeau P, Lewis PN (1985) Biophys J 47:451
- Sawatzki J, Fischer R, Scheer H, Siebert F (1990) Proc Natl Acad Sci USA 87:5903
- Scanlon K, Lanx L, Overend J (1979) Appl Spectrosc 33:346
- Schaarschmidt K (1977) Z Chem 17:299
- Schachtschneider JH (1964) Report 231/64 Shell Development Co, West Hollow Research Center POB 1380 Houston Texas 77001
- Schachtschneider JH (1965) Report 57/65 Shell Development Co, West Hollow Research Center POB 1380 Houston Texas 77001
- Schachtschneider JH, Snyder RG (1963) Spectrochim Acta 19:117
- Schachtschneider JH, Snyder RG (1965) Spectrochim Acta 21:169
- Schäcke G, Schaller KH, Essing HG, Valentin H, Wittgens H, Pfäffl A (1972) Arbeitsmedizin Sozialmedizin Arbeitshygiene 7:292
- Schadt M (1993a) Ber Bunsenges Phys Chem 97:1213
- Schadt M (1993b) Liq Cryst 14:73
- Schaefer C, Matossi F (1930) Der Ramanenffekt. Borntraeger, Berlin
- Schaefer-Siebert D, Budrowski C, Kuzmany H, Roth S (1987) Springer Series Solid State Sciences 76:38. In: Kuzmany H, Mehring M, Roth S (eds) Electronic Properties of Polymers. Springer, Berlin Heidelberg New York London
- Schallert B (1978) Diplomarbeit, Dortmund
- Schallert B (1982) Dissertation, Universität Essen
- Schantz MM, Martire DE (1987) J Chromatogr 391:35
- Schaufele RF, Shimanouchi T (1967) J Chem Phys 47:3605
- Scheele KW (1781) Traite de l'air et du feu, Paris
- Schellman JA (1973) J Chem Phys 58:2882
- Schellman JA, Jensen HP (1987) Chem Rev 87:1359
- Scherer JR, Snyder RG (1980) J Chem Phys 72:5798
- Schmid ED, Brandmüller J, Kiefer W, Schrader B, Schröter HW (1976) (eds) Proceedings of the Vth International Conference on Raman Spectroscopy, HF Schulz Verlag, Freiburg
- Schmid ED, Gramlich V (1979) Ramanspektroskopische Untersuchungen an Nucleinsäuren. In: Aussenegg F (ed). Laser Spektroskopie, Neue Entwicklungen und Anwendungen. Springer, Berlin
- Schmid WJ, Schröter HW (1977) Chem Phys Lett 45:502
- Schmid WJ, Schröter HW (1981) J Raman Spectrosc 10:212
- Schneider JR (1974) Dissertation, Universität Dortmund
- Schneider JR, Schrader B (1975) J Mol Struct 29:1026
- Schneider JR, Schrader B, Bleckmann P (1975) Ber Bunsenges Phys Chem 79:1026
- Schnoeckel H (1975) J Mol Struct 29:123
- Schnoeckel H (1976) Z Naturforsch 31b:1291
- Schnoeckel H (1980) Angew Chem Int Ed Engl 19:323

- Schnoeckel H (1980a) *J Mol Struct* 65:115
Schnoeckel H (1980b) *Z Anorg Allg Chem* 460:37
Schnoeckel H (1984) *Z Anorg Allg Chem* 510:72
Schnoeckel H, Goedecke HJ, Elsper R (1982) *Z Anorg Allg Chem* 494:78
Schnoeckel H, Koeppe R (1989) *J Am Chem Soc* 111:4583
Schnoeckel H, Mehner T, Plitt HS, Schunck S (1989) *J Am Chem Soc* 111:4578
Schoen PE, Priest RG, Sheridan JP, Schnur JM (1979) *J Chem Phys* 71:317
Schoenflies AM (1891) Kristallsysteme und Kristallstruktur. BG Teubner, Leipzig
Schoenflies AM (1923) Theorie der Kristallstruktur. Borntraeger, Berlin
Scholl F, Fuchs H (1968) *Bosch Techn Berichte* 2:235
Schönemann M, Eckermann T, Kunath D, Kriegsmann H (1972) *Exp Tech Phys* 20:43
Schönhofen A, Junge M, Memmer R, Kuball HG (1990) *Chem Phys* 146:211
Schönhofen A, Kuball HG, Puebla C (1983) *Chem Phys* 76:453
Schrader B (1960) Dissertation, TU Berlin
Schrader B (1967) *Chemie Ing Techn* 39:1008
Schrader B (1968) Das Schwingungsspektrum von Molekülkristallen, Habilitationsschrift, Universität Münster
Schrader B (1973) *Angew Chem* 85:925, Int Ed Engl 12:884
Schrader B (1978) Raman and IR Spectroscopy of Molecular Crystals. In: Barrow RF, Long DA, Millen DJ (eds) *Molecular Spectroscopy, A Specialist Periodical Report*, vol 5. The Chemical Society, London, p 235
Schrader B (1980) Infrarot- und Ramanspektrometrie: In: Ullmanns Encyklopädie der Technischen Chemie, Verlag Chemie, Weinheim, p 303
Schrader B (1987) United States Patent 4714345, United Kingdom Patent GB 2 162961, German Patent DE 3 424108 C 2
Schrader B (1988) *Croat Chem Acta* 61:589
Schrader B (1989) *Raman/Infrared Atlas of Organic Compounds*, 2nd edn. VCH Verlagsellschaft, Weinheim
Schrader B (1990) *Fresenius Z Anal Chem* 337:824
Schrader B (1990) Possibilities and Limitations of FT-Raman Spectroscopy in Fourier Transform IR Spectroscopy (FTIR), chapt 4. In: Ferraro JR, Krishnan K (eds). Academic Press, New York London
Schrader B (1994) Sampling techniques, chapt II. In: Chase DB, Rabolt JF (eds) *Fourier Transform Raman Spectroscopy*. Academic Press, Boston
Schrader B, Ansmann A (1975) *Angew Chem* 87:345
Schrader B, Baranović G, Keller S, Sawatzki J (1994) *Fresenius J Anal Chem* 349:4
Schrader B, Bergmann G (1967) *Fresenius Z Anal Chem* 225:230
Schrader B, Bougeard D, Niggemann W (1980) Determination of the Structures of Organic Molecules by Computer-Evaluation and Simulation of IR and Raman Spectra. In: Computational Methods in Chemistry, IBM Research Symposia-Series. Plenum Press, New York
Schrader B, Heinrich P, Wyzgol R (1990a) US patent 4,941,742; Franz patent 2 625 318; UK patent 2 214 291
Schrader B, Hoffmann A, Keller S (1991) *Spectrochim Acta* 47A:1135
Schrader B, Hoffmann A, Podschadlowski R, Simon A (1989) Proceedings of the 7th International Conference on Fourier Transform Spectroscopy, SPIE vol 1145, Bellingham, p 372
Schrader B, Hoffmann A, Simon A, Podschadlowski R, Tischer M (1990b) *J Mol Struct* 217:207
Schrader B, Hoffmann A, Simon A, Sawatzki J (1991) *Vibrat Spectrosc* 1:239
Schrader B, Hoffmann A, Tischer M., Podschadlowski R, Simon A (1989) Proceedings of the 7th International Conference on Fourier Transform Spectroscopy, SPIE vol 1145, Bellingham, p 190
Schrader B, Keller S (1992) SPIE 1575:30
Schrader B, Keller S (1993) Infrared and Raman Spectroscopy, Encyclopaedia of Food Science, Food Technology and Nutrition. Academic Press, London
Schrader B, Keller S, Löchte T, Fendel S, Moore DS, Simon A, Sawatzki J (1995) *J Mol Struct*, in print
Schrader B, Korte EH (1972) *Angew Chem* 84:218, Int Ed Engl 11:226
Schrader B, Meier W (1966) *Z Naturforsch* 21a:480
Schrader B, Meier W (1972) *Fresenius Z Anal Chem* 260:248

- Schrader B, Meier W (1975) Fresenius Z Anal Chem 275:177
- Schrader B, Meier W, Gottlieb K, Agatha H, Barentzen H, Bleckmann P (1971) Ber Bunsenges Phys Chem 75:1263
- Schrader B, Meier W, Steigner E, Zöhrer F (1971) Fresenius Z Anal Chem 254:257
- Schrader B, Nerdel F, Kresze G (1959) Z Anal Chem 170:43
- Schrader B, Nerdel F, Kresze G (1960) Naturwiss 47:198
- Schrader B, Niggemann W, Belz HH, Schallert B (1981) Z Chem (Leipzig) 21:249
- Schrader B, Simon A (1988) Microchim Acta 2:227
- Schrader B, Spiekermann M, Hecht L, Bougeard D (1984) J Mol Struct 113:49
- Schrader B, Steigner E (1970) Liebigs Ann Chem 735:6
- Schrader B, Steigner E (1971) Fresenius Z Anal Chem 254:177
- Schrader B, Steigner E (1973) chapt 9, Raman Spectroscopy of Steroids. In: Hoffman E (ed). Modern Methods of Steroid Analysis. Academic Press, New York
- Schrader B, Tischer M, Podschadlowski R, Schlemmer H (1988) Eleventh International Conference on Raman Spectroscopy, John Wiley & Sons, London, p 957
- Schröder G (1987) Technische Optik. Vogel Buchverlag, Würzburg
- Schrödinger E (1926) Ann Phys 81:109
- Schrötter HW (1982) In: Kiefer W, Long DA (eds) Non-linear Raman Spectroscopy and its Chemical Applications. D Reidel, Dordrecht, p 143
- Schrötter HW (1982) Linear Raman Spectroscopy: A State of the Art Report. In: Kiefer W, Long DA (eds) Non-Linear Raman Spectroscopy and its Chemical Applications, Reidel, Dordrecht, p 3
- Schrötter HW, Berger H, Boquillon JP, Lavorel B, Millot G (1988) High-Resolution Nonlinear Raman Spectroscopy of Rovibrational Bands in Gases. In: Salzer R, Kriegsmann H, Werner G (eds) Progress in Molecular Spectroscopy, Teubner Texte zur Physik, Bd 20. Teubner, Leipzig, p 102
- Schrötter HW, Berger H, Boquillon JP, Lavorel B, Millot G (1990) J Raman Spectrosc 21:781
- Schrötter HW, Bernstein HJ (1961) J Mol Spectrosc 7:464
- Schrötter HW, Bernstein HJ (1964) J Mol Spectrosc 12:1
- Schrötter HW, Boquillon JP (1989) In: Recent Trends in Raman Spectroscopy, Banerjee SB, Jha SS (eds) World Scientific, Singapore, p 113
- Schrötter HW, Boquillon JP (1989) In: Vibrational Spectra and Structure, vol 17B, Bist HD, Durig JR, Sullivan JF (eds) Elsevier, Amsterdam, p 1
- Schrötter HW, Frunder H, Berger H, Boquillon JP, Lavorel B, Millot G (1988) High Resolution CARS and Inverse Raman Spectroscopy. In: Clark RJH, Hester RE (eds) Advances in Non-linear Spectroscopy, vol 15, Wiley, Chichester, p 97
- Schrötter HW, Klöckner HW (1979) In: Weber A (ed) Topics in Current Physics, vol 11, Springer Verlag, Berlin Heidelberg New York
- Schrötter HW, Klöckner HW (1979) Raman Scattering Cross Sections in Gases and Liquids, Chap 4. In: Weber A (ed) Raman Spectroscopy of Gases and Liquids, Topics in Current Physics. Springer, Berlin
- Schrumpt G, Martin S (1982) J Mol Struct 81:155
- Schubert M (1958) Exp Techn Physik 6:203
- Schuegerl B, Kuzmany H (1981) J Chem Phys 74:953
- Schulte A, Lenk TJ, Hallmark VM, Rabolt JF (1991) Appl Spectrosc 45:325
- Schulz KR (1974) Thesis, Karlsruhe
- Schumann K, Perkampus HH (1976) Spectrochim Acta 32A:1651
- Schweitzer D, Gogu DE, Hennig I, Klutz T, Keller HJ (1987) Ber Bunsenges Phys Chem 91: 890
- Sears WM, Hunt JL, Stevens JR (1981) J Chem Phys 75:1599
- Seddon JM (1990) Biochim Biophys Acta 1031:1
- Seder TA, Church SP, Oudekirk AJ, Weitz E (1985) J Am Chem Soc 107:1432
- Seebeck TJ (1823) Pogg Ann d Physik 6:1
- Segal GA, Klein ML (1967) J Chem Phys 47:4236
- Seiber HJ (1983) Siemens Energietechnik 5:8
- Seki HJ (1986) J Electron Spectrosc Relat Phenom 39:289
- Sellers HL, Sims LB, Schaefer L, Lewis DE (1977) QCPE 11:339
- Seppelt K (1976) Angew Chem Int Ed Engl 15:377, 778
- Seppelt K, Oberhammer H (1985) Inorg Chem 24:1227

- Séquaris JML, Koglin E (1987) *Anal Chem* 59:527
- Setchell RE (1977) *Prog Astronaut Aeronaut* 1977:499
- Seth-Paul WA (1969) *J Mol Struct* 3:403
- Seydel U, Brandenburg K, Koch MHJ, Rietschel ET (1989) *Eur J Biochem* 186:325
- Shafer KH, Lucas SV, Jacobsen RJ (1979) *J Chromatogr Sci* 17:464
- Shannon CE (1948) *The Bell System Techn J* 27 379 623
- Shelnutt JA, Rousseau DL, Friedman JM, Simon SR (1979) *Proc Nat Acad Sci USA* 76:4409
- Sherman WF, Stadtmuller AA (1987) *Experimental Techniques in High Pressure Research*. John Wiley, Chichester
- Sherwood PMA (1972) *Vibrational Spectroscopy of Solids*. Cambridge University Press, Cambridge
- Shie M, Dobrov EN, Tikhonenko TI (1978) *Biochem Biophys Res Comm* 81:907
- Shimanouchi T (1957) *J Chem Phys* 26:594
- Shimanouchi T (1968) *Computer Programs for Normal Coordinate Treatment of Polyatomic Molecules*. The University of Tokyo, Tokyo
- Shimanouchi T (1970) In: Eyring H, Henderson D, Jost W (eds) *Physical Chemistry. An Advanced Treatise*, chapt 6, vol 4, Molecular Properties. Academic Press, New York London, p 233
- Shimanouchi T (1970) *Physical Chemistry. An Advanced Treatise*. In: Eyring H, Henderson D (eds), chapt 6, vol IV. Academic Press, New York
- Shimanouchi T, Matsuura H, Ogawa Y, Harada I (1978) *J Phys Chem Ref Data* 7:1323
- Shimanouchi T, Tsuboi M, Miyazawa T (1961) *J Chem Phys* 35:1597
- Shirakawa H, Ikeda S (1971) *Polymer Journal* 2:231-244
- Shirley JA, Hall RJ, Eckbreth AC (1980) *Opt Lett* 5:380
- Shiro Y (1972) *Bull Chem Soc Japan* 44:2371
- Shorygin PP (1978) *Russ Chem Rev* 47:907
- Shorygin PP (1978) *Usp Khim* 47:1997
- Shurcliff WA (1962) *Polarized Light*. Harvard University Press, Cambridge MA
- Siebert H (1953) *Z Anorg Allg Chem* 273:170
- Siebert H (1966) *Anwendungen der Schwingungsspektroskopie in der Anorganischen Chemie*. Springer, Berlin
- Siebrand W, Zgierski MZ (1979) In: *Excited States*, vol 4, Lim EC (ed). Academic, New York, p 1
- Siesler HW (1991) *Makromol Chem Macromol Symp* 52:113
- Siesler HW, Holland-Moritz R (1980) *Infrared and Raman Spectroscopy of Polymers*. Marcel Dekker, New York
- Siiiman O, Lepp A, Kerker M (1983) *Chem Phys Lett* 100:163
- Sikka SS, Kausch HH (1979) *Coll Polym Sci* 257:1060
- Silverstein RM, Bassler CG, Morrill TC (1974) *Spectrometric Identification of Organic Compounds*. John Wiley & Sons, New York
- Simandiras ED, Handy NC, Amos RD (1988) *J Phys Chem* 92:1739
- Siminovitch DJ, Wong PTT, Mantsch HH (1987) *Biochim Biophys Acta* 910:163
- Simon A, Sawatzki J (1991) *FT Raman Microscope*. Bruker Application Note, Karlsruhe
- Singh S, Luck WAP (1981) *J Mol Struct* 74:49, 65
- Skotheim TA (1986) *Handbook of conducting polymers*. Marcel Dekker, New York Basel
- Slivnic J, Smalc A, Lutar K, Zemva B, Frlec B (1975) *J Fluorine Chem* 5:273
- Sloane HJ, Obranski RJ (1977) *Appl Spectrosc* 31:506
- Smekal A (1923) *Naturwiss* 11:873
- Smith AL (1979) *Applied Infrared Spectroscopy*. John Wiley & Sons, New York
- Smith AL (1986) *Trace Analysis by Infrared Spectroscopy*. In: Christian GD, Callig JB (eds) *Trace Analysis*. John Wiley & Sons, New York
- Smith DY (1985) *Dispersion Theory, Sum Rules, and Their Application to the Analysis of Optical Data*. In: Palik ED (ed) *Handbook of Optical Constants of Solids*. Academic, Orlando. p 35
- Smith JE, Sedgwick TO (1975) *Lett Heat Mass Transf* 2:329
- Smith WJ (1965) In: *Handbook of Military Infrared Technology*. US Government Printing Office, Washington DC, p 434
- Smulevitch G, Mauro JM, Fishel LA, English AM, Kraut J, Spiro TG (1988a) *Biochemistry* 27:5477

- Smulevitch G, Mauro JM, Fishel LA, English AM, Kraut J, Spiro TG (1988b) Biochemistry 27:5486
- Smulevitch G, Miller MA, Gosztola D, Spiro TG (1989) Biochemistry 28:9905
- Smulevitch G, Wang Y, Edwards SL, Poulos TL, English AM, Spiro TG (1990a) Biochemistry 29:2586
- Smulevitch G, Wang Y, Mauro JM, Wang J, Fishel LA, Kraut J, Spiro TG (1990b) Biochemistry 29:7174
- Snatzke G (ed) (1967) ORD and CD in Organic Chemistry, Heyden, London
- Snee RD (1977) Technometrics 19:415
- Snyder R, Scherer JR, Gaber BP (1980) Biochim Biophys Acta 601:47
- Snyder RG, Hsu FL, Krimm S (1978) Spectrochim Acta 34A:395
- Sokolov KV, Lutsenko SV, Nabiev IR, Nie S, Yu NT (1991) Appl Spectrosc 45:1143
- Solladié G, Zimmermann RG (1984) Angew Chem 96:335; Angew Chem Int Ed Engl 23:349
- Song JJ, Eesley GL, Levenson MD (1976) Appl Phys Lett 29:567
- Song S, Asher SA (1989) J Am Chem Soc 111:4295
- Sonnich Mortensen O, Hassing S (1980) Polarization and interference phenomena in resonance Raman scattering. In: Clark RJH, Hester RE (eds) Advances in Infrared and Raman spectroscopy, vol 6. Heyden and Sons, New York
- Soper SA, Ratzloff KL, Kuwana T (1990) Anal Chem 62:1438
- Sorensen JM, Arlt W (1979) Liquid-Liquid Equilibrium Data Collection, vol 1. In: Behrens D, Echermann R (eds) Chemistry Data Series, vol 5. Dechema, Frankfurt
- Souvignier G, Gerwert K (1992) J Biophys 63:1393
- Spicker R, Levin IW (1976) Biochim Biophys Acta 433:457
- Spiekermann M (1975) Diplomarbeit, Universität Dortmund
- Spiekermann M (1979) Dissertation, Universität Dortmund
- Spiekermann M, Bougeard D, Oelichmann HJ, Schrader B (1980) Theor Chim Acta 54:301
- Spiekermann M, Bougeard D, Schrader B (1980) J Mol Struct 60:55
- Spiekermann M, Schrader B (1977) Angew Chem 89:200; Int Ed Engl 16:197
- Spiekermann M, Schrader B, D'Orazio M (1976) Proceedings of the 5th International Conference on Raman Spectroscopy, Freiburg, p 346
- Spiro TG (1974) Acc Chem Res 7:339
- Spiro TG (1979) Resonance Raman spectroscopy of heme proteins. In: Theophanides TM (ed) Infrared and Raman spectroscopy of biological molecules. Nato advanced study institute series, Series C, vol 43. D Reidel Publishing Company, Dordrecht
- Spiro TG (1987) (ed) Biological Applications of Raman Spectroscopy, vol 2. Wiley, New York
- Spiro TG, Loehr TM (1975) In: Clark RJH, Hester RE (eds) Advances in Infrared and Raman Spectroscopy, vol 1. Heyden and Son, New York p 98
- Spiro TG, Strekas TC (1972) Proc Natl Acad Sci USA 69:2622
- Spoliti M, DeMaria G, D'Alessio L, Maltese M (1980) J Mol Struct 67:159
- Srinivasan K, Finsterhölzl H, Klöckner HW, Illig D, Schröter HW (1977) Z Naturforsch 32a:1070
- Staat H, Heise HM, Korte EH (1983) Fresenius Z Anal Chem 316:170
- Stallhofer P, Huber D (1983) Solid State Technol:233
- Stansbury EJ, Crawford MF, Welsh HL (1953) Can J Phys 31:954
- Stark E, Luchter K, Margoshes M (1986) Appl Spectrosc Rev 22:335
- Stave MS, Nicholas JB (1993) J Phys Chem 97:9630
- Stegemeyer H, Finkelmann H (1973) Chem Phys Lett 23:227
- Stegemeyer H, Mainusch KJ (1971) Naturwiss 58:599
- Steigmeier EF, Auderset H, Kobel W, Baeriswyl (1987) Synth Met 18:219-224
- Steinborn D (1993) Symmetrie und Struktur in der Chemie. VCH Verlagsgesellschaft, Weinheim
- Stencel JM, Noland DM, Bradley EB, Frenzel CA (1978) Rev Sci Instr 49:1163
- Stephens PJ (1985) J Phys Chem 89:748
- Stephens PJ, Lowe MA (1985) Vibrational Circular Dichroism. In: Rabinovitch BS, Schurr JM, Strauss HL (eds) Ann Rev Phys Chem 36:213
- Stephenson DA, Blint RJ (1979) Appl Spectrosc 33:41
- Steudel R (1982) Homocyclic sulfur compounds. In: Dewar MJS et al (eds) Topics in current chemistry, vol 102. Springer, Berlin, p 149
- Stevenson CL, Winefordner JD (1991) Appl Spectrosc 45:1217
- Stewart JJP (1989) QCPE 581

- Stockburger M, Aishuth T (1986) In: Clark RJH, Hester RE (eds) Spectroscopy of Biological Systems. John Wiley Pub Co, p 483
- Stockburger M, Klusmann W, Gattermann H, Massig G, Peters R (1979) Biochemistry 18:4886
- Stoeckenius W, Bogomolni (1982) Ann Rev Biochem 51:587
- Stoicheff BP (1959) High Resolution Raman Spectroscopy. In: Thompson HW (ed) Advances in Spectroscopy, vol 1. Interscience, New York, p 91
- Stokes GG (1880) Mathematical and Physical Papers, Cambridge
- Stokr J, Jakes J, Schneider B (1977) Coll Czechoslov Chem Commun 42:2287
- Stone AJ (1990) Studies in Physical and Theoretical Chemistry. In: Rivail JL (ed) vol 71. Elsevier, Amsterdam
- Stone M, Brooks RJ (1990) J R Statist Soc B 52:237
- Stoutland PO, Dyer RB, Woodruff WH (1992) Science 257:1913
- Straley JP (1974) Phys Rev A 10:1881
- Stremmel J, Kiefer W (1991a) Can J Chem 69:1732
- Stremmel J, Kiefer W (1991b) J Raman Spectrosc 22:583
- Stremmel J, Kiefer W (1991c) J Chem Phys 95:2391
- Strey G (1969) Spectrochim Acta 25A:163
- Strey G, Mills IM (1976) J Mol Spectrosc 59:103
- Stricker W, Hochenbleicher G (1973) Z Naturforschung 28a:27
- Stricker W, Just T (1979) VDI Berichte 346:111
- Stricker W, Meier W (1994) In: Trends in Applied Spectroscopy, Research Trends, Trivandrum
- Strommen DP, Nakamoto K (1977) J Chem Educ 54:474
- Strong FC (1979) J Chem Educ 56:681
- Studier MH, Appleman EH (1971) J Am Chem Soc 93:2349
- Su C, Subramaniam S, Spiro TG (1991) J Am Chem Soc (in press)
- Suefaka W, Ohsawa M (1979) Appl Surf Sci 3:118
- Sugai S, Shamoto S, Sato M, Ido T, Takagi H, Uchida S (1990) Solid State Commun 76:1990
- Sullivan DH, Connor WC, Harold MP (1992) Appl Spectrosc 46:811
- Sullivan JF (1994) Notations and Conventions in Molecular Spectroscopy, Draft, to be published
- Surewicz WK, Epand RM, Orlowski R, Mantsch HH (1987) Biochim Biophys Acta 899:307
- Surewicz WK, Mantsch HH, Stahl GL, Epand RM (1987) Proc Natl Acad Sci USA 84:7028
- Surewicz WK, Moscarello MA, Mantsch HH (1987) Biochemistry 26:3881
- Surewicz WK, Moscarello MA, Mantsch HH (1987) J Biol Chem 262:8598
- Suschtschinskij MM (1974) Raman Spektren von Molekülen und Kristallen. Akademie Verlag Berlin
- Susi H (1969) In: Timasheff SN, Fasman GD (eds) Structure and Stability of Biological Macromolecules, vol 2. M Dekker Pub Co, New York
- Susi H, Byler DM (1983) Biochem Biophys Res Comm 115:391
- Susi H, Sampugna J, Hampson JW, Ard JS (1979) Biochemistry 18:297
- Suzuki N, Ozaki M, Etemad S, Heeger AJ, Macdiarmid AG (1980) Phys Rev Lett 15:1209-1213
- Svendsen EN, Stroyer-Hansen T, Tangaa T (1979) J Mol Spectrosc 77:244
- Swaid I, Nickel D, Schneider GM (1985) Fluid Phase Equilibria 21:95
- Swalen JD, Rabolt JF (1985) Characterization of Orientation and Lateral Order in Thin Films by Fourier Transform Infrared Spectroscopy. In: Ferraro JR, Basile LJ (eds) Fourier Transform Infrared Spectroscopy, Applications to Chemical Systems. Academic, Orlando, p 283
- Swanson BI, Jones LH (1981) J Mol Spectrosc 89:566
- Sweger DM, Travis JC (1979) Appl Spectrosc 33:46
- Swietlik R, Schweitzer D, Keller HJ (1987) Phys Rev B6:881
- Swinneheart JS, Porro TJ (1973) Angewandte Infrarotspektroskopie Heft 8. Bodenseewerk Perkin Elmer, Überlingen
- Szalontai B, Gombos Z, Lutz M (1991) In: Hester RE, Girling RB (eds) Spectroscopy of Biological Molecules. The Royal Society of Chemistry, p 453
- Szivessy G (1928) Kristalloptik. In: Handbuch der Physik, chap. 11, vol 20: Licht als Wellenbewegung. Julius Springer, Berlin, p 635
- Taboury JA, Bourtyare P, Liquier J, Taillandier E (1984) Nucleic Acids Res 12:4247
- Taboury JA, Liquier J, Taillandier E (1985) Canad J Chem 63:1904
- Tabyaoui A, Lavorel B, Millot G, Saint-Loup R, Chaux R, Berger H (1990) J Raman Spectrosc 21:809

- Tabyaoui A, Lavorel B, Pierre G, Bürger H (1991) *J Mol Spectrosc* 148:100
- Taga K, Schwarzbach C, Stingeder G, Grasserbauer M, Kellner R (1993) *Anal Chem* 65:2288
- Tai MH, Harwit M (1976) *Appl Opt* 15:2664
- Taillandier E, Fort L, Liquier J, Couppez M, Sautiere P (1984a) *Biochemistry* 23:2644
- Taillandier E, Liquier J, Taboury JA (1985) In: Clark RJH, Hester RE (eds) *Advances in Infrared and Raman Spectroscopy*, vol 12. Wiley Pub Co, p 65
- Taillandier E, Taboury JA, Adam S, Liquier J (1984b) *Biochemistry* 23:5703
- Taillandier E, Taboury JA, Liquier J, Gadenne MC, Champagne M, Brahms J (1979) *Biopolymers* 18:1877
- Taillandier E, Taboury JA, Liquier J, Sautiere P, Couppez M (1981) *Biochimie* 63:895
- Takahashi S, Ogura T, Itoh Shinzawa K, Yoshikawa S, Kitagawa T (1991) *J Am Chem Soc* 113:9400
- Takahashi S, Schrader B, Meier W, Gottlieb K (1967) *J Chem Phys* 47:3842
- Talskey G, Mayring M, Kreuzer H (1978) *Angew Chem* 90:854
- Tam CN, Keiderling TA (1993) *J Mol Spectrosc* 157:391
- Tang J, Albrecht AC (1970) Developments in the theories of vibrational Raman intensities. In: Szymanski HA (ed) *Raman Spectroscopy*. Plenum Press, New York London, p 33
- Tannor DJ, Heller EJ (1982) *J Chem Phys* 77:202
- Taraschi T, Mendelsohn R (1980) *Proc Natl Acad Sci USA* 77:2362
- Tasumi M (1977) *Intra- und Intermolecular Vibrations of n-Alkanes and Polyethylene*, chapt 23. In: Barnes AJ, Orville-Thomas WJ (eds) *Vibrational Spectroscopy - Modern Trends*. Elsevier, Amsterdam, p 365
- Tasumi M, Fujiwara M (1987) In: Clark RJH, Hester RE (eds) *Spectroscopy of Inorganic-based Materials*. Wiley Pub Co, p 407
- Tasumi M, Shimanouchi T, Miyazawa T (1962) *J Mol Spectrosc* 9:261
- Teraoka J, Harmon PA, Asher SA (1990) *J Am Chem Soc* 112:2892
- Terhune RW, Maker PD, Savage CM (1965) *Phys Rev Lett* 14:681
- Thakur SN, Goodman L, Ozkabak AG (1986) *J Chem Phys* 84:6642
- Thamann TJ, Lord RC, Wang AHJ, Rich A (1981) *Nucleic Acids Res* 9:5443
- Theophanides TM (ed) (1979) *Infrared and Raman Spectroscopy of Biological Molecules*, Nato Advanced Study Ser C, vol 43. D Reidel, Dordrecht
- Theophanides T, Anastassopoulou J, Fotopoulos N (1993) *Proceedings of the Vth International Conference on the Spectroscopy of Biological Molecules*, Kluwer Acad Publ, Dordrecht
- Thibreau RJ, Brown CW, Heidersbach RH (1978) *Appl Spectrosc* 32:532
- Thibreau RJ, van Haverbeke L, Brown CW (1978) *Appl Spectrosc* 32:98
- Thomas DM (1977) *Appl Spectrosc* 31:515
- Thomas EV, Haaland DM (1990) *Anal Chem* 62:1091
- Thomas jr GJ, Benevides JM (1985) *Biopolymers* 24:1101
- Thomas jr GJ, Hartmann KA (1973) *Biochim Biophys Acta* 312:311
- Thomas jr GJ, Murphy P (1975) *Science* 188:1205
- Thomas jr GJ, Prescott B, Mac Donald-Ordzie PE, Hartman KA (1976) *J Mol Biol* 102:103
- Thompson ME, Baxter SM, Bulls AR, Burger BJ, Nolan MC, Santarsiero BD, Schaefer WP, Bercaw JE (1987) *J Am Chem Soc* 109:203
- Thomsen C, Cardona M (1989) Raman Scattering in High T_c Superconductors. In: Ginsberg DM (ed) *Physical properties of high temperature superconductors I*. World Scientific, Singapore New Jersey London Hong Kong, p 409
- Thulstrup EW, Michl J (1982) *J Am Chem Soc* 104:5594
- Tietze LF, Hübsch T, Voß E, Buback M, Tost W (1988) *J Am Chem Soc* 110:4065
- Timms PL (1976) Techniques of Preparative Cryochemistry. In: Moskovits M, Ozin GA (eds) *Cryochemistry*. John Wiley, New York, p 62
- Timusk T, Tanner DB (1989) Infrared properties of high T_c superconductors. In: Ginsberg DM (ed) *Physical properties of high temperature superconductors I*. World Scientific, Singapore New Jersey London Hong Kong, p 341
- Tinoco I Jr, Freeman MP (1975) *J Phys Chem* 61:1196
- Tobias KM, Jansen M (1987) *Z Anorg Allg Chem* 550:16
- Tödheide K (1972) Water at High Temperatures and Pressures, Chap 13. In: Franks F (ed) *Water - A Comprehensive Treatise*, vol. 1. Plenum Press, New York
- Török F, Pułay P (1978) *J Mol Struct* 46:43

- Tolles WM, Nibler JW, McDonald JR, Harvey AB (1977) *Appl Spectrosc* 31:253
Tolles WM, Turner RD (1977) *Appl Spectrosc* 31:96
Tonge PJ, Carey PR (1990) *Biochemistry* 29:10723
Tonge PJ, Menard R, Storer AC, Ruzsicska BP, Carey PR (1991) *J Am Chem Soc* 113:4297
Tost W (1988) Thesis, Göttingen
Tourin RH (1966) *Spectroscopic Gas Temperature Measurements*. Elsevier, Amsterdam
Tran CD (1984a) *Anal Chem* 56:824
Tran CD (1984b) *J Chromatogr* 292:432
Treando PJ, Lewin IW, Lewis EN (1992) *Appl Spectrosc* 46:553
Treffers RR (1977) *Appl Opt* 16:3103
Tripathi GNR (1983) Time resolved resonance Raman spectroscopy of radiation-chemical processes. In: Talmi Y (ed) *Multichannel Image detectors*, vol 2; ACS Symposium Series No. 236. American Chemical Society, Washington D.C.
Truett WL (1979) *Adv Chem Ser* 174:81
Truett WL, Bayliss MA (1983) *Appl Spectrosc Rev* 18:329
Tsai P, Cooney RP (1980) *J Raman Spectrosc* 9:39
Tsai P, Cooney RP, Heaviside J, Hendra PJ (1978) *Chem Phys Lett* 59:510
Tsai YS, Ma SM, Nishimura S, Ueda I (1990) *Biochim Biophys Acta* 1022:245
Tsankov D, Jordanov B, Korte EH, Schrader B (1984) *Appl Spectrosc* 38:43
Tsuboi M (1969) In: Brame jr EG (ed) *Applied Spectroscopy Reviews*, vol 3. M Dekker Pub Co, p 45
Tsuboi M (1977) *Raman Spectroscopy of Nucleic Acids and Proteins* chapt 25. In: Decius JC, Hexter RM (eds) *Molecular Vibrations in Crystals*. McGraw-Hill, New York, p 405
Tsuboi M, Shuto K, Higushi S (1968) *Bull Chem Soc Japan* 41:1821
Turner JJ, Pimentel GC (1963) *Science* 140:974
Turrell G (1972) *Infrared and Raman Spectra of Crystals*. Academic Press, London New York
Tzinis C, Bahl SK, Davidson P, Risen Jr WM, Baughman RH (1978) *Rev Sci Instr* 49:1725
Udagawa A, Matsui T, Tanaka S (1989) *Analyt Sc* 5:263
Ueba H, Ichimura S, Yamada H (1982) *Surf Sci* 119:433
Ueda T, Shimanouchi T (1968) *J Mol Spectrosc* 28:350
Ueno A, Bennelt CO (1979) *Bull Chem Soc Jpn* 52:2551
Ugawa A, Ojima G, Yakushi K, Kuroda H (1988) *Synth Met* 27:A445
Uhl W (1988) *Z Naturforsch* 43b:1113
Uhmann W, Becker A, Taran Ch, Siebert F (1991) *Appl Spectrosc* 45:390
Urabe H, Hayashi H, Tominaga Y, Nishimura Y, Kubota K, Tsuboi M (1985) *J Chem Phys* 82:531
Urano TI, Hamaguchi H (1992) *Chem Phys Lett* 195:287
Urban MW, Gaboury SR, McDonald WF, Tiefenthaler AM (1990) *Adv Chem Ser* 227:287
Urban MW, Koenig JL (1990) Recent Developments in Depth Profiling from Surfaces Using FT-IR Spectroscopy. In: Durig JR (ed) *Applications of FT-IR Spectroscopy, Vibrational Spectra and Structure*, vol 18, p 127
Urpi L, Ridoux JP, Liquier J, Verdaguer N, Fita I, Subirana JA, Iglesias F, Huynh Dinh T, Igolen J, Taillandier E (1989) *Nucleic Acids Res* 17:6669
Vainer YG, Kuzin MY, Malyavkin LP, Sil'kis EG, Tanana KV, Titov VD (1979) *Sov J Quant Electron* 9:296
Valentini JJ, Esherick P, Owyoung A (1980) *Chem Phys Lett* 75:590
Valyashko VM (1977) *Ber Bunsenges Phys Chem* 81:388
Valyashko VM, Buback M, Franck EU (1980) *Z Naturforsch* 35a:549
Valyashko VM, Buback M, Franck EU (1981) *Z Naturforsch* 36a:1169
van de Ven M, Reijer J, Verwer W, Levine YK, Sheridan JP (1984) *J Raman Spectrosc* 15:86
van Denbussche G, Clercx A, Curstedt T, Johansson J, Jörnvall H, Ruysschaert JM (1991) *Eur J Biochem* 203:201
van Duyne RP (1979) In: Moore CB (ed) *Chemical and Biological Applications of Lasers*, vol 4, Academic, New York
van Eck M, van Dalen JPJ, de Galan L (1983) *Analyst* 108:485
van Eijk CGA, van der Maas JH (1977) *Fresenius Z Anal Chem* 286:80 (1978) 291:308
van Eldik R, Asano T, Le Noble WJ (1989) *Chem Rev* 89:549
van Haverbeke L, Lynch PF, Brown CW (1978) *Anal Chem* 50:315
van Helvoort K, Knippers W, Fantoni R, Stolte S (1987) *Chem Phys* 111:445

- van Wart HE, Sheraga HA (1976) *J Phys Chem* 80:1823
 van Wart HE, Sheraga HA (1978) *Methods Enzymol* 49:67
 Vardeny Z, Ehrenfreund E, Braffman O, Heeger AJ, Wudl F (1987) *Synth Met* 18:183
 Varotsis C, Woodruff WH, Babcock GT (1989) *J Am Chem Soc* 111:6439
 Varotsis C, Woodruff WH, Babcock GT (1990) *J Biol Chem* 265:11131
 Varsanyi S, Szöke S (1969) *Vibrational Spectra of Benzene Derivatives*. Academic Press, New York
 Vauck WR, Müller HA (1988) *Grundoperationen chemischer Verfahrenstechnik*, 7th edn. Verlag Chemie, Weinheim
 VDI (1975) *VDI Handbuch Reinhaltung der Luft*, Vorschrift Nr. 2456, 2459, 2460, VDI Verlag Düsseldorf
 Veirs DK, Rosenblatt GM (1987) *J Mol Spectrosc* 121:401
 Verdaguer N, Aymami J, Fernandez-Forner D, Fita I, Coll M, Huynh Dinh T, Igolen J, Subirana JA (1991) *J Mol Biol* 221 (in press)
 Verdieck JF, Peterson SH, Savage CM, Maker PD (1970) *Chem Phys Lett* 7:219
 Verma SP, Wallach DFH (1983) In: Chapman D (ed) *Biomembrane Structure and Function*. Verlag Chemie, p 167
 Vickers TJ, Mann CK, Marley NA, King TH (1984) *International Laboratory*, Nov/Dec 1984
 Vidrine DW, Mattson DR (1978) *Appl Spectrosc* 32:502
 Vincent JS, Levin IR (1991) *Biophys J* 59:1007
 Vincent JS, Levin IW (1988) *Biochemistry* 27:3438
 Vincent JS, Levin IW (1990) *J Am Chem Soc* 108:3551
 Vincent JS, Revak SD, Cochrane CG, Levin IR (1991) *Biochemistry* 30:8395
 Virdee HR, Hester RE (1984) *J Phys Chem* 88:451
 Visapää A (1965) *Kemian Teollisuus* 22:487
 Visser T, van der Maas JH (1974) *J Raman Spectrosc* 2:563
 Visser T, van der Maas JH (1975) *J Raman Spectrosc* 3:125
 Visser T, van der Maas JH (1978) *J Raman Spectrosc* 7:278
 Vo-Dinh T, Alak A, Moody RL (1988) *Spectrochim Acta* 43B:605
 Vo-Dinh T, Meier M, Wokaun A (1986) *Analyst Chim Acta* 181:139
 Vogt H (1973) *Phys Stat Solid b* 58:705
 Vogt H (1976) In: Proc 5th Int Conf Raman Spectrosc, Schmid ED, Brandmüller J, Kiefer W, Schrader B, Schrötter HW (eds) Schulz Verlag, Freiburg, p 742
 Vogt H (1987) *Phys Rev B* 36:5001
 Vogt H, Neumann G (1976) *Opt Commun* 19:108
 Vogt H, Neumann G (1978) *Phys Stat Solid b* 86:615
 Vogt H, Neumann G (1979) *Phys Stat Solid b* 92:57
 Vogt H, Rossbroich G (1981) *Phys Rev B* 24:3086
 Voisin C, Cartier A, Rivail JL (1992) *J Phys Chem* 96:7966
 Volchek BZ, Purkina AV (1992) Investigation of polymer liquid crystals by infrared spectroscopy. In: Mitchell J Jr (ed) *Appl Polym Anal Charact*, vol 2. Hanser, Munich, pp 311
 Volkmann H (ed) (1972) *Handbuch der Infrarot-Spektroskopie*. Verlag Chemie, Weinheim
 Vollmert B (1979) *Grundriß der Makromolekularen Chemie*. Vollmert-Verlag, Karlsruhe
 Vrbjar N, Kean K, Szabo A, Senak L, Mendelsohn R, Keough KMW (1990) In: Biophysics for 90's, Tenth International Biophysics Congress, p 214
 Vries H de (1951) *Acta Cryst* 4:219
 Vu H, Atwood MR, Vodar B (1963) *J Chem Phys* 38:2671
 Vuks MF (1966) *Opt Spectrosc* 20:361
 Wagner HG, Zellner R (1979) *Angew Chemie* 91:707
 Wagner HH, Schaefer RR (1979) *J Appl Phys* 50:2697
 Wahbi AM, Ebel S (1974) *Anal Chim Acta* 70:57
 Wahbi AM, Ebel S, Steffens U (1975) *Fresenius Z Anal Chem* 273:183
 Wald D (1985) *Gruppentheorie für Chemiker*. VCH Verlagsgesellschaft, Weinheim
 Walker IC, Stamatovic A, Wong SF (1978) *J Chem Phys* 69:5532
 Wall DL, Mantz AW (1977) *Appl Spectrosc* 31:525
 Wallach DFH, Verma SP, Fookson J (1979) *Biochim Biophys Acta* 559:153
 Wallnoefer W, Faulques E, Kuzmany H (1989a) *Synth Met* 28:C533-C538
 Wallnoefer W, Kuzmany H (1989b) unpublished

- Walmsley SH (1968) *J Chem Phys* 48:1438
Walrafen GE (1974) *Phys Bl* 30:540
Walrafen GE (1975) *Appl Spectrosc* 29:179
Walrafen GE (1977) *Appl Spectrosc* 31:295
Walrafen GE, Stone J (1972) *Appl Spectrosc* 26:585
Walther H (ed) (1976) *Laser Spectroscopy*, Springer, Berlin
Wang AHJ, Quigley GJ, Kolpkat FJ, Crawford JL, van Boom JH, van der Marel G, Rich A (1979) *Nature* 282:680
Wang B, Croatto PV, Yoo RK, Keiderling TA (1992) *J Chem Phys* 96:2422
Wang B, Keiderling TA (1993) *J Chem Phys* 98:903
Wang C, Qian S, Johnson CK (1990) *J Phys Chem* 94:8417
Wang IY, Weber A (1978) *Indian J Pure Appl Phys* 16:358
Wang Y, McCreery RL (1989) *Anal Chem* 61:2647
Wang Y, Purrello R, Jordan T, Spiro TG (1991) *J Am Chem Soc* 113:6359
Wang Y, Purrello R, Spiro TG (1989) *J Am Chem Soc* 111:8274
Wang Y, Thomas GA, Peticolas WL (1987) *J Biomol Struct Dyn* 5:249
Warshel A (1977) *Ann Rev Biophys Bioeng* 6:273
Washington MA, Genack AZ, Cummins HZ, Bruce RH (1977) *Phys Rev B* 15:2145
Watson WM, Kohler CF (1979) *Environ Sci Technol* 13:1241
Weast RC (ed) (1977) *Handbook of Chemistry and Physics*, 55th edn. CRC Press, Cleveland
Weber A (1973) *High-Resolution Raman Studies of Gases*. In: Anderson A (ed) *The Raman Effect*, vol 2. Marcel Dekker, New York, p 543
Weber A (1976) *Progress in Raman Spectroscopy of Gases*. In: Schmid ED, Brandmüller J, Kiefer W, Schrader B, Schröter HW (eds) *Proceedings of the 5th International Conference on Raman Spectroscopy*. Schulz HF, Freiburg, p 391
Weber A (1979) *High-Resolution Rotational Raman Spectra of Gases*. In: Weber A (ed) *Raman Spectroscopy of Gases and Liquids*. Topics in Current Physics, vol 11. Springer, Berlin, p 71
Weber A (ed) (1979) *Raman Spectroscopy of Gases and Liquids*, Topics in Current Physics. Springer, Berlin
Weber A, Jennings DE, Brault JW (1984) *Proceedings 9th International Conference Raman Spectroscopy*, Tokyo
Weber A, Porto SPS (1965) *J Opt Soc Am* 55:1033
Weber PM, Rice SA (1988) *J Chem Phys* 88:6107
Wegener W, Cole-Tortosa L (1978) *Lenzinger Ber* 45:190 (1978)
Wegner G (1969) *Z Naturforschung* B24:824
Wegner G (1971) *Makromol Chem* 145:85
Wehry EL, Mamantou G (1979) *Anal Chem* 51:643A
Weidlein J, Müller U, Dehncke K (1981) *Schwingungsfrequenzen, I Hauptgruppenelemente*. G Thieme Verlag, Stuttgart New York
Weidlein J, Müller U, Dehncke K (1982) *Schwingungsspektroskopie, eine Einführung*. G Thieme Verlag, Stuttgart New York
Weidlein J, Müller U, Dehncke K (1986) *Schwingungsfrequenzen, II Nebengruppenelemente*. G Thieme Verlag, Stuttgart New York
Weidlich O, Siebert F (1993) *Appl Spectrosc* 47:1394
Weidlich T, Lindsay SM, Peticolas WL, Thomas GA (1990) *J Biomol Struct Dyn* 7:849
Weidner M, Röseler A (1992) *Phys Status Solidi A* 130:115
Weierstrass K (1856) *Mathematische Werke*, vol 3, p 175, (1967) reprint by Johnson Reprint Corp, New York
Weigel C, Kellner R (1989) *Fresenius Z Anal Chem* 335:663
Weil L, Dure G, Quentin KE (1974) *Wasser Abwasser-Forsch* 7:169
Weimann D, Vogt H (1974) *Phys Stat Solid a23:463*
Weippert A, Funk JM, Materny A, Kiefer W (1993) *J Raman Spectrosc* 24:705
Weippert A, Kiefer W (1992a) *J Raman Spectrosc* 23:707
Weippert A, Kiefer W (1992b) *J Raman Spectrosc* 23:713
Weippert A, Kiefer W (1992c) *Il Nuovo Cimento* 14D:1033
Weir CE, Lippincott ER, Van Valkenburg A, Bunting EN (1959) *J Res Natl Bur Stand Sec A* 63:55
Weitkamp H, Barth R (1972) *Infrarot-Strukturanalyse*. Thieme, Stuttgart

- Weitkamp H, Barth R (1976) Einführung in die quantitative Infrarot-Spektrophotometrie. G Thieme Verlag, Stuttgart
- Weitkamp H, Wortig D (1977) Mikrochim Acta II:315
- Weitkamp H, Wortig D (1983) Mikrochim Acta II:31
- Weitz DA, Moskovits M, Creighton JA (1986) In: Chemical Structure at Interfaces, Hall RB, Ellis AB (eds) VCH, p 197
- Wells RD, Collier DA, Hanvey JC, Shimizu M, Wohrlab F (1988) Faseb J 2:2939
- Welsh HL (1956) Can J Phys 34:737
- Welsh HL, Crawford MF, Thomas TR, Love GR (1952) Can J Phys 30:577
- Welsh HL, Stansbury EJ, Romanko J, Feldman T (1955) J Opt Soc Am 45:338
- Wen ZQ, Barron LD, Hecht L (1993) J Am Chem Soc 115:285
- Wen ZQ, Hecht L, Barron LD (1994) J Am Chem Soc 116:443
- Werner HJ (1981) Mol Phys 44:111
- Weyer LG (1985) Appl Spectrosc Rev 21:1
- Wharton CW, Chittcock RS, Austin J, Hester RE (1988) In: Schmid ED, Schneider FW, Siebert F (eds) Spectroscopy of Biological Molecules. John Wiley and Sons, New York, p 95
- Wheeler O (1959) Chem Rev 59:629
- Whetsel KB (1968) Appl Spectrosc Rev 2:1
- White JU (1942) J Opt Soc Amer 32:285
- Wieboldt RC, Lowry SR, Rosenthal RJ (1988) Microchim Acta I:179
- Wiederkehr RR, Drickamer HG (1958) J Chem Phys 28:311
- Wienecke P, Finsterhölzl H, Schröter HW, Brandmüller J (1986) J Appl Spectrosc 40:70
- Wiesner U, Reynolds U, Boeffel C, Spiess HW (1991) Makromol Chem Rapid Commun 12:457
- Wiesner U, Reynolds U, Boeffel C, Spiess HW (1992) Liq Cryst 11:251
- Wigner E (1931) Gruppentheorie. Vieweg, Braunschweig; reprint: (1944) Edwards, Ann Arbor
- Wilks PA (1986) The Origins of Commercial Infrared Spectrometers. In: Stock JT, Orna MV (eds) The History and Preservation of Chemical Instrumentation. D Reidel, Amsterdam, p 27
- Williams AD, Spragg RA (1982) Perkin Elmer INFRARED Bulletin 96
- Williams JM, Beno MA (1990) Inorganic Chemistry 29:1599
- Willing W, Christoffersen R, Mueller U, Dehncke K (1987) Z Anorg Allg Chem 555:16
- Willis H (1979) Europ Spectrosc News 26:27
- Willner H, Aubke F (1990) Inorg Chem 29:2195
- Wilson EB, Wells AJ (1946) J Chem Phys 14:578
- Wilson jr EB, Decius JC, Cross PC (1955) Molecular Vibrations, The Theory of Infrared and Raman Vibrational Spectra. McGraw-Hill, New York
- Windholz W (ed) (1983) The Merck Index, 10th edn. Merck and Co, Rahway
- Winter J, Kuzmany H (1992) Solid State Commun 84:935
- Winter J, Kuzmany H (1994) In: Kuzmany H, Fink J, Mehring M, Roth S (eds) Proceedings Int. Winterschool on Electronic Properties of Novel Materials, Kirchberg 1994, World Scientific to be published
- Winter J, Kuzmany H (1994) unpublished
- Wittke W, Hatta H, Otto A (1989) Appl Phys A 48:289
- Wokaun A (1984) In: Solid State Physics, vol 38, Seitz F, Turnball D (eds). Academic Press, New York, p 223
- Wokaun A, Baiker A (1986) Chimia 40:2
- Wold S (1978) Technometrics 20:397
- Wold S, Esbensen K, Geladi P (1987) Chemometrics and Int Lab Sys 2:37
- Wolkenstein MN (1941) Dokl Akad Nauk SSSR 30:791
- Wolter H (1956) Optik dünner Schichten. In: Flügge S (ed) Handbuch der Physik / Encyclopedia of Physics, vol 24. Springer, Berlin, p 461
- Wong PTT, Wong RK, Fung MFK (1993) Appl Spectrosc 47:1058
- Wood RW (1928) Nature 122:349
- Wood RW (1929) Phil Mag Ser 7, 7:744
- Wood TH, Klein MV (1979) J Vac Sci Technol 16:459
- Wood TH, Zwemer DA (1981) J Vac Sci Technol 18:649
- Woost B (1983) Dissertation, Universität Essen
- Wu TS, Efron U, Hess LD (1984) Appl Opt 23:3911
- Wyzgol R (1989) Dissertation Universität Essen

- Wyzgol R, Heinrich P, Lebioda K, Lentz E, Hatzilazaru A, Schrader B (1991) Final report for the BMFT research project 02 - WA 8735, Universität Essen
- Wyzgol R, Heinrich P, Schrader B, Lübbbers DW (1989) Determination of Anesthetics in Aqueous Solution of Infrared ATR Spectroscopy. In: Droph R, Spintage R (eds) Innovations in Physiological Anaesthesia and Monitoring. Springer Verlag, Berlin
- Yamada C, Hirota E (1979) *J Mol Spectrosc* 74:203
- Yamada H (1981) *Appl Spectrosc Rev* 17:227
- Yamada H, Amamiya T, Tsubomura H (1978) *Chem Phys Lett* 56:591
- Yamada H, Nagata H, Toba K, Nakao Y (1987) *Surf Sci* 182:269
- Yang W, Griffiths PR, Byler DM, Susi H (1985) *Appl Spectrosc* 39:282
- Yarwood J (1990) *Spectroscopy* 5:34
- Yarwood J (1993) *Anal Proc* 30:13
- Yates JT, Madey TE (1987) (eds) In: *Vibrational Spectroscopy of Molecules on Surfaces*, vol 1. Plenum, New York
- Yen YS, Wong JS (1989) *J Phys Chem* 93:7208
- Yoshino T, Bernstein HJ (1958) *J Mol Spectrosc* 2:213, 241
- Yoshino T, Bernstein HJ (1959) *Proceedings of the Conference on Molecular Spectroscopy*. Pergamon Press, London, p 141
- Yu GS, Che D, Freedmann TB, Nafie LA, (1993) *Tetrahedron Asymmetry* 4:511
- Yu NT, Kuck JFR (1978) *The Spex Speaker* 23 no 3
- Yu NT, Li XY (eds) (1994) *Proc. XIVth Int Conf Raman Spectrosc*, Wiley, London
- Yu NT, Nie S (1990) In: *Laser applications in life science*. SPIE Proceedings, vol 1403
- Yu NT, Nie S (1992) In: *Proc XIIth Int Conf Raman Spectrosc*, Kiefer W, Cardona M, Schaack G, Schneider FW, Schröötter HW (eds) Wiley, Chichester, p 37
- Yu QH, Levy R (1981) *J Luminesc* 24/25:417
- Yu W, Alfano RR (1975) *Phys Rev A* 11:188
- Yuratich MA, Hanna DC (1977) *Mol Phys* 33:671
- Yuratich MA, Hanna DC, Cotter D (1979), *Nonlinear Optics of Free Atoms and Molecules*, Springer, New York
- Zachmann G (1987) *Productronic* 11:78
- Zannoni C (1979) Distribution Functions and Order Parameters. In: Luckhurst GR, Gray GW (eds) *The molecular physics of liquid crystals*. Academic, London, p 51
- Zeigler JM (1989) *Synth Met* 28:C581-C591
- Zeindl S, Bauer F, Sailer K, Ruoff A, Schröötter HW (1993) *Verhandl DPG(VI)* 28:357
- Zeindl S, Sailer K, Bauer F, Schröötter HW, Ruoff A (1994) *J Mol Struct*, submitted
- Zemnach R, Vardeny Z, Brafman O, Ehrendfreund E, Epstein AJ, Weagley RJ, Gibson HW (1985) *Mol Cryst Liq Cryst* 118:423
- Zentel R, Poths H, Kremer F, Schoenfeld A, Jungbauer D, Twieg R, Willson CG, Yoon D (1992) *Polym Adv Technol* 3:211
- Zerbi G (1977) Limitations of Force Constant Calculations for Large Molecules, chapt 17. In: Barnes AJ, Orville-Thomas WJ (eds) *Vibrational Spectroscopy - Modern Trends*. Elsevier, Amsterdam, p 261
- Zerbi G (1977) Molecular Dynamics and Molecular Spectra of Polymers, chapt 24. In: Barnes AJ, Orville-Thomas WJ (eds) *Vibrational Spectroscopy - Modern Trends*. Elsevier, Amsterdam, p 379
- Zerbi G, Castiglion C, Lopez Navarete JT, Bogang T, Gussoni M (1989) *Synth Met* 28:D359
- Zetterer T, Franz M, Schuetzmann J, Ose W, Otto HH, Renk KF (1990) *Phys Rev B* 41:9499
- Zeyher R, Zwicknagel G (1990) *Z Physik* B78:175
- Zheng JB, Snow JB, Murphy DV, Leipertz A, Chang RK, Farrow RL (1984) *Opt Lett* 9:341
- Zhizhin GN, Yakovlev VA (1990a) *Phys Rep* 194:281
- Zhizhin GN, Yakovlev VA (1990b) *J Electron Spectrosc Relat Phenom* 54:449
- Zhou X, Fogarasi G, Liu R, Pulay P (1993) *Spectrochim Acta* 49A:1499
- Ziegler E (1973) Computer in der instrumentellen Analytik. Akademische Verlagsgesellschaft, Frankfurt
- Ziegler LD (1990) *J Raman Spectrosc* 21:769
- Ziegler LD, Chung YC, Wang P, Zhang YP (1989) In: *Time Resolved Spectroscopy*, Clark RJH, Hester RE (eds). Wiley, Chichester, p 55
- Ziegler LD, Chung YC, Zhang YP (1987) *J Chem Phys* 87:4498

- Ziegler LD, Roebber JL (1987) *Chem Phys Lett* 136:377
Ziegler T (1991) *Chem Rev* 91:651
Zinth W, Kaiser W (1988) In: Ultrashort Laser Pulses and Applications, Kaiser W (ed) *Topics in Applied Phys*, vol 60, Springer, Berlin, p 235
Zinth W, Leonhardt R, Holzapfel W, Kaiser W (1988) *IEEE J Quantum Electron* 24:455
Zundel G, Eckert M (1989) *J Mol Struct Theochem* 200:73
Zundel G, Noller H, Schwab GM (1962) *Ber Bunsenges Phys Chem* 66:122, 129
Zupan J, Gasteiger J (1991) *Anal Chim Acta* 248:1
Zupan J, Gasteiger J (1993) *Neural Networks for Chemists*. VCH, Weinheim
Zurmühl R (1965) *Praktische Mathematik, 1 Ausgleichsparabeln*. Springer, Berlin

Subject Index

- ab initio* calculation of vibrational spectra 239,
 AB_3 systems 234
 AB_n system 234
252, 463, 565
Abbe's equation 150
aberrations 102
aberration-tolerance 144
absolute configuration 337, 569
absolute normalized Raman scattering cross section
 151f, 295
absolute Raman scattering coefficients 140
absolute Raman scattering cross sections, crystal
 powders 430
absorbance 17
– apparent 17, 414
absorptance 17
absorption
 – coefficient 17, 130
 – factor 17, 99
 – index 578, 591
ac interferogram 550
accidental symmetric rotor 270
accuracy of analysis 411
acetic acid, IR and Raman spectrum 213
acetic acid tert. butyl ester, IR and Raman spectrum
 211
acetic anhydride, IR and Raman spectrum 213
acetyl chloride, IR and Raman spectrum 213
acetylcholine receptors 257f
acetylene *see* C_2H_2
acetylene derivatives, IR and Raman spectra 202
acoustic branch 38, 315
acoustic modes 248
acousto-optic tunable filter (AOTF) 126
acousto-optically Q-switched Nd:YAG laser 172
acrylonitrile, IR and Raman spectrum 198
active transformation 46
activity measure 460
agitation of current carriers 106
air
– FT Raman spectrum of 281
– Raman spectrum, multireflection cell 281
– rotational Raman spectrum 281
Airy disc 68
Airy equation 583
Al-Al bond 226
Albrecht's A- and B-terms 470f
Albrecht's Theory 376, 390
aldehyde, characteristic frequencies 212
alexandrite laser 136
 AlF/AlF_3 bonding parameters 245
aliasing 620
1-alkenes, NIR spectra 533
n-alkyl benzenes, NIR spectra 534
alkyl carboxylic acid chlorides, NIR spectra 539
1-alkynes, NIR spectra 534
allene, point group 704
all-trans-retinol, IR and Raman spectrum 199f
amide vibrations 195, 357, 618
amino acids, characteristic frequencies 215
ammonia, CARS spectrum 291
amphotericin 368f
amplitude modulation 21
amplitudes 10
analysis without external calibration 429
analytical application of vibrational spectroscopy
 108f
angle between oscillators, determination 239
Angström 1f
angular dispersion 69f
anharmonic force field of benzene 256
anharmonic potential 10f
anharmonicity 26, 256, 519
– constants 279, 482, 667
– electrical 17, 26, 518
– mechanical 17, 26, 518
 m -anisidine, IR and Raman spectrum 210
anisotropic sample 88, 595
anisotropic solvents 324
anisotropy 323
annealing of matrix 301
anomalous polarization 473

- anomalous Raman scattering 383
 anti-carcinogenic substances, interaction with
 nucleic acids 355
 antipodes, discrimination of 342
 anti-Stokes Raman spectrum 3, 18f, 22
 antisymmetric vibrations 44
 AOTF *see* acousto-optic tunable filter
 aplanatic points 131
 apodization function 620
 apparent integrated intensity 422
 apparent transmission 668
 APT *see* atomic polar tensor
 aqueous solutions, Raman spectroscopy 251
 aragonite, space group 319
 argon ion lasers 136
 argon matrix 301
 arrangement of Raman cells 154
 array detectors 136f
 arsenic modified selenium glass 128
 arsenic trisulfide glass 127
 AsCl_5 250
 associative law 44
 ASTERISK 167
 asymmetric top molecules 258, 272f, 294
 A-term scattering 472
 atom-atom interactions 257
 atom-atom potential functions 10, 34, 457
 atomic axial tensor 556
 atomic polar tensor (APT) 554
 ATPase activity 357
 ATR membrane technique 603
 ATR spectra of thiourea single crystal 59
 ATR spectroscopy 430, 576, 593f, 599, 603
 ATR theory 575f, 604
 atropeptin 357, 370
 A-type band of near prolate top 273
 AuCl_4^- , point group 703
 autoclave IR cell 643f
 automatic identity control 441
 automatic quality control 411
 automobile exhaust gases, Raman spectral analysis
 434
 axial vector 51
 – character of transformation 52
 azidomethemoglobin, VCD 555
 azo compounds, characteristic frequencies 215
 1, 1'-azomethylcycloheptane, IR and Raman spectrum 216
 B type bands 273
 B \rightarrow Z conformational transition 350
 back-donation 233
 background 159
 – noise 75
 – ways of reducing 161
 back-scattering arrangement 141ff
 back-thinned CCD 562
 backward scattered CARS 175
 backward scattering Raman effect 141f, 147
 bacterial photosynthetic reaction 618, 636
 bacterial reaction centers 359, 637 f
 bacteriophages 363
 bacteriopheophytin BPh 636
 bacteriorhodopsin (BR) 359f, 369
 – resonance Raman spectrum 487
 – fast reactions 618f, 622, 626f, 630, 638
 Badger's rule 454
 banana, Raman spectrum 220
 band contours 236, 665
 bandshape analysis 275
 bandwidth 67
 Bardeen, Cooper, and Schrieffer, theory of superconductivity 402
 barium fluoride, properties of 128
 base
 – pairing, nucleic acid spectra 346
 – of prism 72
 – stacking, nucleic acid spectra 346
 baseline method 416
 beam condensor 131
 beam splitter 74, 619
 BEDT-TTF-Cu-complex 397
 bending vibrations, number of 33
 benzaldehyde, IR and Raman spectrum 210
 benzene *see* C_6H_6
 benzene derivatives
 – point groups 703, 706, 708
 – substitution pattern 208
 BF/BF_3 bonding parameters 245
 BH_3 249
 B_2H_6 force constants 250
 B_2H_6 point group 705
 biaxial crystals, infrared spectra 318
 binary digit 109
 biological chromophores 466
 biological samples 151, 344ff, 486
 biological systems, resonance Raman spectroscopy
 358f, 486
 biomembranes 364
 biomolecules, infrared and Raman spectroscopy
 344ff, 497, 571
 bipolaron states 396

- birefringence 318f, 336, 582
– circular 88
– linear 88
– retarders 95f
black body radiator 99, 124, 132, 156f, 668
Blackman Harris apodization 621
blank measures 115
Bloembergen 165
BM model (bond moment) 553
bolometer 1
Boltzmann distribution 18, 20, 663, 671f
bond
– angles, Teller-Redlich rule 241 f
– moment 553
– order 10
– polarizability model 567
– strengths 223
– stretching coordinate 448
Born-Oppenheimer approximation 469
boron and phosphorous determination in SiO₂ 437
Bose-Einstein statistics of CO₂ molecule 265
Bouguer-Lambert-Beer law 17, 99
BOXCARS 180
BR *see* bacteriorhodopsine
Bragg's equation 70
brain proteolipid 357
branches
– optical and acoustical 37
– rotation-vibration spectra 259f, 280f, 665f, 674f
Brewster
– angle 93, 575, 588
– polarizers 92
Bridgman's unsupported area principle 643
Brillouin zone 315f, 457
bromomethane 36
Bruker
– interferometer, optical conductance of 153
– notch filter 138
B-term scattering 472
Buckingham type, of interatomic potential 10, 34, 457
buckminsterfullerene 39, 407f, 709
butadiene, infrared absorption 134
butter, Raman spectrum 220
butyl acrylate, polymerization of 540
B₁₂X₁₂²⁻ 252
C₆₀, fullerene 39, 407f
Cabannes 3
cadmium selenide, retarders 95
cadmium sulfide, properties of 128
CADPAC 455
CaF₂ force constants 248
caged GTP 637f
Cahn-Ingold-Prelog nomenclature 337
calcite
– crystal spectra 319
– polarizer 92
– properties of 127
– retarders 95
– space group 319
calcitonin 370
calcium carbonate, crystal spectra 319f
calcium fluoride, properties of 127
calculation of frequencies and intensities in molecules and crystals 445f
calibration
– curve 115, 433
– methods 416f
– plate for VCD measurements 547f
– Raman intensity 162
capillary cell 161
carbocations 688
carbon monoxide, near-infrared absorption 520
carbonyl complexes, number of CO groups in 235
carbonyl compounds, characteristic frequencies 213f
carbonyl group in different environments, characteristic frequencies 212f
carboxylic acid, characteristic frequencies 212
carboxylic acid anhydride, characteristic frequencies 212
carboxylic acid chloride, characteristic frequencies 212
carboxylic acid esters, characteristic frequencies 212
cardiolipin 370
β-carotene 199
carotenoids, IR spectra 359
CARS (coherent anti-Stokes Raman spectroscopy) 167, 172f, 181, 288, 297, 501f
– difference spectroscopy 175
– disadvantages of 173
– of gas-phase molecules 502f
– spectra, of water vapour 294
– spectroscopy in the condensed phase 173
– thermometry 503
Cartesian coordinates of molecules, IUPAC rules 695ff
catalytic activity of cell materials 644
CBrClFI, point group 696

- C-C
 – backbone vibrations 192
 – force constants in diamond 248
 – stretching vibrations, of membranes 365
 $\text{C}=\text{C}$ frequencies in different environments 195
 CCD *see* charge-coupled device
 CCl_2F_2 , trace impurities in air 225
 CCl_3F , trace impurities in air 225
 CCl_4
 – point group 707
 – Raman scattering cross section 296
 CD *see* circular dichroism
 CD_4 , CARS 294
 C_2D_2 , Raman scattering cross section 296
 C_6D_6 , rotational Raman spectrum 292
 CdSe calibration plate for VCD measurements 548
 cell mismatch 417
 cell nucleus, confocal micro Raman spectroscopy 363
 center of symmetry 40
 centrifugal distortion constant 259, 279, 451, 667
 cesium, resonance absorption filter 138
 cesium bromide, properties of 129
 cesium iodide, properties of 129
 CH_4
 – CARS 293f
 – Coriolis resonance 292
 – Fermi resonance 292
 – Raman scattering cross section 296
 – rotation-vibration IR spectrum 271
 C_2H_2
 – point group 711
 – Raman scattering cross section 295f
 – Raman spectrum 288f
 – rotation-vibration IR spectrum 266
 C_2H_4
 – Raman scattering cross section 297
 – Raman spectrum 294
 – rotation-vibration IR spectrum 274
 C_2H_6 , Raman scattering cross section 297
 C_3H_6 , cyclopropane, normal vibrations 205
 C_3H_8 , propane, Raman scattering cross section 297
 C_4H_6 , dimethylacetylene, Raman scattering cross section 295, 297
 C_6H_6 , benzene
 – and C_6D_6 , fundamental vibrations 255
 – ionization detected stimulated Raman spectrum, IDRS 515f
 – Raman scattering cross section 295, 297
 – rotational Raman spectrum 292
 – rotation-vibration spectrum 254, 271
 C_6H_{12} , cyclohexane, Raman scattering cross section 297
 chain molecules, stretching vibrations 30, 192
 chalcedony, Raman spectrum 159
 chalcogenide IR glass fibers 614
 C-halogen vibrations, dependence on constitution and conformation 205f
 characteristic frequencies
 – of carbonyl compounds 213f
 – of $\text{C}=\text{C}$ bonds 196
 characteristic Raman bands of membranes 365
 characteristic vibrations 2, 7, 32, 189f
 – of CH_2 and CH_3 groups, frequencies of 192
 – infrared and Raman intensities 190
 characters of symmetry operators 47, 49
 character table 7, 48, 695ff
 charge flow model (VCD) 552
 charge-coupled devices (CCD) 121, 138
 charge-transfer crystals, infrared and Raman spectroscopy 396ff
 CHCl_3 , Raman scattering cross section 296
 CH_2Cl_2 , Raman scattering cross section 296
 CH_3Cl , Raman scattering cross section 296
 $\text{C}_2\text{H}_3\text{Cl}$, Raman scattering cross section 297
 $\text{C}_2\text{H}_2\text{Cl}_2\text{F}_2$, point group 696
 $\text{C}_2\text{H}_5\text{CN}$, assignment of fundamentals 276
 $\text{CH}_3\text{C}(\text{O})\text{OONO}_2$ (PAN), trace impurities in air 225
 chemical effect of SERS 492
 chemical equilibria, high pressure spectroscopy 642
 chemical kinetics 658
 chemical reactions
 – in matrix 302
 – quantitative study 519
 – under process conditions 679
 chemical sensor 613
 chemical transformations 644
 chemical vapor deposition, matrix isolation 305
 chemometrics 444
 CH_3I
 – P, Q and R subband branches 268
 – rotation-vibration spectrum of 269
 chiral specificity of Contergan 543
 chirality 40
 – amplification of 344f
 – observation 337
 – of the solute molecules 336
 chlorides, NIR spectra 537
 2-chloro-1,3-butadiene, IR and Raman spectrum 198

- chlorophylls
– FT Raman spectra 361
– IR spectra 359
- chloropropane, IR and Raman spectrum 206
- CH_3O , Raman scattering cross section 297
- $\text{C}_2\text{H}_4\text{O}$, acetaldehyde, rotation-vibration spectrum of 275
- cholesteric liquid crystal
– helical structure 334f, 337, 584
– selective reflection 343
- cholesteric structure induced in nematic liquid crystals 335
- cholesterol, effect on phospholipids 369
- Christiansen effect 440, 582
- Christiansen filter 582, 138
- chromatin 362
- chromosomes, confocal micro Raman spectroscopy 363
- CH_3X groups, symmetric deformation 209
- CID *see* circular intensity difference
- circle cell 605
- circular birefringence 84f
- circular dichroism 84f, 343, 543f, 582
- circular intensity difference (CID) 544, 561, 568
- circular intensity sum (CIS) 561
- circular polarizers 86, 339f, 544
- circularly polarized radiation 78, 87, 319, 544, 548
- CIS *see* circular intensity sum
- cis poly(acetylene) 383, 388
- cis to gauche conversion 304
- cis-trans isomerization 381, 387
- Cl_2
– Raman scattering cross section 296
– reaction in liquid 250
- CICIO, produced by matrix photolysis 313
- Cl_2O_6 251
- cladding of optical fibers 104, 614
- classes of symmetry operators 48
- classical Raman effect 135, 637
- classical turning points of wave functions 480
- clearing point T_c 326
- closed cycle refrigerator 301
- closure law 44
- $\text{CN}, -\text{NC}$, characteristic vibration 234
- C_2N_2 , Raman scattering cross section 296
- CNO (fulminate) and -ONC (isofulminate) characteristic vibration 234
- CO
– ATR membrane method 607
– force constants, bond distances, and bond energies 246
- Raman scattering cross section 296
- rotation-vibration spectrum 261f
- CO_2
– Fermi resonance 287f
– force constants, bond distance, and bond energy 246
– high resolution vibration band analysis 263f
– laser 124
– Raman scattering cross section 296
– rotational Raman spectrum 286
– rotation-vibration spectrum 263, 266, 288
- cobalamines 361
- Coblentz 2, 189f
- C-O-C group, stretching vibration 209
- co-deposition for matrix isolation 304, 311
- coherent anti-Stokes Raman spectroscopy (CARS) 167, 172f, 181, 288, 297, 501f
- combination bands of C_6H_6 256
- combination modes 518f, 667
- combustion processes, matrix isolation 305
- complete analytical procedure 112
- compressed gases, vibrational spectroscopy of 641
- concave grating 69
- Condon approximation 472f
- conducting optical elements 103f
- conducting polymers 372f
- confocal microscope 149f, 363
- conformational barriers of enones 197, 686
- conformational equilibria 208
- conformationally sensitive bands of proteins 356
- conformers
– differences in enthalpy and entropy 684f
– 1,3-difluoropropane 686
– matrix isolation 298, 304
- conical sample cell for Raman spectroscopy 146f
- conjugated C=C systems 197f
- conjugated dienes, *s-cis* *versus* *s-trans* 199
- conjugated polymers (CP) 377f, 381f, 387, 392
- contaminations in waste water 615
- continuous-flow helium cryostats 301
- continuous spectrometric control by extraction technique 603
- continuum resonance Raman scattering 476f
- convolution of interferogram by boxcar function 620
- Cooley-Tukey algorithm 620
- coordinate systems 450
- coordination number 230f
- Coriolis coupling 262, 268, 451, 667
- Coriolis resonance 292

- correlation bond order / force constant for C-C bonds 244, 453
- correlation diagram molecule/site/factor group 58, 319
- correlation field interaction 304, 317 *see also* factor group
- Cotton and Krahanzel, carbonyl frequencies 243
- Cotton effect, absorption- (ACE), reflection- (RCE) 336, 341f, 582
- Coulomb force constants 34f
- coumarin 22
- couplet 551
- coupling of oscillators 32
- effect of bond angle 227f
 - effect of mass 229
- CP *see* conjugated polymers
- $\text{Cr}(\text{CO})_5$ 250
- critical temperature /pressure 641
- CrO_4^{2-} 238
- cross-sections of Raman bands 117f, 295f
- crude oil, Raman spectrum 158
- cryo pumping 301
- cryochemistry in a matrix 309f
- cryocooler 174
- Cryolect 305
- crystal quartz, properties 127
- crystals, vibrations in 44ff, 161, 247, 314f, 317, 458
- CS_2
- force constant, bond distance, and bond energy 246
 - IR and Raman spectrum 221, 225, 607
 - Raman scattering cross section 288, 295f
- CsBr , properties of crystals 129
- CSe_2 , IR 249
- CsI , properties of crystals 129
- CSRS (coherent Stokes Raman spectroscopy) 167
- C-type band of near prolate top 273
- cumulated C=C=C bonds 197, 199f
- Curie-Weiss law 399
- cw CARS spectrometer 179
- C-X bonds ($X = \text{Cl}, \text{Br}, \text{I}$) characteristic frequency 207
- cyclic molecules 30, 202f, 205
- cycloaddition 654f
- cyclobutane, point group 703
- 1,3-cyclohexadiene, IR and Raman spectrum 200
- cyclohexane
- NIR spectrum 141
 - point group 704
- cyclooctyne, IR and Raman spectrum 203
- cyclopentadienyl-anion, point group 703
- cyclopropane
- normal vibrations 205
 - point group 703
- cyclopropenes, characteristic vibration 196
- cytochrome 361f, 636
- 2D
- mapping 150
 - scanning techniques 148
- D_2 , Raman scattering cross section 296
- DAC *see* diamond anvil cell
- dc part of interferograms 550
- DCID (dimensionless circular intensity difference) 561
- DCO *see* degenerate coupled oscillator model
- Debye screening length 376
- decadic absorption coefficient 17
- decision limit 116
- deformation force constants 242
- deformation vibrations 12, 192, 448
- degenerate coupled oscillator model (DCO) 551
- degenerate vibrations 44
- degree of freedom, motional 12, 33
- degree of order (liquid crystals) 325
- density of a substance 641
- depolarization ratio 25f, 50f, 161, 236
- deprotonation (and reprotonation) of Schiff base 631
- depths profiling 602
- detection limit 116f, 130, 612f
- detection of pollutants 431, 433, 603ff
- detectivity 107
- detectors 2, 106f, 126f, 136
- detergents, non-denaturing 357
- determination limit 116
- determination of the cell thickness, interference fringes 431
- deuterated poly(ethene) 607
- deuterium exchange rate of nucleic acids 351f
- diacetylene, resonance CARS 508
- diamond
- anvil cell (DAC) 640f,
 - normal frequencies 248, 456
 - properties 129
- diatomic chain, vibrations 314
- 1,ω-dibromoalkanes, NIR 535
- 1,1-dichloroethane, IR and Raman spectrum 200
- 1,2-dichloroethane, IR and Raman spectrum 206
- dichloromethane, IR and Raman spectrum 36
- dichroism 59, 330ff, 582, 592

- circular, Mueller matrix 88
- linear, Mueller matrix 85, 88
- dielectric constant 573, 578, 595
- dielectric mirror 584
- Diels-Alder reactions, high pressure 653
- dienes, conformation 197f
- difference spectrum 302, 418, 441, 626ff
 - proteins 357, 618f
- difference tones 33
- differential Raman scattering cross section 151f, 165, 171, 295f
- diffraction pattern 68, 70
- diffuse reflection techniques 430, 598ff
- diffusion coefficient 611
- diffusion halo 149
- dihedral plane 41
- dimethyl sulfide, IR and Raman spectrum 218
- dimethyl sulfoxide, IR and Raman spectrum 218
- dimethylacetylene, Raman scattering cross section 295
- Dirac, prediction of Raman effect 3
- directional cosines 46
- director (liquid crystals) 325
- discrimination of enantiomers 337
- dispersion
 - of frequencies of a chain molecule 31, 38, 315
 - of refractive index, anomalies 578
- dispersive instruments 68f, 619
- dispersive power (prism) 72
- disulfides, characteristic vibration 215
- di-*tert*-butyl peroxide, decomposition 652f
- divided spinning cell 152
- DNA 345ff
- dodekahedron 39, 709
- D₂O, IR and Raman spectrum 221
- doped conjugated polymers 378ff, 395
- Doppler effect in IR gas spectra 257
- double beam spectrometer 3
- double minimum potential 268
- double spectrograph 137
- DP (dynamic polarization) model 553
- drug - DNA interaction 354f
- dynamic coupling 320
- dynamic polarization model 553
- dynamics of the fluid state under high pressure 641f
- ECD (electronic circular dichroism) 543
- effective medium approximation (IR reflection) 584
- effective solid angle (spherical cell) 144
- effective thickness (ATR) 605
- effective volume (Raman scattering) 149
- efficiency of the Raman process 465
- eigenvalues 447
- elastic scattering 18
- electrical anharmonicity 17, 26, 518
- electric dipole interaction tensors (optical activity) 565
- electrochemical doping 395
- electrodes for SERS 493
- electromagnetic enhancement of SERS 491
- electronic Raman scattering 285, 376
- electrooptical theory 460
- electrostatic interaction 34f, 458
- element-element frequency (third period) 238
- element-hydrogen vibrations 226
- elements of point group 45
- ellipsoids, polarizability and refractive index 317f
- ellipsometric ATR measurement 595
- ellipsometric parameters 577, 589f
- ellipsometry 332, 344, 585, 589, 592
- elliptical polarization 78, 578
- emission spectra 99f, 124, 132, 134, 156f, 668f
- emissivity of tungsten wire 124
- emittance 99
- enantiomers, discrimination, purity 337
- end-on arrangement 148
- endrin, IR and Raman spectrum 204
- energy density 64
- enrichment by membrane extraction 603ff
- enthalpy
 - of conformers 686f
 - of dimerization (AlBr_3) 691
- entrance slit 69f, 74, 143
- entropy
 - change 306, 687
 - information theory 109
- environmental effect on IR absorption 289
- equilibrium rotational constants 279
- ErBa₂Cu₃O₇, Raman lines, 405
- α -error (limit of detection) 116
- β -error (limit of detection) 116
- error function 415
- escherichia coli* 371
- ethane
 - point groups 698, 704
 - torsional Raman spectrum of partially deuterated 292
- ethanol, NIR spectrum 141
- ethene
 - derivatives, characteristic frequencies 196

- overtone spectrum 530
- point groups 698, 702
- polymerization, NIR spectrum 540
- Raman spectrum 294
- Eulerian angle of pure rotation 328
- evanescent wave 575, 593, 604
- excitation profile, resonance Raman effect 467, 475, 485
- excited state properties 482, 485
- exhaust fumes, monitoring 224, 434
- external reflection 392f, 586
- external standards 424
- extraordinary wave 318

- F matrix 243
- F_2 , molecular constants for the electronic ground state of 285
- F_2 , Raman scattering cross section 296
- fabric additives 442
- Fabry-Perot etalon 76f, 184
- factor analysis for proteins 357
- factor group 37, 53, 247f, 317, 404
 - splitting 37, 58f, 194, 317
- Fano effect 400
- Fano line shapes 375
- far-infrared gas cell 660
- far-infrared spectrum 15
- fast Fourier transform algorithm 620
- fast reactions, investigation of 617, 623, 626, 662
- FC *see* Franck-Condon
- $Fe_3(CO)_{12}$ 236
- Fellgett advantage 75, 120
- femtosecond time-resolved CARS 177, 505
- Fermi resonance 33, 292, 518, 527
 - of CCl_4 227
 - of CO_2 227, 288
 - notation 263
 - of $S=Si=O$ 227
- Fermi triad, NIR spectrum of CO_2 529
- Fermi-Dirac statistics 265
- ferricytochrome 370
- ferrocene, point group 705
- ferroelectric modification of thiourea 60
- FHF⁻ frequencies 249
- fiber bundles for Raman spectroscopy 103ff, 146ff
- fiber optics 103ff, 519, 614
- field enhancement, reflection at grazing incidence 597
- finesse 76
- fingerprint region, of nucleic acid spectra 356
- finite field perturbation (FPT) theory 462f

- first-order reactions 632
- fixed partial charge (FPC) (model for VCD) 552
- flash pyrolysis in matrix 306
- flow-through arrangement (spherical Raman cell) 145
- fluid phase spectroscopy 642, 648
- fluorescence 14, 465
 - reduced by filtration 161
 - spectrum of a cyanine dye 158
- fluorine combustion analysis 224
- fluorite, properties of 127
- folded-BOXCARS 181
- food, Raman spectrum 220
- force constants 10, 226, 242f, 446f
 - of carbon-carbon bonds 10, 244
 - of CO_2 and CS_2 228
 - derived from lattice modes 247
 - estimation of 34
 - of PA (polyacetylene) 392
 - physical significance 227, 230, 244, 453
- forward-scattering arrangement 141f, 147
- Fourier-transform spectrometers 75, 125, 518, 589, 619f, 640
- four-wave mixing process 169
- FPC *see* fixed partial charge
- FPT *see* finite field perturbation theory
- Franck-Condon
 - factors 471f
 - integral 377
 - overlap integral 479
- Fraunhofer lines 1
- free carriers, infrared and Raman spectroscopy 373, 400, 410
- free enthalpies of condensation 610
- free-radical polymerization
 - of ethene, NIR spectra 658
 - of styrene, NIR spectra 541
- frequencies
 - difference IR spectrometer 184
 - doubled radiation (hyper Rayleigh scattering) 163
 - of matrix-isolated molecules 304
 - of metal carbonyls 233
 - of model molecules 9, 26ff, 225f
 - of molecule in a crystal lattice 38
- Fresnel rhombus 97, 173
- Fresnel's equations 92, 574, 582, 585f
- FSeSeF, photolysis, matrix isolation 308f
- FSSF isomerization, matrix isolation 308
- FTIR reaction mechanism studies 618
- FTIR techniques 619f

- FT-NIR atlas 518
FT-Raman spectroscopy 4, 136, 143, 156, 161, 361, 637f
fullerenes 39, 407f, 709
fullerite crystal 408
fused silica, properties of 127
fuzzy logic 114
- GaAs Raman scattering 401
gallium arsenide, properties of 128
gangliosides 371
gas phase IR and Raman spectroscopy 253f
gases
– infrared spectra 256ff
– Raman scattering cross sections 295
– Raman spectra 277ff
gaskets 640
GAUSSIAN 455
Gaussian
– distribution 113
– line profile 257
Ge semiconductor detector 153
 GeCl_4 , Raman scattering cross section 296
gel-like to liquid crystalline phase transitions 366
general valence force field (GVFF) 243, 304, 451
geometrical conductance 66
geometrical slit width 71
germanium, properties of 128, 606
GF matrix method, calculation of normal frequencies 248, 456
giant laser pulses 26, 162f, 464f
GIS *see* grazing incidence spectroscopy
Glan-Foucault prism 91
Glan-Thompson polarizer 91, 173
glass temperature 605
globar (glow bar) 124
glucacon 358
glycine, IR and Raman spectrum 217
glycolipids 371
glycophorin 370
G-matrix 242f
Golay cell 126
Goos-Hänchen effect 575
Gordy's rule 454
gramicidin 368f
grating spectrometer 3, 68ff, 124, 136
grazing incidence spectroscopy (GIS) 598
great orthogonality theorem 50
grey body 124
grid polarizers 93f
groove binding drugs (DNA) 354f
- grooves, of gratings 69
group theory 41, 44
GTPase activity 637
guest molecules in stretched polymer foils 334
GVFF *see* general valence force field
- H_2 , Raman scattering cross section 296
half-spheric mirror 146, 148, 150
half-wave plate 95
halfwidth parameter 257
halobacterium halobium 360, 626ff
halogen lamps 124
handcdness 79, 334, 339
– of induced cholesteric solution 336
harmonics 33
'harmonic' vibration 10f
 HBr , Raman scattering cross section 296
 $\text{H}_2\text{C}=\text{CH}_2$, force constant f(CC) 238
HCl
– Raman scattering cross section 296
– Raman spectrum of 278f
 HClO_4 , matrix-isolated species 303
HCN, point group 710
head space analysis, by membrane method 615
heatable cell 659
Heisenberg, prediction of Raman effect 3
helical twisting power, of induced cholesteric solution 336f
helical type of nucleic acids characterization by IR and Raman spectroscopy 347
 α -helix 356f
Hermann/Mauguin symbols 41, 695ff
Herschel 1
Hertzian dipole 23
Herzberg-Teller expansion 376, 470
heterodesmic lattices 53
 β -1,2,3,4,5,6-hexachlorocyclohexane, IR and Raman spectrum 204
 γ -1,2,3,4,5,6-hexachlorocyclohexane, IR and Raman spectrum 204
hexagonal crystal system 318
hexamethylene diisocyanate, IR and Raman spectrum 201
hexamethylenetetramine, lattice modes 61
1-hexyne, IR and Raman spectrum 203
2-hexyne, IR and Raman spectrum 203
HF, abundance of 225
HF complexes, IR spectra 304
 HF_2 IR spectrum 249
HF, Raman scattering cross section 296
 $\text{Hg}(\text{CN})_2$, complexation of 250

- III, Raman scattering cross section 296
- high frequency conductivity 394
- high pressure techniques, application of 640ff
- high resolution
 - CARS spectrum 502
 - cw-CARS 178
 - inverse Raman spectrum 512
 - IR gas spectra 257
 - photoacoustic Raman (PARS) spectrum of CO₂ 515
 - quasi-cw inverse Raman spectrometers 184
 - Raman spectra 187
 - stimulated Raman spectroscopy 183
- high temperature
 - high pressure cell 643
 - species, matrix isolation 305
 - superconductor 402
- higher-order Raman spectral excitation studies 167
- higher-order stimulated Stokes emission 166
- Hilbert transformations 582
- HN=C=NH, FTIR 249
- H₂O
 - IR and Raman spectrum 221
 - point group 699
 - Raman scattering cross section 296
 - Raman spectrum of 295
 - rotation-vibration bands 273f
- H₂O₂
 - matrix isolation in nature 298
 - point group 696
- holographic grating 69
- homeotropic alignment 325, 334
- homodesmic lattices 51
- HOMO-LUMO transition 391
- HONO, trace impurities in air 225
- Hooke's law 9
- horizontal symmetry plane 40
- hormones, interaction with phospholipid bilayers 370
- HORSES 167
- H₂S, Raman spectrum of 294
- H₂S, Raman scattering cross section 296
- H₂Si=CH₂, under matrix conditions 306f
- hot-band transitions 33, 256, 288f, 298, 304, 526, 667
- Hund's coupling cases 282
- Huygens' principle 101
- hydrides, M-H vibrations of 226
- hydrocarbons in water, IR spectroscopy 431, 603f
- hydrogen chloride, molar absorption coefficient at various densities 649
- hydrogen fluoride, proton-donor 304
- hydrophobic substances 603f
- hyper Raman spectroscopy 163f, 172f, 466, 498, 695
- hysteresis curve in first order phase transitions 683
- icosahedron, point group 39, 709
- identification of samples 322
- identity
 - element 44
 - operator 40
 - test 441
- IDSRS *see* ionization detected stimulated Raman spectroscopy
- IF₇, point group 703
- IM *see* inertial motion
- image intensifier 561
- imaging elements 100
- improper rotation 46f
- impurities of oxygen and carbon in Si wafers 437
- inclusion compounds 54
- index ellipsoid 319
- induced cholesteric solution 336f
- induced dipole moment 21, 319
- induced handedness 337
- inductive properties, reflected in the frequencies 233
- inelastic impact 13
- inertial motion 553
- inertial tensor 258
- information
 - channel 108
 - contents of vibrational spectra 412
 - handling 122
 - theory applied to analytical chemistry 111
- infrared
 - absorption 14
 - absorption coefficients 134
 - active vibrations 49
 - emission spectroscopy 134f, 602
 - high-pressure techniques 642f
 - intensity 18, 131f, 459
 - linear birefringence 332
 - molar decadic absorption coefficients of organic molecules 133
 - night vision instrument 162
 - and Raman spectra of calcite and aragonite 321
 - and Raman spectroscopy of chiral substances 543f
 - reflection techniques 572

- refractive indices 332
- rotatory dispersion 336
- rotatory dispersion of carvone 544
- spectra uniaxial crystals 318
- spectrometers 63, 123ff
- spectroscopic ellipsometry 590
- spectrum 15, 16f
- trace analysis 305
- inner vibrations, number of 52
- inorganic substances 223f
- in-plane and out-of-plane deformations 33
- instrument line shape functions 262
- integral
 - absorption coefficient 613, 649
 - Napierian absorption coefficient 18
- integrated absolute normalized Raman scattering
 - cross sections of liquids 151
- integrated intensities 419ff, 524
- intensity
 - parameters, transferable molecular 460
 - of a Raman band 155, 414
 - steps, resolvable 113
 - of Stokes and anti-Stokes lines 19, 25, 153, 671f
 - of vibrational bands 239f
- interaction force constants 12, 242, 454
- intercalating drugs 354f
- interdigitated phase 366f
- interfacial modes 365
- interference
 - filters 76f, 125, 617
 - pattern 68
- interferogram 75, 620
- interferometers 73f, 136, 619
- intermediates, of photocycle 626
- intermolecular and intramolecular interactions 691
- intermolecular forces 309
 - constants 34
- internal coordinates 13, 237, 448
- internal field factor 24, 152, 295
- internal modes 317
- internal reflection 593
 - element 603, 605
 - spectroscopy 393
- internal standard method 426
- internal valence force field 451
- international notation of symmetry elements 40, 695f
- intracavity Raman experiment 294
- intramolecular reactions 632
- invariants of the polarizability 25, 565
- inverse element 44
- inverse Raman scattering (IRS) 167, 182f, 297, 511
- inverse Raman spectroscopy of water vapour 294
- inversion
 - doubling 270
 - operator 40
- ion exchangers, Raman spectrum 159
- ionization detected stimulated Raman spectroscopy (IDSRS) 167, 169, 186, 292, 515
- ionization detected stimulated Raman spectrum of benzene 516
- ionophores, interaction with phospholipid bilayers 368f
- IR absorptions of trapped species 298
- IR cell for the temperature range -180°C to +250°C 660
- IR difference spectroscopy 439
 - for quality control 438
- IR-CD (IR-circular dichroism) 543
- irradiance 64
- IRRAS *see* reflection-absorption IR spectroscopy
- irreducible representations 47f
- IR-reflectance on $\text{YBa}_2\text{Cu}_3\text{O}_7$, phonon anomalies 406
- IRS *see* inverse Raman scattering
- Irtran 1[®] MgF_2 , properties of 127
- Irtran 2[®] ZnS , properties of 128
- Irtran 3[®] CaF_2 , properties of 127
- Irtran 4[®] ZnSe , properties of 128
- Irtran 5[®] MgO , properties of 127
- isomerization, of poly(acetylene) 387
- isomers, matrix isolation 298
- isoprene, IR and Raman spectrum 198
- isothiocyanate, IR and Raman spectrum 201
- isotopic substitution 234, 237, 240
- isotopically substituted molecules, matrix isolation 298, 304
- isotopomers of oxygen 282
- isotropic sample 88
- IUPAC definitions 64f, 115, 695f
- Jacobian matrix 451
- Jacquinot
 - advantage 75f, 124, 618, 625, 637
 - stop 74, 124, 143
- Jones vector 79
- Joule-Thompson expansion cycle 301
- Kaiser, limit of detection 115
- ketones, NIR spectra 537
- KHD *see* Kramers-Heisenberg-Dirac

- kidney stones 322
 kinematic viscosity 612
 kinetic analysis 631
 kinetic energy 445
 Kirchhoff's law 99f, 132f, 156, 160, 668
 Knudsen cell 300, 305, 310
 Kohlrausch 4
 Kramers, prediction of Raman effect 3
 Kramers-Heisenberg
 – dielectric function 375
 – effect 3
 Kramers-Heisenberg-Dirac (KHD)
 – relation 468, 473, 481
 – formulation 481
 Kramers-Kronig
 – integral equations 331
 – relation 375, 582, 585f, 589, 595
 KRS-5, 593, 606
 Kubelka-Munk theory
 – diffuse reflection 598f
 – Raman intensity 139, 149, 156

 Lambert-Beer law 17, 117f, 154, 413f
 Landsberg 3
 Langley 1
 Langmuir-Blodgett films 598
 Lapis lazuli, matrix isolation in nature 298
 laser ablation method for preparation of colloids for SERS 494
 laser spectroscopy 257
 lasers 77f, 136
 lattice vibrations 61, 190, 247, 317
 v^4 -law 24, 151f, 295
 laws of Planck and Kirchhoff 98, 132, 155, 160
 L-cysteine, IR and Raman spectrum 217
 L-cystine, IR and Raman spectrum 217
 LD *see* linear dichroism
 leak rate of the matrix-isolation assembly 300
 leakage (truncation of interferogram) 620
 left-handed cholesteric helical structure: positive reflection Cotton effect 341
 Lehrer 3
 Lennard-Jones potential 10, 457
 lens equation 67, 101
 librations 38, 57, 61, 317
 – number of 52
 LIDAR (*light detecting and ranging*) 434
 light pipe 97, 131, 146, 154
 light-induced proton-pump 359f, 369, 618f
 limit of detection 115f, 130, 612f
 linear bending coordinate 448

 linear birefringence (LB) 84f, 324, 592
 linear dichroism (LD) 84f, 324, 331
 – experiment 86
 linear polarization 78, 86, 89, 318, 545
 linear rotor 248
 line
 – intensities 671
 – splittings 282
 lipid A 371
 lipid bilayer 364
 lipophilin 357
 liquid crystals 323f, 366
 – comprehensive bibliography 324
 liquid-chromatographic fractions, detection of 600
 liquidlike state 649
 lithium fluoride, properties of 127
 living cells, confocal micro Raman spectroscopy 363
 local modes 518
 local symmetry force field 452
 localized molecular orbital (VCD) 552
 lock-in amplifier 545
 logarithmus dualis (information theory) 109
 longitudinal acoustical vibration 194, 316
 longitudinal optical vibration 284, 316
 long-range effects 322f
 loperamide 368
 Lorentzian function 113, 257, 375, 414, 422, 578, 623
 LO-TO splitting 316, 322
 I-type doubling 262
 Luft 3
 Lyddane-Sachs-Teller splitting 316
 lysozyme 358

 magic acids 688f
 magic angle 330
 magnesium fluoride, properties of 127
 magnetic field perturbation method 555
 magnetic vibrational circular dichroism (MVCD) of methane and ammonia 560
 magnesium oxide, properties of 127
 Maiman 4
 Malus, law of 90
 Mandelstam 3
 Martin-Puplett interferometer 550
 mass-selective interferometric IDSR 187
 mass-weighted Cartesian coordinates 447
 material dispersion 72, 102
 matrix effect 301
 matrix isolation, examples in nature 298

- matrix isolation/GC/FTIR system 305
matrix-isolated molecules 297ff
matrix-isolated perchloric acid 303
matrix-isolated species, isotopic substitution 240
Maxwell's relation 374, 574
MCT detector 126, 619
mean square amplitudes 451
mean-field approach 327
Me-B=N-Me 250
mechanical anharmonicity 17, 26, 518
mechanically caused coupling, in the species F-H-F⁻ and F-Xe-F 227
mechanism of chemical reactions 617
Mecke's nomenclature of characteristic vibrations 33, 192
melamine, infrared and Raman spectrum 36
melittin 371
melting point capillary 145
melt-like regions 651
membrane
– processes 609, 613f
– proteins 357, 370, 618
– structure 364
mercury arc lamp 124, 136
mercury-cadmium telluride detector 126
mesomeric properties, reflected in the frequencies 233
mesophase 323
metabolites, discrimination 343
metal 372ff
– aggregates, matrix isolation 310
– carbonyls 236
– molecules, matrix isolation 310
– nitrides, characteristic IR frequencies 252
– oxides, characteristic IR frequencies 252
– sols, substrate for SERS 494
– and superconductors, infrared and Raman spectroscopy 401f
metal-carbon bonds 233
metal-metal bonds 226, 252
metallic reflection 392
metalloporphyrins 361
methane *see* CH₄
methoxyacetonitrile, IR and Raman spectrum 201
3β-methoxyandrost-5-en-17-one, IR and Raman spectrum 219
methyl disulfide, IR and Raman spectrum 216
methyl vinyl ether 304
N-methylamide, IR and Raman spectrum 211
3-methyl-1,2-butadiene, IR and Raman spectrum 200
methylsulfone, IR and Raman spectrum 218
MgCl₂ 235
Michelson interferometer 1, 73, 76, 124, 132, 138, 619
micro analysis 131
micro Raman spectra 151
micro scanning arrangements 148
microscopes 131, 148
microstructure of polybutadiene 439
microwave spectroscopy 256
Mie scattering 598
mineral pigments 322
minimum detectable concentration 116
MIRSI *see* molar integrated Raman scattering intensity
Mn(CO₅)Br, CO-vibrations 243
MnO₄⁻, totally symmetric breathing mode 238
Mo(CO)₆, matrix isolation 305
Mo₂Cl₈⁺, metal-metal bond 239
model calculation 445
modes, standing waves 78
modulation of light by a molecular vibration 22
molar absorption coefficient
– of CO 520, 525
– of ethene in the IR/NIR 656
molar integrated Raman scattering intensity (MIRSI) 651
molecular
– chirality 40, 334f, 344f
– complexes 304, 309
– cross section 117f
– crystals 37, 41f, 54f
– dipole moment, modulation 15f, 20
– enhancement of SERS 492
– force field 256, 451f
– geometry 305
– polarizability 15, 565
– symmetry 42, 695ff
moment of inertia 259
monitoring atmospheric trace gases 124
monochromators 76, 137
monolayer 573, 596
Mo≡N vibration 252
moon, reflection spectrum 2
MOPAC 455
Morse function 10
movable piston 645
moving mirror 68, 619
Mueller matrices 83f, 86, 89
Mulliken rules 695
multichannel advantage 121

- multi-component analysis 8, 412, 427f
- multiple beam interferometer 77
- multiple bonds
 - between atoms of higher periods 245
 - stabilized under matrix conditions 306
- multiple choice questions 110
- multiple monochromators 137
- multiple reflection arrangements 142, 145, 147
- multiple standards 425
- multiplex
 - advantage 75f, 120f, 124, 619, 625
 - CARS 176
 - disadvantage 75, 121, 138
- multiplication table 45
- multi-ROA instrument 564
- MVCD *see* magnetic vibrational circular dichroism
- myelin protein 357
- myoglobin 358
- myotoxin 371

- N₂
 - absolute differential Raman scattering cross section 295
 - molecule vibration 226
 - Raman scattering cross sections 296
- NaCl lattice, force constant 248f
- nanoseconds time resolution 618
- Napierian
 - absorption coefficient 18, 139f
 - Raman scattering coefficient 139
- naphthalene, lattice vibrations 61
- natural line width 253
- ND₄, Raman scattering cross section 296
- Nd:YAG laser 136
- n-doped poly(acetylene) 382
- near-infrared *see* NIR
- nematic liquid crystals 325
- nematic mixture, reflection Cotton effect 341
- nematogenic molecules, structures 327
- neon matrix experiments 301
- NEP (noise-equivalent power) of detectors 107, 113, 118, 126, 153
- Nernst
 - diffusion layer 604, 611f
 - glow 124
- neutral element (group theory) 44
- neutron scattering, inelastic 14
- Newton's law 9, 446
- NH₃
 - character table 699
 - high resolution IR spectrum 268f
- Raman scattering cross section 296
- rotational Raman spectrum 292
- Nicol polarizer 91
- NIR
 - diffuse reflectance techniques 518f
 - high-pressure techniques 642
 - MIR, and FIR spectrometers 123f
 - molar absorption coefficient of n-alkanes 532
 - spectra of CO₂ 526f
 - spectrum of ammonia 530
- NIR-FT-Raman technique 4, 136, 143, 156, 161, 361, 637
- NiSO₄ single crystal NIR absorption spectra 560
- nitriles
 - IR and Raman spectrum 202
 - NIR spectra 537
- nitro groups, characteristic frequencies 215
- nitrogen, absolute differential Raman scattering cross section 295
- N-N single bonds 226
- N→O transition of BR 631
- NO
 - Raman scattering cross section 296
 - rotation-vibration features 261
- NO₄, structure deduced from Raman spectra 251
- N₂O
 - IR spectrum 262
 - Raman scattering cross section 296
 - trace impurities in air 225
- noble gases, matrix isolation 298
- noise 106f, 116, 121
- non-classical Raman spectroscopy 465ff
- non-dispersive spectrometer 3, 126
- non-linear coherent Raman spectroscopy 465ff
- non-linear effects 26
- non-linear Raman spectroscopy 135, 162f, 498f
- non-reversible enrichment 613
- non-rigidity of molecule 259
- normal coordinate 7, 13, 48, 236
 - calculation, program packages for 451
- normal frequency 7
- normal vibrations 7, 13, 48, 236
- normalized Stokes vectors 82
- normalized detectivity for different detectors 107
- north type sugars (DNA) 346, 348, 350, 353f
- notation of Hermann/Mauguin 40, 695f
- notch filters 138
- nucleic acids
 - B→A conformational transition 348
 - IR and classical Raman spectroscopy 345
 - line markers of A, B and Z conformers 347

- nucleophilic substitution of alcohols in magic acid 689
nucleoproteins 362f
numerical aperture 66, 104
nylon, vibrational spectra 193
Nyquist frequency 620
nystatin 368f
- O₂
– inverse Raman spectrum the Q-branch 283f
– Raman scattering cross section 296
– Raman spectrum of the Q-branch 283
- O₃, Raman scattering cross section 296
- OAsCl, matrix isolation 306
- objets d'arts, specular reflection 589
- oblate symmetric top 267, 290
- oblate top 258
- O-branch 280
- O=C=C=C=C=O, structure 249
- OCN and -NCO, characteristic vibrations 234
- OCS, trace impurities in air 225
- octyl ether, IR and Raman spectrum 211
- oligomer conformations, micro Raman spectroscopy 353
- O₃M₆-O-MoO₃²⁻, structure obtained by vibrational spectroscopy 252
- oncogen FTIR 637
- ONF, Raman scattering cross section 296
- on-line analysis 525, 538, 603, 658
- OPCI, matrix isolation 306
- O₂PCl, produced by matrix photolysis 313
- O=P-F, force constant, bond distance 245
- optical activity
– of a fundamental transition 567
– prove 337
– tensors 565
– in the UV/VIS 582
- optical anisotropy of nematics 325
- optical branch 38, 315
- optical cells for high pressure vibrational spectroscopic studies 642
- optical conductance 65ff, 147
– of interference filters 77
– of interferometers 73f, 76
– of prism and grating spectrometers 72f
– per wavenumber 67
- optical constants of crystals 318
- optical elements, imaging and conducting 100
- optical fibers 97, 146f, 605
- optical glass BK7, Raman spectrum 160
- optical high-pressure cell 644f
- optical modes 247f
- optical properties of IR windows 127f
- optical rotatory dispersion (ORD) 343, 543
- optical spectrometers, components 97
- optically active compounds, characterizing the chirality 337
- optically active sample, Mueller matrix 87
- optimization of NIR Raman spectroscopy 144, 148, 161
- optimum thickness of crystal powders for Raman spectroscopy 142
- optothermal effect 126
- ORD *see* optical rotatory dispersion
- order of a group 44
- order parameter 326, 329
- order-disorder phase transition 322, 381
- ordinary wave 318
- organic substances 189f
- orientational order 323, 336
- orientation by strain 195
- oriented gas model 37, 53, 59
- orthogonal transformations 46
- orthorhombic crystal 56, 318
- OsBr₆²⁻, totally symmetric breathing modes 238
- oscillator strength 374, 407
- O=Si, force constants, bond distances and bond energies 246
- O=Si=O, force constants, bond distances and bond energies 246
- O=Si=S, force constants, bond distances and bond energies 246
- out-of-plane bending coordinate 448
- out-of-plane deformation 33
- overtones 2, 256, 296, 480f, 518
- oxamide 61
- oxidation number and force constants 231f
- oxidative degradation 692
- oxidic superconductors, crystal structure 403
- ozone hole, chemical processes leading to 313
- ozonide ion 311
- P and R branches 259, 520, 665
– overtones 522f, 529
- PA *see* polyacetylene
- PANI *see* polyaniline
- parallel band 262, 267, 330
- PARS *see* photoacoustic Raman spectroscopy
- PARS-CARS 185
- passive transformation 46
- PAT *see* polyalkylthiophene
- PDA *see* polydiacetylene

- Pd(CO)₄ 235
 PDNAS *see* poly(di-n-alkylsilane)
 PDNHS *see* poly(di-n-hexylsilane)
 p-doped poly(acetylene) 382
 p-doped Si, Raman spectrum 400
 peak absorption coefficient 613
 peak area measurements 420
 Peltier element 126, 659
 PEM *see* photoelastic modulator
 penetration depth 594, 604f
 pentagonal dodecahedron, point group 39, 709
 perchloric acid, matrix-isolated species 303
 permittivity 573
 perovskite fluorides, calculation of normal frequencies 456
 peroxides, characteristic frequencies 215
 perpendicular band 262, 267, 330
 PHAM *see* poly(heteroarylenemethin) phase
 – correction 621
 – equilibria 519, 642
 – plate with optical retardation of $\pm\pi/2$ 544
 – transition 322, 324, 366, 399f, 658
 – transitions of thiourea 59
 phenylalanine 358
 phonon spectra of DSP (distyrylpyrazine) recorded during polymerization 63
 phospholipids 364, 367, 369f
 photoacoustic effect 3, 602
 photoacoustic Raman spectroscopy (PARS) 167, 185f, 513
 photochemical reactions in a matrix 312
 photocycle of bacteriorhodopsin 28, 621, 634
 photodiode arrays 138
 photodiodes 106
 photoelastic modulators (PEM) 95, 544ff, 590
 photoelimination, in low-temperature matrices 313
 photo-induced absorption 395f
 photolysis 302, 310, 625
 photomultipliers 106
 photophone 1
 photosynthesis 487, 636
 phototransistors 106
 picket fence effect 620
 picosecond-pulsed laser 625
 piezoelectric transducers 545
 pigments, IR and Raman spectra 355, 599
 pinch mode 409
 pinene, VCD 558f
 pitch 334, 336, 339
 PITN *see* poly(isothianaphthene)
- Placzek's theory 4, 24, 152
 planar or homogeneous alignment (nematic liquid crystals) 325
 Planck function 99, 124, 132f, 157
 Planck's and Kirchhoff's law 98, 156, 160
 plane of observation 23
 plasma frequency 374, 491
 plasmon 491
 plastic selenium 595
 plasticizers 608
 Platonic bodies 39, 707ff
 pleochromism of the infrared bands 195
 PMeT *see* poly(3Me-thiophene)
 PMMA 587
 p-nitrobenzoic acid, IR and Raman spectrum 210
 Poincaré sphere 79, 591
 point groups 41, 695ff
 – algorithm for the determination 42
 Poisson statistics 75
 polar fluids, vibrational spectra of 648
 polarity of the bond 230, 245
 polarizability
 – of crystalline phase 317
 – tensor 21, 25, 318, 473
 – theory 4, 26
 – volume 25
 polarization
 – CARS 182
 – optics 89
 – rotator 84, 95
 – sensitive sample, Mueller matrix 84
 – types of 78
 polarized radiation 50, 78ff, 325
 polarizer 548
 – types of 83f, 89f
 polarizing interferometer 558, 564
 polaroids 91
 polarons 380f
 – states 396
 – type ring mode 389
 polar tensors 462
 polar vector 51f
 poly d(A-T), FTIR spectra 349
 poly(acetylene) (PA) 378f, 382
 poly(acetylene) n-doped, IR bands 393
 poly(alkylthiophene) (PAT) 379
 poly(aniline) (PANI) 379, 382, 384, 389, 393, 395
 polycations, effect on charged lipids 369
 polychromator 137f
 polycrystalline silicon, windows 643
 polycrystalline silver halide, fiber for continuous

- extraction technique 614
poly(diacetylene) (PDA) 379, 382, 384, 488
poly(di-n-alkylsilane) (PDNAS) 379
poly(di-n-hexylsilane) (PDNHS) 382, 384, 387f
poly(dimethylsiloxane) 193, 607, 608
polyenes 199
poly(etheresteramide) 607
poly(ethylene) 129, 192ff
poly(heteroarylenemethin) (PHAM) 379
poly(isothianaphthene) (PITN) 379, 382f
polymer chains 195
polymerization
– of ethene 657
– matrix isolation 310
polymers
– characteristic vibrations 192f, 195
– glass temperature 606
poly(3Me-thiophene) (PMeT) 382f
polynucleotides stretched as films 345
poly(octadecylsiloxane) 607f
poly(octylthiophene) 382
– IR bands 393
poly(p-phenylene) 382
poly(p-phenylenevinylene) (PPV) 379, 382, 393
poly(pyrrole) (PPy) 379, 382
poly(thiophene) (PT) 379, 383, 393
Porto's nomenclature 50, 319
potassium bromide, properties of 128
potassium chloride, properties of 128
potassium iodide, properties of 129
potential energy distribution, PED 451
potential functions 10f, 457, 686
Poulter's principle (high pressure cells) 643
Poynting vector 574
PPV *see* poly(p-phenylenevinylene)
PPy *see* poly(pyrrol)
PR separation 276, 666, 670
practical resolving power 68
precision of spectrometric analysis 115
preparative reactions in matrices 311
pre-resonance Raman effect 465f, 638
pressure-tuning FT-IR spectroscopy 641
principal moments of inertia 258
priority sequences, for determination of absolute configuration 337
prism spectrometer 1f, 72, 124, 136
processes interfering with the Raman spectrum 156
prolate top 258, 268
proper axis 40
proteins, IR and Raman spectra 355f, 368, 618f
proton pumping mechanism 626ff, 634
protonation, and force constants 231f
pseudo-diatomic species 237
PT *see* poly(thiophene)
pulsed CARS 175
pulsed deposition technique 301
pulsed light sources 626
pure rotational spectra of homonuclear diatomic molecules 280
pyroelectric detectors 126, 617
pyrolysis reactions, matrix isolation 307

Q-branch 262, 280, 289
QCPE 451
Q-switched ruby laser 172
qualitative analysis 224f
quality control 436f
quantitative analysis 115f, 224f, 411ff
quantitative *in situ* analysis 680
quantitative reflection spectroscopy 430
quantum chemical calculations 246, 462
quantum efficiency 106
quantum number 259, 671
quarter wave plate 95
quartz 642
– glass suprasil, Raman spectrum 160
– retarders 95
– soft mode 323
quasi-cw inverse Raman spectroscopy 183

radiance 64f
– of a Planck black body 132
– per wavenumber 67
radiant energy 64
radiant exposure 64
radiant flux 64f
– flowing from a hot to a cold Planck black body 132
radiant intensity 64
radiant power 64f
– of Raman lines 151, 153
– per solid angle and per wavenumber 98
radiation
– balance of a Raman scattering sample 153
– detectors 97, 106
– sources 97, 124f, 136
– sources, nomenclature of properties 64
RAIRS (reflection absorption IR spectroscopy) 598
Raman
– active vibrations 49
– bands of a chromophore 466
– cells for high-pressure 647

- circular intensity difference 544, 565
- high-pressure techniques 642
- lines, radiant power of 151f, 156
- microscopes 151
- module 125
- optical activity (ROA) 561f, 570f
- polarizability (resonance Raman effect) 469
- spectrometers 63, 135f
- spectrum 18f
- Raman effect 3, 13f
- Raman/exciting radiation ratio (crystal powders) 143
- Raman induced Kerr effect (RIKE) 167
- Raman/infrared atlas 143, 193ff
- Raman intensity 430, 459
 - of conducting polymers 391
- Raman overlap 474
- Raman scattering
 - cross section 24, 117, 151f, 295, 430, 489
 - effective volume 149
 - of crystal powders 139
- Raman spectra
 - of CH_3OH in magic acid 691
 - of crystals 318f
 - of electrolyte solutions 651
 - excited by different laser lines 15
 - in magic acid 689f
 - of nucleic acids 349
- Raman spectroscopy
 - advantage over IR methods 225
 - based on third-order susceptibilities 166
 - in the NIR range, special features 155
 - nonlinear 162ff
 - salt melts 251
 - sample arrangements optimization 143f
- rapid scan FTIR mode 621f, 626
- Rasetti 138
- rate constants 631f
- rate of polymerization 692
- Rayleigh
 - criterion 69
 - filter 76, 137f
 - scattering 14, 18, 75, 135f
 - wings 75
- Rayleigh's rule 32
- R-branch 259
- reaction
 - kinetics 679
 - mechanism of proteins 618
 - products, matrix isolation 306
- reactive molecules 223
- $\text{Re}_2\text{Cl}_8^{2-}$, metal-metal bonds 239
- $\text{Re}_2(\text{CO})_{10}$, low temperature FTIR and Raman spectra 251
- rectangular cell, for Raman spectroscopy 144
- reduced mass 9
- reflectance
 - anomalies 588
 - measurements, NIR 542
- reflection
 - coefficient (free carrier system) 374
 - Cotton effect 336, 341
 - losses 145
 - operator 40
 - standard (gold covered erasive) 600
 - technique 572ff
- reflection-absorption spectroscopy 598f
- refractive index 92, 127, 317
- relative normalized differential Raman scattering
 - cross section 295
- remote analysis 519
- remote sensing of temperature and species 503
- representation of a group 45f
- representative of an operator 45f
- resolvable channels, number of 113
- resolving power 68, 74
- resonance CARS spectroscopy 488, 507, 511
- resonance Raman spectroscopy (RRS) 26, 135, 226, 238, 358, 465ff, 482
 - selection rules 695
- resonance Raman spectrum of Se_3 in solid N_3 310
- resonance Raman theories 376, 390, 468f
- resonance-enhanced multiphoton ionization 515
- reststrahlen bands 572, 581
- retardation factor (deuterium exchange of nucleic acids) 352
- retarders 84, 86, 94ff
- retinal 361, 626, 634, 638
- reversal of the lines 668
- reversibly extracting medium 603
- rigid rotor-harmonic oscillator models 258
- rigid prolate top, rotational energy 267
- RIKE *see* Raman-induced Kerr effect
- ring current mechanism 555
- ROA *see* Raman optical activity
- Rocard 3
- rocking vibration 33, 192
- rotamers, matrix isolation 304
- rotating solid sample cell 661
- rotation operator 40
- rotational
 - constant 259

- cooling 276
- fine structure 236
- isomerism 658, 684
- modes 57, 277, 317
- partition function 664
- photoacoustic Raman PARS spectrum of CO₂ 514
- Raman spectra of N₂ and O₂ 282, 672
- Raman transitions, the selection rules 290
- temperature 664, 670f
- wave functions 265
- Zeeman effect 560
- rotational-vibrational lines 260, 277, 521
- rotations 12
- rotation-vibration
 - bands, notations 263
 - interaction 253f, 268
- rotatory strength 551, 555, 557
- rovibrational Raman spectrum 294
- RRS *see* resonance Raman spectroscopy
- R-SH groups, characteristic frequencies 215
- R-SO_n-R, characteristic frequencies 215
- rubidium, resonance absorption filter 138
- ruby fluorescence (pressure calibration) 640
- Ru₃(CO)₁₂, CO modes in 251
- rule of mutual exclusion 50, 194, 205, 254
 - pure rotational Raman spectra 292
- rules, of gratings 69
- S₃⁻, matrix isolation in nature 298
- S₈, point group 707f
- salmonella minnesota* 371
- sample
 - arrangements 97f, 138f, 145f
 - generation, for matrix isolation 302
 - temperature 25, 150
- sampling points, rate 620
- sapphire
 - cell 145
 - laser 136
 - properties of 127
 - Raman spectrum 160f
 - retarders 95
 - windows for high-pressure cells 642f, 647
- sarcoplasmic reticulum 357
- saturated isocycles, IR and Raman spectra 202
- Savitzky-Golay polynome 121
- S-branch 280
- S=C force constants, bond distances and bond energies 246
- scan
 - duration 622
 - length 620
- scanning micro arrangements for Raman spectroscopy 148
- scanning multichannel instrument 138
- scanning pulsed CARS 173
- scattering
 - activity 24
 - coefficient 141, 414
 - tensor 161
- Scheelite, IR and Raman spectrum of the anion WO₄²⁻ 247
- Schiff's base 626
- Schoenflies symbols 40f, 695ff
- Schrödinger, prediction of Raman effect 3
- Schubert factor 120
- scissoring vibration 33
- SCl₂ 235
- SCN and -NCS, characteristic vibrations 234
- scrambler 319
- S=C=S force constants, bond distances, and bond energies 246
- Se₃, resonance Raman spectrum 310
- sealing of high-pressure optical windows 643
- secondary standard 162
- secondary structures of membrane proteins 357f
- second derivative spectra of amide I band 357
- second order Raman bands of C₆H₆ and C₆D₆ 256
- secular equation 17, 449
- SeF, selenium fluorides 308
- SeF₆, Raman scattering cross section 296
- SeF₅OCN 234
- SEHRS *see* surface-enhanced hyper Raman scattering
- selection rules 44
 - for crystals 247
 - of gas spectra 278
- selective reflection 336f, 584
- selectivity, of detection 304
- self-absorption 669
- self-emission of the sample 668
- semiclassical polarizability theory 469
- semiconductor
 - array detectors 126
 - band gap filters 139
 - infrared and Raman spectroscopy 372ff, 399
 - lasers 124
 - quality control 436
- sensitivity γ (calibration curve) 115
- sensitivity and selectivity, matrix isolation 305
- sensor for real time and on-line control 603

- sequential spectrometers 136
- SERRS *see* surface-enhanced resonance Raman spectroscopy
- SERS *see* surface-enhanced Raman spectroscopy
- SEW *see* surface electromagnetic wave
- SF₂ 235
- SF₆
 - point group 708
 - Raman scattering cross section 296
- Shannon 108
- shape broadening 623
- β -sheet conformations 357
- shielding effect of free carriers 401
- short-lived species 306
- SiCl₄
 - breathing mode 236
 - Raman scattering cross section 296
- side chain melting 387
- Siebert's rule 34
- SiF₂, force constant bond distance 245
- sign conventions to describe the optical activity 341
- signal-to-noise ratio 106, 112, 115f, 424, 619, 625, 637
- silaethene, matrix isolation 307
- silent modes 163, 465
- silicon
 - compounds, double and triple bonds 246
 - properties of 128, 248, 606
 - substitutional carbon and interstitial oxygen as impurities 224
- silver bromide 128, 606
- silver chloride 128, 606
- silver halide, transmission of IR-fibers 614
- simple valence force field 34, 243
- simplified general valence force field 451
- simultaneous spectrometers 138
- single component analysis 424
- single crystals of YBa₂Cu₃O₇, polarized spectra 404
- single crystal spectroscopy 59f, 317f
- single particles, Raman spectroscopy of 151
- single standard methods 424
- singular value decomposition 632
- SiO, matrix-isolated 237
- SiO₂, dimer in solid argon 250
- Si-O-Si stretching 195
- SiS₂, produced by matrix photolysis 313
- SiSi force constants in silicon 248
- site directed mutagenesis 630
- site symmetry model 37, 56
- slit function 414
- smectic phase 323
- Smekal, prediction of Raman effect 3
- SnCl₄, Raman scattering cross section 296
- SnH₄, high resolution infrared and Raman spectroscopy 294
- Snellius' law of refraction 101, 573
- SO₂
 - force constant bond distance 245
 - Raman scattering cross section 296
- sodium chloride
 - properties of 128
 - refractive index 1
- soft modes 323, 400
- solid-state problems 247
- solvents
 - IR and Raman spectrum 222
 - without X-H bonds 146
- sonication 357
- SOS (sum-over-states)-method 463
- sources of background 155
- south type sugars (DNA) 346, 348, 350, 353
- space groups 41
- spacers 643
- spatial resolving power 149
- SPBr, matrix isolation 306
- specific rotation 337
- spectra
 - of N₂ and O₂ for temperature determination 672
 - of polymers 192f, 195
 - subtraction 302, 626ff
- spectral
 - apparatus 124f
 - band width/line width relation 119
 - libraries 587
 - optical conductance 67
 - radiance 63, 98f, 135, 668
 - resolution 119, 465, 622
 - sensitivity of NIR FT Raman spectrometer 156
- spectrograph 138
- specular reflection spectra 586
- spherical cell, for Raman spectroscopy 144f, 161
- spherical rotor 258
- spherical top molecules 270f, 292
- spinning cell 152
- spontaneous nonlinear Raman spectroscopy 163
- spray-on nozzle 301
- SPSIM program package 460
- squaric acid, phase transition 322
- SRGS *see* stimulated Raman gain spectroscopy
- SSF₂, matrix isolation 308

- S=Si=S force constants, bond distances, and bond energies 246
standard addition method 425
standard analyte solutions 416
standing wave 78, 596
Stark spectroscopy 264
static FTIR technique 621f, 625, 628
step scan mode 510, 625f, 640
Sterling principle 301
stimulated anti-Stokes Raman scattering, momentum conservation 166
stimulated Raman effect 164ff, 297
stimulated Raman gain spectroscopy (SRGS) 167, 171, 182f, 511f
Stokes
– and anti-Stokes Raman lines, ratio 25, 150, 162, 671, 679
– hyper Raman scattering 163
– parameters 591f
– vector 79f
– wings 672f
Stokes-Mueller formalism 79f, 84
strained ring systems 195
s-trans diene 197
stratified medium 343
stretched polymers 595
stretching force constants 34, 242, 244
stretching vibration 12, 33, 192, 227
– of CO₂ 227
– of groups with triple bonds 190
– of inorganic compounds 225
– number 33
– in OCN⁻ ion 229
– of rings 31
– of zig-zag chains 31, 194
stroboscope method 624ff, 631, 634, 640
strong coupling 229
strong oscillator 579
strongest hydrogen bond 304
structural examination in inorganic chemistry 223
structure
– and bonding and vibrational spectroscopy 234
– determination 223, 249, 463
– of fluid electrolyte solutions 650
strychnine, IR and Raman spectrum 219
styrene homopolymerization, NIR spectra 541
S-tyrosine-methylester, reflection Cotton effect 341
substances of biological interest, Raman spectrum 220
subtractive double monochromator 137
sulfur, cyclic molecules 251
sulfur fluorides 308
sum-over-states picture 468, 557
sun as an IR source 225
superacids 689
supercomputer 624
superconductors 256, 372ff, 403, 405f
supercritical temperature 650
superpolarizability 159
surface electromagnetic wave (SEW) 602
surface-enhanced hyper Raman scattering (SEHRS) 172, 361, 497
surface-enhanced infrared spectroscopy 602
surface-enhanced Raman spectroscopy (SERS) 135, 361f, 465ff, 489, 493f
– theories 490
surface-enhanced resonance Raman spectroscopy (SERRS) 135, 361
SVFF (simple valence force field) 243
symmetric top 258, 262, 267, 290f
symmetry
– axes 258, 695f
– coordinates 13, 450
– elements 40, 45
– of the vibrations 26, 38f, 44, 695f
– operators 39, 45, 48
– plane 40
symmetry-adapted coordinate 238, 695f
symmetry-allowed higher order combinations 519
syn and anti conformations, of sugar molecules 346
TCNQ 394f
T.D.S. data bank 294
TEA (TCNQ)₂, infrared conductivity 398
techniques in nonlinear coherent Raman spectroscopy 168
TeF₆, Raman scattering cross section 296
Teller-Redlich product rule 241
temperature determination
– by IR spectroscopy 664ff
– by linear Raman spectroscopy 18, 671ff
temperature of a gas, P- and R-branch intensity maxima 265
temperatures in flames 680
terminal and bridging bonds, force constants 231f
tert-butylperoxide, IR and Raman spectrum 216
tetragonal crystals 317
tetraphenylmethane, point group 706
tetrathiofulvalene-tetracyanoquinodimethane 396
theoretical resolving power 68f, 73
thermal

- conductivity, of a solid noble gas 301
- detector 617
- expansion 643
- radiator 98, 156f
- thermocouple 126
- thermodynamic
 - functions 695f
 - temperature 663
- thermoelectric coolers 126, 660
- thermogravimetric analysis with IR spectroscopy 693
- thermopile, detector 1, 617
- thiamine, IR and Raman spectrum 219
- thickness of an IR cell (interference fringes) 431
- thin-layer chromatography detection by SERS 495
- thiocyanate ligands 234
- thiourea
 - single crystal, IR and Raman spectra 59f
 - vibrational spectra 54
- third-order nonlinear susceptibility 164
- three-dimensional lattice 316
- three-wave process 166
- TiCl₄, Raman scattering cross section 296
- time constant of the extraction process 609, 611f
- time resolution 618ff, 634
- time-dependent
 - formulation of Raman scattering 473, 478
 - phenomena 640
 - picture of resonance Raman scattering 475
- time-resolved CARS 176f
- time-resolved IR spectroscopy 250, 621f, 679
- TO mode 580
- Tomsk-Dijon spectroscopy project 294
- torsion coordinate 448
- total angular momentum 259, 262
- total degrees of freedom, number of 52
- total differential Raman scattering cross section 295
- total molecular eigenfunction 265
- total reflection 575
- toxins, effects on lipid layers 371
- trace analysis 117, 130, 225, 432, 495, 603
 - of enantiomers 342f
- trans to cis isomerization 626ff
- trans/gauche ratio, of lipid chains 364
- transferable force fields 452
- transformation matrix 45f
- transient species, resonance Raman spectroscopy 488
- transition
 - element chemistry 226, 251, 311
- point, of phospholipid bilayers 369
- translational vibration 12, 38, 57, 61, 190, 319
- number of 52
- transmission
 - factor 17, 65
 - range, of optical materials 127
- trans-PA (trans-polyacetylene) 382, 386
- transversal optical mode 316, 580
- trapped molecule, shift for high- and low-frequency vibrations 298
- triatomic molecules, stretching vibrations 27
- triatomic and tetraatomic species in solid noble gases 233
- trichlorooctadecylsilane 608
- trigonal crystals 317
- triple helices 354
- triple monochromator 76, 137
- true integrated intensity 423
- tryptophan 358
- TTF-TCNQ 396f
- tunable radiation sources 136, 256
- Tunnel cell 605
- turkey breast, Raman spectrum 220
- β -turns 356
- twisted ethane and ethene, point group 698
- twisted nematic 334
- twisting vibration 33, 192
- two-beam interferometer 1, 74, 619
- two-dimensional NIR FT Raman spectra 361
- Tyndall scattering 75
- tyrosine 358
- UF₆, Raman scattering cross sections 297
- Ultricht Kugel 600
- ultra-high pressure investigations 640
- uniaxial crystals 317f
- universal potential of Kitaigorodsky 34
- α,β -unsaturated aldehydes and ketones 197
- URAS (Ultrarot-Analysator) 3, 126
- Urey-Bradley force field 452
- vacuum
 - instrument 625
 - phototubes 106
- valence angle bending coordinate 448
- valinomycin 368f
- van der Waals forces 456
- variable temperature Raman cell 661
- varnishes on historical violins 589
- VCD (vibrational circular dichroism) 343, 543f, 551

- *ab initio*-calculations 544
- spectrometer 547f
- vertical axis 40
- vertical plane 41
- vibrational
 - cooling 276
 - coupling 226f
 - frequencies, influence of bonding 229
 - frequencies of crystals 456
 - fundamental of pure hydrogen chloride at various densities 649
 - modes of the phosphate groups 346
 - optical activity 543f
 - selection rules 254
 - temperature 25, 150, 162, 663f, 669ff
- vibrational intensity 459
- NIR 519
- vibrational spectra
 - of matrix-isolated molecules 298
 - prediction 246, 445
- vibrational spectroscopy
 - as an analytical method 108
 - of different states of compounds 189ff
 - early history 1ff
 - of fluids 642
 - general survey 7ff
 - at high pressures and temperatures 642
 - in inorganic chemistry, application of 224f
- vibrational states belonging to different symmetry species 50f
- vibrational states of molecules and unit cells, number of 52
- vibrational-rotational band gas/liquid/solid 119
- vibration-rotation interaction constants 259, 279
- vibrations
 - of groups with cumulated double bonds 190
 - of molecules in different states 35f
 - of the unit cell 247
- vibronic part of the polarizability 473
- vinyl chloride 669f
- viruses 363
- VOA *see* vibrational optical activity
- VORD (vibrational optical rotatory dispersion) 343
- wagging vibration 33, 192
- water
 - near infrared absorption spectrum 141
 - normal modes 12
 - at supercritical temperature 650
- wave vector 248, 315
- wavenumber units 9, 63
- weak oscillator 579
- wedged sample layers 339
- Weierstrass lens 131, 146f
- White cells 131
- Wigner-Seitz cell 53
- workstation 624
- XCl₄ molecule splitting of stretching vibration 240
- XeF₂ 235
- XeF₆, fascinating vibrational spectrum 235
- XeOF₄, point group 700
- X-H stretching vibrations (*X* = halogen) 190
- X-ray diffraction analysis 223, 234
- xylene, absorption bands 2
- X=Y=Z systems 199
- yttrium-aluminum garnet laser 136
- Z form helices, Raman lines 351
- Zeeman spectroscopy 264
- zeolithe, Raman spectrum 159
- zero filling 620
- zero point
 - amplitude 24
 - energy 11
- zig-zag chains 31, 192f
- zinc selenide 605f
- zinc sulphide 606
- zinc sulphide retarders 95
- zirconium fluoride, transmission of IR-fibers 614
- ZnSe 605f